

Jong-Hwan Kim
Eric T. Matson
Hyun Myung
Peter Xu (Eds.)

Robot Intelligence Technology and Applications 2012

An Edition of the Presented Papers from the
1st International Conference on Robot Intelligence
Technology and Applications



Springer

Editor-in-Chief

Prof. Janusz Kacprzyk
Systems Research Institute
Polish Academy of Sciences
ul. Newelska 6
01-447 Warsaw
Poland
E-mail: kacprzyk@ibspan.waw.pl

Jong-Hwan Kim, Eric T. Matson, Hyun Myung,
and Peter Xu (Eds.)

Robot Intelligence Technology and Applications 2012

An Edition of the Presented Papers from the
1st International Conference on Robot
Intelligence Technology and Applications



Springer

Editors

Prof. Jong-Hwan Kim
Dept. of Electrical Engineering
KAIST
Korea

Prof. Eric T. Matson
Dept. of Computer and Information
Technology
Purdue University
United States

Prof. Hyun Myung
Dept. of Civil and Environmental Engineering
KAIST
Korea

Prof. Peter Xu
Dept. of Mechanical Engineering
The University of Auckland
New Zealand

ISSN 2194-5357
ISBN 978-3-642-37373-2
DOI 10.1007/978-3-642-37374-9
Springer Heidelberg New York Dordrecht London

ISSN 2194-5365 (electronic)
ISBN 978-3-642-37374-9 (eBook)

Library of Congress Control Number: 2013934352

© Springer-Verlag Berlin Heidelberg 2013

This work is subject to copyright. All rights are reserved by the Publisher, whether the whole or part of the material is concerned, specifically the rights of translation, reprinting, reuse of illustrations, recitation, broadcasting, reproduction on microfilms or in any other physical way, and transmission or information storage and retrieval, electronic adaptation, computer software, or by similar or dissimilar methodology now known or hereafter developed. Exempted from this legal reservation are brief excerpts in connection with reviews or scholarly analysis or material supplied specifically for the purpose of being entered and executed on a computer system, for exclusive use by the purchaser of the work. Duplication of this publication or parts thereof is permitted only under the provisions of the Copyright Law of the Publisher's location, in its current version, and permission for use must always be obtained from Springer. Permissions for use may be obtained through RightsLink at the Copyright Clearance Center. Violations are liable to prosecution under the respective Copyright Law.

The use of general descriptive names, registered names, trademarks, service marks, etc. in this publication does not imply, even in the absence of a specific statement, that such names are exempt from the relevant protective laws and regulations and therefore free for general use.

While the advice and information in this book are believed to be true and accurate at the date of publication, neither the authors nor the editors nor the publisher can accept any legal responsibility for any errors or omissions that may be made. The publisher makes no warranty, express or implied, with respect to the material contained herein.

Printed on acid-free paper

Springer is part of Springer Science+Business Media (www.springer.com)

Preface

Humans attempt to solve a problem by using intelligence and accumulated knowledge based on the given data and information which are available from information technology. However, robots require intelligence technology to solve the problem because they do not possess such intelligence and knowledge to use the data and information properly. One of the major objectives of robotics is to build thinking robots to solve such a problem using the intelligence technology.

In recent years, robots have been built based on cognitive architecture which has been developed to model human cognitive ability. The cognitive architecture can be a basis for intelligence technology to generate robot intelligence. In this edition, the robot intelligence is classified into six categories: cognitive intelligence, social intelligence, behavioral intelligence, ambient intelligence, collective intelligence and genetic intelligence. This classification categorizes the intelligence of robots based on the different aspects of awareness and the ability to act deliberately as a result of such awareness.

The cognitive intelligence is associated with an inference process of robots to generate a complex or unknown context from other contexts. This is strongly related to behavior selection in the task of deciding what to do in a given situation. The related research areas of cognitive intelligence are decision making, memory management, task scheduling, etc. The social intelligence has a concern with the sociability of robots, which is mainly focused on the human-robot interaction. It was not considered as an important issue in the traditional robots such as industrial robots. However, interactive skills are demanded by many application areas, where the robot needs to interact and collaborate with humans. In this aspect, the social intelligence is an essential intelligence for most service robots, which increases the value of the robot itself. Robotic pet, robotic doll and robotic head are well known types of robots, which are specially designed for the researches on social intelligence. The behavioral intelligence is related to the implementation of selected behaviors, which primarily depends on the hardware system of the robot and its driving algorithm. The behavioral intelligence is highly connected to the social intelligence because it has a high correlation with hardware specifications. The ambient intelligence is the ability to gather data and information from the surroundings of the robot. It is mainly made as a sub-system and vision-based object recognition system is one example. The collective intelligence has concerns with

the collaboration of multiple robots, which is realized through cooperative behaviors and/or schooling behaviors in multi-robot systems. The genetic intelligence is related to genetic code, which contains the personality of the robot and the knowledge inherited from its parents. This genetic code can be optimized for a specific desired personality through an evolutionary generative process.

This edition aims at serving the researchers and practitioners in related fields with a timely dissemination of the recent progress on robot intelligence technology and its applications, based on a collection of papers presented at the 1st International Conference on Robot Intelligence Technology and Applications (RiTA), held in Gwangju, Korea, December 16-18, 2012. For better readability, this edition has the total 101 papers grouped into 3 chapters: Chapter I: Cognitive Intelligence, Social Intelligence and Behavioral Intelligence, Chapter II: Ambient Intelligence, Collective Intelligence and Genetic Intelligence, Chapter III: Intelligent Robot Technologies and Applications, where individual chapters, edited respectively by Eric T. Matson, Hyun Myung, Peter Xu along with Jong-Hwan Kim, begin with a brief introduction written by the respective chapter editors.

A century ago, humans had no idea about computers; now, humans cannot even imagine living without computers. Likewise, in the near future, robots will become an essential part of human life. To lead the future of robots, i.e. the symbiosis between humans and robots, this edition introduces the various intelligence technologies and applications. I do hope that readers find the first edition of Robot Intelligence Technology and Applications, RiTA 2012, stimulating, enjoyable and helpful for their further research.

Jong-Hwan Kim
General Chair, RiTA 2012

Contents

Chapter I: Cognitive Intelligence, Social Intelligence and Behavioral Intelligence

Eric T. Matson

Slip Compensation of Mobile Robots Using SVM and IMM	5
<i>Jongdae Jung, Hyoung-Ki Lee, Hyun Myung</i>	
Emergence of Discrete and Abstract State Representation through Reinforcement Learning in a Continuous Input Task	13
<i>Yoshito Sawatsubashi, Mohamad Faizal bin Samusudin, Katsunari Shibata</i>	
Obstacle Detection Using Fuzzy Integral-Based Gaze Control for Mobile Robot	23
<i>Seung-Beom Han, Jeong-Ki Yoo, Jong-Hwan Kim</i>	
Ensembles of Gradient Based Descriptors with Derivative Filters for Visual Object Categorization	33
<i>Enas A.A. Eqlouss, Azizi Abdullah, Siti Norul Huda Sheikh Abdullah</i>	
Transdisciplinary Way of Knowledge Representation in Intelligent Autonomous Systems with Neural Networks	45
<i>B.A. Kalashankar, N.N.S.S.R.K. Prasad</i>	
Differential Trace in Learning of Value Function with a Neural Network ...	55
<i>Katsunari Shibata, Shuji Enoki</i>	
Episodic Memory Design for Predicting the User's Intention	65
<i>Seung-Hwan Choi, Woo-Ri Ko, Jong-Hwan Kim</i>	
Behavior Selection Method for Entertainment Robots Using Intelligence Operating Architecture	75
<i>Woo-Ri Ko, Jong-Hwan Kim</i>	

A Quality Control Model for Trustworthy Crowdsourcing in Collaborative Learning.....	85
<i>Jun Jo, Ann Stevens, Clarence Tan</i>	
Multimodal Human-Robot Interface with Gesture-Based Virtual Collaboration.....	91
<i>Young Eun Song, Mihoko Niitsuma, Takashi Kubota, Hideki Hashimoto, Hyoung Il Son</i>	
Three-Layered Architecture for Tele-operator and Its System Test	105
<i>Koshi Hoshino, Yasuharu Kunii</i>	
Analysis of Physiological Signals for Emotion Recognition Based on Support Vector Machine	115
<i>Makara Vanny, Seung-Min Park, Kwang-Eun Ko, Kwee-Bo Sim</i>	
Human Intention Reading by Fuzzy Cognitive Map: A Human-Robot Cooperative Object Carrying Task	127
<i>Ji-Hyeong Han, Jong-Hwan Kim</i>	
A Simultaneous Generation Method for Gaze Behaviors and Facial Expressions of a Robotic Head	137
<i>Bum-Soo Yoo, Jong-Hwan Kim</i>	
Curvature Path Planning with High Resolution Graph for Unmanned Surface Vehicle	147
<i>Hanguen Kim, Byeolteo Park, Hyun Myung</i>	
Automatic Take-off and Landing Control for Small Unmanned Helicopter.....	155
<i>Satoshi Suzuki</i>	
Development of Crawler Robot with Pile Units to Traverse Loose Soil with Steep Slope	169
<i>Kojiro Iizuka, Hirofumi Komatsu, Takashi Kubota</i>	
Robo-Teacher: A Computational Simulation Based Educational System to Improve Cyber Security	179
<i>Bin Zhang, Kamran Shafi, Hussein A. Abbass</i>	
Comparative Analysis of Arm Control Performance Using Computational Intelligence.....	187
<i>Cesar H. Valencia, Marley M.B.R. Vellasco, Karla T. Figueiredo</i>	
Advanced Sampling Scheme Based on Environmental Stiffness for a Smart Manipulator.....	199
<i>Taku Shimizu, Takashi Kubota</i>	

Walking Pattern Generation on Inclined and Uneven Terrains for Humanoid Robots	209
<i>Young-Dae Hong, Jong-Hwan Kim</i>	
Stable Modifiable Walking Pattern Algorithm with Constrained Optimized Central Pattern Generator	223
<i>Chang-Soo Park, Jong-Hwan Kim</i>	
Optimal EEG Channel Selection for Motor Imagery BCI System Using BPSO and GA	231
<i>Jun-Yeup Kim, Seung-Min Park, Kwang-Eun Ko, Kwee-Bo Sim</i>	
3D Human-Pose Tracking through a Monocular Vision	241
<i>Minho Kim, Sihyun Joo, Sungho Jo</i>	
Operator Standpoint-Based Remote Operation System Considering the Operational Convenience for a Mobile Robot	255
<i>Chang-Seop Shin, Gon-Woo Kim</i>	
Sway Motion Cancellation Scheme Using a RGB-D Camera-Based Vision System for Humanoid Robots	263
<i>Jeong-Ki Yoo, Seung-Beom Han, Jong-Hwan Kim</i>	
Locomotion of Robotic Fish Using the Univector Field Method in a 3-D space	273
<i>In-Bae Jeong, Jong-Hwan Kim</i>	
Humanoid Interface for Artificially Intelligent Role-Based Game Playing	283
<i>Lisa J. Golden, Zachary T. Golden, James Michael McAtee, Eric T. Matson</i>	
Task Planning for Service Robots with Supervisory Control	293
<i>Chung-Woon Park, Jung-Woo Lee, Jong-Tae Lim</i>	
Cognitive Architecture to Composite Emotions from Autonomic Nervous System for Robotic Head	301
<i>Charmasson Amandine, Kim Jong-Hwan, Kambiz Arab Tehrani</i>	
Development and Implementation of Break Falling System for a Biped Robot	315
<i>Seung Je Woo, Sung G. Lee, Jung Seul Ok, Jong Hwan Kim</i>	
Application of Fuzzy Logic in Learning Autonomous Robots Systems	327
<i>Maria Laura Gonzalez, Jorge Salvador Ierache</i>	
Robot Control on the Basis of Bio-electrical Signals	337
<i>Jorge Salvador Ierache, Gustavo Pereira, Iris Sattolo, Juan Irribarren, Nicolás Suiffet</i>	

Experience with the Children-Humanoid Interaction in Rehabilitation Therapy for Spinal Disorders	347
<i>Maria Vircikova, Peter Sincak</i>	
Differential Kinematics of Flexible Manipulator for Calibration of Model Parameters	359
<i>Bum-Joo Lee</i>	
EtherCAT Based Parallel Robot Control System	375
<i>Jung-Hoon Kim, Sun Lim, Il-Kyun Jung</i>	
Real-Time Trajectory Generation for Both Arms of a Humanoid Robot	383
<i>Chang-Young Jung, Jong-Hwan Kim</i>	
Chapter II: Ambient Intelligence, Collective Intelligence and Genetic Intelligence	
<i>Hyun Myung</i>	
Experimental Tests of Autonomous Jellyfish Removal Robot System JEROS	395
<i>Donghoon Kim, Jae-uk Shin, Hyongjin Kim, Donghwa Lee, Seung-Mok Lee, Hyun Myung</i>	
An Examination of Feature Detection for Real-Time Visual Odometry in Untextured Natural Terrain	405
<i>Kyohei Otsu, Masatsugu Otsuki, Genya Ishigami, Takashi Kubota</i>	
Cost Based Navigation for Autonomous Vacuum Cleaners	415
<i>Khaled Al-Wahedi, Aya Darwish, Basma Kodiah</i>	
Image-Based ICP Algorithm for Visual Odometry Using a RGB-D Sensor in a Dynamic Environment	423
<i>Deok-Hwa Kim, Jong-Hwan Kim</i>	
Hybrid Indoor Location Tracking for Pedestrian Using a Smartphone	431
<i>Seon-Woo Lee, Philhwon Jung, Seong-Ho Song</i>	
Overlapped Object Recognition Using Range and Image Data for a Service Robot	441
<i>Honggu Lee, Keonhong Lee, Sungjo Jo</i>	
Novel Scheme of Real-Time Direction Finding and Tracking of Multiple Speakers by Robot-Embedded Microphone Array	453
<i>Daobilige Su, Masashi Sekikawa, Kazuo Nakazawa, Nozomu Hamada</i>	
Development of Software and Hardware of Entry-Level Vision Systems for Navigation Tasks and Measuring	463
<i>S.M. Sokolov, A.A. Boguslavsky, A.I. Vasilyev, O.V. Trifonov</i>	

Development of a Quadrocopter Robot with Vision and Ultrasonic Sensors for Distance Sensing and Mapping	477
<i>Seung-Jae Lee, Jong-Hwan Kim</i>	
2D Image Feature-Based Real-Time RGB-D 3D SLAM	485
<i>Donghwa Lee, Hyongjin Kim, Hyun Myung</i>	
Simultaneous Localization Assistance for Mobile Robot Navigation in Real, Populated Environments	493
<i>Peshala G. Jayasekara, Hideki Hashimoto, Takashi Kubota</i>	
Towards an Ami-Robot Applied to Greenhouses	505
<i>Antonio Bautista-Hernández, Fernando Ramos-Quintana</i>	
Particle Swarm Optimization-Based Distributed Control Scheme for Flocking Robots	517
<i>Seung-Mok Lee, Hyun Myung</i>	
Control Strategies for Heterogeneous, Autonomous Robot Swarms	525
<i>Stefan Thamke, Markus Ax, Lars Kuhnert, Klaus-Dieter Kuhnert, Marco Langerwisch, Thomas Remmersmann</i>	
A Full-functional Simulation and Test Platform for Rotorcraft Unmanned Aerial Vehicle Autonomous Control	537
<i>Ziming Wang, Dalei Song, Juntong Qi, Jianda Han, Yu Miao, Lijun Meng, Shuaike Zhao, Ming Li</i>	
Market-Based Multiagent Framework for Balanced Task Allocation	549
<i>Dong-Hyun Lee, Ji-Hyeong Han, Jong-Hwan Kim, Fellow, IEEE</i>	
Autonomy Balancing in a Manned-Unmanned Teaming (MUT) Swarm Attack	561
<i>Ji Hyun Yang, Marek Kapolka, Timothy H. Chung</i>	
Semi-autonomous Control of Robotic Multi-agents	571
<i>Jae H. Chung, Christopher Kim</i>	
Context-Aware Decision Making for Maze Solving	589
<i>Sheir Afgen Zaheer, Jong-Hwan Kim</i>	
Decentralized Task Re-planning Approaches with <i>en Route</i> Information Rewards	599
<i>Sung-Hoon Kim, Sung-Tae An, Han-Lim Choi</i>	
Improved CAMshift Based on Supervised Learning	611
<i>Nur Ariffin Mohd Zin, Siti Norul Huda Sheikh Abdullah, Azizi Abdullah</i>	
Development of a Fall Detection System with Microsoft Kinect	623
<i>Christopher Kawatsu, Jiaxing Li, C.J. Chung</i>	

Strategic Decision-Making of MASTER Software Agent in Terms of the Behavior of Mobile Robot Agents	631
<i>Mikulas Hajduk, Marek Sukop</i>	
Experimental Study of Grouser's Effect for Planetary Rovers Based on Terramechanics	641
<i>Yuto Nakane, Kojiro Iizuka, Takashi Kubota</i>	
Evolving Story Narrative Using Surrogate Models of Human Judgement ..	653
<i>Kun Wang, Vinh Bui, Eleni Petraki, Hussein A. Abbass</i>	
Distributed Multiobjective Quantum-Inspired Evolutionary Algorithm (DMQEA)	663
<i>Si-Jung Ryu, Jong-Hwan Kim</i>	
Neuro-Evolution of Escape Behaviour under High Level of Deception and Noise	671
<i>Shir Li Wang, Kamran Shafi, Chris Lokan, Hussein A. Abbass</i>	
A Homogeneous Distributed Computing Framework for Multi-objective Evolutionary Algorithm	683
<i>Ki-Baek Lee, Jong-Hwan Kim, Fellow, IEEE</i>	
Personalized Emotional Expressions to Improve Natural Human-Humanoid Interaction	691
<i>Maria Vircikova, Peter Sincak, Dong Hwa Kim</i>	
Adaptive Fuzzy Cognitive Maps Using Interactive Evolution: A Robust Solution for Navigation of Robots	703
<i>Daniel Lorencik, Jan Vascak, Maria Vircikova</i>	
Tuning Fuzzy-Based Hybrid Navigation Systems Using Calibration Maps	713
<i>Napoleon H. Reyes, A.L.C. Barczak, T. Susnjak</i>	
Distributed and Incremental Visual Object Categorization for Humanoid Platform NAO	723
<i>Peter Sincak, P. Smolar, M. Vircik, M. Pala</i>	
Computational Intelligence for Creating Autonomous Robots	733
<i>Pitoyo Hartono</i>	
Chapter III: Intelligent Robot Technologies and Applications	
<i>Peter Xu</i>	
Fostering Students' Spatial Skills through Practice in Operating and Programming Robotic Cells	745
<i>Igor M. Verner, Sergei Gamer, Avraham Shtub</i>	

Innovative Experimental System Supporting Mechatronics Education	753
<i>Fusaomi Nagata, Akimasa Otsuka, Sakakibara Kaoru, Keigo Watanabe, Maki K. Habib</i>	
Humanoids at the Assistive Robot Competition RoboWaiter 2012	763
<i>Igor M. Verner, Dan Cuperman, Amit Cuperman, David Ahlgren, Steve Petkovsek, Vlad Burca, Binay Poudel, Junius Santoso</i>	
Human-Like Robot as Teacher's Representative in a Science Lesson: An Elementary School Experiment	775
<i>Takuya Hashimoto, Igor M. Verner, Hiroshi Kobayashi</i>	
Measuring the Information Quality of e-Learning Systems in KSA: Attitudes and Perceptions of Learners	787
<i>Salem Alkhafaf, Anne T.A. Nguyen, Steve Drew, Vicki Jones</i>	
Research on Distance-First Based Role Assignment Strategy of Soccer Robot	793
<i>Da-Lei Song, Bing-Wei Wu, Xiu-Fang Li, Li-Ping Chen, Chuan-Jun Liu</i>	
An Approach to the Specification of Security Concerns in UML	801
<i>Vinh Xuan Tran, Ninh-Thuan Truong, Anne T.A. Nguyen</i>	
Intelligent Blowing Controller for Autonomous Underwater Flight Vehicle	809
<i>Hyun-Sik Kim</i>	
Fuzzy Visual Navigation Using Behavior Primitives for Small Humanoid Robot	823
<i>Yong-Tae Kim, Su-Hee Noh</i>	
Development of Steer-by-Wire for Manned and Unmanned Electric Vehicle	835
<i>Yong-Jun Lee, Young-Jae Ryoo</i>	
Passive RFID Positioning System Using RF Power Control	845
<i>Sang Yup Lee, Byung-Cheol Min, Dong Hoe Kim, Jae Seok Yoon, Dong Han Kim</i>	
An Islands-of-Fitness Compact Genetic Algorithm Approach to Improving Learning Time in Swarms of Flapping-Wing Micro Air Vehicles	855
<i>John C. Gallagher</i>	
A Collision Control Strategy for Multiple Moving Robots	863
<i>Pejman Kamkarian, Henry Hexmoor</i>	
Communication for Task Completion with Heterogeneous Robots	873
<i>Danielle Erickson, Max DeWees, John Lewis, Eric T. Matson</i>	

Robotic Reasoning with Ontological Semantic Technology	883
<i>Max Petrenko, Christian F. Hempelmann</i>	
The Not So Simple Ontology of a “Primitive” Robot	893
<i>Victor Raskin</i>	
Understanding and Processing Information of Various Grain Sizes	901
<i>Julia M. Taylor</i>	
Software Platform for the Industrial Dual-Arm Robot	911
<i>Taeyong Choi, Hyunmin Do, Chanhung Park, Dongil Park, Seunghwi Lee, Jin Ho Kyung</i>	
Design of Dual-Arm Robot for Cell Production	921
<i>Hyunmin Do, Chanhung Park, Kyoungtaik Park, Jin Ho Kyung</i>	
Dynamic Control of Parallel Manipulator	931
<i>Kap-Ho Seo, Yongsik Park, Sungjo Yun, Sungho Park, Jungsoo Jun, Jeongtack Min</i>	
Design of Rotor and Magnetic Bearings for 200RT Class Turbo Refrigerant Compressor	941
<i>Cheol Hoon Park, Sang Kyu Choi</i>	
Forming Complicated Surface in Shipyard Using Neural Network System	951
<i>Nguyen Truong-Thinh, Tuong Phuoc Tho, Trinh Duc Cuong</i>	
A Method for Controlling Wheelchair Using Hand Gesture Recognition	961
<i>Nguyen Kim-Tien, Nguyen Truong-Thinh, Trinh Duc Cuong</i>	
Position Control of a Quad-Rotor System	971
<i>Seungho Jeong, Seul Jung</i>	
Mathematical Formula Recognition Based on Modified Recursive Projection Profile Cutting and Labeling with Double Linked List	983
<i>Yong-Ho Yoo, Jong-Hwan Kim</i>	
Control for Smart Transportation Vehicle Based on Dynamic model	993
<i>Phan Le Hung, Trinh Duc Cuong, Nguyen Truong Thinh</i>	
Intelligent Camera for Object Identification and Tracking	1003
<i>Donald G Bailey, Gourab Sen Gupta, Miguel Contreras</i>	
Speaker Dependent Visual Speech Recognition by Symbol and Real Value Assignment	1015
<i>Jeongwoo Ju, Heechul Jung, Junmo Kim</i>	

Automatic Image Segmentation Using Saliency Detection and Superpixel Graph Cuts	1023
<i>Sandeul Kang, Hansang Lee, Jiwhan Kim, Junmo Kim</i>	
A Survey: Stereo Based Navigation for Mobile Binocular Robots	1035
<i>Da-Lei Song, Qian-li Jiang, Wei-cheng Sun, Le-le Yao</i>	
Wheel of B2C E-commerce Development in Saudi Arabia	1047
<i>Rayed AlGhamdi, Anne T.A. Nguyen, Vicki Jones</i>	
Author Index	1057

Chapter I: Cognitive Intelligence, Social Intelligence and Behavioral Intelligence

Eric T. Matson

The field of robotics has long studied topics such as manipulation of physical devices, refined embodiment, kinematics and dynamics of physical bodies. A physical body must be controlled by algorithms enabling correct function. Recent trends point toward the shift of focusing on intelligent aspects of robotics, thereby making robots more biological or human, in some cases. Adding intelligence to robots in the cognitive, social and behavioral functions, moves in the direction of drawing ever closer to the goal of creating robots that resemble biological or human-like form and function.

This chapter contains seven groups consisting of thirty seven technical papers. This collection of papers shows a diverse collection of scientific and technical research in the areas of cognitive, social and behavioral intelligence. The groups are Cognitive Intelligence I, Cognitive Intelligence II, Social Intelligence, Behavioral Intelligence I, Behavioral Intelligence II, Behavioral Intelligence III and interactive session papers.

There are three sessions of papers in the cognitive intelligence. Five papers are in the initial **Cognitive Intelligence I** group where topics considered are varied such as obstacle detection, knowledge representation, categorization of visual objects and reinforcement learning.

- 1) Slip Compensation of Mobile Robots Using SVM and IMM
- 2) Emergence of Discrete and Abstract State Representation in Continuous Input Task through Reinforcement Learning
- 3) Obstacle Detection Using Fuzzy Integral-Based Gaze Control for Mobile Robot
- 4) Ensembles of Gradient Based Descriptors with Derivative Filters for Visual Object Categorization
- 5) Transdisciplinary way of Knowledge Representation in Intelligent Autonomous Systems with Neural Networks.

There are four papers are presented in the **Cognitive Intelligence II** group. These papers range from intelligent operating system architectures, to memory design and learning with neural networks to the application of collective intelligence in the form of crowdsourcing.

- 1) Differential Trace in Learning of Value Function with a Neural Network
- 2) Episodic Memory Design for Predicting the User's Intention
- 3) Behavior Selection Method for Entertainment Robots Using Intelligence Operating Architecture
- 4) A Quality Control Model for Trustworthy Crowdsourcing in Collaborative Learning

Social intelligence describes the capability to successfully interact with other actors in a system, where five papers are in the **Social Intelligence** session. There are papers on direct interfaces such as human-robot interface using gestures and tele-operation. There are also papers in the areas of gaze control, physiological signals and reading of human intention using pre-defined cognitive maps.

- 1) Multimodal Human-Robot Interface with Gesture-based Virtual Collaboration
- 2) Three-Layered Architecture with Variable Task Flow for Teleoperator
- 3) Analysis of Physiological Signals for Emotion Recognition based on Support Vector Machine
- 4) Human Intention Reading by Fuzzy Cognitive Map: A Human-Robot Cooperative Object Carrying Task
- 5) Gaze Behavior Selection for Proper Facial Expression of Robotic Head

There are three sections of behavioral intelligence papers. In the initial section, there are five papers presented in the **Behavioral Intelligence I** session. The papers varied from control of ground and air vehicles to the control of robotic arms, to the use of a robotic teaching aide to assist in cyber security.

- 1) Curvature Path Planning with High Resolution Graph for Unmanned Surface Vehicle
- 2) Automatic Take-off and Landing Control for Small Unmanned Helicopter
- 3) Development of Crawler Robot with Pile Units to traverse Loose Soil with Steep Slope
- 4) Robo-Teacher: A Computational Simulation Based Educational System to Improve Cyber Security
- 5) Comparative Analysis of Arm Control Performance Using Computational Intelligence

The four papers presented in the **Behavioral Intelligence II** session included topics smart manipulation and channel selection. Two papers are topically oriented towards humanoid biped walking. One paper on walking on uneven or inclined terrains and the second paper on stable, modifiable walking patterns.

- 1) Advanced Sampling Scheme Based on Environmental Stiffness for a Smart Manipulator
- 2) Walking Pattern Generation on Inclined and Uneven Terrains for Humanoid Robots
- 3) Stable Modifiable Walking Pattern Algorithm with Constrained Optimized Central Pattern Generator
- 4) Optimal EEG Channel Selection for Motor Imagery BCI System using BPSO and GA

Five papers were presented in the **Behavioral Intelligence III** session. The papers represent a varied group of intelligent control. The interaction of human to robot game playing was shown in form of simple, interactive competitive play. Two papers featured vision-oriented intelligence including human pose tracking and sway motion cancellation. The behavior of fish locomotion was covered using the univector field method.

- 1) 3D Human-Pose Tracking through a Monocular Vision
- 2) Operator Standpoint-based Remote Operation System Considered the Operational Convenience for a Mobile Robot
- 3) Sway Motion Cancellation Scheme using a RGB-D Camera-based Vision System for Humanoid Robots
- 4) Locomotion of Robotic Fish Using the Univektor Field Method in a 3-D space
- 5) Humanoid Interface for Artificially Intelligent Role-Based Game Playing

The chapter concludes with nine papers presented in multiple interactive sessions. These papers show a range of topics such as control, social interaction and humanoid function.

- 1) Task Planning for Service Robots with Supervisory control
- 2) Cognitive Architecture for Composite Emotions from Autonomic Nervous System of Robotic Head
- 3) Development and Implementation of Break Falling System for a Biped Robot
- 4) Application of Fuzzy Logic in Learning Autonomous Robots Systems
- 5) Robot Control on the basis of Bio-electrical signals
- 6) Social Interactions between Humanoids & Children
- 7) Differential Kinematics of Flexible Manipulator for Calibration of Model Parameters
- 8) EtherCAT based Parallel Robot Control System
- 9) Real-time Trajectory Generation for Both Arms of a Humanoid Robot

Slip Compensation of Mobile Robots Using SVM and IMM

Jongdae Jung¹, Hyoung-Ki Lee², and Hyun Myung¹

¹ Dept. of Civil and Environ. Engg., KAIST

291 Daehak-ro, Yuseong-gu, Daejeon 305-701, Korea

² Samsung Advanced Institute of Technology, Samsung Electronics Co., Ltd.

Nongseo-dong, Giheung-gu, Yongin, Gyeonggi-do 449-712, Korea

{jdjung, hmyung}@kaist.ac.kr, twinklelee@samsung.com

Abstract. Improvement of dead reckoning accuracy is essential for robotic localization system and has been intensively studied. However, existing solutions cannot provide accurate positioning when a robot suffers from changing dynamics such as wheel slip. In this paper, we propose an interacting multiple model (IMM) framework to detect and compensate for wheel slip. Firstly, two different types of extended Kalman filter (EKF) are designed to consider both no-slip and slip dynamics of mobile robots. Then a support vector machine (SVM) for slip estimation is constructed using real world training data. The trained model is utilized along with the two EKFs in the IMM framework. The approach is evaluated with experiments and the results show that the proposed approach improves positioning and slip compensation compared to the conventional approach.

Keywords: dead reckoning, interacting multiple model, support vector machine, slip detection.

1 Introduction

Dead reckoning (DR) is the most basic approach to a mobile robot's localization problem. Much research work has been done to improve DR accuracy by calculating exact heading angles [1]–[2]. However, performance of DR-based localization is severely degraded when a slip or immobilization occurs during the robot motion. To cope with dynamic changes due to wheel slip, extended Kalman filter (EKF) based adaptation methods can be considered. There are two kinds of such methods; i) the parameter adaptation method such as covariance matrix adaptation and ii) structural adaptation method such as interacting multiple model (IMM). In this paper, we propose a SVM-based IMM framework to improve the DR performance of conventional IMM filters. In our framework, SVM runs independently from sub-filtering process and detects slip occurrence using the sensor data from both encoder and inertial measurement unit (IMU). The calculated SVM output is used in the update of IMM parameters. In this way, we can separate the slip detection from the sub-filtering process and more effectively utilize the multiple model approach.

The remainder of this paper is organized as follows. We will describe conventional IMM framework in Section 2. We then will introduce the SVM-based slip detection in Section 3. Experimental results are given in Section 4, followed by conclusion.

2 Design of IMM Framework

Since the error covariance of encoder is substantially changing depending on the wheel slip conditions, two different EKFs are employed to deal with both no-slip and slip dynamics of robots [3]. In this section, we first design two types of EKFs and then explain the detailed structure of conventional IMM.

2.1 Design of EKFs

A robot moving on an irregular floor experiences three dimensional attitude changes. The attitude of a robot can be described using type I Euler angles, i.e., roll θ , pitch ϕ , and yaw ψ . Euler angles are defined as the angular displacements along the x_b , y_b , and z_b axes where the subscript b means the body fixed frames. The body frame can be thought of as embedded in the robot body so that its x -axis points forward, the y -axis to the left, and the z -axis upward. The defined body-fixed frame is shown in figure. 1.

The state variable \mathbf{x}_k for robot motion can be represented as follows:

$$\mathbf{x}_k = \begin{bmatrix} \mathbf{p}_k^W & \mathbf{v}_k^W & \mathbf{a}_k^W & \boldsymbol{\varphi}_k^W & \boldsymbol{\omega}_k^b \end{bmatrix}^T \quad (1)$$

where \mathbf{p}_k^W , \mathbf{v}_k^W , \mathbf{a}_k^W , $\boldsymbol{\varphi}_k^W$, and $\boldsymbol{\omega}_k^b$ are vectors for the robot's position, velocity, acceleration, angular displacement, and angular velocity, respectively.

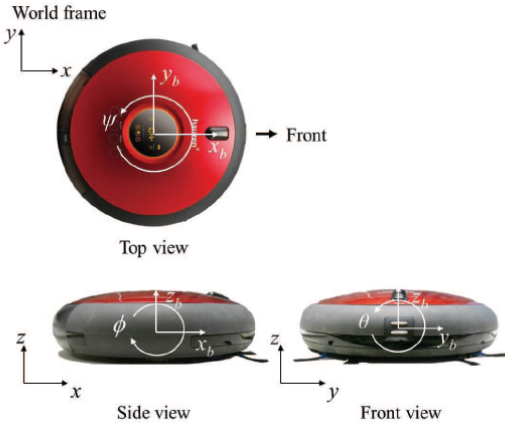


Fig. 1. Inertial and body-fixed coordinate frames

There are two main steps in EKF – prediction and update. In the prediction step, the state transition and the corresponding error covariance are estimated according to the prediction model. In the update step, measurements in current time step are

estimated by using the measurement model and innovations calculated from the difference between the estimated and actual measurements are used in the state and error covariance update. Figure 2 and 3 shows the structure of the EKF for no-slip and slip conditions, respectively. The update of state variable and covariance matrix follows basic framework of EKF and are not described here.

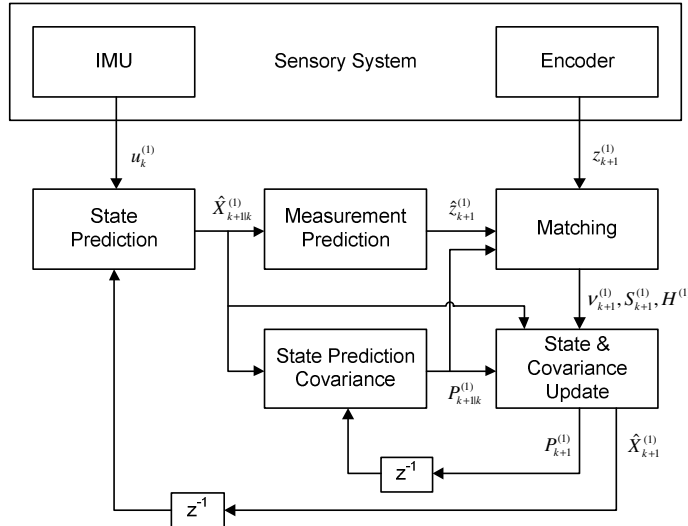


Fig. 2. Structure of EKF for no-slip condition. It uses IMU data as control inputs in state prediction and encoder data as measurements in state update.

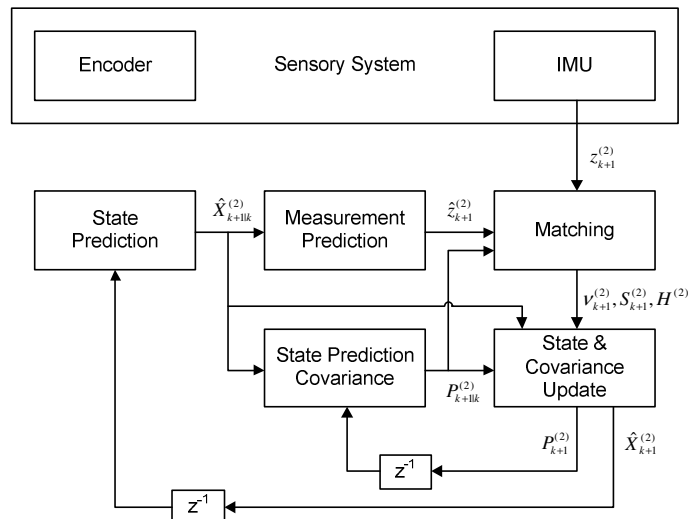


Fig. 3. Structure of EKF for slip condition. It uses robot dynamics model with no control input in state prediction and IMU data as measurements in state update.

2.2 Conventional IMM Filtering

Figure 4 shows the overall structure of the IMM algorithm used in this study. At each time k , a linear combination of the previous estimates (states and covariance) is given as an input to each of n modes. Current measurement \mathbf{z}_k is also given to each sub-filter and innovations are computed along with the corresponding likelihood $\lambda_k^{(j)}$. Mode probabilities $\mu_k^{(j)}$ are used as weights in a linear combination of current model outputs to form desired state and covariance estimates.

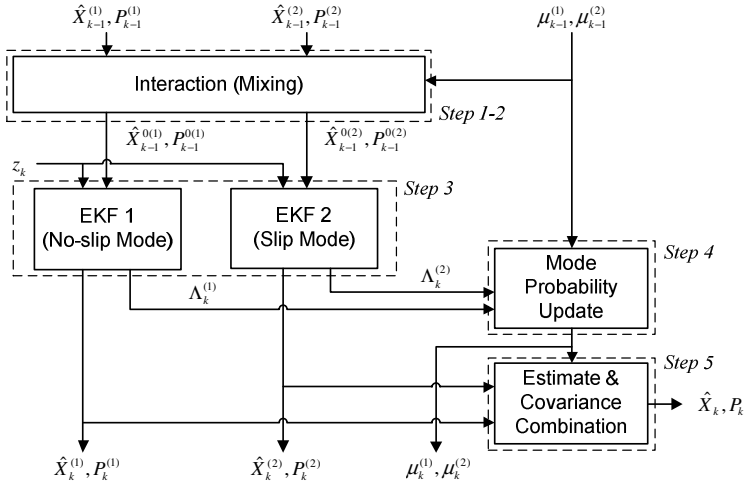


Fig. 4. Structure of the conventional IMM filtering with two modes. Each EKF outputs updated state prediction and likelihood of measurements based on the different prediction and measurement models. Mode probability update is performed based on the likelihood values.

3 SVM-Based IMM (SVMIMM)

Even if the IMM filter can handle the multiple models of the robot's driving dynamics, the update of mode probability based on the likelihood values can lead to errors in slip detection. This is the case when a sub-filter outputs very large innovations caused by the poor performance of its prediction model. Since the likelihood values are calculated based on the sensor covariance S and the innovation v , the corresponding mode probability can be decreased even if that mode is the current mode. In our case, the prediction model for slip mode is just a time update of robot dynamics based on the previous states, and this can lead to the wrong slip detections. Thus an additional slip estimator which runs in parallel with the IMM filter is required to independently track the robot's slip mode. In this study, SVM is employed as a slip estimator [5].

The SVM used in our study used three features as its inputs. The three SVM inputs are i) the difference in forward direction acceleration between encoder and accelerometer, ii) the difference in encoder velocity between the right and left wheels,

and iii) the difference in calculated yaw rate between the gyro and encoder. These SVM inputs have been selected in order to best discriminate between the no-slip and slip conditions of the robot wheels. As it can be seen from the sensor data obtained from a driving robot (see figure 5), the three differences – the difference in forward-direction acceleration between encoder and accelerometer, the difference in encoder velocity between the right and left wheels, and the difference in calculated yaw rate between the gyro and encoder – are dominant around the slip regions. The SVM output is the degree of slip occurrence ξ .

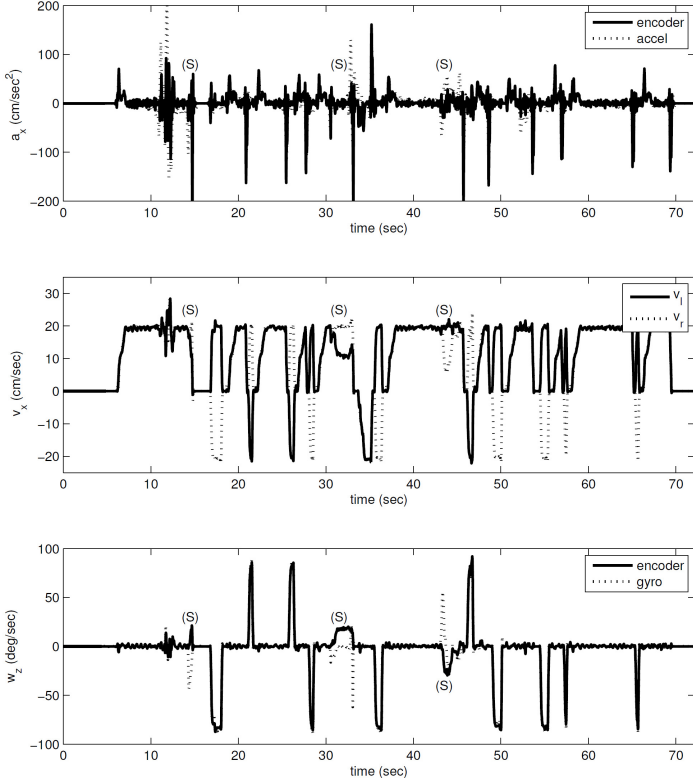


Fig. 5. IMU and encoder data obtained from a set of driving tests. v_l and v_r indicate the left and right wheel velocities. Slip regions are labeled with (S). The three differences – the difference in forward-direction acceleration between encoder and accelerometer, the difference in encoder velocity between the right and left wheels, and the difference in calculated yaw rate between the gyro and encoder – are dominant around the slip regions.

The difference between the conventional IMM and the proposed method lies in the update of mode probability – the proposed method uses SVM output whereas the conventional IMM uses likelihood values. In our method, the mode probability is calculated as:

$$\mu_k^{(1)} \equiv P\{M_k^{(1)} | Z_k\} = 1/c(1 - \xi_k)\bar{c}_1 \quad (8)$$

$$\mu_k^{(2)} \equiv P\{M_k^{(2)} | Z_k\} = 1/c\xi_k\bar{c}_2 \quad (9)$$

where $c = (1 - \xi_k) \bar{c}_1 + \xi_k \bar{c}_2$ is the normalization constant. Since the SVM model have been adapted based on both the encoder and IMU data, it can effectively detect the slip occurrence during the IMM filtering independent of the sub-filtering performances.

4 Experiment

The robot used in our experiment is depicted in figure 1. It has an onboard sensory system which includes two incremental encoders. *MTi-G* IMU with a 3-axis gyro and a 3-axis accelerometer are mounted on top of the robot body.

Figure 6 shows an experimental environment for acquiring the driving data. The environment has several slip-occurring obstacles such as doorsills, a rug, a mat, and a base of a fan. In this environment the robot is commanded to draw a square path roughly in clockwise direction. The robot goes over the doorsill A but not the doorsill B. When the robot is blocked by the doorsill, it moves back and takes a detour. The ground truth of the robot pose (position and heading angle) was measured by *Hawk Digital RealTime System*.

For comparison purposes, we used odometry, normal mode EKF, conventional IMM, and SVMIMM in our estimation.

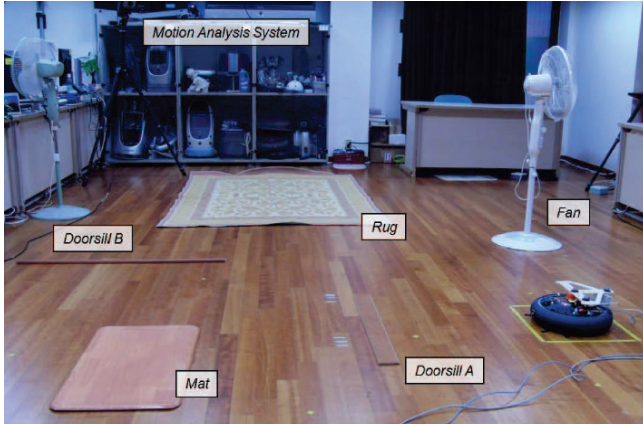


Fig. 6. Experimental setup for the driving test. The environment involves several slip-occurring obstacles such as doorsills and rugs.

Figure 7 shows the estimated trajectories using the data of the first driving test, where the SVMIMM outperforms other algorithms by closely matching the start and end points. By examining the trajectories, we can see that most of the slip regions cause longitudinal errors along the robot path. Since the single EKF cannot compensate for this kind of error, the path error accumulates whenever the slip occurs. Even if the IMM uses multiple EKFs, however, the trajectory of IMM algorithm is similar to (or sometimes worse than) the single EKF. This is because the IMM cannot guarantee the accurate slip detection. When we examine the mode 2

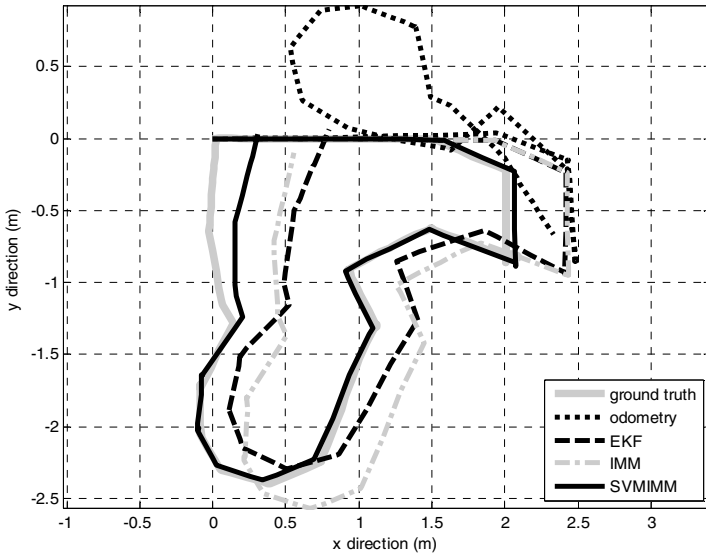


Fig. 7. Estimated trajectories using several algorithms. SVMIMM outperforms other algorithms in the compensation of longitudinal errors caused by wheel slip.

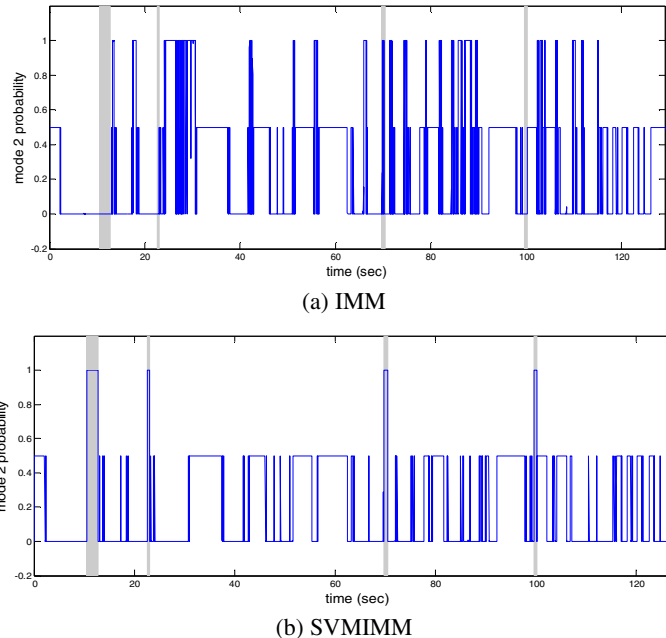


Fig. 8. Estimated mode 2 (slip mode) probabilities from two algorithms for driving data 1. Mode 2 probability should be 0 when the robot is in a normal driving mode and 1 in a slip mode. The probability is set to 0.5 when the robot is stopped. We can see that the SVMIMM algorithm accurately detects the slip regions (shaded areas) compared to the IMM algorithm.

probability results shown in figure 8, we can see that the IMM gives wrong detection results while the SVMIMM accurately detects the slip regions. The reason for this is that the mode probability updates based on the likelihood can be wrong.

5 Conclusion

In this paper, we proposed an SVM based approach to improve the dead reckoning performance of mobile robots based on a framework of IMM EKF. To consider both no-slip and slip dynamics of robots, two different types of EKF are designed according to the sensor characteristics of encoder and IMU sensor.

The SVMIMM, a framework for improving the performance of slip detection and compensation, is introduced in which the update of mode probability is done by using SVM output instead of likelihood of measurements. The proposed method has been implemented using a mobile robot and tested in a slip-occurring indoor environment. Experimental results show that our method outperforms simple EKF and conventional IMM approach in the estimation of robot positions. The calculated slip mode probabilities also indicate that the SVMIMM algorithm accurately detects the slip occurrences.

Acknowledgements. This work was supported by the Energy Efficiency & Resources of the Korean Institute of Energy Technology Evaluation and Planning (grant No. 2011201030001D-11-2-200), funded by the Korean Government Ministry of the Knowledge Economy.

References

1. Ojeda, L., Borenstein, J.: FLEXnav: Fuzzy Logic Expert Rule-based Position Estimation for Mobile Robots on Rugged Terrain. In: Proc. of ICRA, pp. 317–322 (2002)
2. Myung, H., Lee, H., Choi, K., Bang, S., Lee, Y., Kim, S.: Constrained Kalman Filter for Mobile Robot Localization with Gyroscope. In: Proc. of IROS, pp. 442–447 (2006)
3. Lee, H., Choi, K., Park, J., Kim, Y., Bang, S.: Improvement of dead reckoning accuracy of a mobile robot by slip detection and compensation using multiple model approach. In: Proc. of IROS, pp. 1140–1147 (2008)
4. Bar-Shalom, Y., Li, X., Kirubarajan, T.: Estimation with applications to tracking and navigation. John Wiley & Sons, Inc. (2001)
5. <http://www.csie.ntu.edu.tw/~cjlin/libsvm/>

Emergence of Discrete and Abstract State Representation through Reinforcement Learning in a Continuous Input Task

Yoshito Sawatsubashi¹, Mohamad Faizal bin Samusudin^{1,2},
and Katsunari Shibata¹

¹ Department of Electrical and Electronic Engineering, Oita University,
700, Dannoharu, 870-1124 Oita Japan

² Department of Mechatronic, Universiti Malaysia Perlis,
02600 Arau, Perlis Malaysia

bashis8@yahoo.co.jp, ballack83@hotmail.co.jp, shibata@oita-u.ac.jp

Abstract. “Concept” is a kind of discrete and abstract state representation, and is considered useful for efficient action planning. However, it is supposed to emerge in our brain as a parallel processing and learning system through learning based on a variety of experiences, and so it is difficult to be developed by hand-coding. In this paper, as a previous step of the “concept formation”, it is investigated whether the discrete and abstract state representation is formed or not through learning in a task with multi-step state transitions using Actor-Q learning method and a recurrent neural network. After learning, an agent repeated a sequence two times, in which it pushed a button to open a door and moved to the next room, and finally arrived at the third room to get a reward. In two hidden neurons, discrete and abstract state representation not depending on the door opening pattern was observed. The result of another learning with two recurrent neural networks that are for Q-values and for Actors suggested that the state representation emerged to generate appropriate Q-values.

1 Introduction

While we get a huge amount of sensor signals with eyes, ears and other sensors, we can evaluate a state accurately and act appropriately. However, we are not conscious of each individual sensor signal, but rather represent a state with an abstract representation such as “room” and “corridor”, and make an action plan as “open the door, go out the room, and walk along the corridor”. Such discrete and abstract state representation must make our learning efficient and can be an origin of intelligence.

First of all, why can we recognize a “room” even though there are many kinds of rooms? For example, if the wall color is different, the sensor signal will be different completely. What we usually see with our eyes is only part of a room, and the sensor signals change largely by eye, head or body movement. For these reasons, it is highly unlikely that such abstract representation is formed only

from the huge amount of time series sensor signals. We probably recognize the “room” through the accumulation of action learning in a room where we “work or rest”, “open a door to go out the room” and “open a window on a hot day”. The authors call such discrete and abstract representation “concept”. If “concept” as a high-order function is given to a robot, it is expected to behave appropriately even in the real world with various situations.

However, it is hardly possible for us to design each “concept” manually, because it is difficult to define it in words. For example, the place where there are walls, doors and windows is not always a “room”. We recognize a place as a “room” based on the parallel consideration from many aspects, and learning from experiences with our brain as a massively parallel processing and learning system seems to enable it. Therefore, the concept formation is difficult to be achieved by hand-coding.

Tani et al. have proposed a method by which abstract state representation from the time series data as inputs emerge through learning. In the method, the next sensor signals are predicted from the present sensor signals and motor commands, and modular recurrent neural networks (RNNs)[1] or one RNN consisting of neurons with different time constants[2] are introduced. However, generating appropriate actions or achieving a goal is not considered. In their paper, the input was simple sensor signals, but if a visual sensor is used in the real world that is full of trivial information, it must be difficult for the system to predict all the input at every moment. Furthermore, as mentioned above, it seems impossible to divide the time series of huge sensor data into states such as “room” and “corridor” without considering the necessity for action generation.

Therefore, a method is suggested in which a neural network (NN) and reinforcement learning (RL) are combined for the emergence of abstract representation. RL enables to learn appropriate actions for a purpose such as getting a reward and avoiding a penalty. Therefore if RL is combined with a NN with a parallel structure, the NN is optimized based on RL, and the necessary information is extracted in the NN without any explicit directions. It is expected that the discrete and abstract state representation emerges in the NN as extracted necessary information. The authors group has been aiming it already, but in the previous works, binary signals that respond at a state transition were given as inputs, and/or a task with one-step state transition was employed[5][6].

In this paper, as a previous step of the “concept formation”, it is aimed to form a discrete and abstract state representation in a task with multi-step state transition. Then, a simulation task is employed in which an agent moves in an environment with several rooms and doors, and the emergence of discrete and abstract state representation in which the state changes by the door opening is investigated in the hidden layers in a RNN after the mapping from the continuous sensor inputs to the action is learned in it by RL.

2 The Learning System

Here, as shown in Fig. 1, a 5-layer Elman-type RNN is used to learn a task with multi-step state transition. The RNN is trained with back propagation through

time (BPTT)[3] using the training signals generated by RL. As for RL, Actor-Q[4] is used in which Q-learning for discrete action selection and Actor-Critic for the continuous motion are combined. Therefore, in the RNN, there are two types of outputs: for the Q-values and for the Actors. At first, a discrete actions is selected based on the Q-values, and then if the action needs a continuous motion, the motion is generated based on the Actors. The Q-value for the previous action is updated using the Q-value for the present action and reward. The training signal for the Q-value $Q_{d,a_t,t}$ is generated as

$$Q_{d,a_t,t} = Q_{a_t}(\mathbf{s}_t) + TDerror_t = r_{t+1} + \gamma \max_a Q_a(\mathbf{s}_{t+1}) \quad (1)$$

$$TDerror_t = r_{t+1} + \gamma \max_a Q_a(\mathbf{s}_{t+1}) - Q_{a_t}(\mathbf{s}_t) \quad (2)$$

where γ indicates a discount factor, and r_t , \mathbf{s}_t , a_t indicates a reward, state vector, and action at time t respectively. The Actor output is updated using the TD-error derived from the Q-value on behalf of the critic in Actor-Critic. The training signal for the Actor $\mathbf{A}_{d,t}$ is generated as

$$\mathbf{A}_{d,t} = \mathbf{A}(\mathbf{s}_t) + TDerror_t \times \mathbf{rnd}_t \quad (3)$$

where $\mathbf{A}(\mathbf{s}_t)$, \mathbf{rnd}_t indicates the Actor output vector and a random number vector that is added to the Actor output vector for exploration to generate the actual motion commands.

3 Task

As a previous step of the “concept-formation”, a task with multi-step state transition is learned to examine the emergence of discrete and abstract representation from continuous inputs. As shown in Fig. 2, there are several rooms and doors in the task environment, and an agent is initially located at a random place in the central room. When it pushes a switch located at the center of each room, one of the surrounding doors that connects the present room with a next room is opened at random. An episode terminates when the agent passes two rooms and finally arrives at the third room. The agent gets a reward when it arrives at the third room. In the early stage of learning, the agent takes an action almost at random because all the outputs are 0.0 by setting all the initial connection weights to the output layer to 0.0. Through leaning, only with the reward at the goal, the agent is expected to generate appropriate actions and the abstract representation that is useful to achieve the goal.

As shown in Fig. 1, the agent detects the distance to the walls using 8 sensors. Each sensor signal represents the distance from the agent to the wall in one of the eight directions in the form of e^{-3d_i} where d_i indicates the distance to the wall in the i -th direction. The agent also detects the information about the closest switch. The distance from the agent to the switch is also represented as e^{-3d_s} and the angle of the switch direction was given as $\sin\theta$ and $\cos\theta$. Thus, the number of inputs in the RNN was 11 in total. This task needs memory because

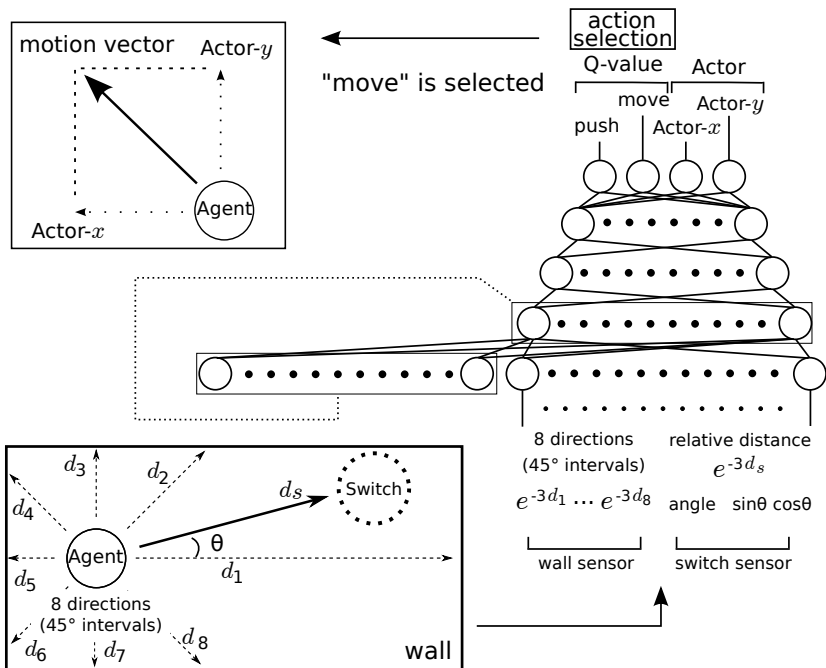


Fig. 1. Learning system consisted of a 5-layer Elman-type RNN, and its inputs and outputs

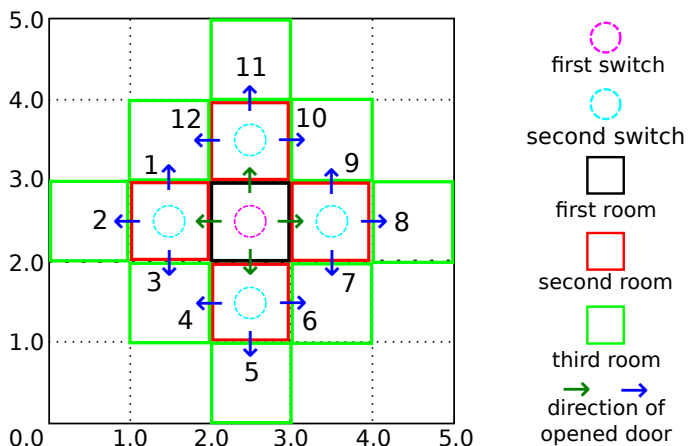


Fig. 2. Task environment with rooms and switches

after opening a door in the second room, the agent cannot discriminate the first room and the third room without referring the past wall sensor signals.

As shown in Fig. 1, the number of outputs in the RNN is 4. Two of them are used as the Q-values of “move” and “push”, and the other two are used as the Actors for the agent move in the x - and y -directions when the action “move” is selected. The size of the move vector is limited in the circle with the radius of 0.5 around the agent.

When the agent moves and arrives at the third room within 35 steps for 30,000 consecutive episodes, learning finishes. If the agent does not arrive at the third room as the goal within 200 steps, the episode is terminated. As an action selection method, “Boltzmann selection” is used, and the temperature is gradually decreased from 1.00 to 0.01 as the learning progresses. The value range of sigmoid function that is used as an output function in each hidden or output neuron is from -0.5 to 0.5. To transform between Q-value output [-0.5, 0.5] in the RNN and actual Q-value [0.0, 1.0], the value is shifted by -0.5 or 0.5. The other parameter settings are shown in Table 1.

Table 1. Parameter setting

initial position of the agent (x,y)	(2.0~3.0, 2.0~3.0)
radius of the switch	0.2
number of layers	5
number of neurons in each layer	11(input)-80-40-20-4(output)
constant input for bias	0.1
reward r at the third room	0.9
punishment for “push” at the outside of the switch	-0.1
discount factor γ	0.9
thr range of exploration vector rnd ($\text{rnd}_x, \text{rnd}_y$)	-0.5~0.5 -0.2~0.2
traced back time in BPTT	30
initial connection weight	
input - hidden1, hidden1 - hidden2	-0.1~0.1, -0.2~0.2
hidden2 - hidden3, hidden3 - output	-0.5~0.5, 0.0
self-feedback, other-feedback	4.0, 0.0
learning rate	
for feedback connections	0.0125
for other connections	0.5

4 Learning Result

The learning finished after 760,675 episodes. After learning, the agent can reach the third room from any grid point with the interval of 0.01 in the central room for any pattern of the room appearance. However, depending on the random sequence used in learning, a few failures occurred.

Fig. 3~Fig. 6 show two sample agent behaviors after learning. In (a), the initial position is (2.1, 2.9), and the direction of the opened door is left at first and then upward in order, and in (b), the initial position is (2.9, 2.1), and the direction of the opened door is downward at first and then right in order. Fig. 3~Fig. 6 show the agent trajectory, the Q-value outputs, and the Actor outputs, a part of the outputs in the top hidden layer at each step respectively.

As shown in Fig. 3, the agent moved on switches and pushed them and arrived at the third room. In both cases, when the agent pushed the second switch, the agent cannot know which door is newly opened only from the present sensor signals. However, from the fact that the agent arrived at the third room without being at a loss, it is considered that the agent could act based on memory. In Fig. 4, as the number of steps increased, the larger of the two Q-values at each step increased monotonically, and is close to the ideal curve. When the agent was located on a switch at the 2nd or 7th step, the value for the “push” action increased even though no explicit signal is given to identify that the agent is on a switch. This means that the agent could recognize it from the continuous inputs. In Fig. 5, it is known that when a new room appears, the Actor changes so as that the movement of the agent is directed to the new room.

Fig. 6 shows the output of characteristic neurons in the top hidden layer. A hidden neuron 1 changed its output only when the agent pushed the first switch. The hidden neuron 2 changed its output only when the agent pushed the second switch. The interesting point is that the output change of the hidden neuron at the door opening is very large and not depending on the direction in which the new room appears.

In a past study[6], it was reported that a discrete representation emerged through the learning in the task that an agent passed on a switch and arrived at a goal. In this case, a binary input indicating whether the agent is on the switch or not is given, so it is rather easy to form discrete state representation by holding the binary input in the RNN. However, in this task, although one of the distance inputs changes discretely when the agent opens the door, it changes only from 0.22 to 0.01 in the range from 0.0 to 1.0. Therefore, it is difficult to explain the sudden change in the hidden neuron only from the input signal, but the change should be explained from the necessity of generating Q-values or Actor outputs.

Then, to examine which output needs such discrete and abstract representation in the hidden neurons, Q-values and Actor outputs are learned separately using two RNNs in the learning of the same task. As the result, the discrete and abstract state representation was formed only in the RNN for Q-values. Fig. 7 and 8 show the Q-value outputs and a part of the output in the top hidden layer at each step respectively in the RNN for Q-values. Note that, the agent pushed the second switch at one step earlier than the previous case. The hidden neurons that change suddenly at the door opening not depending on its direction have the largest connection weight with the Q-value output for the “move” action. It was reported that if the two training signal patterns are similar, the representation in the hidden layer that is close to the output layer is likely to be closer

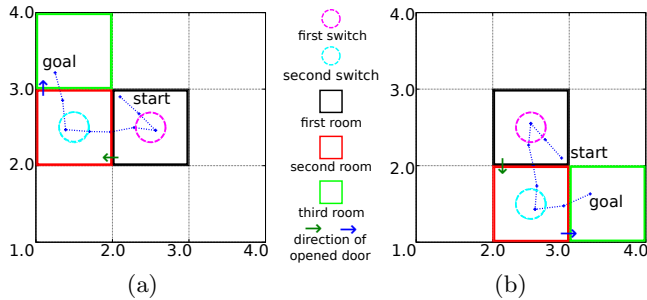


Fig. 3. Two sample trajectories of the agent after learning

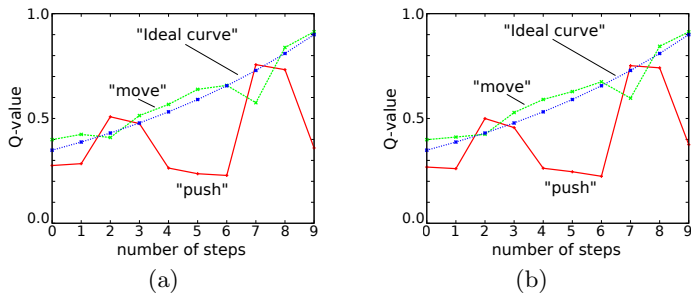


Fig. 4. Change of the Q-values in one episode

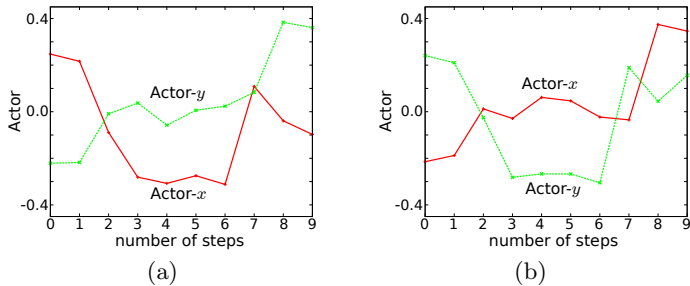


Fig. 5. Change of the Actors in one episode

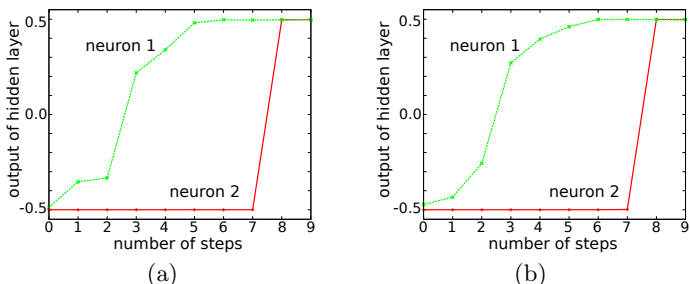


Fig. 6. Discrete change of the outputs in two neurons in the top hidden layer

to each other through learning even though the input patterns are not close[7]. As shown in Fig. 4 (a) and (b), since the Q-values always change in the same way not depending on which door is opened, it can be explained that similar representation not depending on the door opening direction emerges. The reason of emergence of sudden change in the hidden neurons is suggested as follows. In the hidden neurons, the recognition of whether the agent is on a switch or not emerged from the necessity of raising the Q-value for the “push” action and its representation should be discrete to realize the sudden change in the Q-values at the step 2 or 7. The recognition result is held in another hidden neuron to represent the difference in Q-values between before and after the door opening. However, it has not been examined yet, and that is left as a future work.

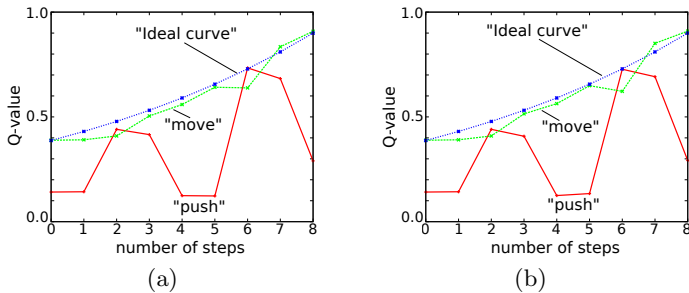


Fig. 7. Change of the Q-values in one episode

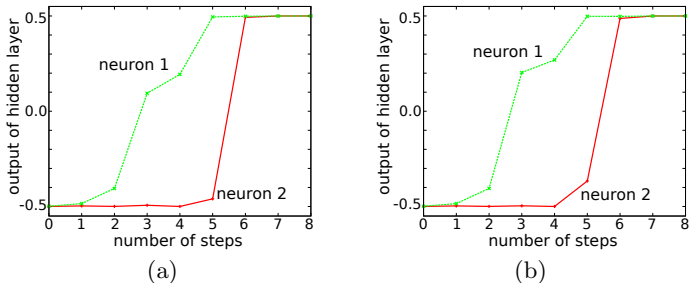


Fig. 8. Discrete change of the outputs in two neurons in the top hidden layer

5 Discussion and Conclusion

In this paper, it was shown that discrete and abstract state representation emerged through Actor-Q reinforcement learning using a recurrent neural network in doors-and-rooms environment. It is interesting that a different input signal changed depending on the opened door, but the representations in the top hidden neurons were almost the same. It is suggested from the learning using two recurrent neural networks that such representation emerge to generate Q-values that is also not depending on the door opening direction.

Although the discrete and abstract representation emerged, emergence of “concept” still seems to be out of reach. In order to form the “concept”, it is required to extract necessary information and to recognize its state flexibly from more kinds of sensor signals that includes trivial information by considering many things simultaneously taking advantage of parallel processing. The large gap between the sensor signals and the state representation requires more intelligence, and that permit us to call a “concept”, the authors hope. From this viewpoint, a visual sensor with many visual cells will be used in a future work.

Anyway, the authors hope that the work in this paper shows the usefulness of the combination of reinforcement learning and a recurrent neural network towards the emergence of “concept”, and becomes a foothold for it.

Acknowledgment. This work was supported by JSPS Grant-in-Aid for Scientific Research #23500245.

References

1. Tani, J., Nolfi, S.: Learning to Perceive the World as Articulated: An Approach for Hierarchical Learning in Sensory-Motor Systems. *Neural Networks* 12, 1131–1141 (1999)
2. Yamashita, Y., Tani, J.: Emergence of functional hierarchy in a multiple timescale neural network model: a humanoid robot experiment. *PLoS Computational Biology* 4, e100220 (2008)
3. Rumelhart, D.E., Hinton, G.E., Williams, R.J.: Learning Internal Representations by Error Propagation. In: *Parallel Distributed Processing*, pp. 318–362. The MIT Press (1986)
4. Shibata, K., Nishino, T., Okabe, Y.: Active Perception and Recognition Learning System Based on Actor-Q Architecture Systems and Computers in Japan 33(14), 12–22 (2002)
5. Samsudin, M.F., Shibata, K.: Emergence of Multi-Step Discrete State Transition through Reinforcement Learning with a Recurrent Neural Network. In: Proc. of ICONIP 2012 (2012) (to appear)
6. Utsunomiya, H., Shibata, K.: Contextual Behaviors and Internal Representations Acquired by Reinforcement Learning with a Recurrent Neural Network in a Continuous State and Action Space Task. In: Köppen, M., Kasabov, N., Coghill, G. (eds.) *ICONIP 2008, Part II. LNCS*, vol. 5507, pp. 970–978. Springer, Heidelberg (2009)
7. Shibata, K., Ito, K.: Adaptive Space Reconstruction on Hidden Layer and Knowledge Transfer based on Hidden-level Generalization in Layered Neural Networks. *Trans. SICE* 43(1), 54–63 (2007) (in Japanese)

Obstacle Detection Using Fuzzy Integral-Based Gaze Control for Mobile Robot

Seung-Beom Han, Jeong-Ki Yoo, and Jong-Hwan Kim

Department of Electrical Engineering, KAIST, 291 Daehak-ro, Yuseong-gu, Daejeon,
305-701, Republic of Korea
{fsbhan,jkyoo,johkimg}@rit.kaist.ac.kr

Abstract. Obstacle detection is one of key issues in robotics because robots should avoid obstacles not to collide with or use them to obtain some information in the environment. Decision making for a proper gaze direction to get more information is also an important issue when there are many obstacles, in particular, dynamic obstacles. To deal with these issues, this paper proposes fuzzy integral-based gaze control for obstacle detection of mobile robots. The fuzzy measures are calculated with the preference degree for five criteria about obstacle detection and the fuzzy integral decides a final gaze direction using the fuzzy measure values and partial evaluation values with respect to the five criteria. Computer simulation demonstrates the effectiveness of the proposed algorithm.

Keywords: Obstacle detection, fuzzy integral, gaze control.

1 Introduction

Obstacle detection is one of important issues for mobile robots. It influences obstacle avoidance, path planning, map building and so on. There are many researches on obstacle detection for mobile robots [1,2] and visually impaired people [3,4,5]. Gaze control is usually researched for giving an attention to a specific object in robotics [6,7]. It is also used to get more useful information with a limited number of sensors in an environment while navigating [8,9,10]. Researches on multi-criteria decision making have been carried out considering user's preference and relationships among criteria using λ -fuzzy measure and Choquet fuzzy integral [11,12,13]. The Choquet fuzzy integral could be used in gaze control.

This paper proposes fuzzy integral-based gaze control for mobile robots to detect obstacles and to explore widely and efficiently in a dynamic environment. λ -fuzzy measure is employed to denote the preference degree for five criteria about obstacle detection. The final gaze direction is decided by the Choquet fuzzy integral using the fuzzy measure values and partial evaluation values with respect to the five criteria.

This paper is organized as follows. Section 2 presents the fuzzy measure and the fuzzy integral. In Section 3, fuzzy integral-based gaze control of mobile robots for obstacle detection is proposed. Computer simulation and results are presented in Section 4. Finally, conclusion and future works follow in Section 5.

2 Fuzzy Measure and Fuzzy Integral

The fuzzy integral is one of multi-criteria decision making methods. The correlation between criteria is calculated by the fuzzy measure. And then, the global evaluation of candidates are calculated by the fuzzy integral using the fuzzy measure values and partial evaluation values with respect to criteria.

To compute the fuzzy measure, weights of criteria are calculated using diamond pairwise comparison diagram shown as Fig. 1 [13]. The shapley value

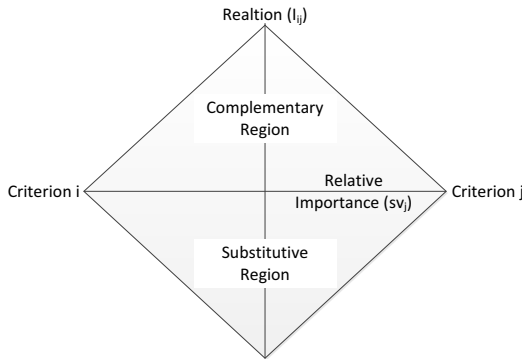


Fig. 1. Diamond pairwise comparison diagram

of the fuzzy measure g , sv_i and sv_j , for the lateral axis in diamond pairwise comparison diagram is defined as

$$\begin{aligned} sv_i &= \{g(\{C_i\}) + g(\{C_i, C_j\}) - g(\{C_j\})\}/2 \\ sv_j &= \{g(\{C_j\}) + g(\{C_i, C_j\}) - g(\{C_i\})\}/2, \end{aligned} \quad (1)$$

where C_i and C_j are criteria, and i and j are the index of criteria.

Weights of criteria w_i are identified by eigenvalue of the ordinal AHP's pairwise comparison matrix. The ordinal AHP's pairwise comparison matrix is defined as

$$C = \begin{pmatrix} c_{11} & \cdots & c_{1n} \\ \vdots & \ddots & \vdots \\ c_{n1} & \cdots & c_{nn} \end{pmatrix}, \quad (2)$$

where $c_{ij} = sv_i/sv_j$, $c_{ii} = 1$, $c_{ji} = 1/c_{ij}$, and n is the number of criteria.

And the hierarchy diagram is estimated using agglomerative hierarchical clustering method. ϕ_s transformation is used to calculate the fuzzy measure efficiently as follows:

$$\phi_s : [0, 1] \times [0, 1] \rightarrow [0, 1],$$

$$\phi_s(\xi, u) = \begin{cases} 1 & \text{if } \xi = 1 \text{ and } u > 0 \\ 0 & \text{if } \xi = 0 \text{ and } u = 0 \\ 1 & \text{if } \xi = 1 \text{ and } u = 1 \\ 0 & \text{if } \xi = 0 \text{ and } u < 1 \\ \frac{s^u - 1}{s - 1} & \text{other cases} \end{cases}, \quad (3)$$

where $s = \frac{(1-\xi)^2}{\xi^2}$, $u = \sum_{i \in A} \omega_i$. ω_i is the weight of criterion, and ξ is interaction degree. The fuzzy measure \mathbf{g} is identified, as follows:

$$\mathbf{g}(X) = \phi_s(\xi_R, \sum_{P \subset R} u_P^R), \quad (4)$$

$$u_P^R = \begin{cases} w_i, \text{ where } i \in P & \text{if } |P| = 1 \text{ and } i \in X \\ 0 & \text{if } |P| = 1 \text{ and } i \notin X \\ \phi_s^{-1}(\xi_R, \phi_s(\xi_P, \sum_{V \subset L} u_V^P)) \times T_P^R & \text{other cases} \end{cases}, \quad (5)$$

$$T_P^R = \frac{\phi_s(\xi_U, \sum_{i \in L} \omega_i)}{\phi_s(\xi_L, \sum_{i \in L} \omega_i)}, \quad (6)$$

where R is root level set and $\phi_s^{-1}(\xi, r)(\xi \in (0, 1))$ is the inverse function of $\phi_s(\xi, r)$. U and L denote an upper level set and a lower level set in the hierarchy diagram, respectively.

Finally, Choquet fuzzy integral calculates the global evaluation of each candidate gaze direction using the fuzzy measure values and partial evaluation value, \mathbf{h} [14].

$$\int_X \mathbf{h} \circ \mathbf{g} = \sum_{i=1}^n (\mathbf{g}(E_i) - \mathbf{g}(E_{i+1})) \mathbf{h}(x_i), \quad (7)$$

where $\mathbf{h}(x_1) \leq \dots \leq \mathbf{h}(x_n)$, $E_i = \{x_i, x_{i+1}, \dots, x_n\}$ and $\mathbf{h}(x_0) = 0$, for $x_i \in X$ and $i = 1, \dots, n$.

3 Fuzzy Integral-Based Gaze Control for Obstacle Detection

Fuzzy integral-based gaze control of mobile robots for obstacle detection is processed as in as Fig. 2. Fuzzy measures are calculated from the user-defined preference. A mobile robot obtains obstacle information (distance, size, velocity and so on) through the sensor system. The candidate gaze directions are calculated by visibility check. Finally, Choquet fuzzy integral decides the gaze angle using the fuzzy measure values and partial evaluation values.

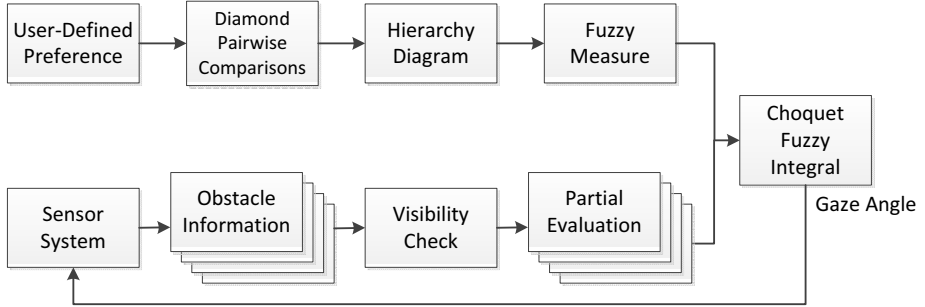


Fig. 2. Fuzzy integral-based gaze control for obstacle detection

3.1 Criteria for Obstacle Detection

In this paper, five criteria are proposed for obstacle detection: distance-based, size-based, velocity-based, uncertain area-based and localization-based criteria. A distance between the robot and the obstacle is an important factor for detection. The partial evaluation function for distance-based criterion C_d is defined as follows:

$$H_d = 1 - \frac{i_{sd}}{n_{obs}}, \quad (8)$$

where i_{sd} and n_{obs} denote the index of the sorted list into the close distance order and the number of obstacles, respectively.

Big size obstacles should be focused in detection. The partial evaluation function for size-based criterion C_s is defined as follows:

$$H_s = 1 - \frac{i_{ss}}{n_{obs}}, \quad (9)$$

where i_{ss} denotes the index of the sorted list into the big size order.

Fast dynamic obstacles should be observed closely in order to detect certainly. The partial evaluation function for velocity-based criterion C_v is defined as follows:

$$H_v = 1 - \frac{i_{sv}}{n_{obs}}, \quad (10)$$

where i_{sv} denotes the index of the sorted list into the fast velocity order.

Keeping gaze on only detected obstacles disturbs to explore environment. So the robot should look around to detect new obstacles. To obtain uncertain area, sample points locate the front of a robot. And sample points in gaze area change from uncertain points to certain points. The partial evaluation function for uncertain area-based criterion C_u is defined as follows:

$$H_u = \frac{n_{up}}{1 + n_{sp}}, \quad (11)$$

where n_{up} and n_{sp} denote the number of uncertain sample points and the number of whole sample points, respectively.

The accurate position of the robot leads to obtain the accurate positions of obstacles. Because the robot calculates the positions of obstacles using the own position. Unscented Kalman filter-based SLAM (UKF-SLAM) is used to estimate the position of the robot [15]. The partial evaluation function for localization-based criterion C_l is defined as follows:

$$H_l = \frac{\sigma}{\tau}, \quad (12)$$

where σ and τ denote the magnitude of robot position components in the error covariance matrix which is computed by UKF-SLAM and a user-defined normalization factor, respectively.

3.2 Weights of Criteria and Fuzzy Measure

Shapley value of the fuzzy measure g , sv_i and sv_j , and the Murofush and Soneda's interaction index I_{ij} are obtained through Grabisch's graphical interpretation as shown in Fig. 3. The ordinal AHP's pairwise comparison matrix and weights are shown as Table 1. The identified fuzzy measures using the process explained Section 2 are provided in Table 2.

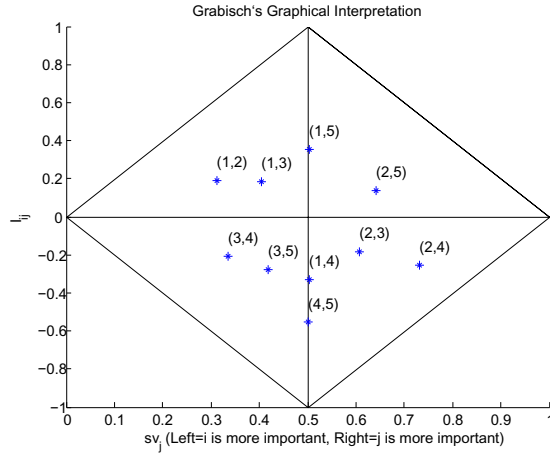


Fig. 3. User-defined diamond pairwise comparison diagram

Table 1. Ordinal AHP's pairwise comparison matrix and weights

	C_d	C_s	C_v	C_u	C_l	w_i
C_d	1.0000	2.2030	1.4729	0.9863	0.9863	0.2406
C_s	0.4539	1.0000	0.6471	0.3669	0.5583	0.1092
C_v	0.6789	1.5455	1.0000	1.9828	1.3912	0.2449
C_u	1.0139	2.7253	0.5043	1.0000	0.9954	0.2073
C_l	1.0139	1.7910	0.7188	1.0046	1.0000	0.1980

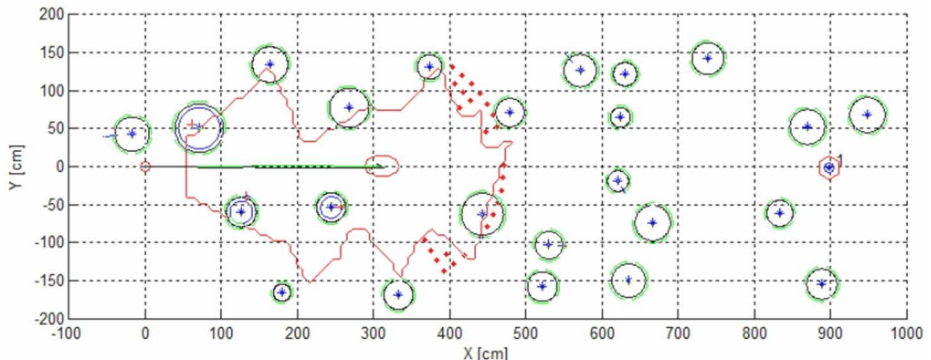
Table 2. Identified fuzzy measures

A	$g(A)$	A	$g(A)$	A	$g(A)$	A	$g(A)$
$\{\emptyset\}$	0.000000	{4}	0.241472	{5}	0.231136	{4, 5}	0.454150
{1}	0.278492	{1, 4}	0.497724	{1, 5}	0.488340	{1, 4, 5}	0.690813
{2}	0.129732	{2, 3}	0.360844	{2, 5}	0.350951	{2, 4, 5}	0.564397
{1, 2}	0.396275	{1, 2, 4}	0.606101	{1, 2, 5}	0.597120	{1, 2, 4, 5}	0.790906
{3}	0.283160	{3, 4}	0.502019	{3, 5}	0.492651	{3, 4, 5}	0.694780
{1, 3}	0.535572	{1, 3, 4}	0.734273	{1, 3, 5}	0.725768	{1, 3, 4, 5}	0.909281
{2, 3}	0.400743	{2, 3, 4}	0.610212	{2, 3, 5}	0.601246	{2, 3, 4, 5}	0.794703
{1, 2, 3}	0.642325	{1, 2, 3, 4}	0.832502	{1, 2, 3, 5}	0.824361	{1, 2, 3, 4, 5}	1.000000

where 1: C_d , 2: C_s , 3: C_v , 4: C_u , 5: C_l .

4 Simulation Environments and Results

In this simulation, there were a mobile robot, static obstacles, dynamic obstacles and one goal in an environment, as shown Fig. 4. The small red circle located (0,0) is the initial position of the mobile robot and big blue circles are obstacles. The size of the blue circle means the size of obstacle and the length of the blue line in the blue circle indicates the speed of the obstacle. The red hexagon is the goal point for the mobile robot to arrive at. The mobile robot assumed to have a RGB-D camera which can move to a desired pan/tilt angle. In Fig. 4, a red polygon denotes explored area. The robot could obtain obstacle information (distance, size, velocity) only within the view area. The robot moved at a speed of 30.0 cm/s and the period of detection process was 100.0ms. The control noise of the mobile robot about the moving distance and angle is assumed Gaussian noise. Its mean was 5.0 cm/s, 1.0°. The observation noise from RGB-D camera about the distance and angle is also assumed Gaussian noise and its mean was 5.0 cm, 10.0°.

**Fig. 4.** Simulation environment

In this simulation, the proposed algorithm was applied 10 times to analyze results of obstacle detection. The average of root mean square error (RMSE) and standard deviations (STD) for the obstacle position error and the robot position error are shown in Table 3. The obstacle position error was the distance between the detected obstacle position and the real obstacle position. The robot position error was the distance between the estimated robot position from UKF-SLAM and the real robot position.

Table 3. Simulation results

Position Error		RMSE (cm)	STD (cm)
Without gaze control	Obstacle	19.5	12.48
	Robot	12.9	9.56
With gaze control	Obstacle	20.3	16.05
	Robot	14.8	12.26

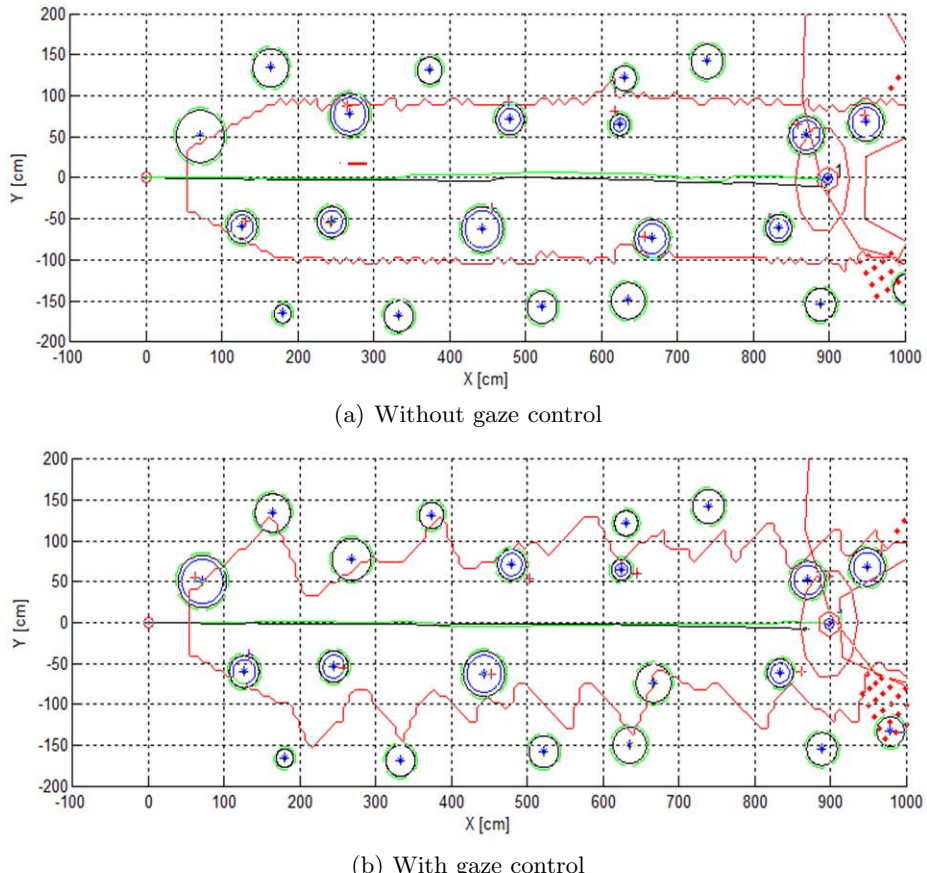


Fig. 5. Simulation results

Results when the robot was using gaze control were very similar to them when the robot was not using gaze control. But the robot applied proposed the fuzzy integral-based gaze control for obstacle detection can explore widely, as shown Fig. 5.

Consequently, the robot applied proposed the fuzzy integral-based gaze control for obstacle detection had small obstacle position error and robot position error. And it can explore widely in dynamic environment.

5 Conclusion

This paper proposed the fuzzy integral-based gaze control of mobile robots for obstacle detection. It makes a mobile robot explore widely and efficiently in a dynamic environment. For the effective detection, five criteria were proposed: distance-based, size-based, velocity-based, uncertain area-based and localization-based criteria. To calculate weights of criteria, diamond pairwise comparison diagram were used and then fuzzy measures were identified. The global evaluations of all the candidate gaze directions were calculated through the Choquet fuzzy integral using fuzzy measures and partial evaluation values. Computer simulation demonstrated the effectiveness of the proposed algorithm in obstacle detection.

Performance improvement should be needed. Real experiments with the mobile robot will be performed as a further work. Also, obstacle avoidance algorithms will be incorporated into the proposed obstacle detection algorithm for navigation in real environment.

References

1. van der Mark, W., van den Heuvel, J., Groen, F.: Stereo based obstacle detection with uncertainty in rough terrain. In: IEEE Intelligent Vehicles Symposium, pp. 1005–1012 (2007)
2. Yankun, Z., Hong, C., Weyrich, N.: A single camera based rear obstacle detection system. In: IEEE Intelligent Vehicles Symposium, pp. 485–490 (2011)
3. Yu, K.H., Yoon, M.J., Jeong, G.Y.: 3d detection of obstacle distribution and mapping for tactile stimulation. In: IEEE International Conference on Mechatronics, pp. 1–6 (2009)
4. Chen, L., Long Guo, B., Sun, W.: Obstacle detection system for visually impaired people based on stereo vision. In: 2010 ICGEC, pp. 723–726 (2010)
5. Lee, C.H., Su, Y.C., Chen, L.G.: An intelligent depth-based obstacle detection system for visually-impaired aid applications. In: 2012 WIAMIS, pp. 1–4 (2012)
6. Ude, A., Wyart, V., Lin, L.H., Cheng, G.: Distributed visual attention on a humanoid robot. In: 2005 5th IEEE-RAS International Conference on Humanoid Robots, pp. 381–386 (2005)
7. Gu, L., Su, J.: Gaze control on humanoid robot head. In: 2006 WCICA, vol. 2, pp. 9144–9148 (2006)
8. Ushida, S., Yoshimi, K., Okatani, T., Deguchi, K.: The importance of gaze control mechanism on vision-based motion control of a biped robot. In: 2006 IROS, pp. 4447–4452 (2006)

9. Frintrop, S., Jensfelt, P.: Attentional landmarks and active gaze control for visual slam. *IEEE Transactions on Robotics* 24(5), 1054–1065 (2008)
10. Yoo, J.K., Kim, J.H.: Fuzzy integral-based gaze control architecture incorporated with modified-univector field-based navigation for humanoid robots. *IEEE Transactions on Systems, Man, and Cybernetics, Part B: Cybernetics* 42(1), 125–139 (2012)
11. Kim, J.H., Han, J.H., Kim, Y.H., Choi, S.H., Kim, E.S.: Preference-based solution selection algorithm for evolutionary multiobjective optimization. *IEEE Transactions on Evolutionary Computation* 16(1), 20–34 (2012)
12. Kim, J.H., Ko, W.R., Han, J.H., Zaheer, S.: The degree of consideration-based mechanism of thought and its application to artificial creatures for behavior selection. *IEEE Computational Intelligence Magazine* 7(1), 49–63 (2012)
13. Takahagi, E.: A fuzzy measure identification method by diamond pairwise comparisons and f_s transformation. *Fuzzy Optimization and Decision Making* 7, 219–232 (2008)
14. Takahagi, E.: On identification methods of l -fuzzy measures using weights and l . *Journal of Japan Society for Fuzzy Theory and Systems* 12, 665–676 (2000)
15. Julier, S.J., Uhlmann, J.K.: A new extension of the kalman filter to nonlinear systems. In: The 11th Int. Symp. on Aerospace/Defence Sensing, Simulation and Controls, pp. 182–193 (1997)

Ensembles of Gradient Based Descriptors with Derivative Filters for Visual Object Categorization

Enas A.A. Eqlouss, Azizi Abdullah, and Siti Norul Huda Sheikh Abdullah

Pattern Recognition Research Group
Center for Artificial Intelligence
Faculty of Information Science and Technology
University Kebangsaan Malaysia 43600 Bangi, Selangor
bello_pearla@yahoo.com, {azizi, mimi}@ftsm.ukm.my

Abstract. This paper describes several ensemble methods that combine multiple edge and orientation based histograms with support vector machine classifiers. The aim is to enhance learning speed and accuracy performance by using the chosen classical primitive filters on different edge and orientation descriptors. For efficiently describe images using these descriptors, the combination of a few basis features or edge filters are used. The stronger filter operator responds to edge-like structures, the more sensitive it to orientation. Thus, using more than one edge filter allows to capture more edge information to completely describe the structure of image content. One problem in combining these different descriptors is that the input vector becomes very large dimensionality, which can increase problems of overfitting and hinder generalization performance. The intuitively designed ensemble methods namely product, mean and majority are then used to combine support vector machines classifiers derived from the multiple orientations of edge operators. The results indicate that the ensemble methods outperform the single and naive classifiers.

Keywords: object categorization, ensemble rules, support vector machines, compass filters.

1 Introduction

An image is an ill-defined entity consisting of many image features such as lines, edges or textures. These features provide a more abstract and informative description of images than pixels for recognition. The images can be of a complex nature, however, it is not impossible to describe the generic meaning by using these low-level features. During the last decade a large number of novel algorithms have been researched for recognition and became one of the most interesting topics in computer vision [1][2][3]. The algorithms use descriptors describing an image and a machine learning algorithm for classification. However, it is common experience for computer vision researches to get low accuracy performance due to complex transformations with high inter-class variations from the query of digital images.

In the literature, it is often difficult to determine which image features are most discriminative to describe the information in an image. Good image features are crucial because they can give a compact representation and help in capturing meaningful patterns

in the image. However, one of the most widely used features in describing images is the construction of edge and orientation features. For this reason, gradient based descriptors such as SIFT[4], histograms of oriented gradients [5] and MPEG-7 edge histogram [6][7] have become popular and nowadays widely used in image recognition systems. In this paper, we show the advantages of using ensembles of a set of edge filters instead of pixel difference in the performance of the well known edge-based descriptors. One problem in gradient computation using pixel differences in these descriptors is sensitive to noise and other artifacts, which can increase problems of feature indexing. A common solution to the problem is to compute smoother approximations of the image derivative using filters such as Gabor filters[8][9][10] and Gaussian-weighted Principle Independent Component Analysis (GPICA) of an image [11]. In contrast to these previous works, here we use a set of classical filters namely Robinson's filters to approximate the whole structure of the image. One problem with a single filter for feature description is that the stronger a filter operator responds to edge-like structures, the more sensitive it to orientation and the operator only respond to edges in a narrow range of orientations. Thus, using more than one edge operator provides wider range of directions and magnitudes for feature description. After that, each gradient based histogram of the operator outputs and giving them as input to a learning classifier such as a support vector machine (SVM) [12] has been shown to lead to promising results.

In [13][10], the authors computed descriptors from feature maps at different scales and orientations using filters. However, when these methods are used to combine many gradient based descriptors in a single large input vector, this may lead to overfitting the data and worse generalization performance. Therefore, in [13], proposes a series of planes where successive convolutions and subsampling operations at different scales to construct feature maps for feature indexing. The system is based on neural network architecture that consists of six different layers, where the last two layers carry out the classification task using the features extracted in the previous layers namely n_1 and n_2 layers. Layer n_2 receives inputs from layer n_1 that contains a number of partially connected sigmoid neurons of the network. In contrast, [10] constructs a set of different feature maps from Gabor Wavelets features at different scales and orientations. After that, the Principle Component Analysis is applied to reduce dimensionality of feature maps and nearest neighbor classifier for classification. In this paper, we describe several ensemble methods that combine multiple descriptors from different feature maps. The aim is to enhance learning speed and accuracy performance by using the chosen classical primitive filters of different edge and orientation descriptors. It basically constructs a set of individual support vector machines classifiers from these descriptors. After that, the ensembles are used for learning and combine probability outputs from all classifiers.

Contributions of this Paper. (1) The ensembles are used for learning and combine multiple outputs of filter based classifiers to enhance learning speed and accuracy performance. (2) We compare the accuracy of the proposed method with single and naive approaches on 20 classes from Caltech-101 dataset.

The rest of the paper is organized as follows: Section 2 reviews the related researches. After that we describe our system for image recognition in section 3. The system basically uses gradient based descriptors compute feature vectors from feature maps that are used to construct support vector machine classifiers. Section 4 describes the ensemble methods

and how we used the support vector machine as classifiers. Experimental results on 20 classes from Caltech-101 dataset are shown in Section 5. Section 6 concludes this paper.

2 Related Work

Edge and orientation are important elements for object recognition purposes than pixels information. These information are typically represented by combination of a few basis features. Recently, most studies are focusing on using multiple edge and orientation information to completely describe images for satisfactory recognition result. Using these information may help in recognizing different structures of images in wider range. The information can be extracted using a single filter such as Sobel or a set of different filters such as compass filters or Gabor filters. However, using multiple filters are more informative for feature indexing due to different orientations or magnitudes of image structure can be extracted.

2.1 Robinson Compass Filters

One advantage using edge operator such as Robinson filters is that a wider range of orientations and magnitudes information can be extracted. It contains eight different filters with orientation spaced at 45° . The main reason why we used this filter is that it is simple and not requiring expensive operation to convolve images. The Robinson filter contains eight major orientations namely vertical right, vertical left, bottom horizontal, top horizontal, bottom right diagonal, top left diagonal, bottom left diagonal and top right diagonal with its coefficients in the range of -2 and 2.

2.2 MPEG-7's Edge Histogram

Human eyes are very sensitive to the intensity changes. Thus, texture information is important to check homogeneity and non-homogeneity between images. We used the MPEG-7 edge histogram [14] to compute texture information. The edge histogram describes a non-homogeneous texture and captures a local spatial distribution of edges. Given an input image, the image is partitioned into 4×4 overlapping blocks or 16 sub-block. After that each sub-block is convolved with the following five orientation filters. As a result each block holds a total of five different orientations or 5-bin for description. The maximum of the most dominant edges is determined by comparing it with other edges' strength. Then the maximum of these results is compared with a threshold. Finally, the descriptor with 80-bin histogram for intensity component is constructed for the input image by excluding the no-edge information. We named them as EH_G to represent the edge histogram with intensity information.

2.3 Histograms of Threshold-Oriented Gradients (HTOG)

Shape is important to discriminate between objects. Local shape histograms are represented by edge orientations within an image subregion quantized into N bins. We model the shape by using intensity signals, and then we compute orientations by detecting the signal changes that are visible and significant in a certain angular range.

The most popular gradient base histogram that extract information about edges and shape is HOG[5] and SIFT[4]. The histogram basically describes an image by a set of local histograms. In contrast to this previous work, here we used histograms that count occurrences of thresholded gradients in a local part of the image. After that, the image is divided into 4×4 sub regions to obtain the spatial relationship between edge attributes. Subsequently, the gradients dx and dy are computed at each point in each region by using the filters in the x and y directions, respectively.

$$\begin{bmatrix} 0 & 0 & 0 \\ 0 & 1 & -1 \\ 0 & 1 & -1 \end{bmatrix} \begin{bmatrix} 0 & 0 & 0 \\ 0 & 1 & 1 \\ 0 & -1 & -1 \end{bmatrix}$$

To compute the magnitude and orientation of the gradient the following formulas are used:

$$m(x,y) = \sqrt{dy^2 + dx^2} \quad (1)$$

$$\Theta(x,y) = \arctan(dy/dx) \quad (2)$$

where m is the magnitude, Θ is the orientation of the gradient, and dy and dx are gradients in vertical and horizontal directions, respectively.

In order to determine the occurrence histogram for different orientations, a threshold is used to choose the strongest edges. The edge is considered as a noise or weak response if $m(x,y)$ is below the threshold (in our experiments set to 10), and not counted in constructing the histogram. Otherwise, all Θ 's which have a magnitude above the threshold are selected and then quantized into N bins. In our experiments, $N = 8$ gave the best results. Finally, the descriptor with 128 bins is constructed for the whole region (consisting of 4×4 blocks). Each bin in the histogram represents the number of occurrences of edges that have a certain orientation. We chose several angular ranges to recognize different structures of images and to enrich the semantic description of the edge information. We found two angular ranges i.e., 180° and 360° to be optimal in our dataset. An angular range of 180° maps angles between 180° and 360° to the range between 0 and 180 degrees. We named the two resulting descriptors HG_{180G} and HG_{360G} to represent the HTOG with intensity information.

2.4 Block-Based SIFT (Scale Invariant Feature Transform)

SIFT[4] describes an image by constructing histograms of gradient orientations around a set of interest points. Thus, we also applied the descriptor as one of our main descriptors. The original SIFT version uses an interest points detector to detect salient locations which have certain repeatable properties. In contrast with this approach, we believe that using fixed partitioning blocks gives a simpler method with the same or better performance on our dataset. Furthermore, using this approach the spatial relationships between the SIFT features can be represented more efficiently, i.e. we do not need clustering and less computational time for constructing the descriptor. Therefore, fixed regions without orientation alignment are constructed over the image and instead of 'salient points' we compute the center of each region.

To compute the descriptor, an input image (whole image) is smoothed with the same smoothing function and differentiated using the same dx and dy filters. After that, the center point of the region is determined by dividing its width and height by 2. The descriptor is then constructed by a circular region around the center point of the region. The circular region radius is determined by taking the $\min(\frac{\text{width}}{2}, \frac{\text{height}}{2})$, where width and height are the sizes of the region. After that, the descriptor breaks apart a window around the center point into 4×4 sub-blocks and calculates a gradient orientation histogram, whereby each gradient is weighted by its magnitude to better reflect strong orientations. Each histogram has 8 bins and in total there are 128 bins per histogram for each region. Our use of SIFT differs from the HTOG in the following ways: it uses a circular region instead of a rectangular block and it does not use a threshold on the magnitude. In this way we compute complementary features with SIFT and HTOG. We also used SIFT descriptors with 180° and 360° angular ranges to enrich its visual information. We named them S_{-180G} and S_{-360G} to represent the SIFT descriptors with intensity information.

3 Ensemble of Gradient Histogram Based Filters

The main idea behind histogram gradient-based filters is to use the most probable edge or orientation frequency distributions to depict different feature map images. Using filters basically may help to recognize different maxima at edge structures of images efficiently and enrich the semantic description of visual information. The stronger a filter operator responds to edge-like structures, the more sensitive it to orientation. Thus, using more than one edge operator allows to capture more edge information to completely describe image content.

The system uses multiple gradient based descriptors to describe feature maps extracted from eight different Robinson filters. It consists of five layers, excepting the input plane that receives an image as a whole of any sizes, without requiring any local pre-processing of the input image such as brightness correction, contrast adjustment, etc. The system starts by convolving pixels neighborhood of an image with eight 3×3 masks (a through h of Fig. 1), resulting eight different magnitude images or feature maps with maxima at edge locations. The different filters used in the stage is to provide wider range of directions and magnitudes for specific structural feature description. After that, gradient based descriptors are applied to compute feature vectors from the feature maps. These descriptors compute the first order image derivatives using these filters as convolution masks. Next, the computed feature vectors are used to construct support vector machine models for predictions. Once trained, for a given test object, SVM probability outputs of all models are then combine using ensemble learning methods for final classification. Fig. 1 shows the overall purposed system.

4 Classification Methods

4.1 SVM Classifier

We employ an SVM [15] to learn to classify the images. The one-vs-one approach is used to train and classify images in the Caltech-101 dataset. For the SVMs, we use

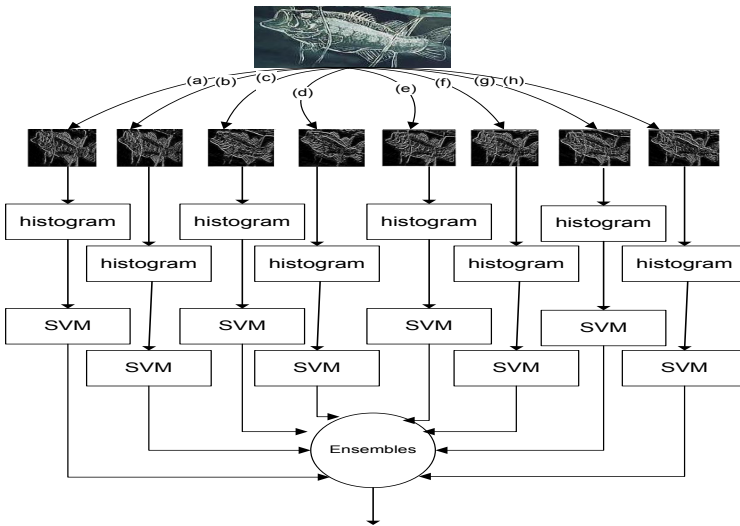


Fig. 1. Architecture of the ensembles of gradient-based descriptors using eight Robinson filters

Radial-Basis-Function (RBF) kernels in all experiments. Initially, all attributes in the training and testing sets were normalized to the interval $[-1, +1]$ by using this equation:

$$x' = \frac{2(x - \min)}{(\max - \min)} - 1. \quad (3)$$

The normalization is used to avoid numerical difficulties during the calculation and to make sure the largest values do not dominate the smaller ones. We also need to find the SVM parameters C and γ that perform best for the descriptors. To optimize the classification performance, the parameters were determined by using the libsvm grid-search algorithm [16]. We tried the following values $\{2^{-5}, 2^{-3}, \dots, 2^{15}\}$ and $\{2^{-15}, 2^{-13}, \dots, 2^3\}$ for C and γ , respectively. The values which gave the best accuracy performance with 5-fold cross-validation are picked and used to train on the training set.

4.2 Ensemble Methods for Combining Classifiers

Our previous works [17][18] showed that combining multiple features and classifiers with ensemble methods significantly increases classification performance. Ensemble methods have received considerable attention in the machine learning community to increase the effectiveness of classifiers. In order to construct a good ensemble classifier, the ensemble needs to construct accurate and diverse classifiers and to combine outputs from the classifiers effectively [19]. There exist several methods to obtain and combine the diverse classifiers. Here we employ three ensemble algorithms namely (1) product rule (2) mean rule [20] and (3) majority voting.

The product rule is one of the simplest and most efficient ways for combining outputs of classifiers [20]. When the classifiers have small errors and operate in independent

feature spaces, it is efficient to combine their (probabilistic) outputs by multiplying them. Thus, we use this product rule to determine the final decision of the ensemble. First the posterior probability outputs $P_j^k(x^k)$ for class j of n different classifiers are combined by the product rule:

$$P_j^p(x^1, \dots, x^n) = \prod_{k=1}^n P_j^k(x^k) \quad (4)$$

where x^k is the pattern representation of the k^{th} descriptor. Then the class with the largest probability product is considered as the final class label belonging to the input pattern.

When estimators of the different classifiers contain large errors, it can be more efficient to combine their estimated probabilities by the mean rule [20] as follows:

$$P_j^m(x^1, \dots, x^n) = \frac{1}{n} \sum_{k=1}^n P_j^k(x^k) \quad (5)$$

Majority voting is the simplest and intuitive rule in combining multiple classifiers. It counts the collective judgement sets or votes for every classifier and applies a score. Let $d_{n,j} \in \{0, 1\}$ denote the decision outputs of the n^{th} classifier M_n , $n=1\dots L$ and $j=1\dots c$, where L is the number of classifiers and c is the number of classes. If the n^{th} classifier selects class j , then $d_{n,j} = 1$ for correct, and zero for error. The vote will result in ensemble decision for t input class if:

$$\sum_{n=1}^L d_{n,t} = \max_{j=1}^c \sum_{n=1}^L d_{n,j} \quad (6)$$

Similar to the product rule and mean rule the class with the largest score is considered as the final class label.

In the experiments we will compare these ensemble methods to the naive approach that combines the feature vectors computed at all feature maps in one large feature vector.

5 Experiments and Results

For our comparison between the different descriptors and ensemble algorithms, a variety of image classes were chosen. The images should be common and familiar to machine vision researchers, and therefore we used a well known dataset, i.e. Caltech-101 [21]. The dataset contains various image sizes and were categorized into 101 different classes. However, in our experiment, only the first 20 classes were chosen for evaluation due to computational restrictions. In the dataset, each image consists of different sizes and contains different viewpoints, which makes the recognition process more challenging.

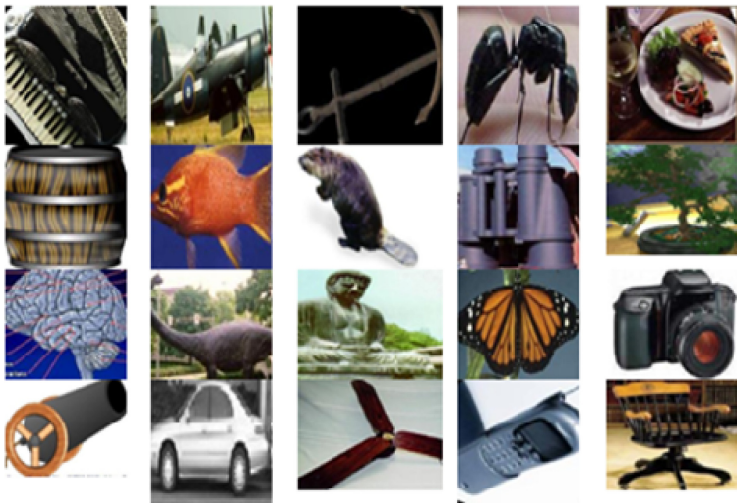


Fig. 2. Image examples with ground truth for different groups namely accordion, airplane, anchor, ant, background, barrel, bass, beaver, binocular, bonsai, brain, brontosaurus, Buddha, butterfly, camera, cannon, car side, ceiling fan, cell phone and chair respectively

5.1 Caltech-20 Dataset

The Caltech-101 is one of the most popular and widely used datasets to demonstrate the performance of object recognition systems [21]. It consists of 101 categories depicting real world object images such as camera, airplanes, bonsai, anchor, etc. In our experiments, we used the first 20 categories (in alphabetical category order) and a total of $20 \times 30 = 600$ images for evaluation. These images are all in JPEG format with medium resolution about 300 x 300 pixels and both in color and gray level representation. Fig. 2 shows the ground truth for the 20 different classes we used of the Caltech-101 dataset.

For evaluating the ensemble methods and the other single descriptors, we used 15 training and 15 testing images for each image class. To compute the performances of the different methods, we choose 10 times different training and test images randomly from a set of candidate images in the 20 classes of the Caltech-101 dataset. Finally, we report the performance using mean and standard deviation to verify significances of the obtained classification results.

5.2 The Detection of Intensity Changes

The process of extracting information from edges and orientations can be divided into three main tasks. The first task is to transform pixels in RGB color space into a more robust color space. In our case, YIQ color model is used to describe intensity information. In YIQ color space, only the Y component is used since this channel represents the intensity information. We used intensity values in the range of [0...255] per pixel, where the value 0 represents the minimum brightness and 255 the maximum brightness. The

second task is to provide feature maps for the grayscale image. In this step, the image will be convolved using eight different Robinson filters. Once the feature maps are constructed, the last step is to apply gradient based descriptors that compute the first order image derivative to describe images and support vector machine algorithm for learning.

Table 1. The average classification accuracy (mean and SD) of the single and combination classifiers. M1=HG_G, M2=HG_{360G}, M3=S_G, M4=S_{360G}, and M5=EH_G. F1-F8=Filter, N=Naive, E1=Product Rule, E2=Mean Rule and E3=Majority Voting. The best result is marked in boldface.

	F1	F2	F3	F4	F5	F6	F7	F8	N	E1	E2	E3
M1	48.50 ±2.94	52.20 ±3.50	49.67 ±1.71	52.13 ±1.74	49.13 ±2.80	50.87 ±2.96	50.37 ±3.44	49.00 2.03	58.83 ±2.17	59.93 ±1.97	60.07 ±1.95	58.73 ±2.22
M2	48.47 ±2.46	50.47 ±1.57	50.0 ±1.97	50.67 ±2.16	48.93 ±2.07	50.20 ±2.49	50.33 ±1.86	50.53 ±2.30	-	60.7 ±1.83	58.0 ±2.04	48.7 ±2.46
M3	52.83 ±2.87	56.37 ±3.70	54.50 ±2.47	55.47 ±3.41	53.87 ±3.70	57.14 ±2.29	53.67 ±2.68	56.03 ±2.10	61.37 ±3.24	61.67 ±3.57	61.43 ±3.55	59.87 ±3.98
M4	51.03 ±2.40	55.30 ±3.25	52.73 ±2.99	54.73 ±3.57	52.50 ±3.44	55.90 ±2.53	52.00 ±2.38	55.60 ±1.92	-	59.67 ±3.47	59.50 ±3.43	58.7 ±2.40
M5	47.93 ±2.12	52.10 ±2.52	46.63 ±2.68	52.23 ±2.51	48.50 ±2.63	52.63 ±2.69	47.87 ±1.90	53.23 ±2.28	59.40 ±2.38	59.37 ±2.57	59.17 ±2.21	57.73 ±2.68

5.3 Results on Caltech-20

Table 1 shows the average classification accuracy and standard deviation of the different descriptors to classify images using the RBF kernel. The result shows that the average classification accuracy for each descriptor is best if all filter classifiers are combined i.e. naive and ensemble methods. It indicates that using a single filter is insufficient to completely describe objects due to narrow range of orientations. In contrast, using a larger set of filters produces wider range of orientations to enrich description of images. Besides, it provides better cooperation between classifiers to improve the final performance of the combination algorithms. In our experiments, we do not report results on HG_{360G} and S_{360G} of the naive method because previous results show that ensemble methods slightly outperform this approach. Thus, we believe both naive and ensembles have sufficiently rich information to describe objects using eight Robinson filters using a single descriptor.

We extended our experiments to combine all classifiers of the different descriptors on 20 classes. We compare the combination based on all filters combined with three ensemble methods namely product rule, mean rule and majority voting. The results are reported in Table 2. In this experiment, combining all classifiers of the different descriptors with the mean rule gives the best performance of 68.23%. This result shows that a combination of the descriptors performed very well with an ensemble of support vector machines. We do not report results on naive combination due to computation restriction of feature vector size. Besides, our previous works [17][18] show naive gives no improvement to increase classification result due to overfitting problem.

Table 2. The average classification accuracy of the different combination classifiers on 20 classes. M=Classifiers based on all filters combined. The best result is marked in boldface.

	Product Rule	Mean Rule	Majority Voting
M	67.93±2.19	68.23±2.16	67.67±2.74

6 Conclusions

In this paper, we have introduced an approach for recognizing objects in digitized images using classical compass filters. We reported a significant comparison of using filters in describing and classifying images namely (a) using a filter with a single feature descriptor, (b) using a set of different filters with a single feature descriptor, and (c) filters with different feature descriptors. The system uses different gradient based descriptors to compute the first order image derivative using eight Robinson's filters as convolution masks. A possible problem using a single filter to compute feature vectors, is that this operator only respond to edges in a narrow range of orientations. Thus, for a completely describe objects using edge information, a wide range of orientations is needed. Still, the best idea to describe images on the 20 classes is to use a combination of different filters and feature descriptors. This may be caused by its ability to keep structural relationships or cooperations between feature maps of the images. Using a single filter only to describe images gives worse result due to losing information about structures.

In future work we want to use color information to enrich semantic information for describing objects. And to use the spatial pyramid approach to construct multiple spatial resolution levels for each convolution mask.

Acknowledgment. The authors want to thank the Faculty of Information Science and Technology, University Kebangsaan Malaysia, for providing facilities and financial support under the exploration Research Grant Scheme No. UKM-TT-07-FRGS0253-2010, UKM-ERGS/1/2011/STG/UKM/02/41 and UKM-ERGS/2011/STG/IKM/2/48(TK). We also want to thank to Sanusi Azmi for helpful comments. The first author also wants to thank to the government of Libya for scholarship.

References

1. Kinnunen, T., Kamarainen, J.K., Lensu, L., Lankinen, J., Kälviäinen, H.: Making visual object categorization more challenging: Randomized caltech-101 data set (2010)
2. Larlus, D., Jurie, F.: Latent mixture vocabularies for object categorization and segmentation. *Image Vision Comput.* 27(5), 523–534 (2009)
3. Winn, J., Criminisi, A., Minka, T.: Object categorization by learned universal visual dictionary (2005)
4. Lowe, D.G.: Distinctive image features from scale-invariant keypoints. *Int. J. Comput. Vision* 60(2), 91–110 (2004)
5. Dalal, N., Triggs, B.: Histograms of oriented gradients for human detection (2005)

6. Manjunath, B.S., Salembier, P., Sikora, T. (eds.): *Introduction to MPEG-7: Multimedia Content Description Language*. Wiley (2002)
7. Won, C.S., Park, D.K., Park, S.J.: Efficient use of mpeg-7 edge histogram descriptor 24(1), 23–30 (2002)
8. Moreno, P., Bernardino, A., Santos-Victor, J.: Improving the sift descriptor with smooth derivative filters. *Pattern Recogn. Lett.* 30(1), 18–26 (2009)
9. Koenderink, J.J., van Doorn, A.J.: Generic neighborhood operators. *IEEE Trans. Pattern Anal. Mach. Intell.* 14, 597–605 (1992)
10. Zhu, J., Vai, M.I., Mak, P.U.: A new enhanced nearest feature space (enfs) classifier for gabor wavelets features-based face recognition (2004)
11. Arlt, B., Brause, R.W., Tratar, E.: Mascot: a mechanism for attention-based scale-invariant object recognition in images. Technical Report 00, 02, Informatik (2009)
12. Vapnik, V.N.: *The nature of statistical learning theory* (1995)
13. Garcia, C., Delakis, M.: Convolutional face finder: A neural architecture for fast and robust face detection. *IEEE Trans. Pattern Anal. Mach. Intell.* 26(11), 1408–1423 (2004)
14. Lux, M., Becker, J., Krottmaier, H.: Caliph and emir: Semantic annotation and retrieval in personal digital photo libraries (2003)
15. Cortes, C., Vapnik, V.: Support-vector networks. *Mach. Learn.* 20(3), 273–297 (1995)
16. Hsu, C.W., Chang, C.C., Lin, C.J.: *A Practical Guide to Support Vector Classification* (2000)
17. Abdullah, A., Veltkamp, R.C., Wiering, M.A.: An ensemble of deep support vector machines for image categorization (2009)
18. Abdullah, A., Veltkamp, R.C., Wiering, M.A.: Ensembles of novel visual keywords descriptors for image categorization (2010)
19. Dietterich, T.G.: Ensemble methods in machine learning (2000)
20. Tax, D.M., Duin, R.P., Breukelen, M.V.: Comparison between product and mean classifier combination rules (1997)
21. Fei-Fei, L., Fergus, R., Perona, P.: Learning generative visual models from few training examples: An incremental bayesian approach tested on 101 object categories. *Comput. Vis. Image Underst.* 106(1), 59–70 (2007)

Transdisciplinary Way of Knowledge Representation in Intelligent Autonomous Systems with Neural Networks

B.A. Kalashankar¹ and N.N.S.S.R.K. Prasad²

¹ IT Consultant, Logica, now part of CGI,
124-125, Divyasree Technopolis,
Yemlur, Bangalore - 560037, India
kba.shetty@gmail.com

² Group Director (Electromagnetic & Optical Systems),
ADA, PO:1718, Vimanapura Post,
Bangalore-560017, India
nnssrkprasad2007@gmail.com

Abstract. Learning is the highly complex and ongoing process in each and every stage of life to enrich our thought processes, in the same way our thought process is involved in the course of acquiring auxiliary knowledge with an existing knowledge. In this perspective human stands ahead on every stage of life, an important difference between intelligent autonomous applications and human intelligence is our ability to exploit common sense knowledge attained from a lifetime of learning and experiences to inform our decision-making and behavior. This allows humans to adapt easily to novel situations where intelligent autonomous systems fail in some cases due to lack of situation-specific rules and generalization capabilities.

In the ongoing research and development, most of the intelligent autonomous systems can do the task as expected, but still fails in the process of acquiring additional knowledge apart from the acquired knowledge. This is due to our way of learning methodologies, domain experience, and way of thought processes where we involved as a disciplinary, multidisciplinary, interdisciplinary and transdisciplinary approach of learning. In order for intelligent autonomous systems to exploit common sense knowledge in reasoning as humans do, understand domain specific basics, then, we need to provide them with human-like reasoning strategies.

In complex situation, in particular, representation of multiple domain knowledge to resolve the problem based on the situation. The domain knowledge should be adapted at multidimensional way or parallel or dynamic way of adapting the knowledge. This leads intelligent autonomous systems to use an alternative when it fails at the particular point of solving the problem, so for better result knowledge should be organized in the better way. Knowledge is dominantly organized in disciplines, as multidisciplinary and interdisciplinary research is developing at the boundaries of the scientific disciplines [8]. In this paper we compare transdisciplinary, interdisciplinary, multidisciplinary and

non-disciplinary forms of knowledge representations and adopt transdisciplinary approach for intelligent autonomous systems with neural networks.

Keywords: Knowledge Representation, Intelligent Autonomous Systems, Expert System, AI, Multidisciplinary, Interdisciplinary, Transdisciplinary and Artificial Neural Networks.

1 Introduction

The Computational Cognitive arose on the background of Turing's theory of computability. In his functionalism, the **hardware of a computer** is related to the **wetware of the human brain**. The **mind** is understood as the **software** of a computer. Turing argues: If human mind is computable, it can be represented by a Turing program (Church's thesis) which can be computed by a universal Turing machine, i.e. technically by a general purpose computer. The embodied mind is obviously a complex dynamical system acting and reacting in dynamically changing situations [9].

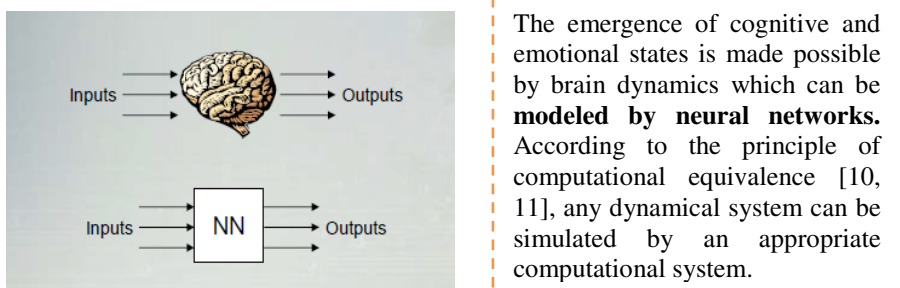


Fig. 1. Human brain represented through NN

Knowledge Representation, as we know our Knowledge is not formally represented, but embodied knowledge, which is learnt by doing, applied by self-organization, and understood by bodily interacting with (social) environments. In a complex world, we have to be able to act and decide with incomplete and fuzzy knowledge under the conditions of bounded rationality [9]. Our brain attain the knowledge on the fly, means when we speak, talk, walk, listen, sense, see, communicate and many more, it acquire and accumulate the knowledge into the existing knowledge, so the common sense of human brain is more intelligent than the current intelligent autonomous systems. In the same aspect the intelligent autonomous systems usually behaves based on the program on each task, the basic fundamental on the autonomous systems behavior is that it behaves consistently on all the scenarios. Whereas human brain cannot do this, which is the major failure of human being on which the autonomous systems has overcome the problem, now we are trying to replicate or inject the emotion and common sense and behavior to intelligent autonomous systems.

The intelligent autonomous systems uses a wide array of knowledge representations, some of these include parametric knowledge, spatial knowledge, and symbolic knowledge. Production of knowledge is dominantly organized in disciplines. At the same time, multidisciplinary and interdisciplinary research is developing at the boundaries of the scientific disciplines. The requirement for multiple disciplinary is emerging at a time when pace and complexity of science and technology is accelerating, such as in the fields of bioinformatics, health, and robotics [7].

In a complex dynamical world, decision-making and acting is only possible under conditions of bounded rationality. Bounded rationality results from limitations on our knowledge, cognitive capabilities, and time.

Our perceptions are selective, our knowledge of the real world is incomplete, our mental models are simplified, and our powers of deduction and inference are weak and fallible. Emotional and subconscious factors affect our behavior. Deliberation takes time and we must often make decisions before we are ready [1] [6]. in simple terms our brain works based on the routine activities, irrespective of the acquired knowledge, so each time if we give little time to recall or revisit the connecting point for current scenario's then our brain can do better then what is expected. In the today's robotics world, the knowledge representation must not be restricted to explicit declarations, which includes the tacit background knowledge, change of emotional states, personal attitudes, and situations with increasing complexity are challenges of modeling information and communication systems.

The current research and development on Artificial Intelligence, Expert System, Artificial Neural Network, Intelligence Autonomous System, we have more focused on the outer layer, middle layer and currently looking into the inner layer in order to represent human intelligence. The human intelligence are gained by the way of multidisciplinary, transdisciplinary and intelligent disciplinary. The word intelligent disciplinary is coined due to when we say the disciplinary it is act of behavior in the intelligent way.

When it comes to the transdisciplinary approach, our brains are well connected network, well established and worlds biggest network, because each and every organ

In this paper we compare disciplinary and non-disciplinary forms of knowledge representation, discuss the evolution of disciplines and transdisciplinary approach in terms of cognitive developmental robotics (CDR). The CDR are widely discussed research area, in that Trans-disciplinary knowledge representation is consider to be a necessary condition to represent and design “subjectivity” in cognitive developmental robotics.

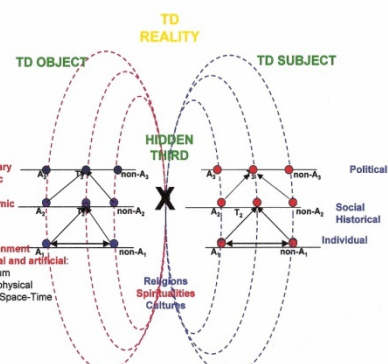


Fig. 2. Transdisciplinary Representation

act independently and dependently on one system, in which each stage brain plays a vital role to provide the intelligence on the fly. Therefore our current intelligent autonomous systems application should be more robust, which can work in multidimensional, round the clock and dynamic in nature, which means inter-relation between the four pillars of the Transdisciplinary approach of learning: how to learn to make while learning to know, and how to learn to be while learning to live together with? In the transdisciplinary vision, there is a transrelation connecting the four pillars of the new system of learning mechanism while representing the knowledge for intelligent autonomous system.

2 Background

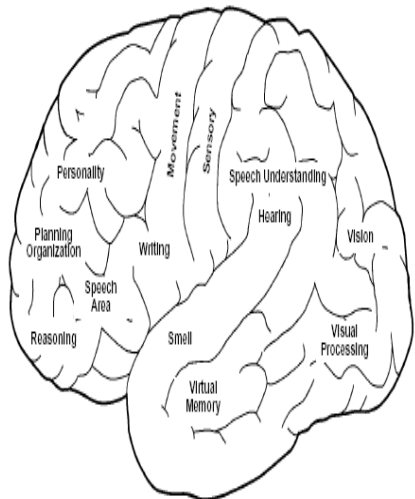
Current learning & knowledge representation should go in across disciplinary, not only interdisciplinary, multidisciplinary and transdisciplinary. Because if there was a supercomputer into which one could load all the knowledge from all existing disciplines, than this supercomputer would be capable of knowing everything while understanding nothing. A user of such computer would have immediate access to any results (content) from any discipline, but would be incapable of understanding their meanings [12]. The meaning is hidden in connections between the different disciplines, with other words, each discipline gives other discipline a meaning and consequently also a new content.

Brain, in the human organism, e.g. walking is a complex bodily self-organization, largely without central control of brain and consciousness: It is driven by the dynamical pattern of a steady periodic motion, the attractor of the motor system. Motor intelligence emerges without internal symbolic representations.

Emotion, Geschwind suggested that some neurological control structures have dual activations, one from below-from the emotions-one from above-the intellect. We smile, cry, and laugh from emotional signals: our attempt to-mimic these acts from intellectual desires or upon receipt of a verbal command to do so recreates neither the true emotion, nor the same motor actions. An observer can often tell which behavior is real, which synthetic.

Learning, “learning-through-action”, the objective is to actively involve learners in interacting with their human and material environment, based on the idea that this will lead to a more profound integration of information than perception. Action necessarily implies operationalisation – the implementation of concepts. The learner not only needs to acquire knowledge and know-how, but must also be able to render them operational in real applications. Therefore the learner becomes “active”, implying a better level of learning.

Human neurons interaction, humans in addition are able to comprehend and modify their world in a cognitive way. All these achievements are entirely based on the parallel processing of billions of neuron in the brain. Through theoretical neuroscience an increasingly better understanding of brain function has emerged during the last decades. Algorithms have been developed to simulate perception and action and also to some degree cognitive properties.



Our brains are neural systems which allow quick adaptation to changing situations during the life-time of an organism. In short: they can learn, assess and anticipate. The human brain is a complex system of neurons self-organizing in macroscopic patterns by neuro chemical interactions. Perceptions, emotions, thoughts, and consciousness correspond to these neural patterns. Motor knowledge for instance is learnt in an unknown environment and stored implicitly in the distribution of synaptic weights of the neural nets.

Fig. 3. Brain Segregation areas to illustrate the ANN implementation

3 Literature Survey

Transdisciplinary approach of representation is a specific form of inter disciplinary in which boundaries between and beyond disciplines are transcended and knowledge and perspectives from different scientific disciplines as well as non-scientific sources are integrated (Flinterman et al, 2001)[5] “Multidisciplinary”, according to Klein, is a process for providing a juxtaposition of disciplines that is additive, not integrative; the disciplinary perspectives are not changed, only contrasted[6]. “Interdisciplinary” is a synthesis of two or more disciplines, establishing a new level of discourse and integration of knowledge [5]. For example, when nuclear physics is combined with medicine it leads to new treatments for cancer. When methods from mathematics were transferred to physics, mathematical physics was born, and when they were transferred to meteorological phenomena or stock market processes, they gave rise to chaos theory; transferring methods from particle physics to astrophysics produced quantum cosmology; and from the transfer of computer methods to art, computer art was generated [8].

The disciplinary, multidisciplinary, interdisciplinary and transdisciplinary are like four arrows shot from but a single bow: knowledge. As in the case of disciplinary, transdisciplinary research is not antagonistic but complementary to multidisciplinary and interdisciplinary research. Transdisciplinary is nevertheless radically distinct from multidisciplinary and interdisciplinary because of its goal, the understanding of the present world, which cannot be accomplished in the framework of disciplinary research [13].

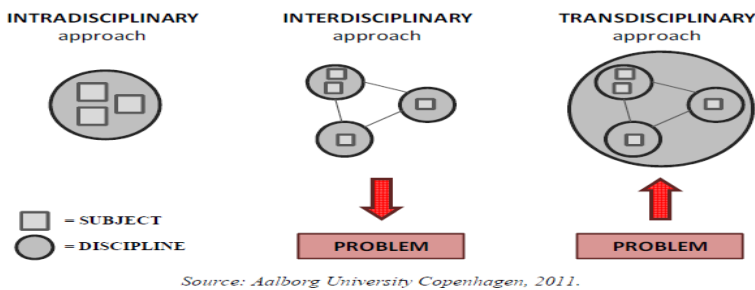


Fig. 4. Comparison of intra-, inter-, and TD approach [12]

Transdisciplinary entails both a new vision and a lived experience. It is a way of self-transformation oriented towards knowledge of the self, the unity of knowledge, and the creation of a new art of living in the society. The report to UNESCO of the International Commission on Education for the Twenty first Century, chaired by Jacques Delors, [7] strongly emphasizes four pillars of a new kind of education: learning to know, learning to do, learning to live together with, and learning to be.

In this context, the Transdisciplinary approach can make an important contribution to the advent of this new type of education.

Table 1: Comparison of disciplinary knowledge (DK) and TD knowledge (TK)

Knowledge DK	Knowledge TK
“IN VITRO”	“IN VIVO”
External world – Object	Correspondence between external world (Object) and internal world (Subject)
Knowledge	Understanding
Analytic intelligence	New type of intelligence – harmony between mind, feelings and body
Oriented towards power and possession	Oriented towards astonishment and sharing
Binary logic	Included middle logic
Exclusion of values	Inclusion of values

Source: B. Nicolescu, *Towards Transdisciplinary Education and Learning*, 2005, p. 3.

Fig. 5. Comparison of disciplinary and transdisciplinary knowledge [12]

AI can be defined as simulation of human intelligence on a machine, so as to make machine efficient identify and use the right piece of knowledge at a given step of solving problem. A system capable of planning and executing the right task at the right time is generally called rational [7].

Neural Network (NN) is an interconnected group of artificial neurons that uses a mathematical or computational model to find patterns in data. The motivation for the development of neural network technology stemmed from the desire to develop an artificial system that could perform intelligent tasks similar to those performed by the human brain [2]. NNs imitate the learning process of human brain to solve many difficult tasks of data management, pattern mapping, pattern recognition etc.

ANNs have the potential for building computing system that do not need to be programmed, simply we can say that ANN is an extremely simplified model of the brain, where it transforms inputs into outputs to the best of its ability[7]:

Expert System, as ES mimics a human expert, it is capable of making mistakes as much as the expert does. For example, if the expert provides wrong rules, the system will make a wrong diagnosis. Also, ES frequently work with incomplete information. Therefore, they provide probabilistic advice, e.g., they are not sure about a certain interpretation or about a diagnosis. In addition to using wrong rules and providing probabilistic answers, the system may ask, like a human expert, wrong questions from the user. However, since we separate the knowledge base from the inference engine and the knowledge is organized in a non-sequential manner (i.e., in independent rules), it is easy to correct mistakes once detected.

4 Proposed Architecture

In the current trends, we begin by placing our argument within the complexity and transdisciplinary literature, and build a theoretical framework for thinking about how complexity is managed through transdisciplinary practice, focusing on two important ways this can be done; the use of collective dialogical processes and building

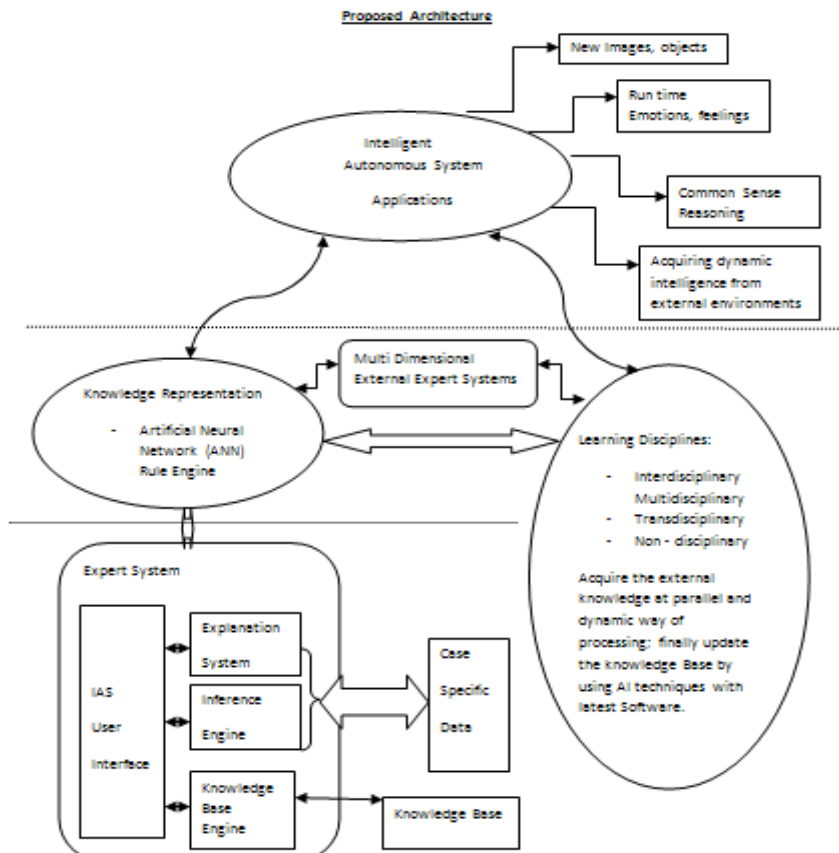


Fig. 6. Flow of IAS interaction with external and internal factors

contextualized holistic frameworks. The following architecture deal with each of the two main points of our argument:

The proposed architecture is to acquire the additional knowledge such as common sense, feelings, and emotions by the way of dynamic and parallel processing , in which the robotics perform the predefined activities, apart from this it also obtain the external entities and pass this information to ANN rule engine system. The ANN rule engine system interact with the expert system in order to differentiate the existing and newly acquired knowledge, finally uses the external system to define the newly acquired knowledge by the way of interdisciplinary, multidisciplinary, transdisciplinary and non transdisciplinary approach of learning.

In the above proposed architecture, simulate the embodied mind, where embodied mind is obviously a complex dynamical system acting and reacting in dynamically changing situations. The emergence of cognitive and emotional states is made possible by brain dynamics which can be modeled by neural networks. But Artificial Neural Networks and artificial minds could have their own intentionality, cognitive and emotional states that cannot be forecast and computed like in the case of natural minds. Limitations of computability are characteristic features of complex systems.

Human experts do not only rely on explicit (declarative) rule-based representations, but also on intuition and implicit (procedural) knowledge [3]. Moreover, as already Wittgenstein knew, our understanding depends on situations. The situations of representations are a severe problem of informatics.

Transdisciplinary knowledge representation is necessary for the above architecture:

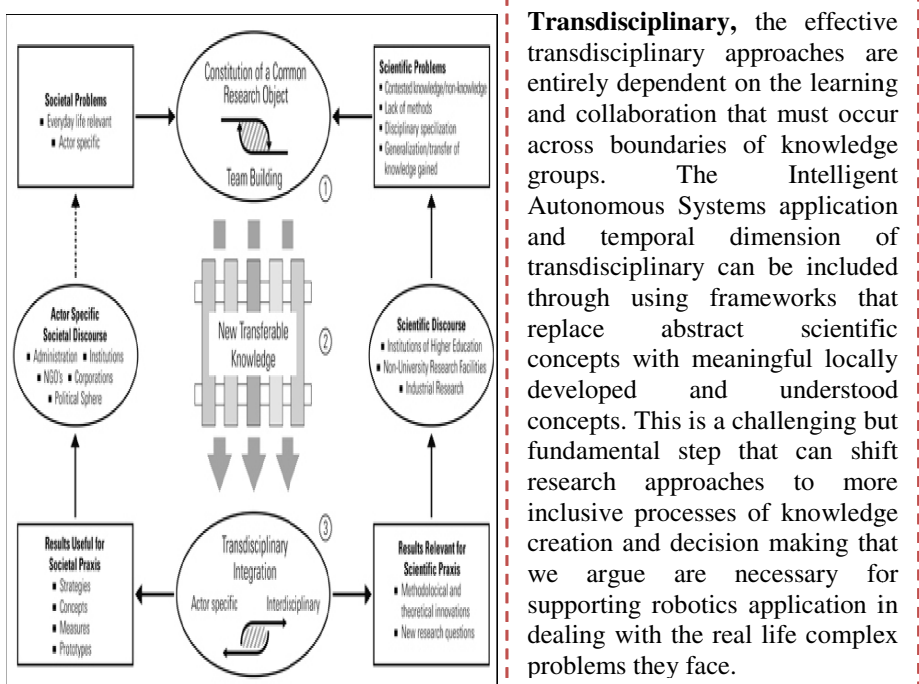
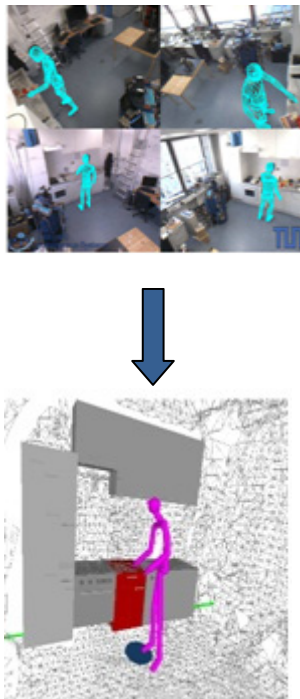


Fig. 7. The Transdisciplinary representation & integration

The intelligent autonomous systems acquire an auxiliary knowledge, when we have robust, dynamic and inter-linked NN rule engine, Multiple Domain Expert System and across learning transdisciplinary knowledge representation. The below figure explains the simple human activities involved in the kitchen, the same knowledge is to be observed into transdisciplinary approach to represent the knowledge for intelligent autonomous systems.



A robot, e.g., needs a complete symbolic representation of a situation, which has to be updated, if the robot's position is changed. How can the robot prevent incomplete knowledge? How can it distinguish between reality and its relative perspective? Situated agents like human beings do not need symbolic representations and constant updating. They look, talk, and interact bodily, e.g., by pointing to things. Even rational acting in sudden situations does not depend on internal representations and logical inferences, but on bodily interactions with a situation (e.g. looking, feeling, and reacting). Thus, we distinguish formal and embodied acting in games with more or less similarity to real life: Chess for instance is a formal game with complete representations, precisely defined states, board positions, and formal operations.

Fig. 8. Sample of Human activities observation to represent the knowledge into robotics

5 Conclusion

In today's intelligent autonomous systems, Robots are innately real-time systems. In servo level the real-time mean tens or hundreds of cycles per second. Current research work focus widely on robotics, where research scholars, innovators, professors, scientists involved in elaborating the existing techniques and methods of knowledge representations. In line with this, we have discussed how to simulate or achieve the human brain behavior and acquiring auxiliary knowledge with an existing knowledge into the intelligent autonomous systems.

In this paper, we have discussed importance of transdisciplinary approach of learning for current intelligent autonomous systems, types of knowledge representations, need of transdisciplinary approach, types and evolution of disciplinary and importance of transdisciplinary knowledge representation. But in the ongoing research and development it is very important to segregate and narrow down the transdisciplinary knowledge representation in each segment, since even in our learning process we are still in the path of perfection to adapt the transdisciplinary approach of learning, which needs to be co-related and inclined with the intelligent autonomous systems applications.

Acknowledgments. I am very grateful to my institution for their constant support. I sincerely thank Dr. N.N.S.S.R.K Prasad for his valuable guidance, suggestions, useful remarks, and productive discussion which helped me to improve the content and presentation of this paper.

References

1. Kalashankar, Prasad, N.N.S.S.R.K.: An Innovative Future Classroom with an Intelligent Autonomous System – in a Transdisciplinary Approach. In: IETET – 2012, GIIMT, Haryana, India (2012)
2. Merleau-Ponty, M.: Phenomenology of Perception. Routledge & Kegan Paul (1962)
3. Dreyfus, H.L.: What Computer's can't do – The Limits of Artificial Intelligence. Harper & Row, New York (1979)
4. Madhavan, R., Yu, W., Biggs, G., Schlenoff, C., Huang, H.M.: IEEE RAS Standing Committee for Standards Activities: History and Status Update
5. Journal of the Robotics Society of Japan, Special Issue on Activities of International Standards for Robot Technologies 29 (May 2011)
6. van den Besselaar, P., Heimeriks, G.: Disciplinary, Multidisciplinary, Interdisciplinary - Concepts and Indicators –8th CSI, Sydney (2011)
7. Russel, S., Norvig, P.: Artificial Intelligence: A Modern Approach. Prentice-Hall, Englewood Cliffs (1995)
8. Apgar, J.M., Argumedo, A., Allen, W.: Building Transdisciplinarity for Managing Complexity: Lessons from Indigenous Practice. International Journal of Interdisciplinary Social Sciences 4(5), 255–270 (2009)
9. Balke, W.-T., Mainzer, K.: Knowledge Representation and the Embodied Mind: Towards a Philosophy and Technology of Personalized Informatics, Germany
10. Mainzer, K.: Thinking in Complexity. In: The Computational Dynamics of Matter, Mind, and Mankind, 4th edn. Springer, New York (2004)
11. Mainzer, K.: KI - Künstliche Intelligenz. Grundlagen intelligenter Systeme. Wissenschaftliche Buchgesellschaft, Darmstadt, Germany (2003)
12. Cerar, J.: Master Thesis on Transdisciplinary Sustainability Development
13. Nicolescu, B.: The transdisciplinary evolution of learning – CIRET

Differential Trace in Learning of Value Function with a Neural Network

Katsunari Shibata and Shuji Enoki

Department of Electrical and Electronic Engineering,Oita University
700,Dannooharu,870-1192 Oita Japan
shibata@oita-u.ac.jp, magic.hands1988@gmail.com

Abstract. Reinforcement learning has a fatal problem of slow learning. To solve this problem, Eligibility-trace has been widely used. However, since the trace throws away old information and takes the present information constantly not depending on whether the information is important or not, long-term learning and short-term learning are incompatible. In this paper, a novel approach called "Differential trace" is proposed, in which the trace is not updated constantly, but according to the change of each neuron's output in a neural network. In other words, the time axis is subjectively adjusted in each neuron. The characteristics of the Differential trace could be observed in the learning of state value in a simple task where one-dimensional continuous environment is divided into 100 states. The learning performance is better in total than the case of Eligibility trace with either of two decay rates.

1 Introduction

In recent years, reinforcement learning[1] which is a way to learn appropriate actions through trials and errors based on reward and punishment as a scalar signal, has been attracting attention because of its autonomous learning ability. It has been shown that through reinforcement learning, necessary functions emerge in a neural network (NN) that connects from sensors to motors[2]. However, reinforcement learning has a fatal problem of slow learning due to the exploration and also extraction of important information from a huge amount of spatio-temporal sensor signals. In the original algorithm, which is called "Onestep" method here, only the value function at the previous time step is learned from the present value and reinforcement signal, and that is also one major reason of slow learning. To solve this problem, Eligibility-trace (E-trace)[3][4] has been widely used that enables to update the values for the past series of states in real-time by holding the information about the visited states in the past. However, the past information in the E-trace decays constantly regardless of whether it is important or not. Therefore, if the trace is set to decay slowly in order to hold the past state, since taken information for a moment is relatively small than the whole information held in the trace, learning for quick motions becomes slow. On the other hand, if the trace decays quickly, the past information can be held only in a short period.

Here, for example, suppose that you are driving a car. Do you think as "go straight, go straight ..., go straight, turn right," with a fixed-time interval? No one might think as such. Rather, you must think as "now go straight, and turn right at the corner with the second signal" and so on. The thinking in the former way is obviously inefficient. Learning of action planning for one day with the sampling rate of 100 msec is very inefficient, while fine actions cannot be learned with the sampling rate of one minute. Accordingly, as in the latter example, important points should be focused and trivial points should be ignored. This means that time passes slowly for the important state and passes quickly for the trivial state. That is to say, if the time axis is adjusted subjectively, learning is expected to be more efficient.

When a robot learns something in the real world, it obtains sensor signals from various sensors, and they change from moment to moment. The quantity of information is huge, and so it is a difficult and intelligent task to know what is important among it. However, a neural network has an ability to represent important information in its hidden layer through learning without any directions from humans. Furthermore, the division of roles among hidden neurons progresses through learning. It can be said that each neuron represents the state subjectively. In the proposed method in this paper, the state change that is the time derivative of the output in each neuron is utilized to adjust how much present information is taken into the traces. The trace, the authors call "differential trace (D-trace)". In each neuron, when the output changes largely, considering that the state changes largely, the traces throw away the information about the old inputs and take the present inputs largely. When the output does not change so much, it is considered that the state does not change largely and there is no need to take the present inputs into the trace. In this way, each neuron takes the inputs in the traces only when its output changes, and keeps the previous traces when its output does not change. Furthermore, as mentioned, each neuron responds different events due to the division of roles among hidden neurons, and so the information held in the traces is different among the hidden neurons. The D-trace promotes the learning for the past event, and the learning promotes the effective memory of the past in the D-trace. The synergetic effect is expected to accelerate reinforcement learning when considering life-long learning where the knowledge or representation acquires through learning can be utilized in the following learning.

In this paper, the algorithm of D-trace is formulated comparing with the E-trace and its characteristics are observed in a simple task in which only value function is learned.

2 “Differential Trace” vs. “Eligibility Trace”

In this section, E-trace, D-trace and the learning of value function using the traces are formulated when they are implemented in a layered neural network (NN). Only the learning of value function is focused and action selection is not considered here. In the original "Onestep" reinforcement learning, each weight

value w in the neural network are updated to decrease TD(Temporal Difference) error as

$$E_t = \frac{1}{2} TDerr_t^2 \quad (1)$$

$$\text{where } TDerr_t = r_{t+1} + \gamma O_{N1,t+1} - O_{N1,t}$$

$$\begin{aligned} \Delta w_{kji,t} &= -\eta \cdot \frac{\partial E_t}{\partial w_{kji}} = \eta \cdot TDerr_t \cdot \frac{\partial O_{N1,t}}{\partial w_{kji}} \\ &= \eta \cdot TDerr_t \cdot \frac{\partial O_{N1,t}}{\partial U_{kj,t}} \cdot \frac{\partial U_{kj,t}}{\partial w_{kji}} \\ &= \eta \cdot TDerr_t \cdot C_{kj,t} \cdot O_{k-1,i,t} \\ &\text{where } C_{kj,t} = \frac{\partial O_{N1,t}}{\partial U_{kj,t}} \end{aligned} \quad (2)$$

where subscript k, j, i indicate the layer number, the number of signal-receiving neuron, and the number of signal-sending neuron in the NN. N indicates the output layer, and there is only one output neuron in the layer that is learned to represent the state value. U and O is the internal state and output of a neuron, and $O = \text{sigmoid}(U)$ where *sigmoid* is the sigmoid function as an output function. r is a given rewards, γ is a discount factor and η is a learning rate. $C_{kj,t}$ indicates the contribution of the neuron j in the layer k to the output, and that is similar to propagated error δ in BP (Error Back Propagation) but no error information is included. It can be computed through backward propagation from the output neuron in the same way as δ . In this algorithm only the present influence of the weight to the output neuron $\partial O_{N1,t}/\partial w_{kji}$ is considered and then the NN is updated so as to reduce the TD error for the present state.

On the other hand, using E-trace e that accumulates the past information in it as a discrete approximation of the first-order lag, the values for the past states also can be updated in real-time as

$$e_{kji,t} = \gamma \lambda e_{kji,t-1} + (1 - \lambda) C_{kj,t} \cdot O_{k-1,i,t} \quad (3)$$

$$\text{where } \lambda \in [0, 1)$$

$$\Delta w_{kji,t} = \eta \cdot TDerr_t \cdot e_{kji,t} \quad (4)$$

where λ is a constant to decide how fast the E-trace decays. If λ is large and close to 1.0, the E-trace decays slowly. Since λ is a constant, the E-trace decays constantly. When E-trace is formulated, generally, no coefficient is multiplied to the second term in Eq(3). However, here, $(1 - \lambda)$ is multiplied to make the E-trace compatible with the other cases. By this, if $C_{kj,t} \cdot O_{k-1,i,t}$ does not change for a long time, the E-trace converges to the value.

Finally, the D-trace d is updated according to the output change of each neuron instead of the constant λ as

$$d_{kji,t} = \gamma (1 - |\Delta O_{kj,t}|) d_{kji,t-1} + |\Delta O_{kj,t}| C_{kj,t} \cdot O_{k-1,i,t} \quad (5)$$

$$\text{where } \Delta O_{kj,t} = O_{kj,t} - O_{kj,t-1}$$

$$\Delta w_{kji,t} = \eta \cdot TD_err_t \cdot d_{kji,t}. \quad (6)$$

When Eq(5) is seen as the difference approximation of first-order lag, large ΔO means small time constant, and the trace value is replaced largely by the present input. It can be considered that the time passes fast. When ΔO is small, the time constant is large, and the time passes slowly. In other words, it is possible to adjust the time axis flexibility according to the change of subjective state ΔO . Since ΔO is calculated in each neuron, it is known that the information that each trace holds is different among neurons.

Fig.1 illustrates the temporal change of E-trace and D-trace. It can be seen that when the output changes, the present input is taken into the D-trace, while the D-trace value is held when the output does not change except for the decay by the discount factor γ .

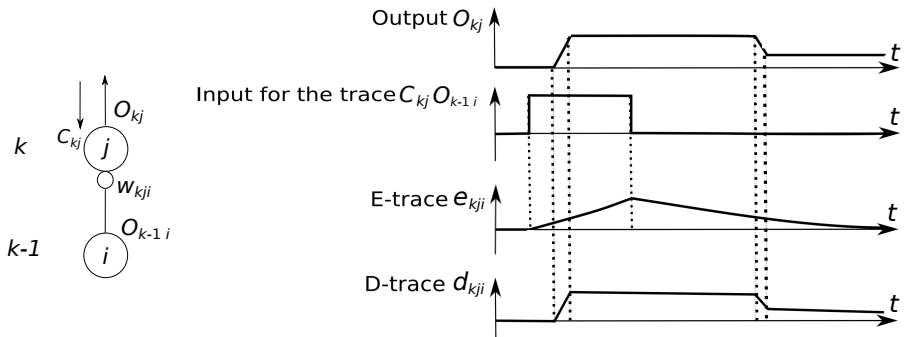


Fig. 1. Comparison of temporal change between E-trace and D-trace

3 Task

In this section, a task in which the characteristics of each trace are easy to be seen is described. As shown in Fig.2, an agent just moves rightward from the left end to the goal at the right end constantly for 10,000 steps with no action selection. When it reaches the goal, reward 1.0 is given. The agent learns the state value during the episode using a 3-layer neural network. The way from start to goal is divided into 100 discrete states and it takes 100 steps to go through each state. There are two types of input signals that respond locally only when the agent is on one state. One type of them takes the value of 1 when the agent is on the corresponding state, and 0 otherwise. The other type inputs change its value linearly from 0 to 1 over 100 steps on the state so that the agent can identify the place in the state. In this task, since each input represents only local information and the generalization ability of the neural network does not work effectively, the effect of holding the past state in the traces can be seen easily.

Parameters used in this learning are shown in Table 1. The learning rate also influences the learning speed, and is roughly optimized through trials and errors. The reason why it is small in the case of Onestep is that some oscillation

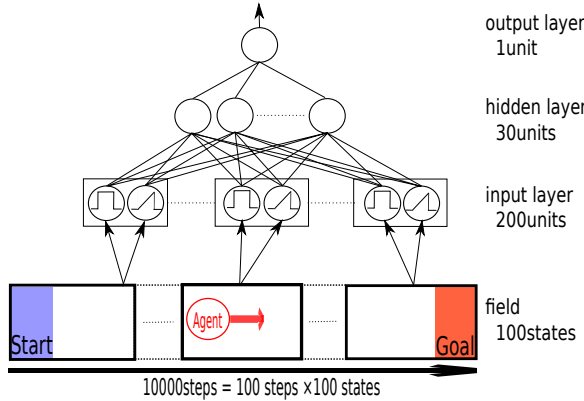


Fig. 2. A task to observe the characteristics of E-trace and D-trace

is observed when the learning is done with the same rate (2.0, 20.0) as the other cases. The discount factor γ was set so as that the state value is 0.2 at the first step and 1.0 at the goal. The sigmoid function whose value ranges from -0.5 to 0.5 is used. The value is linearly transformed to the range of [0.0, 1.0] from the range of [-0.4, 0.4] in the output of the NN. The value is limited from -0.4 to 0.4 even though it is less than -0.4 or more than 0.4 originally. Simulation results are compared among "Onestep", "E-trace" and "D-trace", and in the E-trace case, the results for two different decay rates $\lambda = 0.999$ and $\lambda = 0.99$ are shown.

Table. 1. Learning parameters

number of neurons in each layer		200-30-1	
learning rate (hidden → output)	Onestep	E-trace,D-trace	1.0 2.0
learning rate (input → hidden)	Onestep	E-trace,D-trace	10 20
initial weight of neurons	random [-1.0, 1.0]		
reward	1.0		

4 Learning Result

Fig. 3 shows the learning curve for each case. The vertical-axis indicates the absolute value of the difference between actual state value and the ideal one that is decided from the discount factor γ . Each plot shows the average of the error over one episode.

The learning speed is slower in Onestep learning than the cases of using a trace. In the case of E-trace ($\lambda = 0.99$), learning is faster than in the Onestep learning, but is slower than the other two trace learning. As for the other two cases, learning

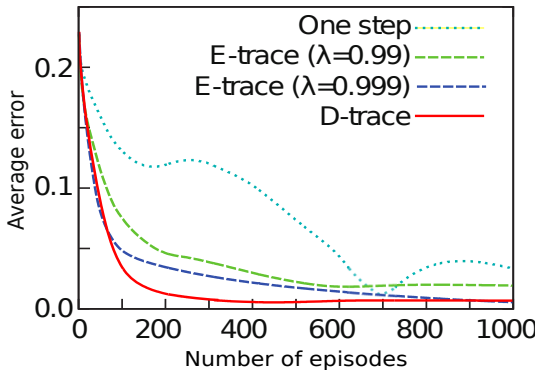


Fig. 3. Change of the average error between the network output and ideal state value during learning is compared among Onestep, E-trace and D-trace

is slightly faster in the case of E-trace($\lambda = 0.999$) at first, but, the difference in D-trace becomes smaller than the case of E-trace($\lambda = 0.999$). In the case of Onestep learning, the difference becomes larger again at around 700th episode after once it became small. Same phenomena are observed also in other cases although the increase is not so large. It was found that such phenomena occur by the influence of local representation of input signals and non-linearity in each neuron. Small learning rate decreases the influence, but learning becomes slow.

To show how the learning progresses in each case, Fig.4 shows the state value at the 100th episode. In the case of Onestep, the value is formed only after around the 7,000th step, and in the case of E-trace($\lambda = 0.99$), the range that the value is formed is a bit wider than the case of Onestep, but appropriate value does not reach in the early states.

On the other hand, in the cases of E-trace($\lambda = 0.999$) and D-trace, the rough shape of the value is formed over whole the episode. However, large high-frequency components are seen in the case of E-trace($\lambda = 0.999$). It is confirmed that the shape is influenced by the initial connection weights. This means that E-trace with a large λ is good at forming a rough shape of value function in a long range, but is not good at forming appropriate value change in a short range. In the case of D-trace, high-frequency components are not so large, and both local and global learning seem to be progressing. Due to the limited number of pages, the result is not shown, but in the case of E-trace for an intermediate decay rate $\lambda = 0.996$, high-frequency component is at the same level as in the case of D-trace, but the global shape is closer to the case of $\lambda = 0.99$.

Fig. 5 shows how D-trace changes as time goes by together with ΔO that is the temporal change in the output of the hidden neuron. Each hidden neuron has one trace for each input, and 200 traces in total. Since the trace shown in Fig. 5 is for the binary input from the 18th state, the value largely increased when the agent reached the 18th state at the 1801st step. After that, the trace increased for 100 steps because the input is 1.0, but the increase ratio is not so

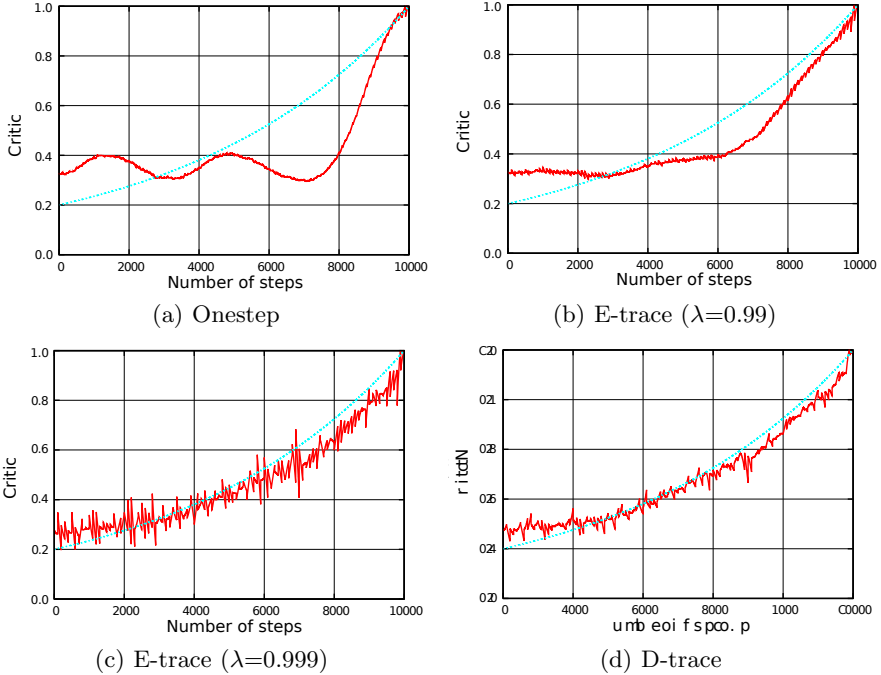


Fig. 4. Comparison of the state value at the 100th episode

large due to the small ΔO . After leaving the state, the value mainly decreased at every 100 step when a state transition occurs. The reduced value is not constant, but depends on the value of ΔO .

Next, it is observed how each trace holds the past information. Fig. 6 shows the trace values of one hidden neuron at the final step in the 100th episode for the 4 cases. Fig. 6 shows the traces for the 100 binary inputs that take always 1.0 when the agent is on the corresponding state. Each trace takes the product of contribution to the output C_{2j} and the input $O_{1,i}$. The contribution C_{2j} depends on the weight to the output and also the derivative of output function in the hidden and output neurons. Therefore, they influence the trace values, but the rough tendency can be seen about which input signal is taken more.

It can be seen that in the case of $\lambda = 0.99$, the value of E-trace for the states close to the goal is large, but that has decayed for the distant states from the goal. On the other hand, in the case of $\lambda = 0.999$, the value is not so large even for the states close to the goal, but the decay is slow and so the trace for the distant state from the goal also has some value. D-trace holds the past information, but in Fig. 6(c), the trace for the input from the 98th state, which is the 3rd state from the goal, takes a larger value comparing with the other trace. The profile is different from that in a different hidden neuron in Fig.6(d). This means that each hidden neuron can hold different past information, and that is supposed to be one reason for the efficient learning.

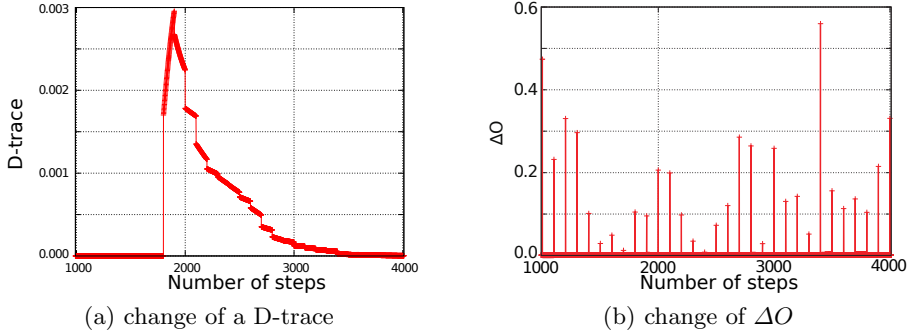


Fig. 5. Change of a D-trace and ΔO of one hidden neuron in the 1000th episode. The D-trace is for the input whose value is 1.0 at the 18th state.

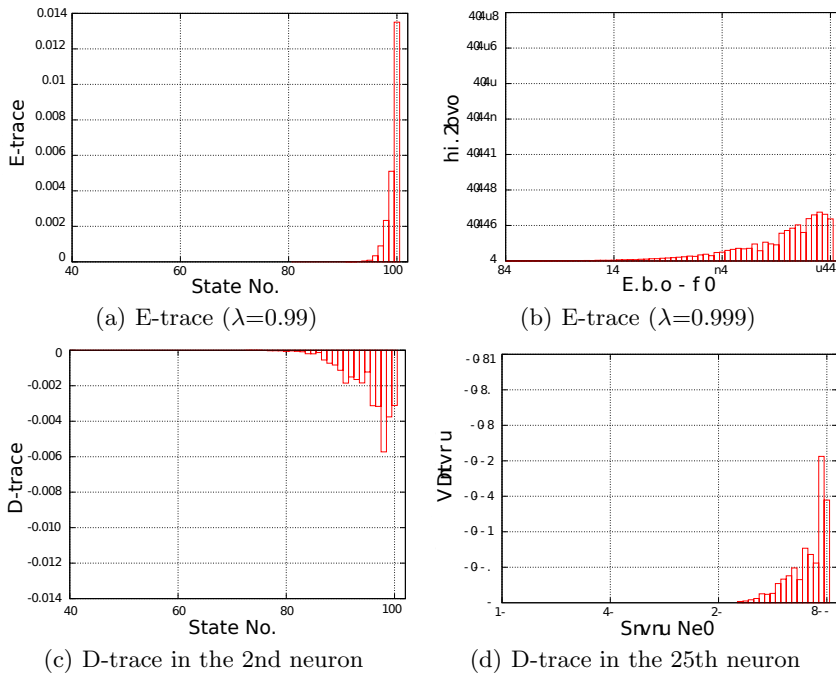


Fig. 6. The trace values for the binary inputs from the 100 states in one hidden neuron at the last(10000th) step in the 100th episode

5 Conclusion

In this paper, a novel approach for learning of value function called "Differential trace (D-trace)" was proposed. That enables to hold the important information for each neuron and to learn the value function for past states efficiently in real

time. In the learning of a simple task in a one-dimensional continuous environment with many local sensors, the characteristics of D-trace was observed, and it was confirmed that the learning performance is better in total than the case of Eligibility trace in either case of fast decay or slow decay.

In the real world, there is a vast amount of information, and so subjective adjustment of time axis must be required to extract important events and to learn effectively. Accordingly, D-trace has a very large potential in the autonomous learning in the real world, and further investigation is strongly demanded. Similar concept has been already introduced in the learning of a recurrent neural network, and it was shown that it works even though the computational cost and necessary memory capacity is as small as $O(N^2)$ where N is the number of neurons[5][6]. The integration of the method and D-trace is expected.

Acknowledgment. This work was supported by JSPS Grant-in-Aid for Scientific Research #23500245.

References

1. Rumelhart, D.E., et al.: Learning Internal Representation by Error Propagation. In: Parallel Distributed Processing, vol. 1, pp. 318–364. MIT Press (1986)
2. Shibata, K.: Emergence of Intelligence through Reinforcement Learning with a Neural Network. In: Mellouk, A. (ed.) Advances in Reinforcement Learning, pp. 99–120. InTech (2011)
3. Sutton, R.S., Barto, A.G.: Reinforcement Learning, pp. 163–192. MIT Press (1988)
4. Bakker, B., Zhumatiy, V., Gruener, G., Schmidhuber, J.: A robot that reinforcement-learns to identify and memorize important previous observation. Intelligent Robots and Systems, 230–235 (2003)
5. Shibata, K., Ito, K., Okabe, Y.: Simple Learning Algorithm for Recurrent Networks to Realize Short-Term Memories. In: Proc. of IJCNN (Int'l Joint Conf. on Neural Networks), pp. 2367–2372 (1988)
6. Samsudin, M.F.B., Hirose, T., Shibata, K.: Practical Recurrent Learning (PRL) in the Discrete Time Domain. In: Ishikawa, M., Doya, K., Miyamoto, H., Yamakawa, T. (eds.) ICONIP 2007, Part I. LNCS, vol. 4984, pp. 228–237. Springer, Heidelberg (2008)

Episodic Memory Design for Predicting the User's Intention

Seung-Hwan Choi, Woo-Ri Ko, and Jong-Hwan Kim

Department of Electrical Engineering, KAIST, 291 Daehak-ro, Yuseong-gu,
Daejeon, 305-701, Republic of Korea
`{shchoi,wrko,johkim}@rit.kaist.ac.kr`

Abstract. These days, people can easily access various services through IT devices. However, in most cases, the user has to spend much time in configuring the right options to get the exact desired service. To solve this kind of service problem, this paper proposes a service system with the episodic memory for predicting the user's intention. The interaction agent is developed for seamless and interactive service with the episodic memory. The episodic memory records the history of the user's requests when the user utilizes the service agent. Also, the reliability of the episode is proposed for predicting user's intention. The effectiveness and applicability of the proposed system are demonstrated through the experiments.

Keywords: episodic memory, intention prediction, interactive service.

1 Introduction

In recent years, various IT devices have been developed and they provide many services to people. The news, expert knowledge, and entertainments are easily accessible through the internet and PC. Mobile devices including smart phone provide various services at anyplace and anytime. Naturally, people, these days, spend much more time to get better service than in the past. However, in most cases, the user has to select options to take the exact service. When the television is turned on, it does not select the channel automatically because it does not know which channel the user wants. Therefore, the user has to select the channel manually. However, if the television is able to understand the user's intention, then it can provide more convenient service to the user.

Lately, there have been research on user intention recognition method to offer a personalized and seamless service for web-browsing [1]-[4], smart home systems [5], [6], healthcare [7], and human-robot interaction [8], etc. The service patterns of the user to build ontology or to cluster users' patterns have been used. Besides, many websites use the cookie which is a piece of text stored on the user's computer by the web browser. It can be used for storing site preferences, shopping cart contents, or anything else that can be accomplished through strong text data. The online shopping site provides the list of products which are searched by the user or recommended based on shopping patterns of the user. This kind of services needs to interact with the user because they should be

updated whenever an undesired service is provided. From this point of view, the interaction between humans is a good guideline. At a restaurant, for example, a customer can choose from many options when he orders a food. Usually, a waiter asks each option one by one. However, a waiter may ask “as usual?” if the customer visits the restaurant often. Most people feel comfortable to the question because it is common in daily life.

This paper proposes a service system with the episodic memory for predicting the user’s intention. The intention prediction algorithm is implemented to the interaction agent with the episodic memory which records histories of the user’s service commands. The structure of the episodic memory and the reliability of the episode are proposed to predict user’s intention. Additionally, the system tries to talk with the user to provide a proper service as is done between humans. Each agent was developed based on modular design approach and, therefore, the proposed system can be easily applied to other systems as well.

The remainder of this paper is organized as follows. Section II describes the data structure of episodic memory for service commands and its maintenance processing. Section III proposes the system for service and the intention prediction algorithm. In Sections IV, the experimental results are described. Finally, the concluding remarks follow in Section V.

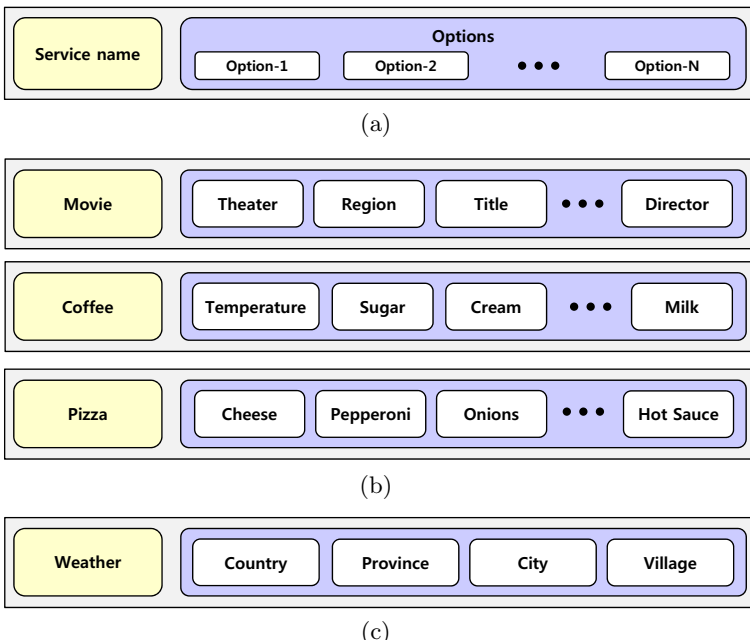


Fig. 1. (a) The structure of the service information. (b) The example structures of the services about movie tickets, coffee, and pizza. (c) The example structure of the service about weather forecast.

2 Episodic Memory for Service Commands

The episodic memory can be used for recommending proper options automatically when the user requests the same service again. In this research, for this kind of seamless service, histories of service command are stored in the episodic memory as an episode. The proposed structure of the episode for representing general services is described in the following subsections.

2.1 The Structure of the Service Information

The service information is a set of essential data for providing services. There are two types of the service information and both one are consist of ‘service name’ and ‘options’ as shown in Fig. 1(a). The first one is that the options of the service information represent the result of the service itself. For example, the services for movie tickets, coffee, and pizza contain all information for service even though they are not physical results as shown in Fig. 1(b). The second one is that the options of the service information are key values to make the result of the service. The service information about weather forecast has four options to represent the address as shown in Fig. 1(c). They are used as key values to access the database which has the weather information.

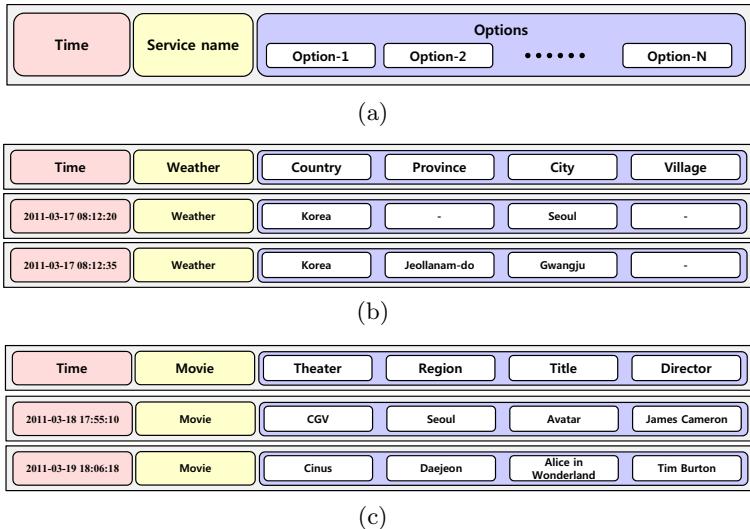


Fig. 2. (a) The structures of the episode. (b) The example episodes of weather forecast. (c) The example episodes of the advance sale of movie tickets.

2.2 The Structure of the Episode for Representing Services

The structure of the episode for representing services is similar to one of the service information because the episode is a history of each requested service command. It additionally has ‘time’ field which records the time when the episode was occurred. Fig. 2 shows the proposed structure of the episode. The episode may have null value for several fields because it is possible to skip the selection of several options by users choice.

2.3 Maintenance

Whenever the user interacts to a service agent, the episode is occurred. However, the episode which is occurred when the service is provided successfully is only meaningful and it is recorded to the episodic memory. Also, the episode should be removed from the episodic memory to adapt to the users new pattern. Every episode is removed after predefined episode life time such as one week or one month.

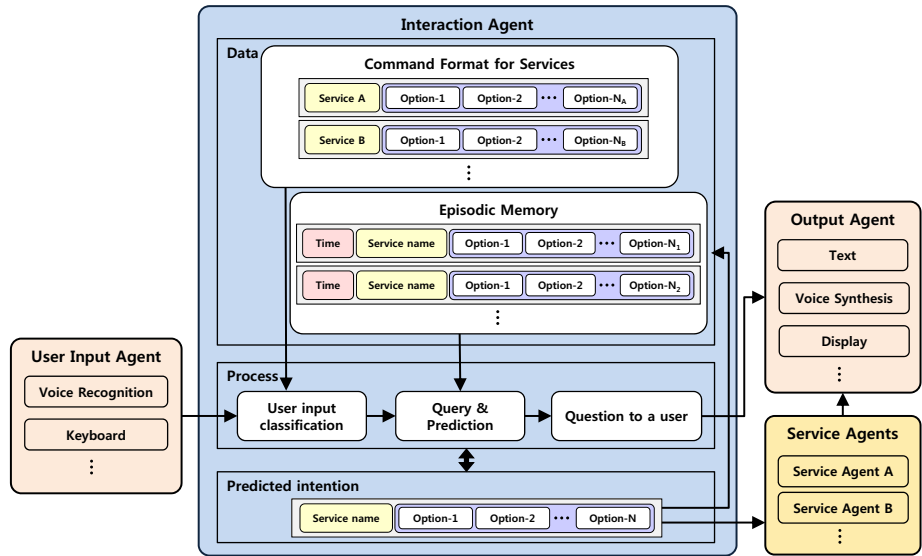


Fig. 3. Overall system for predicting the user’s intention by using episodic memory

3 System for Services

The proposed system consists of the user input agent, the output agent, the interaction agent, and the service agents (Fig. 3). The user input agent transfers text or voice data from the user to the interaction agent. The output agent transfers interaction data from the interaction agent to the user. Also, the service results from the service agents are shown to the user though the output agent.

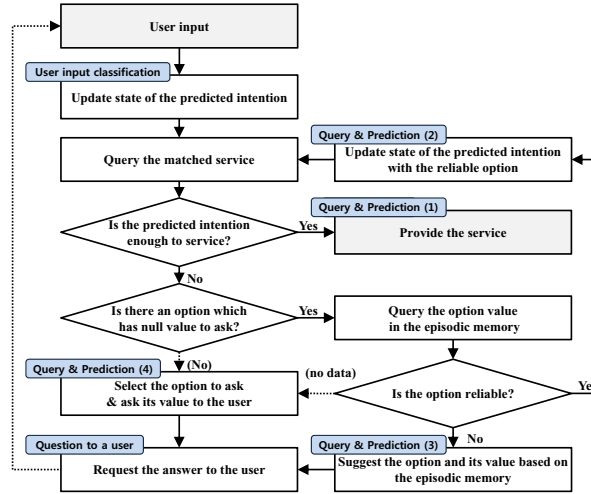


Fig. 4. The flowchart of interaction-based service providing

The service agent should be activated itself by registering the command format for its service to the interaction agent.

The interaction agent updates the status of the predicted intention by using the service agent information and the episodic memory. It reports the selected service to a proper service agent when the status of the predicted intention has enough valid option values to decide the service. The status of the predicted intention is updated by ‘user input classification,’ ‘query and prediction,’ and ‘question to a user’ processes (Fig. 4). The processes are briefly described in the following.

3.1 User Input Classification

The user input classification process is the first step of the processes when the user inputs new data. If the input data is the service name, then the status of the predicted intention is initialized and a new service command is assigned. If it is a value of an option, then it is assigned to the corresponding option of the status of the predicted intention. When the interaction agent asks a question with the expected answer to the user, it can be an answer such as “yes” or “no.” In this case, the expected answer is assigned instead.

3.2 Query and Prediction

The query and prediction process is the step for predicting the best service command. The interaction agent searches for the matched service command in the service agent information which satisfies the status of the predicted intention. If the status of the predicted intention is ready to provide service, then the

predicting result is reported to the corresponding service agent (Case 1). The maximum amount of data that can be managed by the service agent is defined and it is settled when the service agent was registered to the interaction module. If there are too many searched data, it means the status of the predicted intention needs a more specific value for options. If there is an available option in the status of the predicted intention, the interaction agent finds out the option value which has the highest reliability in the episodic memory. The reliability of episode e , $R_e(e)$, and the reliability of the option value v , $R_v(v)$, are defined as follows:

$$R_e(e) = \frac{e_t}{T}, \quad (1)$$

$$R_v(v) = \frac{\sum_j R_e(e'_j)}{\sum_i R_e(e_i)} \quad (2)$$

where e_t is the residual life time of episode e , T is the life time of an episode, $E = \{e_1, e_2, \dots, e_N\}$ is a set of episodes in the episodic memory, N is the number of episodes, $E_v = \{e' | e \text{ has option value } v, e \in E\}$.

The searched option value is assigned to the status of the predicted intention, if its reliability is greater than predefined thread hold such as 0.6 (Case 2). Otherwise, it is assigned only if the user confirms it (Case 3). If there are not enough episodes in the episodic memory to calculate the reliability, then the interaction module selects the option in order and asks its value to the user again (Case 4).

3.3 Question to a User

The question to a user process is the transferring step to request the option value to the user. The interaction agent transfers the question to the output agent and the output agent represents it to message, voice synthesis, or an image. Also, the service agent sends the service result to the output agent to provide it to the user.

4 Experiments

The dialogue agent, the display agent, two service agents, and the interaction agent were implemented for experiments as shown in Fig. 5. The dialogue agent is the program which connects the interaction agent and the user through text and voice interface. Two service agents, the weather forecast agent and the movie ticket agent, generates the result image and sends it to the display agent. The user takes a service through the displayed image.

4.1 The Weather Forecast

4.1.1 Command Format

The service command of the weather forecast agent consisted of three options which were ‘city,’ ‘gu,’ and ‘dong’ as shown in Fig. 6. These are the unit of the administrative district of Korea. The maximum amount of data that can be managed by the weather forecast agent is defined by 1.

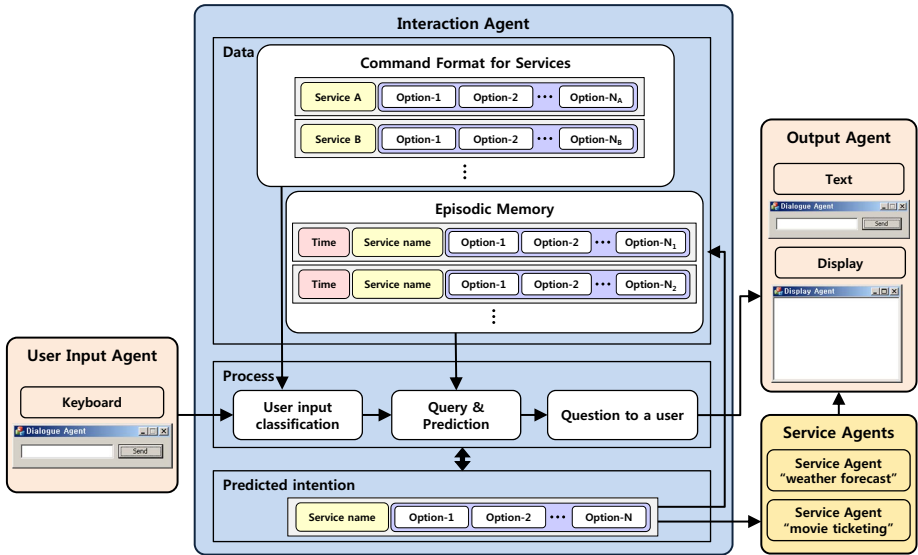


Fig. 5. The system setup for experiments

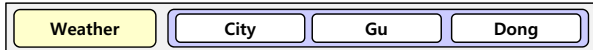


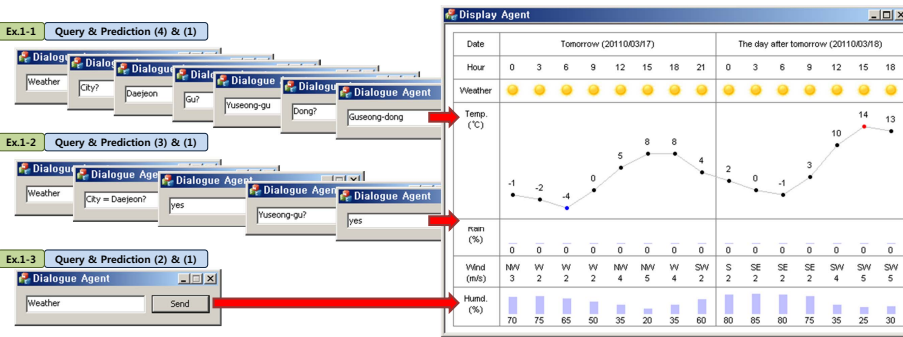
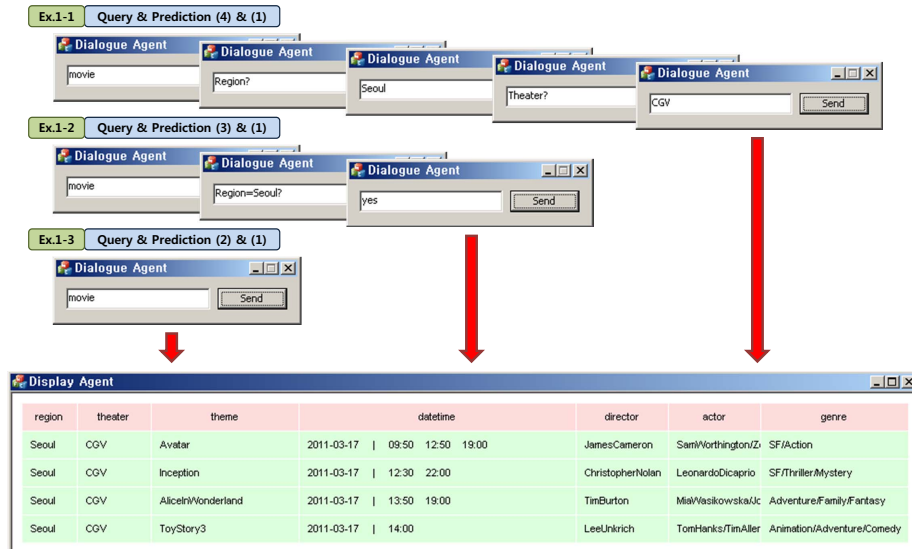
Fig. 6. The command format of the weather forecast agent

4.1.2 Weather Forecast Agent

When the address data from the interactive agent is transferred, the weather forecast agent accesses the corresponding XML data in the internet portal site. The XML data has the information of 'temperature,' 'probability of rain,' 'direction and speed of wind,' and 'humidity' for every three hours during 48 hours from now. This information was represented with the image and it was transferred to the display agent.

4.1.3 Analysis

Fig. 7 shows the experimental results of the proposed system with weather forecast agent. The service was provided when the user inputted the all option value in order at first (Ex. 1-1). After the episodic memory stored several episodes, the service agent tried to interact with more natural communication. The agent suggested 'Daejeon' and 'Yuseong-gu' because they were the most reliable values for this service (Ex. 1-2). Finally, the agent automatically provided the weather in 'Daejeon Yuseong-gu Guseong-dong' without any question (Ex. 1-3).

**Fig. 7.** The experimental results with the weather forecast agent**Fig. 8.** The command format of the movie ticket agent**Fig. 9.** The experimental results with the movie ticket agent

4.2 The Advance Sale of Movie Tickets

4.2.1 Command Format

The service command of the movie ticket agent consisted of eight options which are ‘region,’ ‘theater,’ ‘theme,’ ‘date,’ ‘time,’ ‘director,’ ‘actor,’ and ‘genre’

(Fig. 8). The movie schedule data were collected from internet portal site by using HTML parser before this experiment. The maximum amount of data that can be managed by the movie ticket agent is defined by 10.

4.2.2 Movie Ticket Agent

When the service command is transferred to the movie ticket agent, the agent represents the service result to the image. Then, the result image is transferred to the display agent.

4.2.3 Analysis

Fig. 9 shows the experimental results of the proposed system with the movie ticket agent. Like the experiment with the weather forecast agent, the service was provided when the user inputted the all option values in order at first (Ex. 2-1). After the episodic memory stored several episodes, the service agent suggested reliable option value ‘Seoul’ instead of asking in order (Ex. 2-2). Finally, the agent automatically provided the ticket information without any question (Ex. 2-3).

5 Conclusion

This paper proposed the service system with the episodic memory for predicting the user’s intention. The structure of the episodic memory for representing requested services was defined and implemented. The reliability of the episode memory was proposed to predict user’s intention. Two different types of software agents were implemented for the experiments. Also, the research showed natural and convenient service system successfully by providing the interaction between the prediction algorithm and the user. Moreover, the proposed system can be easily applied to other systems because the user input, the output agent, the software agent and the interaction agent were developed independently. As further works, the algorithm for predicting user’s intention should be improved because the reliability does not consider the relation among options.

Acknowledgement. This research was supported by the MKE(The Ministry of Knowledge Economy), Korea, under the Human Resources Development Program for Convergence Robot Specialists support program supervised by the NIPA(National IT Industry Promotion Agency) (NIPA-2012-H1502-12-1002).

References

1. Ge, J., et al.: Cooperative recommendation based on ontology construction. In: 2008 Int. Conf. Computer Science and Software Engineering, Wuhan, China, pp. 301–304 (2008)
2. Cheng, X., Liu, H.: Personalized services research based on web data mining technology. In: Second Int. Symposium on Computational Intelligence and Design, pp. 177–180 (2009)

3. Lu, L., et al.: Sequence pattern recognition in Web Log Mining. *Mini-Micro Compute Systems* (2000)
4. Si, Y., Yang, S.: A web path mining pattern based on improved AprioriAll algorithm. *Journal of Guangxi Normal University: Natural Science Edition* 25(4), 172–175 (2007)
5. Uhm, Y., et al.: Service reconstruction for improving performance using classified service pattern and a session manager-based architecture in smart homes. In: 5th IEEE Consumer Communications and Networking Conference, pp. 326–330 (2008)
6. Hwang, Z., et al.: Service-oriented multi agent middleware using information fusion and service prediction in pervasive environments. In: Second Int. Conf. on Advances in Future Internet, pp. 25–30 (2010)
7. Ros, M., et al.: A system to supervise behaviours using temporal and sensor information. In: 2010 IEEE Int. Conf. on Fuzzy Systems, Barcelona, Spain, pp. 1–8 (July 2010)
8. Han, J.-H., Kim, J.-H.: Human-Robot Interaction by Reading Human Intention based on Mirror-Neuron System. In: IEEE Int. Conf. on Robotics and Biomimetics, Tianjin, China, pp. 561–566 (December 2010)

Behavior Selection Method for Entertainment Robots Using Intelligence Operating Architecture

Woo-Ri Ko and Jong-Hwan Kim

Department of Electrical Engineering, KAIST, 291 Daehak-ro, Yuseong-gu,
Daejeon, 305-701, Republic of Korea
{wrko,johkim}@rit.kaist.ac.kr

Abstract. To get and hold a user's attention, entertainment robots should be able to think and behave like a human being to show various responses in a certain situation. For this purpose, this paper proposes a behavior selection method for entertainment robots using intelligence operating architecture (iOA). The iOA consists of five parts and 15 modules to implement the robot intelligence, which is motivated by the key functions of human brain. In the internal state part, the strengths of the robot's internal states, i.e. motivation, homeostasis, and emotion, are updated. The sensory information is converted to contexts in the context module. Considering both the internal states and contexts, a behavior which is composed of four expressions, i.e. facial expression, gesture, movement, and voice expression, is selected in the problem solving module. To show the effectiveness of the proposed method, a software entertainment robot is implemented for simulations. The simulation results show that entertainment robots with different characteristics can be created and they can generate various behaviors by the proposed behavior selection method.

Keywords: Behavior selection, entertainment robot, robot intelligence, fuzzy integral, fuzzy measure.

1 Introduction

Nowadays, a number of entertainment robots have been developed, which aim to interact with users in a variety of situations. To receive attention from the user and hold the attention, entertainment robots should think and behave like a human being to show various responses depending on its internal state even in the same situation. For this purpose, there has been much research on the behavior selection method for entertainment robots. An expressive gesture generation algorithm was presented for storytelling application [1]. A system for a spontaneous speech recognition, multi-modal dialogue processing and visual perception of a user was developed for a natural human-robot interaction [2]. A composite facial expression generation method was devised to reflect the robot's emotion [3].

In this paper, the intelligence operating architecture (iOA) is used to construct a behavior selection method for entertainment robots [4]. The iOA consists of five parts and 15 modules to implement the robot intelligence. The robot's internal states, i.e. motivation, homeostasis, and emotion, are updated in the internal state part. In the context

module, external situation is defined as a context. Considering both the internal state and the context, the next proper behavior is selected in the problem solving module, which is composed of facial expression, gesture, movement, and voice expression. To diversify the robot's responses, the characteristics of the robot is formed by assigning different preference degrees for each and every internal state and context.

This paper is organized as follows. Section II presents the intelligence operating architecture (iOA), which explains how the intelligence of robots is generated. The behavior selection method using the iOA is proposed in Section III. The effectiveness of the proposed method is illustrated through the simulations in Section IV. The concluding remarks follow in Section V.

2 Intelligence Operating Architecture (iOA)

As shown in Fig. 1, the iOA consists of five parts and 15 modules to implement the robot intelligence [4]. It is motivated by the key functions of the human brain, such as problem solving in the frontal lobe, actions from the motor cortex, etc. In the perception layer, internal and external sensor data are gathered in the internal and external sensing modules, respectively, and the gathered data are converted to context data in the perception module. The three modules in the internal state part, i.e. motivation, homeostasis, and emotion modules, work for controlling internal states. All data including the internal state strengths and the context are shared with other modules through the memory.

There are three kinds of memory: short-term memory (STM), working memory (WM), and long-term memory (LTM). The STM deals with the data required to be remembered for a short time period. Therefore, sensory data are stored in the STM. The LTM, on the other hand, lasts for a few days to a whole lifetime of a robot. It is composed of three sub memories; episodic memory (EM), semantic memory (SM), and procedural memory (PM). The EM stores the events that are related to time and can be described explicitly. However, the SM holds the knowledge which is factual and concept-based. The PM consists of the information about the way of using a certain object or conducting a specific action. Lastly, the WM contains the information currently required to carry out tasks including reasoning, learning, understanding, etc.

A behavior decision procedure is carried out on the reasoning part. By help of the WM, task planning and scheduling are processed in this part. In the problem solving module, the most proper behavior for the robot is selected. Then, this decision is passed to the execution layer and the selected behavior is generated to the exact action by actuating the motor system in the control module. In this paper, some modules in the iOA are realized to develop a behavior selection method for entertainment robots.

3 Behavior Selection Method

In this section, a behavior selection method based on the iOA is described. The key modules for the behavior selection, namely motivation, homeostasis, emotion, context, and problem solving modules are described in the following.

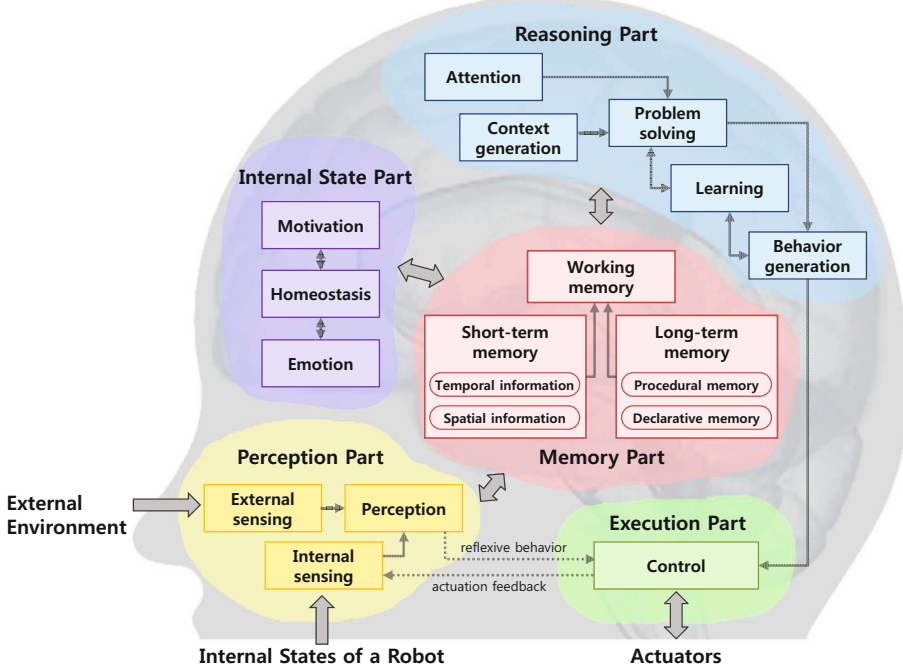


Fig. 1. The intelligence operating architecture (iOA)

3.1 Motivation, Homeostasis, and Emotion Modules

In the motivation, homeostasis, and emotion modules, the internal states of an entertainment robot are defined and the strengths of the internal states are updated. As shown in Table 1, there are eight internal states of the robot. In the motivation module, four motivations, i.e. “curiosity,” “power,” “social contact,” and “tranquility,” are defined based on 16 human basic desires theory [5]. In the homeostasis module, “battery” is defined as the robot’s homeostasis. In the emotion module, an emotion of the robot is represented as a point in a three dimensional coordinates of “arousal,” “valence,” and “stance,” [6].

At time t , the strength of the j th motivation $m_j(t)$, $j = 1, 2, \dots, l$, where l is the number of motivations, is updated by [8].

$$m(t+1) = m(t) + \alpha_j(\bar{m}_j - m_j(t)) + S^T \cdot M_j(t) + \delta_{ij}(t), \quad (1)$$

where α_j is the difference gain, \bar{m}_j is the steady-state value of the j th motivation, S is the stimulus vector, M_j is the strength vector between stimulus and the j th motivation, and $\delta_{ij}(t)$ is the amount of change of the j th motivation strength caused by the previous i th behavior. If the previous i th behavior affects positively on the j th motivation, $\delta_{ij}(t)$ is a positive value. If the previous i th behavior affects negatively on the j th motivation, $\delta_{ij}(t)$ is a negative value. In the same manner, the strengths of homeostasis and emotion are updated. Note that the strengths of motivation and homeostasis are scaled to be

Table 1. The eight internal states of the entertainment robot

Module	Internal state
Motivation	Curiosity (m_1)
	Power (m_2)
	Social contact (m_3)
	Tranquility (m_4)
Homeostasis	Battery (h_1)
Emotion	Arousal (e_1)
	Valence (e_2)
	Stance (e_3)

in $[0, 1]$ and those of emotion are scaled to be in $[-1, 1]$. The normalized strengths of internal states are used in the problem solving module.

3.2 Context Module

In the context module, four contexts are defined for entertainment robots, as shown in Table 2. Since the entertainment robots should entertain more people and respond to the user's voice, "the number of attentive people," "distance to the nearest person," "loudness," and "direction of the loudest sound" are defined as the contexts.

Table 2. The four contexts of the entertainment robot

Context	Scale	Unit
The number of attentive people (c_1)	$0, 1, \dots, 10$	people
Distance to the nearest person (c_2)	$[0, 5]$	meter
Loudness (c_3)	$[0, 100]$	decibel (dB)
Direction of the loudest sound (c_4)	$[-180, 180]$	degree

3.3 Problem Solving Module

In the problem solving module, considering both the robot's internal states and external contexts, the most proper behavior is selected by employing the fuzzy integral. The fuzzy integral is one of the well-known aggregation methods for multi-criteria decision making and it can also reflect the redundancy (negative interaction) or synergy (positive interaction) effects between criteria, i.e. internal states and contexts [7]-[9]. A behavior is composed of four expressions, i.e. facial expression, gesture, movement, and voice expression. A list of expressions is presented in Table 3. The global evaluation value of each expression is calculated by the fuzzy integral with respect to 1) the fuzzy measure values of criteria sets, i.e. internal state and context sets, 2) current internal state strengths and context information, 3) and the partial evaluation values of expressions over criteria. The detailed procedure of behavior selection is described in the following.

Table 3. A list of expressions of the entertainment robot

Expression	Behavior
Facial expression	Normal, anger, disgust, fear, happiness, sadness, surprise, fatigue
Gesture	Raise left hand, raise right hand, raise both hands, lower both arms, wave left hand, wave right hand, wave both hands, hold out left hand, hold out right hand, hold out both hands, rest chin on left hand, rest chin on right hand
Movement	Stand, bow, turn left, turn right, go forward, step back, turn head left, turn head right, bend knee, lean
Voice expression	Hello, hi, nice to meet you, who are you?, bye, have a good day, I am tired

3.3.1 Fuzzy Measure Identification of Criteria Set

To measure the preference degree of a criteria set, i.e. internal state and context set, ϕ_s transformation method is employed for an efficient fuzzy measure identification [10]. In this method, the fuzzy measure values are calculated using a hierarchy diagram of criteria which represents hierarchical interaction relations among criteria. A fuzzy measure $g(A)$, where A is the subset of criteria, is identified as follows:

$$g(A) = \phi_s(\xi_R, \sum_{P \subset R} u_P^R), \quad (2)$$

where R is the root level in the hierarchy diagram, ξ_R is the interaction degree between the criteria sets in the R , ϕ_s is a scaling function [11], and u_Q^P is defined as follows:

$$\phi_s(\xi, u) = \begin{cases} 1, & \text{if } \xi = 1 \text{ and } u > 0 \\ 0, & \text{if } \xi = 1 \text{ and } u = 0 \\ 1, & \text{if } \xi = 0 \text{ and } u = 1 \\ 0, & \text{if } \xi = 0 \text{ and } u < 1 \\ \frac{s^u - 1}{s - 1}, & \text{other cases} \end{cases} \quad (3)$$

$$u_Q^P = \begin{cases} d_i, \text{ where } i \in Q & \text{if } |Q| = 1 \text{ and } i \in A \\ 0 & \text{if } |Q| = 1 \text{ and } i \notin A \\ \phi_s^{-1}(\xi_P, \phi_s(\xi_Q, \sum_{V \subset Q} u_V^Q) \times T_Q^P) & \text{other cases} \end{cases} \quad (4)$$

where $s = (1 - \xi)^2 / \xi^2$, d_i is the preference degree of the i th criterion, and the value of $\phi_s^{-1}(\xi, r)$ is u , which satisfies $\phi_s(\xi, u) = r$. The conversion ratio T_Q^P from Q to P , is computed as

$$T_Q^P = \frac{\phi_s(\xi_P, \sum_{i \in Q} d_i)}{\phi_s(\xi_Q, \sum_{i \in Q} d_i)}, \quad (5)$$

where P is the upper level set and Q is the lower level set in the hierarchy diagram.

3.3.2 Global Evaluation of Expressions Using Fuzzy Integral

The global evaluation value $E(expr_i), i = 1, 2, \dots, n$ of the i th expression $expr_i$, where n is the number of expressions, is calculated by the following Choquet fuzzy integral:

$$\begin{aligned} E(expr_i) &= \int_X h \circ g \\ &= \sum_{j=1}^n \{h_{ij} \cdot \Omega_j(t) - h_{i(j-1)} \cdot \Omega_{j-1}(t)\} g(A), \end{aligned} \quad (6)$$

where $X = \{m_1, m_2, m_3, m_4, h_1, e_1, e_2, e_3, c_1, c_2, c_3, c_4\}$ is the universal set of criteria, $A \subset X$ is the subset of criteria, h_{ij} is the partial evaluation value of the i th expression over the j th criterion, $\Omega_j(t)$ is the strength of the j th criterion, and $g(A)$ is the fuzzy measure value of A , identified by (2). One expression in each expression category is selected, which has the highest global evaluation value.

4 Simulations

4.1 Simulation Setting

To show the effectiveness of the proposed behavior selection method, the simulations are performed on an software entertainment robot, as shown in Fig. 2. In the perception program, the sensory data is converted into context information and the internal state strengths are updated. Considering both the internal state and context, a behavior which is composed of four kinds of expressions is selected in the expression and behavior selection program. A selected behavior is generated and executed in the behavior generation and execution programs, respectively. The communication of data between programs is performed by the communication server program.

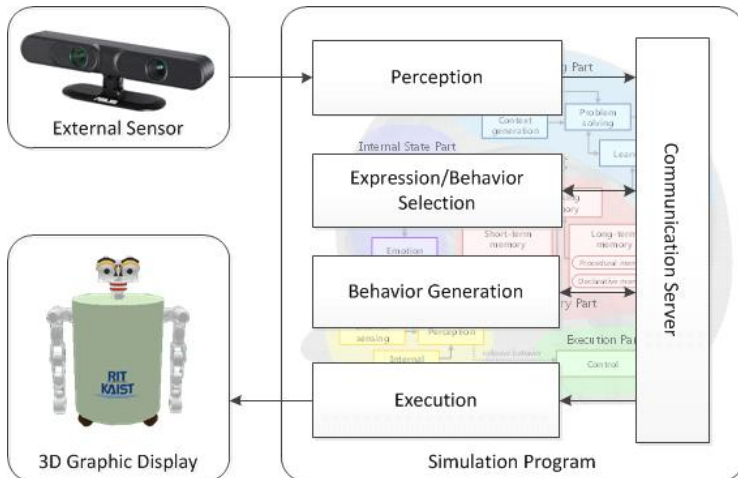


Fig. 2. The structure of the simulation program

To measure the performance of the proposed method, the mean of behavior generation frequency was calculated from 10 sets of the experiment results gathered for one hour, which is the same as one day in the virtual world. The behavior was selected in every 2.5 sec, and therefore the number of total generated behaviors were 1,440. Note that the partial evaluation values of expressions were pre-given by an expert.

4.2 Simulation 1: The Generation Frequencies of Four Expressions

In this simulation, the behavior generation frequencies of four expressions were computed, as shown in Fig. 3. The generation frequency of “fatigue” facial expression was about 5% and that of “normal” facial expression was about 21%. The generation frequency of “raise both hands” gesture was about 4% and that of “wave right hand” was about 14%. The generation frequency of “bend knee” movement was about 1% and that of “bow” movement was about 18%. The generation frequency of “bye” voice expression was about 7% and that of “hi” voice expression was about 22%. In summary, various expressions and behaviors could be generated through the proposed behavior selection method.

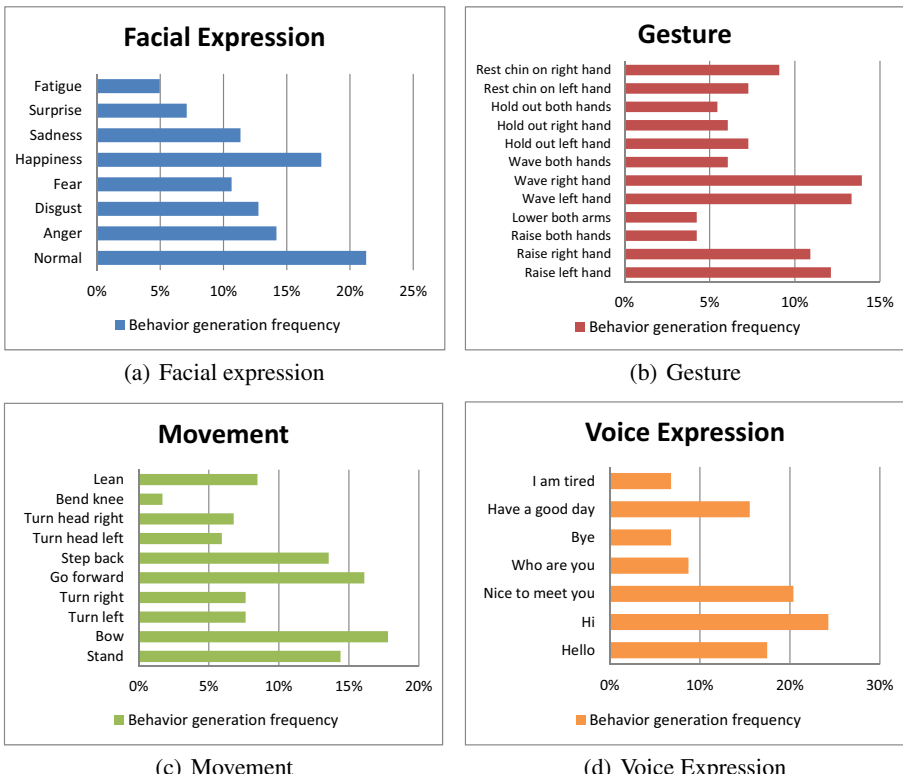


Fig. 3. The behavior generation frequencies of four expressions

4.3 Simulation 2: Three Entertainment Robots with Different Characteristics

In this simulation, three entertainment robots with different characteristics were created by assigning different preference degrees for each and every internal state and context, as shown in Table 4. For a cheerful entertainment robot, the preference degrees for “curiosity,” “power,” and “social contact” were given to be higher than the others. For a safety-first one, the preference degrees for “tranquility” and “distance to the nearest person” were given to be higher than the others. For a sentimental one, the preference degrees for emotions, i.e. arousal, valence, and stance, were given to be higher than the others.

Table 4. Three entertainment robots with different characteristics

Characteris-tics	Motivation				Homeostasis		Emotion			Context		
	m_1	m_2	m_3	m_4	h_1	e_1	e_2	e_3	c_1	c_2	c_3	c_4
Cheerful	0.174	0.174	0.174	0.043	0.043	0.043	0.043	0.043	0.087	0.087	0.087	0.043
Safety-first	0.050	0.050	0.050	0.200	0.200	0.050	0.050	0.050	0.050	0.200	0.050	0.100
Sentimental	0.050	0.050	0.050	0.050	0.050	0.200	0.200	0.200	0.050	0.050	0.050	0.050

The behavior generation frequencies for the three entertainment robots were computed, as shown in Fig. 4. For the cheerful one, “holding out both hands” was the most frequent gesture expression whose generation frequency was about 16%. For the safety-first one, “stepping back” was the most frequent movement whose generation frequency was about 23%. For the sentimental one, “sadness” was the most frequent facial expression whose generation frequency was about 20%. In summary, different characteristics could be generated through the proposed method.

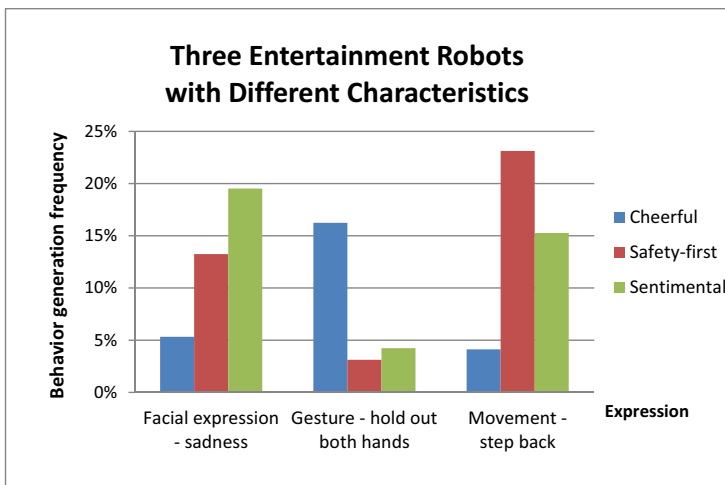


Fig. 4. The behavior generation frequencies for the three entertainment robots

5 Conclusions

This paper proposed the behavior selection method for entertainment robots using the iOA which consists of five parts and 15 modules to implement the robot intelligence. The internal state strengths and context information were obtained in the internal state and context modules, respectively. Considering them, a behavior which is composed of four expressions, i.e. facial expression, gesture, movement, and voice expression, was selected in the problem solving module. Each expression was evaluated by the Choquet fuzzy integral of the partial evaluation values with respect to the preference degrees of the internal states and contexts. The effectiveness of the proposed method was demonstrated through the simulations with a software entertainment robot in the 3D virtual environment. The results showed that the robot could generate various behaviors through the proposed behavior selection method. Moreover, by assigning different preference degrees, various entertainment robots with different characteristics could be created.

Acknowledgement. This research was supported by the MKE (The Ministry of Knowledge Economy), Korea, under the Human Resources Development Program for Convergence Robot Specialists support program supervised by the NIPA (National IT Industry Promotion Agency) (NIPA-2012-H1502-12-1002)

References

1. Pelachaud, C., Gelin, R., Martin, J.-C., Le, Q.A.: Expressive Gestures Displayed by a Humanoid Robot during a Storytelling Application. Paper presented at New Frontiers in Human-Robot Interaction (AISB), Leicester (2010)
2. Stiefelhagen, R., Fugen, C., Gieselmann, P., Hozapfel, H., Nickel, K., Waibel, A.: Natural Human-Robot Interaction using Speech, Head Pose and Gestures. Paper presented at IEEE/RSJ International Conference on Intelligent Robots and Systems (IROS), Sndai, Japan, pp. 2422–2427 (2004)
3. Yoo, B.-S., Cho, S.-H., Kim, J.-H.: Fuzzy Integral-based Composite Facial Expression Generation for a Robotic Head. Paper Presented at IEEE International Conference on Fuzzy Systems 2011, pp. 917–923 (2011)
4. Kim, J.-H., Choi, S.-H., Park, I.-W., Zaheer, S.A.: Intelligence Technologies for Robots That Think. IEEE Computational Intelligence Magazine (2012) (under review)
5. Reiss, S.: Who am I? The 16 Basic Desires that Motivate Our Actions and Define Our Personalities. Berkley Trade (2002)
6. Breazeal, C.: Emotion and sociable humanoid robots. International Journal of Human Computer Interaction (2003) (in press)
7. Sugeno, M.: Theory of fuzzy integrals and its applications. PhD dissertation, Tokyo Institute of Technology (1974)
8. Kim, J.-H., Ko, W.-R., Han, J.-H., Zaheer, S.A.: The degree of consideration-based mechanism of thought and its application to artificial creatures for behavior selection. IEEE Computational Intelligence Magazine 7(1), 49–63 (2012)

9. Ko, W.-R., Hyun, H.-S., Kim, H.-J., Choi, S.-H., Kim, J.-H.: Behavior Selection Method for Intelligent Artificial Creatures Using Degree of Consideration-based Mechanism of Thought. Paper presented at IEEE International Conference on Systems, Man and Cybernetics (2011)
10. Takagagi, E.: A fuzzy measure identification method by diamond pairwise comparisons and ϕ_s transformation. *Fuzzy Optimization and Decision Making* 7(3), 219–232 (2008)
11. Narukawa, Y., Torra, V.: Fuzzy measure and probability distributions: Distorted probabilities. *IEEE Transactions on Fuzzy System* 13(5), 617–629 (2005)

A Quality Control Model for Trustworthy Crowdsourcing in Collaborative Learning

Jun Jo, Ann Stevens, and Clarence Tan

School of Information and Communication Technology, Griffith University,
Parkland Dr. Southport, QLD, Australia

j.jo@griffith.edu.au, ann.stevens@griffithuni.edu.au,
clarence@bondwireless.com

Abstract. Crowdsourcing is getting more popular in various on-line communities. This method allows many people to share and learn knowledge through collaborations. However, fraud or inaccurate information often causes crucial problems and the quality and accuracy of the knowledge became a major issue. This paper investigates the effects of crowdsourcing in education. Inquiry-based learning will be employed as an educational technology. This paper will then introduce a quality control model that integrates trustworthy crowdsourcing into collaborative learning. A new method for credit rating will be introduced.

Keywords: crowdsourcing, trustworthy, online teaching, collaborative learning.

1 Introduction

Crowdsourcing, for example Wiki, is an innovative approach to Internet-based collaboration, allowing many users to share information and solve complex problems collaboratively. This technology is getting more popular in various Internet applications.

Surowiecki [8] examined several cases of crowd wisdom at work and stated that the very success of a solution is dependent on its emergence from a large body of solvers. Under the right circumstances, groups are remarkably intelligent, and are often smarter than the smartest people in them. The unprecedented level of collaboration and meaningful exchanges between people from every imaginable geographical location, which is the concept of crowdsourcing, is made possible to foster using the technology [2]. There is, however, an inherent weakness in crowdsourcing that there is no clear difference between “the wisdom of the crowd” and “the mob that rules.” What is missing is a measure of discernment [7].

Untrustworthy contents and incredible authors are potentially dangerous and always the major concerns in education environment in general and collaborative learning in particular. The significance of the research is to overcome the potential online fraud and to propose a model, which is appropriate and safe for educational settings. The new learning model will increase the learning performance by employing an inquiry system.

This paper will introduce a quality control model that integrates trustworthy crowdsourcing into collaborative learning. The main objectives of the model include: to protect the learners from untrustworthy information, to motivate students to get actively involved in learning, and to improve the quality of knowledge.

2 Crowdsourcing in Education

The success of GoldCorp, InnoCentive and iStockPhoto has proven crowdsourcing to be beneficial in solving scientific and business cases; and showcasing talented artists. This has prompted educators and researchers to investigate and extend its benefits to the education community. To insure the credibility of the crowd and the trustworthiness of information they provide, it is substantial to develop a quality control model.

It is an educational concern that majority of the online discussions viewed and found by people casually searching online for knowledge or solutions, do not involve a credible content expert as a mentor. Therefore, the trustworthiness of the solution offered by the forum is questionable and could potentially mislead the people or learners seeking for reliable solutions [6].

Due to the above concern, majority of the education institutions only facilitate and restrict the online collaborative learning to the enrolled students as part of the institution based e-Learning or Learning Management System (LMS). The collaboration is initiated, monitored and controlled by the online facilitator, which also has a task of delivering the contents. It is more of a closed-door virtual classroom where collaboration with outsiders, the crowd, whose contributions could improve the learning outcome, is restricted or does not exist due to technology, security and educational policies.

Inquiry-Based Collaborative Learning through Social Media

The proposed model is not an alternative of either traditional classroom teaching, or the online LMS. It is a model to support the main stream learning approach in which the learners have more power in their learning direction, expressing their argument and challenge others' arguments.

Brand & Moore [1] published relevant research on the proposed inquiry-based strategy and its relevance to learning motivation with a positive conclusion. The teachers reported that the emphasis on inquiry-based strategies influenced students' performances in other areas of their learning, which was also reinforced through lessons emphasizing interdisciplinary connections. The students' increased interests and motivation improved their attitudes toward learning and researching new ideas. Rather than being powerless and dependent on the institution, learners need to be empowered to think and to learn for themselves. Thus, learning needs to be conceived of as something a learner does, not something that is done to a learner [4].

The learning activities involved in the inquiry-based approach must be extended beyond posting questions and answers. The learners are expected to challenge each other. Surowiecki [8] believed that the 'wisdom of crowds' is derived not from averaging solutions, but from aggregating them.

The constructivist perspective supports that learners learn through interaction with others. Learners work together as peers, applying their combined knowledge to the solution of the problem. The dialogue that results from this combined effort provides learners with the opportunity to test and refine their understanding in an ongoing process [9].

The social media promotional campaign has successfully convinced a large number of collaborative learning systems to use the social media platform to trial its capability and effectiveness, and to provide service for collaborative learning, using the constructivist perspective and inquiry-based learning strategy. Inquiry to a network of trusted friends for a solution to a problem normally gathers expected number of response and enhances the motivation to participate in knowledge sharing, yet knowing that the trustworthiness of the responses are in question.

The growing interest of learning through inquiry and its response posted through social media is accordance with Dewey's theory on inquiry-based collaborative learning. Dewey, in one of his interpretations on experience, argued that inquiry is the only method of having an experience. Inquiry is triggered by difficult situations, and inquiry is the means through which it is possible to transform this situation through the mediation of thinking and action. Dewey viewed education and teaching as a means to support, through inquiry, the direction of experience [5].

Learning Challenges, Reward and Motivation

The majority of the crowdsourcing participants, Howe [2] believed, are not primarily motivated by money, and they are donating their leisure hours to the cause. They are contributing their excess capacity, or "spare cycles" to indulge in something they love to do. Nowadays, spare times are increasingly being spent producing online information and media to be shared with other users.

Huberman [3] highlighted attention seeking as the key to motivation in crowdsourcing. Instant and low-cost or free access to online information across geographic and institutional boundaries, has devalued information. People value what's scarce, not plentiful. The precious entity they now seek is attention, such as to be viewed, followed and liked by many in social media environment. This attention is social in nature. To source better quality and timely response, often the science, business and art sectors offer attractive financial incentives for ideas and solutions initiated from their crowdsourcing platforms.

The education sector, such as schools, is again restricted to offer financial rewards to the valued participants. The rewards offered for participation are normally based on quantitative evaluation method, for example, the duration of participation. Participants become more of passive learners and lose motivation to search and share information over a quality discussion. In order to obtain rewards, higher marking percentage for example, some participate in the discussion many times, without concern about the quality and accuracy of the answers. Their involvement in online collaborative learning is often ceased at the completion of the course. Online collaborative learning is long overdue for an innovative reward system. This research investigates an appropriate reward method to encourage active, dynamic and high quality contributions, while discouraging insincerity or untrustworthy involvement.

3 A Quality Control Model for Trustworthy Crowdsourcing in Collaborative Learning

The Quality Control Model for Trustworthy Crowdsourcing is composed of five modules: the Learning Module, the Knowledge Classification Module, the Knowledge Repository, the Credit Information Database, and the Credit Rating Module, Figure 1. The overall process involves the creation of knowledge (the learning materials) by the crowd users (learners), knowledge classification and credit rating.

The knowledge, with a credit rating, is made available to the learners through the Learning Module. The inquiry-based learning program will be provided and managed by the educators. A learner should use the preset schema and clearly describe concepts and relations, when creating questions and answers. This will help the Knowledge Classification Module make it easy to store, search and rate the credit of the knowledge. The Knowledge Repository stores learning materials with the information such as the related inquiries and topics.

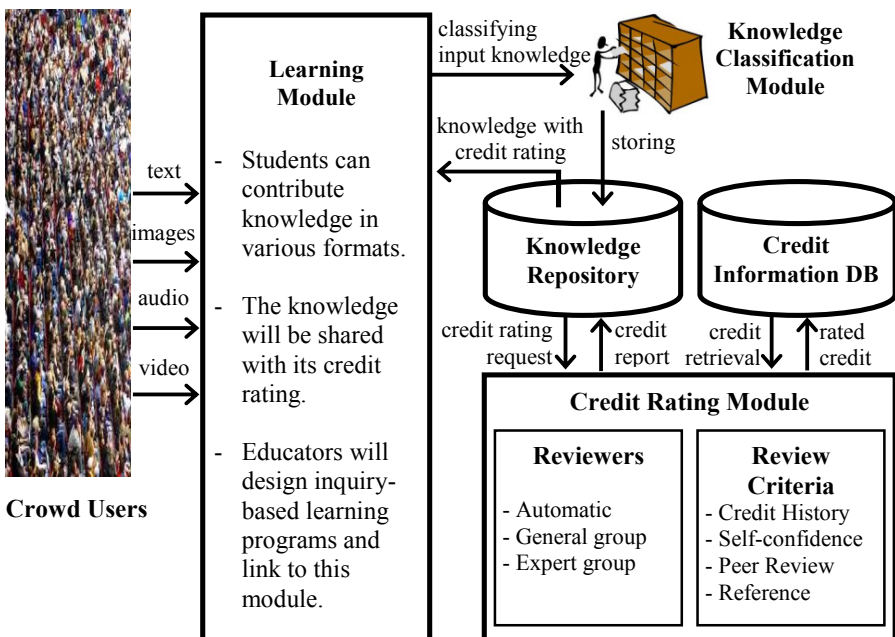


Fig. 1. A conceptual model of learning system based on trustworthy crowdsourcing

When a learner creates and submits new knowledge to the system, the Credit Rating Module grades the level of trustworthiness of the information. The process considers a number of variables to calculate the credit rating, including previous credit history, A_k , and self-confidence, D_i , of the user. It also conducts peer-review and refers to relevant cases from the Internet. The review task can be implemented

automatically using a mathematical equation, peer-review by other anonymous users and an expert group, who may be paid by the service provider.

The trustworthiness value (Q_i) is the sum of anonymous rating by peer review (P_i), rating(s) by expert(s) ($\sum R_j C_{ij}$), and the author credit rating and confidence ($A_k D_i$). Here R_j stands for the article rating given by an expert and C_{ij} is the credit rating of the expert. In the situation where there are multiple experts conducting the review, the ratings will be combined and divided by the number of the reviewers (N).

$$Q_i = w_1 (P_i) + w_2 \left(\frac{\sum R_j C_{ij}}{N} \right) + w_3 (A_k D_i)$$

Each of the variables will be given different weight based on their value. For example, the review result from experts is considered to be more influential than the feedback from the anonymous. The Credit Information Database contains the credit information of the users including authors and experts.

The anonymous peer-review algorithm (P_i) is a simple algorithm based on the method that eBay is using, where the positive feedback percentage is calculated based on the total number of positive and negative feedback ratings.

$$P_i = \frac{\text{Positives}}{\text{Positives} + \text{negatives}}$$

For example, if the total number of positive and negative feedback ratings are 134 and 20, the value of P_i is:

$$\frac{134}{134 + 20} = 87\%$$

4 Conclusion

While crowdsourcing and collaborative learning exist in web environment have been for a number of years, its trustworthiness has been one of the major issues. This research investigated and addressed the strengths and weaknesses of crowdsourcing and the collaborative learning environment. This paper introduced a trustworthy crowdsourcing-based collaborative educational model integrating the two concepts.

One of the key elements in the model is the credit rating module that invites experts, general public as well as automatic assessment algorithms, in order to rate the quality of information contributed by the crowd. The review criteria include previous credit history, self-confidence, peer review and reference. When designing the model, its implementation on mobile computing, which includes mobile phones and tablets was taken into consideration, align with the concept of ubiquitous computing. The system will be implemented and applied for a real learning situation.

References

1. Brand, B.R., Moore, S.J.: Enhancing Teachers' Application of Inquiry- Based Strategies Using a Constructivist Sociocultural Professional Development Model. *International Journal of Science Education* 33(7), 889–913 (2011)
2. Howe, J.: *Crowdsourcing: How the Power of the Crowd Is Driving the Future of Business*. Random House Business Books, Great Britain (2008)
3. Huberman, B.A., Romero, D.M., Wu, F.: Crowdsourcing, attention and productivity. *Journal of Information Science* 35(6), 758–765 (2009)
4. Huffaker, D.A.: Dimensions of Leadership and Social Influence in Online Communities. (Doctoral dissertation). Retrieved from ProQuest Dissertations and Theses. (Accession Order No. UMI 1451129) (2009)
5. Illeris, K.: *Contemporary theories of learning: learning theorists... in their own words*. Taylor & Francis (2009)
6. Moturu, S.T., Liu, H.: Quantifying the trustworthiness of social media content. *Distributed Parallel Databases* 29, 239–260 (2011)
7. Roman, D.: Crowdsourcing and the question of expertise. *Communications of the ACM - Finding the Fun in Computer Science Education* 52(12), 12 (2009)
8. Surowiecki, J.: *The Wisdom of Crowds: Why the Many Are Smarter Than the Few and How Collective Wisdom Shapes Business, Economies, Societies and Nations* Little, BrownISBN 0-316-86173-1 (2004)
9. Tam, M.: Constructivism, instructional design, and technology: Implications for transforming distance learning. *Educational Technology & Society* 3(2), 50–60 (2000)

Multimodal Human-Robot Interface with Gesture-Based Virtual Collaboration

Young Eun Song¹, Mihoko Niitsuma², Takashi Kubota¹,
Hideki Hashimoto², and Hyoung Il Son³

¹ The University of Tokyo, 7-3-1 Hongo, Bunkyo-ku, Tokyo, Japan
tdsong@ee.t.u-tokyo.ac.jp, kubota@isas.jaxa.jp

² Chuo University, 1-13-27 Kasuga, Bunkyo-ku, Tokyo, Japan
niitsuma@mech.chuo-u.ac.jp, hashimoto@elect.chuo-u.ac.jp

³ Max Planck Institute for Biological Cybernetics, Spemannstraße 38,
72076 Tübingen, Germany
hyoungil.son@tuebingen.mpg.de

Abstract. This paper proposes an intuitive teleoperation scheme by using human gesture in conjunction with multimodal human-robot interface. Further, in order to deal with the complication of dynamic daily environment, the authors apply haptic point cloud rendering and the virtual collaboration to the system. all these functions are achieved by a portable hardware that is proposed by authors newly, which is called "the mobile iSpace". First, a surrounding environment of a teleoperated robot is captured and reconstructed as the 3D point cloud using a depth camera. Virtual world is then generated from the 3D point cloud, which a virtual teleoperated robot model is placed in. Operators use their own whole-body gesture to teleoperate the humanoid robot. The Gesture is captured in real time using the depth camera that was placed on operator side. The operator receives both the visual and the vibrotactile feedback at the same time by using a head mounted display and a vibrotactile glove. All these system components, the human operator, the teleoperated robot and the feedback devices, are connected with the Internet-based virtual collaboration system for a flexible accessibility. This paper showcases the effectiveness of the proposed scheme with experiment that were done to show how the operators can access the remotely placed robot in anytime and place.

1 Introduction

Human beings have studied and developed telecommunication method for a long time to solve the question, "How can one make more efficient collaboration with others in remote areas?". Early efforts such as audio teleconference (ATC), video teleconference (VTC) and computer mediated communication (CMC) have enabled people to collaborate with each other even until recently. Then, as means of communication on the Internet has made much progress, virtual face-to-face interaction scheme which is called "the virtual collaboration system" has been studied vibrantly in recent years. The virtual collaboration system emerged from

the VTC at first, then, other various approaches have been presented including the application of the immersive 3D virtual reality (VR) to increase the sense of presence. In immersive 3D VR, operators are surrounded with VR, which makes it seems as if they are inside of a different place. Therefore, It is possible for the operators to feel the remote places as close to the real world when they interact with objects or other people in a certain virtual world through their own avatars, and that allows complicated collaboration tasks between them possible. There is a crucial factor of the immersive 3D VR. In order to reflect the operator in the virtual world as the avatar, continuous capturing of the operator's pose is necessary. For such activity, application of the *intelligent space (iSpace)* concept would be ideal. iSpace concept had been proposed by Hashimoto laboratory at the University of Tokyo since 1996. The iSpace makes surrounding space to have intelligence by using *distributed intelligent network device (DIND)*, and the DIND observes all events including human movements in the space [8,5]. However the conventional iSpace necessitate operators to not deviate from the sensor range, since DINDs are fixed in specific places it makes nearly impossible to transfer the device around. To overcome these space restraints and to make iSpace system more flexible, a new type of DIND is required. As a soultion, this paper presents the mobile iSpace, a personal portable devices.

Although the avatar is placed in the virtual world where the remote environment is reconstructed and linked, there still is a limitation as to what people can actually interact with. The real Objects in the remote environment are limited due to its absence of perception. To fulfill this shortage of the ordinary virtual collaboration system, the bilateral teleoperation system is necessary. Recently, the teleoperation systems carry out a decisive role where the environments are dangerous, unstructured and under-recognized; such as bomb disposal, rescue or space exploration with the abilities of robot that are precise, and mechanically strong. The robotic surgery might be a good example [1]. The bilateral teleoperation system links the real and the virtual world together physically, which then can support the virtual collaboration to the remote places when it lacks fidelity. As a matter of fact, in order to link the remote places via the virtual collaboration, two of the teleoperation technologies are required. Those are the input and the output systems. The former is for transmission of the control references from the human operators to the robot, while the later is for reflection of the remote environmental information back to human. In the case of the input devices, conventionally, researchers have used joystick like control sticks or keypads. But, with such method, the more the task is getting complicated, the more workload is increasing in geometric progression, and also the operators have to be trained enough prior to the session. To solve these problems, recently, researchers have applied the gesture capture devices as a input system to control robots by moving simultaneously with operator's own motions. The early studies captured only the hands of operators to control the end effectors of the robots by using marker based optical systems or exoskeleton motion capture devices. However these kinds of systems often disturb the natural movements of operators and also had to be installed beforehand. Once again, it brings to a

conclusion to stress the importance of having portable device which can capture the whole body gesture to sustain the natural movement of the operator. it also means more natural and intuitive teleoperation system for virtual collaboration is possible with such device. Thus, the primary objectives of this paper would be categorized into three parts. First of all, this paper proposes the mobile iSpace consisted of the minimum hardware set, i.e. a RGB-D camera, a head mounted display (HMD) and a vibrotactile gloves, for the gesture capture and immersive 3D visual and tactile feedback respectively. And secondly, a multimodal haptic feedback scheme is achieved by portable devices like vibrotactile gloves and the HMD, instead of using massive exoskeleton devices to implement force and visual feedbacks. Finally, the rendering of the multimodal haptic feedback states are designed to perform the haptic illusion related with the cognitive channel to achieve natural perception with portable devices.

The arrangement of paper is as in the following. The gesture-based teleoperation control is illustrated in Section 2. In Section 3, multimodal feedback is detailed. Finally, Section 4 concludes this paper by summarizing while discussing the future works.

2 Gesture-Based Teleoperation Control

2.1 System Overview

To present much better natural and intuitive teleoperation environment than other typical end-effector-only teleoperation schemes, this work applies the whole body gesture-based teleoperation system that the usual movements of human operators are directly carried out tasks with the teleoperated robots. And this leads operators not only to prevent the danger from lack of reality but also to support much more dexterous tasks. However, there are problems with the conventional the whole body gesture-based teleoperation systems that those systems need hulking or fixed hardwares. This work, therefore, shows a noble system that consists of *the mobile iSpace* and *the virtual collaboration arena (VirCA)* to provide more flexible accessibility. The VirCA is developed by the *Cognitive Informatics Research Group of MTA SZTAKI*, and is one of the successful virtual collaboration system [4]. The whole system structure is shown in Figure 1. Once, the operators set up the mobile iSpace, they can access to the VirCA as the robot avatars via the Internet. The mobile iSpace is a sine qua non of this system to make surrounding environments have intelligence, both operator side and the remote side. In the operator side, the mobile iSpace plays a role in capturing human gesture and providing feedbacks to the operator. And in the remote side, the mobile iSpace offers the realtime 3D reconstruction of surroundings. As a matter of fact, those factors are the key functions of the virtual collaboration system for the connecting the participants. In contrast to the traditional iSpace DINDs which have limited sensor range and poor mobility, the mobile iSpace provides excellent mobility and flexibility to make space has a intelligence wherever and whenever it is needed. As shown in Figure 1 the mobile iSpace consists of a depth camera, a tactile glove and a head mounted display

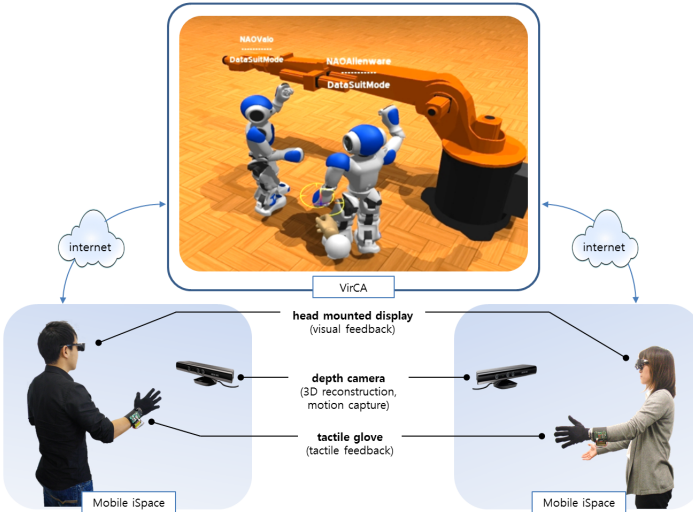


Fig. 1. Human and robot participants in the virtual collaborative teleoperation system

(HMD), which are the minimum hardware set which can satisfy essential conditions of the virtual collaboration system. Moreover, all the component parts of the mobile iSpace have accessibility to the VirCA. In order to organize this distributed system, all the sensors and feedback devices of the mobile iSpace and the VirCA are implemented with CORBA standard for data transfer, thanks to the RT-Middleware [2]. So all the system components exist as modules online [2]. This system, therefore, supports cloud computing to make sure that operators can share their surrounding environmental information or hardware accessibility without any limitations if the Internet connection is available. Operators can check which components are accessible and they can connect them and share information simply online. And the shared information is included and visualized in the VirCA. And the VirCA give visual feedback to the HMD and also tactile feedback to the tactile gloves of the mobile iSpace. The gesture capture data from the depth camera is transferred to the virtual robot, which is visualized in the VirCA. And the virtual robot is connected with the real robot in a remote place. So eventually, the remote placed robot is moved simultaneously with human operators gesture and the operators feel like as if they exist in the remote place by the feedback devices of the mobile iSpace.

2.2 Human Gesture Capture

The positions and orientations of 15 joints of the human operator, i.e. head, neck, shoulders, elbows, torso, hands, hips, knees and feet, are transmitted to the applied humanoid type robot. We use quaternions to express the orientations

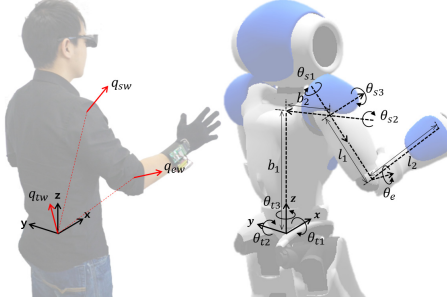


Fig. 2. The coordinate of the applied humanoid type robot

not only to solve the gimbal-lock problem inherent in Euler angles, but also to reduce the data amounts. In the case of quaternions, it needs only four numbers, which consists of one real number and three imaginary numbers, to express rotation while the Euler angles need nine. However, the robot uses the Euler angles to control the every joint, therefore, quaternions from the human gesture have to be converted into the Euler angles, e.g. the quaternions q_{tw} , q_{sw} and q_{ew} , which represent the rotation of the human torso, shoulder and elbow individually, is converted into the Euler angles θ_{t1} , θ_{t2} , θ_{t3} (torso), θ_{s1} , θ_{s2} , θ_{s3} (shoulder) and θ_e (elbow) (see Figure 2). The torso quaternion q_{tw} is expressed as $q_{tw} = [q_{tw0} \ q_{tw1} \ q_{tw2} \ q_{tw3}] = q_{tw0} + q_{tw1}i + q_{tw2}j + q_{tw3}k$. q_{tw0} is a real part and q_{tw1} , q_{tw2} and q_{tw3} are imaginary parts. If we consider a rotation about the unit vector, u by an angle θ . The quaternion that computes this rotation is

$$q_{tw0} = \cos\left(\frac{\theta}{2}\right), \quad [q_{tw1} \ q_{tw2} \ q_{tw3}] = u \sin\left(\frac{\theta}{2}\right) \quad (1)$$

Then we obtain $q_{tw} = \cos\left(\frac{\theta}{2}\right) + i \sin\left(\frac{\theta}{2}\right) + j \sin\left(\frac{\theta}{2}\right) + k \sin\left(\frac{\theta}{2}\right)$. So that the Euler rotations (R_x , R_y and R_z) by the angles (θ_{t1} , θ_{t2} and θ_{t3}) we compute that

$$\begin{aligned} R_x(\theta_{t1}) &= \cos\left(\frac{\theta_{t1}}{2}\right) + i \sin\left(\frac{\theta_{t1}}{2}\right) \\ R_y(\theta_{t2}) &= \cos\left(\frac{\theta_{t2}}{2}\right) + j \sin\left(\frac{\theta_{t2}}{2}\right) \\ R_z(\theta_{t3}) &= \cos\left(\frac{\theta_{t3}}{2}\right) + k \sin\left(\frac{\theta_{t3}}{2}\right) \end{aligned} \quad (2)$$

By combining the quaternion representations of the Euler rotations we get

$$\begin{aligned} q_{tw} &= R_z(\theta_{t3})R_y(\theta_{t2})R_x(\theta_{t1}) \\ &= \left[\cos\left(\frac{\theta_{t3}}{2}\right) + k \sin\left(\frac{\theta_{t3}}{2}\right) \right] \left[\cos\left(\frac{\theta_{t2}}{2}\right) + j \sin\left(\frac{\theta_{t2}}{2}\right) \right] \left[\cos\left(\frac{\theta_{t1}}{2}\right) + i \sin\left(\frac{\theta_{t1}}{2}\right) \right] \\ &= \left[\cos\left(\frac{\theta_{t1}}{2}\right) \cos\left(\frac{\theta_{t3}}{2}\right) \cos\left(\frac{\theta_{t2}}{2}\right) + \sin\left(\frac{\theta_{t1}}{2}\right) \sin\left(\frac{\theta_{t3}}{2}\right) \sin\left(\frac{\theta_{t2}}{2}\right) \right] \\ &\quad \left[\sin\left(\frac{\theta_{t1}}{2}\right) \cos\left(\frac{\theta_{t3}}{2}\right) \cos\left(\frac{\theta_{t2}}{2}\right) - \cos\left(\frac{\theta_{t1}}{2}\right) \sin\left(\frac{\theta_{t3}}{2}\right) \sin\left(\frac{\theta_{t2}}{2}\right) \right] \\ &\quad \left[\cos\left(\frac{\theta_{t1}}{2}\right) \sin\left(\frac{\theta_{t3}}{2}\right) \cos\left(\frac{\theta_{t2}}{2}\right) + \sin\left(\frac{\theta_{t1}}{2}\right) \cos\left(\frac{\theta_{t3}}{2}\right) \sin\left(\frac{\theta_{t2}}{2}\right) \right] \\ &\quad \left[\cos\left(\frac{\theta_{t1}}{2}\right) \cos\left(\frac{\theta_{t3}}{2}\right) \sin\left(\frac{\theta_{t2}}{2}\right) - \sin\left(\frac{\theta_{t1}}{2}\right) \sin\left(\frac{\theta_{t3}}{2}\right) \cos\left(\frac{\theta_{t2}}{2}\right) \right] \end{aligned} \quad (3)$$

For Euler angles we get

$$\begin{bmatrix} \theta_{t1} \\ \theta_{t2} \\ \theta_{t3} \end{bmatrix} = \begin{bmatrix} \tan^{-1} \left(\frac{2(q_{tw0}q_{tw1} + q_{tw2}q_{tw3})}{1 - 2(q_{tw1}^2 + q_{tw2}^2)} \right) \\ \sin^{-1} (2(q_{tw0}q_{tw2} - q_{tw3}q_{tw1})) \\ \tan^{-1} \left(\frac{2(q_{tw0}q_{tw3} + q_{tw1}q_{tw2})}{1 - 2(q_{tw2}^2 + q_{tw3}^2)} \right) \end{bmatrix} \quad (4)$$

The robot shoulder quaternion is converted to the relative orientation (q_{sr}) from world orientation (q_{wr}) based on the torso orientation (q_{tw}) is computed as $q_{sr} = q_{tw}^{-1}q_{sw}$ where the q_{sr} is $q_{sr} = q_{sr0} + q_{sr1}i + q_{sr2}j + q_{sr3}k$. With the same way on this quaternions, the Euler angles of robot shoulder are shown as

$$\begin{bmatrix} \theta_{sr1} \\ \theta_{sr2} \\ \theta_{sr3} \end{bmatrix} = \begin{bmatrix} \tan^{-1} \left(\frac{2(q_{sr0}q_{sr1} + q_{sr2}q_{sr3})}{1 - 2(q_{sr1}^2 + q_{sr2}^2)} \right) \\ \sin^{-1} (2(q_{sr0}q_{sr2} - q_{sr3}q_{sr1})) \\ \tan^{-1} \left(\frac{2(q_{sr0}q_{sr3} + q_{sr1}q_{sr2})}{1 - 2(q_{sr2}^2 + q_{sr3}^2)} \right) \end{bmatrix} \quad (5)$$

The robot elbow quaternion is converted to the relative orientation (q_{er}) from world orientation (q_{ew}) based on the shoulder world orientation (q_{sw}) is computed as $q_{er} = q_{sw}^{-1}q_{ew}$ where the q_{er} is $q_{er} = q_{er0} + q_{er1}i + q_{er2}j + q_{er3}k$. The Euler angle of elbow is shown as

$$\theta_e = \tan^{-1} \left(\frac{2(q_{er0}q_{er3} + q_{er1}q_{er2})}{1 - 2(q_{er2}^2 + q_{er3}^2)} \right) \quad (6)$$

Although quaternions have advantages for expressing the orientations, they do not represent the 3D position information. Therefore, the forward kinematics vector transformation for an open kinematics chain needs to be represent another way. We apply dual quaternions for representing both rotation and translation in a single vector that shown as

$$Q(q, p) = ([\cos(\frac{\theta}{2}), \sin(\frac{\theta}{2}) < i, j, k >], < p_x, p_y, p_z >) \quad (7)$$

where the unit quaternion q expresses orientation of a joint and the vector $p = < p_x, p_y, p_z >$ represents corresponding translational displacement. Considering the orientation vectors first, since the x -axis, y -axis and z -axis of the reference coordinate frame are the unit line vectors along the rotation axes of the first joint (θ_{t1}), the second joint (θ_{t2}) and the third joint (θ_{t3}) individually, the quaternion vectors that represent the orientation are expressed as

$$\begin{aligned} q_1 &= \cos\left(\frac{\theta_{t1}}{2}\right), \sin\left(\frac{\theta_{t1}}{2}\right) < 1, 0, 0 > \\ q_2 &= \cos\left(\frac{\theta_{t2}}{2}\right), \sin\left(\frac{\theta_{t2}}{2}\right) < 0, 1, 0 > \\ q_3 &= \cos\left(\frac{\theta_{t3}}{2}\right), \sin\left(\frac{\theta_{t3}}{2}\right) < 0, 0, 1 > \end{aligned} \quad (8)$$

Orientations of the shoulder joints ($\theta_{s1}, \theta_{s2}, \theta_{s3}$) are determined as follows using the same approach described above.

$$\begin{aligned} q_4 &= \cos\left(\frac{\theta_{s1}}{2}\right), \sin\left(\frac{\theta_{s1}}{2}\right) < 1, 0, 0 > \\ q_5 &= \cos\left(\frac{\theta_{s2}}{2}\right), \sin\left(\frac{\theta_{s2}}{2}\right) < 0, 1, 0 > \\ q_6 &= \cos\left(\frac{\theta_{s3}}{2}\right), \sin\left(\frac{\theta_{s3}}{2}\right) < 0, 0, 1 > \end{aligned} \quad (9)$$

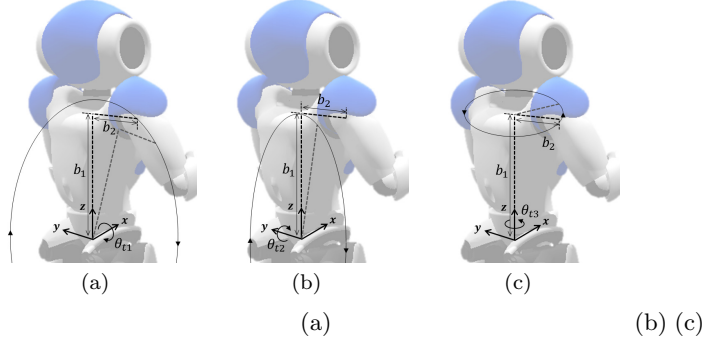


Fig. 3. (a) The body traces a circle on the yz -plane; (b) The body traces a circle on the xz -plane; (c) The body traces a circle on the xy -plane

Because, there is one joint (θ_e) on z -axis in the robot elbow that can be denoted as

$$q_7 = \cos\left(\frac{\theta_e}{2}\right), \sin\left(\frac{\theta_e}{2}\right) < 0, 0, 1 > \quad (10)$$

The position vectors are assigned in terms of reference coordinate frame as follows. When the first joint of robot torso (θ_{t1}) is rotated anticlockwise direction around the x -axis of reference coordinate frame by an angle of θ_{t1} , the body traces a circle in the yz -plane as given Figure 3a. Using the following vector p_1 , any point on the circle can be determined. The second joint position vector p_2 and the third joint position vector p_3 are determined as follows using the same approach (see Figure 3b,c).

$$\begin{aligned} p_1 &= < 0, -b_1 \sin \theta_{t1} + b_2 \cos \theta_{t1}, b_1 \cos \theta_{t1} + b_2 \sin \theta_{t1} > \\ p_2 &= < b_1 \sin \theta_{t2}, 0, b_1 \cos \theta_{t2} > \\ p_3 &= < -b_2 \sin \theta_{t3}, b_2 \cos \theta_{t3}, 0 > \end{aligned} \quad (11)$$

Since rotation of the first joint of robot shoulder (θ_{s1}) do not create any displacement, the position vector p_4 is

$$p_4 = < 0, 0, 0 > \quad (12)$$

Because, the second joint of robot shoulder (θ_{s2}) is rotated anticlockwise direction around the y_s -axis, the link l_1 traces a circle in the $x_s z_s$ -plane with position vector p_5 as shown Figure 4a. The third joint of robot shoulder position vector p_6 is determined as follows using the same approach (see Figure 4b).

$$\begin{aligned} p_5 &= < l_1 \cos \theta_{s2}, 0, -l_1 \sin \theta_{s2} > \\ p_6 &= < l_1 \cos \theta_{s3}, l_1 \sin \theta_{s3}, 0 > \end{aligned} \quad (13)$$

And the elbow joint (θ_e) is rotated anticlockwise direction around the z_e -axis (see Figure 4c), the position vector p_7 can be determined

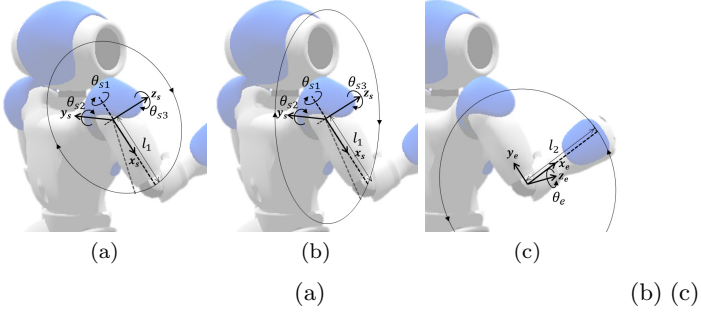


Fig. 4. (a) The link l_1 traces a circle on the $x_s z_s$ -plane; (b) The link l_1 traces a circle on the $x_s y_s$ -plane; (c) The link l_2 traces a circle on the $x_e y_e$ -plane

$$p_7 = \langle l_2 \cos \theta_e, l_2 \sin \theta_e, 0 \rangle \quad (14)$$

Finally, the kinematics transformations using the dual quaternions for the applied humanoid robot defining the spatial relationships between successive linkages can be represented as in the following

$$\begin{aligned} Q_1(q_1, p_1) &= ([\cos \bar{\theta}_{t1}, \sin \bar{\theta}_{t1} < 1, 0, 0 >], \\ &< 0, -b_1 \sin \theta_{t1} + b_2 \cos \theta_{t1}, b_1 \cos \theta_{t1} + b_2 \sin \theta_{t1} >) \end{aligned} \quad (15)$$

$$Q_2(q_2, p_2) = ([\cos \bar{\theta}_{t2}, \sin \bar{\theta}_{t2} < 0, 1, 0 >], < b_1 \sin \theta_{t2}, 0, b_1 \cos \theta_{t2} >) \quad (16)$$

$$Q_3(q_3, p_3) = ([\cos \bar{\theta}_{t3}, \sin \bar{\theta}_{t3} < 0, 0, 1 >], < -b_2 \sin \theta_{t3}, b_2 \cos \theta_{t3}, 0 >) \quad (17)$$

$$Q_4(q_4, p_4) = ([\cos \bar{\theta}_{s1}, \sin \bar{\theta}_{s1} < 1, 0, 0 >], < 0, 0, 0 >) \quad (18)$$

$$Q_5(q_5, p_5) = ([\cos \bar{\theta}_{s2}, \sin \bar{\theta}_{s2} < 0, 1, 0 >], < l_1 \cos \theta_{s2}, 0, -l_1 \sin \theta_{s2} >) \quad (19)$$

$$Q_6(q_6, p_6) = ([\cos \bar{\theta}_{s3}, \sin \bar{\theta}_{s3} < 0, 0, 1 >], < l_1 \cos \theta_{s3}, l_1 \sin \theta_{s3}, 0 >) \quad (20)$$

$$Q_7(q_7, p_7) = ([\cos \bar{\theta}_e, \sin \bar{\theta}_e < 0, 0, 1 >], < l_2 \cos \theta_e, l_2 \sin \theta_e, 0 >) \quad (21)$$

The forward kinematics can be determined multiplying all of the Q_i matrices, where $i=1,2,\dots,7$. Therefore, the pose of the end effector of robot x can be determined as

$$x(q, p) = Q_7 Q_6 Q_5 Q_4 Q_3 Q_2 Q_1 \quad (22)$$

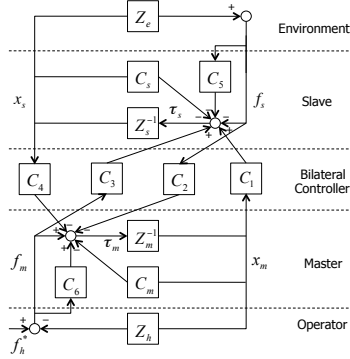


Fig. 5. Generalized four-channel control architecture for teleoperation system

2.3 Gesture-Based Teleoperation

The generalized four-channel (4C) control architecture is widely used to represent the teleoperator's control architecture, which is presented in Fig. 5. The bilateral teleoperation system shown in Fig. 5 consists of the operator (Z_h), the master (Z_m), the slave (Z_s), the environment (Z_e). These components are usually modeled as second-order linear-time-invariant (LTI) dynamic model (i.e., $Z_i = M_i s + B_i + K_i / s, i = h, m, s, e$ where $M_i \in \Re^{3 \times 3}$, $B_i \in \Re^{3 \times 3}$, and $K_i \in \Re^{3 \times 3}$ is the positive definite inertia, damping, and stiffness matrix, respectively.) . And there is the bilateral controller which has two position controllers (C_1 and C_4) and two force controllers (C_2 and C_3). Additionally, there are local feedback controllers C_m and C_s and local feedforward controllers C_6 and C_5 for the master and the slave, respectively. Finally, f_h^* denotes the exogenous control inputs generated by the human operator.

In this paper, motivated by this practical perspective, we use the position-position (PP where $C_2 = C_3 = 0$) control architectures. The PP control architecture is the most widely used controllers in the bilateral teleoperation systems where force information of the slave robot is unavailable. We employed a proportional-derivative (PD) controller for the position controllers. The position controllers are designed as $C_i = K_i^D + K_i^P / s, i = 1, 4$ where $K_i^D, K_i^P \in \Re^{3 \times 3}$ are the positive definite/symmetric derivative and proportional gain matrices. A symmetric scalar gain matrix $K_i^f, i = 2, 3, 5, 6 \in \Re^3$ is defined for the force controllers.

2.4 Stability Analysis

From two-port network theory [7], the input-output relationship between positions and forces of the master and the slave in teleoperation system is defined using hybrid matrix formulation as given below.

$$\begin{bmatrix} f_m \\ -\dot{x}_s \end{bmatrix} = \begin{bmatrix} h_{11} & h_{12} \\ h_{12} & h_{22} \end{bmatrix} \begin{bmatrix} \dot{x}_m \\ f_s \end{bmatrix} \quad (23)$$

where f_m , x_m , f_s , and x_s are the force and the position of the master and the slave, respectively.

The operator dynamics, though passive, is generally adaptive and changing while the environment impedance is either unknown or inadequately modeled. Stability analysis based on the two-port network model of the teleoperation system alone rather than the whole system including the operator and the environment is therefore more appropriate. When the two-port network of the teleoperation remains stable under all possible uncoupled passive terminations, the teleoperation system is said to be absolutely stable. Absolute stability is used in this paper to analyze the stability robustness of the teleoperation system. Absolute stability is a less conservative condition compared to passivity. Llewellyn's criterion for absolute stability is expressed in terms of hybrid matrix parameters as follows [7,6].

- h_{11} and h_{22} have no poles in the right half plane.
- Any poles of h_{11} and h_{22} on the imaginary axis are simple with real and positive residues.
- The followings holds for all real values of ω :

$$\begin{cases} \Re(h_{11}) \geq 0 \\ \Re(h_{22}) \geq 0 \\ 2\Re(h_{11})\Re(h_{22}) - \Re(h_{12}h_{21}) - |h_{12}h_{21}| \geq 0 \end{cases} \quad (24)$$

Theorem 1. *The position-position control architecture for teleoperation system is absolutely stable for all frequency range if $B_m \geq 0$, $B_s \geq 0$, and $B_m K_s - B_s K_m = 0$.*

Proof. The above proof is based on the hybrid matrix representation of the teleoperation system wherein all the three conditions of absolute stability given by the Llewellyn's criteria, are satisfied one by one. The detailed proof is completely mathematical and can be understood easily from the authors' previous work in [9].

We, finally, designed the bilateral controllers based on Theorem 1 for a stable teleoperation system.

3 Multimodal Feedback

The visual and tactile feedback are rendered based on the reconstructed virtual world (see Figure 6). First, the remote environment is captured as the 3D point cloud by using depth and color information of the RGB-D camera. And using the 3D point cloud map, the virtual world is reconstructed and applied for the virtual collaboration system. Then, the virtual collaboration system renders the visual and tactile feedbacks which are implemented by the mobile iSpace.

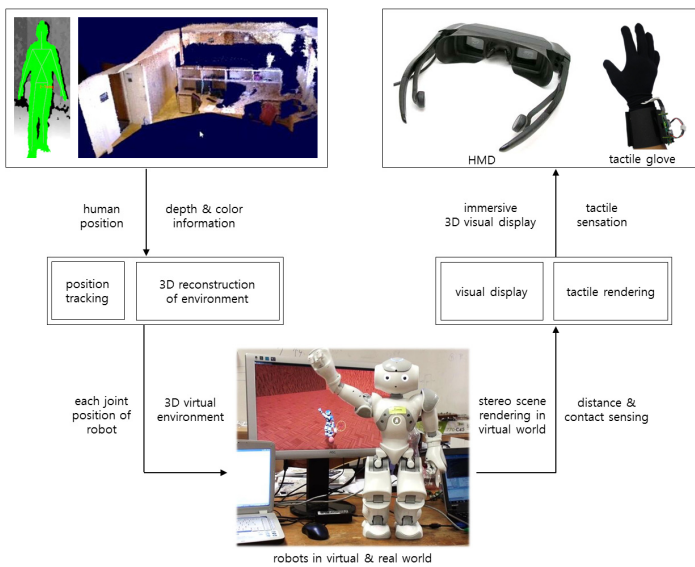


Fig. 6. System structure of the teleoperation and multimodal feedback system



Fig. 7. (a) Real objects and reconstructed virtual objects; (b) Real space and reconstructed virtual space

3.1 Visual Feedback

To handle a dynamically changing unknown remote environment, this system applies the 3D point cloud instead of using a 3D map which is built by 3D CAD tools. Consequently, this system provides a more realistic 3D map automatically and quickly. The 3D point cloud map is reconstructed by combining each 3D point cloud based on the location of the depth camera. As a result, Some objects in the real environment and the reconstructed virtual objects by 3D point clouds are shown in Figure 7a, and the real environment and the virtual environment are shown in Figure 7b. For the visual feedback, this system uses stereoscopic 3D images on the HMD which are provided from virtual stereo camera which are placed on the eyes of the virtual humanoid robot. Eventually operators can interact with remote environment having 3D immersive virtual reality, to make them feel as if they are inside the remote environment.

3.2 Tactile Feedback

In order to enable realization of a dexterous and accurate teleoperation task, researchers have applied human cognitive perception on rendering force or tactile feedback recently. Especially, the cognitive perception has advantages when letting operators define distance in the virtual environment with his or her own hands [3]. In this work, therefore, the tactile feedback is rendered based on the distance between the robot hand and certain objects. To rendering the tactile feedback, the vibrotactile glove which has vibration motors on fingertips is applied as feedback actuator as shown in Figure 8a. The frequency (F) and the magnitude (M) of the vibration motors are control inputs to express the distance (d) from a certain object as shown in Figure 8b. The rendering scheme is as in the following. If the d is too far, in other words the robot hand is out of range (r_0) from the object, then there is no feedbacks like as $|d| > r_0$:

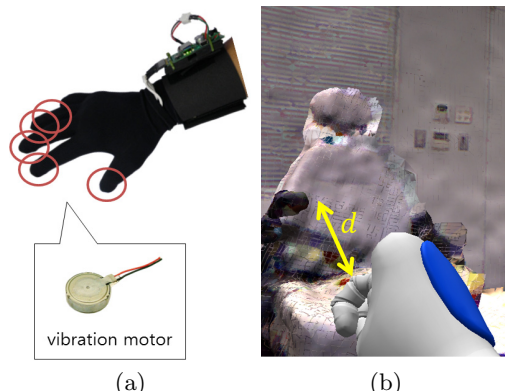


Fig. 8. (a) The vibrotactile glove; (b) The frequency (F) and the magnitude (M) of the vibration motors are rendered based on the distance (d)

$F(Hz) = 0$, $M(V) = 0$. But if the robot hand is in the range of the object like $|d| < r_0$, the feedbacks are rendered as

$$F(Hz) = a \cdot \frac{1}{|d|}, \quad M(V) = M_0 \quad (r_0 > d > 0) \quad (25)$$

$$F(Hz) = F_0, \quad M(V) = b \cdot |d| \quad (d < 0) \quad (26)$$

where the F_0 , M_0 , a and b are constant parameters. So before contact the object, the frequency (F) is changing based on the distance (d) having same magnitude (M_0), and after contact the object, the frequency (F) is constant and magnitude (M) is changing based on the distance (d). Therefore the operator can perceive how much close from the object and also how much entered to the object based on his or her cognitive perception.

4 Conclusions

The natural and intuitive teleoperation system for virtual collaboration by using only portable and personal devices is introduced in this paper. Despite the limited hardware set, to support the sense of reality we introduce the mobile iSpace concept. The mobile iSpace offers the real time 3D reconstruction, human whole body gesture capture and multimodal haptic feedback. First, the remote space is captured by a RGB-D camera as a point cloud and 3D map is reconstructed from the point clouds, and then a human operator controls the applied humanoid type robot by their own gesture having the 3D immersive visual feedback and tactile feedback by the HMD and vibro tactile gloves individually. Eventually, the human operator could interact with the virtual object using their cognitive perception. Since the presented system connects two remote space via the virtual collaboration system, we can simulate certain tasks beforehand and also have more flexible view. Moreover, as a matter fact, these days, not only the social network system but also real time communication systems are rising, thus this proposed system can be easily applied to our daily life.

References

1. Intuitive surgical inc., <http://www.intuitivesurgical.com>
2. Ando, N., Suehiro, T., Kitagaki, K., Kotoku, T.: Rt (robot technology)-component and its standardization-towards component based networked robot systems development. In: Proceedings of the SICE-ICASE International Joint Conference, pp. 2633–2638 (2006)
3. Galambos, P.: Vibrotactile feedback for haptics and telemanipulation: Survey, concept and experiment. Acta Polytechnica Hungarica 9(1), 41–65 (2012) (in print)
4. Galambos, P., Baranyi, P.: VirCA as virtual intelligent space for RT-Middleware, pp. 140–145 (2011)
5. Hashimoto, H.: Intelligent space: Interaction and intelligence. Artificial Life and Robotics 7(3), 79–85 (2003)

6. Hashtrudi-Zaad, K., Salcudean, S.: Analysis of control architectures for teleoperation systems with impedance/admittance master and slave manipulators. *The International Journal of Robotics Research* 20(6), 419–445 (2001)
7. Haykin, S.: Active network theory. Addison-Wesley, Reading (1970)
8. Lee, J., Hashimoto, H.: Intelligent space concept and contents. *Advanced Robotics* 16(3), 265–280 (2002)
9. Son, H.I., Bhattacharjee, T., Lee, D.Y.: Control design based on analytical stability criteria for optimized kinesthetic perception in scaled teleoperation. In: Proceedings of the SICE-ICASE International Joint Conference, pp. 3365–3370 (2009)

Three-Layered Architecture for Tele-operator and Its System Test

Koshi Hoshino and Yasuharu Kunii

Dept. of Electrical and Electronic Engineering, Chuo University
1-13-27 Kasuga, Bunkyo-ku, Tokyo 112-8551, Japan
{koushi_11,kunii}@hmsl.elect.chuo-u.ac.jp

Abstract. In this paper, we discuss an intelligent system architecture for teleoperators (e.g., planetary exploration rovers). This architecture offers advanced flexibility (variability), efficiency, scalability, and transparency. The architecture is composed of two software layers (first and second) and one hardware layer (third). The software layer is divided into two layers to achieve both efficient task construction by the users and management of software modules by the system. To maintain a variable structure and improve accessibility to information, we connect modularized software and hardware via a network. Moreover, to achieve high-speed data communication between software modules, we use a shared memory. Through the proposed architecture we can efficiently perform repairs and consequently enhance the functionality of teleoperator systems. Therefore, our proposed architecture can provide significant contributions to the development and operation of teleoperators.

Keywords: system architecture, teleoperation, RT-Middleware.

1 Introduction

In this paper, we discuss a system architecture for teleoperators (remote mobile robots). In general, teleoperators are required to achieve stable performance while performing advanced missions in various environments. In order to get that capability, various system architectures for robots are proposed [1]-[6]. Teleoperators are composed of many functions (e.g., action planning, recognition, motion control) and various subsystems (e.g., moving mechanisms, communication system, and various sensors such as cameras). Because teleoperator systems are multifunctional they tend to be bulky and complex. Conversely, the systems are required to be scalable and efficiently adapt to any situation. Therefore, these systems should be capable of efficiently performing advanced tasks by freely combining various elements of the robot via a network.

A problem with most of the existing software architectures of teleoperator systems is that it is difficult to operate a robot when system failures occur in remote locations[7]-[9]. This is because it is difficult to dynamically modify functions of the

robot. From this viewpoint, it is highly desirable for an architecture to have advanced scalability and variability. Moreover, to operate the robot safely, it is important to know the state of the system.

For these reasons, we designed a system architecture that emphasizes the flexibility (variability) of the structure of functions and transparency of data. In this paper, we introduce, implement, and evaluate an intelligent system architecture for teleoperators. We show that our architecture provides flexibility (variability), scalability, and transparency. We realize advanced variability by defining real and virtual connections in different layers. Our implementation is based on RT-Middleware[10]. Finally, we evaluate our architecture by comparing its performance against components composed by genuine RT-Middleware.

2 Software Architecture for Teleoperated Systems

In general, teleoperators operate in locations where humans cannot easily perform activities. Moreover, the environment of these locations are not necessarily well-known. Thus, the system must be flexible and should be able to change the structure of its functions accordingly. Moreover, to operate the robot safely, it is important to know the state of the system during its operation. Therefore, we designed a system by emphasizing the flexibility (variability) of the structure of functions and transparency (accessibility) of data.

2.1 Modularized Software Network

To efficiently perform system modifications, modularization and networking are important. Modularization allows us to clearly define each function of the system and efficiently modify it. Networking allows us to easily modify parts of the system. Hence, these two characteristics are important when building a flexible system.

In our proposed architecture, each function is modularized and connected via a network. Furthermore, advanced variability is achieved by defining real and virtual connections in different layers. In the next section, we describe each layer of our architecture.

2.2 Three-Layered Architecture

Our proposed architecture is shown in figure 1. It is composed of two software layers (first and second) and one hardware layer (third). To achieve both efficient task construction by the users and management of software modules by the system, the software layer is divided into two layers.

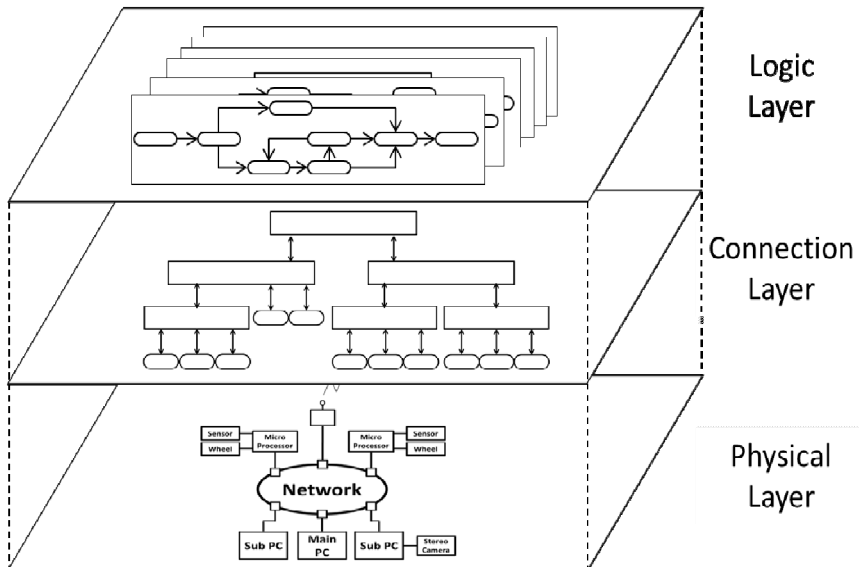


Fig. 1. Three-layered architecture

2.2.1 Logic Layer

In this first layer, we improve the efficiency of composing tasks by introducing a method that enables users to intuitively compose tasks. Users collect the necessary modules according to the intended task flow and connect them, as shown in figure 2. Our method allows free swapping, adding, replacing, and deleting modules. For a robot to operate in remote locations, it must be able to switch multiple tasks (composed of a module's behavior logic) in a flexible manner depending on the situation. Thus, the system can rebuild its functions effectively and respond quickly when problems arise.

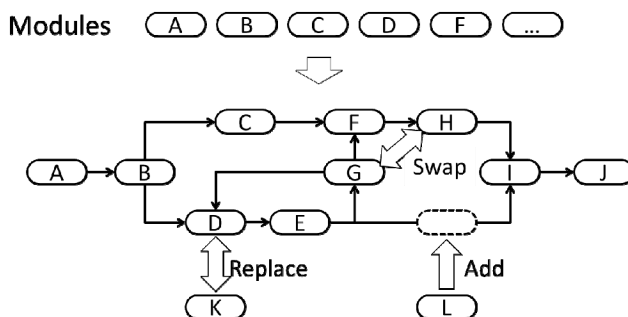


Fig. 2. Example of creating a task flow

2.2.2 Connection Layer

Because of the cost associated with connecting tasks, the actual switching of connections defined in the first layer is not realistic. For this reason, the second layer manages the actual modules of the system and virtually realizes task dependencies defined in the first layer. This action is performed by the database node module (DNM), which relays information between functions of modules. Specifically, all modules are connected to DNM, as shown in figure 3, and data is exchanged between them at high-speeds via shared memory. DNM realizes a network list by transmitting the destination addresses for each module that contains task dependencies defined by the user in the first layer. Hence switching of module connections is achieved by changing reference pointers, and the timing of the switches is managed by DNM. Moreover, system transparency is improved because DNM contains the data of all modules. To achieve load balancing, DNM can be arranged in a hierarchical structure (see figure 4). Specifically, the Newman algorithm can be used to cluster modules, which can then be placed at each layer of the hierarchical DNM structure [11][12]. Moreover, this structure facilitates the identification of failure causes, because the range is limited.

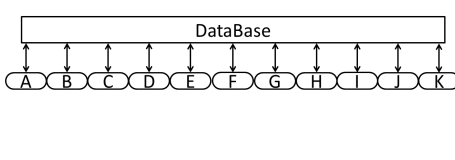


Fig. 3. Connection of modules in DNM

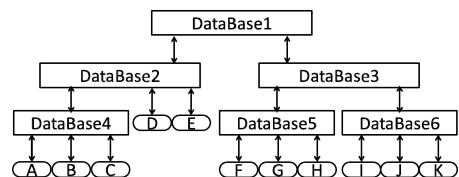


Fig. 4. Hierarchical connection of modules in DNM

2.2.3 Physical Layer

In the third layer, all hardware is connected via a network as shown in figure 5. It is possible to directly access any function, and connections can be changed using software without any physical restrictions. Thus, the system provides advanced variable structure and accessibility. In addition, it increases fault tolerance by minimizing the units that are lost when system failures occur.

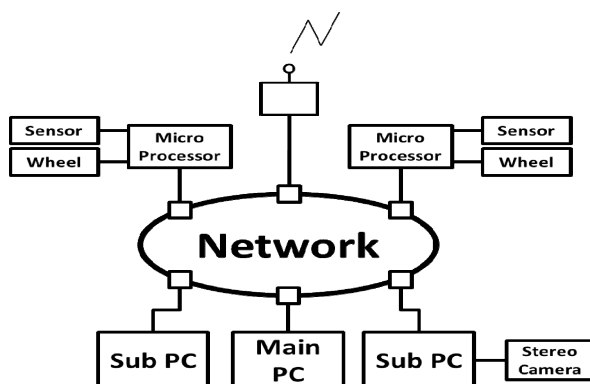


Fig. 5. Hardware Connection via Network

3 Realization of Variability for Task Flow

To realize the proposed architecture, the system is required to dynamically switch tasks, and share data between multiple DNM s. In this section, we describe in detail these functionalities.

3.1 Dynamically Task Switching

To dynamically switch tasks, we must dynamically change the connections between modules that comprise a task. Managing the execution of all modules by DNM is not preferred, because overhead increases. Thus, DNM only provides information about the connections, and each module manages its own execution. Specifically;

1. Each module is connected to the DNM and assigned a dedicated shared memory space. The capacity of the memory is provided by each output port number.
2. Using the netlist information of each module, DNM sets references between input ports and the output port of the appropriate module. Input ports continuously monitor the connections to the output ports.
3. When the execution of a module is complete, the value of each output port is updated. When an input port receives the updated information, it reads the value of the output port.

3.2 Data Sharing between Multiple DNM s

In this architecture, high-speed data communication between modules is achieved using shared memory. However, when modules are present between different DNM s, communication between modules cannot be achieved, because the shared memory space of each DNM is independent. To overcome this problem, it is necessary to send and receive data between DNM s using the netlist. Therefore, DNM is equipped with a function that automatically finds the route to a destination using the information of the netlist, and synchronizes the data of shared memory spaces. Moreover, because this architecture implementation is based on RT-Middleware (CORBA), DNM s communicate via CORBA.

4 Simulation Results and Evaluation

4.1 Data Communication Time

To evaluate the performance of our system, we compare the data communication time of our virtual inter-module connections with that of conventional RT-Middleware. The results of this comparison are shown in figure 6. The results indicate that the communication time of the virtual connections of this architecture is considerably lower than that of conventional RT-Middleware. Therefore, we conclude that the data communication in this system is efficient.

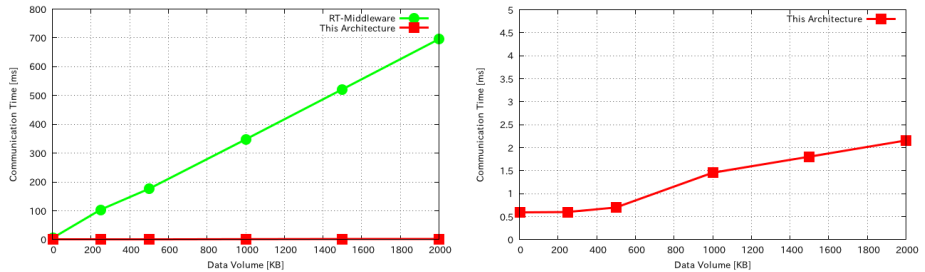


Fig. 6. Communication time of 10 modules using RT-Middleware and our proposed architecture (*left*) Communication time of our proposed architecture plotted in a reduced scale of time (*right*)

4.2 Variability

To compare variability, we measured the task switching speed of actual connections using RT-Middleware and that of the virtual connections used in our proposed architecture. The results of the comparison are shown in figure 8. The results show that the switching speed of our architecture is faster than that when using the RT-Middleware. Therefore, we confirm that our architecture offers efficient operation and task execution.

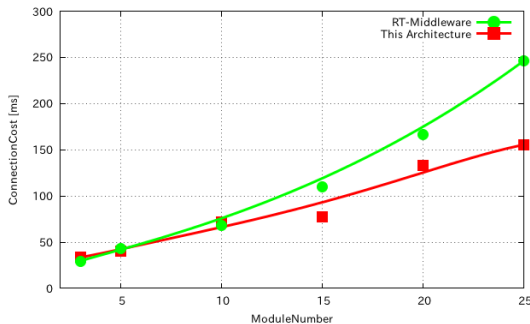


Fig. 7. Switching time of module connections

5 Tele-navigation System with 3 Layered Architecture

5.1 Tele-Navigation System on Rover Test Bed Micro6

We implemented tele-navigation system of our rover Micro6 (figure 8), an experimental mobile robot aimed for planetary exploration, using the proposed architecture. Its system task flow is shown in figure 9. To acquire terrain data as DEM, we used a stereo camera unit on the top of the sensor mast in the middle of the

rover, and an operator selects landmarks (LMs) based on image data captured and sent by the rover (Autonomous LM registration should be done in near future). Based on measured terrain information sent from the rover, the operator can create a command path toward the goal point as sequential waypoint data. Along its trip, the operator watches its status data and traverse result. Therefore, the operator can check the result at each waypoint. If problem is identified, the path can be changed or its motion terminated by the operator or the rover itself.

The system task flow in figure 9 is realized on the logical layer by the operator, and converted to tree style networking structure like shown in figure 10 on the connection layer. Here, software operation GUI was designed and shown in figure 11. Task Generation Interface, via which users could intuitively generate tasks, is given and Module Connection Interface, which is visualization tool allowing users to monitor the connection status in the connection layer, is also provided. As a result, the operator can create tasks on the logic layer, and supervise connection status in the connection layer.

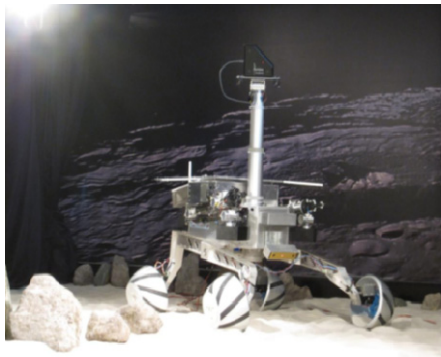


Fig. 8. Tele-operated Rover Test bed: Micro6

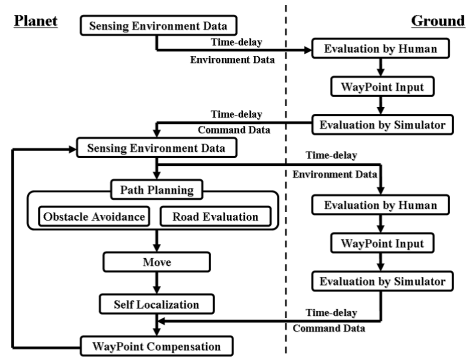


Fig. 9. System task flow

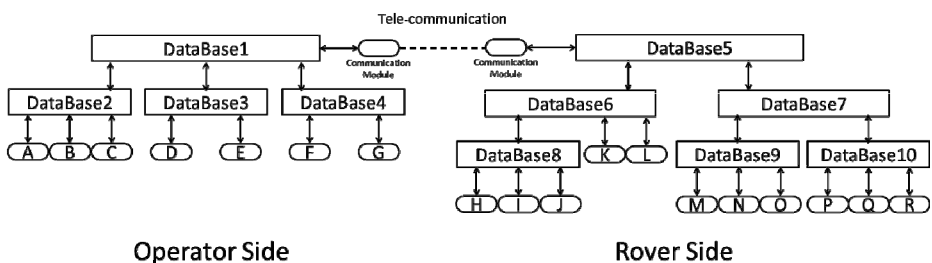


Fig. 10. Actual connection of tele-navigation system

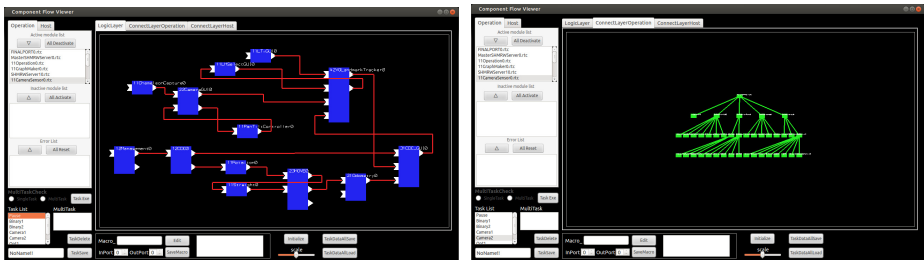


Fig. 11. Graphical User Interface of Task Generation (*left*) and Module Connection (*right*)

5.2 Task Switching Test for the Architecture

Navigation function on the rover consists of manual and autonomous path planning methods. For evaluation of task switching mechanism on the architecture, we switch those tasks (methods) during its travel. Those two tasks are presented in figure 12. In the manual task, the operator designates way-point frequently in the case of terrain with many obstacles. In the second one, the rover generates a route autonomously without any instructions by the operator in simple environment.

During the travel of the rover, the operator can switch these tasks flexibly depending on its situation. Actually, network connections on the system have never been changed even if the user changes task flows on the logic layer, because a task flow connection is virtually realized on the connection layer like shown in figure 10. However, the operator is not necessary to recognize their actual connections.

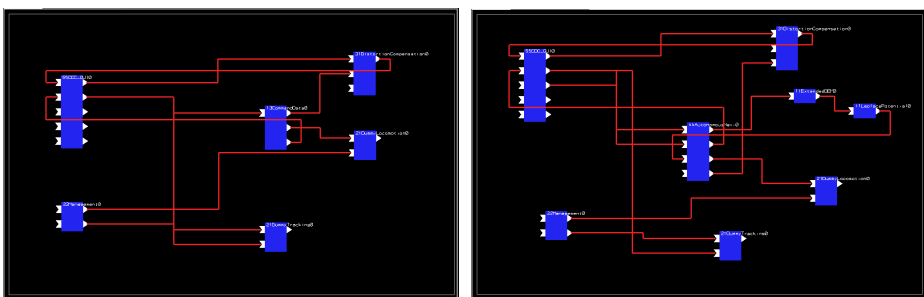


Fig. 12. Tasks of controlled by operator (*left*) and autonomous travel (*right*)

5.3 Implementation experiment

We performed experiments in Izu-Oshima, under scenarios that the rover cruises for long range traversability on a planetary surface. The remote-control host system, the communications antenna, and the survey instrument for true value measurement were prepared on site. A rock 50 meters away from the start point was set as an observation target, and the rover drove in its direction. Besides, the operator switched two tasks depending on the situation.

Figure 13 shows an actual traversal result of the rover in our field tests, and the positions of the trajectory and LMs are the true values measured with a laser survey instrument. Because of existing proportional errors that depend on the distance to the LMs from the camera, there was differences between the measured LM positions and their true positions. Therefore, following the initial path, the potential received from obstacles increases, and the risk of collisions occurring increased. However, our Command path Data Compensation (CDC) algorithm effectively avoided the obstacles, and the rover was able to safely cruise.

Finally, the rover travelled to the goal without colliding with obstacles for about 50 [m] in this Tele-Navigation experiment as shown in figure 14. In addition, from this experimental result, we confirmed that the architecture is possible to flexible and efficient operating of large-scale system and the system works without problems.

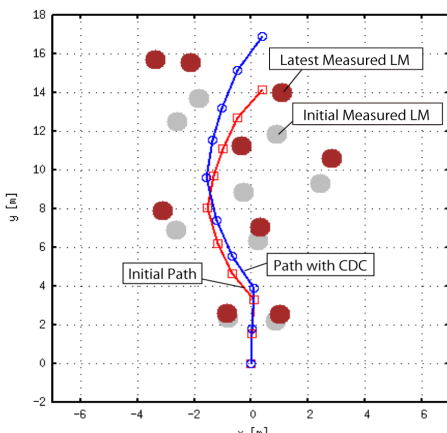


Fig. 13. Moving track of the rover

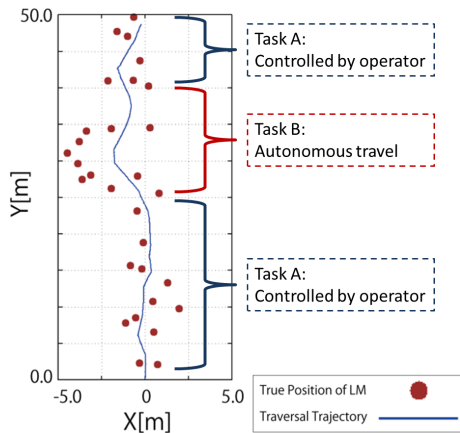


Fig. 14. Trajectory of cruising long distance

6 Conclusion

In this paper, we proposed a system architecture for teleoperators that offers advanced flexibility (variability), efficiency, scalability, and transparency. The architecture provides significant contributions to the development and operation of teleoperators. In future work, we plan to further improve the efficiency of our proposed architecture by incorporating a task scheduler in the logic layer.

References

1. Volpe, R., Nesnas, I., Estlin, T., Mutz, D., Petras, R., Das, H.: The CLARAty architecture for robotic autonomy. In: Proc. IEEE Aerospace Conf., pp. 121–132 (2001)
2. Volpe, R., Peters, S.: Rover Technology Development and Infusion for the 2009 Mars Science Laboratory Mission. In: Proc. Int'l SAIRAS (2003)

3. Estlin, T., Castano, R., Gaines, D., Bornstein, B., Judd, M., Anderson, R.C., Nesnas, I.: Supporting increased autonomy for a Mars Rover. In: Proc. Int'l SAIRAS (2008)
4. Ando, N., Suehiro, T., Kitagaki, K., Kotoku, T., Yoon, W.K.: Composite component framework for RT middleware (robot technology middleware). In: Proc. Int'l Conf. on IROS, pp. 1330–1335 (2005)
5. Ando, N., Suehiro, T., Kitagaki, K., Kotoku, T., Yoon, W.K.: RT-middleware: distributed component middleware for RT (robot technology). In: Proc. Int'l Conf. on ASME, pp. 3933–3938 (2005)
6. Ando, N., Suehiro, T., Kotoku, T.: A software platform for component based RT-system development: OpenRTM-aist. In: Carpin, S., Noda, I., Pagello, E., Reggiani, M., von Stryk, O. (eds.) SIMPAR 2008. LNCS (LNAI), vol. 5325, pp. 87–98. Springer, Heidelberg (2008)
7. Ando, N., Kurihara, S., Biggs, G., Sakamoto, T., Nakamoto, H., Kotoku, T.: Software Deployment Infrastructure for Component Based RT-Systems. J. RM 23(3), 350–359 (2011)
8. Newman, M.E.J., Girvan, M.: Finding and evaluating community structure in networks. J. Phys. Rev. E 69 (2004)
9. Newman, M.E.J.: Fast algorithm for detecting community structure in networks. J. Phys. Rev. E 69 (2004)

Analysis of Physiological Signals for Emotion Recognition Based on Support Vector Machine

Makara Vanny, Seung-Min Park, Kwang-Eun Ko, and Kwee-Bo Sim*

School of Electrical and Electronics Engineering, Chung-Ang University
221, Heukseok-dong, Dongjak-gu, Seoul 156-756, Korea
{makaravanny,sminpark,kkeun}kbsim@cau.ac.kr

Abstract. Emotion recognition is one of the important part to develop in human-human and human-computer interaction. In this paper, we focused on the experimental paradigm and feature extraction to extract features from the physiological signals. The experimental paradigm for data acquisition used MULTI module equipment of biofeedback 2000 x-pert which combined multi-sensor such as skin conductance, skin temperature, and blood volume pulse to collect physiological signals from the subject's fingertip of the non-dominant hand. And an approach for the emotions recognition based on physiological signals such as fear, disgust, joy, and neutrality that international affective picture system (IAPS) was used to elicit emotion. These were selected to extract the characteristic parameters, which will be used for classifying emotions. Support vector machine (SVM) is a popular technique for classifying emotion recognition and perform high accuracy for classification. The experiment results showed that the methodology by using experimental paradigm, feature extraction and especially multi-class support vector machine (MSVM) provided significant improvement in accuracy for classification emotion recognition states.

Keywords: emotion recognition, biofeedback system, physiological signals, international affective picture system (IAPS), support vector machine (SVM).

1 Introduction

Biofeedback system is an important autonomic nervous system (ANS) measure in psychophysiological signal for emotion recognition to develop human computer interaction. This system provides a service health care for human and proves to be a particularly successful new therapy. For emotion is a concept involving three components such as subjective experience, expressions and biological arousal. And it is a psychophysiological process that produced by the limbic system activity in response to a stimulus.

In this paper, multi-class support vector machine (MSVM) was employed to improve accuracy for emotion classification. There are many ways that the researcher used to express and elicit emotions through visualization, audition, gesture and tone of voice, body movement, facial expressions, and others to detect which respond to

the affective state. In this work, visualization of IAPS was employed to elicit emotions for the experimental paradigm and it was an affective picture standard to induce the emotions for the subject [1]. And some emotions were difficult to induce and recognize by people, and inner emotional experiences was not expressed outwardly. Then, the physiological patterns may be used to recognize distinct emotions through the remained questions [2].

The physiological signals of interest in this analysis are: SC, SKT, and BVP. Skin conductance changing is related to the activity of sweat gland which is controlled by the sympathetic nervous system and skin conductance is used as an indication of psychological or physiological arousal.

SKT may be taken as a representative sample of bodily activity correlated with changes in affective states. A fall in the skin temperature of the extremities in response to mental work: stress, fear, and pain. Conversely, a rise in the skin temperature showed about the relaxation and sleep state.

BVP changes in the blood flow causes fluctuations in the brightness of the reflected or transmitted light. These fluctuations are filtered out, amplified, and displayed as the BVP parameter relative change in blood flow.

Statistical analysis is a crucial algorithm which used to extract the features of raw signals for processing emotion recognition classification. SVM is a popular algorithm which presented the ability with the good result of classifying to classify four emotions such as fear, disgust, joyful and neutral. The remains parts of this paper will be proved in the next step such as the related work, feature extraction, classification, the result of experimental paradigm, and the conclusion and future work.

2 Related Works

The emotion recognition system was recognized by using physiological signals through the different ways that this system was proposed by some researchers. The physiological signals can vary depending of the range of number of emotional categories and whether the systems are user dependent or independent as the following descriptions:

The emotion recognition system was able to recognize eight emotions and performed with the accuracy of 81.25% for a single subject. Four biometric sensors of physiological signals were collected over a period of 20 days. The statistical features were then calculated over a period of one-day, and hybrid of SFFS and FP were used to select and classify respectively. This system was developed by Picard et al. [3].

Posner et al. proved an analog, continuous mapping of emotions based on a weighted combination of arousal intensity and emotional valence which is represented by two-dimensional space [4].

The emotion recognition system was user-independent emotion detection system by utilizing three physiological signals that the physiological data were collected from 50 children aged from 5 to 8 years old to recognize 4 emotions of sadness, anger, stress, and surprise. The accuracy of 78.43% and 61.76% were achieved for three and four emotion respectively. In pattern classification, SVM was employed to classify emotion recognition. This system was developed by Kim et al. [5].

The emotion recognition system was used 5 types of bio-sensors to attach on the subjects to make the experiment. IAPS was used to elicit emotion for subjects and feature extraction employed six statistical features of physiological signals. To optimize the work procedure, genetic algorithm was used for feature selection. And four types of classification methods were employed to classify emotion after comparing the accuracy of these methods [6].

Our previous work, we used mean and standard deviation of raw signal to extract the features for classifying emotions. In the experimental paradigm was used another method to induce emotion for the subjects which was different to experimental paradigm in this work. And the experimental results proved that the accuracy of emotion recognition was low accuracy for classification.

Thus, our purpose in this work, throughout the researchers above and our previous work, we concentrate on experimental paradigm to get the meaningful data and eigenvalue with eigenvector to extract the features. And support vector machine was employed for classification to improve accuracy of emotion recognition.

3 Experimental Paradigm for Physiological Data Acquisition

In our work, we divide two steps for defining the method to extract the data collections that we describe as the following:

3.1 Equipment Method

The equipment for acquisition of emotion-specific physical signals is MULTI module of biofeedback 2000 x-pert combined multi-sensor such as SC, SKT and BVP. These three physiological signals are selected to record the raw data for extracting the emotion recognition features. This equipment is attached on the finger tip of the non-dominant hand of subject as the following figure 1. The temperature and relative humidity of the experimental room were between 20 °C and 26 °C.

SC is measured by recording the electrical potential and it has the sample rate of 2 KHz. It is a square wave signal with frequency 20 Hz and amplitude of ± 1.42 V is applied to the skin. The maximum measuring range for SC is defined from 0 to 50 μ S and resolution 0.001 μ S with maximum error of 0.65 μ S.

SKT is processed in the sensor and transmitted to the multi-module in digital form and data rate of 4 values per second. Within a range of 10-40 °C and the temperature is measured at a resolution of 0.01°C and with an accuracy of 0.5°C.

BVP is the measurement of the mean flow of blood near the surface of the skin with the range of the value is 0-100% at a resolution of 0.25%. And the range of parameter is 30-200 bpm (beats per minute) at a display resolution of 1 bpm. The sample rate is 500 Hz and integration time constant of 100 ms with 10 data rate per second.



Fig. 1. The experiment procedure in our laboratory

Figure 1 showed that the way how to attach the sensor, radio module, and connect the radio pyramid to the software biofeedback 2000X-pert in the computer.

3.2 Emotion Induction Method

Subjects and emotion elicitation protocol: four subjects (three males and one female, aged from 25 to 30 years old) graduate students are healthy subjects and not taken any medicine in a week for making the experimental paradigm. The participants were introduced how to induce emotions and make the experiment before we start the experiment. The consent form the participant is seated in a comfortable chair in front of a computer screen at an approximate distance of 70 cm. All target emotion states are elicited from the subject by using IAPS image slide-show to induce emotion.

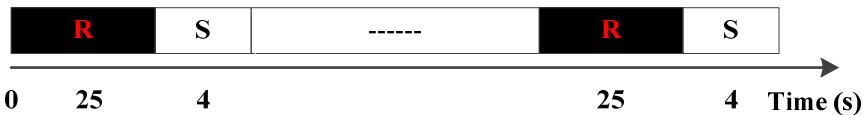


Fig. 2. The process of eliciting emotions for the subjects (R = rest and S = stimulus)

Data collection: One session takes the time of 4 minutes 50 seconds that each emotion displays 10 images and one image is displayed 4 seconds to induce emotion. In order to process the experiment, we first start showing the black screen which represent the rest time for the subject, after we show the image to elicit emotion. The black screen is also shown in the time duration of 25 seconds and it was shown between of the images to stimulus emotion that it was done 10 times until finish the experiment of each session. There are 10 trials in one session as shown in the Figure 2 and these 10 trials of image stimuli are displayed the same emotion in a session.

The accuracy strongly depends on the data sets or experimental data which were obtained in laboratory conditions because the observation and verification showed that the results were achieved for specific users in specific contexts and it is very difficult to label emotion classes in physiological signals such as waveforms without uncertainty.

4 Feature Extraction

4.1 Preprocessing

We first verify that the data were recorded properly during the experimental session by generating and examining plots of each of the channels over time as the following figure 3. The data acquisition of each physiological signal was segmented according to the time duration of the stimulating sections as you can see in the Figure 2. And these segments were prepared to process for the next step, means that we cut the meaningful signal as the trial from the session of the experiment procedure.

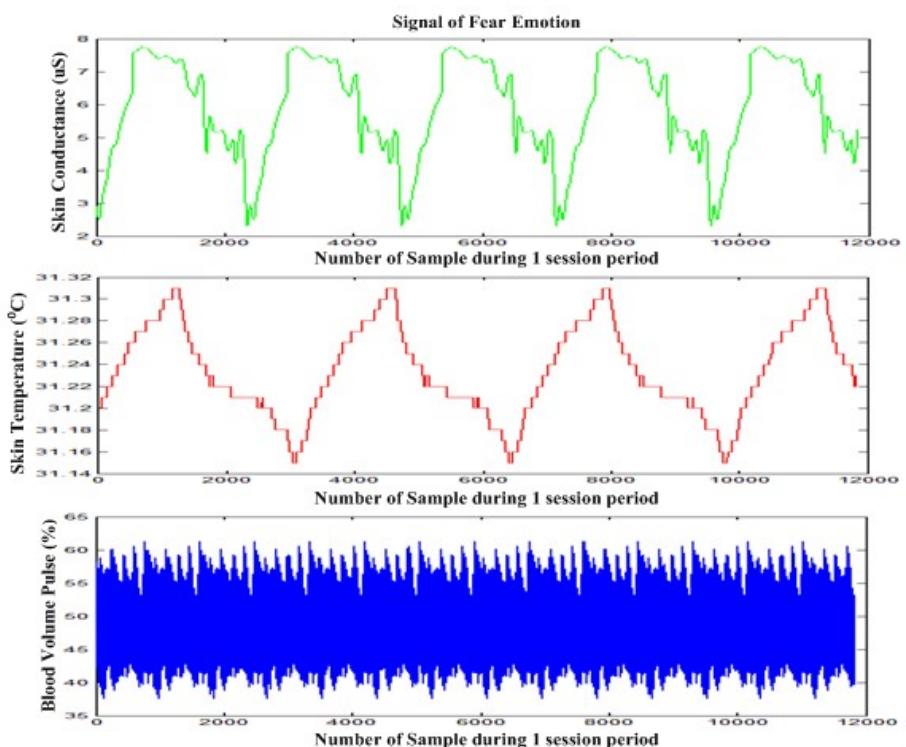


Fig. 3. The raw signal of fear emotion during one session period

Figure 3 showed characteristic raw signal of fear emotion which was plotted by physiological signals such as skin conductance, skin temperature, and blood volume pulse. This signal was cut in 10 trials subject to the time stimulus of the subject.

We will get the property of the raw signal of fear emotion for a trial as shown in below figure 4.

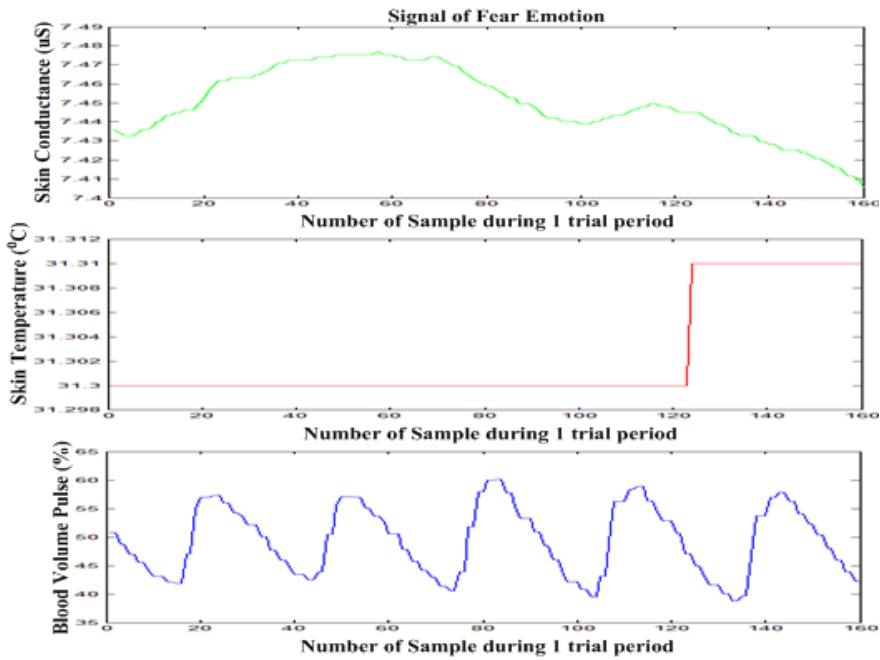


Fig. 4. The raw signal of fear emotion of one trial cut from the session

4.2 Feature Extraction Method

Eigenvalue and eigenvector were employed to extract the features from the raw data for feature extraction. The process of this method was calculated through the step as follows. After we got the raw data of each trial, we used the raw data of skin conductance (x), raw data of skin temperature (y), and raw data of blood volume pulse (z) to make a 3 dimensional data set (dimensions x, y, z) and the result was the calculation of covariance matrix between two dimensional space which were arranged as bellows:

So, we obtained 3 matrices (size: 160-by-2) that we got from the combination of x, y, and z. We assume that matrix $A = [x \ y]$, $B = [x \ z]$, and $C = [y \ z]$.

Next, we calculated the covariance matrix A , B , and C which were given as the following formula (1).

$$\text{Cov}(X) = \frac{1}{n-1} XX^T \quad (1)$$

Where $\text{Cov}(X)$ is a covariance matrix. X is a matrix and X^T is a transpose matrix. For n is the length of row of the matrix X that we make the covariance matrix to be a square matrix (n -by- n)

After that, we calculate the eigenvalue and eigenvector of the covariance matrix of all two separate dimensions by supposing:

$T = Cov(A)$, $U = Cov(B)$, and $V = Cov(C)$ as the equation (2) can be written as:

$$\mathbf{P} \cdot \mathbf{v} = \lambda \cdot \mathbf{v} \quad (2)$$

Where \mathbf{P} is a square matrix n -by- n and \mathbf{v} is the eigenvector and λ is the eigenvalue

Thus, we receive 160 features from four subjects and four emotions for classification by using this method.

5 Classification Method and Experimental Results

The classification was most important step to recognize emotion. The multi-class support vector machine was used to classify emotional states of physiological signals and to improve the accuracy result of recognition.

5.1 Classification Method

In this paper, we use a tree-structure multi-class SVM, whose aim is to optimize the class patterns [7]. The process of this method will be shown as the following given steps.

First, we review a two-class pattern recognition problem. Given l labeled training data $\{(x_i, y_i)\}$, where $x_i \in R^n$, $y_i \in \{-1, 1\}$, and $i = 1, 2, \dots, l$. The learning of a two-class SVM is formulated as a convex quadratic programming (QP) problem by calculating the Lagrange multipliers $\{\alpha_i\}_{i=1}^l$ that maximize the function:

$$Q(\alpha) = \sum_{i=1}^l \alpha_i - \frac{1}{2} \sum_{i=1}^l \sum_{j=1}^l \alpha_i \alpha_j y_i y_j K(x_i, x_j) \quad (3)$$

Subject to : $\sum_{i=1}^l \alpha_i y_i = 0, \quad 0 \leq \alpha_i \leq C \text{ for } i = 1, 2, \dots, l$

Where C is a user-specified positive constant and $K(x_i, x_j)$ is a kernel function

The Gaussian kernel is chosen in this condition and we can optimize the problem 1 by using the function:

$$f(x) = \sum_{i=1}^l \alpha_i^* y_i K(x_i, x_j) + b \quad (4)$$

Where b means the bias

In this section, we describe the SVM learning algorithm for a k -class pattern recognition problem as the following steps.

Step 1: Let $\Gamma = \{1, 2, \dots, k\}$, and put Γ into a table which is indexed. Calculate the distances d_{ij} of all pairwise classes by equation below.

$$\begin{cases} d_{ij} = \frac{Ed_{ij}}{\gamma_i + \gamma_j} \\ \gamma_i = \frac{\sum_{m=1}^{n_i} \|x_m^i - c_i\|}{n_i} \end{cases} \quad (5)$$

Where Ed_{ij} is the Euclidian distance between i th class and j th class patterns, and γ_i is the distance between patterns in i th class and center point of i th class patterns.

Step 2: Find the furthest pair (i^*, j^*) in Γ , and let x^i belong to class1 and x^{j^*} belong to class -1.

Step 3: Compare d_{ii^*} with d_{ij^*} , where $i \in \Gamma \setminus \{i^*, j^*\}$. If $d_{ii^*} < d_{ij^*}$, x^i is distributed to Class1. If not, x^i is distributed to class -1. Thus, two subsets Γ_1 and Γ_{-1} are obtained.

Step 4: Calculate μ by using equation (6 (a)).

$$\begin{cases} (a) \mu = \frac{\min(n_1, n_{-1})}{\max(n_1, n_{-1})} \\ (b) \mu' = \frac{\min(n_1 + n_F, n_{-1} - n_F)}{\max(n_1 + n_F, n_{-1} - n_F)} \\ (c) v_e = \frac{d_{eA}}{d_{eB}} \end{cases} \quad (6)$$

Parameter μ represents the balance of distribution of four-class patterns, if $n_1 \prec n_{-1}$, calculate v_e by using formula (6(c)), where $e \in \Gamma_{-1}$. If not, calculate v_e where $e \in \Gamma_1$. Select a class x^e that the corresponding v_e is smallest. And calculate μ' by using formula (6(b)), where $n_F = n_e$.

If $\mu \succ \mu'$, go to step 5, else, if $n_1 \prec n_{-1}$, put x^e in class 1, and let $\Gamma_1 = \Gamma_1 \cup e$ and $\Gamma_{-1} = \Gamma_{-1} \setminus e$, if $n_1 \succ n_{-1}$, put x^e into class -1, and let $\Gamma_1 = \Gamma_1 \setminus e$ and $\Gamma_{-1} = \Gamma_{-1} \cup e$. Then repeat to step 4.

Step 5: We solve the equation (3) with the subsets Γ_1 and Γ_{-1} , and get a classifier.

Step 6: Delete Γ from the table and put Γ_1 and Γ_{-1} into the table. If the number of elements in each subset listed in the table equals 1, stop the algorithm. Else, let Γ be one of subsets in the table, in which the number of elements is larger than 1. And then go to Step 2.

5.2 Experimental Results

In Figure 5 represents the data of physiological signals of each emotion which is plotted in 2-D and 3-D space of single subject, it proves that the data of different emotions of single subject is separated and spread out for classification.

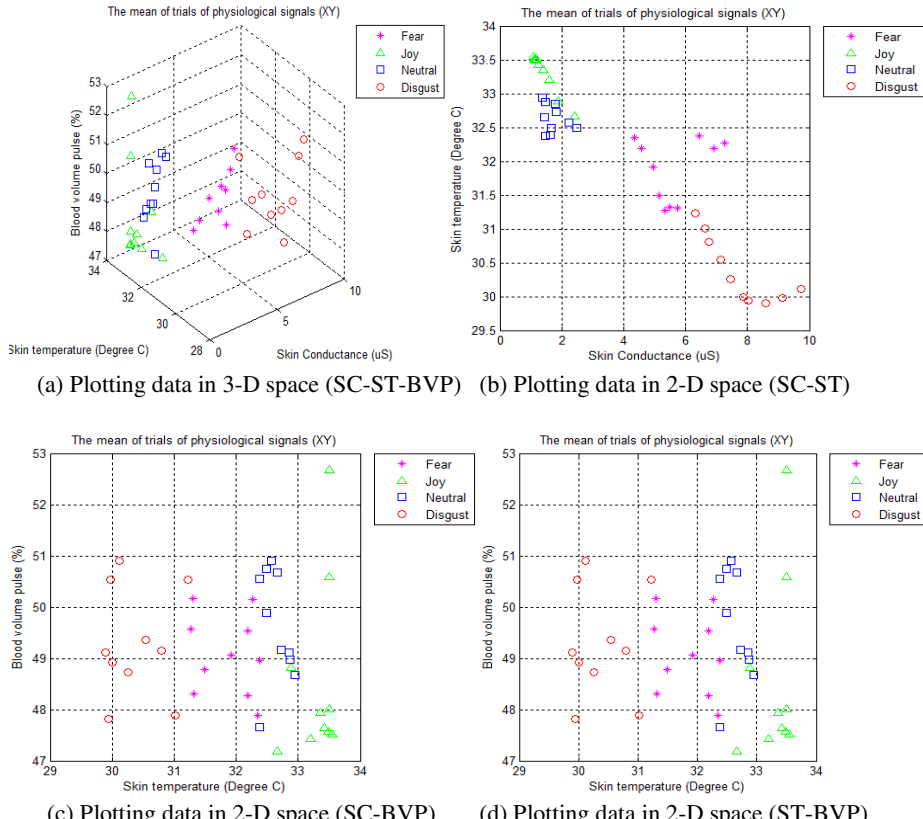


Fig. 5. Physiological data distribution for each emotional state

Table 1 proves the experimental results of four emotions of single subject, subject 1 exists the high accuracy of 100 % of fear and joy emotion from the 1st column but low accuracy of 40% of fear and disgust emotion from the 2nd column. Subject 2 has the high accuracy of 100% of disgust and neutral emotion in the 1st column with the low accuracy of 40% of neutral emotion in the 2nd and 3rd column, likewise the low accuracy of 40% of joy emotion is in the 4th column. For subject 3 proves that the 1st column shows the high accuracy of 100% of fear, joy, and neutral emotion but in the 3rd column proves the low accuracy of 40% of disgust and joy emotion. Subject 4 certifies that in the 1st column appears the high accuracy of 100% of joy and neutral emotion, in contrast the low accuracy of 40% of disgust emotion is in the 1st, 2nd, 3rd and 4th column.

Table 1. The accuracy of experimental results of each single subject, in this table: 1st, 2nd, 3rd columns represent the 2-D space which are combined by two axes of skin conductance-skin temperature, skin conductance-blood volume pulse, and skin temperature-blood volume pulse, respectively. And 4th column is a 3-D space which is constructed by three axes of skin conductance, skin temperature, and blood volume pulse.

Emotion	Subject 1				Subject 2				Subject 3				Subject 4			
	1st	2nd	3rd	4th												
Fear (%)	100	80	40	60	60	60	40	60	100	80	80	80	80	60	60	60
Disgust (%)	60	60	40	60	100	60	60	80	60	60	40	60	40	40	40	40
Joy (%)	100	60	60	80	40	60	60	40	100	60	40	60	100	60	60	60
Neutral (%)	60	60	60	60	100	40	40	60	100	60	60	60	100	60	60	60

Thus, according to the result in table 1 shows that the high accuracy of each subject in the 1st column is more efficient than the other columns in this experimental result, on the other hand the low accuracy is appeared in the 3rd column of this work much more than the other columns.

6 Conclusion

In this paper, we showed that using multi-class support vector machine was more efficient than other methods for classification in this work. And eigenvalue and eigenvector were used to optimize the feature for feature extraction. The accuracy of experimental result proved that the high accuracy of this work was located in the 1st column and low accuracy was located in the 3rd column. Although in this paper had a trouble with experimental paradigm in this time, we still make the progressive and will re-prepare the experiment for this work by improving the accuracy of emotion recognition. We assume that the methods are employed for feature extraction and classification in this paper, are efficient for emotion recognition.

In the future work, we will reach the experimental method to improve the meaningful data of elicited emotions such as video-clip and multi-modal stimuli (the combination of visualization and audition). And power spectrum as same as the other optimization methods for feature extraction will be used to optimize the feature for the feature extraction step as well as the comparison of classification methods with support vector machine will be employed to classify emotion recognition for improving the accuracy of classification. And we will show the way how to study multi-subjects classification in the next work.

Acknowledgements. This work was supported by the National Research Foundation of KOREA [NRF] grant funded by the KOREA government [MEST] [No.2011-0029861].

References

1. Lang, J., Bradley, M., Cuthbert, N.: International Affective Picture System (IAPS). Technical Manual and Affective Rating, Center for Research in Psychophysiology, University of Florida (1999)
2. Cacioppo, T., Tassinary, G.: Inferring Psychological Significance from Physiological Signals. *American Psychologist* 45(1), 16–28 (1990)
3. Vyzas, E., Picard, W., Healey, J.: Toward Machine Emotional Intelligence, Analysis of Affective Physiological State. *IEEE Trans. Pattern Analysis and Machine Intelligence* 23(10), 1175–1191 (2001)
4. Posner, J., Russell, A., Peterson, S.: The circumflex model of affect,” An integrative approach to affective neuroscience, Cognitive development and psychopathology. *Development and Psychopathology* 17(3), 715–734 (2005)
5. Kim, H., Bang, W., Kim, R.: Emotion Recognition System using Short-term Monitoring of Physiological Signals. *Medical and Biological Engineering and Computing* 42(3), 417–427 (2004)
6. Gu, Y., Tan, S., Wong, K., Ho, M., Qu, L.: Using GA-based Feature Selection for Emotion Recognition from Physiological Signals. In: Int. Symposium on Intelligent Signal Processing and Communication System, Bangkok (2008)
7. Jun, G., Youguang, C., Min, Z., Su, W., Xiaoping, L.: An Efficient Support Vector Machine Algorithm for Solving Multi-class Pattern Recognition Problems. In: Second Int. Conf. on Computer Modeling and Simulation, vol. 2, pp. 461–465 (2010)

Human Intention Reading by Fuzzy Cognitive Map: A Human-Robot Cooperative Object Carrying Task

Ji-Hyeong Han and Jong-Hwan Kim

Department of Electrical Engineering, KAIST, 291 Daehak-ro, Yuseong-gu,
Daejeon, 305-701, Republic of Korea
{jhhhan,johkim}@rit.kaist.ac.kr

Abstract. Considering the symbiosis between humans and robots in coming years, robots should be able to infer the implicit human intention for the efficient human-robot interaction. This paper focuses on the human-robot cooperation problem among the various fields of human-robot interaction. The human intention reading method using fuzzy cognitive map for the efficient human-robot cooperation is proposed along with the algorithm which decides the appropriate behavior of a robot with the recognized human intention. The effectiveness of the proposed method is demonstrated through computer simulation on human-robot cooperative object carrying task.

Keywords: Human-robot interaction, human intention reading method, fuzzy cognitive map.

1 Introduction

The symbiosis era of humans and robots is approaching in no distant future because of the rapid development of the robot technology and artificial intelligence (AI). For this coming era, the natural and rational human-robot interaction (HRI) is needed. In this manner, HRI researches have grown up and there have been many researches on various HRI fields. Among these researches, the efficient cooperation between humans and robots is one of crucial issues. Through the efficient human-robot cooperation, each can get particular benefits from the other.

To achieve the efficient human-robot cooperation, robots need to read the human intention without the explicit human commands. A robot can infer the human intention by recognizing the explicit human commands, such as verbal dialog. However, in this case, a human has a cognitive burden, since he/she has to make an explicit command all the time. Therefore, a robot should have a capability to recognize the human intention based on the implicit human information, such as human behavior, gesture, and position. There were several researches on intention reading algorithm and social robotics [1]-[6].

The one of typical applications for human-robot cooperation is human-robot cooperative object carrying task. There were several researches on human-robot cooperative object carrying [7]-[12]. Most of the researches have focused on the control issue after a robot and a human grab the object. Some researches considered the human intention by force or torque sensing, but it was still after grabbing the object. However, in the real world environment, there can be several objects and a robot should decide which

object and which side of an object a human wants to carry. Also, there can be several goal points to carry an object. There is a lack of research which considers the human intention before grabbing an object as well as with the case of several possible objects and goal points. Therefore, this paper proposes the human intention reading method which recognizes the human intended object, side, and goal point using fuzzy cognitive map (FCM) for the efficient human-robot cooperative object carrying task. FCM, which was proposed by Kosko, is a symbolic representation for modeling the complex system [13]. FCM has been applied to the various research fields [14].

In this paper, human intention reading method using FCM is proposed for the efficient human-robot cooperative object carrying task. To demonstrate the effectiveness of the proposed method, computer simulation on human-robot cooperative object carrying task is carried out.

This paper is organized as follows. Section 2 briefly explains FCM. Section 3 describes the formulation of the target problem and proposes the human intention reading method using FCM. In Section 4, the simulation results for the human-robot cooperative object carrying task are discussed. Finally, concluding remarks follow in Section 5.

2 Fuzzy Cognitive Map

Fuzzy Cognitive Map (FCM) is a graphical representation which consists of concept nodes and weighted arrows [13]. The weighted arrows are connecting the concept nodes and represent the causality between the connected concept nodes. This graphical representation is able to show clearly which concept influences other concepts and how much influence. This section briefly explains FCM representation and update formulation.

2.1 Fuzzy Cognitive Map Representation

Figure 1 is a simple FCM example which consists of four concept nodes and six weighted arrows. As shown in figure 1, FCM is able to model the causal relationship between concept nodes. Each concept node has a concept variable, such as C_1, C_2, C_3 , and C_4 in figure 1. Each concept variable has a number α_i which represents its value in the interval $[0, 1]$. The causality from C_i to C_j is represented by the arrow which starts from C_i , which is called a causal variable, and ends to C_j , which is called an effect variable. The degree of causality between concepts is represented by weight, W_{ij} in interval $[-1, 1]$. There are three kinds of causalities between concepts as follows:

- 1) $W_{ij} > 0$: the positive causality.
- 2) $W_{ij} = 0$: no relationship.
- 3) $W_{ij} < 0$: the negative causality.

At each time step, the value of concept variable C_i , α_i , is calculated as follows:

$$\alpha_i^t = f \left(\sum_{\substack{j=1 \\ j \neq i}}^n \alpha_j^{t-1} W_{ji} + \alpha_i^{t-1} \right) \quad (1)$$

where α_i^t and α_i^{t-1} are the values of concept C_i at time step t and $t - 1$, respectively, α_j^{t-1} is the value of concept C_j at time step $t - 1$, W_{ji} is the interconnection weight

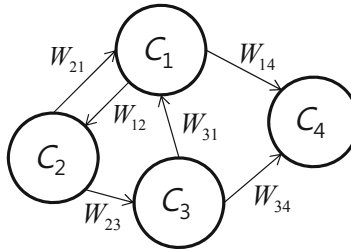


Fig. 1. A simple fuzzy cognitive map example

from concept C_j to concept C_i , and W_{ii} is zero. The function f is a threshold function for normalizing concept value in interval $[0, 1]$. Usually, the following unipolar sigmoid function is used as the threshold function in FCM.

$$f(x) = \frac{1}{1 + e^{-\lambda x}}, \lambda > 0 \quad (2)$$

where λ determines the steepness of the function f .

3 Problem Formulation and the Proposed Human Intention Reading Method

The problem trying to solve in this paper is human-robot cooperative object carrying task. For efficient cooperation between a human and a robot, the robot should recognize the human intention, such as the human intended object and the human intended goal point. To solve this issue, the human intention reading method using FCM is proposed in this paper. This section explains the problem formulation and then detailed descriptions of the proposed method follow.

3.1 Problem Formulation

Figure 2 shows the simulation environment of human-robot cooperative object carrying task. There are two blocks (B1 and B2), two goal points (G1 and G2), three robot agents (R1, R2, and R3), and a human agent (H). The goal of the task is carrying each block to any goal points. A goal point is able to have only one block and the indices of the blocks and the goal points are irrelevant. Two agents are needed to carry a block and they have to be at opposite sides of the block. After all blocks are grabbed by agents, they are carried to goal points.

The initial positions of all agents and blocks are random. The human agent moves manually by a user using keyboard and mouse inputs. The robot agents move autonomously and the details of the robot agent behavior decision process will be explained in the following Subsection 3.2. The blocks move randomly up, down, left, right, or stay with probability of 0.2 until they are grabbed by an agent. The locations of goal points are fixed.

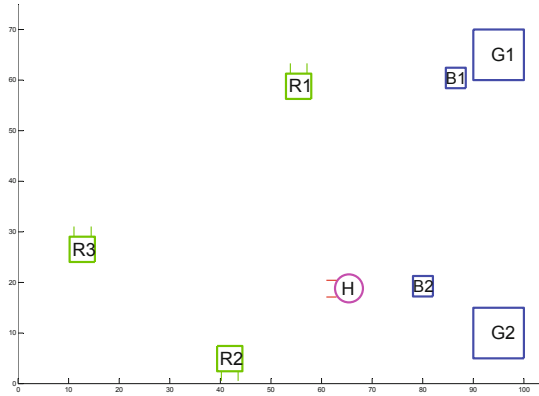


Fig. 2. The simulation environment of human-robot cooperative object carrying task

3.2 Human Intention Reading Method Using FCM

The problem trying to solve has two blocks, three robot agents, and a human agent and two agents are needed to carry a block. Therefore, there are two teams which consist of two robot agents and a human and a robot agents. To a human and a robot agents team carry a block successfully to a goal point, a human and robot cooperation is essential. To achieve the efficient human-robot cooperation, a robot should read the human intention by observing the human movement. Three kinds of human intentions are defined in this problem as follows.

- 1) Which block does a human want to carry?
- 2) Which side of the block does a human want to grab?
- 3) Which goal point does a human want to go?

FCM is applied to recognize the human intentions 1) and 3). Figure 3 shows the defined FCM. There are four input concept nodes, i.e., D_1 , D_2 , A_1 , and A_2 . The input concept node D_n represents the distance between the human position and B_n and G_n positions for the human intention 1) and 3), respectively. The input concept node A_n represents the angle between the human direction and B_n and G_n for the human intention 1) and 3), respectively. There are two output concept nodes for each block and goal point, i.e., B_1 , B_2 and G_1 , G_2 , for the human intention 1) and 3), respectively. The subscript of each node is the index of the block or the goal point.

The values of the input concept nodes D_n and A_n , α_{D_n} and α_{A_n} , are defined as follows:

$$\begin{aligned}\alpha_{D_n} &= 1/(1 + d_n) \\ \alpha_{A_n} &= 1/(1 + a_n)\end{aligned}\quad (3)$$

where d_n is the distance between the human and B_n or G_n and a_n is the angle between the human direction and B_n or G_n . Since the block or goal point with small d_n and a_n shall be the human intended one, α_{D_n} and α_{A_n} are defined one over d_n and a_n . Plus one in the denominator of Equation 3 is to prevent dividing by zero. The values of the output concept nodes B_n and G_n for the human intentions 1) and 3), respectively, are initially

zero and updated by Equation 1. When FCM reaches the equilibrium point, the output concept node which has the biggest value is selected as the human intended block or goal point.

Two different weights of FCM are defined to recognize the human intentions 1) and 3), respectively. Each of them is defined as follows:

$$W_{block} = \begin{bmatrix} 0 & 0 & 0 & 0 & 0.5 & -1 \\ 0 & 0 & 0 & 0 & -1 & 0.5 \\ 0 & 0 & 0 & 0 & 1 & -1 \\ 0 & 0 & 0 & 0 & -1 & 1 \\ 0 & 0 & 0 & 0 & 0 & -1 \\ 0 & 0 & 0 & 0 & 1 & 0 \end{bmatrix}, W_{goalpoint} = \begin{bmatrix} 0 & 0 & 0 & 0 & 1 & -1 \\ 0 & 0 & 0 & 0 & -1 & 1 \\ 0 & 0 & 0 & 0 & 0.5 & -1 \\ 0 & 0 & 0 & 0 & -1 & 0.5 \\ 0 & 0 & 0 & 0 & 0 & -1 \\ 0 & 0 & 0 & 0 & -1 & 0 \end{bmatrix} \quad (4)$$

where W_{block} is for recognizing the human intention 1) and $W_{goalpoint}$ is for recognizing the human intention 3). The order of columns and rows is $D_1, D_2, A_1, A_2, B_1/G_1$, and B_2/G_2 from left to right and from up to down, respectively. W_{block} is defined to consider that the angle is more important than the distance. On the other hand, $W_{goalpoint}$ is defined to consider that the distance is more important than the angle.

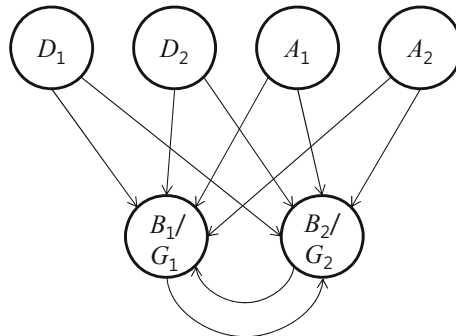


Fig. 3. The defined FCM to recognize the human intentions 1) and 3)

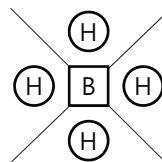


Fig. 4. The relative position between a human and a block to recognize the human intention 2)

To recognize the human intention 2), the simple relative position between a human and a block is used as shown in figure 4. H and B in figure 4 represent a human and a block, respectively. There are four possible human intentions, i.e., up, down, left, or right sides of the block.

Algorithm 1 shows the overall procedure for a human-robot cooperative carrying task using the proposed human intention reading method with FCM.

Algorithm 1. The overall algorithm for a human-robot cooperative object carrying task

Initially, all of the agents and blocks are randomly located.

while All blocks are grabbed by agents. **do**

- i) Recognize the human intended block using FCM with W_{block} .
- ii) Recognize the human intended side of the intended block from i) using the relative position between a human and the intended block.
- iii) The closest robot to the human intended block makes a team with a human. The robot goes to the opposite side of the human intended side of the human intended block.
- iv) The other robots make a team and go to the other block. The closest robot to the other block chooses the desired side first and another robot goes to the opposite side.

end while

After all blocks are grabbed by the agents, the agents carry the block to the goal point.

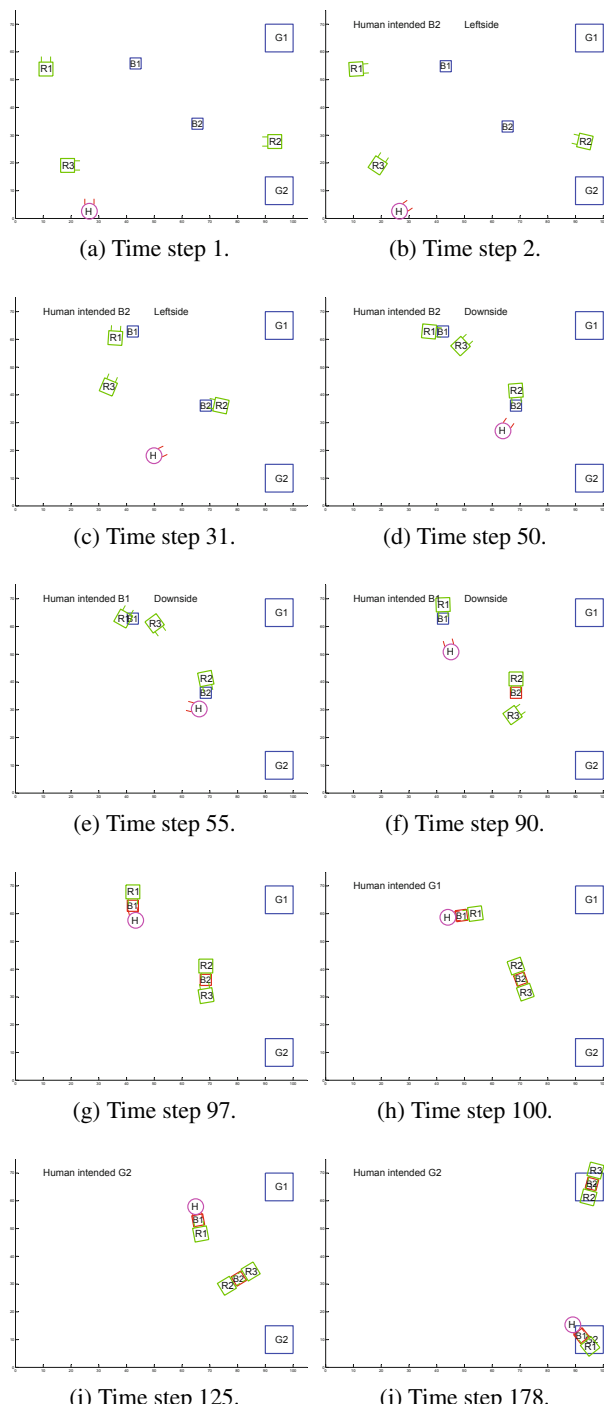
while All blocks are carried to the goal point. **do**

- i) Recognize the human intended goal point using FCM with $W_{goalpoint}$.
- ii) The robot in a human-robot team goes to the human intended goal point with a human.
- iii) The other team goes to the other goal point.

end while

4 Simulation Results

To show the effectiveness of the proposed method, a human-robot cooperative object carrying task was simulated in MATLAB environment. Figure 5 shows the snapshots of simulation result in time order and figure 6 shows the values of FCM output concept nodes during simulation. Initially all of the agents and blocks were located randomly (figure 5(a)). Firstly, the human wanted to grab B2. The human intention was recognized as B2-leftside (figure 5(b)), since the value of FCM output concept node B_2 was bigger than one of B_1 as shown in figure 6(a). So R2, which was the closest robot to B2, made a team with the human and went to the B2-rightside and other robots, R1 and R3, went to B1 (figure 5(c)). Since the recognized human intention was changed to B2-downside as the human approached B2, R2 moved from B2-rightside to B2-upside (figure 5(d)). Suddenly, the human changed his/her mind to grab B1. The human intention was recognized as B1-downside (figure 5(e)), since the value of FCM output concept node B_1 was bigger than one of B_2 as shown in figure 6(a). So R1, which was the closest robot to B1, made a team with the human and grabbed B1-upside and R3 changed its direction to B2 (figure 5(f)). When a block was grabbed, the color was changed to red. Finally, all the blocks were grabbed and simulation was in next stage, i.e., carrying the object to a goal point (figure 5(g)). Firstly, the human wanted to carry B1 to G1. The human intention was recognized as G1, since the value of FCM output concept node G_1 was bigger than one of G_2 as shown in figure 6(b). So the human-robot team went to G1 and the robot-robot team went to G2 (figure 5(h)). And then suddenly the human changed his/her mind to carry B1 to G2. The human intention was recognized as G2, since the value of FCM output concept node G_2 was bigger than one of G_1 as shown in figure 6(b). Therefore, the human-robot team went to G2 and the robot-robot team changed

**Fig. 5.** Simulation results in time order

their directions to G1 (figure 5(i)). Finally, all the blocks were carried to different goal points successfully and the simulation was over (figure 5(j)).

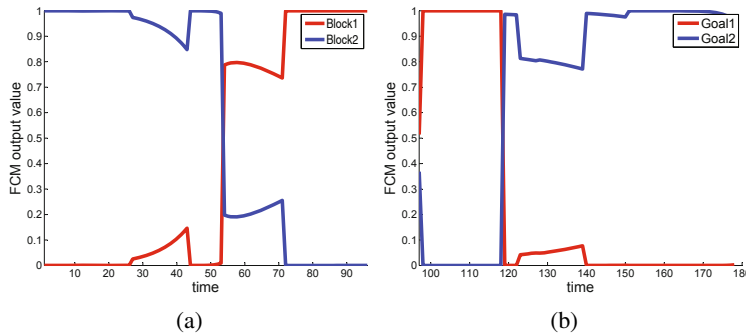


Fig. 6. The values of FCM output concept nodes during simulation. (a) The values of B_1 and B_2 . (b) The values of G_1 and G_2 .

5 Conclusion and Future Works

This paper proposed the human intention reading method for the efficient human-robot cooperative object carrying task. FCM was applied to the human intention reading method. The three kinds of human intentions, i.e., which block, which side of a block, and which goal point, were defined and they were recognized by the proposed method with the defined FCM. The effectiveness of the proposed method was demonstrated through computer simulation on the human-robot cooperative object carrying task with two blocks and two goal points. The proposed method recognized the human intention in real time and even if the human intention was suddenly changed, the proposed method inferred it instantly. Also, the robot behavior decision process with the recognized human intention was defined for the efficient cooperation between a human and a robot.

FCM was the useful method to understand the human intention as shown in this paper. It could represent the various abstracted concepts as nodes and their relationships as weighted edges intuitively and the human intention usually consisted of the abstracted conceptions. Therefore, FCM would be the competitive method to solve the problem which could be defined by the various concepts such as the human intention issue. For future work, the weights of FCM could be adjusted by using Hebbian learning or other learning methods.

Acknowledgment. This research was supported by the MKE (The Ministry of Knowledge Economy), Korea, under the Human Resources Development Program for Convergence Robot Specialists support program supervised by the NIPA (National IT Industry Promotion Agency)(NIPA-2012-H1502-12-1002).

References

1. Schrempf, O.C., Hanebeck, U.D., Schmid, A.J., Wörn, H.: A novel approach to proactive human-robot cooperation. In: IEEE RO-MAN 2005, pp. 555–560 (2005)
2. Schrempf, O.C., Hanebeck, U.D.: A generic model for estimating user intentions in human-robot cooperation. In: Proc. of the 2nd Int. Conf. on Informatics in Control, Automation and Robotics, pp. 250–256 (2005)
3. Schmid, A.J., Weede, O., Wörn, H.: Proactive robot task selection given a human intention estimate. In: IEEE RO-MAN 2007, pp. 726–731 (2007)
4. Omori, T., Yokoyama, A., Okada, H., Ishikawa, S., Nagata, Y.: Computational Modeling of Human-Robot Interaction Based on Active Intention Estimation. In: Ishikawa, M., Doya, K., Miyamoto, H., Yamakawa, T. (eds.) ICONIP 2007, Part II. LNCS, vol. 4985, pp. 185–192. Springer, Heidelberg (2008)
5. Gray, J., Breazeal, C., Berlin, M., Brooks, A., Lieberman, J.: Action parsing and goal inference using self as simulator. In: IEEE RO-MAN 2005, pp. 202–209 (2005)
6. Breazeal, C., Gray, J., Berlin, M.: An embodied cognition approach to mindreading skills for socially intelligent robots. *Int. J. Robotics Research* 28, 656–680 (2009)
7. Yamada, Y., Umetani, Y., Daitoh, H., Sakai, T.: Construction of a human/robot coexistence system based on a model of human will/intention and desire. In: Proc. IEEE Robotics and Automation, vol. 4, pp. 2861–2867 (1999)
8. Fernandez, V., Balaguer, C., Blanco, D., Salichs, M.A.: Active human-mobile manipulator cooperation through intention recognition. In: Proc. IEEE ICRA, vol. 3, pp. 2668–2673 (2001)
9. Arai, H., Takubo, T., Hayashibara, Y., Tanie, K.: Human-robot cooperative manipulation using a virtual nonholonomic constraint. In: Proc. IEEE ICRA, vol. 4, pp. 4063–4069 (2000)
10. Inoue, Y., Toghe, T., Iba, H.: Cooperative transportation system for humanoid robots using simulation-based learning. *Applied Soft Computing* 7, 115–125 (2005)
11. Sisbot, E.A., Clodic, A., Alami, R., Ranan, M.: Supervision and motion planning for a mobile manipulator interacting with humans. In: Proc ACM/IEEE HRI 2008, pp. 327–334 (2008)
12. Pereira, F.G., de Sä, F.B., Ferreira, D.B., Vassallo, R.F.: Object transportation task by a human and a mobile robot. In: IEEE Int. Conf. Industrial Tech., pp. 1445–1450 (2010)
13. Kosko, B.: Fuzzy cognitive maps. *Int. J. Man-Machine Studies* 24, 65–75 (1986)
14. Glykas, M.: Fuzzy cognitive maps advances in theory, methodologies, tools and applications. *STUDFUZZ*, vol. 247 (2010), doi:10.1007/978-3-642-03220-2

A Simultaneous Generation Method for Gaze Behaviors and Facial Expressions of a Robotic Head

Bum-Soo Yoo and Jong-Hwan Kim

Department of Electrical Engineering, KAIST, 291 Daehak-ro,
Yuseong-gu, Daejeon, 305-701, Republic of Korea
{bsyoo,johkim}@rit.kaist.ac.kr

Abstract. Human robot interaction (HRI) is one of emerging areas in robotics. When robots communicate with people, non-verbal communication including facial expressions, gestures and gaze plays an important role to express their emotion and intention effectively. Thus, many researches are carried out to generate proper non-verbal communications that would make robots to be considered as social agents. This paper proposes a method of generating facial expressions and gaze directions simultaneously. When external environment is perceived, robot's emotion is changed either instantly or gradually. The emotion is used to generate facial expressions using the fuzzy measures and fuzzy integral. At the same time, a fuzzifier is applied to the perceived information to produce useful human information. The human information includes the number of faces and the size of faces, which can be used to approximate distances from the robot to faces. The human information is used to select a gaze behavior among four candidate behaviors. Through the proposed method, robots can generate proper facial expressions and gaze behaviors at the same time. The effectiveness of the proposed method is demonstrated through the simulation and the experiments with a robotic head, developed in the RIT Laboratory, KAIST.

Keywords: Human robot interaction, gaze behavior selection, face detection, facial expression.

1 Introduction

Conventional robots were mainly used for industrial purpose. In this period, robots worked instead of people for tedious and repetitive tasks. However, with the development of robot technology, robots are expected to be partners of humans in future [1]. Thus, researches on HRI is one of emerging areas and is required more attention to keep pace with robot technology.

In HRI, it is necessary to use non-verbal communication to deliver robots emotion and intention effectively. According to the psychologist Mehrabian, 55% of information is delivered by non-verbal communication [2], [3]. Among various non-verbal communication methods, facial expressions of a robot are mainly

used to express emotions and its gaze direction has a large influence on social interactions. For example, if a robot is able to keep eye contact with a human while she/he is talking, she/he may get more comfortable impression from the robot. Thus, gaze direction is one of an essential elements in HRI.

Many researches are carried out to generate humanlike gaze. Saliency map which integrates information from attractive visual features to one global map was introduced to make stimulus driven gaze direction system [4]. Affects of faces on human's attention system was described and showed that faces are strong attractors [5]. The architecture to autonomously learn gaze control was introduced [6]. Its performance was demonstrated by showing that the robot could look at objects that human partners were explaining. Human partners felt robots were concentrating on their explanations. A small size humanoid robot which can gaze at a moving object by controlling its eyes and head was introduced [7]. The gaze control was applied to the navigation of humanoid robots in a dynamic environment [8]. The gaze direction was selected based on four criteria and internal preferences by using the fuzzy measure and fuzzy integral.

This paper proposes a method of generating facial expressions and human-like gaze behaviors. When external environment is perceived, robot's emotion is changed both instantly and gradually. At the same time, a fuzzifier is applied to the perceived information to produce useful human information. The human information includes the number of faces and the size of faces, which can be used to approximate distances from the robot to faces. Derived human information is used to select a proper gaze behavior among four candidate behaviors by the fuzzy rule-based system. Facial expressions are generated from emotions using the fuzzy measures and fuzzy integral. Since the relationship among emotions is ambiguous, the fuzzy measure is used to reflect the ambiguity. In addition, the fuzzy measure can cover a non-linearity which facial expressions have. With the proposed method, robots can generate proper facial expressions and gaze behaviors at the same time. The effectiveness of the proposed method is demonstrated through the experiments with a robotic head with 19 degrees of freedom, developed in the RIT Laboratory, KAIST.

The rest of paper is organized as follows: Section II describes gaze control method according to the perceived information and emotion update equations. Section III describes the definition related to fuzzy logics and facial expression generation algorithm. Section IV describes simulation and experimental results and concluding remarks on Section V.

2 Gaze Control

2.1 Gaze Behavior Selection

A proper gaze behavior is chosen based on human information in the environment. From visual information three criteria such as the number of faces (c_1), average face size (c_2) and the maximum face size (c_3) are obtained and fuzzified. The sizes of faces are used to approximate the distance from the robot to

Table 1. Rule set related to human information

Number of faces (c_1)	Average size (c_2)	Maximum size (c_3)	Gaze behavior
Few	-	Small	Look default direction
Few	-	Medium	Look one face
Several	Small	-	Look center of faces
Several	Medium	Small	Look center of faces
Several	Medium	Medium	Look faces one by one
Several	Large	-	Look faces one by one
Many	Small	-	Look center of faces
Many	Medium	-	Look center of faces
Many	Large	-	Look faces one by one
-	-	Large	Look one face

each face. According to the three criteria, robot's gaze behavior is decided. For example, if a face is too big, which means the face is too close, robot should see only that face and if there are several faces, robot has to give a gaze to all faces one by one sequentially or see to the center of all faces. With the three criteria robot selects a proper gaze behavior among four candidate behaviors: look default direction, look one face, look the center of all faces and look faces sequentially. Selection is decided by a fuzzy rule-based system which is shown in Table 1.

Fig. 1 shows the membership functions for each criterion. The rules with **max-min** inference are applied to the result of fuzzifier and the rule with the largest inference value is selected. Since the visual information contains lots of noise, sometimes gaze behavior changes from time to time. Once the gaze behavior is changed frequently and robot is to be vibrating which will cause more noise in visual information and will get worse results. Thus, selection period is dynamically changed from 33 msec to one sec based on current visual information. Note that 33 msec means regeneration period of visual information from 30 fps camera. For example, if a robot detects faces after no face situation for a while, selection period is set to be one sec instantly and decreased gradually.

just after no face situation.

2.2 Emotion Transition

When a robot receives visual information, emotions are changed. Emotions (E) are expressed with six parameters according to the psychologist Ekman's theory which defines human's basic emotions as anger (e_1), disgust (e_2), fear (e_3), happiness (e_4), sadness (e_5) and surprise (e_6) [9]. It is assumed that robots always want to interact with people. Thus, if people are in their vision, their happiness is increasing. Robots will get disgusted when people are positioned too close to robots like several centimeters. When the visual information is perceived, fuzzy membership functions are applied to derive human information and emotions are updated as follows:

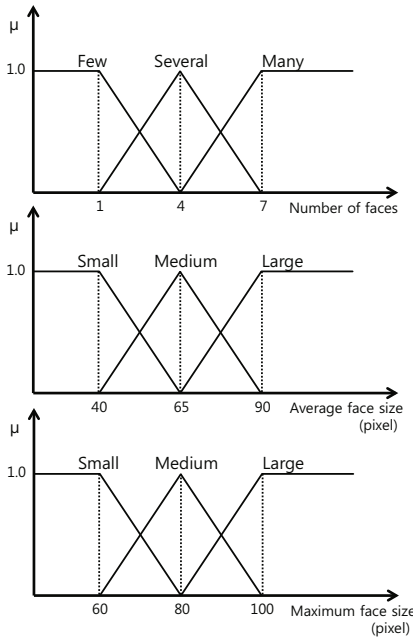


Fig. 1. Membership functions for the three criteria

$$E_{t+1} = E_t + A_1 u_1 + A_2 u_2 + \dots + A_n u_n \quad (1)$$

where u_i are the visual information including the human information. A_i is a 6×1 vector containing the relationship between the visual information including the human information and the emotions. The emotions are updated as follows:

$$E_{t+1} = E_t + (E_{nor} - E_t) \times \Delta E_t \quad (2)$$

where E_{nor} is the normal emotion and Δ represents the amount of change in a control period. The meaning of the normal emotion is a converging emotion when there is no input for a while. Emotions slowly converge to the normal emotion. The normal emotion also changes as the visual information is perceived as follows:

$$E_{nor} = E_{nor} + B_1 u_1 + B_2 u_2 + \dots + B_n u_n \quad (3)$$

where B_i is a 6×1 vector containing the relationship between the visual information including the human information and normal emotions.

3 Facial Expression

3.1 Fuzzy Measure and Fuzzy Integral

The Sugeno λ -fuzzy measure and the Choquet integral are used to generate facial expressions. The fuzzy measure is defined in the following [10].

Definition 1: A fuzzy measure on the set X of symbols is a set function $g : P(X) \rightarrow [0, 1]$ satisfying the following axioms;

- i) $g(\emptyset) = 0, g(X) = 1$;
- ii) $A \subset B \subset X$ implies $g(A) \leq g(B)$.

The Sugeno λ -fuzzy measure satisfies the following [11]:

$$g(A \cup B) = g(A) + g(B) + \lambda g(A)g(B). \quad (4)$$

In the above equation, g represents the fuzzy measure, λ represents the interaction degree. If $\infty > \lambda > 0$, two symbols are in a negative correlation and $g(A \cup B)$ is overestimated. If $0 > \lambda > -1$, two symbols are in a positive correlation and $g(A \cup B)$ is underestimated.

The Choquet fuzzy integral is defined in the following [12].

Definition 2: Let h be a mapping from finite set X to $[0,1]$. For $x_i \in X, i = 1, 2, \dots, n$, assume $h(x_i) \leq h(x_{i+1})$ and $E_i = \{x_i, x_{i+1}, \dots, x_n\}$. The Choquet fuzzy integral of h over X with respect to the fuzzy measure g is define as

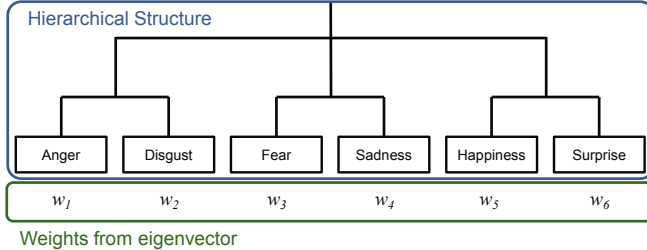
$$\int_X h \circ g = \sum_{i=1}^n (h(x_i) - h(x_{i-1}))g(E_i), \quad h(x_0) = 0. \quad (5)$$

In the above equation, all fuzzy measures should be calculated before the global evaluation.

3.2 Facial Expression Generation

Facial expressions are generated with the fuzzy integral and fuzzy measure [13]. The fuzzy measure can deal with the ambiguity of crisp sets. Since people may not easily assign the degree of evidence to be in one of emotions, the fuzzy measure is used to deal with the ambiguity. In addition, the fuzzy measure can cover a non-linearity which facial expressions have. To identify all fuzzy measures, the diamond pairwise comparison method is used [14]. Six basic emotions are used to express robot's emotion and are used as criteria in generating facial expressions. Human's facial expressions do not contain only one emotion. They can contain composite emotions. According to the Ekman, when two emotions are expressed at the same time, each emotion is expressed separately in parts of face, and composite facial expressions are produced in a big picture. To make composite facial expressions, face is divided into three parts and the algorithm is applied separately.

Based on the Ekman's theory, every two emotions pair among six basic emotions is compared with the diamond pairwise comparison method. The comparison reflects two informations: relative importance and relationship between all two emotion pairs. The relative importance means which emotion is appeared between two emotions in that part of face. The relationship means positive or negative corelation between two emotions which is assigned according to the

**Fig. 2.** Hierarchical structure

Ekman's theory. With the relative importance, the pairwise comparison matrix is generated and weight vector, $W = \{w_1, w_2, \dots, w_6\}$, is calculated by the eigenvalue and eigenvector. Since the derived weight vector contains only the importance of each emotion, the relationship among emotions should be considered.

From the relationship among emotions, dissimilarity graph is obtained. The dissimilarity graph consists of six clusters according to the number of basic emotions. Two clusters in the dissimilarity graph are merged step by step until only one cluster remains. Result of merging process is used to generate hierarchical structure in Fig. 2. Weight vector from the pairwise comparison matrix is placed at the bottom-level of the hierarchical structure. To reflect the relationship among emotions, the weight vector moves the top-level of the hierarchical structure with ϕ_s transformation [15]. The top-level weights are used as the fuzzy measure, which is expressed g in (5). Partial evaluation values are obtained from current emotion. Let $S_i = \{s_{i1}, s_{i2}, \dots, s_{i6}\}$, $i = 1, 2, \dots, 6$ be an ideal emotion. The ideal emotion means that the corresponding emotion is fully expressed. The ideal emotion states s_{ij} is defined as follows:

$$s_{ij} = \begin{cases} 0 & \text{if } i \neq j \\ 1 & \text{if } i = j. \end{cases} \quad (6)$$

Thus, $S = \{S_1; S_2; \dots; S_6\}$ is the 6×6 identity matrix. The current emotion should be close to S_i to express the i -th emotion. In addition, in expressing the i -th emotion, the i -th emotion state is more important than other emotions. Thus, the partial evaluation value of the i -th emotion H_i is calculated as follows:

$$H_i = I - (s_{ii} - e_i) \times (I - |S_i - E|), \quad (7)$$

where I is the 1×6 vector with elements are all ones and $H = \{H_1; H_2; \dots; H_6\}$ is a partial evaluation matrix. The partial evaluation H_i in (7) is integrated with the fuzzy measure from Fig. 2 by the Choquet integral and the maximum value of emotion is expressed through facial expression. The algorithm is applied to each part of faces separately. Because when a composite facial expression is produced, different parts of face express different emotions. Thus, each part has different relative importance for emotions.

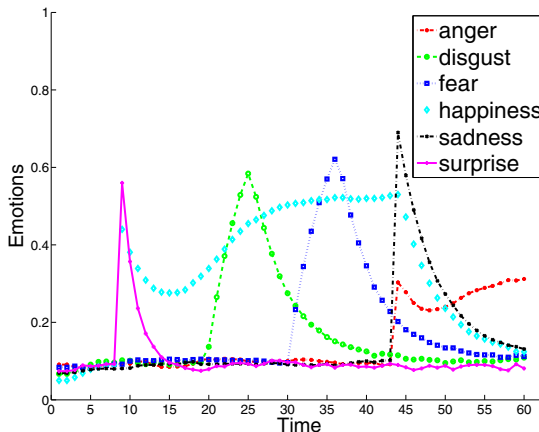


Fig. 3. Emotion variation

4 Simulation and Experimental Results

4.1 Simulation

HRI was performed through computer simulation and the robotic head's emotions were observed. Fig. 3 shows the variation of its emotions during HRI. Initially, every emotion is in a similar level with small degree. When human faces appeared, happiness and surprise increased instantly because it wanted to interact with people. Soon, surprise, the shortest emotion among six basic emotions, quickly decreased and happiness was continuously maintained high. When a face was approaching too close, the robotic head got disgusted. When the robotic head thought there were too many faces in a vision, it got afraid and fear increased. When faces were disappeared from the vision, the robotic head became sad and anger increased.

4.2 Experiment

HRI was performed in real environment. When there was no face in a vision, the robotic head looked default direction with anger facial expressions. When a face appeared, it was surprised and happiness increased. At the same time, the robotic head changed its gaze behavior from look default direction to look one detected face and turned its gaze direction to the face. Since there was no significant change in human information, the robotic head continuously pursued the face. Fig. 4 shows snapshots for pursuing the detected face. The gaze behavior selection was performed in every 33 msec, which was not enough to transit from one gaze behavior to other gaze behavior. Thus, FIR filter was applied to every data received from the camera and the gaze behavior was tuned to change if the



Fig. 4. Gaze selection. (a) robot looks default direction (b) robot detects a face (c) robot pursues the detected face

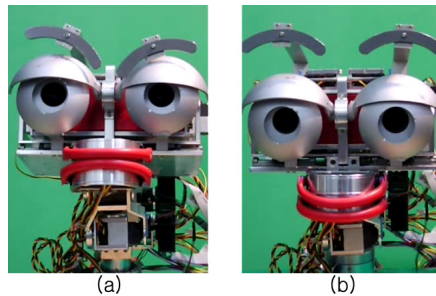


Fig. 5. Produced facial expressions. (a) anger (b) happiness and surprise

global evaluation of a certain gaze behavior was larger than that of previously selected gaze behavior plus predefined threshold.

Fig. 5 shows the facial expressions of robotic head. Fig. 5(a) shows anger facial expression of the robotic head. It made anger facial expression when there were no faces in a vision for a while. Fig. 5(b) shows happiness and surprise composite facial expression. It made the composite facial expression when it detected faces just after no face situation.

5 Conclusions

This paper proposed a generation method for facial expressions and gaze behaviors simultaneously and the proposed method was demonstrated its effectiveness through the experiments with the robotic head developed in the Robot Intelligence Technology Lab., KAIST. From the visual information, human information was derived through the fuzzifier defined by fuzzy membership functions. The human information was used to select a gaze behavior by the proposed fuzzy rule-based system. At the same time, the visual information affected its emotion which would be expressed through facial expressions. Facial expression generation was performed with the fuzzy measure and fuzzy integral. Experiments showed that facial expressions and gaze behaviors were generated properly according to the current situation.

Acknowledgement. This research was supported by MKE (The Ministry of Knowledge Economy), Korea, under the Human Resources Development Program for Convergence Robot Specialists support program supervised by the NIPA (National IT Industry Promotion Agency) (NIPA-2012-H1502-12-1002).

References

1. Breazeal, C.L.: Social interactions in HRI: the robot view. *IEEE Trans. Man Cybern. C Appl. Rev.* 34(2), 181–186 (2004), doi:10.1109/TSMCC.2004.826268
2. Mehrabian, A.: Nonverbal Communication. Aldine-Atherton (1972)
3. Mehrabian, A.: Communication without words. *Psychology Today* 2(4), 53–56 (1968)
4. Koch, C., Ullman, S.: Shifts in selective visual attention: towards the underlying neural circuitry. *Human Neurobiology* 4, 219–227 (1985)
5. Cerf, M., Harel, J., Einhäuser, W., Koch, C.: Predicting human gaze using low-level saliency combined with face detection. *Advances in Neural Information Processing Systems* 20, 241–248 (2008)
6. Mohammad, Y., Okada, S., Nishida, T.: Autonomous development of gaze control for natural human-robot interaction. Paper presented at 2010 Wrks on Eye Gaze in Intell Human Mach Interaction, Hong Kong, China, pp 63–70 (February 2010), doi: 10.1145/2002333.2002344
7. Itoh, H., Fukumoto, H., Wakuya, H., Furukawa, T.: Developing a robot that performs tasks of developmental scales: on gaze control by eye-head coordination. Paper presented at SICE Annual Conference 2011, Waseda University, Tokyo, Japan, pp 2488–2491 (September 2011)
8. Yoo, J.-K., Kim, J.-H.: Fuzzy Integral-based Gaze Control Architecture Incorporated with Modified-univector Field-Based Navigation for Humanoid Robots. *IEEE Trans. on Systems, Man and Cybernetics - Part B* 42(1), 125–139 (2012)
9. Ekman, P., Friesen, W.: Unmasking the face: a guide to recognizing emotions from facial expressions. Prentice Hall, Englewood Cliffs (1975)
10. Sugeno, M.: Theory of fuzzy integrals and its applications. Ph.D. dissertation, Tokyo Institute of Technology (1974)
11. Sugeno, M.: Fuzzy measures and fuzzy integrals - a survey. *Fuzzy Automata and Decision Processes*. North Holland, Amsterdam (1977)
12. Grabisch, M., Nguyen, H.-T., Walker, E.-A.: Fundamentals of uncertainty calculi, with applications to fuzzy inference. Kluwer, Boston (1995)
13. Yoo, B-S., Cho, S-H., Kim, J-H.: Fuzzy integral-based composite facial expression generation for a robotic head. Paper presented at Int. Conf. on Fuzzy Syst., Taipei, Taiwan, pp 917–923 (June 2011), doi: 10.1109/FUZZY.2011.6007468
14. Takahagi, E.: A fuzzy measure identification method by diamond pairwise comparisons and ϕ_s transformation. *J. Fuzzy Optimization Decision Making* 7, 219–232 (2008), doi:10.1007/S10700-008-9032-3
15. Narukawa, Y., Torra, V.: Fuzzy measure and probability distribution: distorted probabilities. *IEEE Trans. Fuzzy Syst.* 13, 617–629 (2005), doi:10.1109/TFUZZ.2005.856563

Curvature Path Planning with High Resolution Graph for Unmanned Surface Vehicle

Hanguen Kim, Byeolteo Park, and Hyun Myung

Dept. of Civil and Environmental Engg, KAIST
291 Daehakro, Yuseong-gu, Daejeon, 305-701, Rep. of Korea
`{sskhk05, starteo, hmyung}@kaist.ac.kr`

Abstract. In this paper, we propose a curvature path planning algorithm for unmanned surface vehicles (USVs). To control the USV automatically, various robot navigation techniques can be applied and numerous researchers are working on a grid map-based path planning algorithms. However, the most grid map-based path planning methods for the USVs consider only two-dimensional (x, y) plane without considering vehicle's maximum curvature. Since the most of the USVs are typically highly under-actuated, the ship tends to result in failure and sometimes induces hazardous collision situation when the ship follows the resultant path generated by the two-dimensional path planning algorithm. To solve this problem, we construct a non-uniform grid map which can reflect the geometric cost. Next we extend the dimension to reflect the kinematic constraint of the USV. Finally, to consider the vehicle's dynamic constraint, we propose a new cost function. The result of the proposed algorithm has been demonstrated through the simulation on the real map and the results show that the proposed algorithm generates the most plausible and efficient path.

Keywords: path planning, vehicle navigation, unmanned surface vehicle.

1 Introduction

Recently, the development of the USV that can replace functions of manned surface vehicle has been progressed actively at various nations. In order to manage the USV effectively in a wide area, the robot navigation technology is essential. In the field of robot navigation, grid-based representation is generally used in localization, mapping, SLAM (Simultaneous Localization And Map-building) and path planning. The ship navigation problem can likewise be solved using a grid-based representation. Many researchers have adopted ideas from robot navigation technology to the ship navigation problem because it is somewhat similar to that of robotics [1].

In the area of grid map-based path planning method, many research such as A* algorithm have been conducted. The most grid map-based path planning methods focus on finding the shortest path. The most important kinematic factor for operating the USV is a curvature radius due to the speed of the USV. Accordingly, in case of generating the shortest path which does not satisfy kinematic constraints of the USV for actual operation, existing grid map-based path planning methods have a disadvantage that it is difficult to follow a resultant path.

Though various researches have been done in the field of oceans engineering to solve the navigation problem with kinematic constraints of ocean robot, most research topic is focused on the obstacle avoidance rather than path planning [2]. More advanced approaches to path planning such as genetic algorithms or fuzzy set theory have recently been reported [3, 4]. However, they have not given much consideration to the actual turning capability of the USVs, which is critical not only in path planning but also in vehicle maneuvering itself. Therefore, to deal with the kinematic constraints of the USV, this paper focuses on the 3-D (x, y, θ) path planning considering curvature radius.

In this paper, we propose a grid map based path planning algorithm considering curvature radius of the USV. The proposed algorithm generates the graph reflecting the ocean environments and maximum curvature of the USV. In addition, the algorithm suggests the cost map reflecting curvature radius and the path applying the kinematic constraints of the USV. In Section 3, we simulate the proposed algorithm and discuss the result.

2 Path Planning Algorithm

2.1 Curvature Path Planning Algorithm

In this paper, we propose the curvature path planning for the USV. Basically, the basic A* which is a kind of grid map-based path planning algorithm consists of the g and h cost functions. The g cost sums up a travelled path cost until the current node and the h cost calculates an admissible heuristic cost from the current node to the goal. Thus, to find the shortest path, the cost function is defined as follows:

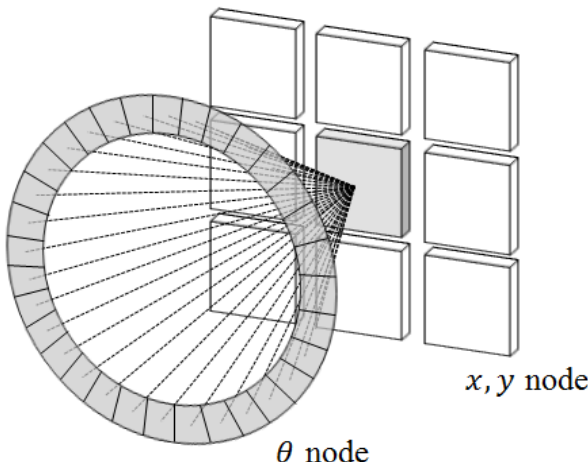


Fig. 1. The structure of the 3-D (x, y, θ) graph

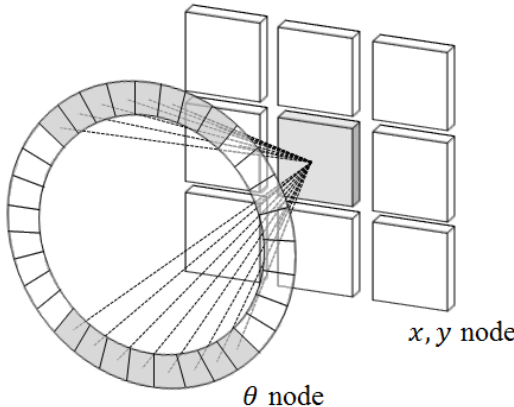


Fig. 2. Generation of the final 3-D (x, y, θ) graph

$$f(n) = g(n) + h(n) \quad (1)$$

To generate the path which considers the vehicle's dynamics and to extend to higher dimension, first of all, the structure of the graph should be modified. More specifically, the conventional three dimensional (x, y, θ) A* has a 3-D graph which is represented by angular resolution of 45 degrees. As a result, it cannot satisfy the vehicle's kinematic constraint. Thus, we extend the grid's dimension by considering the grid resolution per rotation angle of the vehicle.

Figure 1 shows the structure of the 3-D (x, y, θ) graph, θ node comes under each (x, y) node. In this paper, we generate the 3-D graphs which are represented by angular resolution of 5 degrees. When configuring the graph like Figure 1, the number of nodes increases depending on the map size. Thus, to generate the 3-D graph effectively, we do not include the part of occupied area which is a kind of terrain information.

Turning radius r is defined as the ratio of speed V to yaw rate R as follows:

$$r = \frac{V}{R}. \quad (2)$$

By using equation (2), the maximum curvature of the USV is calculated and the θ nodes at which the USV cannot be operated are restricted. The 3-D graph is generated finally as shown in Figure 2. The generated graph has (x, y, θ) coordinate.

Although it is almost impossible to precisely predict the motion of the USV because of the dynamic and unstable characteristics of the ocean environment, a Maritime Security Committee in IMO (International Maritime Organization) established a regulation (MSC. 137(76)) called "Standards for Ship Maneuverability" [5]. This document limits the maximum curvature angle diameter of the surface vehicle to 5 times the ship length.

2.2 Design of the Cost Function for Unmanned Surface Vehicle

To generate the plausible and efficient path, the resultant path should be applied to the kinematic constraints of the USV and also the grid map should consider the terrain, buoy and fairway information. Thus, in this paper, we generate the cost map which can incorporate the ocean environments such as the terrain, buoy, fairway, etc. Then, the cost map is used in the cost function. Figure 3 shows the grid map example of the Busan ports area in South Korea and the result of the cost map. In Figure 3(b), the bright parts of the cost map indicate where the USV is easy to operate.

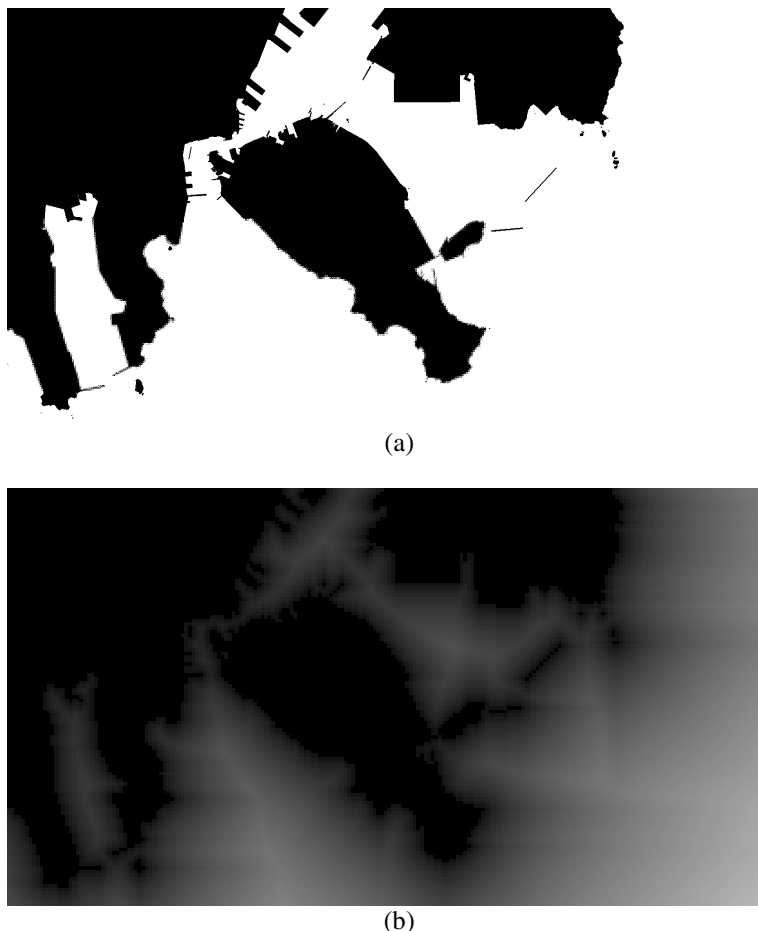


Fig. 3. The grid map of Busan port (a) and the cost map (b)

Using the cost map and the vehicle's maximum curvature angle in equation (2), we have designed the cost function of curvature path planning algorithm. The cost function is as follows:

$$g(n) = w_p C_m(n) + w_c C_w. \quad (3)$$

$$h(n) = w_h d_g. \quad (4)$$

where w_p , w_c , w_h indicate the weights of the cost map, current curvature radius, and heuristic cost, respectively. And C_m is a value of the cost map, C_w is a current curvature radius of the USV, also d_g is a Euclidean distance between the current node and the goal node. As a result, the proposed cost function can adjust the resultant path by controlling the weight value.

3 Simulation Results

In this paper, the proposed algorithm has been demonstrated through the simulation with the real map – the Busan ports area in South Korea. The simulation condition is shown in Table 1.

Table 1. Simulation Condition

Parameters (Unit)		Value
Max Yaw rate	$^{\circ}/s$	8
Max Ship Speed	<i>knots</i>	40
Ship Beam	<i>m</i>	4
Ship Length	<i>m</i>	12
Grid map Resolution	<i>m/pixel</i>	200

The angular resolution of the grid map is 5 degrees and the maximum curvature radius is set to $5^{\circ}/m$. The size of grid map is 209 x 115 pixels (width and height). The specification of the USV is defined by the standard form of the high speed small vessels. The resultant paths are shown in Figure 4. From inside the Busan harbor, each resultant path has an arbitrary goal point. We set the angular configuration with the magnetic meridian to 0 degree, and angle is increased with the clockwise direction. The average path generation time is about 4 seconds on Intel Core i5 with 3GB RAM. In our simulation results, the proposed path planning algorithm showed the most plausible and efficient path.

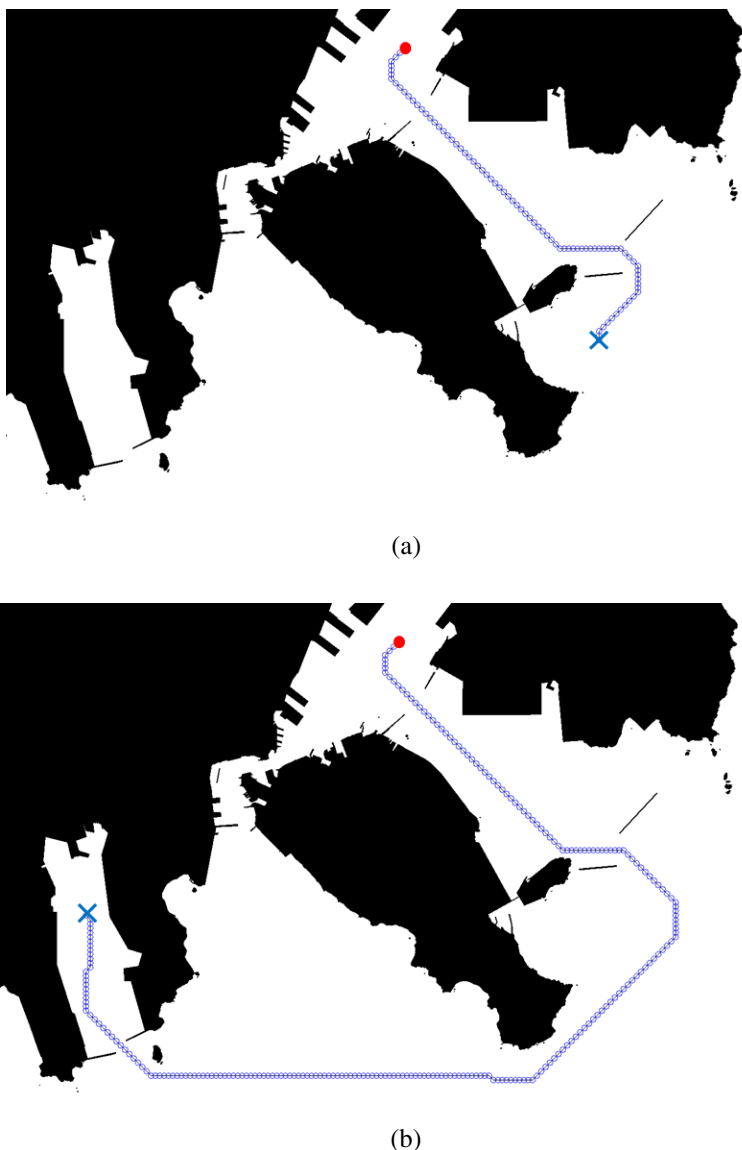
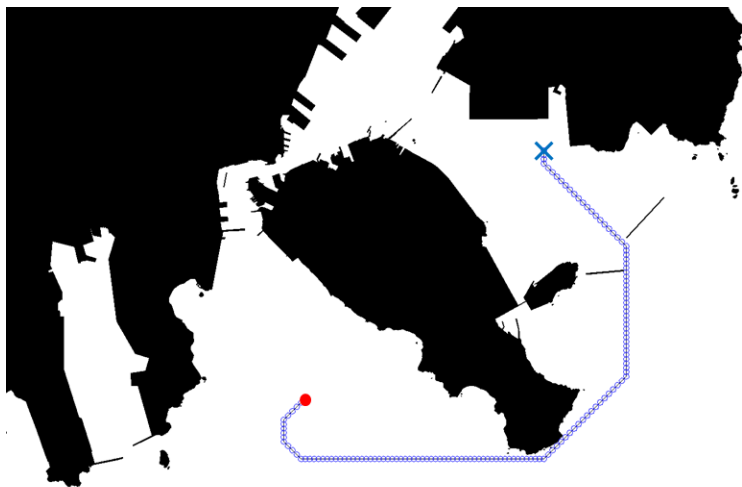
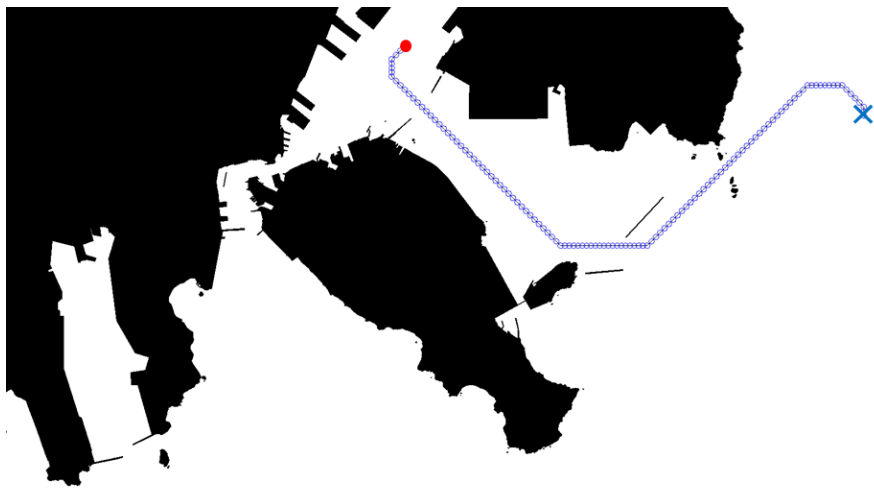


Fig. 4. Simulation results for various start (red dot) and end (blue cross) points



(c)



(d)

Fig. 4. (continued)

4 Conclusion

The curvature path planning algorithm for autonomous navigation of the USV is proposed in this paper. To satisfy the kinematic constraints of the USV, we proposed a 3-D (x, y, θ) A* with high resolution θ nodes. To apply to the ocean environments, we proposed a new cost map and cost function. The performance of the proposed

algorithm has been demonstrated through the simulation using the map of Busan ports area in South Korea. Consequently, the proposed path planning algorithm considering the cost map and the kinematic constraints of the USV shows the most plausible and efficient path. In the future, we will perform an optimization of the proposed algorithm, and design a path planning algorithm that incorporates seaway rule according to each region.

Acknowledgements. This research was supported by the MKE(The Ministry of Knowledge Economy), Korea, under the Human Resources Development Program for Convergence Robot Specialists support program supervised by the NIPA(National IT Industry Promotion Agency) (NIPA-2012-H1502-12-1002). This work was also financially supported by Korea Ministry of Land Transport and Maritime Affairs (MLTM) as U-City Master and Doctor Course Grant Program.

References

1. Lee, T., Chung, H., Myung, H.: Multi-resolution path planning for marine surface vehicle considering environmental effects. In: Proc. of IEEE OCEANS Conference, Spain, pp. 1–9 (2011)
2. Szlapczynski, R.: A new method of ship routing on raster grids with turn penalties and collision avoidance. *The Journal of Navigation* 59, 27–42 (2006)
3. Szlapczynski, R.: A New Method of Ship Routing on Raster Grids, with Turn Penalties and Collision Avoidance. *The Journal of Navigation* 59, 27–42 (2006)
4. Smierzchalski, R., Michalewicz, Z.: *Innovations in Robot Mobility and Control*. Springer (2005)
5. Society of Naval Architects and Marine Engineers: Technical Committees – Ship Technical Operations: Panel O-44 : IMO Activities Archive – Standards for Ship Maneuverability

Automatic Take-Off and Landing Control for Small Unmanned Helicopter

Satoshi Suzuki

Young Researchers Empowerment Center, Shinshu University
3-15-1 Tokida, Ueda-shi, Nagano 386-8567, Japan
s-s-2208@shinshu-u.ac.jp

Abstract. In this study, a control scheme and controller design for automatic take off and landing of a small unmanned helicopter are proposed. First, acceleration feedback controller is designed for stabilizing horizontal motion of the helicopter. In acceleration feedback controller, horizontal acceleration is estimated by using Kalman filter, and desired attitude to cancel out horizontal acceleration is generated by using estimated acceleration. Second, altitude controller by using ultrasonic sensor is designed to stabilize altitude of the helicopter near ground. Finally, each control system is verified by flight experiment, and automatic landing experiment is also carried out.

Keywords: Small Electric Helicopter, Automatic take-off and landing.

1 Introduction

In the last decade, unmanned aerial vehicle (UAV) technology has improved drastically, and UAVs are now used not only in research and development but also for various practical purposes such as aerial photography, surveillance, and crop dusting. UAVs are safer and more convenient than manned aircrafts, and they can be potentially employed in a wide range of applications. It is necessary to achieve autonomous control of UAVs in order to reduce operator burden in practical tasks. Therefore, several researchers have focused on autonomous control of various types of UAVs such as fixed-wing UAVs [1] and [2], helicopter-type UAVs [3]-[5], tilt-rotor-type UAVs [6], tail-sitter-type UAVs [7], and airship-type UAVs [8].

Recently, small UAVs weighting less than 10 kg have attracted considerable attention owing to their ease of carriage and handling. Accordingly, we have investigated methods for achieving autonomous control of a small unmanned helicopter, which is one kind of small UAVs. It is extremely difficult to achieve autonomous control of small helicopter as compared to large ones, owing to the payload limitation and sensor restriction. In general, larger sensors have greater accuracy. Hence, the sensors that can be mounted on small helicopter don't have enough accuracy for requirements specification. In our previous study, we designed an autonomous navigation, guidance, and control system for a small helicopter by using only small and light weight sensors [9]. Consequently, we have already



Fig. 1. Overview of Small electric helicopter

achieved hovering and 3-dimensional guidance control of 2 kg electric helicopter by using designed guidance and control system. However, we have not yet achieved automatic take off and landing (TOL), although it is also necessary for fully autonomous control of small unmanned helicopter. Besides, automatic TOL is also important for convenience and easiness of practical operation because take-off and landing is most difficult in manual operation of small helicopter. In this study, we aim at realizing automatic TOL of the small electric helicopter. However, some sensors used in current control system could not be used for automatic TOL because the outputs of the sensor become inaccurate near ground. To avoid the problem, we propose a new control scheme for automatic TOL.

In this paper, control system design for automatic TOL of a small electric helicopter is presented. In the control system, we use only acceleration feedback and a range sensor. In acceleration feedback controller, horizontal acceleration is estimated by using Kalman filter, and desired attitude is generated to cancel out the horizontal acceleration. Altitude controller by using ultrasonic sensor is designed to stabilize altitude of the helicopter near ground. Finally, each control system is verified by flight experiment, and automatic landing experiment is also carried out.

2 Experimental Setup

Experimental setup including small electric helicopter, all sensors and electric devices for control of the helicopter are introduced. Figure 1 shows an overview of

Table 1. Configurations of control device

Main board	SUZAKU-V SZ410
Attitude sensor	IMU-05 by HIROBO
GPS module	u-blox LEA-6S
Barometer	SCP 1000
Photo reflector	BTE 003B
Wireless module	XBee-Pro
CPU core	PowerPC 405
CPU clock	350 MHz
OS	Linux 2.6
Weight (with box)	312 g

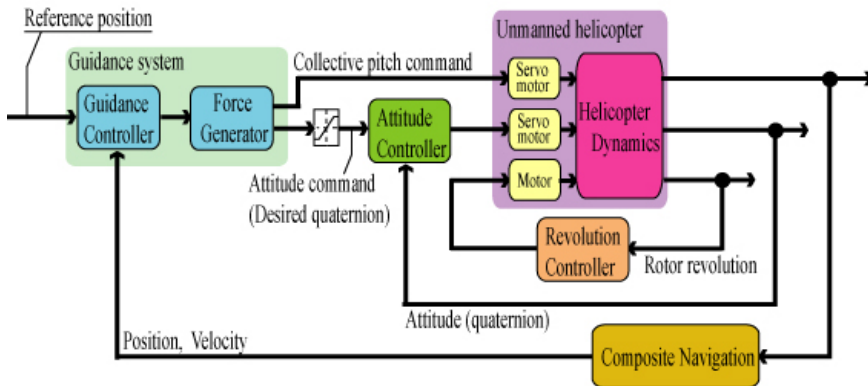


Fig. 2. Navigation, guidance, and control system for small helicopter

our 2 kg small helicopter, this helicopter was originally designed for a hobby-use radio-controlled helicopter. Next, configuration of a control device is shown in Table 1. The control device consists of a Field Programmable Gate Array (FPGA) board, a small attitude sensor, a small light weight GPS module, a barometer, a photo-reflector module for measuring rotor revolution, and a wireless module. The configuration of our control device is nearly identical to that of an autopilot system [10].

3 Overview of Autonomous Control System for Small Helicopter

In this section, autonomous navigation, guidance, and control system for small unmanned helicopter, which have been developed in previous study [9], are briefly introduced. Figure 2 shows the block diagram of entire control system. The system consists of attitude controller, rotor revolution controller, composite navigation system, and guidance system. In particular, details of composite navigation system and guidance system are introduced in following section.

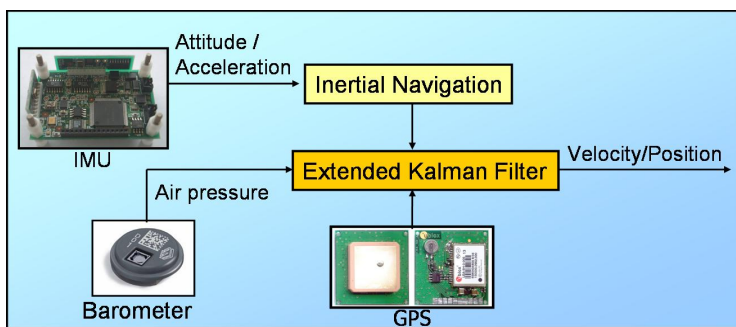


Fig. 3. Block diagram of composite navigation system

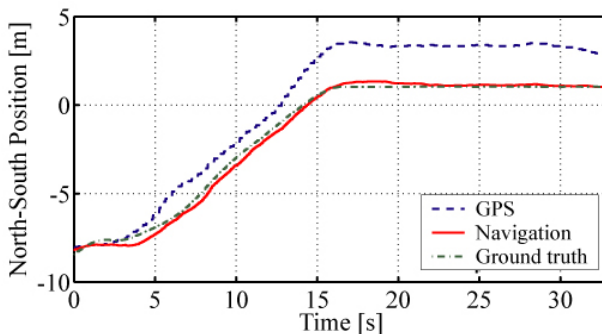


Fig. 4. Result of composite navigation system

3.1 Composite Navigation System

Because of payload limitation of small helicopter, we can only use small and light weight sensors. However, accuracy of these sensors, especially small GPS module, is not enough for the autonomous control of the helicopter. Therefore, composite navigation system, which integrates the output of small GPS and the other sensors, is necessary for compensating the error of the small GPS module. Figure 3 shows the overview of designed composite navigation system. In the system, we use inertial navigation and barometric height measurement for compensating GPS error, and these data are integrated by using Extended Kalman Filter (EKF).

An example of estimation result of composite navigation system is shown in figure 4. From the figure, it can be concluded that the composite navigation system was able to estimate accurate position even though the GPS module had a large error.

3.2 Guidance System

The guidance system for stabilizing the helicopter at an arbitrary point in 3-dimensional space is introduced. The helicopter performs translational motion by changing the magnitude and direction of the thrust generated by the main rotor, and it is equivalent to changing collective pitch angle of the rotor and the attitude of the

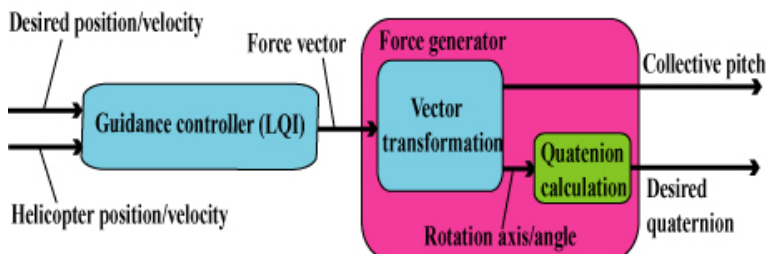


Fig. 5. Overview of guidance system

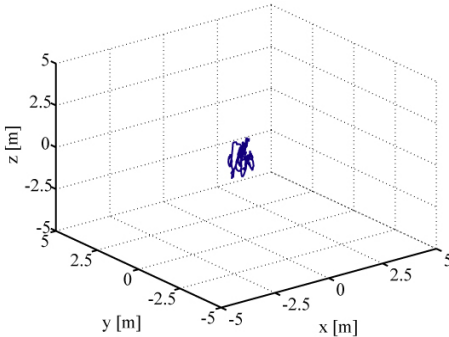


Fig. 6. Hovering experiment

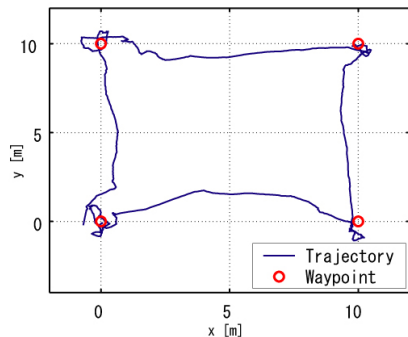


Fig. 7. Waypoint flight

helicopter. Therefore, guidance system has to calculate appropriate collective pitch angle and attitude. Our guidance system consists of two parts, guidance controller and force generator. The overview of guidance system is shown in figure 5. Guidance controller calculates the desired force vector required for stabilizing the position and velocity of the helicopter, and it was designed by using Liner Quadratic Integrator (LQI). Force generator calculates the appropriate collective pitch angle of the rotor and the quaternion which expresses desired attitude for achieving the desired force by using the rotor thrust. The force generator consists of simple vector transformation and quaternion calculation.

Experimental results of 3-dimensional guidance control using designed guidance system are shown in figure 6 and figure 7. Figure 6 shows the 3-D trajectory in the hovering experiment. In this figure, the reference position has been fixed at the origin. This figure shows that 95 % of the entire flight trajectory was included in the 0.5 m ball centered at the origin. Figure 7 shows horizontal trajectory of waypoint flight. The figure clearly shows that the helicopter accurately passed each waypoint. From the results, it can be said that precise autonomous flight was achieved by using designed guidance system.

4 Control System Design for Automatic Take-off and Landing

In this section, we design the control system for automatic TOL of a small helicopter. For the control of the small helicopter, GPS and barometer were used for measuring position and velocity. However, GPS and barometer have some problems at their accuracy when they are used for automatic TOL. In the case of GPS, radio signals from satellites are reflected by terrestrial objects such as trees or buildings near ground, hence the signals reach receiving antenna by two or more paths. This phenomenon is called multi-path of radio signal, and so the multi-path causes inaccuracy of the GPS position and velocity data. On the other hand, when the helicopter is near ground, rotor downwash is compressed between the main rotor and ground surface. As a result, air pressure measured by the barometer drastically increases, and so the altitude calculated from the air pressure become to be inaccurate.

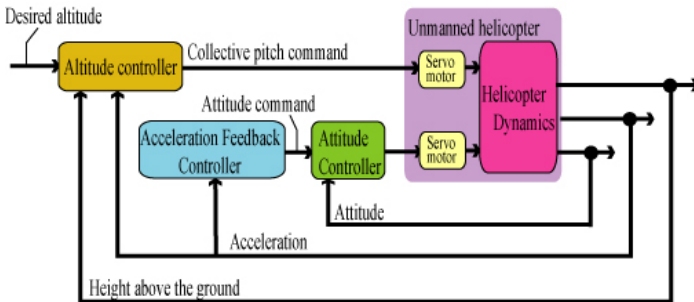


Fig. 8. Control system for automatic take-off and landing

For these reasons, GPS and barometer cannot be used for measuring the position and height in the case of automatic TOL. Therefore, we should design the system without using GPS and barometer. We propose a control scheme using only accelerometer and range sensor. Entire control system for automatic TOL is shown in figure 8. In the following section, details of acceleration feedback controller and altitude control system using range sensor are introduced.

4.1 Acceleration Feedback Control

Acceleration feedback controller is used to stabilize the horizontal motion of the helicopter in automatic TOL. The linear acceleration of the helicopter used for control, can be measured by accelerometer included in attitude sensor. However, the output of the accelerometer is quite noisy, thus it cannot be directly used for control. Therefore, it is necessary to estimate the linear acceleration by using Kalman filter. At first, coordinate systems used for design are defined as figure 9. In this figure, first coordinate system is the local level frame denoted by R -frame; its origin is fixed at the center of gravity of the helicopter. Z_r lies along the direction of gravity, X_r lies in local level plane, and along the forward direction of the helicopter, Y_r along the rightward direction. This frame rotates about Z_r in conjunction with the yaw motion of the helicopter. Second coordinate system is the body frame, and it is denoted by B -frame; its origin is fixed at the same point as the origin of R -frame. X_b lies along the forward direction, Y_b along the rightward direction, and Z_b along the downward direction of the helicopter. The output of the accelerometer is expressed as a vector in this frame.

To design Kalman filter, process model of the system has to be derived. First, state space equation is derived. In the following, we only derive the equations for longitudinal and pitching direction of the helicopter. However, the equations for lateral and rolling direction could be obtained using same procedure. For simplicity of the model, we consider the following assumption.

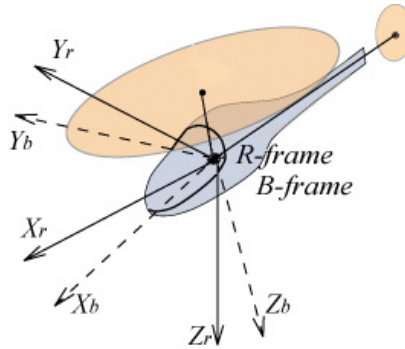


Fig. 9. Coordinate systems

- Roll and pitch angle of the helicopter is sufficiently small, and yaw rate has been stabilized and equal to zero.
- Flapping angle of the main rotor and stabilizer bar of the helicopter is sufficiently small.
- Magnitude of the thrust of the main rotor is equal to weight of the helicopter in steady state such as hovering.

Under these assumptions, the linear acceleration put on the helicopter is represented as follows:

$$a_{xr} = -\frac{T}{M} \cos \phi \sin \theta \equiv -g \theta \quad (1)$$

Here, a_{xr} is X_r and axis component of the linear acceleration. T is the thrust of the main rotor, M is mass of the helicopter, θ denotes pitch angle of the helicopter, and g is gravitational acceleration. Moreover, time derivatives of pitch angle are obtained under assumptions as:

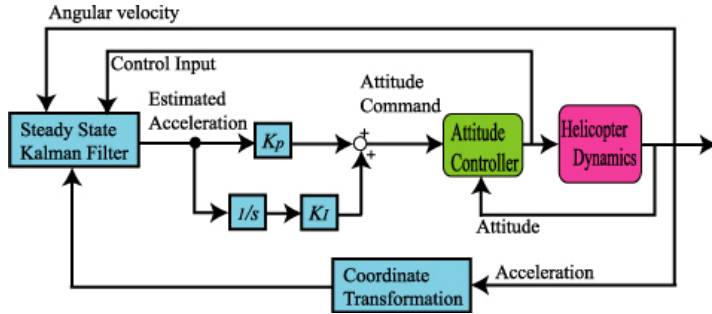
$$\dot{\theta} = q \cos \phi - r \sin \phi \equiv q \quad (2)$$

Here, ϕ denotes roll angle, p , q , and r represent roll, pitch and yaw angular velocity. Therefore, time derivative of (1) is derived as follows:

$$\dot{a}_{xr} = -gq \quad (3)$$

On the other hand, the rotational equation of motion of the small helicopter has been derived in [11] as:

$$\begin{bmatrix} \dot{q} \\ \dot{a} \\ \dot{c} \end{bmatrix} = \begin{bmatrix} 0 & M_a / I_{yy} & 0 \\ -1 & -1/\tau_b & K_3 / \tau_b \\ -1 & 0 & -1/\tau_s \end{bmatrix} \begin{bmatrix} q \\ a \\ c \end{bmatrix} + \begin{bmatrix} 0 \\ K_1 / \tau_b \\ K_2 / \tau_b \end{bmatrix} \delta_{lat} \quad (4)$$

**Fig. 10.** Acceleration feedback control system

Here, a is the flap angle of the main rotor, c is the flap angle of the stabilizer, δ is the input, I_{yy} are the moment of inertia, and τ_b , τ_s , and $K_1 - K_3$ are appropriate constants. From (3) and (4) following state space equations are obtained.

$$\begin{bmatrix} \dot{a}_{xr} \\ \dot{q} \\ \dot{a} \\ \dot{c} \end{bmatrix} = \begin{bmatrix} 0 & -g & 0 & 0 \\ 0 & 0 & L_b/I_{yy} & 0 \\ 0 & -1 & -1/\tau_b & K_3/\tau_b \\ 0 & -1 & 0 & -1/\tau_s \end{bmatrix} \begin{bmatrix} a_{xr} \\ q \\ a \\ c \end{bmatrix} + \begin{bmatrix} 0 \\ 0 \\ K_1/\tau_b \\ K_2/\tau_b \end{bmatrix} \delta_{lat} \quad (5)$$

Next, measurement equation is derived. The linear acceleration on R -frame can be measured by accelerometer. Moreover, angular velocity of the helicopter can be measured by gyro sensor. Therefore, the measurement equations are derived as follows:

$$\begin{bmatrix} a_{xr} \\ q \end{bmatrix} = \begin{bmatrix} 1 & 0 & 0 & 0 \\ 0 & 1 & 0 & 0 \end{bmatrix} \begin{bmatrix} a_{xr} \\ q \\ a \\ c \end{bmatrix} \quad (6)$$

We designed the steady-state Kalman filter by using state space equation and measurement equation mentioned above. Finally, the acceleration feedback control system is constructed using Kalman filter and Proportional-Integral (PI) controller as figure 10.

4.2 Altitude Control Using Ultrasonic Sensor

From the aforementioned problem of GPS and barometer, we should use other sensor to measure the height above ground for automatic TOL. Considering size, weight, and maximum range of the sensor, we choose small ultrasonic sensor. The key specifications of the sensor are listed in Table 2. However, the ultrasonic sensor is potentially affected by acoustic noise caused by the main rotor of the helicopter.

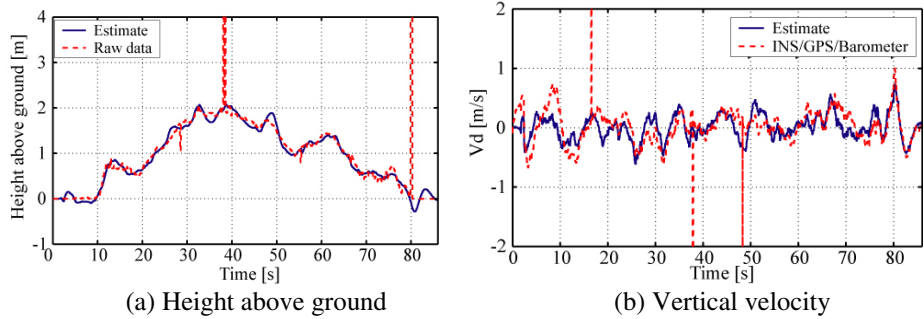


Fig. 11. Estimation results of Kalman filter

Moreover, the sensor cannot measure the vertical velocity, although it is also necessary for the altitude control. Therefore, we design Kalman filter by using ultrasonic sensor and accelerometer to estimate the height above ground and the vertical velocity of the helicopter. The process model is derived as:

$$\begin{bmatrix} \dot{h} \\ \dot{v}_d \\ \dot{b}_a \end{bmatrix} = \begin{bmatrix} 0 & -1 & 0 \\ 0 & 0 & -1 \\ 0 & 0 & 0 \end{bmatrix} \begin{bmatrix} h \\ v_d \\ b_a \end{bmatrix} + \begin{bmatrix} 0 \\ 1 \\ 0 \end{bmatrix} a_{zr} + \begin{bmatrix} 0 \\ 0 \\ 1 \end{bmatrix} w \quad (13)$$

$$\begin{bmatrix} h \\ v_d \\ b_a \end{bmatrix} = \begin{bmatrix} 1 & 0 & 0 \\ 0 & 1 & 0 \end{bmatrix} \begin{bmatrix} h \\ v_d \\ b_a \end{bmatrix}$$

Here, h is the height above ground, v_d , the vertical velocity, b_a , the bias error of accelerometer, a_{zr} , the vertical acceleration, and w is white noise. Steady state Kalman filter is designed by using the process model. Experimental results of the altitude estimation using Kalman filter is shown in figure 11. In this experiment, ultrasonic sensor was mounted on the helicopter, and altitude estimation system using Kalman filter was implemented on embedded computer. In each figure, solid line represents the estimate of height and velocity, which was estimated by designed Kalman filter. From figure 11 (a), it is shown that the height above ground could be estimated even if the output of the ultrasonic sensor has considerable noise at 40 s and 80 s. Besides, it is also shown that vertical velocity could be estimated from figure 11(b). Finally, estimated height and vertical velocity is input to conventional altitude controller, which was proposed in previous study [9].

Table 2. Specifications of ultrasonic sensor

Vendor	MaxBotix
Product name	XL-MaxSonar-EZ1
Size	19.9×22.1×25.1 [mm]
Weight	5.9 [g]
Range	20-765 [cm]

5 Experiment

Flight experiments were carried out to verify designed acceleration feedback system and the altitude control system using ultrasonic sensor. Finally, automatic landing experiment was also carried out.

5.1 Acceleration Feedback Control

First, horizontal motion control experiment was performed by using only acceleration feedback system. The experiment was carried out at out of doors, and wind velocity in the experiment was approximately 1-2 m/s. Figure 12 shows horizontal velocity in this experiment. The horizontal velocity was measured by composite navigation system, however it was not used for horizontal motion control. From the figure, it is clear that the horizontal motion of the helicopter can be stabilized by using only acceleration feedback.

5.2 Altitude Control Using Ultrasonic Sensor

Next, altitude control experiment was carried out using estimated height, vertical velocity, and altitude controller designed in previous study. Figure 13 shows the results of the experiment. In the figures, dashed line represents reference, and solid line represents the experimental data. From the figures, it is clear that altitude and vertical velocity of the helicopter could be stabilized by the controller. The error of altitude control is approximately within 0.5 m, and it is enough for the automatic TOL.

5.3 Automatic Landing Experiment

Finally, automatic landing experiment was carried out by using designed control system. However, performance of acceleration feedback has not yet been enough for the landing control. Therefore, in this case, horizontal motion was stabilized using conventional guidance system with INS/GPS composite navigation. Figure 14 and figure 15 shows the results. From the results, it is clear that the helicopter safely landed without falling down.

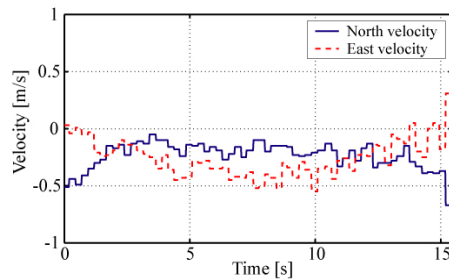
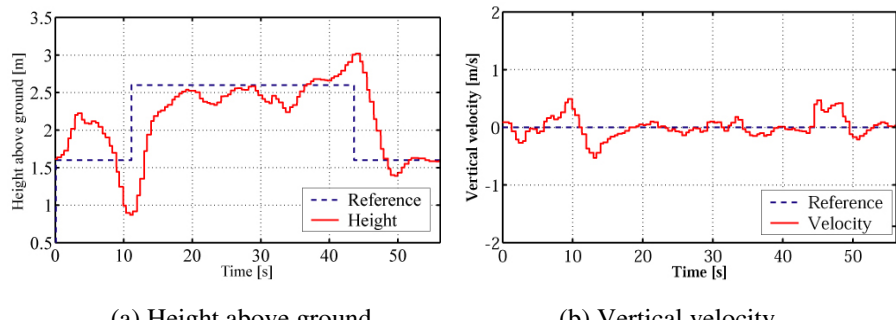


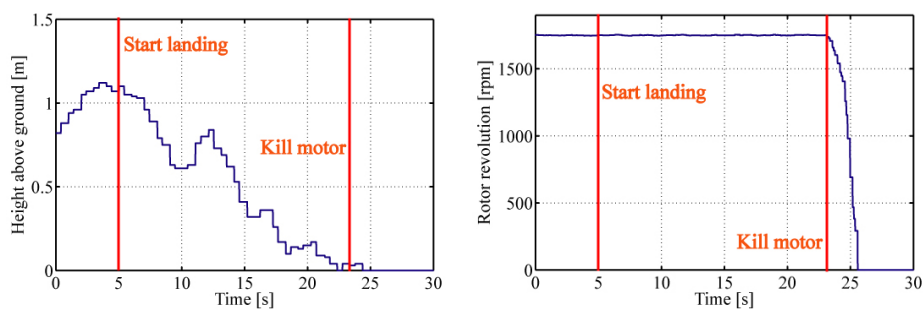
Fig. 12. Horizontal velocity in acceleration feedback experiment



(a) Height above ground

(b) Vertical velocity

Fig. 13. Altitude control using ultrasonic sensor



(a) Height above ground

(b) Rotor revolution

Fig. 14. Automatic landing experiment

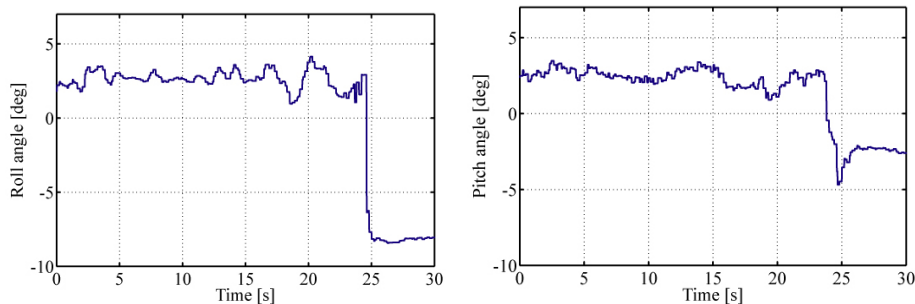


Fig. 15. Attitude during automatic landing

6 Conclusion

In this study, a control scheme and controller design for automatic take off and landing of the unmanned helicopter were proposed. Acceleration feedback controller was designed for stabilizing the horizontal motion of the helicopter. To avoid the problem of GPS and barometer near ground, altitude controller using ultrasonic sensor was proposed. Finally, each control system was verified by flight experiment, and it is shown that proposed control systems are efficient for automatic take off and landing. Moreover, automatic landing control was achieved by using proposed control scheme.

In future works, we'll carry out the automatic landing experiment with acceleration feedback, and realize fully autonomous flight of small unmanned helicopter including automatic take off and landing.

References

1. Oh, C.K., Barlow, G.J.: Autonomous Controller Design for Unmanned Aerial Vehicles using Multi-object Genetic Programming. In: Proceedings of Congress on Evolutional Computation 2004, vol. 2, pp. 1538–1545 (2004)
2. Eklund, J.M., Sprinkle, J., Sastry, S.: Implementing and Testing a Nonlinear Model Predictive Tracking Controller for Aerial Pursuit/Evasion Games on a fixed wing Aircraft. In: Proceedings of 2005 American Control Conference, vol. 3, pp. 1509–1514 (2005)
3. Mettler, B.: System Identification Modeling of a Small-Scale Unmanned Rotorcraft for Flight Control Design. Journal of American Helicopter Society 47(1), 50–63 (2002)
4. Kim, H.J., Shim, D.H.: A Flight Control System for Aerial Robots: Algorithm and Experiment. Journal of Control Engineering Practice 11, 1389–1400 (2003)
5. Shen, S., Michael, N., Kumar, V.: Autonomous Multi-floor Indoor Navigation with a Computationally Constrained MAV. In: Proceedings of IEEE International Conference on Robotics and Automation 2011, pp. 20–25 (2011)
6. Lee, J.H., Min, B.M., Kim, E.T.: Autopilot Design of Tilt-rotor UAV using Particle Swarm Optimization Method. In: Proceedings of the 2007 International Conference of Control, Automation and Systems, pp. 1629–1633 (2007)

7. Stone, H., Wong, K.C.: Preliminary Design of a Tandem-wing Tail-sitter UAV using Multi-disciplinary Design Optimization. In: Proceedings of International Aerospace Congress, pp. 707–720 (1997)
8. Lee, S.J., Kim, S.P., Kim, T.S., Kim, H.K., Lee, H.C.: Development of Autonomous Flight Control System for 50 m Unmanned Airship. In: Proceedings of 2004 Intelligent Sensors, Sensor Networks Information Processing Conference, pp. 457–461 (1997)
9. Suzuki, S.: Low Accuracy Sensor-based Navigation and Fully Autonomous Guidance Control of Small Electric Helicopter. In: Proceedings of IEEE International Conference on Robotics and Automation 2011, pp. 4442–4448 (2011)
10. Chao, H., Cao, Y., Chen, Y.: Autopilots for Small Unmanned Aerial Vehicles: A Survey. International Journal of Control, Automation, and Systems 8(1), 36–44 (2010)
11. Nonami, K., Kendoul, F., Suzuki, S., Wang, W., Nakazawa, D.: Autonomous Flying Robots Unmanned Aerial Vehicles and Micro Aerial Vehicles. Springer (2010)

Development of Crawler Robot with Pile Units to Traverse Loose Soil with Steep Slope

Kojiro Iizuka¹, Hirofumi Komatsu¹, and Takashi Kubota²

¹ International Young Researcher Empowerment Center, Shinshu University,

3-15-1 Tokida, Ueda, Nagano, 386-8567, Japan

{Iizuka, 10fa414b}@shinshu-u.ac.jp

² Japan Aerospace Exploration Agency, 3-1-1 Yoshinodai, Tyo-ku,

Sagamihara, 252-5210, Japan

Kubota@jaxa.isas.jp

Abstract. Rovers are the most important devices for planetary exploration. Rovers are required to traverse many situation of ground, on various form's stones, loose soil, steep slope etc. There are some technologies that large obstacles such as stones can be avoided by using cameras or lasers. However, it is extremely difficult for rovers to traverse loose soil, especially "loose soil with steep slope". If the area being traversed is sloped, these rovers might not work. During a lunar exploration mission, rovers must be able to traverse slopes. Lunar surfaces are mainly characterized by loose soil called regolith, and the ground is very steep around craters. We developed a crawler robot to adapt such condition. Proposed rover has an ability to traverse loose soil with steep slope. It is to use the shearing strength of soil. This means that we use characteristic of soil that the shearing strength of deeply soil areas was very strong compared with surface of ground. If the rovers can make use of the deep area of loose soil, they may be able to support their weight on slopes with loose soil. Therefore, we employ piles to penetrate into the deep area of loose soil. We combined the crawler robot and piles units. The experimental results are shown the high performance of the proposed crawler robot with piles units on uneven ground and loose soil.

Keywords: Crawler robot, Piles, Loose soil, Steep soil.

1 Introduction

Rovers are the most important devices for planetary exploration; these rovers must traverse planetary surfaces in order to collect precise information regarding the origin and age of planets. In the past, lunar explorations were undertaken by the Soviet Union [1] and the United States [2]. The NASA Mars mission in 1996 was accomplished using the micro rover Sojourner, which traversed and explored the surface of Mars. Sojourner transmitted important data and detailed pictures of Mars to Earth [3]. The Sojourner mission revealed the importance of moving exploration. In

planetary explorations, rovers are required to traverse rough terrain that often includes craters and rear cliffs (Crater is the trace which a meteorite hit. Cliffs is the wall which becomes bare without being covered with soil.), which are scientifically important locations that need to be explored. Hence, it is important that the rovers do not tip over or get stuck while traversing such terrain. Rovers may be required to reach the top of a slope. Figure 1 shows an example scene on the lunar surface [4], which presents many irregularities for rovers to traverse. It is difficult for some types of wheels or crawlers to traverse these surfaces because they may sink into the soil or destroy the surface of the soil during locomotion, especially the area like slope around craters. Figure 2 shows the poor condition when MER traverses loose soil on MARS[3]. On such condition, there is a locomotion robot which can traverse loose soil with steep slope as shown fig.3 [5]. We developed a newel rover which can traverse loose soil with steep slope as shown fig.4 [6]. This proposed rover has piles to support itself weight. Fig.5 shows motion concepts. While the piles of the outer body penetrate into soil, the inner body can move forward as shown fig.5(a). The outer body can move during the piles of the inner body are penetrated into soil (fig.5(b)).

This paper proposes the crawler robot combined piles unit. The crawler robot can move without bulldozing influence and turning. Moreover, it is not easy to sink into soil because the crawler robot has a flat contacting surface to ground. We carry out the running experiments using the proposed one. The running ground used the experiments is loose soil with steep slope. As evaluation, we use the slip ratio.

In Section 2, the supporting force is described for the robot on loose soil with steep slope. In Section 3, the supporting force of the pile is measured. In Section 4, the proposed crawler robot is described. The running experiments are carried out in section 5. Finally, the conclusion of this study is presented in Section 6.

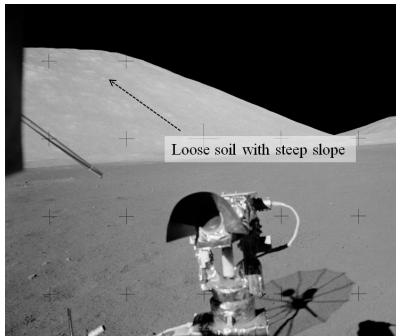


Fig. 1. Lunar surface (NASA) [4]

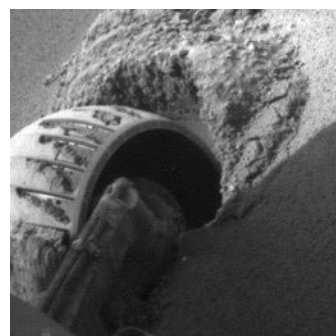


Fig. 2. Poor condition of MER (NASA/JPL) [3]

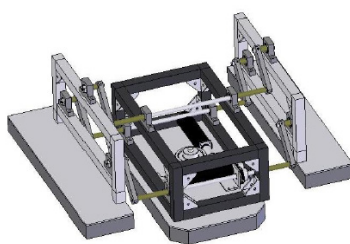


Fig. 3. Track walker (Tohoku Univ.) [5]

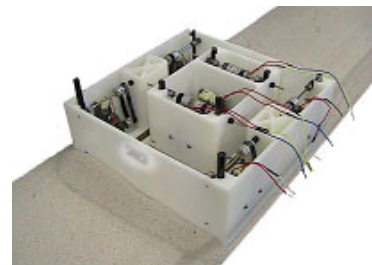
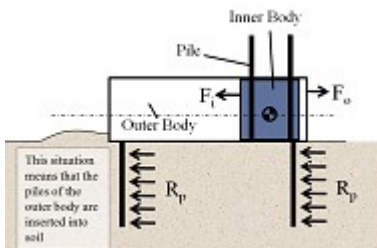
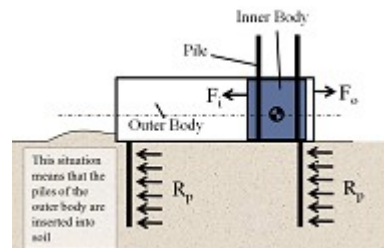


Fig. 4. Proposed rover [6]



(a) Inner body motion (Piles of outer body penetrate)



(b) Outer body motion (Piles of inner body penetrate)

Fig. 5. Motion concept of proposed rover

2 Supporting Force During Locomotion on Loose Soil with Steep Slope

When locomotion systems traverse steep slopes with loose soil, they are burdened with their own weight due to gravity. This means that the influence of gravity increases with the slope. We use the deep area of soil in order to prevent this influence. In shallow soil areas, the pile can easily move forwards and backwards. However, in deep soil areas, the pile cannot move easily. For moving in deep soil areas, we need a force stronger than that in the shallow soil area. We consider this reason. Figure 6 shows the shearing torque of the soil at various depths (20, 40, and 60 mm) using the vane shearing tester. We measured the shearing stress of Toyoura soil and regolith stimulant. When the depth of the soil increases, the shearing strength of the soil becomes large. Therefore, we consider a unique method that enables the rover to support its weight using this characteristic of loose soil. Figure 7 shows the model for simulating the relationship between the supporting force and the length of the pile. The pile is held the upper part. H is length from surface of loose soil to bottom of pile. When the pile is given resistance from soil, the rotation of pile does not work by moment force. There are many proposed method to calculate the

supporting force of the pile on other researches. Brinch Hansen (1961)[7] proposed the method that is calculated the supporting force , when the pile is assumed to rotate about a single point. Kasch et al. (1977)[8] will result in a very conservative solution using Rankine's passive states. Reese (1977)[9] developed a computer program that widely used to predict the performance of piles subjected to the supporting force. Broms(1965)[10] solution is widely used for calculation of lateral bearing capacity of piles because of its simplicity. We employed the short pile for proposed rover. The theory of Broms focuses on many case of pile (small and large of diameter) which is holding a part of head of it. The supporting force can be calculated by simple equation by the theory of Broms. Moreover, the theory of Broms can adapt cohesive soil and sandy soil. Therefore, we decided to use the theory of Broms. The supporting force F_s is then described using the length and diameter d of pile, density of soil, γ and coefficient of passive ground pressure, K_p , as follows:

$$F = \frac{2}{3} H^2 d \gamma K_p \quad (2)$$

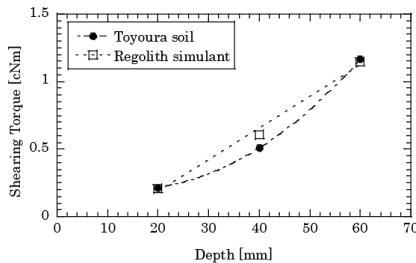


Fig. 6. Shearing stress into loose soil

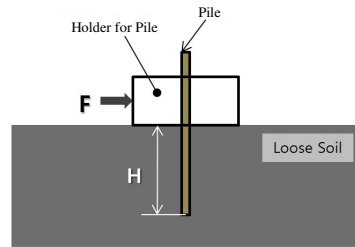
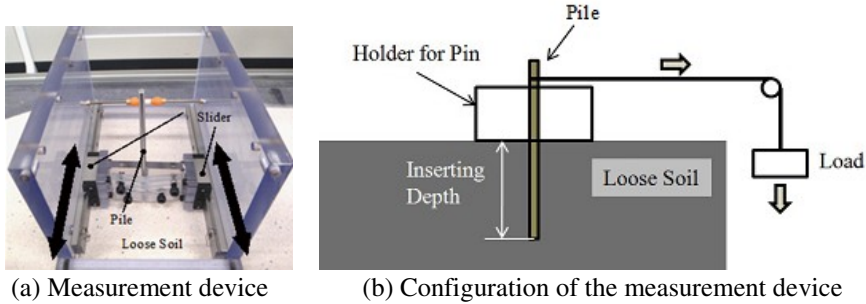


Fig. 7. Simulating model using supporting force and pile

3 Measurement of a Supporting Force

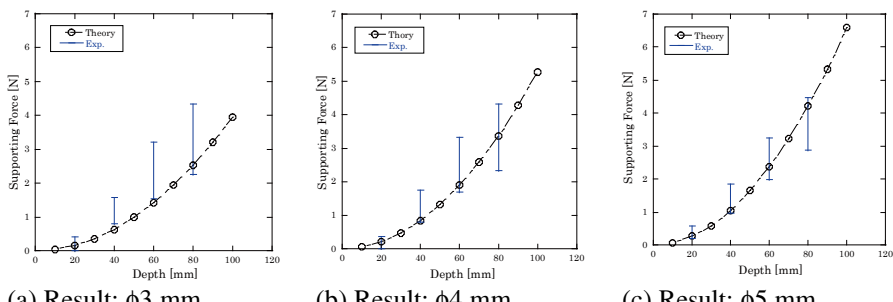
In Section 2, we mentioned that it was important to use deep soil areas when traversing steep slopes with loose soil. Therefore, we measure the supporting force and the resistance force when the pile is penetrated into the soil. Figure 8 (a) shows an overview of the device used to measure the supporting force using a pile. Figure 8 (b) shows the configuration of the measurement device. The pile is installed at the center of this device. This device can then move forward and backward. The pile is added at various loads using a pulley. We using Toyoura soil for this measurement.

**Fig. 8.** Device to measure supporting force

In the measurements, we use piles with diameters $\phi 3$ mm, $\phi 4$ mm and $\phi 5$ mm. We carry out the experiments of 20 times to measure the supporting force. We use the momentary value that a pile begins to work into soil as the point to judge the supporting resistance. Figure 9 shows the measurement results. In this figure, the results of each theory and measurement are shown. And the simulation parameter is shown table.1. When the penetrating depth increases, the supporting force increases. The results of both the simulation and experiment showed that the supporting force increased when the depth of the penetrated pile increased and the diameter of the piles was large. The measurement results are uneven, but resemble a simulation result. From both results, it can be seen that the supporting force of the $\phi 3$ mm pile is smaller than that of the other piles. When the diameter of the pile increases, the supporting force also increases.

Table 1. Simulation Psxzparameter

Parameter	Value	Unit	Description
H	20, 40, 60, 80, 100	mm	Depth of Soil
D	3, 4, 5	mm	Diameter of pile
γ	2.64	Kg/l	Density of soil
K_p	3.93212		Coefficeinet of Passive ground pressure
ϕ	33	deg	Friction angle

**Fig. 9.** Measurement Results

4 Proposed Crawler Robot with Pile Units

The effect of the pile was showed in section 3. Therefore, we will combine the piles to the crawler robot. The performance of the crawler robot is very high. The crawler robot can move on rough terrain including rock etc. However, when the crawler robot traverses loose soil with steep slope, they have large slip condition. This is the reason why the crawler robot cannot support its weight at slope. If the crawler robot has the piles to support its weight, one will have high mobility system. From this consideration, we propose the crawler robot with pile units. Fig.10 shows the conceptual design. This robot has three bodies. One is inner body. Other bodies are outer body (both side). The proposed robot has 12 motors. The four motors are used for driving and the four motor are for penetrating piles. The two motors are set to the swing up mechanism for the outer body (sub-crawler). The fro-back systems using two motors are installed between inner and outer body. This robot has 4 piles units. There are 2 piles unit on inner body. The outer body has each one pile unit as shown fig.11. Moreover, this robot can hold up the edge of the outer body to get over various obstacles such as rocks.

On Figure 12, the developed crawler robot is showed by various views, (a) Overview, (b) Top view, (c) Front View and (d) Side view. We will carry out the running experiments using this robot. The dimension is 500mm×500mm×500mm (including the height of piles units). The whole weight is 14.7 kg. The stroke of outer bodies toward the main body is 300 mm.

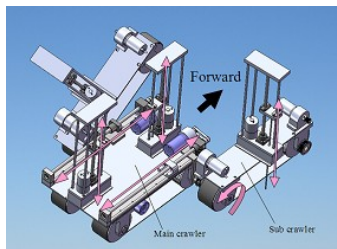


Fig. 10. Crawler robot with piles units

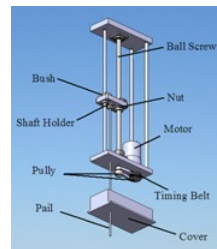


Fig. 11. Piles units

Fig.13 shows the running mechanism of the proposed robot. When the piles of inner body are penetrated into soil, the outer body can move front direction. Then, the inner body can move during the piles of the outer bodies are penetrated into soil. Fig.14 shows a principal of locomotion of proposed one. If the pile of the inner body is penetrated into soil, the outer body can move front direction such as figure. The piles of outer bodies are held up into box at this time. Pile gets the resistance force from soil (deeper than around surface) to support the whole bodies.

In experiments, we measure slip ratio of this robot's motion on loose soil with steep soil.

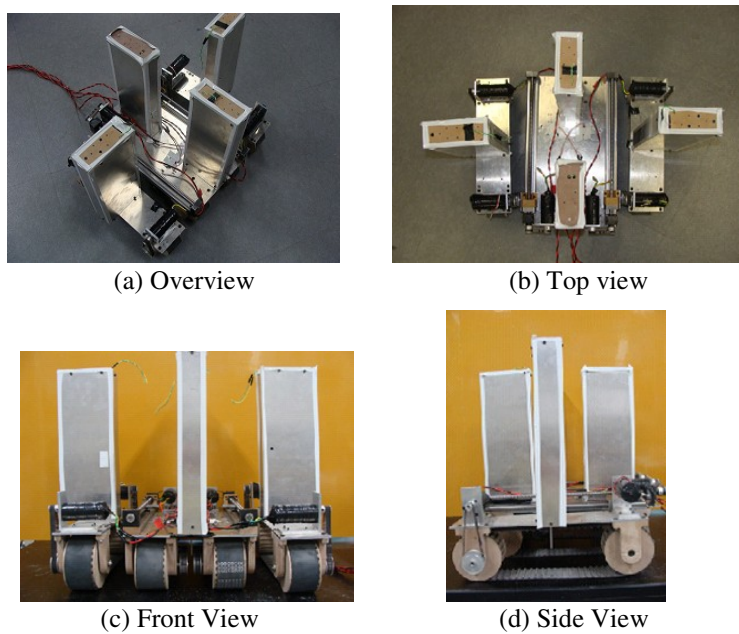


Fig. 12. Proposed Crawler robot with piles units

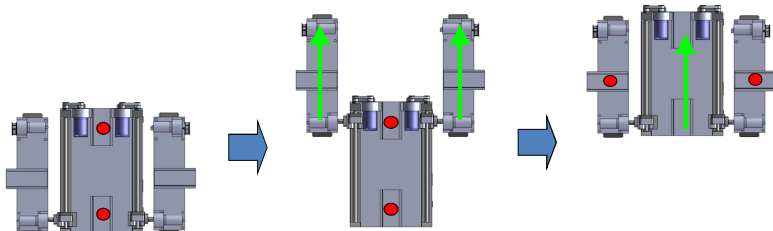


Fig. 13. Running mechanism of the proposed robot with pile motion

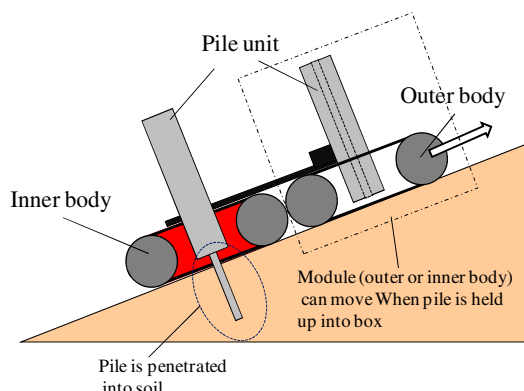


Fig. 14. A principal of locomotion of proposed crawler robot

5 Running Experiments

5.1 Preliminary Running

We carry out the running experiments to confirm the running performance in natural soil field. The view of the experiment is shown in fig. 15. There are various situation in natural field such as small hole. But the developed crawler robot can traverse smoothly. Moreover, the robot can steer using differential motion on loose soil smoothly.

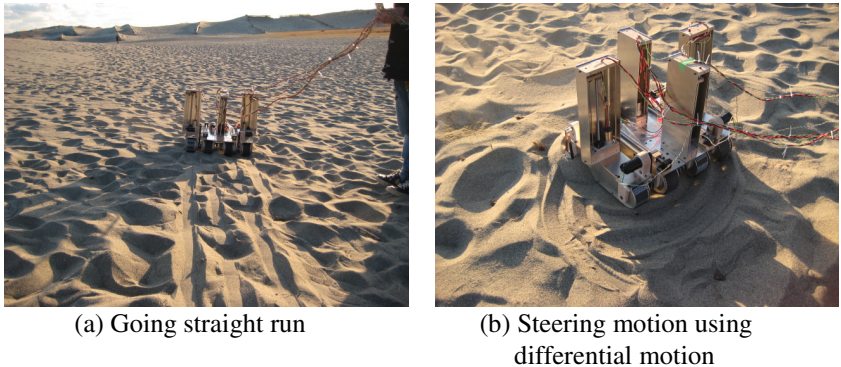


Fig. 15. Running experiments using natural soil field (Nakadajima sandhill)

5.2 Running Experiments on Loose Soil with Steep Slope

We will confirm the effective of the piles which are installed into the proposed robot. In case of this robot without pile motion, this robot traverses loose soil using only crawler belts. In case of one with pile motion, the fro-back systems which are set on inner body are used. When the fro-back systems are used, the crawler belts are rotated at same time. Fig.15 shows the overview of experiment. The slope of loose soil is set. We will carry out the running experiment without and with pile motion.

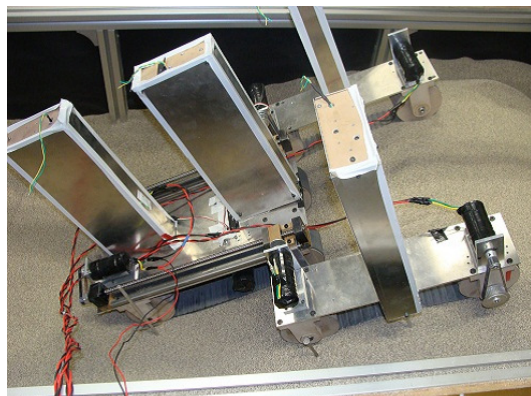


Fig. 16. Overview of running experiment using loose soil with steep soil

6 Results and Discussion

Figure 17 shows the slip ratio versus slope angle. The horizontal axis represents slope which made traversed to the proposed robot. The vertical axis is the slip ratio. In case of the proposed crawler robot without pile units, when the slope increases, the slip ratio increases rapidly (red point and line). When the slope for traversing becomes over 10 deg, the tendency of slip ratio becomes large. The sinkage is low because the proposed robot has crawler belt even if the slope is high. The normal stress of the crawler belt is smaller than the circular rigid wheels. But the slip behaviour is occurred notably. From results, one could not move over 20° slope. On the other hand, the slip ratio of one with pile units does not increase (blue points and line) on various slopes. The proposed robot could climb on loose soil with steep slope by using pile units. This results show that employment of piles is effect to support itself weight and traverse.

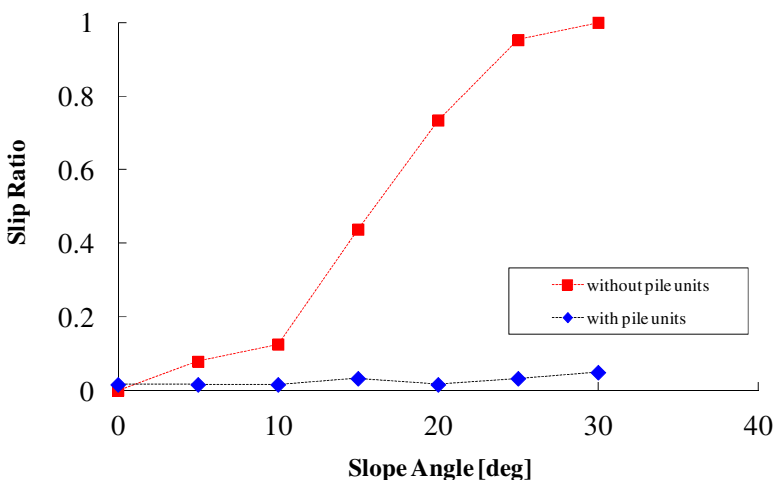


Fig. 17. Slip ratio when the crawler robot with and without pile units traverses loose soil with steep slope

7 Conclusion

We developed the crawler robot with pile units. These piles are used to support itself weight when the robot are traversing loose soil with steep slope. This crawler robot has three bodies, two outer bodies (sub-crawlers) and one inner body. During each piles insert into soil alternately, the proposed crawler robot can move on loose soil with steep slope. The experiments using loose soil with steep slope to measure slip ratio shows the effective of proposed concept. From the experiments, we understood an effective scheme using piles to traverse loose soil with steep slope. We believe that the proposed crawler robot is very effective mobile tools as planetary rovers or rescue robot etc which traverse uneven ground.

Acknowledgements. This research has been supported in part by NSK Foundation for the Advancement of Mechatronics, JAPAN.

References

- [1] Soviet Lunar Missions,
<http://nssdc.gsfc.nasa.gov/planetary/lunar/lunarussr.html>
- [2] NASA, <http://www.hq.nasa.gov/alsj/alsj-LRVdocs.html>
- [3] NASA/JPL, Mars Exploration Rovers,
<http://www.jpl.nasa.gov/missions/mer/>
- [4] Apollo 17 Image Library,
<http://www.hq.nasa.gov/alsj/a17/images17.html>
- [5] Yoshida, K., Nagatani, K., Tadakuma, K., Kinoshita, H.: Design and Development of Surface-contact-type Mobile Robot to Traverse on Weak Soils and Steep Slopes. In: Proceeding of the JSME Conference on Robotics and Mechatronics, 2P1-D17(DVD-ROM) (2009) (in Japanese)
- [6] Iizuka, K., Komatsu, H.: Development of Lunar Rover that uses Characteristic of Loose Soil. In: Proc. of International Symposium on Robotics and Intelligent Sensors, pp. 219–224 (2010)
- [7] Hansen, B.J.: The Ultimate Resistance of Rigid Piles Against Transversal Forces. Danish Geotechnical Institute (Geoteknisk Institut) Bull 12, 5–9 (1961)
- [8] Kasch, V.R., et al.: lateral load test of drilled shaft in clay. Research report 211-1 Texas transportation institute, Texas A and M University (1977)
- [9] Reese, L.C.: Handbook on Design of Piles and Drilled Shafts under Lateral Loads. US Department of Transportation, Federal highway Administration (1984)
- [10] Broms, B.B.: Design of Laterally Loaded Piles. Journal of the Soil Mechanics and Foundations Division 91, 79–99 (1965)

Robo-Teacher: A Computational Simulation Based Educational System to Improve Cyber Security

Bin Zhang, Kamran Shafi and Hussein A. Abbass

School of Engineering and Information Technology,
University of New South Wales,
Canberra, Australia

Bin.Zhang@student.adfa.edu.au, {k.shafi,h.abbass}@adfa.edu.au

Abstract. Various threats and security issues exist in the cyber environment. For information assurance, we need to fully understand the concept of Cyber Intelligence (CI) which includes the identification, tracking, analysis and countering of security threats in cyberspace. In order to achieve this, we focus on educating and training CI for organizations and individuals via effective smart systems design and implementation using artificial intelligence (AI) techniques to build an interactive and adaptive learning environment. Based on investigation of basic theories and CI concepts, a simulation model is proposed. Interaction and adaptation are then integrated or designed upon simulation. Such a learning environment aims to impart a thorough and comprehensive understanding of cyber intelligence and provide enhanced learning experience.

Keywords: Cyber Intelligence, Education, Training, Simulation, Optimization.

1 Introduction

The cyberspace is a broad concept involving information exchange and utilization in any form via any technique or media. It contains not only the physical and technical implementation, but also the social interactions developing in this virtual reality [1]. In fact, it can be thought of as the interconnection of human intelligence through information communication.

It's a fact that we have to confront cyber security issues while enjoying the benefits from cyberspace. However, it is also difficult and complicated to deal with cyber attacks and address vulnerabilities. So many things are involved and intermingled. It contains not only the physical and technical implementation, but also human beings and interactions. From this perspective, not only anti-virus packages, intrusion detection systems and security enhanced systems are necessary, but also a comprehensive endeavor is required for managing our security objectives. We need to fully understand the concept of Cyber Intelligence and impart the knowledge to human beings located in the center of cyberspace to raise the level of security and information assurance. Hence, effective educational and training tools are in urgent need to improve the current situation of CI learning.

2 Background

Knowledge relies on education and training for imparting. Current education and training methods exploit one or a combination of several categories of techniques. The first kind is formal training sessions, which are instructor-led spot or video courses, brown-bag seminars and so on [2]. Usually they are predefined and the success is greatly determined by the lecturer to engage the audience. What's more, they are probably more appropriate approaches for common knowledge rather than complex concepts which require high level of learner involvement and interaction. The second category is computer or web based models and tools for education, which are still traditional teaching method equipped with advanced information and communication technology and add a certain extent of flexibility since users can determine their own pace of training. However, they are generally passive and monotonous ways with low level of user participation and not able to challenge the user for further elaboration. The third category is featured by artificial intelligence techniques that have been introduced into education to encourage interaction. However, they are also based on scripted knowledge and usually integrate predefined exercises, associated solutions and remediation actions when solutions of the users deviated. They are good for drill-and-practice activities but not so satisfying for complex pedagogies [3].

To improve the current situation, or at least complement or provide an alternate to current methods, we require the educational tools to be more flexible, autonomous and adaptive. The learning environment in this paper is designed to contribute to fill the gap between the limitations of traditional teaching methods and high requirements of complex pedagogical activities for cyber intelligence concepts.

3 Framework of Interactive Learning Environment for Cyber Intelligence (ILECI)

In order to enhance people's awareness of and capabilities to deal with cyber security issues, our learning environment should be able to carry out pedagogical activities via a virtual intelligent platform using appropriate artificial intelligence techniques. Briefly, methods of teaching and learning, pedagogic and curriculum design principles from the domain of education are incorporated into our learning environment and mapped against advanced techniques in the artificial intelligence domain to provide users with a unique way of improving their understanding of cyber intelligence.

From a high-level point of view, there are several components required to realize our educational purposes. First, various cyber intelligence concepts should be investigated and distilled into a set of target learning outcomes. Second, simulation scenarios extracted from and reflecting these concepts and outcomes should be presented with the intelligent environment for the trainee to interact with. Hence, a scenario-based, exploration-oriented framework is adopted by our training system. Third, both the intelligent system and the trainee coevolve towards the instructional objectives which are evaluated by our optimization engine. During the learning loop, the system records and stores the state and actions of the students for data mining purposes. It identifies different operation patterns and adapts itself to adjust the learning process to better challenge and assist the user to understand cyber intelligent concepts.

In conclusion, the system design relies on the combination of simulation, optimization and data mining to achieve its goal. A simulation engine is required to reflect the environment dynamics and changes. An optimization engine should be in place to implement decision making mechanism. Data mining techniques are needed to realize adaptation. This comprehensive method will be used to develop an intelligent learning environment that offers flexible, autonomous, interactive and adaptive capabilities in support of the learning process. The overall framework of our learning environment is shown in Figure 1.

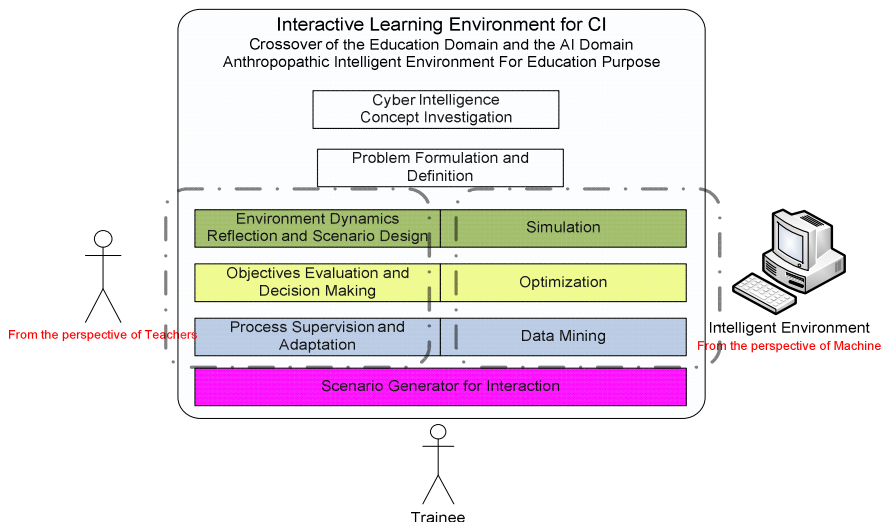
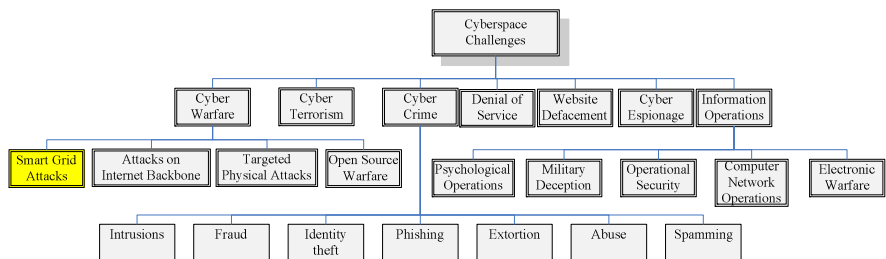


Fig. 1. Framework of the Learning Environment

The learning environment monitors and evaluates the trainee's solution in the simulation environment and compares it with its own optimized solution to decide whether a solution is appropriate or requires pedagogical intervention (e.g., challenge or help with an incorrect solution, praise for a good solution). For a certain number of unsuccessful attempts, data mining engine is invoked to assess the trainee's performance. The key difference between our intelligent system and traditional educational tools is that the system is able to challenge the user by understanding the simulation dynamics.

There is a great quantity of security issues in the cyberspace to be researched and categorized. The ILECI framework is intended to cover various cyber threats as shown in Figure 2. As the first component, we study the security issues of modern power systems which we called Espionage in Smart Grid and start with access point layout design in Advanced Metering Infrastructure (AMI). AMI is an integral part of the smart distribution grid [4]. This infrastructure incorporates current information and communication technologies for sensing, metering and measurements in order to realize full visibility and pervasive control [5, 6].

**Fig. 2.** Cyber Threats [7]

4 Advanced Metering Infrastructure – An Application of ILECI

4.1 Advanced Metering Infrastructure

Meter Reading System (MRS) enables utilities to read the consumption records, alarms and status from residential meters remotely. Nowadays, two-way communication is supported by advanced digital meters at all customer service locations [6] in smart distribution grid.

These smart meters are usually deployed or integrated with various sensors, actuators and appliances within the customer's premises to form a home area network (HAN) using the low-power and advanced wireless network technologies such as ZigBee (IEEE 802.15.4) [8]. Based on this, several adjacent HANs constitute a neighborhood area network (NAN) sharing an access point of the distribution grid to communicate with the utility's operational centre. An access point receives periodic input from each NAN within its reception range and then relays or uploads the centralized information to the power utility using long-haul communication technologies such as Ethernet, GPRS/CDMA [9].

The layout of access points is of great importance for utility because they affect the intelligence of the grid significantly. If an access point of the distribution network isn't able to work properly due to cyber attacks, it would result in a loss of reception of the whole neighborhood area. Hence, the reliability and robustness of access points and their layout are key factors for an accurate information collection, which supports the correct and efficient decision making of utilities.

There are several requests to deploy access points, which are not too difficult to figure out, including:

- Reduce the number of access point devices since the enormous size of service area;
- Maintain the coverage of access points for an acceptable level of service;
- Increase the overlap of coverage areas of access points for the sake of redundancy;
- Make full utilization of the covering capability of access points.

These requests also provide perspectives to measure or evaluate access point layout. On top of that, the difficult part is to identify the relationships between these requirements. For example, what are the priorities of these items? How they compromise with each other for our overall objective of layout design? Where should my layout go? Is there still a solution better than mine?

4.2 Teaching Objectives

Narrow down to the access point layout design, the learning environment aims to support the trainee to understand how the access point layout relates to keeping an acceptable level of service in order to tolerate faults or mitigate the impact of challenges or attacks to normal operation. As mentioned earlier, the issues such as deployment cost (determined by the number of APs), coverage, redundancy and access point utilization are included. Apparently, Conflict exists and it usually implies a cost vs. performance trade-off among them. How the layout affects the distribution network and the implications between its subitems are left for the trainee to explore.

4.3 Operating Mechanics

The components and their roles are described as following:

- Scenario Generator: First, the scenario generator is responsible to create certain scenarios and interfaces for user interaction. It supports automated scenario generation mainly determined by house density in a service area. Second, it bridges the underlying components, such as the simulation engine, and the user. On one hand, it catches the user input and action and transfers the recorded data to simulation engine. On the other hand, it reflects the output from simulation engine in scenarios.
- Simulation Engine: Simulation Engine is the control centre of this teaching robot. First, it monitors the learning process and evaluates the user solution in order to cover the teaching content step by step. Second, it compares the user solution to optimized solution from optimization engine to offer feedback or challenge. Last but not least, it recalls the scenario generator for demonstration.
- Optimization Engine: Optimization Engine provides the basis for decision making of this teaching robot. Only through an integrated optimization process, can the system know what is good dynamically. Among various optimization techniques, the famous multi-objective genetic algorithm NSGA-II (Non-Dominated Sorting Genetic Algorithm-II) [10] is adopted for its efficiency and the versatility of genetic algorithms in the field of optimization.

5 Experiment

For the learning environment, the main window (as shown in Figure 3) consists of a design region, which takes most part of the whole screen, an information region, an operations region and a directions region.

The information shows statistics of user solution and the status of the nearest access point nearest to the cursor.

The operations region, at first, accepts a parameter called density (from 0 to 1) for the initializing button to generate a distribution of houses in the design region. Secondly, the user solution can be saved or restored through relevant button. Last, the operations region allows the user to do the optimization at the background and open a watch window, if needed, to see how your solution deviates from the optimized solutions in the Pareto Front. If the density is changed, you are required to do the optimization before you can use the watch window.

The last component of the main window is the Directions region. It provides guide information when you get stuck or need help to proceed. It will reveal the principles gradually during your solution design process. At first, it shows information regarding how to basicly use this learning environment.

The most time and energy-consuming process begins when the user starts to design an access point layout solution.

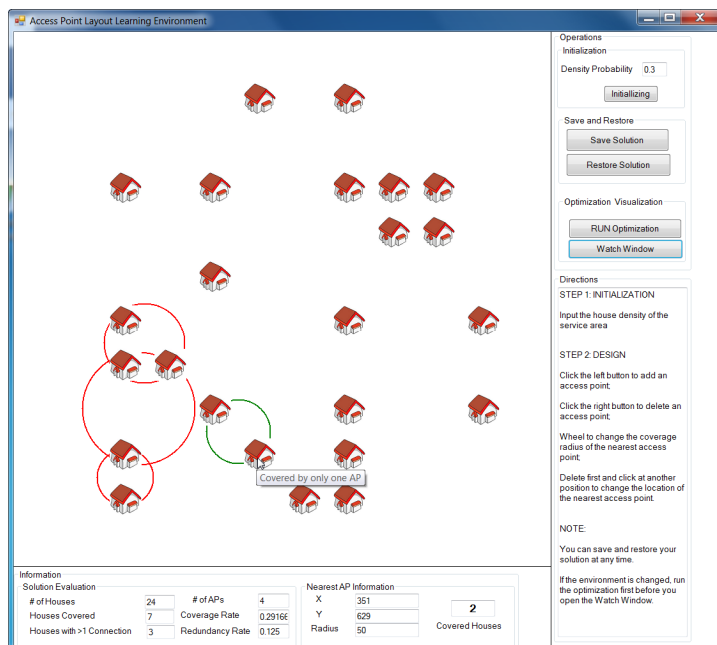


Fig. 3. Explore the Design Process

We can click at any position in the design region to add an access point or remove it by clicking the right button. Once an access point is deployed, the user doesn't have to operate it by touching it exactly. In fact, the access point nearest to the mouse cursor will respond automatically. If you want to move one access point to another place, remove it first and click at the new location to add a new access point. You can also roll the wheel in the middle of the mouse to change the coverage radius of an access point, forward for increase and backward for decrease.

When you are operating, the statistics of your not-completed-yet solution will be displayed as shown in Figure 3. You can get your immediate information about your move to make clear what happened after that and its effect on your design. The green access point is the nearest one that responds to your operation. In the information region, we can see that it has covered 2 access points. However, it may not be so explicit to decide that whether a house (HAN) is covered sometimes, especially when the house is located at the edge of the coverage area of an access point. In this case you can move your mouse to that house, a pop-up tip will appear to inform you how many access points it is being covered.

When you are struggling with the solution design, one big problem is that you are not sure about what the information displayed means and where my solution will possibly go. That's why we introduce the watch window. It shows how much your solution deviates from the optimized ones and you task is to move your solution towards the optimized ones until your solution is not worse than them, which means at least your solution is not dominated by any of them. It would be great if yours dominates one or several optimized solutions.

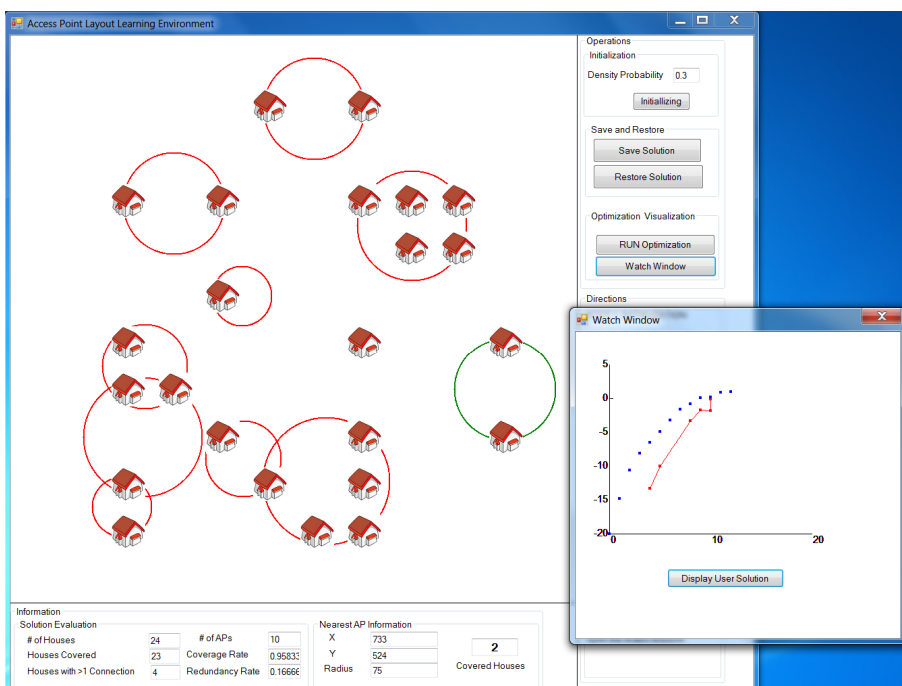


Fig. 4. Watch Window for Visual Evaluation

When you open the watch window, shown in Figure 4, the solutions in the Pareto Front are represented by blue dots. They are determined by the optimization algorithm and the objective functions embedded. The user solution represented by the red dots and lined up in the figure reflects the trainee exploration and is shown for your comparison and analysis. This evolution process of user solutions will be recorded and indicates how you come up with better solutions step by step.

Although it is just a demonstration of an individual example, it's interesting to note that the evolution process of user solution is not monotone improving, which means the gap between the user solution and the Pareto Front keeps decreasing. The gap can be enlarged at some time. The drift is struggling for the user but a process of essence during which the ineffable and deep knowledge, usually the most important part of a concept, is explored and digged by the trainee. In fact, theoretically, the track of user solutions can be of any form until he makes sure about the design principles.

6 Conclusion and Future Work

In this paper, we demonstrate how the simulation combined with optimization is used for cyber intelligence education through the learning environment design and implementation. NSGA-II plays an important role, with the help of the simulation engine, makes the environment intelligent to guide the trainee to find the principles of access point layout design. This is also an application demonstration of evolutionary computation in the field of education. Definitely this kind of computational intelligence is potential and rewarding to make a difference to current situation.

Apparently, this is just a prototype. For the next step, we would:

- Integrate the data mining engine for better reflection of system dynamics;
- Investigate and integrate more evolutionary computation methods and verify the performance of these algorithms, especially those with fast convergence.
- Test the effectiveness of the system widely by making more people involved to improve the logic flow and interface user-friendliness.

References

1. Morningstar, C., Farmer, F.R.: The lessons of Lucasfilm's habitat. In: *Cyberspace: First Steps* 1991, pp. 273–302. MIT Press (1991)
2. Cone, B.D., et al.: A video game for cyber security training and awareness. *Computers & Security* 26(1), 63–72 (2007)
3. Conati, C.: Intelligent tutoring systems: new challenges and directions. In: *Proceedings of the 21st International Joint Conference on Artificial Intelligence 2009*, pp. 2–7. Morgan Kaufmann Publishers Inc., Pasadena (2009)
4. Hart, D.G.: Using AMI to realize the Smart Grid. In: *2008 IEEE in Power and Energy Society General Meeting - Conversion and Delivery of Electrical Energy in the 21st Century* (2008)
5. Momoh, J.: *Smart Grid: Fundamentals of Design and Analysis*. John Wiley & Sons (2012)
6. Brown, R.E.: Impact of Smart Grid on distribution system design. In: *2008 IEEE in Power and Energy Society General Meeting - Conversion and Delivery of Electrical Energy in the 21st Century* (2008)
7. Abbass, H.: computational Red teaming and cyber challenges (2009), <http://mams.rmit.edu.au/fpowkftaovbo.pdf>
8. Bennett, C., Highfill, D.: Networking AMI Smart Meters. In: *Energy 2030 Conference, ENERGY 2008*. IEEE (2008)
9. McDaniel, P., McLaughlin, S.: Security and Privacy Challenges in the Smart Grid. *IEEE Security & Privacy* 7(3), 75–77 (2009)
10. Deb, K., et al.: A fast and elitist multiobjective genetic algorithm: NSGA-II. *IEEE Transactions on Evolutionary Computation* 6(2), 182–197 (2002)

Comparative Analysis of Arm Control Performance Using Computational Intelligence

Cesar H. Valencia, Marley M.B.R. Vellasco, and Karla T. Figueiredo

ICA – Applied Computational Intelligence Laboratory
Electric Engineering Department

Pontifical Catholic University of Rio de Janeiro (PUC-Rio)

R. Marquês S. Vicente 225 – Gávea, Rio de Janeiro, RJ, Brasil

{chvn, marley, karla}@ele.puc-rio.br

Abstract. Several models of computational intelligence have been proven to be useful in robotic devices control. This work evaluates three models to solve the inverse kinematics problem of a robotic manipulator with two degrees of freedom, which is used to position objects in conjunction with the *CoroBot* platform. They were initially developed the direct and inverse kinematic models using the homogeneous transformation matrices, extracting from these, the training, testing and validation data used in the three models. This paper takes advantage of the great potential of artificial neural networks, in order to determine the feasibility and response of the experiments performed, keeping in focus the possible applications and modification of design and training parameters. The models used are Feedforward Neural Networks, Neuro-Fuzzy Systems and finally Echo State Networks.

Keywords: Neural Networks, Neuro-Fuzzy Systems, Echo State Networks, Robotic, Inverse Kinematic.

1 Introduction

Traditionally, the positioning of robotic manipulators is performed using classical control techniques [1]. In some cases, models of computational intelligence are used, such as Neuro-Fuzzy (ANFIS) [2] and Neural Networks (NN) [3].

In this case, the platform used did not show many published studies using control by intelligent techniques. In [4] is proposed a design methodology of neural networks applied to mobile robotic platforms, and [5] develops a training cooperative robot for inspection in an unfamiliar area.

Recurrent neural networks Echo State Networks (ESNs) presented in [6], is a model that has recently been successfully used in problems of prediction of chaotic systems [7], nonlinear dynamics [8], and identification and control systems [9].

The objective of this work was to determine the recurrent neural networks ESNs performance in the inverse kinematics solution problem, embedded in the commercial platform *CoroBot*. Additionally, this problem was also solved using Multilayer Perceptron Networks (MLP), and Neuro-Fuzzy Models to establish a comparison between traditional computational models of intelligence and the ESN.

The paper is organized as follows: section two presents the mathematical foundations of ESNs, as well as the steps of sampling and calculation of weights that make up the training. Section three presents results solving the problem using the three computational intelligence models selected, and finally section four presents conclusions.

2 Reservoir Computing (Echo State Networks)

ESNs are a Recurrent neural Network (RRN) inspired by recent neuropsychological experiments [10], which main characteristic is the presence of at least one feedback loop. According to [11], recurrent neural networks are those that use at least one output neuron of the network at n -time and use it as input to other neurons in a $n + 1$ time.

Figure 1 shows the basic structure including the reservoir with internal units.

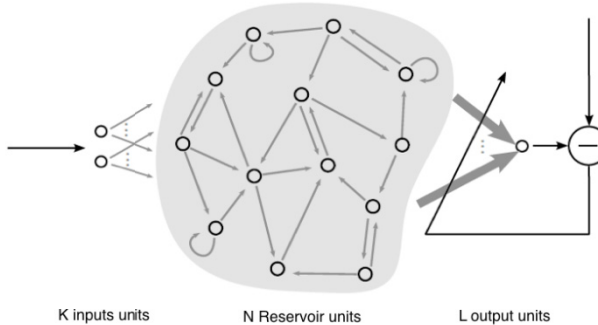


Fig. 1. Reservoir Computing, only the RNN-to-output weights are adapted. [11]

The most important element in ESNs is the reservoir, which contains a large number of internal units which are interconnected randomly and / or self-connected. According to [12] after the reservoir is formed with randomly interconnected neurons, it remains fixed, however, during the training process, the connections weights going from the reservoir to the output are modified.

The weight updates can be performed off-line using linear regression, or on-line using recursive minimum least squares methods.

The state of activation of neurons in the reservoir can be obtained using Equation 1.

$$x(n) = \varphi(w^e u(n) + w^R x(n-1) + w^{rr} d(n-1)) \quad (1)$$

Where $x(n)$ is the internal state of the reservoir in a $\varphi(\cdot) = (\varphi_1, \dots, \varphi_N)^T$ time, and they are sigmoid activation functions, $d(n-1)$ is the action potential of the output unit to an earlier time, $u(n)$ is an input vector, w^e , w^R and w^{rr} are the weights matrix for the input units, the reservoir and the recurrent connections respectively. The output of an ESN is given by equation 2.

$$d(n) = \varphi^s \left(w^s \cdot \begin{bmatrix} x(n) \\ d(n-1) \end{bmatrix} \right) \quad (2)$$

Where φ^s may be linear or sigmoid, depending on the task complexity, and w^s is the matrix containing the weights of the output connections, this is determined after the training.

Using K units as input, N units in the reservoir, and L units in output, the dimensions of matrices are: $w^e \in \mathbb{R}^{N*K}$, $w^R \in \mathbb{R}^{N*N}$, $w^{rr} \in \mathbb{R}^{N*L}$ and $w^s \in \mathbb{R}^{L*N}$.

The training was carried out in two stages: first sampling occurs, and then calculating the weights that are presented in the next section.

2.1 Sampling

Sampling the internal signals is determined by equation 3 for the operating range $n = A_p, \dots, A_q$ and they are stored in the matrix J sized $(A_q - A_p) + 1 * K$, where A_p e A_q are the initial and final values of the sample strip, respectively.

$$x(n) = (x_1(n), \dots, x_K(n)) \quad (3)$$

2.2 Calculating the Output Weights

The second step is the weights calculation (equation 4), which are stored in the matrix w^s to the output unit $d(n)$, and it could be seen that the output signal $y(n)$ is estimated with the series combination of linear internal activation $x_i(n)$ according to equation 4.

$$y(n) \approx d(n) = \sum_{i=1}^K w_i^s x_i(n) \quad (4)$$

The output signal $y(n)$ is stored in matrix U of size $(A_q - A_p) + 1 * L$. It is recommended that the value A_p is sufficiently distant so that dynamics of the network is not determined by the initial states.

2.3 Training Error

Equation 5 is used to obtain the mean square error for training data.

$$MSE_{train} = \frac{1}{(A_q - A_p) + 1} \sum_{n=p}^q \left(y(n) - \sum_{i=1}^K w_i^s x_i(n) \right)^2 \quad (5)$$

The offline calculation of the weights of regression is equivalent to multiplying the J pseudo-inverse with U matrix as shown in equation 6.

$$w^s = J^{-1}U \quad (6)$$

2.4 Testing Error

To obtain the test error, equation 7 is used. Where the generated output $d(n)$ is the network trained data set in the range for testing, A_e and A_f are the initial and final values of the test strip respectively.

$$MSE_{test} = \frac{1}{(A_f - A_e) + 1} \sum_{n=e}^f (y(n) - d(n))^2 \quad (7)$$

3 Results

3.1 Simulations Using Different Models of Computational Intelligence

This section shows the obtained results with the three computational intelligence models used. After acquiring the data sets for every angle of the manipulator, two criteria were established to evaluate performance for each model. The first one is the Mean Squared Error (MSE) calculated according to equation 8.

$$MSE = \frac{1}{N} \sum_{n=1}^N (y(n) - d(n))^2 \quad (8)$$

The second evaluation criteria is the maximum angular difference obtained by applying the model developed for each arm angles. Such difference could be positive (MP) or negative (MN), and was obtained using equation 9.

$$D\alpha = \alpha_{MM} - \alpha_{MIC} \quad (9)$$

Where, α_{MM} is the angle according to the mathematical model, and α_{MIC} is the angle according to the computational intelligence model.

3.1.1 Neuro-Fuzzy Models (ANFIS)

The first computational intelligence model used was Neuro-Fuzzy. The 24,000 generated patterns were divided into 70% training, 15% for validation, and 15% for testing.

The number of linguistic terms for each variable and the number of times used to generate the fuzzy models were altered to obtain the lowest MSE and the lowest possible $D\alpha$. All terms used are Gaussian type, which was standardized for all experiments as shown in [13] and [14].

Table 1 shows the results obtained for the three configurations proposed. The number of terms for each input variable was changed at 3, 5 and 7, as well as the number of epochs at 20, 40 and 80. Higher values were disregarded because the results did not show a significant improvement, and represent a high computational cost.

Table 1. Results Neuro-Fuzzy Models

Linguistic Terms	Epochs	MSE	α	Error (degrees)
3	20	$7.9e^{-4}$	θ_1	$M_p:0.11^\circ ; M_N:0.09^\circ$
		$2.2e^{-3}$	θ_2	$M_p:0.39^\circ ; M_N:0.19^\circ$
	40	$4.9e^{-4}$	θ_1	$M_p:0.10^\circ ; M_N:0.07^\circ$
		$1.4e^{-3}$	θ_2	$M_p:0.15^\circ ; M_N:0.17^\circ$
	80	$2.2e^{-4}$	θ_1	$M_p:0.08^\circ ; M_N:0.03^\circ$
		$1.1e^{-3}$	θ_2	$M_p:0.35^\circ ; M_N:0.15^\circ$
5	20	$7.2e^{-5}$	θ_1	$M_p:0.05^\circ ; M_N:0.02^\circ$
		$1.9e^{-4}$	θ_2	$M_p:0.04^\circ ; M_N:0.08^\circ$
	40	$2.4e^{-5}$	θ_1	$M_p:0.03^\circ ; M_N:0.01^\circ$
		$7.2e^{-5}$	θ_2	$M_p:0.02^\circ ; M_N:0.05^\circ$
	80	$1.9e^{-5}$	θ_1	$M_p:0.03^\circ ; M_N:0.01^\circ$
		$5.5e^{-5}$	θ_2	$M_p:0.01^\circ ; M_N:0.04^\circ$
7	20	$1.3e^{-5}$	θ_1	$M_p:0.02^\circ ; M_N:0.05^\circ$
		$3.8e^{-5}$	θ_2	$M_p:0.39^\circ ; M_N:0.19^\circ$
	40	$1.0e^{-5}$	θ_1	$M_p:0.02^\circ ; M_N:0.01^\circ$
		$2.9e^{-5}$	θ_2	$M_p:0.01^\circ ; M_N:0.04^\circ$
	80	$9.9e^{-6}$	θ_1	$M_p:0.02^\circ ; M_N:0.01^\circ$
		$2.7e^{-5}$	θ_2	$M_p:0.01^\circ ; M_N:0.04^\circ$

Figure 2 shows the structure used in the Neuro-fuzzy model. The input values are the positions (y, z) and the output is the angle of articulation.

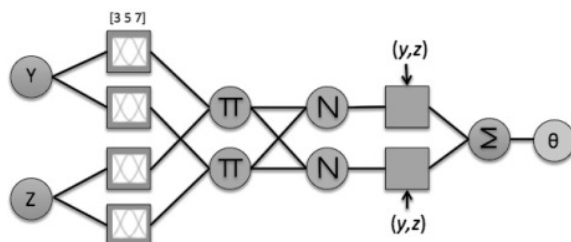


Fig. 2. ANFIS Structure

3.1.2 MLP Networks

The use of neural networks MLP follows the fact that these are considered universal approximators and have a great diversity of configuration. In results reported by other authors in control tasks such as robotic manipulators [15], [16] and [17] MLP Networks achieved such goals.

Table 2. Results MLP Networks

Type	Neurons	α	MSE	Error (degrees)
FFnet 1layer	10	θ_1	3.07e-1	MP:6.0° ; MN:3.0°
		θ_2	6.60e-1	MP:3.0° ; MN:11°
	20	θ_1	6.32e-2	MP:2.2° ; MN:1.3°
		θ_2	3.03e-1	MP:1.3° ; MN:2.8°
	30	θ_1	8.06e-2	MP:1.7° ; MN:1.0°
		θ_2	7.37e-2	MP:1.3° ; MN:2.2°
	40	θ_1	6.06e-2	MP:1.7° ; MN:0.7°
		θ_2	5.83e-2	MP:1.3° ; MN:2.5°
	10	θ_1	5.85e-1	MP:8.2° ; MN:2.0°
		θ_2	1.33	MP:2.0° ; MN:5.7°
Fitnet 1 layer	20	θ_1	8.42e-2	MP:1.8° ; MN:1.3°
		θ_2	2.20e-1	MP:2.0° ; MN:2.7°
	30	θ_1	1.79e-1	MP:1.5° ; MN:1.2°
		θ_2	7.91e-2	MP:1.2° ; MN:2.3°
	40	θ_1	9.39e-2	MP:1.5° ; MN:1.0°
		θ_2	5.23e-2	MP:0.7° ; MN:1.5°
	10-15	θ_1	3.40e-3	MP:0.6° ; MN:0.45°
		θ_2	1.10e-3	MP:0.31° ; MN:0.5°
FFnet 2 layers	20-15	θ_1	1.21e-4	MP:0.37° ; MN:0.14°
		θ_2	1.12e-4	MP:0.07° ; MN:0.22°
	30-15	θ_1	1.54e-4	MP:0.13° ; MN:0.06°
		θ_2	2.30e-4	MP:0.05° ; MN:0.1°
	10-15	θ_1	2.00e-3	MP:1.0° ; MN:0.4°
		θ_2	1.82e-4	MP:0.3° ; MN:0.5°
	20-15	θ_1	2.14e-4	MP:0.5° ; MN:0.18°
		θ_2	7.70e-5	MP:0.06° ; MN:0.18°
Fitnet 2 layers	30-15	θ_1	1.38e-4	MP:0.15° ; MN:0.06°
		θ_2	1.51e-4	MP:0.05° ; MN:0.12°

For this work were evaluated 14 different types of neural networks, using the same, training, validation and testing data set used in Neuro-Fuzzy model.

Parameters such as number of neurons and number of hidden layers were changed for each variant configuration. Table 2 presents the results for each type of network employed. The activation function for all networks in the hidden layer, or layers, was hyperbolic sigmoid tangent. Implementation and testing was performed using Matlab 2010b.

Two types of network models were used. The first was FeedforwardNet, which represents the traditional shape MLP network. The second one was FitNet, which is applied to determine the relationship between input / output values to subsequently use them in a MLP network.

The use of two layers was an alternative that offered best response during the design of networks, obtaining the angular difference better than with one hidden layer.

Figure 3 shows the structures used in the first and second layers. The input values are the positions (y , z) and the output is the θ angle.

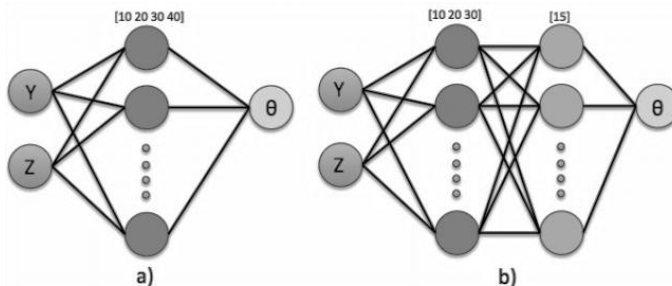


Fig. 3. MLP Network Structure

3.1.3 Reservoir Computing (Echo State Networks)

The final model used for comparison with the previous ones were the ESNs [18], which were presented in section 2. The data set used is the same as in previous models. The percentages for training sets, validation and testing were maintained.

Table 3 shows the results obtained using ESNs. The parameters modified for testing were the dispersion¹, the internal units and the number of reservoir units.

¹ In the case of reservoir internal units is the weighting matrix w^R that have non-zero value and were randomly selected.

Table 3. Results Echo State Networks

w^R	N	MSE	α	Error (degrees)
30%	50	1.925e ⁻⁶	θ_1	M _P :0.145° ; M _N :0.179°
		2.563e ⁻⁶	θ_2	M _P :0.195° ; M _N :0.192°
	100	1.301e ⁻⁶	θ_1	M _P :0.048° ; M _N :0.062°
		1.766e ⁻⁶	θ_2	M _P :0.054° ; M _N :0.065°
	300	1.333e ⁻⁶	θ_1	M _P :0.050° ; M _N :0.025°
		2.002e ⁻⁶	θ_2	M _P :0.056° ; M _N :0.027°
	600	1.414e ⁻⁶	θ_1	M _P :0.027° ; M _N :0.015°
		1.769e ⁻⁶	θ_2	M _P :0.031° ; M _N :0.022°
	1000	2.255e ⁻⁶	θ_1	M _P :0.058° ; M _N :0.040°
		2.693e ⁻⁶	θ_2	M _P :0.067° ; M _N :0.048°
50%	2000	3.239e ⁻⁶	θ_1	M _P :0.025° ; M _N :0.051°
		3.361e ⁻⁶	θ_2	M _P :0.026° ; M _N :0.055°
	50	3.037e ⁻⁶	θ_1	M _P :0.123° ; M _N :0.084°
		3.100e ⁻⁶	θ_2	M _P :0.020° ; M _N :0.087°
	100	2.799e ⁻⁶	θ_1	M _P :0.069° ; M _N :0.047°
		2.885e ⁻⁶	θ_2	M _P :0.075° ; M _N :0.053°
	300	1.617e ⁻⁶	θ_1	M _P :0.035° ; M _N :0.018°
		1.982e ⁻⁶	θ_2	M _P :0.037° ; M _N :0.021°
	600	2.310e ⁻⁶	θ_1	M _P :0.025° ; M _N :0.015°
		2.505e ⁻⁶	θ_2	M _P :0.025° ; M _N :0.015°
80%	1000	1.680e ⁻⁶	θ_1	M _P :0.032° ; M _N :0.018°
		1.819e ⁻⁶	θ_2	M _P :0.033° ; M _N :0.019°
	2000	3.362e ⁻⁶	θ_1	M _P :0.048° ; M _N :0.014°
		3.546e ⁻⁶	θ_2	M _P :0.049° ; M _N :0.017°
	50	3.223e ⁻⁶	θ_1	M _P :0.164° ; M _N :0.021°
		3.926e ⁻⁶	θ_2	M _P :0.177° ; M _N :0.022°
	100	1.583e ⁻⁶	θ_1	M _P :0.035° ; M _N :0.063°
		1.749e ⁻⁶	θ_2	M _P :0.041° ; M _N :0.066°
	300	1.368e ⁻⁶	θ_1	M _P :0.031° ; M _N :0.028°
		1.550e ⁻⁶	θ_2	M _P :0.042° ; M _N :0.033°
	600	2.670e ⁻⁶	θ_1	M _P :0.042° ; M _N :0.031°
		2.693e ⁻⁶	θ_2	M _P :0.047° ; M _N :0.038°
	1000	1.954e ⁻⁶	θ_1	M _P :0.036° ; M _N :0.019°
		2.113e ⁻⁶	θ_2	M _P :0.037° ; M _N :0.021°
	2000	4.240e ⁻⁶	θ_1	M _P :0.020° ; M _N :0.039°
		4.218e ⁻⁶	θ_2	M _P :0.021° ; M _N :0.040°

Figure 4 shows the structure used in ESNs. Once again, the input values are the positions (y, z) and the output is the angle.

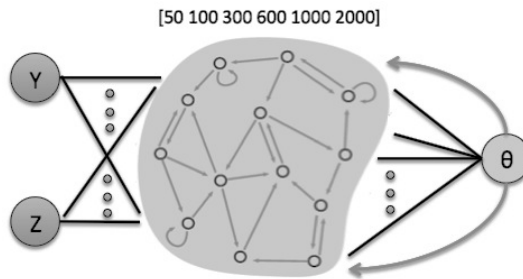


Fig. 4. Echo State Networks Structure

4 Conclusions

The results confirmed the feasibility of using computational intelligence models to robotic manipulators control.

Table 4 presents the best results for each model used, revealing that the ESNs provided the best performance.

Table 4. Results Echo State Networks

Model	$D\alpha$	MSE	Error (degrees)
ANFIS	θ_1	$9.9e^{-6}$	$M_p:0.02^\circ ; M_n:0.01^\circ$
	θ_2	$2.7e^{-5}$	$M_p:0.01^\circ ; M_n:0.04^\circ$
MLP Networks	θ_1	$1.54e^{-4}$	$M_p:0.13^\circ ; M_n:0.06^\circ$
	θ_2	$7.70e^{-5}$	$M_p:0.06^\circ ; M_n:0.18^\circ$
ESNs	θ_1	$2.31e^{-6}$	$M_p:0.025^\circ ; M_n:0.015^\circ$
	θ_2	$2.50e^{-6}$	$M_p:0.025^\circ ; M_n:0.015^\circ$

The models developed using MLP networks have proved to be good at learning, getting low MSE values, and $D\alpha$ values that could be used for various applications of manipulators. It was also observed that the complexity of the patterns presented made necessary the use of two layers to ensure results.

In the design of the networks, the FitNet had a better answer for most experiments, considering the fact that the curve fit function was performed by the best.

The models utilizing ANFIS had a superior performance than models with MLP networks, and less number of epochs, which means a low computational cost, the results showed responses to $9.9E-6$ MSE error, in the best case.

Increasing the number of linguistic terms in the input variables showed a significant improvement greater than the number of epochs increase in the results. The angular difference reached values lower than MLP networks getting errors of up to 0.01° .

The design of ESNs showed greater complexity derived from the characteristics to be considered for the reservoir. A large number of tests was conducted to achieve the results.

ESN model performance results exceeded all previous models and maintained a moderate computational cost compared to previous models. All results showed an error with MSE values lower than the best results of the other models.

Two design parameters determined the general behavior of ESNs. One was the weights dispersion of the units within the reservoir, when the dispersion increases the network performance decreases. The second parameter was the number of internal units, which showed better results in amounts in the range 50 to 600.

References

1. Tondu, B.: Kinematic modelling of anthropomorphic robot upper limb with human-like hands. In: IEEE International Conference on Advanced Robotics, pp. 1–9 (2009)
2. Adhyaru, D., Patel, J., Gianchandani, R.: Adaptive Neuro-Fuzzy Inference System based control of robotic manipulators. In: IEEE International Conference on Mechanical and Electrical Technology, pp. 353–358 (2010)
3. Young, H., Lewis, F., Dawson, D.: Intelligent optimal control of robotic manipulator using neural networks. *Automatica* 36(9), 1355–1364 (2000)
4. Bhamhani, B., Valbuena-Reyes, L., Tanner, H.: Spatially distributed cellular neural networks. *International Journal of Intelligent Computing and Cybernetics* 4(4), 465–486 (2011)
5. Cheng, K., Dasgupta, P.: Multi-Agent coalition formation for distributed area coverage: analysis and evaluation. In: IEEE International Conference on Web Intelligence and Intelligent Agent Technology, vol. 3, pp. 334–337 (2010)
6. Jaeger, H.: The “echo state” approach to analysing and training recurrent neural networks – with an Erratum note 1. *GMD Report* (148), 1–47 (2010)
7. Xi, J., Shi, Z., Han, M.: Analyzing the state space property of echo state networks for chaotic system prediction. In: IEEE International Joint Conference on Neural Networks, vol. 3, pp. 1412–1417 (2005)
8. Bian, X., Mou, C.: Identification of non-linear dynamic model of UUV based on ESN neural network. In: IEEE 30th Chinese Control Conference, pp. 1432–1437 (2011)
9. Ni, S., et al.: Predictive Control of Vehicle Based on Echo State Network. In: IEEE International Conference on Intelligence Science and Information Engineering, pp. 37–40 (2011)
10. Jaeger, H.: Reservoir riddles: suggestions for echo state network research (extended abstract). In: IEEE International Joint Conference on Neural Networks, vol. 3, pp. 1460–1462 (2005)
11. Lukoševičius, M., Jaeger, H.: Reservoir computing approaches to recurrent neural network training. *Computer Science Review* 3(3), 127–149 (2009)
12. Ganesh, K., Shishir, B.: Effects of spectral radius and settling time in the performance of echo state networks. *Neural Networks* 22(7), 861–863 (2009)
13. Aghajarian, M., Kiani, K.: Inverse kinematics solution of PUMA 560 robot arm using ANFIS. In: IEEE International Conference on Ubiquitous Robots and Ambient Intelligence, pp. 574–578 (2011)

14. Yang, M., Lu, G., Li, J.: An inverse kinematics solution for manipulators based on fuzzy. In: IEEE International Conferences on Info-tech and Info-net, vol. 4, pp. 400–404 (2001)
15. Pham, D., Castellani, M., Fahmy, A.: Learning the inverse kinematics of a robot manipulator using the Bees Algorithm. In: IEEE International Conference on Industrial Informatics, pp. 493–498 (2008)
16. Wang, L., Chai, T., Yang, L.: Neural-Network-Based Contouring Control for Robotic Manipulators in Operational Space. *IEEE Transactions on Control Systems Technology* (99), 1–8 (2011)
17. Wei, L.-X., Wang, H.-R., Li, Y.: A new solution for inverse kinematics of manipulators based on neural network. In: IEEE International Conference on Machine Learning and Cybernetics, vol. 2, pp. 1201–1203 (2003)
18. Xue, Y., Yang, L.: Development of a new recurrent neural network toolbox (RNTool). A Course report on training recurrent multilayer perceptron and echo statenetwork (2006)

Advanced Sampling Scheme Based on Environmental Stiffness for a Smart Manipulator

Taku Shimizu¹ and Takashi Kubota²

¹ Dept. of Electrical Engineering and Information Systems, The University of Tokyo

taku@ac.jaxa.jp

² ISAS/JAXA

Abstract. Extraction of rock samples using robotic arms is an essential technique for planetary exploration. By sampling and analyzing the rocks, we can gain knowledge, not only about the planetary body itself but also about other bodies and the space environment as a whole. In conventional missions, images of the surface are captured and sent to Earth so that the human operator can decide a sampling strategy. However, in such missions, communication delays with Earth are inevitable, and a large number of scientists and engineers are involved in the decisions, which makes the procedure time-consuming, expensive and limited in efficiency. For these reasons, automated extraction processes are required to increase the scientific return. In this study, a novel intelligent manipulator system which samples the rocks semi-automatically by measuring environmental stiffness is proposed. To make such a system autonomous in an unknown environment, vision-based approaches are usually preferred. However, information obtained from cameras is difficult to process. In this paper, another technique based on measuring applied forces is presented, and we demonstrate its effectiveness for the detection of buried rocks.

1 Introduction

In planetary exploration, robotic systems need to be robust with regard to their environment because they can acquire only limited information in advance. To increase the robustness, methods based on visual information have been proposed until now[1][2][3]. However, visual information contains only indirect information about the environment and images require a significant amount of processing. Thus, estimating the state of the surroundings with visual information only is difficult. On the other hand, environmental stiffness provides direct information.

In this study, the effectiveness of a method based on measurement of applied force in an unknown environment is demonstrated using a novel intelligent manipulator system. First, the system detects the rocks to be sampled using a stereo camera, and assesses the possibility of extraction using the information of environmental stiffness. Then it extracts the desired rock with a 4-DOF manipulator.

2 Manipulation System

The developed rover is shown in Fig. 1. And the manipulator system is settled in front of the rover.

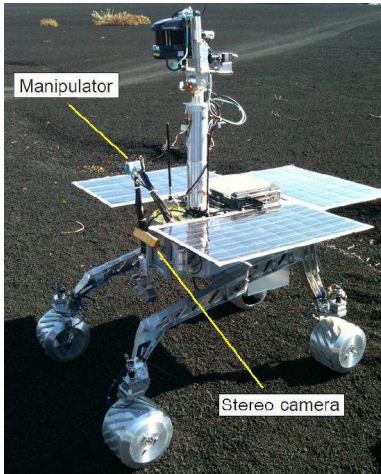


Fig. 1. Overview of the Micro6

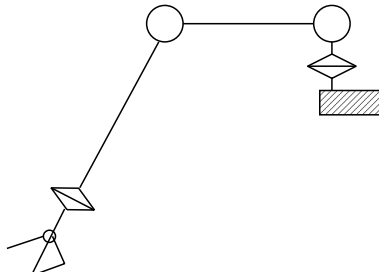


Fig. 2. Structure of the manipulator

2.1 External Sensor

Before beginning the operations, information on the surroundings must be obtained. For this purpose, we added a stereo camera at the base of the manipulator. A 3D model of the objects is obtained by processing image pairs captured from these cameras. Stereo cameras are suitable external sensors for space applications because they are lighter than other 3D sensors such as LRFs(Laser Range Finders).

2.2 Robotic Arm

The schematic diagram of the 4-DOF robotic arm designed for the system is shown in Fig. 2. Each joint of the manipulator is driven by the Ultra Sonic Motor (Fig. 3). The USM's rotation is created by the friction between the rotor and a piezoelectric element vibrating at ultrasonic frequencies. Because of this unique technology, USM has the following features which make it a suitable motor for robotic arm on space systems[4][5].

- Maintain position with no current
- Achieve high torques and slow rotation speeds
- Small and light

However, shortcomings are:

- Bad motor efficiency
- Difficult motion modeling

Despite the bad motor efficiency, the total power consumption will be reduced since sampling tasks require the arm to be kept most of the time in a stationary position, which can be maintained by the USM without current.



Fig. 3. Appearance of the ultrasonic motor

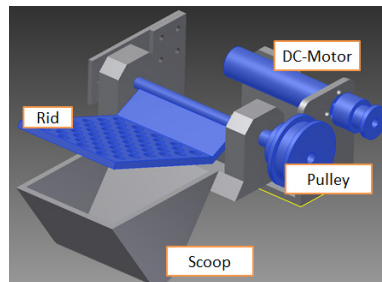


Fig. 4. Schematic diagram of the end effector

The USM is also interesting for its reduced weight. A significant gain can be achieved on the total weight of the joint, not only from the motor itself but also from the reduced weight of the reduction gear.

2.3 End Effector

As described in Fig. 4, the end effector has a fixed bucket and a movable mesh lid. By using this effector, rocks can be sampled in two ways: "Scooping (Fig. 5)" and "Picking up(Fig. 6)".

Scooping is desirable from the point of view of the scientist because the influence of the external force applied on the rock can be minimized. However, scooping cannot be performed when the soil in the periphery of the rock is solid. On the other hand, picking up can be performed regardless of the surroundings of the rock, by applying an external force. In other words, scooping is agreeable for the sampling but can not be applied when the environmental stiffness is high. In that case, we should approach with picking up.



Fig. 5. Sampling of scooping mode



Fig. 6. Sampling of picking up mode

As for the actuator, we chose a DC motor for the end effector. As stated above, while the USM has desirable characteristics for a robotic arm, it is difficult to control. DC motors are easy to model and to control, so that we can easily estimate the reaction force applied on the lid. Simultaneously, there is no need to perform consistent torque for the end effector, power consumption will not increase.

3 Environmental Stiffness Estimation

Common techniques to measure applied forces include using force sensors or strain gauges. However, in the system being discussed, no additional sensors are used for measuring the force. In this section, the principle of sensor-less force estimation is explained and the parameters needed for estimating the torque are identified.

3.1 Principle

The control circuit for the DC motor used on the end effector is shown in Fig. 7. As shown in Fig. 4, the motor torque is transmitted via a built-in gear head and a timing belt. The motor is connected to the driver IC and V_m [V] is applied in proportion to the voltage generated from the micro controller V_m^* [V]. The motor current I_m [A] and the angle of the motor θ_m [deg] then be measured simultaneously.

The torque generated by the motor is written as

$$T_m = K_t \cdot I_m. \quad (1)$$

Where K_t [Nm/A] means motor's torque constant.

Then, if we define the reduction ratio of the gear head and timing belt as R , transmission efficiency as η [%], Coulomb frictional force as F_c [Nm], inertia of the motor and end effector as J_m , J_e [Nms²], the torque of the end effector T_e [Nm] can be written as follows:

$$T_e = (T_m - J_m \ddot{\theta}_m)R\eta - F_c - J_e \ddot{\theta}_e \quad (2)$$

Then, with the assumption that rotational speed of the motor is constant, T_e can be written as

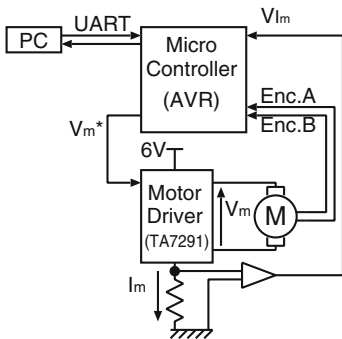
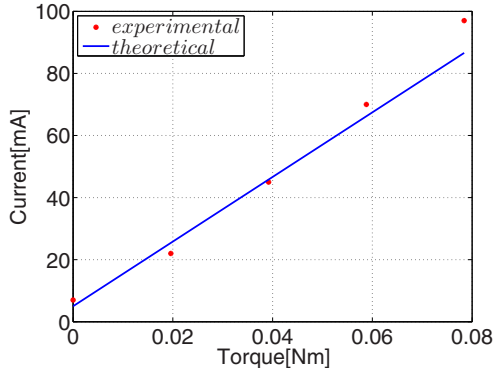
$$T_e = T_m R\eta - F_c. \quad (3)$$

Therefore, T_e can be estimated and controlled by I_m with the knowledge of F_c and η only.

3.2 Parameter Identification

Transmission Efficiency. Using Eq. (1) to (3), variation of the motor current when the load increases ΔT_e is expressed as follows:

$$\Delta I_m = \frac{1}{K_t R \eta} \Delta T_e \quad (4)$$

**Fig. 7.** DC motor control circuit**Fig. 8.** Current versus applied torque when velocity control is implemented

Thus, by applying a known load torque under velocity control and by measuring the motor current, we can identify $\frac{1}{K_t R \eta}$.

Fig. 8 shows the experimental result when the applied torque varies under velocity control with $\dot{\theta}_e^* = 90$. The points represent the measured motor current and the straight line is the fitted line. η is identified as 0.38. This value includes the default efficiency of the gear head module: 60%.

Coulomb Frictional Force. By transforming Eq. (1) and Eq. (3), Coulomb frictional force F_c is expressed as

$$F_c = K_t R \eta I_m - T_e. \quad (5)$$

Therefore, by measuring the current when moving at constant velocity with no load, F_c can be estimated. And as a result, F_c was identified as $6.7 \times 10^{-3} [Nm]$. This value can be ignored compared to the value expected for sampling rocks and estimating environmental stiffness.

3.3 Detecting Buried Rock

Detecting buried rock is done by detecting the displacement of the rock when horizontal force is applied with end effector.

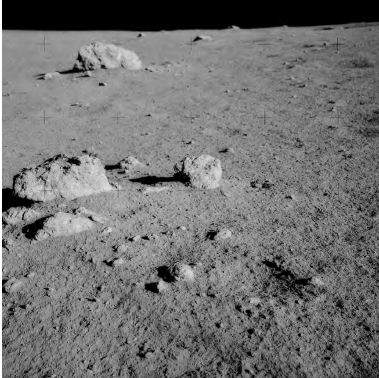
First, the weight of the rock $W[g]$ is estimated with the volume of the rock $V_r[\text{mm}^3]$ with the assumption that the rock's density is $\sigma[g/\text{mm}^3]$.

$$W = V_r \cdot \sigma \quad (6)$$

Then, apply the force $F_e[N]$ in proportion to W . In this case, the force is determined as the required force to roll the cubic rock with the weight of W .

$$F_e = \frac{T_e}{l_e} \quad (7)$$

$$= Wg \times 10^{-3} [N] \quad (8)$$

**Fig. 9.** Moon surface[9]**Fig. 10.** Mars surface[10]

Where, l_e [m] is the radius of the end effector, g [m/s²] is gravitational acceleration of the planet.

When applying the force F_e , if the displacement of the rid angle exceeds the threshold calculated with the stiffness of the robotic arm itself, the rock is estimated as "not buried". To the contrary, if the displacement is lower than the threshold, the rock is regarded as "buried".

4 Rock Detection

Several methods have been proposed for rock identification using visual information. The approach proposed by Leena *et al.*[6] classify the rocks in pre-defined classes using features identified from the spectrum and the texture. Robert *et al.*[7] identifies the rocks by prior estimation of their size, shape and color. However, these methods need prior information about the rocks, so the alternative approach developed by Takanashi *et al.*[8] was preferred, although it was initially proposed for obstacle avoidance.

Fig. 9 and Fig. 10 show the surface of the Moon and Mars. As it can be observed from these pictures, there is only little diffusion of light because of the reduced atmospheres. Therefore, rocks can be easily identified from the shade (for the surfaces) and the variance (for the contours). Finally, by combining these information, we can distinguish the regions where the surfaces and contours coincide with the rock.

4.1 Surface Detection

The surface of the rock is in contrast with the surroundings: brighter where sunlight is cast and darker in its shadow. The brightness of the point (p, q) in the image is defined as

$$A(p, q) = \frac{1}{w_a^2} \sum_{i=p-\frac{w_a-1}{2}}^{p+\frac{w_a-1}{2}} \sum_{j=q-\frac{w_a-1}{2}}^{q+\frac{w_a-1}{2}} x(i, j). \quad (9)$$

Where w_a is the size of the window used for noise reduction, $x(i, j)$ is the brightness of the point (i, j) in the raw image. After $A(p, q)$ has been calculated, the threshold is determined as follows:

$$Th_{aw} = \overline{A(p, q)} + t_{aw} \cdot \sigma_a \quad (10)$$

$$Th_{ab} = \overline{A(p, q)} - t_{ab} \cdot \sigma_a \quad (11)$$

Where $\overline{A(p, q)}$ is the average of $A(p, q)$ and σ_a is the standard deviation of $A(p, q)$. t_{aw} and t_{ab} are the design parameters that define the percentage of the detected area.

By using this threshold, the area where $A(p, q) > Th_{ab}$ or $A(p, q) < Th_{aw}$ are defined as the faces of the rocks.

4.2 Contour Detection

The variance of the image is used for contour detection. First, the value of the variance $V(p, q)$ at point (p, q) is calculated from the following equation.

$$V(p, q) = \frac{1}{w_v^2} \sum_{i=p-\frac{w_v-1}{2}}^{p+\frac{w_v-1}{2}} \sum_{j=q-\frac{w_v-1}{2}}^{q+\frac{w_v-1}{2}} (A(p, q) - x(i, j))^2 \quad (12)$$

Where w_v is the size of the window used for noise reduction. Then, a threshold Th_v is defined as follows:

$$Th_v = \overline{V(p, q)} + t_v \cdot \sigma_v^2 \quad (13)$$

Here, $\overline{V(p, q)}$ is an average value of $V(p, q)$, σ_v is the standard deviation of $V(p, q)$. t_v is a design parameter.

By using this threshold, the areas where $V(p, q) > Th_v$ are identified as the contours of the rocks.

4.3 Volume Estimation

After the rock is distinguished by proposed scheme, three demensional position of five representative points, A,B,C,D and its center p_0 is extracted as shown in Fig. 11. First, p_0 is extracted as a highest point of the rock. And then, A,B,C,D is extaracted to maximize the difference of the distance between AC and BD.

Using the information about the representative point, the volume of the rock V_r is approximately calculated as the twice of the volume of the quadratic prism consisted by these five representative points.

As described in Fig. 12, there is a possibility of estimating the volume smaller than true value in this estimation method. However, smaller volume estimation connects to the interpretation that the rock is "buried" in proposed scheme. So the problem does not have bad influence on the interpretation.

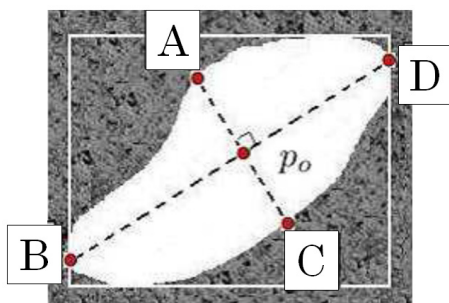


Fig. 11. Detection of the representative points

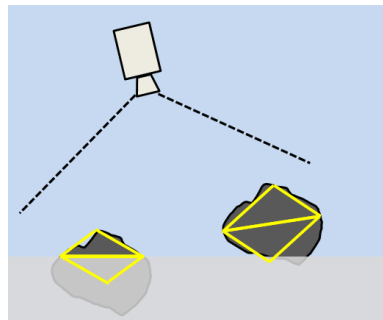


Fig. 12. Miscalculation of the volume with buried rock

5 Experiment

5.1 Procedure

The procedure of the sampling is as follows:

1. Image capture
The image of the surface of the planet is taken using the stereo camera.
2. Image processing
The rocks are detected in the image and their positions and shapes are calculated.
3. Environmental stiffness estimation
After the rock to be sampled has been identified by the operator, the system estimates the environmental stiffness automatically and decides a sampling strategy.
4. Rock Sampling
The rock of interest is sampled using the chosen strategy.

In this section, this procedure is applied for buried rocks and unburied rocks. Finally, the efficiency of the system is validated. In this research, rocks are scattered at random and buried rocks are intentionally made by pushing it towards ground.

5.2 Result

Fig. 13 shows the image taken from the cameras, Fig. 14 shows the result of rock detection and Table. 1 shows the properties of the rocks detected in the image.

In this case, the rock No.5 is chosen to be extracted by the operator. Then, the robotic arm approaches the rock and applies the force on the sides of the rock. Although judging the state of the rocks using only visual information seems difficult, the system correctly estimated the burying of the rock from the displacement and the gscoping method was successfully applied.

To further validate this performance, the same experiment is performed for a buried rock. Fig. 15 shows the image taken from the cameras, Fig. 16 shows the result of rock detection and Table. 2 shows the properties of the rocks.



Fig. 13. Raw image of the terrain when the rock is not buried

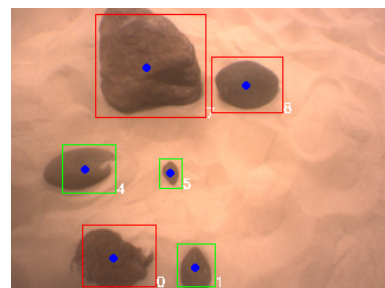


Fig. 14. Processed image of the terrain when the rock is not buried

Table. 1. Output of processed image of the terrain when the rock is not buried

No.	Distance [mm]	length [mm]	width [mm]	weight [g]
0	601	111	90	2204
1	651	87	44	834
4	687	75	73	1010
5	747	41	31	170
7	790	179	140	12979
8	876	108	85	2797



Fig. 15. Raw image of the terrain when the rock is buried

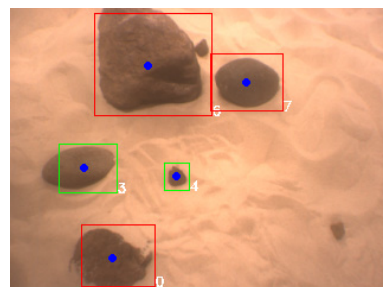


Fig. 16. Processed image of the terrain when the rock is buried

In this case, No.4 was the rock of interest and the system correctly assessed the state of the rock as buried. Thus, the rock was extracted in "Picking up" successfully.

In these examples, the proposed system worked very well. However, some problems became distinct in some trial. For example, when the rock is completely buried and when just tip of the rock was visible, the rid of the end effector could not apply the force to the rock. So the proposed method could not be applied. More over, in other trial, the rock was moved by the pushed sands while the end effector is approaching with scooping way and the capture ended up in failure.

Table. 2. Output of processed image of the terrain when the rock is buried

No.	Distance [mm]	<i>length</i> [mm]	<i>width</i> [mm]	<i>weight</i> [g]
0	597	110	88	2277
3	681	81	71	1183
4	733	39	34	229
6	784	191	140	13304
7	874	141	128	5716

6 Conclusion

A novel intelligent manipulator system is proposed which samples the rocks semi-automatically using a method based on the estimation of ground stiffness. The accuracy of the rock identification algorithm and the efficiency of the ground stiffness approach are demonstrated through experiments. Simultaneously, some problems of this system became distinct by experiments.

In this paper, the environmental stiffness itself is not measured appropriately. However, we can measure environmental stiffness by applying this system without no additional sensor. With the acquired prospect about the efficiency of measuring force on manipulator system, we will continue developing more efficient manipulator system.

Reference

1. Theobald, D.A., Jesse Hong, W., Madhani, A., Hoffman, B., Niemeyer, G.: Autonomous Rock Acquisition. In: AIAA Forum on Advanced Developments in Space Robotics (1996)
2. Huntsberger, T., Cheng, Y., Stroupe, A., Aghazarian, H.: Closed Loop Control for Autonomous Approach and Placement of Science Instruments by Planetary Rovers. In: IEEE/RSJ IROS 2005, August 2-6 (2005)
3. Barnes, D., Shaw, A., Pugh, S.: Autonomous Sample Acquisition for the ExoMars Rover. In: ESA Workshop on Advanced Space Technologies for Robotics and Automation (2006)
4. Kunii, Y., Oda, H., Otsuka, M., et al.: Micro Manipulator with Ultra Sonic Motor for Planetary Exploration. In: ROBOMECH 2000 (2000)
5. Das, H., Bao, X., Bar-Cohen, Y., Bonitz, R., et al.: Robot manipulator technologies for planetary exploration. In: SPIE Smart Structures and Materials (March 1999)
6. Lepisto, L., Kunttu, I., Autio, J., Visa, A.: Rock Image Classification Using Non-Homogenous Textures and Spectral Imaging. In: WSCG 2003, February 3-7 (2003)
7. Crida, R.C., de Jager, G.: Rock Recognition using feature classification. In: COMSIG 1994 (1994)
8. Takanashi, S., Kubota, T.: Study on Autonomous Traverse of Exploration Rover using Monocular Camera. In: Annual Conference of the Robotics Society of Japan, vol. 28 (2010)
9. <http://www.hq.nasa.gov/alsj/>
10. <http://www.jpl.nasa.gov/missions/mer/>

Walking Pattern Generation on Inclined and Uneven Terrains for Humanoid Robots

Young-Dae Hong and Jong-Hwan Kim

Department of Electrical Engineering, KAIST
291 Daehak-ro, Yuseong-gu, Daejeon 305-701, Republic of Korea
{ydhong,johkim}@rit.kaist.ac.kr

Abstract. This paper introduces a walking pattern generation method on an inclined terrain in both pitch and roll directions, and uneven terrain. The walking pattern generation method is based on a modifiable walking pattern generator (MWPG) which allows a zero moment point (ZMP) variation in real-time. As a navigational command set, a 3-D command state (CS) is defined, which consists of single and double support times, sagittal and lateral step lengths, and foot height of the swing leg. In the single support phase, the primary dynamics of the humanoid robot on the inclined terrain is modeled as a 3-D linear inverted pendulum model (LIPM) with constant center of mass (CoM) height, and the dynamic equation of the 3-D LIPM is derived to obtain the sagittal and lateral CoM motions. Using the sagittal and lateral CoM motions, the sagittal and lateral CoM trajectories are generated to satisfy the sagittal and lateral step lengths of the swing leg. The foot trajectories of the swing leg are generated according to the commanded sagittal and lateral step lengths, and foot height. In the double support phase, the vertical CoM trajectory is generated to satisfy the foot height of the swing leg from the single support phase. The walking pattern generation method is implemented on a simulation model of the small-sized humanoid robot, HanSaRam-IX (HSR-IX) and the effectiveness is demonstrated through computer simulations.

Keywords: Humanoid robot, 3-D command state (CS), modifiable walking pattern generator (MWPG), locomotion on inclined and uneven terrains, 3-D linear inverted pendulum model (LIPM).

1 Introduction

In the robotics society, a humanoid robot is a representative research topic. A lot of humanoid robots have been developed [1]–[3] and many walking pattern generation methods for stable walking have been studied [4]–[7]. In most of walking pattern generation methods, it is assumed that the terrain is flat. However, there exist not only flat but also inclined or uneven terrains in real environment. Therefore, recently, various walking pattern generation methods were developed for walking on the inclined terrain [8]–[11] and uneven terrain [12]–[16].

This paper presents a novel walking pattern generation method on various environments for humanoid robots. Particularly, the walking pattern generation method on an inclined terrain in both pitch and roll directions, and uneven terrain is introduced. In the previous researches on walking pattern generation on the inclined terrain and uneven terrain, the humanoid robot was unable to modify independently elements of a walking pattern, i.e. single and double support times, sagittal and lateral step lengths, and foot height of the swing leg without any additional footstep for adjusting the center of mass (CoM) motion. Thus, in this paper, the walking pattern generation method is developed to solve this problem. The walking pattern generation method is based on the conventional modifiable walking pattern generator (MWPG) which allows the zero moment point (ZMP) variation in real-time by closed form functions [5], [6]. The conventional MWPG can be applied only on the flat terrain.

The walking pattern generation method in this paper extended the MWPG to independently modify the elements of the walking pattern on the inclined terrain and uneven terrain. As a navigational command set, a 3-D command state (CS) is defined, which consists of the single and double support times, sagittal and lateral step lengths, and foot height of the swing leg. The CoM trajectories in the single and double support phases are generated to satisfy the 3-D CS. In the single support phase, the primary dynamics of the humanoid robot on the inclined terrain is modeled as a 3-D linear inverted pendulum model (LIPM) with constant CoM height, and the dynamic equation of the 3-D LIPM is derived to obtain the sagittal and lateral CoM motions. Using the sagittal and lateral CoM motions, the sagittal and lateral CoM trajectories are generated to satisfy the sagittal and lateral step lengths of the swing leg. The foot trajectories of the swing leg are generated according to the commanded sagittal and lateral step lengths, and foot height. In the double support phase, the vertical CoM trajectory is generated to satisfy the foot height of the swing leg from the single support phase. The walking pattern generation method is implemented on a simulation model of the small-sized humanoid robot, HanSaRam-IX (HSR-IX), developed at the Robot Intelligence Technology laboratory, KAIST and the effectiveness is demonstrated through computer simulations.

This paper is organized as follows. Section 2 presents the walking pattern generation method. The 3-D CS is presented, the CoM trajectory generations in the single and double support phases are described, and the foot trajectory generation of the swing leg is also explained. In Section 3, the simulation results are presented and finally conclusions follow in Section 4.

2 Walking Pattern Generation

The walking of the humanoid robot consists of single and double support phases, and in the single support phase, the primary dynamics of the humanoid robot on the flat terrain is modeled as a 3-D LIPM [4]. In the 3-D LIPM, it is assumed that the support leg is a weightless telescopic limb and the mass is concentrated as a single point without vertical motion. Consequently, it is possible to decouple the sagittal and lateral CoM motion equations.

In the conventional 3-D LIPM, it is assumed that the ZMP is fixed at the contact point. Consequently, in the single support phase, the CoM motion of the 3-D LIPM is unmodifiable, which means that the humanoid robot is unable to modify independently the elements of the walking pattern, i.e. the single and double support times, the sagittal and lateral step lengths, and the foot direction of the swing leg. However, in the MWPG, by allowing the ZMP variation, the CoM position and velocity can be changed independently at any time during the single support phase [5]–[7]. Thus, the MWPG enables the humanoid robot to modify the elements of the walking pattern independently by the ZMP functions without any extra footstep for adjusting the CoM motion. In this paper, for modifiable walking on the inclined terrain and uneven terrain as well as flat terrain, the conventional MWPG is extended.

2.1 3-D CS

As a navigational command set, the conventional CS is insufficient to walk on various environments [5]–[7]. Thus, the foot height of the swing leg should be considered in the CS. In this paper, the 3-D CS is defined as a novel navigational command set as follows:

Definition 1. *3-D CS is defined as*

$$\text{3-D CS} \equiv [T_{l/r}^{ss} \ T_{l/r}^{ds} \ S_{l/r} \ L_{l/r} \ H_{l/r}]$$

where

$T_{l/r}^{ss}$: single support time;

$T_{l/r}^{ds}$: double support time;

$S_{l/r}$: sagittal step length of left/right leg;

$L_{l/r}$: lateral step length of left/right leg;

$H_{l/r}$: foot height of left/right leg.

2.2 CoM Trajectory Generation in Single Support Phase

Fig. 1 shows the 3-D LIPM on the inclined terrain in both pitch and roll directions. The following equations present the sagittal and lateral CoM motions of the 3-D LIPM on the inclined terrain.

Sagittal CoM motion:

$$\begin{bmatrix} x_f \\ v_f T_c \end{bmatrix} = \begin{bmatrix} \cosh(\frac{T}{T_c}) \sinh(\frac{T}{T_c}) \\ \sinh(\frac{T}{T_c}) \cosh(\frac{T}{T_c}) \end{bmatrix} \begin{bmatrix} x_i \\ v_i T_c \end{bmatrix} - \frac{1}{T_c} \begin{bmatrix} \int_0^T \sinh(\frac{T}{T_c}) \bar{p}(t) dt \\ \int_0^T \cosh(\frac{T}{T_c}) \bar{p}(t) dt \end{bmatrix} + \begin{bmatrix} -gT_c^2 \sin \theta_v (-1 + \cosh(\frac{T}{T_c})) \\ -gT_c^2 \sin \theta_v \sinh(\frac{T}{T_c}) \end{bmatrix} \quad (1)$$

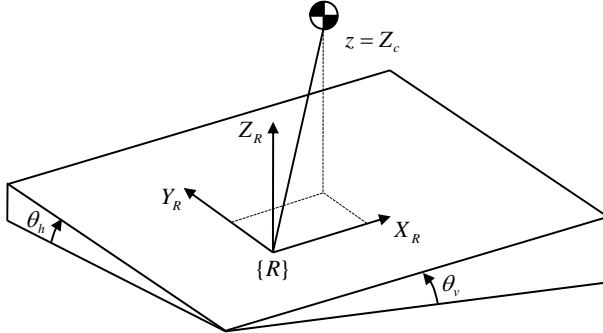


Fig. 1. 3-D LIPM on inclined terrain

Lateral CoM motion:

$$\begin{bmatrix} y_f \\ w_f T_c \end{bmatrix} = \begin{bmatrix} \cosh\left(\frac{T}{T_c}\right) \sinh\left(\frac{T}{T_c}\right) \\ \sinh\left(\frac{T}{T_c}\right) \cosh\left(\frac{T}{T_c}\right) \end{bmatrix} \begin{bmatrix} y_i \\ w_i T_c \end{bmatrix} - \frac{1}{T_c} \begin{bmatrix} \int_0^T \sinh\left(\frac{T}{T_c}\right) \bar{q}(t) dt \\ \int_0^T \cosh\left(\frac{T}{T_c}\right) \bar{q}(t) dt \end{bmatrix} + \begin{bmatrix} -g T_c^2 \sin \theta_h (-1 + \cosh(\frac{T}{T_c})) \\ -g T_c^2 \sin \theta_h \sinh(\frac{T}{T_c}) \end{bmatrix} \quad (2)$$

with

$$T_c = \sqrt{\frac{Z_c}{g \cos \theta_v \cos \theta_h}}$$

where $(x_i, v_i)/(x_f, v_f)$ and $(y_i, w_i)/(y_f, w_f)$ represent the initial/final position and velocity of the CoM in sagittal and lateral planes, respectively. T is the remaining single support time. $p(t)$ and $q(t)$ are the ZMP functions for sagittal and lateral CoM motions, respectively. $\bar{p}(t) = p(T-t)$ and $\bar{q}(t) = q(T-t)$.

Using the above sagittal and lateral CoM motions (1) and (2), the sagittal and lateral CoM trajectories in the single support phase are generated to satisfy the sagittal and lateral step lengths. The CoM position and velocity in the sagittal and lateral planes are defined as a walking state (WS) of the 3-D LIPM and the WS is derived for the commanded CS [5]–[7]. Then, the sagittal and lateral CoM trajectories satisfying the WS are generated by (1) and (2).

2.3 CoM Trajectory Generation in Double Support Phase

In this paper, the vertical CoM trajectory in the double support phase is generated to satisfy the foot height of the swing leg from the single support phase, $H_{l/r}$ instead of using the constant CoM height. As shown in Fig. 2, the CoM height maintains the constant Z_c during the single support phase, and then it moves to $Z_c + H_{l/r}$ during the double support phase by the cubic spline interpolation with Z_c at $t = 0$ and $Z_c + H_{l/r}$ at $t = T_{l/r}^{ds}$ as follows:

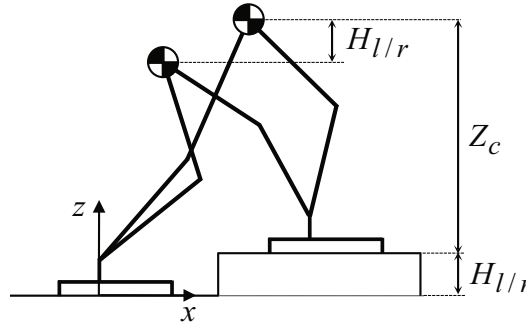


Fig. 2. Vertical CoM motion in double support phase

$$z(t) = -2 \frac{H_{l/r}}{T_{l/r}^{ds}} t^3 + 3 \frac{H_{l/r}}{T_{l/r}^{ds}} t^2 + Z_c. \quad (3)$$

Note that the vertical CoM trajectory is defined with respect to the local coordinate frame attached on the support leg. In the double support phase, the sagittal and lateral CoM motions travel with constant velocity.

2.4 Foot Trajectory Generation

The sagittal and lateral foot trajectories of the swing leg, (x_{foot}, y_{foot}) are generated by the cubic spline interpolation with the sagittal and lateral step lengths at the previous footstep, $(-S_{r/l}^{pre}, -L_{r/l}^{pre})$ at $t = 0$ and $(S_{l/r}, L_{l/r})$ at $t = T_{l/r}^{ss}$ as follows:

$$x_{foot}(t) = -2 \frac{S_{l/r} + S_{r/l}^{pre}}{T_{l/r}^{ss}} t^3 + 3 \frac{S_{l/r} + S_{r/l}^{pre}}{T_{l/r}^{ss}} t^2 - S_{r/l}^{pre} \quad (4)$$

$$y_{foot}(t) = -2 \frac{L_{l/r} + L_{r/l}^{pre}}{T_{l/r}^{ss}} t^3 + 3 \frac{L_{l/r} + L_{r/l}^{pre}}{T_{l/r}^{ss}} t^2 - L_{r/l}^{pre}. \quad (5)$$

The vertical foot trajectory of the swing leg, z_{foot} is generated by a cycloid function. To satisfy the foot height $H_{l/r}$, the trajectory Δz_{foot} is added, which is generated by the cubic spline interpolation with the foot height of the swing leg at the previous footstep, $-H_{r/l}^{pre}$ at $t = 0$ and $H_{l/r}$ at $t = T_{l/r}^{ss}$ as follows:

$$z_{foot}(t) = r \left(1 - \cos \left(\frac{2\pi t}{T_{l/r}^{ss}} \right) \right) + \Delta z_{foot}(t) \quad (6)$$

with

$$\Delta z_{foot}(t) = -2 \frac{H_{l/r} + H_{r/l}^{pre}}{T_{l/r}^{ss}} t^3 + 3 \frac{H_{l/r} + H_{r/l}^{pre}}{T_{l/r}^{ss}} t^2 - H_{r/l}^{pre}$$

where r denotes the radius of the cycloid circle.

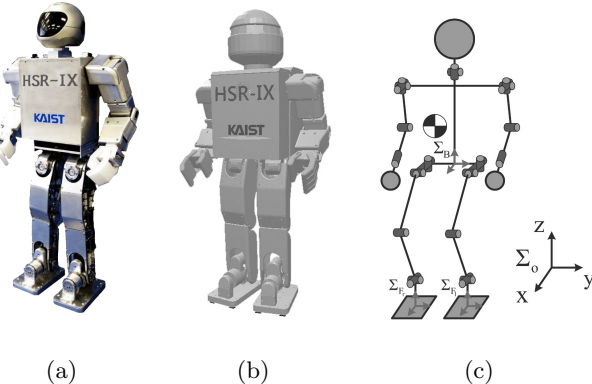


Fig. 3. (a) HSR-IX. (b) Simulation model. (c) Configuration.

3 Simulation Results

3.1 HanSaRam-IX

The proposed algorithm was implemented on the simulation model of the small-sized humanoid robot, HSR-IX in Fig. 3. The simulation model of HSR-IX was modeled by Webots which is the 3-D robotics simulation software and enables users to conduct the physical and dynamical simulation [17]. HSR has been in continual development and research by the Robot Intelligence Technology laboratory, KAIST [6]. Its height and weight are 52.8 cm and 5.5 kg, respectively. It has 26 DOFs which consist of 12 DC motors with harmonic drives in the lower body and 16 RC servo motors in the upper body (two servo motors in each hand control). The on-board Pentium-III compatible PC, running RT-Linux, calculates the proposed algorithm every 5 msec in real-time. To measure ground reaction forces on the feet and the real ZMP trajectories while walking, four force sensing resistors are equipped on each foot.

3.2 Modifiable Walking on Inclined Terrain

To verify the modifiable walking on the inclined terrain in pitch and roll directions, the 3-D CS list in Table 1 was used for the simulation, in which sagittal and lateral step lengths were independently changed while maintaining the same walking period at each footstep. The 3-D CS can be predefined or provided by the footstep planning algorithm [18], [19]. Fig. 4 shows the snapshot of the walking simulation on the inclined terrain in pitch and roll directions. HSR-IX walked stably on the inclined terrain in pitch and roll directions by modifying the sagittal and lateral step lengths of the swing leg according to the commanded 3-D CS list at every footstep. Fig. 5 shows the generated walking pattern, CoM, and ZMP trajectories when the terrain was inclined upward and leftside simultaneously ($\theta_v = 15^\circ$ and $\theta_h = 5^\circ$). As the figure shows, the CoM trajectory which

Table 1. Commanded 3-D CS list for walking simulation on inclined terrain in pitch and roll directions (time and length units were given in seconds and centimeters, respectively.)

Steps	$T_{l/r}^{ss}$	$T_{l/r}^{ds}$	$S_{l/r}$	$L_{l/r}$	$H_{l/r}$
1 st (right foot)	0.8	0.4	4.0	-6.0	0.0
2 nd (left foot)	0.8	0.4	4.0	6.0	0.0
3 rd (right foot)	0.8	0.4	1.0	-10.0	0.0
4 th (left foot)	0.8	0.4	4.0	6.0	0.0
5 th (right foot)	0.8	0.4	4.0	-6.0	0.0
6 th (left foot)	0.8	0.4	2.0	9.0	0.0
7 th (right foot)	0.8	0.4	4.0	-6.0	0.0
8 th (left foot)	0.8	0.4	4.0	6.0	0.0
9 th (right foot)	0.8	0.4	4.0	-6.0	0.0
10 th (left foot)	0.8	0.4	2.0	9.0	0.0
11 th (left foot)	0.8	0.4	4.0	-6.0	0.0
12 th (right foot)	0.8	0.4	4.0	6.0	0.0
13 th (left foot)	0.8	0.4	0.0	-6.0	0.0

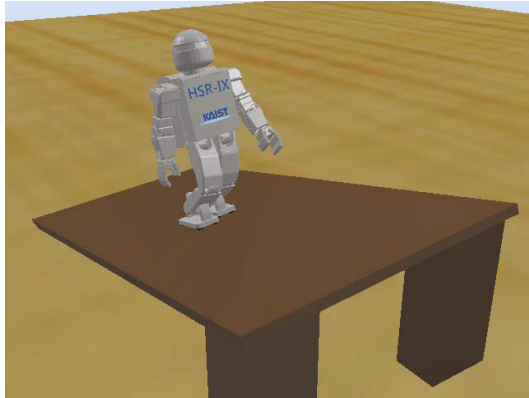


Fig. 4. Snapshot of the walking simulation on inclined terrain in pitch and roll directions

was shifted forward and left simultaneously was generated for stable walking. It can be shown that the ZMP trajectories in x -axis and y -axis follow the foot trajectories with a small variation. The small variation was mainly caused by the dynamic difference between the robot and the 3-D LIPM. However, the ZMP trajectories were within the upper and lower boundaries of foot trajectories. Accordingly, the robot was able to walk stably on the inclined terrain in both pitch and roll directions.

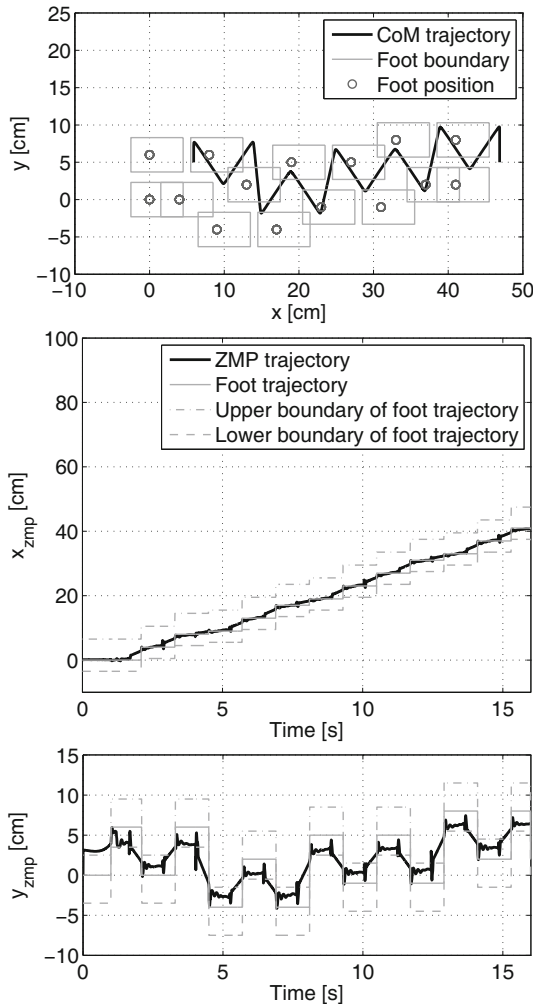


Fig. 5. Generated walking pattern, CoM, and ZMP trajectories when the terrain was inclined upward and leftside simultaneously in the simulation ($\theta_v = 15^\circ$ and $\theta_h = 5^\circ$).

3.3 Modifiable Walking on Uneven Terrain

In the simulation environment, there were five boards with different heights (0.5, 1.0, and 1.5 cm) and sizes, and the 3-D CS list for the simulation was determined according to the information about the terrain. Table 2 shows the commanded 3-D CS list, in which sagittal and lateral step lengths, and foot height of the swing leg were independently changed while maintaining the same walking period at

Table 2. Commanded 3-D CS list for walking simulation on uneven terrain (time and length units were given in seconds and centimeters, respectively.)

Steps	$T_{l/r}^{ss}$	$T_{l/r}^{ds}$	$S_{l/r}$	$L_{l/r}$	$H_{l/r}$
1 st (right foot)	0.8	0.4	7.0	-6.0	0.0
2 nd (left foot)	0.8	0.4	7.0	6.0	1.0
3 rd (right foot)	0.8	0.4	7.0	-6.0	-1.0
4 th (left foot)	0.8	0.4	7.0	6.0	1.0
5 th (right foot)	0.8	0.4	5.0	-11.0	-1.0
6 th (left foot)	0.8	0.4	7.0	6.0	1.0
7 th (right foot)	0.8	0.4	7.0	-6.0	0.5
8 th (left foot)	0.8	0.4	8.0	9.0	-1.0
9 th (right foot)	0.8	0.4	6.0	-9.0	0.5
10 th (left foot)	0.8	0.4	7.0	6.0	-1.0
11 th (right foot)	0.8	0.4	8.0	-6.0	0.0
12 th (left foot)	0.8	0.4	7.0	6.0	0.0
13 th (right foot)	0.8	0.4	0.0	-6.0	0.0

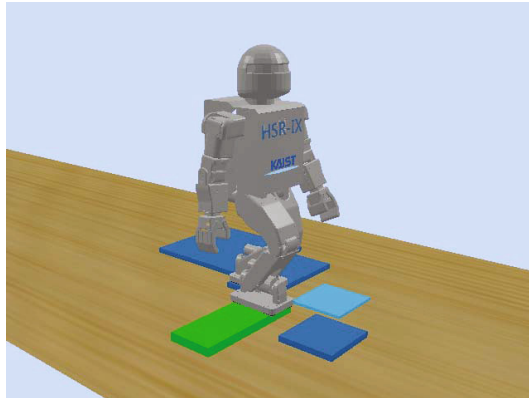


Fig. 6. Snapshot of the walking simulation on uneven terrain

each footstep for walking on the uneven terrain. Fig. 6 shows the snapshot of the walking simulation on the uneven terrain. HSR-IX walked stably on the uneven terrain by modifying the sagittal and lateral step lengths, and foot height of the swing leg according to the commanded 3-D CS list at every footstep. Fig. 7 shows the generated CoM trajectories with respect to the global coordinate frame attached on the terrain. As shown in the figure, in the single support phases, the sagittal and lateral CoM trajectories were generated to satisfy the

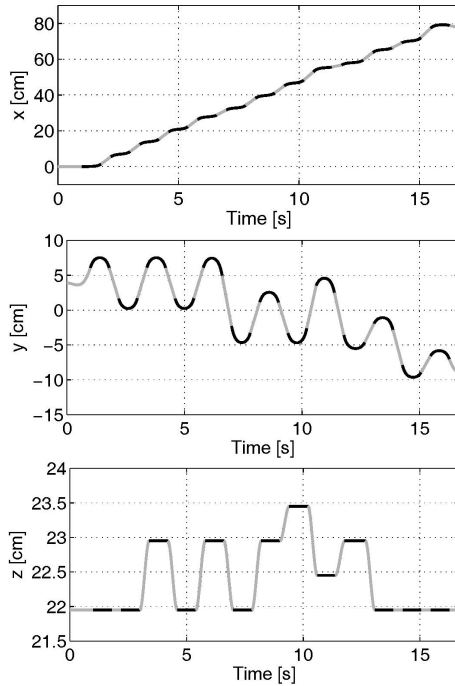


Fig. 7. Generated sagittal, lateral and vertical CoM trajectories with respect to the global coordinate frame attached on the terrain. The thick and thin lines represent the CoM trajectories in the single and double support phases, respectively.

sagittal and lateral step lengths in the 3-D CS list by (1) and (2), and the vertical CoM trajectory maintained the constant value. In the double support phases, the vertical CoM trajectory was generated to satisfy the foot heights of the swing leg from the single support phases by (3). In addition, the foot trajectories of the swing leg were generated by (4), (5), and (6). Fig. 8 shows the measured ZMP trajectories in the walking simulation. It can be seen that the ZMP trajectories in the x -axis and y -axis followed the foot trajectories with a small variation. The small variation of the ZMP trajectories was mainly due to the dynamic difference between HSR-IX and the 3-D LIPM. However, the ZMP trajectories were within the upper and lower boundaries of foot trajectories, which means that HSR-IX could walk on the uneven terrain while maintaining stability.

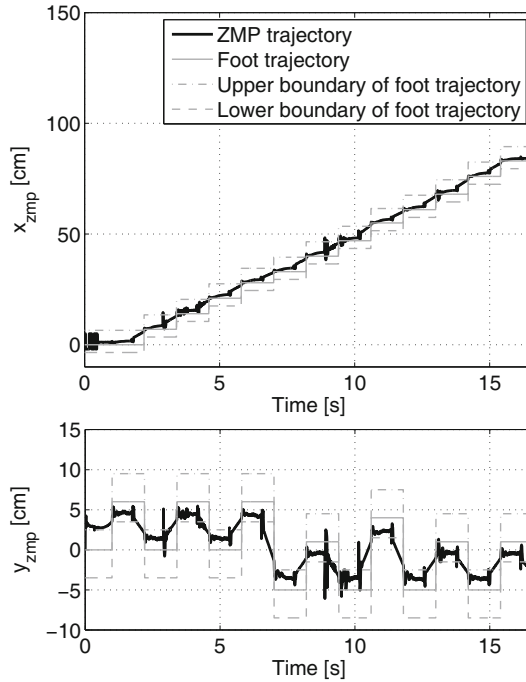


Fig. 8. Measured ZMP trajectories in the walking simulation on uneven terrain

4 Conclusion

In this paper, the novel walking pattern generation method based on the MWPG was introduced for modifiable walking on the inclined terrain in pitch and roll directions, and uneven terrain. As a novel navigational command set, the 3-D CS was defined and then, the CoM trajectories in the single and double support phases were generated to satisfy the 3-D CS, also the foot trajectory of the swing leg was generated. The effectiveness of the walking pattern generation method was verified through simulations using the simulation model of the small-sized humanoid robot, HSR-IX. Consequently, by using the walking pattern generation method, the humanoid robot could walk stably on the inclined terrain in both pitch and roll directions, and uneven terrain following the commanded 3-D CS list by modifying the sagittal and lateral step lengths, and foot height of the swing leg at every footstep.

Acknowledgments. This research was supported by Basic Science Research Program through the National Research Foundation of Korea (NRF) funded by the Ministry of Education, Science and Technology (2012-0000150).

References

1. Sakagami, Y., Watanabe, R., Aoyama, C., Matsunaga, S., Higaki, N., Fujimura, K.: The intelligent ASIMO: system overview and integration. In: Proc. IEEE/RSJ Int. Conf. Intell. Robot. Syst., pp. 2478–2483 (2002)
2. Akachi, K., Kaneko, K., Kanehira, N., Ota, S., Miyamori, G., Hirata, M., Kajita, S., Kanehiro, F.: Development of humanoid robot HRP-3P. In: Proc. IEEE-RAS Int. Conf. Humanoid Robots, pp. 50–55 (2005)
3. Ogura, Y., Aikawa, H., Shimomura, K., Kondo, H., Morishima, A., Lim, H.-O., Takanishi, A.: Development of a new humanoid robot WABIAN-2. In: Proc. IEEE Int. Conf. Robot. Autom., pp. 76–81 (2006)
4. Kajita, S., Kanehiro, F., Kaneko, K., Fujiwara, K., Yokoi, K., Hirukawa, H.: A realtime pattern generator for biped walking. In: Proc. IEEE Int. Conf. Robot. Autom., vol. 1, pp. 31–37 (2002)
5. Lee, B.-J., Stonier, D., Kim, Y.-D., Yoo, J.-K., Kim, J.-H.: Modifiable walking pattern of a humanoid robot by using allowable ZMP variation. *IEEE Trans. Robot.* 24(4), 917–925 (2008)
6. Hong, Y.-D., Lee, B.-J., Kim, J.-H.: Command state-based modifiable walking pattern generation on an inclined plane in pitch and roll directions for humanoid robots. *IEEE/ASME Trans. Mechatron.* 16(4), 783–789 (2011)
7. Hong, Y.-D., Kim, J.-H.: 3-D Command state-based modifiable bipedal walking on an uneven terrain. *IEEE/ASME Trans. Mechatron.* (December 2011), 10.1109/TMECH.2012.2182777
8. Shih, C.-L., Chiou, C.-J.: The motion control of a statically stable biped robot on an uneven floor. *IEEE Trans. Syst. Man, Cybern. B, Cybern.* 28(2), 244–249 (1998)
9. Chew, C.-M., Pratt, J., Pratt, G.: Blind walking of a planar bipedal robot on sloped terrain. In: Proc. IEEE Int. Conf. Robot. Autom., vol. 1, pp. 381–386 (1999)
10. Kajita, S., Kanehiro, F., Kaneko, K., Fujiwara, K., Harada, K., Yokoi, K., Hirukawa, H.: Biped walking pattern generation by using preview control of zero-moment point. In: Proc. IEEE Int. Conf. Robot. Autom., vol. 2, pp. 1620–1626 (2003)
11. Huang, W., Chew, C.-M., Zheng, Y., Hong, G.-S.: Pattern generation for bipedal walking on slopes and stairs. In: Proc. IEEE-RAS Int. Conf. Humanoid Robots, pp. 205–210 (2008)
12. Nishiwaki, K., Kagami, S.: Walking control on uneven terrain with short cycle pattern generation. In: Proc. IEEE-RAS Int. Conf. Humanoid Robots, pp. 447–453 (2007)
13. Takubo, T., Imada, Y., Ohara, K., Mae, Y., Arai, T.: Rough terrain walking for bipedal robot by using ZMP criteria map. In: Proc. IEEE Int. Conf. Robot. Autom., pp. 788–793 (2009)
14. Hirukawa, H., Hattori, S., Kajita, S., Harada, K., Kaneko, K., Kanehiro, F., Morisawa, M., Nakaoka, S.: A pattern generator of humanoid robots walking on a rough terrain. In: Proc. IEEE Int. Conf. Robot. Autom., pp. 2181–2187 (2007)
15. Zheng, Y., Lin, M.C., Manocha, D., Adiwahono, A.H., Chew, C.-M.: A walking pattern generator for biped robots on uneven terrains. In: Proc. IEEE/RSJ Int. Conf. Intell. Robot. Syst., pp. 4483–4488 (2010)

16. Aoyama, T., Sekiyama, K., Hasegawa, Y., Fukuda, T.: 3-D biped walking over rough terrain based on the assumption of point-contact. In: Proc. IEEE/RSJ Int. Conf. Intell. Robot. Syst., pp. 3163–3168 (2010)
17. Michel, O.: Cyberbotics Ltd. WebotsTM: Professional mobile robot simulation. Int. J. Advanced Robot. Syst. 1(1), 39–42 (2004)
18. Hong, Y.-D., Kim, Y.-H., Han, J.-H., Yoo, J.-K., Kim, J.-H.: Evolutionary multi-objective footstep planning for humanoid robots. IEEE Trans. Syst. Man. Cybern. C, Appl. Rev. 41(4), 520–532 (2011)
19. Hong, Y.-D., Kim, J.-H.: An evolutionary optimized footstep planner for the navigation of humanoid robots. Int. J. Humanoid Robot. 9(1) (March 2012)

Stable Modifiable Walking Pattern Algorithm with Constrained Optimized Central Pattern Generator

Chang-Soo Park and Jong-Hwan Kim

Department of Electrical Engineering, KAIST,
291 Daehak-ro, Yuseong-gu, Daejeon, 305-701, Republic of Korea
{cspark,johkim}@rit.kaist.ac.kr

Abstract. In this paper, stable modifiable walking pattern algorithm is proposed using evolutionary optimized central pattern generator (CPG). Sensory feedback pathways in CPG are proposed, which use force sensing resistor (FSR) signals. For the optimization of CPG parameters, two-phase evolutionary programming (TPEP) is employed. Modifiable walking pattern generator (MWPG) generates position trajectory of center of mass (COM) of humanoid robot and CPG generates sagittal swing foot position trajectory. The effectiveness of the proposed scheme is demonstrated by simulations using a Webots dynamic simulator for a small sized humanoid robot, HSR-IX, developed in the Robot Intelligence Technology (RIT) Lab, KAIST.

Keywords: Modifiable walking pattern generator (MWPG), central pattern generator (CPG).

1 Introduction

Despite the complexity of high-DOF systems, these days many humanoid robots have been developed and their performance has been improved a lot [1]-[4]. However, their control algorithm still needs to be improved further to perform a practical task. In this regard, research on developing robust walking patterns of humanoid robots plays one of important roles in this field.

For generation of robust walking patterns of humanoid robots, there are two typical approaches, such as dynamic model based approach and biologically inspired approach. In the former, A 3-D linear inverted pendulum model (3-D LIPM) is one of popular schemes [5]– [8]. The 3-D LIPM decouples the sagittal and lateral center of mass (COM) motion equations in single support phase. A modifiable walking pattern generator (MWPG) extends the conventional 3-D LIPM for the zero moment point (ZMP) variation by the closed form functions and allows the bipedal robot to modify the walking pattern in real-time while walking [9], [10]. In the latter, central pattern generator (CPG) is widely used [11]-[14]. It can generate rhythmic output signals without rhythmic central input or sensor signal. Also, it can alter generated signals to deal with environmental disturbance using sensor feedback.

This paper proposes a stable MWPG algorithm with constrained optimized CPG. The proposed scheme generates position trajectory of the humanoid robot's COM using the MWPG. Also, to minimize the disturbance by the COM position error, the CPG

generates the sagittal swing foot position trajectory and sensor feedback in CPG modifies the generated sagittal swing foot position trajectory. The sensor feedback gets the disturbance information using signals of force sensing resistor (FSR) sensors attached on the sole of foot. To optimize the parameters of the CPG, two-phase evolutionary programming (TPEP) is employed considering equality constraints [15], [16]. The effectiveness of the proposed scheme is demonstrated by computer simulations with the Webots model of a small sized humanoid robot HSR-IX developed in the Robot Intelligence Technology (RIT) Lab., KAIST.

This paper is organized as follows. In Section II, stable MWPG using constrained optimized CPG is proposed. In Section III, simulation results are presented and finally concluding remarks follow in Section IV.

2 Stable MWPG Using CPG

This section presents the proposed stable MWPG using constrained optimized CPG. In this paper, to generate the trajectory of COM, the MWPG is employed [9], [10]. The bipedal walking is composed of single and double support phases. In the single support phase, the primary dynamics of the bipedal robot is modeled as a 3-D LIPM [5]. The MWPG extends the conventional 3-D LIPM for the ZMP variation by the closed form functions and allows the bipedal robot to modify the walking pattern in real-time while walking. Meanwhile, the sagittal swing foot position trajectory is generated by the constrained optimized CPG for stable bipedal walking.

2.1 Neural Oscillator

In this paper, the neuron is developed to generate rhythmic signal for humanoid robots. The neuron is biologically inspired to generate a rhythmic signal, defined as follows (Fig. 1) [17]:

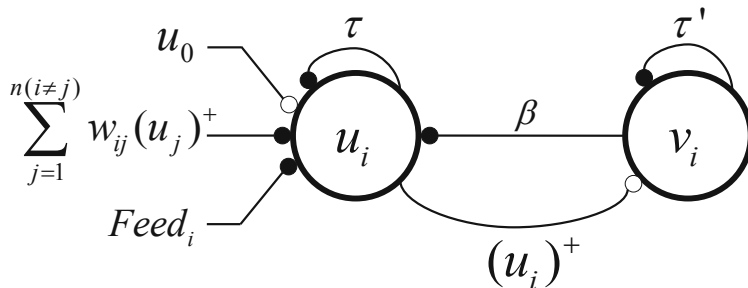


Fig. 1. Neuron structure. The lines ending with black and white circles are inhibitory and excitatory connections, respectively.

$$\tau \dot{u}_i = -u_i - \sum_{j=1}^N w_{ij}(u_j)^+ - \beta v_i + u_0 + Feed_i, \quad (1)$$

$$\tau' \dot{v}_i = -v_i + (u_i)^+ \quad (2)$$

$$(u_i)^+ = \max(0, u_i) \quad (3)$$

where u_i is the inner state of the i th neuron, v_i is the self-inhibition state of the i th neuron, u_0 is the constant input signal, o_i is the output signal, w_{ij} is the connecting weight between i th and j th neurons, τ and τ' are time constants, β is the weight of the self-inhibition, and $Feed_i$ is the sensory feedback signal which is necessary for stable biped locomotion, of the i th neuron. u_0 , τ , τ' and w_{ij} are constant parameters. τ and τ' decide the output wave shape and frequency, u_0 determines the output amplitude and w_{ij} determines the phase difference between i th and j th neurons. In this paper, the neural oscillator is composed of two neurons, each of which consists of two mutually excited neurons: an extensor neuron (EN) and a flexor neuron (FN) to generate rhythmic signal [17]. The CPG structure generates the rhythmic signal as follows (Fig. 2):

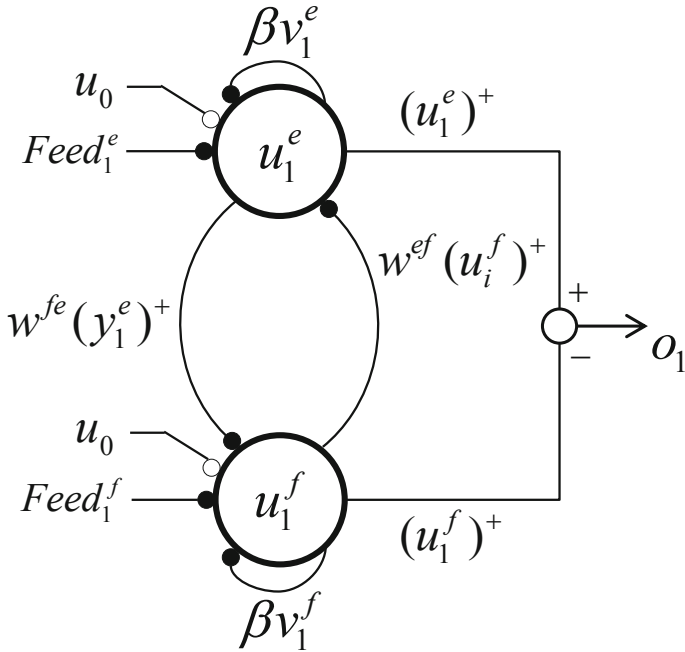


Fig. 2. CPG structure

$$\tau \dot{u}_1^e = -u_1^e - w(u_1^f)^+ - \beta v_1^e + u_0 + Feed_1^e, \quad (4)$$

$$\tau' \dot{v}_1^e = -v_1^e + (u_1^e)^+ \quad (5)$$

$$\tau \dot{u}_1^f = -u_1^f - w(u_1^e)^+ - \beta v_1^f + u_0 + Feed_1^f, \quad (6)$$

$$\tau' \dot{v}_1^f = -v_1^f + (u_1^f)^+ \quad (7)$$

$$o_1 = (u_1^e)^+ - (u_1^f)^+ \quad (8)$$

where the superscripts e and f denote the EN and the FN, respectively.

2.2 Swing Foot Trajectory Generation by CPG

Using the NO, the sagittal foot trajectory is generated as follows:

$$x_{foot} = -S^{pre} + \frac{S + S^{pre}}{2A_1} o_1 \quad (9)$$

where x_{foot} is the sagittal position of the swing foot. S and S^{pre} are the sagittal step lengths at the present footstep and previous footstep, respectively. A_1 is the amplitude of o_1 . o_1 should become minimum value $-A_1$ at beginning single support phase and o_1 should become maximum value A_1 at end single support phase to satisfy step length.

The sensor feedback of the NO alters x_{foot} to compensate the disturbance by the COM position error. The sensor feedback gets the information from four FSRs of each foot, which are attached to each corner of the sole of the foot. The sensory feedback is designed as follows:

$$Feed_1^e = k_f |x_{zmp}^d - x_{zmp}^r| \quad (10)$$

$$Feed_1^f = -Feed_1^e \quad (11)$$

with

$$x_{zmp}^r = \frac{\sum_{i=1}^4 (f_i^l x_i^l + f_i^r x_i^r)}{\sum_{i=1}^4 (f_i^l + f_i^r)}$$

where k_f is the scaling factor. x_{zmp}^d is the desired sagittal ZMP and x_{zmp}^r is the real sagittal ZMP [18]. f_i^r and f_i^l are the ground reaction forces (GRFs) measured at the right and left feet, respectively, by FSRs. x_i^l and x_i^r are the sagittal positions of FSRs on left and right soles.

2.3 Constrained Optimization for CPG

The objective of this optimization is to obtain the desired output signals and to minimize the oscillation of the ZMP while bipedal walking. To obtain the desired output signals, time constants of the CPG should be optimized. When the magnitude of the NO output signal generated by the CPG reaches the minimum (maximum) value, the time

T_1^{min} (T_1^{max}) should be equal to time at beginning (ending) single support phase. Thus, $T_1^{max} - T_1^{min}$ should be equal to the single support time T_{ss} . When the magnitude of output signal reaches zero, the time T_1^0 should be equal to the middle value of T_{ss} . To satisfy the objective and these constraints, the following objective function is defined to obtain the time constants and the scaling factors in the sensory feedback, by the TPEP [16]:

$$\text{Minimize } f = f_x + P \quad (12)$$

subject to

$$\begin{aligned} (T_1^{max} - T_1^{min}) - T_{ss} &= 0 \\ T_1^0 - \frac{T_{ss}}{2} &= 0 \end{aligned}$$

with

$$f_x = \sum_{T=0}^{T_{ss}} |x_{zmp}^d - x_{zmp}^r|$$

where P is the penalty which is given if humanoid robot loses its balance and collapses. f_x means the sum of the differences between the desired ZMP and the real ZMP while bipedal walking.

3 Simulations

The effectiveness of the proposed algorithm was demonstrated by computer simulations with the Webots model of a small sized humanoid robot, HSR-IX (Fig. 3). HSR-IX is the latest one of HSR-series. HSR is a small-sized humanoid robot that has been in continual redesign and development in RIT Lab, KAIST. Its height and weight are 52.8cm and 5.5kg, respectively. It has 26 DOFs that consist of 14 RC servo motors in the upper body and 12 DC motors with harmonic drives for reduction gears in the lower body. Webots is the 3-D robotics simulation software. Users can conduct the physical and dynamical simulation using Webots [19].

3.1 CPG Parameters Setting Using TPEP

In the simulation, Z_c was set as 23.35cm. The self inhibition weight, β , and the input signal, u_0 were set as 2.5 and 2.9, respectively. The connecting weights were set as 2.5 to make the phase difference between EN output and FN output to π [17]. Table 1 shows the parameter settings for the constrained optimization by TPEP. The initial values of inner states and self-inhibition states were set as Table 2 to make initial value of o_1 to the minimum value at beginning of single support phase. For the constrained optimization of the CPG, the simulation model of HSR-IX modeled by Webots, was employed. The constrained optimized parameters were obtained by TPEP as Table 3.

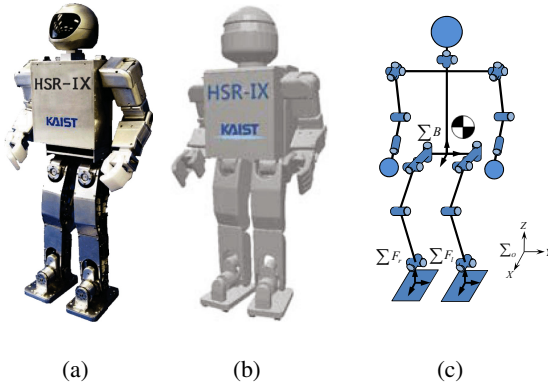


Fig. 3. (a) HSR-IX. (b) Simulation model. (c) Configuration

Table 1. The parameters setting for TPEP

Single support time (s)	T_{ss}	0.8
Double support time (s)	T_{ds}	0.4
Penalty	P	∞

Table 2. Initial values of inner states and self-inhibition states

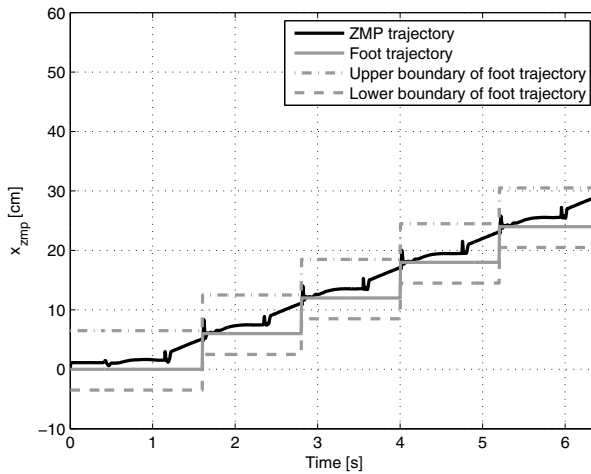
u_1^e (s)	-0.0068	u_1^f	0.9723
v_1^e (s)	0.1902	v_1^f	0.7771

Table 3. Constrained optimized parameters by TPEP

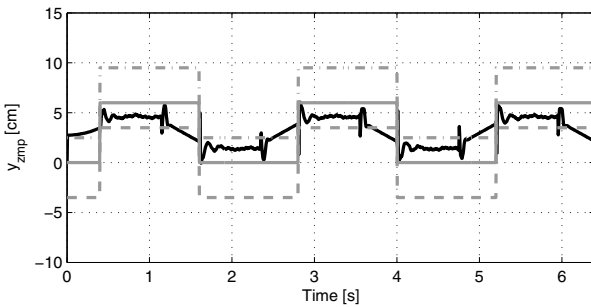
Time constants	τ	0.315
	τ'	0.207
Scaling factor	k_f	-3.21

3.2 Walking Simulation Using CPG

In this simulation, to increase the oscillation of the ZMP, the error term Δx was added to the generated sagittal COM position trajectory by MWPG while bipedal walking. When Δx increased by 0.5cm, f_x increased by 30.3% without sensor feedback and 27.27% with sensor feedback compared at $\Delta x = 0$. In this result, the increment of Δx caused Δx was reduced by 10.6% using the CPG with sensor feedback. Fig. 4 shows the measured ZMP trajectory. As shown in the figure, the ZMP trajectories were within the allowable ZMP variation region. It means the HSR-IX could walk stably with the proposed algorithm.



(a)



(b)

Fig. 4. The measured ZMP while bipedal walking with sensor feedback

4 Conclusion

This paper proposed a stable MWPG algorithm with constrained optimized CPG. The MWPG was employed to generate COM position trajectory. The sagittal swing foot position trajectory was generated using CPG. Also, for stable bipedal walking, sensor feedback in CPG modified generated signals to deal with the disturbance. Sensor feedback got the disturbance information using FSRs. TPEP was employed to optimize parameters of CPG considering some constraints. In order to demonstrate the performance of the proposed scheme, computer simulations were carried out with the Webots model of the small sized humanoid robot, HSR-IX developed in the RIT Lab., KAIST.

Acknowledgments. This research was supported by Basic Science Research Program through the National Research Foundation of Korea (NRF) funded by the Ministry of Education, Science and Technology (2012-0000150).

References

1. Sakagami, Y., Watanabe, R., Aoyama, C., Matsunaga, S., Higaki, N., Fujimura, K.: The intelligent ASIMO: system overview and integration. In: Proc. IEEE/RSJ Int. Conf. Intell. Robot. Syst., pp. 2478–2483 (2002)
2. Akachi, K., Kaneko, K., Kanehira, N., Ota, S., Miyamori, G., Hirata, M., Kajita, S., Kanehiro, F.: Development of humanoid robot HRP-3P. In: Proc. IEEE-RAS Int. Conf. Humanoid Robots, pp. 50–55 (2005)
3. Ogura, Y., Aikawa, H., Shimomura, K., Kondo, H., Morishima, A., Lim, H.-O., Takanishi, A.: Development of a new humanoid robot WABIAN-2. In: Proc. IEEE Int. Conf. Robot. Autom., pp. 76–81 (2006)
4. Park, I.-W., Kim, J.-Y., Lee, J., Oh, J.-H.: Online free walking trajectory generation for biped humanoid robot KHR-3(HUBO). In: Proc. IEEE Int. Conf. on Robot. Autom., pp. 1231–1236 (2006)
5. Kajita, S., Kanehiro, F., Kaneko, K., Fujiwara, K., Yokoi, K., Hirukawa, H.: A realtime pattern generator for biped walking. In: Proc. IEEE Int. Conf. Robot. Autom., pp. 31–37 (2002)
6. Motoi, N., Suzuki, T., Ohnishi, K.: A bipedal locomotion planning based on virtual linear inverted pendulum mode. *IEEE Trans. Ind. Electron.* 56(1), 54–61 (2009)
7. Erbatur, K., Kurt, O.: Natural ZMP trajectories for biped robot reference generation. *IEEE Trans. Ind. Electron.* 56(3), 835–845 (2009)
8. Sato, T., Sakaino, S., Ohashi, E., Ohnishi, K.: Walking trajectory planning on stairs using virtual slope for biped robots. *IEEE Trans. Ind. Electron.* 58(4), 1385–1396 (2001)
9. Lee, B.-J., Stonier, D., Kim, Y.-D., Yoo, J.-K., Kim, J.-H.: Modifiable Walking Pattern of a Humanoid Robot by Using Allowable ZMP Variation. *IEEE Trans. Robot.* 24(4), 917–925 (2008)
10. Hong, Y.-D., Lee, B.-J., Kim, J.-H.: Command state-based modifiable walking pattern generation on an inclined plane in pitch and roll directions for humanoid robots. *IEEE/ASME Trans. Mechatron.* 16(4), 783–789 (2011)
11. Taga, G.: Emergence of bipedal locomotion through entrainment among the neuro-musculo-skeletal system and the environment. *Physica D: Nonlinear Phenomena* 75(1.3), 190–208 (1994)
12. Aoi, S., Tsuchiya, K.: Stability analysis of a simple walking model driven by an oscillator with a phase reset using sensory feedback. *IEEE Trans. Robot.* 22(2), 391–397 (2006)
13. Righetti, L., Ijspeert, A.J.: Programmable central pattern generators: an application to biped locomotion control. In: Proc. IEEE Int. Conf. Robot., pp. 1585–1590 (2006)
14. Park, C.-S., Hong, Y.-D., Kim, J.-H.: An Evolutionary Central Pattern Generator for Stable Bipedal Walking by the Increased Double Support Time. In: Proc. IEEE Int. Conf. Robot. Bio., pp. 497–502 (2011)
15. Myung, H., Kim, J.-H.: Hybrid evolutionary programming for heavily constrained problems. *BioSystems* 38(1), 29–43 (1996)
16. Kim, J.-H., Myung, H.: Evolutionary programming techniques for constrained optimization problems. *IEEE Trans. Evol. Comput.* 1(2), 129–140 (1997)
17. Matsuoka, K.: Sustained oscillations generated by mutually inhibiting neurons with adaptation. *Biol. Cybern.* 52(6), 367–376 (1985)
18. Vukobratovic, M., Borovac, B.: Zero-moment point-thirty live years of its life. *Int. J. Humanoid Robot.* 1(1), 157–173 (2004)
19. Michel, O.: Cyberbotics Ltd. WebotsTM: Professional mobile robot simulation. *Int. J. Advanced Robot. Syst.* 1(1), 39–42 (2004)

Optimal EEG Channel Selection for Motor Imagery BCI System Using BPSO and GA

Jun-Yeup Kim, Seung-Min Park, Kwang-Eun Ko, and Kwee-Bo Sim*

School of Electrical and Electronics Engineering, Chung-Ang University
221, Heukseok-dong, Dongjak-gu, Seoul 156-756, Korea
{jy915, sminpark, kkeun, kbsim}@cau.ac.kr

Abstract. A motor imagery brain-computer interface system is used to translate a subject's intention into a control command of machine, such as electrical wheelchair, robot manipulator, and so on. The overall process of classification of the motor imagery EEG signals is based on the acquisition of raw data from multiple channel of scalp when the subject tries to imagine the movement of limbs. So far, we have been concentrated which channel are activated by the imagination of the movement of limbs. Therefore, we have expected that the more channels are selected, the better results can be acquired. However, the problem is that using many channels causes other problems. When applying a common spatial pattern (CSP), which is a spatial feature extraction, many channels cause an overfitting problem, in addition there is difficulty using this technique for medical analysis. To overcome these problems, we suggest a binary particle swarm optimization (BPSO) as an optimal channel selection method. This paper examines selecting optimal channels and their combination, and comparing accuracy and the number of selected channels obtained from BPSO and simple genetic algorithm.

Keywords: EEG Channel Selection, Brain-Computer Interface, Binary Particle Swarm Optimization, Common Spatial Pattern, Support Vector Machine.

1 Introduction

A brain activity associated with user's intention is measured by brain-computer interface and the recorded brain activity is translated into control signals. There are two ways to record brain activity; one is invasive method and the other is non-invasive method. Invasive method implants electrodes on the surface of cortex by surgery which includes opening the skull. The signals measured in this way have little artifacts, excellent quality and good spatial resolution. The drawback, however, is that it could be dangerous due to the surgery. Non-invasive method puts electrodes on the skin. That is the reason why it is likely to be sensitive and has low amplitude and could have artifacts and noise. Electroencephalography (EEG) is one of non-invasive methods. Because EEG obtained from non-invasive methods contains many artifacts,

* Corresponding author.

meaningful signals must be extracted with noise eliminated at the same time. CSP is one of the methods which extract important signals. One of the major challenges in BCI is that each person has different activated brain regions even though they perform the experiment in the condition that the experiment of environment and paradigm are exactly the same. In order to overcome this problem, we use as many channels as was feasible. However, the use of multiple channels causes other problems, such as overfitting, and appearance of artifacts from other channels, among other things. We suggest a method which makes it possible to find optimal channels for each subject with the number of used channels decreasing and with high accuracy maintaining by applying a binary-PSO prior to feature extraction. We compared the accuracy of the optimal channel combination and the accuracy of all channels. CSP was applied as an extraction method, and SVM was applied for classification. We applied PCA to reduce the dimension when the dimension was too large. This paper is structured as follows: section 2 contains related works such as feature selection and feature extraction. Experiment data is described in section 3. Proposed method and result are given in section 4 and 5, respectively

2 Related Works

2.1 Linear Filtering

EEG is one of non-invasive methods so it contains a lot of artifacts. We need to remove those artifacts to obtain better classification. Linear filtering is good at removing artifacts which are located at specific frequency. EMG artifacts can be removed by low-pass filter and EOG artifact can be removed by high-pass filter. Linear filter was commonly used in early studies to remove artifacts in EEG signal [1]. This algorithms has disadvantages which occurs when the neurological phenomenon of interest and the EOG or the EMG are overlapped in the same frequency band.

2.2 Particle Swarm Optimization

The PSO algorithm was developed by Kennedy and Eberhart in 1995 [2]. It is based on the simulation of social behavior of birds and it has been gotten attention throughout the world in that it performs as much as Genetic algorithm (GA) does even though it has fewer variables and is much simpler than GA. The individuals referred as to particles are defined as the potential solution of a search space and are flown through hyper-dimensional search space. The particles fly over the search space with a certain velocity. Individuals swarm members can profit from the discoveries and previous experience of all other members of the school. When each particle is searching for a final optimal solution in the search space, they consider the present optimal solution, as well as the previous optimal solution. So the velocity of each particle is influenced by its own best position found so far and the best solution that was found so far by its neighbors. Each particle continues to search for the optimal solution using the fitness value and update. The best solution of the swarm is called

gbest, and the best solution of each particle is called pbest. Eventually the swarm will converge to optimal positions. The position and velocity of the particles are updated as follows:

$$v_{k+1}^i = w v_k^i + c_1 r_1 (p_k^i - x_k^i) + c_2 r_2 (gbest - x_k^i) \quad (1)$$

$$x_i(t+1) = x_i(t) + v_i(t+1) \quad (2)$$

Where i denotes each particles; c_1 is cognitive component and c_2 is social component. c_1, c_2 that control how far a particle will move in a single trial are constant value. w is inertial weight value which constrains previous velocity. r_1, r_2 are arbitrarily random values between 0 and 1. When $c_1 > c_2$, velocity update weights on the force emerging from the tendency to return to its own best solution found so far more than the force emerging from the attraction of the best solution found so far in its neighborhood, vice versa.

2.3 Binary Particle Swarm Optimization

BPSO is a discrete version of PSO [3]. The velocity is updated in the same way as PSO. The difference between PSO and BPSO is that the particles consist of either a 0 or 1 in BPSO, and the update rule for each position is different. The update equations are as follows:

$$S(v) = (1 + e^{-v})^{-1} \quad (3)$$

$$x_{k+1}^i = 1 \text{ if } \tau < S(v_{k+1}^i) \quad (4)$$

$$x_{k+1}^i = 0 \text{ if } \tau > S(v_{k+1}^i) \quad (5)$$

where τ is a random value between 0 and 1. We consider the channel space as the solution space, and each particle's position can have a value of either 0 or 1.

2.4 Genetic Algorithm

Genetic algorithm was developed by John Holland in 1970's in order to understand the adaptive processes of natural systems and to design artificial systems [4]. It is based on reproduction which a child's gene is made from his parents. Gene search process is divided into 4 steps; initialization, fitness evaluation and reproduction, crossover, and mutation. In initialization step, population consisted of individuals which have potential to be a solution of given task is made. Initial individuals are randomly distributed in the solution space. Fitness evaluation which performs environment in natural system is computed after each individual is encoded. According to their relative fitness values, individuals in the present population are selected for reproduction. As fitness values from a certain individual are higher than fitness value from the rest, the certain individual has more chance to be selected and reproduced while the other individual is likely to be removed. The selected individuals get reproduced from crossover and produce new individuals by

exchanging their own gene information. Crossover usually tries to get changed only with the information which the present population has. Mutation offers a new method which provides new information by randomly flipping at least one gene's information of selected individuals with low mutation probability. The 4 steps are repeated until the new population finds optimal value.

2.5 Common Spatial Pattern

The Common Spatial Pattern (CSP) allows spatial filters which maximize the variance of signal of one class and minimize the variance of signals of the other class at the same time[4]. CSP filters are good at detecting amplitude of sensorimotor rhythms and discriminating mental states which are characterized by ERD/ ERS effect because variance of band-pass filtered signals is equal to band-power. The main purpose of CSP is that the multi-channel EEG is projected into low-dimensional spatial subspace by projection matrix. This transformation can maximize the variance of two-class signal matrices. For the analysis, the raw EEG data of one trial is represented as $N \times T$ matrix, where N is the number of channels and T is the number of samples per channel. The normalized spatial covariance of the EEG can be obtained from:

$$C_1 = \frac{E_1 E_1^T}{\text{Trace}(E_1 E_1^T)}, \quad C_2 = \frac{E_2 E_2^T}{\text{Trace}(E_2 E_2^T)} \quad (6)$$

where E_1^T means the transpose of E_1 and $\text{trace}(x)$ means the summation of diagonal elements of matrix (x). The averaged normalized covariance \bar{C}_1, \bar{C}_2 can be calculated by averaging over all the trials of each group.

$$\bar{C}_1 = \frac{1}{n_a} \sum_{j=1}^{n_a} C_1(j), \quad \bar{C}_2 = \frac{1}{n_b} \sum_{j=1}^{n_b} C_2(j) \quad (7)$$

Where n_a means the number of class 1 of all trials and n_b means the number of class 2 of all trials. The composite spatial covariance is as follows:

$$C_c = \bar{C}_1 + \bar{C}_2 = U_c \lambda_c U_c^T \quad (8)$$

where U_c is the matrix of eigenvectors and λ_c is the diagonal matrix of eigenvalues. The eigenvalues are sorted in descending order. The whitening transformation is shown as:

$$P = \sqrt{\lambda^{-1}} U_c^T \quad (9)$$

Whitening transformation transforms the average covariance matrices as:

$$S_1 = P \bar{C}_1 P^T, \quad S_2 = P \bar{C}_2 P^T \quad (10)$$

S_1 and S_2 share common eigenvector and the sum of corresponding eigenvalues will always be one:

$$S_1 = U\Sigma_1 U^T \quad S_2 = U\Sigma_2 U^T \quad (11)$$

$$\Sigma_1 + \Sigma_2 = I \quad (12)$$

From equation (10) ~ (12), we can explain the eigenvector with the largest eigenvalue for S_1 has the smallest eigenvalue for S_2 . The projection matrix W is denoted as:

$$W = U^T P \quad (13)$$

The original EEG signal can be transformed into uncorrelated components with the projection matrix as shown:

$$Z = WX \quad (14)$$

3 Proposed Methods

3.1 Binary PSO for Channel Selection

We applied Binary PSO algorithm for channel selection in BCI system. The flow chart of BPSO applied in BCI is depicted in Fig. 1. In order to avoid overfitting in feature extraction, we need to remove features which could be artifacts and have noise on them by using BPSO.

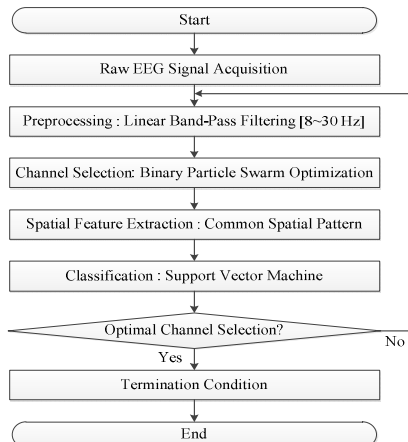


Fig. 1. Flow chart of Binary Particle Swarm Optimization applied in BCI

We keep doing Feature selection until we select optimal features. We consider the channel space as the solution space, and each particle's position can have a value of either 0 or 1, where 0 means that we do not use the channel, and 1 means that we use the channel. In the BCI dataset IV-data 1, they use 59 channels; therefore, we used 59 dimensions and let the particles have a value of 0 or 1. The first step is to initialize particle position and velocity, c_1 , and c_2 . After initializing, we chose only particles

with a value of 1. With channels consisting of the position of each particle, we applied CSP as the feature extraction method and SVM for the classification. After the classification, we estimated the accuracy (%). When the dimension was too big to calculate, we applied PCA in order to reduce the size of the dimension. We set the fitness function according to the accuracy obtained through the classification. The fitness function is as follows:

$$\text{Fitness} = 0.7 \times (\text{accuracy}) + 0.3 \times \left(\frac{\# \text{ of total channel} + 1 - \# \text{ of selected channel}}{\# \text{ of total channel}} \right) \quad (15)$$

$$\text{accuracy} = \frac{\# \text{ of correctly classified data}}{\# \text{ of test data}} \quad (16)$$

Even though we consider both accuracy and the number of selected channel, we put more impact on accuracy than the number of selected channel. The particle position, velocity, pbest, and gbest are then updated, unless the iteration exceeds the maximum set value. The particle position and velocity are updated by equations (1), (3), (4), and (5). When $\text{fitness}(x_{k+1}^i)$ is bigger than $\text{fitness}(pbest^i)$, $pbest^i$ is updated to the x_{k+1}^i . When $\text{fitness}(gbest)$ is less than $\text{fitness}(x_{k+1}^i)$, $gbest$ is updated to the x_{k+1}^i . When the iteration exceeds the maximum value, we consider gbest to be the optimal channel combination. Among the 7 subjects who imagined left or right hand or foot movements, we selected subjects b, d, and e, who only imagined either the left or right hand movements, to analyze the signals. The parameters were set as follows: The number of particles is set to 50 and the iteration maximum value was set to 100, c_1, c_2 were set to 2, and r_1, r_2 , and τ were set to a random value between 0 and 1. The n-th inertia weight is as follows

$$w(n) = w_{max} - (w_{max} - w_{min}) \frac{n}{h} \quad (17)$$

where w_{max} is set to 0.9, and w_{min} is set to 0.6, and h represents the maximum value of the iteration.

3.2 Genetic Algorithm for Channel Selection

We applied GA algorithm for channel selection in BCI system. The process of GA for channel selection is the same as the process of BPSO. In GA algorithm, we also use the same fitness function as described in (15). The parameter setting is as follow. We used 50 individual and set maximum iteration as 100. We set crossover probability as 0.8 and mutation probability as 0.011.

4 Simulation and Results

4.1 Experimental Condition

BCI dataset IV-dataset 1 is used in this study [5]. Healthy 7 subjects take part in the experiment and 59 electrodes depicted in Fig. 2 are used. For each subject two classes of motor imagery were selected from the three classes (left hand, right hand, and foot).

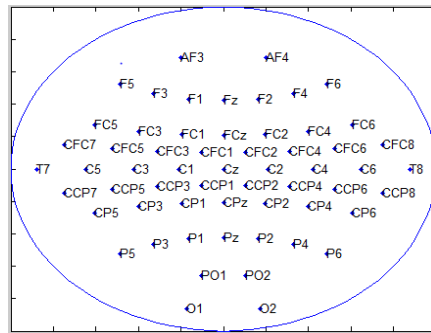


Fig. 2. Position of 59 EEG electrodes used for data acquisition

4.2 Experimental Results

Fig. 3 is a comparison between the accuracy acquired by all channels and the selected channels. For a selected channel by BPSO and GA, the accuracy of each subject was calculated 5 times.

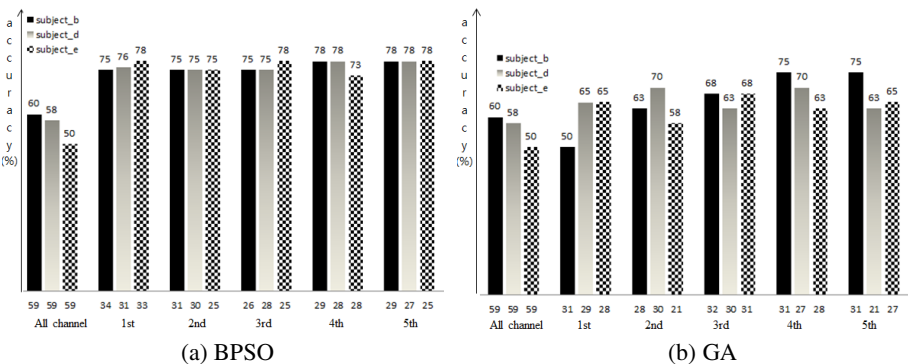


Fig. 3. Comparison between the accuracy rate acquired by all channels and the selected channels by using (a) PSO, and (b) GA

As shown in Fig.3 (a), the optimal channel selection using the proposed BPSO method improved 15~18 % for subject b over all channel and 17~20 % for subject d and 23 ~28% for subject e. On the other hand, as shown in Fig.3 (b), the optimal channel selection using the proposed GA method improved 3~15 % for subject b, 5~12 % for subject d, and 8~15% for subject e over all channel. In the sense of accuracy, BPSO algorithm is better than GA at finding channel combination which makes the system have higher accuracy. In the sense of the number of selected channels, BPSO selected 29 channels on average and GA selected 31 channels on average for subject b. As we executed experiment 5 times, we did not get the same optimal channel combination so we estimated the frequency of channel selection. The maximum frequency is set to 5 and we chose channels which selected more than or equal to 3 when executing experiment 5 times.

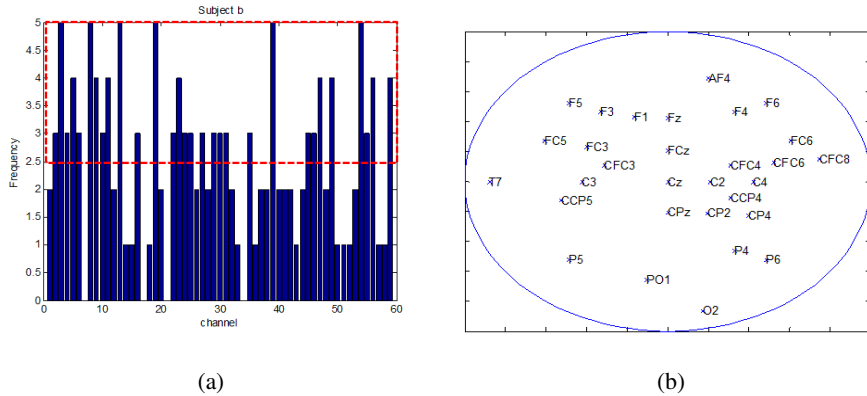


Fig. 4. (a) Histogram of selected channels for subject_b by BPSO , (b) Selected channels for subject_b which have frequencies more than 3.

Fig. 4 (a) illustrates frequency of selected channels for subject b by BPSO and a square box means that inside of a box has frequencies more than or equal to 3 times and the corresponding channels are depicted Fig. 4(b). The number of channels which have more than 3 frequencies is 25.

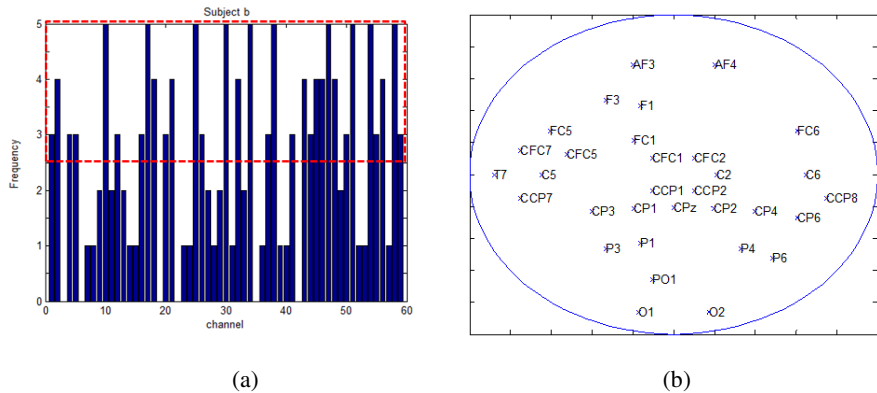


Fig. 5. (a) Histogram of selected channels for subject_b by GA, (b) Selected channels for subject_b which have frequencies more than 3

Fig. 5 (a) illustrates frequency of selected channels for subject b by GA and Fig.5 (b) depicts selected channels for subject b which have frequencies more than 3. The number of channels which selected more than or equal to 3 by BPSO is 30 and the number of channels which selected more than or equal to 3 by GA is 32.

5 Conclusion

Instead of using all channels, this paper proposed an optimal channel selection method by BPSO and GA. With the both proposed method, we used a smaller number of channels with higher accuracy and optimal channels selected by BPSO have higher accuracies than channel selected by GA and the number of selected channels is almost similar. In the future, we will adjust the fitness function in order to get the same optimal channel combination every time the calculation is performed.

Acknowledgements. This work was supported by the National Research Foundation of KOREA[NRF] grant funded by the KOREA government[MEST][No.2011-0029861].

References

1. Zhou, W., Gotman, J.: Removing eye-movement artifacts from the EEG during the intracarotid amobarbital procedure. *Epilepsia* 46, 409–414 (2005)
2. Kennedy, J., Eberhart, R.C.: Particle swarm optimization. In: Proceedings of IEEE International Conference on Neural networks, pp. 1942–1948 (1995)
3. Kennedy, J., Eberhart, R.C.: A discrete binary version of the particle swarm algorithm. In: IEEE International Conference on Systems Man and Cybernetics, vol. 5, pp. 5104–5108 (1997)
4. Engelbrecht, A.P.: Computational Intelligence: An Introduction, 2nd edn. John Wiley & Sons, Ltd. (2007)
5. Ramoser, H., Gerking, J.M., Pfurtscheller, G.: Optimal spatial filtering of single trial EEG during imagined hand movement. *IEEE Trans.*, 441–446 (1998)
6. Blankertz, B., Dornhege, G., Krauledat, M., Müller, K.-R., Curio, G.: The non-invasive Berlin Brain–Computer Interface: fast acquisition of effective performance in untrained subjects. *Neuroimage*, 539–550 (2007)

3D Human-Pose Tracking through a Monocular Vision

Minho Kim, Sihyun Joo, and Sungho Jo

Dept. of Computer Science, KAIST
291 Daehak-ro, Yuseong-gu, Daejeon 305-701, Korea
`{minokino,zently,shjo}@kaist.ac.kr`

Abstract. We develop an algorithm for 3D human-pose tracking through a monocular vision. The algorithm is based on body-silhouette shape matching combined with particle-filter-based selected-region tracking in the 2D view. The selected-region tracking, combined with human-body structural data, restricts the temporal interpretation of 3D human poses to those best corresponding to the 2D silhouette shapes. The experimental results demonstrate that our approach performs real-time human-motion tracking with good quality and reasonable robustness.

Keywords: 3D visual tracking, Monocular vision, Silhouette.

1 Introduction

Tracking 3D human motion through a vision sensor is very useful in many applications and has been extensively investigated. Various approaches to tracking 3D human motion have been attempted such as ICP-based tracking of silhouettes in a multicamera system [1], a model-based tracking method from multiple-view sequences [2], body-silhouette combination with a skeletal model through offline training [3], tracking by combining region fitting and dense optical flow as well as SIFT feature tracking [4], real-time tracking using several particle filters with a flexible body model and a stereo camera [5], and a nonlinear point-distribution model to encapsulate 3D skeletal structure and 2D silhouettes [6]. We present a novel algorithm for 3D human-motion tracking from a monocular vision. Our algorithm includes two main steps: the 2D tracking of important human body regions and the matching of a 3D human-body model with its corresponding 2D silhouette shape. 3D motion tracking is achieved by finding a 3D model pose that best corresponds to the instantaneous 2D-image information, constrained by the 2D positions of important body parts. A designated human-body model enables the application of analytic algorithms to facilitate the implementation. Our approach requires no preliminary training before execution.

2 2D Tracking of Head, Hands, and Legs

2.1 2D Body Silhouette Acquisition

To acquire the body silhouette, we subtract the background from the image at each time step by a simple real-time executable method adapted from [7]. For every pixel

(u, v) in the 2D image sequence of the background, each pixel is designated by a tuple with elements representing the expected color value, standard deviation of the color value, variation of brightness distortion, and chromaticity distortion. Each pixel is classified into the foreground only when the chromaticity difference is greater than a certain threshold or the brightness distortion is much less than that of the background. The body silhouette is then identified as the largest continuous, dark foreground area. The borderline of the body silhouette is smoothed through a low-pass filter operation.

2.2 Particle Filter-Based Tracking

Important human body regions in the 2D image plane are tracked by applying the particle filter method. Body components such as hands, feet and head, whose positions govern the overall human pose, are tracked. Each individual particle representing a target object at time t is described by a state \bar{x}_t which represents the center-point position vector of the object, its velocity vector, and its acceleration vector. A first-order autoregressive (AR) model represents the transition of \bar{x}_t .

$$\bar{x}_t = A \bar{x}_{t-1} + \bar{\epsilon}_{t-1} \quad (1)$$

where $A = \begin{pmatrix} 1 & 0 & 1 & 0 & 0 & 0 \\ 0 & 1 & 0 & 1 & 0 & 0 \\ 0 & 0 & 0.8 & 0 & 1 & 0 \\ 0 & 0 & 0 & 0.8 & 0 & 1 \\ 0 & 0 & 0 & 0 & 0.5 & 0 \\ 0 & 0 & 0 & 0 & 0 & 0.5 \end{pmatrix}$ and $\bar{\epsilon}_{t-1}$ is a random variable vector in

which each element is distributed according to a Gaussian probability distribution with a zero mean and covariance.

The 2D instantaneous image from the camera is converted to the HSV color space, where $HU(u, v)$ and $SA(u, v)$ represent the hue and the saturation values, respectively, at pixel (u, v) . Each particle stores information on the lower and upper boundary values of the hue, h_L and h_U as well as the lower and upper boundary values of the saturation, s_L , and s_U . The measurement of a particle, \bar{z}_t , is a collection of pixel positions in a rectangular window centered at \bar{p}_t , with a constant width w and height h . The particle measurement likelihood $p(\bar{z}_t | \bar{x}_t)$ is calculated by

$$p(\bar{z}_t | \bar{x}_t) = \frac{1}{wh} \sum_{(u,v) \in \bar{z}_t} IN(u, v) \quad (2)$$

where $IN(u, v) = \begin{cases} 1 & \text{if } h_L \leq HU(u, v) \leq h_U \quad s_L \leq SA(u, v) \leq s_U \\ 0 & \text{otherwise} \end{cases}$

Tracking individual objects separately may cause problem when similar objects, e.g., two hands, intersect. Two particle filters are likely to chase only a single hand with the highest measurement likelihood value. To prevent the problem, the probabilistic exclusion principle is applied, as given in [8]. Furthermore, by applying partitioned sampling [9] to an aggregated particle $\bar{x}_{a,t} = (\bar{x}_{1,t}, \bar{x}_{2,t}, \dots, \bar{x}_{n,t})$, the curse of the dimensionality problem is alleviated. The measurement likelihood $p(\bar{z}_{a,t} | \bar{x}_{a,t})$ for the aggregated particle can be calculated as follows:

$$p(\bar{z}_{a,t} | \bar{x}_{a,t}) = R(\bar{x}_{a,t}, \bar{z}_{a,t}) I(\bar{x}_{a,t}, \bar{z}_{a,t}) D(\bar{x}_{a,t}, \bar{z}_{a,t}) \quad (3)$$

where $R(\bar{x}_{a,t}, \bar{z}_{a,t}) = p(z_{1,t} | \bar{x}_{1,t}) p(z_{2,t} | \bar{x}_{2,t}) \dots p(z_{n,t} | \bar{x}_{n,t})$

$$I(\bar{x}_{a,t}, \bar{z}_{a,t}) = \begin{cases} 0 & \text{if } \bar{z}_{i,t} \cap \bar{z}_{j,t} \neq \emptyset, \text{ for } \forall i \neq j \\ 1 & \text{otherwise} \end{cases}$$

$D(\bar{x}_{a,t}, \bar{z}_{a,t}) = \min\left(1, \frac{d_m - d_{ref}}{d_{ref}}\right)$, $d_m = \max\|\bar{p}_{i,t} - \bar{p}_{j,t}\|$ for $\forall i \neq j$, and d_{ref} is a constant.

3 3D Human Body Representation

3.1 Human Body Model

The 3D human body model consists of rigid limb segments interconnected by joints such as the shoulder, elbow, hip, knee, and ankle (see Fig. 1). We represent the shapes of body segments as superquadrics [10]. The superquadrics can be described analytically by simple mathematical formulae. A point (x, y, z) on the surface of the superquadrics is analytically expressed by:

$$\begin{aligned} x(u, v) &= a_1 C(v, \epsilon_1) C(u, \epsilon_2), y(u, v) = a_2 C(v, \epsilon_1) S(u, \epsilon_2), z(u, v) = a_3 S(v, \epsilon_1) \\ C(\eta, \epsilon) &= \text{sgn}(\cos\eta)|\cos\eta|^\epsilon, S(\eta, \epsilon) = \text{sgn}(\sin\eta)|\sin\eta|^\epsilon \end{aligned} \quad (4)$$

where $-\frac{\pi}{2} \leq v \leq \frac{\pi}{2}$, $-\pi \leq u \leq \pi$, the constants a_1, a_2 , and a_3 determine the sizes of the superquadrics along x, y, and z axis, respectively, $-\frac{\pi}{2} \leq v \leq \frac{\pi}{2}$, and $\text{sgn}(q) = +1$ if $q > 0$ and -1 otherwise.

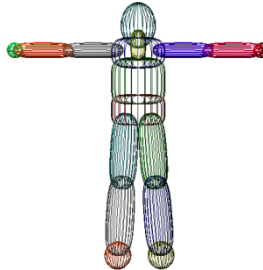


Fig. 1. Human body model

3.2 Camera Model

The perspective projection camera model describes the relation between the 3D positions of the human body segments and their corresponding pixel positions in the 2D image with respect to the camera position. This work uses a frustum projection with a symmetric view volume with respect to the camera view axis represented by a following matrix [10]:

$$P = \begin{pmatrix} \frac{n}{r} & 0 & 0 & 0 \\ 0 & \frac{n}{t} & 0 & 0 \\ 0 & 0 & -\frac{f+n}{f-n} & -\frac{2fn}{f-n} \\ 0 & 0 & -1 & 0 \end{pmatrix} \quad (5)$$

where n indicates the distance between the camera and the near clip plane, f the distance between the near plane and the far clip plane, r half of the width of the near clip plane, and t half of the height of the near clip plane.

A position in Cartesian coordinates, $\bar{p}_e = (x, y, z)$, can be transformed into a pixel position in the 2D image plane, (u, v) :

$$u = \left(1 + \frac{\left(\frac{n}{r}\right)x}{-z}\right) \left(\frac{W}{2}\right), v = H - \left(1 + \frac{\left(\frac{n}{t}\right)y}{-z}\right) \left(\frac{H}{2}\right) \quad (6)$$

where W and H denote the width and the height of the image, respectively.

4 Matching the 3D Body Model to the 2D Silhouette Shape

The 3D human body model is projected onto the 2D image plane from a camera viewpoint to compute the borderline of the human-body model. We then attempt to match the projected 2D contour of each body component with the corresponding area of the 2D silhouette shape. The matching procedure is implemented in the following order: head, trunk, arms, and legs. The prior information from the 2D tracking facilitates the hierarchical matching.

4.1 Model Matching Method

Matches of the body components, head, trunk, and extremities, share a common matching method. A tangent line at a point (u_{m_j}, v_{m_j}) on the curve of a projected model component has the form:

$$v_{m_j} \cos \theta - u_{m_j} \sin \theta = d_{m_j} \quad (7)$$

where θ is the orientation of the line with respect to the u axis in the 2D projected plane and d_{m_j} is the signed length of the line defining the perpendicular distance of the point from the origin.

Similarly a tangent line at a point (u_{s_j}, v_{s_j}) on the contour of the corresponding silhouette is described by:

$$v_{s_j} \cos \theta - u_{s_j} \sin \theta = d_{s_j} \quad (8)$$

where d_{s_j} is the signed length of the line defining the perpendicular distance from the origin.

Then, the signed perpendicular distance error between the two lines is defined as $e_j = d_{s_j} - d_{m_j}$ [11] which describes the discrepancy between the curves of the

projected model part and the corresponding silhouette. Given a selected point on the contour of a projected model, a normal vector must be computed to find a comparable point on the contour of the silhouette. The two points should be matched by consensus.

4.1.1 Normal Vector Sampling

Because each body component is composed of superquadrics, a normal vector \bar{n} can be retrieved from any point in the body-model surface as follows.

$$\bar{n} = (n_x, n_y, n_z) = \left(\frac{\cos^{2-\epsilon_1}(\eta) \cos^{2-\epsilon_2}(\omega)}{a_1}, \frac{\cos^{2-\epsilon_1}(\eta) \sin^{2-\epsilon_2}(\omega)}{a_2}, \frac{\sin^{2-\epsilon_1}(\eta)}{a_3} \right) \quad (9)$$

The boundary between the visible and invisible parts of a body-model component determines the contour of the component. Any point along the contour should satisfy the condition $\bar{l} \cdot \bar{n} = 0$ where $\bar{l} = [l_x, l_y, l_z]^T$ is a vector from the camera position to the point. The contour can then be described by, as ω varies from $-\pi$ to π ,

$$\eta = \tan^{-1} \left(-\frac{a_3}{l_z} \left(\frac{l_x}{a_1} \cos^{(2-\epsilon_2)}(\omega) + \frac{l_y}{a_2} \sin^{(2-\epsilon_2)}(\omega) \right) \right)^{\frac{1}{2-\epsilon_2}} \quad (10)$$

The 3D position of the contour can then be computed by plugging the η values above into (4). Points are sampled from the contour of a body-model component such that the distance between two sequential sample points is equal to a predefined distance, ensuring that all the sample points faithfully represent the contour. From each sample point a vector normal to the image plane is drawn, either outward or inward, to select a proximal point on the curve of the silhouette. The selected point is designated as the corresponding sample point to be matched. When a set of the sample points is represented by $\bar{p}_m = \{(u_{mj}, v_{mj})\}_{j=1}^{N_m}$ where N_m is the number of the effective samples, a set of corresponding points from the contour of the silhouette is given by $\bar{p}_s = \{(u_{sj}, v_{sj})\}_{j=1}^{N_m}$, with the associated normal vectors at the sample points and corresponding points on the silhouette denoted as \bar{n}_m and \bar{n}_s , respectively; together, they are stored in a set $(\bar{p}_m, \bar{p}_s, \bar{n}_m, \bar{n}_s) \in NV_m$. To suppress false positives, each match should satisfy the following condition:

$$\bar{n}_m \cdot \bar{n}_s \leq \varepsilon \ll 1 \quad (11)$$

where ε is a positive threshold value.

4.1.2 Jacobian Matrix Calculation

Suppose there are M parameters $r_1, \dots, r_M \in \mathbb{R}$ to be found to minimize the error. For all N_m elements in NV_m , the gradient $\frac{de_j}{dr_i}$ is calculated. Using (6),

$$\frac{du}{dr_i} = \left(\frac{n}{r} \right) \left(\frac{w}{2} \right) \left(\frac{1}{z} \right) \left(\frac{x}{z} \left(\frac{dz}{dr_i} \right) - \frac{dx}{dr_i} \right) \quad (12)$$

$$\frac{dv}{dr_i} = - \left(\frac{n}{t} \right) \left(\frac{h}{2} \right) \left(\frac{1}{z} \right) \left(\frac{y}{z} \left(\frac{dz}{dr_i} \right) - \frac{dy}{dr_i} \right) \quad (13)$$

Also, taking the derivative of e_j with respect to r_i yields:

$$\frac{de_j}{dr_i} = \sin\theta \left(\frac{du}{dr_i} \right) - \cos\theta \left(\frac{dv}{dr_i} \right) \quad (14)$$

By plugging (12-13) into (14), each gradient component is computed. Then, the error Jacobrian matrix, J_e , whose elements are the gradient component, is obtained.

4.1.3 Parameter Optimization

The parameters $\bar{r} = [r_1 \dots r_M]^T$ are computed by the minimization of

$$\|J_e \bar{r} - \bar{e}\|^2 + \lambda^2 \|\Lambda(\bar{r} - \bar{r}_0)\|^2 \quad (15)$$

where $\bar{r} = \bar{r}^* - \bar{r}_0$, \bar{r}_0 is an initial parameter vector, \bar{r}^* is an optimal parameter vector, and \bar{r}_0 is an initial guess for \bar{r} .

The constant λ controls the effectiveness between the initial guess and new data, and Λ is a diagonal matrix whose diagonal entries are the reciprocals of the standard deviation of each parameter. A modified Levenberg-Marquardt (LM) algorithm [11][12] finds the solution:

$$\begin{aligned} [J_e^T \quad \Lambda^T] \begin{bmatrix} J_e \\ \lambda^2 \Lambda \end{bmatrix} \bar{r} &= [J_e^T \quad \Lambda^T] \begin{bmatrix} \bar{e} \\ \lambda^2 \Lambda \bar{r}_0 \end{bmatrix} \\ (J_e^T J_e + \lambda^2 \Lambda^T \Lambda) \bar{r} &= J_e^T \bar{e} + \lambda^2 \Lambda^T \Lambda \bar{r}_0 \end{aligned} \quad (16)$$

Its computation is iteratively processed. To efficiently control the convergence to a solution, λ is increased by multiplication by a factor $c > 1$ when the error value is large and decreased by division by the factor when the error value is small. Prior information is extracted from the 2D particle-filter-based tracking. \bar{r}_0 is assumed to be a zero vector initially and the above iterative algorithm converges quickly and finds a reliable solution in real time. In the case of hands and legs, each limited motion range is further considered to find solutions that are geometrically feasible. A bounded constraint $\alpha \leq r_i \leq \beta$ is described by a quadratic penalty function $(r_i - r_{c,i})^2 \leq \sigma_i$ where $r_{c,i} = (\beta + \alpha) / 2$, and $\sigma_i = (\beta - \alpha) / 2$. A modified cost function is defined by adding the constraint term to (16):

$$\|J_e \bar{r} - \bar{e}\|^2 + \lambda^2 \|\Lambda(\bar{r} - \bar{r}_0)\|^2 + \|C_e^{-\frac{1}{2}}(\bar{r} - \bar{r}_c)\|^2 \quad (17)$$

where $C_e = \text{diag}(\sigma_i^2)$ which is a constant diagonal matrix and $\bar{r}_c = [r_{c,1}, r_{c,2}, \dots, r_{c,M}]^T$.

Then, modified algorithm aims to find a solution of:

$$(J_e^T J_e + \lambda \Lambda^T \Lambda + C_e^{-1}) \bar{r} = J_e^T \bar{e} + (\lambda \Lambda^T \Lambda + C_e^{-1}) \bar{r}_0 \quad (18)$$

During the iterations, it is verified that each iteration result lies within the predefined boundary. If the result lies outside of the boundary, the corresponding diagonal value in C_e^{-1} is multiplied by a factor and its evaluation is again implemented. This procedure is thus guaranteed to find a solution that satisfies the boundary constraint.

4.2 Matching the Head in the Model and the Silhouette

The projected head model component is elliptical. Therefore, its contour is described by the following parametric equations, assuming that the center of the ellipse is located at (x_c, y_c, z_c) in the 3D space (x, y, z) . As t varies from $-\frac{\pi}{4}$ to $\frac{5\pi}{4}$,

$$x = x_c + a_h \cos t \cos \phi - b_h \sin t \sin \phi, y = y_c + a_h \cos t \sin \phi + b_h \sin t \cos \phi, z = z_c \quad (19)$$

where a_h and b_h are coefficients denoting head size.

The range of t value draws the partial curve of the ellipse which resembles the head contour. The z axis is parallel to the camera view direction. Here, z_c approximately indicates the distance from the camera to the human head. The parameters to be determined are $\bar{r} = [x_c, y_c, z_c, \phi]$. This parameter selection yields the following derivatives:

$$\frac{dx}{dx_c} = \frac{dy}{dy_c} = \frac{dz}{dz_c} = 1, \frac{dx}{d\phi} = (y - y_c), \frac{dy}{d\phi} = -(x - x_c), \frac{dz}{d\phi} = 0 \quad (20)$$

These are plugged into (12-13) to compute the error Jacobian, which is required to find optimized parameter values. To more accurately compute these parameters, an optimization is done in two steps. First, the optimization takes into account the head part as a partial ellipse. Then, after finding coarse parameter values, the neck and shoulder line is extended from the fragmented part of the ellipse using a simple B-spline curve. Additional points along the B-spline curve are sampled and the same optimization method is applied.

4.3 Matching the Trunk in the Model and the Silhouette

To represent natural trunk poses, the 3D trunk model consists of three components as shown in Fig. 1. This three-component trunk model is useful for approximating round-shaped human torso poses. The position of the top part is constrained by the head position as follows:

$$\bar{p}_T = [x_c + \gamma b_h \sin \phi, y_c - \gamma b_h \cos \phi, z_c] \quad (21)$$

where γ is a scaling factor to fit the neck length.

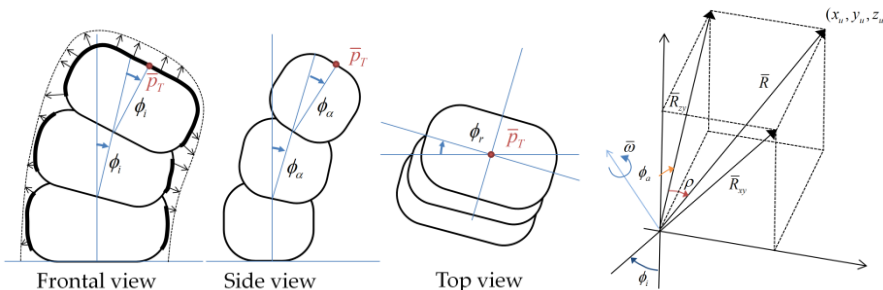


Fig. 2. Trunk model components and parameters

Each trunk component's position can be described with three parameters using spherical coordinates: the inclination (ϕ_i), the azimuth (ϕ_a), and the rotation (ϕ_r) angles. To draw the naturally smooth contour of the human trunk, it is assumed that ϕ_i and ϕ_a between the top and middle parts equal those between the middle and bottom parts, respectively. This assumption enables the trunk-pose match between the contours of the trunk model and its corresponding silhouette by selecting three parameters $\bar{r} = [\phi_i, \phi_a, \phi_r]$ as shown in Fig. 2. However, because the trunk is represented by a combination of three superquadrics, the contour of the trunk volume is not smooth. Therefore, selected partial contours of the three superquadrics are only used for matching, and normal vectors are sampled only from the lines. The thick lines in Fig. 2 illustrate these selected partial contours. To apply the optimization in Section 4.1, the gradients must be computed. First, an algorithm to compute $\frac{d\bar{p}}{d\phi_i}$ is investigated, where \bar{p} is any point on the contour in the 3D space. Let $[x_u, y_u, z_u]$ denote the joint position between the top and the middle trunk components while the origin denote the joint position between the middle and the bottom trunk components. A vector, \bar{R} , can be drawn to connect the two joints. Let \bar{R}_{xy} and \bar{R}_{zy} represent the component vectors of \bar{R} projected onto the xy plane and zy plane, respectively, as shown in Fig. 2. Then,

$$x_u = |\bar{R}_{xy}| \sin \phi_i, y_u = |\bar{R}_{xy}| \cos \phi_i = |\bar{R}_{zy}| \cos \phi_a, z_u = |\bar{R}_{zy}| \sin \phi_a \quad (22)$$

where $|\bar{R}_{xy}|^2 + z_u^2 = |\bar{R}_{zy}|^2 + x_u^2 = |\bar{R}|^2$.

$$|\bar{R}_{xy}| = |\bar{R}| \left(\frac{1}{\sin^2 \phi_i + \left(\frac{\cos \phi_i}{\cos \phi_a} \right)^2} \right), |\bar{R}_{zy}| = |\bar{R}| \left(\frac{1}{\sin^2 \phi_i + \left(\frac{\cos \phi_a}{\cos \phi_i} \right)^2} \right) \quad (23)$$

As an intermediate step in the calculation of the gradient $\frac{d\bar{p}}{d\phi_i}$, an angle, ρ , is designated by:

$$\rho = \cos^{-1} \left(\frac{|\bar{R}_{zy}|}{|\bar{R}|} \right) \quad (24)$$

From (23) and (24),

$$\frac{1}{(\cos \rho)^2} = \sin^2 \phi_a + \left(\frac{\cos \phi_a}{\cos \phi_i} \right)^2 \quad (25)$$

Assuming ϕ_a is fixed,

$$\frac{d\rho}{d\phi_i} = \frac{\cos^2 \phi_a}{\cos^2 \phi_i} \tan \phi_i \cos^2 \rho \cot \rho \quad (26)$$

In addition, a rotation vector, $\bar{\omega}$, as illustrated in Fig. 2, is computed by:

$$\bar{\omega} = \frac{\bar{R} \times \bar{R}_{zy}}{|\bar{R} \times \bar{R}_{zy}|} \quad (27)$$

An algebraic relationship [13] indicates:

$$\vec{p}_a = \bar{\omega} \times (\bar{p}_a - \bar{q}) \quad (28)$$

$$\begin{bmatrix} \frac{d\bar{p}_a}{d\rho} \\ 1 \end{bmatrix} = \begin{bmatrix} 0 & -\omega_z & \omega_y & \omega q_x \\ \omega_z & 0 & -\omega_x & \omega q_y \\ -\omega_y & \omega_x & 0 & \omega q_z \\ 0 & 0 & 0 & 1 \end{bmatrix} \begin{bmatrix} \bar{p}_a \\ 1 \end{bmatrix} \quad (29)$$

where $\bar{\omega} = (\omega_x, \omega_y, \omega_z)$, and $(-\omega \times \bar{q}) = (\omega q_x, \omega q_y, \omega q_z)$.

So far, it is assumed that the lower joint position is constantly at the origin for simplicity. However, the joint position, in fact, changes. By taking into account the fact that the trunk parameters are constrained by \bar{p}_T as fixed from the head matching, the computation of the gradient relies on the changing joint position. With respect to the global 3D space coordinate,

$$\frac{d\bar{p}}{d\rho} = \frac{d\bar{\delta}}{d\rho} - \frac{d\bar{p}_a}{d\rho} \quad (30)$$

$$\text{where } \frac{d\bar{\delta}}{d\rho} = \left[= -\frac{|\bar{R}| \cot \phi_i (\cot^2 \phi_i + 1)^{\frac{3}{2}}}{(\cos^2 \phi_a + \cot^2 \phi_i)^2}, \frac{|\bar{R}| \tan \phi_i (\tan^2 \phi_i + 1)^{\frac{3}{2}}}{(\tan^2 \phi_i + \sec^2 \phi_a)^2}, -\frac{|\bar{R}| \cos^2 \phi_i \sin \phi_a}{(\cos^2 \phi_a + \cot^2 \phi_i)^{\frac{3}{2}}} \right].$$

Combining (26) and (30), the gradient is computed:

$$\frac{d\bar{p}_c}{d\phi_i} = \frac{d\rho}{d\phi_i} \frac{d\bar{p}_c}{d\rho} \quad (31)$$

Similarly, the gradient $\frac{d\bar{p}_c}{d\phi_a}$ can be calculated under the assumption that ϕ_i is fixed. Finally, as for ϕ_r , any point on the contour of the silhouette shape can be rotated with respect to \bar{p}_T along the y axis. Here \bar{p}_T plays a role analogous to \bar{q} in (28), and the rotation vector is $[0, 1, 0]^T$. Hence:

$$\begin{bmatrix} \frac{d\bar{p}}{d\phi_r} \\ 1 \end{bmatrix} = \begin{bmatrix} 0 & 0 & 1 & q_z \\ 0 & 0 & 0 & 0 \\ -1 & 0 & 0 & -q_x \\ 0 & 0 & 0 & 1 \end{bmatrix} \begin{bmatrix} \bar{p} \\ 1 \end{bmatrix} \quad (32)$$

4.4 Matching the Arms and Legs in the Model and the Silhouette

To determine the postures of the arms, followed by those of the legs, the positions of the hands and feet estimated through the particle filter are used to restrict their poses. Unlike with the head matching, the hand and leg regions are sufficiently small that

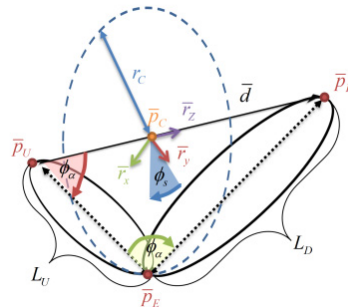


Fig. 3. Arm model components and parameters

they can be modeled as spheres in the body model; hence, the 2D particle-filter-based tracking is sufficient for localization. Each arm is modeled as two rigid segments that are pin-jointed in the middle. An end of the upper arm is fixed at the shoulder's position once the trunk is posed; let \bar{p}_U represent the fixed shoulder position. The end of the lower arm is similarly fixed at the hand's position; let \bar{p}_D represent the fixed hand position. We can apply inverse kinematics to locate the elbow at the pin-joint. Fig. 3 illustrates that the elbow location \bar{p}_E should lie on a circle. The swivel angle (θ_s), which defines a point on the circle, is selected as the parameter to be determined. Here, $\bar{d} = \bar{p}_D - \bar{p}_U$ indicates the direction of the rotational axis for drawing the circle. In addition, the depth value (d_z) is computed to secure the arm pose in the 3D space. Two parameters then fix the arm posture $\bar{r} = [\phi_s, d_z]$. To apply the optimization described in Section 4.1, first, the gradient $\frac{d\bar{p}}{d\theta_s}$ is computed. Any points on the contour of the silhouette are rotated with respect to \bar{p}_U along a rotation vector of $\bar{\omega} = \frac{\bar{d}}{|\bar{d}|}$.

Here \bar{p}_U replaces \bar{q} in (28). Therefore:

$$\begin{bmatrix} \frac{d\bar{p}}{d\theta_s} \\ 1 \end{bmatrix} = \begin{bmatrix} 0 & -\omega_z & \omega_y & dq_x \\ \omega_z & 0 & -\omega_x & dq_y \\ -\omega_y & \omega_x & 0 & dq_z \\ 0 & 0 & 0 & 1 \end{bmatrix} \begin{bmatrix} \bar{p} \\ 1 \end{bmatrix} \quad (33)$$

where $\bar{\omega} = (\omega_x, \omega_y, \omega_z)$, and $(-\bar{\omega} \times \bar{p}_U) = (-\bar{\omega} \times \bar{q}) = (\omega q_x, \omega q_y, \omega q_z)$.

Unfortunately, $\frac{d\bar{p}}{dd_z}$ cannot be easily calculated using the algebraic rotation formulation. Instead, an approximation is employed:

$$\frac{d\bar{p}}{dd_z} \cong \frac{\bar{p}(\theta_s, d_z + \Delta d_z) - \bar{p}(\theta_s, d_z)}{\Delta d_z} \quad (34)$$

where $\bar{p}(\theta_s, d_z)$ denotes a 3D point on the contour described by the parameters. Next, $\bar{p}(\theta_s, d_z)$ is obtained through the following procedure. Let L_U and L_D represent the lengths of the upper and the lower arms, respectively.

Then, three unit vectors are defined, as shown in Fig. 3:

$$\bar{r}_z = \bar{\omega}, \bar{r}_y = \frac{\bar{r}_b - (\bar{r}_b \cdot \bar{r}_z)\bar{r}_z}{|\bar{r}_b - (\bar{r}_b \cdot \bar{r}_z)\bar{r}_z|}, \bar{r}_x = \bar{r}_y \times \bar{r}_z \quad (35)$$

where \bar{r}_b is an predefined, arbitrary vector chosen here as $[0, 1, 0]^T$.

Then, geometrically, $\cos \phi_a = \frac{|\bar{d}|^2 - L_U^2 - L_D^2}{2 L_U |\bar{d}|}$, $\cos \phi_i = \frac{|\bar{d}|^2 - L_U^2 - L_D^2}{2 L_U L_D}$ and the position of elbow is:

$$\bar{p}_E = L_U \cos \phi_a \bar{r}_z + L_U \sin \phi_a (\cos \phi_s \bar{r}_y + \sin \phi_s \bar{r}_x) \quad (36)$$

The shoulder joint orientation is represented using a rotation matrix M_r [12]:

$$M_r = [\hat{x} \quad \hat{y} \quad \hat{z}] \quad (37)$$

where $\hat{z} = \frac{\bar{p}_E}{|\bar{p}_E|}$, $\hat{y} = \frac{\bar{d} - (\bar{d} \cdot \hat{z})\hat{z}}{|\bar{d} - (\bar{d} \cdot \hat{z})\hat{z}|}$, $\hat{x} = \hat{y} \times \hat{z}$

Then, a 3D point described by the parameters ϕ_s , and d_z with respect to the shoulder joint local coordinate is given by:

$$\bar{p}(\phi_s, d_z) = \begin{cases} M_r \bar{p}_0 & \text{If a point is in the upper arm} \\ M_r \bar{L}_U + R_y(\phi_i) \bar{p}_0 & \text{If a point is in the lower arm} \end{cases}$$

where $\bar{L}_U = \bar{p}_U - \bar{p}_E$, and $R_y(\phi_i)$ is a rotation matrix that rotates the z axis towards the x axis by ϕ_i . Here, \bar{p}_0 is a local space coordinate of the targeting point.

The arm pose is determined by finding the two parameter values through the optimization procedure given in Section 4.1. Boundary constraints are imposed on the optimization to enforce a geometrically feasible posture. Each parameter is bounded by $\theta_{s,l} \leq \theta_s \leq \theta_{s,h}$, $d_{z,l} \leq d_z \leq d_{z,h}$ where $\theta_{s,l}$ and $\theta_{s,h}$ equal 0 and 2π , respectively, $d_{z,l}$ and $d_{z,h}$ are determined by finding two positions located along a vector connecting the viewpoint \bar{p}_V to \bar{p}_D and whose lengths are equal to $L_U + L_D$. When $\bar{p}_U = [p_{U,x}, p_{U,y}, p_{U,z}]^T$, two solutions of the following equation denote $d_{z,l}$ and $d_{z,h}$, respectively.

$$\sqrt{(at - p_{U,x})^2 + (bt - p_{U,y})^2 + (ct - p_{U,z})^2} = L_U + L_D \quad (38)$$

from a parametric line equation from \bar{p}_V to $\bar{p}_D = (at, bt, ct)$ where t is a parameter.

The legs have the same model structure as the arms. Therefore, the method for matching an arm can be applied directly to matching a leg.

4.5 Overall 3D Body Model Pose

The proposed algorithm using the hierarchical fitting can realize a 3D posture with 11 parameter tunings. The head position is determined by 4 parameters (x_c, y_c, z_c, ϕ) . Once the head is positioned, the trunk, consisting of 8 DOFs in the body model, is positioned by three parameters (ϕ_i, ϕ_a, ϕ_r) . Two parameters, (ϕ_s, d_z) , are used to fit each arm, each consisting of 4 DOFs. As for each arm, each leg is positioned by two parameter tuning. The entire set of parameter values is initialized according to an initial human pose. The body model is initially fitted with the human pose. Once execution begins, the overall tracking procedure is implemented as shown in Fig. 4.

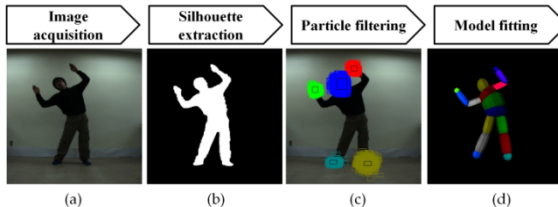


Fig. 4. Overall procedure

5 Experiments and Conclusion

3D real-time human body pose tracker based on the proposed algorithm was realized and tested with some scenarios. The real-time image frames were recorded through a

monocular camera at size of 480×480 pixels. 1000 particles were used in the 2D particle filter tracking, and the size of the tracking window of each body extremity is 35×40 pixels for the head tracking, 20×20 pixels for each hand tracking, and 25×15 pixels for each foot tracking respectively. Initially, ‘T’-like human pose as in Fig. 1 is taken, and the HV color histogram bin in each tracking window is used to assign the lower and upper boundary values of the hue and saturation.

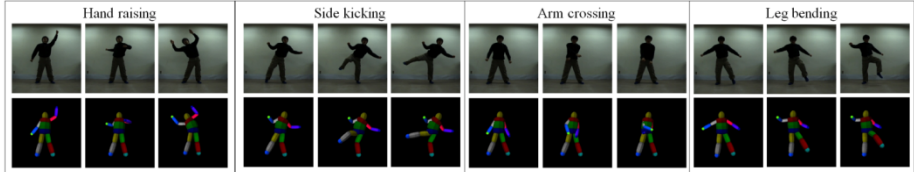


Fig. 5. Experimental results

Fig. 5 illustrates snapshots of instantaneous body pose sequences taken from the pose tracking of continuous human motion. The overall human motion consists of hand raising, side kicking, arm crossing, and leg bending gestures. To evaluate the performance, we compared the body poses in 2D vision images and estimated by the algorithm by checking relative positions between two body extremities in terms of pixels. It was because we did not measure actual 3D body pose with any sensors. In comparison with human motion, motion tracking was successfully. The overall average error of the corresponding positions between the body poses in the images and estimated by the algorithm is 2.7 pixels. In comparison with the human heights, 170 cm which is 165 pixels, the error, which approximates 2.8 cm, is practically insignificant. The results show that the three-component trunk model was effective at representing natural torso poses, and the depths of body extremities were robustly identified. The whole visual-tracking task was conducted at 9-10 fps with a non-fully optimized code. In average, the silhouette subtraction took about 40ms, 2D particle filter tracking took about 50 ms, and the model matching took about 20ms.

We proposed a new approach to find best fitting of a 2D silhouette shape to a 3D body model pose in real time, and thus to implement real-time body motion tracking through a monocular camera. Generally, algorithms for matching a 3D body model with a 2D silhouette region may not yield a unique solution. However, our approach identified the best pose by carrying out 2D tracking of the head and body extremities, which provided clues to the 3D body pose and, furthermore, by restricting the feasible motion ranges of some joints, which prevented the generation of unnatural human poses. This new approach opens up possibilities of building low-cost 3D human-pose tracking systems using monocular vision devices only.

Acknowledgements. This work was supported in part by the Korean government (MEST) under the KRF grant (No. 2010-0015226) and in part by the Korean government (MKE) under Human Resources Development Program for Convergence Robot Specialists.

References

1. Demirdjian, D., Darrell, T.: 3-D articulated pose tracking for unthethered deictic reference. In: Int. Conf. Machine Learning (2002)
2. Yamamoto, M., Sato, A., Kawato, S.: Incremental tracking of human actions from multiple views. In: IEEE Comput. Soc. Conf. Computer Vision and Pattern Recognition (1998)
3. Orrite-Urunuela, C., Rincon, J.M., Herrero-Jaraba, J.E., Rogez, G.: 2D silhouette and 3D skeletal models for human detection and tracking. In: IEEE Comput. Soc. Conf. Computer Vision and Pattern Recognition (2004)
4. Brox, T., Rosenhahn, B., Gall, J., Cremers, D.: Combined region and motion-based 3D tracking of rigid and articulated objects. *IEEE Trans. Pattern Analysis and Machine Intelligence* 32(3), 402–415 (2010)
5. Hecht, F., Azad, P., Dillmann, R.: Markerless human motion tracking with a flexible model and appearance learning. In: Int. Conf. Robotics and Automation, Kobe, Japan, May 12–17 (2009)
6. Bowden, R., Mitchell, T.A., Sarhadi, M.: Non-linear statistical models for the 3D reconstruction of human pose and motion from monocular image sequences. *Image and Vision Computing* 18, 729–737 (2000)
7. Horprasert, T., Harwood, D., Davis, L.S.: A statistical approach for real-time robust background subtraction and shadow detection. In: IEEE Int. Conf. Computer Vision (1999)
8. MacCormick, J., Blake, A.: A probabilistic exclusion principle for tracking multiple objects. *Int. J. Comput. Vision* 39(1), 57–71 (2000)
9. MacCormick, J., Isard, M.: Partitioned sampling, articulated objects, and interface-quality hand tracking. In: Vernon, D. (ed.) *ECCV 2000, Part II. LNCS*, vol. 1843, pp. 3–19. Springer, Heidelberg (2000)
10. Yang, H.-D., Lee, S.-W.: Reconstruction of 3D human body pose from stereo image sequences based on top-down learning. *Pattern Recognition* 40, 3120–3131 (2007)
11. Lowe, D.G.: Fitting parameterized three-dimensional models to images. *IEEE Trans. Pattern Analysis and Machine Intelligence* 13(5), 441–450 (1991)
12. More, J.: The Levenberg-Marquardt algorithm: implementation and theory. *Numerical Analysis* (1977)
13. Murray, R.M., Li, Z., Sastry, S.S.: A mathematical introduction to robotic manipulation. CRC Press, Inc. (1994)

Operator Standpoint-Based Remote Operation System Considering the Operational Convenience for a Mobile Robot

Chang-Seop Shin and Gon-Woo Kim^{*}

School of Electronics Engineering, Chungbuk Nat'l University
52 Naesudong-ro, Heugdeok-gu, Cheongju, Chungbuk 361-763, South Korea
gwkim@cbnu.ac.kr

Abstract. The remotely operated mobile robot is usually controlled in the viewpoint of the mobile robot using the conventional remote operation system. However, it is a little hard to control the mobile robot efficiently when the mobile robot exists in the field of view of the operator. Therefore, we propose the operator standpoint-based remote operation system considering the operational convenience for controlling a mobile robot. For implementing the proposed system, the accurate measurements of the orientation of both the mobile robot and the remote operation system are needed. In order to measure the absolute orientation of the mobile robot and the remote operation system, we exploit the magnetic compass. We also propose the efficient remote operation algorithm in the field of view of the operator using the coordinate transformation method. Finally, we present some experimental results for evaluating the validity of the proposed algorithm. The proposed method can be easily adapted to the common remote operation system by the switching mode approach.

Keywords: remote operation, mobile robot, omnidirectional, compass.

1 Introduction

Recently, the applications of the intelligent mobile robot has been drastically increased in the various fields, such as vacuum cleaning, surveillance, rescue, exploration, guidance, military purpose, etc. [1, 2]. In many applications, the mobile robot should be partially or fully operated by the human operator because of the technical limitations of the autonomous mobility. Especially, the remote operated mobile robots are surely feasible for the applications in the hazardous environments like space, nuclear plants, battlefield, underwater, and so forth [1].

Remote operation is the method to remotely operate a mobile robot with a joystick or other control device which may be plugged directly into the robot, may be connected by wireless or may be a component to the remote controller. This approach is typically applied to robotic applications to keep the operator out of the dangerous situation.

^{*} Corresponding author.

The method of the remote operation should be applied differently whether a mobile robot exists in the field of view of the operator or not. It is because the operator usually feels difficulty in operation under the situation of controlling a mobile robot while watching it. A remotely operated mobile robot is out of sight of the operator in general. In this case, the operator fully depends on the information from a mobile robot such as visual, range, map, etc. In the other case, however, the operator mainly depends on the information of his own sense. At this time, the mismatch between the viewpoint of the operator and the orientation of a mobile robot can be occurred. Under this situation, the operator is not able to operate a mobile robot efficiently, but the conventional remote operation system has not been concerned about this situation. Therefore, it is needed to improve the efficiency to operate a mobile robot for the various situations.

In this paper, we propose the operator standpoint-based remote operation system considering the operational convenience for controlling a mobile robot in order to improve the efficiency to operate a mobile robot for the various situations. For implementing the proposed system, the accurate measurements of the orientation of both the mobile robot and the remote operation system are needed. In order to measure the absolute orientation of the mobile robot and the remote operation system, we exploit the magnetic compass. We also propose the efficient remote operation algorithm in the field of view of the operator using the coordinate transformation method.

2 Background

2.1 Related Works

There are many research groups studying about remotely operated mobile robots for the various applications [1]. However, the operation-centric remote operation system has not been concerned in this research area.

For implementing the proposed algorithm, we should be interested in the joystick control, the kinematics and control of the omni-directional mobile robot and the usage of the magnetic compass. Seo et al. [4] developed the joystick controller for electric wheelchair. They proposed the control algorithm using the cumulate and the derivative operation for the unskilled operation of the handicapped person. Some researches for the control algorithm of the omni-directional mobile robot and the measurement algorithm of the orientation using the magnetic compass have been presented [5, 6, 7, 8, 9, 10, 11]. Lee et al. [8] used a magnetic compass for the azimuth tracking control of an omni-directional mobile robot. They also proposed the filtering method for reducing the noise of the compass data.

2.2 Configuration of the Proposed Remote Operation System

The proposed remote operation system is composed of two components which are the remote operator and the remotely operated mobile robot as shown in Fig. 1. The remote operator consists of microcontroller, joystick, compass sensor and Bluetooth module for the communication by wireless. Fig. 2. shows the operation range and the

coordinate system of the joystick. The joystick is composed of two potentiometers with $10\text{ K}\Omega$ and 5 V of the input voltage. In order to obtain the resolution of 1° , we divide the output levels into 50 steps using 10-bit ADC for x and y axis, respectively. Finally, we can obtain the 2-dimentional discrete data (x_j, y_j) from the joystick as shown in Fig. 2. To measure the orientation of the remote operator, the magnetic compass sensor is utilized with the resolution of 0.5° and the repeatability of 1° .

The mobile robot is developed in the type of the omni-directional mobile robot using three 90-degree Swedish wheels arranged in an equilateral triangle. The same magnetic compass sensor is used for measuring the orientation angle of the mobile robot.

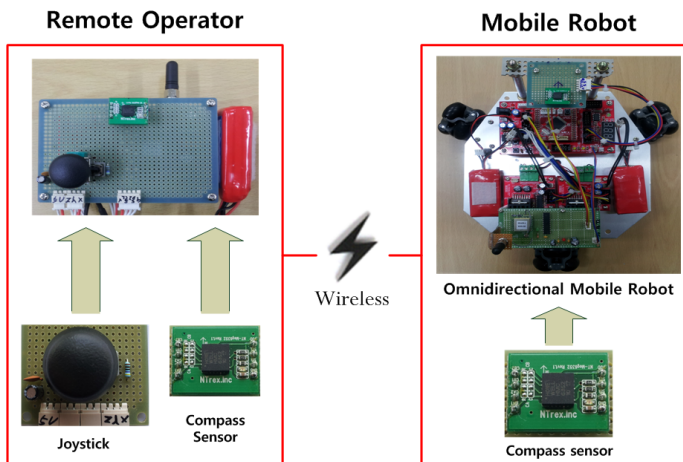


Fig. 1. The configuration of the proposed remote operation system

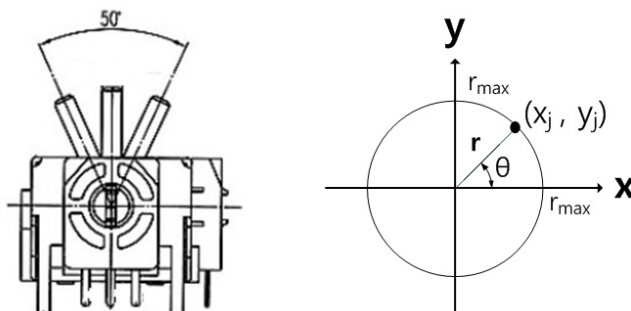


Fig. 2. The operation range (left) and the coordinate system of the joystick (right)

The remote operator periodically sends the 2-dimentional control data (x_j, y_j) from the joystick and the compass data to the mobile robot. Then, the robot transforms the operational direction aligned with the reference frame of the remote operator using two compass data from the remote operator and the mobile robot.

3 Operator Standpoint-Based Remote Operation System

In this section, we propose the operator standpoint-based remote operation system considering the operational convenience for controlling a mobile robot in order to improve the efficiency to operate a mobile robot for the various situations. The efficient remote operation algorithm is discussed in the field of view of the operator using the coordinate transformation method.

3.1 Definition of the Reference Frames

Firstly, we have to define some reference frames for the coordinate transform. We define the reference frames as shown in Fig. 3. In Fig. 3, $\{G\}$ represents the global reference frame, the robot local reference frame is defined as $\{R\}$, and the remote operator local reference frame is also defined as $\{P\}$. We align the frame $\{G\}$ with the earth-centered coordinate frame. The angular differences between the global reference frame and each local reference frame are given by α_r and α_p , which are obtained using the magnetic compasses of the mobile robot and the remote operator, respectively.

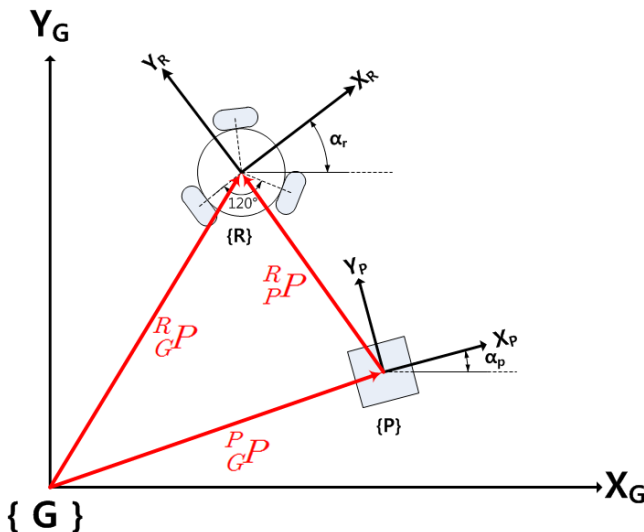


Fig. 3. Definition of the reference frames: the global reference frame $\{G\}$, the robot local reference frame $\{R\}$, and the remote operator local reference frame $\{P\}$.

3.2 Operator Standpoint-Based Remote Operation Algorithm

In the conventional remote operation system, the input data from the joystick are generally converted to the translational and the rotational velocity in the viewpoint of the robot local reference frame. In this case, we don't need to consider the orientation

of the remote operator. For the operator standpoint-based remote operation, however, we should consider the orientation angles both the mobile robot and the remote operator.

The angle difference θ_r between the robot local reference frame and the remote operator local reference frame can be easily obtained as shown below.

$$\theta_r = \alpha_p - \alpha_r \quad (1)$$

For aligning the operational direction with the remote operator local reference frame, the angle difference θ_r is used.

In order to generate the operator-centric control input, the 2-dimentional control data (x_j, y_j) from the joystick should be properly modified. Firstly, the joystick data can be converted to the velocity vector in the robot local reference frame:

$$\begin{bmatrix} \dot{x}_r \\ \dot{y}_r \end{bmatrix} = \frac{v_{\max}}{r_{\max}} R\left(\frac{\pi}{2} + \theta_r\right) \begin{bmatrix} x_j \\ y_j \end{bmatrix} \quad (2)$$

where $R(\theta) = \begin{bmatrix} \cos \theta & \sin \theta \\ -\sin \theta & \cos \theta \end{bmatrix}$

In (2), v_{\max} is the maximum linear velocity of the mobile robot; r_{\max} is the positive maximum value of the joystick data.

The control input of each wheel can be computed using the kinematic model of the omni-directional mobile robot [2]. When ϕ_i represents the i th wheel position of the mobile robot, the relation between the angular velocity of the wheels and the velocity of the mobile robot can be obtained:

$$\begin{bmatrix} \dot{\phi}_1 \\ \dot{\phi}_2 \\ \dot{\phi}_3 \end{bmatrix} = \frac{1}{r} \begin{bmatrix} -\sin(\alpha_r + \varphi_1) & \cos(\alpha_r + \varphi_1) \\ -\sin(\alpha_r + \varphi_2) & \cos(\alpha_r + \varphi_2) \\ -\sin(\alpha_r + \varphi_3) & \cos(\alpha_r + \varphi_3) \end{bmatrix} \begin{bmatrix} \dot{x}_r \\ \dot{y}_r \end{bmatrix} \quad (3)$$

The three omni-wheels are located at an angle $\varphi_i (i=1, 2, 3)$ relative to the robot local reference frame. In this paper, we have $\varphi_1 = 0^\circ$, $\varphi_2 = 120^\circ$, and $\varphi_3 = 240^\circ$. And r is the radius of the omni-wheel.

For the operator standpoint-based remote operation, we can finally compute the operator-centric control input using the 2-dimentional control data (x_j, y_j) from the joystick as shown below:

$$\begin{bmatrix} \dot{\phi}_1 \\ \dot{\phi}_2 \\ \dot{\phi}_3 \end{bmatrix} = \frac{v_{\max}}{r \cdot r_{\max}} \begin{bmatrix} -\sin(\alpha_r + \varphi_1) & \cos(\alpha_r + \varphi_1) \\ -\sin(\alpha_r + \varphi_2) & \cos(\alpha_r + \varphi_2) \\ -\sin(\alpha_r + \varphi_3) & \cos(\alpha_r + \varphi_3) \end{bmatrix} \cdot R\left(\frac{\pi}{2} + \theta_r\right) \cdot \begin{bmatrix} x_j \\ y_j \end{bmatrix} \quad (4)$$

Even if the orientation angle of the mobile robot has been changed according to the operational input, the orientation for the control can be always aligned with the

remote operator local reference frame using the proposed algorithm. It can provide the operational efficiency for the operator when the mobile robot exists in the field of view of the operator.

4 Experiments

For evaluating the validity of the proposed remote operation system, we compared the performance of the operation by the inexperienced operator at two different positions. Fig. 4. shows the experimental setup. The mission of the operation is that the operator should control the robot along the fixed square path within 1.6 m x 1.6 m space. The operator should also perform this mission at two different positions which are taken at the aligned and the perpendicular orientations between the heading direction of the mobile robot and the viewpoint of the operator in Fig. 4.

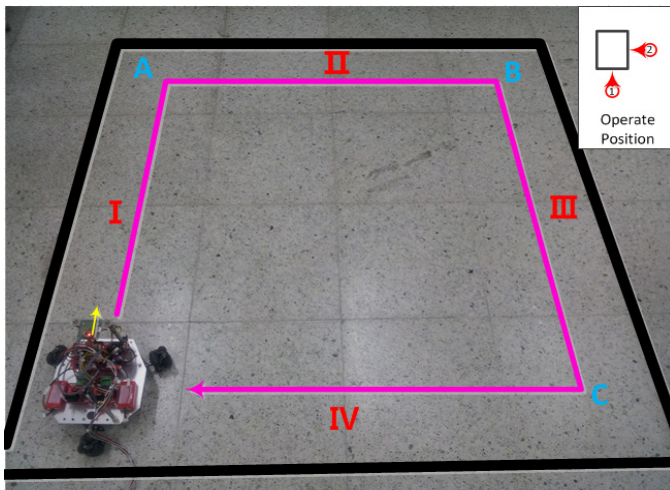


Fig. 4. Experimental setup: the path to be controlled by the operator and the different positions of the operator (*top right*)

Fig. 5. and Fig. 6. show the experimental results for both the conventional operation and the operation standpoint-based operation when the operator controls the mobile robot at the operation position ②. In these figures, I, II, III and IV represent each straight path and A, B and C indicate each corner as shown in Fig. 4. In Fig. 5., there are some improper operations caused by the confusion of the orientation of the mobile robot. Especially, the operator repeatedly made the incorrect control input right after the mobile robot reached at the corner as shown in Fig. 5. (*bottom*). However, we were able to examine that the operator can properly control the mobile robot along the path using the proposed operation standpoint-based remote operation system as shown in Fig. 6.

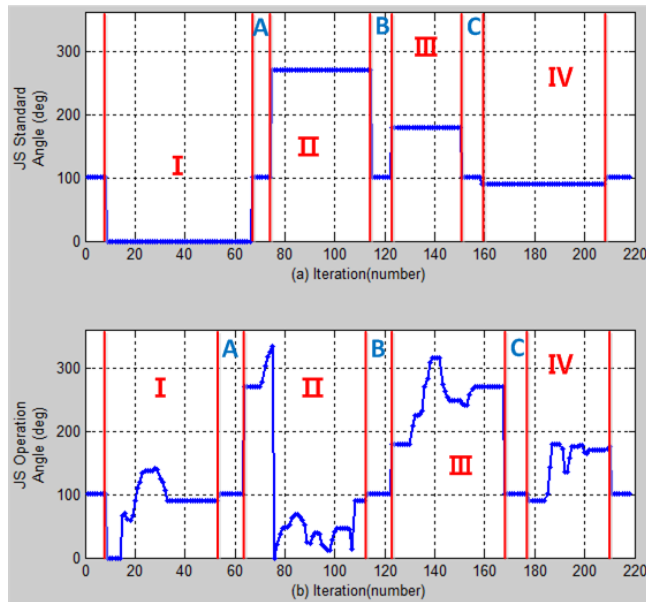


Fig. 5. Experimental results: the performance of the conventional operation with the reference operation pattern (top) and the user's operation pattern (bottom)

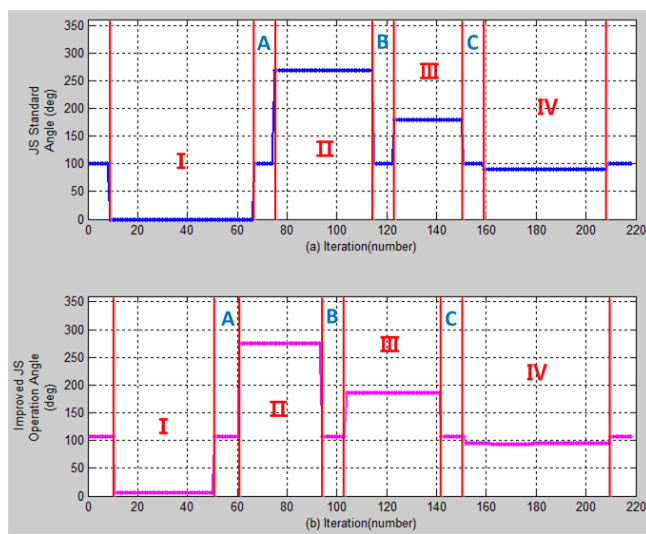


Fig. 6. Experimental results: the performance of the operation using the proposed algorithm with the reference operation pattern (top) and the user's operation pattern (bottom)

5 Conclusion

In this paper, we showed that the proposed operator standpoint-based remote operation system is more efficient than the conventional system in the field of view of the operator. The experimental results have shown the validity and the efficiency of the proposed algorithm. The proposed algorithm can be effectively adapted to the teleoperation system as one of the switching modes for the operation. In the future work, we will improve the remote operation system using the joystick with the yaw motion in order to generate the rotation motion and also propose the modified algorithms that can be applied to the different types of the mobile robot, such as differential-drive, steer-drive, etc.

Acknowledgements. This research has been supported in part by the project ‘Development of inspection equipment technology for harbor facilities’, funded by Korea Ministry of Land, Transportation, and Maritime Affairs and by the ‘Leaders INdustry-university Cooperation’ project, supported by the Ministry of Education, Science & Technology (MEST).

References

1. Siciliano, B., Khatib, O.: *Handbook of Robotics*. Springer (2008)
2. Siegwart, R., Nourbakhsh, I.R., Scaramuzza, D.: *Introduction to Autonomous Mobile Robots*. The MIT Press (2004)
3. Corke, P.I.: *Robotics, Vision and Control*. Springer (2011)
4. Seo, M.J., Yoon, C.M., Heo, J.H., Kim, D.J., Lee, T.H., Ahn, J.W.: Development Joystick controller for Electric Wheelchair. The Korean Institute of Electrical Engineers (KIEE) Electrical Machinery and Energy Conversion Systems Department, pp. 315–317 (2010)
5. Ashmore, M., Barnes, N.: Omni-drive robot motion on curved paths; The fastest path between two points is not a straight-line. In: 15th Australian Joint Conference on Artificial Intelligence, pp. 225–236 (2002)
6. Park, S.J., Jeong, J.S.: A Study on Characteristics of a Terrestrial Magnetism Sensor with Bluetooth. *Information Security Paper* 6(3), 37–47 (2006)
7. Jung, J.B., Shin, W.J., Lee, S.S.: Heading Error Compensation and Navigation Control of Mobile Robot using a Magnetic Sensor. In: 2000 Conf. of the Korea Institute of Signal Processing and Systems, vol. 1(1), pp. 117–120 (2000)
8. Lee, J.H., Jung, S.: Azimuth Tracking Control of an Omni-Directional Mobile Robot (ODMR) Using a Magnetic Compass. *Institute of Control, Robotics and Systems* 15(1), 132–138 (2009)
9. Watanabe, K.: Control of an Omni Directional Mobile Robot. In: *International Conference on Knowledge-Based Intelligent Electronic Systems*, pp. 51–60 (1998)
10. Ojeda, L., Borenstein, J.: Experimental Results with the KVH C-100 Fluxgate Compass in Mobile Robot. In: *IASTED International Conference Robotics and Applications*, pp. 1–7 (2000)
11. Park, G.D., Lee, J.M.: Inclination and Non-horizontal Error Correction of Magnetic Compass by the Law of Gravity. *Institute of Electrical Engineers* 60(3), 606–611 (2011)

Sway Motion Cancellation Scheme Using a RGB-D Camera-Based Vision System for Humanoid Robots

Jeong-Ki Yoo¹, Seung-Beom Han², and Jong-Hwan Kim²

¹ Digital Media and Communications R&D Center, Samsung Electronics,
Suwon 443-742, Republic of Korea

yoojeongki@gmail.com

² Department of Electrical Engineering, KAIST,
291 Daehak-ro, Yuseong-gu, Daejeon 305-701, Republic of Korea
{sbhan, johkim}@rit.kaist.ac.kr

Abstract. When a humanoid robot walks dynamically, it generates sway motion which is reflected as an oscillative sine wave-like pattern at its center-of-mass (CoM) trajectory. In order to cancel out such motion from the coordinates of detected obstacles, this paper proposes a sway motion cancellation scheme incorporated with walking pattern generator of humanoid robots along with a RGB-D camera-based vision system. After the preprocessing for the depth information from the RGB-D camera using attitude reference system (ARS)-generated roll and pitch angles of the vision module, the coordinates of detected obstacles are estimated using the ground filtered 3D points. Then, the sway motion cancellation scheme is applied to the coordinates of detected obstacles not only for the lateral direction of the robot but also for the sagittal one by referring the CoM trajectory collected from the walking pattern generator. The proposed sway motion cancellation scheme and the RGB-D camera-based vision system are verified by experiments using a small-sized humanoid robot, HanSaRam-IX (HSR-IX).

Keywords: Humanoid robot navigation, sway motion cancellation, depth camera-based vision module, RGB-D sensor.

1 Introduction

The researches for humanoid robots have been performed mainly focusing on the walking issues [1–4]. By the virtue of such researches to generate dexterous walking patterns, various fields of researches for mobile robots such as vision processing, navigation, task planning and human-robot interaction, etc. has been employed for humanoid robots [5–8]. In addition, due to the limited capacity of visual perception of humanoid robot, gaze control researches were also performed [9, 10]. There was an approach employing fuzzy measure and fuzzy integral for the gaze control of humanoid robots [11].

Due to the trait of walking process, humanoid robots keep swinging mainly along the lateral direction. For the precise acquisition of information for surrounding environment, such sway motion-originated side effect in the coordinates of objects have to be canceled out in advance before starting the vision processing. If the vision processing

is performed without sway motion cancellation, oscillative CoM patterns would be reflected in each estimated coordinate of a detected obstacle whenever the robot walks. Thus, the sway motion cancellation is the one of essential preprocessing procedures for robust navigation of humanoid robots. Dune et al. proposed a sway motion cancellation strategy for visual servoing [12]. They used the predictive walking pattern generator information as reference signals to cancel out sway motion in Y-axis of HRP-2 robot. Note that they only focused on lateral direction of walking without considering sagittal one. Started from this research, the vision-based 3D model tracking research considering sway motion cancellation was also performed [13]. In the research, the previously proposed sway motion cancellation framework was adopted to match 3D object models with vision information. However, as they did not consider sway motion cancellation in the sagittal direction. Moreover, their approach required a precise prediction model due to the synchronization inaccuracy between components of their navigation system.

This paper proposes a sway motion cancellation scheme incorporated with humanoid walking pattern generation algorithm along with RGB-D camera-based vision system. As a RGB-D camera, a Microsoft Kinect sensor is used in this paper. HSR-IX, which was developed at the Robot Intelligence Technology laboratory, KAIST, uses modifiable walking pattern generation (MWPG) method to generate walking patterns [4, 14]. By using the center-of-mass (CoM) trajectory obtained from the walking pattern generator in the robot, the side effect caused by the sway motion during walking can be canceled out from the coordinates of detected obstacles which are obtained by the RGB-D camera-based vision system. In addition, the proposed sway motion cancellation scheme considers sagittal direction of walking as well as lateral one by The proposed scheme and system are verified by experiments using HSR-IX.

This paper is organized as follows. Section 2 explains how the vision system is implemented using a RGB-D camera. Section 3 presents the proposed sway motion cancellation scheme for humanoid robots. Then, Section 4 describes the result of experiments along with the developed experimental system, and concluding remarks follow in Section 5.

2 RGB-D Camera-Based Vision System

In order to implement a vision system which is capable of providing depth information as well as color information, a RGB-D camera is employed as a vision sensor incorporated with attached ARS sensor to compensate roll and pitch angles of the vision module as shown in Fig. 1 [15–17]. The roll and pitch angles of the vision system against the gravity direction, $\boldsymbol{\theta}_{ars} = [\theta_r, \theta_p]^T$, are used to get rid of the 3D points belong to the ground by compensating the rotation of the vision module [17].

$\boldsymbol{\theta}_{ars}$ is obtained through a Bluetooth connection between the ARS sensor and a Linux-based vision processing server which calculates the coordinates of obstacles using OpenNI and OpenCV libraries [18, 19]. Since the conversion process of a RGB-D point to one in the world coordinate one using OpenNI library have to be applied point by point, it takes about 23 ms for converting a 640 x 480 resolution RGB-D image using an Intel CoreDuo 2.3 GHz computer with 2G RAM. To decrease this world coordinate conversion time, a look-up table for depth conversion is pre-generated and used.

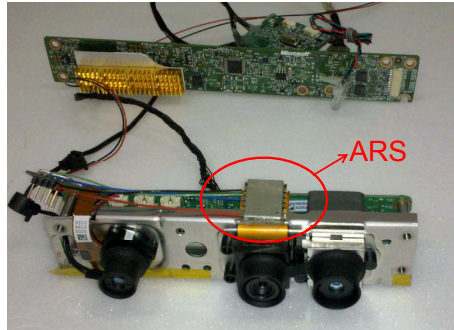


Fig. 1. Vision module with attached ARS sensor

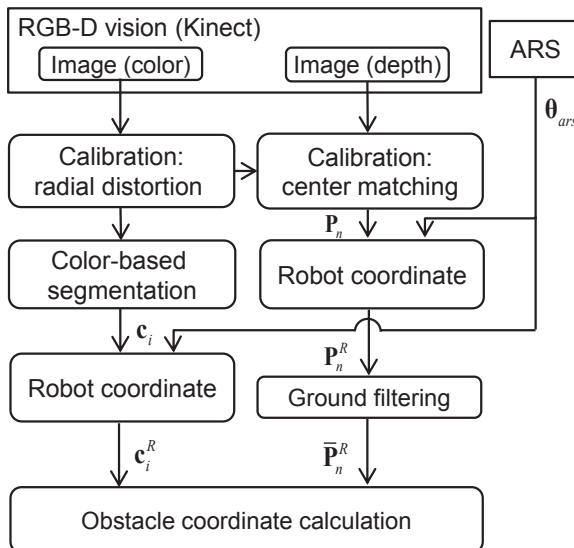


Fig. 2. Vision processing procedure

By using this look-up table approach, depth conversion time for one image could be decreased under 9 ms in average. Fig. 2 describes the vision processing procedure including ground filtering, color-based obstacle detection, and the generation of coordinates for detected obstacles from robot orientation.

After the preprocessing to eliminate the effect of radial distortion using the intrinsic matrix of RGB camera, color-based segmentation with the obstacle color set is performed using equally-spaced seeds for adaptive flooding of segments [19]. Then, the derived center points c_i of thresholded segments are converted to ones in the real world coordinate, c_i^R using the rotation matrix $R(\theta_{ars})$ and the world coordinate generation function of OpenNI [18]. Incorporated with this color image-based process, depth image-based vision processing is also performed simultaneously. Note that the initial

calibration to match the centers of color and depth-based images is performed in advance as shown in Fig. 2. Then the 3D points in the depth image, \mathbf{P}_n , are converted to ones in the robot coordinate system, $\bar{\mathbf{P}}_n^R$ by using the intrinsic parameters obtained from the process of the calibration [20]. After that, the ground points are filtered out to decrease computation time. That is, ones under the threshold are filtered out to obtain obstacle-related 3D points. In case of the HSR-IX, the threshold is set to -52 cm since the height of the robot is 52 cm. After that, the filtered points are moved by 52 cm along the Z-axis in order to compensate for the height of the robot. As a result, 3D points possibly belonging to obstacles, $\bar{\mathbf{P}}_n^R$, could be distinguished from the ground points. Since cylinder-shaped obstacles are used for this system, their center positions could be obtained by using the trait of the shape. The coordinates of obstacles are calculated as follows:

$$\hat{\mathbf{P}}_{o_i}^R = T(\text{mean}(\|\mathbf{Pset}_{o_i}^{near}\|_2), r_{obs}), \quad (1)$$

with

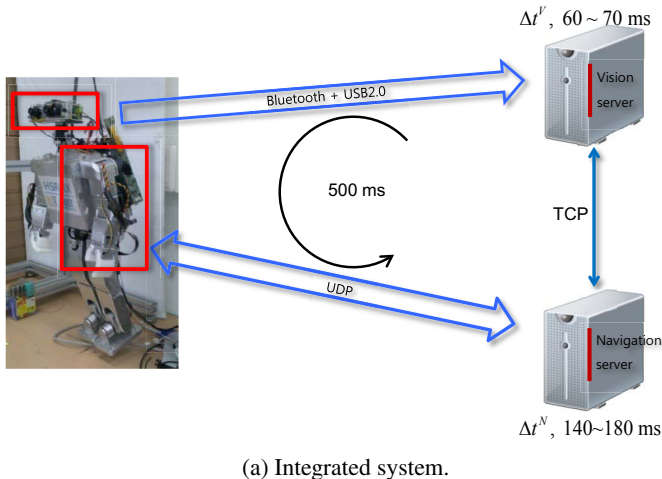
$$\begin{aligned} \mathbf{Pset}_{o_i}^{near} &= \{\bar{\mathbf{P}}_n^R \mid \|\bar{\mathbf{P}}_n^R - \bar{\mathbf{P}}_{c_i}^R\|_2 < \lambda, \bar{\mathbf{P}}_{n_{min}}^R \in \mathbf{A}_i\}, \\ n_{min} &= \arg \min (\|\bar{\mathbf{P}}_n^R\|_2, \bar{\mathbf{P}}_n^R \in \mathbf{A}_i), \\ \mathbf{A}_i &= \{\bar{\mathbf{P}}_n^R \mid \left\| \frac{n}{\mathbf{c}_i^R - \bar{\mathbf{P}}_n^R} \right\|_2 < \alpha r_o, \text{col}(\bar{\mathbf{P}}_n^R) = i\}, \end{aligned}$$

where α is an initial threshold coefficient used for adjusting the boundary to select 3D points of the corresponding obstacle, n_{min} is the index of the nearest point from the robot among \mathbf{A}_i , λ means the small distance threshold for selecting closer points than αr_o , $\text{mean}(\beta)$ calculates the mean coordinate of β , r_o is the radius of obstacles, $\text{col}(C)$ checks the color index of corresponding 3D point C , and $T(D, E)$ translates 3D point D along the direction of E with the additional distance of E . In this paper, α and λ are assigned as 2.0 and 5 cm, respectively.

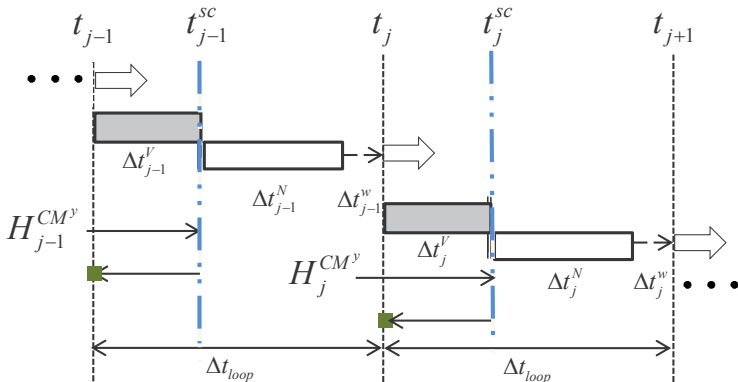
3 Sway Motion Cancellation

Fig. 3 shows the system integration and communication diagrams between servers. To guarantee the constant vision processing period, vision and navigation modules are individually implemented using separate servers. The robot transmits its internal states including the CoM coordinate trajectory and supporting leg information to the navigation server at every 20 ms. This information is used for the sway motion cancellation in Section 4. In Fig. 3b, t_j is the periodic instant at the j th control instant which the vision sensor takes the corresponding RGB-D information, t_j^{sc} is the instant of the sway motion cancellation at the beginning of the navigation process, Δt_j^V , Δt_j^N , and Δt_j^W mean vision processing, navigation and delay periods, respectively. After finishing one loop of the navigation process, the navigation server waits to transmit the corresponding walking command for Δt_j^W to maintain the synchronization between servers.

As shown in the figure, the visual information is periodically acquired at every Δt_{loop} . The navigation server performs sway motion cancellation using Δt_j^V at every t_j^{sc} . After finishing the calculation of navigation process, the navigation module calculates Δt_j^W , and waits to transmit the walking command for the corresponding control period. Through this waiting process, the navigation server can transmit its walking command at every exact control period. In this paper, Δt_{loop} was set to 500 ms to maintain the



(a) Integrated system.



$$\Delta t_j^w = \Delta t_{loop} - (\Delta t_j^V + \Delta t_j^N), \Delta t_{loop} = 500 \text{ ms}$$

	: vision processing time (Δt_j^V)
	: navigation processing time (Δt_j^N)
	: waiting time to transmit a command (Δt_j^w)
	: command to the robot
	: sway motion cancellation instance

(b) Communication diagram of the proposed system.

Fig. 3. Developed system environment

whole processing periods consistent since the processing time periods of vision and navigation servers are not consistent. In order to obtain the exact Y coordinate of CoM of the robot at t_j , CM_j^y , the navigation server retraces the history of CM^y , $H_j^{CM^y}$, from the sway motion cancellation time t_j^{sc} using the vision processing time Δt_j^V . $H_j^{CM^y}$ stores CM^y values received from the robot through an UDP connection.

Though the sway motion-caused side effect for the obstacle detection is mainly shown along the lateral direction of the robot, Y-axis, we can find that the sway motion is also revealed in the X-coordinates of detected obstacles as a smaller oscillative pattern. In the sagittal direction, as described above, the oscillative pattern of X-coordinates for the detected obstacles is mainly caused by the compliance of legs and control inaccuracies. However, since such oscillative pattern is synchronized with CM_j^y pattern, it could be also diminished by using CM_j^y as for the case of lateral direction. Thus, these two directions of sway motion can be considered simultaneously. The sway motion cancellation for the sagittal direction of the robot is performed using the 2nd order polynomial-based estimation for the affect of sway motion according to the distances of obstacles from the robot along the X-axis. This is because the accuracy of 3D coordinate conversion decreases as the distances of the obstacles are increases. By measuring the peak and valley values of the coordinates of detected obstacles, the magnitude of fluctuation synchronized with the sway motion from the robot has been measured. Using the measured coordinates, sway motion in sagittal direction is modeled as 2nd order polynomial as follows:

$$\bar{\mathbf{P}}_{o_j}^R = R(\theta_{j-1}^*)^{-1}\hat{\mathbf{P}}_{o_i}^R - [A_{sag} \ 1]^T CM_j^y \quad (2)$$

with

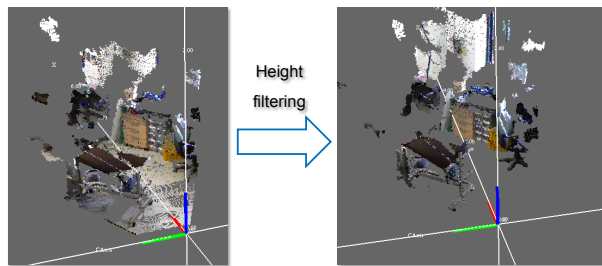
$$A_{sag} = p_1 \hat{x}_{ci}^2 + p_2 \hat{x}_{ci} + p_3,$$

where $\hat{\mathbf{P}}_{o_i}^R = [\hat{x}_{o_j}, \hat{y}_{o_j}]^T$ is the detected coordinates of the j th obstacle, θ_{j-1}^* is the $j-1$ th pan angle θ_{j-1}^* , and $\bar{\mathbf{P}}_{o_j} = [\bar{x}_{o_j}, \bar{y}_{o_j}]^T$ is the finally obtained sway motion canceled coordinates of i th obstacle. $\theta_j^* = [\theta_{P_j}^*, \theta_{T_j}^*]^T$ is the pan/tilt angle for j th period. In this paper, the parameters for the 2nd order polynomial for (2) are assigned as $[p_1, p_2, p_3] = [0.0298, -0.0160, -0.0002]$.

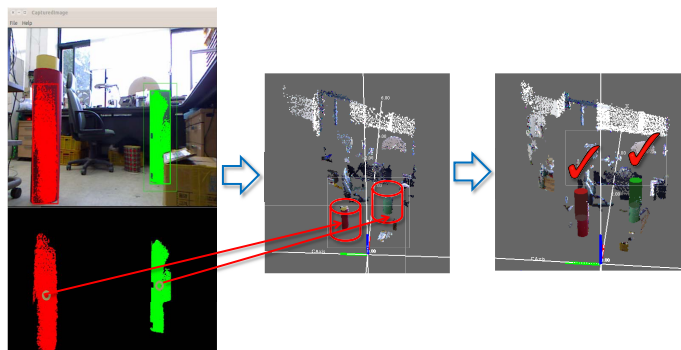
4 Experimental Results

Fig. 4 shows the result of obstacle detection using the proposed vision system. As described in Section 2, after the ground filtering, RGB-D information-based obstacle detection was performed. In the figure, red and green obstacles were denoted using 3D cylinders according to the result of the obstacle detection process.

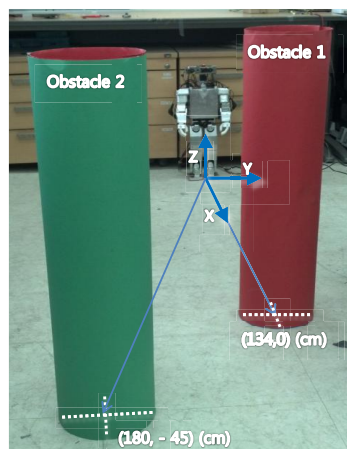
Fig. 5 shows the experimental setup used for sway motion cancellation experiments. As shown in the figure, two obstacles with red and green colors were used for the sway motion cancellation experiments. In order to verify the proposed sway motion cancellation scheme, sway motion cancellation experiment was performed. In the experiment, the robot walked in place along with rotating its panning angle with $20\sin(\pi/33)t_j$ where t_j is the j th time step. Note that, as the tilt angles were compensated by using



(a) Ground filtering process.



(b) Obstacle detection.

Fig. 4. Obstacle detection result**Fig. 5.** Experimental setup for sway motion cancellation

$R(-\theta_{j-1}^*)$ in advance which is described in Section 3, the effect of tilt angle change was not considered in this experiment. Fig. 6 shows the result of the experiment. The truncated periods of x_{o_2} and y_{o_2} in Fig. 6c and Fig. 6d means that the corresponding obstacle was out of sight at that periods. As shown in Fig. 6, the sway motion cancellation scheme was successfully canceled the oscillative pattern in the coordinates of obstacles generated by the sway motion of the robot during walking. As described in Section 4, the sway motion canceled coordinates of obstacles were calculated after the compensation process of head rotation.

The performance of this sway motion cancellation scheme is also verified by comparing the mean values of the maximum variations for each of periods of sway motion canceled and the original coordinates of the two obstacles as presented in Table 1. As presented in the table, the proposed sway motion cancellation scheme was successfully canceled its affect in the coordinates of the obstacles.

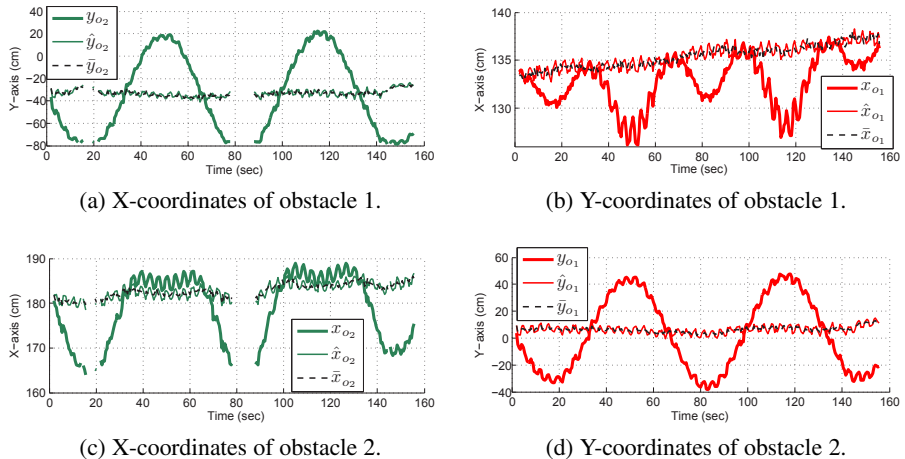


Fig. 6. Initial and sway motion-canceled coordinates of obstacles

Table 1. Statistical result of the mean of the maximum variations for each of periods

	Coordinate	Original (cm)	Sway motion-canceled (cm)	Improvement ratio (%)
Obstacle 1	x	1.409	0.582	41.3
	y	5.976	2.324	38.8
Obstacle 2	x	2.611	0.920	35.2
	y	5.310	2.841	53.5

5 Conclusion

This paper proposed a sway motion cancellation scheme incorporated with the CoM trajectory of the humanoid robot along with a RGB-D camera-based vision processing

module. By using the depth information preprocessed by rotation using the roll and pitch angles from the attached ARS sensor, the obstacle detection and calculation of their coordinates could be performed efficiently. In particular, ground filtering process decreased the number of candidate 3D points for the calculation of obstacle coordinates, and incorporation between color and depth information was effectively considered. Using the developed vision system, sway motion cancellation scheme was applied for the coordinates of obstacles considering the coordinate of CoM. The proposed scheme was verified through experiments using HSR-IX, and showed effective sway motion cancellation performance.

Acknowledgment. This research was supported by Basic Science Research Program through the National Research Foundation of Korea (NRF) funded by the Ministry of Education, Science and Technology (2012-0000150).

References

1. Sakagami, Y., Watanabe, R., Aoyama, C., Matsunaga, S., Higaki, N., Fujimura, K.: The intelligent ASIMO: system overview and integration. Paper presented at IEEE/RSJ International Conference on Intelligent Robots and Systems, pp. 2478–2483 (September 2002)
2. Akachi, K., Kaneko, K., Kanehira, N., Ota, S., Miyamori, G., Hirata, M., Kajita, S., Kanehiro, F.: Development of humanoid robot HRP-3P. Paper presented at IEEE-RAS International Conference on Humanoid Robots, Tsukuba, Japan, pp. 50–55 (December 2005)
3. Yoo, J.-K., Lee, B.-J., Kim, J.-H.: Recent progress and development of the humanoid robot HanSaRam. *Robot. and Auton. Syst.* 57(10), 973–981 (2009), doi:10.1016/j.robot.2009.07.012
4. Lee, B.-J., Stonier, D., Kim, Y.-D., Yoo, J.-K., Kim, J.-H.: Modifiable walking pattern of a humanoid robot by using allowable ZMP variation. *IEEE Trans. Robot.* 24(4), 917–925 (2008), doi:10.1109/TRO.2008.926859
5. Gutmann, J.-S., Fukuchi, M., Fujita, M.: 3D perception and environment map generation for humanoid robot navigation. *J. Robot. Res.* 27(10), 1117–1134 (2008), doi:10.1177/0278364908096316
6. Okada, K., Kojima, M., Sagawa, Y., Ichino, T., Sato, K., Inaba, M.: Vision based behavior verification system of humanoid robot for daily environment tasks. Paper presented at IEEE/RAS Int. Conf. on Humanoid Robot., pp. 7–12 (December 2006), doi:10.1109/ICHR.2006.321356
7. Asfour, T., Azad, P., Vahrenkamp, N., Regenstein, K., Bierbaum, A., Welke, K., Schöder, J., Dillmann, R.: Toward humanoid manipulation in human-centred environments. *Robot. Auton. Syst.* 56(1), 54–65 (2008), doi:10.1016/j.robot.2007.09.013
8. Hale, J.G., Pollick, F.E.: ‘Sticky hands’: learning and generalization for cooperative physical interactions with a humanoid robot. *IEEE Trans. Syst. Man Cybern. C* 35(4), 512–521 (2005), doi:10.1109/TSMCC.2004.840063
9. Seara, J.F., Schmidt, G.: Intelligent gaze control for vision-guided humanoid walking: methodological aspects. *Robot. Auton. Syst.* 48(4), 231–248 (2004), doi:10.1016/j.robot.2004.07.003
10. Yoo, J.-K., Kim, J.-H.: Navigation framework for humanoid robots integrating gaze control and modified-univector field method to avoid dynamic obstacles. Paper presented at IEEE/RSJ Int. Conf. Intell. Robot. and Syst., Taipei, Taiwan, pp. 1683–1689 (October 2010), doi: 10.1109/IROS.2010.5650381

11. Yoo, J.-K., Kim, J.-H.: Fuzzy integra-based gaze control architecture incorporated with modified univector field navigation for humanoid robots. *IEEE Trans. Syst. Man Cybern. B Cybern.* 42(1), 125–139 (2012), doi:10.1109/TSMCB.2011.2162234
12. Dune, C., Herdt, A., Stasse, O., Wieber, P.-B., Yokoi, K., Yoshida, E.: Cancelling the sway motion of dynamic walking in visual servoing. Paper presented at IEEE/RSJ Int. Conf. Intell. Robot. Syst., Taipei, Taiwan, pp. 3175–3180 (October 2010), doi:10.1109/IROS.2010.5649126
13. Dune, C., Herdt, A., Marchand, E., Stasse, O., Wieber, P.-B., Yoshida, E.: Vision based control for humanoid robots. Paper presented at IROS Workshop on Vis. Control of Mob. Robot., pp. 19–26 (2011)
14. Hong, Y.-D., Lee, B.-J., Kim, J.-H.: Command state-based modifiable walking pattern generation on an inclined plane in pitch and roll directions for humanoid robots. *IEEE/ASME Trans. Mech.* 16(4), 783–789 (2011), doi:10.1109/TMECH.2010.2089530
15. Kinect description (2011), <http://en.wikipedia.org/wiki/Kinect> (accessed October 15, 2011)
16. Disassemble process of Kinect (2011), <http://www.ifixit.com/Teardown/Microsoft-Kinect-Teardown/4066/1>(accessed October 15, 2011)
17. MyArs-USB of With Robot (2011),
<http://www.withrobot.com/entry/myARS-USB>(accessed October 15, 2011)
18. OpenNI official web site (2011), <http://75.98.78.94/default.aspx> (accessed October 15, 2011)
19. OpenCV official web site (2011), <http://opencv.willowgarage.com> (accessed October 17, 2011)
20. Burrus, N.: Kinect calibration (2012),
<http://nicolas.burrus.name/index.php/Research/Kinect> (accessed July 17, 2012)

Locomotion of Robotic Fish Using the Univector Field Method in a 3-D Space

In-Bae Jeong and Jong-Hwan Kim

Department of Electrical Engineering, KAIST,
291 Daehak-ro, Yuseong-gu, Daejeon, 305-701, Republic of Korea
{ibjeong,johkim}@rit.kaist.ac.kr

Abstract. This paper proposes a univector field navigation method and a tracking controller for robotic fish locomotion in a three-dimensional space. Univector fields are designed to generate a path to the goal position avoiding obstacle collision. The tracking controller is to convert the direction vector into control signals to track the path obtained from the univector field method. Parameters which are needed for univector field generation and the tracking controller are optimized using Quantum-inspired Evolutionary Algorithm(QEA). The effectiveness of the proposed locomotion algorithm and controller is demonstrated by computer simulation.

1 Introduction

Animals such as birds and fishes have efficient characteristics which are well optimized through evolution, and those characteristics have inspired a lot of robotic researches. Since it is known that locomotion of real fish has higher efficiency compared to propeller-driven underwater vehicle [1], extensive researches about mimicking the propulsion mechanism have been done [2,3,4]. However there are few researches about locomotion of robotic fish in three dimensional space, which involves upward and downward movement as well as planar movement.

In this paper, a locomotion algorithm based on univector field navigation method and the tracking controller are proposed. The proposed univector field generates a path to the goal avoiding obstacles, and the tracking controller converts the vector into actuator signals. Quantum-inspired Evolutionary Algorithm is adopted to optimize parameters to enhance the algorithm and the controller to make an efficient path.

The remainder of this paper is organized as follows. Section 2 introduces preliminaries on the robotic fish Fibo and its simulator, and describes QEA briefly. Section 3 explains how the univector field and the controller are designed. Evaluation function is defined to optimize parameters in this section. The simulation results with the optimized results are shown in Section 4. Conclusions follow in Section 5.

2 Preliminaries

This section describes previous works. Robotic fish Fibo and its specifications are introduced and the hydrodynamic forces used to implement a simulator of Fibo are described. QEA, which is the optimization algorithm used to optimize the parameters for univector field method, is briefly explained.

2.1 Robotic Fish, Fibo

A robotic fish named Fibo was developed in 2010 in the RIT lab., KAIST. Fibo3, the latest version of Fibo, consists of four links connected with three joints as shown in Fig. 1. Fibo is categorized into carangiform using oscillating wing.

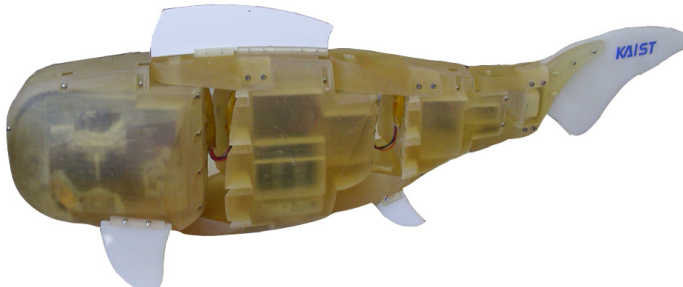


Fig. 1. Fibo3

For fish-like swimming, Lighthill's travelling wave was adopted [5]. The travelling wave equation is as follows:

$$y_{body}(x, t) = (c_1 x + c_2 x^2) \sin(kx - 2\pi f t) \quad (1)$$

To generate sinusoidal signals for the joints of Fibo, a CPG controller was proposed and the parameters of the CPG controller were optimized to track the travelling wave form [6].

Fibo can locate its position from the image captured from the vision sensor. It processes the image to recognize the patterns of markers which are attached to the floor and calculates its position from the information. Fibo detects obstacles using three ultrasonic sensors. It also can submerge using the artificial air bladder, which is made up of a ballast tank and a center of gravity controller. To communicate Fibo uses bluetooth on the surface and low-frequency RF under water. Table 1 shows the specifications of Fibo3.

Table 1. Fibo3 specifications

Size(L × H × W)	105 × 19 × 23 cm
Weight	18.6 kg
Velocity	0.8 BL/s
Sensors	Ultrasonic proximity sensor Vision based localization sensor Inclinometer
Communication	Bluetooth & Low frequency RF

2.2 Fibo Simulator

A simulator for Fibo was implemented on Webots [7] to create and test software for the robotic fish. Webots is a development environment used to model, program and simulate mobile robots. While it supports physical characteristics such as weight, gravity, friction, etc., but does not support hydrodynamic forces. It is needed to implement the physical characteristics to simulate the robotic fish.

To calculate the hydrodynamic forces, the following assumptions are given to simply the modeling [8]:

1. The body of the robotic fish can be considered as N jointed plates.
2. The robotic fish swims in still water and is not affected by reflected waves in the environment.
3. The deformation of the robotic fish can be ignored except for the motion of the joints.
4. The motion is analyzed only in two-dimensions, which is the most important propulsion situation.

The forces acting on a link are buoyancy and drag force, and the drag force is divided into three forces: pressure on the link, approach stream pressure, and friction drag.

The buoyancy force is applied in the opposite direction to gravitational force and the magnitude is:

$$\mathbf{B} = -V_{body,i} \cdot \rho_{water} \cdot \mathbf{g} \quad (2)$$

where $V_{body,i}$ is the volume of the i th link, ρ_{water} is the density of water, and \mathbf{g} is the gravitational acceleration.

The pressure force acting on the i th link is as follows:

$$\mathbf{F}_i^\perp = -\frac{1}{2} \cdot \rho_{water} \cdot C_d \cdot A_i^\perp \cdot \mathbf{v}_i^\perp |\mathbf{v}_i^\perp| \quad (3)$$

where C_d is the drag coefficient, A_i^\perp is the effective area, and v_i^\perp is the perpendicular velocity.

The approach stream pressure and the friction force are

$$\mathbf{F}^\parallel = -\frac{1}{2} \cdot \rho_{water} \cdot C_L \cdot A^\parallel \cdot \mathbf{v}_0^\parallel |\mathbf{v}_0^\parallel| \quad (4)$$

$$\mathbf{F}_i^\parallel = -\frac{1}{2} \cdot \rho_{water} \cdot C_f \cdot A_i^\parallel \cdot \mathbf{v}_i^\parallel |\mathbf{v}_i^\parallel| \quad (5)$$

where C_L and C_f are the drag coefficients, A and A_i^\parallel are the effective areas, and v_i^\parallel is the velocity along the parallel direction where the robotic fish is heading.

The hydrodynamic forces were implemented in Webots using Physics plugins. Fig. 2 shows the simulated environment and Fibo.

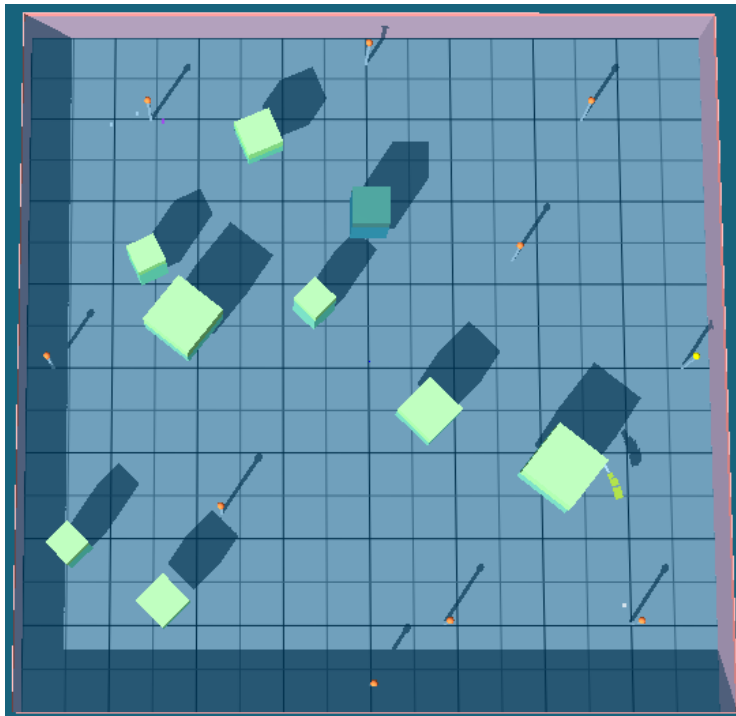


Fig. 2. Fibo simulator

2.3 QEA

Quantum-inspired evolutionary algorithm (QEA) is an evolutionary algorithm based on the concept and principles of quantum computing. QEA uses Q-bit as the smallest unit of information instead of binary bit. Q-bit is defined as a pair of numbers, (α, β) , which satisfies $|\alpha|^2 + |\beta|^2 = 1$. $|\alpha|^2$ and $|\beta|^2$ represent probabilities of Q-bit being observed in ‘0’ and ‘1’ state, respectively. A Q-bit individual is defined as a string of Q-bits as

$$\left[\begin{array}{c} \alpha_1 | \alpha_2 | \dots | \alpha_m \\ \beta_1 | \beta_2 | \dots | \beta_m \end{array} \right] \quad (6)$$

where m is the number of Q-bits.

The QEA procedure is described in Algorithm 1.

Since the Q-bit individual represents linear superposition of all possible states probabilistically, more diverse individuals are observed during the process and therefore QEA is able to explore the search space with a small number of individuals. The detailed explanations of QEA and its structure are described in [9].

```

begin
     $t \leftarrow 0$ 
    initialize  $Q(t)$ 
    make  $P(t)$  by observing the states of  $Q(t)$ 
    evaluate  $P(t)$ 
    store the best solutions among  $P(t)$  into  $B(t)$ 
    while not termination-condition do
         $t \leftarrow t + 1$ 
        make  $P(t)$  by observing the states of  $Q(t - 1)$ 
        evaluate  $P(t)$ 
        update  $Q(t)$  using Q-gates
        store the best solutions among  $B(t - 1)$  and  $P(t)$  into  $B(t)$ 
        store the best solution  $b$  among  $B(t)$ 
        if migration-condition then
            | migrate  $b$  or  $b_j^t$  to  $B(t)$  globally or locally, respectively
        end
    end
end

```

Algorithm 1. QEA Procedure

3 Univector Field Navigation Method for Fibo

3.1 Univector Field Generation

A univector field N for the robot navigation is defined as [10]

$$N : W \longrightarrow I \quad (7)$$

where W is the workspace of Fibo in R^3 and I is a set of unit vectors with arbitrary directions. These unit vectors are used as the desired heading direction of Fibo. Since the magnitude of the vectors in the field is assumed to be unity at all points, the univector field N can be represented in terms of its angles as follows:

$$F : W \longrightarrow \begin{bmatrix} \theta \\ \phi \end{bmatrix} \quad (8)$$

where θ is the polar angle and ϕ is the azimuthal angle. The ranges of θ and ϕ are $[-\pi, \pi]$ and $[0, 2\pi)$, respectively.

In this paper, two types of univector fields are used: base univector field(BUF) and avoiding univector field(AUF). BUF makes the robot move to the destination and defined simply as follows:

$$F_{BUF}(\mathbf{p}) = |\mathbf{g} - \mathbf{p}| \quad (9)$$

where \mathbf{p} is the current position of Fibo and \mathbf{g} is the goal position.

AUF is the essential part for obstacle avoidance of Fibo. For each obstacle, repulsive force is applied along the perpendicular direction to the surface of the obstacle. AUF for the i th obstacle O_i is defined as:

$$F_{AUF_i}(\mathbf{p}) = \begin{cases} \hat{\mathbf{n}} & \text{if } D_i(p) < R \\ \mathbf{0} & \text{otherwise} \end{cases} \quad (10)$$

where $\hat{\mathbf{n}}$ is the normal vector, $D_i(p)$ is the distance between the position p and the obstacle O_i , and R is the effective radius that repulsive forces affect.

It is needed to determine an appropriate R to generate an avoiding path. A colliding path will be generated if R is too small. If R is too large, a long way around will be generated.

The final univector field is obtained by compositing BUF and AUFs.

3.2 Univector Field Tracking Controller

A tracking controller is needed to track the univector field. Fibo needs three control signals: turning angle, slope, and buoyancy.

The turning angle signal changes the heading angle of Fibo. The slope signal determines the inclination of Fibo so that it goes upward or downward when it is swimming forward. The buoyancy signal controls the ballast tank. It is used when Fibo is not swimming but it needs to sink or float.

Let \mathbf{g} be the goal position, \mathbf{p} and \mathbf{p}_s the current position and the posture of Fibo, respectively, $F(\mathbf{p})$ the vector obtained from the univector field,

$$\mathbf{g} = [g_x, g_y, g_z]^T \quad (11)$$

$$\mathbf{p} = [p_x, p_y, p_z]^T \quad (12)$$

$$\mathbf{p}_s = [\theta_p, \phi_p]^T \quad (13)$$

$$F(\mathbf{p}) = [\theta_d, \phi_d]^T \quad (14)$$

The signals are given as follows:

$$S_{turn} = K_t \cdot (\phi_d - \phi_p) \quad (15)$$

$$S_{slope} = K_s \cdot \theta_d \quad (16)$$

$$S_{buoyancy} = K_b \cdot (\theta_d - \theta_p) \quad (17)$$

where K_t is the turning coefficient, K_s is the slope coefficient, and K_b is the buoyancy coefficient.

The coefficients should be well chosen since the coefficients determine the tracking performance.

3.3 Optimization of Controller Parameters

There are four parameters which need optimization: three for the tracking controller and one for AUF. Since QEA uses a string of Q-bits, it is needed to set the numbers of Q-bits and range for each parameter. The number and the range for each parameter is as shown in Table 2.

Table 2. Parameters to be optimized

Parameter	Number of bits	Range
K_t	8	[0, 2]
K_s	10	[0, 10]
K_b	10	[0, 10]
R	8	[0, 2]

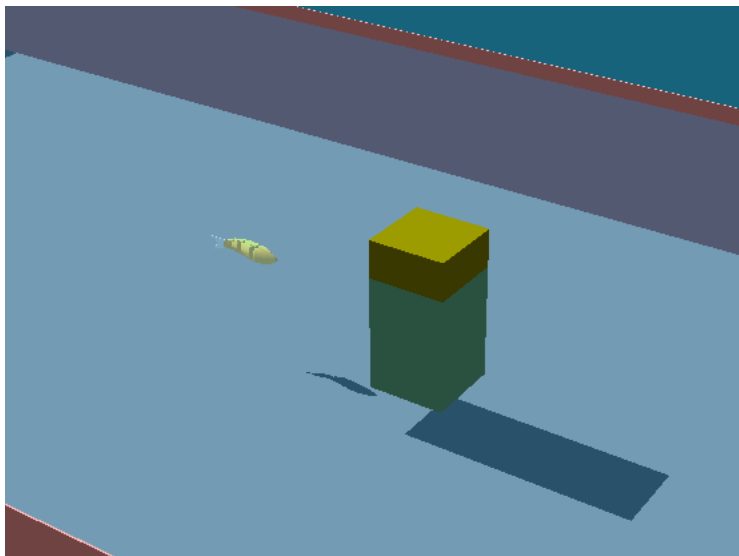
To evaluate an individual, two environments are used. One environment has no obstacle and the other has a blocking obstacle between Fibo and the goal. The initial position of Fibo is set to $[0, 0, 0]^T$ and the goal position is set to $[5, 0, -1]^T$.

The evaluation function for an individual x is defined as follows:

$$\begin{aligned} e(x) = & T_o\left(\frac{\pi}{4}\right) + T_o\left(\frac{\pi}{2}\right) + T_o\left(\frac{3\pi}{4}\right) + T_o(\pi) \\ & + T_b\left(\frac{\pi}{4}\right) + T_b\left(\frac{\pi}{2}\right) + T_b\left(\frac{3\pi}{4}\right) + T_b(\pi) \end{aligned} \quad (18)$$

where $T_o(\phi)$ and $T_b(\phi)$ are the measured times to reach to the goal for the initial posture $[0, \phi]$ in each environment. If $e(x) < e(y)$, x is a better individual than y .

Fig. 3 shows the environment which has an obstacle.

**Fig. 3.** Environment with an obstacle

4 Experimental Results

Using QEA optimization, the optimized values for the parameters were obtained as shown in Table 3.

Table 3. Optimized values of parameters

Parameter	Optimized value
K_t	2.00
K_s	3.63
K_b	8.07
R	0.49

Setting the optimized values to the univector field and the tracking controller, Fibo followed the path and reached the goal position. The trajectories of Fibo with each initial posture are shown in Fig. 4

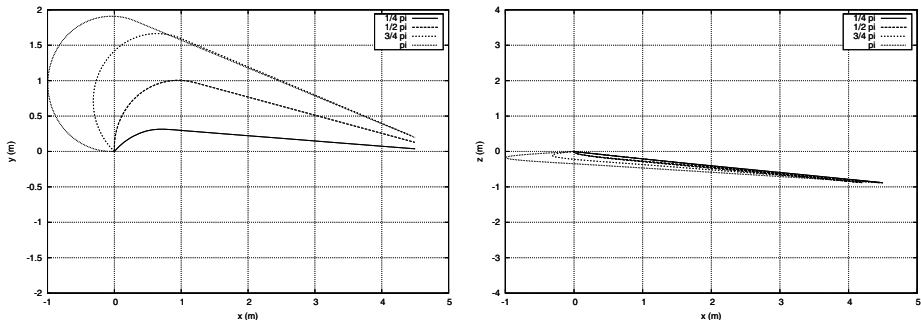


Fig. 4. Trajectories without obstacle

During optimization, K_t tended to be optimized to the maximum value in the given range. Since K_t is a major factor which determines the maneuverability, Fibo turned to the direction heading to the goal more quickly with larger K_t . Fig. 5 shows the effect of K_t . However, as K_t increases, Fibo began to oscillate when it is heading directly to the goal position. The oscillation did not affect the elapsed time to reach the goal, but It is needed to choose K_t heuristically for natural movements.

Obstacle avoidance is shown in Fig. 6. The circle represents an obstacle. It is shown that Fibo reached the goal avoiding the obstacle. Note that Fibo took a long way around the obstacle when the initial posture is $\pi/4$, since Fibo is not able to rotate without translational movement.

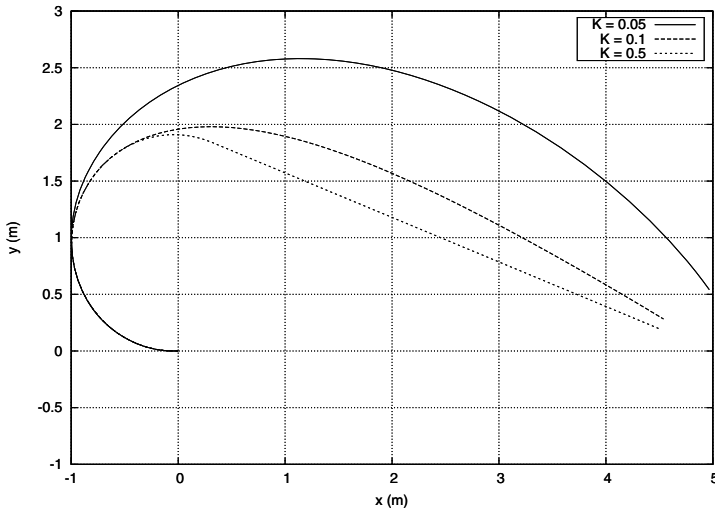


Fig. 5. Trajectories for different K_t

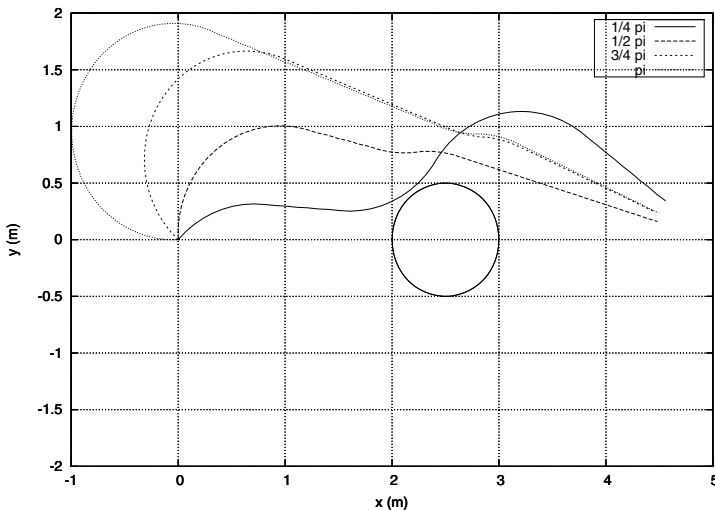


Fig. 6. Obstacle avoidance

5 Conclusion and Further Works

In this paper, univector field and tracking controllers were proposed for the locomotion of the robotic fish, Fibo in a three-dimensional space. Univector field was designed to generate a heading direction to the desired position and the tracking controllers were implemented to track the path obtained from the univector field. To generate an effective path, parameters for the univector field and the controllers were optimized with QEA.

Simulation results confirmed that Fibo moved to the goal position avoiding obstacle collision with the proposed navigation method.

The proposed navigation method is easy to implement and runs fast, but it inherits the problems of potential field methods such as local minimum and dead-lock state. Hybrid navigation method which is integrated with global navigation algorithms shall be researched as a further work. Furthermore, improving AUF is needed to reduce detour and a navigation algorithm which predicts the position of moving obstacles and avoids the obstacles shall also be researched.

Acknowledgement. This research was supported by the MKE (The Ministry of Knowledge Economy), Korea, under the Human Resources Development Program for Convergence Robot Specialists support program supervised by the NIPA (National IT Industry Promotion Agency) (NIPA-2012-H1502-12-1002).

References

1. Triantafyllou, M.S., Triantafyllou, G.S.: An efficient swimming machine. *Scientific American* 262(3), 40–48 (1995)
2. Sfakiotakis, M., Lane, D., Davies, J.: Review of fish swimming modes for aquatic locomotion. *IEEE J. Oceanic Engineering* 24(2), 237–252 (1999)
3. Kato, N.: Control performance in the horizontal plane of a fish robot with mechanical pectoral fins. *IEEE J. Oceanic Engineering* 25(1), 121–129 (2000)
4. Yu, J., Tan, M., Wang, S., Chen, E.: Development of a biomimetic robotic fish and its control algorithm. *IEEE Trans. Systems, Man, and Cybernetics - Part B: Cybernetics* 34(4), 1798–1810 (2004)
5. Lighthill, M.J.: Note on the swimming of slender fish. *J. Fluid Mechanics*, doi:10.1017/S0022112060001110
6. Jeong, I.-B., Park, C.-S., Na, K.-I., Han, S., Kim, J.-H.: Particle Swam Optimization-based Central Pattern Generator for Robotic Fish Locomotion. In: Proc. IEEE Congress on Evolutionary Computation (2011)
7. Michael, O.: Webots: Professional Mobile Robot Simulation. *Int. J. Advanced Robotic Systems* 1(1), 39–42 (2004)
8. Zhou, C., Hou, Z.-G., Cao, Z., Wang, S., Tan, M.: Motion modeling and neural networks based yaw control of a biomimetic robotic fish. *Information Sciences*, doi:10.1016/j.ins.2011.02.015
9. Han, K.-H., Kim, J.-H.: Quantum-Inspired Evolutionary Algorithm for a Class of Combinatorial Optimization. *IEEE Trans. on Evolutionary Computation* 6(6), 580–593 (2002)
10. Kim, Y.-J., Kim, J.-H., Kwon, D.-S.: Evolutionary Programming-Based Univector Field Navigation Method for Fast Mobile Robots. *IEEE Trans. on Systems, Man, and Cybernetics - Part B: Cybernetics* 31(3), 450–458 (2001)

Humanoid Interface for Artificially Intelligent Role-Based Game Playing

Lisa J. Golden, Zachary T. Golden, James Michael McAtee, and Eric T. Matson

M2M Lab/RICE Research Center
Department of Computer Information Technology
Purdue University, West Lafayette, IN, USA
`{lpliu, zgolden, ematson}@purdue.edu, jmmcater@gmail.com`

Abstract. Innovations of technology can change the way humans interact with their world. The demand for robotic technology is not exclusively influenced by the component specifications of what a robot is built of, but instead driven by the applications and potential of a robot. Humanoid robots are the best interface for human and robotic interaction because they are ergonomically designed to physically mimic a person thereby benefiting mankind by having the potential to physically operate in an environment designed for society. Moreover, humans are more apt to treat humanoid robots as companions because humans are more likely to project a personality onto the robot. This paper attempts to explore two topics: the advantages of entertainment based applications for humanoids as a vehicle for role-based game playing, and exploring the model for humanoid interaction with either a human adversary or a humanoid adversary. This paper also mentions entertainment based application implementations on systems with limited resources. We utilized the DARwIn-OP as a vehicle to demonstrate a fundamental application of basic artificial intelligence. In playing the role-based game of tic-tac-toe, we created a model for human to humanoid robot interaction as well as humanoid robot to humanoid robot interaction.

Keywords: role based game playing, tic-tac-toe, artificial intelligence, humanoid interaction, multi-agent systems.

1 Introduction

Humanoid robots are the best robotic interface for human to robot interaction because humanoid robots have the ability to convey more meaningful and complex information to the human in comparison to a traditional modern computer such as a desktop. Humanoid robots also have the potential to be ideal for environments ergonomically designed for human operation because they are physically similar to a person. As a result, the incorporation of humanoid robots into our world leads to tremendous possibilities. Research has been done towards the advancement of humanoid robot technology by creating function orientated humanoid robots and entertainment orientated humanoid robots. These humanoid robots are valuable to our society because humans prefer robots with lifelike human features and are therefore

more willing to treat humanoid robots as a companion instead of an object, facilitating their adoption into human society [11].

This paper examines humanoid robot interaction with either a human or a humanoid as adversaries in role-based game play. In order to demonstrate this application, an physically-interfaced, role-based game of tic-tac-toe is implemented. The DARwIn-OP, the humanoid player in this application, is an intelligent agent that must evaluate its environment in order to determine the best playing move to maximize its goal of winning the game. This research explore the advantages of entertainment based application design on humanoid robots, explore the model for humanoid robot interaction with both human and humanoid robot adversaries, and discuss the implementation heuristics of tic-tac-toe and how their correlate with function on a system with limited resources.

There are two goals of this paper. The first goal is to attempt to examine the advantages of an entertainment focused application designed on humanoid robots as the vehicle for role-based game playing. The second goal of this paper is to create a model for humanoid robot interaction with adversaries in the form of either a human or robotic opponent. Additionally, this paper mentions considerations for implementing entertainment based applications on systems with limited resources. These goals are central to maximizing the potential of a humanoid robot and must be considered when designing an entertainment based application.

In section 2 background material is described. Section 3 shows the combination of intelligent agents and the play of tic-tac-toe. Section 4 describes the realization of the system built to evaluate this research. Section 5 draws conclusions of this research.

2 Background

2.1 Related Works

Several organizations and research groups have been interested in humanoid robots in the development of function orientated applications or entertainment based companionship applications. Humanoid robots have the ability to communicate complex and detailed information in ways that other forms of modern technology such as personal computers cannot because humanoid robots can pass on information through body language. Body language is interpretable by humans and can be used with function based robots to assist people in daily tasks, or to add entertainment value to companionship based robots, such as with instrument playing [13][14] or dancing [15].

Body language in function based robots can encourage a consumer to interact with the humanoid robot. Honda Corporation has developed a function based robot named ‘Domestic Robot’. ‘Domestic Robot’ was designed to model a butler, conquering navigation and traversal challenges that are necessary to move through a home. ‘Domestic Robot’ could climb stairs, move in any direction, and maintain balance on

uneven surfaces [4]. While a functioning butler-type robot and applications built on the robot could be of interest to society, the robot must be extremely accurate in its traversal else the robot could endanger the safety of humans around the robot.

A more feasible way to utilize humanoid robots in society is developing entertainment and companionship focused applications for humanoids. Entertainment and companionship focused applications have been previously popular for other lifelike robots. AIBO (Artificially Intelligent roBOt) not only looks like a robotic dog, but also has programmed dog-like body language. Researchers that developed AIBO confirmed that humans were more likely to project ‘living’ characteristics on robots exhibiting life-like characteristics than a different type of robot [5]. Therefore, it would not be absurd to assume that humans would project lifelike qualities on humanoid robots as well.

Body language expression for humanoid robots also may include facial body language. Research in humanoid advancement has also been done in facial expression development. The inclusion of facial expression to body language is excellent for the human-robotic interface as it increases the functionality of body language communication. Research at MIT led to the development of a robot named KISMET which has the ability to change gaze direction, control ‘facial expression’ and body posture, and voice quality [7]. Additional levels of communication may benefit companionship based applications for humanoids because a human may feel more entertained by playing with facially expressive robots.

2.2 Human to Robot Social Interaction and DARwIn-OP

Personality is essential for socially interactive robotics because personality gives humans the feeling of social presence [2]. Research has also shown that humans enjoy interacting with robots exuding a playful personality [3]. In order for humanoids to be successful in entertainment and companionship applications, humans must be encouraged to interact with the robot. Natural cues such as gaze and gesture is critical for social humanoid to human interaction because humans already understand these behaviors and can react accordingly [2][6][7]. To create a personality for our game contestant, we focused on the development of body language via manipulation of limbs and gaze direction.

The DARwIn-OP, acronym for *Dynamic Anthropomorphic Robot with Intelligence-Open Platform* is an excellent humanoid robot model for the development of entertainment and companionship focused applications. The DARwIn-OP, shown in Figure 1, enables for the modification of software as well as hardware for research or application development. Development to create a personality on DARwIn-OP can integrate sound and vision capabilities, motion management, wireless communication, and force sensing resistors located in specially purchased feet [8]. These sensor and actuator networks allow for complex demonstrations of game play possibilities and methods of human to robot interaction.



Fig. 1. DARwIn humanoid robot (ROBOTIS)

2.3 Tic-Tac-Toe with Limited System Resources

One of the most fundamental ways demonstrating basic artificial intelligence is the implementation of tic-tac-toe [10]. Tic-tac-toe, also known as ‘Noughts and Crosses’ is a popular game played by two adversaries. The game is played with an initially empty 3x3 grid. Each player is represented by a unique marking to indicate their positions in the game. This role-based game rotates in turn after a player makes a single movement choice. The goal of the game is to have three of the player’s unique markings placed consecutively with each other in the grid either horizontally, vertically, or diagonally. This game utilizes artificial intelligence because each robot must evaluate their environment and make a decision that maximizes their probability of reaching their goal. Figure 2 shows the tic-tac-toe board being utilized in a game of two DARwIn robots.

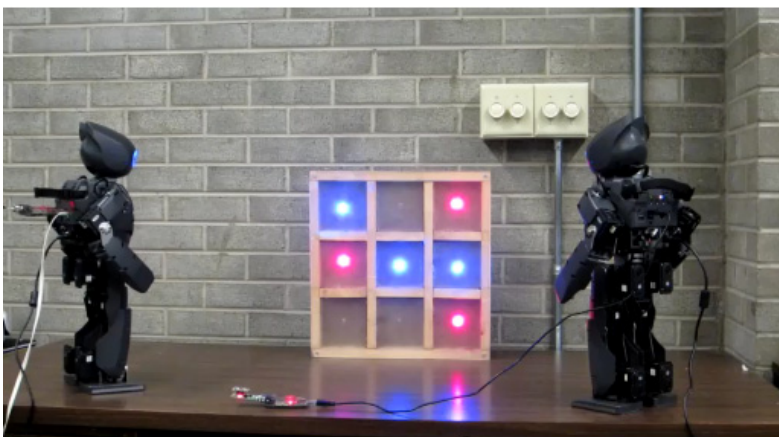


Fig. 2. DARwIn's playing tic-tac-toe

Humanoid robots may have limited system resources when compared to the resources available to a desktop computer. This paper discusses a good heuristic, defined in this paper as a heuristic that always accomplishes its goal for tic-tac-toe on a system with limited resources. Heuristics for role-based game play must take in account the available RAM, hard disk space, and lower clocking speed of humanoid systems. For the game of tic-tac-toe, there are many existing heuristics that vary in space and time complexity for that guarantee an agent win. For humanoid robot game application development, the best heuristic for game play is the heuristic that is most good while running smoothly on the system.

3 Intelligent Robotic Agents and Tic-tac-toe

From the point of view of the audience, the humanoid robot intelligent agents behave as rational agents in their environment; each determining the most advantageous playing choice to meet their goal of winning the game. Tic-tac-toe is one of the most fundamental ways to demonstrate artificially intelligent adversarial game play, due the simple environment and limited resource requirements, of the game. Everything that concerns the humanoids in relation to meeting its performance goal is completely accessible and plainly displayed on the tic-tac-toe board. In this straightforward, deterministic environment, each decision made by the agent is entirely a result of the agent's percept sequence. The environment remains static while the agent is deliberating, therefore the agent does not need to continuously update its sensors while deciding on a move. The number of moves an agent must consider is discrete as there a limited amount of unoccupied playing locations on the board. Depending on the algorithm used to implement tic-tac-toe, this application could be written episodically, only evaluating and making a decision based on the current game state, or non-episodically, keeping track of future game states in order to make a decision.

A multi-agent environment must take the actions made by both intelligent agents into account. Each intelligent agent uses sensors to perceive its environment. In this case, the environment includes the locations representing movement decisions made by the adversary and the agent as well unoccupied playing locations on the board that the agent must consider when deliberating its next turn. In order for the agents to affect their environment, each agent must notify the board and the opponent agent of its movement choice and update the percept sequence.

In the application model described in this paper, when two DARwIn-OP take roles as adversaries, each agent views its environment differently. Our model is implemented with a master-slave relationship: the master determining the best possible move for itself by evaluating its percept sequence, afterwards determining the best possible move for its opponent. Once the move for its opponent has been determined, the master communicates the move to the slave. The master and slave take action on their environment by wirelessly communicating with the board. This gives the audience the illusion of completely separate humanoids playing against each other. While the environment is still accessible, deterministic, static, and discrete, the master is the only intelligent agent. The board and the slave are not intelligent agents because they do not make intelligent decisions; only react to information passed to them.

When a DARwIn-OP plays against a human, the humanoid is the intelligent agent. In our model, the human communicates with the humanoid by typing on a computer that sends a wireless message to the humanoid and the board. The humanoid communicates to the human by communicating to the board to light up the appropriate location. The human can then look at the game environment and determine what movement choice the humanoid made. The environment is still accessible, deterministic, static, and discrete.

The robotic-based intelligent agents added entertainment value by incorporating body language. When an agent evaluated the game state and determined that it was in a position to win, the agent performed a designated win stance and nodded its head to signal triumph. When the humanoid agent evaluated the game state and determined that it was in a position to lose, the agent collapsed to its knees and bowed its head downwards to defeat. When the game resulted in tie, or referred to in tic-tac-toe as a ‘cat’s game’, the agents bowed once to signal a ‘good play’.

4 Realization

The application was constructed using two DARwIn-OP humanoid robots. These robotic agents communicated with each other and a separately designed board using ZigBee communication. Each intelligent agent contained a copy of the tic-tac-toe algorithm as well as the ZigBee communication protocol. When the application began, one of the humanoid robots would designate itself as the master player and designate the other humanoid robot into being the slave. Appropriate portions of the program code were activated respectively for the master and slave agent. The master made a play by determining the best move for itself and acting on its environment by updating its percept sequence. The master determined the best move for its opponent and updated its percept sequence accordingly. The board accepted ZigBee input from the agents and lit up the appropriate board square with a color representing input from each agent.

The board, shown in Figure 2, is designed with one ATMEGA 128, 8 bit microprocessor available from ATMEL Co., 1 ZigBee receiver, 9 *super bright* red LEDs, 9 *super bright* blue LEDs, and two power regulators: one for the ATMEGA 128 and one for the ZigBee receiver. One pair of super bright red and blue LEDs was placed in each square of the tic-tac-toe grid. The ZigBee receiver received input from the master agent and the slave agent and passed information into the ATMEGA 128 chip to light up the appropriate square with the appropriate LED. The board served no other function other than to communicate the state of the game with the human adversary or the audience. The intelligent agent held their own internal representation of the board which updated when the agent updated their percept sequence.

This project implemented a real entertainment and companionship application for a humanoid robot. In this research, a real application is better than a theoretical model because real applications must account for everything present in the agent environment for functionality, thereby being accurate in design. Body language associated with agent movement accessed human attraction and movement popularity, and our models had to be robust in wireless communication due to surrounding wireless interference to avoid miscommunications.

4.1 Tic-Tac-Toe Heuristics

The application was designed episodically because it simplified the environment for the intelligent agent. The goal of our agents is to play a good game of tic-tac-toe. ‘Good’ being defined as the agent reaching its goal where the initial player will either win or tie with the adversary.

The algorithm consists of three main consecutive steps:

- Test for the goal move for the playing agent win
- Test for a move to prevent the opponent from winning
- Assign a random movement based on prior knowledge of movement choices which maximize the probability of an agent win.

Note: If a movement choice for a step is determined, the following steps are not considered.

Prior knowledge of movement choices that maximize the probability of the playing agent win simplifies the algorithm because it prunes the algorithm from deliberating spaces that are less productive to an agent win. In this case, it also prevents the agent from having to compute a search tree to identify all possible game states that could take place from the considering game state. All squares in the tic-tac-toe grid do not have equal probability for being supportive to a game win. For example, the center square gives the greatest probability for an agent win because there are four ways for three consecutive placements of the agent mark: middle-horizontal, middle-vertical, left-diagonal, and right-diagonal. All squares have certain probabilities in participating in an agent win, and the squares with the greatest probabilities are the randomly assigned movement choice in the third step.

Another heuristic for tic-tac-toe construction generates a search tree detailing every possible combination of game states that could result from each episode in the game. This algorithm is also known as ‘minimax’. The minimax heuristic has the advantage of allowing the agent to play a good game of tic-tac-toe without having prior statistic about the probabilities of winning in each board location. The algorithm generates a search tree during every turn from the current episode to the terminal state of the board. The terminal states are evaluated and utility values are assigned during the generation of the algorithm to determine the best movement choice.

An agent implementing our algorithm is not an ideal rational agent, while the agent that uses the minimax algorithm to generate an entire search tree can be an ideal rational agent. An agent implementing our algorithm might choose to move into a square that is not immediately in the best interest of the agent such as the following case: The movement for the X player in the third game grid is not ideally rational because moving in the corner-left space does not increase the utility for the X agent in terms of winning. However, these game choices will still lead to a good game because a movement choice such as the one indicated in the third grid can only be chosen after the agent determined that neither the opponent nor it could make a move to win the game. Movements such as these increase the possibility of a tied game but will not contribute to an opponent win. The minimax algorithm allows the agent to be ideally rational because it uses utility values from every possible game state to determine the next best move.

4.2 Hardware Consideration

The minimax algorithm would be acceptable to implement for a game of tic-tac-toe on the DARwIn-OP due to the small possibility of states, however the heuristic used in games that generate a multitude of possibilities are entirely dependent on the system resources of the platform.. Deep Blue had advanced evaluation hardware that achieve search speeds of 500,000 positions to 700,000 positions per second. [1] The same algorithm could not be used with the DARwIn-OP and produce the same result. Another major limitation in hardware for any robotic system is energy consumption. For example, robotic movement and gesticulation such as walking requires continuous movement with bent knees, therefore continuously loading motors [3]. Entertainment applications must also take in account how much power a humanoid is capable of expending in the time it takes to play a role based game application.

5 Conclusion

This paper attempts to explore the advantages of entertainment based application for humanoids as a vehicle for role-based game playing, designing game play applications on a system with limited resources, and exploring the model for humanoid interaction with either a human adversary or a humanoid adversary. Humanoids are the best interface for human to robot communication because humans are more likely to be social with humanoids. Humanoids can also communicate with humans in a more complex manner than another type of machine. Adapting heuristics to humanoid system specifications must be considered when building applications for current humanoids because more affordable humanoids tend to have more limited computational power when compared to the average desktop computer. Humanoids and humans can communicate through several methods: an intermediary that processes communication between the human and the humanoid, or the human and humanoid can directly communicate depending on the sensor capabilities of the robot.

Entertainment based applications have an obvious usefulness in game applications. However, entertainment focused applications can have other benefits to society as well. In a study conducted with children with autism, children with autism related social difficulties were more willing to collaborate with adults after playing with a child-like humanoid robot Kaspar [12]. Entertainment focused humanoids can benefit society not only by being pleasurable and fun, but can also serve as an aid and interaction interface to those who perceive social collaboration as difficult.

References

1. Campbell, M., Hoane Jr., A., Hsu, F.: Deep Blue. *Artificial Intelligence* 134, 57–83 (2002)
2. Lee, K., Peng, W., Yan, C.: Can Robots Manifest Personality?: An Empirical Test of Personality Recognition, Social Responses, and Social Presence in Human-Robot Interaction. *Journal of Communication*, ISSN 0012-9916
3. Yamasaki, F., Hosoda, K., Asada, M.: Consumption Based Control for Humanoid Walking. In: Intl. Conference on Intelligent Robots and Systems (October 2002)

4. Harai, K., Hirose, M., Haikawa, Y., Takenda, Y.: The Development of Honda Humanoid Robot. *Robotics and Automation* 2, 1321–1326 (1998)
5. Fujita, M.: On activating human communications with pet-type robot AIBO. *Proceedings of the IEEE* 92(11), 1804–1813 (2004)
6. Takanori, S.: An Overview of Human Interactive Robots for Psychological Enrichment. *Proceedings of the IEEE* 92(11), 1749–1758
7. Breazeal, C.: Emotion and Sociable Humanoid Robots. *Journal of Human-Computer Studies* 59(1-2), 119–115, ISSN 1071-5819
8. Ha, I., Asama, H., Jeakweon, H., Hong, D.W.: Development of open humanoid platform DARwIn-OP. In: 2011 Proceedings of SICE Annual Conference (SICE), pp. 2178–2181 (September 2011)
9. Goatz, J., Kiesler, S.: Cooperation with a robotic assistant. *Extended Abstracts on Human Factors in Computer Systems*, 578–579
10. Russel, S., Norvig, P.: *Artificial Intelligence: A Modern Approach*, 2nd edn. Prentence-Hall, Englewood Cliffs (2003)
11. Walters, M., Syrdal, D., Dautenhahn, K., Boekhorst, R., Koay, K.: Avoiding the uncanny valley: robot appearance, personality, and consistency of behavior in an attention-seeking home scenario for a robot companion. *Autonomous Robots* 24(2), 159–178 (2008)
12. Wainer, J., Dautenhahn, K., Robins, B., Amirabdollahian, F.: Collaborating with Kaspar: Using an autonomous humanoid robot to foster cooperative dyadic play among children with autism. In: 2010 10th IEEE-RAS International Conference on Humanoid Robots (Humanoids), pp. 631–638 (December 2010)
13. Solis, J., Takanishi, A., Hashimoto, K.: Development of an Anthropomorphic Saxophone-Playing Robot. In: Angeles, J., Boulet, B., Clark, J.J., Kövecses, J., Siddiqi, K. (eds.) *Brain, Body and Machine. AISC*, vol. 83, pp. 175–186. Springer, Heidelberg (2010)
14. Kusuda, Y.: Toyota's violin-playing robot. *Industrial Robot: An International Journal* 35(6), 504–506 (2008)
15. Or, J.: Towards the Development of Emotional Dancing Humanoid. *International Journal of Social Robotics* 1(4), 367–382 (2009)

Task Planning for Service Robots with Supervisory Control

Chung-Woon Park, Jung-Woo Lee, and Jong-Tae Lim

Dept. of Electrical Engineering, KAIST
373-1 Guseong-dong Yuseong-gu Daejeon, 305-701, Korea
`{kp225, jungwoo}@kaist.ac.kr, jtlim@stcon.kaist.ac.kr`

Abstract. Without an appropriate task planning scheme for service robots (SRs) in a ubiquitous robotic companion (URC) environment, the SRs degrade the system performance and they do not achieve the desired goal and the customers' requirements. In addition, the system resources might be wasted. In this paper, we propose a new task planning scheme for SRs to balance a desired goal and the system resources with a supervisor. In particular, we propose a high work-metric SR selection scheme using work metric (WM) information to provide the flexible trade-off with the limited communication resources. As a result, the proposed scheme not only reduces a significant communication feedback overload but also considers task planning in an URC environment. Simulation results show that the proposed scheme achieves the high customers' requirements with the limited communication resources.

Keywords: task planning, service robots, feedback aware, supervisory control.

1 Introduction

Industrial robots for working in factory environment were broadly studied and led to enormous development in the 20th century [1]. But the research subjects are moving to Service Robotics with the busy life style of humans in the 21st century. Humans have great concern in healthy life and do not want to get 3D jobs (difficult, dangerous and dirty) as well as repeated simple jobs. For these reasons, service robots (SRs) which do these jobs instead of humans are the main focus of research nowadays.

As SRs perform their jobs in the same environment as humans, SRs should have essential abilities humans have. They should recognize faces, gestures, characters, objects, speech and atmosphere. They should find their way to reach the goal without collisions and destructions, and accomplish the task at hand successfully. They should grab and deliver some objects. They should communicate with humans based on emotion. These all research subjects are included in Service Robotics area.

One of the key points of the future SRs is the concept of network computing. By connecting existing standalone robots to the communications network, some of their computations are performed on remote, distributing their loads over the network. This distribution is expected to raise customers' satisfaction because it can increase the

number of services available, which would not be possible with standalone robots. Moreover, their prices could also be lowered than ever because they do not need to have expensive computing devices any more expensive computations are now done on remote servers [2]. Many challenges are waiting to be faced in front of us when designing URC home service robots. Some of the challenges are the execution and coordination of active services launched locally or remotely, the integration of modules developed by different teams, controlling accesses to robot's resources from different modules or services, designing an efficient protocol architecture that is best suited for intelligent URC home service robots [3]-[6].

In addition, each robot is communicated with the central task planner where a basic task planner allocates the dedicated feedback communication resources to all robots requires a significant communication feedback overload. Thus, without an appropriate task planning scheme for SRs in an URC environment, the SRs degrade the system performance and they do not achieve the desired goal and customers' requirements and the system resources is wasted. In this paper, we propose a new task planning scheme for SRs to balance a desired goal and system resources with a supervisor. In particular, we propose a high work-metric SR selection scheme using work metric (WM) information to provide the flexible trade-off with the limited communication resources. Only a robot with the work-metric(WM) higher than a given threshold feeds back its states information. The rest of this paper is organized as follows: Section 2 presents the system model. The proposed scheme is presented in Section 3 and Section 4 demonstrates simulation results. The conclusion is drawn in Section 5.

2 System Model

We consider a service robot network with a supervisor as shown Fig. 1.

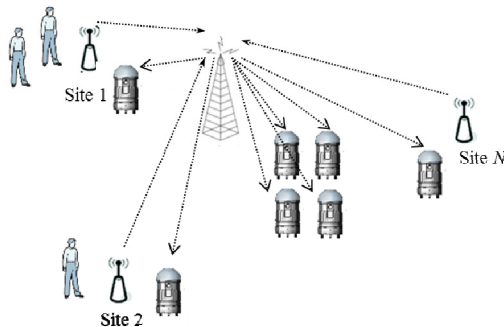


Fig. 1. Communication network architecture for service robots with a supervisor

In system architecture, there is N SRs and a supervisor. We assume that there is a task planner in the supervisor communicating with multiple SRs over independent communication channels. The customers are generated according to a Poisson process

of intensity λ . Each time every SR measures their state vector \mathbf{H} . State vector \mathbf{H} consists of the location information, the work load information, and the capability of the work load. The work metric Z_i of SR i is defined as follows

$$Z_i = f(\mathbf{H}_i) \quad (1)$$

We further assume that the states information of a new robots is measured and known to the task planner when robots join the SR networks. The maximum work-metric (WM) task planning selects SR i^* as follows:

$$i^* = \arg \max_i Z_i(t) \quad (2)$$

Note that $Z_{i^*}(t)$ is the WM of SR i at time t .

3 Proposd Scheme

3.1 Task Planning

To achieve the customers' requirement, the traditional task planning scheme requires all the state information \mathbf{H} from all the SRs for metric calculation in (1). However, it requires significant channel resources and the channel overhead increases as the number of SR increases. To reduce the amount of channel communication information between the supervisor and SRs, we propose a new task planning scheme that induces only the SRs who has WM exceeding the threshold to enter the source of workplace and send their WM to the supervisor as shown in Figure 2. Each SR independently measures their WM and sends a WM in each time to the supervisor if their WM is higher than the WM threshold Z_{th} where Z_{th} is the threshold value for WM. Then, the supervisor performs the task planning based on the feedback information. If there is no SR whose WM is larger than threshold Z_{th} , then supervisor looks for any SR who is idle state. Each user sets the initial threshold as $Z_{th}(0)$. Then, the threshold is dynamically determined during the service period and transmitted by the supervisor, which results in the WM information being fed back only by selective SRs that have a high probability being selected for the current work.

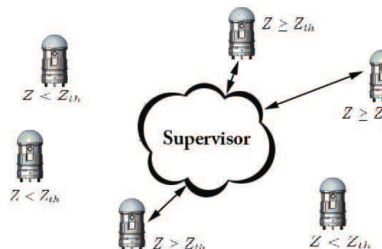


Fig. 2. Task Planning over WM threshold Z_{th}

3.2 Work Metric Threshold Control

Since the purpose of the proposed scheme is to reduce the complexity of task planning by lowering the channel overhead resources between the supervisor and SRs, the threshold control is important issue. If the WM threshold value Z_{th} is too small, the larger number of SRs will tend to respond, the channel overhead for task planning is still high and it makes the channel overhead reduction scheme to be non-effective. However, if WM threshold value Z_{th} is too large, there may be no SR responding, which results in the supervisor not having any information regarding the WM of the SRs. Then, it is difficult for the supervisor to task planning based on that information. Therefore, determining the proper threshold value is important issues in order to maintain a proper number of SRs that feeds back their WM information, which results in the channel overhead reduction scheme to be effective.

In this paper, a method is modified that limits the number of SRs that feeds back the WM, which is represented by n_F , to the target number of SRs that feed back their WM, which is represented by n_T , with δ probability

$$Pr(n_F < n_T) = \delta \quad (3)$$

can be guaranteed by adjusting the threshold value, Z_{th} as follows

$$Z_{th}(t+1) = \begin{cases} Z_{th}(t) + \Delta, & \text{if } n_F \geq n_T \\ Z_{th}(t) - \frac{1-\delta}{\delta} \Delta, & \text{elsewhere} \end{cases} \quad (4)$$

For the case where n_F is equal to or larger than n_T , Z_{th} is increased by Δ , and as a result, n_F is likely to be reduced in the next time. On the other hand, when n_F is smaller than n_T , Z_{th} is decreased by $\frac{1-\delta}{\delta} \Delta$ which is likely to increase the n_F in the next time slot. The step sizes of the threshold increasing and decreasing are set to Δ , and $\frac{1-\delta}{\delta} \Delta$ respectively, which make the cumulative offset of Z_{th} in the long term be 0.

4 Simulation Result

In this section, we evaluate the performance of the proposed task planning scheme under a URC environment. We consider a single SR network with a supervisor and randomly distributed $N=12$ SRs. SRs are located in the 20 by 20 space and are moving randomly. Depending on the state information \mathbf{H} such as location information, etc., the WM of each SR Z is determined. The customers are generated according to a Poisson process of intensity $\lambda=1$ per unit time and located in the space randomly. There is a task planner in the supervisor communicating with multiple SRs over independent communication channels.

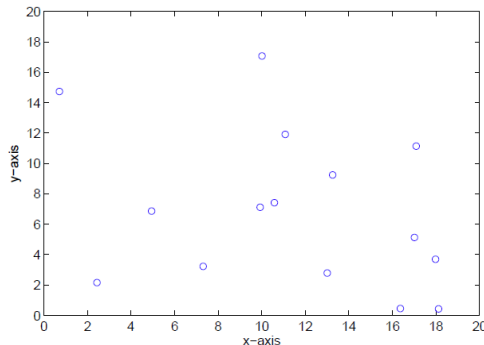


Fig. 3. Initial randomly distributed location SRs

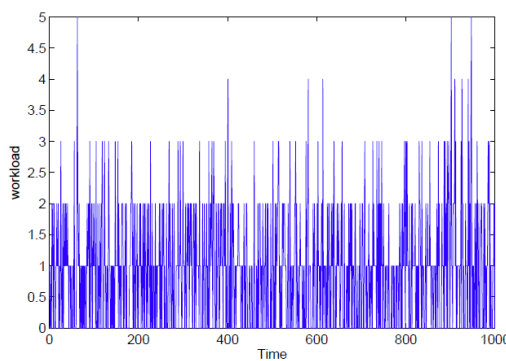


Fig. 4. Workload versus time

Figure 3 shows that initially random distributed location of SRs. As shown in the Fig. 3, SRs are located in the 20 by 20 space and are moving randomly. Figure 4 shows the customer service traffic versus time. Since the customers are generated according to a Poisson process, an appropriate task planning scheme for service robots (SRs) has to achieve the desired goal and customers' requirements. Figure 5 shows the input arrival and service output versus time. As shown in Fig. 5, the service

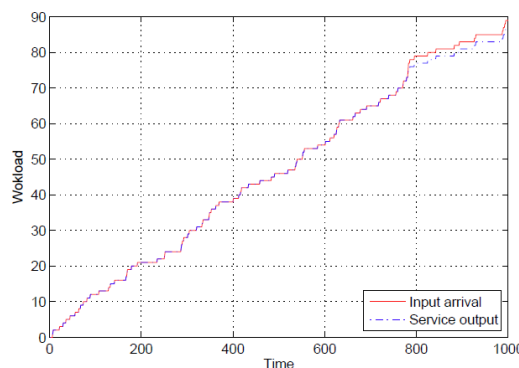


Fig. 5. Input arrival and service output versus time

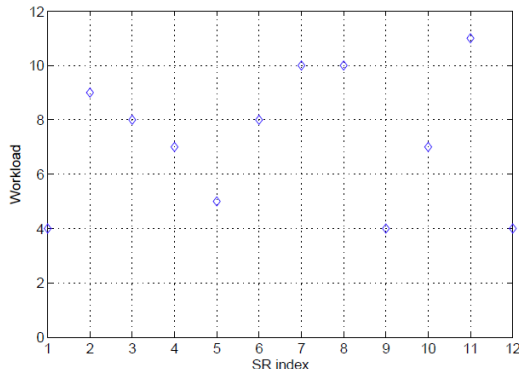


Fig. 6. Distribution of service output

output of the proposed scheme achieves the customers' input requirements. This is because the proposed scheme guarantees to select a SR in highest WM region at a given time and considers an outage situation. Thus, the proposed scheme achieves the higher effective service output using the limited communication channel. Figure 6 shows the distribution of service output.

5 Conclusion

In this paper, we propose a new task planning scheme for SRs to balance a desired goal and system resources with a supervisor. In particular, we propose a high work-metric SR selection scheme using work metric (WM) information to provide the flexible trade-off with the limited communication resources. As a result, the proposed scheme not only reduces a significant communication feedback overload but also considers task planning in an URC environment. Simulation results show that the proposed scheme achieves the high customers' requirements with the limited communication resources.

Acknowledgements. This work is supported by the NRRC for Robot Intelligence Technology.

References

1. Ahn, H.-S.: Advances in Service Robotics. In-Tech, Vienna (2008)
2. Park, J.-S.: Ubiquitous Robotic Companion (URC) Protocol Specification Version 2.0 (May 2005)
3. Ahn, H.S., Sa, I.-K., Choi, J.Y.: PDA-based mobile robot system with remote monitoring for home environment. *IEEE Trans. Consum. Electron.* 55(3), 1487–1495 (2009)
4. Yun, W.-H., Kim, D., Yoon, H.-S.: Fast Group Verification System for Intelligent Robot Service. *IEEE Trans. Consum. Electron.* 53(4), 1731–1735 (2007)

5. Rezaei, S., Sengupta, R.: Kalman Filter-Based Integration of DGPS and Vehicle Sensors for Localization. *IEEE Trans. Contr. Syst. Technol.* 15(6), 1080–1088 (2007)
6. Schleicher, D., Bergasa, L.M., Ocana, M., Barea, R., Lopez, M.E.: Real-Time Hierarchical Outdoor SLAM Based on Stereovision and GPS Fusion. *IEEE Trans. Intell. Transp. Syst.* 10(3), 440–452 (2009)
7. Kim, H., Han, Y.: An Opportunistic Channel Quality Feedback Scheme for Proportional Fair Scheduling. *IEEE Commun. Lett.* 11(6), 501–503 (2007)

Cognitive Architecture to Composite Emotions from Autonomic Nervous System for Robotic Head

Charmasson Amandine¹, Kim Jong-Hwan¹, and Kambiz Arab Tehrani²

¹ Dept. of Electrical Engineering
KAIST

Daejeon, Republic of Korea

² Dept. of Embedded System
ESIGELEC
Rouen, France

charmasson.amandine@gmail.com, johkim@rit.kaist.ac.kr,
kambiz.tehrani@esigelec.fr

Abstract. In this paper, methods are proposed for generating facial expression defined by Ekman's facial expression database from a robotic head. This paper gives rise to how to generate two emotions at the same time and how to solve problems between two conflicting emotions. Among others, it uses a cognitive architecture and some biological values in generating several probabilities from the hidden Markov model. The cognitive architecture is characterized by three main parts: perception and decoding module for simulating brain system, thalamus, amygdala, hypothalamus and hippocampus; learning module to memorize the data and transmit the behavior of an emotion to the emotion module which will generate facial expression to the robotic head from a given environment. This paper presents two basic emotions, not only one as we have already tested. However, according to psychologists, some conflicts exist between emotions. This research develops a table of compatibility of emotions from the Robert Plutchik's research, who is one of the precursors of emotional intelligence. To use Robert Plutchik's Emotion database and Paul Ekman Emotion database, we decide to work with the 6 universal basic emotions, anger, disgust, fear, joy, sadness and surprise, which can be combined. The problem of conflicting composite emotion can be solved by using the properties of the biological stimuli. By this way, the composite emotion is made possible.

Keywords: Facial Expression, Cognitive Architecture, Composite Emotion, Biological and Physiological brain System, Hidden Markov Model.

1 Introduction

Emotion is a prickly manifestation as a response of our physiological and biological system in relation with what can be perceived from an environment. The process still remains complicated for the psychologists and the biologists, but the interest about emotional system is growing every day. For now, we know how the body reacts according to a specific environment to protect ourselves. The development of an

emotion derives from how we have to act to keep a straight face from a particular situation. To confront the situation, some biological stimuli are created from the nervous system in such a way that we can control the situation. The heart rate, the breathing change, the muscle tensing, the perspiring, the temperature of body, or the act of crying, are just a response to an environment to fight against a situation, to protect ourselves, to integrate a social group... Up until now, in artificial intelligence, some studies had been done about the recognition or about how to generate one emotion.

Often, the face formulates not just only one emotion but several ones. Even if an emotion is overwhelming, we can perceive a combination of emotions. However, some problems can occur considering some conflicts from a combination of emotions, how to generate several emotions, or how to integrate the notion of the degree of an emotion... Indeed, generally, psychologists work on the Paul Ekman's model which uses and experiments 6 basic emotions, anger, disgust, fear, joy, sadness and surprise. This model is known to be universal and some biological tests have been done to understand how it works, biologically. The goal, here, is to use the biological values, the model of the nervous system to generate and simulate emotions accounting for the degree of an emotion and the combination between several emotions to emulate these kinds of emotion for facial expression for a robotic head. The cognitive architecture is completed by a brain system and nervous system to convey the good data to an emotion module which will affect the appropriate emotion to the robotic head.

This paper is organized as follows: The second part reviews the related work. The part 3 studies the brain and the nervous system mechanisms as well as the cognitive and the composite architecture. The part 4 presents how to solve the problem of conflicting composite emotions. The part 5 is intended for the experiment results and the last part gives a conclusion.

2 Related Work

This part reviews how these studies trend.

2.1 Emotion Process

According to Klaus Scherer who defined the precise nature of the emotions as a change of state based on an organic system synchronized with the appraisal of an external or internal stimulus in the interest of the person who generates the emotion. These changes of states take place in cognitive system, psychological system, motivational system, and motor system – facial expression. Thanks to the results of the appraisal, it is possible to predict the kind and the intensity of the emotion from a given event.

Most emotion's theories support the idea that an emotion depends on how to react in view of a certain situation and the signification of the outcome. These outcomes are for the survival or the well-being of the person. The system acts as follows: Is the information from this environment good for me? Am I able to fight this situation? To give more explicit details about the process that will deeply study what is the repercussion of an emotion among the 6 basics ones : The fear permits to run away

from a danger, the disgust makes us move away from everything which is considered bad for our health, the surprise supplies enough energy to confront an unknown situation, for the joy and the sadness, the human can't survive if he doesn't live in a group that's why the joy permits to better integrate with the society and the sadness to draw the other members' attention . Regarding the autonomic nervous system, it acts in function of the situation.

For instance, when someone is afraid of a danger, the kidneys send a lot of adrenalins in the blood, under the influence of this substance, the organism acts to prepare the person to run away. The pupil dilates to see a maximum of information from this environment. The lungs fill with the air and the breathing becomes faster, the heart beats quicken to supply the muscles with oxygen. The face pales, because the system irrigates the legs in priority. The cooling system of the body reacts and the person sweats, that's what we call the cold sweat.

But first, the emotional process must detect the information from an external or internal environment to generate the appropriate emotion. The limbic system interferes to perceive and decode this information. Thanks to the decoding, it is possible to know what kind of situation the person has to confront. The notion of limbic system was established by Paul Broca, it defines a group of structure from the brain. The hippocampus, the amygdala, the fornix, the thalamus, the hypothalamus, the prefrontal cortex among others, work for the limbic system. They play a part in the process to perceive, to sort, to treat, to compare, to memorize and to command the vital reflexes.

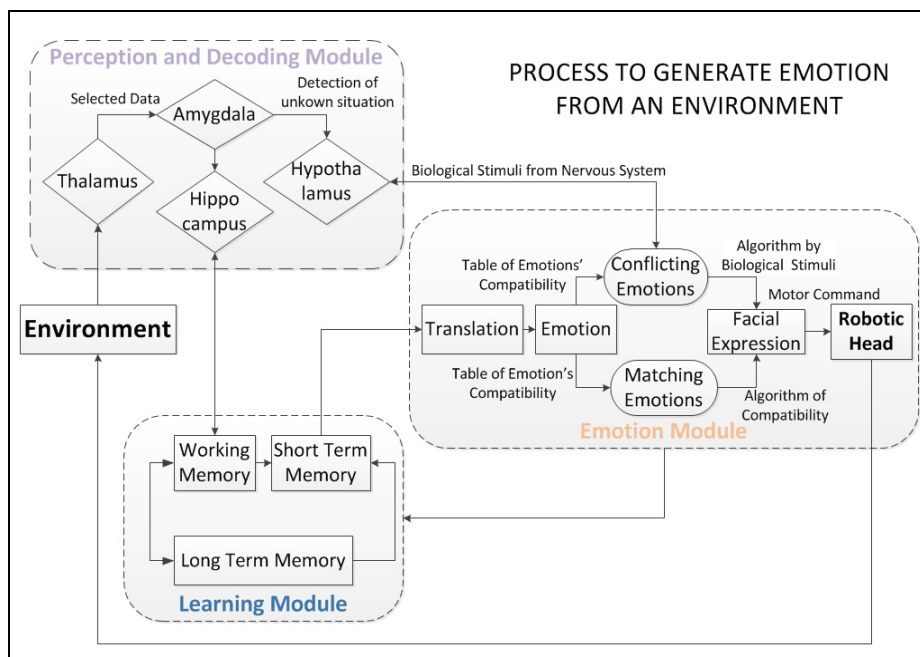


Fig. 1. Schema of the Cognitive Architecture in its overall

One of the basic notions about emotion is the work of Robert Plutchik who notably works on the composite of emotions. The famous Plutchik's Wheel [1] explains the relation between the different basic emotions according to the intensity as well as the similarity of emotions.

2.2 Facial Expression

The facial expression is an important aspect for the behavior and for the communication to interact with humans or robots. Several studies have been done about the recognition and the simulation of facial expression. They play a very important part, notably for Paul Ekman who is considered as one of the best psychologists in his category. He established the list of the 6 basic emotions: anger, disgust, fear, joy, sadness and surprise. After having created a list for the emotions, he developed the Facial Action Coding System (FACS) to do a classification of every human facial expression and to list all the face's muscles which work to express the largest possible panel of emotions. The database comports several sequences from several individuals for each emotion.

2.3 Robotic Head

To generate a facial expression from a given emotion, a robotic head is necessary to simulate the emotions and move according to the part of the face established by Paul Ekman. The robotic head was created by [2] [3] to simulate facial expressions. Different parts of the head can be controlled by motor commands to move mainly the neck, the jaws, the lips, the eyelids, and the eyebrows. Each emotion is generated by a vector to control the movement of the robotic head. These values will be used as outputs of this cognitive architecture.

To know more about this Robotic Head, please read the papers [2] and [3].

3 The Cognitive and Composite Architecture

The cognitive architecture is composed of three main modules and interacts with a given environment, as we can see on the Fig.1.

3.1 Perception and Decoding Module

An emotion is generally a way to confront a situation. This situation comes about an external or internal environment. The data of this environment are perceived by the thalamus which is going to select the good information. It plays the part of the sorting module in the limbic system. The data then, are sent to the amygdala. The amygdalae are involved in the recognition and the appraisal of the emotion to interpret the situation and to may act in this condition. Then, the hippocampus will do the transfer

between the memory, the known situation and the unknown situation. Once the data are recognized, the brain transmits the elements to the hypothalamus. This part of the brain commands the vital reflexes from the autonomic nervous system. As it is explained in the related work, each emotion is a feedback of a precise situation. The biological stimuli are not created by chance but by following some rules to survive in this environment. Each stimulus is in connection with a part of the face to move. For example the breathing change is in connection with the jaws. Indeed, the relation between our breathing and the movements of our mouth is understood. The muscle tensing will be in relation with the movements of the neck, the act of crying will be related to the movements of the eyelids. Each stimulus used in this architecture interrelates with the part of the Robotic Head that is associated with. The values of the stimuli are extracted from a study about the evidence of the response patterning of emotions [4][5].

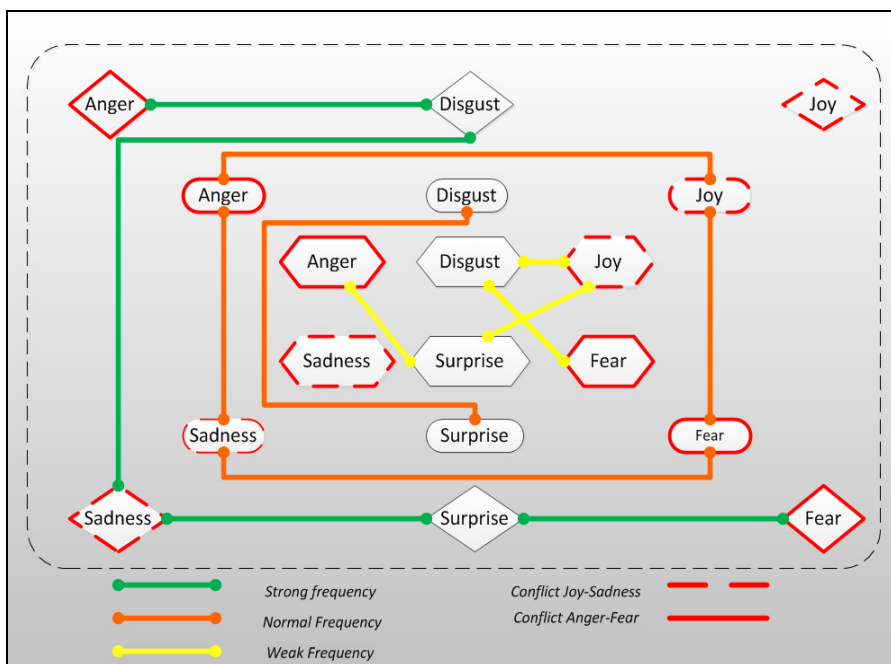


Fig. 2. Composite between the 6 basic emotions

3.2 Emotion Module

This research is based on the composition of several emotions. But, to generate only one emotion from the 6 basic emotions, it will be the association of the same emotion. To compose an assembling of emotions, model of Plutchik and the frequency about each basic emotion are used.

Table 1. Compatibility's Table according to the Frequency of an Emotion. The top line is the main emotion X and the left column is the second emotion Y. ρ is the compatibility parameter. The values are represented by $\rho(X, Y)$. for $\rho=(X, Y)$.

Compatibility's Table according the Frequency of an Emotion

	Joy=0	Anger=1	Fear=2	Sadness=3	Disgust=4	Surprise=5
Joy=0	1(0;0)	0,5(1;0)	0,5(2;0)	0(3;0)	0,25(4;0)	0,25(5;0)
Anger=1	0,5(0;1)	1(1;1)	0(2;1)	0,5(3;1)	0,75(4;1)	0,25(5;1)
Fear=2	0,5(0;2)	0(1;2)	1(2;2)	0,5(3;2)	0,25(4;2)	0,75(5;2)
Sadness=3	0(0;3)	0,5(1;3)	0,5(2;3)	1(3;3)	0,75(4;3)	0,75(5;3)
Disgust=4	0,25(0;4)	0,75(1;4)	0,25(2;4)	0,75(3;4)	1(4;4)	0,5(5;4)
Surprise=5	0,25(0;5)	0,25(1;5)	0,75(2;5)	0,75(3;5)	0,5(4;5)	1(5;5)

As we show on the Fig. 2, according to Plutchik, some combinations of emotions exist. But there are some conflicts too, between the Joy and the Sadness as well as between the Anger and the Fear. The associations that are not represented mean that the frequency of the apparition of these ones is too low to be generated. To know how the mixing must be done; the frequency plays a very important part in the cognitive architecture and the algorithm to send the good movement to the robotic head. The Table 1 shows how the frequency of a combination is characterized. The numeration of the emotions is done as follows: Joy = 0, Anger = 1, Fear= 2, Sadness= 3, Disgust= 4, Surprise = 5 and Neutral = 6. The top line (X) represents the predominant emotion, and the left column (Y) represents the secondary emotion. By this way, it would be possible to generate a largest panel of emotions with several degrees.

Five parts of the robotic head can move based on the basic emotions. The robotic head moves according to the defined characteristics of an emotion for every part of the head. But some parts are more expressive than the others. Indeed, the movements of the neck are less expressive than the movements of the eyelids for instance. As follows, in ascending order of the degree of expression for each face's part: Neck > Jaws > Eyelids > Eyebrows = Lips. The different components of the head are articulated by means of some vectors already defined [2][3].

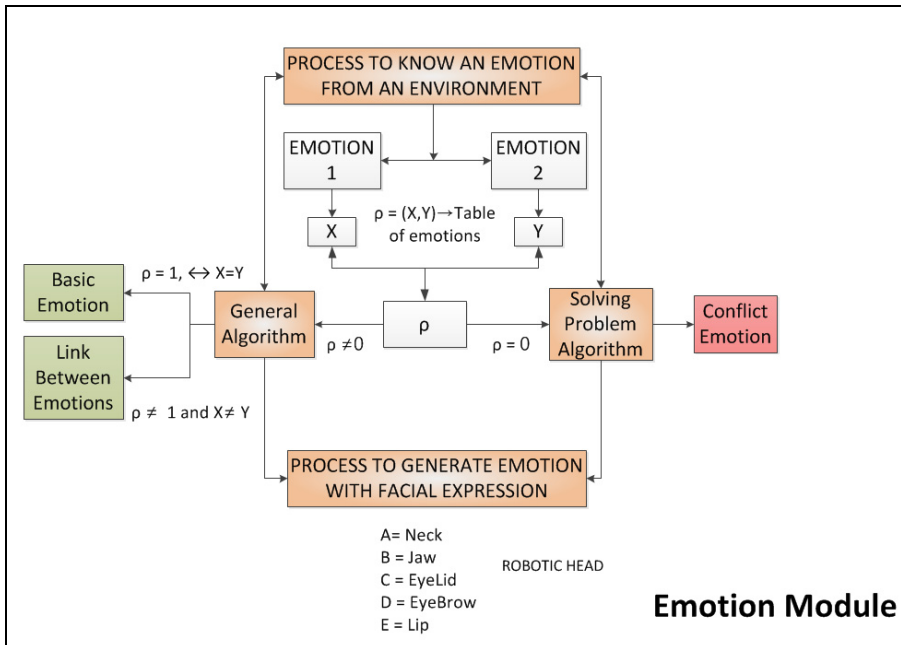


Fig. 3. Detailed representation of the Emotion Module to determinate if there is conflict or not

The frequency of a combination is combined with the importance of the expressive part of the head. A probability is then defined, inspired of the hidden Markov model [6] (HMM) and Viterbi algorithm. An HMM is defined by four elements: The state, the initial probabilities, the transition probabilities and the probability to transmit a certain output. The outputs of our algorithm are the different vectors to drive the facial expressions.

The Fig. 4 shows the functioning of the algorithm to obtain the appropriate movement for the robotic head. ρ represents the compatibility parameter between the emotion X and the emotion Y defined by the Plutchik model.and:

$$\forall (X, Y) \in \{1, 6\}^2, \exists \rho \in [0, 1] \text{ such as}$$

$$(X, Y) = \rho$$

The compatibility parameter can have five values:

- If $\rho=1$, it means the composite is composed by two same emotions so we have a pure emotion and in this case only one emotion will be generated by the Robotic Head.
- If $\rho=0,75$ it means the compatibility between the two emotions is very good and the movement of the Robotic Head will be generated by one of the schemas of the general algorithm. Fig. 4.

- If $\rho = 0,50$, the concordance is good and the composite emotion follows the schema of the Fig. 4.
- If $\rho = 0,25$, it means the relation between the two emotions is pretty low and usually this combination is not expressed by Humans. The secondary emotion can be perceived or not at all.
- If $\rho = 0$, there is a conflict between the emotions. In this case, we will solve the problem by using the biological stimuli to generate the appropriate movement.

Furthermore, the probability to obtain a movement knowing the state of ρ , can be defined by the equation as follows:

$$f(\rho) = \frac{e^{(0,75-\rho)*(0,5-3\rho)}}{1,2}.$$

That's how, the formula permits to find the probability considering each value of the parameter ρ and the predominance of the main emotion X.

By this way, the probability of X, $P(X)$ and the probability of Y, $P(Y)$, can be found by means of the parameter ρ , knowing $P(X) = f(\rho)$.

The HMM uses different dimensions, to get the output; that is to say to get the movement we want, in accordance with the following formula:

$$P(Movement) = \sum_{Emotion} P(Movement|Emotion)P(Emotion).$$

$$\begin{cases} Emotion = X, Y \\ Movement = X \text{ movement}, None, Y \text{ movement.} \\ f(\rho) = P(X) \end{cases}$$

To simulate the HMM in the program of the robotic head, a precise law must be defined. The HMM needs values on each branch of its model. It is in this perspective that the different laws are in relation with the parameter of compatibility. So each path of the HMM is simulated by the following law for the program:

$$Probability_Law(\rho) = \left\{ \rho, 1 - \left(\rho + \frac{f(\rho)}{4} \right), \frac{f(\rho)}{4} \right\}.$$

3.3 Learning Module

This module represents the part where the data are stocked and how the data are memorized. A memorization of the different states is important. That is to say, each time a composite of an emotion is generated, the data will be kept in the long term memory. In this way, it will be able to stock the data that is necessary to know how to simulate the right composite emotions. Then after generating n times an emotion, the process will be able to choose which pattern is the best way to express this emotion by the robotic head.

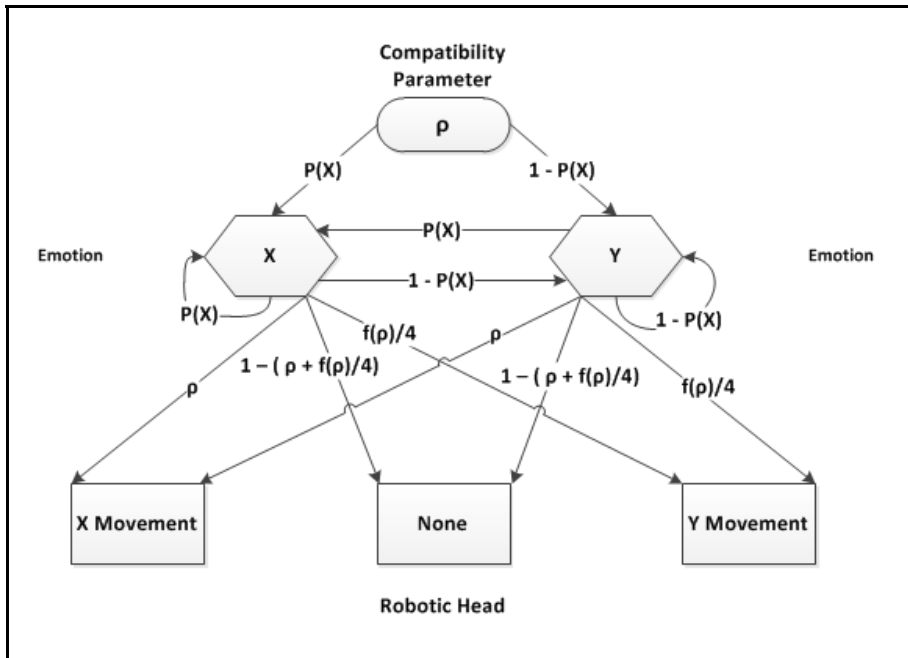


Fig. 4. Representation of the Algorithm to generate a facial expression from a composite emotion

4 Solving the Problem of Conflicting Emotions

As we can see on the Fig. 3, the composition of emotions can follow two different patterns, either the general algorithm with a compatibility parameter different from 0, or conflicting composite emotions. The joy-sadness combining and the anger-fear combining are totally conflicting.

Even if, according to Plutchik's Theory, these emotions are a problem considering the internal system, we can generate two conflicting emotions in the same time. For instance, if the state is joy, then in the external environment, the system perceives a sad event. Even if the event makes the person sad, in the memory, the state of joy is still present. That is by this way, taking into account that the memory can be an environment, conflicting emotions can be generated.

By this eventuality, it is important to find a way to solve this problem.

The psychologist Klaus Scherer, did some studies about the response of the internal system at the hands of basic emotions. That's how, it can be decided to use these stimuli to generate a new HMM, by employing the response of breath, the act of crying and the muscles tensing to move respectively the jaws, the eyebrows and the neck. The other part will automatically generate the main emotion to give more strength to this new emotion. The method transforms the values obtained by Scherer to have probability values spread from 0 and 1.

Table 1. Adapted values to biological stimuli for emotion according to Scherer

Measure	Conflicting Emotions		Conflicting Emotions	
	Joy	Sadness	Anger	Fear
Breathing change	0.16	0.19	0.29	0.36
Muscles Tensing	0.08	0.20	0.32	0.40
Crying/Sobbing	0.09	0.58	0.16	0.17

5 Experiments and Results

5.1 Parameter Setting

The composite emotion follows the rules of some probability laws and algorithms in relation with the compatibility and the hidden Markov model.

The robotic head works in receiving the appropriate value for the appropriate DC motors or servomotors. It demands three main parts: the header, the cognitive architecture part, and the flag. This kind of signal “0xFF, 0xFF, 0xFF (255, 255, 1)” is required in the header to initialize and send information to the Robotic Head.

Generating an emotion consists of sending the good value of the selected emotion which corresponds to the wished movement. The upper part of the robotic head needs 8 values that are associated with the motors of the eyelids and the eyebrows. The lower part also needs 8 values to move the motors of the neck, the jaws and the lips.

At first, the initialization of each part of the head with a pattern of the HMM is done. That is to say, the composite emotion follows a specific pattern according to its importance to the emotion recognition. The lips and the eyelids compulsorily use the path of the main emotion, to ensure the predominance of the main emotion. The Other parts – the Neck, the Jaws and the Eyebrows – use more or less a random path, according to the laws of the HMM. (Fig. 4)

Depending on the movement of the neck and the compatibility, it will generate a specific path to obtain the movement of the jaws and as far as to obtain the movement of the Eyebrows knowing the two last movements.

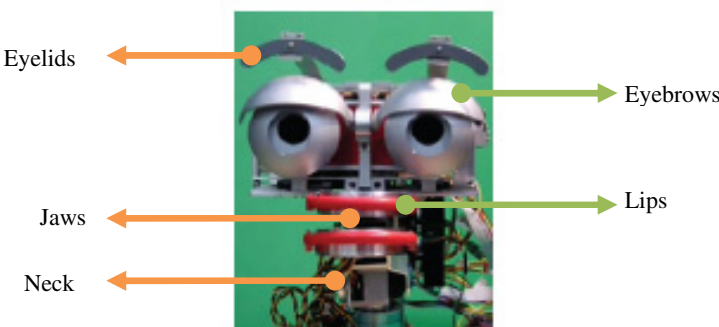


Fig. 5. Robotic Head [2], green arrows represent the part generated by the main emotion, the orange arrows represent the parts using the HMM

5.2 Simulation and Experiments Results.

The experiments are based on the results of the composite emotions. Using the protocol, previously enunciated, the values of the motor which are necessary are finally obtained. We can see a sample, about what is sent to the Robotic Head, once the HMM had been done, on the Fig. 5, from a C and C++ code. (Fig.6).

The outcome of this cognitive architecture has been tested. The tests are done, first, for the general algorithm and secondly for the solving problem by using biological stimuli. Foremost, by testing each emotion with the compatibility equal to 0.25, the average to have a good composite emotion is around 76%, and only 6% just generate the main emotion. For the compatibility equal to 0.50, the average to obtain a good composite emotion is around 96% and only 4% generate the pure main emotion. It means the law and the HMM for this compatibility is totally appropriated. For compatibility equal to 0.75, the average is 88% with an error of 4%. The method to compose emotion gives very good results. (Table 3 and Table 4).

Table 2. Results of the experiments per compatibility

Compatibility = 0.25		
Expected results	Main Emotion/Neutral	Error
76%	18%	6%

Compatibility = 0.50		
Expected results	Main Emotion/Neutral	Error
96%	0%	4%

Compatibility = 0.75		
Expected results	Main Emotion/Neutral	Error
88%	8%	4%

Table 3. Percentages of the different composite emotions between different pattern.

Difference	
Between $\rho = 0.25$ and $\rho = 0.50$	Between $\rho = 0.50$ and $\rho = 0.75$
12%	16%

The experiments which test the method for compatibility equal to 0 using biological stimuli are shown in the Table 2. Then, results are obtained by considering which emotion is the main one. The percentages of the results are shown in the Table 5. Although the percentage to get a composite emotion is low for SADNESS/JOY and FEAR/ANGER, these are the expected results because according to Scherer these compositions should not exist.

Table 4. Percentages of the different composite emotions between different patterns. The red squares show the unexpected outcomes.

	JOY/SADNESS			SADNESS/JOY			ANGER/FEAR			FEAR/ANGER		
	NECK	JAWS	EYES	NECK	JAWS	EYES	NECK	JAWS	EYES	NECK	JAWS	EYES
Neutral	72	40	48	72	52	12	28	40	72	28	48	84
Main Em	4	16	0	20	24	72	36	16	16	44	28	8
2nd Em	24	44	52	8	24	16	36	44	12	28	24	8
Comp. Em	88%			52%			64%			44%		

6 Conclusion

Facial Expression, for modeling the emotion, is one of the most important researches for the virtual humans. The cognitive architecture based on physiological and biological stimuli, permits on the one hand to be closer to the human process and on the other hand to solve some problems by imitating a real human. Even though the researches about the link between each emotion and the appraisal of our external and internal body stay pretty fuzzy, it is a way we have to follow to make Humanoid Robot, more Human than Robot.

```
CompositeEmotion_servo1[8] = {112.400002, 148.490005, 130.470001, 125.500000, 128.000000, 100.410004,
76.500000, 110.470001}
```

```
CompositeEmotion_servo2[8] = {133.360001, 122.519997, 147.589996, 113.339996, 125.480003, 125.470001,
129.509995, 128.000000}
```

Fig. 6. Sample of the signal sending to the Robotic Head at the end of the HHM. These values match the angle of the corresponding motor.

Furthermore, the hidden Markov model permits to simulate a largest panel of emotion just with 6 basic emotions. Unfortunately, generating several emotions at the same time, remains a subject that is not enough developed in the recognition and the simulation of emotion.

This kind of research gives a new dimension to generate emotions.

```

float X6 = Table_Mouth[emotionChoice1][0];
float X7 = Table_Mouth[emotionChoice1][1];
float X8 = Table_Mouth[emotionChoice1][2];

float Y5 = Table_EyesBrow[emotionChoice1][0];
float Y6 = Table_EyesBrow[emotionChoice1][1];
float Y7 = Table_EyesBrow[emotionChoice1][2];
float Y8 = Table_EyesBrow[emotionChoice1][3];

float CompositeEmotion_servo1[8] = {X1, X2, X3, X4, X5, X6, X7, X8};
float CompositeEmotion_servo2[8] = {Y1, Y2, Y3, Y4, Y5, Y6, Y7, Y8};

```

Fig. 7. Sample of the code for the General Algorithm

References

1. Plutchik, R.: The Nature of Emotions. American Scientist (retrieved April 14, 2011)
2. Yoo, B.-S., Cho, S.-H., Kim, J.-H.: Fuzzy Integral-based Composite Facial Expression Generation for a Robotic Head. In: Proc. IEEE International Conference on Fuzzy Systems (June 2011)
3. Yoo, B.-S., Cho, S.-H., Kim, J.-H.: Facial Expression Generation Using Fuzzy Integral for Robotic Heads. In: Proc. FIRA Robot World Congress, Kaohsiung, Taiwan (August 2011)
4. Scherer, K.R., Wallbott, H.G.: Evidence for Universality and Cultural Variation of Differential Emotion Response Patterning. Journal of Personality and Social Psychology 66(2), 310–328 (1994)
5. Scherer, K.R.: Psychological Models of Emotion, vol. 4(1), pp. 9–38 (1984)
6. Rabiner, L.R.: A Tutorial on Hidden Markov Models and Selected Application in Speech Recognition, Fellow. IEEE

Development and Implementation of Break Falling System for a Biped Robot

Seung Je Woo^{1,*}, Sung G. Lee^{2,*}, Jung Seul Ok^{3,*}, and Jong Hwan Kim³

¹ Department of Electrical Engineering, Stanford University, Stanford, California, USA

² Department of Electrical and Computer Engineering, Georgia Institute of Technology, Atlanta, Georgia, USA

³ Dept. of Electrical Engineering, Korea Advanced Institute of Science and Technology
291 Daehak-ro, Yuseong-gu, Daejeon 305-701, Korea
sjwoo@stanford.edu, sleet656@gatech.edu,
ockjs@lanada.kaist.ac.kr, johkim@rit.kaist.ac.kr

Abstract. The development of humanoid robots is becoming more popular these days. While the robotics community is outputting varieties of enabling results for humanoid robots to perform many different types of tasks such as locomotion or entertainment, there has not been much research on securing their safety in motion. A way to make humanoid robots prepare for some dangerous incidents should be given attention in order to prevent the developers from losing expensive and important parts of robots and efforts they put in. The main focus of this research is to make a robot break-fall when external forces are exerted behind the robot. This paper is organized as follows: the research robotic platform that is used in order to test break-fall motions of robots is introduced. Various methods of break-fall motions are designed and evaluated. We conclude that among the types of motion we investigated, motion type C-2, stretching arms forward & bending knees & damping motion, is the best break-fall motion. Application of our algorithm to other practical robots may result in reduction of precarious incidents of robots falling down, which will be beneficial for robot developers.

Keywords: feedback system, robot safety, sensor control, Kalman filter.

1 Introduction

Robots are beginning to leave the lab environment and becoming more directly involved with human beings nowadays. Many scientists are working on building robots and making them more applicable to human society [1-2]. The development of biped robots – humanoids – is one of such example. They, like humans, have two legs supporting their bodies. Most of those working on developing humanoids aim to make robots resemble human beings both visually and in intelligence [3-4].

Regardless of how intelligently the robots are designed, unforeseen accidents do occur. Many have witnessed robots caught up in traumatic accidents. Some accidents

* These authors contributed equally to this work.

are such that the developers of the robots would likely not only lose some expensive and important parts of the robots, but also the tremendous amount of effort they put in to develop the robots.

With the above fact in mind, we would like to find a way to make humanoid robots prepare for deleterious incidents. In order to protect robots from breaking down due to unexpected falling, we propose a simple controller that executes pre-designed motions to implement break-fall. The motions are designed based on energy and mechanical considerations at the moment of impact.

2 Background

2.1 Related Works

There has been considerable amount of research done on topic for making humanoid robot locomotion that focused on the robots moving without falling. Lee et al. suggest a way to modify walking pattern in order not to fall down from the external force [5]. Morisawa et al. present the method of having the robot stop within one step when danger is detected by planning an emergency stop motion in real-time [8]. However, just as it is impossible for human beings to avoid falling altogether, there are bound to be situations where it is physically impossible for biped robots to keep standing [9-11], e.g. if overwhelmingly large force has been applied from behind. In such cases, an unwary robot will fall, which has a large potential to cause damage to vital parts of the robot. This could lead to a tremendous loss of time and money during development of the robot. Bipeds must thus be equipped with capabilities to protect the more vital parts of its structure, such as the processor, the sensors such as the camera, and so on.

Some work has been done on securing the safety of robots when a fall is unavoidable. The work by Fujiwara et al analyzes scenarios of falling and proposes an algorithm for break-falling [6]. Fujiwara et al. use an optimal control approach to plan falling motions to reduce damages to the robot [12]. Another approach is presented in a work by Ruiz-del-Solar et al., where a human-based search for joint angle values that minimizes the robot's damage when falling is done [13].

2.2 Hardware

An accelerometer and a gyroscope are used for sensors. They are attached securely to the back of a robot and are responsible for measuring the state of the robot. As Fig. 1 shows, two directional and one rotational sensors are used. Since the sensors then should be attached upright, what we are to measure are x-axis and z-axis acceleration and axis rotation.

The humanoid robot platform is made from the BIOLOID robot kit from Robotis. A PXA255 processor board is used as the main processor and ATmega128 board is used for peripheral purposes, such as motor control and ADC.

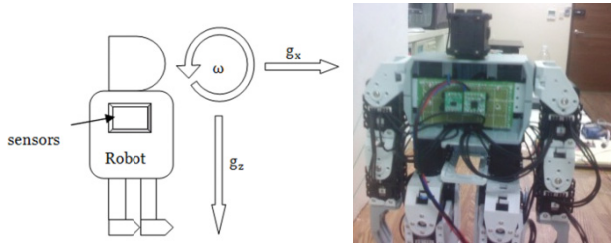


Fig. 1. The axes and naming for measurements (*left*) and the picture of sensors attached to the robot(*right*)

3 The Kalman Filter for Falling Prediction

We assume that it is sufficient to observe the angle and angular velocity of robot for detecting unavoidable falling when the initial state is fixed and external force which causes the fall is the same every time, since it is the angular position, velocity, and acceleration that gives the most direct information about whether the robot is falling or not. Now, we aggregate sensors' outputs and estimate angular state of robot so that robot can detect and react to the falling. To obtain angle and angular velocity, we implement a filter based on Kalman filter [3]. As Kalman filter does, the filter aggregates current inferences and weighted sum of observed inputs according to accuracies of inputs, and expects inferences in next time step, recursively. The future state is predicted from previous angle and angular velocity obtained from the gyroscope. The familiar formula for predict process is as follows:

$$\begin{aligned} \theta_{predict} &= \theta + \omega dt + \frac{1}{2} \alpha dt^2 & \sim \text{Cov}(\theta_{predict}) &= N_\theta + N_\omega dt + \frac{1}{2} N_\alpha dt^2 \\ \omega_{predict} &= \omega + \alpha dt & \sim \text{Cov}(\omega_{predict}) &= N_\omega + N_\alpha dt \\ \alpha_{predict} &= \frac{3lg_0 \sin \theta}{L^2} & \sim \text{Cov}(\alpha_{predict}) &= \left(\frac{3lg_0 \cos \theta}{L^2} \right)^2 N_\theta \end{aligned}$$

where l is length from the base of foot to center of mass of the robot, g_0 is the standard average gravitational acceleration on Earth's surface, and L is the height of the robot. In the above formulation, the robot body approximates the rod of length L with uniform mass, the sensor is positioned at height l of length L , and the angular acceleration is generated by the gravity so that we have $\alpha_{predict}$ as above. We update the predicted future value with observation g_z , g_x , and roll from the accelerometer and the gyroscope. We can simply get θ (angle), ω (angular velocity), and α (angular acceleration) which are states of interest for us in this research from given information about g_x , g_z accelerations and roll angular velocities. To process the information from the sensors to get the angular states that we want, we need to convert the relationship between them. Here is a model for information processing which converts g_x , g_z and roll to θ , ω , and α .

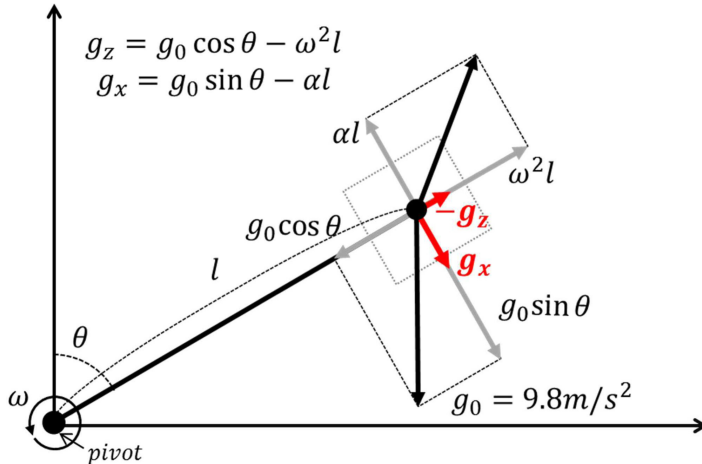


Fig. 2. The a model for information processing which converts g_x, g_z and roll to θ , ω , and α

Based on this model, we can easily get θ , ω , and α . Following is the result:

$$\theta_{measure} = \pm \cos^{-1} \left(\frac{g_z + \omega^2 l}{g_0} \right)$$

$$\omega_{measure} = \omega$$

$$\alpha_{measure} = \frac{1}{l} \left[\sqrt{g_0^2 - (g_z + \omega^2 l)^2} - g_x \right]$$

In the above, the sign of $\theta_{measure}$ is determined by sign of predicted θ . In this measuring model, the difficult part extracting their reliabilities since measuring parameters may follow normal distributions with each variance but results from functions of them may not follow simple distributions. Therefore we assume that every variance is small enough so that variance of result will be similar to $f'(x)$. $f(x)$ near a can be assumed as:

$$f(x) \cong f(a) + f'(a)(x - a)$$

Therefore, variances of the measurements are:

$$Cov(\theta_{measure}) = \frac{1}{\epsilon + g_0^2 - X^2} (N_g + N_{\omega^2} l^4)$$

$$Cov(\omega_{measure}) = N_{roll}$$

$$Cov(\alpha_{measure}) = \frac{1}{l^2} (X^2 N_X + N_g)$$

Here, $X = g_z + \omega^2 l$, $N_X = \frac{1}{\epsilon + g_0^2 - X^2} (N_g + N_{\omega^2} l^4)$, and $N_{\omega^2} = 2N_\omega(N_\omega + 2\omega^2)$. $\epsilon = 0.01$ is used to avoid division by zero. N_g is variance of g_z and g_x measurements and N_{roll} is variance of roll angular velocity. We denote our Kalman filter with approximated distribution as Kalman AD filter.

3.1 Design and Simulation of Kalman Filter

This version of Kalman filter takes centripetal force from ω into account, so it does not give poor results as the previous Kalman filter. Reversing this logic, if the model of the desired value does not follow Kalman AD filter but follows Kalman filter, Kalman AD filter would not be applicable. Thus, we can see that the modeling process for Kalman filter before implementation is a very important step.

The following graph is the result of Kalman AD filter. It initially follows θ very well, but loses track after collision at 0.8 second. It does not, however, keep on increasing like the θ obtained from integrating ω . The reason for the gap after collision is because the value of α is extremely large so that sensor values of g_x , g_z , and roll are limited at voltage source's range, V_{CC} and V_{DD} . Another reason is that sensors output low pass filtered results, but collisions are impulsive changes in voltage. It has high frequency contents, and is distorted by the sensor output, and this results in more difficulty for Kalman filtering.

Given enough time, however, the filter variance will begin to become smaller, and reliability will be back up. Otherwise, we can give the filter an initial value again to reset it, because the filter is recursive. The gap between Kalman AD filter result and θ is analogous to inability of humans to keep balance when they only rely on vestibular organ and semicircular canal. Opening the eyes to see the current status is analogous to resetting Kalman filter to set initial state again.

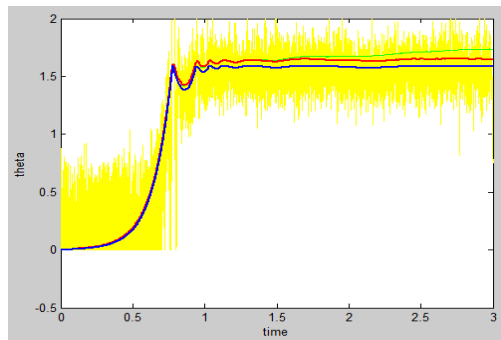


Fig. 3. Ideal dropping model simulation. Measuring θ using Kalman AD filter: Blue: θ , red: Kalman AD filter, green: integration, yellow: model

Following is the table of mean square errors of results from individual filters. We can see that Kalman AD filter has the smallest error. Kalman common filter that assumes small ω and inverse tangent method can be seen to perform no meaningful filtering.

Table 1. Mean square error [unit: rad²]

Filter	Mean Square Error in θ
Measured N_θ	0.0564
$\tan^{-1} g_x/g_z$	2.4808
$\int_{[0,t]} wdt$	0.0069
Kalman common filter	6.9789×10^5
Kalman AD filter	0.0023

4 Possible Break-Fall Motions

First of all, we need to measure when no robot control is involved (motion A). This motion is expected to bring the strongest force to the robot, as the body of the robot directly touches the ground.

Motion B breaks falling with arms only. The motion raises moment of inertia, which decreases the increase of angular acceleration in response to gravitational pull. This action will also result in higher center of mass, which increases the torque gravity places on the robot. These two phenomena would unavoidably happen, since initial positions of all motions are fixed to be upright standing position. This motion does not try to decrease Δt , the time duration from the moment the robot touches the ground and comes to a complete stop, but touches the ground faster by using its arms. This stops some portion of potential energy from being converted to kinetic energy.

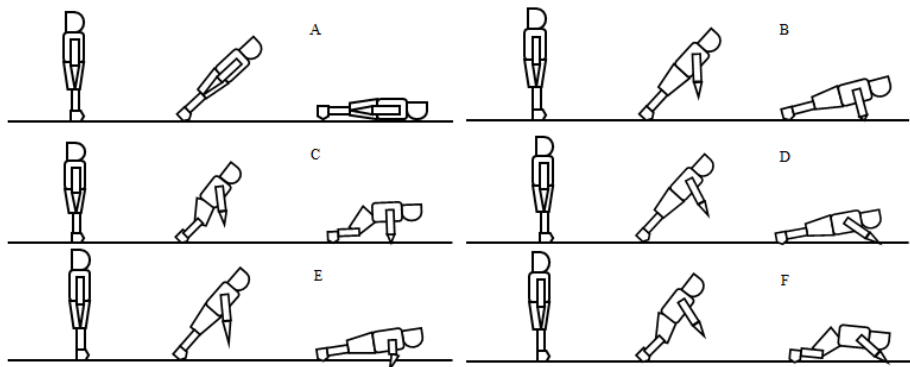


Fig. 4. Possible break falling motions: from left to right, top to bottom, A, B, C, D, E, and F

Motion C is a power-hungry motion using 10 motors all at once. This motion achieves much smaller time to touch the ground by using knees and hands. Torques on the motors that supply the torque for contact force are decreased to increase Δt . This action is expected to be safer for the robot. In real experiment, we tried two variations of motion C, motion C-1 and motion C-2. Motion C-1 does not employ low-torque motor method but motion C-2 does.

Motion D does not have a large difference in falling time compared to unguarded falling. Shoulder torque is minimized in attempt to maximize Δt . This result can be compared to Motion B to check which motion is superior to the other.

Motion E is similar to Motion D, except that arms are outstretched horizontally, instead of vertically.

Motion F both experiments with moderate reduction in falling time and reducing motor torque at once. Falling time is reduced by slightly bending the knees, and positioning the arms horizontally and bent inwards, ready to support itself. Torques in all arm motors are reduced in attempt to increase Δt .

When should the break-fall motion be executed? One possible way to figure out when may be to compute the time that remains to impact the ground. In general, this is a function of the angular states of the robot. In order to find the time,

$$\begin{aligned}\tau &= I\alpha = lF\sin\theta \\ I &= \int r^2 dm = \frac{1}{3}mL^2 \\ F &= mg_0\end{aligned}$$

Combining these equations,

$$\ddot{\theta} = \frac{d^2\theta}{dt^2} = \frac{3lg_0 \sin\theta}{L^2}$$

Moment of inertia I is calculated by approximating the robot as a rod of uniform mass.

This differential equation occurs when in the study of motions of a pendulum, where the fact that θ is small is used to allow the approximation $\theta \approx \sin\theta$. This assumption cannot be made in our work, and hence such simplifying approximations cannot be made. Thus we have no closed form solution for the differential equation. Numerical methods must be used to approximate the time remaining until impact.

The time it takes to fall down, however, take at most a few seconds. We want to avoid spending time in calculations because we may not have enough time left to react by the time the robot realizes it is falling. Hence, since in this work we investigate break-fall from a uniform initial state, we simply set a threshold angle and once the robot's angular position goes past this angle, we execute the break-fall motion.

5 Experiment

5.1 Experiment Method

We set up the experiment environment as shown in the figure below. The puller is the system that pulls a robot down such that the robot falls down.

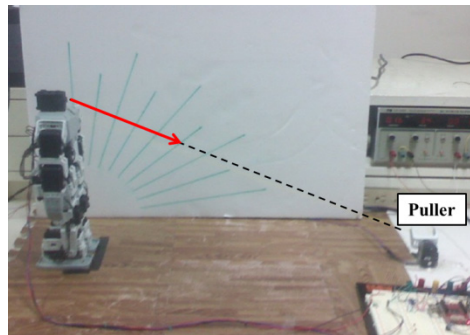


Fig. 5. Experiment environment

The experiment would begin by having the puller pull on the robot to make it fall down. When we detect that the angular position of the robot exceeded the threshold, we send signals to the motor controller so that the robot takes motions against falling. After the robot falls completely, we analyze the video and the sensor data to find out difference in performance between each motion.

5.2 Experimental Results

We present ADC value of g_x recordings from only motion A and C-2 in Fig. 6 due to limit of page space. Since when the robot hits the ground, the direction g_x is direction of normal force, g_x well presents shock power on the robot. To see effect of each motion on reducing shock power, we summarize value of maximum peak-to-peak g_x , first bounce interval, and relative first contact time in Table 2. The relative first contact time is the time difference between first contact times of motion A and other motion.

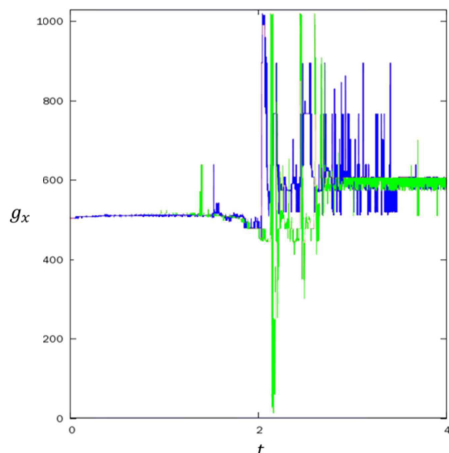


Fig. 6. Sensor data recordings from different break-fall motions (A: green, C-2: blue)

Table 2. Summarized characteristics of break fall motions

Falling motion	Peak-to-peak g_x (m/s ²)	First bounce interval (ms)	Relative first contact time (ms)
A	127.9	106	-0
B	102.8	89	-44
C-1	83.6	130	-59
C-2	60.5	243	-73
D	100.1	144	-20
E	108.6	131	-21
F	95.4	83	-62

Experiments with various motions show that motion C-2, which combines the lower-torque motor technique and high final center of mass position to minimize kinetic energy, is the most effective, as measured by the maximum acceleration. Maximum acceleration can be translated to maximum impulsive force, the minimizing of which is the goal of this paper.

Motion F had the potential to be very effective break-fall motion by also utilizing two techniques. Motion F focused more on lower-torque motors, while motion C-2 emphasized higher final center of mass position more. Unfortunately, the leg movement sequence was slightly too fast for motion F for its small-torque motors to work.

Analysis of result graphs are made difficult by the fact that the maximum ADC value of acceleration we can see 1023, which is the maximum ADC digital output value. Almost all motion results show maximum acceleration to be 1023, with the exception of motion C-2, which is the best motion, with maximum acceleration around 900. Another factor that makes analysis hard is that although various efforts have been made to maximize Δt , it is still not very distinguishable.

6 Conclusion

In this paper, we worked through physical analysis of break-falling and concluded that maximizing Δt and stopping the fall as soon as possible is vital to successful minimization of maximum impulsive force. We came up with 5 candidate break-fall motions, where Δt and impact time considerations are made in each falling motion. We implemented and tested these motions on our research platform by actually making the robot fall. A hazard signal was provided by the Kalman filter running on PXA255 processor once the robot reached the threshold angular position, to indicate that the robot is falling, and then ATmega128 board initiated the break-fall motion.

Δt was maximized by lowering the torques of motors that come into contact with the ground so that less normal force could be applied on the motor. Stopping the falling motion as quickly as possible to minimize kinetic energy was realized by reaching out the arms and bending the knees. After experimentation, the most promising motion was motion C-2, where both maximizing Δt technique and minimizing impact time technique was employed. While all other motions showed

maximum measurable value of g_z , motion C-2 alone showed smaller g_z , which is a very good indication that it is indeed an effective motion. Motion F, on the other hand, could have been very effective as well, but its moving sequence did not let lower-torque motor technique come into play, and a large part of the ability to minimize impulsive force has been lost. In any case, motion C-2 and all other motions indicate that our technique for minimizing impulsive force based on physical analysis is indeed effective.

Much more precise analysis of motions could have been performed if we had the accelerometer to measure up to higher acceleration. All motions except for motion C-2 indicate that the acceleration the sensor experiences is the maximum value the sensor can measure. It is very likely that these motions result in higher acceleration than the measurable maximum value. If we had accelerometer to measure wider ranges of g , we could have had much more reliable data to perform analysis and comparison between motions.

Future works include expansion of the results to cases where the robot falls sideways and backwards, not just in forward direction, and while the robot is moving. The ideas developed in this work combined with the tools of optimal control may boost the break-fall performance by factors. Also, it will be very useful to test the break-fall with a humanoid robot of a human-like size, considering that larger the size of the robot, the more vulnerable it is to the damage from a fall.

Acknowledgements. This research has been supported in part by URP (Undergraduate Research Participation) Program at KAIST. We thank In-Won Park for helpful discussions.

References

1. Millan, J.R., Renkens, F., Mourino, J., Gerstner, W.: Noninvasive Brain-Actuated Control of a Mobile Robot by Human EEG. *IEEE Transactions on Biomedical Engineering* 51(6), 1026–1033 (2004)
2. DiSalvo, C.F., Gemperle, F., Forlizzi, J., Kiesler, S.: All robots are not created equal: the design and perception of humanoid robot heads. In: *Proceedings of the 4th Conference on Designing Interactive Systems: Processes, Practices, Methods, and Techniques*, pp. 321–326 (2002)
3. Miller, W.T.: Real-Time Neural Network Control of a Biped Walking Robot. *IEEE Control Systems*, 41–48 (February 1994)
4. Kim, J.-H., Lee, C.-H., Lee, K.-H.: Evolutionary Generative Process for an Artificial Creature’s Personality. *IEEE Transactions on Systems, Man, and Cybernetics - Part C* 39(3), 331–342 (2009)
5. Lee, B.J., Stonier, D., Kim, Y.D., Yoo, J.K., Kim, J.H.: Modifiable Walking Pattern of a Humanoid Robot by Using Allowable ZMP Variation. *IEEE Transactions on Robotics* 24(4), 917–925 (2008)
6. Fujiwara, K., Kanahiro, F., Kajita, S., Kaneko, K., Yokoi, K., Hirukawa, H.: UKEMI: Falling Motion Control to Minimize Damage to Biped Humanoid Robot. In: *Proceedings of the 2002 IEEE/RSJ Intl. Conference on Intelligent Robots and Systems*, pp. 2521–2526 (October 2002)
7. Kalman, R.E.: A New Approach to Linear Filtering and Prediction Problems. *Journal of Basic Engineering* (1960)

8. Morisawa, M., Kajita, S., Harada, K., Fujiwara, K., Kanehiro, F., Kaneko, K., Hirukawa, H.: Emergency Stop Algorithm for Walking Humanoid Robots. In: IEEE/RSJ International Conference on Intelligent Robots and Systems, pp. 31–37 (2005)
9. Kanehiro, F., Kaneko, K., Fujiwara, K., Harada, K., Kajita, S., Yokoi, K., Hirukawa, H., Akachi, K., Isozumi, T.: The First Humanoid Robot that has the Same Size as a Human and that can Lie down and Get up. In: Proceedings of the 2003 IEEE International Conference on Robotics & Automation, pp. 1633–1639 (2003)
10. Renner, R., Behnke, S.: Instability Detection and Fall Avoidance for a Humanoid using Attitude Sensors and Reflexes. In: Proceedings of the 2006 IEEE/RSJ International Conference on Intelligent Robots and Systems, pp. 2967–2973 (2006)
11. Harada, K., Kajita, S., Kaneko, K., Hirukawa, H.: Dynamics and Balance of a Humanoid Robot During Manipulation Tasks. *IEEE Transactions on Robotics*, 568–575 (2006)
12. Fujiwara, K., Kajita, S., Harada, K., Kaneko, K., Morisawa, M., Kanehiro, F., Nakaoka, S., Hirukawa, H.: Towards an Optimal Falling Motion for a Humanoid Robot. In: 2006 6th IEEERAS International Conference on Humanoid Robots, pp. 524–529 (2006)
13. Ruiz-del-Solar, J., Palma-Amestoy, R., Marchant, R., Parra-Tsunekawa, I., Zegers, P.: Learning to fall: Designing low damage fall sequences for humanoid soccer robots. *Robotics and Autonomous Systems* 57, 796–807 (2009)

Application of Fuzzy Logic in Learning Autonomous Robots Systems

María Laura González¹ and Jorge Salvador Ierache^{1,2}

¹ Information Advance Systems Laboratory. Engineering School.

University of Buenos Aires, Universidad de Morón, Cabildo 134,

(B1708JPD) Morón, Buenos Aires, Argentina 54 11 5627 2000 int 189

² Institute of Intelligent Systems and Robotics Experimental Teaching,

FICCTE, UM Universidad de Morón, Cabildo 134, (B1708JPD) Morón, Buenos Aires,

Argentina 54 11 5627 2000 int 189

jierache@unimoron.edu.ar

Abstract. Autonomous Robots Systems (ARS) can learn by establishing plans, executing them in a given environment and analyzing the results of the execution. The logic used among this process is usually the classic logic, which most of the times ends up being too restrictive and not consistent with the world the ARS is facing. This paper proposes the application of fuzzy logic to address this issue and improve the ARS learning curve considerably.

Keywords: Robots, Fuzzy Logic, Machine Learning, Autonomous Systems.

1 Introduction

This paper extends previous work learning in Intelligent Autonomous Systems [1, 2] by implementing fuzzy methods in the comparison of situations (registered by the proximity sensors of the robot) and actions (made by robot actuators or wheels) between theories that form ARS basis of knowledge [3, 4, 5].

The Learning Life Cycle in Autonomous Robots Systems [1, 2] can be considered as a number of perceptions of the surrounding world and actions performed as a response to those perceptions. Each perception/action cycle might help to improve the ARS intelligence by applying stored knowledge or generating new one. This “unit of knowledge” is usually defined as theory [1,2] and it has the following structure:

$$\langle C, A, F, P, K, U \rangle$$

where "C" is the initial situation (conditions obtained by the distance sensors of obstacles), "A" is the action to be performed (by their actuators-wheel speed of the robot), F is the final situation (post-conditions), P means the times that the theory was successfully applied (final situation F was obtained), K means the times that the action A was applied to C, U means the utility level reached by applying the action to the initial situation.

In this scenario, the ARS will sense the initial situation through its sensors and look in the stored theories for one that matches in order to determine the action to be performed. After the action is done through its effectors, the ARS will sense the final situation and analyze the results of this perception/action cycle which includes the addition (or not) of a new theory and the re-ordering of the stored ones. Among these pages we will demonstrate that the application of fuzzy logic to the ARS learning process can certainly improve it by generating fewer theories but certainly more effective than a controller that doesn't apply this kind of logic. The main reason for this improvement is that the world where the robot is moving, its perceptions and consequent actions performed, is better modeled with fuzzy variables, sets and functions that give flexibility and allows little and expectable deviations caused by the sensoring.

The following sections will explain how to apply fuzzy logic to this learning process (section 2), suggest an experimentation plan and analyze its results (section 3) and finally draw some conclusions and future research lines (section 4). We will use E-Puck mini-robot simulation provided by Webots for all the experiments defined.

2 General Description of the Fuzzy Controller

First we need to define some fuzzy concepts that our controller will implement [6]:

Fuzzy Variables: distance to an obstacle for the input and speed applied to the wheels for the output. As the ARS is moving in a labyrinth with a given complexity the input is telling the controller how far is a wall which might stop its movement, and the output is allowing the robot to rotate in different angles to avoid them while it's moving.

Fuzzy Sets: Possible values for distance variable are: Clear (C), Very Far (VF), Far (F), Medium (M), Near (N), Very Near (VN), while for speed variable are Very Fast Backward (VFB), Fast Backward (FB), Medium Backward (MB), Slow Backward (SB), Still (S), Slow Forward (SF), Medium Forward (MF), Fast Forward (FF), Very Fast Forward (VFF). This configuration for both sets have been achieved after many testing simulations with different combinations trying to find the one that makes the ARS moving more stable while sorting the different labyrinths.

Fuzzy Membership Functions: we chose the trapezoidal function to represent our fuzzy variables and sets. Again, the values chosen for each of the trapezoids have been experimentally determined after many testing simulations to determine the better configuration (the one that allows a reasonable predictable movement).

At the beginning of each perception/action cycle the E-Puck robot [7] will sense the initial situation "Si" through its 8 sensors. The controller will assign to each sensed value a certain degree of membership to each of the fuzzy sets using the corresponding fuzzy membership function. The highest degree of membership determines which fuzzy set matches that value. Then it will build a baseline vector with

eight positions, assigning the linguistic labels obtained previously. For example Si: [C, C, VF, M, M, M, VF, C]. At this point we have the initial situation in fuzzy terms.

Selected theory returns a vector A (Action), with two positions, one for each speed to be applied to each wheel ARS. For example Ai: [VFF, FF].

The controller will now look in the ARS knowledge base for a theory with the same initial situation in order to apply the action specified in that theory (this implies same values for each position of Si vector). If it finds more than one candidate it will choose the one with higher utility, P and K. If no matching theory is found it will generate a random action.

In this search the controller performs we find one of the biggest differences with Classic Logic implementation: *to determine equality the values that are compared are fuzzy labels, not numbers*. This brings a level of granularity in the possible comparisons that helps to use in a situation which is very similar to another (but not exactly the same) the action used in that situation, which will probably be more helpful than a random action generated as a consequence of no matches found among the available theories. As we can see, fuzzy logic's perception of the world is more realistic and useful than Classic one.

As the action is expressed in fuzzy terms in the theory, the controller needs to deal with defuzzification process in order to send to each wheel a value of speed that can be interpreted and applied. There are several methods commonly used in this process, our controller implements the Mean of Maximum method which chooses the value that maximizes the membership function.

After applying the selected action the E-Puck robot [7] will now sense the final situation, which will also follow the fuzzyfication process described earlier. Now the controller needs to determine if a new theory has been created or an existing one needs to be reinforced. If it finds a theory which matches the initial situation, action and final situation, then it will reinforce its P and K. If it finds a theory which matches the initial situation and action, it will reinforce K and save the new theory in order to be able to use it in future perception/action cycles. Finally, if it doesn't find a theory that matches any of those values, it will simply save the new theory.

Our controller has the ability to apply some methods which can make the learning process faster and better: mutation, cooperation and collaboration [1, 2].

Mutation allows creating new theories from existing ones, and it can be helpful at those moments when the learning process seems to be stucked. Cooperation and collaboration on the other hand let 2 different ARS to share their knowledge (stored as theories) according to the stage in the Learning Life Cycle and the layer involved [1, 2]: [a] Layer BIO (Built In Operators) where operators are implanted into a "Born" ARS by its creator, [b] Layer TBO (Trained Base Operations) where operators are learned by a "Newbie" ARS in a simulated scenario, [c] Layer WIO (World Interaction Operators) where operators are learned by interaction of a "Trained" ARS with other ARSs to finally turn into a "Mature" ARS. The objective of the ARS is to autonomously learn theories also called operators (action models) that may predict the effects of the actions on the environment, through the observation of the consequences of these actions and to advance in their evolution state (Born, Newbie, Trained, Mature).

Learning Life Cycle starts as Born, it turns to Newbie after 600 perception/action cycles, then Trained after another 600 perception/action cycles and finally Mature after 600 more perception/action cycles. Cooperation is applied among ARS that have reached the same level of evolution while collaboration [2] implies an ARS with a higher level of evolution than the one receiving its knowledge.

3 Experimentation and Result Analysis

Now we will present the design of the experiments, the results and their analysis. We simulated E-Puck robot [7] behavior by using Cyberbotics Webots 6 mobile robot simulator developed in the Laboratory of Micro-Informatics of the Swiss Federal Institute of Technology, Lausanne, Switzerland (EPFL) [8]. Figure 1 shows the experimentation scenarios used according to the level of evolution reached by the ARS. For utility calculation we chose a method which compares the actual speed performed by the robot with the one calculated by applying Braitenberg quotients [9]. The more similar both values are, the higher the utility of the action taken by the ARS will be (in the range 0-1). We consider that a theory is successful when it has a value between 0.75 and 1. On the other hand we consider that a plan is successful when the final situation achieved matches the expected one. The controller will compare the fuzzy labels of each sensor in order to determine this equality.

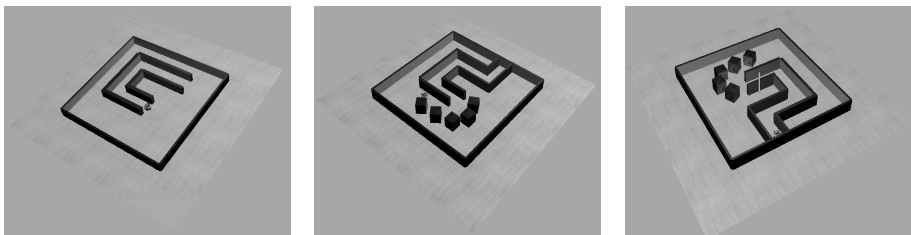


Fig. 1. Experimentation settings scenarios for Born, Newbie and Trained ARS

We have considered the following ARS configurations for fuzzy and classic ARS:

1. ARS with no learning accelerator method applied (None)
2. ARS that applies de collaboration (Colab)
3. ARS that applies cooperation (Coop)
4. ARS that applies collaboration and cooperation (Colab-Coop)
5. ARS that applies mutation (Mut)

We applied the following metrics [1,2] to analyze the results obtained from the comparison between proposed fuzzy ARS and classic ARS: New situations, New theories, Percentage of successful theories, Percentage of successful plans, Percentage of random actions.

3.1 Experiment Design

Each of the ARS configurations performed simulations that lasted 600 perception/action cycles. Every 20 cycles we generated a new entry in the report shown in table 1. Theories are generated by the interaction of ARS with its environment (operating scenario). We selected trained stage of evolution for all the comparisons between Fuzzy and Classic ARS. The cooperations were made between two trained ARS and collaborations the between a trained and a mature one.

Table 1.

Cycles	New Situations	New Theories	% of Successful Theories	% of Successful Plans	% of Random Actions
1	1	0	0	0	0
20	2	4	2	8	19
..
600	116	472	128	459	193

[a] *New situations* is a quantitative variable in the interval [0,600 cycles] and indicates the number of new situations that have been generated by the ARS during the current simulation

[b] *New theories* is a quantitative variable in the interval [0,600 cycles] and indicates the number of new theories that have been generated by the ARS during the current simulation

[c] *Percentage of successful theories* is a quantitative variable that indicates the percentage of new successful theories (theories with utility higher than 0.75)

[d] *Percentage of successful plans* is a quantitative variable that indicates the percentage of new successful plans (plans where the final situation matches the expected one in the theory applied)

[e] *Percentage of random actions* is a quantitative variable that indicates the percentage of new random actions (actions generated when no applicable theory was found)

3.2 Graphs and Discussion of the Experimentation Results

We present a synthesis of the results of the comparison between fuzzy logic vs. classic one. Figure 2 shows that classic controller generates three times -or more- the amount of new situations that fuzzy one does for every configuration. The main reason of this difference is that classic controller compares numerical values while fuzzy one compares fuzzy labels, so the granularity of available different situations is considerably higher (and the probability of matching situations is considerably lower).

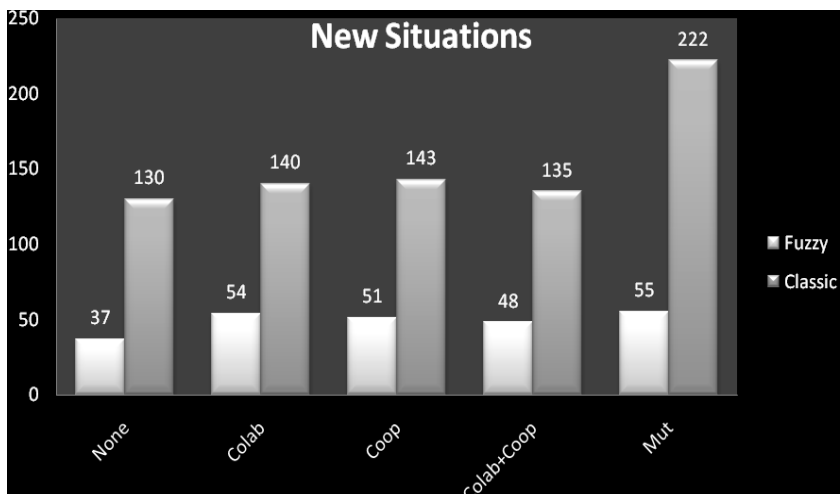


Fig. 2. Fuzzy vs Classic - New Situations

Figure 3 shows that classic controller generates a greater number of new theories for every configuration. Again, the main reason of this difference is that classic controller compares numerical values while fuzzy one compares fuzzy labels, so the granularity of available different theories is considerably higher (and the probability of matching theories is considerably lower).

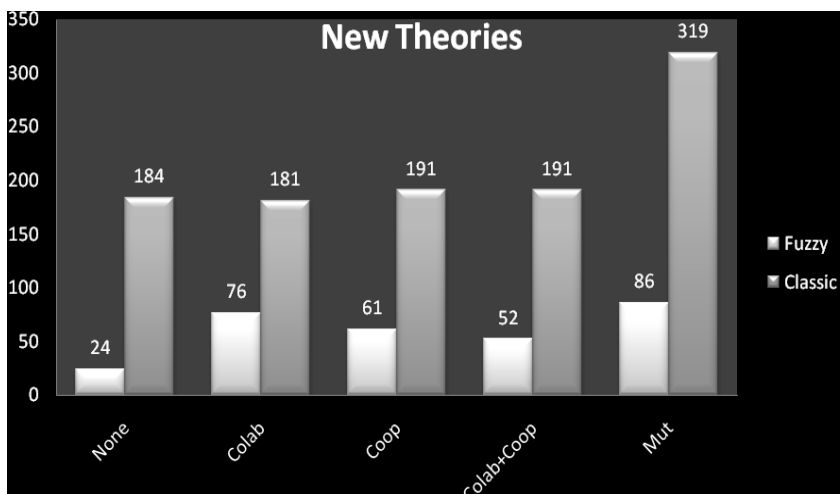


Fig. 3. Fuzzy vs Classic - New Theories

We might think that this higher amount of new theories generated by Classic controller leads to a faster and better learning process, but quantity doesn't mean quality and we will demonstrate it with the analysis of the following three metrics.

Figure 4 shows that fuzzy controller has a higher percentage of successful theories for every configuration. This means that although it has a smaller number of available theories to apply, they are more useful than the ones generated by the classic controller

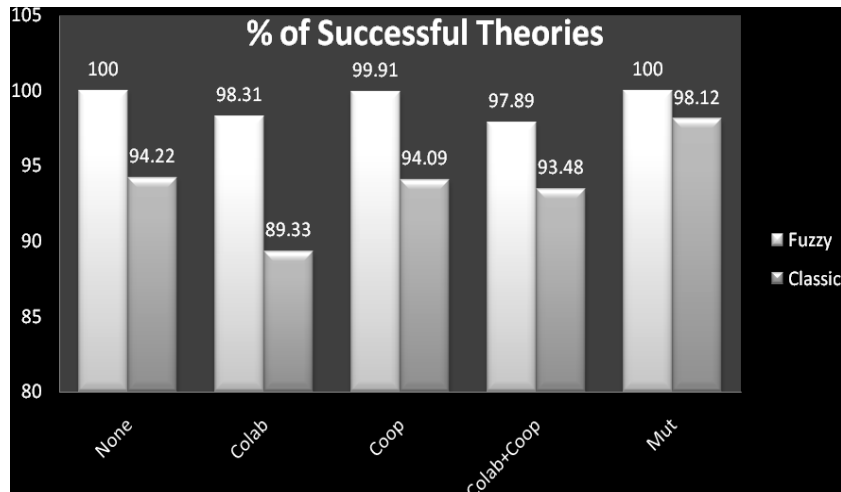


Fig. 4. Fuzzy vs Classic - Percentage of Successful Theories

Figure 5 shows that fuzzy controller has a higher percentage of successful plans for every configuration. This means that although it has a smaller number of available theories to apply, it generates more plans where the final situation matches the predicted one, making the robot behaviour more predictable and stable.

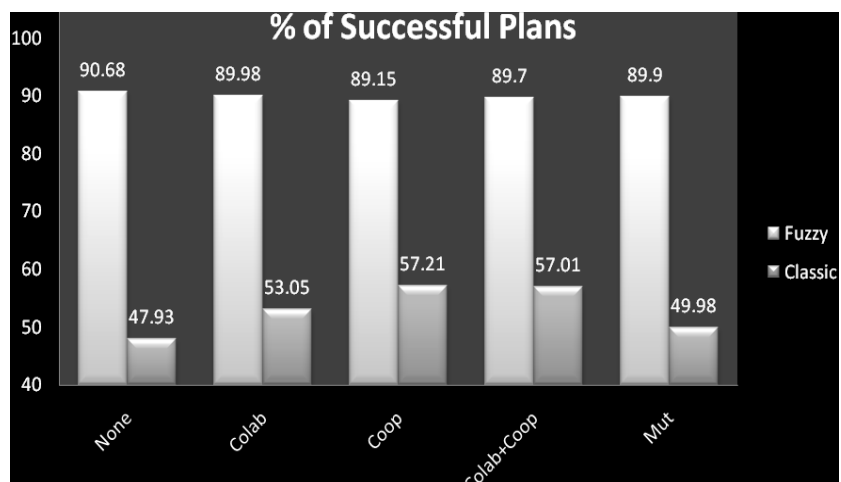


Fig. 5. Fuzzy vs Classic - Percentage of Successful Plans

Figure 6 shows that fuzzy controller has a significantly smaller percentage of random actions applied for every configuration. This means that the robot faces less unknown situations where it doesn't know what to do.

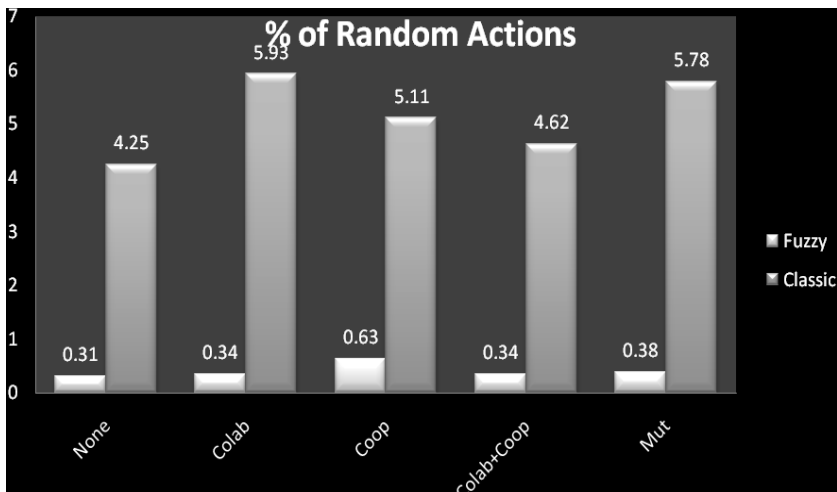


Fig. 6. Fuzzy vs Classic - Percentage of Random Actions

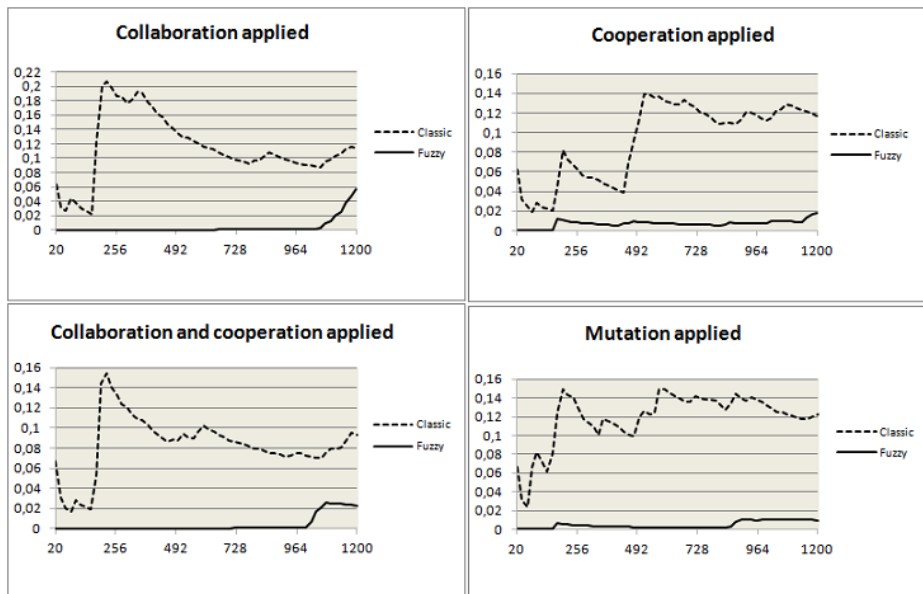


Fig. 7. Random Actions/Successful Plans

Figure 7 shows that Fuzzy controller has a significantly smaller rate of Random Actions/Successful Plans for every configuration. As the Fuzzy Controller has very small percentages of Random Actions and very high percentages of Successful Plans

for every configuration, we have this insignificant value for the rate Random Actions/Successful Plans and therefore we confirm the fact that the theories generated for a Fuzzy Controller are mostly successful.

4 Conclusions and Future Research Lines

According to the results achieved during the experimentation, we can conclude that the application of fuzzy logic in the implementation of an ARS controller optimizes the learning process, generating higher percentages of successful theories and plans and lower percentages of random actions applied. The knowledge stored as theories is smaller but more useful than classic one. As a future research line we could consider the implementation of full fuzzified theories, which implies the fuzzyfication of P, K and utility parameters. and the adaptation of the membership functions during the learning life cycle in autonomous robots systems

References

1. Ierache, J., Garcia Martinez, R., De Giusti, A.: Learning Life Cycle in Autonomous Robots Systems. In: Bramer, M. (ed.) Artificial Intelligence and Practice II. IFIP, vol. 276, pp. 451–455. Springer, Boston (2008)
2. Ierache, J., García-Martínez, R., De Giusti, A.: Learning by collaboration in intelligent autonomous systems. In: Bramer, M. (ed.) IFIP AI 2010. IFIP AICT, vol. 331, pp. 143–152. Springer, Heidelberg (2010)
3. García-Martínez, R., Borrajo, D.: Planning, learning, and executing in autonomous systems. In: Steel, S. (ed.) ECP 1997. LNCS (LNAI), vol. 1348, pp. 208–220. Springer, Heidelberg (1997)
4. García Martínez, R., Borrajo, D.: An Integrated Approach of Learning, Planning and Executing. Journal of Robots and Robotic Systems 29, 47–78 (2000)
5. García-Martínez, R., Borrajo, D., Maceri, P., Britos, P.: Learning by knowledge sharing in autonomous intelligent systems. In: Sichman, J.S., Coelho, H., Rezende, S.O. (eds.) IBERAMIA–SBIA 2006. LNCS (LNAI), vol. 4140, pp. 128–137. Springer, Heidelberg (2006)
6. Matellan, V., Fernandez, C., Molina, J.: Genetic learning of fuzzy reactive controllers. Robotics and Autonomous Systems 25, 33–41 (1998)
7. E-Puck, “Robot e-puck”, web (2012), <http://www.e-puck.org/>
8. Webots, “Simulador Webots”, web (2012), <http://www.cyberbotics.com/>
9. Braitenberg, V.: Vehicles: Explorations In Synthetic Psychology. MIT Press (1984)

Robot Control on the Basis of Bio-electrical Signals

Jorge Salvador Ierache^{1,2}, Gustavo Pereira¹, Iris Sattolo¹, Juan Irribaren¹,
and Nicolás Suiffet¹

¹ Instituto de Sistemas Inteligentes y Enseñanza Experimental de la Robótica FICCTE
Universidad de Morón, Cabildo 134, (B1708JP) Morón, Buenos Aires,
Argentina 54 11 5627 2000 int 189

² Information Advance Systems Laboratory. Engineering School. University of Buenos Aires
Universidad de Morón, Cabildo 134, (B1708JP) Morón, Buenos Aires,
Argentina 54 11 5627 2000 int 189
jierache@unimoron.edu.ar

Abstract. This article shows the experiences carried out in the context of human/robot communication, on the basis of brain bio-electrical signals, with the application of the available technologies and interfaces which have facilitated the reading of the user's brain bio-electrical signals and their association to explicit commands that have allowed the control of biped and mobile robots through the adaptation of communication devices. Our work presents an engineering solution, with the application of technological bases, the development of a high- and low-level communication framework, the description of experiments and the discussion of the results achieved in field tests.

Keywords: Robots, Brain Machine Interface, Bio-Electrical Signal, Human Machine Interfaces.

1 Introduction

The application of bio-electrical signals for the control of systems, robots, applications, games and devices in general presents an original approach as it opens up new possibilities for the interaction of human beings and computers in a new dimension, where the electrical biopotentials registered in the user are specifically exploited; these biopotentials include the EMG (electromyogram), the EEG (electroencephalogram) and the EOG (electro-oculogram), which are bio-electrical signals generated by activity patterns in the user's muscles, brain and eyes. The idea of moving robots or facilitating the application of devices for the physically disabled people by controlling them only through the brain activity, with no use of manual controls, has fascinated researchers.

In this regard, several works have been presented; the first ones resorted to the implantation of intracranial electrodes in the motor cortex of primates [1], [2]. Non-invasive works for humans resorted to EEG signals, applied to mental command exercises, such as moving the computer cursor [3], [4] based on the use of Brain-Machine Interface (BMI). Millan et. al [5] show how two people are able to move a robot by using a simple electroencephalogram on the basis of recognizing three

mental states, which are associated to robot commands. The works presented by Saulnier et al. [6] focused on controlling robot speed and further inferring the user's stress level, thus influencing on the social behavior of domestic robots, in this case of a robotic vacuum cleaner. Millan et al's seminal work [5] uses the EEG as a unique bio-electrical signal, on the basis of the work of two people to support robot navigation; in contrast to this, our work presents the preliminary result by applying a low-cost BMI, used in secondary works like that by Saulnier et al[6] that includes bio-electrical signals corresponding to the electroencephalogram, the electro-oculogram and the electromyogram. Unlike Saulnier et al's work, in which speed control is implemented on the basis of the electromyogram and the user's stress level is inferred on the basis of the electroencephalogram, our work focuses on the execution of a navigation pattern task by a robot, by comparing the manual control and brain control operating times during the beginning of a user's learning curve, with results that show that the brain control requires in general terms twice as long as the manual control for the execution of the same navigation pattern. However, in the context described our work introduces an improvement in the brain control times slightly exceeding the manual control in the execution tests of the same navigation pattern, which we call brain control with auto-focus. In our research work the V1 Robosapiens Biped robot from the Woo Wee Robotics family [8] was used for the preliminary tests and as main robot a simple mobile one on the basis of an NXT Lego was assembled [9].

In the second part of this work it is presented the problem to be solved in the context of the use of a BMI for the control of robot behaviors, the difficulty in the process of selection of robot behaviors. In the third part it is proposed the solution, with a description of the BMI used, the brain control of each robot behavior, and the features of the integration framework. Finally in the fourth part the comparative results obtained from the tests carried out with manual control, brain control and brain control with auto-focus are discussed, being the latter presented as a solution for the selection of robot behavior through brain-actuated control.

2 Problem

Our initial objective was to explore an engineering solution that allows us to achieve a primary integration of a BMI and a robot so as to be used by a user who does not need to have previous experience in meditation techniques or specific training in mental concentration.

For the brain control of a robot, two commands were set out: one enabling the control of behavior **selection** and another one making it possible the **execution** of robot behavior on the basis of its own controllers (for example moving forward in the case of the biped robot or turn right in the case of the mobile robot), with no major difficulties when associating the **execution** to a muscular bio-electrical signal stimulus.

Nevertheless, the **selection** of a behavior (in our context those behaviors corresponding to the menu of the family of robot behavior) through brain control, on the basis of bio-electrical signals coming from the electroencephalogram, **was not practical for the user**, due to the difficulty in controlling the menu of behavior selection **in a stable way**.

3 Solution Description

It is established an experimental architecture having two communication models; the first model, and main study subject, is called high-level communication model: “user-computer”; this model was implemented with an low-cost OCZ NIA BMI[10], which is used in an experimental way in videogames and makes it possible the association of brain signal patterns with the computer keyboard and computer mouse. Taking this into account, it was determined a simple profile for robot operation that associates and characterizes in the first place the control for the execution of the mental command on the basis of the detection of muscle signals, in our case through a slight eyelid movement, and in the second place the selection of the robot high-level commands, working in this case on the basis of Alpha brainwaves. This type of bioelectrical signals did not guarantee the user an adequate control in the displacements through the menu of command selection of the robot’s control framework. For this reason it was implemented the option of auto-focus application for brain control mode in the framework in order to improve the user’s management in the selection process. The second communication model, called low-level communication model: “computer-robot”, was implemented in the case of the V1 Robosapiens through an IR Tower [11], and in the case of the NXT mobile robot its Bluetooth communication capabilities were exploited. The communication with robots done via IR was based on the results obtained in the capture and reproduction of commands controlled from a computer [12].

3.1 Brain-Machine Interface

The Neural Impulse Actuator (NIA) was used as a brain-machine interface / BMI [10]. It is composed of a driver control unit (figure 1) and a headband with three diamond-shaped sensors, which is put on the user’s forehead (figure 2), manufactured using carbon fiber nanotechnology. The driver control unit is connected to the computer and fed via a USB 2.0; the software that comes with the NIA allows the calibration, training and definition of the control profiles that make up the applications.

The preparation of the profile to control the robot makes it necessary to think about the intuition of the robot behavior that is intended to be controlled. BMI capabilities are different from those of a keyboard, so control strategies are to be adjusted consequently to take advantage of the more limited reaction times and the higher level of immersion in robot behavior.



Fig. 1. BMI-NIA



Fig. 2. Headband – NIA

The BMI-NIA has an application having a control and configuration panel to allow auto-calibration of the recorded biosignals (Fig.3) through its components: the electro-oculogram that detects eye glancing (eye movement activity), the electroencephalogram that records Alpha brain waves (9-13 Hz, present in the following situations: wakefulness, normal alertness and consciousness) and the beta waves (14-30 Hz, present in the situation of being relaxed, calm, lucid, or not thinking), and finally through the electromyogram that detects muscle amplitude. Moreover, the application has some tools for the creation and editing of profiles that allow the association of biosignals with keyboard commands.

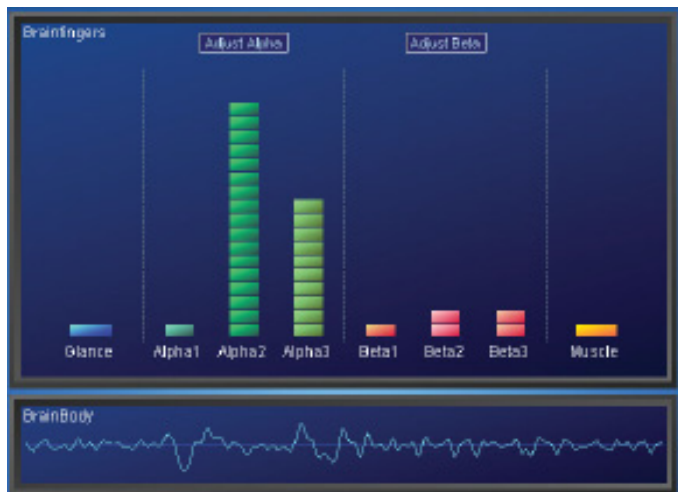


Fig. 3. Biosignal panel

For the creation of profiles in the BMI-NIA, switch events are firstly considered; they are thought to select actions that require precise timing for these switch events, like for example jumping in an action game, turning right in the case of a mobile robot or taking a step to the right in the case of a biped robot. The switch events can further be assigned a single data transfer, single mouse click or keystroke or a hold function. In the latter case, the action bound to the key will continue as long as the switch event remains active. The BMI-NIA allows us to bind the profile up to three different switch events. The BMI-NIA considers as a second step for the creation of a profile, the creation of up to four joysticks (horizontal, vertical, parallel). Each vertical joystick allows the definition of up to four different zones, for each zone up to three switch events may be stated; moreover, several modalities may be assigned to each zone (on/off, hold the key for a certain time, a single click, delay the activation for a defined time, repeat at a defined interval, repeat and hold, etc.) Every biosignal can be used in one or more parallel joysticks that use the same input biosignal; the result is equal to pressing two or three keys on the keyboard simultaneously. Four zones, two left ones and two right ones, can also be assigned to the horizontal joystick; it is applied with the “glance” biosignal coming from the electro-oculogram. This signal follows the lateral eye movements and could be used so that the robot may

turn right or left. The same as in the case of the vertical joystick, up to three switch events and modes are defined for each zone. Each joystick can be separately adjusted with respect to the level, amplification and smoothing of biosignals.

3.2 Brain-Actuated Control of Robot's Behavior

The communication of robot behaviors is implemented in two communication models (Fig.4), a high-level one between the BMI-NIA and the framework, and a low-level one between the latter, by means of the communication transmission device, and the robot.

The high level communication model, developed for the integration of the mental commands with the behaviors associated to the mobility of the Robosapiens V1 and the NXT respectively, functions between the BMI-NIA and the framework, where the selection and execution of motion behaviors for the biped robot and the mobile robot take place, by means of the mental commands captured by the BMI-NIA according to the profile for the robot control. The profile associates and characterizes firstly the control for the execution of mental commands on the basis of a switch event bound, in our case, to the “spacebar” key in single mode, being its activation controlled by muscle biosignal, with a gentle eyelid movement.

Secondly, for the selection of the robot's high-level commands it was defined in the profile a vertical joystick (1°), which is activated on the basis of the Alpha 1 waves, being the event bound to the “F” key, in zone ZI. To improve the user's control in the displacement by means of the **selection** menu, the framework enables the activation of auto-focus. The auto focus is BMI-independent; it is used in our framework to make a sequence of the commands according to the test pattern. Although the auto focus functionality assists the user, it does not replace the event of the command mental **selection**; it only makes a controlled sequence, unlike the brain control mode (without the use of the auto focus) that does not control command sequencing, thus requiring a bigger effort on the part of the user.

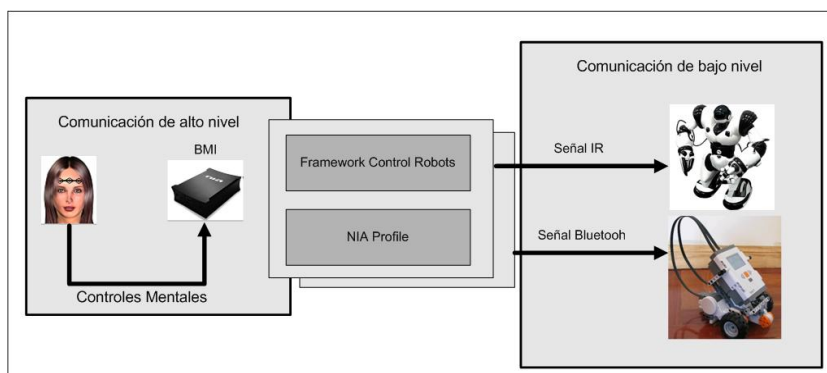


Fig. 4. Robot- BMI-NIA Integration

The framework configuration (Fig.5) for the fulfillment of the tests in the 'brain control with auto-focus' mode adopted the following command path: left-stop, forward-stop, right -stop. The execution of the 'forward' command was set to 2 seconds and the turns to 50 seconds. For the brain control (without auto-focus) tests said function was deactivated and it was used the same framework as in the manual control, with the same time parameters for the execution of forward and turn motions.

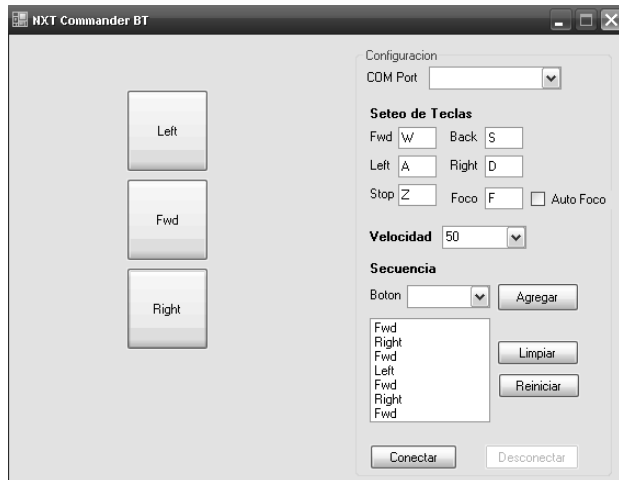


Fig. 5. Mobile Robot Framework

4 Result Discussion

Even though all the features of the BMI-NIA have not been mastered so far, we can comment that whenever used it is to be calibrated; although it was found out that calibration has not always been necessary, it is better to calibrate it before each test session period. On several occasions, the desired results were not achieved, particularly in the first attempts due partly to the equipment sensitivity to electromagnetic fields, and it was also found out that the user could exert some influence when touching the BMI-NIA. Throughout the initial trainings, the users became tired and needed some rest after approximately 30 minutes. At the beginning, the user makes muscular motion in an exaggerated way, but with practice and the improvements on profile calibration, the muscle movements are minimized. The tests performed with the biped robot were oriented to the free execution of mental commands and were the basis for the preparation of more complex tests with the mobile robot. One of the functional tests of free execution of the biped robot was video-documented [12]. The mobile robot tests were carried out in an experimentation area (2.00 meters x 1.50 meters) on which four check-points (Cp), distributed according to a pattern (Fig.6) were marked. The first test case was that of the manual control (MC) of the robot controlled by the user; for this case three training sessions and three test sessions were performed. The second test case was that of the brain control (BC); nine previous training sessions and three test sessions were carried out.

The third test case was performed in order to check the work proposal, regarding the application of brain control with auto-focus (BC-AF) in the command to be executed, according to the navigation pattern; for this mode six training sessions and three test sessions were carried out.

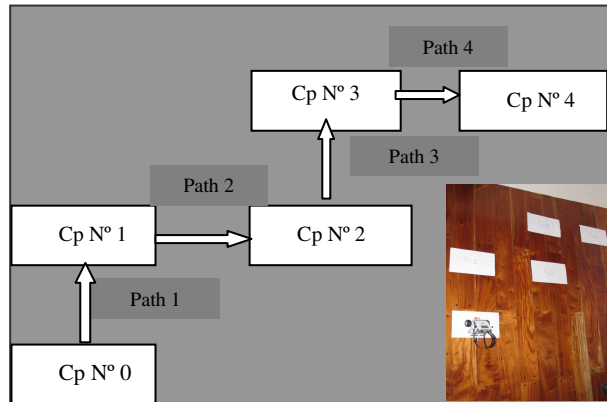


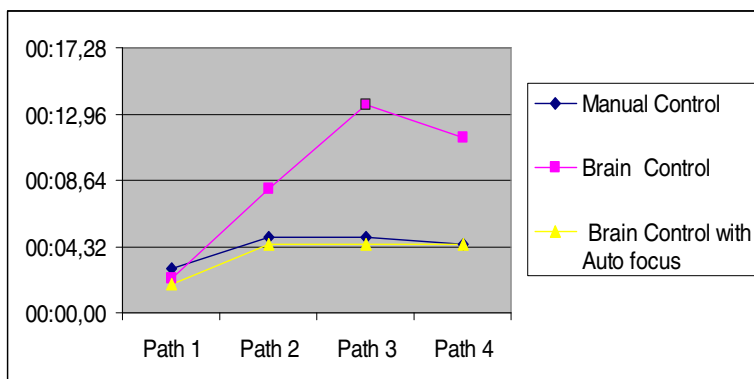
Fig. 6. Mobile Experimentation Pattern

For each test session, the partial times of each path defined between each check-point (Cp) –as detailed in table 1 “Mobile robot experimentation outcomes”- were obtained. The preliminary outcomes indicated that the combination of brain control with auto-focus (BC-AF) was quicker than the manual control solution; however, in general terms the Brain control (BC) solution was slower than the manual control (MC) solution. Table 1 shows the comparative average results obtained in the three test sessions corresponding to each control case (manual, brain, brain with auto-focus, respectively): (a) the time per path between each check point, (b) the total time to perform the pattern, (c) the time difference between manual control and brain control, (d) the time difference between manual control and brain control with auto-focus, (e) final percentages between manual control and brain control, final percentages between manual control and brain control with auto-focus. The second section of Table 1 shows the cumulative times between paths and the total time. Finally, to summarize we could state that the brain control with auto-focus was 11.32 % better than the manual control, though the manual control was 111 % better than the brain control (without auto-focus).

Fig. 7 shows the comparative distribution of average times of the test sessions for each path: with manual control, brain control and brain control with auto-focus, respectively. Finally Fig.8 shows the total time for each path, for each test according to the control type (manual control, brain control and brain control with auto-focus, respectively). To complete the navigation pattern, the second brain control test (test 2 BC) was the one which took longer (45.47 seconds) and the third test of brain control with auto-focus (test 3 BC-AF) was the one that took less time (13.93 seconds) to complete the same navigation pattern. Some parts of the mentioned tests were video-documented: brain control [13], brain control with auto-focus [14]

Table 1. Mobile robot experimentation outcomes

Type of Control	Manual	Brain	Brain Control
Average time between Path	Control (MC)	Control (BC)	with Auto focus (AF)
Path 1	00:02,85	00:02,19	00:01,84
Path 2	00:04,92	00:08,09	00:04,43
Path 3	00:04,91	00:13,60	00:04,50
Path 4	00:04,44	00:11,47	00:04,43
Total Time	00:17,13	00:36,16	00:15,19
Delta Time MC-BC		19,03	
Delta Time MC-BC + AF			1,94
% MC-BC		111%	
% MC-BC+AF			11,32%
CumulativeTime	Manual	BC	BC-AF
Path 1	00:02,85	00:02,19	00:01,84
Path 2	00:07,78	00:11,09	00:06,27
Path 3	00:12,69	00:24,69	00:10,76
Path 4	00:17,13	00:36,16	00:15,19
Total Time	00:17,13	00:36,16	00:15,19

**Fig. 7.** Average time between paths

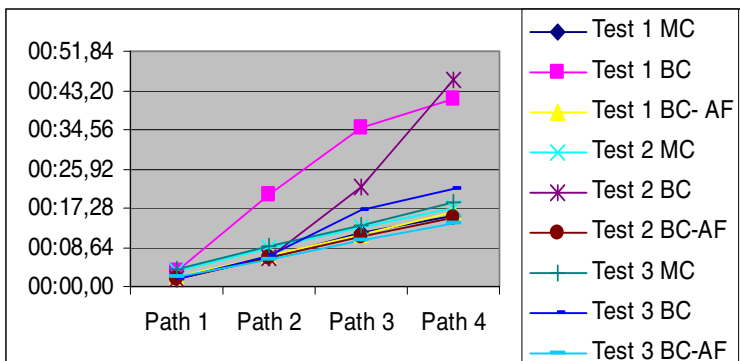


Fig. 8. Total time for each test

5 Conclusions and Future Research Lines

Due to the experience and the outcomes obtained in the preliminary tests of human-robot integration through brain-actuated control, we could enter a new dimension of communication. As a result of the tests performed in a real environment with physical limitations, for example the slight floor undulation, the final outcome was that the brain control with auto-focus mode slightly exceeded the manual control. Although the manual control exceeded the brain control in terms of time for the execution of the navigation pattern, this is to be considered in a preliminary framework within the beginning of the user's learning curve with BMI memory. In conclusion, this experience allows us to appreciate the wide potential of applications, especially those oriented to physically disabled people, as well as human interaction in a direct way with context-centered applications, and the future potential of human-robot collaboration among other possible fields. Our future research lines will focus on the development of an integrating framework for robots, the interaction with the robot perception through its environment sensorization, and the study of new BMIs (Emotiv) [15] as well as the continuity of the users' practice and experimentation, adapting their memory to the context of BMI applications [16].

References

1. Wessberg, J., Stambaugh, C.R., Kralik, J.D., Beck, P.D., Laubach, M., Chapin, J.K., Kim, J., Biggs, S.J., Srinivassan, M.A., Nicolelis, M.A.L.: Real-time prediction of hand trajectory by ensembles of cortical neurons in primates. *Nature* 408, 361–365 (2000)
2. Nicolelis, M.A.L.: Brain-machine interfaces to restore motor function and probe neural circuits. *Nature Rev. Neurosci.* 4, 417–422 (2003)
3. Wolpaw, R., McFarland, D.J., Vaughan, T.M.: Brain-computer interface research at the Wadsworth center. *IEEE Trans. Rehab. Eng.* 8, 222–226 (2000)
4. del Millán, J.R.: Brain-computer interfaces. In: Arbib, M.A. (ed.) *Handbook of Brain Theory and Neural Networks*, 2nd edn. MIT Press, Cambridge (2002)

5. Millán, J., Renkensb, F., Mouriñoc, J., Gerstnerb, W.: Non-Invasive Brain-Actuated Control of a Mobile Robot by Human EEG. *IEEE Trans. on Biomedical Engineering* 51 (June 2004)
6. Saulnier, P., Sharlin, E., Greenberg, S.: Using Bio-electrical Signals to Influence the Social Behaviours of Domesticated Robots. In: *HRI 2009*, La Jolla, California, USA, March 11–13. ACM (2009) 978-1-60558-404-1/09/03
7. WowWeeRobotics (2012), <http://www.wowwee.com/en/products>
8. RS, http://www.wowwee.com/static/support/robosapien/manuals/Robosapien_Manual.pdf
9. NXT (2012), <http://mindstorms.lego.com/eng/Overview/default.aspx>
10. NIA, http://www.ocztechnology.com/products/ocz_peripherals/nia-neural_impulse_actuator
11. USB-UIRT (2012), <http://www.usbuirt.com/>
12. Video Bípedo (2012), <http://www.youtube.com/watch?v=-04JjfMcdfU>
13. Video Brain control, <http://www.youtube.com/watch?v=LhKV50jNgcY>
14. Video Brain control con auto foco,
<http://www.youtube.com/watch?v=hD9CvQlNxho>
15. Emotiv (2012), <http://www.emotiv.com>
16. Jorge, I., Gustavo, P., Juan, I.: Demostración de integración de Interfases Lectoras de Bioseñales aplicadas al Control de un Robot. Congreso Educación en Tecnología y Tecnología en Educación UNNOBA (2012) ISBN 978-987-28186-3-0

Experience with the Children-Humanoid Interaction in Rehabilitation Therapy for Spinal Disorders

Maria Vircikova and Peter Sincak

Center for Intelligent Technologies,
Dept. of Cybernetics and Artificial Intelligence, Technical University of Kosice,
9 Letna, Kosice 040-01, Slovakia
{Maria.Vircikova,Peter.Sincak}@tuke.sk

Abstract. This paper deals with the social human-robot interaction with children towards the application outside tightly controlled and constrained laboratory environments. We present our experience of using the Nao humanoid robotic platform in a role of a physiotherapist for rehabilitation and prevention of scoliosis in a children's hospital and an elementary school in Slovakia. Before and between the exercise units, children could freely interact with a robot, what contributed to building-up robot-children relationship. The results indicate the potential of humanoids to enhance the quality of life of children in an entertaining and effective way.

Keywords: applications, human-robot interaction, human environment, observation of interaction, robotherapy, social robotics.

1 Introduction

Social robotics is an emerging field with the focus on interaction-oriented robots, which are being developed to join human environments. Comparing social and industrial robots, the social are capable to engage people in natural exchange. Human interactive robots are already used in the human environment, such as schools, hospitals and in homes, assigned many kinds of tasks and also have already been proposed as supplementary tools for rehabilitation. According to [6], beyond the basic capabilities of moving and acting autonomously, the field has focused on the use of the robot's physical embodiment to communicate and interact with users in a social and engaging manner.

In this paper, we focus on the motivational issue of the humanoid robot Nao immersed in the real environment with children to raise their interest in exercise as a part of the therapy. For Tapus, Mataric and Scassellati [6], motivation is recognized as the most significant challenge in physical rehabilitation and training. Socially assistive robotics technology has the potential to provide novel means for monitoring, motivating, and coaching.

This study will therefore address the following research question:

What effects can be observed when we put a humanoid robot in the role of the physiotherapist to exercise with children?

The purpose of this paper is to share our experience learned about the implementation of systems for social HRI with child users towards application in the human environments, outside tightly controlled and constrained laboratories.

As said, there are many projects which use humanoids for the autism therapy with children. Our motivation was principally to motivate children to exercise, as there is a wide application potential, as the problem of scoliosis in today's society is growing and also children tend to become overweight. In general, it is fundamental to ensure adequate motor skill development during childhood. Exercises can help strengthen children's back and improve their posture to prevent spinal disorders like scoliosis. As children tend to discover the world around them, with special interest in technology, we used a humanoid robot as a trainer to exercise with children for scoliosis treatment. The advantages of using humanoid robots for rehabilitation or prevention exercises consist in their motion - they resemble human's body in shape and their motion is precise and repeatable. This paper moves beyond these factors presenting our observations of positive influence of the interaction between children and the robot on their interest in the exercise. The second advantage of the implementation of the robot to show patients exercises is that the human physiotherapist does not have to perform exercises and thus can observe patients, correct their movements and help the weaker ones.

There is a need to encourage children to get more exercise, not only with purpose to prevent spine disorders, but in general to help prevent health complications, e.g. from getting overweight, from getting heart disease or diabetes at an early age. The core aim of this research is to fuse play and rehabilitation techniques using a robotic design to induce child-robot interaction, in which the criteria is to achieve is to be entertaining and effective for the children.

2 Related Works

Human-Robot Interaction is exploring the potential for partner robots to interact with people in daily life. It raised a significant number of studies which report observations of non-technical individuals interacting with robots with the aim to assist people in the daily real-world. Many projects use a robot-assisted therapy with the aim to improve people's moods, and exceptional interest is in the work with autistic children, e.g. [7], [8], [9], [10], [11] and facing aging population, e.g. [12], [13], [14], [15], [16], [17]. Such projects believe that during the process of machine migration to the human society they will be considered beneficial and intuitive partners. The future cooperation between machines and us how we believe it will be can be summed up with these words: machines fully adapting to man – that man no longer has to adapt his behaviour to machines.

Tanaka[2] did a study where a small humanoid robot kept attending at a nursery school on a daily basis for more than three months. This research focused on children's touch behaviour on the robot. A group around Kozima[3] build and evaluates a humanoid robot that is intended to help normal and handicapped children learn to communicate socially with other people. They report that the embodied interaction is

the key activity in the social communication, where one sees invisible mental states, such as intention and belief, in the visible posture and movement of others.

Kanda [4] develops a humanoid that reads human relationships from their physical behaviour. The robot recognizes friendly relationships among humans by simultaneously identifying each person in the interacting group. He made a practical and long-term experiment with autonomous humanoid robots human society. Students in an elementary school interacted with the robots over 18 days. They expected that the robots human-like form and behaviour would evoke spontaneous communication from the children. The results suggest that the communicative relationships between children and the robots did not endure for more than one week in general. However, some children developed sympathetic emotions for the robot. Authors find necessary to identify methods to promote longer lasting interactive relationships. The second issue is that, when using a robot to show patients the exercises, a human physiotherapist or a doctor can observe patients during the therapy process and can help each of them individually.

A similar study as us was conducted by Ros et. al.[5] presenting insights gleaned from a series of child-robot interaction experiments carried out in a hospital paediatric department. We agree with them that social interaction with robots is challenging, but there is a point of entry to human-robot interaction which is, in some respects at least, easier. Children, for reasons not fully understood, respond much more readily and strongly to social robots. As such, human-robot engagement is significantly more easily attained with younger children than it is with adolescent or adult users.

Gockley and Mataric [19] focus on the role of embodiment and implemented an autonomous mobile robot aimed at the role of a monitoring and encouragement system for stroke patient rehabilitation. Their results show that the presence and behavior of the robot can influence how well people comply with their physical therapy.

You et al. [20] reported field trials of using robot in an English learning classroom, where the robot plays as a partner of a teacher. They observed most students in the three classes had a positive attitude to this robot, and had great interest in the robot's performance.

3 The Experimental Scenario

3.1 Basic Set-Up

The aim of the proposed research is to develop companion robots able to engage child users and support them in exercising, important for their physical condition. An interaction scenario was designed, consisting of the following parts:

1. The robot is introduced to the children.
2. Children can freely interact with him.
3. The exercises are shown by the robot and children try to imitate his movements.



Fig. 1. Children and the humanoid robot environment

We use a humanoid-type robot Nao, developed by the French company, Aldebaran robotics. Since he is about the size of a child, children are not afraid of him. We present two human-robot interaction (HRI) experiments. First, we observed the robot in the hospital at the department of oncology. In the second, the robot was inserted in the elementary schools. In both cases it was used for robotherapy.

The subjects, in both environments of the hospital and the school, are 50 children, aged between 5-7. This sample of subjects was chosen deliberately, as children of this age are playful, interested in the unknown and thus are not limited by fear of the unknown. On the other hand, the problem of children of this age is their concentration. The majority of children is not able to repeat the same activity during a longer time. This is the main priority for satisfactory results of the rehabilitation exercises. The experiment was 2 days long.

3.2 The Pre-rehabilitation Phase

Firstly, we introduced the humanoid robot to children. We explained children his capabilities and skills and showed them several entertaining performances, prepared by the students involved in the project. The performance, e.g. various kinds of robotic dances or robotic theatres, raises the interest in children for the robot. We tried to enjoin children to participate in the future activity of exercising with the robot.

In the next step we left children interact with the robot. They could communicate with him - touching him or talking to him. Together with the students we prepared a set of interactive behaviours. Here is the place for the techniques of artificial intelligence, in the areas of human identification and face recognition, natural language communication, implementation of the emotional technology and programming a loop of interactive behaviours. We argue that the interactivity is the key element of success in the area of social robotics.



Fig. 2. Introducing Nao in the hospital



Fig. 3. Introducing Nao in the school



Fig. 4. Child-robot interaction in the hospital environment



Fig. 5. Child-robot interaction in the school environment

3.3 The Rehabilitation Process

In this part we used a humanoid robot as a tool to peak children's interest to do exercise which can help to increase the effectiveness of the therapy. We programmed a set of exercises for the scoliosis reduction.

There is a need to encourage children to get more exercise, not only with the purpose to prevent spine disorders, but in general - to help prevent health complications, such as from getting overweight, from getting heart disease or diabetes at an early age, [17]. However, children often become bored easily, especially with routines. In children the scoliosis tends to present as a cosmetic problem, whereas scoliosis in adults more often presents with pain and neurological symptoms. These exercises reduce the symptoms of spinal disorders, as they improve cosmetic appearance, reduce pain, improve breathing and function levels, reduce the existing curvature and in some cases avoid the need for scoliosis surgery. We discussed the design of the exercises with a professional physiotherapist with the purpose to correct or lessen the curvature to help to prevent the possibility of surgery in the future. The exercise should posses the following qualities:

- The motions during the exercises should be slow pacing of the duration of 20 minutes.
- The movement is slow, without fitfulness.
- A sudden, violent movement and swing should be avoided.
- At the beginning the range of exercises is of little extent and this range during the exercise process is gradually increasing until the marginal position.
- Patients can feel slight tension but not pain.
- The training should be performed in static, less demanding positions (standing, sitting or lied down) to reduce muscle tension while maintaining balance.



Fig. 6-10. Children exercising with the robot

4 The Observations and Comments

4.1 Contributions of the Robot's Involvement

Based on the video material documenting the interactions, a qualitative analysis was conducted. We observed contributions of the robot implementation in the therapy process for the scoliosis treatment from the following perspectives:

- 1. The Rise of the Children's Interest in the Therapy.** The robot from the point of view of children changed boring, repetitive exercises into joyful and exciting play. The results of this part are discussed in the section 4.2.

2. **The Effectiveness of the Work of the Human Physiotherapist.** Our work has focused on applications of socially assistive robotics in health care and education, where human supervision can be significantly augmented and complemented by intelligent machines. As the robot was performing the exercise units, the human trainer could monitor the children and help them individually.
3. **Involvement of the Students.** The exercise units were programmed by students of the 1st of the Master course of the subject called Interactive Systems. They were involved in this work with the objective to help students to understand how people perceive robots. The knowledge of human-robot interaction enables students to study of how humans interact with robots, and how best to design and implement robot systems capable of accomplishing interactive tasks in human environments. Students had to design the user interface, to test it during the real-time interaction with people without any technical background and then to analyze results and finally, to repeat the process. People's opinions and reactions towards robots serve as valuable feedback not only for their projects.

4.2 Evaluation of the Children-Humanoid Interaction

We discuss the following effects of the humanoid platform on children's motivation in the rehabilitation therapy:

- *Interest.* Only the arrival of Nao generated unprecedented interest of children, supported by the sound of greeting him, gestures of waving, sparkling eyes, smiles, noise and loud voices and children asked to touch him. When the children saw the robot for the first time, all of them gathered around the robot. All of the children wanted to interact with him with much excitement. In the context of HRI, younger children are willing to view the robot as more than an ordinary mechanical object. Children have the tendency to attribute human characteristics and behaviours to robots, at least to anthropomorphic robots, as previously analyzed by Ros[5].
- *Docility.* Children motivated by the interest in the robot started to subordinate to all of the verbal instructions without any complains. The human physiotherapist reported that it was unusual when exercising with human trainer.
- *Joy of exercise.* Children were happy of all of the motions and tried to imitate the humanoid's motions as accurately as they could. They said the exercise was "*like to play with a good friend.*"
- *Correctness.* The kinetics of each child is individual. Motorically weaker children in the process of exercises were supervised by a human physiotherapist himself. This had time to help children individually, as his job of the instructor was performed by the robot. This leads to the raise of the accuracy and perfection of each of the motions.

- *Repeatability.* Children, while maintaining obedience and concentration, had no problem with repetition of the exercises. They had a break when they could interact with the robot and got to know what he can do between the first and the second unit of exercises. This time of joy and fun was motivational and relaxing. All of the children wished to continue after the rehabilitation training finished.
- *Other comments.* We do not compare the two selected environments in more details, as it is clear that children in the hospital, treated for oncology disease, are more quiet and do not show joy or interest in comparable manner as the healthy children do. However, the most amazing moment we experienced together with our students, was when a nurse of the children's oncology department said us that "she had not seen these children smiling and even laughing, some of them, for months." The human therapist, in both cases, agreed that the robot fascinated children, evoke their positive emotions and as a result they wanted to do their utmost during the exercise process.

5 Conclusion

The purpose of this paper was to present our scenario of a humanoid robot as an instructor in the physical therapy in the environment with children. We tried to find an effective structure of the overall children-robot interaction process to motivate children to exercise with the robot. We report that the joy of children rose from the interaction, the accuracy of the motions and their repeatability - as the robot does not become tired and all of the children wanted to continue when the exercise finished.

The important part of the scenario was a free interaction, when the majority of the children established a closer relationship with the robot, perceiving him as a peculiar friend. We feel that the most difficult challenge in the future is coping with the loss of desire to interact with the robot on a long-term basis. The verbal communication of the robot together with its gestures raises children's interest and admire. The mutual interaction during the exercises is important, as it could have both the motivational and educational character.

Acknowledgements. Research partly supported by a number of projects including the project implementation of "Development of the Center of Information and Communication Technologies for Knowledge Systems" (ITMS project code: 26220120030) supported by the Research & Development Operational Program funded by the ERDF. These results are also thanks to the project "Center of Competence of knowledge technologies for product system innovation in the industry and service", with ITMS project number: 26220220155 for the years 20012-2015 and also the research is partly supported by the National Research and Development Project Grant 1/0667/12 "Incremental Learning Methods for Intelligent Systems" 2012-2015.

References

1. Kanda, T., Hirano, T., Eaton, D.L., Ishiguro, H.: A practical experiment with interactive humanoid robots in a human society. *Humanoids* (2003)
2. Tanaka, F., Movellan, J.R.: Behavior Analysis of Children's Touch on a Small Humanoid Robot: Long-term Observation at a Daily Classroom over Three Months. In: The 15th IEEE International Symposium on Robot and Human Interactive Communication, RO-MAN 2006 (2006)
3. Kozima, H., Nakagawa, C., Kosugi, D., Yano, Y.: A Humanoid in Company with Children. In: 4th IEEE/RAS International Conference on Humanoid Robots (2004)
4. Kanda, T., Ishiguro, H.: Reading human relationships from their interaction with an interactive humanoid robot. In: Orchard, B., Yang, C., Ali, M. (eds.) IEA/AIE 2004. LNCS (LNAI), vol. 3029, pp. 402–412. Springer, Heidelberg (2004)
5. Ros, R., et al.: Child-Robot Interaction in The Wild: Advice to the Aspiring Experimenter. In: Proceedings of the ACM International Conference on Multi-modal interaction (2011)
6. Tapus, A., Mataric, M., Scassellati, B.: Socially Assistive Robots, The Grand Challenges in Helping Humans Through Social Interaction. *IEEE Robotic and Automation Magazine* 35–42 (2007)
7. Libby, S., Powell, S., Messer, D., Jordan, R.: Spontaneous play in children with autism: A reappraisal. *Journal of Autism and Developmental Disorders* 28, 487–497 (1998)
8. Pierce-Jordan, S., Lifter, K.: Interaction of social and play behaviors in preschoolers with and without pervasive developmental disorder. *Topics in Early Childhood Special Education* 25(1), 34 (2005)
9. Hobson, R., Lee, A., Hobson, J.: Qualities of symbolic play among children with autism: A social-developmental perspective. *Journal of Autism and Developmental Disorders* 39, 12–22 (2009)
10. Robins, B., Dautenhahn, K., Dickerson, P.: From isolation to communication: A case study evaluation of robot assisted play for children with autism with a minimally expressive humanoid robot. In: Int. Conf. Adv. in Computer-Human Interactions, pp. 205–211 (2009)
11. Kozima, H., Nakagawa, C., Yasuda, Y.: Interactive robots for communication-care: a case-study in autism therapy. In: IEEE Int. Workshop Rob. and Human Interactive Com., pp. 341–346 (2005)
12. Bahadori, S., Cesta, A., Grisetti, G., Iocchi, L., Leone, R., Nardi, D., Oddi, A., Pecora, F., Rasconi RoboCare, R.: An integrated robotic system for the domestic care of the elderly. In: Proceedings of Workshop on Ambient Intelligence AI*IA 2003, Pisa, Italy (2003)
13. Broadbent, E., Stafford, R., MacDonald, B.: Acceptance of healthcare robots for the older population: review and future directions. *Int. J. Soc. Robot* 1, 319–330 (2009)
14. Broekens, J., Heerink, M., Rosendal, H.: Assistive social robots in elderly care: a review. *Gerontechnology* 8, 94–103 (2009)
15. Pollack, M.E.: Intelligent technology for an aging population: the use of AI to assist elders with cognitive impairment. *AI Mag.* 26, 9–24 (2005)
16. Schraft, R.D., Schaeffer, C., May, T.: Care-O-botTM: The concept of a system for assisting elderly or disabled persons in home environments. In: Proceedings of the 24th Annual Conference of the IEEE Industrial Electronics Society: IECON, Aachen, Germany, pp. 2476–2481 (1998)
17. Sparrow, R., Sparrow, L.: In the hands of machines? The future of Aged Care Mind Mach. 16, 141–161 (2006)

18. The National Institute of Arthritis and Musculoskeletal and Skin Diseases, Questions and Answers about Scoliosis in Children and Adolescents (2008),
<http://www.niams.nih.gov/HealthInfo/Scoliosis>
19. Gockley, R., Mataric, M.J.: Encouraging physical therapy compliance with a hands-Off mobile robot. In: Proceedings of the 1st ACM SIGCHI/SIGART Conference on Human-robot Interaction (HRI 2006), pp. 150–155. ACM (2006)
20. You, Z.J., Shen, C.Y., et al.: A Robot as a Teaching Assistant in an English Class,” Advanced Learning Technologies, 2006. In: Sixth International Conference on Advanced Learning Technologies, pp. 87–91, 5-7 (2006)

Differential Kinematics of Flexible Manipulator for Calibration of Model Parameters

Bum-Joo Lee

Department of Electrical Engineering, Myongji University, San 38-2, Nam-Dong, Yongin,
Kyunggi-Do, 449-728, Republic of Korea
bjlee@mju.ac.kr

Abstract. In this paper, a noble algorithm was proposed which improves the accuracy of the manipulation of the robot by calibrating the model parameters such as the Denavit-Hartenberg parameters, joint compliances, and CM positions of the links. Even though the mechanical parts are manufactured and assembled accurately, always small differences between the designed and the actual system exist due to both the geometric and the unmodeled error. In order to resolve these problems, the proposed algorithm employs an estimation system which consists of a structured light module with a stationary camera and a screen. After derivation of the Jacobian which represents the relationship between the model parameters and the laser points on the screen, the model parameters are updated by using an iterative estimation algorithm such as least-squares manner. This algorithm is advanced by considering the joint flexibility from the previous work which used a rigid link model [1]. Effectiveness of the proposed algorithm was verified by the computer simulation with a 6 DOF manipulator robot.

1 Introduction

The kinematic information of the links of a manipulator is essential for the control of the robotic systems. Especially in the research of an articulated link manipulator which consists of a series of links such as a robotic arm, finger, or leg, accuracy of the model directly influence the performance of the manipulator's task. Consequently, it is important to know the parameters which determine the mathematical model of the robot. Although a 3D cad tool provides accurate information of the model, however, the geometry of the actually manufactured robot commonly does not match the designed one. Subsequently, the difference between the models reduces the accuracy of the manipulation significantly. Inaccuracies in the model parameters of the robotic systems arise from two kinds of errors: geometrical and unmodeled errors. The geometrical errors are caused by an inaccurate manufacturing, assembling, were, etc. The unmodeled errors are commonly caused by the approximation such as joint and link flexibilities, thermal dynamics, etc. Therefore, in order to improve the accuracy and/or the stability of the manipulation, it is required to calibrate the model parameters and use an advanced robot model together.

There were a lot of research related to the kinematical identification and calibration of the manipulator robot. A methodology that uses laser was introduced to capture robot

position data in order to model stiffness of the robot manipulator [2] and to predict kinematic parameters [3–7]. O'Brian et al. also employed a magnetic motion capture data to determine the kinematic parameters [8]. Renaud et al. [9] and Rauf et al. [10] used a vision-based measuring device and a partial pose measurement device for kinematic calibration of parallel mechanisms, respectively. Gatti and Danieli demonstrated a pose-matching procedure for calibration, which provides a low cost and easy-to-use external metrology system [11]. Santolaria et al. recently demonstrated a continuous data capture technique by using a ball bar gauge and a cooling probe to estimate kinematic parameters of articulated arm coordinated measuring machines [12]. It was concluded that the parameter error was minimized in the measured positions, whereas the error increased in very different positions because the optimization technique was only based on the position information of end-effector. To overcome this problem, Ye et al. [13] and Iurascu and Park [14] demonstrated a kinematic calibration method using differential kinematics and iterative algorithms to determine parameters.

In the previous paper, a novel algorithm was proposed to estimate entire kinematic parameters of the robot manipulator by using a structured laser module(SLM), a stationary camera and a screen [1]. In the algorithm, by using the Jacobian which represents the relationship between the kinematical parameters and the laser points on the screen, iterative estimation scheme such as the Extended Kalman filter (EKF) was adopted. For the kinematic model, Denavit-Hartenberg (D-H) convection is used and all the joints and the links were modeled as rigid.

In this paper, the previously proposed method was extended by using the flexible joint model. To improve the accuracy of the manipulation, three types of model parameters were estimated: D-H parameters, joint compliances, and CM positions of the links. Similarly with the previous work, SLM system with a stationary camera and a screen was adopted to estimate the model parameters. The proposed technique is verified with a 6 DOF humanoid leg system by computer simulation.

This paper is organized as follows. In Section 2, problems are defined and described with a flexible joint model. Subsequently, in Section 3 and 4, mathematical model and Jacobians are represented, respectively. In Section 5, the effectiveness of the proposed algorithm is verified by simulational experiment. Lastly, concluding remarks follow in Section 6

2 Problem Definition

In order to control robot manipulator precisely, it is essential to know the kinematical parameters of the manipulator. However, there always exist model errors in link lengths and link twists during manufacturing and/or assembling the robot system. These undesirable errors reduce accuracy during the manipulation and sometimes make the system unstable. These may cause more problems in a complex articulated linkage system such as a humanoid robot. Small error in each joint is accumulated and eventually it makes a significant difference between the model and the actual system as shown in Fig. 1 where the transparent image with the solid line represents the designed posture with the model parameters. While the colored image represents actual posture.

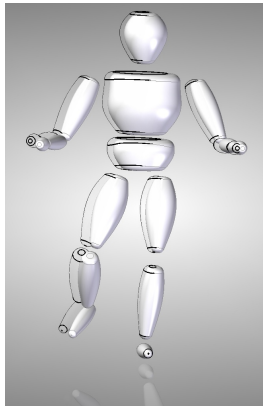


Fig. 1. Misestimated robot posture

In the previous work, a novel systematic algorithm was proposed to measure the errors in the kinematical parameters by using a structured laser module (SLM) and a stationary camera system. With the algorithm, the kinematical errors were successfully measured. Consequently, it enhanced the accuracy in the forward and inverse kinematics. Since the algorithm uses a lot of standstill postures of the manipulator with rigid kinematical model, however, if the mass of the link of the manipulator is large or the stiffness of the joint is small, then observation errors arise due to the gravitational force. This undesirable effect is depicted in Fig. 2 where θ_r and θ_f represent joint angles under rigid and flexible joint model, respectively, and θ_e and τ_g represent an expected angle and a gravitational torque. Normally, in the rigid model it is assumed that the θ_e is equal to the θ_r , while it is different from θ_f .

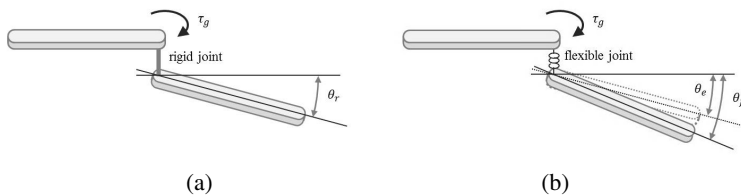


Fig. 2. Influence of joint flexibility. (a) Rigid joint. (b) Flexible joint.

In order to estimate the model parameters, the measurement system is configured as shown in Fig. 3. The proposed system consists of a SLM attached on a manipulator, a stationary camera and a screen. Note that the base frame σ^G is attached on the screen

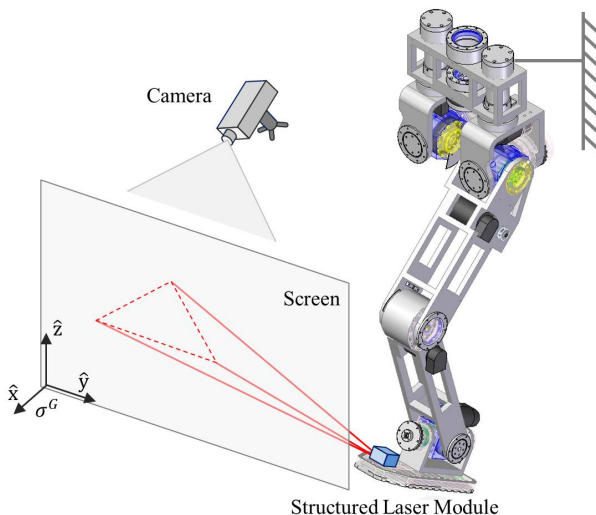


Fig. 3. Overall system to estimate the kinematical parameters using SLM

and the stationary camera is used to measure positions of the laser points on the screen. When all kinematical parameters including joint compliances and mass positions are accurately known, predicted laser points on the screen with the given robot posture must be equal to the measured point by the stationary camera. Since there are some model errors, however, this case does not happen generally as mentioned above. The proposed method uses the differences between predicted laser points from the current model parameters and the actually measured points to update the model parameters. To do this, it needs the relationships between the variations of the model parameters and the laser points. This is commonly accomplished by Jacobian matrix. A detailed mathematical model and a derivation of the Jacobians are described in Section 3 and 4, respectively.

3 Mathematical Model

3.1 Kinematical Model

In the proposed algorithm, D-H notation is utilized to describe the kinematical motion because the notation uses minimum number of parameters to represent the coordinate system attached on the each link as shown in Fig. 4. Here α and β are the joint offset angle and the twist angle between the joint axes, respectively, and d and l are the distance between links and the length of the link, respectively. Also, θ and ϕ are the joint angle and the twisting angle due to the joint flexibility, respectively.

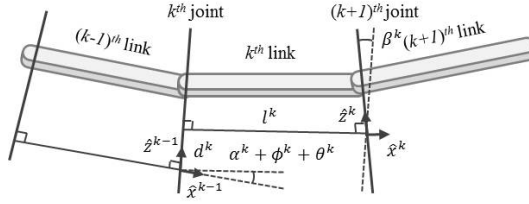


Fig. 4. Coordinate frames of revolute joints with D-H notation

3.2 Differential Kinematics

End-effector's posture is determined from the D-H parameters and twisting angles due to the joint flexibility as represented in Eq. (1).

$$\begin{aligned}\pi_e &= f(\lambda, \phi) \\ &= \begin{bmatrix} r_e \\ \delta_e \end{bmatrix}^T\end{aligned}\quad (1)$$

where λ and ϕ are both vectors for the D-H parameters and the twisting angles, respectively, π_e is 6×1 vector which consist of position(r_e) and orientation(δ_e) of the end-effector in 3D space. By differentiating Eq. (1), differential kinematic motion is obtained as follows:

$$d\pi_e = \frac{\partial f}{\partial \lambda} d\lambda + \frac{\partial f}{\partial \phi} d\phi \quad (2)$$

At the stationary state, the twisting angles are represented as following implicit function:

$$\phi = h(c, \lambda, p_m, \phi) \quad (3)$$

where c and p_m represent joint compliance and mass position, respectively. If the twisting angles are not too large, in other words, the rigidity of the joint is big enough, the effect of nonlinearity for the compliance can be negligible. Consequently, the joint compliance can be modeled as linear. From the Hooke's law, the twisting angles are simply expressed as multiplication of the compliances and the joint torques.

$$\phi = D_\chi \gamma(\lambda, p_m, \phi) \quad (4a)$$

$$= D_\gamma \chi \quad (4b)$$

where γ means the joint torque vector and D_χ means diagonalized matrix of a vector x . By differentiating Eq. (4), differential of the twisting angles are derived as follows:

$$\begin{aligned}
d\phi &= \frac{\partial h}{\partial \chi} d\chi + \frac{\partial h}{\partial \lambda} d\lambda + \frac{\partial h}{\partial p_m} dp_m + \frac{\partial h}{\partial \phi} d\phi \\
&= D_\gamma d\chi + D_\lambda \frac{\partial \gamma}{\partial \lambda} d\lambda + D_\chi \frac{\partial \gamma}{\partial p_m} dp_m + D_\phi \frac{\partial \gamma}{\partial \phi} d\phi
\end{aligned} \tag{5}$$

By solving Eq. (5) algebraically for $d\phi$, differential relationship among the compliances, the D-H parameters and the mass positions is derived as follows:

$$d\phi = \left(I - D_\chi \frac{\partial \gamma}{\partial \phi} \right)^{-1} \left(D_\gamma d\chi + D_\lambda \frac{\partial \gamma}{\partial \lambda} d\lambda + D_\chi \frac{\partial \gamma}{\partial p_m} dp_m \right) \tag{6}$$

By substituting Eq. (6) into Eq. (2), differential kinematic motion is finally expressed as differentials of the D-H parameters, the compliances and the mass positions as follows:

$$d\pi_e = \frac{\partial \pi_e}{\partial \lambda} d\lambda + \frac{\partial \pi_e}{\partial \chi} d\chi + \frac{\partial \pi_e}{\partial p_m} dp_m \tag{7}$$

where,

$$\begin{aligned}
\frac{\partial \pi_e}{\partial \lambda} &= \frac{\partial f}{\partial \lambda} + \frac{\partial f}{\partial \phi} \left(D_k - \frac{\partial \gamma}{\partial \phi} \right)^{-1} \frac{\partial \gamma}{\partial \lambda} \\
\frac{\partial \pi_e}{\partial \chi} &= \frac{\partial f}{\partial \phi} \left(D_k - \frac{\partial \gamma}{\partial \phi} \right)^{-1} D_k D_\gamma \\
\frac{\partial \pi_e}{\partial p_m} &= \frac{\partial f}{\partial \phi} \left(D_k - \frac{\partial \gamma}{\partial \phi} \right)^{-1} \frac{\partial \gamma}{\partial p_m}
\end{aligned}$$

Eq. (7) represents the relationship among the variation of the kinematical parameters, the compliances and the mass positions for the end-effect posture. Applying estimation

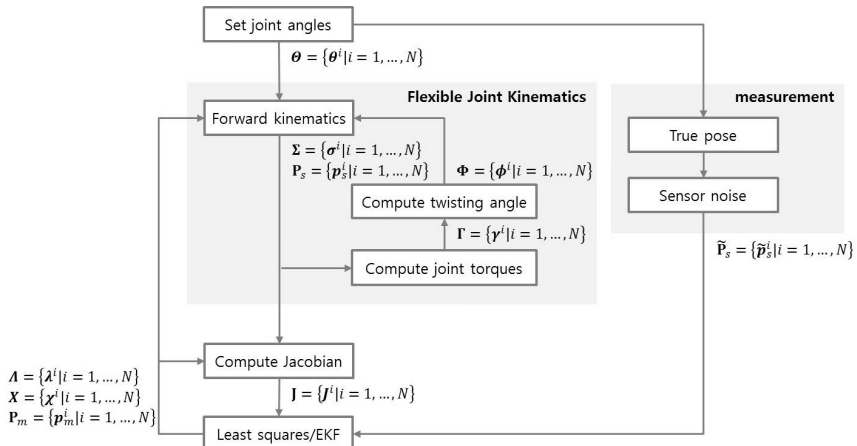


Fig. 5. Block diagram of overall algorithm flow

algorithm such as Least-squares manner or Extended Kalman filter, kinematical parameters can be effectively calibrated. This overall algorithm is summarized in the block diagram as described in Fig. 5. Note that Jacobians of Eq. (7) will be derived concretely in the Section 4.

4 Derivation of Jacobian

4.1 End-Effector Posture Derivatives w.r.t D-H Parameters and Twisting Angles

Since the computation of the Jacobian accompanies partial derivatives, it is generally not easy to derive the Jacobian matrix. Fortunately, however, the Jacobian of articulated linkage system can be computed systematically. Fig. 6 illustrate general D-H coordinate frames which is used in the proposed algorithm. Jacobian is computed by the exactly same manner commonly used in kinematics, except that the parameters are D-H parameters, $\lambda = [\dots \alpha^k \ d^k \ l^k \ \beta^k \ \dots]^T$, including the twisting, $\phi = [\dots \theta^k \ \dots]^T$, angles. The Jacobian is constituted by differential translation and differential rotation with respect to the corresponding parameters. Differential translation and differential rotation by the translational parameters such as d^k and l^k are unit vector in the direction of the translation and zero vector, respectively. Also, differential translation and differential rotation by the rotational parameters such as α^k , β^k and θ^k are cross product of rotational axis vector and distance vector from the rotational axis to the end-effector and unit axis vector, respectively. Eq. (8) represents these formulas.

$$\begin{bmatrix} \hat{z}^{k-1} \times (r_e - r_\sigma^{k-1}) & \hat{z}^{k-1} \hat{x}^k \hat{x}^k \times (r_e - r_\sigma^k) & \hat{z}^{k-1} \times (r_e - r_\sigma^{k-1}) \\ \hat{z}^{k-1} & 0 & 0 \\ \dots & \dots & \dots \end{bmatrix} \quad (8)$$

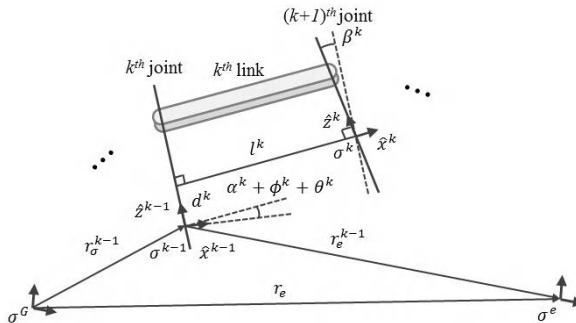


Fig. 6. Coordinate frames for Jacobian Computing

Partial Derivative w.r.t. D-H Parameters($\frac{\partial f}{\partial \lambda}$)

Applying Eq. (8), partial derivatives of the end-effector posture with respect to the D-H parameters are computed as follows:

$$\frac{\partial f}{\partial \lambda} = \left[\begin{array}{c} \frac{\partial f}{\partial \lambda_o} \frac{\partial f}{\partial \lambda_e} \\ \underbrace{\begin{array}{c} \hat{z}^G \times (r_e - r_\sigma^0) \hat{z}^G \hat{x}^0 \hat{x}^0 \times (r_e - r_\sigma^0) \\ \hat{z}^G \quad 0 \quad 0 \quad \hat{x}^0 \end{array}}_0 \\ \dots \underbrace{\begin{array}{c} \hat{z}^{k-1} \times (r_e - r_\sigma^{k-1}) \hat{z}^{k-1} \hat{x}^k \hat{x}^k \times (r_e - r_\sigma^k) \\ \hat{z}^{k-1} \quad 0 \quad 0 \quad \hat{x}^k \end{array}}_k \\ \dots \underbrace{\begin{array}{c} \hat{z}^{n-2} \times (r_e - r_\sigma^{n-2}) \hat{z}^{n-2} \hat{x}^{n-1} \hat{x}^{n-1} \times (r_e - r_\sigma^{n-1}) \\ \hat{z}^{n-2} \quad 0 \quad 0 \quad \hat{x}^{n-1} \end{array}}_{n-1} \\ \underbrace{\begin{array}{c} \hat{x}_T \hat{y}_T \hat{z}_T \hat{x}_{R_x} \times (r_e - r_{R_x}) \hat{y}_{R_y} \times (r_e - r_{R_y}) \hat{z}_{R_z} \times (r_e - r_{R_z}) \\ 0 \quad 0 \quad 0 \quad \hat{x}_{R_x} \quad \hat{y}_{R_y} \quad \hat{z}_{R_z} \end{array}}_n \end{array} \right] \quad (9)$$

where $0 \leq k \leq n$

Note that λ consists of λ_o which is the general D-H parameters and λ_e which is a parameter used to determine end-effector coordinate frame without redundancy or deficiency. Therefore, the number of columns for the sub-matrix corresponding to each joint is four, except the number of columns for the final sub-matrix corresponding to the end-effector is six.

Partial Derivatives w.r.t. Twisting Angles($\frac{\partial f}{\partial \phi}$)

With similar manner, partial derivatives of end-effector posture with respect to the twisting angles are computed as follows:

$$\frac{\partial f}{\partial \phi} = \left[\underbrace{\begin{array}{c} \hat{z}^0 \times (r_e - r_\sigma^0) \\ \hat{z}^0 \end{array}}_1 \dots \underbrace{\begin{array}{c} \hat{z}^{k-1} \times (r_e - r_\sigma^{k-1}) \\ \hat{z}^{k-1} \end{array}}_k \dots \underbrace{\begin{array}{c} \hat{z}^{n-1} \times (r_e - r_\sigma^{n-1}) \\ \hat{z}^{n-1} \end{array}}_n \right] \quad (10)$$

where $1 \leq k \leq n$

4.2 Joint Torque Derivatives w.r.t. D-H Parameters, Twisting Angles and CM Positions

For the sake of simplicity, the proposed algorithm measures sensor data during standstill state. Consequently, torques applied to each joint are only caused by gravitational force. Fig. 7 illustrates coordinate frames and CM positions for revolute joints. Since the k^{th} joint torque, τ^k , is affected by from k^{th} link to the last link, it is required to compute CM position from the k^{th} link to the last link as shown in Eq. (11).

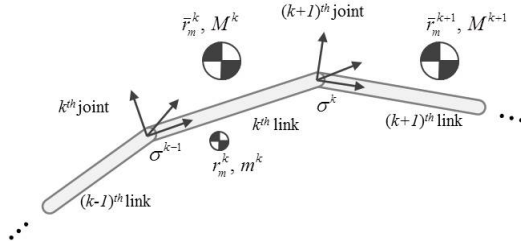


Fig. 7. Coordinate frames and CM positions for revolute joints

$$\begin{aligned}\bar{r}_m^k &= \frac{m^k r_m^k + m^{k+1} r_m^{k+1} + \cdots + m^n r_m^n}{m^k + m^{k+1} + \cdots + m^n} \\ &= \frac{1}{M^k} \sum_{j=k}^n m^j r_m^j\end{aligned}\quad (11)$$

where r_m^k and m^k represent CM position and mass of the k^{th} link, respectively. Subsequently, by using triple product formula, joint torque is computed as follows:

$$\tau^k = (f^k \times g^k) \cdot h^k \quad (12)$$

and

$$f^k = \bar{r}_m^k - r_\sigma^{k-1} \quad (13a)$$

$$g^k = M^k g \quad (13b)$$

$$h^k = \hat{z}^{k-1} \quad (13c)$$

where f^k is the distance vector between the k^{th} joint to the center of total mass from the k^{th} link to the last link, and g^k is the gravitational force due to the total mass after k^{th} link, lastly, h^k is the joint unit vector. Differentiating Eq. (12), differential of the joint torque with respect to the D-H parameters, the CM positions and the twisting angles are derived as follows:

$$d\tau^k = \frac{\partial \tau^k}{\partial \lambda} d\lambda + \frac{\partial \tau^k}{\partial p_m} dp_m + \frac{\partial \tau^k}{\partial \phi} d\phi \quad (14)$$

where detailed partial derivatives are as follows:

$$\begin{aligned}\frac{\partial \tau^k}{\partial \lambda} &= (f^k \times g^k)^T \frac{\partial h^k}{\partial \lambda} + (g^k \times h^k)^T \frac{\partial f^k}{\partial \lambda} + (h^k \times f^k)^T \frac{\partial g^k}{\partial \lambda} \\ &= (f^k \times g^k)^T \frac{\partial h^k}{\partial \lambda} + (g^k \times h^k)^T \frac{\partial f^k}{\partial \lambda}\end{aligned}\quad (15a)$$

$$\begin{aligned}\frac{\partial \tau^k}{\partial p_m} &= (f^k \times g^k)^T \frac{\partial h^k}{\partial p_m} + (g^k \times h^k)^T \frac{\partial f^k}{\partial p_m} + (h^k \times f^k)^T \frac{\partial g^k}{\partial p_m} \\ &= (g^k \times h^k)^T \frac{\partial f^k}{\partial p_m}\end{aligned}\quad (15b)$$

$$\begin{aligned}\frac{\partial \tau^k}{\partial \phi} &= \left(f^k \times g^k \right)^T \frac{\partial h^k}{\partial \phi} + \left(g^k \times h^k \right)^T \frac{\partial f^k}{\partial \phi} + \left(h^k \times f^k \right)^T \frac{\partial g^k}{\partial \phi} \\ &= \left(f^k \times g^k \right)^T \frac{\partial h^k}{\partial \phi} + \left(g^k \times h^k \right)^T \frac{\partial f^k}{\partial \phi}\end{aligned}\quad (15c)$$

where

$$\begin{aligned}\frac{\partial f^k}{\partial \lambda} &= \left[\frac{\partial f^k}{\partial \lambda_o} \frac{\partial f^k}{\partial \lambda_e} \right] \\ &= \underbrace{\left[\hat{z}^G \times (\bar{r}_m^k - r_\sigma^{k-1}) \ 0 \ 0 \hat{x}^0 \times (\bar{r}_m^k - r_\sigma^{k-1}) \right]}_0 \\ &\quad \dots \underbrace{\hat{z}^{j-1} \times (\bar{r}_m^k - r_\sigma^{k-1}) \ 0 \ 0 \hat{x}^j \times (\bar{r}_m^k - r_\sigma^{k-1})}_j \\ &\quad \dots \underbrace{\hat{z}^{k-2} \times (\bar{r}_m^k - r_\sigma^{k-1}) \ 0 \ 0 \hat{x}^k \times (\bar{r}_m^k - r_\sigma^{k-1})}_{k-1} \\ &\quad \underbrace{\frac{M^k}{M^k} \hat{z}^{k-1} \times (\bar{r}_m^k - r_\sigma^{k-1}) \ \frac{M^k}{M^k} \hat{z}^{k-1} \ \frac{M^k}{M^k} \hat{x}^k \ \frac{M^k}{M^k} \hat{x}^k \times (\bar{r}_m^k - r_\sigma^k)}_k \dots \\ &\quad \underbrace{\frac{M^l}{M^k} \hat{z}^{l-1} \times (\bar{r}_m^l - r_\sigma^{l-1}) \ \frac{M^l}{M^k} \hat{z}^{l-1} \ \frac{M^l}{M^k} \hat{x}^l \ \frac{M^l}{M^k} \hat{x}^l \times (\bar{r}_m^l - r_\sigma^l)}_l \dots \\ &\quad \underbrace{\frac{M^{n-1}}{M^k} \hat{z}^{n-2} \times (\bar{r}_m^{n-1} - r_\sigma^{n-2}) \ \frac{M^{n-1}}{M^k} \hat{z}^{n-2} \ \frac{M^{n-1}}{M^k} \hat{x}^{n-1} \ \frac{M^{n-1}}{M^k} \hat{x}^{n-1} \times (\bar{r}_m^{n-1} - r_\sigma^{n-1})}_{n-1} \\ &\quad \underbrace{\frac{M^n}{M^k} \hat{x}_T \ \frac{M^n}{M^k} \hat{y}_T \ \frac{M^n}{M^k} \hat{z}_T \ \frac{M^n}{M^k} \hat{x}_{R_x} \times \hat{r}_x \ \frac{M^n}{M^k} \hat{y}_{R_y} \times \hat{r}_y \ \frac{M^n}{M^k} \hat{z}_{R_z} \times \hat{r}_z}_n\end{aligned}$$

where $\hat{r}_x = r_m^n - r_{R_x}$, $\hat{r}_y = r_m^n - r_{R_y}$, $\hat{r}_z = r_m^n - r_{R_z}$. (16a)

$$\begin{aligned}\frac{\partial h^k}{\partial \lambda} &= \frac{\partial \hat{z}^{k-1}}{\partial \lambda} \\ &= \underbrace{\left[\frac{\partial \hat{z}^{k-1}}{\partial \alpha^0} \ \frac{\partial \hat{z}^{k-1}}{\partial d^0} \ \frac{\partial \hat{z}^{k-1}}{\partial l^0} \ \frac{\partial \hat{z}^{k-1}}{\partial \beta^0} \ \dots \ \underbrace{\frac{\partial \hat{z}^{k-1}}{\partial \alpha^j}}_0 \ \underbrace{\frac{\partial \hat{z}^{k-1}}{\partial d^j}}_j \ \underbrace{\frac{\partial \hat{z}^{k-1}}{\partial l^j}}_0 \ \underbrace{\frac{\partial \hat{z}^{k-1}}{\partial \beta^j}}_0 \right]}_0 \\ &\quad \dots \underbrace{\left[\frac{\partial \hat{z}^{k-1}}{\partial \alpha^{k-1}} \ \frac{\partial \hat{z}^{k-1}}{\partial d^{k-1}} \ \frac{\partial \hat{z}^{k-1}}{\partial l^{k-1}} \ \frac{\partial \hat{z}^{k-1}}{\partial \beta^{k-1}} \ \underbrace{0}_k \ \dots \ \underbrace{0}_n \right]}_{k-1} \\ &= \underbrace{\left[\hat{z}^G \times \hat{z}^{k-1} \ 0 \ 0 \ \hat{x}^0 \times \hat{z}^{k-1} \ \dots \ \underbrace{\hat{z}^{j-1} \times \hat{z}^{k-1}}_j \ 0 \ 0 \ \hat{x}^j \times \hat{z}^{k-1} \ \dots \right]}_0 \\ &\quad \underbrace{\hat{z}^{k-2} \times \hat{z}^{k-1} \ 0 \ 0 \ \hat{x}^{k-1} \times \hat{z}^{k-1} \ 0 \ 0 \ \hat{x}^{k-1} \ \dots \ 0 \ 0 \ \hat{x}^{k-1}}_{k-1} \underbrace{\dots \ 0 \ 0 \ \hat{x}^{k-1}}_k \ \dots \ \underbrace{0 \ 0 \ \hat{x}^{k-1}}_n \text{ where } 0 \leq j \leq (k-1)\end{aligned}\quad (16b)$$

$$\frac{\partial f^k}{\partial p_m} = \frac{1}{M^k} \left[\underbrace{0}_1 \cdots \underbrace{0}_{j-1} \cdots \underbrace{0}_{k-1} \underbrace{m^k R^k}_k \cdots \underbrace{m^l R^l}_l \cdots \underbrace{m^n R^n}_n \right] \quad (16c)$$

where $1 \leq j \leq (k-1), k \leq l \leq n$

$$\begin{aligned} \frac{\partial f^k}{\partial \phi} &= \left[\underbrace{\hat{z}^0 \times (\bar{r}_m^k - r_\sigma^{k-1})}_1 \cdots \underbrace{\hat{z}^{j-1} \times (\bar{r}_m^k - r_\sigma^{k-1})}_j \cdots \underbrace{\hat{z}^{k-2} \times (\bar{r}_m^k - r_\sigma^{k-1})}_{k-1} \right. \\ &\quad \left. \underbrace{\frac{M^k}{M^k} \hat{z}^{k-1} \times (\bar{r}_m^k - r_\sigma^{k-1})}_k \cdots \underbrace{\frac{M^l}{M^k} \hat{z}^{l-1} \times (\bar{r}_m^l - r_\sigma^{l-1})}_l \cdots \underbrace{\frac{M^n}{M^k} \hat{z}^{n-1} \times (\bar{r}_m^n - r_\sigma^{n-1})}_n \right] \\ &\text{where } 1 \leq j \leq (k-1), k \leq l \leq n \end{aligned} \quad (16d)$$

$$\frac{\partial h^k}{\partial \phi} = \left[\underbrace{\hat{z}^0 \times \hat{z}^{k-1}}_1 \cdots \underbrace{\hat{z}^{j-1} \times \hat{z}^{k-1}}_j \cdots \underbrace{\hat{z}^{k-2} \times \hat{z}^{k-1}}_{k-1} \underbrace{0}_k \cdots \underbrace{0}_n \right] \quad (16e)$$

where $1 \leq j \leq (k-1)$

4.3 Laser Point Jacobian

After obtaining the relationships between the kinematical parameters including the compliances and the CM positions and the end-effector position, it needs to find the relationship between end-effector position and laser point that is beamed onto the screen. The position of the laser point from the end-effector to the screen can be represented as follows:

$$p_s^k = R_l^k \begin{bmatrix} 0 \\ 0 \\ \rho^k \end{bmatrix} + p_l^k \quad \text{where } k = 0, 1, 2 \quad (17)$$

where p_l and p_s are the positions of the laser attached the end-effector and the laser point on the screen, respectively. Also, ρ represents distance between the laser to the laser point on the screen. Since the x-component of the laser point on the screen must be zero, following equation is obtained.

$$\begin{aligned} p_{sx}^k &= (R_{lz}^k \rho^k + p_l^k)_x \\ &= R_{lxz}^k \rho^k + p_{lx}^k \\ &= 0 \end{aligned} \quad (18)$$

By solving Eq. (18), ρ^k is calculated as follows:

$$\rho^k = -\frac{p_{lx}^k}{R_{lxz}^k} \quad (19)$$

Similarly, the x-component of the differential of the point on the screen is also zero. This yields

$$\begin{aligned} dp_{sx}^k &= d(R_{lx}^k \rho^k + p_l^k)_x \\ &= (d\delta_{ly}^k R_{lzz}^k - d\delta_{lz}^k R_{lzy}^k) \rho^k + R_{lzx}^k d\rho^k + dp_{lx}^k \\ &= 0 \end{aligned} \quad (20)$$

By solving Eq. (20), $d\rho^k$ is obtained as follows:

$$d\rho^k = \frac{(d\delta_{ly}^k R_{lzz}^k - d\delta_{lz}^k R_{lzy}^k) p_{lx}^k - R_{lzx}^k dP_{lx}^k}{(R_{lzx}^k)^2} \quad (21)$$

By differentiating after substituting Eq. (19) and (21) into Eq. (17), the y-component of the differential transform is obtained as follows:

$$\begin{aligned} dp_{sy}^k &= (d\delta_{lz}^k R_{lzx}^k - d\delta_{lx}^k R_{lzy}^k) \rho^k + R_{lzy}^k d\rho^k + dp_{ly}^k \\ &= \left(-\frac{R_{lzy}^k}{R_{lzx}^k} \right) dp_{lx}^k + dp_{ly}^k + \left(\frac{R_{lzz}^k}{R_{lzx}^k} p_{lx}^k \right) d\delta_{lx}^k + \left(\frac{R_{lzy}^k R_{lzz}^k}{(R_{lzx}^k)^2} \right) d\delta_{ly}^k \\ &\quad + \left(\frac{(R_{lzz}^k)^2 - 1}{(R_{lzx}^k)^2} p_{lx}^k \right) d\delta_{lz}^k \end{aligned} \quad (22)$$

Also, the z-component of the differential transform is obtained as follows:

$$\begin{aligned} dp_{sz}^k &= (d\delta_{lx}^k R_{lzy}^k - d\delta_{ly}^k R_{lzx}^k) \rho^k + R_{lzz}^k d\rho^k + dp_{lz}^k \\ &= \left(-\frac{R_{lzz}^k}{R_{lzx}^k} \right) dp_{lx}^k + dp_{lz}^k + \left(-\frac{R_{lzy}^k}{R_{lzx}^k} p_{lx}^k \right) d\delta_{lx}^k + \left(\frac{1 - (R_{lzy}^k)^2}{(R_{lzx}^k)^2} p_{lx}^k \right) d\delta_{ly}^k \\ &\quad - \left(\frac{R_{lzy}^k R_{lzz}^k}{(R_{lzx}^k)^2} p_{lx}^k \right) d\delta_{lz}^k \end{aligned} \quad (23)$$

From Eq. (22) and (23), Jacobian of laser point on the screen by end-effector posture is given by

$$dp_s^k = J_s^k d\pi_{el}^k \quad (24)$$

where

$$J_s^k = \begin{bmatrix} -\frac{R_{lzy}^k}{R_{lzx}^k} 1 & 0 & \frac{R_{lzz}^k}{(R_{lzx}^k)^2} p_{lx}^k & \frac{(R_{lzz}^k)^2 - 1}{(R_{lzx}^k)^2} p_{lx}^k \\ -\frac{R_{lzz}^k}{R_{lzx}^k} 0 & 1 & -\frac{R_{lzy}^k}{R_{lzx}^k} p_{lx}^k & \frac{1 - (R_{lzy}^k)^2}{(R_{lzx}^k)^2} p_{lx}^k - \frac{R_{lzy}^k R_{lzz}^k}{(R_{lzx}^k)^2} p_{lx}^k \end{bmatrix}$$

5 Simulational Results

5.1 Simulation Environment

The effectiveness of the proposed algorithm was verified by computer simulation with 6 DOF humanoid leg robot as shown in the Fig. 8. For the calibration, 25 test postures

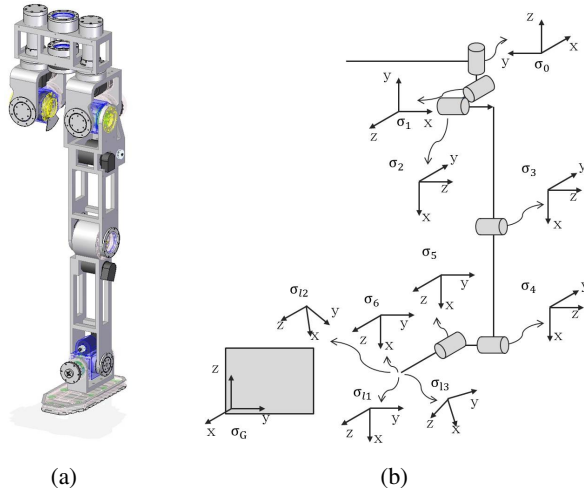


Fig. 8. Coordinate frames of 6 DOF humanoid robot leg. (a) 3D design. (b) coordinate system.

which consisted of joint angles were arbitrary selected. By using theses postures, laser pointers on the screen corresponding to the each posture were calculated. From the initially biased guess to the true value, least-squares algorithm was iterated. As shown in Fig. 9, when the iteration increases the error norm between the measured and the

Table 1. Distance errors of laser points on the screen

	Mean	STD	Max.	Min.
Initial guess	0.3017	0.0115	0.3291	0.2916
After calibration	0.0156	0.0082	0.0341	0.0049

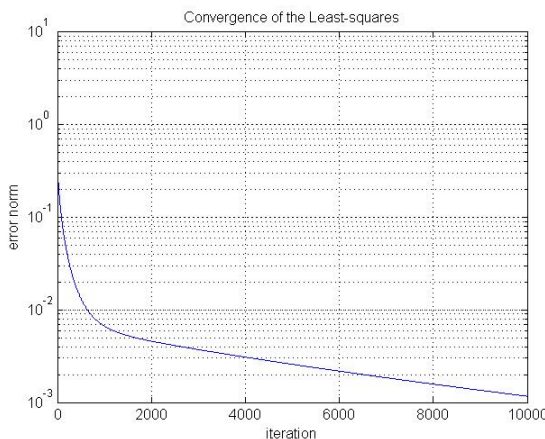


Fig. 9. Convergence of the error norm between the estimated parameters and the true parameters

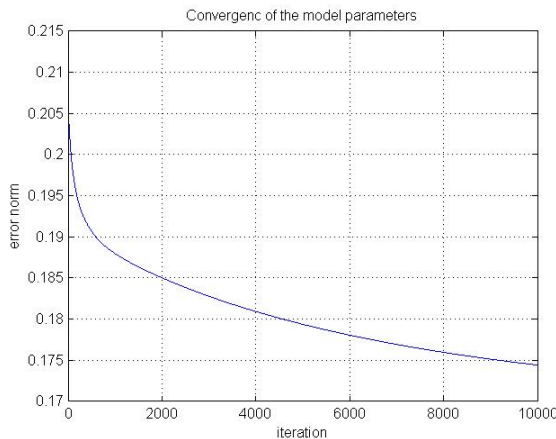


Fig. 10. Convergence of the error norm between the estimated parameters and the true parameters

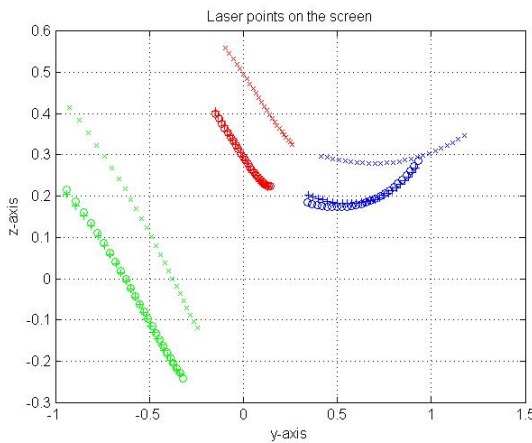


Fig. 11. Test Laser points on the screen

calibrated laser points goes to zero. Consequently, the error norm of model parameters decreases as shown in Fig. 10.

To investigate whether or not the estimated model parameters are effective on the arbitrary postures besides the test postures, new test postures were also selected and examined as shown in Fig. 11. Circle symbol(\circ) represents laser points with true parameters while cross(\times) and plus($+$) symbols represent laser points with inaccurate and calibrated model parameters, respectively. After calibration, laser points on the screen had come close to the ideal ones. The distance errors between the true points and the calculated points with the estimated parameters were compared with the errors between the true points and the calculated points with the initially guessed parameters. As shown in Table 1, accuracy was improved in every category.

6 Conclusion

In this paper, differential kinematics of a flexible manipulator was derived to calibrate the model parameters such as the D-H parameters, the joint compliances, and the mass positions. By using the Jacobian matrix which represents the relationship between the model parameters and the laser points on the screen, the model parameters were iteratively updated. Consequently, the difference between the measured and the computed laser points on the screen were effectively decreased. Computer simulation with a 6 DOF humanoid leg robot was carried out and confirmed that the proposed algorithm could calibrate the model parameters automatically. Applying the algorithm to the actual robotic system is left as a further work.

References

1. Park, I.-W., Lee, B.-J., Cho, S.-H., Hong, Y.-D., Kim, J.-H.: Laser-Based Kinematic Calibration of Robot Manipulator Using Differential Kinematics. *IEEE/ASME Trans. Mechatronics* pp(99), early access articles
2. Alici, G., Shirinzadeh, B.: Enhanced stiffness modeling, identification and characterization for robot manipulators. *IEEE Trans. Robot.* 21(4), 554–564 (2005)
3. Newman, W., Birkhimer, C., Horning, R.: Calibration of a motoman P8 robot based on laser tracking. In: Proc. IEEE Int. Conf. Robot. Autom., San Francisco, CA, pp. 3597–3602 (April 2000)
4. Omodei, A., Legnani, G., Adamini, R.: Three methodologies for the calibration of industrial manipulators: Experimental results on a SCARA robot. *J. Robot. Syst.* 17(6), 291–307 (2000)
5. Omodei, A., Legnani, G., Adamini, R.: Calibration of a measuring robot: Experimental results on a 5 DOF structure. *J. Robot. Syst.* 18(5), 237–250 (2001)
6. Alici, G., Shirinzadeh, B.: A systematic technique to estimate positioning errors for robot accuracy improvement using laser interferometry based sensing. *Mech. Mach. Theory* 40, 879–906 (2005)
7. Alici, G., Jagielski, R., Sekercioglu, Y., Shirinzadeh, B.: Prediction of geometric errors of robot manipulators with particle swarm optimization method. *Robot. Auton. Syst.* 54, 956–966 (2006)
8. O'brian, J., Bodenheimer, R., Brostow, G., Hodgins, J.: Automatic joint parameter estimation from magnetic motion capture data. In: Proc. Graph. Interface, pp. 53–60 (May 2000)
9. Renaud, P., Andreff, N., Lavest, J.-H., Dhome, M.: Simplifying the kinematic calibration of parallel mechanisms using vision-based methodology. *IEEE Trans. Robot.* 22(1), 12–22 (2006)
10. Rauf, A., Pervez, A., Ryu, J.: Experimental results on kinematic calibration of parallel manipulators using a partial pose measurement device. *IEEE Trans. Robot.* 22(2), 379–384 (2006)
11. Gatti, G., Danieli, G.: A practical approach to compensate for geometric errors in measuring arms: Application to a six-degree-of-freedom kinematic structure. *Meas. Sci. Technol.* 19(1), 015107-10-015107-12 (2008)
12. Santolaria, J., Aguilar, J., Yagye, J., Pastor, J.: kinematic parameter estimation technique for calibration and repeatability improvement of articulated arm coordinate measuring machines. *Precis. Eng.* 32, 251–268 (2008)
13. Ye, S., Wang, Y., Ren, Y., Li, D.: Robot calibration using iteration and differential kinematics. *J. Phys.: Conf. Series* 48, 1–6 (2006)
14. Iurascu, C.C., Park, F.C.: Geometric algorithms for kinematic calibration of robots containing closed loops. *J. Mech. Design* 125, 23–32 (2003)

EtherCAT Based Parallel Robot Control System

Jung-Hoon Kim, Sun Lim, and Il-Kyun Jung

Intelligent Robotics Research Center, Korea Electronics Technology Institute(KETI)
brain2012@gmail.com, sunishot@keti.re.kr

Abstract. In this paper, we describe the control strategy of high speed parallel robot system with EtherCAT network. This work deals the parallel robot system with centralized control on the real-time operating system such as window RTX, intime etc. Most control scheme and algorithm is implemented master platform on the PC, the input and output interface is ported on the slave side. The data is transferred by maximum 20 us-second with 1000 bytes. EtherCAT is very high speed and stable industrial network. The control strategy with EtherCAT is very useful and robust on Ethernet network environment. In this study, we propose the centralized parallel robot control mechanism approach. The experiment and simulation result using selected approach is omitted.

Keywords: EtherCAT network, parallel robot system, real time control.

1 Introduction

The Parallel Robot as Shown in Fig 1(a)(b) is one of the successful industrial robot in many application domains, pick-and-place, packing even assembling. Because of this, Parallel Robot have many advantages compared to traditional serial robots, such as speed and accuracy. based on the end-effector of parallel robot can move a light weight objects at a speed of several meter per second, and has high accuracy within a limited range as shown in Fig 1(c).[1]



Fig. 1. Parallel Robots

FlexPicker of ABB(*Left*), 650H of Adept(*Center*), Work Envelope of 650H Parallel Robot(*Right*)

In addition, a mechanism that operates in a limited range to ensure safety in exceptional circumstances due to a device that acts as an element of performance and safety were met. In recent years, several devices in end-effector by installing a complex assembly and operation is possible as shown in Fig 2.[2]

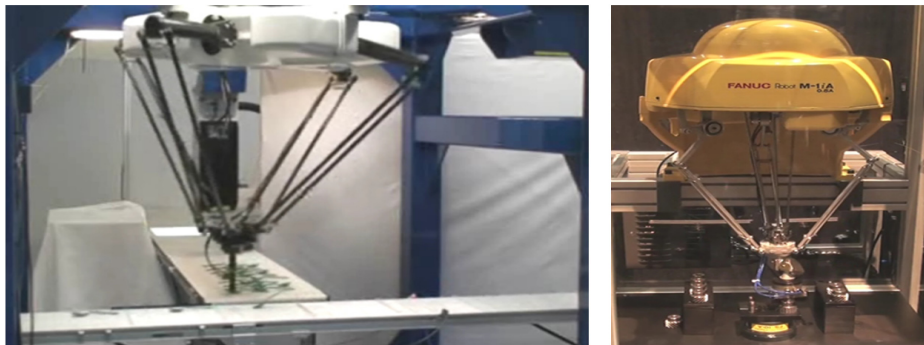


Fig. 2. Parallel Robots in Industrial Field. Pick-and-Place(left) and Assembling (right).

However, demand in industry turned to small quantity batch production, As the conversion process can be done easily and quickly rose in the interest of the system. At the traditional robot environment, the changes in the process of time it took several months. In addition, if the accuracy requirements of the job took a long time used to verify. In this paper, we present a centralized parallel robot control system for rapid process changes. The proposed system changes manufacturing process through the software and a number of parallel robots have the flexibility to expand as high-speed synchronization via industrial networks by supporting to improve the performance of a parallel robot control.

This paper is structured as follow: In Section 2, the background technologies of presented system are described. In Section 3, Control strategy and concept of the system are described. Finally, Section 4 describes the concluding remark.

2 Background

2.1 Real-Time Operating System

Most of the robot control systems are being developed using window operating system. Windows has many advantage of easy developing environment, such as, supporting abundant device drivers and multitasking. However it cannot support hard real time capabilities since the windows is not designed for the real-time system originally to emphasize the graphic display and to use the multi task in viewed same time. Moreover it is difficult and takes a lot of time to develop the device drivers in windows operating system.[6][7] Basically a real time O/S is suitable to implement a real time control system. The commercial QNX and VxWorks have the hard real time

capabilities. However, the price is too high to be used for education and research purposes. Their support of device drives for custom designed controllers are so weak that the expendability is very low [8]. Thus our system is ported to window real time operating system , such as, window-RTX. This OS have an advantage of the similar window OS and hard real time is guaranteed.

2.2 EtherCAT

EtherCAT is Real Time Ethernet technology based on the Ethernet. Its objective is to maximize the utilization of the full duplex Ethernet bandwidth[3]. The network communication system employs the Master/Slave principle. The master node send the packet frames to the slave nodes. The slave node extract data from and insert data in to packet frames. Telegram processing principles are utilized “on the fly”. In this way, by performing EtherCAT can use ninety percent of bandwidth without packet collision[4][5]. Also EtherCAT provide distributed clock function for synchronization with each slave node. It can be improve the control capability of parallel robots

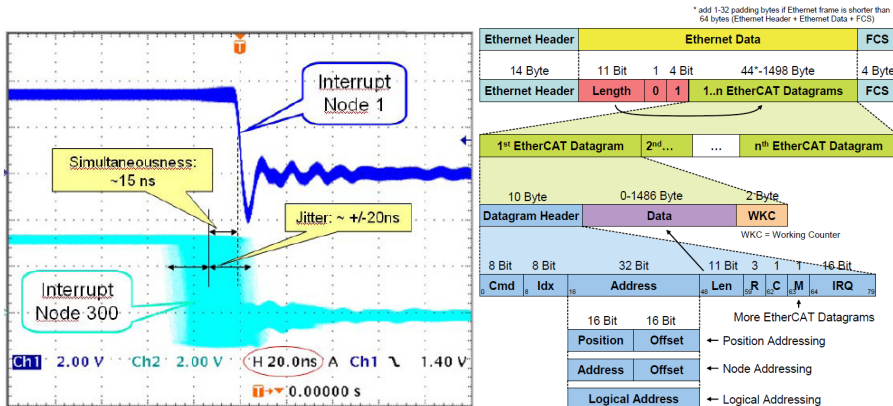


Fig. 3. Accuracy Result of Distributed Clock by EtherCAT (left) and EtherCAT Datagram (right)

3 EtherCAT Based Parallel Control Strategy

Figure 3. illustrate the Delta robot that is one of the industrial robots more used today and is the most successful robots which have been designed. The parallel robot is useful its applications include pick, place and packing products in the food, medical and cosmetic industry, as well as in assembly process of electronic device. The parallel robot is made up of an active joint with joint motor and passive joint which are linked together three independent rigid arms. The actuators are placed for each arm as shown in Fig 3. right side.

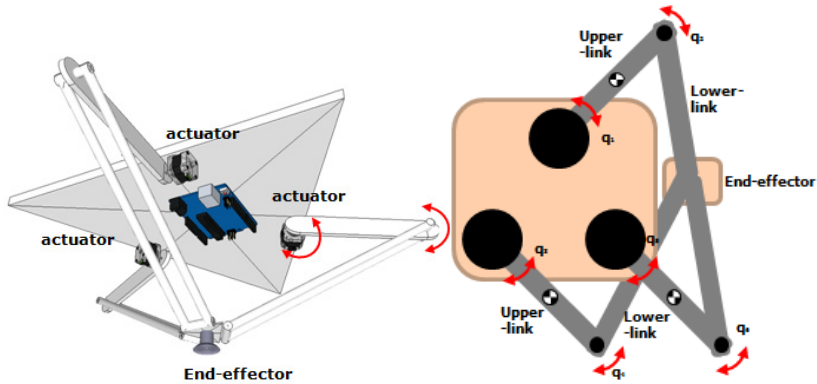


Fig. 4. The Parts of parallel robot (*left*) and configuration (*right*)

3.1 Parallel Robot Master Controller

Master Controller is made up of industrial PC platform and EtherCAT Master Stack. The system is implemented window OS such as window 7-32bit, with window RTX. The parallel robot control scheme and safety mechanism is running on window RTX for real-time and periodic computing work. The monitoring and user interface is implemented window side. The data is shared between window and RTX with inner interface socket communication. Figure 6. illustrate the Master Controller structure. This structure is very practical on industrial controller.

The control scheme is detailed in figure 4. The robot control attempts to achieve motion control using parallel robots under unknown manufacturing tolerances and inaccuracies by migrating the measurement from joint space and task space. This problem is solved by the on and off calibration of the parallel body. However this is very hard and time consuming work so most field engineer want to avoid this work and automatically find the parameter by program. Thus the control objective of this paper is described as bellows;

Find the control law below condition is satisfied as

$$\lim_{t \rightarrow \infty} \begin{bmatrix} x_i^* \\ y_i^* \\ z_i^* \\ t_i^* \end{bmatrix} - \begin{bmatrix} x_i \\ y_i \\ z_i \\ t_i \end{bmatrix} = 0 \longrightarrow \begin{bmatrix} e_i^x \\ e_i^y \\ e_i^z \\ e_i^t \end{bmatrix} = 0 \quad (1)$$

and

$$\tau(t) \leq \alpha < \infty$$

where * upper script mean the command and lower script i mean the i-index parallel robot platform. x, y, z, t are a Cartesian space axis, individually x-axis, y-axis, z-axis and time domain. The task space control is very difficult because feedback of the end-effector on the cartesian space is not useful measure on real-time. Thus most control

scheme is designed on the joint space of parallel robot. This control block diagram is represented on Figure 4. This work attempts to achieve precise motion control using parallel robot that encounters manufacturing tolerances, assembly errors and thermal deformations without periodic calibration through only joint space measurements.

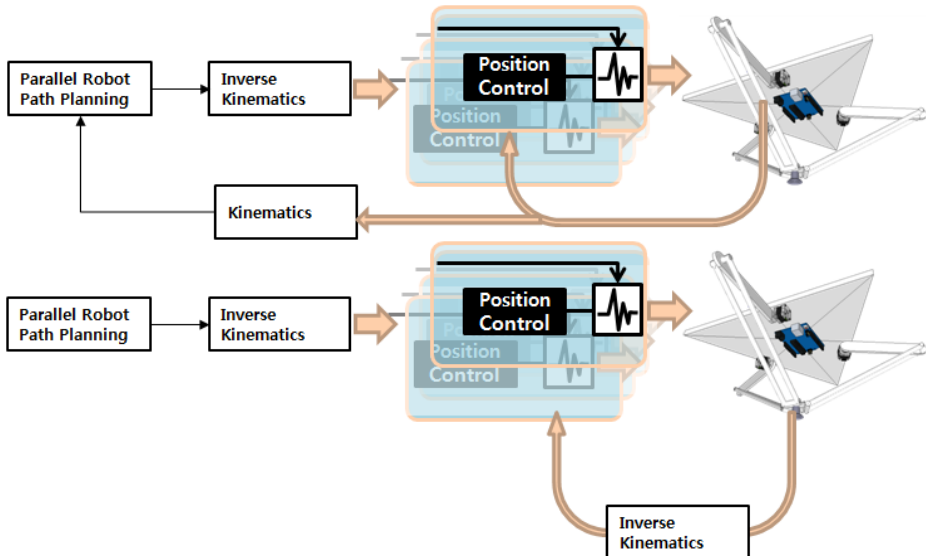


Fig. 5. The Joint space control block diagram(upper) and the task space control block diagram(lower)

The parallel robot path planning block is the generation block of motion on the cartesian space trajectory or regulation. This block make the x,y,z and time trajectory that is input of the inverse-kinematics block. The inverse-kinematic block generate the joint space motor position trajectories. Figure 5 show the Parallel robot control block diagram. The detail description of individual block is mentioned below.

The parallel robot dynamic equation of motion in the configuration space can be written as follows

$$M(q)\ddot{q} + b(q, \dot{q}) + g(q) = \tau(t) \quad (2)$$

where $M(q)$ is the parallel robot positive definite inertia matrix, $b(q, \dot{q})$ is a vector of coriolis and centripetal forces, $g(q)$ is the gravity term while $\tau(t)$ is the generalized torque vector acting on the generalized coordinate vector. Most practical system have the physical measurement uncertainty so taking the dynamical inaccuracies into consideration, one can write the following relations

$$\begin{aligned} M(q) &= M_n(q) + \Delta M(q) \\ b(q, \dot{q}) &= b_n(q, \dot{q}) + \Delta b(q, \dot{q}) \\ g(q) &= g_n(q) + \Delta g(q) \end{aligned} \quad (3)$$

where $M_n(q), b_n(q, \dot{q}), g_n(q)$ are respectively the nominal value inertia matrix, nominal vector of coriolis and centripetal forces and the nominal gravity term. These value are measured by the calibration tool or 3D cad software. Δ symbol stands for the deviation between these terms and the actual ones.

Rewriting (2)

$$M_n(q) + b_n(q, \dot{q}) + g_n(q) + \Delta M(q) + \Delta b(q, \dot{q}) + \Delta g(q) = \tau(t) \quad (4)$$

$$M_n(q) + b_n(q, \dot{q}) + g_n(q) + d(t) = \tau(t)$$

where $d(t) = \Delta M(q) + \Delta b(q, \dot{q}) + \Delta g(q)$ is disturbance term that is canceled by the disturbance observer which is described as follows

The dynamic uncertainties such as the un-modeled dynamics are considered as disturbances, then a disturbance observer is designed to estimate such disturbances and used to generate compensation term.

$$\hat{d}(t) = \tau(t) - \tau^*(t) \quad (5)$$

where $\hat{d}(t)$ is disturbance estimation value and $\tau^*(t) = M_n(q) + b_n(q, \dot{q}) + g_n(q)$ is a calculation value with nominal value.

Moreover, it can be estimated through the following low pass filter for avoiding noise sensitivity,

$$\hat{d}(t) = \frac{h}{s+h} [\tau(t) - \tau^*(t)] \quad (6)$$

where h is the single observer gain which controls how fast the estimated signal converges to the actual disturbance.

Then, the control law is represented as follow

$$\tau(t) = \frac{1}{M_n} [b_n(q, \dot{q}) + g_n(q) - k\epsilon(t) + \hat{d}(t)] \quad (7)$$

where k is the control gain for reducing convergence time and regulation error.

The stability is proved by the lyapunov function that is omitted in this work.

Overall this control scheme is running on the RTX side. Therefore the control signal is periodically calculated and transferred to the slave node with distributed clock by the EtherCAT network. Also the parallel robot path planning, inverse kinematics and disturbance observer is running on the same side. This guaranteed the synchronization time clock and calculation with same source such as joint space angle and velocity.

In order to investigate the influence and performance of motion control operation in the presence of both kinematical and dynamical inaccuracies, experiments will test on the test setup environment. The experiment setup consists of a parallel robot namely, NT-parallel robot. First experiments are conducted using measurement taken from the actuator's encoder. Then next experiments are conducted using measurement of the end effector's exact position by vision or laser scanner.

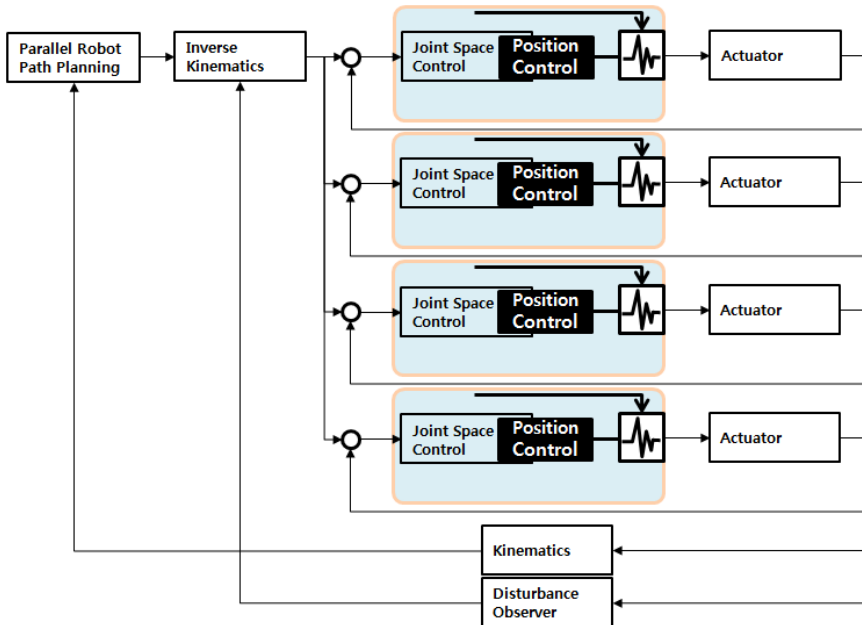


Fig. 6. The Parallel robot control block diagram

The proposed fame work is described as below

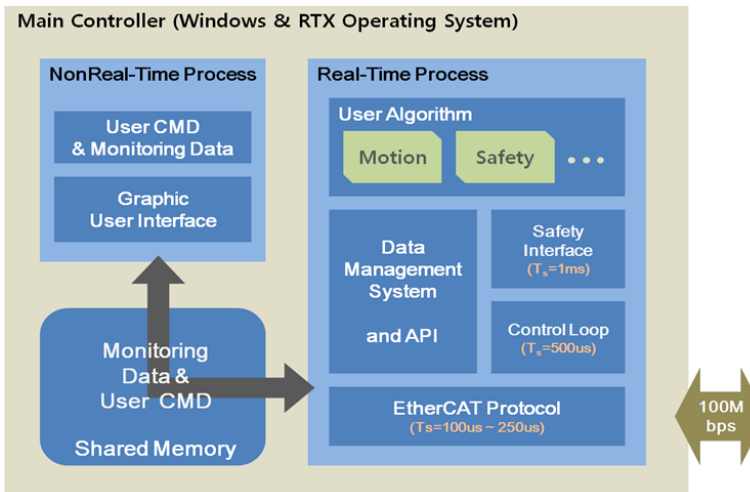


Fig. 7. Master control scheme

4 Conclusion and Future Work

This paper proposed the control scheme of the parallel robot system. For the high speed and precision motion control, we equipped the widow real time operating system, e.x. window RTX, and 100Mbps industrial communication network such as EtherCAT. The comparison between the nomal PC-based control system and real time based control system with EtherCAT results will be obtained on the same parallel robot hardware. Also we will prove the feasibility and performance of the proposed control frame work without any change of the parallel robot hardware. This is very important on the parallel robot motion real time tracking, e.g. fast cycle.

Acknowledgements. This work was supported by the Industrial Strategic technology development program, 10041965, Development of a parallel link robot with 6kg payload and 0.43 sec cycling time, funded by the Ministry of Knowledge Economy (MKE), Korea

References

1. Li, Y.: Design and application of a new 3-DOF translational parallel manipulator. In: IEEE Workshop on Advanced Robotics and Its Social Impacts, ARSO 2007, December 9-11, pp. 1–6 (2007)
2. Khalil, I.S.M., Golubovic, E., Sabanovic, A.: High precision motion control of parallel robots with imperfections and manufacturing tolerances. In: 2010 IEEE Conference on Emerging Technologies and Factory Automation (ETFA), September 13-16, pp. 1–7 (2010)
3. Song, II.-S.: Implementation and analysis of the embedded master for EtherCAT. In: 2010 International Conference on Control Automation and Systems (ICCAS), October 27-30, pp. 2418–2422 (2010)
4. Rostan, M.: EtherCAT enabled advanced control architecture. In: 2010 IEEE/SEMI Advanced Semiconductor Manufacturing Conference (ASMC), July 11-13, pp. 39–44 (2010)
5. Prytz, G.: A performance analysis of EtherCAT and PROFINET IRT. In: IEEE International Conference on Emerging Technologies and Factory Automation, ETFA 2008, September 15-18, pp. 408–415 (2008)
6. Tapia, E., Intille, S., Larson, K.: EUROM ICR0 1991 Workshop on Real-Time Systems. Universite Paris XI PARIS-9-RSAY, France, June 12-14 (1991)
7. Lee, C.H., Mavroidis, C.: PC based control of mechatronic systems under MS-windows NT workstation. IEEE/ASME Trans. on Mechatronics 6(3), 311–321 (2001)
8. Lages, W.F., Hemerly, E.M.: Linux as a software platform for mobile robots. Submitted to IEEE Transactions on Software Engineering (200)

Real-Time Trajectory Generation for Both Arms of a Humanoid Robot

Chang-Young Jung and Jong-Hwan Kim

Department of Electrical Engineering, KAIST, 291 Daehak-ro, Yuseong-gu, Daejeon,
305-701, Republic of Korea
cyjung,johkim@rit.kaist.ac.kr

Abstract. This paper proposes a real-time trajectory generation algorithm for both arms of a humanoid robot. Since it is hard to find a closed form of inverse kinematics for each arm of seven degrees of freedom, the damped least-squares method is employed to obtain the inverse kinematics. The trajectory is generated by the minimum-jerk method to maximize the position accuracy. Considering the performance in computation time, a software SD/FAST is used to find a Jacobian matrix of the arm. Computer simulation was performed to verify the effectiveness of the proposed algorithm using a Webot simulator for the upper body of Mybot developed in the RIT Lab., KAIST. The results show that the proposed algorithm generates trajectory in real-time and it is robust to singularity.

Keywords: Humanoid robot, Robot arms trajectory generation, Damped least square, Minimum-jerk.

1 Introduction

Two-arm system of a humanoid robot consists of a trunk and two arms each of which can be regarded as an independent manipulator. Based on each manipulator control, the robot can manipulate both arms simultaneously and dexterously. Once the robot is given a task like pointing or reaching a position, it has to provide its arm's trajectory to reach the position. To make this possible, this paper proposes a novel algorithm that generates trajectories for both arms in real-time.

The research of manipulator has a long history. It first starts with the problem of inverse kinematics. As the number of robot's joint increases, nonlinear terms of inverse kinematics greatly increase. Therefore, it is impossible to find a closed form of inverse kinematics of the manipulator. Several methods have been introduced including neural network mapping [1], rapidly random tree in configuration space [2][3], and iterative method [4]. Even though the inverse kinematic equations are obtained, the generation of proper trajectory is still a difficult problem.

In this paper, an efficient real-time trajectory generation algorithm for both arms of humanoid robot is proposed by employing methods used in robot manipulator control. The damped least-squares method is used to obtain inverse

kinematics of the arm of seven degrees of freedom. After finding the inverse kinematics, the minimum-jerk trajectory generation method is used to get the trajectory of the arm. Proposed algorithm is expected to be used as a core algorithm in task planning of both arms, where both arms need to be manipulated to do a commanded action. The effectiveness of the proposed algorithm is demonstrated through computer simulation using a Webot simulator for a model of Mybot, developed in the RIT Lab, KAIST.

This paper is organized as follows. Section 2 describes an arm of Mybot and its kinematics. Section 3 proposes a real-time trajectory generation algorithm for both arms of a humanoid robot. Section 4 presents simulations and the results for the Mybot arms. Concluding remarks along with future work follow in Section 5.

2 Kinematics of an Arm

SD/FAST which is a software developed by Symbolic Dynamics Inc. is used to obtain kinematic and dynamic equations of a humanoid arm [6]. This software uses Kane's formulation and symbolic manipulation to formulate the nonlinear equations of a multi-body mechanical system [5]. As each arm has seven degrees of freedom(**DOF**), the robot has redundant DOFs in 3D Cartesian space. The feature of left arm is presented in Fig. 1. Entire torso of Mybot consisting of two arms and trunk is also presented in Fig. 2.

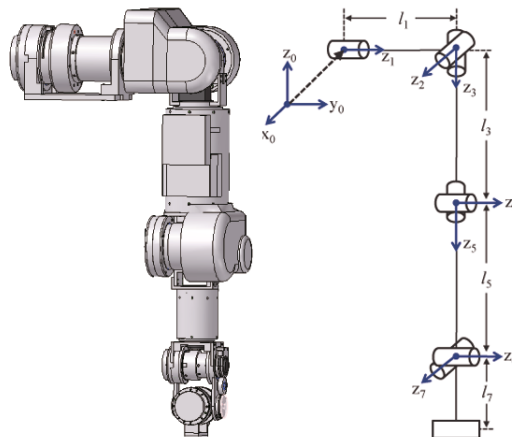


Fig. 1. Hardware Design of 7 DOF Mybot arm

As shown in Fig. 2, two arms are located on the upper side of trunk. Therefore, there are three Cartesian coordinate systems in the right arm, left arm and trunk. The coordinate system of trunk is considered as a global or base coordinate system. Each arm has its own coordinate system of which the origin is

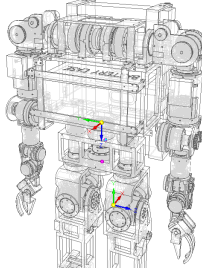


Fig. 2. Mybot's two arms and trunk

located at the first joint of arm, and every coordinate system is easily derived only by multiplying translation transformation matrix to base frame. Therefore, in the rest of the paper, the trajectory generation method for only one arm is described. For the other arm, the same procedure is adopted. In other words, the same trajectory generation algorithm is applied for both arms with each arm's own coordinate system. The nominal values of left arm's physical feature used in SD/FAST are summarized in Table 1. ‘SH’, ‘EL’, and ‘WR’ represent shoulder, elbow, and wrist, respectively and ‘X’, ‘Y’, and ‘Z’ repectively mean the corresponding rotation axis with respect to the base frame.

Jacobian matrix \mathbf{J} , which transforms angular velocity into end-effector velocities in Cartesian space, is given as a 6×7 matrix as follow:

$$\begin{bmatrix} v_x \\ v_y \\ v_z \\ \omega_x \\ \omega_y \\ \omega_z \end{bmatrix} = \mathbf{J}(\mathbf{q}) \begin{bmatrix} \dot{q}_1 \\ \dot{q}_2 \\ \dot{q}_3 \\ \dot{q}_4 \\ \dot{q}_5 \\ \dot{q}_6 \\ \dot{q}_7 \end{bmatrix} \quad (1)$$

where v and w denote linear and angular velocities of end-effector in the Cartesian coordinate system, respectively. The vector \mathbf{q} represents joint angle, and $\dot{\mathbf{q}}$ indicates joint angular velocity. A velocity propagation method, which finds angular velocity of each joint from the base frame, is used to calculate the Jacobian matrix above.

3 Trajectory Generation Algorithm

The overall algorithm is shown in Algorithm 1. If the target position and target rotation are given to the robot, the algorithm generates tarajecotry of an arm to reach the position. The following notations are used:

$$\mathbf{p}^0 = [x^0 \ y^0 \ z^0 \ \psi^0 \ \theta^0 \ \phi^0]^T, \quad \mathbf{p}^N = [x^N \ y^N \ z^N \ \psi^N \ \theta^N \ \phi^N]^T \quad (2)$$

Table 1. Nominal values of dynamic parameter of 7 DOF humanoid arm

Name	Link	Length (m)	Mass (kg)	Inertia ($\text{kg} \cdot \text{m}^2$)
SHY	1	0.2 (0.1)	1.0	0.1 0.01 0.01 0.01 0.05 0.01 0.01 0.01 0.1
SHX	2	0.0	0.8	0.03 0.005 0.005 0.005 0.08 0.005 0.005 0.005 0.08
SHZ	3	0.2 (0.1)	1.0	0.15 0.01 0.01 0.01 0.15 0.01 0.01 0.01 0.05
ELY	4	0.0	0.5	0.05 0.005 0.005 0.005 0.01 0.005 0.005 0.005 0.05
WRZ	5	0.2 (0.1)	0.5	0.04 0.004 0.004 0.004 0.04 0.004 0.004 0.004 0.008
WRY	6	0.0	0.3	0.03 0.003 0.003 0.003 0.006 0.003 0.003 0.003 0.03
WRX	7	0.05 (0.05)	0.2	0.006 0.003 0.003 0.003 0.03 0.003 0.003 0.003 0.03

where \mathbf{p}^0 and \mathbf{p}^N represent initial pose and final pose of robot arm, respectively, and $[x, y, z]^T$ and $[\psi, \theta, \phi]^T$ represent the position and orientation, respectively. As the number of samples, \mathbf{N} increases, more interpolation points are generated in trajectory. After interpolated joint values \mathbf{q}_{ref}^i are obtained, the robot follows the trajectory by assigning joint values.

This algorithm is applied to both arms identically. As mentioned earlier, since each arm has its own coordinate system, the algorithm is separately adopted by each arm based on its own coordinate system. Once the target position is given based on global coordinate system, the position value is converted into each arm's coordinate system and the algorithm is carried out.

Proposed algorithm employs the damped least-squares method [7] in order to calculate inverse kinematics. Since robot arm has 7 degrees of freedom with redundant joints, it is hard to find a closed form of inverse kinematics. The damped least-squares method, also called as Levenberg–Marquardt method, finds inverse kinematics by using linear velocity, angular velocity and Jacobian matrix iteratively. The obtained solution is numerically stable [8]. The cost function of the damped least-squares method is defined as follows [5]:

$$L(\mathbf{p}, \mathbf{q}) = (\mathbf{p}^{j+1} - \mathbf{p}^i)^T r_1 (\mathbf{p}^{j+1} - \mathbf{p}^i) + (\mathbf{p}^{j+1} - \mathbf{p}^{-j})^T r_2 (\mathbf{p}^{j+1} - \mathbf{p}^{-j}) + (\mathbf{q}^{j+1} - \mathbf{q}^{-j})^T r_3 (\mathbf{q}^{j+1} - \mathbf{q}^{-j}) \quad (3)$$

Algorithm 1. Trajectory Generation Algorithm

```

1: procedure DAMPED LEAST-SQUARES(p)                                ▷ generating q from p
2:   p0, pN ← p                                              ▷ N: the number of samples
3:   while errornorm < e do                                         ▷ errornorm = pdesired − pcurrent
4:     Δq ← L(p, q)                                                 ▷ L(p, q) : Levenberg-Marquardt method
5:     q = q + Δq
6:     pcurrent ← FK(q)                                              ▷ FK : Forward Kinematics
7:   end while
8:   return qref0, qrefN
9: end procedure

10: procedure MINIMUM-JERK TRAJECTORY(qref0, qrefN)
11:   qrefi, q̇refi, q̈refi ← qref
12:   return qrefi                                                     ▷ i : N samples
13: end procedure

```

where j is the iteration number, r_1, r_2 and r_3 are constants. When partial derivative according to ${}^{j+1}\mathbf{q}$ of \mathbf{L} is zero, the joint value error becomes a minimum. Therfore, after taking partial derivative and rearranging the formula, $\Delta^j \mathbf{q}$ can be expressed as follows:

$$\Delta^j \mathbf{q} = \mathbf{J}^T \left(\mathbf{J} \mathbf{J}^T + \lambda^2 \mathbf{I} \right)^{-1} \Delta \mathbf{p} \quad (4)$$

where r_1 and r_2 is set to 1 and r_3 is set to λ^2 . Accuracy and feasibility of the result are determined by the damping factor λ . The detailed formulations can be obatined from [5]. In order to solve the above equation, matrix inversion calculation is required. It is achieved by using a LDLT decomposition [5].

After calculating inverse kinematics, the outputs obtained by the damped least-squares are only initial and final joint values of required pose. The entire trajectory, which connects between start position and end position, should be generated. In the view of joint space, joint values between initial and final joint values should be determined by the interpolation method. There are many methods that generate a trajectory between two points. The following minimum-jerk trajectory method is used to maximize the accuracy of joint position:

$$\begin{aligned}
\mathbf{q}_{ref}^i &= \mathbf{q}^0 + (\mathbf{q}^N - \mathbf{q}^0) (10k_3 - 15k_4 + 6k_5) \\
\dot{\mathbf{q}}_{ref}^i &= \frac{(\mathbf{q}^N - \mathbf{q}^0)}{N} (30k_2 - 60k_3 + 30k_4) \\
\ddot{\mathbf{q}}_{ref}^i &= \frac{(\mathbf{q}^N - \mathbf{q}^0)}{N^2} (60k_1 - 180k_2 + 120k_3)
\end{aligned} \quad (5)$$

with

$$k_1 = \frac{i}{N}, \quad k_2 = k_1^2, \quad k_3 = k_1^3, \quad k_4 = k_1^4, \quad k_5 = k_1^5$$

where i is the sample point index. As the jerk is a rate of acceleration, the position error is increased as the jerk increases. Furthermore, minimum-jerk trajectory not only minimizes the position error, but also it makes the trajectory similar to human arm trajectory [9].

4 Computer Simulations

Webots simulator, which is a development environment to model, program and simulate mobile robots, was used to test the proposed algorithm. The 3D model and its nominal values are given in Fig. 2 and Table 1. The algorithm was implemented by C++, and the simulation was performed on a desktop computer. In the given experimental environment, real world's physics were not considered in order to concentrate on testing the feasibility of generating trajectory to the given position. The target position set \mathbf{q}^N could be obtained from user in various ways. In this experiment, the target position sets in Fig. 3 were applied to the robot to measure the time for generating trajectories for two arms. The accuracy was determined by analyzing error norm, $\sum_i |p_{i,desired} - p_{i,current}|$.

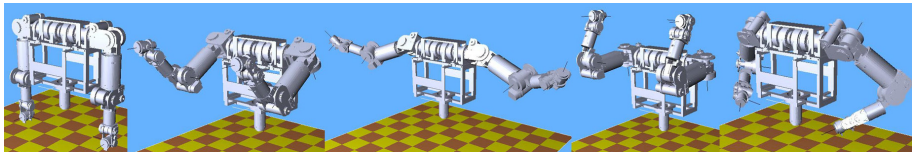


Fig. 3. Test position sets

$$\begin{aligned}
 StartPosition : \mathbf{p}^0 &= [0.0 \ 0.0 \ -0.45 \ 0.0 \ 0.0 \ 0.0]^T \\
 Position1 : \mathbf{p}^1 &= [0.3 \ 0.0 \ 0.0 \ 0.0 \ 0.0 \ 0.0]^T \\
 Position2 : \mathbf{p}^2 &= [0.2 \ 0.3 \ -0.15 \ 0.0 \ 0.0 \ 0.0]^T \\
 Position3 : \mathbf{p}^3 &= [0.1 \ 0.0 \ 0.1 \ 0.0 \ 0.0 \ 0.0]^T \\
 Position4 : \mathbf{p}^4 &= [0.1 \ 0.12 \ -0.18 \ 0.0 \ 0.0 \ 0.0]^T
 \end{aligned} \quad (6)$$

For given target position sets, the experimental results are summarized in Table 2 and Fig. 4. The trajectories in Fig. 4 present left arm end-effector's trajectory in Cartesian coordinate system. Fig. 4 (a) shows the trajectory of each position set (7), and all of them are drawn in one graph in Fig. 4 (b).

Every position sets start from leftmost pose in Fig. 3. Smooth trajectories are generated as shown in Fig. 4. Both horizontal and vertical motion trajectories were generated successfully.

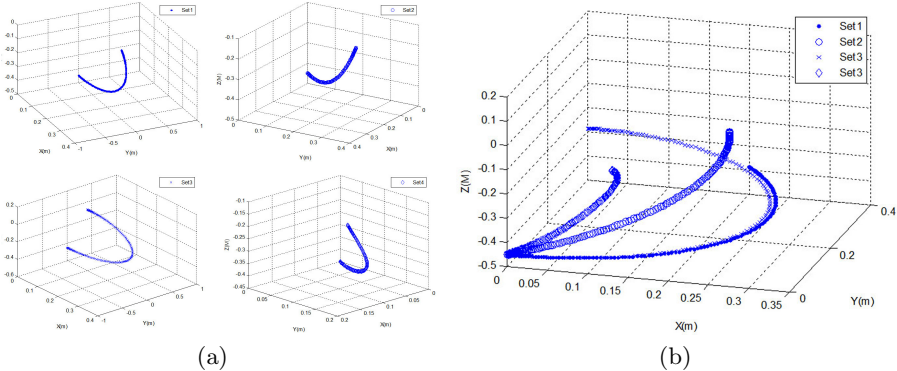


Fig. 4. End-effector trajectories for test sets

Table 2. Damped least-squares iteration number and computation time

Set	iteration	computation time (ms)	error norm (m)
Position set 1	2612	37.0542	0.000001
Position set 2	2586	50.1257	0.000001
Position set 3	2568	35.9959	0.000001
Position set 4	2518	54.0743	0.000001

The computation time can be varied according to the computation power. In this simulation, the computation time took more than 30ms but below 60ms. However, trajectory generation is not required to be performed in every control period which is usually less than 30ms. While following a current trajectory, the robot can generate the next trajectory in 60ms for the next motion. Modern robot real-time system is required under 1ms on motion trajectory generation. However, due to iterative way of finding a inverse kinematics, it is hard to reduce computation time by using this generation algorithm. Though it has a limitation on trajectory generation time for fast control system, the robot can make a path by itself not just only following pre-programmed path according to given command. Therefore, proposed algorithm can be applied to the real-time trajectory generation of both arms of a humanoid robot.

5 Conclusions

This paper proposed a real-time trajectory generation algorithm for both arms of a humanoid robot. Once the target position in Cartesian coordinate system was given, the damped least-squares method was used to find inverse kinematics of start and final positions. After obtaining the inverse kinematics, the algorithm generated an interpolated trajectories which are minimum-jerk trajectories. Computer simulation demonstrated its effectiveness successfully. That is, the proposed

trajectory generation algorithm shows real-time ability and robustness to singularity. The proposed algorithm is expected to be utilized in robot motion and task planning applications.

For the future work, robot's dynamics and real world physics should be considered to be applied to a real robot. The robot should control its arm by torque based on generated trajectory. In addition, the algorithm still makes a trajectory without considering self body collision. In other words, the algorithm generates a trajectory which crosses the trunk or the other hand for reaching a certain position. The algorithm has to make an trajectory with self body collision avoidance as well as external obstacles.

Acknowledgements. This research was supported by the MKE (The Ministry of Knowledge Economy), Korea, under the Human Resources Development Program for Convergence Robot Specialists support program supervised by the NIPA (National IT Industry Promotion Agency) (NIPA-2012-H1502-12-1002).

References

1. Hemion, N.J., Joublin, F., Rohlfing, K.J.: Integration of Sensorimotor Mappings by Making Use of Redundancies. Paper Presented at the IEEE World Congress on Computational Intelligence, Brisbane, Australia, June 10-15 (2012)
2. Bertram, D., Kuffner, J., Dillmann, R., Asfour, T.: An Integrated Approach to Inverse Kinematics and Path Planning for Redundant Manipulators. Paper Presented at the IEEE International Conference of Robotics and Automation, Orlando, Florida (May 2006)
3. Vande Weghe, M., Ferguson, D., Srinivasa, S.S.: Randomized Path Planning for Redundant Manipulator without Inverse Kinematics. Paper Presented at the IEEE International Conference of Robotics and Automation Society, Roma, Italy (November 2007)
4. Subudhi, B., Morris, A.S.: Soft Computing methods applied to the control of a flexible robot manipulator. *Applied Soft Computing* 9, 149–158 (2009)
5. Park, I.-W.: Kinematic Calibration, Optimal Trajectory Generation, and MOEA-based Optimal Posture Control of Humanoid Robot. Dissertation, KAIST (2012)
6. Hollars, M., Rosenthal, D., Sherman, M.: SD/FAST. Symbolic Dynamics, Inc. (1991)
7. Nakamura, Y., Hanafusa, H.: Inverse kinematic solutions with singularity robustness for robot manipulator control. *ASME J. Dyn. Syst. Meas. Control* 108, 163–171 (1986)
8. Wampler, C.: Manipulator inverse kinematic solutions based on vector formulation and damped least-squares methods. *IEEE Trans. Syst., Man Cyber.* 16, 93–101 (1986)
9. Flash, T., Hogan, N.: The coordination of arm movements: an experimentally confirmed mathematical model. *J. Neuroscience* 3, 1688–1703 (1985)

Chapter II: Ambient Intelligence, Collective Intelligence and Genetic Intelligence

Hyun Myung

Sensors installed on a robot itself can offer very limited information due to limited field of view and limited range of the sensors. Without help of ubiquitous sensor networks installed in environment, the robot's behavior is largely dependent on the restricted information. Ambient intelligence can take benefit of sensory information gathered from environment and enable the robot to behave more intelligently by perceiving and aggregating all the sufficient information. Collective intelligence emerged by interactions among multiple robots can be regarded as an extension of ambient intelligence. In this context, multiple robots can be regarded as various sources of sensory information. To achieve more complex intelligent behavior, soft computing techniques such as evolutionary computation can be used instead of classical hard computing techniques. By only providing the representation of the problem in the form of genetic coding, a properly designed objective function can guide the robot to fit to a desired fitness function.

The chapter is composed of four segments of different topics which cover broad spectrum of topics related to robot intelligence discussed above; Ambient Intelligence, Collective Intelligence, Genetic Intelligence, and Embodied and Developmental Robotics.

The first topic in this chapter is *Ambient Intelligence*. In Wikipedia, Ambient Intelligence (AmI) is said to be related to electronic environments that are sensitive and responsive to the presence of people. The ambient intelligence paradigm comprises of pervasive computing, ubiquitous computing, context awareness, and human computer interaction. In the robotics sense, the ambient intelligence enables a robot to acquire environmental information using ubiquitous sensor networks distributed in the environment as well as sensors embedded in the robot itself. The following papers treat various kinds of examples related to the above mentioned issues.

- 1) *Experimental Tests of Autonomous Jellyfish Removal Robot System JEROS*
- 2) *An Examination of Feature Detection for Real-Time Visual Odometry in Untextured Natural Terrain*
- 3) *Cost Based Navigation for Autonomous Vacuum Cleaners*
- 4) *Visual Odometry from RGB-D Sensor in a Dynamic Environment*
- 5) *Hybrid Indoor Location Tracking for Pedestrian Using a Smartphone*
- 6) *Overlapped Object Recognition Using Range and Image Data for an Service Robot*
- 7) *Novel scheme of real-time direction finding and tracking of multiple speakers by robot-embedded microphone array*

- 8) *Development of software and hardware of entry-level vision systems for navigation tasks and measuring*
- 9) *Map Building using Quadrocopter based on Vision and Ultrasonic Sensor Fusion*
- 10) *2D Image Feature-Based Real-Time RGB-D 3D SLAM*
- 11) *Simultaneous Localization Assistance for Mobile Robot Navigation in Real, Populated Environments*
- 12) *Towards an Ami-Robot Applied to Greenhouses*

The second topic in this chapter is *Collective Intelligence*. Collective intelligence is a theory that describes a type of shared or group intelligence that emerges from the collaboration and competition of multiple robots. A group of robots can cooperate or compete with each other to achieve a common desired objective. The result of this collective intelligence can be implemented by either distributed or centralized way. The tasks that are difficult to solve for an individual robot can be solved using this collective intelligence approach by utilizing intelligence of multiple robots within an environment. Multi-robot system or swarm robot system can be used to implement collective intelligence as the following papers show.

- 1) *Particle Swarm Optimization-based Distributed Control Scheme for Flocking Robots*
- 2) *Control Strategies for heterogeneous, autonomous Robot Swarms*
- 3) *A Full-functional Simulation and Test Platform for Rotorcraft Unmanned Aerial Vehicle Autonomous Control*
- 4) *Market-based Multiagent Framework for Balanced Task Allocation*
- 5) *Autonomy balancing in a manned-unmanned teaming (MUT) swarm attack*
- 6) *Aemi-Autonomous Control of Robotic Multi-Agents*
- 7) *Context-aware Decision Making for Maze Solving*
- 8) *Decentralized Task Re-Planning Approaches with en Route Information Rewards*
- 9) *Improved CAMshift based on Supervised Learning*
- 10) *Development of a Fall Detection System with Microsoft Kinect*
- 11) *Strategic decision-making of MASTER software agent in terms of the behavior of mobile robot agents*

Genetic intelligence is closely related to evolutionary computation. By representing a problem with a chromosome and genes, and describing fitness of this chromosome in the form of objective function, evolutionary computation effectively solves a solution using meta-heuristics inspired by genetics. The problems hard to be solved due to their inherent complexity, or the problems that do not have gradient information that is necessary for classical optimization methods or hard computing techniques, can be candidates for the application of evolutionary approach. The robots that use this problem solving capability can be regarded to have genetic intelligence. The following papers present some examples of this approach.

- 1) *Experimental study of Grouser's Effect for Planetary Rovers Based on Terramechanics*
- 2) *Evolving Story Narrative using Surrogate Models of Human Judgement*

- 3) *Distributed Computing Approach for Multiobjective Quantum-inspired Evolutionary Algorithm*
- 4) *Neuro-evolution of Escape Behaviour under High Level of Deception and Noise*
- 5) *Homogeneous Distributed Computing Framework for Multi-Objective Evolutionary Algorithm*

Embodied and Developmental Robotics deals with the application of intelligence to make robots evolve their behavior using interactions or iterative means. The following papers present concrete methods for implementing embodied and developmental robotics.

- 1) *Towards Intelligent Social Machines: Personalised Computational Expressions of Emotions as a Tool to Improve Human-Robot Interaction*
- 2) *Adaptive Fuzzy Cognitive Maps using Interactive Evolution: A Robust solution for Navigation of Robots*
- 3) *Tuning Fuzzy-based Hybrid Navigation Systems Using Calibration Maps*
- 4) *Distributed and Incremental Visual Object Recognition for Humanoid Platform NAO*
- 5) *Computational Intelligence for Creating Autonomous Robots*

The hybridization and integration of the ambient intelligence, collective intelligence, genetic intelligence, and embodied and developmental robotics may be the next step to achieve more emergent and proactive robot intelligence in the years to come.

Experimental Tests of Autonomous Jellyfish Removal Robot System JEROS

Donghoon Kim, Jae-uk Shin, Hyongjin Kim, Donghwa Lee,
Seung-Mok Lee, and Hyun Myung^{*}

URL(Urban Robotics Lab.), KAIST, Daejeon, 305-701, Korea
{dh8607, jacksju, hjkim86, leedonghwa, semoyi, hmyung}@kaist.ac.kr

Abstract. Recently, the increase in population of jellyfish is becoming a great menace to the oceans ecosystem, which leads to drastic damage to the fishery industries. To overcome this problem, a jellyfish removal system with trawl boats equipped with the jellyfish removal net has been suggested by NFRDI. However, the system needs large ships which need to be operated by a lot of human operators. Thus, this paper represents the design and implementation of an autonomous jellyfish removal robot system, called JEROS. The JEROS consists of an autonomous surface vehicle (ASV), a grid for jellyfish removal, and an autonomous navigation system. Once jellyfish are detected using a camera, the jellyfish removal scenario is started with generating efficient path to remove the jellyfish. Finally, the jellyfish is sliced up with the grid installed underneath the JEROS by following the generated path. The prototype of the system was implemented, and its feasibility was demonstrated through outdoor experiments and field tests.

Keywords: jellyfish removal, surface vehicle, navigation, vision processing, object detection.

1 Introduction

Many scientists have warned that drastic growth of jellyfish population causes a serious problem, and the causes of the proliferation have been regarded as the factors including climate change, pollution from the land runoff, over-fishing, and marine structures. In addition to that, the jellyfish have caused a severe damage to fishery industries and power plants. In Korea, the proliferation of harmful jellyfish such as *aurelia aurita* and *nemopilema nomurai* is becoming a serious problem. The jellyfish have induced the damage of nearly 300M USD per year to fishery industries, seaside power plants, and etc. In order to cope with this problem, some jellyfish removal systems have been developed. In Japan, trawl boats equipped with blades have been used to cut off the jellyfish. The jellyfish removing system also has been developed to remove the jellyfish near the water intake pipe of power plants using a camera and a pump [1]. National Fisheries Research and Development Institute (NFRDI) in Korea has developed a system with trawl boats equipped with the jellyfish removal nets [2].

^{*} Corresponding author.

However, the system needs to be operated by large ships and a lot of human operators. Urban Robotics Laboratory at KAIST proposed a jellyfish removal robot system using ASV-based robot which reduces the consumption of man power, time, and capital [3].

An autonomous swarm robot system for jellyfish removal, called JEROS (Jellyfish Elimination RObotic Swarm) has been designed as shown in figure 1. In this research, the design and implementation of the JEROS are described. The JEROS was designed as a SWATH-type [4] surface vehicle which is stable to disturbances compared to other monohull-type AUVs, and a grid which consists of a frame and thin wires is installed underneath the JEROS to slice up the jellyfish. An autonomous navigation system for jellyfish detection and removal is also embedded, and the scenario of the system consists of 3 steps. The first step is detecting jellyfish using a camera and vision processing algorithm. In the next step, path which leads the JEROS to jellyfish is generated. Finally, following the generated path using guidance and control algorithm makes the robot cut off the jellyfish. In the next section, design and implementation of the ship, electrical parts, the autonomous navigation system, and vision-based jellyfish detection algorithm will be explained. And the navigation tests at a pond and field tests using prototype are also described.

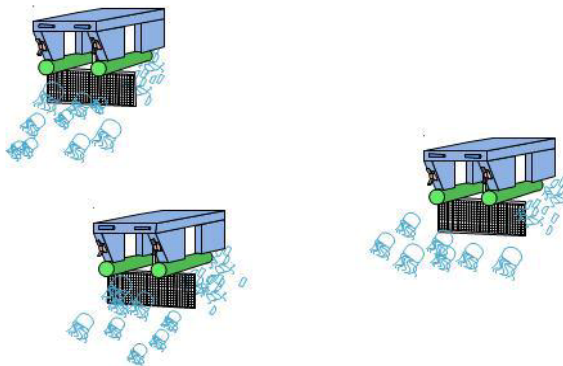


Fig. 1. Concept of JEROS

2 Design and Implementation of JEROS

2.1 Design of Ship

In this research, the JEROS was designed as a SWATH-type ASV. The ship consists of two hulls, one body, one grid, and some links as shown in figure 2. The two hulls connected to the body by 6 narrow links provide buoyancy, and the hull volume in the surface is minimized. Thus, the SWATH-type ship provides high level of stability to disturbances such as wave, current, and wind compared to monohull-type ASVs, and the ship is able to sustain its speed in rough head seas by minimizing the hull volume. The two thrusters were attached to the rear of the hulls to reduce friction of the fluid and enhance the thrusting performance. The grid attached underneath the robot consists of a frame and thin wires for slicing up the jellyfish as shown in figure 2.

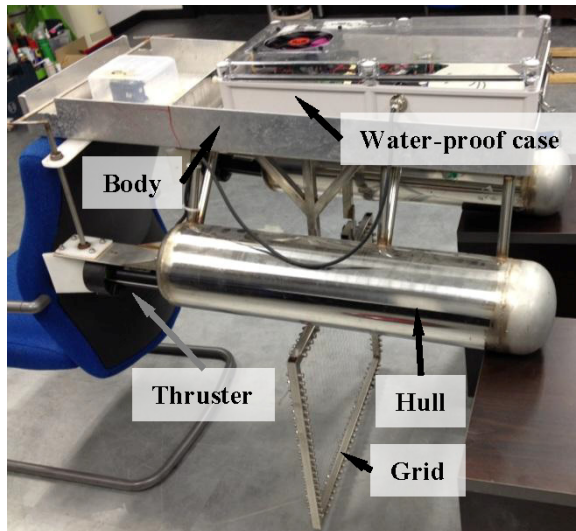


Fig. 2. Autonomous surface robot platform JEROS

2.2 Electrical Parts

The electrical parts which consist of sensors, processors, and controllers were embedded on the body of the JEROS with the water-proof case and a cooling fan as shown in figure 3. The sensor parts consist of a camera, GPS, and IMU. The camera is used to detect jellyfish underneath the sea surface. GPS provides location information with 1.5m accuracy and IMU provides absolute attitude with respect to global coordinate system. A single board computer (SBC) and a microprocessor for processing the guidance, navigation and control algorithm of the JEROS were also included in the electrical parts. The electrical parts are listed in Table 1.

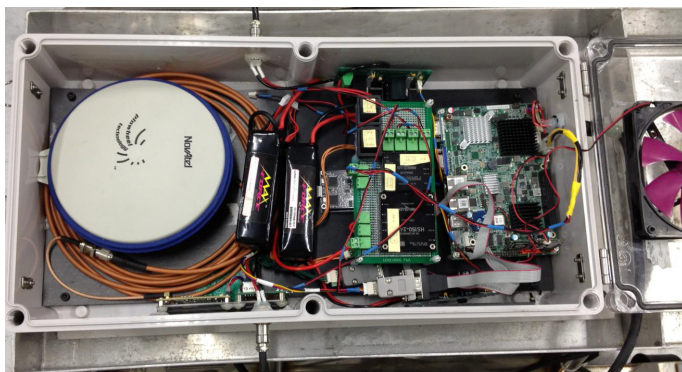


Fig. 3. Electrical parts embedded in the water-proof

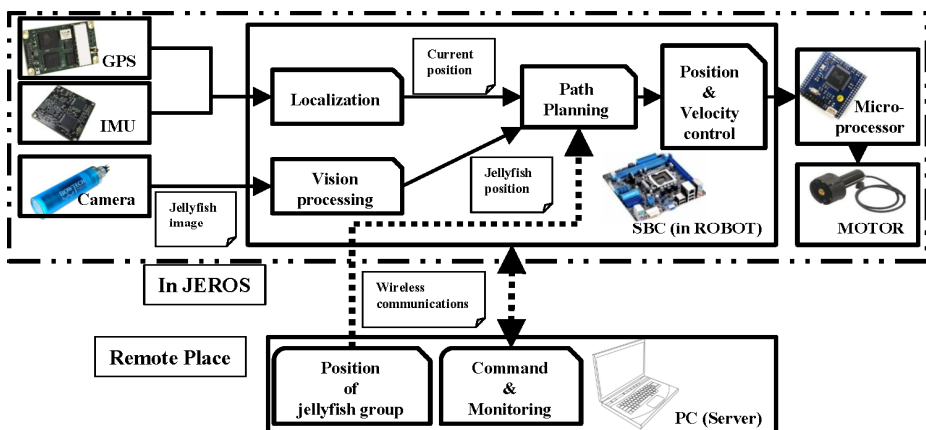
Table 1. Electrical Parts of JEROS

Device	Name	Manufacture
GPS	OEMV-1	Novatel
IMU	MySen-B	MySen
Camera	DIVECAM-550C	Bowtech
Computer(SBC)	Core 2 Duo Board	Intel
Microprocessor	TMS320F2808	Texas Instrument
Thruster	BTD150	SeaBotix

2.3 GNC System

The Guidance, Navigation, Control (GNC) system is made up of a localization module, a vision processing module, a position and velocity control module, and a monitoring module. These are processed on the SBC, microcontroller, and external server computer. The architecture of the system is shown in figure 4.

The localization module estimates current position and heading angle of the JEROS using GPS and IMU, respectively. The vision processing module computes relative position to the jellyfish using jellyfish images from the camera, which is used to plan efficient path for jellyfish removal. The generated path is followed using a guidance algorithm in the position and velocity control module. The monitoring module was implemented to observe the status of the JEROS at a remote place through wireless communication. While monitoring, manual control is also available by transmitting simple commands or path information to the JEROS.

**Fig. 4.** Block diagram describing the overall architecture of the GNC system

2.4 Robot Navigation

The overall navigation system is designed as the block diagram shown in figure 5, which consists of the localization module, the path planning module, and the position and velocity control module. The navigation system starts with the position of jellyfish detected in the vision processing module, and then the path from the current position of the JEROS to the jellyfish position for jellyfish removal is generated as a sequence of virtual way-points in the path planning module. After that, the generated path is followed asymptotically using the line-of-sight (LoS) guidance algorithm [5]. The velocity and heading angle of the JEROS are controlled by two thrusters in the microprocessor. Finally, the jellyfish is cut off with the grid.

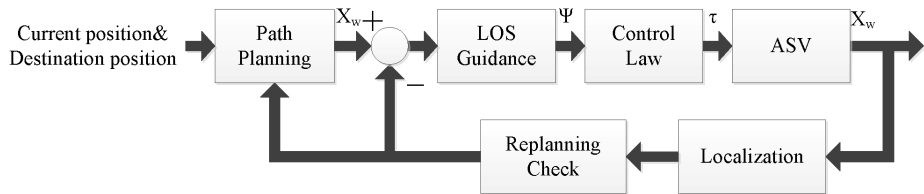


Fig. 5. Block diagram describing the architecture of navigation system

The path consists of some way-points, starting position, and target position as shown in figure 6. The LoS guidance algorithm provides the heading angle to minimize the heading angle error and to follow the paths between the contiguous way-points as follows:

$$\psi_{err} = \psi_d - \psi^* \quad (1)$$

where ψ^* and ψ_d are the current and desired heading angle of the robot, respectively. The current heading angle is provided by IMU, and the desired heading angle is calculated using the LoS vector. The LoS vector is a vector from the current position $P^* = (x^*, y^*)$ to the LoS point $P_{los} = (x_{los}, y_{los})$. The LoS point is a target point to track the path. The desired heading angle can be calculated as:

$$\psi_d = \tan^{-1} \left(\frac{y_{los} - y^*}{x_{los} - x^*} \right), -\pi \leq \psi_d \leq \pi \quad (2)$$

The LoS point and desired heading angle depend on a Circle of Acceptance (CoA) which is defined as a circle centered at the current position with radius R_0 . The LoS point is an intersection point of the CoA and the generated path. For this reason, the robot can get back to the path rapidly depending on the radius R_0 when the robot is far away from the path. During the following of the path, the robot must switch the way point to the next one when it comes close to the next way point, and the robot has to plan a new path when it gets far away from the path more than distance R_0 .

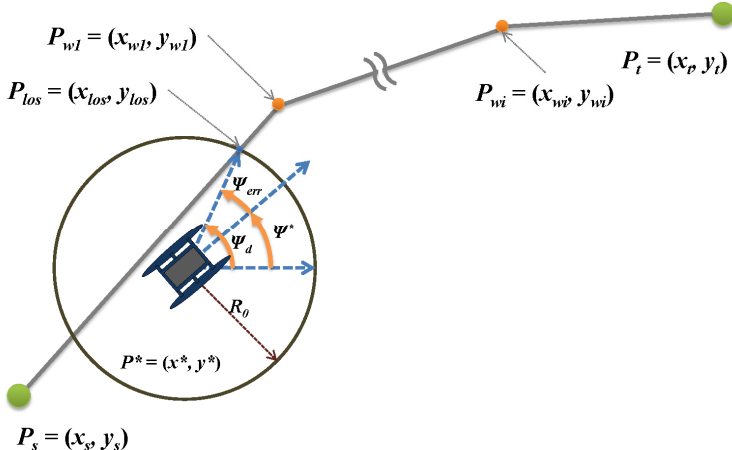


Fig. 6. Configuration of the navigation system for the JEROS

2.5 Image Processing for Jellyfish Detection

The related studies on the detection of jellyfish based on vision system have focused on surveys of underwater environment. Therefore the almost detection algorithms have performed in underwater environment [6]. In this research, a surface vehicle type robot is used, so the jellyfish detection algorithm is studied on the surface of the ocean. One CMOS camera connected to the SBC is used for vision system.

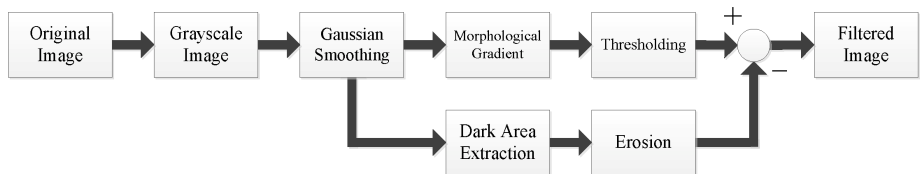


Fig. 7. Block diagram describing the image processing sequence for jellyfish detection

The jellyfish detection algorithm is performed every processing step based on the image from the camera sensor, as illustrated in figure 7. First, the input image is converted to a binary scale image. Then the outlines of objects are detected by applying the morphological gradient operation. However, due to the rolling of the sea wave, dark regions appear that is impediment to extract the edge of jellyfish. In order to solve this problem, after detecting the dark areas in the original image, the erosion operation and the morphological gradient operation are applied sequentially. The processed dark area is subtracted from the original image. Finally, blob labeling is performed and jellyfish is detected. These pre-processing steps are applied to the real jellyfish images on the surface of the ocean, and the results are shown in figure 8.

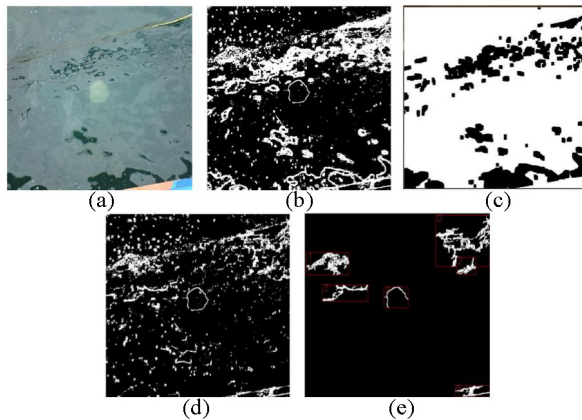


Fig. 8. Image processing results to the real jellyfish image. (a) The original jellyfish image (b) The result of the morphological gradient operation (c) Extracting the dark areas (d) The result of subtracting the dark areas form the original image (e) Blob labeling and jellyfish detection.

3 Experiments

3.1 Navigation Tests

The feasibility of the navigation system was demonstrated through outdoor experiments at a pond in KAIST. The prototype has a weight of about 35kg in air

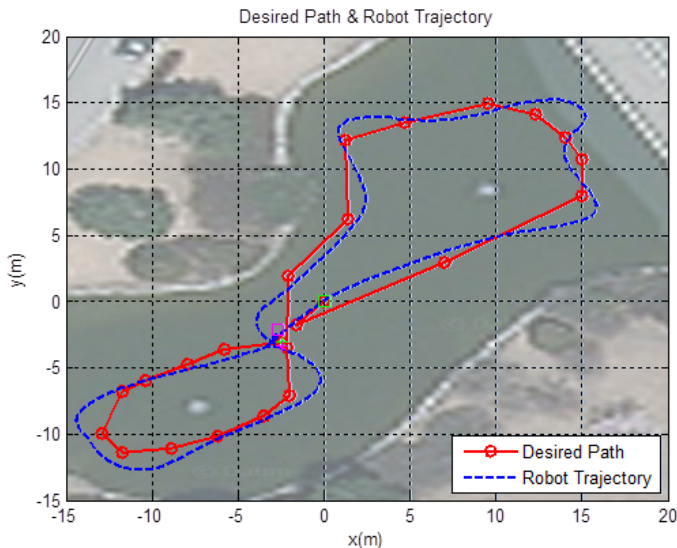


Fig. 9. Result of path following test at a pond in KAIST. The result shows the desired path (red solid line) and trajectory (blue dashed line) of the robot.

and a dimension of 1m x 0.6m x 0.5m. The test area is about 1200m², and there are two fixed obstacles as shown in figure 9. The desired path was set arbitrarily as a closed loop, and the path is illustrated as red solid line on figure 9. The prototype autonomously navigated following the path using the navigation system, and blue dashed line on figure 9 shows the trajectory followed by the prototype.

3.2 Field Tests

In order to verify the feasibility of the prototype, field tests were conducted twice in saemanguem and shihwaho, in the west coast of Korea. The reason for selecting two test sites is that an enormous number of jellyfishes are inhabited and wave level is lower than the other coast.

At first, the balance of the prototype was adjusted using some weights and buoys to enhance the stability against the waves as shown in figure 10, and then, the feasibility was demonstrated by following arbitrary paths.

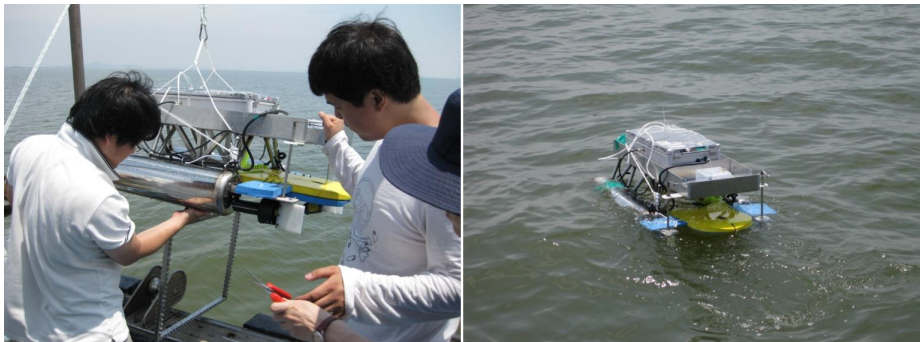


Fig. 10. Field tests in shihwaho

4 Conclusion

In this paper, we represented the development and experiments of an ASV-based jellyfish removal robot system, JEROS. The robot system was designed and implemented to detect and remove jellyfish using the GNC system. The GNC system consists of the vision processing module for jellyfish detection, the navigation module for localization and path planning, and the position and velocity control module for guidance and control. The feasibility of the prototype was demonstrated through the outdoor navigation tests and the field tests. Future research will focus on enhancement of the ship for stability to the waves and on a cooperative jellyfish removal strategy using swarm robot system. And the efficiency of the JEROS will be investigated through various field tests.

Acknowledgment. This research was supported by Basic Science Research Program through the National Research Foundation of Korea (NRF) funded by the Ministry of Education, Science and Technology (grant number 2012-0003897). It was also supported by the Ministry of Knowledge Economy (MKE), Korea, under the Human Resources Development Program for Convergence Robot Specialists support program supervised by the National IT Industry Promotion Agency (NIPA) (NIPA-2012-H1502-12-1002). Additionally, it was supported by Korea Ministry of Land, Transport and Maritime Affairs(MLTM) as U-City Master and Doctor Course Grant Program.

References

1. Matsuura, F., Fujisawa, N., Ishikawa, S.: Detection and Removal of Jellyfish Using Underwater Image Analysis. *Journal of Visualization* 10(3), 259–260 (2007)
2. National Fisheries Research and Development Institute, Separating and cutting-off system of jellyfish, KOR. Patent 10-0646453-00-00, November 8 (2006)
3. Korea Advanced Institute of Science and Technology, Apparatus for Removing Jellyfish, KOR. Patent 10-1145521-00-00, May 4 (2012)
4. Robertson Dinsmore, SWATH: Small SWATH Research Vessels, Small Research Vessel Compendium, UNOLS (2004)
5. Fossen, T.I.: Marine Control Systems: Guidance, Navigation and Control of Ships, Rigs and Underwater Vehicles, *Marine Cybernetics* (2002)
6. Rife, J., Rock, S.M.: Segmentation methods for visual tracking of deep ocean jellyfish using a conventional camera. *IEEE Journal of Oceanic Engineering* 28(4), 595–608 (2003)

An Examination of Feature Detection for Real-Time Visual Odometry in Untextured Natural Terrain

Kyohei Otsu¹, Masatsugu Otsuki², Genya Ishigami², and Takashi Kubota²

¹ The University of Tokyo, 7-3-1 Hongo, Bunkyo, Tokyo, Japan
kyon@ac.jaxa.jp

² ISAS/JAXA, 3-1-1 Yoshinodai, Chuo, Sagamihara, Kanagawa, Japan

Abstract. Estimating the position of a robot is an essential requirement for autonomous mobile robots. Visual Odometry is a promising localization method in slippery natural terrain, which drastically degrades the accuracy of Wheel Odometry, while relying neither on other infrastructure nor any prior knowledge. Visual Odometry, however, suffers from the instability of feature extraction from the untextured natural terrain. To date, a number of feature detectors have been proposed for stable feature detection. This paper compares commonly used detectors in terms of robustness, localization accuracy and computational efficiency, and points out their trade-off problems among those criteria. To solve the problem, a hybrid algorithm is proposed which dynamically switches between multiple detectors according to the texture of terrain. Validity of the algorithm is proved by the simulation using dataset at volcanic areas in Japan.

Keywords: Visual odometry, Outdoor environment, Feature detection.

1 Introduction

Exploring ultimate environments such as planetary surfaces and deep sea is a challenging but beneficial task for human beings. Several missions have attacked such environments, e.g., the Mars Science Laboratory (MSL) program by NASA¹. Due to the severe conditions of the environments, autonomous mobile robots are regarded as an effective method for such missions. One of the essential techniques of autonomous mobile robots is localizing themselves. Especially in such environments, robots have to estimate their position without any external infrastructure (such as GPS satellites) nor prior knowledge about the location.

To date, numerous localization methods for mobile ground vehicles have been proposed and implemented in mobile ground vehicles. The most popular methods are Wheel Odometry (WO) and Inertial Measurement Unit (IMU) or the combination of them. These methods offer high resolution with low cost sensors. Even so, these approaches have several challenges: WO is vulnerable to

¹ <http://mars.jpl.nasa.gov/msl/>

wheel slips, and inertial sensors are prone to drift. These shortages can be crucial when exploring the environment containing loose terrain and steep slopes. Doppler sensors are used as velocity sensors insensitive to wheel slips, while they are applicable only for fast-moving robots. Active ranging sensors, such as ultrasonic sensors and Laser Range Finders (LRF), are also typically used to localize robots. These sensors measure the distance from the robot to objects, and the robot estimates its current position from the physical relationship with the objects. However, these active sensors have a drawback to consume much electric power, so they are not feasible under the energy-limited environment.

Recently, the focus is on another powerful sensor, vision sensor, which is less energy-consuming but provides rich information about the environment. A technique to estimate motion by using visual input is called Visual Odometry (VO). It is regarded as a promising localization method with the help of the rapid improvement of computational resources in recent years. The basic principle of VO is an iteration of estimating the camera relative pose by finding the feature point correspondences between images, which is a key technique of two-view Structure from Motion (SfM) problem. VO is immune to wheel slips and also more stable for the drift error since it can cancel the drift by vision approaches (e.g., Bundle Adjustment [1] or loop-closing technique of Simultaneous Localization and Mapping (SLAM) problem [2]). VO can also be easily installed into the system since visual sensors are recently mounted on most robots due to the variety of their possible usage.

SLAM is, on the other hand, another powerful localization method actively researched in the robotic field. Radio sensors and vision sensors tend to be used for the input to SLAM algorithms. The method is very useful for the robot navigation since it creates a map as well as localizing the robot. However, the algorithm is complex and requires much computational resources, which may bring difficulty in installing into low-performance onboard computers. From the viewpoint, VO focuses on calculating a robot trajectory, which requires far less computational power and promotes easy installation onto a system.

VO is becoming more and more popular due to these advantages. Still, it has several challenges evolved from properties of vision:

1. **Stability:** feature point tracking should be robust to the terrain appearance. VO becomes stable if every pair of images exhibits adequate correspondence of features.
2. **Accuracy:** the robot should be accurately localized even if the algorithm uses error-prone images. The accuracy can be improved by using statistical methods.
3. **Computational Efficiency:** most onboard computers equipped on mobile robots are not computationally powerful. To execute real-time VO the algorithm efficiency is an issue to be concerned.

Generally speaking, these criteria depend on the appearance of ground and cannot be fully estimated beforehand. In addition, these are trade-off in many cases.

Several implementations of real-time VO have been presented (e.g., [3–5]). Regardless of these successful results, VO in an outdoor environment has a

crucial problem on detecting feature points from the untextured terrain. VO assumes that the terrain exhibits rich texture so that the feature points are easily tracked. However, in contrast to indoor environments, particular outdoor scenery makes the point tracking difficult. In fact, the VO localization in the Mars Exploration Rover (MER) mission by NASA/JPL revealed that the rovers found many areas which have little visual features on the ground surfaces in the real ultimate environment [6].

In order to address the challenge of VO in untextured terrain, roughly two approaches have been proposed. One simple but effective approach is to use a proper feature detection algorithm. A number of detectors have been proposed to detect points with intended properties. The detail of common detectors will be discussed in Sect. 2. Since these detectors focus on the different characteristics of the image, the proper detector for certain scenery depends on the terrain appearance and the intended properties.

The other approach is to divide images into several blocks and find the most characteristic point in each region [7, 8]. This method enables feature detection even in feature-less terrain. However, this approach has several shortages, e.g., forcing extraction from extremely low textured region causes low matching rate because of using too weak characteristic points.

The proposed method adopts the former approach, i.e., using the effective feature detector. The rest of the paper is organized as follows: in Sect. 2, the commonly used detectors are discussed and evaluated by using dataset at volcanic fields. In Sect. 3, a hybrid algorithm of several detectors is introduced, which is designed to overcome shortages of the common detectors. In Sect. 4, the comparative study of the common and proposed detectors is presented. Finally, Sect. 5 concludes the paper.

2 Conventional Feature Detectors

Detector Description. The main focus of this paper is to detect stable features from the smooth terrain which shows difficulty in tracking features. A lot of feature detectors have been proposed. Generally speaking, these can be divided into two groups:

Corner Detectors. These detectors find corners in given images, since corners tend to exhibit invariance to the change of the view. This group involves the methods such as Harris [9], Shi-Tomasi [10], and FAST [11, 12] detectors.

Scale-space Feature Detectors. These detectors can obtain scale invariant features. This characteristic benefits VO as it is robust to scale changes and enables longer tracking. However, these invariance may degrades the computational efficiency to some extent. SIFT [13], SURF [14], and STAR based on CenSurE [15] can be classified into this group.

The algorithms mentioned above are implemented in OpenCV Library [16] and widely used in various applications including VO. Typically, corner detectors such as Harris and FAST are used in VO, since they are high-speed and accurately located. Yet, these corners are sometimes difficult to find in untextured

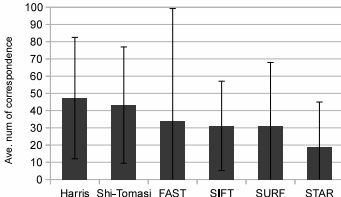


Fig. 1. The average number of correspondences between features

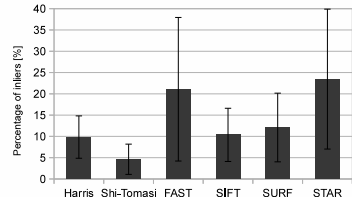


Fig. 2. The percentage of correct matches in the all extracted features

Table 1. Average runtime per frame (320x240 grayscale images on Intel Core 2 Quad 2667MHz CPU)

Detectors	Harris	Shi-Tomasi	FAST	SIFT	SURF	STAR
Ave. runtime [ms]	11.87	14.36	1.32	54.98	27.90	9.86

natural terrain. The quantity of features can be improved by changing parameters such as threshold, but it can be prone to increase noise and outliers. SIFT and SURF are also used if scale change is a big concern. These algorithms require large computational time, and lose pixel-level accuracy in exchange for scale invariance. Agrawal et al. [15] proposed a novel detector called CenSurE, that is scale invariant but has a better computational property, as a feature detector in their real-time VO implementation [4]. STAR detector is implemented based on CenSurE.

Performance Test. A performance test for these detectors is conducted by using the dataset including more than 900 stereo image pairs of volcanic areas (See examples in Fig. 3). Statistical results are shown in Fig. 1 and 2. The accurate VO localization requires a certain number of persistent feature correspondences in order to compensate errors statistically. More than 20-30 correct matches are typically regarded to be enough for estimation. Harris corner detector shows better performance than the others. However, Harris and similar Shi-Tomasi detectors cannot present high matching rate in matching process, which can affects the matching efficiency and accuracy.

The timing result on a laptop machine is presented in Table 1. In terms of the average detection time for an image, the corner detectors are superior to the scale-space feature detectors except STAR detector. STAR detector shows high computational efficiency, while it is not stable at least for this parameter setting and dataset. FAST detector is the most efficient detector of all. Its detection is fast, and repeatability and distinctiveness is high. Even so, its high performance depends on terrain, i.e., FAST detector is not robust to all kind of terrain.

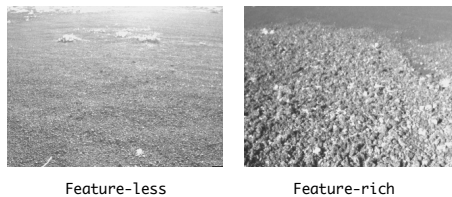


Fig. 3. The examples of terrain types

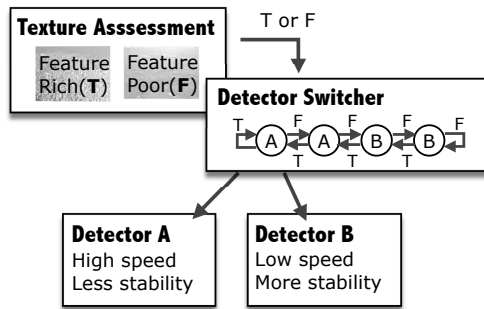


Fig. 4. Saturating counter with four states

These results give an implication. Harris detector shows stability as well as localization accuracy; and FAST detector is highly efficient but not robust. This trade-off problem can be solved by adopting a hybrid method which simultaneously makes use of these advantages.

3 Adaptive Detector Selection

The proposed algorithm switches feature detectors so as to improve the stability and accuracy while maintaining computational efficiency. The switching rule is described in this section.

In the proposed scheme, an appropriate feature detector is selected according to the texture of ground. The examples of the different textures in natural terrain are shown in Fig. 3. For the terrain which has large features on the ground surfaces (referred as ROUGH), high-speed feature detectors are preferred in order to obtain the total performance efficiency. On the other hand, if the robot is on the terrain with little features (referred as SMOOTH), detectors should be sensitive and stable. The terrain type is estimated from the result of feature detection and tracking. For instance, the number of detected features and/or percentage of successful tracking can be referred to be a condition of switching.

The proposed method switches among multiple detectors which have different properties. These detectors are selected out of the conventional detectors based on the usability against different terrain. One should be high-speed to improve the total performance, and another should be sensitive to be capable of detecting

features even from the SMOOTH terrain. The detectors should be two or three in order not to increase the cost of switching.

The cost of switching is explained as follows. In the developing VO system, the features are matched by calculating the normalized correlation between the feature points detected in every pair of succeeding frames. Feature matching cannot be done if the both frames use different feature detectors, since each detectors focus on different characteristics. Therefore, if the selected detector is different between the succeeding frame pairs, it requires excess detection process. This surely deteriorates the computational performance.

The simplest method to switch among the detectors may be selecting a high-speed detector for all ROUGH terrain and a sensitive and stable detector for all SMOOTH terrain. However, the strategy performs poorly for a certain terrain, e.g., the intermediate terrain between SMOOTH and ROUGH. Such environment causes frequent switching between the detectors and the efficiency should be decreased by the excessive calculation.

One approach to avoid the excessive switching is to use a saturating counter that is used for branch prediction in the field of computer architecture (Fig. 4). This technique is known to be simple but quite effective to make a prediction on future branches. The saturating counter is composed of a state machine with several states. The number of states can be adjusted considering the type of the explored environment. This counter can mitigate the excessive cost of switching.

4 Experiments

4.1 Experimental Setup

Field experiments have been conducted in two off-road environments: Ura-Sabaku desert at Izu-Oshima and Aso Volcano located in Japan. These spots are covered with volcanic products as well as partial rocks and rollings. Two experimental rovers (Fig. 5) developed by JAXA are used to collect the dataset. The camera specifications for rovers are shown in Table 2. The collected images are more than 900 stereo pairs in total.

The readers might think the frame rates in Table 2 are too slow. This is because of the hardware constraints related to communication and scheduling problems. However, the traversing speed of the rovers are not so fast (approximately 0.1m/sec), so the low frame rate does not cause a big problem.

4.2 Adaptive Detector Selection

Detector Combination. To improve the performance of the proposed hybrid detector, finding proper combination of detectors should be essential. According to the guideline of selecting detectors in the previous section, three detectors (Harris, FAST, and SIFT) are chosen and combined to form hybrid detectors.

The performance is compared in Fig. 6 for effective percentage of correct matches and processing time including switching cost. Figure 6(a) shows a statistical result of repeatability and distinctiveness, presenting the sorted percentage of correct matches for every frame with more than 20 matches. Figure 6(b)

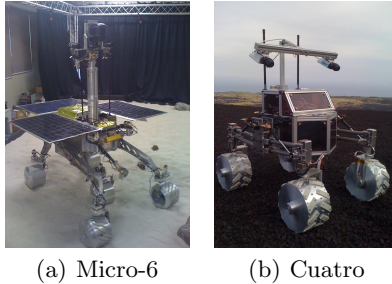


Fig. 5. Appearance of the experimental rovers

Table 2. Camera specification of the experimental rovers

	Micro-6	Cuatro
FOV(degree)	40x30	87x65
Resolution	320x240	640x400
Frame rate(Hz)	0.25	0.69
Baseline(m)	0.270	0.475
Height from ground(m)	1.450	0.770

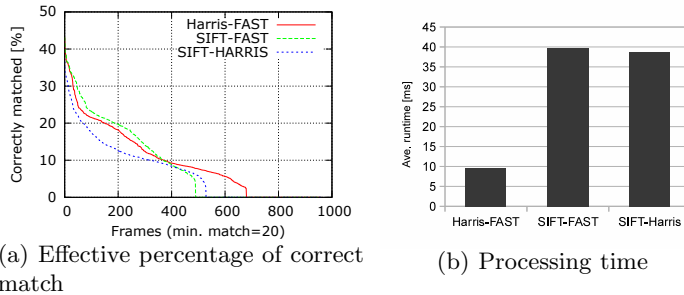
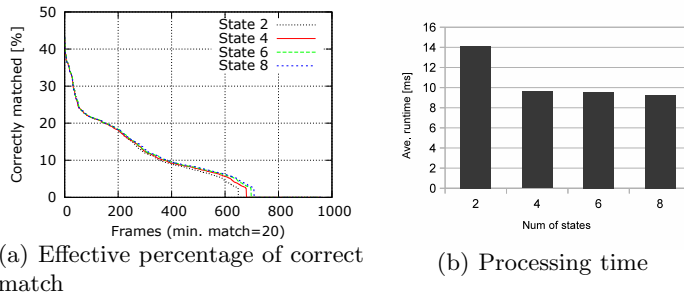
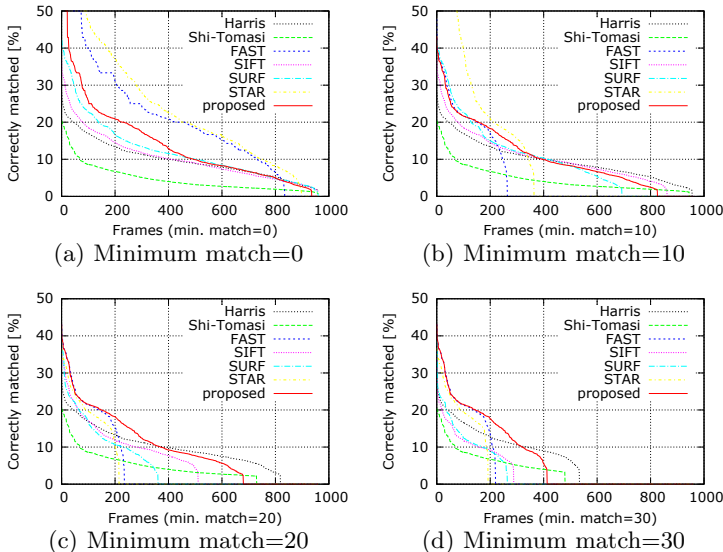
shows the averaged time for processing each frame. Apparently, the combination of Harris and FAST is effective: 4 times faster, highly stable as well as having higher matching rate. This combination is determined to be used for this dataset.

The Saturating Counter. The performance evaluation with respect to the number of states in the saturating counter is shown in Fig. 7. The number of states varies from 2 to 8. Note that the saturating counter with 2 states corresponds to the simplest method which uses the high-speed detector for all ROUGH terrain and the sensitive detector for all SMOOTH terrain. The result in Fig. 7 shows that the state greater than 4 is slightly better in stability, and 1.5 times better in efficiency. For simplicity, the saturating counter with 4 states is adopted.

4.3 Comparison with the Conventional Detectors

The proposed method is compared to Harris, Shi-Tomasi, FAST, SIFT, SURF and STAR detectors. Figure 8 presents how much of the detected points are correctly matched for the frames with more than 0, 10, 20, 30 matches respectively. In general, 20-30 matches are enough for reducing errors by statistical methods. A good detector should exhibit high matching rate for the frames with the certain number of matches. The proposed method could successfully obtain the benefits of the both combined detectors.

Figure 9 shows the percentage of frames with fewer than N correct matches, which means how many frames will fail if a threshold for inliers are given to assure the reliability of motion estimation. Harris, Shi-Tomasi and the proposed

**Fig. 6.** Performance evaluation over detector combination**Fig. 7.** Performance evaluation over the number of state in the saturating counter**Fig. 8.** Statistical results on stability and accuracy: the sorted percentage of correct matches for minimum of N match frames

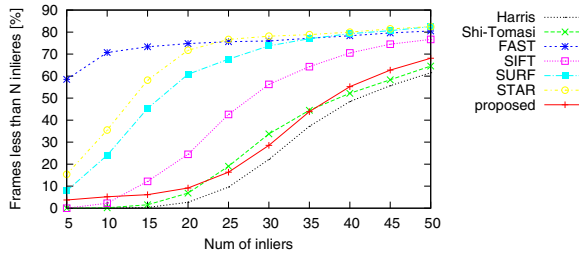


Fig. 9. Missed frames: the percentage of frames as a function of the number of correct matches

Table 3. Comprehensive evaluation

Detector	Type	Stability	Accuracy	Efficiency
Harris	Corner	+++	+++	++
Shi-Tomasi	Corner	+++	+	++
FAST	Corner	+	++	++++
SIFT	Scale-space	++	+++	+
SURF	Scale-space	+	++	++
STAR	Scale-space	+	++	+++
Proposed	Corner	+++	+++	+++

detector have less than 10% missed frames with minimum of 20 inliers even for the extremely untextured dataset.

The result for the processing time also supports the superiority of the proposed method. In the same setup in Table 1, the proposed method could detect from an image with 9.63 msec. This can vary with dataset; for example, the proposed method would perform better for the dataset containing ROUGH images at a high rate, since it choose the high-speed detector in most images.

Finally, the comprehensive analysis is shown in Table 3. The detectors are compared in terms of the criteria: stability, accuracy, and efficiency. This table shows the effectivity of the proposed method for this dataset with more than 900 images in the volcanic areas.

5 Conclusions

This paper compares the conventional feature detectors in untextured natural terrain, in terms of stability, localization accuracy, and computational efficiency. In order to address the trade-off problems which is clarified by the examination, a new hybrid detector is proposed. The algorithm of the detector is switching among multiple detectors according to the texture of terrain. In the process of dynamic detector switching, a saturating counter for predicting future branches is adopted in order to mitigate the excessive cost of switching.

The proposed algorithm has been verified by using datasets collected at volcanic areas, covered with feature-less volcanic products and a few rocks. The method is validated as a robust and efficient algorithm through the comprehensive analysis.

References

- Triggs, B., McLauchalan, P., Hartley, R., Fitzgibbon, A.: Bundle adjustment – a modern synthesis. *Vision Algorithms: Theory and Practice*, 153–177 (2000)
- Open source software for SLAM and loop-closing, <http://openslam.org>
- Nister, D., Naroditsky, O., Bergen, J.: Visual odometry for ground vehicle applications. *J. of Field Robotics* 23, 3–20 (2006)
- Konolige, K., Agrawal, M.: Large-scale visual odometry for rough terrain. In: *International Symposium on Research in Robotics (ISRR 2007)*, vol. 66 (2007)
- Howard, A.: Real-time stereo visual odometry for autonomous ground vehicles. In: *IEEE/RSJ Int. Conf. on Intelligent Robots and Systems (IROS 2008)*, pp. 3946–3952. IEEE (2008)
- Maimone, M., Cheng, Y., Matthies, L.: Two years of visual odometry on the mars exploration rovers. *J. of Field Robotics* 24(3), 169–186 (2007)
- Johnson, A.E., Goldberg, S.B., Cheng, Y., Matthies, L.H.: Robust and efficient stereo feature tracking for visual odometry. In: *IEEE International Conference on Robotics and Automation (ICRA 2008)*, pp. 39–46 (2008)
- Tamura, Y., Suzuki, M., Ishii, A., Kuroda, Y.: Visual odometry with effective feature sampling for untextured outdoor environment. In: *IEEE/RSJ Int. Conf. on Intelligent Robots and Systems (IROS 2009)*, pp. 3492–3497. IEEE (2009)
- Harris, C., Stephens, M.: A combined corner and edge detector. In: *Alvey Vision Conference, Manchester, UK*, vol. 15, pp. 147–151 (1988)
- Shi, J., Tomasi, C.: Good features to track. In: *IEEE Conference on Computer Vision and Pattern Recognition (CVPR 1994)*, pp. 593–600. IEEE (1994)
- Rosten, E., Drummond, T.: Fusing points and lines for high performance tracking. In: *IEEE International Conference on Computer Vision (ICCV 2005)*, vol. 2, pp. 1508–1515. IEEE (2005)
- Rosten, E., Drummond, T.W.: Machine learning for high-speed corner detection. In: Leonardis, A., Bischof, H., Pinz, A. (eds.) *ECCV 2006, Part I*. LNCS, vol. 3951, pp. 430–443. Springer, Heidelberg (2006)
- Lowe, D.: Distinctive image features from scale-invariant keypoints. *Int. J. of Computer Vision* 60(2), 91–110 (2004)
- Bay, H., Ess, A., Tuytelaars, T., Van Gool, L.: SURF: Speeded-up robust features. *Computer Vision and Image Understanding* 110(3), 346–359 (2008)
- Agrawal, M., Konolige, K., Blas, M.R.: CenSurE: Center surround extremas for realtime feature detection and matching. In: Forsyth, D., Torr, P., Zisserman, A. (eds.) *ECCV 2008, Part IV*. LNCS, vol. 5305, pp. 102–115. Springer, Heidelberg (2008)
- Bradski, G.: The OpenCV Library. *Dr. Dobb's Journal of Software Tools* (2000)

Cost Based Navigation for Autonomous Vacuum Cleaners

Khaled Al-Wahedi, Aya Darwish, and Basma Kodiah

The Petroleum Institute, Abu Dhabi, UAE

{kalwahedi,aytsalim,bankodiah}@pi.ac.ae

Abstract. In this paper, the *Autonomous Vacuum Cleaner Navigation Problem* is defined, formulated, and a solution is provided. In the design of an Autonomous Vacuum Cleaner (AVC), the most critical aspect is its navigation. An AVC is required to sweep the whole environment in order to clean it, and hence, this problem belongs to a category of problems known as *Coverage Problems*.

We propose a cost-based navigation algorithm that, at each stage, assigns costs to all the possible moves the AVC can make. These costs are based on certain navigation rules that are preprogrammed into the AVC. After all the rules are applied, the move with the lowest total cost is considered the winning move, and is the one selected by the AVC. The algorithm is tested via simulation, and the simulation results are presented.

1 Introduction

In a typical robot navigation problem, the robot is required to travel from point A to point B in some environment along the shortest collision free path, i.e. while avoiding obstacles. The autonomous vacuum cleaner navigation problem differs from this typical problem in two ways; the first is that the AVC is required to traverse the whole environment, which is typically a room; and the second is that the AVC is not supposed to avoid obstacles, instead it is required to get as close as possible to the obstacles, in order to clean around them. This AVC problem belongs to a large group of problems known as area coverage problems, or just coverage problems [1], with applications such as floor cleaning, floor painting, and landmine detection.

These differences are what makes the autonomous vacuum cleaner navigation problem an interesting and a unique navigation problem. Solutions exist for this problem, and commercial products based on these solutions also exist. However, these solutions, as we will see next, are far from perfect. What we propose in this paper is a new navigation algorithm that is efficient and at the same time comprehensive, as it is easily adaptable to handle more complex environments.

The performance of coverage algorithms in general can be expressed in terms of two important measures; namely the *effectiveness*, and the *efficiency* of coverage [2]. Effectiveness is proportional to the total area covered, and efficiency is inversely proportional to the total distance travelled.

Autonomous or robotic vacuum cleaners have been available commercially for at least ten years now. As far as their navigation is concerned, they rely mainly on one of two navigation schemes; behavior-based navigation, and mapping-based navigation.

1.1 Behavior-Based Navigation

In behavior-based navigation, the AVC navigates by mimicking the behaviors of animals searching for food. In other words, this scheme is comprised of a collection of simple behaviors that the AVC switches between as it moves around. These simple behaviors include spiral movement, zigzag movement, wall following, and changing direction with random angles (See. Fig.1.) It is expected that the collective effect of these behaviors is a thorough cleaning of most of the room.

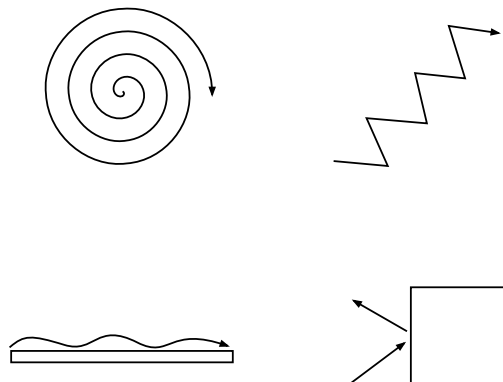


Fig. 1. Different behavior patterns that are used in behavior-based navigation

Behavior-based navigation is a simple algorithm to program, and it is easy to implement. It also does not require the use of sensors to sense the environment. However, it is random by nature, and it does not have a guaranteed performance. In other words, the AVC will take longer to clean the room, and it is not guaranteed to completely cover the whole room [3].

1.2 Mapping-Based Navigation

On the other hand, mapping-based navigation relies on building and continuously updating a map for the environment. The AVC needs to also localize itself in this map, and therefore techniques like *Simultaneous Localization And Mapping* or SLAM are used in mapping-based navigation.

Mapping-based navigation is a costly algorithm, as it relies on building a complete map of the room, and it is heavily sensor-dependent. In an ideal environment, it has a guaranteed level of performance, and it can cover the whole area of the room. Also, since it builds a map of the environment, it does not usually wander aimlessly in the room, although, that can happen sometimes [4].

1.3 SLAM

Simultaneous Localization And Mapping (SLAM) is the process of building a map of an unknown environment by a mobile robot, while at the same time navigating the environment using that map. What makes this process challenging is that the robot needs to build the map and localize itself in the map simultaneously. Accurate localization requires an accurate map, and an accurate map cannot be built without accurate localization. Figure 2 illustrates the different steps of the SLAM process.

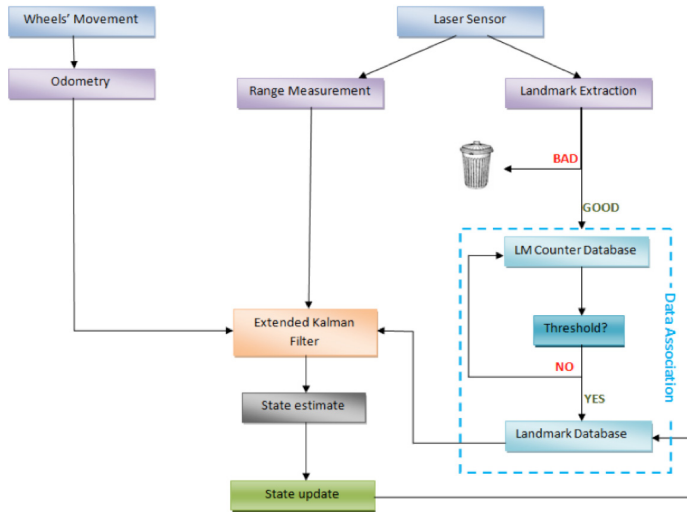


Fig. 2. The different components of the SLAM algorithm

2 Problem Statement

The Autonomous Vacuum Cleaner Navigation Problem can be stated as follows: Given a vacuum cleaner in an a priori unknown environment, design a navigation system that will satisfy two criteria simultaneously; maximize the total area cleaned, and minimize the total distance traveled.

The problem can be formulated as a multi-objective optimization problem as follows: Find $p \in \mathcal{P}$ that will maximize $F_1(p)$ and minimize $F_2(p)$, where \mathcal{P} is the infinite set of all possible paths p , $F_1(p)$ is the total area cleaned, and $F_2(p)$ is the total distance traveled.

3 The Proposed Navigation Algorithm

As a solution to the autonomous vacuum cleaner navigation problem, we propose a new algorithm that combines the simplicity of the behavior-based algorithm,

and the guaranteed performance of the mapping-based algorithm. The proposed algorithm is capable of completely covering the area of the room, without building and maintaining a map for it.

In our approach, at each step, the navigation problem is reduced to selecting one of four possible moves: forward, back, right, and left. Each of these four moves is assigned a cost according to a set of navigation rules. The move with the lowest cost after all the rules are applied will be selected as the next move.

3.1 Initial Setup

The room is modeled as a grid of $m \times n$ square cells. Each cell is marked “free” initially, unless it belongs to an obstacles, where it is marked “blocked” permanently. The AVC starts from a corner in the room, and it can only move in four directions. The AVC completely occupies a cell, and it can only sense the eight surrounding cells (See Fig. 3.)

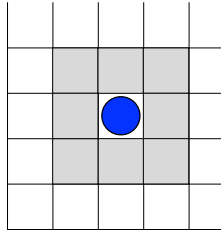


Fig. 3. The vacuum cleaner (the circle in the middle) is able to sense the eight surrounding cells only

3.2 The Cost Function

If at time t , the AVC is in location (x, y) , then it has to select one of four locations to move to at time $t + 1$. These four locations are $(x + 1, y)$, $(x - 1, y)$, $(x, y + 1)$, and $(x, y - 1)$. The selection process involves evaluating a cost function for each of the four locations. This cost function has the form

$$\sum_{i=1}^n C_{r_i}, \quad (1)$$

where C_{r_i} is the cost resulting from applying navigation rule r_i out of the n applicable rules.

3.3 The Navigation Modes

During navigation, the AVC switches between two navigation modes; the first is the *normal navigation mode*, which is the default mode that the AVC starts in; and the second is the *obstacle avoidance mode*, which the AVC switch to when

it encounters an obstacle. The AVC needs to apply different rules depending on which mode it is in.

The AVC starts in the normal navigation mode, and the selection of the next move is done according to the rules of this mode¹. When the AVC determines that its next move will make it hit an obstacle, it switches to the obstacle avoidance mode. In this mode, the objective of the AVC is to circle around the obstacle, and once that is done, the AVC returns back to the normal navigation mode (See. Fig. 4.)

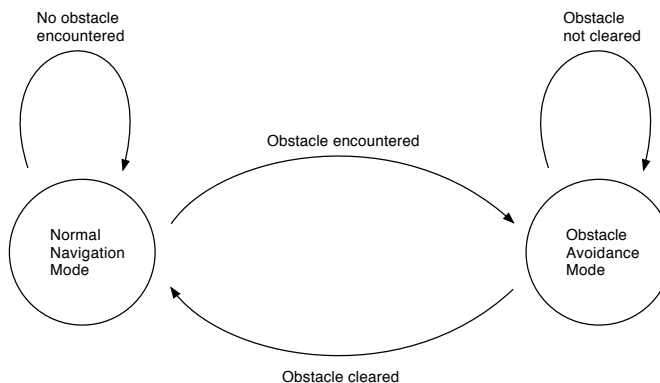


Fig. 4. The two navigation modes for the autonomous vacuum cleaners

3.4 The Navigation Rules

In the normal navigation mode, the following rules are applied:

1. *Move Straight*: This rule dictates to the AVC that it is always better to keep moving in a straight line. Therefore, this rule assigns a low cost to the move that makes the AVC continue straight. It assigns medium cost to both turning right and left, and it assigns high cost to going backward.
2. *Least Visited*: This rule dictates to the AVC that it is always better to visit the least visited cells first. Every time a cell is visited, its visitation counter is incremented, so the costs assigned to the four moves are proportional to the visitation counts of the cells they lead to. The free or non-cleaned cells have been visited zero times before, so they are preferable over the already visited cells. This rule is also useful in case the AVC is stuck in a certain spot, because eventually the number of visitations to that spot will increase to a point that will cause the AVC to prefer another route. Finally, this rule can be used to prohibit the AVC from going into obstacles. We can assign obstacles a very high visitation number from the beginning, therefore, the AVC will never select a move that will lead it to go into an obstacle.

¹ These rules and the rules of the other mode will be discussed in details next.

3. *Push Towards Wall:* This rule is not a straightforward rule, however it is important to ensure that no spots are left uncleaned in the room. Since the AVC starts at a corner in the room, the collective effect of all the navigation rules is a spiral movement that terminates in the center of the room. In case some spots were missed on an outer orbit as a result of moves necessitated by obstacle avoidance requirements, this rule ensures that the AVC is knocked back to that outer orbit in order to clean those spots. In such case, the rule assigns a low cost to the move in that direction, and a high cost to the other moves.

In the obstacle avoidance mode, the following rules are applied:

1. *Move Straight:* Same as in the normal navigation mode.
2. *Least Visited:* Same as in the normal navigation mode.
3. *Move Around Obstacles:* This rule prefers the move that will keep the obstacle on the same side of the AVC over other moves. When the AVC encounters an obstacle, it has to decide to go right or left. Once that is decided, then the obstacle becomes on one side of the AVC, and this rule ensures that it remains on that side as long as the AVC is in the obstacle avoidance mode. Thus, it effectively allows the AVC to circle around the obstacle. The rule assigns a low cost to the move that will keep the obstacle on that side, and a high cost to the other moves.

These navigation rules can be prioritized by fine-tuning the costs they assign to the moves. A high priority rule should reward and penalize moves more substantially than a low priority rule. A final remark here is that this rule-based navigation algorithm is adaptable. It can be complemented with additional rules, so that it is able to handle more complex environments.

3.5 Simulation Example

In order to prove the validity of the proposed algorithm, we present here a simulation example of a typical room consisting of a sofa and a table (See Fig. 5.).

In this example, the AVC effectively cleans the whole room, and it does so efficiently without visiting the same cell twice . The simulation results are shown in figure 6.

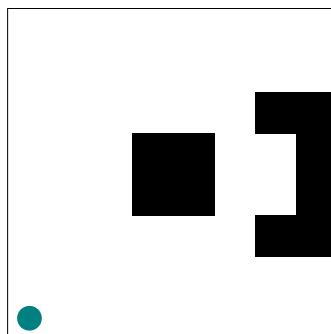


Fig. 5. A simulation example. The AVC is shown as a circle.

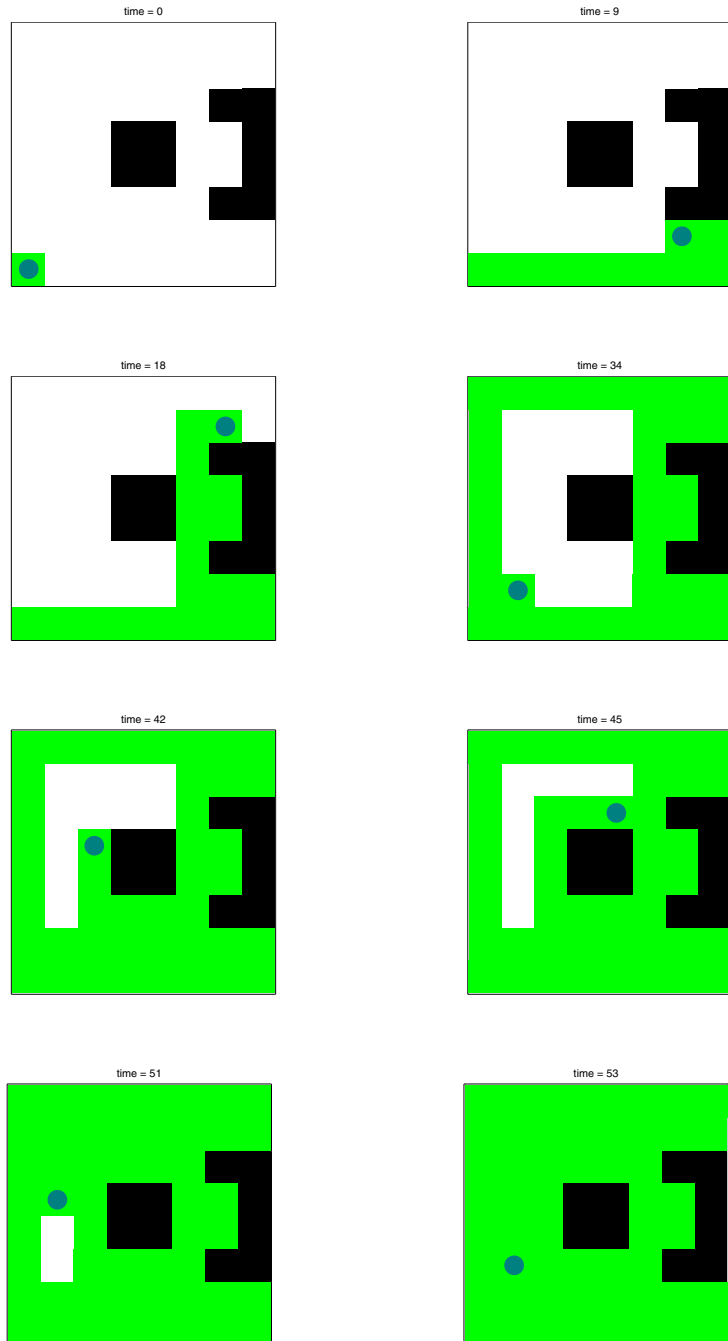


Fig. 6. The simulation results of the example in fig. 5 shown as snapshots. Each snapshot has a time stamp on the top.

4 Conclusion

In this paper we presented a novel algorithm for the autonomous vacuum cleaner navigation problem. Similar to the behavior-based algorithm, our algorithm relies on simple and basic rules to decide how to navigate, however it is not random in nature. Similar to the mapping-based algorithm, our algorithm is deterministic, and it guarantees a certain level of performance, however it is not an expensive algorithm, i.e. it does not need to build a map of the environment.

One of the main features of the algorithm is that it can deal with both static and dynamic obstacles, since it does not create a map of the environment (i.e. it does not store the locations of the obstacles.) Not creating a map for the environment makes sense, because environments like the living room, for example, typically change often. This dynamic nature is the result of the frequent existence of moving obstacles (people, pets, etc) and the not so frequent relocation of furniture.

The work presented here is a work in progress. The algorithm is not perfect, and it is still not able to completely clean environments with high complexity. However, as we already mentioned, the algorithm is adaptable, and it can be complemented with additional navigation rules. Furthermore, additional research is also needed in prioritizing the rules as we briefly mentioned before.

References

1. Choset, H.: Coverage for robotics – A survey of recent results. *Annals of Mathematics and Artificial Intelligence* 31, 113–126 (2001)
2. Wong, S.: Performance Metrics for Robot Coverage Tasks. In: Proc. 2002 Australasian Conference on Robotics and Automation, Auckland, New Zealand (November 2002)
3. <http://www.youtube.com/watch?v=8DuKBtv-La4>
4. <http://www.youtube.com/watch?v=H0o8s-6f5S8>
5. Sung, J.-Y., et al.: Housewives or Technophiles?: Understanding Domestic Robot Owners. In: HRI 2008, Amsterdam, Netherlands (March 2008)
6. Brooks, R.: The relationship between matter and life. *Nature* 409(6818), 409–411 (2001)
7. Thrun, S.: Robotic Mapping: A Survey. School of Computer Science, Carnegie Mellon University (2002)
8. Csorba, M.: Simultaneous Localization and Map Building. PhD thesis, University of Oxford (1997)
9. Palleja, T., et al.: Modeling floor-cleaning coverage performances of some domestic mobile robots in a reduced scenario. *Robotics and Autonomous Systems* 58(1), 37–45 (2010)
10. Durrant-Whyte, H., Bailey, T.: Simultaneous localization and mapping: part I. *IEEE Robotics & Automation Magazine* 13(2), 99–110 (2006)
11. Bailey, T., Durrant-Whyte, H.: Simultaneous localization and mapping (SLAM): part II. *IEEE Robotics & Automation Magazine* 13(3), 108–117 (2006)

Image-Based ICP Algorithm for Visual Odometry Using a RGB-D Sensor in a Dynamic Environment

Deok-Hwa Kim and Jong-Hwan Kim

Department of Robotics Program, KAIST,
291 Daehak-ro, Yuseong-gu, Daejeon 305-701, Republic of Korea
{dhkim,johkim}@rit.kaist.ac.kr

Abstract. This paper proposes a novel approach to calculate visual odometry using Microsoft Kinect incorporating depth information into RGB color information to generate 3D feature points based on speed up robust features (SURF) descriptor. In particular, the generated 3D feature points are used for calculating the iterative closest point (ICP) algorithm between successive images from the sensor. The ICP algorithm works based on image information of features differently from previous approaches. This paper suggests one of the modified versions for a state-of-the-art implementation of the ICP algorithm. Such an approach makes accurate calculation of the rigid body transformation matrix for visual odometry in a dynamic environment. From this calculation step, dynamically moving features can be separated into outliers. Then, the outliers are filtered with random sample consensus (RANSAC) algorithm for accurate calculation of the rigid body transformation matrix. The experiments demonstrate that visual odometry is successfully obtained using the proposed algorithm in a dynamic environment.

Keywords: Visual Odometry, RGB-D Sensor, Iterative Closest Point Algorithm, Dynamic Environments, SLAM.

1 Introduction

Mobile robots containing wheels use their encoder values for odometry information. However, aerial vehicles or humanoid robots cannot directly use their encoder values for odometry information. Because of this constraint, visual odometry has become more important than another sensor values in their fields. Actually, the robotics and computer vision communities have developed many techniques and algorithm for 3D mapping and visual odometry using range scanner [5, 6], stereo cameras [3], monocular cameras [4, 7] and RGB-D sensors [1, 2, 10].

Most visual odometry systems require the spatial alignment of successive camera frames. To deal with the alignment problem, the ICP algorithm [11] has been used. This algorithm is to minimize the difference between the two sets of the points. It is often employed to reconstruct 2D or 3D surfaces from different scans.

If there are some unreliable points in a set of features, the systems using those points will be unstable. To solve this problem, RANSAC algorithm, which is very simple and useful algorithm, has been used widely [12].

There have been many researches on visual odometry using a RGB-D sensor based on the ICP and RANSAC algorithms. However, dynamic environments have not been considered in those researches. Considering dynamic environment applications, this paper proposes a novel approach to calculate visual odometry with the modified ICP algorithm based on image information.

2 Visual Odometry System Using a RGB-D Sensor

Many researchers proposed visual odometry systems using a RGB-D sensor. Those visual odometry systems follow similar algorithm [1, 10]. This chapter introduces the algorithm for getting the visual odometry information. Visual odometry information can be obtained by five procedures. First of all, it needs to get feature points. Visual odometry system works based on rotation-invariant feature points. For the feature detection, SURF algorithm [8] is employed. SURF algorithm have many parallel processing computation, so it can be applied to graphic processing unit (GPU) processing for boosting speed. From the SURF algorithm, the feature information, which contains feature position, feature scale, etc, can be obtained. After getting features, feature matching algorithm is computed between prior frame and current frame. The next step to get odometry information is 3D reconstruction using the camera intrinsic parameters (focal lengths, principal points) and the depth information. It can be done from the proportional equation between the focal length and the depth information, easily. After the step, the inliers detection has to be computed by re-projection using the homography between the prior image plane and the current image plane. The homography is found by RANSAC algorithm. From this step, matched features can be refined.



Fig. 1. The Image matching result with SURF GPU algorithm

Using the matched features, the rigid body transformation matrix [9] is calculated. It is computed by singular value decomposition (SVD) method for decomposing the cross-dispersion matrix $[C]$. The cross-dispersion matrix is computed from

$$[C] = \frac{1}{n} \sum_{i=1}^n (y_i - \bar{y})(x_i - \bar{x})^T,$$

where x_i is the position of the i -th point measured in the prior image; y_i the position of the i -th point measured in the current image; \bar{x} the mean position of the prior image; \bar{y} the mean position of the current image. It can be decomposed to $[U]$, $[W]$, $[V]$ by SVD where $[U]$ and $[V]$ are the orthogonal matrices, and $[W]$ is the diagonal matrix which contains the singular values of matrix $[C]$. For calculating the rigid body transformation matrix, rotation matrix is computed from

$$[R] = [U][V]^T.$$

And translation vector is estimated by

$$\mathbf{t} = \bar{y} - [R]\bar{x}.$$

Through the combination of $[R]$ matrix and t vector, the rigid body transformation matrix can be computed. Based on this matrix, estimation for odometry information is conducted.

For more accurate estimation of the transformation matrix, RANSAC algorithm is applied. The result from this procedure is used for initial rigid body transformation matrix. However, there still remain errors in this transformation matrix. More compensation algorithm is needed.

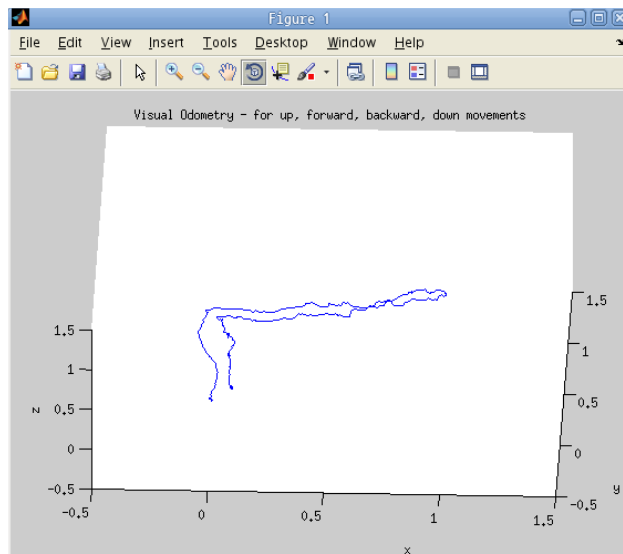


Fig. 2. The odometry information from up, forward, backward, down movements

For more compensation of rigid body motion, this paper uses ICP algorithm. This algorithm has been used for 2D or 3D reconstruction in the vision field. It consists of 3 procedures. Firstly, finding closest points from feature sets is required. KD-tree searching algorithm is used for searching closest points. In this paper, this procedure is modified to use the image information and it is discussed in detail in the next

section. And next procedure is finding the rigid body transformation matrix from the closest point sets. To find the matrix, the SVD method is applied. After then, update procedure is computed. This update step can make new closest sets of feature. From the result of iterative searching for transformation matrix, odometry information gets more precise.

Those overall procedures produce visual odometry information. Figure 2 shows the result from the continuous up, forward, backward and down movements for visual odometry. In the next section, accurate visual odometry algorithm in a dynamic environment (consisting of static and dynamic objects) is proposed.

3 The Image-Based ICP Algorithm in a Dynamic Environment

In a dynamic environment, visual odometry cannot be correctly computed because dynamic movements affect unfit matching in a part of getting closest sets in the ICP algorithm. In this section, the ICP algorithm based on images is proposed for the dynamic environment applications.

3.1 The Image-Based ICP Algorithm

The ICP algorithm based on images is different from original one in detecting the closest sets of features. At a part of finding closest sets in ICP algorithm, an image information with the 3D position information of the feature is combined. This image information can contribute to the precise detection of matched features.

Algorithm 1. The image based ICP

```

 $T \leftarrow T_0$ 

for  $i=0$  to  $\text{max\_iteration}$  do

     $M \leftarrow \text{FindClosestSetPoint}(T \times X, Y, \Psi_x, \Psi_y);$ 
     $T \leftarrow \text{GetNewTransformationMatrixUsingRansac}(M, T \times X);$ 
     $\epsilon \leftarrow \text{ComputeError}(Y, T \times X);$ 

    If ( $\epsilon < \epsilon_0$ ) break;

end
```

If the features are matched more precisely, they can be divided into inliers and outliers. Dynamic obstacle features are classified into the outliers because those features have different movements from the others.

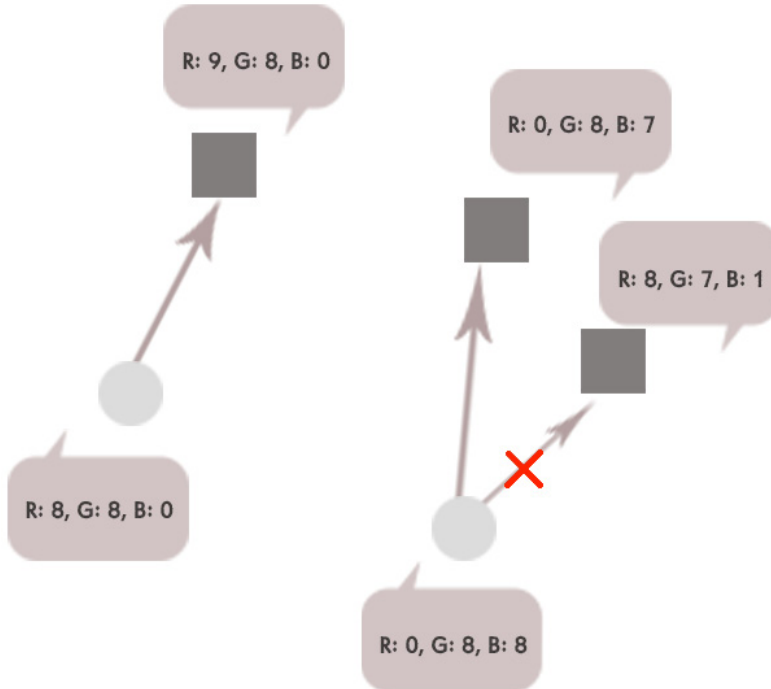


Fig. 3. Diagram of finding closest set of feature using the proposed algorithm

Algorithm 1 shows the image-based ICP algorithm. “*FindClosestSetPoint*” function has two more parameters Ψ_x, Ψ_y , where Ψ_x is a set of RGB for the prior image features; Ψ_y is a set of RGB for the current image features. This function uses KD-tree searching algorithm which is faster than raw searching algorithm for getting the closest sets. After then, solving the rigid body transformation matrix using RANSAC algorithm follows.

Figure 3 shows the diagram of finding closest set of feature using the image-based ICP algorithm. Each finding procedure considers euclidean distance but also normalized RGB distance.

3.2 Benefits of the Image Based ICP Algorithm

This paper proposes a novel visual odometry algorithm to be used in a dynamic environment. It is very robust to dynamic obstacles. Therefore, it can be applied to the real life for computing visual odometry. For example, aerial vehicles are very hard to get odometry information from their motors. In that field, this visual odometry algorithm using RGB-D sensor can be applied.

4 Experiments

The proposed algorithm was tested with RGB-D sensor as known as the Kinect sensor. Experimental environments were Gentoo OS, Intel i5 3.3GHz Quad-core

processor, NVIDIA GTX 560 GPU and 6GB RAM. Average computation time was 152.0 ms per frame. The experiments were carried out in a static environment and in a dynamic environment.

4.1 The Experiment Result in a Static Environment

Experiments in a static environment were conducted in a room where there were no movements excluding the Kinect sensor and experimenter. Experimenter grabbing the Kinect sensor moved it upward, forward, backward, and downward.

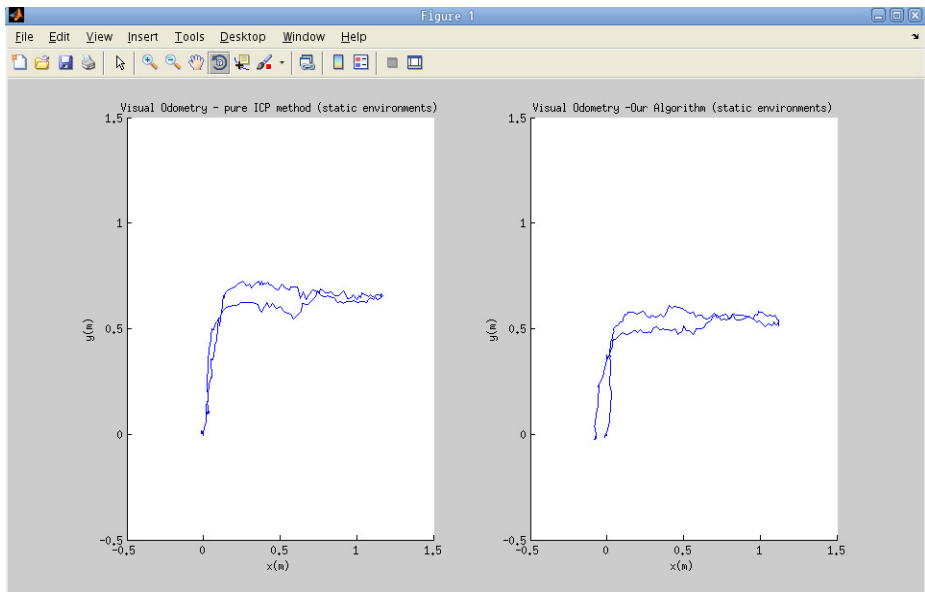


Fig. 4. The experiment result in a static environment for up, forward and return movements: (left) using the conventional ICP algorithm; (right) using the image-based ICP algorithm

Figure 4 is a result of experiment in a static environment. Left graph is a result of visual odometry using the conventional ICP algorithm. Right graph is a result of visual odometry using the image-based ICP algorithm. Both algorithms have showed similar results in a static environment. From this result, the image-based ICP algorithm also can be applied to calculate visual odometry in a static environment.

4.2 The Experiment Result in a Dynamic Environment

For the realization of a dynamic environment, experimenter roamed around a room, as Fig. 5 shows. In this environment, calculating the visual odometry was performed using a fixed Kinect sensor.

Figure 6 shows a result of the experiment with the proposed visual odometry algorithm compared with the conventional ICP.

The left graph is a result of the conventional ICP algorithm. It shows a result of unstable computation for the visual odometry. This result came from no inliers detection in the ICP algorithm. The outliers which came from roaming people were not filtered to solve rigid body transformation matrix. However, the right graph shows a very stable computing result for the visual odometry in a dynamic environment with the fixed Kinect. The proposed algorithm has additional filtering steps, such as the closest set detection based on images and outlier suppression using the RANSAC algorithm, in the ICP algorithm. As a result, the visual odometry using the RGB-D sensor by the proposed algorithm can be more accurate than the conventional ICP algorithm in a dynamic environment.



Fig. 5. A Dynamic environment

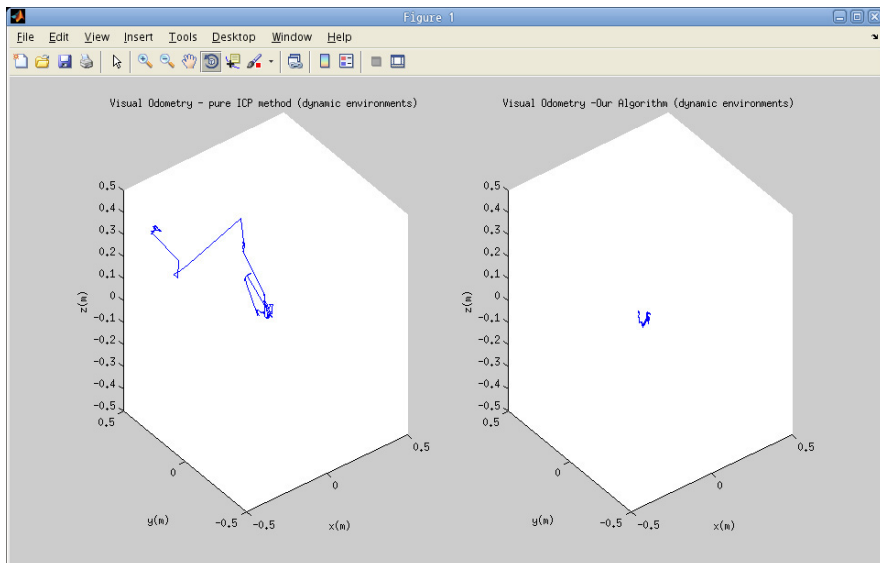


Fig. 6. The experiment result in a dynamic environment with a fixed RGB-D camera: (left) using the conventional ICP algorithm; (right) using the image-based ICP algorithm

5 Conclusion

This paper proposed the image-based ICP algorithm for calculating visual odometry. It was demonstrated that the proposed algorithm was very robust to dynamic obstacles. In this algorithm, RGB information of feature point was used for finding the closest set points in the ICP algorithm. After finding the closest set points, RANSAC algorithm was computed for solving the rigid body transformation matrix with eliminating outlier effect of dynamic object features. Such overall procedures contributed to promote accurate calculation of odometry information in a dynamic environment. However, the proposed algorithm still has a problem in computation

time caused by RANSAC algorithm. Therefore, we need to solve the real-time problem considering the case of fast movements of the RGB-D sensor. Furthermore, the SLAM system has to be considered for our further works using the proposed visual odometry algorithm.

Acknowledgements. This research was supported by the MKE (The Ministry of Knowledge Economy), Korea, under the Human Resources Development Program for Convergence Robot Specialists support program supervised by the NIPA (National IT Industry Promotion Agency) (NIPA-2012-H1502-12-1002)

References

1. Huang, A.S., Bachrach, A., Henry, P., Krainin, M., Maturana, D., Fox, D., Roy, N.: Visual Odometry and Mapping for Autonomous Flight Using an RGB-D Camera. Paper Presented at International Symposium on Robotics Research (ISRR), Flagstaff, AZ, USA (August 2011)
2. Steinbrucker, F., Sturm, J., Cremers, D.: Real-Time Visual Odometry from Dense RGB-D Images. Paper Presented at IEEE International Conference on Computer Vision Workshops, Barcelona, Spain, pp. 719-722 (November 2011)
3. Nourani-Vatani, N., Roberts, J., Srinivasan, M.V.: IMU aided 3D visual odometry for car-like vehicles. Paper Presented at 10th Australasian Conference on Robotics & Automation, Canberra, ACT, Australia, pp. 1-8 (December 2008)
4. Kneip, L., Chli, M., Siegwart, R.: Robust Real-Time Visual Odometry with a Single Camera and an IMU. Paper Presented at The 22nd British Machine Vision Conference, University of Dundee, pp. 16.1-16.11 (September 2011)
5. Baglietto, M., Sgorbissa, A., Verda, D., Zaccaria, R.: Human Navigation and Mapping with a 6DOF IMU and a laser scanner. Paper Presented at Robotics and Autonomous Systems 59, 1060-1069 (2011), doi:10.1016/j.robot.2011.08.005
6. Hornung, A., Wurm, K.M., Bennewitz, M.: Humannoid Robot Localization in Complex Indoor Environments. Paper Presented at IEEE/RSJ International Conference on Intelligent Robots and Systems, Taipei, Taiwan, pp. 1690-1695 (October 2010)
7. Davison, A.J., Reid, I.L., Molton, N.D., Stasse, O.: MonoSLAM: Real-Time Single Camera SLAM. Paper Presented at IEEE Transactions On Pattern Analysis And Machine Intelligence 29(6), 1052-1067 (2007), doi:10.1109/TPAMI.2007.1049
8. Bay, H., Ess, A., Tuytelaars, T., Van Gool, L.: Speeded-Up Robust Features (SURF). Paper Presented at Computer Vision and Image Understanding 110(3), 346-359 (2008), doi:10.1016/j.cviu.2007.09.014
9. Challis, J.H.: A Procedure for determining rigid body transformation parameters. Paper Presented at Journal of Biomechanics 28(6), 733-737 (1994), doi:10.1016/0021-9290(94)00116-L
10. Henry, P., Krainin, M., Herbst, E., Ren, X., Fox, D.: RGB-D Mapping: Using Depth Cameras for Dense 3D Modeling of Indoor Environments. Paper Presented at International Symposium on Experimental Robotics, Delhi, India (December 2010)
11. Segal, A.V., Haehnel, D., Thrun, S.: Generalized-ICP. Paper Presented at Robotics: Science and Systems, Seattle, USA (June 2009)
12. Fischler, M.A., Bolles, R.C.: Random sample consensus: a paradigm for model fitting with applications to image analysis and automated cartography. Paper Presented at Communications of the ACM 24(6), 381-395 (1981), doi:10.1145/358669.358.692

Hybrid Indoor Location Tracking for Pedestrian Using a Smartphone

Seon-Woo Lee, Philhwan Jung, and Seong-Ho Song

Dept. of Electronic Engineering, Hallym University
1 Hallymdaehak-gil, Chuncheon 200-702, Korea
{senu, philhwani, ssh}@hallym.ac.kr

Abstract. In this paper, a hybrid indoor location tracking method is proposed for pedestrian using a set of inertial sensors embedded in smartphones. The method is composed of two localization techniques; one is dead-reckoning using inertial sensors and the other is Wi-Fi fingerprinting. The proposed method uses the concept of combined map of topological and geometric map. Introducing user-select points of interest in his/her workplace we can reduce the cost of building a radio map for Wi-Fi fingerprinting method. The dead-reckoning method can track incremental movements of user by detecting steps. Based on acceleration signals we proposed a method to estimate the orientation and position of the phone in a pocket of pants. Experiments verified the performance of the method.

Keywords: indoor location tracking, dead-reckoning, Wi-Fi fingerprinting, smartphone, hybrid method.

1 Introduction

Smartphones have recently been becoming the closest mobile device that users keep close by and use the most frequently throughout the day. In addition, smartphones have various sensors and communication devices. That means that a smartphone is an excellent and convenient device to collect and recognize the user's context that can provide useful context-aware services. Among numerous contexts the location information is a core context. Tons of location-based services therefore have been developed. The GPS is the best solution for outdoor environments, however it is not available in indoor environments. There has been a fair amount of studies recognizing the location of a mobile device in indoor environments [1]. Especially there have been some works that used smartphones as sensing platforms [2, 3]. In [2], the authors have developed a smartphone-based indoor positioning method by using inertial sensors embedded in the phone. Using a set of inertial sensors a mobile device can track a pedestrian via dead-reckoning method. Some works [4, 5] used shoe-mounted sensors and another [6] used body-mounted sensors. Wi-Fi based localization method [7] using smartphones could be a promising and convenient solution for indoor positioning system, because Wi-Fi is becoming more and more ubiquitous and all smartphones have an Wi-Fi device.

In daily life, many people usually move between certain places in their working area. We focused that the places are limited generally, so the number of such places is not many although user moves around all day long. We call these places as *point of interest* (abbreviated as PoI). Almost paths user moves in workplace can be segmented a series of paths from a start PoI to an end one. If we can recognize where user is among the pre-determined PoIs and also transition between PoIs, then it is possible to provide useful context-aware and location-based services from tracking results based on topological and symbolic map.

In our work, Wi-Fi fingerprinting technique was selected to detect such PoIs because the infra structure of Wi-Fi is usually built almost workplaces and indoor environments. The Wi-Fi fingerprinting technique requires a signal strength map at each reachable calibration place *a priori*. The map building *a priori* is the most costly task. In our scheme, the PoIs are selected by user himself, so it could be customized and its number is not many. The user easily can collect a radio signal at the PoIs and build his/her own map.

We want to detect user's movements more specifically when the user walks between two PoIs, so we added dead-reckoning localization technique by using inertial sensors. Like other inertial navigation systems a smartphone can detect walk-steps using accelerometer and update the position estimate forward by the step length in the direction determined by a geomagnetic field sensor. This means dead-reckoning approach is based on geometric map.

Consequently, we developed a hybrid method to track a pedestrian by using a smartphone. The suggested method uses two positioning techniques; one is Wi-Fi fingerprinting method and the other is dead-reckoning method. We claim the proposed method to track a user based on a combined map of both geometric and topologic maps. This means that our method can provide tracking information such as "now the user is walking to a PoI B departs from a PoI A, and the location of the user is a certain point on a path from the PoI A to the PoI B, which is represented by 2-dimensional coordinate data". When the user arrives at the PoI B, then the method confirms the current location of the user is at PoI B by Wi-Fi fingerprinting technique. Energy-efficient management of sensors [8] is very important and essential requirements for system-level applications of smartphones. To do this task, we developed simple sensor management method based on the state of the device. We evaluated the performance of the proposed method via experiments by implementing on a smartphone.

2 Hybrid Tracking Method

2.1 Overview

We used a 'Google Nexus One' of HTC company. The phone has inertial sensors such as 3-axis accelerometer (BMA150, Bosch co.) and 3-axis geomagnetic field sensor (AK8973, Asahi Kasei co.). It also has a light sensor and proximity sensor like other smartphones. The directions of axes of sensors are as follows: x-axis is from left to right of the phone, y-axis is from bottom to up, and z-axis is from phone to sky.

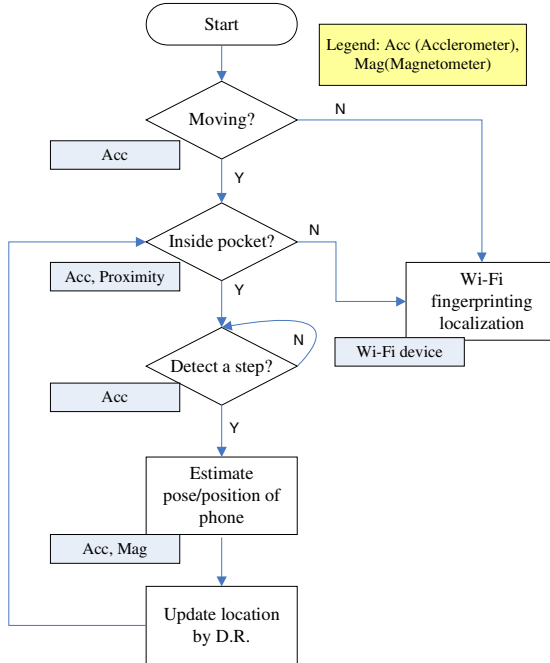


Fig. 1. Flowchart of the proposed tracking method

There are many situations in carrying a smartphone by people. Someone puts it into a pocket of pants or a coat, various types of bags, or keeps it in hand while moving. We are developing a method to estimate the possession style (i.e. position on user's body) of the smartphone while moving. In this work, we assume that user possesses a smartphone in a pocket of pants. There are a couple of reasons to determine the possession style. First one is that many people carry a smartphone in a pocket of pants regardless of ages or sex. Second is that step detection is easier from the sensor data at the position. We also assume that a phone is positioned vertically.

The overall operation of the proposed tracking method is shown in Figure 1 as a flow chart. In the Figure, the left lower boxes represent the sensors used to do the data processing. We used a simple sensor management scheme for energy-efficient operation. Our scheme is simple but useful. We define two types of states; *staying* and *moving*. The *staying* means that user does not move or the device is on a desk. The *moving* means user moves with his/her smartphone. By using an accelerometer we can estimate the state, and then we turn sensors on or off based on the estimated state. When the device is in *moving* state, it starts dead-reckoning technique. In the case of *staying*, the device starts a Wi-Fi fingerprinting processing.

In *moving* state, we can estimate whether the device is in a pocket or not by using the proximity sensor and accelerometer. Then we compute a standard deviation of three acceleration signals to decide whether the user walks or not. If user starts to walk, then the system tries to detect a step by a method which will be explained in next section. If a step is detected, the current location is updated with measured direction of movement by using a geomagnetic field sensor.

When the user stays, then the device turns a Wi-Fi device on and scan radio signals from access points(AP) to determine the current place among the PoIs by comparing the current radio fingerprint and the pre-built PoIs' fingerprints.

2.2 Step Detection

In this subsection, we describe a method to detect a step by using an accelerometer. As explained previously, the position of a smartphone is assumed at a pocket of pants, and the direction of phone is fixed. We will explain a method in detail to estimate the pose of phone in next section.

To detect a step we firstly processed the raw acceleration signals to eliminate the gravity component by using a first-order high pass filter. And then we compute a signal (called energy signal) from three acceleration signals as follows:

$$E(k) = \sqrt{x(k)^2 + y(k)^2 + z(k)^2} \quad (1)$$

where the $x(k)$, $y(k)$, and $z(k)$ represents three filtered acceleration signals along 3-axes. The Android 2.3 platform (a.k.a Gingerbread) does not provide a fixed sampling period and it only provides four kinds of delay functions. Among them we selected SENSORY_DELAY_GAME type for reading sensor signals. The official document describes its period is about 20ms, but we could find it is about 60ms from experiments. So we consider the sampling frequency is around 16.7Hz.

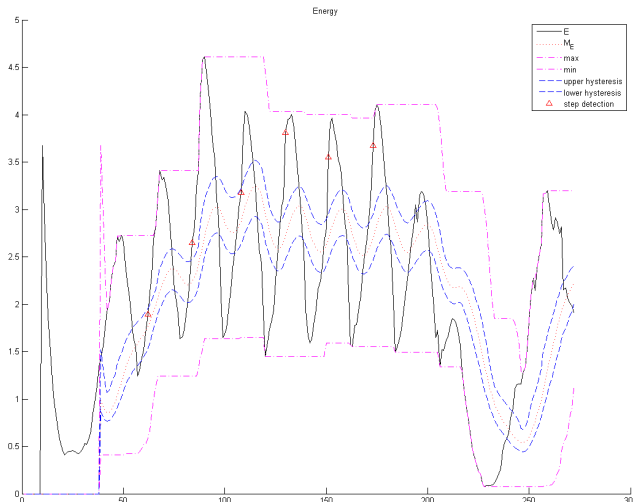


Fig. 2. Typical trajectories of computed various signals and detection of new step

Figure 2 shows the typical trajectories of the energy signal, its mean and upper/lower threshold values when a user walks. In Figure 2, we can easily find gait cycles. To detect a step we first compute a mean of 10 samples of the energy signal at every sampling time, i.e. $\bar{E}(k) = \sum_{i=0}^9 E(k-i)$. We also compute again a mean of

the 30 averaged values, i.e., $M_E(k) = \sum_{i=0}^{29} \bar{E}(k-i)$. Using these values we test the following condition to determine each new step:

$$\bar{E}(k) > M_E(k) + H_U, \text{ where } H_U = 0.2(\max \bar{E}(k) - M_E(k)) \quad (2)$$

Here the H_U is an upper hysteresis value that is computed as 20% of the difference between a maximum value of averaged energy signal and the mean of averaged energy signal. Figure 3 shows these computed values and when the device detects a new step with red triangle symbol. Using this simple comparison method based on a threshold we could obtain good detection performance for many people. The performance will be shown in next section.

2.3 Estimation of the Phone's Orientation and Position

It is the most important to detect the direction of movements correctly in dead-reckoning approach for pedestrian, because small errors on direction could make big location error. This problem is an inherent characteristic of all dead-reckoning based localization technique. Many dead-reckoning based localization methods require that sensing units are attached on a certain position of user's body and also the system knows the direction of axes of inertial sensors, so that the system could measure the direction of movement.

However it is not impractical condition in the case of using a smartphone. So we propose a method to estimate the accurate orientation of the phone in a pocket of pants. Even though we assumed that the phone's orientation is portrait, we should know the relative orientation of the device with respect to body. First we easily determine whether the orientation of trackball is up or down by using a y-axis acceleration signal.

It is however not easy to discriminate whether the direction of LCD is inward or outward with respect to body. From experiments we could find that the value of upward component of z-acceleration, u_z in a rotation matrix R is different respect to the direction of LCD. Figure 3 shows the typical trajectory of the transformed

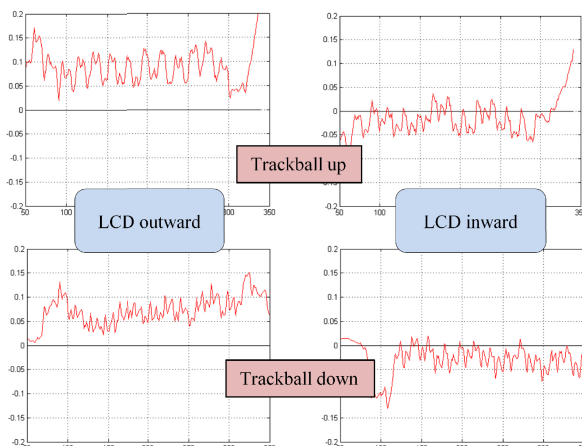


Fig. 3. Typical trajectories of upward component of z-acceleration

acceleration signal u_z while user walks. The left two graphs represent its direction is outward and the right ones show inward. The averaged value of u_z is positive for the outward case, on the contrary the values are negative for the inward case. The rotation matrix R is a transformation matrix from local (device) coordinate system to world coordinate system as shown in equation (3). The world coordinate system has three axes; north, east and upward (toward sky) directions. We can easily obtain the rotation matrix from a standard API (*getRotationMatrix*) of Android platform.

$$R = \begin{bmatrix} e_x & e_y & e_z \\ n_x & n_y & n_z \\ u_x & u_y & u_z \end{bmatrix} \quad (3)$$

Under the assumption of orientation of a phone in a pocket, the phone could move around in the pocket while user walks. From our experiments we could assume that the phone would be positioned at two places in the pocket, one is front place and the other is side place. Movement of the device could make wrong heading measurement. So we propose a method to estimate the position of a phone among two places. The developed method uses a ratio of variances of x and z-axis acceleration as a following equation:

$$r_{xz} = \sigma_z^2(k)/\sigma_x^2(k) \quad (3)$$

where $\sigma_{x,z}^2$ is a variance of 20 samples of high-pass filtered x/z-axis accelerations. As shown in Figure 4, when the device is at front place of a pocket, then the ratio value is smaller than the case of the device at side place. We introduced a threshold value to discriminate the position.

As described in Figure 1, when the system detects a step, then it tries to estimate the orientation and position inside a pocket. Based on the estimation for orientation and position of the phone, we determine the heading direction of user's movement by using a geomagnetic field sensor. In our work we introduced a quantization technique for the heading sensor signal to overcome a problem derived from heading fluctuations due to device movements. In our experiments, the $\pi/2$ level was used for quantization. By using an average step length and the heading measurement, the dead-reckoning method can compute new location information as 2-dimensional coordinate values.

2.4 PoI Recognition by Wi-Fi Fingerprinting

When the current state is *staying*, the system turns the Wi-Fi device on, and tries to estimate the current location by using pre-built radio map. If the system determines the location among the PoIs, then the current location is changed to the pre-determined position of the PoI. Detection of a PoI means that the system can recognize a starting point of user movements. Dead-reckoning needs to know where a starting point is. In addition the detection of PoI can be used to correct the location information of user. It means that the accumulated error evolved by dead-reckoning could be eliminated. If we select more PoIs in an workplace, then it is possible to correct the position error more frequently.

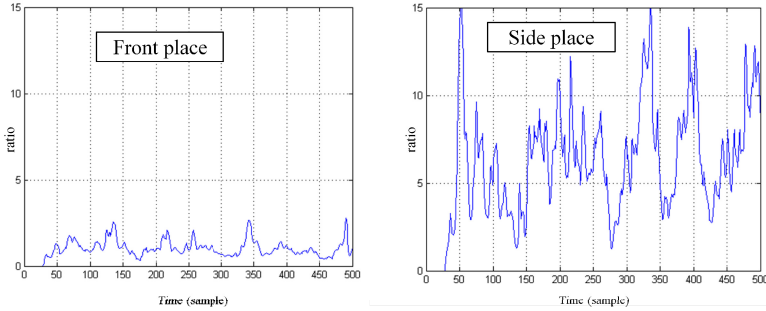


Fig. 4. Trajectories of the ratio of x/z-acceleration variances

We developed a simple application program of Android platform to build a radio map for user-select PoIs. At the PoIs, user just executes the application, then it collects all radio signals from seeable access points, computes statistics data for each AP, and store the data into a database automatically for two minutes. The data for an AP include PoI ID, date and time of measurement, BSSID, and the mean, standard deviation, minimum, maximum and median values of RSSI. The stored data in the database could be a topological radio map as:

$$(\text{PoI}_i, \{\overrightarrow{SS_j}, j \in N_i\}) \quad (4)$$

where the $\overrightarrow{SS_j}$ is the radio fingerprint having statistical data of signal strength for the j -th AP in the place of i -th PoI (PoI_i), the N_i is the number of reachable APs at the PoI_i .

To determine the PoI for a given radio fingerprint, we try to find a PoI satisfying that there exist more than 3 APs which satisfy the small error between the mean of RSSI of each AP as follows:

$$|m_j^{\text{current}} - m_j^i| < Th_{\text{wifi}} \cdot \delta_j^i, \text{ where } (m_j^i, \delta_j^i) \in \overrightarrow{SS_j}, j \in N_i \quad (5)$$

where the (m_j^i, δ_j^i) is a mean and standard deviation value of the $\overrightarrow{SS_j}$ vector, respectively. We used only to compare the mean values of signal strength. This method showed good performance despite its simplicity. In addition experiments showed that we can adjust the size of the PoIs by adjusting the threshold value.

3 Experiments

3.1 Step Detection Performance

To evaluate the performance of step detection method, we let 15 subjects walk for 30 meters along a straight path. The subjects are 4 female and 11 males who are between 21 to 33 years old. We asked they walk in slow, normal, and fast speed. The average numbers of steps for three speeds are 19, 21 and 23 steps. The result showed that the average stride length is 1.4m, and the average pace (speed) is 1.08m/s.

The experimental results are shown in Table 1. Total number of steps for normal, slow and fast walking are 304, 39, and 51, respectively. The total average detection rate is 96%.

Table 1. Detection rate of steps for three speeds

Detection rate	Slow	Normal	Fast
Mean	96%	96%	95%
Minimum	86%	75%	83%

3.2 Wi-Fi Fingerprinting Localization Performance

We selected 5 PoIs for our experiments in the same floor of one building. For experiments we have built a radio map for the PoIs, and then executed the localization program at the PoI while we moved the device a little in a circular region. The results told us that the radius of recognizable region of a PoI is around 0.6m with the condition of $\text{Th}_{\text{wifi}} = 6$.

The recognition performance of the proposed Wi-Fi fingerprinting method is listed in Table 2. The total average recognition ratio is 87.4%. From experiments we could find the movements of the device would make failures more easily than other effects such as the phone's direction and/or existence of person/objects. That is another reason to introduce the switching method depending on the state of the phone.

Table 2. Performance of Wi-Fi fingerprinting method

PoI	Success	Fail	Ratio (%)
1	92	8	92
2	90	10	90
3	89	11	89
4	80	20	80
5	86	14	86
sum	437	63	87.4

3.3 Tracking Performance

Figure 5 shows the captured screens of the developed tracking application and the explaining boxes on the screens. As an example, Figure 5 (a) shows the result of the proposed tracking method when a user walked from PoI#1 (his seat) to PoI#3 via PoI#2, and then returned to his seat (PoI#1). Before starting to walk, the system knows where the user is currently at PoI#1 by using Wi-Fi fingerprinting method. While he walks to PoI#2, the dead-reckoning method tracks the movement by detecting steps and his heading as shown by a series of triangle shaped points in the figures.

When the state is changed to the staying, then Wi-Fi fingerprinting method tries to find the PoI where he is. If the system could determine a PoI, then the location is corrected to the pre-determined position of the detected PoI, as shown in both plots by a red circle and a red arrow. This correction has an important role to eliminate the accumulated error by dead-reckoning method, so as to increase the accuracy of the tracked position. The longer path tracking by dead-reckoning could make bigger error. We can find this drawback also in our experimental results. The error of final position of the path2 is bigger than that of the path1 in Figure 5 (a).

Figure 5 (b) shows the tracking result when a user walked to PoI#4 from PoI#1, and then returned to his seat again. The result shows the tracking capability of the proposed method could enable the applicability for many kinds of location-based services such as personal navigation system for complex huge buildings.

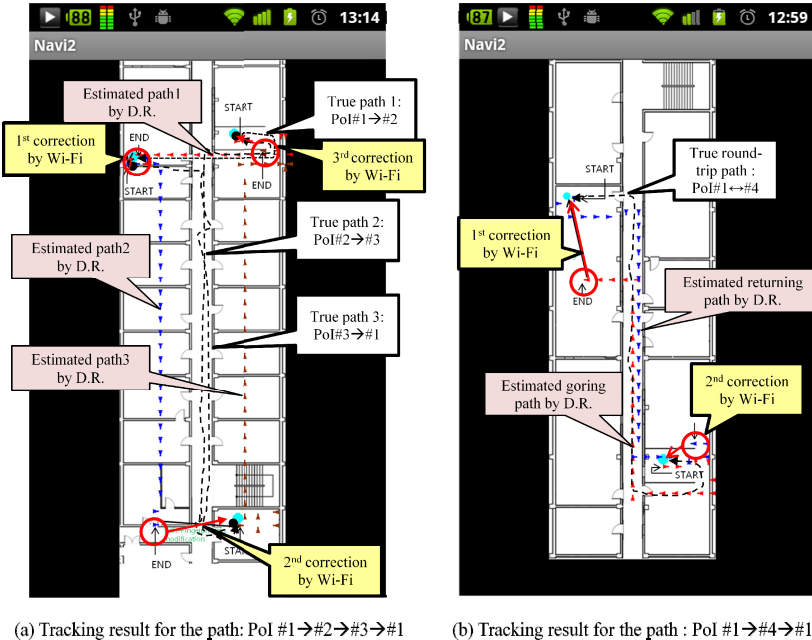


Fig. 5. The tracking result of the proposed hybrid method

4 Conclusion and Future Works

In this paper, we suggested a hybrid tracking method for a pedestrian by using a smartphone. The hybrid method is composed of a dead-reckoning method to track incremental movements of a user by detecting steps, and Wi-Fi fingerprinting method to recognize places which could be a departing or arriving place. Introducing such places as point of interest (PoI) we could segment a long path into several short paths, so the detection of PoIs could eliminate the accumulated position errors of dead-reckoning. An energy-efficient sensor management scheme was also suggested for running the proposed tracking method. We proposed a simple but useful method to detect steps and it results in the average detection rate of 96% from experiments. Based on acceleration signals we proposed a method to estimate the orientation and position of the phone in a pocket of pants in order to measure the heading direction of user with a geomagnetic field sensor. The developed tracking method was implemented on a smartphone, "Nexus One" of HTC company. The experimental results showed the usefulness and limitations of the proposed method.

For future works, we are going to find a method to recognize walking behaviors and count walk-steps for various possession styles not only in a front pocket of pants but also in many kinds of pockets of pants or a jacket, in various bags, in his/her arm. To do this we will use a gyroscope sensor additionally embedded in the latest smartphones. We also have to increase the recognition ratio of the Wi-Fi fingerprinting localization method.

Acknowledgements. This work was in part supported by Business for cooperative R&D (Grants No. C0037241) between Industry, Academy, and Research Institute funded Korea Small and Medium Business Administration in 2012, and by Mid-career Researcher Program (No.2012-0005324) through the National Research Foundation of Korea(NRF) funded by the Ministry of Education, Science, and Technology.

References

1. Liu, H., Darabi, H., Banerjee, P., Liu, J.: Survey of Wireless Indoor Positioning Techniques and Systems. *IEEE Transactions on Systems, Man, and Cybernetics, Part C: Applications and Reviews* 37(6), 1067–1080 (2007)
2. Chon, J., Cha, H.: LifeMap: A Smartphone-Based Context Provider for Location-Based Services. *IEEE Pervasive Computing* 10(2), 58–67 (2011)
3. Shin, H., Cha, H.: Wi-Fi Fingerprint-Based Topological Map Building for Indoor User Tracking. In: 2010 IEEE 16th International Conference on Embedded and Real-Time Computing Systems and Applications (RTCSA), pp. 105–113 (2010)
4. Foxlin, E.: Pedestrian tracking with shoe-mounted inertial sensors. *IEEE Computer Graphics and Applications* 25(6), 38–46 (2005)
5. Ojeda, L., Borenstein, J.: Non-GPS Navigation for Security Personnel and First Responders. *Journal of Navigation* 60(3), 391–407 (2007)
6. Lee, S.-W., Mase, K.: Activity and location recognition using wearable sensors. *IEEE Pervasive Computing* 1(3), 24–32 (2002)
7. Cypriani, M., Lassabe, F., Canalda, P., Spies, F.: Wi-Fi-based indoor positioning: Basic techniques, hybrid algorithms and open software platform. In: 2010 International Conference on Indoor Positioning and Indoor Navigation (IPIN), pp. 1–10 (2010)
8. Wang, Y., Lin, J., Annavaram, M., Jacobson, Q.A., Hong, J., Krishnamachari, B., Sadeh, N.: A framework of energy efficient mobile sensing for automatic user state recognition. In: Proceedings of the 7th International Conference on Mobile Systems, Applications, and Services (MobiSys 2009), p. 179 (2009)

Overlapped Object Recognition Using Range and Image Data for a Service Robot

Honggu Lee, Keonhong Lee, and Sungho Jo

Dept. of Computer Science, KAIST
291 Daehak-ro, Yuseong-gu, Daejeon 305-701, Korea
`{Nickplay, diskedit, shjo}@kaist.ac.kr`

Abstract. We propose an algorithm for object recognition in indoor service robots. The problem of object recognition is one of the key challenges in the creation of realistic robotic services. Despite great advancements in the past, sufficiently accurate object recognition for service robots in real-world environments remains problematic. Our algorithm uses image and range data information that is available on a service robotic platform to execute the segmentation and classification steps. The segmentation decision rule is applied to correctly segment objects even in overlapped placements. In the classification step, the bag of words is employed with feature descriptors that are constructed from image and range information of segmented regions. In experiments, a working service robotic platform recognizes objects of similar shapes and colors. In addition, we test the recognition capability of overlapped objects. The results demonstrate the feasibility of the proposed algorithm.

Keywords: Camera, Laser range finder, Object recognition, Service robot.

1 Introduction

Computer vision techniques have contributed hugely to the progress of robotic object recognition. However, they have difficulty in distinguishing featureless or similar textures. In addition, they are unreliable with changing light conditions such as an object shadowed by a near object. Therefore, attempts have been made to overcome the shortcomings of 2D image-based object recognition by exploiting 3D shape information [1–3]. 3D range data information is useful when an object’s textures are featureless. Various techniques, including local surface descriptor matching [1] and skeleton graph matching [2] have been proposed for range-data based classification [3]. Gould et al. [5] attempted to enhance object detection by augmenting a 2D image-based detector with 3D depth information and focused this system on a real-time robotic application. However, their method requires searching descriptive features over the whole image region to detect a specific object. They employed high-resolution 3D sensing to further improve the detection performance [6]. Marton et al. [7] used a composite sensor with a time-of-flight camera, a color stereo camera, a thermal camera, and a laser range finder to categorize kitchen objects in a table setting. They combined Markov and Bayesian logic networks to capture complex

features and design classifiers. Despite its applicability to a robotic system, a complicated sensory organization is less preferred. A real-time performable object classification in 3D laser range data for an autonomous mobile robot has been proposed previously [8]. The AdaBoost learning approach was applied to construct a cascade of classifiers that were based on image and range data.

In this paper, we aim to solve the object recognition problem for indoor service robots. We propose a new recognition algorithm that reinforces performance through fusion of visual and range information. Our algorithm consists of multiple procedures that can be easily streamlined for execution in a robotic platform. First step is the object segmentation that uses the combined information of 2D image data from a camera and 3D range data from a laser range finder (LRF). Multisensor-based segmentation enhances correct segmentability. Our algorithm extracts fixation points during the segmentation step and employs a segmentation decision rule to confirm segmented objects based on image and range information. The other step is the classification based on 2D image information augmented by 3D shape information. Because our method identifies a specific object of interest through segmentation and focuses on it, the classification process is computationally simple and robust. To recognize objects, we apply the classification algorithm called the bag of key points [4], which is based on features from the segmented regions. We propose a modification to impose 2D image and 3D shape information into descriptors for the recognition.

2 System and Scenario

2.1 Robotics Platform and Sensors

Robotics technology progress has resulted in advanced service robot platforms [9-11]. These service robot platforms all have visual and range sensors. Multimodal sensor equipment in a service robot has become the default. We developed a working service robot platform that is also equipped with sensors including a monocular camera and an LRF, to be used for object recognition, as shown in Fig. 1(b) and (c). The camera can capture 1024×768 images at 30 frames per second. Our recognition algorithm is embedded into the robot platform for evaluation.

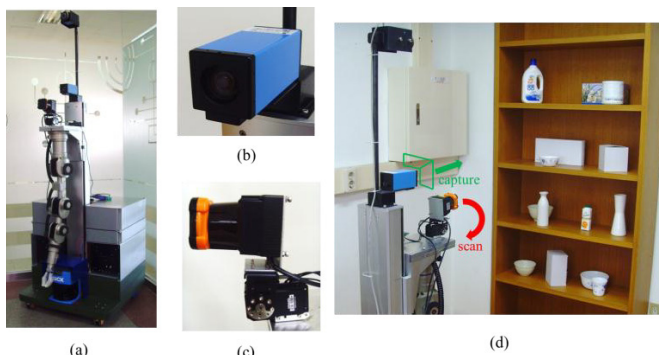


Fig. 1. (a)The service robot platform with (b) a monocular camera, and (c) a rotating LRF, and (d) experimental setting

2.2 Scenario

We set the experimental environment as shown in Fig. 1(d). The service robot platform was placed in front of the shelves where various objects were located. Some of objects are similar in shape or texture. During object learning sessions, the objects were separately placed from the viewpoint of the robot platform. While the camera of the robot platform took an image of the area, the LRF was rotated vertically and scanned the frontal area in order to obtain range data points. To gain sufficient training data, the objects' orientations and locations were changed arbitrarily. We conducted object recognition experiments while some of the objects were arbitrarily located or overlapped from the robot's viewpoint.

3 Algorithm

The proposed algorithm consists of several steps such as data acquisition, object segmentation, and classification. Extrinsic calibration that was proposed in [12] is executed to identify the physical geometric relationship between the two sensors. Next, the range low-resolution data points are mapped to the high-resolution image data based on their physical relationship. To identify objects from the original data, the segmentation process is performed using the obtained image and range data. The data from segmentation process are used as training data to learn specific objects or as test data to recognize learned objects.

3.1 Data Acquisition

Each acquired camera image is undistorted through intrinsic calibration as in [13]. The laser range finder scans the frontal region with a scan speed of 25 ms at 0.25° resolution by panning. The 3D range data acquired through this scanning process contain depth or 3D shape information of the surface of the detected space. Fig. 2(a) illustrates an example of a captured camera image and Fig. 2(b) shows the corresponding 3D range data that were acquired by scanning the region.

3.2 Object Segmentation

The real-time segmentation of range data is performed by the application of an algorithm that is explained in [14]. This method clusters range data points by estimating the normal vectors of data points in a neighborhood and the Euclidean and angular distance between data points. As a result, object segmentation is realized as demonstrated in Fig. 2(c). Point clouds with distinct colors indicate different objects of interest. The background part is removed considering the size of known objects. The segmentation is only based on the range data information. Sometimes a wrong judgment is realized. For example, the object at the bottom right was recognized as two segmented objects in Fig. 2(c). Image data information is used to reinforce the segmentation judgment.

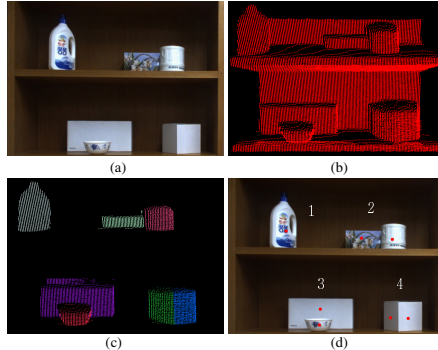


Fig. 2. The procedure of object segmentation. Four cases are labeled from 1 to 4.

Using the geometric relationships from the extrinsic calibration, the range data points of each object are projected onto the image plane (u, v). Next, the attention points of objects of interest are identified by verifying a central point among the projected range data points. Given a set of the projected data points $S = \{\vec{p}_i = (u_i, v_i), i = 1, \dots\}$ of a specific object, we identify a central point $\vec{p}_c = (u_c, v_c)$ that satisfies $\vec{p}_c = \arg \min_{\vec{p}_c \in S} \sum_{i=1}^n \|\vec{p}_c - \vec{p}_i\|^2$. The central point is called the medoid. Because the medoid is only one of many data points, it is always located on the object. The above formulation resembles the k -medoids algorithm when $k=1$, which calculates a medoid over all of the data. The Partitioning Around Medoids (PAM) method solves this problem [15]. The central point is regarded as an attention point of the object. The red dots in Fig. 2(d) show the selected attention points of the objects. Sometimes multiple attention points are assigned on an identical object. Each attention point is a fixation point that is enclosed by a contour through image-based active segmentation. By applying the active image segmentation with fixation [16], each object is segmented on the image plane. When a non-occluded object is pointed by a fixation point (case 1 in Fig. 2(d)), the image segmentation easily identifies the object. If both range and image-based segmentations (see Fig. 3(a)) indicate the same region by inducing a fixation point, we confirm a segmented object.

However, cases become complicated when an object is multi-segmented or multiple objects occluding each other. In case 2 in Fig. 2(d), the active image segmentations are executed at every fixation points. The image segmentation results can be different; a segmentation contour obtained from a fixation point encloses other segmentation contours from other fixation points or includes other contours. The left and right fixation points of case 2 in Fig. 2(d) were extracted from the segmented range data as in Fig. 3(b). Fig. 3(b) illustrates the results of the image segmentations with the left and right fixation points of case 2 in Fig. 2(d) respectively. Fig. 3(c), which are the results of case 3 in Fig. 2(d) from the segmented range data show a case of image segmentations that include each other. Fig. 3(d), the results of case 4 in Fig. 2(d) from the segmented range data, also has a relationship that includes one another.

We formulate the relationships as follows. Let A and B be segmented object image regions extracted from two different fixation points, and C be their overlapped image

region. When a pixel (u, v) is inside of an enclosed segmentation region, $s_O(u, v) = 1$, and otherwise, $s_O(u, v) = 0$, where O indicates a segmented object.

For all u, v ,

$$s_C(u, v) = 1 \text{ if } s_A(u, v) = 1 \text{ and } s_B(u, v) = 1,$$

$$s_C(u, v) = 0 \text{ otherwise.}$$

Then,

$$A \text{ includes } B \text{ if } \left| \frac{\sum_u \sum_v s_C(u, v)}{\sum_u \sum_v s_B(u, v)} - 1 \right| < \delta, \quad B \text{ includes } A \text{ if } \left| \frac{\sum_u \sum_v s_C(u, v)}{\sum_u \sum_v s_A(u, v)} - 1 \right| < \delta.$$

($\delta = 0.05$, which is empirically selected considering image resolution.)

In addition, A and B are disjoint (no intersection) if $\frac{\sum_u \sum_v s_C(u, v)}{\sum_u \sum_v s_B(u, v)} < \delta$ or $\frac{\sum_u \sum_v s_C(u, v)}{\sum_u \sum_v s_A(u, v)} < \delta$. When the two segmented image regions are disjointed, we conclude that they indicate different objects. Otherwise, we check one more step as follows. When the range data-based segmentation indicate multiple segments, but the image-data segmentations result in inclusive relationships (see cases 2 to 4 in Fig. 3), we consolidate their separation evaluation by proposing an additional method. Generally, these cases occur when two objects are overlapped or an object has highly distinguished surfaces.

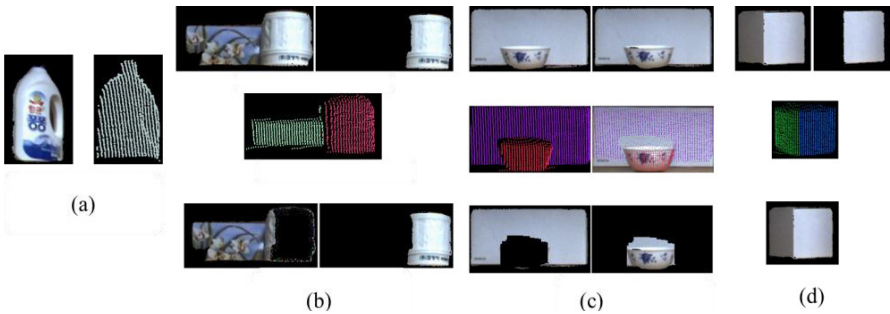


Fig. 3. Segmentation result of (a) case 1, (b) case 2, (c) case 3, and (d) case 4

During the collection of the range data, the LRF is rotated to scan the objects vertically (see Fig. 1(c)). Each scan consists of laser beams over a horizontal line as in Fig. 4(a). The horizontal laser beams spread out at a uniformly fixed angle. The range data points are projected onto a 2D view plane with respect to the LRF. Based on the range data-based segmentation, the projected data points are binarily labeled to indicate a segmentation region of a binary image as shown in Fig. 4(b). The projected data points labeled as one indicate an object of interest, whereas data points labeled as zero indicate any other regions than the object. Next, the dilation of the binary image by the structuring element defined in Fig. 4(d) is processed [17].

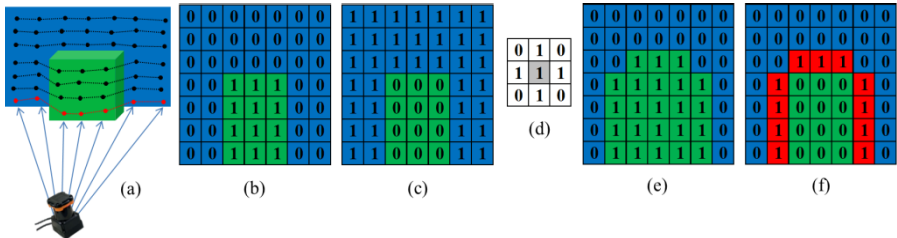


Fig. 4. Extraction of border of overlapped object segments

This process results in a binary image as in Fig. 4(e). Fig. 4(c) describes a complementary image of Fig. 4(b). The intersection of Fig. 4(c) and (e) describes the border labeled as one around the object and is placed in the region just outside of the object. For each of the original 3D range data points that correspond to the points of the border, we apply the k nearest neighbor algorithm [18]. We then count how many nearest neighbor data points are associated in the region outside of the object. Let the total number of points on the border (number of one's in Fig. 4(f)) be N_b and the 3D data points corresponding to the points of the border be denoted by $\vec{x}_b(i)$, $i = 1, \dots, N_b$. Also, R_O represents data points associated in the object. Then, the following segmentation decision is applied.

```

Let  $N_c := 0$ 
For  $i = 1$  to  $N_b$ 
   $\{ \vec{x}_{n,i}(j) \mid j = 1, \dots, k \} = k$ -nearest neighbor points of  $\vec{x}_b(i)$ 
  If  $\nexists \vec{x}_{n,i}(j) \in R_O$  Then  $N_c = N_c + 1$ 
End
Return  $c = \frac{N_c}{N_b}$ 

```

If $|c - 1| < \varepsilon$, then the two adjacently segmented regions (an object of interest and the region outside of the object) indicate separated objects; otherwise, they indicate that an object is not separated ($\varepsilon = 0.1$ which is empirically selected considering the scanning resolution and LRF noise).

The decision rule states that the separation between the object and other regions is confirmed if the nearest neighbor points of the border are located outside of the object region. If some numbers of nearest neighbor points of the border are within the object region, it implies that the two regions are connected locally somewhere. In this situation, we merge the two segmentations into one object region. Cases 2 and 3 in Fig. 3 are examples of object separation. In case 2 when object image A includes object image B , the object image textures are obtained simply. The two object images are $A-B$ and B . In case 3 when images A and B include each other, object image regions that correspond to the binary images from the projected range data in Fig. 4(b) and (c) are selected to extract both object image textures. Case 4 shows an example of segmentations that are finally merged to indicate one object. The overall segmentation decision based on the range and image segmentation is summarized in Fig. 5.

Image relationship	Range relationship	Decision	Segmentation decision rule
A includes B, and B includes A	Not separated	Merge	a
	separated	Separate	b
A only includes B	Not separated	Merge	c
	separated	Separate	d
A and B are disjointed		Separate	e

Fig. 5. Overall segmentation result between two object segments

3.3 Object Classification

The bag of words method was originally proposed for text categorization [19]. However, it has been applied for visual categorization and its successful performance has been verified [4, 20]. It has practical appeal because of its computational efficiency and simple operation. In addition, it is robust in different lighting conditions, partial occlusion, and orientation changes. We apply the bag of words extensively for object classification in our application. Features are extracted from the image and range data information. To construct the image data descriptor, we use the method proposed in [4]. This method prepares a set of clusters. Each cluster collects features obtained from a category of images. By extracting the SIFT (or SURF) descriptors from the images of the VOC2008 dataset, which has been widely used [21], and applying the k -means, we construct our clusters. The number of clusters is set to 1000, as suggested in [4]. Given an image segment, we compute the SIFT (or SURF) descriptors and compare each descriptor to the representative descriptors of clusters. Next, each descriptor is assigned to a closest cluster. The total number of assigned descriptors in each cluster slot is counted. The assigned counts over the 1000 slots describe the image data descriptor. The range data provide the shape information. Features that contain the 3D shape information are adapted from a previous study [22].

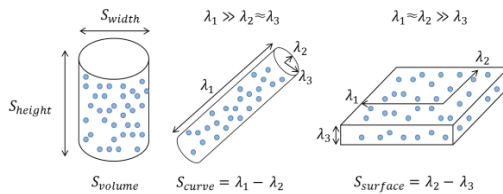


Fig. 6. Shape features

Fig. 6 illustrates the features obtained from the range data points. Let each data point be represented by $\vec{x}_i = (x_i, y_i, z_i) \in O$ where O is a set of data points from the object in 3D Cartesian space. x , y , and z represent element values along horizontal, vertical and depth axes from a viewpoint. When N data points are in the set, covariance matrix, M , of the data points is computed by

$$M = \frac{1}{N} \sum_{i=1}^N (\vec{x}_i - \bar{m})(\vec{x}_i - \bar{m})^T, \quad (\bar{m} = \frac{1}{N} \sum_{i=1}^N (\vec{x}_i - \bar{m})). \quad (1)$$

Then, the first to third major principal components, λ_i , $i=1,2,3$, of M are computed. It was proposed that the relative scales between the principal components, as in Fig. 6, designate three feature values, S_{volume} , S_{curve} , and $S_{surface}$ [22]. The features represent information on the object volume, curviness, and surfaceness respectively. However, our data points are partially measured along a viewpoint, and depth information is not provided correctly. Therefore, we substitute S_{volume} with the width, S_{width} , and height, S_{height} , of the object that are measured from a viewpoint. The width and height are defined as follows.

$$S_{width} = \max\{x_i | i = 1, \dots, N\} - \min\{x_i | i = 1, \dots, N\} \quad (2)$$

$$S_{height} = \max\{ y_i | i = 1, \dots, N \} - \min\{ y_i | i = 1, \dots, N \} \quad (3)$$

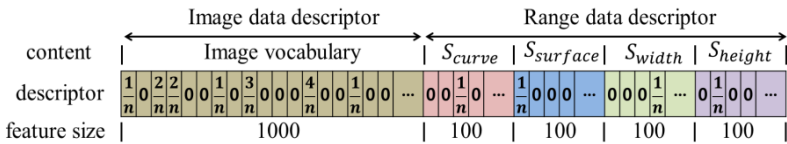


Fig. 7. Data descriptor for bag of word (n is selected to set the total sum of nonzero values in slots to be one)

Fig. 7 illustrates the composition of bag of words descriptors that includes both image vocabulary and shape features. Taking into account the maximum and minimum of each shape feature over the sample data, each feature values are categorized into 100 slots per shape feature. The associated slot value is one when a shape feature value from a sample data set is in a slot, while the rest of the slot values are zero. Because four shape features are considered, a total feature vector, which consists of the image and range data descriptors, is sized at 1400. The feature vector is finally normalized for the total sum of descriptor values to be one.

We use the Support Vector Machine (SVM) algorithm [23] for the construction of classifiers for object recognition. Let \vec{v}_i be a feature vector for each sample, $i=1,\dots,N_S$, where N_S is the total number of positive and negative samples. The SVM decision function is described by

$$f(\vec{v}) = \text{sign}(\sum_i s_i \alpha_i K(\vec{v}, \vec{v}_i) + b) \quad (4)$$

where $K(\vec{v}, \vec{v}_i) = \exp(-\gamma \|\vec{v} - \vec{v}_i\|^2)$, $\gamma > 0$, α_i and b are parameters to be determined by the SVM, and s_i is +1 for each positive sample and -1 for each negative samples. An object with the highest positive value of $f(\vec{v})$ among the learned objects is selected. If all of the classifiers result in negative values, no object is recognized.

4 Experiments

These experiments evaluate the proposed algorithm using 14 objects as shown in Fig. 8. During the training session, each classifier was constructed using 30 positive samples from each trained object and 500 negative samples. The negative samples were constructed by taking image vocabulary chosen randomly from the VOC2008

dataset and shape descriptors chosen randomly from the measured range data points of objects other than the trained object. Each positive sample consisted of an image vocabulary descriptor from a segmented image of the trained object and shape descriptors from measured range data points of the object.

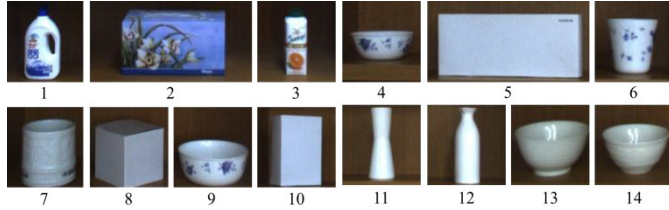


Fig. 8. 14 objects used in experiments

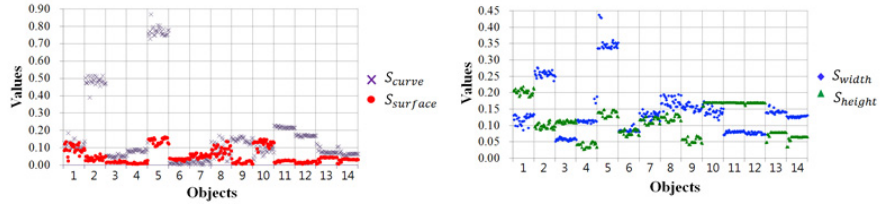


Fig. 9. Values of shape features

	1	2	3	4	5	6	7	8	9	10	11	12	13	14	Ratio
1	30	0	0	0	0	0	0	0	0	0	0	0	0	1.00	
2	0	30	0	0	0	0	0	0	0	0	0	0	0	1.00	
3	0	0	30	0	0	0	0	0	0	0	0	0	0	1.00	
4	0	0	0	29	0	0	0	1	0	0	0	0	0	0.97	
5	0	0	0	0	15	0	0	0	0	0	0	0	0	0.50	
6	0	0	0	0	30	0	0	0	0	0	0	0	0	1.00	
7	0	0	0	0	0	30	0	0	0	0	0	0	0	1.00	
8	0	3	0	0	0	0	26	1	0	0	0	0	0	0.87	
9	0	0	0	4	0	0	0	0	26	0	0	0	0	0.87	
10	0	1	1	0	0	0	0	0	28	0	0	0	0	0.93	
11	0	0	0	0	0	0	0	0	26	0	4	0	0	0.87	
12	0	1	1	0	0	0	0	0	0	1	3	23	1	0.77	
13	1	1	0	0	0	0	0	0	0	0	28	0	0	0.93	
14	0	0	0	0	0	0	0	0	0	0	0	30	1.00		
total recognition ratio														0.91	

(a)

(b)

	1	2	3	4	5	6	7	8	9	10	11	12	13	14	Ratio
1	30	0	0	0	0	0	0	0	0	0	0	0	0	1.00	
2	0	30	0	0	0	0	0	0	0	0	0	0	0	1.00	
3	0	0	30	0	0	0	0	0	0	0	0	0	0	1.00	
4	0	0	0	30	0	0	0	0	0	0	0	0	0	1.00	
5	0	0	0	0	21	0	0	9	0	0	0	0	0	0.70	
6	0	0	0	0	30	0	0	0	0	0	0	0	0	1.00	
7	0	0	0	0	0	30	0	0	0	0	0	0	0	1.00	
8	0	3	0	0	0	0	26	1	0	0	0	0	0	0.87	
9	0	0	0	4	0	0	0	0	26	0	0	0	0	0.87	
10	0	1	1	2	0	0	0	0	26	0	0	0	0	0.87	
11	0	0	0	0	0	0	0	0	30	0	1	0	0	1.00	
12	0	1	1	0	0	0	0	0	0	1	26	1	0	0.87	
13	0	0	0	0	0	0	0	0	0	0	29	1	0	0.93	
14	0	0	0	0	0	0	0	0	0	0	0	30	1.00		
total recognition ratio														0.94	

(c)

(d)

Fig. 10. Performance results of object recognition

Fig. 9 illustrates the shape descriptor values of the 30 positive samples per object. It is clearly shown that the shape features are effective to distinguish objects. In some cases, the distinction is subtle. For example, objects 11 and 12 had a small difference in S_{curve} , and objects 13 and 14 had slightly different features. The test session

evaluated recognition performance using 30 test samples that were obtained arbitrarily from each object. Two different classification schemes were applied for comparison. One scheme relied on image information only and, therefore, image descriptors only. The other scheme included shape information and used the full set of descriptors. Either SURF or SIFT descriptors were used to identify the image information after the SIFT detector was applied [23].

Fig. 10 summarizes the results. Each left column and top row indicates the ground truth objects and the recognition results respectively. Image only-based classification results are shown in Figs. 10(a) (using the SIFT descriptor) and (b) (using the SURF descriptor). The SIFT descriptor outcome had relatively better performance. The classification performances were improved generally in both cases when shape information is included. Object 8 was not well classified using only the SURF descriptor, however, the range data information improved its recognition rate up to 80% as shown in Fig. 10(d). The SIFT descriptor only resulted in a low classification rate for object 5. The rate was improved with the use of the shape information as shown in Fig. 10(c). The overall results indicate that the proposed algorithm was effective for object classification and attained high recognition rates of 94% on average.

Next, we conducted experiments in which objects were overlapped. There was no learning session. Instead, we used the non-overlapped objects learned from the previous experiment. As shown in Fig. 11, 15 cases of two overlapped objects were set up arbitrarily. The objects were selected randomly from the 14 objects in Fig. 8.



Fig. 11. Overlapped objects selected for experiments

As a consequence, 30 object recognitions were performed. In Fig. 12, the experimental results are categorized by comparing image only- and both image and range-based segmentations as well as classifications. We used the SIFT descriptor for image only-based classifications. Using both image and range data, objects were correctly segmented in all of the cases. In the recognition results, each number in parenthesis indicates a wrongly recognized object when the recognition failed. “Null” indicates that no object was recognized, which means no classification generated a positive value. The image only-based classification (a) was performed with the image only-based segmentation, but the image only-based classification (b) was performed with both image and range-based segmentations. The performance of (b) was better than (a). The inclusion of the range information for classification (c) improved the performance further. There was no case that (b) was successful while (c) failed. In (c), interestingly, object 12 was recognized even with no image descriptor in case D. 23 objects out of 30 (76.7% recognition rate) were successfully recognized. These results indicate that the inclusion of the range information in both the segmentation and recognition steps improved performance significantly.

	object	Segmentation		Rule	Recognition	
		image only	+ range		image only	+ range
A	2	Fail	Success	d	Fail(9)	Success
	4	Fail	Success		Fail(9)	Fail(9)
B	6	Fail	Success	b	Success	Success
	7	Fail	Success		Fail(6)	Success
C	3	Fail	Success	b	Fail(4)	Success
	4	Fail	Success		Fail(2)	Success
D	5	Fail	Success	b	Success	Success
	12	Fail	Success		Fail(5)	Success
E	1	Success	Success	e	Success	Success
	13	Success	Success		Fail(7)	Success
F	6	Fail	Success	b	Fail(1)	Fail(7)
	8	Fail	Success		Fail(2)	Success
G	6	Fail	Success	b	Success	Success
	9	Fail	Success		Fail(6)	Success
H	9	Success	Success	d	Success	Success
	13	Fail	Success		Fail(9)	Fail(2)
I	2	Success	Success	e	Success	Success
	12	Success	Success		Fail(5)	Success
J	3	Fail	Success	d	Success	Success
	9	Success	Success		Fail(4)	Fail(4)
K	6	Fail	Success	b	Success	Success
	11	Fail	Success		Fail(6)	Fail(10)
L	1	Success	Success	d	Success	Success
	2	Fail	Success		Success	Success
M	9	Success	Success	e	Fail(4)	Success
	12	Success	Success		Success	Success
N	1	Success	Success	e	Success	Success
	7	Success	Success		Success	Success
O	5	Fail	Success	b	Fail(2)	Success
	6	Fail	Success		Success	Success

Fig. 12. Performance result of overlapped object recognition

5 Conclusion

This work presented an algorithm of object recognition that used range and image data for an indoor service robot. Two types of sensory data were mingled to realize object segmentation, even in cases of overlapping objects. Experimental results demonstrated that object recognition based on segmentation was effective. Furthermore, mixed range and image data utilization successfully enhanced the recognition rate. Using the proposed algorithm, an indoor service robot can recognize objects of interest that are located a certain distance away. For better recognition, the robot should be able to move around and glance at the objects to obtain further data.

Acknowledgements. This work was supported in part by the Agency for Defense Development (ADD) under Grant UD110111ID, the Korean government (MEST) under the KRF grant (No. 2010-0015226) and in part by the Korean government (MKE) under Human Resources Development Program for Convergence Robot Specialists.

References

1. Sundar, H., Silver, D., Gagvani, N., Dickinson, S.: Skeleton based shape matching and retrieval. In: Int. Conf. on Shape Modeling and Applications, p. 130 (2003)
2. Li, X., Guskov, I.: 3D object recognition from range images using pyramid matching. In: IEEE Int. Conf. on Computer Vision, pp. 1–6 (2007)
3. Tangelder, J., Veltkamp, R.: A survey of content based 3D shape retrieval methods. In: Int. Conf. on Shape Modeling and Applications, pp. 145–156 (2004)
4. Dance, C., Willamowski, J., Fan, L., Bray, C., Csurka, G.: Visual categorization with bags of keypoints. In: ECCV Int. Workshop on Stat. Learn. in Comp. Vision (2004)

5. Gould, S., Baumstarck, P., Quigley, M., Ng, A.Y., Koller, D.: Integrating visual and range data for robotic object detection. In: Workshop on Multi-camera and Multi-modal Sensor Fusion (2008)
6. Quigley, M., et al.: High-accuracy 3D sensing for mobile manipulation improving object detection and door opening. In: IEEE Int. Conf. on Rob. & Autom. (2009)
7. Marton, Z.-C., et al.: Probabilistic categorization of kitchen objects in table settings with a composite sensor. In: IEEE/RSJ Int. Conf. Intell. Rob. & Syst. (2009)
8. Nüchter, A., Surman, H., Hertzberg, J.: Automatic classification of objects in 3D laser range scans. In: Conf. on Intelligent Autonomous Systems, pp. 963–970 (2004)
9. Ng, A.N., Gould, S., Quigley, M., Saxena, A., Berger, E.: STAIR: the STanford Artificial Intelligence Robot project. In: Proc. AAAI Robotics Workshop (2007)
10. Jain, A., Kemp, C.C.: EL-E: an assistive mobile manipulator that autonomously fetches objects from flat surfaces. Auton. Rob. 28(1), 45–64 (2010)
11. Rusu, R.B., et al.: Rea-time perception-guided motion planning for a personal robot. In: IEEE/RSJ Int. Conf. on Intell. Robt. And Sys., pp. 4245–4252 (2009)
12. Unnikrishnan, R., Hebert, M.: Fast extrinsic calibration of a laser rangefinder to a camera. Technical Report CMU-RI-TR-05-09, Robotics Institute, Carnegie Mellon University (2005)
13. Zhang, Z.: A flexible new technique for camera calibration. IEEE Trans. on Patt. Anal. & Mach. Intell. 22(11), 1330–1334 (2000)
14. Klasing, K., Wollherr, D., Buss, M.: Realtime segmentation of range data using continuous nearest neighbors. In: IEEE Int. Conf. on Rob. & Autom., pp. 2431–3436 (2009)
15. Theodoridis, S., Koutroumbas, K.: Pattern Recognition, 3rd edn., pp. 635–639. Academic Press (2006)
16. Mishra, A., Aloimonos, Y., Fah, C.L.: Active segmentation with fixation. In: IEEE Int. Conf. on Comp. Vision, pp. 468–475 (2009)
17. Gonzalez, R., Woods, R.: Digital Image Processing, pp. 518–519, 549. Addison-Wesley Publishing Company (1992)
18. Wu, X., Kumar, V., Ross Quinlan, J., Ghosh, J., Yang, Q., Motoda, H., McLachlan, G.J., Ng, A., Liu, B., Yu, P.S., et al.: Top 10 algorithms in data mining. Knowledge and Information Systems 14(1), 6–8 (2008)
19. Sahlgren, M., Cöster, R.: Using bag-of-concepts to improve the performance of support vector machines in text categorization. In: Conf. on Computational Linguistics, pp. 487–513 (2004)
20. Yang, J., Jiang, Y.G., Hauptmann, A.G., Ngo, C.W.: Evaluating bag-of-visual-words representations in scene classification. In: Int. Workshop on Multimedia Information Retrieval, pp. 197–206 (2007)
21. Everingham, M., Van Gool, L., Williams, C.K.I., Winn, J., Zisserman, A.: The PASCAL Visual Object Classes Challenge 2008 (VOC 2008) Results (2008)
22. Lalonde, J.F., Vandapel, N., Huber, D.F., Hebert, M.: Natural terrain classification using three-dimensional ladar data for ground robot mobility. Journal of Field Robotics 23(10), 839–861 (2006)
23. Bauer, J., Sunderhauf, N., Protzel, P.: Comparing several implementations of two recently published feature detectors. In: Proc. of the Int. Conf. on Intell. Rob. & Syst. (2007)

Novel Scheme of Real-Time Direction Finding and Tracking of Multiple Speakers by Robot-Embedded Microphone Array

Daobilige Su¹, Masashi Sekikawa¹, Kazuo Nakazawa², and Nozomu Hamada²

¹ Signal processing Lab, School of Integrated Design Engineering, Keio University

² Department of System Design Engineering, Keio University

Hiyoshi 3-14-1, Yokohama 223-8522 Japan

{su, sekikawa}@hamada.sd.keio.ac.jp,

{nakazawa, hamada}@sd.keio.ac.jp

Abstract. Recently, interest on artificial robot audition is growing for developing human-robot interaction. The main purposes of an artificial audio system mounted on mobile robot are localizing sound sources, separating speech signal that is relevant to a particular speaker such as robot's master, and processing speech sources to extract useful information such as master's uttering commands. This paper reports a novel proposed method of a speaker's direction tracking algorithm, and a realization of the real tracking system on a mobile robot. Basic approach of this study belongs to a category of direction finding known as sparseness-based one which employs time-frequency decomposition and disjoint property between different speech signals. The novel points in the proposed source tracking exist on a reliable data selection from time-frequency cells and the application of mean shift tracking to the kernel density estimator derived from these reliable time-frequency components. A wheel-based mobile robot is developed and built-in audio processing system. Experiments are conducted and demonstrate the ability to localize in real environments.

Keywords: robot audition, sound source localization, microphone array, kernel density estimator, mean shift tracking.

1 Introduction

For robot audition system the sound source tracking problem by it draws lots of attentions recently [1]-[6]. The same issues have also been studied in a wide field of applications, such as, automatic camera steering for surveillance and video conference, and acoustic discrimination between individuals in real multi-speaker environments. In this paper we are particularly interested in a speaker's direction of arrival (DOA) tracking by microphone array mounted on mobile robots, where the problem is in the moving sources as well as moving sensor framework. In addition, the method should be sufficiently robust against environmental noise and other speaker's voices. That is, it is required a better directional sensitivity and better anti-interference ability. Under the assumption of fixed source location, there have been

proposed a large amount of studies. Among them, approaches based on the sparseness of time-frequency (T-F) component in speech signals are very attractive because of their capability for underdetermined case where the sources outnumber the sensors. This study is also based on the sparseness of speech signal in T-F domain.

In the context of fixed sensor array, several methods of tracking moving source have been proposed. Most popular approaches are adaptive beamforming tracking [4] and particle filter or sequential Monte Carlo method [4][6]. The methods treat two kinds of localization issues: namely, tracking the source position such as exact position tracking in an environment and the source direction tracking. The former problem can be solved by combining the estimation by individual microphone arrays. Another type of problem integrates two-types of microphone arrays one of which is mounted on mobile robot and the others are on the room's walls [2]. The acoustic source tracking system in mobile robot has been developed in the context of moving sensors/sources condition. This moving sensor/source problem would be different from that of fixed source/sensor location especially with respect to the number of data available because of real time processing.

As obviously recognized in general estimation problem, the use of reliable data promises an accurate result. Thus, the deletion of outliers from observations is effective for statistical estimation algorithms. Basically the T-F sparseness approach attempts to cluster in the T-F cell distribution on which spatial cues such as direction angles are labeled. Thus the existence of outliers must disturb the clustering process, and tends to fail in detecting source positions. The idea of the T-F cell selection have been proposed by [7] and by an author of this paper [8] and [9]. This paper will present a modified T-F cell selection related with [9].

The main contributions of this paper are the following twofold. (a) Applying mode-seeking mean-shift algorithm to the directivity likelihood in terms of kernel density estimator for time-varying source directions finding. (b) Implementing the above audition system upon a mobile robot and demonstrating and evaluating the tracking capability through real experiments.

The rest of this paper is structured as follows. In section 2, the proposed DOA estimation method for arbitrary array configuration is presented, and our direction tracking algorithm based on the mean shift algorithm and the kernel density estimator approach is proposed. Section 3 summarizes the implementation of our mobile robot and signal processing system mounted on it. In section 4, tracking experiments and their results are demonstrated, and the paper is concluded in section 5.

2 Proposed Method

2.1 Speaker's Direction Finding by Arbitrary Microphone Arrangement

Observation Model: Considers an array of M microphones with arbitrary configuration satisfying non-spatial aliasing condition where the inter-sensor distance is bounded, for instance, 4cm inter-sensor distance for 8kHz sampling. The observation $x_m(\tau)$ at m -th microphone ($m=1,\dots,M$) is modeled by the following convolutive mixture of N source signals $s_i(\tau)$ ($i=1,\dots,N$).

$$x_m(\tau) = \sum_{i=1} \sum_{k=1} h_{mi}(k) s_i(\tau - k) \quad (1)$$

where $h_{mi}(k)$ is the impulse response from i -th source to m -th microphone. The method proposed in this paper is applicable to the underdetermined case where the sources outnumber the sensors, namely $N > M$.

In the time-frequency domain by transformed by STFT (Short-Time Fourier Transform) the mixed observations $x_m(\tau)$ of (1) is represented

$$X_m(k, l) = H_{mi}(l) S_i(k, l) \quad (2)$$

where $X_m(k, l), S_i(k, l)$ are the STFT's of $x_m(\tau), s_i(\tau)$ respectively, $H_{mi}(l)$ is the DFT of $h_{mi}(\tau)$, l is the index of discrete frequency bin, k is the time-frame index. Let $\mathbf{r}_m = [x_m, y_m, z_m]^T$ ($m = 1, \dots, M$) denote the location of the m -th sensor in 3-D space, and assume the first sensor is located at the origin ($\mathbf{r}_1 = \mathbf{0}$) without loss of generality.

Time Delay and Phase Difference: A source direction vector referred to as the propagation direction vector is defined by

$$\mathbf{a}(\phi, \theta) = \begin{bmatrix} \sin \theta \cos \phi \\ \sin \theta \sin \phi \\ \cos \theta \end{bmatrix}^T \quad (3)$$

where $\phi (-\pi < \phi \leq \pi)$ denotes the azimuth angle of source direction, $\theta (-\pi/2 \leq \theta \leq \pi/2)$, and $\mathbf{a}(\phi, \theta)$ constitutes a unit sphere.

An acoustic signal with a propagation direction vector $\mathbf{a}(\phi)$ induces time delays τ_m ($m = 2, \dots, M$) of arrival between m -th sensor and the first or the reference sensor as follows.

$$\tau_m = -\mathbf{r}_m^T \mathbf{a}/c \quad (4)$$

where c is the travelling speed. The vector-matrix formulation of above is represented by

$$\boldsymbol{\tau} = -\frac{\mathbf{R} \mathbf{a}(\phi)}{c} \quad (5)$$

where $\boldsymbol{\tau} = [\tau_2, \dots, \tau_M]^T$, $\mathbf{R} = [\mathbf{r}_2, \dots, \mathbf{r}_M]^T$

Define the following phase difference vector from the observations.

$$\boldsymbol{\varphi}(l) = [\varphi_{12}(l), \dots, \varphi_{1M}(l)]^T, \quad \varphi_{1m}(l) = \angle X_m(l) - \angle X_1(l), \quad (6)$$

then from (5) we have the following relationship

$$\boldsymbol{\tau} = \frac{1}{\kappa(l)} \boldsymbol{\varphi}(l) \quad (7)$$

where $\kappa(l) = \frac{2\pi f_s l}{L}$, f_s is sampling frequency.

Phase Difference and propagation vector: Let's define a mapping

$$\mathcal{R}: \mathbf{a}(\phi, \theta) \rightarrow \boldsymbol{\varphi}(k, l), \quad (8)$$

in specific, \mathcal{R} can be represented by

$$\mathcal{R}(\mathbf{a}(\phi, \theta)) = -\frac{\kappa(l)}{c} \mathbf{R}\mathbf{a}(\phi, \theta) \quad (9)$$

The inverse operation of \mathcal{R} , that is

$$\mathcal{R}^{-1}: \boldsymbol{\varphi}(k, l) \rightarrow \mathbf{a}(\phi, \theta) \quad (10)$$

can be obtained by our previous method proposed in [9], by exploiting Gram-Schmidt orthogonalization in $\boldsymbol{\varphi}$ -space.

Reliable T-F cell selection: In real observations, due to multiple sources interaction, environmental noise and computational errors in STFT, the estimated phase difference vector $\hat{\boldsymbol{\varphi}}(k, l)$ (symbol $\hat{\cdot}$ is used for estimated value) does not give the propagation vector $\hat{\mathbf{a}}$ on the unit sphere. When we set

$$\hat{\mathbf{a}}_{(k,l)} = \mathcal{R}^{-1}[\hat{\boldsymbol{\varphi}}(k, l)], \quad (11)$$

reliable T-F cells, denoted by $(k, l) \in A$, will be selected by the following rule.

$$1 - \varepsilon < \|\hat{\mathbf{a}}_{(k,l)}\| < 1 + \varepsilon \quad (12)$$

where ε is sufficiently small positive value.

In multiple sources case, all $\hat{\mathbf{a}}_{(k,l)}, (k, l) \in A$ would generate N clusters each of which corresponds one of the sources.

Kernel Density Estimator: Besides the sell selection above, the power threshold and the consistency criteria [8] are applied to determine a set of reliable propagating direction vectors. Then we apply the kernel density estimator or the Parzen window technique for this set of data, and consequently, the local minimum points or modes of the resulted density function corresponds to the source directions. Applying this solely for a set of selected data denoted by $(\hat{\phi}_{ki}^{l_i}, \hat{\theta}_{ki}^{l_i})$, where k means the time frame index of the observation, l_i is the frequency bin of underlying reliable cell and I is the number of T-F cells in the set A. The kernel density estimator with respect to the direction angles can be formulated as follow.

$$\hat{p}(\phi_t, \theta_t) = \frac{1}{I} \sum_{i=1}^I \frac{1}{\epsilon(l_i) \delta(l_i)} K\left(\frac{\phi_t - \hat{\phi}_{ti}^{l_i}}{\epsilon(l_i)}, \frac{\theta_t - \hat{\theta}_{ti}^{l_i}}{\delta(l_i)}\right) \quad (13)$$

where $\epsilon(l_i)$ and $\delta(l_i)$ are the band widths of 2-D kernel function $K(\phi, \theta)$ with respect to ϕ and θ respectively, and which can be respectively represented by

$$\begin{aligned} \epsilon(l_i) &= \frac{1}{\kappa(l) \|\cos \theta \cos \phi \mathbf{r}_x + \cos \theta \sin \phi \mathbf{r}_y - \sin \theta \mathbf{r}_z\|_{\theta=\hat{\theta}_{ti}^{l_i}, \phi=\hat{\phi}_{ti}^{l_i}}} \hbar, \\ \delta(l_i) &= \frac{1}{\kappa(l) \|-\sin \theta \sin \phi \mathbf{r}_x + \sin \theta \cos \phi \mathbf{r}_y\|_{\theta=\hat{\theta}_{ti}^{l_i}, \phi=\hat{\phi}_{ti}^{l_i}}} \hbar \end{aligned} \quad (14)$$

where the band width \hbar is determined by experiment. See more detail in [9].

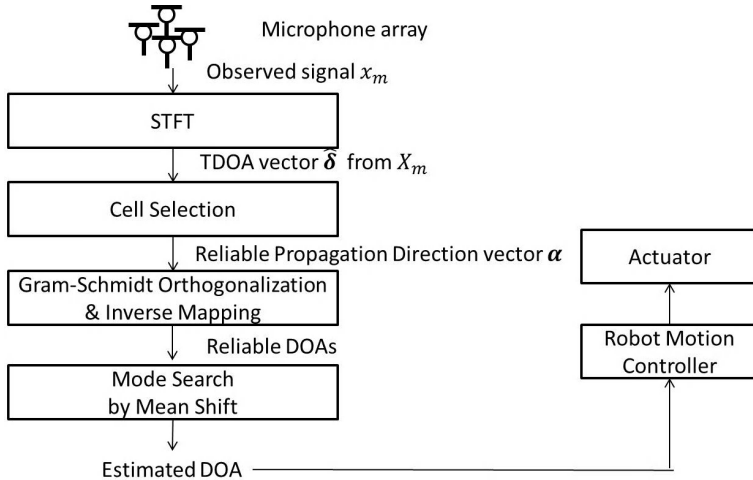


Fig. 1. Flow of the proposed system operation

2.2 Direction Tracking by Mean-Shift Algorithm

The DOA estimation problem discussed 2.1 results in the seeking of the local maximums or the modes of the obtained density estimator (13). In our system the mean-shift algorithm is employed for this purpose because of its low computational cost. In general, the mean shift algorithm is an effective clustering and mode seeking technique which does not require a prior knowledge of the number of clusters, and does not constrain the cluster distribution [10]. Our autonomous robot system needs to find and track the direction of a specific person as a robot master. The direction of the source is represented by its azimuth and elevation angles, and these time-varying values are recursively estimated by use of the mean shift algorithm. In our formulation the individual source directions correspond to the local maximum points of the kernel density estimator (13). Fig. 2 (a) shows one example of reliable T-F cell (blue dots) distribution on the unit sphere of $\mathbf{a}(\phi, \theta)$, and the figure (b) is an expanded image of the lower-left part of the sphere. These can be obtained by applying the

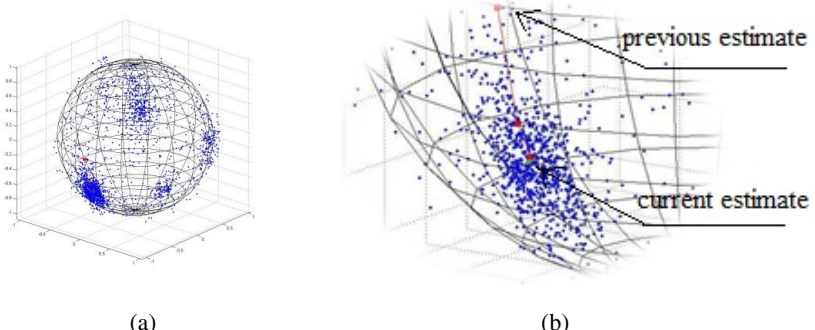


Fig. 2. Reliable T-F cell distribution and mean shift recursion

proposed DOA estimation algorithm for real-life observation in a noisy environment. The initial point and the successively updated mode estimates (red points) by mean-shift algorithm are also indicated in Fig. 2(b). It shows how the mean-shift algorithm could track the robot master direction starting from a previous estimate. Here, the red point on the top is the previous direction and it converges to the local maximum which should be the current master direction.

3 Implementation

3.1 Software Architecture

Programming Environment

In the realized signal processing system, the Linux Ubuntu 10.04.4 LTS is used as the operating system, on which the driver was installed for multichannel synchronal sampling A/D board. On top of these, we use ROS (Robot Operation System) Electric Version [11] as the main programming architecture.

Software Architecture: ROS Nodes and Topics

In ROS, each node is a process that can publish/subscribe or be client/server to another node. The communication between nodes is made by ROS topic. The software architecture represented by ROS nodes and topics in our system are shown in Fig. 3 in which rectangles represent ROS nodes and arrows represent ROS topics. The nodes for *Audio Sensor*, *Actuator* and *Communication* are nodes that deal with external devices and nodes for *DOA*, *Tracking*, *Speaker Iden* and *Speech Recog* constitute the “brain” for the robot. The construction of *Speaker Iden* node and *Speech Recog* node is our long-term objective for future works.

The function of each node is described as below. The node for *Audio Sensor* is responsible for continuously mining the audio data from microphone array and publishing it for other nodes. Each frame of audio data is 8k length under 16 kHz sampling frequency. The node for *DOA* will subscribe to the data from *Audio Sensor* node and estimate the DOA of TF cells with reliable cell selection. Then it will publish these data for *Tracking* node. The node for *Tracking* adopts the Mean Shift algorithm for tracking the robot master. In multi speaker’s case, it may track only the predefined robot master which is determined by *Speaker Iden* node. The *Speaker Iden* node will determine robot master. In single speaker’s case it will tell if the current speaker is predefined robot master. In multi speaker’s case, it can tell which one is robot master. Then it sends the message to the *Tracking* node which one it should track. The node for *Speech Recog* is to get the audio data from *Audio Sensor* node and master direction from *Tracking* node for translating voice command from robot master. In single speaker case, depending on whether one master is being tracked, it will choose to translate the voice command or keep idle. In multi speaker’s case, it solely translates the voice command by robot master by speech separation technique based on DOA. The node for *Actuator* is to subscribe to *Speech Recog* node and *Tracking* node for getting the voice command and speaker direction so that the robot could follow the simple task such as “move forward” or even more sophisticated task such as “follow me”. The node for *Communication* is reserved for the future usage.

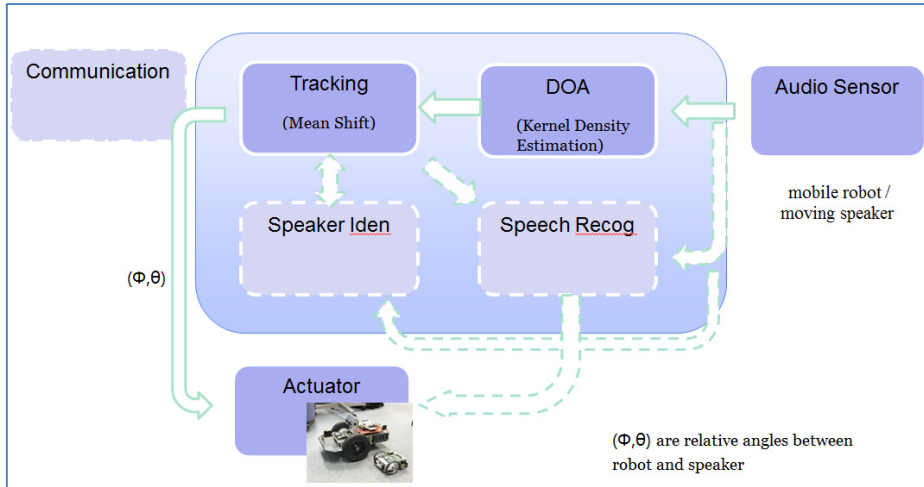


Fig. 3. Software Architecture

3.2 Hardware System

The hardware of our robot platform consists of two parts: (a) audio signal processing, (b) robot controller, and these are connected by Bluetooth module.

(a) Audio signal Processing

As a signal capturing a tetrahedral microphone array with four omni-directional microphones is mounted, and uses analog amplifier followed by the synchronized 16-channel analog-to-digital converter with 16bits and 16 kHz sampling frequency.

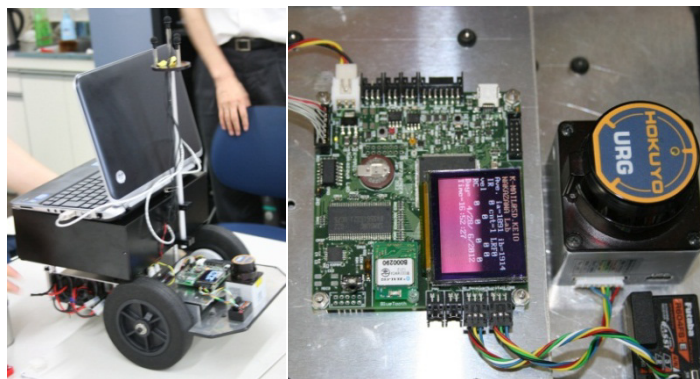


Fig. 4. Robotic Platform

(b) Robot Controller

The motor control system of the robot is composed of several modules with connecting the SH2A (Renesas Electronics R5F72167ADF, 200MHz) CPU with

ROM, SRAM, and SDRAM. The robot's steering mechanism is the two powered wheel steering, and the driving motor is the Maxon A-max22 (6W) with reduction gear ratio 25.6:1. The rotation angle control is performed by the rotary encoder system (HEDL5540, 500CPT). In this setup the motor control is controlled solely by the velocity. The electric battery mounted in this robot is set to 28v3.9AH and its life is about 5 hours.

4 Experiments and Results

The scene of audio source tracking experiment is shown in Fig.5. Real time tracking of two moving speakers is illustrated in Fig. 6. Other experimental results will be presented.



Fig. 5. Scene of experiments

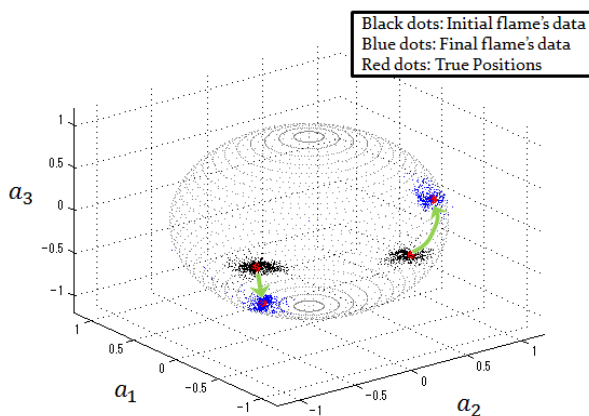


Fig. 6. Experimental results for two sources real time tracking

5 Conclusions

An artificial robot audition system for detecting and tracking of sound sources is proposed. A novel DOA estimation method presented here is applicable for arbitrary array configuration and even for underdetermined case by exploiting the time-frequency approach. The modes of the proposed kernel density estimator for a set of selected data determine the corresponding source directions. Then mode seeking issue can be solved by the mean shift algorithm which is proved to be suitable for real time tracking. The developed mobile robot systems on which audio signal processing and robot controller system are mounted are connected by a wireless link. To verify the effectiveness of our system in real environments several experiments are conducted and tracking ability is evaluated. For future problems, speaker identification and speech recognition by applying the speech separation mechanism are required for realizing real time human-robot communication system.

Acknowledgements. The authors would like to appreciate Dr Toshiyuki Murakami and Dr. Yasue Mitsukura for their valuable suggestions on this study. The first author especially appreciates the committee of EMARO (Europian Master on Advnced Robotics) program for their support.

References

1. Kwon, B., Park, Y., Park, Y.-S.: Sound Source Localization for Robot Auditory System Using the Summed GCC Method. In: International Conference on Control, Automation and Systems 2008, COEX, Seoul, Korea, October 14-17 (2008)
2. Nakadai, K., Nakajima, H., Murase, M., Okuno, H.G., Hasegawa, Y., Tsujino, H.: Real-Time Tracking of Multiple Sound Source by Integration of In-Room and Robot-Embedded Microphone Arrays. In: International Conference on Intelligent Robots and System, Beijing, China, October 9-15 (2006)
3. Huang, J., Ohnishi, N., Sugie, N.: Building ears for robots: sound localization and separation. *Artif. Life Robotics* 1, 157–163 (1997)
4. Valin, J.-M., Michaud, F., Rouat, J.: Robust localization and tracking of simultaneous moving sound sources using beamforming and particle filtering. *Robotics and Autonomous System* 55, 216–228 (2007)
5. Hosoya, K., Ogawa, T., Kobayashi, T.: Robot auditory system using head-mounted square microphone array. In: The 2009 IEEE/RSJ International Conference on Intelligent Robotics and Systems, St. Louis, USA, October 11-15 (2009)
6. Asoh, H., Hara, I., Asano, F., Yamamoto, K.: Tracking human speech events using a particle filter. *IEEE Trans.*, 1153–1156 (2005)
7. Arberet, S., Gribonval, R., Bimbot, F.: A Robust Method to Count and Locate Audio Sources in a Multichannel Underdetermined Mixture. *IEEE Trans. SP* 58(1), 121–133 (2010)
8. Ding, N., Hamada, N.: DOA Estimation of Multiple Speech Source from a Stereophonic Mixture in Underdetermined Case. *IEICE Trans. Fundamentals* E95-A(4), 735–744 (2012)

9. Fujimoto, Ding, N., Hamada, N.: Multiple Sources' Direction Finding by using Reliable Component on Phase Difference Manifold and Kernel Density Estimator. In: IEEE ICASSP 2012, pp. 2601–2604 (March 2012)
10. Cheng, Y.: Mean Shift, Mode Seeking, and Clustering. IEEE Transactions on Pattern Analysis and Machine Intelligence 17(8), 790–799 (1995)
11. <http://www.ros.org/wiki/>

Development of Software and Hardware of Entry-Level Vision Systems for Navigation Tasks and Measuring

S.M. Sokolov, A.A. Boguslavsky, A.I. Vasilyev, and O.V. Trifonov

Keldysh Institute for applied mathematic Russian Academy of Sciences, Moscow
`sokolsm@list.ru, {anbg, ahvac, tob}@imail.ru`

Abstract. The article describes methodical and practical aspects for equipping mobile facilities with computer vision systems in order to solve navigation and measuring tasks. There is an overall schematic of software and algorithmic support of the integrated information system based on computer vision for mobile facilities. There described principles of building-up such systems and there provided possible options for software and hardware arrangements. There emphasized questions concerning the automation for operations of calibration of some components of measuring section and that of interconnection of various heterogeneous systems. There are examples of implementing integrated information system for navigation and measuring tasks.

Keywords: vision system, global and local navigations, architecture of on-board systems, component programming, real time, and noncontact measurements.

1 Introduction

Goal-oriented shift of mobile facilities is not possible without solving the navigation task. With the traffic control by a person this task has been quite successfully solved since the times of the first sailors and travelers. For providing navigation for automatic devices there are also known a lot of successful solutions using inertial navigation systems, ultrasonic systems, radars, LIDARs, and navigation satellite systems. Most of these solutions assume some motion in large open spaces (aviation, cosmonautics, sailing, and long-distance communication) or in clearly determined conditions inside the premise.

The provision of goal-oriented motions in complicated, changing conditions along complicated trajectories and without permanent visibility of satellites, requires an integration of various navigation means and mainly active use of visual information enabling to effectively select, describe and find orienting points in the environment. Until recently the automation of collection and processing of visual data with the required accuracy and in real time scale in the available computer base was impossible. That is why modern navigation and guidance systems as an integrative source use a human-operator who summarizes the data from all the transmitters,

analyses television and other images of the scene, makes necessary measurements, and executes directions of the orienting points or target designation. This sort of tasks requires serious nervous and physical tension, makes the operator tired and is not always performed with the required velocity and accuracy. With the development of means for visual data collection and processing and with the rise of computer capacities, there become open more and more possibilities of automating visual operations, in particular, those of image identification, creation of synthetic images integrating data from several ranges, and improvement of the quality of original images. Automation partly takes some routine burden from the operator and, in some cases, enables to automatically solve the navigation task at full volume.

The complexity and variety of visual data processing tasks, absence of unified formalisms for describing complicated scenes, have resulted to the situation when existing software and hardware solutions for visual tasks differ in big variety and poor integration of program platforms and environments for integrating systems of transmitters and execution of algorithmic supply of the upper level, i.e. the managerial level [10]. The overcoming of above-mentioned difficulties makes the system developers any time overcome the “zero” cycle of supplying the source environment of development and integration of already known / available algorithms in execution for specific task.

Another problem on the way of installing technical visual systems is the complexity of their calibration and bringing various data to the unified coordinate grid, removal of “human factor” from the correspondent algorithms.

It is worthy to pay special attention on the problem of providing reproducibility of the system operation. This problem of setting-up the software is especially acute for the real time visual systems. In real time scale it is necessary to record both the processed data and the condition parameters for all the elements of the information system of the mobile features.

We propose the homogenous environment of development and frame of application programs enabling to successfully solve a wide range of tasks, requiring interconnection of many subsystems based on the system for visual data collection and processing as the most resource-intensive and complicated one in algorithmic supply [8].

2 VS Structure and Means

Automated integrated information system of the mobile features shall solve the following tasks.

- Collect data from all the components of the so-called navigation cross, i.e. operator's instructions; cartographic; satellite; transmitters/registering subsystems, i.e. visual (may be from various field of views and/or multispectral); range data; inertial; reckoning [1, 3].

- Synchronizes the collected data.
- Determines position and orientation of the mobile features on which there installed information system or position of the surveillance objects in the vision area of the vision system.
- Shows to the operator the cartographic or other information characterizing relative position of surveillance objects or information system and external objects.

Based on the experience of development of several dozens of computer vision systems and analysis of software and hardware component of the technical visual system available on market there have been defined elements and means both for the stage of development/setting-up the specific information system, and for the creation of on-board version of the software [2, 4, 5, 9, 10].

Main components of the system:

- DBMS and special Data Base;
- Heterogeneous distribution computing environment (with wire and wireless communication channels);Header: 1,4 cm;
- Unified packages of data exchange;
- Transformers of external digital/analogue signals into the signals of common bus (CAN, USB, GigE);
- Computing units (IBM PC of compatible architecture);
- GigE Vision cameras;
- GPS/GLONASS receivers;
- Accelerometers;
- Supply units;
- Software and algorithmic supply (based on language C++);
- External transmitters (optionally).

We'll comment the choice of the above-mentioned components. The specific peculiarity of applying the Data Base in the reviewed Computer Vision Systems is the necessity to store various data, among which there are big volumes of data from different type transmitters. Due to this fact the structure of the Data Base (hereinafter DB) is built up on the basis of relational model with the use of references to the external files with the data from different transmitters. For example, these may be files of video sequence or range measurements. For the data of every type in the relational Data Base there stored a heading enabling to operatively extract data in linkage to the position/time in the process of measurements. Separate way of data storage enables to reduce time to store big structured data files of the relational DBMS, which is necessary in order to provide operation in real time.

Specific attention should be paid to communication channels in computing environment of the information system. Taking into account the mobility of the whole system and possibility of applying several vision fields in one Computer Vision System wireless channels are more preferable. With account of achievements in the carrying capacity (up to 2 images of high definition with 25Hz frequency),

remoteness, reliability in data transmitting and availability of corresponding equipment, the system communications are based on wireless Ethernet network with unified packages of data exchange. In case of necessity to provide exchange with other buses, transformers are used.

Among computing facilities IBM PC gives preference to compatible architecture and evaluators equipped with cross-software for programming with the use of general computers.

Camcorders of any range are one of the most important elements of the Vision System. Big spectrum of proposals and various, quite often contradictory requirements of the visual analysis tasks require special examination of the features of this component of the computer viewing.

Definition of the above-mentioned components of VS with the enlisted characteristics together with software patterns enable to operatively, minimizing the total cost of ownership, create, set up, and follow a wide range of information systems based on the Vision Systems [3, 4, 5, 6, 9, 10].

3 Principles of Setting Up Software and Hardware Support of VS

As said before differential peculiarity of the described developments is an automatic computer analysis of incoming data in real time. Intellectual information systems propose not a postponed analysis of shot video-information "manually", but receiving finished data for control tasks or making solutions about sending maintenance teams to the indicated addresses. Specific algorithmic support [10] enables to reach such results, and the following principles of building-up the software and hardware support.

- Component hardware support;
- COTS (commercial off-the-shelf) technology (when creating prototypes);
- Open system: external data of additional systems or under standard protocol, or in discussed format; extensible data base; portability of the hardware;
- Control over the real time scale;
- Provision of reducibility of the system operation.

The framework is a prototype of the VS application, which is designed for completion in a specific applied task.

The framework architecture based on three parallel subsystems (fig. 1):

- subsystem for video capturing (visual data input)
- user interface subsystem (GUI)
- image processing subsystem

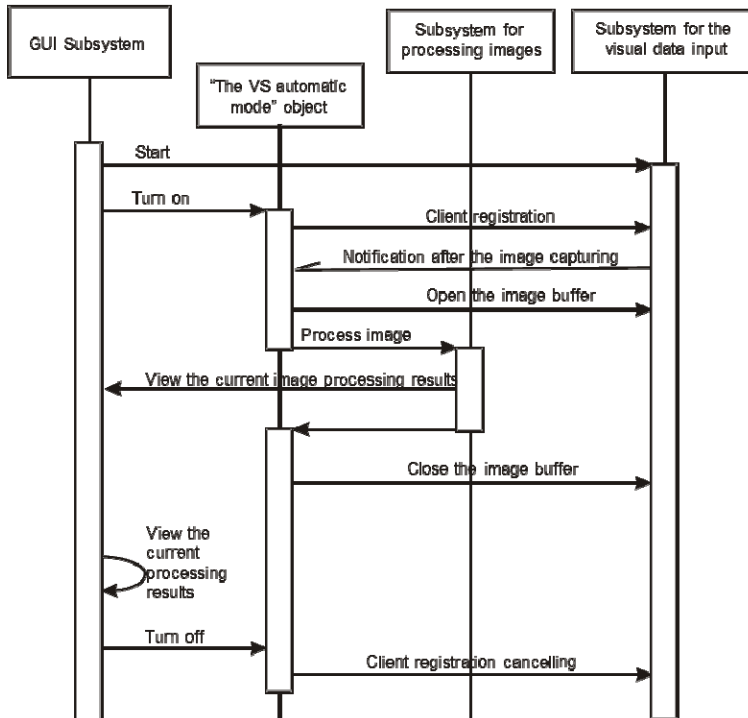


Fig. 1. VS operative mode. Subsystem coordination task: implemented in modes objects.

High-level algorithms design (for concrete VS) is based on the composition of algorithms for processing images of various classes (fig 2).

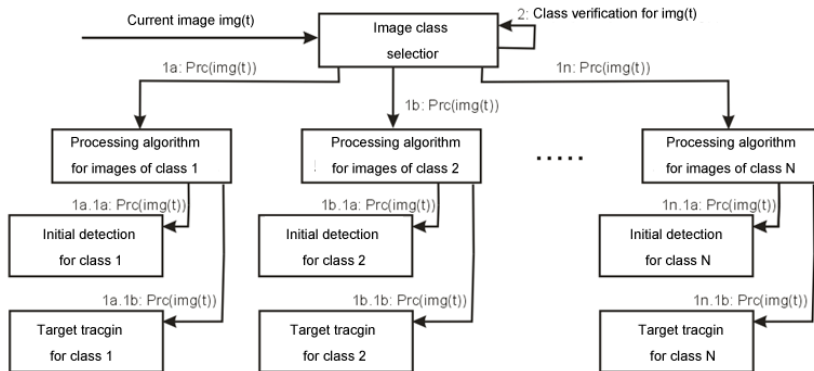


Fig. 2. Operations of the VS software for the current image processing

COTS technology enables to arrange information systems remaining within the economic expediency and within short time.

Following the concept of open systems provides operative interconnecting in the system of data of various sensor systems, reusing of the data base structure in various information systems, software portability to various software and hardware platforms.

Control over the real time scale on all the stages of the development of the information systems provides creation of systems for information support of real time.

Reproducibility of the system operation gives a possibility of adjusting the algorithmic support of processing of real scenes and increases reliability of obtaining processing results. Reproducibility is assured with the data base structure providing the storage of tails from various transmitters binding to the time of measurements and/or motion trajectory of mobile features.

4 Options for Software and Hardware Arrangements

General scheme of software algorithmic support and principles of building up the integrated information system based on computer vision for mobile features assume various options of specific software and hardware arrangements. These arrangements are determined by conditions of the information system operation, desired independence indices, variety of solving tasks, and required accuracies, issues of economic expediency.

In the description of the software and hardware arrangements we will keep this division of the described information systems into hardware blocks, i.e. data acquisition unit (DAU), computing control block (CCB), communication block (CB), block for display and further processing (BDFP). DAU is a block which task is registration in this or that form of electric signal corresponding to concerned physical magnitude. Most often this form is a digital signal; although with exceptions requiring additional devices converting analog signal into the digital form. Examples of DAU are the following: digital/analog camcorder, 3D scan, accelerometer, compass, strap-down inertial reference system. CCB is a block which task is to range the operation of data acquisition modules and processing of incoming data with the purpose to receive necessary information. CCB implementation is an evaluator equipped with software and algorithm support. Examples of computing control blocks are the following: mobile system block, server, DSP. BDFP is a block which task is to reflect information received from CCB to the operator and, if necessary, to additionally process the received data (including the integration of information received from several CCB). BDFP implementation is an evaluator equipped with software and algorithm support and results reflecting devices. BDFP examples are the following: laptop, workstation. CB is a block which purpose is to supply the other information system blocks with data exchange. CB implementation is a communication channel.

As said in the introduction, until recently in the information systems of mobile systems the most frequently used was the segregation of data acquisition unit on the mobile facility with the subsequent, postponed analysis of the collected data on the fixed or movable, though more powerful computer aids with direct human participation.

The purpose of our developments is to create VS in real time scale. VS modules are arranged with account of maximum automation of collecting and processing visual data and advanced independence level. Human participation is assumed in the most complicated conditions and with more degree of uncertainty in describing visual analysis and interest subject.

We'll give examples of unified options to arrange information systems.

DAU with monocular camcorder, CCB (mobile system block of low energy consumption), CB (Wi-Fi transmitter with system POE), accumulator integrating construct, i.e. thermal coating and multi-purpose fitting.

DAU with stereo-system, CCB (mobile system block of low energy consumption), CB (Wi-Fi transmitter with system POE), accumulator integrating construct, i.e. thermal coating and multi-purpose fitting (fig.1).

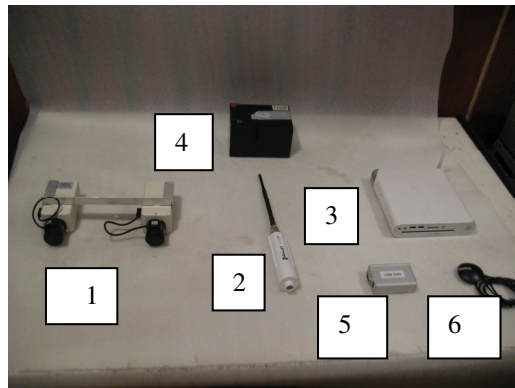


Fig. 3. An example of the stereo VS module hardware

1- data acquisition unit - a stereocamera; 2 - communication block - Wi-Fi transmitter; 3 - computing control block; 4 - the power unit - the accumulator; 5-converter USB-CAN; 6- GPS aerial

DAU with monocular camcorder and structured lighting block based on spherical drives of direct control, CCB with BDFFP (laptop with specific software and algorithm supply), external position detectors (strap down inertial reference system), and odometer.

These options have been successfully used when creating VS: for operative mapping [10]. For control of infrastructure objects of automobile, railway, subway [5].

5 Automation of Auxiliary Operations

When implementing VS, solving the task of information support in total, the obstacle on the way of successful practical use is often adjusting and auxiliary operations requiring big quality manual actions.

When creating a video path of VS, there usually encounter two contradicting requirements: the biggest possible one-time coverage of the environment (wide angle of the vision area) and high accuracy of measurements at different distances from the camcorder to the object. The most attractive (simple and quite available) method of overcoming this contradiction is the choice of the optical system with the wide visual angle and transformer light-signal with big quantity of elements. Similar optical system requires the removal of optical distortion (presence of the transformation eliminating harmonic distortions of the optics). This task is not a new one and there are a lot of corresponding algorithms which main point is to present to the system the prototype objects with known geometrical correlations and indication of visions of these objects on the images [11-15].

For application of video cameras for the purpose of measurements of objects coordinates of an observable scene their preliminary calibration - definition of internal parameters of the camera is required. Thus for stereocamera definition of mutual position and mutual cameras orientation (external camera parameters) is required also.

The most widespread approach of camera's parameters definition is the photogrammetric approach. It is based on minimizing the reprojection error. For the account distortions in model of the perspective camera (restoration of an ideal projection) is used the following reception.

$$\vec{D}(\vec{p}_d - \vec{p}_0) = -f \cdot \begin{bmatrix} \frac{x}{z} & \frac{y}{z} \end{bmatrix}^T \quad (1)$$

where \vec{p} - point co-ordinates on an image plane, \vec{p}_0 - co-ordinates of the main point (crossing of an optical axis and an image plane), f - camera focal length, $[x \ y \ z]^T$ - spatial coordinates of an observable point in cameras system of coordinates; \vec{p}_d - coordinates observed (and deformed owing to distortion) points on the image concerning its center, \vec{D} - a vector function defining distortion model, for example, polynomial Brown model [15].

$$\vec{D}(\vec{\rho}) = \vec{\rho} + \vec{\rho} \cdot \sum_{i=1}^N k_i \cdot \|\vec{\rho}\|^{2i} + \begin{bmatrix} \|\vec{\rho}\|^2 + 2\rho_x^2 & 2 \cdot \rho_x \rho_y \\ 2 \cdot \rho_x \rho_y & \|\vec{\rho}\|^2 + 2\rho_y^2 \end{bmatrix} \cdot \begin{bmatrix} t_1 \\ t_2 \end{bmatrix} \quad (2)$$

where k_i - radial distortion parameters (usually no more than three parameters), t_i - tangential distortion parameters (usually two parameters).

For the purpose of calibration of internal camera's parameters, and definitions of mutual position and orientation of stereocamera have been developed two program modules: the first - for marking of observable points of a scene on images (fig. 4), the second - for calculation of parameters of each camera and a stereosystem (tab.1,2).

The key thing for practice is a segregation of visions of objects on the image. This task is traditionally allotted on a person who "if necessary" (in making calibration measurements) shows to the system about one hundred of points corresponding to the

datum points of the prototype object. In our approach we follow auto-calibration methods.

Operations of determining prototype objects on the images are executed automatically. On fig. 4c there is an example of automatic segregation of distinguished points of the prototype objects. The control points recognition rate is about 93%. Automation reduces calibration time approximately in 10 times.

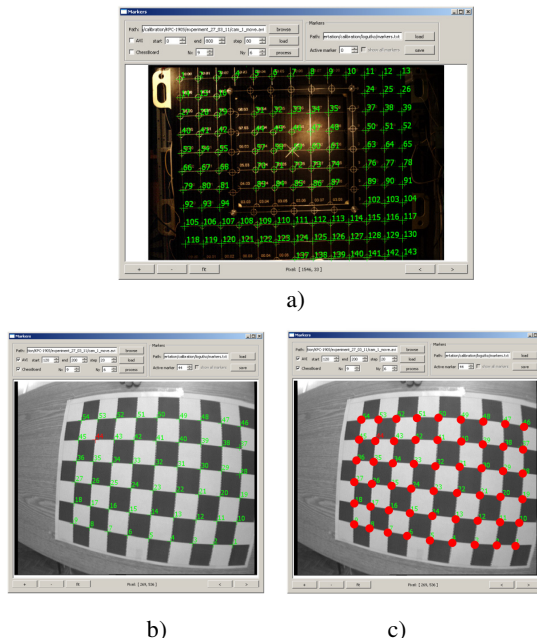


Fig. 4. An example of the interface for work with the module of preparation the test data:
a) - a control table of the test object; b) - the image of the test object with designations of control points; c) - result of automatic extraction of control points; the passed points can be specified by operator.

In the calculation module calibration with the distortion account in the form of restoration of an ideal projection (1), (2) is realized. The example of calculation of parameters of a stereosystem is resulted in tables 1 and 2.

Table 1. Parameters of the left field of view camera

<i>Focal length (on width/height), in pixels</i>	(538.761; 574.814)
<i>Coordinates of the main point, in pixels</i>	(362.103; 268.525)
<i>Radial distortion factors (r_1, r_2, r_3)</i>	-0.41487 0.338228 -0.134554
<i>Tangential distortion factors (t_1, t_2)</i>	0.00924159 -0.00609062

Table 2. Parameters of the right field of view camera

<i>Focal length (on width/height), in pixels</i>	(538.761; 574.814)
<i>Coordinates of the main point, in pixels</i>	(362.103; 268.525)
<i>Radial distortion factors (r_1, r_2, r_3)</i>	-0.41487 0.338228 -0.134554
<i>Tangential distortion factors (t_1, t_2)</i>	0.00924159 -0.00609062

Comparison of results of measurements by means of a stereosystem before calibration are shown in drawings 5 and 6. In drawing 5 distance to observable object, in drawing 6 an error of measurement of the relative sizes of observable object (object's size is 1,5 m). The distance from object to chambers varied from 2 to 5m, thus the greatest errors (fig. 6) were observed, at a finding of object on the brink of images.

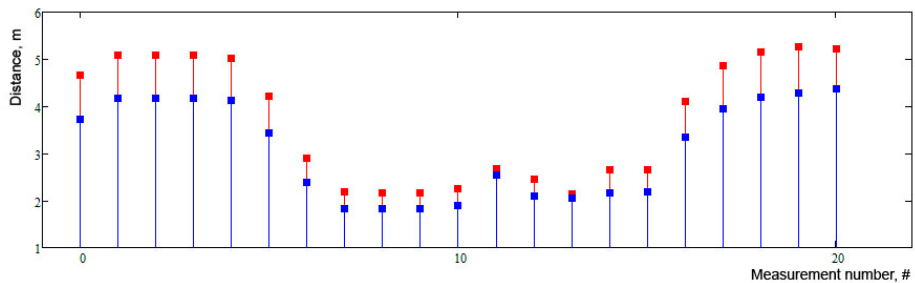


Fig. 5. Estimation of distance to object of interest by means of calibrated (red color) and not calibrated (dark blue color) stereosystem. On an axis of abscises the measurement number, on an axis of ordinates distance to object, m is shown. With increase of a distance to an object of interest the role of calibration parameters grows.

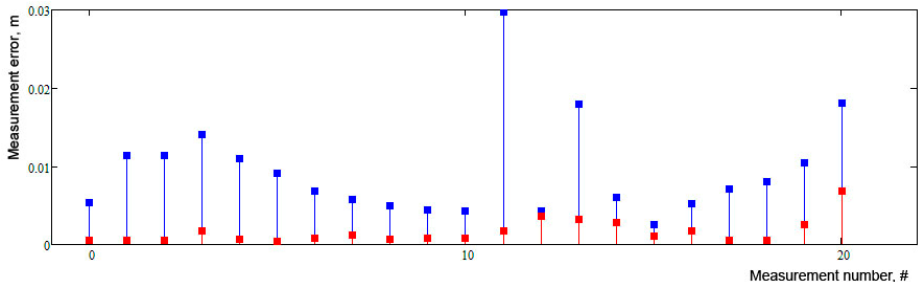


Fig. 6. Estimation of accuracy of measurement of the object size by means of calibrated (red color) and not calibrated (dark blue color) stereosystem. On an axis of abscises the measurement number, on an axis of ordinates a measurement error, m is shown. The chart shows value of calibration for measurement accuracy.

6 Experiment

Working capacity and accuracy of offered decisions was tested on measurement of distances to the set/specifyed objects in stereosystem field of views. Indoor the laboratory stereosystem (fig. 3) (camera focal length 3.5 mm, image sizes 720x576 pixels, stereo base 200 mm) was used and distances from 1 to 5 m. Outdoor - stereosystem on a vehicle (fig. 7) (camera focal length 3.5 mm, image sizes 720x576 pixels, stereo base 1450 mm) were measured and distances from 5 to 300 m [9].



Fig. 7. Mobile complex for operative mapping with the mounted stereosystems

When segregating the distinguished points for measuring distances in cases of unknown in advance or unclearly described objects in the considered VS there may be applied several complementary methods, i.e.:

- Using the model of the object image to find images corresponding to the model, in various vision areas.
- Application of the forecast for positioning the distinguished points of the object images found in one of the vision areas to reduce the search domain in the other areas. For the purpose of computation of positioning the distinguished points there may be applied a calculation with the use of calibration parameters of the utilized stereo-system.
- In complicated cases when auto-detecting is not possible to perform, the indication of the distinguished points is be performed by an operator with account of automatic search tools in the restricted area of interest (fig. 8).



Fig. 8. An example of high-precision extraction of characteristic points on images of objects of interest. In the left field of vision the image is extracted automatically, in right site more precise extraction is carried out with participation of the operator.

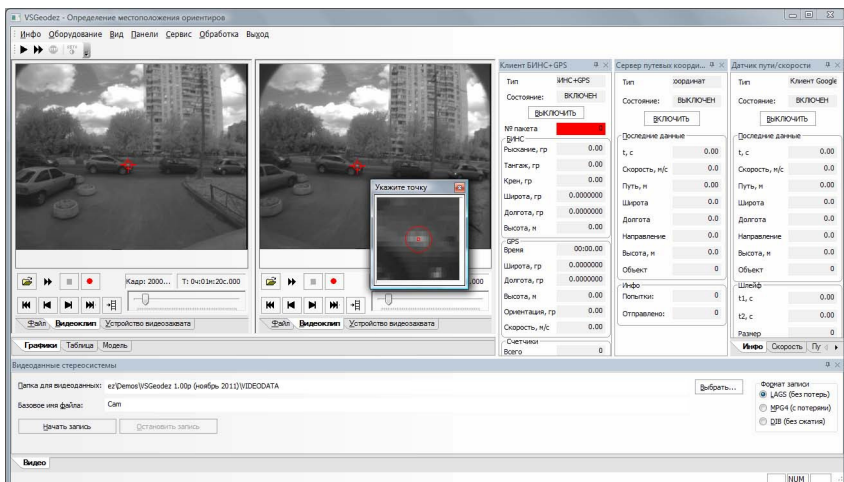


Fig. 9. The screen of the program realizing a binding and measurement of objects from a board of a moving vehicle on the basis of association of the visual data of a stereosystem, platformless inertial navigating system, satellite navigating system, onboard notation of a way

Measurements of the objects sizes in field of view economically expedient stereosystem with the account of correctly spent calibration are carried out with precision not worse 1 % in a wide range.

Integration and cooperative processing of signals GPS/GLONASS and local navigation system. When the signal of GPS receiver disappears for a short duration (till 30 sec) the current coordinates of the mobile facility are approximated based on reckoning the distance covered and accepting hypothesis of keeping the straight line motion with the mobile facility. In cases if the information system is equipped with the strap down inertial reference system or system of accelerometers, it is possible to reconstruct a more complicated motion trajectory of the mobile facility and, as a consequence, possible to determine a position of the mobile facility in the

Geographical Reference System even having long-term omissions of satellite signals (till 20 min). For approximation there may be used the latest error-free information referring the motion direction received from GPS and data of the on-board odometer of the mobile facility. Data from all subsystems are synchronized according to the time of on-board computer network.

For vehicle navigation the inverse problem is solved: definition of geographical coordinates of the vehicle according to measurements of position of coordinates of known objects in stereosystem field of view. Positioning of a vehicle on the basis of position calculation on external reference points allows remaining in borders of accuracy GPS/GЛОНАСС of a binding (without use of the last).

7 Conclusion

The work proposes, describes and discusses methodical and practical issues of creating navigation and measuring systems of mobile facilities based on Vision System. The work shows that the level of developing tools of building-up video-data, computer and communication features in incorporation with specific software and algorithmic support and observing the principles of modern program systems enables to create complex cost-effective information systems with active use of visual data.

The special attention is given questions of visual system calibration and allocation of characteristic points of the image in the course of measurements.

The combination of the automated technologies and riches of aprioristic knowledge of manual processing of images allows reaching split-hair accuracy and reliability of objects coordinates measurements on the basis of the visual data.

Efficiency of the proposed approaches and solutions is proved with examples of successful implementation in the operating systems.

Measurements of the objects sizes in field of view economically expedient stereosystem with the account of correctly spent calibration are carried out with precision not worse 1 % in a wide range.

Positioning of a vehicle on the basis of position calculation on external reference points allows remaining in borders of GPS/ГЛОНАСС accuracy of a binding (without use of the last).

Acknowledgements. This research has been supported in part by RFBR grants №11-08-01945 and №11-08-13166.

References

1. Platonov, A.K., Zueva, E.J., Kirilchenko, A.A., Sokolov, S.M.: Formalistic to designing of algorithms of mobile systems information support (path planning, navigation, reliability), Keldysh Institute for applied mathematics RAS. Moscow. Preprint №19, 32 pg (2008) (in Russian)
2. Boguslavsky, A.A., Kirilchenko, A.A., Platonov, A.K., Sokolov, S., Trifonov, O.V., Yaroshevsky, V.S.: Construction of the environment description in information support systems of mobile robotics complexes. In: Mechatronics, Automation and Control, 12, pg. 50, the appendix, pp.15–24 (2008) (in Russian)

3. Sokolov, S.M., Boguslavsky, A.A., Platonov, A.K., Kiy, K.I., Gorelik, L.I., Filachev, A.M., Fumin, A.I.: An IR Channel-Based Automated Driver Assistance System. In: 12th International Conference on Systemics, Cybernetics and Informatics, WMSCI 2008, vol. I, pp. 126–131 (2008)
4. Platonov, A.K., Sokolov, S.M., Boguslavsky, A.A., Trifonov, O.V.: Multipurpose system of vehicles information support. In: Proceedings of the International Conference Progress of Vehicles and Systems 2009, Volgograd, pp. 95–96 (2009) (in Russian)
5. Platonov, A.K., Sokolov, S.M., Sazonov, V.V., Boguslavsky, A.A., Trifonov, O.V., Kuftin, F.A., Vasilev, A.I., Moksin, K.A.: Hardware-software complex of mobile systems navigation facility. Questions of Defensive Technics (1-2), 47–55 (2010) (in Russian)
6. Sokolov, S.M., Platonov, A.K., Boguslavsky, A.A., Kuftin, F.A., Moksin, K.A.: Contactless odometry as a part of onboard navigating systems. News SFU. Engineering Science 3, 64–68 (2010) (in Russian)
7. Sokolov, S., Boguslavsky, A.A.: Component technology of debugging for real time vision system. In: Proceedings of the 1st Conference Methods and Means of the Information Processing, Moscow, pp. 304–310 (2003) (in Russian)
8. Sokolov, S.M., Boguslavsky, A.A.: Component a skeleton for working out of the real time Vision system software. In: Proceedings of the 2nd Conference Methods and Means of the Information Processing, Moscow, pp. 337–343 (2005) (in Russian)
9. Sokolov, S., Boguslavsky, A.A., Vasilev, A.I., Trifonov, O.V., Nazarov, V.G., Frolov, R.S.: A mobile complex for operative creation and updating of navigation maps. News SFU. Engineering Science 3, 157–166 (2011) (in Russian)
10. Sokolov, S.M., Boguslavsky, A.A.: Intellectual Images Processing for a Realtime Recognition Problem. In: 2nd International Conference on Complexity, Informatics and Cybernetics, IMCIC 2011, vol. II, pp. 406–411 (2011)
11. Clarke, T.A., Fryer, J.G.: The Development of Camera Calibration Methods and Models. Photogrammetric Record 16(91), 51–66 (1998)
12. Salvi, S., Armangu, X., Batlle, J.: A comparative review of camera calibrating methods with accuracy evaluation. In: Pattern Recognition (2002)
13. Tsai, R.Y.: A Versatile Camera Calibration Technique for High-Accuracy 3D Machine Vision Metrology Using Off-the-Shelf TV Cameras and Lenses. IEEE J. of Robotics and Automation RA 3(4), 323–344 (1987)
14. Zhang, Z.: A flexible new technique for camera calibration. IEEE Trans. on PAMI 22(11), 1330–1334 (2000)
15. Brown, D.C.: Close-Range Camera Calibration. Photogrammetric Engineering XXXVII(8), 855–866 (1971)

Development of a Quadrocopter Robot with Vision and Ultrasonic Sensors for Distance Sensing and Mapping

Seung-Jae Lee and Jong-Hwan Kim

Department of Electrical Engineering, KAIST,
335 Gwahangno, Yuseong-gu, Daejeon 305-701, Republic of Korea
{sjlee,johkim}@rit.kaist.ac.kr

Abstract. The objective of this paper is to build a map using a quadrocopter. In order to explore the surroundings and build a map, ultrasonic sensors and a camera sensor are used. As ultrasonic and camera sensors get information separately, they have to be synchronized. Through this synchronization, the location of the quadrocopter can be determined. At that point, the four cardinal points can be calculated by rotating the quadrocopter. The map is then built through the reconstruction of information collected from a camera and ultrasonic sensors. The effectiveness of this scheme is demonstrated in a real environment.

Keywords: Quadrocopter, Localization, Synchronization.

1 Introduction

Unmanned Aerial Vehicle(UAV)s have been mainly used in military field for reconnaissance, observation, information gathering and so on. However, they are also used in the private field, such as remote sensing, environmental monitoring, and cartography, because of the development and diffusion of the technology. The fixed-wing UAVs are easy to control compared with rotary-wing UAVs. However, they cannot stay in one place for a long period of time. Thus, they have to rotate in the same circle continuously. They also cannot quickly change their direction. To solve these problems, many researchers have used the rotary-wing UAVs like a quadrocopter. This uses four propellers and can quickly change its direction. Until the early 2000s, research papers about quadrocopters were concentrated on the stable control issue like remote control [1]. Since mid-2000s, many research papers about additional functions of a quadrocopter have been published. Some of these functions are, for example, obstacles avoidance, safe field filming with a camera and position localization using infrared and ultrasonic sensors [2]. There is also another research about a quadrocopter localization and navigation using camera and ultrasonic sensors [3]. In the recent years, a quadrocopter using a laser scanner and a camera sensor was subject of research too [4]. This was made for real-time autonomous navigation in multi-floor indoor environments using an aerial vehicle. A laser scanner scans horizontal spaces and a camera sensor, which is installed in the front side of the quadrocopter, supports positioning. The laser scanner scans the height of the horizontal map according to changes of the quadrocopter's height and

then a computer builds the whole map. In image processing, finding a particular object and recognizing it as a marker is hard work. There is a paper related to marker finding [5]. There are also many papers about localization by using specific markers [6] or using several ultrasonic sensors [7]. But in this experiment, the marker finding method is used. The goal of this paper is to build a map using a quadrocopter. For this purpose, a quadrocopter needs to know the horizontal distances around it and its location. The horizontal distance of the four cardinal points is obtained from four ultrasonic sensors which are located on the top side of the quadrocopter. The location of the quadrocopter is determined by the markers obtained from the camera sensor. The quadrocopter used in this paper [8] has properties such as 10 minutes of runtime with 2 cell 1000mAh Li-polymer batteries and a weight of 244g including battery and Micro Indoor Hull. Its maximum capacity is 400g when 2 cell batteries are used. In this research, a quadrocopter is equipped with a camera sensor and ultrasonic sensors. By integrating x and y positions from a camera and z position from a bottom ultrasonic sensor, it estimates its position. Other ultrasonic sensors are used to avoid obstacles. By using the information obtained from a camera and ultrasonic sensors, it can have some knowledge about its surroundings. Then, the map is built through the reconstruction of that information. The proposed method corresponds to a quick map-building process with low costs. This scheme can be used for accidents explorations such as collapsed buildings, when it is too dangerous for humans to enter.

2 The Method for Localization of the Quadrocopter

For localization, a camera sensor is used to detect a marker and measure the location of the quadrocopter in 3D coordinates and the rotation angles of x , y , z axis related to marker axis. Fig. 1 shows the image, which is obtained from a camera. Since it is a 2D-camera which can represent (x', y') , it cannot represent the real world 3D coordinates directly. Therefore, z' is calculated by using proportional expression. In real world, the

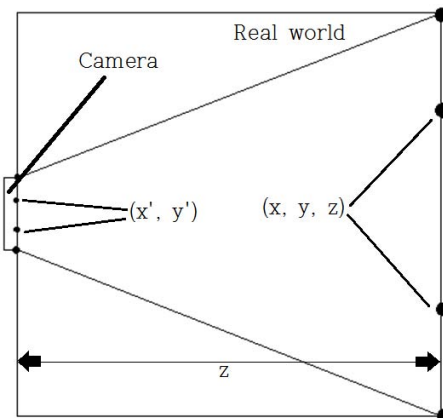


Fig. 1. Camera picture of real world

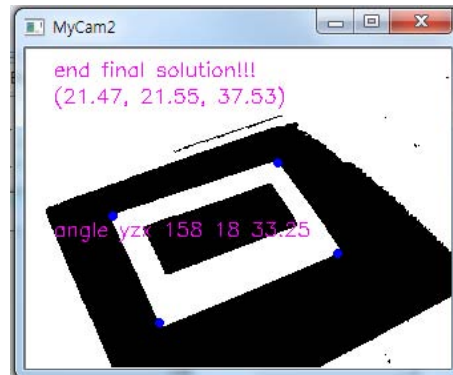


Fig. 2. Location of camera from marker

exact point is located in the direction of vector (x', y', z') . So if z' is decided, the exact one among four markers which are located at each corner can be found by matching the length of the rectangle. By matching the side lengths of a virtual marker and a real marker, the real 3D coordinates of each corner of the marker can be calculated. Then the location of the camera from a marker and the angle of rotation for each axis can be calculated by coordinate transformation from the camera coordinate to the marker one as shown in Fig. 2.

3 Experimental Results and Analysis

A global variable was defined and counted every time step when the distance data obtained from the five ultrasonic sensors were received. The data from the ultrasonic sensors and the camera sensor were matched with a count number. By using these data, the quadrocopter could build a brief map. When five ultrasonic sensors were used, the minimum response time was 20 ms. So 30 ms time delay was defined between distance detection from each sensor. By placing sensors on top of the quadrocopter, it could measure up direction distance. It could avoid upper obstacles when it goes up. Experimental setup for this research was shown in Fig. 3. On the left and the right side, chairs were found. The desks were in the front and back sides. The boxes were at the bottom of the front side.



Fig. 3. Images of surroundings



Fig. 4. Quadrocopter with sensors

3.1 Sensor Information Collection

Fig. 4 shows the complete form of the quadrocopter. The ultrasonic sensors are located on the top, at four directions, and a camera sensor is located at the bottom of the quadrocopter. In this experiment, two types of data were saved. In the first data, the distances obtained from the five ultrasonic sensors were saved. The sequence of the saved data was in order of time, front, left, back, right, and top. In the second data, the camera sensor data were saved. The sequence of the saved data was in order of ultrasonic sensors time, (x, y, z) position, and the angle rotation for three axes.

The camera data were saved in every one or two time step. In the first experiment, the process from departure to landing (about 80 sec) was measured. The overall time from departure, stay at 100 cm height, to landing was 698 time steps for ultrasonic sensor timer. The camera capture time was from 115 to 663 time steps, and 271 pictures were taken. It took two time steps to localization and it was slower than camera capture. It occurred because a marker was not detected. If a marker was not detected, the camera did not capture a picture in this research. Top direction distance changes from 299 cm to 181 cm. Camera location z height was changed from 47 cm to 153 cm. Top distance was changed about 118 cm and z height was changed about 106 cm. Top distance could have an error because of leaning and sensors detection angle. While departure, there was a little rotation and the quadrocopter went up straight. Localization time could be matched with distance data from sensors, and the combination of data provided the information about surroundings. For example, time steps from 115 to 154, the quadrocopter's rotation with y axis was between 6° and 13° , z axis is between -3° and 5° , and x axis was between 177° and 180° . The height was changed from 37 cm to 86 cm (Fig. 3.1). It went up about 48.64 cm. During that time, z distance was changed to 44 cm. If the height was increased, the top sensor distance was decreased. Front sensor distance sustained from 74 cm to 77 cm until 148 time steps, then was changed to 62 cm. Left sensor distance stayed between 36 cm and 43 cm, excluding the early time. Back sensor distance also stayed between 48 cm and 53 cm. Right sensor distance stayed at near 50 cm and was changed to 23 cm approximately. Rotations for three axes were almost same during the experiment, so it could estimate the shape of four directions according to height (Fig. 6). The quadrocopter's lean angle and position are not considered in Fig. 6. About 90 cm, there was the change of distance. The next chair was far, so the left distance increased a lot. Right chair back was blocked by other things with the desk,

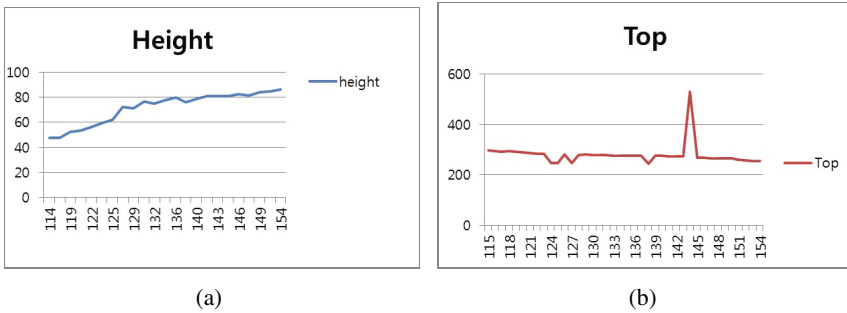


Fig. 5. Height and top distance change according to time

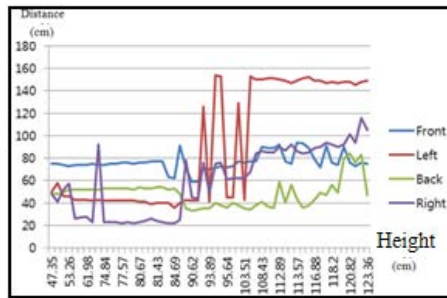


Fig. 6. Distance of horizontal ultrasonic sensors depend on height

so its distance increased a little. Since the lean angle and position of the quadrocopter were not considered this time, it had a huge error and it was hard to know the map surroundings.

3.2 Mapping by Fusion

To measure the quadrocopter's location and leaning angle, the data should be filtered. If the rotation angle, x and y coordinate are the same, the distance data is measured from each parallel plane. By command and filter, the quadrocopter went upward and downward with minimum rotation. In the second experiment, time step was from 0 to 427 time steps for ultrasonic sensors. The camera was started at 25 time steps, and finished at 391 time steps. 99 pictures were captured. Fig. 7(a) shows all distances of ultrasonic sensors with all time, and Figs. 7(b) and 7(c) show distance and height data vs filtered time. If the quadrocopter leans too much, ultrasonic sensors data were excluded. Also, if the marker was not recognized, that time was also filtered. By comparing Figs. 7(c) and 7(d), sudden distance changes were reduced. Its data was depending on time, so it was not able to be used in map building. Fig. 7(d) shows us height changes, it goes up for a long time and go down later. These data and Fig. 7(c) data can be used for map building. This means that each height has four direction distance data, when quadrocopter stably goes up and down.

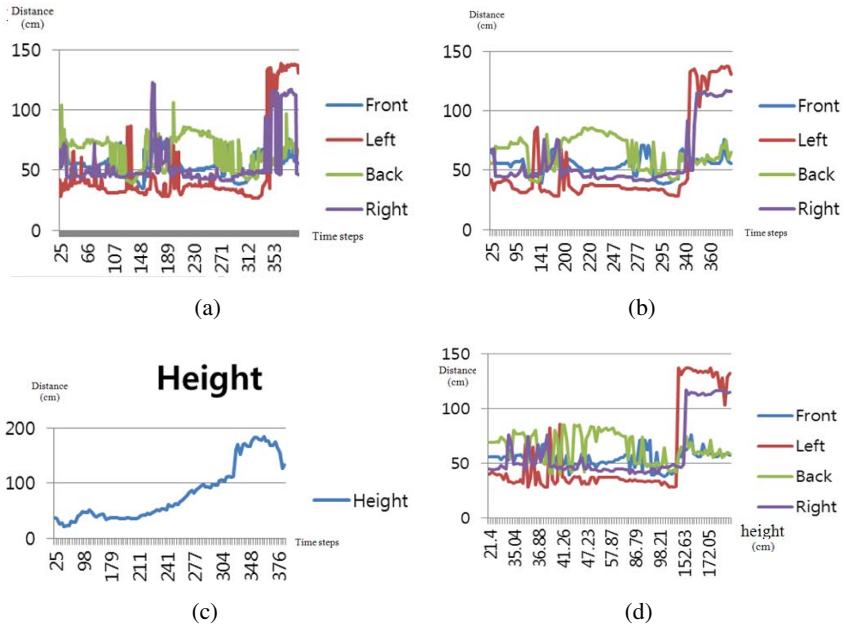


Fig. 7. (a) Distance of horizontal ultrasonic sensors vs time. (b) Distance of horizontal ultrasonic sensors vs time (filtered). (c) Height vs time (Filtered). (d) Distance of horizontal ultrasonic sensors vs height.

Fig. 8 shows each side map according to height. In the front case, boxes and computer were located. Front distance was about 50 cm, and maintained. A height of 90 cm to 110 cm was detected from the desk, because this part had shorter distance. We can estimate that the desk is located about 100 cm as middle. In the left part, almost all the data were about 40 cm until 112 cm. After that, the book shelf was detected with a distance about 130 cm. Back part distance changed a lot. Its reason was that ultrasonic sensor detected the nearest distance of range, and back part was consisted of many objects. Because of these reasons, distance changed a lot, but we could see about 90 cm to 110 cm, it detected the desk. Desk height is same as desk located in front. The right data does not show the chair range of sensor after height about 130 cm. Sensor detects shortest distance of detection range, so errors occurred from 30 cm to 40 cm.

Fig. 9 shows the bottom image obtained by the camera which is a collection of images made as one using panorama. From these data, we could build a map about four directions, bottom and top. Four sides (front, left, back, right) map was made as well with some errors. From this experiment, the quadrocopter could measure all directions of distance including top direction. Computer could make a map of the surroundings by these methods. The bottom side picture could be made as one by using panorama.

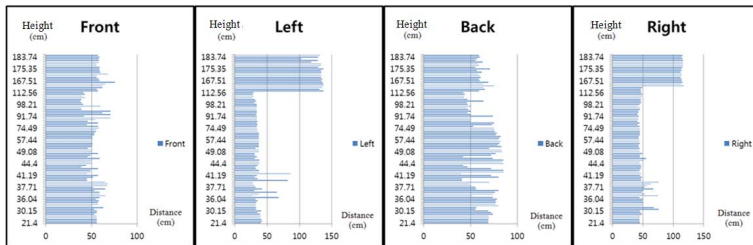


Fig. 8. Distance of horizontal ultrasonic sensors depend on height

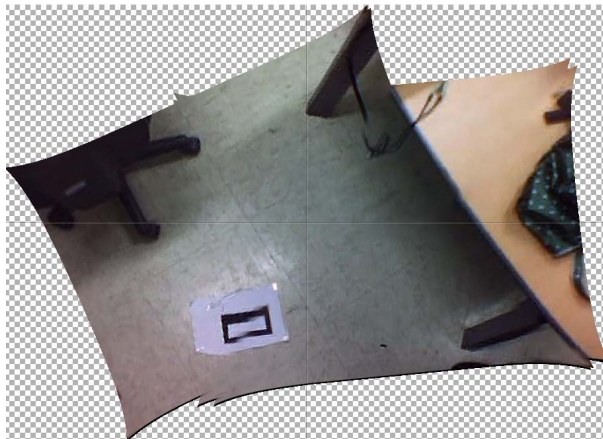


Fig. 9. Bottom image with panorama

4 Conclusion

This paper proposed a map building method using a quadrocopter which was operated with additional equipments like an AVR controller, sensors and a zigbee. A hardware and software for controlling the quadrocopter along with localization were developed. In the experiment, a quadrocopter went up and down without rotation. The bottom map was made by a camera sensor and four direction distance maps depending on heights were made by ultrasonic sensors and a camera sensor. With rotation, the whole map could be built by processing the saved data. If the autonomous movement of a quadrocopter is implemented and the efficient moving algorithm is provided along with this experimental result, a quadrocopter could be used in various fields of society with low costs.

Acknowledgment. This research was supported by the MKE (The Ministry of Knowledge Economy), Korea, under the National Robotics Research Center for Robot Intelligence Technology support program supervised by the NIPA (National IT Industry Promotion Agency) (NIPA-2012-H1502-12-1002).

References

1. <http://www.multicopter.kr/main/index.php?>
2. Park, S., Won, D.H., Kang, M.S., Kim, T.J., Lee, H.G., Kwon, S.J.: RIC (Robust Internal-loop Compensator) Based Flight Control of a Quad-Rotor Type UAV. In: IEEE/RSJ International Conference on Intelligent Robots and Systems, pp. 3542–3547 (2005)
3. Bouabdallah, S., Siegwart, R.: Full control of a quadrotor. In: IEEE/RSJ International Conference on Intelligent Robots and Systems, pp. 153–158 (2007)
4. Shen, S., Michael, N., Kumar, V.: Autonomous Multi-Floor Indoor Navigation with a Computationally Constrained MAV. In: IEEE International Conference on Robotics and Automation (ICRA), pp. 20–25 (2011)
5. Millonig, A., Schechtner, K.: Developing Landmark-Based Pedestrian-Navigation Systems. *IEEE Transactions on Intelligent Transportation Systems* 43–49 (2007)
6. Wang, L., Zhao, G.: A Localization System for Mobile Robots Based Vision. In: 8th World Congress on Intelligent Control and Automation (WCICA), pp. 6671–6675 (2010)
7. Zhao, F.-J., Guo, H.-J., Kenichi, A.: A Mobile Robot Localization Using Ultrasonic Sensors in Indoor Environment. In: Proceedings of 6th IEEE International Workshop on Robot and Human Communication, RO-MAN 1997, pp. 52–57 (1997)
8. <http://www.multicopter.kr/goods/view.php?seq=152>

2D Image Feature-Based Real-Time RGB-D 3D SLAM

Donghwa Lee¹, Hyongjin Kim¹, and Hyun Myung^{1,2}

¹ Department of Civil and Environmental Engineering, KAIST,
291 Daehak-ro, Yuseong-gu, Daejeon 305-701,
Republic of Korea
² Robotics Program, KAIST,
291 Daehak-ro, Yuseong-gu, Daejeon 305-701,
Republic of Korea
{leedonghwa, hjkim86, hmyung}@kaist.ac.kr

Abstract. This paper proposes a real-time RGB-D (red-green-blue depth) 3D SLAM (simultaneous localization and mapping) system. Kinect style sensors give RGB-D data which contains 2D image and per-pixel depth information. 6-DOF (degree-of-freedom) visual odometry is obtained through the 3D-RANSAC (three-dimensional random sample consensus) algorithm with image features and depth information. For speed up extraction of features, parallel computation is performed on a GPU (graphics processing unit) processor. After a feature manager detects loop closure, a graph-based SLAM algorithm optimizes trajectory of the sensor and 3D map. Experimental results show the processing rate over 20 Hz.

Keywords: SLAM, 3D SLAM, RGB-D camera, image features, 3D-RANSAC.

1 Introduction

There have been many researches for the SLAM (Simultaneous Localization and Mapping) problem over the past decade. The initial studies focused on two-dimensional environments, hence they were usually applied to mobile robots [1, 5, 10]. Recently, a variety of 3D SLAM algorithms supports 6-DOF (degree-of-freedom) pose optimization, therefore the SLAM technique is employed in various platforms like quadrotors, underwater robots, etc [7–9].

In the early 3D SLAM studies, expensive sensors like 2D and 3D-LRFs (laser range finders) were mainly used. But with the advent of cheap sensors like the Microsoft Kinect sensor, rapid development of the 3D SLAM area has begun [2–4, 6]. The Kinect sensor contains a depth sensor and a color camera (figure 1). The depth sensor obtains depth data using the IR (infrared) projection method [12]. Figures 1(b) and (c) show a color image and depth data from the Kinect sensor. The Kinect style sensors are called the RGB-D (red-green-blue depth) camera since they give the color image and the depth data concurrently.

Recently, the robotics and computer vision communities have focused on 3D SLAM techniques using the RGB-D camera data. Peter Henry *et al.* [6] used a FAST (Features from Accelerated Segment Test) and the ICP (Iterative Closest Point) method for visual odometry estimation. TORO (Tree-based netwORk Optimizer) SLAM algorithm

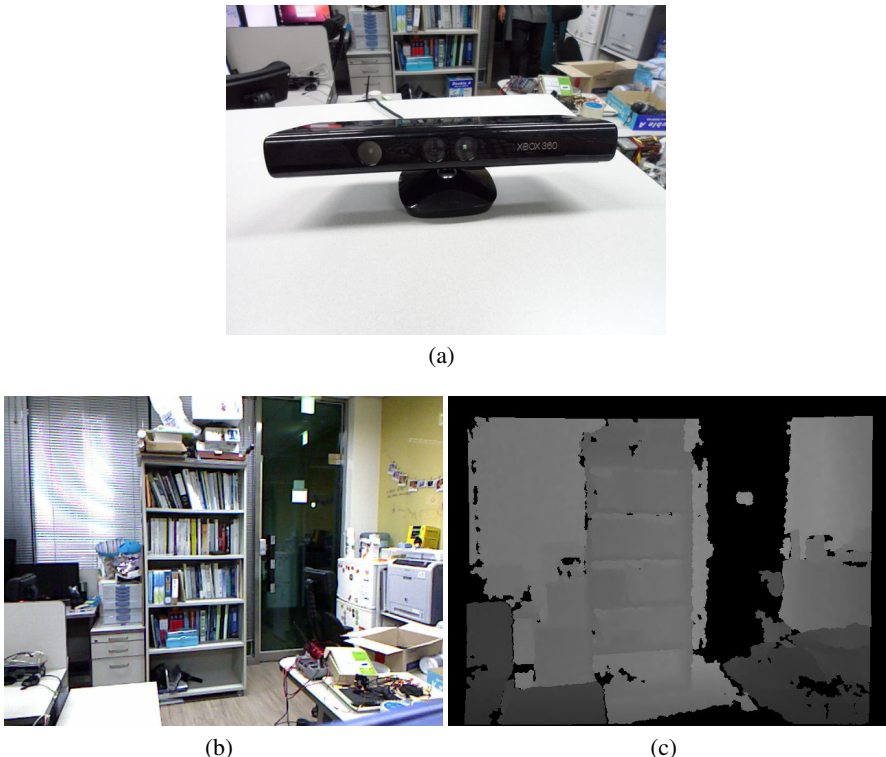


Fig. 1. RGB-D sensor system. (a) Microsoft Kinect sensor. (b) RGB color image. (c) Per-pixel depth data.

optimizes the full trajectory and 3D model. Loop closure detection also makes use of the FAST features. But this work did not operate in real-time. Microsoft Research presented KinectFusion [11] which maps 3D model at 30 Hz using the Kinect sensor and a GPU (Graphics Processing Unit) processor. The GPU processors are specialized in parallel computing, hence they processed the depth data for aligning and mapping 3D model in real-time. But this work has weakness in drift noise, since they did not use the loop closure detection and SLAM techniques. Felix Endres *et al.* [6] implemented and evaluated 3D SLAM with a variety of feature descriptors, the ICP algorithm, and the g2o (General framework for Graph Optimization) SLAM framework. On average, this work has the processing speed of 3 Hz.

In this paper, we propose RGB-D 3D SLAM system which has the processing rate over 20 Hz. The image feature detection is performed on the GPU processor. Visual odometry estimation uses the 3D-RANSAC (RANdom SAmples Consensus) algorithm with image features and the depth data. A feature manager detects loop closure, and then the iSAM (Incremental Smoothing And Mapping) graph-based SLAM algorithm optimizes the full trajectory. iSAM is a high-speed online SLAM core algorithm based on sparse linear algebra [7].

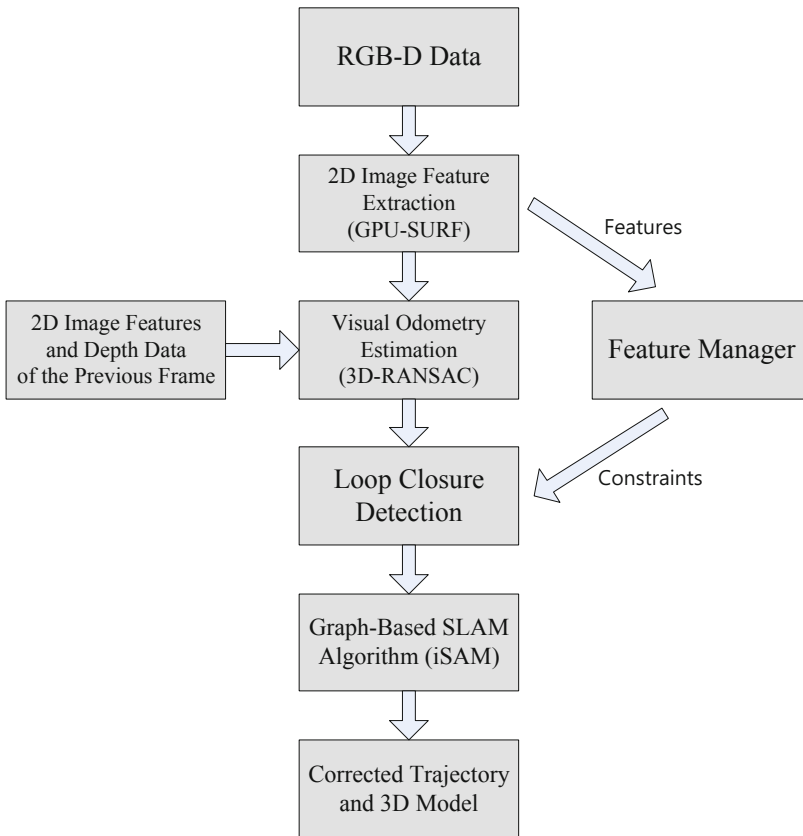


Fig. 2. Overview of the proposed RGB-D 3D SLAM system

The remainder of this paper is organized as follows. The second section presents the proposed 3D SLAM system. The third section provides experimental results. Finally, the last section offers concluding remarks.

2 Proposed 3D SLAM System

Our approach utilizes only 2D RGB image and depth data from a RGB-D sensor. Processing steps of our system are illustrated in figure 2. First of all, 2D image features are extracted. Each feature can be located at a point in three-dimensional coordinate space with depth information. The features are used for 6-DOF visual odometry estimation with feature matching and 3D-RANSAC algorithm. Second, a feature manager gathers the whole features from the previous frames. Through comparison between the current and the preceding features, the current frame is matched to a past trajectory of the sensor. This matching procedure is called loop closure detection. Next, the full trajectory of the sensor is formed by a constraint graph with the visual odometry estimation and



Fig. 3. 2D image feature extraction and matching on a GPU processor. (Left) Previous image frame. (Right) Current image frame.

loop closure detection. After optimizing the constraint graph by the online graph-based SLAM algorithm, the corrected trajectory and the 3D map can be obtained. The whole steps are performed in real-time. Detailed explanation of this system is given in the next subsection.

2.1 Feature Extraction, Matching and 3D-RANSAC

For 6-DOF pose estimation, we extract 2D image features from the incoming color image of the sensor and match to the feature of the previous frame as shown in figure 3. We use SURF algorithm, which is less robust than SIFT algorithm, but its computational speed is faster. Although SURF has speed advantage, it is still hard to implement in real-time on CPU. Recently, GPU-based parallel computing has been applied to the feature extraction algorithms. The GPU-based algorithm allows real-time computational performance. In this system, the feature extraction procedure can handle all of the image data from the sensor in real-time (30Hz image frequency) with GPU-SURF algorithm in OpenCV 2.4.0.

In image feature procedure, feature matching algorithm has heavy computational load. The GPU computing has been also applied to the feature matching algorithm. We used GPU-based brute-force algorithm in OpenCV 2.4.0 for finding the correspondence of the features.

Using the depth information, each feature point has its position in three-dimensional coordinate space. After feature matching between the current and the previous frames, 3D-RANSAC algorithm estimates 6-DOF pose with correspondence and 3D position of the features. 3D-RANSAC algorithm in Point Cloud Library 1.5.1 was used in our implementation.

2.2 Feature Manager and Loop Closure Detection

For visual odometry estimation, it is necessary to keep the features of the previous image frame. But the constraints between the current frame and the frames of the past

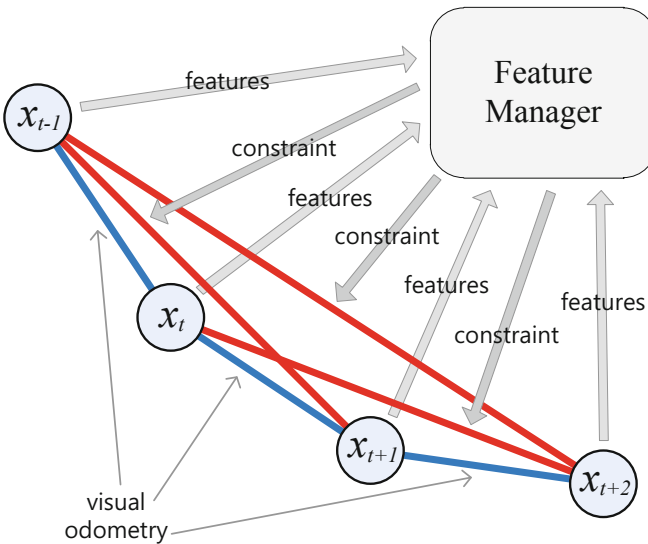


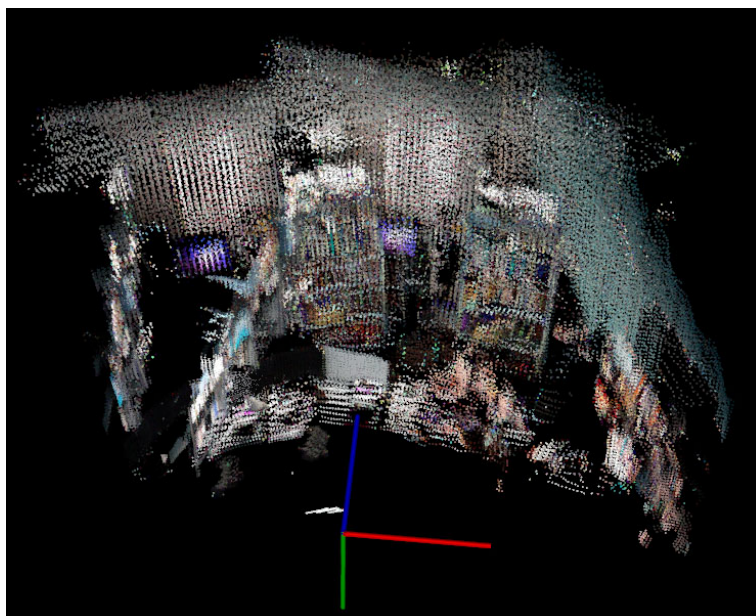
Fig. 4. Feature manager and loop closure detection

trajectory is necessary to optimize the full trajectory by graph-based SLAM algorithms. So, we designed a feature managing part named feature manager as shown in figure 4. After estimating visual odometry, the features of the current frame is sent to the feature manager. The feature manager checks duplication using the matching algorithm between the incoming features and the existing features gathered from the past frames. The features which have no correspondence to the past features are added to the feature manager as new features. Through the duplication check, related frames of the past trajectory are found, which is called loop closure detection. The features of the current frame are matched to the features from the related frames. And a 6-DOF pose constraint is obtained from the 3D-RANSAC algorithm.

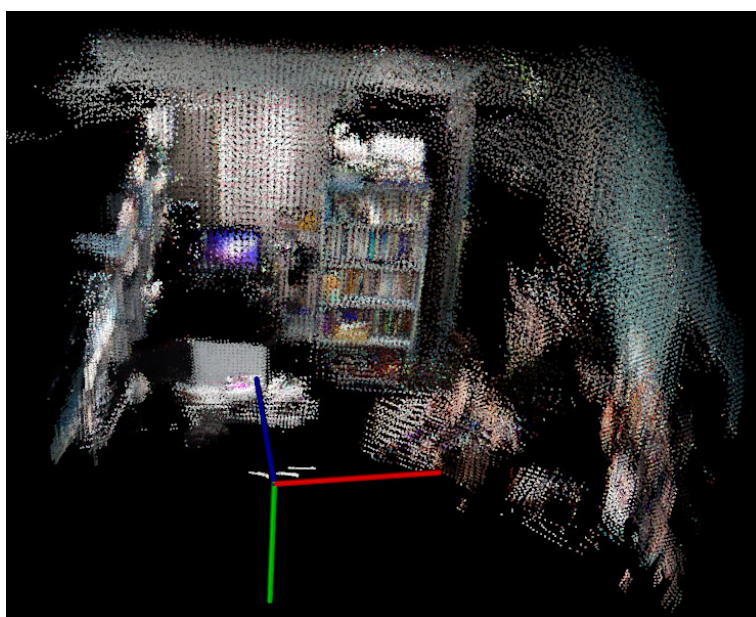
2.3 Graph-Based SLAM Algorithm

In a graph-based SLAM algorithm, a graph form consisting of nodes and edges is required. The nodes represent the trajectory of a sensor and positions of landmarks. But, in the pose graph SLAM, the trajectory of a sensor is only included to the nodes. And an edge denotes a constraint between two nodes.

In our system, we construct the nodes using only the trajectory of the sensor. The edge information between the current and the previous frames is obtained by the 6-DOF visual odometry estimation. The other edges are determined with the loop closure detection procedure.



(a)



(b)

Fig. 5. Experimental results. (a) 3D model by only visual odometry. (b) Optimized 3D model by graph-based 3D SLAM algorithm.

Table 1. Average processing time of the system components

System components	Runtime (ms)
2D feature extraction (GPU-SURF)	17.2
Odometry estimation (Feature matching and 3D RANSAC)	5.9
Loop closure detection	8.1
SLAM algorithm (iSAM)	5.4
Total	36.6

Recently, a variety of graph-based SLAM algorithms has been introduced. In this paper, we use iSAM algorithm to optimize the sensor trajectory for real-time implementation. iSAM solves graph-based SLAM problem using sparse linear algebra and graphical models so that computational time is reduced drastically.

3 Experiments

We have conducted experiments in a room-size environment with the Microsoft Kinect RGB-D sensor. The Kinect uses a structured light for depth information, and its valid range is about 0.5m to 5m. The sensor gives a 2D RGB color image and depth data at 30 frames per second, both with 640×480 resolution. The 3D SLAM system is implemented on a Intel Core i7 CPU with 8 GB of memory. For accelerating the computation of the feature extraction with GPU, an Nvidia GT 560 Ti graphic card supporting the CUDA language is used.

Experimental results of the proposed 3D SLAM algorithm are presented in figure 5. Every node of the pose graph has 3D point cloud data which is transformed by the 6-DOF pose of each node and drawn in 3D space. Figure 5(a) shows 3D reconstruction results with only visual odometry data. The sensor trajectory is drifted by odometry estimation noise, so the result shows a misaligned 3D model. In figure 5(b), the nodes are optimized by the iSAM algorithm, hence the 3D model is aligned correctly.

Table 1 shows the average processing time of the proposed system in the experiments. The feature extraction part takes most of the time, 17.2 milliseconds, on average. The total processing time per frame is 36.6 milliseconds, therefore the rate of the proposed system is above 20 Hz.

4 Conclusion

This paper proposed a real-time RGB-D 3D SLAM system using only an RGB-D sensor. The visual odometry is obtained from the image features, the depth data and the 3D-RANSAC algorithm. The feature manager detects loop closure, and then the graph-based SLAM algorithm optimizes the full trajectory and the 3D model. The GPU processor accelerates operation speed of the system, and the average processing rate on a desktop PC is above 20 Hz.

The depth data is used only for the 3D position of the image features. We think that various applications of the depth data are possible while maintaining the speed of the

system operation. Also, we will evaluate the trajectory and the 3D model with ground truth data in the future.

Acknowledgment. This work was supported partly by the R&D program of the Korea Ministry of Knowledge and Economy (MKE) and the Korea Evaluation Institute of Industrial Technology (KEIT). (The Development of Low-cost Autonomous Navigation Systems for a Robot Vehicle in Urban Environment, 10035354) This work was also partially funded by Samsung Electronics, Co. Ltd. This work was also financially supported partly by Korea Ministry of Land, Transport and Maritime Affairs (MLTM) as U-City Master and Doctor Course Grant Program.

References

1. Dissanayake, M., Newman, P., Clark, S., Durrant-Whyte, H., Csorba, M.: A solution to the simultaneous localization and map building (SLAM) problem. *IEEE Transactions on Robotics and Automation* 17(3), 229–241 (2001)
2. Endres, F., Burgard, W., Cremers, D.: A Benchmark for the Evaluation of RGB-D SLAM Systems. In: Proc. of 2012 IEEE/RSJ International Conference on Intelligent Robots and Systems, IROS (August 2012)
3. Endres, F., Hess, J., Engelhard, N., Sturm, J., Cremers, D., Burgard, W.: An evaluation of the RGB-D SLAM system. In: Proc. of 2012 IEEE International Conference on Robotics and Automation (ICRA), pp. 1691–1696 (2012)
4. Engelhard, N., Endresa, F., Hessa, J., Sturmb, J., Burgarda, W.: Real-time 3D visual SLAM with a hand-held RGB-D camera. In: Proc. of the RGB-D Workshop on 3D Perception in Robotics at the European Robotics Forum, Västerås, Sweden (2011)
5. Hahnel, D., Burgard, W., Fox, D., Thrun, S.: An efficient FastSLAM algorithm for generating maps of large-scale cyclic environments from raw laser range measurements. In: Proc. of 2003 IEEE/RSJ International Conference on Intelligent Robots and Systems (IROS), vol. 1, pp. 206–211 (2003)
6. Henry, P., Krainin, M., Herbst, E., Ren, X., Fox, D.: RGB-D mapping: Using Kinect-style depth cameras for dense 3D modeling of indoor environments. *The International Journal of Robotics Research* 31(5), 647–663 (2012)
7. Kaess, M., Ranganathan, A., Dellaert, F.: iSAM: Incremental smoothing and mapping. *IEEE Transactions on Robotics* 24(6), 1365–1378 (2008)
8. Krainin, M., Maturana, D., Fox, D.: Visual odometry and mapping for autonomous flight using an rgb-d camera. In: Proc. of The 15th International Symposium on Robotics Research, ISRR (2011)
9. Kummerle, R., Grisetti, G.: g2o: A General Framework for Graph Optimization. In: Proc. of 2011 IEEE International Conference on Robotics and Automation, ICRA (2011)
10. Michael, M., Sebastian, T., Daphne, K.: FastSLAM 2.0: An Improved Particle Filtering Algorithm for Simultaneous Localization and Mapping that Provably Converges. In: Proc. of The 18th International Joint Conference on Artificial Intelligence (2003)
11. Newcombe, R., Izadi, S., Hilliges, O., Molyneaux, D., Kim, D., Davison, A., Kohli, P., Shotton, J., Hodges, S., Fitzgibbon, A.: KinectFusion: Real-time dense surface mapping and tracking. In: Proc. of 2011 10th IEEE International Symposium on Mixed and Augmented Reality (ISMAR), pp. 127–136 (2011)
12. Zhang, Z.: Microsoft Kinect Sensor and Its Effect. *IEEE Multimedia* 19(2), 4–10 (2012)

Simultaneous Localization Assistance for Mobile Robot Navigation in Real, Populated Environments

Peshala G. Jayasekara¹, Hideki Hashimoto², and Takashi Kubota³

¹ Dept. of Electrical Engineering and Information Systems, The University of Tokyo

² Dept. of Electrical, Electronics and Communication Engineering, Chuo University

³ Inst. of Space and Astronautical Science (ISAS), Jaxa

peshala@ac.jaxa.jp, hashimoto@elect.chuo-u.ac.jp,

kubota@isas.jaxa.jp

Abstract. Developing autonomous mobile robots that can coexist with human in populated environments is still considered a big challenge. To address this problem the authors propose a novel scheme to assist mobile robots by providing localization information externally. This scheme combines the autonomous navigation and target tracking research fields to arrive at a structured assistance system for autonomous mobile robots. In the proposed scheme, the environment is sensed using a laser range finder and camera based sensor unit. Using Rao-Blackwellized particle filter technique, the robots that need assistance are continuously tracked. In contrast with conventional laser range finder based tracking systems, the placement of sensor is changed to a level above average human height and the mobile robots are modified by attaching a cylindrical pole. The experiments show the validity of the proposed scheme for simultaneous localization assistance for multiple mobile robots. Two mobile robots were simultaneously navigated in given trajectories using assistance data, successfully.

Keywords: localization, mobile robots, target tracking, particle filter.

1 Introduction

Daily human environments are dynamic, unpredictable and populated. These real environments pose many challenges for conventional self-contained autonomous mobile robots even if they are equipped with as many sensors as possible. Adaptability to real environments comes at a cost of the mobile robot's computational capability, which, due to its size and mobility, is limited. As a result, considering the state-of-art technologies, it is difficult to expect a capable mobile robot navigating all by itself in complex human environments even in near future.

Humans tend to depend on some assistance, sometimes even unintentionally, to minimize both the effort and time put into navigation. This human behavior can be imitated and can be used in the field of autonomous navigation for mobile robots. This idea motivates the need for a proper assistance scheme for autonomous navigation and such an assistance system can act as the missing building block to

provide fully autonomous capabilities for mobile robots for navigation in human environments. More specifically, the project objective is to develop a structured assistance system for mobile robots navigating in crowded human environments. The case where such a localization assistance system would not have any prior knowledge about the mobile robots, their shape or their features is considered. Furthermore, the authors intend to reduce the on-board sensors, eliminate the need for any other tags and consider minimum environment modification. The mobile robots will therefore not be equipped with any tags, heading reference systems (e.g. gyro sensors) and rely on information it obtains from the assistance system.

In order to realize a structured mobile robot assistance scheme, two important aspects should be considered; the nature of assistance it provides and a suitable methodology to implement it. In this research, the authors have narrowed the scope of the assistance system to provision of only localization information. Conventional Laser Range Finder (LRF) based scan matching and camera based localization techniques can easily fail in complex human environments due to inability to see landmarks (occlusion), or complexity of the environment. Other localization systems [1]-[4] need the environment to be modified severely and to undergo time consuming calibration procedures.

To implement the proposed assistance system, target tracking techniques have been utilized. There has been considerable research done on tracking moving targets [5]-[9]. However, in these works, tracked information is often used from the viewpoint of the tracker (e.g. for surveillance purposes and etc.) and seldom used for the benefit of the targets being tracked. As described in [10] target tracking can be effectively used to extract localization of mobile robots and assist multiple mobile robots in autonomous navigation; the authors have named the system as intelligent assistance (IA), for it can intelligently track only the mobile robots in a populated environment and it differentiate between them when providing assistance. In this paper the authors present their latest results of the IA system. The rest of the paper is organized as follows: section 2 presents related work; section 3 describes the system architecture; the experiments and results are given in section 4; section 5 concludes the paper reviewing the work undertaken and drawing conclusions about key parts of the work and finally, discussing future directions.

2 Related Works

In this section similar assistance systems for mobile robots are described. Robots can get assistance from three main sources: ambient intelligence, humans and from other robots.

Intelligent space (iSpace), proposed by Hashimoto Laboratory [11], is an ambient intelligent space that has ubiquitous distributed sensory intelligence and actuators for manipulating the space. Robot localization using on-board and distributed sensors has been proposed for iSpace in [12][13]. The proposed system follows the same idea of [12], and the authors extend this concept for a more general assistance scheme for multiple mobile robots for general environments even outside iSpace.

Autonomous City Explorer Project [14] attempts to address the problem of autonomous mobile robot navigation in natural, populated environments with external human assistance. The robot extracts information using its vision system. Vision

based human interaction methodologies need very high computational power embedded into the robot and can be a major bottleneck in the system. The ambiguity in information perception can lead to inconsistencies in information perception.

As the third option, mobile robots can seek help from other mobile robots in the environment using cooperative localization (CL) technique. Ref. [15]-[18] provide some of the example implementations of CL. All these approaches are based on information exchange between mobile robots, where each mobile robot shares its belief with the other members of the group. Amount of transmitted information, computational complexity and the initial correspondence problem are some major issues that cannot be overlooked for a mobile robot which has limited resources. Moreover, if inter-robot communication is not possible, i.e., if the mobile robots do not have a protocol for communication with each other (robots can belong to different owners), then cooperative localization cannot be established to increase individual localization accuracy. Comparing with these techniques, the proposed technique belongs to the assistance by ambient intelligence category.

3 System Architecture

A mobile robot, which needs assistance to navigate in the environment, is expected to carry out an initialization phase, in which an Ethernet wireless connection between the robot and IA will be established for communication. In the initialization phase, the robot is detected by the tracking initializer of the IA vision subsystem. The mobile robots are detected by an LRF, simultaneously. After correctly associating camera observations with corresponding LRF observations, this fused information is used for tracking mobile robots by a particle filter (PF) based tracker. Output from the PF tracker will be fed-back to mobile robots as assistance information. The schematic diagram of the proposed system is given in Fig. 1(left).

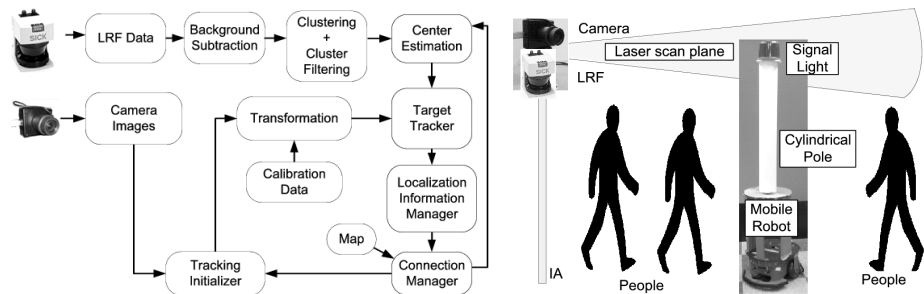


Fig. 1. The Schematic diagram of the proposed system(left) and robot modification(right)

3.1 Sensor Unit

A SICK LMS 291 LRF and a Point Grey Dragonfly2 IEEE firewire camera based sensor unit is used to detect mobile robots. The need for fusion of camera with LRF arises because the differentiation between different targets cannot be done using only LRF data.

3.1.1 Laser Range Finder Data Processing

Utilizing a background subtraction method, mobile robots are detected as foreground objects. The LRF scan plane is changed (section 3.2) and at this scan level the background hardly changes. Thus, background subtraction method for detection is robust. The laser scan points are clustered using a nearest neighbor classifier and filtered for possible noise. LRF cluster means are then adjusted to estimate the center position of the mobile robot.

3.1.2 Camera Based Target Tracking Initialization

The assistant system has no prior knowledge of the robots to be served. Therefore, there should be a mechanism to initialize the tracking of each mobile robot. It can be expected that the mobile robots be occluded in the populated environment and the assistant has to automatically find some clue to detect it. The proposed scheme for initial attachment is by using a blinking signal light (red bulb), with a known frequency of blinking, attached to the cylindrical pole of the mobile robot. The blinking frequency is agreed upon by both parties at the time of initialization. The sensor unit captures the blinking light using camera and associates it with LRF range information. This technique serves as a simple solution to the LRF data association problem. The reader is referred to [19] for algorithm.

3.2 Mobile Robot Modification

Different mobile robots have different base shapes. And, the LRF cluster center varies depending on the mobile robot's base shape as well as its heading angle. To be able to detect mobile robots in crowded environments and to track the same position of robots at all times the robot platform is modified by attaching a vertical lightweight "Polystyrene" cylindrical pole with its height greater than average human height. The IA's LRF placement is also changed to an overhead level at 2m from ground. This is illustrated in Fig. 1(right). The lightweight pole is used only with the intention of improved tracking. Thus, it adds no additional burden to the structure of the robot, not making itself a large-scale robot as such.

3.3 Multiple Target Tracking in Clutter

The problem of data association makes multiple target tracking a much harder task than single target tracking. In multiple target tracking, the algorithm has to estimate which targets produced the measurements, before it is able to use the measurements in actual tracking. If the correct data associations were known, the multiple target tracking problem would reduce to tracking each of the single targets separately [6].

The Rao-Blackwellized Monte Carlo data association (RBMCDA) algorithm proposed by Sarkka et al. [20] estimates data associations with a sequential importance resampling (SIR) PF and the other parts with a Kalman filter (KF) or extended Kalman filter (EKF). This idea can be directly used in the multiple-targets-in-clutter case, where the dynamic model of the targets is linear and the measurement

model of the targets is nonlinear, and the measurements are to be associated with corresponding targets. Due to the conditional independences between the targets, the full KF prediction and update steps for all targets can be reduced to independent single target predictions and updates. Because the targets are a priori independent, conditional on the data associations C_k , the targets will remain independent during tracking. This simplifies RBPF computations as follows:

1. The KF prediction steps can be done for each target in each particle separately. i.e., there is no need to do KF prediction to the joint mean and covariance of all targets, but only for each target.
2. The optimal importance distribution can always be used as the importance distribution for the data association.
3. The marginalized measurement likelihoods can be computed for each target separately.
4. The measurement updates can also be performed for each target separately. This means that the EKF update is actually performed only to one target in each particle.

3.3.1 State Space Model

Target state should be chosen in such a way that localization information of a target could be obtained from its state. Target state X is represented using its position (x, y) and velocities (\dot{x}, \dot{y}) in the two dimensional Cartesian coordinates:

$$X = [x \ y \ \dot{x} \ \dot{y}]^T \quad (1)$$

In doing so, not only its position but also its heading direction can be estimated. The reason is that most robots are nonholonomic, and the non-holonomic constraints limit the robots' velocities in each configuration (x, y, θ) . Thus, if the interval between two successive measurements is small, its heading angle can be computed using:

$$\theta_k = \arctan(\dot{y}_k, \dot{x}_k) \quad \text{for } \dot{x}_k > \text{threshold}_{\dot{x}_k} \ \& \ \& \ \dot{y}_k > \text{threshold}_{\dot{y}_k} \quad (2)$$

This is illustrated in Fig. 2(left). Equation (2) makes sure θ is not calculated when the robot is stationary or rotating with small translational velocities, which in turn results in noisy θ calculations. In such robot movements the heading angle sent by IA will be invalid; this is notified by a data tag for validity of heading angle. Therefore, the heading angle undergoes discontinuities. The thresholds defined in (2) are chosen experimentally (0.015-ms^{-1} was used as the threshold for both directions). A discretized Wiener process velocity model [21] is used as the dynamic model of a target while a nonlinear range-bearing model is used as the measurement model.

$$X_{k+1} = A_{cv} X_k + w_k \quad \text{with} \quad A_{cv} = \begin{bmatrix} 1 & 0 & \Delta T & 0 \\ 0 & 1 & 0 & \Delta T \\ 0 & 0 & 1 & 0 \\ 0 & 0 & 0 & 1 \end{bmatrix} \quad (3)$$

$$Z_k = h(X_k) + v_k \quad \rightarrow \quad \begin{bmatrix} r_k \\ \theta_k \end{bmatrix} = \begin{bmatrix} \sqrt{x_k^2 + y_k^2} \\ \arctan(y_k, x_k) \end{bmatrix} \quad (4)$$

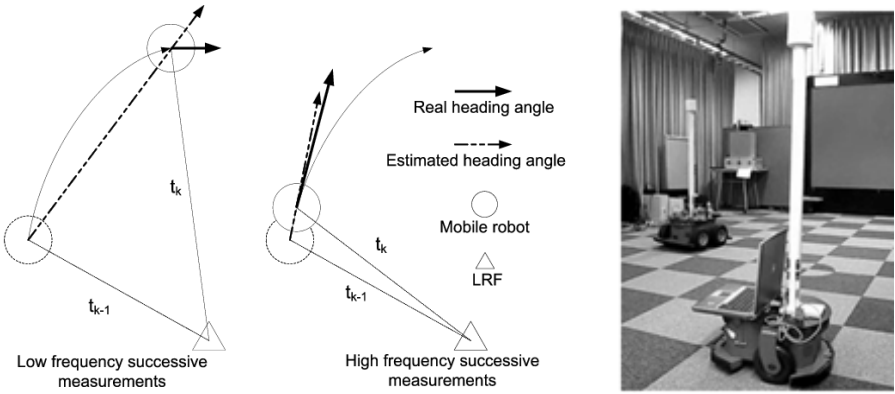


Fig. 2. The Illustration of the validity of heading angle estimation approach(left) and a snapshot of the assisted navigation experiments(right)

A_{cv} is the state-transition matrix, ΔT is the sampling interval, w_k is process noise, Z_k is measurement and v_k is measurement noise.

3.3.2 Algorithm Implementation

In accordance with the method proposed by Sarkka in [6], the final Rao-Blackwellized particle filter (RBPF) implementation is as follows:

1. Perform KF predictions for the means $m_{k-1}^{(i)}$ and the covariances $P_{k-1}^{(i)}$ of particles $i=1,\dots,N$.

$$\begin{aligned}\bar{m}_k^{(i)} &= A_{k-1} m_{k-1}^{(i)} \\ \bar{P}_k^{(i)} &= A_{k-1} P_{k-1}^{(i)} A_{k-1}^T + Q_{k-1}\end{aligned}\quad (5)$$

2. Draw new data association C_k for each particle in $i = 1,\dots,N$ from importance distribution:

$$\pi(C_k^{(i)} | Z_{1:k}, C_{1:k-1}^{(i)}) = p(Z_k^{(i)} | Z_{1:k}, C_{1:k-1}^{(i)}) \quad (6)$$

Using Bayes' rule on (6), and assuming that the current data association does not depend on previous data associations, i.e., $p(C_k^{(i)} | C_{1:k-1}^{(i)}) = p(C_k^{(i)}) = const$:

$$p(C_k^{(i)} | Z_{1:k}, C_{1:k-1}^{(i)}) \propto p(Z_k | C_k^{(i)}, Z_{1:k-1}, C_{1:k-1}^{(i)}) \quad (7)$$

Now a new association can be drawn from (7).

3. Calculate new unnormalized weights as follows:

$$w_k^{*(i)} = w_{k-1}^{*(i)} \frac{p(Z_k | Z_{1:k-1}, C_{1:k}^{(i)}) p(C_k^{(i)} | C_{1:k-1}^{(i)})}{p(C_k^{(i)} | Z_{1:k}, C_{1:k-1}^{(i)})} \quad (8)$$

4. Next, the weights calculated in the previous step are normalized.
5. Then, EKF update step is performed for each of the particles, conditioned on the drawn data association variable:

$$V_k^{(i)} = Z_k - h(\bar{m}_k) \quad (9)$$

$$S_k^{(i)} = \frac{\partial h}{\partial x} \Big|_{\bar{m}_k} \bar{P}_k^{(i)} \left[\frac{\partial h}{\partial x} \Big|_{\bar{m}_k} \right]^T + R_k \quad (10)$$

$$K_k^{(i)} = \bar{P}_k^{(i)} \left[\frac{\partial h}{\partial x} \Big|_{\bar{m}_k} \right]^T [S_k^{(i)}]^{-1} \quad (11)$$

$$\bar{m}_k^{(i)} = \bar{m}_k^{(i)} + K_k^{(i)} V_k^{(i)} \quad (12)$$

$$P_k^{(i)} = \bar{P}_k^{(i)} - K_k^{(i)} S_k^{(i)} [K_k^{(i)}]^T \quad (13)$$

6. The effective number of particles is given by:

$$n_{eff} = \left[\sum_{i=1}^N (w_k^{(i)})^2 \right]^{-1} \quad (14)$$

If n_{eff} is too low, then perform resampling. The parameters used in the RBPF are provided in Table 1.

Table 1. Filter Parameters

EKF(s)	LRF std r LRF std theta target std x target std y target std vel x target std vel y	0.1(m) 1.0(deg) 0.1(m) 0.1(m) 1.0(ms ⁻¹) 1.0(ms ⁻¹)
PF	Particles resampling	100 Systematic[22]

3.4 Robot-Side Implementation

In this section the robot-side implementation to make use of IA information and how a robot can reduce its self-localization uncertainty using this information are explained.

3.4.1 EKF Based Sensor Fusion

An EKF based sensor fusion mechanism is implemented at the robot-side to obtain its pose by fusing intelligent assistance data with odometry measurements; no attitude, heading reference sensors are used. The need for data fusion arises because of the fact that heading angle estimation undergoes discontinuities in intelligent assistant as explained in section 3.3.1.

1. **System model:** a nonlinear system model for the state transition in the form:

$$\begin{aligned} x_k &= g(x_{k-1}, v_k, w_k) + \epsilon_k \\ \begin{bmatrix} x_k \\ y_k \\ \theta_k \end{bmatrix} &= \begin{bmatrix} x_{k-1} + v_k \Delta T \cos(\theta_{k-1}) \\ y_{k-1} + v_k \Delta T \sin(\theta_{k-1}) \\ \theta_{k-1} + \omega_k \Delta T \end{bmatrix} \end{aligned} \quad (15)$$

where x represents the state vector, v_k , ω_k represents control inputs and ε_k is a Gaussian random vector that models uncertainty introduced by the state transition.

2. **Measurement model:** a linear measurement model in the form:

$$Z_k = Hx_k + \delta_k \quad (16)$$

where H is the identity matrix. Both assistance and odometry measurements are similar in structure to the state vector, and therefore, the same measurement model can be used to update the filter.

3. **Sensor fusion:** Sensor fusion takes place at the KF update step, where the filter is updated sequentially using all the sensor measurements for that particular instance. For e.g., for the problem at hand, the KF update step is performed twice for both intelligent assistance data and odometry data after the KF prediction step. However, the mismatch of timestamps of the two measurements prevents us from applying such an update straightaway. This is overcome by interpolating one measurement to the other measurement's timestamp. For more details the reader is referred to [19].
4. **Odometry rectification:** As odometry data can drift arbitrary over time, the raw odometry cannot be used as it is in the EKF. The interpretation of odometry data is changed continuously so that the odometry error accumulated up to a given point of time is eliminated. The interpretation is changed based on the pose estimation output of the EKF. The rectification of raw odometry is done by using three variables for rotation and translation in 2D coordinates; θ offset, x offset and y offset.

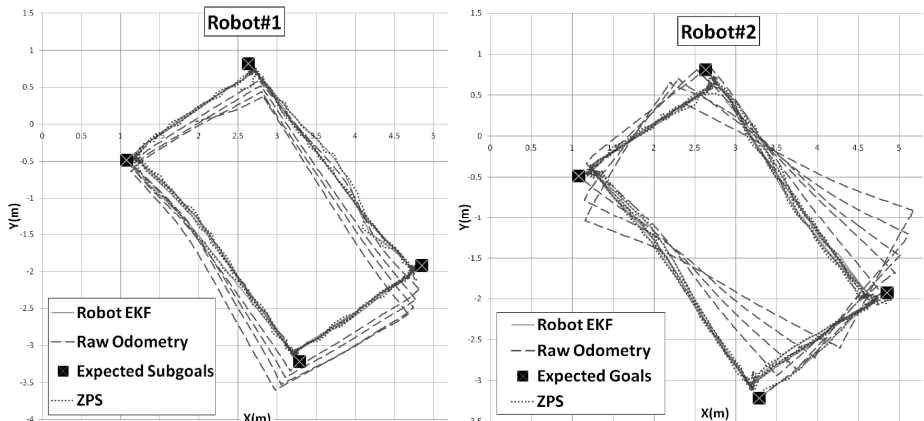


Fig. 3. Comparison between real odometry data, robot EKF output and ZPS output

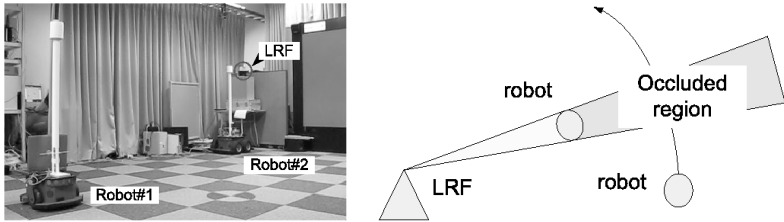


Fig. 4. Behavior in occlusions(left), illustration(right)

4 Experimental Results

4.1 Assisted Navigation Experiments

After extraction of localization, the next step is to feedback this information to mobile robots as assistance. When the LRF scan plane is changed as described in section 3.2, no matter how complex or crowded the environment is, there won't be any disturbance for the tracking procedure. Therefore, conducting the experiment in a crowded or complex environment, over conducting the experiment in a simpler environmental setting, has no difference. Thus, Hashimoto laboratory's experimental space has been used for the purpose. In the experimental setting, as shown in Fig. 2(right), the mobile robot(s) is given four sub-goals (in a rectangle) to navigate using IA's assistance. The mobile robot does not contain any sensors apart from its built-in odometry. Assisted navigation experiments are conducted for both single and dual robots and their raw odometry versus the EKF pose output is examined to identify how well the assistance information has helped the robots to minimize the localization error and how well it can navigate on a given trajectory using IA support. The results are given in Fig. 3. An ultrasonic zone position system (ZPS) gives ground-truth data.

Mobile robots are considered to have achieved the goals when they arrive at the goal within a predefined radius of tolerance. This explains why the robots had started navigating towards the next sub-goal without arriving at a particular pinpoint goal position (Fig. 3). The reason for choosing such a rectangular path was to examine the behavior of robot pose estimation when the heading angle provided by the intelligent assistant is invalid; at sharp corners in the trajectory the robots will be making pure rotations without any translation velocity and only the position information from IA will be valid. Nevertheless, it is evident from the two figures that the pose estimation is not severely affected because of the EKF based sensor fusion implementation at robot-side. It can be clearly observed that, even after one cycle of navigation via the four given sub-goals, the raw odometry had considerably deviated from its actual localization. However, by fusing intelligent assistance data with odometry and changing the odometry interpretation the mobile robots have managed to fulfill the navigation task successfully.

4.2 Occlusions

Occlusions are unavoidable in a single LRF-camera based implementation. In these experiments, the behavior of the tracker when the targets being tracked are occluded, is examined.

Regardless of the number of mobile robots present in the environment, a particular mobile robot will have only two states of occlusion with respect to a single sensor unit; either in occlusion or not in occlusion. And, when the robots are moving arbitrarily, the chances that a robot is continually occluded are low. The worst-case scenario occurs when one mobile robot is not moving and thereby creating an endless occlusion region while another mobile robot is moving inside the occluded region. The experiments are chosen to examine the behaviors of these situations.

Two mobile robots, one to create the occlusion region and the other to traverse in the occluded region, are used. The experimental setting is shown in Fig. 4. In the first experiment, one stationary mobile robot is placed near the sensor unit, which creates the occluding region as described in Fig. 4, and the other robot is moved passing the occluded region in a curved trajectory. In the second experiment, the moving robot comes to a complete stop inside the occluded region and then starts moving again passing the occluded region. The IA extracts the localization information of both mobile robots. The tracking results for the two experiments are provided in Fig. 5.

In the first experiment, where the robot is passing through the occlusion region, the tracker does not receive any measurements regarding that occluded robot. Therefore, its state is only predicted but not updated using measurements. As can be seen from Fig. 5 (middle), the position is predicted from the last updated state in a straight line due to the nature of the motion model described in section 3.3.1. In the second experiment, where the robot is stationary inside the occluded region, the tracker again does not receive any measurements regarding that occluded robot. Prediction of its state will occur, which results in an inconsistent behavior as illustrated in Fig. 5 (right); IA outputs the state of a moving robot even if the robot is at a stop. And, the moment it starts receiving measurements from that particular mobile robot, state estimation jumps from the last predicted state to correct the state and converges to its actual localization. However, this is not guaranteed if the robot's trajectory has been deviated too much. To overcome this problem, the proposed method utilizes a timer-based implementation, in which the robot's endless state prediction is only allowed up to a predefined time interval; i.e. if the tracker could not associate any measurements with the particular robot within the given time interval, the target is imply dropped out from tracking.

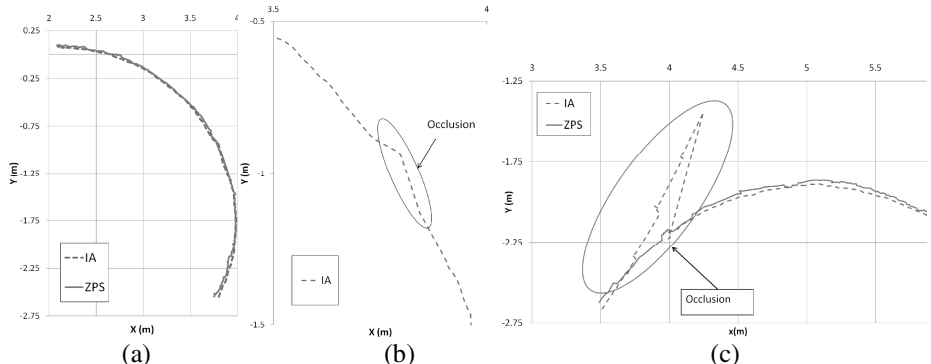


Fig. 5. Comparison between IA and ZPS measurements: (a) while a robot is passing an occluded area; (b) IA result enlarged; (c) while a robot is stationary in an occlusion area

5 Conclusion

By imitating how humans navigate in complex environments with external assistance, the same behavior was mimicked for mobile robots by introducing and developing a structured assistance scheme, named intelligent assistance. Mobile robots are detected using a LRF and a camera based sensor unit and tracked by employing the PF technique. The experiment results show the validity and the applicability of IA for multiple robot assistance, with an IA throughput: 10Hz, position estimation error: 5.5cm and heading angle error: 4.75°. Even though the robots are modified to be taller than human height it does not give the notion of converting them to large-scale robots because the modification is just an attachment of a lightweight pole. Thus, the psychological effect for human can be assumed to be small. The proposed system is, however, only valid for 2D navigation and environments with height differences (e.g. steps) are not considered; yet, constant slopes can be supported by an inclined LRF plane by IA.

By incorporating localization assistance information with rather noisy odometry measurements and a proper implementation at robot-side, the self-localization uncertainty of mobile robots is reduced and thereby the robots could be navigated in expected trajectories, even without any heading reference system, with a minimized error.

As for future work, the proposed LRF tracking technique can be easily utilized in the opposite direction, especially for SLAM; that is, LRF sensors can be attached to robots at a higher lever to scan an overhead plane. In many state-of-art SLAM implementations the observation model for LRF has to tackle the problem of outliers when the space is occupied with people [23]. With an overhead scan plane, landmark extraction process would be robust.

It was assumed that humans in the environment are not affected by the modified robots. However, additional experiments should be conducted to verify the psychological effects for human. IA for mobile robots is a broad concept. In this research the authors have focused only on the assistance in the form of localization and the authors would like to extend this research to provide path planning assistance and obstacle avoidance assistance in future.

References

1. Priyantha, N.B.: The Cricket Indoor Location System. Massachusetts Institute of Technology, PhD Thesis (2005)
2. Orr, R., Abowd, G.: The Smart Floor: A mechanism for natural user identification and tracking. In: Proceedings of the Conference on Human Factors in Computing Systems (CHI 2000), pp. 275–276 (2000)
3. Hada, Y., Takase, K.: Multiple mobile robot navigation using the indoor global positioning system (iGPS). In: Proceedings of IEEE/RSJ International Conference on Intelligent Robots and Systems, vol. 2, pp. 1005–1010 (2001)
4. Hasegawa, T., et al.: Robot Town Project: Sensory Data Management and Interaction with Robot of Intelligent Environment for Daily Life. In: International Conference on Ubiquitous Robots and Ambient Intelligence, URAI 2007 (2007)

5. Brscic, D., Hashimoto, H.: Tracking of Humans Inside Intelligent Space using Static and Mobile Sensors. In: 33rd Annual Conference of the IEEE Industrial Electronics Society IECON, pp. 10–15 (2007)
6. Sarkka, S., Vehtari, A., Lampinen, J.: Rao-Blackwellized Particle Filter for Multiple Target Tracking. *Information Fusion Journal* 8(1), 2–15 (2007)
7. Kurazume, R., Yamada, H., Murakami, K., Iwashita, Y., Hasegawa, T.: Target tracking using SIR and MCMC particle filters by multiple cameras and laser range finders. In: International Conference on Intelligent Robots and Systems, IROS, pp. 3838–3844 (2008)
8. Nakamura, K., et al.: Tracking pedestrians using multiple single-row laser range scanners and its reliability evaluation. *Systems and Computers in Japan* 37(7), 1–11 (2006)
9. Shao, X., et al.: Detection and tracking of multiple pedestrians by using laser range scanners. In: IEEE/RSJ International Conference on Intelligent Robots and Systems IROS, pp. 2174–2179 (2007)
10. Jayasekara, P.G., Song, Y.E., Sasaki, T., Hashimoto, H.: Intelligent Assistance in Localization for Mobile Robots. In: The 8th France-Japan and 6th Europe-Asia Congress on Mechatronics, Yokohama, Japan, November 22-24, pp. 317–322 (2010)
11. Lee, J.H., Hashimoto, H.: Intelligent space - concept and contents. *Advanced Robotics* 16(3), 265–280 (2002)
12. Brscic, D., Hashimoto, H.: Model Based Robot Localization using Onboard and Distributed Laser Range Finders. In: IEEE/RSJ International Conference on Intelligent Robots and Systems, pp. 1154–1159 (2008)
13. Brscic, D.: Mobile Robot Control Scheme based on Distributed and Onboard Sensors,” University of Tokyo, PhD Thesis (2008)
14. Lidoris, G., Rohrmuller, F., Wollherr, D., Buss, M.: The Autonomous City Explorer (ACE) project — mobile robot navigation in highly populated urban environments. In: IEEE International Conference on Robotics and Automation ICRA 2009, pp. 1416–1422 (2009)
15. Fox, D., Burgard, W., Kruppa, H., Thrun, S.: A probabilistic approach to collaborative multi-robot localization. *Autonomous Robots: Special Issue on Heterogeneous Multi-Robot Systems* 8(3), 325–344 (2000)
16. Howard, A., Mataric, M.J., Sukhatme, G.S.: Localization for Mobile Robot Teams Using Maximum Likelihood Estimation. In: International Conference on Intelligent Robot and Systems (IROS 2002), vol. 3, pp. 2849–2854 (2002)
17. Howard, A.: Multi-robot simultaneous localization and mapping using particle filters. In: Proc. Robot. Sci. Syst., Cambridge (2005)
18. Martinelli, A., Pont, F., Siegwart, R.: Multi-Robot Localization Using Relative Observations. In: Proceedings of the 2005 IEEE International Conference on Robotics and Automation, ICRA, pp. 2797–2802 (2005)
19. Jayasekara, P.G.: Simultaneous Localization Assistance for Multiple Mobile Robots using Target Tracking Techniques. University of Tokyo, Master Thesis (2011)
20. Sarkka, S., Vehtari, A., Lampinen, J.: Rao-Blackwellized Monte Carlo data association for multiple target tracking. In: Proceedings of the Seventh International Conference on Information Fusion, vol. I, pp. 583–590 (2004)
21. Bar-Shalom, Y., Li, X.-R., Kirubarajan, T.: *Estimation with Applications to Tracking and Navigation*. Wiley Interscience (2001)
22. Arulampalam, M.S., Maskell, S., Gordon, N., Clapp, T.: A tutorial on particle filters for online nonlinear/non-Gaussian Bayesian tracking. *IEEE Transactions on Signal Processing* 50(2), 174–188 (2002)
23. Thrun, S., Burgard, W., Fox, D.: *Probabilistic Robotics*. The MIT Press (2005) ISBN: 0-262-20162-3

Towards an Ami-Robot Applied to Greenhouses

Antonio Bautista-Hernández and Fernando Ramos-Quintana

Dept. of Computer Science, Tecnológico de Monterrey, Campus Cuernavaca
Autopista del Sol km 104, Colonia Real del Puente, C. P. 62790, Xochitepec, Morelos
`{A01091034, fernando.ramos}@itesm.mx`

Abstract. This work proposes the use of the concept of Ambient Intelligence to facilitate some tasks to be performed by a mobile Ami-Robot within a greenhouse of tomato plants. Although, the application of this Ami-Robot will be mainly focused on the navigation, inspection and fumigation tasks, we report in this work the navigation task. A particular mobile robot with basic functions has been built for this application. In addition, we have developed a monitor system based on Petri Nets, whose main purpose is to track the navigation tasks being performed by the robot and serve as monitor for the producer through a graphical interface. A set of sensors, guide lines and code bars are installed within the green house to facilitate the navigation of the Robot. This Ambient Intelligence, wherein the robot acts as the recipient of all the information, is being tested within a real greenhouse environment. So far, the design and development of this application promise to be easier than a traditional robot application from a hardware and software point of view.

Keywords: Ambient Intelligence, AMI, Mobile Robots, Sensor networks, Greenhouse.

1 Introduction

The research and developments of robots within greenhouse environments is not something new, there are several works that have dealt with such domain AGROBOT [1, 2], AURORA [3] and the Fruit Harvester Robot developed by Kondo et al [4]. Some works are mainly focused on solving problems derived from risky tasks such as fumigation [5,6] or the exhaustive ones as recollection and inspection [6] or even the basic ones like navigation [3,7,8,9]. However the proposed solutions attempt to solve those problems using old, limited, centralized and expensive techniques, for instance, using vision system or proximity sensors for navigation [3, 6, 5].

The use of Ambient Intelligence yields some advantages like the decentralization of the system, making the sub systems easier to be developed, cheaper and with less degree of complexity. In Table 1 a comparison of the two techniques is made, analyzing some basic tasks within a Greenhouse.

One successful case in the use of Robots Mixed with Ambient Intelligent is the work of Alessandro Saffiotti and Mathias Broxvall [10, 11], who created a framework called PEIS where the Robot is a part of the ambient, there is a vision system

Table 1. Technique Comparison

Task/Technique	Traditional Robot	AMI Robot
Navigation	Visual navigation -Implementation of complex algorithms to identify roads, routes, localization, orientation, etc.	AMI assisted navigation yields: -Position -Orientation -Direction There's no need of any visual system, unless some symbols are used to assist the robot.
Fumigation	-Visual plant identification. -Positioning of instruments by visual means.	-AMI assisted plant identification using, IRF tags IRF, symbols, codes, etc. -Preprogrammed fumigation routines.
Monitoring	-Visual plant identification. -Positioning of instruments by visual means.	- AMI gets all the monitoring information using a sensor network.

integrated into the environment which is used for the localization task. The localization system of the robot in this experiment is not efficient, so it uses the PEIS vision system for tracking its position, thereby the robot is being assisted continuously by the environment to achieve its task. They integrated all the systems and robots as part of the environment assuming that in the future robots will be integrated in the entire environment to carry-out several other tasks, which can be seen as a very optimistic scenario.

Another successful work is the project of Graeser [12], which consists in a human welfare robot mounted on a wheelchair for paralyzed patients. In Graeser's work the ambient is used to provide the robot with a better object localization system using an artificial skin on the serving table, and it also uses RFIS to the identification of objects.

In the present application for greenhouses a more practical and concrete work is made, the robot is assisted by the environment, using the Ambient Intelligence to facilitate the achievement of the tasks, similar to a person inside his office or house would do when assisted by Ambient Intelligence like the scenarios proposed by European Commission Community Research [13]. The localization system of the robot uses discrete spaces with a unique identifier, using as reference the beginning of the navigation route.

2 Proposed Model

The Ambient Intelligence approach can take advantage of the systemic concept within a Greenhouse by creating sub systems that work individually in a specific task. In this way all the information can be gathered and shared as in a network to achieve more complex tasks. In our case the Robot acts as a human working inside a Greenhouse, like in a common AMI scenario [13], wherein the human user would receive the needed information to make better decisions in an easier way. Figure 1 illustrates the idea of the approach proposed herein in this paper, where the circles represent the

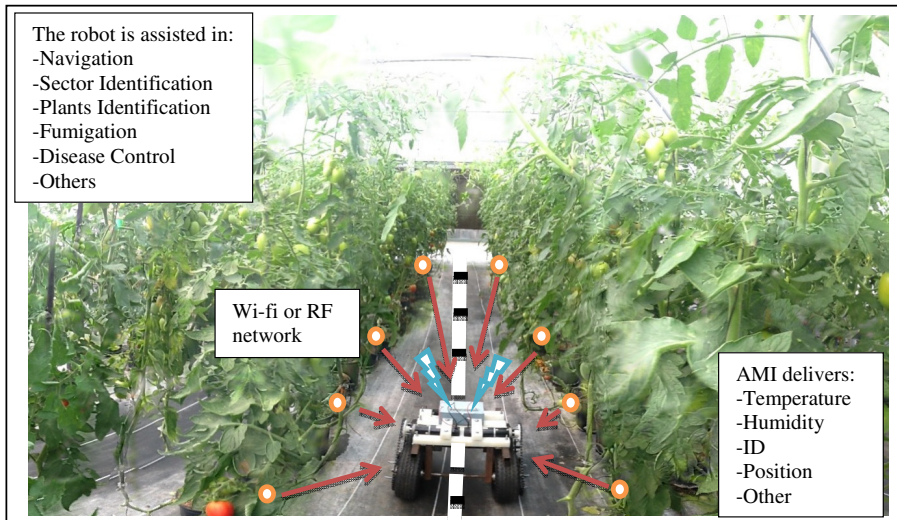


Fig. 1. The AMI-Robot inside the greenhouse

sensor modules spread over the environment, the white line is the path guide and the black squares are the physical discrete places of the corridor identifiers.

To achieve our goals, a decentralized and modular architecture was designed, wherein the Robot, acting as one user, is the receiver of all the information. In this way, more elements can be added to the system without doing complex changes.

The Architecture model is shown in Figure 2. In this model green circles represent the ambient information to be provided to the robot, thus, this information is processed and interpreted to help the robot to carry-out its tasks. Orange trapezoids represent the components associated with the robot's sensorial system, which are the means through which it receives all the information from the ambient. Blue squares represent the processes executed by the robot. As can be seen, the Ambient Intelligence is spread to the environment in a modular way, so it is possible to add/remove modules.

The Robot is the receiver of all the information, the sensor modules information (temperature, humidity and plants ID) is received by an RF module mounted on the Robots platform, the guides and visual ID provides the robot location through the Robot sensors, when mixing these with the map server information a plan can be made, executed and tracked, see Figure 2.

The following section aims at showing a comparison of the involved problematic in a classical approach and our proposed method concerning the navigation task. In order to do that, we show an example of a predefined navigation plan shown in Figure 3, which is an abstraction of one of the scenarios quite similar to a layout of our real green houses.

2.1 A Discussion of Two Navigation Tasks: A Classical Approach vs. an Ami-Robot Approach

In order to compare these two approaches we first characterize the predefined navigation plan propose in this work as follows:

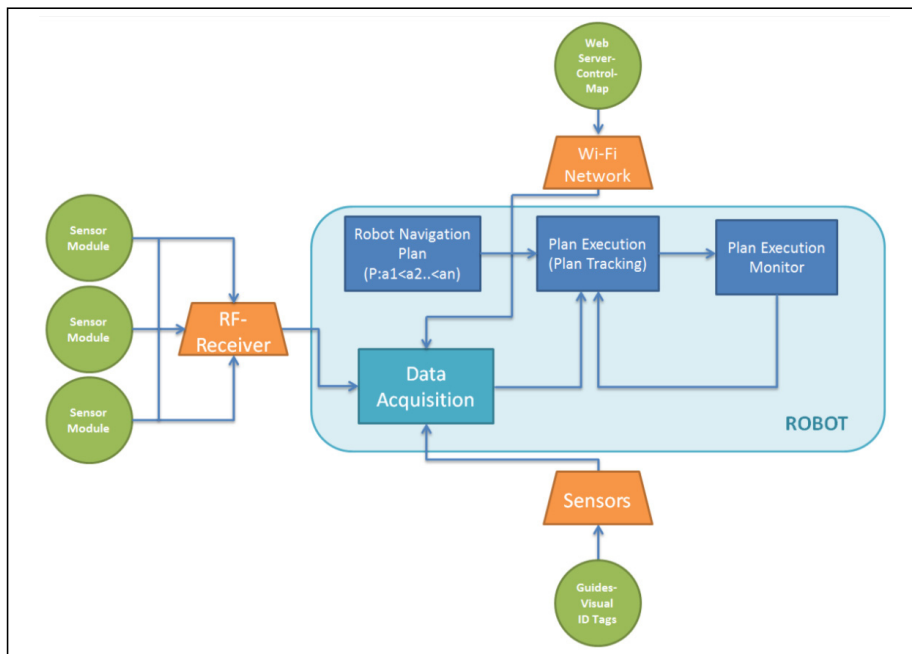


Fig. 2. The architecture model

- a) The Start place of the path and the Goal place to be reached. These are characterized by a code located at a place near the initial point of the Start or Final place, both associated with the navigation plan.
- b) Codes for the intermediate places located sequentially between the Start and the Goal places.

The codes for intermediate places contain also data representing a section of the green house. In the case of Figure 3, four sections are represented. There are also represented transition sections from one section to another, for instance, the transition from section 1 to section 2 as shown in Figure 3.

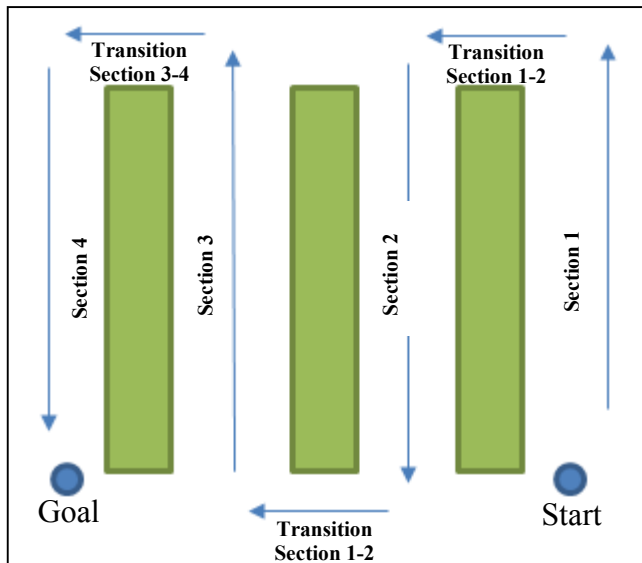


Fig. 3. Characterization of Predefined Navigation Plan used in the Ami-Robot Approach

Table 2 below shows the main problems to be solved for each approach in the case of a navigation task.

Table 2. Problems to be solved associated with each approach

Problems to be solved	Classical Approach	AMI Approach
Map construction	The robot should be provided with sophisticated sensor systems and algorithms to explore the place and build a map. This task is seriously difficult even within controlled environments. Rui Lin work is a great example [15].	A set of predefined maps are designed in depending on a particular green-house layout.
Localization problem	The robot requires a vision system and proximity sensors, sometimes lasers, to recognize where it is located at each instant. Given that the environment is a non-controlled one, serious problems of noise emerge hindering this task, among others. In addition, sophisticated algorithms, from AI field, are needed, because the uncertain information involved. Rui Lin work is a great example [15].	The localization is known at each instant using the barcodes located at strategic places to be reached of the predefined path. This is a basic way to get this information, but it can be upgraded using the Cricket position system from MIT[14].
Obstacle avoidance.	The robot needs a sensorial or vision system, along with complex algorithms to avoid obstacles.	The predefined route can be obstacle free.

3 Current Developments of the Project

In this section, we discuss the current state of the main subsystems of the whole system.

3.1 The Sensorial Network System

The sensor network used to get the information from the plants like position, humidity and temperature was made using the Xbee System, it is an RF component that creates a network between all the components in the same channel. The sections wherein plants are located are divided by areas, thus a RF component is attached to each section and connected to the temperature and humidity sensors using a dsPIC.

The information gathered by the RF components is sent to the network as a string coding data of Humidity, Temperature, Plant section and an ID of the component that can be used for localization or for building a database with the history of the corresponding plants. This string is shown below:

PppTttHhhMM

Where: **P** is the ID identifier of plants, **pp** represents an ID number of plants, **T** and **H** are Temperature and Humidity identifiers respectively, **tt** and **hh** are the values of temperature and humidity respectively and **M** is a module Identifier from 00 to 99, which can be adjusted according to the greenhouse size. Each module gathers a fixed number of plants temperatures and humidity, so using two digits for the number of plant is enough for our purpose, the same with temperature ($^{\circ}\text{C}$) and humidity (%), these values will not be higher than 99°C or 99% of humidity.

The modules used in the development of the sensorial network are composed of:

- Xbee Module XB24-ACI-001 2.4GHz Frequency Band and 250 kbps RF Data Rate.
- Microcontroller dsPIC30F4011 for each plant section.
- Temperature sensor LM35 with linear output and sensing from -55 to 150°C .
- Humidity sensor SMTHS10 with linear output from 0 to 100% RH (Relative Humidity).
- 9v Battery coupled to a 7805 5v 1A voltage regulator.

3.2 The robot

The robot is a basic mobile robot that has been built for this application, equipped with a motion system, a data receiver system, and a set of sensors that serve to interact with the ambient will help in the navigation task. The motion system is implemented using two DC motors, connected to a power stage. The data receiver consists of a similar Xbee to the one used in the sensor modules, but configured as a receiver. The receiver is connected to the robot computer using the Xbee RS232

interface. The sensors mounted in the robot platform consist in a frontal and rear proximity with the only purpose of avoiding collisions, and a bar code reader connected to the computer, that is used to obtain the robot position along its working route. It also incorporates a platform used to mount the robot computers, electronics, mechanics and sensors. The Robot still under development can be seen in Figure 4.

The components used for the robot are:

- 2 DC motors with a maximum input of 24V and 5A.
- 2 2N3055 for the power stage with 60V and 15A as maximum output.
- Xbee Module XB24-ACI-001 2.4GHz Frequency Band and 250 kbps RF Data Rate.
- 6 Sharp GP2Y0A02YK0F Proximity sensors with analog output from 2.8V at 15cm to .4V at 150cm.

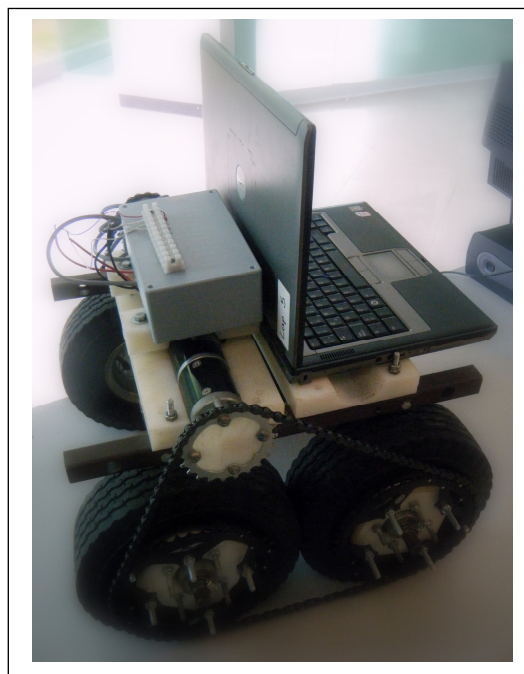


Fig. 4. The robot for the navigation task

3.3 The Robot Navigation System (RNS)

The RNS is composed of predefined navigation plans and a monitor to track the robot navigation.

3.3.1 The Navigation Plan

A set of predefined navigation plans are available, which are adaptable to specific environments inside the greenhouse.

A navigation plan can be defined as follows:

navigation_plan (*pi, pf*) :- **move** (*pi, pi+1*) < **move** (*pi+1, pi+2*) < < **move** (*pf-1, pf*),

Where, **pi** represents the initial place of the robot and **pf** the final one or the end of the plan. The atomic action in this case is defined as **move** (*pj, pj+1*), which represent the movement from any place **pj** to its neighbor **pj+1**. Thus, a navigation plan is achieved when the sequence of movements are satisfied. At the same time, each move action is accomplished when the following assertions are satisfied:

move (*pj, pj+1*) :- **robot_loc** (*pj*) & **free** (*pj+1*).

Sensors will determine if the robot is located at **pj** and the availability of **pj+1** to allow the movement of the robot to such place.

As we can see, the plan is assumed to be a totally ordered sequence of movements, where the symbol “**<**” represents a strict total order, which means that **move** (*pj, pj+1*) should be executed before **move** (*pj+1, pj+2*).

3.3.2 Aid Elements for Navigation

The Greenhouse is equipped with lines and bar codes along its corridors, to assist in the robot navigation system, this let us avoid the use of any vision system, saving money and system complexity. This system can be upgraded to a Cricked position system for example [14].

3.3.3 Monitoring System

A Graphic User Interface has been developed to keep track of the AMI Robot navigation and monitor the tasks being executed. The GUI can be seen in figure 5. This GUI uses Petri Nets, which are bipartite directed graphs that offer, in this application, the opportunity of tracking the correct direction of the robot movements. In this application, place-nodes (circles) represent geographic locations of the corridors in the green house. Meanwhile, transition-nodes (rectangles) represent active conditions to link two neighbor places by performing a basic movement action. One example of a basic movement, which is composed of two nodes and one transition, is illustrated in figure 6 below:

Pj and Pj+1 represent two neighbor places to be linked through the transition firing. The circle node colored in black inside the place Pj is known as token, which is a resource representing that the robot is at place Pj and that the place Pj+1 is available or free to be occupied. Once these conditions are satisfied then the transition is fired and the token goes inside the place Pj+1. This basic unit is repeatead within the whole Petri Net representing the whole path of the navigation plan.

We have to point out that a navigation plan of the robot has associated a particular graph topology, in such a way that we can know, through the Petri Net, where the robot is located at each instant and it also makes it possible to configure the map and assign the tasks to the robot.

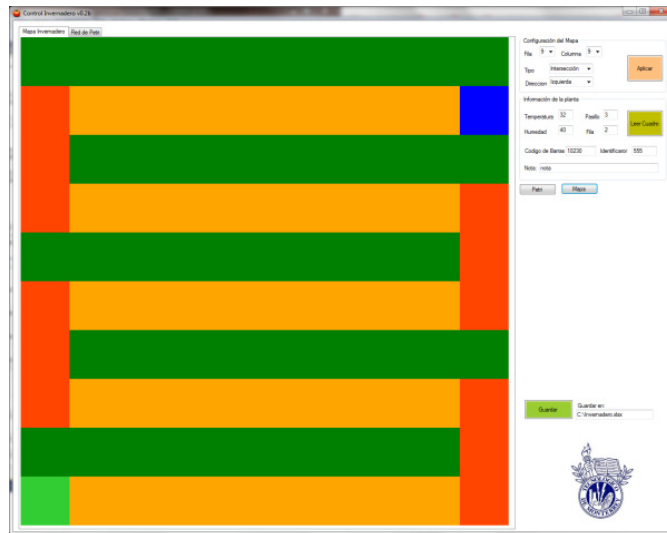


Fig. 5. Graphic User Interface showing the map configuration

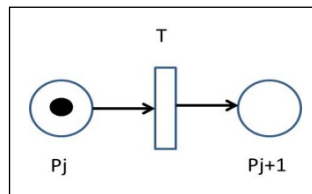


Fig. 6. Basic movement represented by Petri Nets

The places in the Petri Net are the blue circles, which represent at the same time physical discrete places of the corridor. The transition becomes available according to the direction that the robot will move to; this is defined by the user, so the arrows represent that direction, which are the same arrows representing the direction of the Petri Net, see figure 7.

Each transition is triggered only when the resources (token) are available, the resources are the information received by the robot, that is, the number of the corridor section and the data gathered by the sensors in that specific section.

3.4 Procedure

The robot uses its sensing system that interacts with the ambient to know its location, so it can be tracked and compared with the navigation plan. If the goal is reached then the program stops, if not, it will send to the robot the advance to the next position command, and so on and so forth, as shown in figure 8.

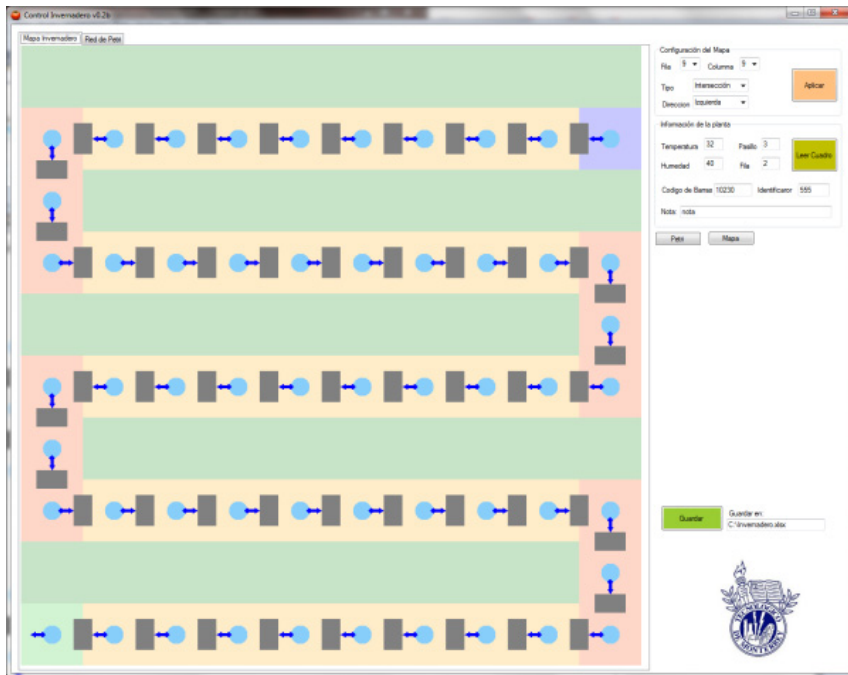


Fig. 7. GUI displaying the Petri net over the map that represents, geographically, the places to be visited

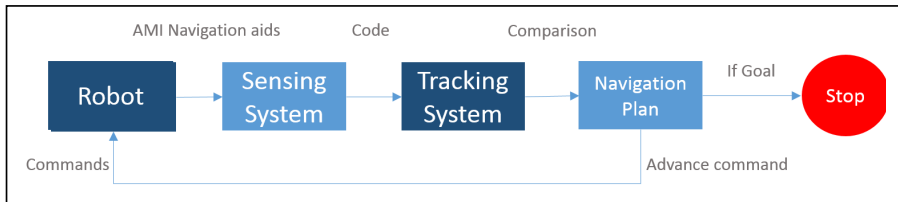


Fig. 8. General system working procedure

4 Conclusions and Discussion

In this work, three main steps should be related properly to assure a correct achievement of the robot navigation task within the green house: 1) the navigation plan; 2) the plan execution; 3) and the monitoring of the navigation task. The contribution of the Ambient Intelligent approach to facilitate the achievement of such a task by the robot is quite evident, because the localization of the robot, the decision for a movement to be executed and the fact of knowing how the task is progressing with respect to the plan, provides the robot with very practical tools to become the tasks easier to be carried-out.

On the other side, with such facilities it is not necessary to build robots provided neither with sophisticated sensorial systems nor complex algorithms. We can say that the ambient intelligent approach can become feasible, from a practical point of view, some developments that seemed to be very complex to be built under other conditions.

For the navigation task, we have obtained promissory results building a simple mobile robot able to execute basic movements and provided with a non-complex architecture to maintain the communication with the sensorial system, which is installed within the green house to guide and monitor the progress of the task. In addition, the producer or user will be able to follow the progress of the robot within the greenhouse at each instant by using the monitor system based on Petri Nets. This kind of system is easier to be operated by non-expert users, such as the producer of tomato in our greenhouses.

References

1. Dario, P., et al.: The AGROBOT Project for Greenhouse Automation. AGRICOLA; ProQuest Agricultural Science Collection; ProQuest Agriculture. Journals. *Acta Horticulturae* (361), 85–92 (1994)
2. Buemi, F.F., Massa, M.M., Sandini, G.G., Costi, G.G.: The AGROBOT Project. *Advances in Space Research: The Official Journal of the Committee on Space Research (COSPAR)* 18(1-2), 185–189 (1996)
3. Mandow, A., Gomez de Gabriel, J.M., Martinez, J.L., Munoz, V.F., Ollero, A., Garcia-Cerezo, A.: The autonomous mobile robot AURORA for greenhouse operation. *IEEE Robotics & Automation Magazine* 3(4), 18–28 (1996)
4. Kondo, N.N., Monta, M.M., Fujiura, T.T.: Fruit Harvesting Robots in Japan. *Advances in Space Research: The Official Journal of the Committee on Space Research (COSPAR)* 18(1-2), 181–184 (1996)
5. Xia, C., Li, Y., Tae-Soo, C., Jang-Myung, L.: A stereo vision based method for autonomous spray of pesticides to plant leaves. In: *IEEE International Symposium on Industrial Electronics*, pp. 909–914 (2009)
6. Li, Y., Xia, C., Lee, J.: Vision-based pest detection and automatic spray of greenhouse plant. In: *IEEE International Symposium on Industrial Electronics*, pp. 920–925 (2009)
7. Janos, S., Matijevics, I.: Implementation of potential field method for mobile robot navigation in greenhouse environment with WSN support. In: *8th Intelligent Systems and Informatics (SISY)*, pp. 319–323 (2010)
8. Kashiwazaki, K.: Greenhouse Partner Robot System. In: *Robotics (ISR), 2010 41st International Symposium on and 2010 6th German Conference on Robotics (ROBOTIK)*, pp. 1–8 (2010)
9. Palamas, G., Houzard, J., Kavoussanos, M.: Relative Position Estimation of a Mobile Robot in a Greenhouse Pathway. In: *IEEE International Conference on Industrial Technology, ICIT 2006*, pp. 2298–2302 (2006)
10. Broxvall, M., Gritti, M., Saffiotti, A., Seo, B.-S., Cho, Y.-J.: PEIS Ecology: integrating robots into smart environments. In: *Proceedings 2006 IEEE International Conference on Robotics and Automation, ICRA 2006*, pp. 212–218 (2006)
11. Saffiotti, A., Broxvall, M., Gritti, M., Leblanc, K., Lundh, R., Rashid, J.: The PEIS-Ecology project: Vision and results. In: *IEEE/RSJ International Conference on Intelligent Robots and Systems, IROS*, pp. 2329–2335 (2008)

12. Graeser, A.: Ambient intelligence and rehabilitation robots — A necessary symbiosis for robust operation in unstructured environments. In: 2010 9th International Symposium on Electronics and Telecommunications (ISETC), pp. 9–16 (2010)
13. Ducatel, Bogdanowics, Scapolo, Scenarios for Ambient Intelligence. ISTAG, European Commission Community Research (2010)
14. Priyantha, N.B., Chakraborty, A., Balakrishnan, H.: The Cricket location-support system. In: Proceedings of the 6th Annual International Conference on Mobile Computing and Networking (MobiCom 2000), pp. 32–43. ACM, New York (2000)
15. Lin, R., Wang, Z., Sun, R.: Vision-based mobile robot localization and mapping using the PLOT features. In: International Conference on Mechatronics and Automation, ICMA 2012, pp. 1921–1927 (2012)

Particle Swarm Optimization-Based Distributed Control Scheme for Flocking Robots

Seung-Mok Lee and Hyun Myung

Dept. of Civil & Environmental Engg. and Robotics Program, KAIST
291 Daehak-ro, Yuseong-gu, Daejeon 305-701, Korea
`{seungmok, hmyung}@kaist.ac.kr`

Abstract. This paper proposes a Nash equilibrium-based model predictive control (MPC) scheme incorporating a cooperative particle swarm optimization (CPSO) to deal with the control of flocking robots whose state vectors are coupled in a cost function. In conventional distributed MPC, the stability is assured by guaranteeing a bounded error between what a subsystem plans to do and what neighbors believe that the subsystem plans to do over a finite prediction horizon. This condition is referred to as compatibility constraint, and the closed-loop control performance largely depends on the responses computed at the previous time step. As an alternative of the compatibility constraint, the distributed CPSO is suggested in an MPC framework, which guarantees the stability without enforcing the compatibility constraint. A numerical simulation is performed on a group of nonholonomic mobile robots to demonstrate the effectiveness of the proposed MPC scheme incorporating CPSO.

Keywords: cooperative particle optimization (CPSO), model predictive control (MPC), Nash equilibrium, flocking.

1 Introduction

In distributed model predictive control (MPC) of multiple subsystems, one of the key issues is to find conditions guaranteeing stability while reducing the computational burden of optimization processes [1]-[6]. To guarantee the stability in the conventional distributed model predictive control (MPC), it is assumed that each subsystem does not deviate too far from its previous computed state trajectory, referred to as the state compatibility constraint or it is assumed that the updating time is sufficiently short [1],[2]. A drawback of this approach is that the system responses can be slow. A sufficiently short update period is used to relax the compatibility constraint, but the closed-loop control performance tends to depend on the update period.

CPSO algorithm is a variant of PSO, employing multiple swarms to optimize different variables of the solution in a cooperative coevolution framework. An early attempt to apply the CC framework to PSO was made by Bergh and Engelbrecht [7], resulting in two cooperative PSO algorithms, namely CPSO-S_K and CPSO-H_K. Recent studies by Li and Yao [8],[9] suggested cooperative coevolving PSO (CCPSO) and

CCPSO2, and their performance was validated on benchmark functions of up to 1,000 dimensions. In fact, the CPSO and its variants were originally developed to deal with high-dimensional optimization problems.

This paper proposes a modified version of the CPSO to find optimal strategies for formation control of flocking robots operated by distributed MPC scheme. It is assumed that each robot is assigned with its own optimization problem and communicates information only with neighboring robots. Thus, each robot has a particle swarm to optimize its cost function value, and the optimization problem is solved by the particle swarm.

The rest of this paper is organized as follows. In Section 2, formation control problem is defined in a distributed MPC framework. Section 3 proposes a novel CPSO-based distributed MPC scheme. Section 4 then presents a simulation result for multi-robot formation control problem. Finally, conclusion is presented in Section 5.

2 Problem Formulation

The formation control problem can be stated as follows: Consider a group of nonholonomic mobile robots. For each robot j , using its own state $[x_j, y_j, \theta_j]^T$ and its neighboring states $[x_i, y_i, \theta_i]^T$, given a reference path X_r and a desired formation pattern P , find a controller such that a group of robots maintain the desired formation pattern P while the center of the formation tracks the reference path X_r . The motion state of the j -th robot defined by $X_j=[x_j, y_j, \theta_j]^T$ can be described by

$$\begin{bmatrix} \dot{x}_j \\ \dot{y}_j \\ \dot{\theta}_j \end{bmatrix} = \begin{bmatrix} v_j \cos \theta_j \\ v_j \sin \theta_j \\ \omega_j \end{bmatrix} \quad (1)$$

where X_j is described by its position (x_j, y_j) and orientation θ_j ; v_j and ω_j are the linear and angular velocities of each robot, respectively.

In order to solve the formation control problem in a distributed way, let us define the formation and tracking error of the robot j as

$$e_j = \begin{bmatrix} e_{jx} \\ e_{jy} \\ e_{j\theta} \end{bmatrix} = \begin{bmatrix} \cos \theta_j & \sin \theta_j & 0 \\ -\sin \theta_j & \cos \theta_j & 0 \\ 0 & 0 & 1 \end{bmatrix} p_{je} \quad (2)$$

where

$$z_{je} = \sum \{(P_j - P_i) - (X_j - X_i)\} + \mu_j (\tilde{X}_j + P_j)$$

in which the former summation part is the formation error and the latter part is the tracking error. Also, $\tilde{X}_j = [\tilde{x}_j, \tilde{y}_j, \tilde{\theta}_j]^T = X_r - X_j$, $P_j = [p_{jx}, p_{jy}, 0]^T$, and $\mu_j=1$ if the

reference X_r is available to robot j , and $\mu_j=0$ if X_r is not available to robot j . The error e_j is obtained by multiplying a rotation matrix in a robot fixed frame with z_{je} . P_j is a desired relative position of robot j to form a desired pattern of flocking.

By differentiating e_j with respect to time, and then substituting (1) into the resulting equation, the error state equation can be obtained as follows:

$$\begin{aligned}\dot{e}_{jx} &= \omega_j e_{jy} + \sum_{i \in N_j} (v_i \cos \theta_{ij} - v_j) + \mu_j (v_r \cos \tilde{\theta}_j - v_j) \\ \dot{e}_{jy} &= -\omega_j e_{jx} + \mu_j v_r \sin \tilde{\theta}_j + \sum_{i \in N_j} v_i \sin \theta_{ij} \\ \dot{e}_{j\theta} &= \sum_{i \in N_j} (\omega_i - \omega_j) + \mu_j (\omega_r - \omega_j)\end{aligned}\quad (3)$$

where $\theta_{ij}=\theta_i-\theta_{ij}$; N_j denotes a set of neighbors of robot j ; v_r and ω_r are the desired linear and angular velocities, which can be derived by differentiating X_r . The error state equation (3) can be generally rewritten as a nonlinear nominal system as follows:

$$\dot{e}_j(\tau) = f(e_j(\tau), u_j(\tau), u_{N_j}(\tau)) \quad (4)$$

where $u_{N_j}(t)=(..., u_i, ...)$, $i \in N_j$, denotes the concatenated vector of the control inputs of the neighbors of robot j , and $u_j=[v_j, \omega_j]^T$.

The cost function to be minimized for each robot j in a distributed MPC framework is designed as follows:

$$J_j(t, e_j(t), u_j(t)) = g_j(e_j(t+T)) + \int_t^{t+T} L_j(\tau, e_j(\tau), u_j(\tau)) d\tau \quad (5)$$

where $g_j(e_j(t+T))=e_j(t+T)^T e_j(t+T)$ is a terminal state penalty function, $L(t, e_j(t), u_j(t))=e_j(t)^T Q e_j(t)+u_j(t)^T R u_j(t)$ is a running cost function, and Q and R are positive definite symmetric weight matrices. At time t , the open-loop optimization problem in a distributed MPC framework can be formulated as

$$\min_{u_j} J(t, e_j(t), u_j(t))$$

subject to

$$\begin{aligned}\dot{e}_j(\tau) &= f(e_j, u_j(\tau), u_{N_j}(\tau)) \\ 0 \leq v_j(\tau) &\leq V_{\max} \\ \|\omega(\tau)\| &\leq \Omega_{\max}\end{aligned}$$

where $\tau \in [t, t+T]$, and V_{\max} and Ω_{\max} are the maximum control inputs.

3 CPSO-Based MPC Framework for Flocking Robots

In this section, we propose a method that optimizes the control input sequence over a prediction horizon by using CPSO for formation control of flocking robots. A cost function for each robot is defined as a coupled form by the future state trajectories of the neighboring robots, and a particle swarm is assigned to each robot in order to minimize the cost function value.

Let $S_j \cdot \mathbf{x}_l^i$ be the current position of the i -th particle of the j -th swarm at generation l , $S_j \cdot \mathbf{y}_l^i$ the personal best of the i -th particle of the j -th swarm, and $S_j \cdot \hat{\mathbf{y}}_l^i$ the global best particle of the j -th swarm. Each particle $S_j \cdot \mathbf{x}_l^i$ represents the predicted control input sequence of robot j at t_k , $u_j(\tau; t_k) = [v_j(\tau; t_k), \omega_j(\tau; t_k)]^T$ over a prediction horizon T .

The process of the proposed CPSO algorithm is shown in Fig. 1. Each robot j receives global best particles found by neighboring robots and predicts the future states of the neighbors. Based on the predicted states, the future control input sequence $u_j(\tau; t_k)$ for $\tau \in [t_k, t_k+T]$ is optimized by minimizing (5) via CPSO. At generation l , the j -th robot evaluates the cost function value of $S_j \cdot \mathbf{x}_l^i$ for all i using the global best particles $S_i \cdot \hat{\mathbf{y}}_{l-1}^i$ where $i \in N_j$. The concatenated vector $u_N(t)$ in (4) is constructed using the received best particles from neighbors of robot j . Then, the cost of $S_j \cdot \mathbf{x}_l^i$ is evaluated by replacing $u_j(t)$ in (5) with $S_j \cdot \mathbf{x}_l^i$. After evaluating the cost of $S_j \cdot \mathbf{x}_l^i$, its personal best $S_j \cdot \mathbf{y}_l^i$ is checked, and then the global best $S_i \cdot \hat{\mathbf{y}}_l^i$ is checked for update. After one generation of the process, each robot transmits its global best particle to neighboring robots. At each generation, the process of evaluating cost, updating personal best and global best particle, and updating velocity and position of each particle is repeated based on the updated global best particles of neighboring robots. When the robots reach an equilibrium state in which all the robots cannot further minimize their cost, the states of the robots are updated using $S_j \cdot \hat{\mathbf{y}}_l^i$ in the time interval $[t, t+\delta t]$.

The update rule to determine the particles' position in the next generation can be described as follows:

$$\begin{aligned} S_j \cdot \mathbf{x}_{l+1}^i &= S_j \cdot \mathbf{x}_l^i + S_j \cdot \mathbf{v}_{l+1}^i, \\ S_j \cdot \mathbf{v}_{l+1}^i &= w_l S_j \cdot \mathbf{v}_l^i + c_1 r_1 (S_j \cdot \mathbf{y}_l^i - S_j \cdot \mathbf{x}_l^i) + c_2 r_2 (S_j \cdot \hat{\mathbf{y}}_l^i - S_j \cdot \mathbf{x}_l^i). \end{aligned} \quad (6)$$

A block diagram of the proposed CPSO-based MPC is shown in Fig. 2. After the process of estimating robots' current states, the future control input sequence $u_j(\tau; t_k)$ is minimized by the CPSO process. When the CPSO process is finished, the first part of the control input sequence is applied to its robot.

At each update time step t_k , particles of each robot should be initialized in order to re-search optimal control input sequence. When initializing the particles of the j -th robot, the global best particle found at the last update time step is chosen again as one of the candidate solutions for the next time step. The fact that the optimization process starts with the best particle found at the last update time step leads to improved convergence performance.

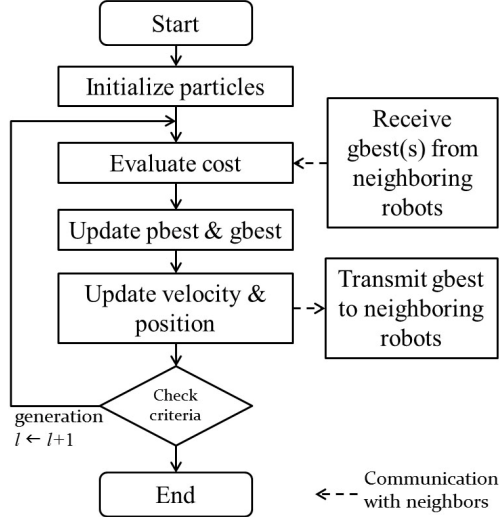


Fig. 1. Flowchart of the CPSO process

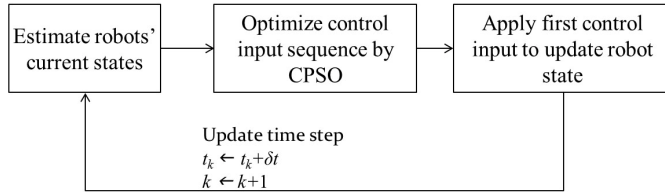


Fig. 2. Block diagram of the CPSO-based MPC Framework

4 Simulation Results

A numerical simulation is performed to validate the effectiveness of the proposed CPSO-based MPC scheme. For the optimization processes by the proposed CPSO, each robot has a particle swarm with a population size of 50, and the maximum number of generations is limited to 100. The inertia weight w_l starts with 0.9 and linearly decrease to 0.4. The search space is limited to real-valued variables within $[-V_{max}, V_{max}]$ and $[-\Omega_{max}, \Omega_{max}]$ for v_j and ω_j , respectively, where $V_{max}=0.5\text{m/s}$ and $\Omega_{max}=1.57\text{rad/s}$. The acceleration coefficients are $c_1=2.0$ and $c_2=2.0$.

The number of prediction horizon steps is 10, while the prediction time interval are selected to be $\delta t=0.1\text{s}$. Thus, the prediction horizon is 1s. The weight matrices Q and R are set to be diagonal where $Q=\text{diag}[0.1, 0.1, 0.01]$ and $R=\text{diag}[0.1, 0.1]$.

Five mobile robots are used to test the algorithm. The reference path is a circle path given by $x_r(t)=2\cos(0.05t)$, $y_r(t)=2\sin(0.05t)$, and $\theta_r(t)=\text{atan}2(\dot{y}_r, \dot{x}_r)$. Initially, the robots are located at $X_1=[2.0, -1.0, 0.0]^T$, $X_2=[2.25, -1.0, 1.57]^T$, $X_3=[2.5, -1.0, 1.57]^T$, $X_4=[1.75, -1.0, 1.57]^T$, and $X_5=[1.5, -1.0, 1.57]^T$, respectively. The desired formation pattern P is a regular pentagon formation, i.e., $p_{1x}=0.5$, $p_{1y}=0.0$,

$p_{2x}=0.1545$, $p_{2y}=0.4755$, $p_{3x}=-0.4045$, $p_{3y}=0.2939$, $p_{4x}=-0.4045$, $p_{4y}=-0.2939$ $p_{5x}=0.1545$, and $p_{5y}=-0.4755$ as shown in Fig. 3. To measure the performance of the algorithm, an error function of t is defined:

$$E(t) = \sum_{j=1}^M e_j^T(t) Q e_j(t). \quad (7)$$

The resulting trajectories of the group of the robots are shown in Fig. 4. It is shown that the five robots maintain a regular pentagon formation while the center of the formation tracks the given reference path using the transmitted information from neighboring robots. Fig. 5 shows the stable total error which converges to zero during maneuvers.

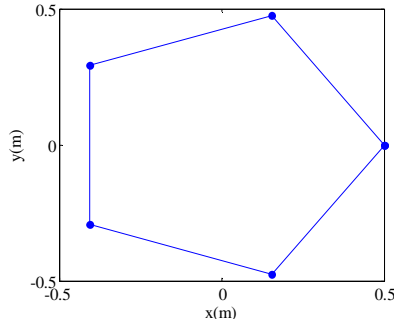


Fig. 3. Desired formation pattern

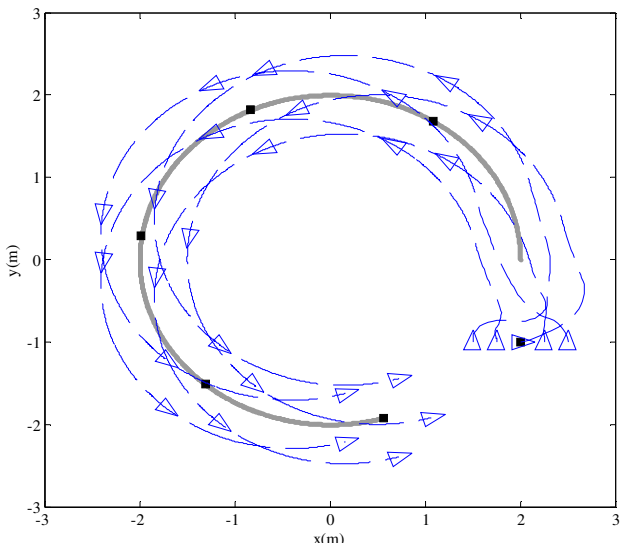


Fig. 4. Trajectories and sampled positions of five robots are indicated with their heading angles. The gray line denotes the reference path and the black squares denote the center of the formation. The positions are sampled at every 20s.

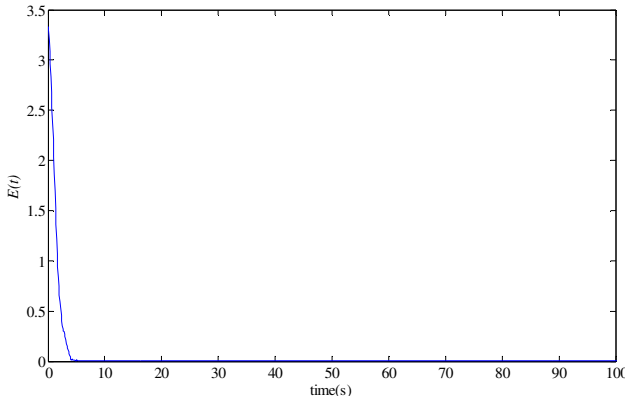


Fig. 5. Total error during maneuvers

5 Conclusion

In this paper, a distributed MPC scheme incorporating CPSO was proposed for multi-robot formation control problem. For the optimization process in MPC, a Nash equilibrium strategy was used to solve the optimization problem by exchanging particle information which has the best experience among neighboring subsystems. In the simulation, using the proposed MPC scheme, it was found that the robots moved to track a given reference path, while maintaining a desired formation pattern successfully.

Future works may include investigations of the stability, robustness, improvement of convergence speed, and comparative studies between the proposed method and conventional MPC schemes. The final goal of this research is the development of real-time cooperative MPC scheme according to the Nash equilibrium strategy.

Acknowledgements. This research was supported by the MKE(The Ministry of Knowledge Economy), Korea, under the Human Resources Development Program for Convergence Robot Specialists support program supervised by the NIPA(National IT Industry Promotion Agency) (NIPA-2012-H1502-12-1002). It was also supported by Basic Science Research Program through the National Research Foundation of Korea (NRF) funded by the Ministry of Education, Science and Technology (grant number 2012-0003897). Additionally, it was supported by Korea Ministry of Land, Transport and Maritime Affairs(MLTM) as U-City Master and Doctor Course Grant Program.

References

1. Dunbar, W.B., Murray, R.M.: Distributed receding horizon control for multi-vehicle formation stabilization. *Automatica* 42(4), 549–558 (2006)
2. Dunbar, W.B., Caveney, D.S.: Distributed receding horizon control of vehicle platoons: stability and string stability. *IEEE Trans. Autom. Control* 57(3), 620–633 (2012)

3. Fontes, F.A.C.C.: A general framework to design stabilizing nonlinear model predictive controllers. *Syst. Control Lett.* 42, 127–143 (2001)
4. Keviczky, T., Borrelli, F., Balas, G.J.: Decentralized receding horizon control for large scale dynamically decoupled systems. *Automatica* 42(12), 2105–2115 (2006)
5. Gu, D., Hu, H.: A stabilizing receding horizon regulator for nonholonomic mobile robots. *IEEE Trans. Robot.* 21(5), 1022–1028 (2005)
6. Chen, J., Sun, D., Yang, J., Chen, H.: Leader-follower formation control of multiple nonholonomic mobile robots incorporating a receding-horizon scheme. *Int. J. Robot. Res.* 29(6), 727–747 (2010)
7. van den Bergh, F., Engelbrecht, A.: A cooperative approach to particle swarm optimization. *IEEE Trans. Evol. Comput.* 8(3), 225–239 (2004)
8. Li, X., Yao, X.: Tackling high dimensional nonseparable optimization problems by cooperatively coevolving particle swarms. In: Proc. IEEE Congress on Evolutionary Computation (CEC), pp. 1546–1553 (2009)
9. Li, X., Yao, X.: Cooperatively coevolving particle swarms for large scale optimization. *IEEE Trans. Evol. Comput.* 16(2), 210–224 (2012)

Control Strategies for Heterogeneous, Autonomous Robot Swarms

Stefan Thamke¹, Markus Ax¹, Lars Kuhnert¹, Klaus-Dieter Kuhnert¹,
Marco Langerwisch², and Thomas Remmersmann³

¹ Dept. of Realtime Learningsystems, University of Siegen
Hoelderlinstr. 3, 57076 Siegen, Germany

{stefan.thamke, markus.ax}@uni-siegen.de
{lars.kuhnert, kuhnert}@fb12.uni-siegen.de

² Institute of Systems Engineering, Leibnitz University of Hannover
Appelstraße 9A, 30167 Hannover, Germany
langerwisch@rts.uni-hannover.de

³ Fraunhofer Institute for Communication, Information Processing and Ergonomics
Neuenahrer Straße 20, 53343 Wachtberg
thomas.remmersmann@fkie.fraunhofer.de

Abstract. Having robots as reliable and robust mobile sensor platforms in unknown environments is getting more and more attractive. The control of each robot as a single machine is often complicated enough. But if there are more than one robots in a given scenario, the task get's even harder. The operators then do not only have to care about steering their robot, but they also have to cooperate with each other. In this paper we describe the results of a research project regarding control strategies for a group of heterogeneous, autonomous robots. The swarm receives orders from a central control station, that uses a Battle Management Language, which is abstract, but human readable. An abstract language postulates a certain degree of intelligence within each robot of the cooperation, because the orders are mostly more complex than simple moves from A to B. There is a command hierarchy within the swarm, but every robot implements its own control strategies, to fulfill the overall goal of the orders. The technical as well as the operational realizations are described and discussed mostly with the focus on the unmanned aerial robots.

Keywords: unmanned aerial vehicles, control strategies, autonomous robots.

1 Introduction

Today single robots are getting more and more robust and reliable in terms of navigation, map building and data preprocessing. Therefore the next step is to combine several heterogeneous machines into a swarm. Even more interesting is the combination of ground and airborne systems at the same time to make use of each ones complementary features.

Unmanned ground vehicles (UGVs) are very useful for various tasks of reconnaissance and transportation, if they are tele-operated, or even autonomous. In that case

human operators are greatly supported and do not have to enter possibly dangerous areas personally. Depending on their size, ground robots do have a high operating distance by being able to carry energy reserves, combined with huge loading capacities for cargo. Their handicaps on the other side are a typically limited maneuverability in heavy terrain and their relatively slow speeds.

Unmanned aerial vehicles (UAVs), especially ones that are capable of vertical takeoff and landing (VTOL), usually present complementary characteristics. Since they normally do not have to cope with obstacles they are highly maneuverable and can traverse great distances very fast. But their energy reserves are typically very low, which is directly proportional to loading capacity and flight duration.

Within the presented project, three different research groups had to incorporate their individual systems into one scalable organization. Each of these groups uses its own software implementation and communication protocol, which makes it necessary to define precise interfaces for global communication processes. Existing standards have been used to solve this problem and to enable even more systems to be integrated into the organization with very little implementational effort. This paper is focused mainly on the aerial parts of the project, but the overall concepts for all partners will be presented as well.

Generally ground air cooperation is a fast rising field of research, since UAV platforms are getting cheaper and more robust. But the amount of published results coping with the fusion of heterogeneous systems from different institutions is quite small. In [1] an UAV was used to enhance the localization quality of the ground vehicle. In [2] and [3] simulation tools are used to test theoretical control approaches. This completely eliminates the need for a communication middleware, since software implementations on the real system are completely faded out. In [4] UAVs are used to discover interesting areas in an urban surveillance scenario. After that is done, the ground vehicles are sent to these locations to execute further reconnaissance tasks.

2 Project Description

For military as well as for civil organizations it gets more and more important to have suitable tools at hand, while coping with (partly) unknown environments. Especially in dangerous areas like war zones or contaminated sites after a nuclear or chemical disaster, the need for unmanned and even autonomous robots will increase. Since there is not the one robot to solve all problems connected with reconnaissance, the cooperation of heterogeneous robots and the potential for a unified control method is evaluated using a realistic military scenario.

Our goal is to analyze the feasibility of a robot swarm, consisting of unmanned ground and aerial vehicles within a reconnaissance scenario. The main focus lies on the definition and standardization of interfaces used to control unmanned robots without having to know everything about their, often proprietary, software installations. The research is done in cooperation between the University of Siegen (EZLS), the Leibniz University of Hannover (RTS), and the Fraunhofer Institute for Communication, Information Processing and Ergonomics (FKIE).

In the following sections the most important components of the project will be described:

2.1 Battle Management Language

The main focus for evaluation lies on the concept of interpretation of an abstract but human readable language. The North Atlantic Treaty Organization (NATO) developed the battle management language (BML) as an unambiguous language used to command and control units and technical equipment conducting military tasks. Additionally there is a possibility for reporting information about the current status of units and the environment. Currently it is used for real troops and simulation purposes. The language is readable for machines in order to enable simulations and therefore should be usable for robot control too. Having a common standard for communication also enables the interoperability between forces from different members of the coalition.

The German version of BML is realized in the *Command and Control Lexical Grammar (C2GL) Specification* [5] and is used as the command language for this project. C2GL is human readable and the sentences are constructed by following a set of formal and context-free rules of a type 2 grammar. Thus sentences like “move to position-X as soon as possible” can be generated from a rule like “order → task where when”. The arrow means that the symbol on the left side is transformed into a sentence defined by the rule on the right side of it. The non-terminal symbols *task*, *where* and *when* are defined by rules too and are transformed accordingly until only terminal symbols remain which represent a complete order.

An important part in reconnaissance scenarios is of course the information coming back from the reconnaissance unit. C2GL defines rules for so called *reports*, which are sent back to the control station. Reports do not intend the receiver to do something, but to inform him about something. They are also in most cases not as precise as orders, because a lot of information that is gathered through reconnaissance is normally attained without the counterpart knowing about being observed, or because of noisy sensor data. There are rules for various kinds of reports within C2GL (see [5]). The interesting ones for this project are task- and status reports. They inform the controller about the process of order execution, or the technical condition of the robots.

2.2 Robot Operating System

Choosing a language for expressing commands and reports raises the question of information transport. Since we do have a multi robot scenario, messages have to be distributed between these systems and the control station. Instead of implementing a proprietary interface, we chose the robot operating system (ROS) [6] as our communication middleware.

ROS does not fulfill the tasks of process management or scheduling, like traditional operating systems do. It is rather a communication service lying on top of a traditional operating system. The main goals in the development of ROS are to build a free and Open-Source, multi-lingual, peer-to-peer platform.

Since the commands and reports must be compatible to C2GL a ROS message is defined, which encapsulates all necessary data fields needed for communication. Additionally a converter is written, that translates pure C2GL messages into the ROS format and vice versa. This makes it very easy to connect processes from different partners together, because the interface is strictly defined and it is mostly platform and language independent.

2.3 User Interface

The graphical user interface (GUI) is designed by the FKIE. It is the standard user interface, which is used to communicate with military simulation environments employed by the NATO. Therefore it is natively only able to use C2GL as a communication protocol. Since ROS is used as the communication middleware, we implemented a C2GL to ROS connector, which translates between the two interfaces where possible. For many things that can be expressed in ROS there are no analogies in C2GL, like pictures, or generally sensor data. So we added a separate communication channel between the connector and the GUI which transports all not in C2GL expressible information.

2.4 UGV HANNA

The University of Hannover takes care of all work concerning the ground robot part of the project. They are using the unmanned ground vehicle *RTS HANNA* [7][8]. This robot is based on a Kawasaki Mule 3010, which is equipped with a drive-by-wire system from PARAVAN GmbH. It can move with up to 40 Km/h and has a maximum payload of 600kg. For environment perception the robot features 2D and 3D laser scanners and cameras. Together with a high precision localization module, backed by differential GPS and inertial sensors, it delivers high resolution occupancy grid maps of a given area, as well as live-video.



Fig. 1. Unmanned aerial vehicle PSYCHE 1000

2.5 UAV Psyche 1000

Within this project the University of Siegen utilizes two UAVs *Psyche 1000* (see Fig. 1) which are modified drones *MD4-1000*, originally built by Microdrones¹. They are electronically driven helicopters with four rotors, so called quadrocopters, providing a maximum flying weight of 6 kg. Having four rotors leads to a system which is controlled only by changes in rotational speed of each rotor. Every one of this rotors is driven by its own brushless engine. That makes the UAV almost completely maintenance free. In

¹ www.microdrones.com

comparison to a conventional helicopter design with a lot of moving parts like a swash plate, the possibility for technical failures is widely reduced.

The UAVs do have a high precision position stabilization and location estimation system. As in most localization systems a GPS receiver is used to obtain information about the absolute position. Together with measurements from accelerometers, gyroscopes, a magnetometer and a barometer the manufacturer provides the user a filtered position estimation. We extend the capabilities of the UAVs by adding a system on a chip running a specialized embedded Linux distribution that supports both a communication channel with the base station and other robots, as well as autonomous flight control. Our control modules utilizes the localization and attitude estimations from the UAV and generates signals that are fed back into the proprietary control software of the drone. The interface we use is the same, as the original radio control connection. This allows us to make use of all position stabilization functionalities provided by the manufacturer, as we electronically simulate a human operator. By the flick of a switch a real operator can obtain control over the UAVs at any given time for safety reasons.

Communication from and to the UAV is realized with two wireless connections. The original radio control device is connected over a bi-directional low-bandwidth, but high distance 2.4Ghz channel. It sends control commands to the UAV and receives information about the height, attitude and battery level, that are shown on a built-in LCD. The second channel is a 5Ghz Wireless LAN connection, used to transmit data with high bitrates.

Since this project is mainly focused on reconnaissance, the drones are equipped each with a 14.7 MP zoom camera. Since the UAVs have to alter their attitude to make changes in movement, a fixed mounting of the cameras would result in mostly blurry images. To resolve this, they are mounted within a moveable frame, which is deflected by two servos. The angle control input is taken from the attitude estimation made by the manufacturer. Pictures are accessible in two versions. One way is the live video preview, which is normally used on the camera display. These pictures do have a resolution of 320x240 pixels, an average file size of 9kB and are available at 15Hz. The second way is the single picture mode, where a high resolution picture is taken. In this case the pictures do have a resolution of up to 4416x3312 pixels and an average file size of 4MB.

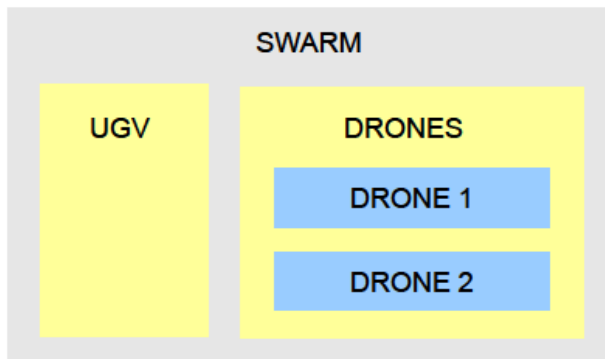


Fig. 2. Schematic hierarchy of the different robot groups, down to single robots that can be commanded

2.6 Scenarios

During the design process for the project we decided to formulate a scenario which is close to reality in terms of given propositions and usability. The basic task is to do reconnaissance in a roughly known area using a swarm of three heterogeneous, unmanned robots. In order to give the operator a clear overview of the environment, one UGV will traverse a known road map of the territory and deliver a occupancy grid map, while two UAVs provide image intelligence from above. To simplify the control process for the human operator the robots can be accessed separately, or in different groups (see Fig. 2). By standard, all orders are sent to the whole swarm only once. But if the current circumstances demand different behaviors, all orders can be given to every other entity within the hierarchy as well.

As mentioned above, BML is a rather high-level language, what makes it easy to read for machines but not very versatile in altering commands. We selected six commands from the pool and defined actions for the different types of robots to perform. Commands are described by so called BML orders. Each order has specific production rules defined by the C2GL rule set. Every one of them begins with the header, consisting of the *sender*, the *addressee* and the *sendingTime*. The header is followed by the order body (OB), which contains all information needed for the task.

All commands do share some common symbols. *Tasker* and *Taskee* are the names of entities that give, respectively receive orders. *At-Where* and *Route-Where* are spatial modifiers, describing a point, a list of points or an area. *Start-When* and *End-When* are temporal modifiers, and define when the command must be executed, or finished. And finally *Label* is set to a unique name for each given task.

1) *Move*: As the name implies this command moves robots from their current position to a specified point, which is the most basic ability the swarm has to be capable of. The rule for this order hast the following structure:

$$OB \rightarrow move \text{ } Tasker \text{ } Taskee \text{ } At\text{-}Where \text{ } Start\text{-}When \text{ } (End\text{-}When) \text{ } Label$$

If this command is send to the whole swarm it is processed by the ground vehicle in first place. It calculates a path from its current position to the target point, using the information from a previously known road map. While executing the order, the vehicle generates continuously (with a frequency of 1Hz) new *move* commands for the drone swarm, using its own position as the target point. All drones will then process these new messages and therefore follow the vehicle on its way to the destination in a formation depending on the number of UAVs.

2) *Patrol*: Sometimes it might be more interesting for the operator to have a look from different perspectives at the ground vehicle while it is moving. Therefore now the drones orbit around the ground vehicle, while it is traversing a number of target points. During this time the cameras of the drones are always headed towards the ground vehicle. The *patrol* command is structured as follows:

$$OB \rightarrow patrol \text{ } Tasker \text{ } Taskee \text{ } Route\text{-}Where \text{ } Start\text{-}When \text{ } (End\text{-}When) \text{ } Label$$

From the technical perspective the execution of this order is quite similar to *move*. The UGV traverses all the points given by the order using the information from the known road map. The UAVs now receive a patrol order from the UGV each second with its own position. With this information they calculate their position on an orbit around the UGV, using the absolute time from the GPS receiver and the knowledge of the number of drones in the swarm. Additionally the required angles for the camera are continuously updated using the position difference between each drone and the UGV.

3) *Observe*: This command lets the swarm approach a given point of interest. When this point is reached, all robots will deliver live video to the control station.

OB → observe Tasker Taskee At-Where Start-When (End-When) Label

If this command is given to the swarm, the ground vehicle internally uses the *move* command to guide the UAVs to the point of interest, so that the target is in the field of view of its camera. When approaching the destination the *observe* order is given once to the drones. They start to orbit around the target, by continuously generating patrol commands addressing themselves with a fixed target point.

4) *Distribute*: While the previous commands only took care of single points, or a route defined by points, the next ones describe actions taken on areas defined by polygons. Now the *At-where* in rule (4) does not consist of a single point, but of three or more, depending on the complexity of the polygon describing the area.

OB → distribute Tasker Taskee At-Where Start-When (End-When) Label

As the result of this command the swarm moves to the area of interest, lead by the UGV using *move* orders and then splits up. All robots distribute themselves equally within the area and send back live video to create an overview. The final positions for the robots are calculated by determining the center of gravity (CG) of polygons. The UGV uses the CG of the initial polygon and finds the closest point on a road within the map. When this point is reached the UAVs receive the *distribute* order, containing the polygon and split it up into smaller parts, depending on the number of drones. Then they apply the same algorithm as the UGV on this smaller polygons to determine their final positions for this scenario.

5) *Guard*: In comparison to the Distribute command, Guard is more challenging from the drones point of view. The ground vehicle executes the same behavior as during the Distribute scenario, except that it sends a single Guard command to the drone swarm, when it reaches the target area. The UAVs split up the given area into smaller parts, depending on the number of drones, and then traverse this smaller areas continuously while delivering high-resolution pictures to the control station.

OB → guard Tasker Taskee At-Where Start-When (End-When) Label

The waypoints needed for the UAVs to traverse the area are generated by overlaying the polygon with lines that are parallel to the line that divides the original polygon into smaller ones. The intersection points between this lines and the polygon boundaries are used for navigation, which leads to a saw tooth pattern of movement.

6) Reconnaissance: This is the most complex command for the swarm. The ground vehicle traverses all known roads within the given target area and builds up an occupancy grid of the environment while the drones deliver images from above.

OB → reconnaissance Tasker Taskee At-Where Start-When (End-When) Label

The ground vehicle guides the drone swarm to the target area using the move command. When the area is reached, one UAV is given the reconnaissance command, which lets it traverse all corner points of the polygon and deliver high resolution pictures from there. The second UAV is continuously given the patrol command to follow the ground vehicle as described above.

3 UAV Hard-/Software Modules

Besides the software implemented by the manufacturer, that takes care of stabilization and localization of the UAV, we added an additional system which executes supplementary tasks and generates the control signals for flight maneuvers, like the ones described in the last chapter. This system consists of a ARM9 system on a chip (SOC) with a total of 128MB of RAM and several interfaces like USB 2.0 and three serial connections. It is realized as a densely packed circuit measuring 54x54mm in size and 30g in weight.

3.1 Psyche Embedded Linux

As the operating system for this SOC we use a custom made Linux distribution. The kernel is highly adapted to the used hardware and the included libraries are reduced to a minimum to save as much resources as possible for user applications.

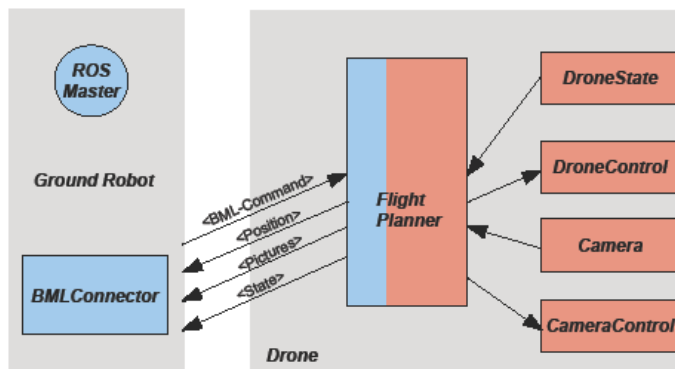


Fig. 3. ROS integration into the system. Blue parts show ROS modules. Red parts show proprietary UAV modules.

3.2 Psyche Software Environment

The main proprietary software modules running on the UAV are sketched with red color in Fig. 3. A more detailed information about the architecture is given in [9], but core functionalities should be mentioned shortly:

1) *DroneState*: This module makes all data coming from the drone available to a client via a UDP connection. Examples for types of data are position and attitude informations, battery status, wind-speed, etc.

2) *DroneControl*: Through this module users send orders to the UAV. Those are basically waypoints, or lists of waypoints attributed with a desired velocity and attitude.

3) *Camera*: Users are able to access the pictures shot with the USB attached camera through a TCP connection by using this module. Both, the low- and high-resolution pictures mentioned above are transported to the clients.

4) *CameraControl*: This module allows the user to remotely adjust all parameters of the camera. Typical use cases are zoom, exposure time, desired resolution and also the tilt angle of the moveable camera frame.

3.3 Reactive Collision Avoidance

Although all robots in the swarm are commanded from the control station, there is no central path planning system for the UAVs. The flying formations are chosen carefully to avoid small gaps between the drones, but while formation changes distances may fall below the safety limit. Therefore each drone is equipped with a software module, that realizes a reactive collision avoidance.

Due to a lack of sensors that are able to detect other UAVs during flights, the drones permanently publish data about their positions and movements via a UDP broadcast connection. This communication is established via an ad-hoc wireless network. WLAN is chosen, because it is very cheap and easy to implement into the system and it is stable and reliable when used for short distance communication, which is always given, if the threat of collision is present.

3.4 ROS Interface

ROS is used as the communication layer within this project, so every robot has to have the ability to publish and receive messages. Therefore the software parts, which implement the algorithms for task execution, also build a bridge between ROS and the proprietary interfaces on the robots. This part is called *Flight planner* in the case of the UAVs and its interfaces are shown in Fig. 3. The implementation on the UGV is mostly identical and not separately described here. The drones receive commands from an operator or from the ground vehicle in form of BML orders, embedded in ROS messages. The messages are processed and depending on the current scenario, different kinds of data are sent back to the control station. In this stage of the project such data mainly consists of reports of the robots positions (*geometry msgs/Pose*), pictures or videos (*sensor msgs/CompressedImage*) from interesting points and occupancy grids (*nav msgs/OccupancyGrid*) for operator defined areas.

3.5 Scenario Interpretation

As mentioned above all algorithms needed for the execution of the different scenarios are implemented within the *Flight planner* module onboard of the UAVs and accordingly on the UGV. The Planner is realized as a state machine with transitions triggered by incoming new, or completions of existing orders. If a new order arrives the first thing to check is the *Taskee* entry of the BML message. The different entities, that can be used as tasks are shown in Fig. 2. If the message must be processed on the given robot the next barrier is the level of the *Tasker*. If this level is higher, or on the same level as the currently active one, the message is further handled. Otherwise it is dismissed.

If the order has to be executed, the robots will start a behavior as described in 2.5. Thus the state machines makes a transition into the appropriate state and the level for the current tasker is set, for further comparisons. If the order is fully processed, before a new one arrives the tasker level is reset to the lowest one possible, so that orders from each entity are processed again.

4 Results

This project shows, that it is possible to control a heterogeneous robot swarm by a very abstract, but formal and context-free language. Using an abstract language requires a certain degree of autonomy on the robots, depending on the degree of abstractness. If this autonomy is available, a single operator can take care of many cooperating systems, without getting overstrained by caring too much about single robots. All scenarios described above were successfully demonstrated at a designated test ground with one ground robot and two aerial robots. All tasks were assigned to the whole robot swarm by a single operator using a simple and intuitive graphical user interface. Mission times, longer than 30 minutes without manual intervention or malfunctions of the systems were effectively shown.

But since the communication channel is strongly constrained by using a formal language, there are some information that cannot be transferred. Rather simple values like desired flying height, or an attitude cannot be expressed in BML. Even more problematic is the task of transmitting sensor data. To overcome this problem, either the language has to be extended to be able to handle binary data. Or the robot swarm has to be more intelligent. In this case sensor data has to be preprocessed on the individual robot and only the higher level interpretation of the information is transferred in the form of BML reports.

References

1. Kuhnert, L., Ax, M., Langer, M., Nguyen Van, D., Kuhnert, K.-D.: Absolute high-precision localisation of an unmanned ground vehicle by using real-time aerial video imagery for geo-referenced orthophoto registration. In: Dillmann, R., Beyerer, J., Stiller, C., Zoellner, J.M., Gindel, T. (eds.) Autonome Mobile Systeme 2009. Informatik aktuell, pp. 145–152. Springer, Heidelberg (2009)

2. Phan, C., Liu, H.H.T.: A cooperative UAV/UGV platform for wildfire detection and fighting. In: Asia Simulation Conference 7th International Conference on System Simulation and Scientific Computing, ICSC 2008, October 10-12, pp. 494–498 (2008)
3. Tanner, H.G.: Switched UAV-UGV Cooperation Scheme for Target Detection. In: 2007 IEEE International Conference on Robotics and Automation, April 10-14, pp. 3457–3462 (2007)
4. Hsieh, M.A., Cowley, A., Keller, J.F., Chaimowicz, L., Grocholsky, B., Kumar, V., Taylor, C.J., Endo, Y., Arkin, R.C., Jung, B., Wolf, D.F., Sukhatme, G.S., MacKenzie, D.C.: Adaptive teams of autonomous aerial and ground robots for situational awareness. *Field Reports. J. Field Robot* 24, 991–1014, November 11-12 (2007)
5. Schade, U., Hieb, M.R., Frey, M., Rein, K.: Command and control lexical grammar (c2gl) specification. Fraunhofer FKIE, Tech. Rep (2010)
6. Quigley, M., Gerkey, B., Conley, K., Faust, J., Foote, T., Leibs, J., Berger, E., Wheeler, R., Ng, A.: Ros: an open-source robot operating system. In: ICRA Workshop on Open Source Software (2009)
7. Langerwisch, M., Reimer, M., Hentschel, M., Wagner, B.: Control of a semi-autonomous ugv using lossy low-bandwidth communication. In: The Second IFAC Symposium on Telematics Applications (TA), Timioara, Romania (October 2010)
8. Hentschel, M., Wagner, B.: Autonomous robot navigation based on openstreetmap geo-data. In: 13th International IEEE Conference on Intelligent Transportation Systems (ITSC) (September 2010)
9. Ax, M., Kuhnert, L., Langer, M., Schlemper, J., Kuhnert, K.-D.: Architecture of an autonomous mini unmanned aerial vehicle based on a commercial platform. In: Joint 41th Symposium on Robotics and 6th German Conference on Robotics (June 2010)

A Full-functional Simulation and Test Platform for Rotorcraft Unmanned Aerial Vehicle Autonomous Control

Ziming Wang¹, Dalei Song¹, Juntong Qi¹, Jianda Han¹, Yu Miao², Lijun Meng²,
Shuaike Zhao², and Ming Li²

¹ Shenyang Institute of Automation, Chinese Academy Science(CAS),
No.114 Nanta Street, Shenyang, Liaoning Province, 110016, China

wangziming@sia.cn

² Liaoning Benxi Power Supply Company
No.6 Yinghua Street, Benxi, Liaoning Province, 117000, China
strongmiao@hotmai.com

Abstract. In this paper, a prototype Hardware in the loop (HIL) simulation and test platform for ServoHeli40 and ServoHeil120 rotorcraft unmanned aerial vehicles have been developed in Shenyang Institute of Automation, Chinese Academy of Science. This simulation system includes a 3D flight and scenery simulator, a flight control systems, a ground control station, and a RC pilot controller. Based on a semi-decoupled flight dynamic model, which is acquired from a frequency domain system identification method using real flight hovering data, an autonomous PID controller is implemented and verified in both simulation and real flight tests. To fulfill agricultural, marine and industrial applications, the application oriented functionalities of the flight control system has been developed and fully tested before deployment in the field. And it is also beneficial to further research such as human factors in operating UAV systems and UAV task load issues.

Keywords: unmanned helicopter, hardware in the loop simulation, system identification.

1 Introduction

Unmanned Aircraft Systems (UAS) is a solution for missions that are “dull, dirty, or dangerous” for human piloting manned aircraft. At present, Unmanned Aerial Vehicles (UAVs) perform reconnaissance as well as attack missions over the battlefields. UAVs are also deployed in civilian applications such as search and rescue, transportation, and scientific research including environmental observation, geological survey, and precision agriculture monitoring, etc.

Compared to fixed wing UAVs, Rotorcraft Unmanned Aerial Vehicles (RUAVs) can be operated in many unique modes such as vertical take-off and landing, hovering, lateral flight, pirouette, and bank-to-turn, etc. Due to its versatility in maneuverability and agility, RUAVs are capable of flying in and out restricted area

and hovering for a long period of time without being noticed, which makes RUAVs suitable for accomplishing many military and civilian applications. However, the nonlinear and inherently unstable dynamics nature makes research experiments highly costly and risky. Therefore, to minimize unnecessary losses during field testing and enhance the system reliability, a simulation and test platform is really necessary for algorithm and system function testing in early stages during the RUAU system development.

After several years of supports from national funded research programs and cooperation with industrial partners, ServoHeli RUAVs are custom made and manufactured in our institute. ServoHeli-40 aerial vehicle, shown in Fig. 1, is a high quality helicopter, which is custom designed by us using a RC technical grade helicopter operating with a remote controller. The modified system allows the payload of more than 10 kilograms, which is sufficient to take the whole airborne avionics box and the communication units to achieve autonomous flight control. The fuselage of the helicopter is constructed with sturdy duralumin, and composite body and the main rotor blades are replaced with heavy-duty carbon fiber reinforced ones to accommodate extra payloads. The vehicle is powered by a ZENOAH engine which generates 9hp at about 10000 rpm, a displacement of 80cc and practical angular rate ranging 2,000 to 16,000 rpm. The length of the fuselage is 2120mm, and the width is 320mm. The total height of the helicopter is 730mm, the diameter of main rotor blades and tail blades are 2150mm and 600mm respectively. Designing and packing the avionics box appropriately under the fuselage of the helicopter are two major tasks to implement the unmanned helicopter system. In the actual flight environment, the weight and the size of the avionics box are strictly limited to achieve best functions and performance under the take-off weight constraint. The airborne control box, which is shown in Fig. 2, is a compact aluminum alloy package mounted on the landing gear under the engine, where is about the center mass of the entire platform. The center of gravity of the box lies on the IMU device, where is not the geometry center of the system, that assures the navigation data from IMU accurate. The compass and the IMU are taken as the horizontal center of the gravity of the avionics system and the other components are installed on the same line.

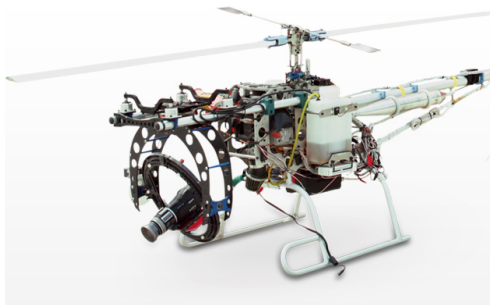


Fig. 1. ServoHeli 40 RUAU

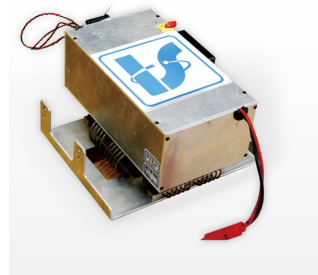


Fig. 2. Onboard flight control system

To operate the ServoHeli RUAU and its onboard payloads, a ground control station (GCS) is designed to communicate with the onboard avionics via a 900MHz radio data link. As the communication established, the onboard avionics transmits the helicopter's flight status, including GPS position and 3axis compass information, aircraft attitude data, filtered and estimated velocities and acceleration data, control inputs and outputs, RUAU operating modes as well as task management information to the GCS 50 times per second. After parsing incoming data packets, GCS displays the flight trajectory, waypoints, target location, as well as the battery and gas level, engine temperatures and revolutions. The GCS also uploads task information to the onboard controller, such as task waypoints, target location, and payload control commands.

A prototype Hardware in the loop (HIL) simulation and test platform for ServoHeli40 RUAUs has been developed in Shenyang Institute of Automation, Chinese Academy of Science. It is composed of 3D flight and scenery simulator, flight control system (FCS), ground control station (GCS), and a RC pilot controller. The 3D flight and scenery simulator runs a RUAU aerodynamic model in Matlab/Simulink environment, which is identified by using data collected from real RUAU manual hovering experiments, and the simulator generates simulated navigational sensory information includes GPS data, RUAU attitude data, 3-axis flight velocity data, 3-axis RUAU acceleration data, 3-axis angular rate data, and 2-axis wind disturbances at 50Hz. It also displays 3D flight progress in Flightgear, a widely known open source flight simulator. The flight control system (FCS) is the core avionics of the system, which accepts the simulated navigational information sent from 3D flight and scenery simulator and executes the autonomous control algorithm iteratively in an UC/OS real time system 50 times per second. Ground control station (GCS) is built in a water-proofed pelican case, and it establishes a wired or wireless data communication link with FCS. GCS software parses the data packets and demonstrates the flight trajectory, RUAU attitude, velocities, accelerations and other essential navigation information simultaneously in user friendly interfaces. It also interacts with the FCS task management via the communication link, such as flight path\waypoints planning, flight modes switching, and RUAU system health monitoring, as well as various payload operations. RC pilot controller enriches the entire system to be capable of RC pilot training and potentially to be a safety redundant during the full autonomous flight or scenarios like encountering hazards in the air.

Full autonomous flights have been simulated and tested in this platform, and it has demonstrated the advantage in accelerating the algorithms and system function development cycle in an advanced approach. This simulation platform can be also deployed in human factor study of operation procedures, UAV crew task load and application-guided operation training.

2 System Identification

In reference [1], a parameterized state-space model is presented that explicitly accounts for the stabilizer bar and rotor system based on first principles. The model can be expressed in the following form

$$\begin{pmatrix}
X_u & 0 & 0 & -w_0 & 0 & -g & X_a & 0 & 0 & X_r & 0 & 0 & 0 \\
0 & Y_v & w_0 & 0 & g & 0 & 0 & Y_b & 0 & Y_r & 0 & 0 & 0 \\
L_u & L_v & 0 & 0 & 0 & 0 & 0 & L_b & L_w & 0 & 0 & 0 & 0 \\
M_u & M_v & 0 & 0 & 0 & 0 & M_a & 0 & M_w & 0 & 0 & 0 & 0 \\
0 & 0 & 1 & 0 & 0 & 0 & 0 & 0 & 0 & 0 & 0 & 0 & 0 \\
0 & 0 & 0 & 1 & 0 & 0 & 0 & 0 & 0 & 0 & 0 & 0 & 0 \\
0 & 0 & 0 & -1 & 0 & 0 & -1/\tau_f & A_b/\tau_f & 0 & 0 & 0 & A_c/\tau_f & 0 \\
0 & 0 & -1 & 0 & 0 & 0 & B_d/\tau_f & -1/\tau_f & 0 & 0 & 0 & A_c/\tau_f & 0 \\
0 & 0 & -v_0 & u_0 & 0 & 0 & Z_a & Z_b & Z_r & 0 & 0 & 0 & 0 \\
0 & N_y & N_p & 0 & 0 & 0 & 0 & N_w & N_r & -N_{fb} & 0 & 0 & 0 \\
0 & 0 & 0 & 0 & 0 & 0 & 0 & 0 & K_r & -K_{rfb} & 0 & 0 & 0 \\
0 & 0 & 0 & -1 & 0 & 0 & 0 & 0 & 0 & 0 & -1/\tau_s & 0 & 0 \\
0 & 0 & -1 & 0 & 0 & 0 & 0 & 0 & 0 & 0 & 0 & C_{lon}/\tau_s & 0 \\
0 & 0 & -1 & 0 & 0 & 0 & 0 & 0 & 0 & 0 & 0 & D_{lon}/\tau_s & 0
\end{pmatrix}
\begin{pmatrix}
\Delta \dot{u} \\
\Delta \dot{v} \\
\Delta \dot{p} \\
\Delta \dot{q} \\
\Delta \dot{\theta} \\
\dot{a} \\
\dot{b} \\
\dot{\Delta r} \\
\dot{\Delta v} \\
\dot{\Delta r} \\
\dot{c} \\
\dot{d}
\end{pmatrix}
+
\begin{pmatrix}
0 & 0 & 0 & 0 \\
0 & 0 & 0 & Y_{ped} \\
0 & 0 & 0 & 0 \\
0 & 0 & 0 & 0 \\
0 & 0 & 0 & 0 \\
A_{lat}/\tau_f & A_{lon}/\tau_f & 0 & 0 \\
B_{lat}/\tau_f & B_{lon}/\tau_f & 0 & 0 \\
0 & 0 & 0 & Z_{col} \\
0 & 0 & 0 & N_{ped} \\
0 & 0 & 0 & N_{col}
\end{pmatrix}
\begin{pmatrix}
\Delta \delta_{lat} \\
\Delta \delta_{lon} \\
\Delta \delta_{ped} \\
\Delta \delta_{col}
\end{pmatrix}
= A\Delta X + B\Delta Y \quad (1)$$

where u, v, w are longitudinal, lateral and vertical velocities, p, q, r are roll, pitch and yaw angle rates, φ and θ are the angles of roll and pitch, respectively; a and b are the first harmonic flapping angles of main rotor, c and d are the first harmonic flapping angles of stabilizer bar, r_{fb} is the feedback control value of the angular rate gyro, δ_{lat} is the lateral control input, δ_{lon} is the longitudinal control input, δ_{ped} is the yawing control input, and δ_{col} is the vertical control input. All the symbols except gravity acceleration g in A and B are unknown. Thus, all the states and control inputs in (1) are physically meaningful and defined in body-axis coordinates, which is described in Fig. 3.

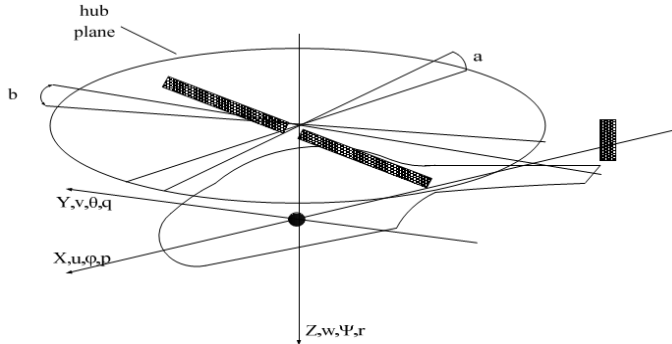


Fig. 3. Helicopter body-fixed coordinate

For effective hovering identification, the original model in [1] is decomposed into three groups (longitudinal, lateral, and yaw-heave coupling), and a semi-decoupled model is obtained [2]. Each group has a decoupled system matrix, and the coupling characteristics are presented only in the control matrix. Thus, the number of unknown parameters and control inputs is reduced and the control loops are semi-decoupled. Then, to identify the unknown parameters in the MIMO semi-decoupled model, a new cost function is proposed to make the traditional method of SISO system frequency estimation [3] applicable to the MIMO state-space models. The proposed cost function is presented in the additional form of the frequency error of every input-output pair for transfer matrix, and the parameters are identified by minimizing the cost function. The simplified model and proposed identification method free the

selection of initial estimation and constraint is not required. The simplified model structure is in the formation of Equation 2, and its Z-transformation is Equation 3. Bode diagrams and response of both step and impulse inputs of the four control channels in the identified model are illustrated through Fig 4-7.

$$y_{t+1} = a_1 y_{t-1} + a_2 y_t + b_1 u_t \quad (2)$$

$$G(z) = \frac{b_1 z}{z^2 - a_2 z - a_1}, T = 0.02s \quad (3)$$

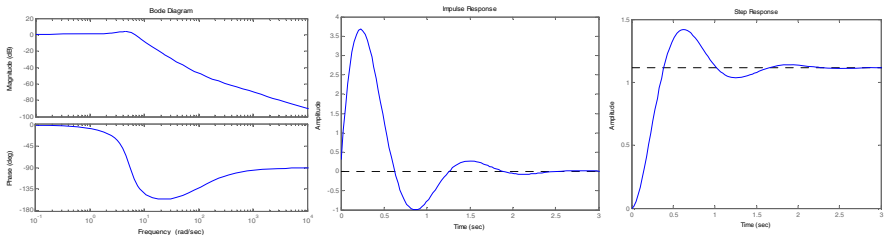


Fig. 4. Bode diagram, step response and impulse response of longitudinal control channel

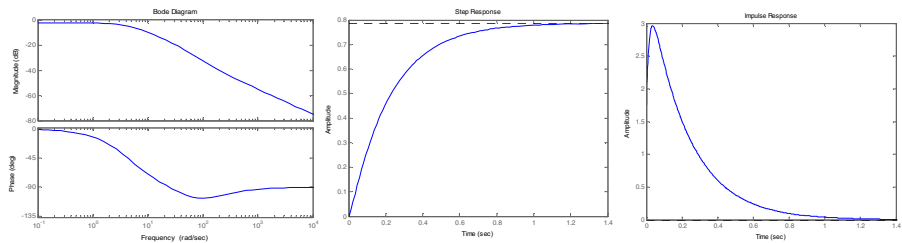


Fig. 5. Bode diagram, step response and impulse response of lateral control channel

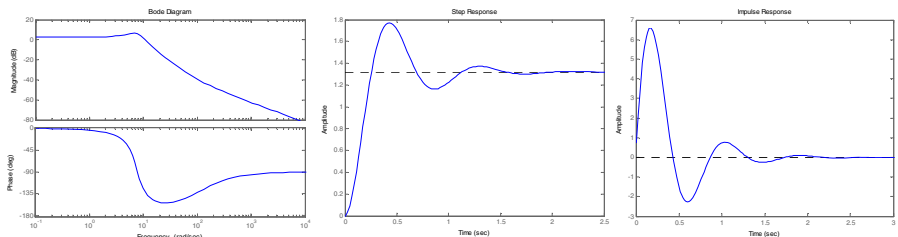


Fig. 6. Bode diagram, step response and impulse response of yaw control channel

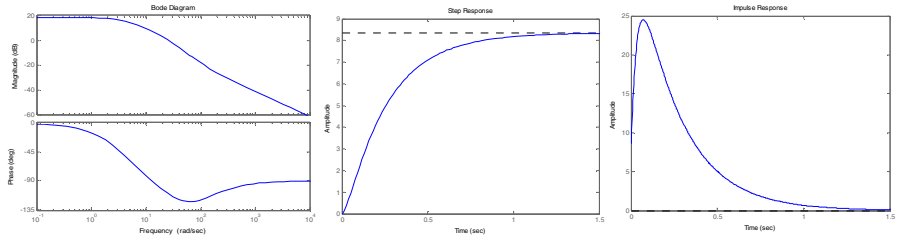


Fig. 7. Bode diagram, step response and impulse response of vertical control channel

With the proposed system identification approach, a decoupled four channel helicopter numerical model has been concluded. Results in [4] validates that this model represents ServoHeli40 RUAV hovering dynamics, and satisfied dynamics in the rest of flight envelope, like lateral flight and agile maneuvering. And based on this model, a PID feedback controller has been implemented and well tuned and tested in both simulation environment and real flight testings.

3 Hardware in the loop Simulation System Configuration

To fulfill the urgent need in the software design and preliminary testing of a flight control system, researchers have built variety of software in the loop simulation systems to address the issue. However, simple software simulation system is not capable of testing and researching RUAV safely and effectively in terms of control algorithm, system function, and system integration. Therefore, hardware in the loop simulation in RUAV's research stage is significantly valuable and has practical meanings, especially in the flight control systems designing as the system has high complexity, multi-variable model and unpredictability due to environment and weather variations. Hence, to build a flight control system simulation environment to perform system control mechanism and system functionality testing is a crucially indispensable approach.

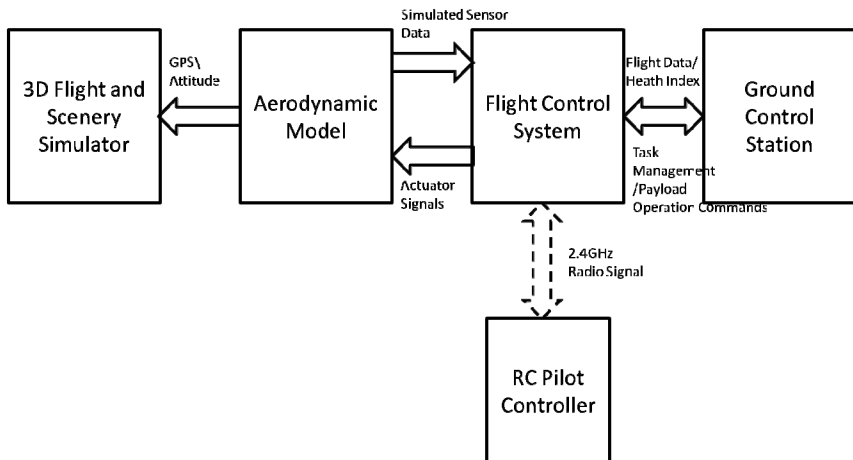


Fig. 8. Hardware in the loop simulation system diagram

Prototype hardware in the loop (HIL) simulation and test platform for ServoHeli40 RUAVs has been developed in Shenyang Institute of Automation, Chinese Academy of Science. It is composed of a 3D flight and scenery simulator, a flight control system (FCS), a ground control station (GCS), and a RC pilot controller. A system diagram is shown in Fig.8, and Fig.9 illustrates a minimum system setup in the lab. The identified ServoHeli40 RUAU flight dynamic model, green block in Fig.10, is run in a Matlab Simulink block on the 3D flight and scenery simulator computer. By propagating the flight dynamic model from an initial known location such as runway 28L at San Francisco International Airport (KSFO) with some other initial settings like a target position in X_{ref} , Y_{ref} , and Z_{ref} , and reference flight speed V_{xref} , V_{yref} , V_{zref} , then simulated navigational sensor information, including GPS information, attitude data, 3-axis flight velocities, accelerations and angular rates, are calculated iteratively when the dynamics is invoked by the Simulink model. Two input channels of the dynamic model are reserved to simulate environmental factors and variations, such as adding signals descript random wind/gust property or representing measurement noise in reality in the form of probability density functions.

With the updated simulated flight information, two formatted data packets are produced. One data stream is fed into a preconfigured Simulink block named "Flightgear 6DOF Animation". This block packs the flight data, including GPS and Euler angles, and then feeds them into Flightgear simulator based on TCP/IP protocol. In Flightgear, a virtualized flight vehicle and flight progress is then simultaneously rendered with rich background objects, like buildings, grassland and configurable clouds and weather conditions; the other stream goes into the grey block labeled "TO_FCU_SERIAL", which sends the data packets to the FCS unit via RS-232 serial communication link. With the simulated navigation sensor data, the high level guidance and control decision is achieved in the FCS unit iteratively by evaluating the control algorithm. And the RUAU control commands, in terms of pitch angle, roll angle, yawing and vertical control, are sent back into the Simulink dynamic model through another RS-232 serial port. Then in the next iteration, these commands will be taken into the flight dynamics calculation and control response will be reflected in the navigation information as well as the Flightgear animation display.



Fig. 9. Simulation system setup

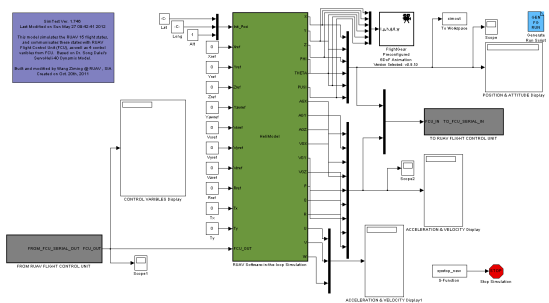


Fig. 10. Simulink model of RUAU flight dynamics

4 Autonomous Control Algorithm Verification and Application Testing

One of the significant purposes is to verify the control logic of the autonomous flight control algorithm and to conduct preliminary tests to validate system function before the system is delivered to industrial partners. In this section, two industry oriented applications are presented with both simulation and real flight testing results.

4.1 Agricultural Application - Autonomous Precision Agricultural Spraying

One of the important RUAV applications is to perform precision agricultural spraying instead of high cost low productivity human spraying or by other large size heavy duty machines. Autonomous agricultural spraying by RUAVs provides accurate chemical delivery and high efficiency operation. Meanwhile, it also limits the harm to human beings during and reduces the heavy workload. In addition, it is the ideal solution for large scale farmland.

We developed an autonomous precision agricultural spraying system for a farming base in Xinjiang Province. The critical requirements are: a) spraying the pesticide or chemicals at a certain height above the plants due to various crops have dissimilar nature in different growing stages; b) as the crops are planted with 3-5 meters between furrows, to equally deliver the chemicals to the crops, the RUAV needs to keep a parallel flight trajectory with a constant speed within the farmland boundaries; c) it requires to cover approximately 500 square meters per minute. According to the partner's requirements, a polygon path planning algorithm has been developed and simulated in the simulation system firstly and then tested in a real farming land and will be tested soon in Xinjiang in late autumn. One of infield flight testing result is shown in Fig. 11. In this figure, the GPS flight trajectory from takeoff to landing is shown. The longer edges are the flight trajectories along the field furrows and the shorter ones are the flight trajectories where the RUAV moved laterally between field furrows. Total flight duration is about 10 minutes. During the operation time, it covered about 6000 square meters. This yields approximately 600 square meters per minute, which confirms that the autonomous path planning algorithm offers convincing performance in real application.

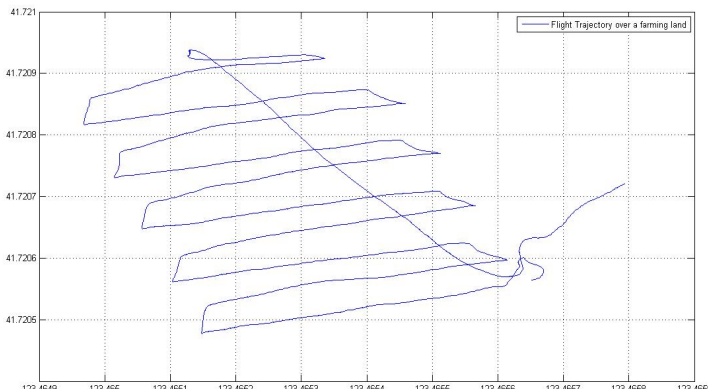


Fig. 11. Flight trajectory during spraying over a farmland

4.2 Marine Application – Autonomous Non-stationary Platform Landing

New challenges are raised with a growing desire of operating UAVs in marine environment with the adverse turbulences over the flight deck and the complicated and unpredictable ship motion. RUAU's operational flexibility, including vertical take-off and landing hovering at a certain height, especially the longitude and lateral maneuverability provides unique capabilities to complete this high risk routine. On the other hand, turbulent gust and low visibility of the landing pad on the deck makes RUAUs are sensitive and vulnerable to these external turbulences during the procedure of the accurate landing tasks. A fundamental issue for a successful landing operation is to accurate estimate the deck displacement and attitude, and then by cooperating this information to adjust the RUAU landing attitude and velocity to compensate the undesirable condition. Lab experiment setup is quite dissimilar from maritime reality and experimental opportunities are also limited to investigate the problem intensively in the lab environment. Therefore, a fully developed simulation system is ideal to assess this cooperative landing algorithm, which can be easily transferred to the flight control system for real flight tests.



Fig. 12. RUAU landing on a carrier deck

In the simulation system, a moving objective, a carrier, with random but adjustable turbulences is introduced, shown in Fig.12. Besides the RUAU dynamic model, a ship dynamics model is run in Simulink on another computer. A ship dynamics [5] and a spectrum based wave dynamic model [6] are integrated in the block to best reflect carrier movement and displacement in the rough sea condition in reality. The cooperative carrier information including GPS location, attitude information, velocities and etc are sent to the RUAU FCS via a RS-232 serial port. In order to assist accurate landing on the target pad, a virtual camera view is custom configured in the Flightgear view system in the "preference.xml". The virtual camera is set fixed at the belly of the helicopter with a (0, 0, -3.5) offset from the center mass of the

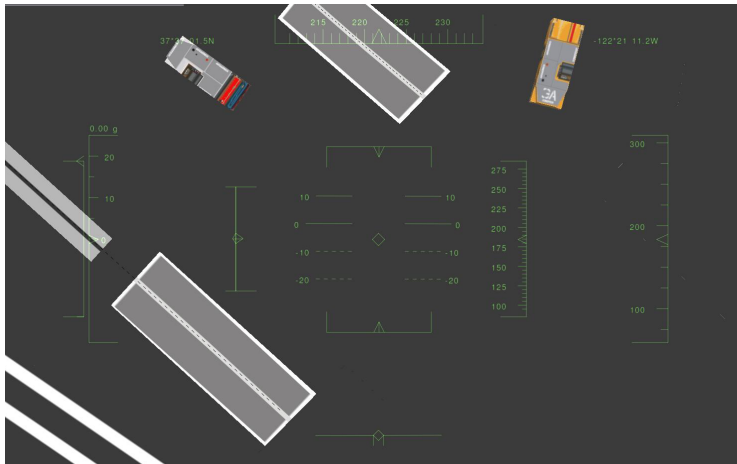


Fig. 13. Downward looking camera view of landing pad

helicopter. The camera view can be specified in two modes: stabled downward looking and body fixed attitude downward looking. The stabled downward looking offers a deck view without taking the RUAV attitude into consideration; and the body fixed downward looking camera view provides a dynamic view as the RUAV changes its own gesture, illustrated in Fig.13. The results of cooperative landing algorithm in simulation and inflight tests will be discussed in future publications.

5 Conclusion

UAVs are widely used in both military and civilian applications, especially, rotorcraft UAVs are ideal for many civilian purposes, like agriculture, geo survey, and power line inspections. However, safety and stability concerns keep the technology from deployment. In this paper, a simulation and testing platform for RUAV software and autonomous control algorithm is introduced, and it has been proved that it is a safe and effective approach during the researching stage of the RUAV control system to reduce the cost and danger compared with real flight testing, and to accelerate the system development. Furthermore, the simulation system shows its flexibility in integrating extra function of the control system. In additional, it is suitable for the operator and crew training once the RUAV becomes a mature product available to the customers who are unfamiliar to the UAV industry.

In the future, different identification approaches and high order model structures will be applied to improve the fidelity of the RUAV system dynamics. Dynamic models of next generation of ServoHeli RUAV with 120kg in weight and quad rotors will be incorporated to the current system to form a series of flight systems. As the system function expends, the simulation system will be revised to be able to test more system functions and working conditions such as power line inspection tasks, autonomous border patrol, and etc. Several proposed topics and research work such as a system solution for GPS denied environment navigation and GPS loss link scenario navigation system will be conduct on this system.

References

1. Mettler, B., Dever, C., Feron, E.: Scaling Effects and Dynamic Characteristics of Miniature Rotorcraft. *Journal of Guidance Control and Dynamics* 3, 466–478 (2004)
2. Song, D., Qi, J., Han, J.: Model Identification and Active Modeling Control for Small-Size Unmanned Helicopters: Theory and Experiment. *AIAA Guidance Navigation and Control*, Toronto, Canada (2010)
3. Haykin, S., De Freitas, N.: Special Issue on Sequential State Estimation. *Proceedings of the IEEE* 92(3), 423–574 (2004)
4. Qi, J., Song, D., Dai, L., Han, J., Wang, Y.: The New Evolution for SIA Rotorcraft UAV Project. *Journal of Robotics*, Vol 2010(743010) (2010)
5. Zhang, X., Yin, Y., Jin, Y.: Ship motion mathematical model with six degrees of freedom in regular wave. *Journal of Traffic and Transportation Engineering* 7(3), 40–43 (2007)
6. Yang, H., Sun, J.: Wave Simulation Based on Ocean Wave Spectrums. *Journal of System Simulation* 14(9), 1175–1178 (2002)

Market-Based Multiagent Framework for Balanced Task Allocation

Dong-Hyun Lee, Ji-Hyeong Han, and Jong-Hwan Kim, *Fellow, IEEE*

Department of Electrical Engineering, KAIST,
335 Gwahangno, Yuseong-gu, Daejeon 305-701, Republic of Korea
{dhlee,jhhan,johkim}@rit.kaist.ac.kr

Abstract. This paper proposes a market-based multiagent task allocation framework for allocating tasks in a balanced manner based on the energy levels of robots. In this framework, a market-based agent is designed for trading tasks considering the robot capabilities, task requirements and energy level of the robot. The framework utilizes a bid weight for distributing the tasks in a balanced manner without frequent using of particular robots. To demonstrate the effectiveness of the proposed framework, a simulation experiment was carried out for a cleaning mission consisting of collecting, carrying, sorting and disposal tasks.

Keywords: Multirobot coordination, Market-based task allocation, Balanced task allocation.

1 Introduction

Market-based coordination approach for multirobot system has been developed with considerable popularity and it has been widely used in the areas of exploration and dynamic team formation [1, 2, 3, 4]. The concept of the market-based task allocation was started from the contract net protocol [5]. Many approaches have since adopted similar strategies for multiagent task allocation. Beaumont and Chaib-draa proposed to use multiagent planning and coordination techniques for resource management in command and control systems [6]. Dias proposed *Traderbots*, consisting of *OpTrader* and *RoboTrader* [7]. Gerkey and Mataric implemented an auction-based task allocation system, MURDOCH, where the publish/subscribe communication model was used for efficient resource usage [8]. Vokrinek et al. presented an abstract architecture of a multiagent solver consisting of three types of agents, task agent, allocation agent and resource agent [9].

Although there have been various researches on market-based approach, most of the market-based approaches did not take much consideration on distributing tasks in a balanced manner. In the proposed approach, two types of bid weights, global and local bid weights are defined for adjusting the relative importance of the task quality over task cost.

This paper is organized as follows. Section 2 defines atomic tasks and three types of compound tasks. In Section 3 and Section 4, bid and utility generation processes are described. The proposed framework is applied in a cleaning mission and simulation results are discussed in Section 5. Finally, concluding remarks and future work are described in Section 6.

2 Task Definition

In this framework, two levels of tasks, atomic and compound tasks, are defined. The atomic task is the minimum unit of a task which can not be divided into smaller sub-tasks. The compound task consists of the atomic tasks and three types of compound tasks, i.e., sequential, synchronous parallel, and asynchronous parallel compound tasks, are defined.

The sequential compound task requires the atomic tasks to be performed sequentially. The i th sequential compound task in a mission, $Task^{i,S}$, $i \in \{1, 2, \dots, M\}$, is defined as

$$Task^{i,S} = \{task_1^{i,S}, task_2^{i,S}, \dots, task_v^{i,S}\} \quad (1)$$

with

$$task_j^{i,S} \in Task^A, \quad task_j^{i,S} \succ task_k^{i,S} \quad (j < k)$$

where M and v are the number of compound tasks in the mission and the number of atomic tasks in $Task^{i,S}$, respectively, $Task^A$ is the set of atomic tasks, and $task_j^{i,S} \succ task_k^{i,S}$ denotes that the priority of $task_j^{i,S}$ is higher than $task_k^{i,S}$. The priority of the atomic task in the sequential compound task represents the execution order.

The synchronous parallel compound task consists of the atomic tasks that should be performed in parallel with synchronized manner. The i th synchronous parallel compound task in the mission, $Task^{i,SP}$ is defined as

$$Task^{i,SP} = \{task_1^{i,SP}, task_2^{i,SP}, \dots, task_h^{i,SP}\} \quad (2)$$

with

$$task_j^{i,SP} \in Task^A, \quad task_j^{i,SP} \succeq task_k^{i,SP} \quad (j < k)$$

where h is the number of the atomic tasks in $Task^{i,SP}$. The priority of the atomic tasks in the synchronous parallel compound task represents the master and slave relationship such that the robot which gets the atomic task with higher priority becomes a master which takes the initiative in task execution.

The asynchronous parallel compound task consists of the atomic tasks that can be performed asynchronously in parallel. Unlike the synchronous parallel compound task, a single robot can perform one or more atomic tasks of the asynchronous parallel compound task as far as it can perform the atomic tasks in parallel. The i th asynchronous parallel compound task in the mission, $Task^{i,AP}$ is defined as

$$Task^{i,AP} = \{task_1^{i,AP}, task_2^{i,AP}, \dots, task_y^{i,AP}\} \quad (3)$$

with

$$task_j^{i,AP} \in Task^A, \quad task_j^{i,AP} \succeq task_k^{i,AP} \quad (j < k)$$

where y is the number of the atomic tasks in $Task^{i,AP}$. The priority of the atomic tasks in the asynchronous parallel compound task represents the master and slave relationship which is similar to the case of the synchronous parallel compound task.

3 Bid Generation

The bid is defined as the list of the task quality, task cost and normalized energy level of the bidder. The bid of a robot for a task is calculated by the capabilities of the robot and the requirement of the task.

3.1 Robot Capabilities and Task Requirements

To describe the robot capabilities and task requirements, the robot capability matrix and task requirement matrix are provided [10]. The robot capability matrix consists of capability vectors and each capability vector contains the information about the quality and energy consumption rate of the capability which are defined by the hardware resource of the capability. The robot capability matrix of the i th robot, $Robot_i$, R_i^{cap} , $i = 1, 2, \dots, n$, is defined as

$$R_i^{cap} = [cap_{i1} \ cap_{i2} \dots \ cap_{im}] \quad (4)$$

where n and m represent the number of the robots and capabilities, respectively, and the k th capability vector of $Robot_i$, cap_{ik} , $k = 1, 2, \dots, m$, is defined as

$$cap_{ik} = [q_{ik} \ e_{ik} \ p_{ik}]^T \quad (5)$$

where q_{ik} ($0 \leq q_{ik} \leq 1$) is the capability quality, and e_{ik} ($e_{ik} \geq 0$) and p_{ik} ($p_{ik} \in \{0, 1\}$) represent the energy consumption rate and its unit, respectively. If p_{ik} is set to one, the unit of e_{ik} is set to J/m , and if p_{ik} is zero, the unit is set to J/s . The robot should be able to monitor its capabilities in real time to make sure they are operating properly.

The task requirement matrix consists of requirement vectors. Each robot has the task requirement matrices such that when one of the tasks is auctioned, the robot searches for the task and gets the task requirement matrix of the task. The task requirement matrix of the j th atomic task, $task_j$, T_j^{req} , $j = 1, 2, \dots, l$, is defined as

$$T_j^{req} = [req_{j1} \ req_{j2} \dots \ req_{jm}] \quad (6)$$

where l represents the number of the atomic tasks, and the k th requirement vector of T_j^{req} , req_{jk} , $k = 1, 2, \dots, m$, is defined as

$$req_{jk} = [h_{jk} \ w_{jk}^{cap}]^T \quad (7)$$

where h_{jk} ($h_{jk} \in \{0, 1\}$) denotes the requirement of the k th capability for $task_j$, which is set to one if the k th capability is required for the task and zero if not, and w_{jk}^{cap} ($0 \leq w_{jk}^{cap} \leq 1$) is the capability weight which decides the importance of the capability quality on the task.

3.2 Bid Values

The task quality of a robot represents how well it can perform the auctioned atomic task in terms of the quality. The task quality of $Robot_i$ for $task_j$, Q_{ij} is defined as

$$Q_{ij} = \sum_{k=1}^m h_{jk} \cdot w_{jk}^{cap} \cdot q_{ik} \quad (8)$$

where h_{jk} and w_{jk}^{cap} are from (7), and q_{ik} is from (5). The equation implies that if the bidder has high qualities for the required capabilities, it can get high task quality for the task.

The task cost is defined as the estimated energy consumption of the bidder to complete the auctioned atomic task. The task cost of $Robot_i$ for $task_j$, C_{ij} is defined as

$$C_{ij} = \alpha_{ij} \cdot d_{ij} + \beta_{ij} \cdot t_{ij} \quad (9)$$

with

$$\alpha_{ij} = \sum_{k=1}^m h_{jk} \cdot p_{ik} \cdot e_{ik} \quad (9.a)$$

$$\beta_{ij} = \sum_{k=1}^m h_{jk} \cdot (1 - p_{ik}) \cdot e_{ik} \quad (9.b)$$

where α_{ij} and β_{ij} are the energy consumption rate per meter and per second, respectively, d_{ij} and t_{ij} are the estimated travel distance and estimated time, respectively, h_{jk} is from (7), and p_{ik} and e_{ik} are from (5).

The normalized energy level of the robot is used to consider the energy level of the robot in task allocation. The auctioneer is able to consider the normalized energy level of each bidder or the sum of the normalized energy levels of the bidders to adjust the relative importance between the task quality and task cost, and distribute tasks in a balanced manner. Since the robots might have different energy capacities, the energy level of each robot is normalized. The normalized energy level of $Robot_i$ for $task_j$, L_{ij} is defined as

$$L_{ij} = \frac{E_i - C_i(A_i, j) - E_i^{Min}}{E_i^{Max} - E_i^{Min}} \quad (10)$$

where E_i , E_i^{Min} and E_i^{Max} are the current, minimum and maximum energy level of $Robot_i$, respectively, and $C_i(A_i, j)$ represents the estimated energy consumption of the robot for the tasks in the set A_i and $task_j$.

4 Utility Generation

Utility represents the bidder's fitness on the auctioned atomic task. The utility is the weighted sum of task quality and task cost. The bid weight is used to adjust the relative importance of task quality over task cost.

4.1 Bid Weight

The proposed framework provides two types of bid weights, global and local bid weights. The function type of the global bid weight for $task_j$, $w_{glo}^{bid}(G_j)$ is defined as

$$w_{glo}^{bid}(G_j) = \alpha \cdot \exp(\lambda \cdot (G_j - 1)) \quad (11)$$

with

$$G_j = \frac{\sum_{i=1}^b L_{ij}}{b} \quad (11.a)$$

where α is the initial value of the bid weight, λ is the decrease rate, b is the number of the bidders, and L_{ij} is the normalized energy level of $Robot_i$ for $task_j$ from (10).

When the local bid weight is used, the bid weight generation module calculates each bidder's bid weight based on the bidder's normalized energy level. The local bid weight of $Robot_i$ for $task_j$, $w_{loc}^{bid}(L_{ij})$ is defined as

$$w_{loc}^{bid}(L_{ij}) = \alpha \cdot \exp(\lambda \cdot (L_{ij} - 1)) \quad (12)$$

where α and λ are the initial value of the bid weight and the decrease rate, respectively. In the system with the local bid weight, if the bidder has higher normalized energy level than others, the auctioneer considers that the bidder has not worked as much as others and the bidder is able to perform a task qualitatively since it still has energy to spare. This enables the system to allocate tasks in a balanced manner.

4.2 Utility

The utility is generated by using the bid values and the bid weights. The utility of $Robot_i$ for $task_j$, U_{ij} is defined as

$$U_{ij} = 0.5 \cdot (w^{bid} \cdot \hat{Q}_{ij} - (1 - w^{bid}) \cdot \hat{C}_{ij} + 1.0) \quad (13)$$

with

$$\hat{Q}_{ij} = \frac{Q_{ij}}{\sum_{i=1}^b Q_{ij}} \quad (13.a)$$

$$\hat{C}_{ij} = \frac{C_{ij}}{\sum_{i=1}^b C_{ij}} \quad (13.b)$$

where w^{bid} ($0 \leq w^{bid} \leq 1$) is the bid weight which can be set either as the global or local bid weight, \hat{Q}_{ij} and \hat{C}_{ij} are the normalized task quality and normalized task cost, respectively, and b is the number of the bidders. In the equation, 0.5 and 1.0 are used to set the range of the utility as $0 \leq U_{ij} \leq 1$.

5 The Case of a Cleaning Mission

To demonstrate the effectiveness of the proposed framework, a simulation experiment was carried out for a cleaning mission. The cleaning mission consists of several compound tasks and the robots work together to allocate and execute the compound tasks.

5.1 Heterogeneous Robots

For the mission, the eight heterogeneous robots with different kinds of capabilities are defined. There are five capabilities, localization, color recognition, mobility, gripper, and block storage. Each of them has different characteristics depending on the hardware resource as shown in Table 1. In the table, q , e and p are the capability quality, energy consumption rate and its unit, respectively from (5), and LOC , COL , MOB , $GRIP$ and $STOR$ are the localization, color recognition, mobility, gripper and storage capabilities, respectively, and LRF , USS , HQC , LQC , OD , $DD RH$ and RS are the laser range finder, ultrasonic sensors, high quality camera, low quality camera, omnidirectional drive, differential drive, robot hand and robot storage, respectively. The gripper capability is used to pick up a block, and the block storage capability enables a robot to store the blocks. Since the storage capability does not use any kinds of active actuators, it does not consume any energy.

The hardware resources of the robots for their capabilities are shown in Table 2.

Table 1. Five Capability Vectors With Different Hardware Resources

	Capability	Hardware resource	<i>q</i>	<i>e</i>	<i>p</i>
<i>LOC</i>	<i>LRF</i>		0.9	30.0	0
	<i>USS</i>		0.6	10.0	0
<i>COL</i>	<i>HQC</i>		0.9	3.0	0
	<i>LQC</i>		0.6	1.5	0
<i>MOB</i>	<i>OD</i>		0.9	210.0	1
	<i>DD</i>		0.6	150.0	1
<i>GRIP</i>	<i>RH</i>		1.0	2.0	1
<i>STOR</i>	<i>RS</i>		1.0	0.0	0

Table 2. Hardware Resources of The Robots

	<i>LOC</i>	<i>COL</i>	<i>MOB</i>	<i>GRIP</i>	<i>STOR</i>
<i>Robot</i> ₁	<i>LRF</i>	<i>HQC</i>	<i>OD</i>	<i>RH</i>	N/A
<i>Robot</i> ₂	<i>LRF</i>	<i>LQC</i>	<i>OD</i>	<i>RH</i>	N/A
<i>Robot</i> ₃	<i>LRF</i>	<i>HQC</i>	<i>DD</i>	<i>RH</i>	N/A
<i>Robot</i> ₄	<i>LRF</i>	<i>LQC</i>	<i>DD</i>	<i>RH</i>	N/A
<i>Robot</i> ₅	<i>USS</i>	N/A	<i>DD</i>	N/A	<i>RS</i>
<i>Robot</i> ₆	<i>USS</i>	N/A	<i>OD</i>	N/A	<i>RS</i>
<i>Robot</i> ₇	<i>LRF</i>	N/A	<i>DD</i>	N/A	<i>RS</i>
<i>Robot</i> ₈	<i>LRF</i>	N/A	<i>OD</i>	N/A	<i>RS</i>

5.2 Compound Tasks

There are four compound tasks in the mission, block collecting task ($Task^{1,AP}$), tray carrying task ($Task^{2,SP}$), white block cleaning task ($Task^{3,S}$), and black block cleaning task ($Task^{4,S}$). The descriptions of the atomic tasks of the four compound tasks are summarized in Table 3. To complete the mission, the mixed blocks should be sorted by their color, and the trays with the sorted blocks, $Tray_2$ and $Tray_3$, should be carried in designated zones, D_1 and D_2 , respectively, as shown in Fig. 1(c) and 1(d). Since the block sorting task should be completed before the tray carrying task, the white and black block cleaning tasks are defined as the sequential compound tasks, $Task^{3,S}$ and $Task^{4,S}$, respectively. The white and black block sorting atomic tasks are defined as $task_1^{3,S}$ and $task_1^{4,S}$, respectively, and $Tray_2$ and $Tray_3$ carrying atomic tasks are defined as $task_2^{3,S}$ and $task_2^{4,S}$, respectively.

For each compound task, the task requirements of the atomic tasks are defined using the task requirement matrices as in Table 4. In the table, $task_{All}^{2,SP}$ represents all of the atomic tasks in $Task^{2,SP}$. Since they require the same capabilities, the task capability matrices of them are also identical.

Table 3. Descriptions of The Atomic Tasks In The Mission

Description		
$Task^{1,AP}$	$task_1^{1,AP}$	Finding and picking up blocks in $Room_1$
	$task_2^{1,AP}$	Carrying blocks to $Tray_1$
$Task^{2,SP}$	$task_1^{2,SP}$	Carrying the front of $Tray_1$ to $Room_2$
	$task_2^{2,SP}$	Carrying the back of $Tray_1$ to $Room_2$
$Task^{3,S}$	$task_3^{2,SP}$	Carrying the left of $Tray_1$ to $Room_2$
	$task_4^{2,SP}$	Carrying the right of $Tray_1$ to $Room_2$
$Task^{3,S}$	$task_1^{3,S}$	Sorting white blocks to $Tray_2$
	$task_2^{3,S}$	Carrying $Tray_2$ to D_1
$Task^{4,S}$	$task_1^{4,S}$	Sorting black blocks to $Tray_3$
	$task_2^{4,S}$	Carrying $Tray_3$ to D_2

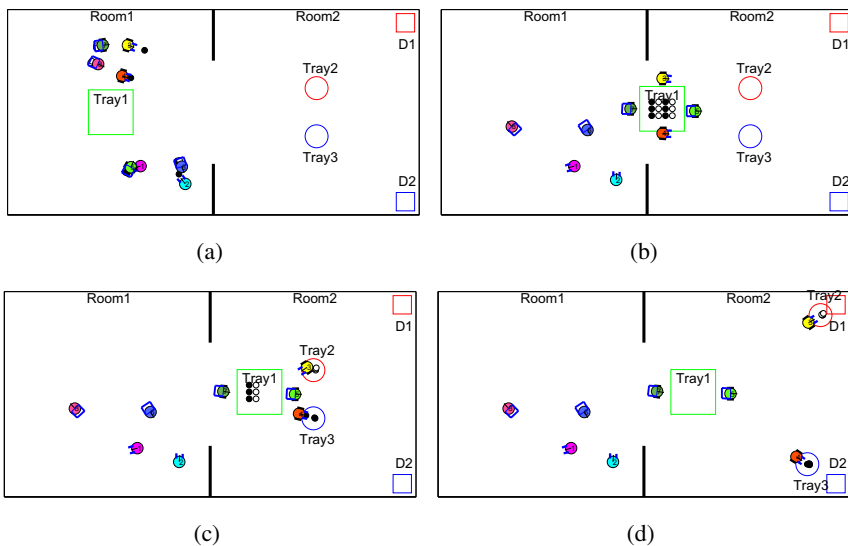
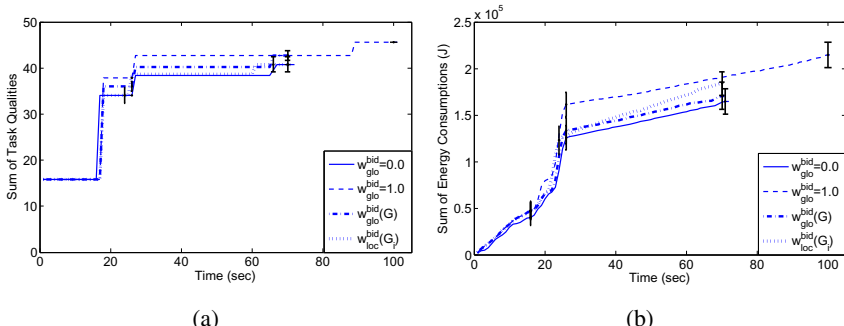
**Fig. 1.** (a) Robots collect the blocks in $Room_1$ to $Tray_1$. (b) Four robots work together to carry $Tray_1$ to $Room_2$. (c) Two robots sort white and black blocks. (d) After sorting, trays are carried to designated places.

Table 4. Task Requirement Matrices of The Atomic Tasks

	<i>LOC</i>	<i>COL</i>	<i>MOB</i>	<i>GRIP</i>	<i>STOR</i>
<i>task</i> ₁ ^{1,AP}	<i>h</i>	1	1	1	0
	<i>w</i> ^{cap}	0.5	0.8	0.5	1.0
<i>task</i> ₂ ^{1,AP}	<i>h</i>	1	0	1	0
	<i>w</i> ^{cap}	0.7	0.0	0.5	0.0
<i>task</i> _{All} ^{2,SP}	<i>h</i>	1	0	1	0
	<i>w</i> ^{cap}	1.0	0.0	0.8	0.0
<i>task</i> ₁ ^{3,S}	<i>h</i>	1	1	1	0
	<i>w</i> ^{cap}	0.5	0.8	0.5	1.0
<i>task</i> ₂ ^{3,S}	<i>h</i>	1	0	1	0
	<i>w</i> ^{cap}	0.8	0.0	0.8	0.0
<i>task</i> ₁ ^{4,S}	<i>h</i>	1	1	1	0
	<i>w</i> ^{cap}	0.5	0.8	0.5	1.0
<i>task</i> ₂ ^{4,S}	<i>h</i>	1	0	1	0
	<i>w</i> ^{cap}	0.8	0.0	0.8	0.0

**Fig. 2.** The result of the mission with different types of bid weights. (a) Sum of the task qualities. (b) Sum of the energy consumptions.

5.3 Simulation Results

In the simulation experiment, robots completed the mission with four different types of bid weights, $w_{glo}^{bid} = 0.0$, $w_{glo}^{bid} = 1.0$, $w_{glo}^{bid}(G)$ and $w_{loc}^{bid}(G_i)$. In the experiment, α and λ from (11) and (12) were set to 0.9 and 6.0, respectively. For each bid weight, the mission was performed five times, and the blocks in *Room*₁ were randomly scattered for each trial.

Fig. 2 shows the sum of the task qualities and the sum of energy consumptions of the robots with different types of bid weights. In the case of using $w_{glo}^{bid} = 0.0$, the system

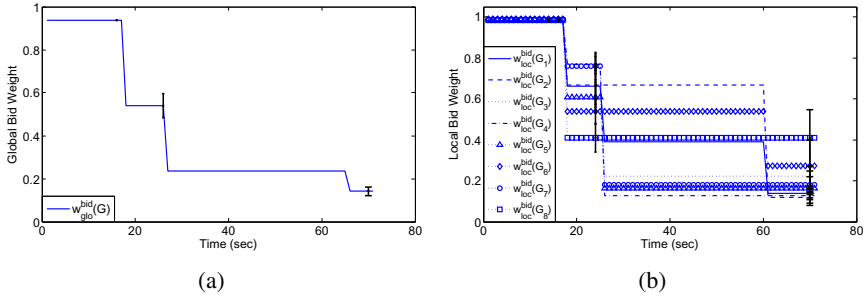


Fig. 3. The changes of bid weights. (a) $w_{glo}^{bid}(G)$. (b) $w_{loc}^{bid}(G_i)$.

tried to minimize the sum of task costs such that it was able to minimize the sum of the energy consumptions as shown in Fig. 2(b). However, the sum of task qualities was worse than any other cases as shown in Fig. 2(a). It implies that the auctioneer allocated tasks to the bidder which can perform the task with lowest task cost regardless of its task quality. Likewise, the system using $w_{glo}^{bid} = 1.0$ was able to maximize the sum of task qualities, while it consumed more energy than any other cases.

To compare the results with $w_{glo}^{bid}(G)$ and $w_{loc}^{bid}(G_i)$, the changes of the bid weights during the mission were measured as shown in Fig. 3. When $w_{glo}^{bid}(G)$ was used, the result was similar to the case with $w_{glo}^{bid} = 1.0$ during the early stage of the mission. As the mission progressed, however, the result was getting close to the result with $w_{glo}^{bid} = 0.0$. It was because of the decrease of the sum of the normalized energy levels caused the decrease of the global bid weight as shown in Fig. 3(a). The result with w_{loc}^{bid} did not show any specific tendency like the other cases. This was because the local bid weight was decided by each bidder's normalized energy level. Fig. 3(b) shows the changes of the local bid weights of the robots during the mission where the differences between the local bid weights were reduced as the mission progressed. The reduction of the differences between the local bid weights implies that the tasks were distributed in a balanced manner such that most of the robots were assigned tasks and worked with consuming their energy.

The energy levels of the robots with four types of bid weights were measured as shown in Fig. 4. In the case of using $w_{glo}^{bid} = 0.0$, when robots performed $Task_1^{AP}$, the robots with next to each other organized a team to minimize energy consumptions. As a result, four sub-teams, $Robot_1$ with $Robot_5$, $Robot_2$ with $Robot_6$, $Robot_3$ with $Robot_7$, and $Robot_4$ with $Robot_8$ were organized and worked together to complete $Task_1^{1,AP}$. Likewise, the robots which could minimize the overall cost for $Task_2^{SP}$ worked together to complete the task. For $Task_3^S$, $Robot_3$ and $Robot_4$ which had performed $Task_2^{SP}$ worked together until the mission was completed since they were the closest robots which can perform block sorting and tray carrying. As a result, $Robot_3$ and $Robot_4$ worked more than others.

In the case of using $w_{glo}^{bid} = 1.0$, the robots with high task qualities organized a team for $Task_1^{1,AP}$ and $Task_2^{2,SP}$. $Robot_1$ worked together with $Robot_8$ and $Robot_4$ worked together with $Robot_5$ although the initial positions between them were not close. After

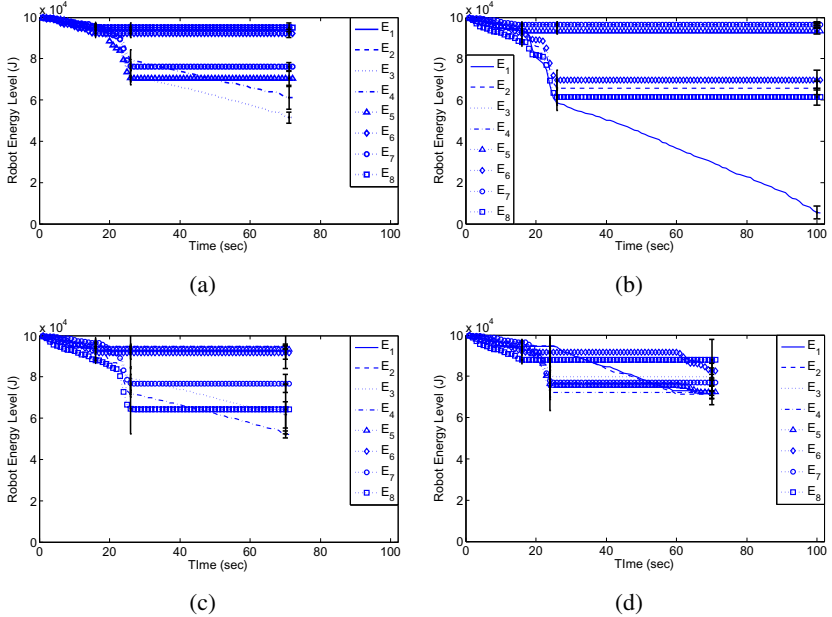


Fig. 4. The energy levels of the robots. (a) $w_{glo}^{bid} = 0.0$. (b) $w_{glo}^{bid} = 1.0$. (c) $w_{glo}^{bid}(G)$. (d) $w_{loc}^{bid}(G_i)$.

completing $Task^{2,SP}$, $Robot_1$ took the rest of the tasks since it had the highest task qualities for the tasks although its energy level was relatively lower than others. As a result, the differences of the energy levels of the robots were increased at the end of the mission as shown in Fig. 4(b). In the case of using the function type global bid weight, the results of task allocations were similar to the case with $w_{glo}^{bid} = 1.0$. However, as the mission progressed, the result of task allocations became similar to the case with $w_{glo}^{bid} = 0.0$. This was because of the decrease of the sum of the normalized energy levels of the robots. As a result, the differences of the energy levels of the robots at the end of the mission was similar to the result from $w_{glo}^{bid} = 0.0$ as shown in Fig. 4(c). In the case of using the local bid weight, most of the normalized energy levels of the robots were decreased evenly as shown in Fig. 4(d). There was no remarkable energy decrease of any specific robot such as $Robot_1$ in the case with $w_{glo}^{bid} = 1.0$ or $Robot_3$ and $Robot_4$ in the case with $w_{glo}^{bid} = 0.0$ and $w_{glo}^{bid}(G)$, and the size of the differences between the energy levels of the robots was lower than any other cases. It implies that the system with the local bid weight is able to distribute the tasks in a balanced manner.

6 Conclusion

This paper proposed a market-based multiagent task allocation framework for bid adjustment and balanced task allocation. The proposed framework was applied to the cleaning mission and the results with different types of bid weights were compared

in a simulation experiment. In the case of using the global bid weight, the system was able to adjust the relative importance between maximizing the sum of task qualities and minimizing the sum of energy consumptions, while it did not guarantee the balanced task allocation since the identical global bid weight was applied to calculate all of the utilities of the bidders. On the other hand, the system with the local bid weight was able to distribute the tasks in a balanced manner considering each individual's normalized energy level, while the overall profits such as maximizing the sum of task quality and minimizing the sum of energy consumptions were not as good as the system with the global bid weight.

Acknowledgment. This research was supported by the MKE (The Ministry of Knowledge Economy), Korea, under the National Robotics Research Center for Robot Intelligence Technology support program supervised by the NIPA (National IT Industry Promotion Agency) (NIPA-2012-H1502-12-1002).

References

1. Dias, M.B., Kalra, N., Zlot, R., Stentz, A.: Market-based multi-robot coordination: A survey and analysis. *Proceedings of IEEE* 94, 1257–1270 (2006)
2. Sariel, S., Balch, T., Stack, J.R.: Real time auction based allocation of tasks for multi-robot exploration problem in dynamic environments. In: *AAAI Workshop*, pp. 27–33 (2005)
3. Sariel, S., Balch, T.: Efficient bids on task allocation for multi-robot exploration. In: *Proc. Int. Conf. Artif. Intelli.*, pp. 116–121 (2006)
4. Berhault, M., Huang, H., Keskinocak, P., Koenig, S., Elmaghreby, W., Griffin, P., Kleywegt, A.: Robot exploration with combinatorial auctions. In: *Proc. IEEE Conf. Intell. Robot. Syst.*, pp. 1957–1962 (2003)
5. Smith, R.G.: The contract net protocol: High-level communication and control in a distributed problem solver. *IEEE Trans. Comput.* 29, 1104–1113 (1980)
6. Beaumont P., Chaib-draa B.: Multiagent coordination techniques for complex environments: The case of a fleet of combat ships. *IEEE Trans. Syst., Man, Cybern., Part C*, 37, 373–385 (2007)
7. Dias, M.B.: Traderbots A new paradigm for robust and efficient multi-robot coordination in dynamic environments. Ph.D. dissertation, Robotics Institute, Carnegie Mellon University (2004)
8. Gerkey, B.P., Mataric, M.J.: Sold!: Auction methods for multirobot coordination. *IEEE Trans. Robot. Autom.* 18, 758–768 (2002)
9. Vokrinek, J., Komenda, A., Pechoucek, M.: Abstract architecture for task-oriented multiagent problem solving. *IEEE Trans. Syst., Man, Cybern., Part C* 41, 31–40 (2011)
10. Lee, D.-H., Han, J.-H., Kim, J.-H.: A preference-based task allocation framework for multi-robot coordination. In: *Proc. IEEE Conf. Robot. Bio.*, pp. 2925–2930 (2011)

Autonomy Balancing in a Manned-Unmanned Teaming (MUT) Swarm Attack

Ji Hyun Yang, Marek Kapolka, and Timothy H. Chung

MOVES Institute, Naval Postgraduate School,
Monterey CA, USA

{jyan1, mkapolka, thchung}@nps.edu

Abstract. In this paper, we describe a framework for developing an interactive feedback model of manned-unmanned teaming (MUT) operational mode selections for a broad spectrum of unmanned vehicle (UV) autonomy levels. Though the highest autonomy levels are within reach as technology continues to advance, lower level autonomy or human manual control will still be needed depending on mission scenarios and dynamic situations. Understanding when and how we change the autonomy level of MUT is critical to ensure system safety and to maximize system performance. Thus, we propose to integrate feedback from various human state variables (i.e., physiological and behavioral signals such as heart rate, skin conductance level, and postures) for estimating human workload and interest level and key task performance measures (accuracy and speed for assigned missions, task interaction) into MUT systems so that the MUT adapts its mode automatically as needed. We developed RESCHU-SA (Research Environment for Supervisory Control of Heterogeneous Unmanned Vehicles Swarm Attacks), a modified version of the RESCHU simulator originally developed at MIT. We designed a human-in-the-loop experiment to collect baseline data for varying levels of autonomy using the RESCHU-SA along with a physiological sensor BioHarness. Different levels of autonomy include 1) high level autonomy using an auction algorithm or nearest-neighbor assignment algorithm, 2) low level autonomy using manual assignment, and 3) interactive autonomy which allows operators to change between high and low autonomy level. The purpose of the research is to investigate the level of autonomy that should be given to unmanned vehicles (UVs) to successfully complete a mission using a MUT in a swarm attack scenario.

Keywords: autonomy balancing, manned-unmanned teaming (MUT), UV swarms, assignment, physiological signal, auction algorithm.

1 Introduction

Future Navy operational capabilities are expected to include teams or swarms of UVs controlled by a single operator. In order to make this happen, numerous research studies are focusing on developing highly automated systems that will require little operator supervision. Accordingly, human operators will soon encounter UVs with a

broad spectrum of autonomous control levels ranging, for example, from a remotely controlled UV to fully autonomous swarms of UVs. Depending on missions and situations, an appropriate autonomy control level should be selected, and thus, the MUT mode selection problems represent non-trivial research and reflect operational issues for successful mission completion.

Automation and mode selection has been studied mostly in the aviation domain [e.g., 1, 2] focusing on pilot-autopilot interaction difficulties such as mode awareness or mode confusion. Unlike pilots responsible for flying vehicles, human operators in MUT fulfill the role of supervisory control, monitoring and directing reconnaissance or surveillance tasks. Thus, MUT mode interaction or mode selection should involve more knowledge-based decision making than rule-based decisions [3] as in pilot-autopilot interaction.

Knowing human operators' states and capacities is critical to the MUT's successful mission completion. For example, Rodas [3] suggested a laboratory experiment estimating the optimal number of heterogeneous UVs for each operator based on performance variables using the RESCHU (Research Environment for Supervisory Control of Heterogeneous Unmanned Vehicles) simulator originally developed at MIT. In addition, many physiological signals have been shown to be correlated with various aspects of human states, e.g., heart rate/skin conductance level and stress level [4], postures and interest level [5, 6], and pupil diameter and attention [7].

Mental workload, situational awareness, and trust in automation of human operators differ between the various automation levels of human-UV teams, and selecting proper human-UV team modes will be a critical element for successful and efficient mission completion. An example could be selecting between a master-slave mode vs. teammate mode by monitoring human operators' attention levels, workload levels, trust levels, and task performance. NPS researchers plan to collect human-UV data in support of the development of a model and/or measures of UV operator cognitive capacity that can be used to predict the optimal human-UV mode in which humans can effectively execute control under various operational scenarios and mixtures of UV types.

The purpose of the proposed study is to develop a simulation test-bed for RESCHU-SA, and collect baseline physiological data when operating RESCHU-SA under different autonomy levels. Section II describes basic functionality of RESCHU-SA and Section III elaborates design of a human-in-the-loop experiment. Section IV provides an autonomy balancing model using a physiological feedback model.

2 Development of RESCHU-SA

2.1 Difference between RESCHU-SA and RESCHU

We developed RESCHU-SA (Research Environment for Supervisory Control of Heterogeneous Unmanned Vehicles in Swarm Attacks), a modified version of the RESCHU simulator originally developed at MIT. In the original version of RESCHU, the user gives commands to a relatively small number of UAVs and UUVs, guiding them to stationary ground targets while avoiding hazard areas. When the UXVs reach the target areas, the user is prompted to complete an image identification task, and if

they succeed they are awarded points. In our version of RESCHU-SA, the user protects a stationary high value unit (HVU) from a swarm of red UAVs by assigning a large swarm of blue UAVs either using the auction algorithm or manual assignment. If the red UAVs reach the HVU the HVU will take damage and eventually be destroyed. If a blue UAV reaches a red UAV it will engage it and potentially destroy it. To assist the user in managing such a large number of UAVs, RESCHU-SA has several changes to the user interface and implements an auction algorithm for automatically assigning blue UAVs to red UAVs.

Our version of RESCHU also connects to the Zephyr BioHarness and displays physiological data about the user while they are using the program. Our version also uses relevant scales and speeds (the scenario takes place in a 20NM square area, the UAVs move at 200 knots) in simulating the motion of the UAVs.

2.2 MUT Swarm Attack Scenario

A large swarm of adversarial UVs attacked a surface target with groups of defensive UVs responding to thwart the attack. Though scenarios can be envisioned where autonomous sea, land, or air unmanned systems may act in groups in order to achieve a goal or attack a specific target, this study examines the threat in the aerial domain, and seeks countermeasures for swarms of UAVs involved in a saturation attack against a HVU owned by the blue team [8].

As unmanned systems become more ubiquitous in current and future warfare due to lowering barriers to entry, such as cost and technical expertise, the employment tactics of these UVs is necessarily changing. In particular, the notion of saturation attacks, where one side uses significant numbers to overwhelm the defenses of the opponent, highlights one such tactic that represents a challenge to HVU or installation protection missions. To counter such swarm attacks, a variety of defensive measures may be considered; however, to combat both numbers and cost advantages of the attacking swarm, a defensive swarm of capable UVs can be designed to defeat this threat.

2.3 RESCHU-SA Functionality

Working features of the current version of RESCHU-SA include: 1) target assignment mode: automatic assignment using an auction algorithm or nearest-neighbor assignment, manual assignment, and interactive mode; 2) real-time updating of scenario variables: location and damage levels of reds vs. blues, HVU damage level, logic dictating what happens when UxVs meet; 3) physiological monitoring: graphical and text representation of respiration rate, heart rate, and posture in real time from Bio-Harness; 4) configuration files: autonomy mode, automatic assignment algorithm type, squad size used in the auction algorithm, number of blue and red UxVs, speed of blue and red UxVs, and initial location of blue and red UxV swarms, and 5) log file saving user action, performance, and physiological data. Figure 1 shows the current version of RESCHU-SA interface.

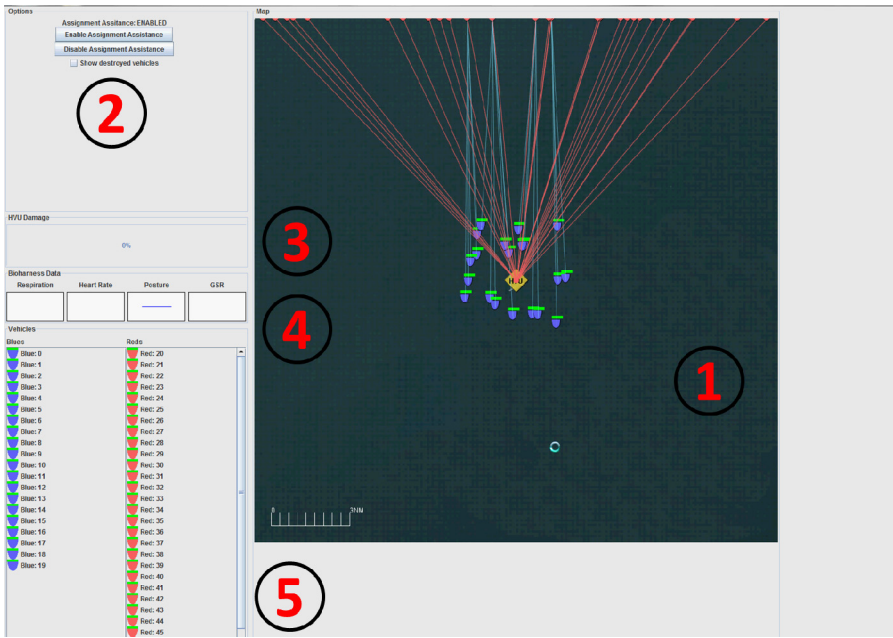


Fig. 1. RESCHU-SA interface: 1-area of operation; 2- assignment mode panel; 3-HVU damage level indicator; 4- physiological data monitor; 5-blue and red health monitoring panel.

3 Human-in-the-loop Experiment Design

The purpose of the experiment is to examine feasibility of the proposed research idea, collect baseline data, and investigate appropriate levels of UV swarm autonomy given a set of scenario variables. The human operator's workload and attention level (using physiological measures) along with mission completeness (using simulator performance measures) should be considered to decide the “appropriateness” of the autonomy level.

3.1 Experiment Schedule and Participants

Experiment was conducted at Camp Roberts, a California Army National Guard Installation just north of Paso Robles, California, on 3 August 2012. The exercises were sponsored by Special Operations Command (USSOCOM) and are referred to as Tactical Network Testbed (TNT) experiments. Participants were either volunteers participating in TNT or Naval Postgraduate School (NPS) students between the ages of 20 and 55 who are in good health and who are not allergic to any of the materials present in the equipment. Subjects were warned of exposure to the stated materials in the recruitment form, on the informed consent form, and verbally by the experimenter. During the informed consent process, subjects were reminded that should they feel discomfort due to the equipment, they may withdraw from the study at any time without penalty.

3.2 Equipments

Subjects were placed in front of a 24-inch LCD monitor on which they worked through the RESCHU-SA simulation used to command a UV swarm to defend a high-value target from multiple attackers. During this task and its tutorial, subjects were outfitted with a Zephyr Technologies BioHarness, which provided various physiological measures such as heart rate and breathing rate wirelessly.

3.3 Scenario Definition

The mission goal of MUT was to assign a swarm of defensive UVs to a swarm of adversarial UVs attacking the HVU to protect from HVU loss. When a blue engaged a red, there was an 80% chance the blue would destroy the red (i.e., its probability of kill), and get damaged in the process. There was a 20% chance that the red will destroy the blue. If a damaged blue engaged a red and destroyed the red, the blue also was destroyed. Every time a red reached the HVU, the latter's damage increased by 10%. The “HVU destroyed” message was displayed after the HVU damage reached 100%. These probability parameters can be set in a configuration file.

3.4 Autonomy Levels in Assignment Tasks

We considered the following three different levels of autonomy endowed to the UVs in the team: 1) highest level autonomy mode: full autonomous swarms using an auction algorithm, 2) interactive mode: human operators could choose between automatic and manual assignment, 3) low level autonomy mode: manual assignment. For each autonomy mode, tasks were assigned to either one or both of UVs or human operators as shown in Table 1. Various efforts have sought to develop taxonomies for autonomy levels, such as in [9] at the National Institute of Standards and Technology, and additional tasks beyond the three listed in Table 1 may be included in upcoming studies.

In this paper, we investigate the problem of best assigning defensive assets to attacking agents. Though one can formulate a mathematical program, which provides an optimal assignment, the computational complexity of the problem as well as the absence of uncertainty in the model both render this approach impractical for realistic operations. An alternative to seeking an optimal solution is to trade optimality for reduced computational complexity. Auction or market-based algorithms using economic principles have been used to assign agents to tasks in previous work [11]. Auction-based solutions are dependent on the problem being solved, and in the present case, we have a market in which blues attempt to purchase reds via auction. In each round of the auction blues are each given an equal amount of money and the cost they are willing to pay for each red is based on Euclidean distance (blues bid higher for closer reds). The iterative negotiation among agents may yield suboptimal assignments, according to the objective function of minimizing distances (and hence, time until intercept) between blues and reds; however, the auction-based structure helps facilitate decentralized optimization, which is an operational enabling capability. Details of the specific formulation and implementation may be found in [8].

Table 1. Task allocation for each autonomy mode

Tasks	High level autonomy mode	Interactive autonomy mode	Low level autonomy mode
Mission assignment	UVs	UVs/Human	Human
Route planning	UVs	UVs/Human	UVs/Human
Flight control	UVs	UVs	UVs

The nearest-neighbor assignment algorithm assigns blues to the closest reds, and can be represented as a linear mathematical program, with costs as the Euclidean distance between all pairs of blue and red agents [9]. When manually assigning targets, left click selects a vehicle (the user can also drag to select multiple vehicles) and right click assigns any selected blue vehicles to the clicked red. The interactive mode allowed operators re-assign a subset of blues to reds when in high autonomy mode and change between high and low autonomy modes. When blues and reds were re-assigned, the auction algorithm or nearest-neighbor algorithm did not re-assign any blue that already had a target. It only re-assigned blues that either did not have a target, or blues whose target was destroyed. If the user assigned the blue to a target, autonomy respected that until the blue destroyed its target, at which point that blue was automatically assigned a new target by either auction or one-on-one algorithm.

3.5 Procedure

Participants were briefed on the nature of the RESCHU-SA and had a BioHarness recording apparatus strapped to them. Participants were informed that this apparatus requires contact with the skin, and so may elicit allergic reactions in some people. This process took no more than five minutes. From here, participants were given an orientation and background to the program that they used. This took ten to twenty minutes. The data collection phase took about ten to twenty minutes. In the data collection phase, participants were asked to monitor, interact with, or take control of and assign an array of virtual blue UV swarms to an adversary forces and accomplish HVU protection within a given time.

3.6 Dependent Variables

RESCHU-SA variables: HVU damage level (0-100%), each blue's damage level (0-100%), and number of manual assignments.

Physiological variables: heart rate (25-240 BPM), respiration rate (3-70 BPM), posture ($\pm 180^\circ$), and skin conductance level.

3.7 Example Data

Subject A showed the best performance in both the automatic and manual modes (0% HVU damage) whereas Subject B showed the best performance in the interactive

mode (50% HVU damage). However, both subjects preferred interactive mode regardless of their performance. Their physiological data are shown in Figure 2.

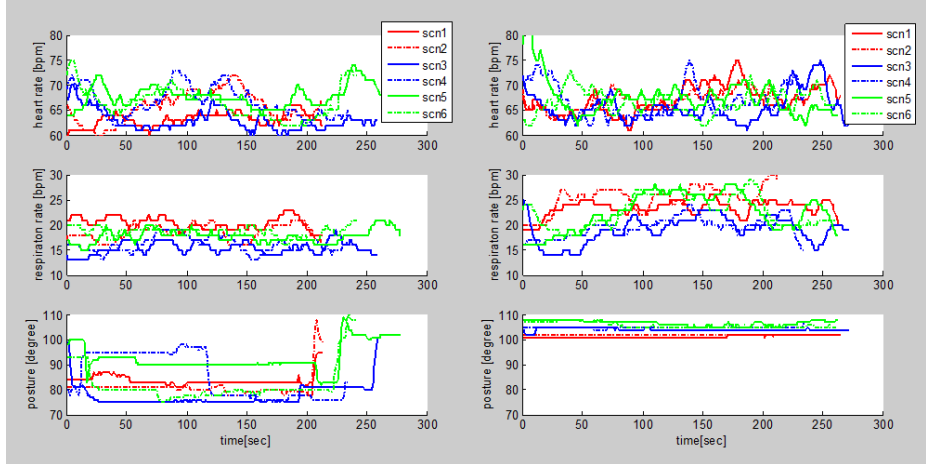


Fig. 2. Physiological data from subject A and subject B

4 Feedback Control Design for MUT Autonomy Balancing

4.1 Human State Measures and Estimation

In some instances, physiological measures are more sensitive to initial changes in workload than performance-based measures. For example, cardiac measures reflected changes in attentional demand from single- to dual-task driving with an n-back task, whereas lane-keeping measures did not [12]. Many other physiological signals have been shown to be correlated with various aspects of human states, such as heart rate variability, galvanic skin response (GSR), and stress level [13], and postures and interest level [5, 6]. For example, changes in heart rate before a decision was made predicted the type of decision made during a gambling task [14]. If eye-tracking data are also available, Index of Cognitive Activity [7] will be included as well to estimate the attention level of humans.

Based on the above estimation, our model will provide an appropriate level of autonomy for the unmanned vehicles in MUT. This process is recursive and can be understood in a feedback control framework as shown in Figure 3. Data which will be collected on the TNT experiment for three different levels of autonomy will serve as baseline data to build the MUT feedback model in a swarm attack. Effectiveness of the proposed feedback model will be validated through another set of human-in-the-loop experiments by comparing overall system performance between the system with the autonomy balancing feedback model and without, i.e., using a manual autonomy balancing method.

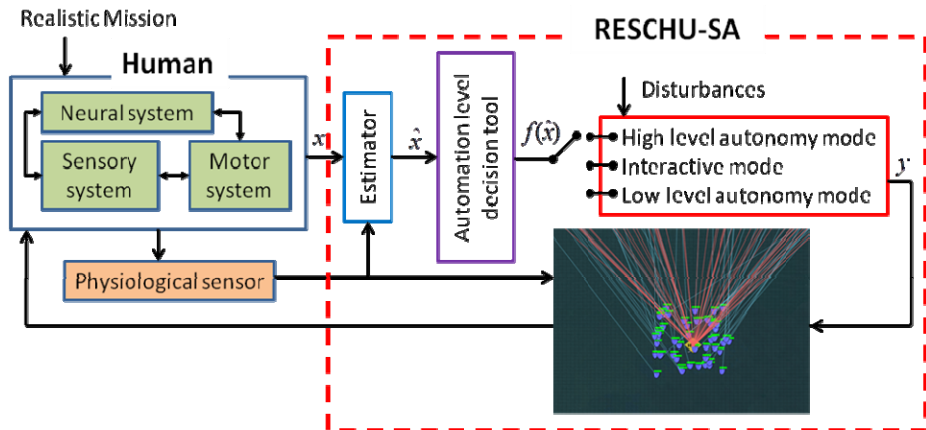


Fig. 3. Schematic diagram of MUT autonomy balancing feedback model in a swarm attack scenario

Acknowledgements. This research has been supported in part by the NPS Chair of Technical Operations. The authors acknowledge the support of Dr. Missy Cummings and Human Automation Lab at MIT for providing us with RESCHU source code. The authors also thank Mr. Jesse Huston for preparing IRB paperwork.

References

1. Javaux, D.: An algorithmic method for predicting pilot-mode interaction difficulties. In: Proceedings of 17th AIAA/IEEE/SAE Digital Avionics Systems, pp. E21/1–E21/8 (1998)
2. Pritchett, A.R.: Aviation automation: General perspectives and specific guidance for the design of modes and alerts. *Reviews of Human Factors and Ergonomics* 5(1), 82–113 (2009)
3. Rodas, M.O., Szatkowski, C.X., Veronda, M.C.: Predicting an adequate ratio of unmanned vehicles per operator using a system with a mission definition language. In: 2011 IEEE First International Multi-Disciplinary Conference on Cognitive Methods in Situation Awareness and Decision Support (CogSIMA), pp. 159–162 (2011)
4. Cacioppo, J.T., Tassinary, L.G., Bernston, G.G.: *Handbook of psychophysiology*, 3rd edn. Cambridge University Press (2007)
5. Lee, S.W., Mase, K.: Activity and location recognition using wearable sensors. *IEEE Pervasive Computing* 1(3), 24–32 (2002)
6. Ahn, H.I., Teeters, A., Breazeal, C., Picard, R.W.: Stoop to conquer: Posture and affect interact to influence computer users' persistence. Paper presented at the The 2nd International Conference on Affective Computing and Intelligent Interaction, Lisbon, Portugal (2007)
7. Marshall, S.P.: Identifying cognitive state from eye metrics. *Aviation, Space, and Environmental Medicine* 78(suppl. 5), B165–B175 (2007)
8. Day, M.: Multi-Agent Task Negotiation Among UAVs to Defend Against Swarm Attacks. Master's Thesis, Naval Postgraduate School (2012)

9. Murty, K.G.: Operations Research: Deterministic Optimization Models, 1st edn. Prentice Hall, Inc., Englewood Cliffs (1995)
10. Huang, H. (ed.): Autonomy levels for unmanned systems framework. Framework models, version 1.0, vol. II. National Institute, Gaithersburg (2007)
11. Gerkey, B.P., Mataric, M.J.: A formal analysis and taxonomy of task allocation in multi-robot systems. *The International Journal of Robotics Research* 23(9), 939–954 (2004)
12. Lenneman, J., Backs, R.: Cardiac autonomic control during simulated driving with a concurrent verbal working memory task. *Human Factors* 51(3), 404–418 (2009)
13. Cacioppo, J.T., Tassinary, L.G., Bernston, G.G.: Handbook of psychophysiology, 3rd edn. Cambridge University Press (2007)
14. Lee, P., Chang, C., Hsiao, T.: Can human decisions be predicted through heart rate changes? Second World Congress on Nature and Biologically Inspired Computing Kitakyushu, Fukuoka, Japan (2010)

Semi-autonomous Control of Robotic Multi-agents

Jae H. Chung¹ and Christopher Kim²

¹ Department of Mechanical Engineering
Stevens Institute of Technology
Hoboken, New Jersey 07030

jae.chung@stevens.edu

² Horace Mann School
4440 Tibbett Avenue,
Bronx, New York 10471
chriskim@optonline.net

Abstract. The teleoperation systems involving cooperative multi-robots to cope with different tasks on a single target with a team of homogeneous robots have been developed with (1) modified potential field based leader-follower formation, (2) adaptive multi-robotic impedances, (3) compensation for contact forces. However, most of the homeland security applications, e.g. military reconnaissance, exploration, and etc, need a team of heterogeneous robots to work on the multi-task simultaneously on the multi-target with a robot-task-target pairing. Therefore, the main contribution of this paper is to propose the cooperative teleoperation control method integrating not only (1-3) but also the robot-task-target pairing for a multi-robot multi-task multi-target defensive application.

The robot-task-target pairing is derived from the proven auction algorithm for multi-robot multi-task multi-target cases, which optimizes effects-based robot-task-target pairing based on a heuristic algorithm. The pairing method for the robot-task-target pairing is developed to produce a weighted attack guidance table (WAGT), which includes the benefits of assignments of robotic combinations (subteams) to tasks and targets. Therefore, the optimal robot-task-target pairs are computed based on WAGT with the heuristic algorithm. Simulation studies illustrate the efficacy of the teleoperation system with the proposed control method for multi-task multi-target scenarios.

1 Introduction

Cooperative control methods of multi-robotic systems [1–7] have been studied extensively in recent years. Multi-robot systems with the cooperative control methods can complete the function that a single robot cannot achieve through cooperation and also improve dexterity of robots to enlarge application fields of robots. Generally speaking, the robotic cooperation is classified into two categories. One is the cooperation without force interactions among robots (unconstrained motion tasks) and the other is with them (constrained motion tasks).

In the former type of cooperation, task planning is one of the main technical problems, but the same positional controller as that of single robot can be used and it can be realized very easily. Therefore, this type of cooperation has been practically used for target captures or enclosure [1–4]. In the latter type of cooperation, under the interactions of forces, design of the control strategies, which can keep inner forces between robots to be desired values and also ensure the stability of the controllers, becomes the most critical problem. This has been seen for target transports as the force or impedance controller has been commonly used [5–7]. Furthermore, those mentioned control methods have been developed only based on a known environment for one common task or target. However, real applications, e.g. military reconnaissance or operation, space or underwater exploration, search and rescue, and etc., require robots to handle many tasks or target simultaneously in an unknown environment. Hence, this paper focuses on development of the control method to collaborate a robotic team to work on multiple tasks or targets in an uncertain environment, which has been rarely seen in publications.

In the applications, due to the limitations of the current sensors and computer decision-making technologies, navigating robots in the unknown environment prohibits the use of fully autonomous systems [5–7]. Therefore, it is required that human decision making be involved in the systems. Teleoperators, in which a human operator is an integral part of the control, are suggested to integrate the human decisions to the control loop of the systems. With the teleoperators, the human operator remotely controls the robot, called the slave robot that locally works on a task in the unknown environment, via another robot, called the master robot that reads human commands and shows sensory data from the slave robot to the human operator. The teleoperators for a cooperative multi-robotic system is grouped into two types of the systems regarding the number of the master and slave robots, Single-Master Multi-Slave System (SMMS) [6, 7] and Multi-Master Multi-Slave System (MMMS) [5]. In order to minimize the required human resources and amplify the human effort, only the SMMS teleoperation [6, 7] has been considered in this paper.

Besides the unknown environment problem, the mentioned applications are normally complicated. Therefore, heterogeneous robots are necessary in this case. Furthermore, some collaboration technologies for the heterogeneous robots are concerned in particular in the multi-robot research. From a practical point of view, the individuals of a robotic team that are often different in design, structure, sensor configuration as well as intelligence, cannot be the homogeneous system. Heterogeneous robots can play the advantages of a single structure robot in a given area to achieve an overall optimal allocation. Because the team is formed by different robots, they should be paired before accomplishing assigned tasks on targets. So far in [8–12], some heterogeneous multi-robot pairings have been proposed. Nonetheless, they did not produce a stable and fast convergence to a global optimum [9–12] and were not used to pair multiple robots, tasks, and targets [8], not to mention the fact that none of them was about the unknown environments.

Therefore, in this paper, the primary objective is to propose a control method for a SMMS system to cooperatively control a mobile multi-functional robotic swarms for a multi-task multi-target scenario with multi-robot multi-task multi-target pairings. Primary components of the proposed control method are (1) modified potential field based leader-follower formation [13] and (2) multi-robot multi-task multi-target pairings. During the operation, a human operator only concentrates on controlling a leader robot chosen online among all slave robots. All other slave robots autonomously make a formation with regard to the positions and velocities of the leader robots. As soon as the leader robot is approaching the region of interest, the team is autonomously split into several subteams, and in each subteam, a subteam leader is online appointed based on the its functionalities and proximity to a paired target after all tasks and targets are paired to subteams. Each subteam leader supervises subteam followers to execute the paired task on the paired target when the subteam followers move with respect to their subteam leader motion. The subteam avoids obstacles and approaches the paired target in a modified potential field based leader-follower formation.

The rest of this paper is organized as follows. In Section 2, the control method that integrates the primary components to control multi-subteams to execute multi-tasks simultaneously for a multi-target approach is proposed. In Section 3, the effectiveness of the task achievement of the SMMS teleoperation system with the proposed control method were evaluated through simulation studies. Section 4 concludes this paper and shows future research directions.

2 Semi-autonomous Teleoperation Control Method for a Multi-task Multi-target Scenario

This paper extends the preliminary concepts of the semi-autonomous teleoperation control method [13] which was only focused on a single-target into a multi-target operation, i.e. several simultaneous target captures and transports, in a complicated environment. The primary difference between the team robot coordinations to complete multi-tasks for multi-targets and a single task for a single target is a pairing method.

Therefore, in this paper, we propose the multi-robot multi-task multi-target pairing method to advance the semi-autonomous teleoperation control method that was seen in our paper [13] to form subteams to perform paired tasks on paired targets. The concept of the pairing method is that all robots act largely independently in terms of planning for themselves but are able to take into account team resources by working on the tasks with other team members. With the pairing method proposed in this paper, the leader robot in the teleoeration system not only takes any human command from the master robot but also works as an auctioneer to send and show all bid data e.g. target locations and their base prices that are also online shared by all other robots called team followers. Any team robot is online appointed as the leader robot by the human operator via the master robot if the original one fails. All follower robots act as bidders to form a subteam by themselves in order to maximize a sum of all follower

bid values and bid on the targets when the corresponding task on the targets is performed by the cooperation of the subteam. In the subteam, the bidder with the maximum bid value is selected as a subteam leader that is responsible for monitoring and coordinating all subteam member actions. According to the largest bid proposed by the subteam, the auctioneer, the leader robot, decides which subteam wins the bid with the restriction that each task and target are only gained by one subteam per auction. If all subteam bid values are smaller than the base price, or any slave robot can not compute the bid value due to lacking of the information surrounding the targets, the auctioneer obtains the bid. If any one of the subteams of the bidders already completes the task on the target, it will inform the auctioneer to cancel the bid.

After being paired to the task and target by using the proposed pairing method, the subteam robots will move to the targets in the modified potential field based leader-follower formation suggested in [13] and perform the paired task, e.g. the transportation or capture of the target.

2.1 Multi-robot Multi-task Multi-target Pairing Method

Consider such a scenario, in a two-dimensional and limited rectangular environment X with n_c square cells, n_p slave robots pursue n_e targets, for $n_p > n_e$. The set of the robots is denoted by a matrix of $A = [a_1, a_2, \dots, a_{n_p}]$ where a_j is the j^{th} robot matrix. The j^{th} robot capability vector for the t^{th} task is denoted by \hat{C}_j^t , $1 \leq j \leq n_p$, and the set of targets is expressed as a target matrix of $T = [T_1, T_2, \dots, T_{n_e}]$ where T_{n_e} is the n_e^{th} target matrix. The vector representing the capability required to accomplish the t^{th} task on the T^{th} target is denoted by \bar{C}_t^T , $1 \leq T \leq n_e$. Agent $A \cup T$ denotes the teams of robots and targets. For simplification, we assume that both space and time can be quantized, therefore the environment can be regarded as a finite collection of cells, denoted by $X_c = 1, 2, \dots, n_c$. There exist some static obstacles with fixed sizes and regular shapes, and their locations are determined by the mapping $m : X_c \rightarrow 0, 1$, for $\forall x \in X_c, M(x) \geq 1$ indicates that the cell x is occupied by obstacles. $\forall x \in X_c, M(x) \leq 0$ indicates that the cell x is free. Each of the heterogeneous team robots needs different capabilities to complete different tasks on different targets, such as the target capture and transportation.

Robot Capability. The weighted capability vectors of the j^{th} robot with u functionalities to complete the i^{th} task can be defined as

$$\hat{C}_j^i = w_j^i \text{diag}\{b_{j1}^i, b_{j2}^i, \dots, b_{ju}^i\} [c_{j1}^i \dots c_{ju}^i]^T \quad (1)$$

where u is the maximum number of the individual functionality with which the j^{th} robot can complete the i^{th} task. c_{jk}^i is a capability value for the j^{th} robot with k^{th} functionality to do the i^{th} task. w_j^T is a positive integer such that for the given target T and robot j , the following is satisfied. If the robot is assigned to the target, $w_j^T = 0$, otherwise, $w_j^T = 1$. The $u \times u$ dimension diagonal matrix of

b_{ju}^t is used to estimate the percentage of possibility of using the $u \times 1$ dimensional capability vector C_j^i to do the i^{th} task by the j^{th} robot successfully. However, if Robot j does not have the capability c_{jk}^i , then the b_{jk}^t is 0.

Capability Required to Execute Tasks on Targets. It is assumed that there are p tasks which need to be done independently and simultaneously. All tasks are represented by the matrix of t that contains a set of the separate task matrices of $\{t_1, \dots, t_p\}$ in the system for $p \leq n_e$, i.e. one task can be paired to two or more targets, but each target can only be paired to one task. The capability vector that is required to accomplish Task i on Target k is defined as

$$\bar{C}_k^i = \text{diag}\{\beta_{i1}^k, \beta_{i2}^k, \dots, \beta_{iu}^k\} C_{ku} \quad (2)$$

where the $u \times u$ dimension diagonal matrix of β_{iu}^k is used to describe the percentage of possibility of using the $u \times 1$ dimension capability vector C_{ku} with which the robot can finish the i^{th} task on the k^{th} target. $C_{ku} = [c_{k1}, \dots, c_{ku}]^T$ when the total number of the functionalities is u . c_{tu} is the capability vector that is required to complete the t^{th} task with the u^{th} functionality. However, if the t^{th} task can not be done successfully by any robot with the capability C_{tu} on the k^{th} target, then the β_{tu}^k is 0. Otherwise, β_{tu}^k is 1.

Subteam Capability. For Subteam f , the subteam capability vector is a sum of capability vectors of all subteam robots, Robot $a - b$, from the team to do the i^{th} task cooperatively. It is defined that Subteam f is formed by the subteam robots, i.e. Robot $a - b$, by assuming that all subteam robots have a capability to do the i^{th} task on the k^{th} target. For Subteam f made by the subteam robots from the team to do i^{th} task, if $\hat{C}_j^i \geq 0$, then the subteam capability vector $Q((a - b), i, f)$ is defined as

$$Q((a - b), i, f) = \sum_{j=a}^b \hat{C}_j^i \quad (3)$$

where the $Q(f) = [Q((a-b), 1, f) \dots Q((a-b), i, f)]$ is a positive matrix that contains subteam capability vectors for Task $1 - i$. $a - b$, $\forall a \geq b$, is the total number of the robots in Subteam f . a is the first and b is the last indices of the elements in the matrix $Q((a - b), i, f)$ for Task i and Subteam f . Subteam f is able to perform Task i on Target k if the condition, $\bar{C}_k^i \leq Q((a - b), i, f)$, is satisfied. Robot j is selected as a subteam leader when its magnitude of the capability vector \hat{C}_j^i is largest in Subteam j . The subteam leader knows all capability information about its subteam members.

Bidding Winner Determination. In order to determine that the capability of each subteam is the most suitable for a specific task and target, the following equation is written to compute the bid value of Subteam f for Task i and Target k .

$$\hat{B}(k, i, j) = (Q((a - b), i, f) - \bar{C}_k^i)(1 - X_{ij}^k) \quad (4)$$

Table 1. Weighted Attack Guidance Table (WAGT)

Subteam 1	\dots	Subteam n
$[\hat{B}(1, 1, 1), \dots, \hat{B}(1, k, 1)]m_{1,1}$	\dots	$[\hat{B}(1, 1, n), \dots, \hat{B}(1, k, n)]m_{1,n}$
$[\hat{B}(2, 1, 1), \dots, \hat{B}(2, k, 1)]m_{2,1}$	\dots	$[\hat{B}(2, 1, n), \dots, \hat{B}(2, k, n)]m_{2,n}$
$\dots\dots\dots$	\dots	$\dots\dots\dots$
$[\hat{B}(t, 1, 1), \dots, \hat{B}(t, k, 1)]m_{t,1}$	\dots	$[\hat{B}(t, 1, n), \dots, \hat{B}(t, k, n)]m_{t,n}$

where X_{ij}^k is the positive integer weight for Subteam j for Target k . If Task i is the most preferred by Subteam f to be done on Target k when $\hat{B}(k, i, f)$ is the maximum bid value of Subteam f for Task i and Target k by comparing the bid values for other tasks and targets, then $X_{if}^k = 0$. Otherwise, $X_{if}^k = 1$. Different subteams are formed by different combinations of the slave robots with their bid values computed with Eq (4), all of which are placed into Table 1. In Table 1, $m_{k,f}$ is the positive integer weight for Subteam f to bid on all tasks on Target k . If $(Q_{(y_a-y_b,i,f)}$ is smaller than the base price which is a positive integer, or Target k has already been assigned to Subteam f , $m_{k,f}$ is 0. Otherwise, $m_{k,f}$ is 1. By arranging $m_{k,f}$ and B_{if}^k into Table 1, called Weighted Attack Guidance Table (WAGT), each row of WAGT corresponds to a target with Tasks (1 to i) and Robot Subteam (1 to f) when i is the total number of the tasks, and f is the total number of the subteams formed in the team. In addition, each column of WAGT corresponds to Subteam that accomplishes Tasks (1 to i) on Targets (1 to k) when k is the total number of the targets. Therefore, there are the k rows and $2f$ columns in WAGT. The scanning proceeds from the first to the last column. Hence, Subteams specified in column i takes precedence over Subteams specified in column $i+2$. The maximum value in each row of WAGT is the most preferred bid for the subteam corresponding to the column number to do the task on the target corresponding to the row number. Therefore, with WAGT, the optimization of the robot-target pairing can be formulated in the following to determine the bidding winner.

Given Subteam f , Target k , and Task i in WAGT, an assignment of a subteam is found in such a format that WAGT is satisfied, and its objective function in Eq. (5) is maximized within the given constraints in Eqs. (6) and (7) where the decision variables are the magnitudes of the subteam and task capability vectors, i.e. $(Q_f$ and $\bar{C}_k^i)$, and X_{ij}^k and $m_{k,f}$. Therefore, for Target k and Subteam $1-f$ as seen in Table 1, the objective function is to find the maximum of the magnitude of $ObjFun(k) = \sum_{j=0}^f \sum_{i=0}^t \hat{B}(k, i, j)m_{k,j}$

$$\text{maximize } \text{Magitude}(ObjFun(k)) \quad (5)$$

Subject to

$$\sum_{j=1}^{j=n} m_{k,j} > 0 \quad (6)$$

$$\sum_{j=1}^{j=n} \hat{B}(k, i, j) \geq 0 \quad (7)$$

where $m_{k,j}$ is the positive integer weight for Subteam j and Target k . Initially, $m_{k,j}$ is equal to one if no subteam is assigned to any target. However, if Subteam j is assigned to Target k , $m_{j,k}$ is equal to zero. Hence, Subteam j that proposes the maximum affordable value of the magnitude of $(\hat{B}(k, i, j)m_{k,j})$ can win Task i on Target k by solving Eqs (5) within the constraints Eqs. (6) and (7). By using the robot-task-target pairing method, the optimal pairs are computed based on given WAGT. In order to make the system be able to split its team into some subteams to execute different tasks on different targets simultaneously, our proposed control method in [13] is advanced by integrating the robot-task-target pairing method into the teleoperation system. The robot-task-target pairing method is created to enable the system based on the found pairs to form subteams, appoint the robots as a subteam leader and followers, pair the tasks to the subteams, and generate the position and force reference inputs to the subteams to work on the given targets. The other components of the proposed control method for the SMMS teleoperator are similar to those we have developed in [13].

2.2 SMMS Teleoperator with the Proposed Modifications

The SMMS teleoperator with integrating the control methods are modified into Figure 1. Figure 1 represents the overall architecture of the modified teleoperation system. The master and slave subsystems in Figures 1a and 1b, respectively, are connected over the wireless internet. The difference from the one in [13] is that the slave subsystem with the proposed control methods is operated fully autonomously for the following reason. The team formed by the slave robots is required to be divided into subteams to simultaneously perform the task on the target when the robots in the subteam are successfully paired to the proper tasks and targets with the multi-robot multi-task multi-target pairing method.

The modified system shown in Figure 1 is formulated into the following equations of motion.

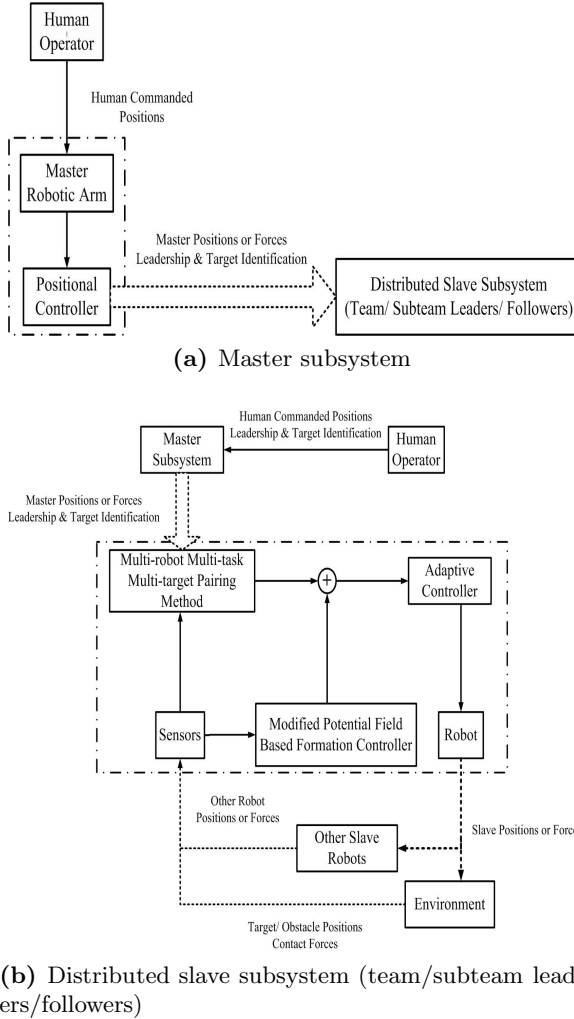
Master:

$$M_m \ddot{e}_m + B_m \dot{e}_m + K_m e_m = 0 \quad (8)$$

i^{th} Slave:

$$M_{si} \ddot{e}_{si} + B_{si} \dot{e}_{si} + K_{si} e_{si} = (1 - W)(U_T + U_o) + (1 - \sigma)(1 - \lambda)U_f + v_{si}^T \tilde{a}_{si} + C_e \delta F_{si} \quad (9)$$

where U_f is the virtual bonding between robots. U_T is the virtual attraction to the target while U_o is the virtual repulsion from the obstacles. C_e is the force compensator to regulate the contact force acting against the target to make a firm grip. W is the sensor based compenstaor to adjust the transparency of the SMMS system

**Fig. 1.** Modified SMMS Systems

based on the human induced error detection. U_f , U_T , U_o , C_e , and W were proposed in [13]. $v_{si} = [z_{si} \dot{x}_{si} x_{si}]^T$, $z_{si} = \mu(\sigma\ddot{x}_m + (1-\sigma)\ddot{x}_{sdi}) - \beta_1\dot{e}_{si} - \beta_0 e_{si}$, β_1 and β_0 are positive constants chosen such that $s^2 + \beta_1 s + \beta_0$ is a stable (Hurwitz) polynomial when s is the Laplace operator. $\tilde{a}_{si} = W [\hat{M}_{si} - M_{si} \hat{B}_{si} - B_{si} \hat{K}_{si} - K_{si}]^T \hat{M}_{si}$, \hat{B}_{si} , and \hat{K}_{si} are the estimated slave impedance matrices. x_m and x_{si} are the master and the i^{th} slave robot position vectors, respectively. x_{sdi} is the reference position vector of the i^{th} slave robot. M_m is the inertia matrix of the master robot. K_m is the control parameters for the linear diagonal master matrices. M_{si} is the inertia matrices of the i^{th} slave robots. B_{si} is the slave impedance matrix. K_{si} is the control parameters for the linear diagonal slave matrices. σ and λ are the control parameters of

Table 2. SMMS simulations for a multi-target mission

Simulations	Control objectives	Robot types
Sim (1)	pairing method	Homogeneous
Sim (2)	pairing method	Heterogeneous

the i^{th} slave robot. When the robot is selected as a team leader, σ is turned into one; otherwise, it becomes zero. When the robot is appointed as a subteam leader, λ becomes one; otherwise, λ is zero. B_m is the master adaptive impedance matrix. $e_{si} = x_{si} - (\sigma x'_m + (1 - \sigma)X'_{ideal})(\alpha_1 + (1 - \alpha_1)\psi_{pos})$. x_{si} is the slave current robot positions. $\alpha_1 = |sgn(e_{si}^2)|$, which is the constant positive integers switching between zero and one in order to determine the output of the target matrix. ψ_{pos} is the matrix, $[0 \ 0 \ 1]^T$ to produce its reference position vectors transformed from X'_{ideal} x'_m and x'_{si} are the delayed transmitted x_m and x_{si} , respectively. X_{ideal} is the slave subteam robot reference position vectors. $\delta F_{si} = F_{si} - F_{ideal}(1 - \alpha_1)\psi_{force}$ is a difference between reference and measured forces of the slave robots when F_{ideal} is the reference force vectors and F_{si} is the measured forces of the slave robots. ψ_{force} is the matrix, $[0 \ 1 \ 0]^T$ to produce its reference force vectors transformed from F'_{ideal} . By using Eqs. (8) and (9), the motion of the SMMS systems can be understood and modeled. The slave team leader path remotely controlled by the human operator is adapted to have good tracking of the master robot positions unless the path is too close to an obstacle and/or too far from the target. The team leader's transparency is compromised. Otherwise, it is adaptively enhanced. When the team is close enough to the region full of targets, the team becomes autonomous and can be split into subteams paired to tasks and targets by using multi-robot multi-task multi-target pairing algorithm to solve Eqs (5) within the constraints in Eqs (6) and (7). The target and task matrices are generated and transformed into the reference positions and forces for the robots to accomplish the designated tasks on the assigned targets. During navigation to the targets, due to no contact force, $\delta F_{si} = 0$, only the robot-obstacle, robot-target, and robot-robot distances can be sensed. If there are too long robot-target distances and/or too short robot-obstacle distances, all slave team robots could autonomously adjust their routes to adapt the formation to approach the target and avoid the obstacles. Furthermore, the subteam leader-follower formation can be maintained or distorted by integrating (1) the virtual robot-robot bondings with different strengths based on which two team robots are connected, (2) the attraction to the target with regard to robot-target distances, and (3) the repulsion from the obstacles with regard to robot-obstacle distances. In such a formation, all followers in the subteam move with regard to the subteam leader's motion. After the target is reached, the slave robots will perform the assigned tasks, such as target capture or transportation relying on the task and target matrices. During target transportation, the contact force against the target by each subteam robot is adjusted, which could cause the subteam robots to have a firm grip of the target while the target is being moved from place to place.

3 Simulation Results

In simulations, the teleoperation control methods with the multi-robot multi-task multi-target pairing method for the homogeneous and heterogeneous robots were simulated in the presence of time-varying communication delays of 0.1-0.0 (seconds) to generate results for performance improvement studies. The maximum delays were defined as 0.1 seconds in the simulations because for the earth application, there is a critical value, beyond which the system tends to become unstable [14]. In Figure 2(a), a master robot was a joystick connected to a laptop with 1.6 GHz Processor and 8 GB memory. In Figure 2(b), virtual slave robot models were programmed in Matlab 7.11 with a realtime simulation toolbox. In all the simulations, there were six virtual static obstacles and two virtual targets in a virtual environment. The target and robot positions were assumed to be known, and the obstacles and targets were modeled in Matlab 7.11 as mass-spring-damper systems [13]. The seven slave robots were run to approach the two static targets, Target A (TA) and B (TB), while avoiding the static obstacles. Two simple tasks, transportation and capture, were considered in the simulations. TB was expected to be moved from place to place by at least three mobile robots when TA was expected to be captured. TB was placed on a movable platform with four passive omni-directional wheels tightly touching the ground. TB would be damaged if the slave robots pushed too hard; however, the slip between the surfaces of TB and the slave robot arms would occur if they pushed too lightly.

The simulations were set up with the following parameters. The robot-robot safety distance was 3m. The minimum robot-obstacle distance was 5m. Six circular obstacles had the radii of 5m. The six obstacles, Ob1, Ob2, Ob3, Ob4, Ob5, and Ob6, were situated at (30, 60), (50, 40), (70, 20), (70,-20), (50,-40), and (30,-60), respectively. Two circular targets had the radii of 5m. Two targets, TA and TB, were situated at (90, 30) and (90, -30), respectively. The seven slave robots, R1, 2, 3, 4, 5, 6, and 7, were initially located at (0, 15), (0, 10), (0, 5),

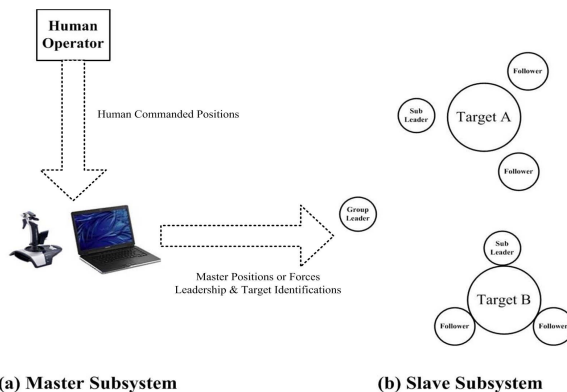


Fig. 2. SMMS Teleoperation Simulation Setups

Table 3. Robot Combinations (Robot Subteams)

Subteam	Combos	Subteam	Combos	Subteam	Combos
Sub1	R1 R2 R3	Sub13	R1 R5 R6	Sub25	R2 R6 R7
Sub2	R1 R2 R4	Sub14	R1 R5 R7	Sub26	R3 R4 R5
Sub3	R1 R2 R5	Sub15	R1 R6 R7	Sub27	R3 R4 R6
Sub10	R1 R4 R5	Sub22	R2 R4 R7	Sub34	R4 R6 R7
Sub11	R1 R4 R6	Sub23	R2 R5 R6	Sub35	R5 R6 R7
Sub12	R1 R4 R7	Sub24	R2 R5 R7		

(0, 0), (0, -5), (0, -10), and (0, -15), respectively. Only the x-y plane motion was considered. Each slave robot had the radii of 3m. TB was expected to move from (90, -30) to (130, -30) along the x-direction. In the simulations, the following parameters were used:

$M_m = 3 \text{ kg}$, $K_m = 6 \text{ Ns/m}$, $M_{si} = 30 \text{ kg}$, $B_{si} = 1.0 \text{ Ns/m}$, $K_{si} = 60 \text{ N/m}$, $/mu = 10$, $k_e = 100$, $b_e = 60$, $r_{imin} = 5$, $r_{smin} = 5$, $k_f = 1$, $\alpha = \rho = 1$, $\beta_1 = 10000$, $\beta_0 = 500$, $\phi = 100$, and $\Lambda_i = \varphi = \gamma = \gamma_w = 1$

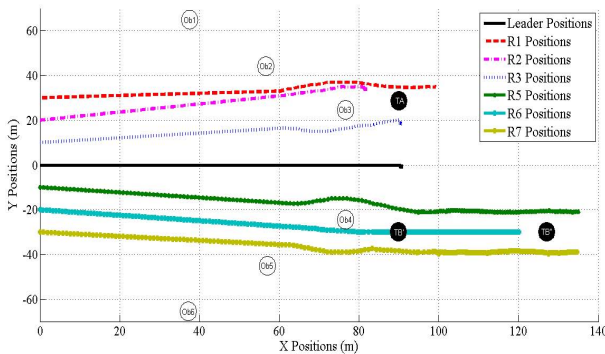
In the simulations, no friction, gravity, and air resistance were assumed in the virtual environment. If the contact force magnitude exceeds 15 N, the robots were assumed to be damaged. The slip was programmed to occur between the contact surfaces of robotic tip point and the target surface only if the static friction condition [1] was not met when the friction coefficient was 0.5 [1]. The simulations, Sim (1) and (2), as listed in 2 were conducted by the same operator for consistency. All slave robots were programmed to move at an average speed of 0.1 m/s in the virtual environment in order to evaluate the effectiveness of the proposed systems by measuring the length of time taken to complete those tasks. In Table 3, those robots could form subteams Sub1 - Sub35 in order to transport TB while capturing TA in the simulations. Each subteam had only three homogeneous or heterogeneous robots, but a robot could not be placed into two different subteams at the same time.

3.1 Simulation 1

In Sim (1), the seven robots were holonomic mobile platforms, each of which had two active wheels and did not have a gripper, and they formed a slave team. The human operator remotely controlled the team leader, R4 while all other slave robots, R1-3 and R5-7, were coordinated with the team leader to approach the targets. In Figure 3, all robots could avoid the obstacles while keeping a constant distance from each other. With the multi-robot multi-task multi-target pairing method in Eqs (1) - (4), the WAGT table for TA and TB, Table 4, was produced based on which the subteams were properly paired to tasks and targets. Bids in Table 4, (Ta, Tb) where Ta was the bid value for TA when Tb was for TB, were calculated in Eq. (4) as an inverse of the sum of target-robot distances in a subteam minus the base price when the base price for t_1 was 30 and t_2 was

Table 4. Weighted Attack Guidance Table (WAGT) for Target A and B in Sim (1)

Subteam	Bids	Subteam	Bids	Subteam	Bids
Sub1	(41,69)	Sub13	(39,73)	Sub25	(38,76)
Sub2	(40,69)	Sub14	(39,74)	Sub26	(39,74)
Sub3	(40,70)	Sub15	(38,75)	Sub27	(39,75)
Sub10	(40,72)	Sub22	(39,74)	Sub34	(38,78)
Sub11	(39,73)	Sub23	(39,75)	Sub35	(38,79)
Sub12	(39,73)	Sub24	(39,75)		

**Fig. 3. Sim (1) - Actual Path Trajectories**

10. The reasons were that in order to start with the tasks, the robots needed to maintain at least 30(m) from TB for t_1 when only keeping at least 10(m) from TA for t_2 because the robots need more space to do t_1 than t_2 . As results of Table 4, Sub1 was paired to TA and the task of the target capture when Sub35 was paired to TB and the task of the target transportation.

In Figure 4, the simulation results showed that the contact forces were maintained at the desired value 10 (N) at most of the time. Those recorded contact forces during the simulation were so desired value that a firm grip of TB was achieved while not being too large to break the robots or TB. Moreover, in Figure 6, the force errors varied from 0.0 to 0.9(N), and a force error average was 0.45 (N) when in Figures 5, the position errors were recorded from 0 to 0.12 (m), and a position error average was 0.05 (m). The position and force errors were as low as those within an acceptable range when the tasks were completed simultaneously in 1250 seconds. Therefore, the performance of the SMMS teleoperator for multi-robot multi-task multi-target pairing was enhanced.

3.2 Simulation 2

In Sim (2), the three heterogeneous robots, R1-3, were holonomic mobile platforms with grippers atop, and the other four robots, R4-7, were nonholonomic

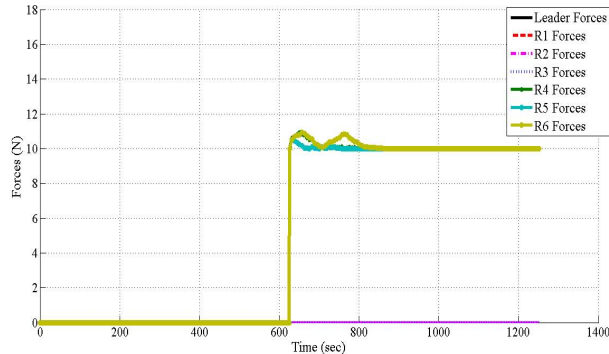


Fig. 4. Sim (1) - Slave Forces

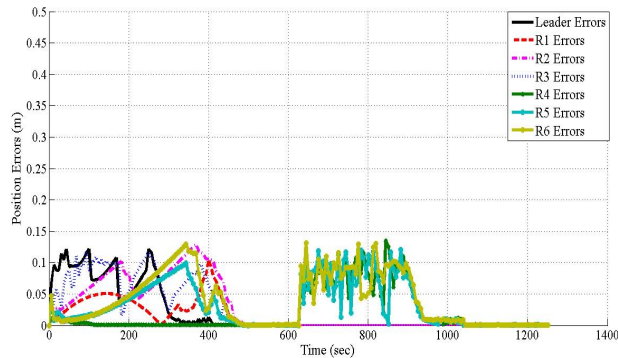


Fig. 5. Sim (1) - Slave Position Errors

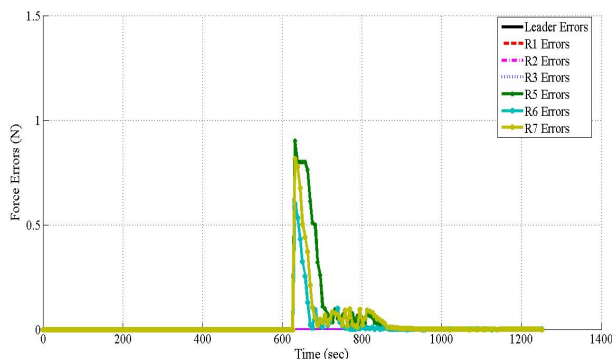
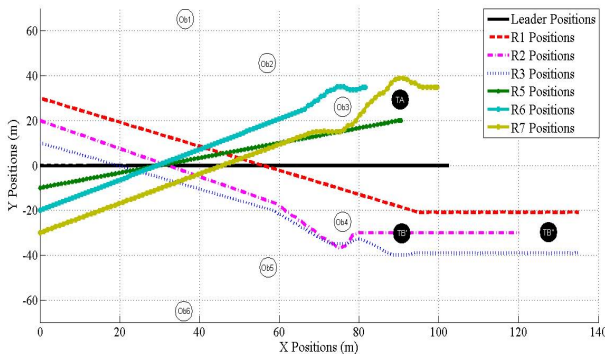


Fig. 6. Sim (1) - Slave Force Errors

Table 5. Weighted Attack Guidance Table (WAGT) for Target A and B in Sim (2)

Subteam	Bids	Subteam	Bids	Subteam	Bids
Sub1	(41,369)	Sub13	(239,173)	Sub25	(238,176)
Sub2	(140,269)	Sub14	(239,174)	Sub26	(239,174)
Sub3	(140,270)	Sub15	(238,175)	Sub27	(239,175)
Sub10	(240,172)	Sub22	(239,174)	Sub34	(328,78)
Sub11	(239,173)	Sub23	(239,175)	Sub35	(338,79)
Sub12	(239,173)	Sub24	(239,175)		

**Fig. 7. Sim (2) - Actual Path Trajectories**

mobile platforms without grippers atop. The obstacles, targets, and tasks were equivalent to the ones specified in Sim (1).

With the multi-robot multi-task multi-target pairing method, bids in Table 5, (T_a, T_b) where T_a was the bid value for TA when T_b was for TB, were calculated in Eq. (4) as an inverse of the sum of the product of robot capability values and all target-robot distances in a subteam minus the base price when the base price for the transportation was 30 and the capture was 10. In addition, the robot capability values for R1-3 were one for the capture if those were ten for the transportation; however, the robot capability values for R4-7 were ten for the capture if those were one for the transportation. The reasons were that in order to start with the tasks, the robots needed to maintain at least 30(m) from TB for the transportation when only keeping at least 10(m) from TA for the capture because the robots need more space to do transportation than capture. Furthermore, the holonomic mobile platforms with grippers atop were more suitable in a target transportation than the nonholonomic mobile platforms without grippers atop. Hence, every robot had different capability values ranging from zero to one. As results of Table 5, Sub35 was paired to TA and the task of the target capture when Sub1 was paired to TB and the task of the target transportation.

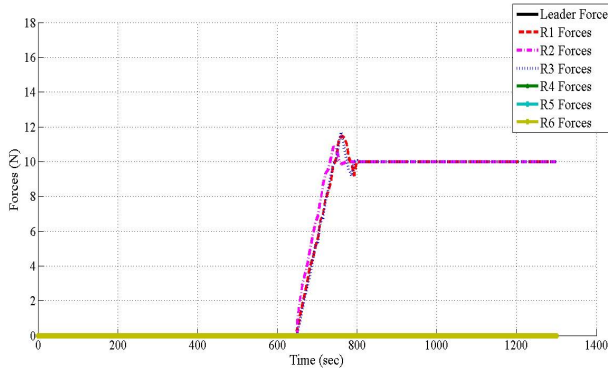


Fig. 8. Sim (2) - Slave Forces

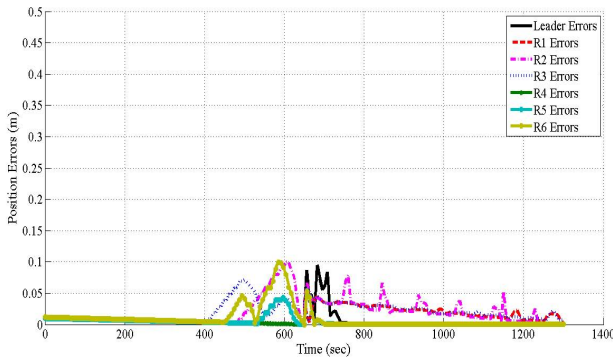


Fig. 9. Sim (2) - Slave Position Errors

In Figure 8, the simulation results showed that the contact forces were also maintained at the desired value 10 (N) at most of the time, which represented an achievement of a firm grip of TB and no damage of the robot and TB due to too large contact forces. Moreover, in Figure 10, the force errors varied from 0.0 to 0.85(N), and a force error average was 0.25 (N) when in Figures 9, the position errors were recorded from 0 to 0.35 (m), and a position error average was 0.08 (m). By comparing the results in Sim(1) and Sim(2), their recorded force and position errors were similar, and their mission completion time was not quite different when the time taken to complete Sim(1) and Sim(2) were 1250 and 1300 seconds, respectively. Therefore, the performance of the proposed SMMS system with the control methods and multi-robot multi-task multi-target pairing method could not be affected if the slave robots were heterogeneous or homogeneous.

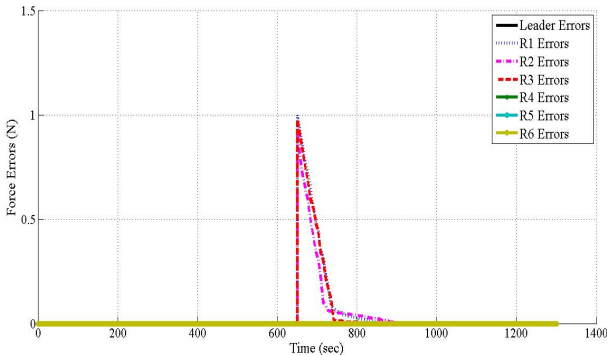


Fig. 10. Sim (2) - Slave Force Errors

4 Conclusion and Future Work

The adaptive control method including the above mentioned major components is developed for the SMMS mobile teleoperations to execute multi-tasks on multi-targets and improve the performance in terms of the effectiveness of the task achievement and the system transparency no matter whether the slave robots are homogeneous or heterogeneous as seen from the simulation results. Moreover, heterogeneous robots with the proposed control method can avoid obstacles and track targets because the major components in the method, (1) the modified potential field based leader-follower formation, (2) adaptive master-slave impedance, (3) compensators for contact forces and human errors, and (4) the multi-robot multi-task multi-target pairing method, enable each robot to generate its path based on sensed robot-obstacle/target/robot distances and contact forces. Nonetheless, the multi-robot multi-task multi-target pairing method could generate a suboptimal solution in general since multi-robot multi-task multi-target pairing algorithm is heuristic.

Therefore, our future work will be to further evaluate the performance of using multi-robot multi-task multi-target pairing method to verify the performance and quality of the pair solutions. In addition, we will look into the proposed control method for a SMMS mobile teleoperator working in much complicated tasks and environments, e.g. an uncertain task that may include unconstrained, constrained, transition, or some motions combining two or all of them in an unknown area, which has not been mentioned in our papers. We will implement the proposed control method into a SMMS system hardware for further experimental validation by comparing the experiments with the simulations to highlight the expected performance enhancements even if the real time delays may vary irregularly.

References

1. Ota, J., Miyata, N., Arai, T., Yoshida, E., Kurabatashi, D., Sasaki, J.: Transferring and regrasping a large object by cooperation of multiple mobile robots. In: Proceedings of the IEEE/RSJ International Conference on Human Robot Interaction and Cooperative Robots (1995)
2. Fong, T., Thorpe, C., Baur, C.: Multi-robot remote driving with collaborative control. *IEEE Transactions on Industrial Electronics* 50(4), 699–704 (2003)
3. Pongpunwattana, A., Rysdyk, R.: Real-time planning for multiple autonomous vehicles in dynamic uncertain environments. *Journal of Aerospace Computing, Information, and Communication* 1(12), 580–604 (2004)
4. Farkhatdinov, I., Ryu, J.-H.: Teleoperation of multi-robot and multi-property systems. In: 6th IEEE International Conference on Industrial Informatics, INDIN 2008, pp. 1453–1458 (1999)
5. Yamamoto, Y., Fukuda, S.: Trajectory planning of multiple mobile manipulators with collision avoidance capability. In: Proceedings of the IEEE International Conference on ICRA 2002 (2002)
6. Lee, D., Martinez-Palafox, O., Spong, M.: Bilateral teleoperation of multiple cooperative robots over delayed communication networks: Theory. In: Proceedings of the IEEE International Conference on Robotics and Automation, ICRA (2005)
7. Lee, D., Spong, M.: Bilateral teleoperation of multiple cooperative robots over delayed communication networks: Application. In: Proceedings of the 2005 IEEE International Conference on Robotics and Automation, ICRA (2005)
8. Bogdanowicz, Z.R., Coleman, N.P.: New algorithm for optimization of effect-based weapon-target pairings. In: International Conference Scientific Computing, CSC 2008 (2008)
9. Liu, B., Qin, Z., Wang, R., Bing Gao, Y., Ping Shao, L.: A hybrid heuristic particle swarm optimization for coordinated multi-target assignment. In: 4th IEEE Conference on Industrial Electronics and Applications, ICIEA, pp. 1929–1934 (2009)
10. Lee, Z.J., Lee, C.Y., Su, S.F.: An immunity-based ant colony optimization algorithm for solving weapon-target assignment problem. *Applied Soft Computing Journal* 2(1), 39–47 (2002)
11. Dias, M.B., Zlot, R.M., Kalra, N., Stentz, A.: Market-based multirobot coordination: a survey and analysis. *Proceedings of the IEEE* 94(7), 1257–1270 (2006)
12. Shi, Z., Wei, J., Wang, Z., Zhang, Q., Liu, L.: Grouping delegation task allocation model for multi-robot collaboration system. In: IEEE International Conference on Computer Science and Automation Engineering (CSAE), vol. 4, pp. 440–446 (2011)
13. Cheung, Y.: Adaptive semi-autonomous teleoperation of a multi-agent robotic system. PhD thesis, Stevens Institute of Technology (2009)
14. Hashtrudi-Zaad, K., Salcudean, S.: Adaptive transparent impedance reflecting teleoperation. In: Proc. of the 1996 IEEE Int. Conf. Robotics and Automation (1996)

Context-Aware Decision Making for Maze Solving

Sheir Afgen Zaheer and Jong-Hwan Kim

Department of Electrical Engineering, KAIST, 291 Daehak-ro,
Yuseong-gu, Daejeon, Republic of Korea
{sheir,johkim}@rit.kaist.ac.kr

Abstract. This paper proposes a context-aware decision making framework for a maze solving robot. The proposed architecture utilizes a fuzzy integral based decision making scheme to select the best behavior according to the current environmental context of the robot. The simulation results show that despite having no prior information about the arrangement of the maze, the proposed cognitive architecture for context-aware decision making successfully enabled the robot to find its way through the maze.

Keywords: Fuzzy integral, Multi-criteria decision making, Maze Solving Robot.

1 Introduction

Over the past few decades, cognitive decision making in intelligent robots and artificial agents have been a popular research area. The human cognitive intelligence seems to be the main inspiration behind all this interest. However, the functional architecture of human cognitive process is still not an established science; this leads to a variety of interpretations and understandings about its functionality. Some researchers are inclined towards symbolic-based cognitive architectures [1]-[2], while others pursue the development of emergent architectures [3]. There is some research on hybrid architectures as-well [4], these architectures result from the combination of both the symbolic and the emergent schemes. Our work is mainly inspired from some of the more recent researches that use personal and environmental aspects (or symbols) as criteria for cognitive decision making [5]-[6].

This project proposes a framework based on context-aware decision making for a maze solving robot. The problem setup consists of a simulated robot, spawned at the starting point of a maze. The maze is a square-shaped arena with randomly placed walls (Fig. 1). The robot is spawned at the starting position of the maze without any information about the map of the maze. Therefore, the robot needs to solve the maze based on its real time interaction with the environment inside the maze. The location of the destination point is the only prior information that the robot has. Though there have been some previous researches on maze solving by robots, most of them use a run or two to map the environment inside the maze before coming up with the solution path [7]-[8]. Another research was aimed at similar kind of cognitive architecture for maze solving [9]. The robot in this research, however, had an additional benefit of being able to look at maze from the top of the maze's walls. The core of the proposed context-aware decision making is a two criteria decision process. Choquet fuzzy integral has been

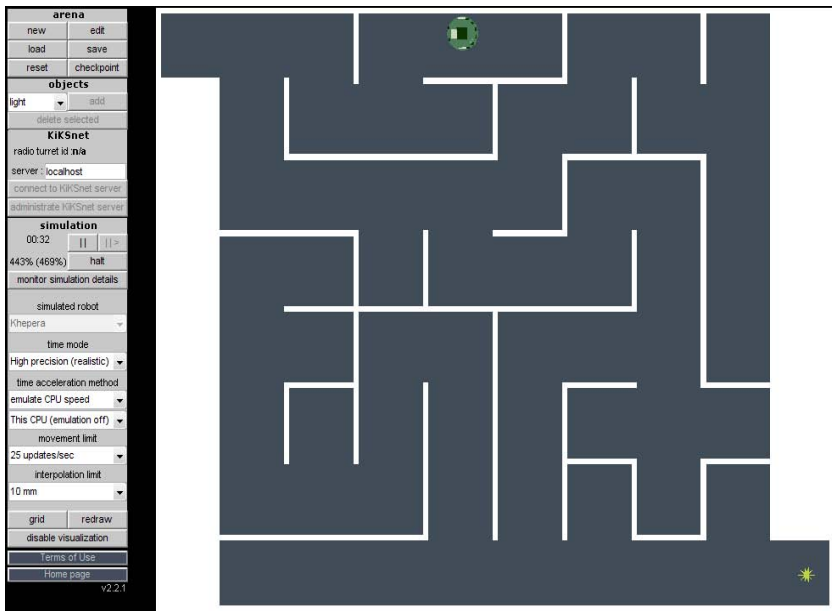


Fig. 1. A Snapshot of simulated maze

found to be an effective aggregator for such decision making problems [6]. In our work, we have used KiKS (a Khepera robot simulator) [10] for simulating Khepera robot and mazes. Khepera is a small differential wheeled robot with an array of ultrasonic sensors attached to its circular periphery.

This paper is organised as follows: Section 2 explains the proposed framework for context-aware decision making to solve a maze. Section 3 describes the simulations results. Finally, discussions and conclusions follow in section 4.

2 Decision Making Framework for The Maze Solving Robot

This paper proposes a decision making framework for a mobile robot that enables it to find its way through an unknown maze. The overall architecture of the proposed framework is summarized in Fig. 2. This framework consists of four layers: the perception layer, the reasoning layer, the memory layer and the execution layer. Each layer consists of some modules through which it performs its share of tasks. Following subsections provide the functional description of all these layers and modules.

2.1 The Perception Layer

The perception layer is mainly responsible for interpreting the sensory readings and transforming them into meaningful information. The components of this layer are the array of sensors on the robot and the perception module.

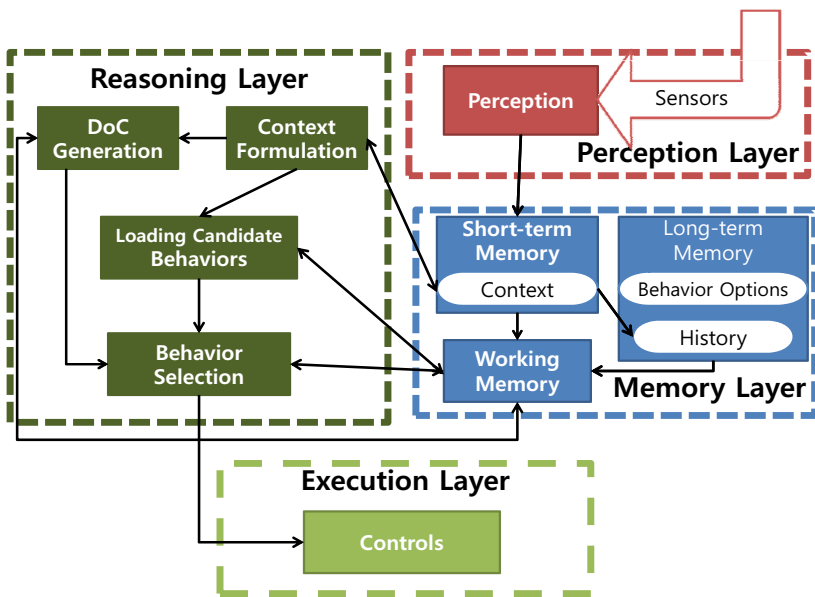


Fig. 2. The architecture of the decision making framework for the maze solving robot

Sensors: As mentioned before, the robot considered in this setup has an array of eight sensors along its periphery. All these sensors are identical ultrasonic distance sensors. These sensors provide a 10-bit proximity reading, i.e. from 0-1024; where 1024 implies a physical contact. In addition to that there are two wheel encoders as-well. These encoders can be used to obtain the information about the robot's heading and the distance travelled.

The Perception Module: Based on readings provided by the sensors, the perception module receives an array of ultrasonic sensor readings and the odometric readings from the encoders. The perception module is responsible for meaningful interpretation of this information. First, it translates the proximity readings into the free space available to the left, right and in front of the robot. Secondly, it uses the odometric information to determine the heading of the robot and its position relative to the starting point of the maze.

2.2 The Memory Layer

As the name suggests the memory layer is responsible for information storage. Based on the type of information stored, the memory layer can be divided into three components: short term memory, long term memory and working memory.

The Short-Term Memory: The short term memory, in this case, is responsible for the storage of current context only. The short term memory interacts with the perception layer and the context formulation module in the reasoning layer to perform its functionality.

Table 1. List of local situations and corresponding Candidate behaviors

Local situation	Description	Candidate behaviors
Backwards only	The robot can only go back, it's a dead end	180 degree turn
One way Forward	Straight path with walls on left and right	Go straight
One way Left	Only open area is towards left	Turn left
One way Right	Only open area is towards right	Turn right
Two way Forw/Left	A junction with open areas in forward and left directions	Go straight; Turn left
Two way Forw/Right	A junction with open areas in forward and right directions	Go straight; Turn right
Two way Left/Right	A junction with open areas in right and left directions	Turn left; Turn right
Three way	A '+' like junction where the robot can go in an any direction	Turn left; Turn right; Go straight

The Long-Term Memory: The long term memory stores two types of information: behavior options and history. The behavior options module stores the list of possible behaviors associated with each context situation. (For details on this, refer to section 2.3) The history modules stores the past context information, in order to keep track of the previously visited sites inside the maze. This particular information is used by behavior selection module.

The Working Memory: This particular part of the memory is responsible to hold information that is being used in the on-going decision making, including the history and the behavior options, whenever required by the reasoning layer.

2.3 The Reasoning Layer

The reason layer is the core of the proposed framework for context-aware decision making. This is where the intelligent decision making stems from. As shown in Fig. 2, the reasoning layer consists of four phases: Context formulation, Degree of consideration (DoC) generation, loading candidate behaviors and Behavior Selection. All these phases are explained in the following subsections.

Context Formulation: As the name suggests, this phase is responsible for building the context. The built context in this application setup consisted of three information variables: position of the robot, heading of the robot and the current local situation. The list of local situations and their description is provided in Table 1 (first two columns).

Degree of Consideration Generation: As mentioned in the previous section, there are two criteria for determining the output behavior for the robot. These two criteria are:

- i) The change in the Euclidean distance to destination (ΔD)
- ii) Distance to the next obstacle in that direction (d_o)

This phase of the decision making process is responsible for the generating the DoCs for both these criteria. The DoCs, in this case, are represented by λ -fuzzy measures. Since there are only two criteria, ΔD and d_o , their union can be written as [11]:

$$g(\Delta D \cup d_o) = g(\Delta D) + g(d_o) + \lambda g(\Delta D)g(d_o) = 1, \quad (1)$$

where $g(\cdot)$ represents the λ -fuzzy measure for a criterion or a set of criteria, and λ is the interaction degree index. However, in this case, the criteria are considered to be uncorrelated. The justification for this consideration is based on the fact that an increase or decrease in ΔD has no effect on d_o and vice versa. Hence, λ is zero in this case, and (1) simplifies into:

$$g(\Delta D \cup d_o) = g(\Delta D) + g(d_o) = 1. \quad (2)$$

The next step is to define the DoC values, i.e. the fuzzy measures, for both criteria. However, the DoC values in this case are not constant. They vary as the robot moves around. The DoC value for ΔD is defined as a function of the absolute distance from the destination position before the current behavior selection.

$$g(\Delta D) = g_{max} - \left(\frac{D_c}{D_T} \times (g_{max} - g_{min}) \right), \quad (3)$$

where g_{max} and g_{min} are the maximum and minimum permissible values for the DoC of ΔD . D_c is the current euclidean distance of the robot from the destination point, and D_T is the diagonal length of the maze. From (2), the DoC for d_o can be defined as:

$$g(d_o) = 1 - g(\Delta D). \quad (4)$$

Loading Candidate Behaviors: In this problem setup, all robot behaviors are not applicable for each context. Therefore, depending on the current context, a list of possible behaviors needs to be provided. Possible contexts and the associated behaviors are summarized in Table 1. The information in this table is available in behavior options module of the long term memory. This phase of decision making receives the context from the context formulation and then, loads the candidate behaviors from the long term memory through working memory.

Behavior Selection: The final step in the reasoning layer was to select the best behavior from the loaded candidate behaviors. Now that all the DoC values and the candidate behaviors are available, an aggregation operation for global evaluation is required. The aggregator used here is the discrete Choquet fuzzy integral [12].

$$\int_X h \circ g = \sum_{i=1}^n (h(x_i) - h(x_{i-1}))g(E_i), \quad (5)$$

where n is the number of criteria, $h(\cdot)$ is the partial evaluation value, and E_i is the subset of the criteria set X consisting x_i and all others that have a higher partial evaluation value than x_i . In this application, there are two criteria, $x_1 = \Delta D$ and $x_2 = d_o$. Therefore, before evaluating each candidate behavior, partial evaluation values over

Table 2. Lookup table for partial evaluation values over ΔD , i.e. $h(\Delta D)$

Change in distance along axis		Horizontal axis		
Vertical axis	Positive	Zero	Negative	
Positive	0.05	0.25	0.5	
Zero	0.25	Not applicable	0.75	
Negative	0.5	0.75	0.95	

each criteria, $h(\cdot)$, are required. For the first criterion, i.e. ΔD , the partial evaluation for a particular candidate behavior over ΔD is obtained from a lookup table (Table 2). As shown in the table, the partial evaluation value depends on whether the selected behavior results in an increase or decrease in Euclidian distance to the destination point. The partial evaluation over the second criteria, i.e. d_o , is defined as a function of proximity of the next obstacle in the direction that results from the current candidate behavior. Numerically, it is given as:

$$h(d_o) = 1 - \frac{PV_c}{PV_{max}}, \quad (6)$$

where PV_c is the current proximity value measured by the ultrasonic sensor, and PV_{max} is the maximum proximity value when the sensor is touching the obstacle.

Finally, the candidate behavior with the highest global evaluation value from (5) is selected as the winning behavior. However, this behavior is not sent directly to the execution layer. Instead, the history in the long term memory is first checked. If the history tells that the current context, including the robot position, has already been visited, it means that the previously selected behavior at this particular location of the maze was not correct. If such a case arises, the behavior with the next highest evaluation value is selected. This helps the robot to avoid making the same mistake.

2.4 The Execution Layer

The execution layer is responsible to ensure proper implementation of the behavior selected through the reasoning process. The control module in this layer translates the behavior command into the respective motor velocities.

3 Results

Once, the cognitive architecture for maze solving was designed, the next step was to test it. Different simulated mazes were constructed for this purpose. Three mazes that vary in size and complexity are discussed here.

- i) 40 x 40 cm maze
- ii) 60 x 60 cm maze
- iii) 100 x 100 cm maze

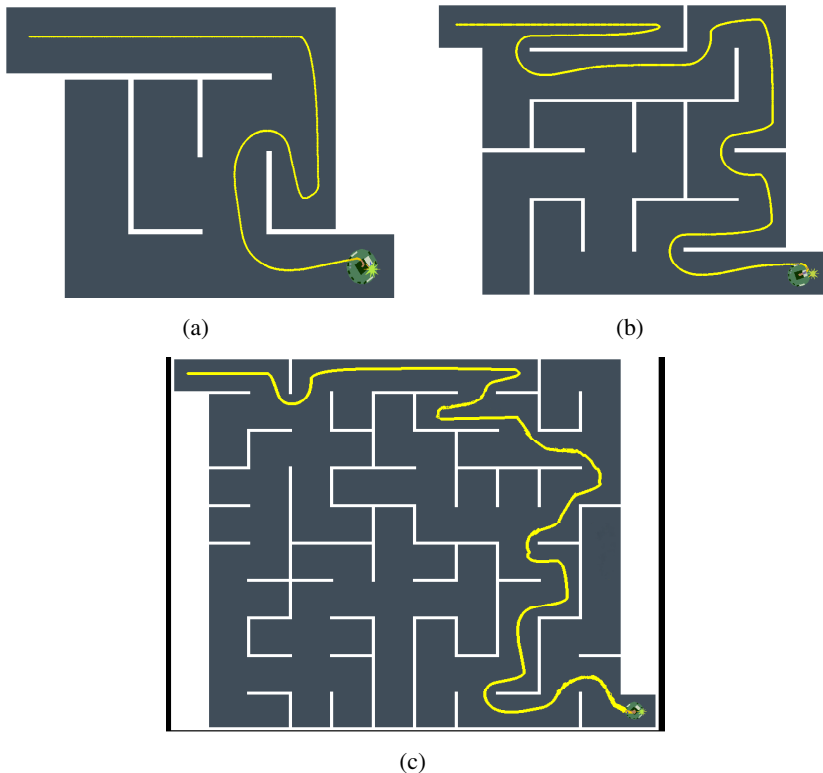


Fig. 3. Robot's trajectory (a) 40 x 40 cm maze (b) 60 x 60 cm (c) 100 x 100 cm

The resulting trajectories of the robot, while attempting to solve these mazes with the proposed architecture, are shown in Fig. 3. It is evident from the figure that the robot was able to successfully reach the destination point. However, we can easily see that the proposed decision making framework does not guarantee an optimal path. This limitation can be attributed to the fact that the robot's instantaneous knowledge about the structure of the maze is limited to a small region of maze that lies within the range of its sensors. Therefore, the decision made by the proposed decision making scheme, though the most viable decision within the visible context, may lead the robot to a dead end later on.

Moreover, we also compared our algorithm with wall follower algorithm for maze following robot. We selected this algorithm for comparison because unlike other algorithms for maze solving robots, the wall following algorithm does not require a pre-run to map the maze. Trajectory result for one run of the wall following algorithm is shown in Fig. 4. It can be seen that the wall following algorithm just tracks the wall until it eventually leads to the end of the maze. The comparative results for the context-aware decision making (CDM) algorithm versus the wall following (WF) algorithm are shown in Table 3. The table shows the average maze solving time over 10 randomly generated mazes. The results show that the proposed algorithm performed better than the wall following algorithm.

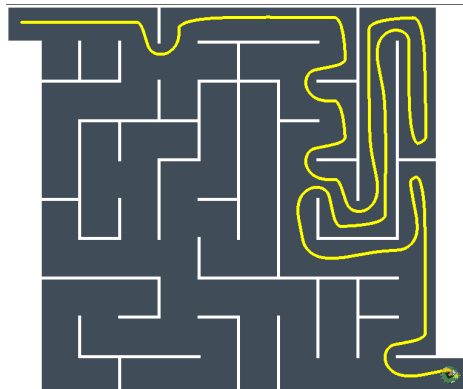


Fig. 4. Robot's trajectory for wall following algorithm

Table 3. Comparative results for the context-aware decision making algorithm versus the wall following algorithm

Maze Size	CDM (seconds)	WF (seconds)
40 x 40	97	123
60 x 60	152	187
100 x 100	203	314

4 Discussion and Conclusion

This paper proposed a cognitive architecture for a mobile robot that enabled it to find its way through the maze. The results show that the robot with the proposed cognitive architecture for behavior selection was able to navigate its way through the maze. Simulations with different maze sizes were conducted. Though the robot was successful in finding the destination point through the maze, it did show some tendency to make suboptimal decisions. In summary, the proposed method for maze solving leads to the successful solution but, in its current form, it cannot be claimed as the best or the optimal method. This work is in its preliminary stages yet. In future, we aim at improving the decision making process by including more context information and criteria. Moreover, we also aim to incorporate a learning module to enable the robot to learn and re-adjust the parameters of DoC generation for different criteria.

Acknowledgment. This research was supported by the MKE (The Ministry of Knowledge Economy), Korea, under the National Robotics Research Center for Robot Intelligence Technology support program supervised by the NIPA (National IT Industry Promotion Agency) (NIPA-2010-N02100128).

References

1. Laird, J.E., Newell, A., Rosenbloom, P.S.: SOAR: An architecture for general intelligence. *Artif. Intell.* 33(1), 1–64 (1987)
2. Kieras, D.E., Meyer, D.E.: An overview of the EPIC architecture for cognition and performance with application to human-computer interaction. *Hum.-Comput. Interact.* 12(4), 391–438 (1997)
3. Brooks, R.: A robust layered control system for a mobile robot. *IEEE J. Robot Autom.* 2(1), 14–23 (1986)
4. Bughart, C., et al.: A cognitive architecture for a humanoid robot: a first approach. Paper Presented at IEEE-RAS International Conference on Humanoid Robots, December 5 (2005)
5. Kim, J.-H., Cho, S.-H., Kim, Y.-H., Park, I.-W.: Two-layered confabulation architecture for an artificial creature's behavior selection. *IEEE Trans. Syst. Man Cybern C, Appl. Rev.* 38(6), 834–840 (2008)
6. Kim, J.-H., Ko, W.-R., Han, J.-H., Zaheer, S.A.: The degree of consideration-based mechanism of thought and its application to artificial creatures for behavior selection. *IEEE Comput. Intell. Mag.* 7(1), 49–63 (2012)
7. Jiang, H., Wang, H., Tian, Y.: Design and realization of a maze robot. Presented at International Conference on Consumer Electronics, Communications and Networks, April 16-18 (2011)
8. Dang, H., Song, J., Guo, Q.: An Efficient Algorithm for Robot Maze-Solving. Presented at 2nd International Conference on Intelligent Human-Machine Systems and Cybernetics, August 26-28 (2010)
9. Wyeth, G., Browning, B.: Cognitive Models of Spatial Navigation from a Robot Builder's Perspective. *Adaptive Behavior* 6(3-4) (1998)
10. Storm, T.: KiKS is a Khepera simulator (2010),
<http://www.tstorm.se/projects/kiks/>
11. Berres, M., Meyer, K.D.: λ -additive fuzzy measures on measure spaces. *Fuzzy Sets and Systems* 27, 159–169 (1988)
12. Gilboa, I., Schmeidler, D.: Additive representations of non-additive measures and the Choquet integral. *Ann. Oper. Res.* 52(1), 43–65 (1994)

Decentralized Task Re-planning Approaches with *en Route* Information Rewards

Sung-Hoon Kim, Sung-Tae An, and Han-Lim Choi

KAIST, 291 Daehak-ro, Yuseong, Daejeon 305-701, Korea
{shkim86,stan,hanlimc}@kaist.ac.kr

Abstract. This paper presents extensions to the consensus-based bundle algorithm (CBBA) for distributed task planning to take into account rewards obtained *en route* in the information-gathering missions. The key idea is to incorporate acquired information on the fly when defining scores of the assigned tasks in the re-plan process so that agents can react to the changes in the environment with correct awareness of the executed task scores. Two methods are proposed to quantify this *en route* acquired information – linear heuristic and entropy-based reward. Numerical simulation results demonstrate that the proposed methods facilitate agents to perform more tasks and thus achieve higher overall scores.

1 Introduction

Gathering information is an essential part for modern autonomous systems in either military or commercial applications. Such applications consist of several tasks such as reconnaissance tasks followed by persistent surveillance, threat identification, target tracking and post-event reconnaissance [28]. These tasks are based on gaining information around the task location even though the objective and operation area of the tasks are different for each application. Therefore, the amount of the information acquired through the task should be considered when multiple tasks are allocated and scheduled for multiple agents.

Typical task allocation methods can be classified into two categories. Centralized methods [2,5,9,17,29,31,33] consist of making all of the decisions in one place [19]. All the tasks to be performed are collected, allocated and scheduled by a central system which is typically on the ground. Thus, they can handle much more computationally expensive procedures to allocate tasks to each agent with optimality while each robot agent can be smaller and more inexpensively developed. However, all the agents should be connected with the central system via certain communication networks through whole missions; thus resulting in smaller operational ranges which can be dealt with the team of agents.

Several types of distributed task allocation methods [4,10,14,30] have been proposed to alleviate this disadvantage of centralized methods. These distributed and decentralized task allocation algorithms can be used in environments where communications may be unreliable due to high latency, high cost, or simply being unavailable [18]. Therefore, decentralized methods generally involve consensus algorithms [1,22–24,26,27] to converge on a consistent situational awareness among agents of team and auction algorithms [6,7,15,16] to deduce suboptimal solutions efficiently.

The consensus-based bundle algorithm (CBBA) developed by one of the present authors is a decentralized task assignment algorithm that has recently been extensively used in the field of UAV (unmanned aerial vehicles) task planning [3,8,11,25,32]. The primary concept of the CBBA framework is to achieve conflict-free assignment of tasks to agents in a decentralized manner via some consensus process in the plan space (as opposed to the problem parameters space). This plan consensus process ensures that all the agents in the network agree upon who is the best agent to do a certain task and what is the maximum score the winning agent would obtain from the task, leading to provable finite time convergence and minimum performance guarantees. Details of the method can be found in [11].

Although the framework of CBBA allows for handling more generic/complex mission plan & re-plan situations, in its typical implementations, the score for an assignment (i.e., an agent-task pair) is determined by the reward obtained when an agent *arrives* at the task location and stays there for specified task duration with penalty on task tardiness. This model is valid when the task is defined as such and/or the length-scale of the mission space is relatively long; however, this model does not particularly represent the situation where agents can accumulate information rewards on the fly and/or when the length-scale of the mission space is relatively short compared to the agent's motion scale.

As such, this work extends the CBBA method in order to explicitly take into account the rewards obtain *en Route* to the task locations. The key extension is, when re-plan, to calculate the partial information reward on the way to task the agent is headed to. To achieve this without significantly increasing computational/communication costs, two methods termed Heuristic and Entropy methods, respectively, are proposed. The Heuristic method is based on the assumption of linear increment in the on the fly information, while the Entropy method takes into account the entropy reduction by measurement sequences with the identical Fisher information metric. Monte-Carlo simulations on multi-UAV task planning/re-planning scenarios with pop-up tasks verifies the proposed approaches.

2 Heuristic Method

The information quantity from the sensor which can be represented as a single scalar value can adjust to the value of the current task for a decreasing reward. In the Heuristic method, two values are determined when specific tasks are assigned to agents; the maximum task value, v_{max} and the total task value, v_{tot} . The total task value is the reward that can be gathered from the task if agents complete the task. The total value is estimated by consuming time through the path. Originally the total task value, v_{tot} is defined by the DMG rule, but in this paper the task value is also affected by the amount of information. During the task, the value of the certain task is decreased as much as the amount of information gathered. The discounted value will reduce the attractiveness of the task and change the bundles according to the newly evaluated tasks. The value of information is increasing during the path and at last it equals the maximum task value v_{max} .

The slope of gathering information shown in Fig. 1 and 2 depicts the fact that the integration of value through the path is the same as the total value from the task.

$$\begin{aligned}
 v_{tot} &= \int_{t_{dep}}^{t_{arr}} \frac{v_{max}}{\Delta t} (t - t_{dep}) dt \\
 v_{tot} &= \frac{1}{2} v_{max} (t_{arr} - t_{dep})
 \end{aligned} \tag{1}$$

Information value represents the quality of information and defines acquired data from the sensor at a specific time. The Heuristic approach assumes that quantity of information is increasing when it comes to the task area. The amount of information obtained from a specific moment from the target is determined by integrating all the values until that moment. The integrated value until the agent reaches the task is equal to the total value. Therefore, in the Heuristic method, at the moment of task completed; agents acquire the entire reward from integrating information value through the path, which is same as total value.

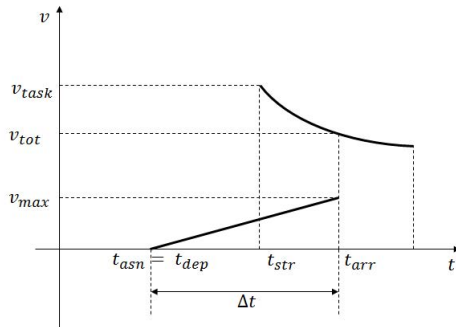


Fig. 1. The case of UAV reaches to the task after it started

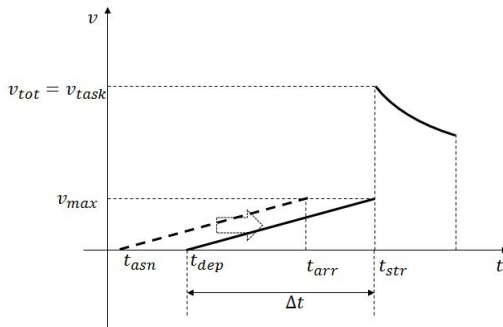


Fig. 2. The case of UAV reaches to the task before it started

In the Heuristic Method, acquired information increases as the distance decreases to the target area due to the accumulation of information during travel. The UAV is assumed to move in a constant speed to the task area, therefore when the task is assigned to a specific agent, the duration time is calculated for the estimated arrival time to the

target. In the case that the arrival time is curtailed, agents can acquire the entire reward without reduction. On the other hand the maximum reward decreases exponentially and this determines the rate of change of gathered information in each step. Upon completion the integrated information quantity from departure to arrival to task is the same as the maximum reward of target.

At each iteration, UAVs identify their current operating task and considers the task which preceded the current task (line 3). If these two tasks are different, agents assume that the new task is assigned, and updates the information of time characteristics. Assigned time is defined by the current time (line 4), and the arrival time is calculated by Δt which is determined by the normal velocity of the vehicle (line 5). Estimated time of arrival can be used for comparison with the start time of the task and to predict the acquired reward from the task by the DMG rule (line 7-12). If the Estimated time of arrival falls before the task start time, agents stay at their current position before departing to the task to arrive on time (line 10,11).

Algorithm 1. Heuristic Method

```

1: for  $i = 1 : N$  do
2:    $m_{idx} = agents(i).task(1)$ 
3:   if  $m_{idx} \neq agents(i).curTask$  then update  $m_{idx}$  task's properties
4:      $t_{asn} = t$ 
5:      $\Delta t = distance / normVel$ 
6:      $t_{arr} = t_{asn} + \Delta t$ 
7:     if  $t_{arr} \geq t_{start}$  then
8:        $V_{tot} = exp^{\lambda(t_{arr}-t_{start})} \times V_{initial}$ 
9:     else
10:       $t_{arr} = t_{start}$ 
11:       $t_{dep} = t_{asn} + (t_{start} - t_{arr})$ 
12:       $V_{tot} = V_{initial}$ 
13:    end if
14:  end if
15: end for

```

3 Entropy Method

Information theory is introduced from Shannon, and it can be used to represent the uncertainty of probability distribution. Entropy is formulated as the expectation of the negative of the log-likelihood

$$H(x) = E[-\ln p(x)] = - \int_{-\infty}^{\infty} p(x) \ln p(x) dx \quad (2)$$

$p(x)$ can be expressed as a state probability of the target and it can be described as a Gaussian distribution with mean \bar{x} and covariance P . And the PDF is given by [20]

$$p(x) = | -2\pi P |^{-1/2} \exp \left(\frac{1}{2} (x - \bar{x})^T P^{-1} (x - \bar{x}) \right) \quad (3)$$

Algorithm 2. Entropy Method for agent i at iteration t

```

1: procedure SELECT TASK( $\theta^2(t-1)$ ,  $\tau^2$ )
2:   if  $m_idx = agents(i).curTask$  then
3:      $\sigma^2(t) = \theta^2(t-1)$ 
4:      $\theta^2(t) = fn(\sigma^2(t), \tau^2)$ 
5:      $v_{tot}(t) = H(t)$ 
6:   end if
7: end procedure

```

The entropy of this Gaussian probability distribution with n-dimensional vector x is represented by [21]

$$E[\ln p(x)] = -\frac{1}{2} \ln[(2\pi e)^n |P|] \quad (4)$$

The covariance of probability can be represented as the uncertainty of target position, and each iteration of target detection from obtained sensors reduces this uncertainty. The sensor characteristics expressed by the likelihood probability and target detecting probability is calculated by the Bayesian theorem. The Bayesian method is represented as follows:

$$p(x|z) = \frac{p(z|x)p(x)}{\int(p(z|x)p(x)dx)} = \frac{p(z|x)p(x)}{p(z)} \quad (5)$$

It is assumed that the sensor detecting process is a Markov process. Also, it can be formulated as the recursive form for using theorem in discrete simulations:

$$p(x|Z^k) = \frac{p(z(k)|x)p(x|Z^{k-1})}{(p(z(k)|Z^{k-1}))} \quad (6)$$

The prior and likelihood probability is a normal distribution with same mean value but with a different variance. In the Bayesian recursive criterion; posterior probability of the target state is used as a prior probability of the next step, which makes the posterior probability sharper with a smaller variance. If the variance of the posterior probability, prior probability, and likelihood probability is defined as θ^2 , σ^2 , and τ^2 then the change of posterior variance in every step is

$$\theta^2 = \frac{\sigma^2 \tau^2}{\sigma^2 + \tau^2} \quad (7)$$

The calculated posterior variance is used as the prior probability variance in the next step, and substitution of prior probability reduces the posterior probability variance in every iteration. In certain iteration t , the posterior probability variance can be estimated as follow:

$$\tau_{t+1}^2 = \frac{\sigma_t^2 \tau_t^2}{\sigma_t^2 + \tau_t^2}$$

$$\begin{aligned}\frac{1}{\tau_{t+1}^2} &= \frac{1}{\tau_t^2} + \frac{1}{\sigma_t^2} \\ \tau_t^2 &= \frac{\tau_1^2 \sigma^2}{\sigma^2 + \tau_1^2(t-1)}\end{aligned}\quad (8)$$

The variance of posterior probability can be transformed into entropy [12,13] by using eq(4). The equation is represented by

$$H(t) = -\frac{1}{2} \ln(\theta^2) - \frac{1}{2} \ln(2\pi \exp) \quad (9)$$

If there is no change of operating tasks, agents update variance of posterior probability by using prior and likelihood probability variances (line 4). The prior probability which is used in this calculation is the posterior probability of the previous step (line 3). The resulting variance can be represented by the reduced amount of entropy and can be directly changed to the total task reward (line 5).

4 Result

Three methods are used to calculate the reward which can be acquired through the completion of tasks. The first is the original CBBA, which can acquire the reward when agents reach the task. The current CBBA does not consider the information acquired during the path to the task.

The Heuristic Method reflects sensor behavior for gathering information, and it is assumed that information increases linearly as agents get closer to the task area. So the accumulated information is formulated in proportion to the distance between the vehicle and the target.

Lastly, the Entropy Method uses the Bayesian recursive rule for calculating the variance of posterior probability. In every step, sensors compensate their measurement values; updating the variance of the prior probability based on the posterior probability in the previous step. A general tendency of increasing information through the path is non-linear and when compared to the Heuristic Method, different results occur.

The simulation is held in a certain modified condition. The agent was set up, and initially one task was located in the mission field. In the first bidding, the agent gets the task as a bundle and moves to the target area. If there are multiple UAVs, according to the type of vehicles, utilize a compatibility matrix and each type of agent was assigned to the tasks that certain UAV can perform.

The simulation area is confined to an indoor experiment facility named KARPE (KAIST Arena with Real-time Positioning Environment), about 9m long and 5m wide. The normal velocity of each vehicle is about 0.1 m/s. At first one task was positioned in a space and it added one in a certain period. Simulations are held in three ways, the original CBBA, the Heuristic CBBA and the Entropy information CBBA. The global score, which is the sum of the total score of each vehicle, and paths, are compared with each other. The scores are altered according to the position and the number of tasks and agents. However with the result in a specific situation, a general tendency of each method can be evaluated.

Each CBBA method has the same independence variables such as the CBBA regeneration time period, number of popup tasks, and time intervals of new tasks generated. During the whole simulation, agents do not reach the task before the task has started. Therefore, in the case that the estimated agent arrival time is prior to the task start time, the agent lingers for a while and reaches the task on time. In the beginning, in three methods, agents are assigned to the same tasks while making the same bundles, because heuristic and entropy approaches cannot affect the initial condition of tasks. During the simulation, however, each method draws quite different paths and scores.

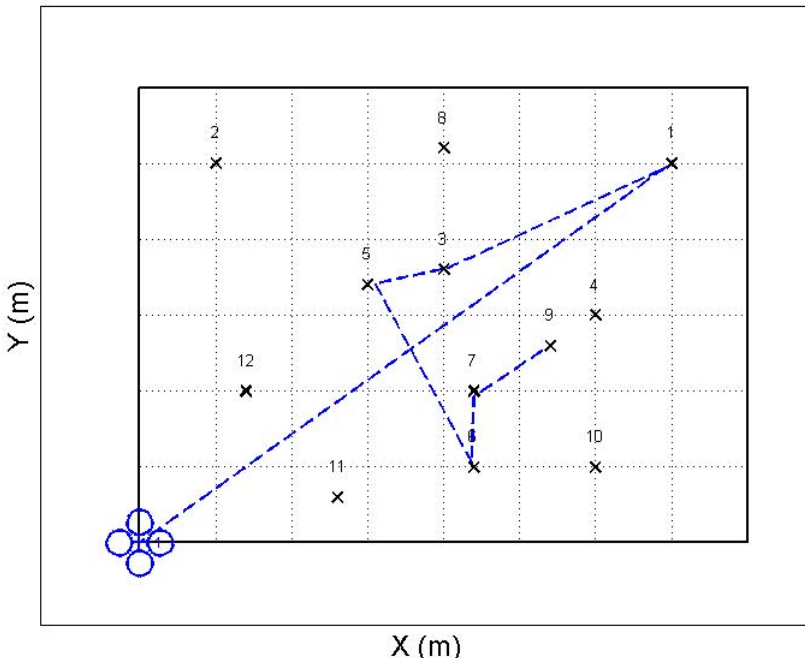


Fig. 3. Result of path in Original CBBA

In the original CBBA simulation, in every distinct step, CBBA is operated and assigns new bundles to the vehicles. And during the specific task, agents can change their routes to other tasks. However, when agents are assigned to the new task and proceeds toward it, the distance between the current task and the agent is shorter but the value of the task is unchanged. Consequently, the attractiveness of the task is increasing and before the closer task is generated, the agent follows the current task.

The main change in the Heuristic CBBA is that the value of the task is decreasing when the agent approaches the task, but still the current task has major influence over the vehicle. Consequently, the resulting path of the Heuristic method shows similar behavior to the original method. In spite of this characteristic, a difference of path can be found easily on the graph. Because the Heuristic method has similar paths but acquires the information during the path, the global score in the Heuristic method is greater than the original CBBA method.

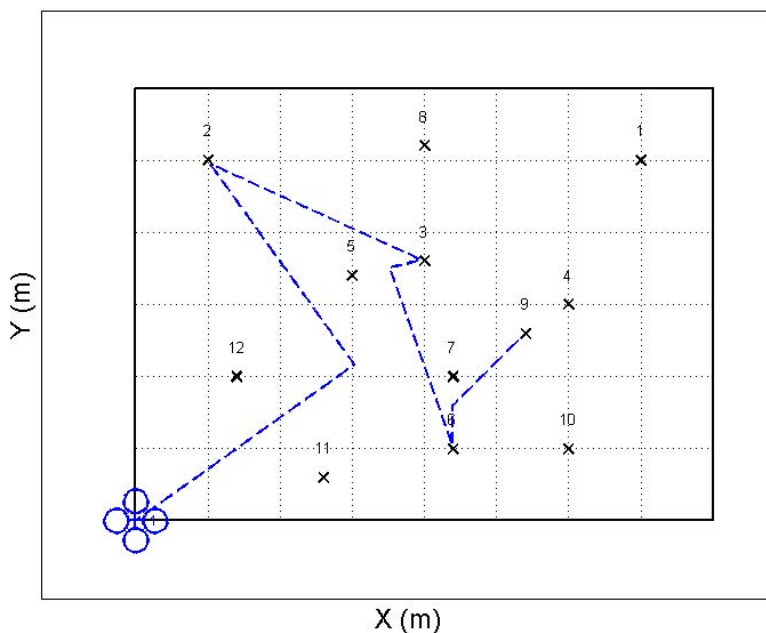


Fig. 4. Result of path in Heuristic CBBA

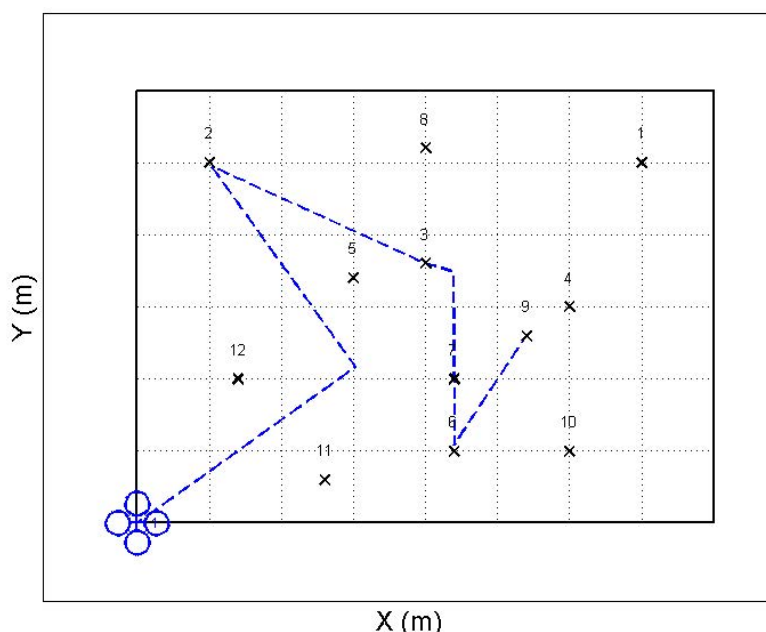


Fig. 5. Result of path in Entropy CBBA

Table 1. Global score of each information method

	Original CBBA	Heuristic CBBA	Entropy CBBA
Global Score	2184.5	2218.7	2570.7
Deviation	343.6	338.2	332.2

The Entropy method changes both the value and attractiveness of task nonlinearly. Therefore, the direction of the path is totally different with the original path, and can find assignment changes during the path. The simulation is operated in randomly task distributed environment and performed over 100 times and determine the mean and deviation value of global scores. The global score and deviation of these three methods are as follow:

Based on the score, it is hard to say which method is better than the others, because real sensor characteristics are not reflected in the simulations. The simulations represent the possibility of path changes when the gathered information through the path is considered with CBBA.

5 Conclusion

This article has presented approaches to efficiently incorporate information obtained *en Route* to the task location for decentralized task planning, specifically, in the consensus-based bundle algorithm framework. A linear heuristic and an entropy-based scheme are proposed to quantify the reward of partial execution of the task. Numerical simulations on multi-UAV task (re-)planning demonstrate that the proposed extensions provide higher overall mission performance. Future work includes performance evaluation in more structured/realistic scenarios.

References

1. Alighanbari, M., How, J.P.: An unbiased kalman consensus algorithm. In: American Control Conference, p. 6 (June 2006)
2. Alighanbari, M.: Task assignment algorithms for teams of uavs in dynamic environments. Master's thesis, Massachusetts Institute of Technology (2004)
3. Argyle, M., Casbeer, D.W., Beard, R.: A multi-team extension of the consensus-based bundle algorithm. In: Proceedings of the American Control Conference, pp. 5376–5381 (2011)
4. Beard, R.W., McLain, T.W.: Coordination variables, coordination functions, and cooperative-timing missions. Journal of Guidance, Control and Dynamics 28(1), 150–161 (2005)
5. Bellingham, J., Tillerson, M., Richards, A., How, J.P.: Multi-task allocation and path planning for cooperating UAVs. In: Cooperative Control: Models, Applications, and Algorithms, pp. 23–41. Springer (2003)
6. Bertsekas, D.P.: Auction algorithms for network flow problems: A tutorial introduction. Computational Optimization and Applications 1, 7–66 (1992), doi:10.1007/BF00247653
7. Bertsekas, D.P.: Auction algorithms auction algorithms. In: Floudas, C.A., Pardalos, P.M. (eds.) Encyclopedia of Optimization, pp. 73–77. Springer, US (2001)

8. Casbeer, D.W., Millet, P.T., Akella, M.R.: An extension of consensus-based auction algorithms for decentralized, time-constrained task assignment. In: Proceedings of the American Control Conference, pp. 6324–6329 (2010)
9. Cassandras, C.G., Li, W.: A receding horizon approach for solving some cooperative control problems. In: Proceedings of the 41st IEEE Conference on Decision and Control, vol. 4, pp. 3760–3765 (December 2002)
10. Castanon, D.A., Wu, C.: Distributed algorithms for dynamic reassignment. In: Proceedings of the 42nd IEEE Conference on Decision and Control, vol. 1, pp. 13–18 (December 2003)
11. Choi, H.L., Brunet, L., How, J.P.: Consensus-based decentralized auctions for robust task allocation. *IEEE Transactions on Robotics* 25(4), 912–926 (2009)
12. Choi, H.L., How, J.P.: Efficient targeting of sensor networks for large-scale systems. *IEEE Transactions on Control Systems Technology* (99), 1 (2011)
13. Cover, T.M., Thomas, J.A., Wiley, J., et al.: Elements of information theory, vol. 6. Wiley Online Library (1991)
14. Curtis, J.W., Murphey, R.: Simultaneous area search and task assignment for a team of cooperative agents. In: 2003 AIAA Guidance, Navigation, and Control Conference and Exhibit (2003)
15. Dias, M.B., Zlot, R., Kalra, N., Stentz, A.: Market-based multirobot coordination: A survey and analysis. *Proceedings of the IEEE* 94(7), 1257–1270 (2006)
16. Gerkey, B.P., Mataric, M.J.: Sold!: auction methods for multirobot coordination. *IEEE Transactions on Robotics and Automation* 18(5), 758–768 (2002)
17. Jin, Y., Minai, A.A., Polycarpou, M.M.: Cooperative real-time search and task allocation in uav teams. In: Proceedings of the 42nd IEEE Conference on Decision and Control, vol. 1, pp. 7–12 (December 2003)
18. Johnson, L., Choi, H.L., Ponda, S., How, J.P.: Allowing non-submodular score functions in distributed task allocation. In: IEEE Conference on Decision and Control, CDC (2012)
19. Le Pape, C.: A combination of centralized and distributed methods for multi-agent planning and scheduling. In: Proceedings of the 1990 IEEE International Conference on Robotics and Automation, vol. 1, pp. 488–493 (May 1990)
20. Lee, W.-S.: Cooperative guidance of multiple uavs for improved target tracking. PhD thesis, KAIST (2011)
21. Manyika, J., Durrant-Whyte, H.F.: Data fusion and sensor management: A decentralized information-theoretic approach (1994)
22. Moallemi, C.C., Van Roy, B.: Consensus propagation. *IEEE Transactions on Information Theory* 52(11), 4753–4766 (2006)
23. Olfati-Saber, R., Murray, R.M.: Consensus problems in networks of agents with switching topology and time-delays. *IEEE Transactions on Automatic Control* 49(9), 1520–1533 (2004)
24. Olshevsky, A., Tsitsiklis, J.N.: Convergence rates in distributed consensus and averaging. In: 2006 45th IEEE Conference on Decision and Control, pp. 3387–3392 (December 2006)
25. Ponda, S.S., Johnson, L.B., Choi, H.-L., How, J.P.: Distributed planning strategies to ensure network connectivity for dynamic heterogeneous teams. *IEEE Journal on Selected Areas in Communications* 30(5), 861–869 (2012)
26. Ren, W., Beard, R.W., Atkins, E.M.: Information consensus in multivehicle cooperative control. *IEEE Control Systems* 27(2), 71–82 (2007)
27. Ren, W., Beard, R.W., Kingston, D.B.: Multi-agent kalman consensus with relative uncertainty. In: Proceedings of the 2005 American Control Conference, vol. 3, pp. 1865–1870 (June 2005)
28. Satterly, M.T., Stubbs, L.C.D., Gilbert, M.G.D., Iler, M.C.L., Glen, C.K.B.: Intelligence preparation of the battlespace - an airman’s introduction. *Air Chronicles* 26 (1999)

29. Schumacher, C., Chandler, P.R., Rasmussen, S.R.: Task allocation for wide area search munitions. In: Proceedings of the 2002 American Control Conference, vol. 3, pp. 1917–1922 (2002)
30. Shima, T., Rasmussen, S.J., Chandler, P.: Uav team decision and control using efficient collaborative estimation. In: Proceedings of the 2005 American Control Conference, vol. 6, pp. 4107–4112 (June 2005)
31. Turra, D., Pollini, L., Innocenti, M.: Fast unmanned vehicles task allocation with moving targets. In: 43rd IEEE Conference on Decision and Control, CDC 2004, vol. 4, pp. 4280–4285 (December 2004)
32. Whitten, A.K., Choi, H.-L., Johnson, L.B., How, J.P.: Decentralized task allocation with coupled constraints in complex missions. In: Proceedings of the American Control Conference (2011)
33. Xu, L., Ozguner, U.: Battle management for unmanned aerial vehicles. In: Proceedings of the 42nd IEEE Conference on Decision and Control, vol. 4, pp. 3585–3590 (December 2003)

Improved CAMshift Based on Supervised Learning

Nur Ariffin Mohd Zin^{1,*}, Siti Norul Huda Sheikh Abdullah², and Azizi Abdullah²

¹ Faculty of Computer Science and Information Technology, Universiti Tun Hussein Onn Malaysia, 86400 Parit Raja, Malaysia
ariffin@uthm.edu.my

² Center for Artificial Intelligence Technology, Faculty of Information Science and Technology, Universiti Kebangsaan Malaysia, 43600 Bangi, Malaysia
{mimi, azizi}@ftsm.ukm.my

Abstract. CAMshift algorithm refers on back-projected distribution of target object's colour to locate the location of the target object in the subsequent frame. However, this mechanism becomes inaccurate when one or more foreign objects that share the same colour features with the target object are very close to one another, resulting these objects are in the same search window. Therefore, this study proposed the embedment of two binary classifiers trained by SVM into the existing CAMshift. These classifiers were modeled to verify the back-projected distribution under 4 types of representations and to distinguish target and non target objects. The aim is to maintain the search window to cover only the target object during tracking. Experiments were conducted to verify the performance of the classifier under three environments namely easy, adjacent and cluttered. Results have shown that the classifier has managed to classify true detection with up to 80%.

Keywords: CAMshift, Support Vector Machine, object tracking.

1 Introduction

Mean-shift algorithm [1] is a mode-seeking algorithm which is based on targeting the similarity distribution of colour histogram of the target in the next frame. Despite of its efficacy in tracing object, however, its implementation is solely based on static images, where it does not concern on updating the subsequent images while tailoring significant shape changes. Besides, it is insensitive in perceiving size deformation and colour. Driven by these disadvantages, Bradski proposed CAMshift algorithm [2] to address these issues. In his work, Bradski refined Fukunaga method by adapting continuously probability distribution computed in each frame, enabling it to dynamically adjust its parameter accordingly in a consecutive image sequence [3]. However, a study by [4] has stated that CAMshift algorithm is very dependent on the probability distribution of the target object's colour. Unfortunately, relying solely on colour distribution can lead to inaccuracy during tracking as there are certainties that the target object share the same colour with other objects. As for example, if two objects with same colour are located nearby, the search window will expand causing

* Corresponding author.

it to cover two objects instead of focusing only to the target object. Theoretically, the search window is constructed by referring to the center location of probability distribution, regardless how large the distribution is. On a situation when two objects are nearby, the area of back-projected probability distribution becomes larger which render the center location is made up from two distributions, causing two or more objects share the same search window. This issue is depicted in Figure 1. Therefore, this study proposed the embedment of two binary classifiers trained by SVM, namely back-projected classifier and target and non-target classifier. The back-projected classifier is used to discriminate between 4 types of back-projected representations of target object. While the target and non-target classifier is modelled to distinguish between target and non-target objects and finally construct a search window based on the highest probability value of sub-image that has the possibility to have the image of target object.

The rest of this paper is organized as follows. Section 2 provides a thoroughly explanation on CAMshift algorithm and Support Vector Machine. While the details of the proposed method is presented in Section 3. In section 4, experimental setup is discussed along with results obtained in section 5. Lastly, a concise conclusions and future works are detailed in Section 6.

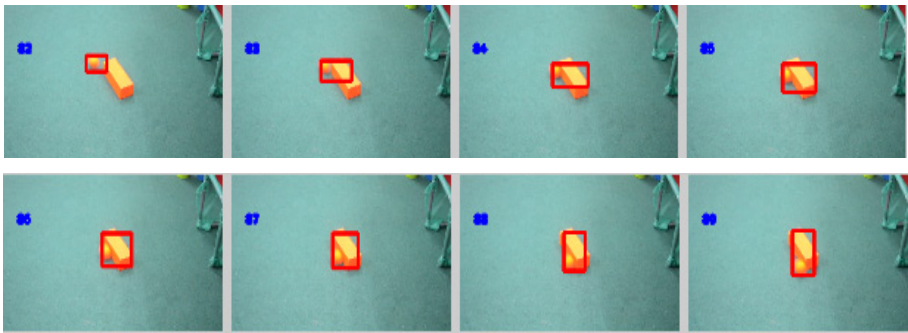


Fig. 1. Target object share the same search window with another object

2 Related Works

2.1 CAMshift Algorithm

CAMshift algorithm is a derivation from Mean-Shift algorithm with some modifications. It differs as Mean-Shift algorithm only concerns on single image while CAMshift algorithm is intended for tracking objects in video sequences [5]. This is explained as Mean-Shift algorithm searches within a fixed window size. On contrary, a dynamical search window is utilized in CAMshift where it adjusts its window size corresponding to each video frame, depending on the size of target object. The significance of its advent prevails when Bradski stressed out on four points that a potent tracking algorithm should be [2]; 1) Able to track moving object with the presence of noise, other faces, and hand movements; 2) It should run fast and works efficiently in real time while consuming very few system resources; 3) Able to serve

as part of a user interface that is in turn part of the computational tasks that a computer might routinely be expected to carry out; 4) Compatibility with variety of cameras and requires no calibration.

Inherently, CAMshift operates in 5 steps. 1) It starts with initialization of window. 2) Secondly, initial location of search window for target's probability distribution is constructed. In this case, the probability distributions correspond on the target's colour. 3) Thirdly, the back-projected probability distribution of target's colour is calculated within the ROI area. 4) Once done, Mean-shift algorithm is employed to obtain the new location (centroid) of target. The location is detected by computing spatial moments of zeroth, first and second [6]. Spatial moments of zeroth and first order are calculated to get the target's centroid. While, second order is computed to adjust the radius, height and width of the search window corresponding to the target object's new formation. These results are stored in memory. 5) Lastly, for the subsequent frame, the results from step 4 are used to center the search window and set the current value as initial value for the next frame. Step 3 is repeated until the mean location moves less than a preset threshold.

2.2 Support Vector Machine

Support Vector Machine (SVM) is a powerful supervised learning algorithm presented by Vapnik [7] which has been broadly used for classification and regression problems. It has gained prominence during years as it is robust, accurate, promising and classify effectively even with a small number of training data [8]. Originally, it was developed to classify two classes, or well known as a binary classifier. However, after years, its use has been extended to handle multiple classification tasks and regression problems. The exertion of SVM is huge, ranging from computer vision fields such as character and text recognition [9] to image classification on satellite [10]. Fundamentally, SVM can be divided into 4 types; 1) C-SVM for classification 2) Nu-SVM for classification 3) Epsilon-SVM for regression 4) Nu-SVM for regression.

Given an input training data constituting two vectors in an n dimensional space, SVM constructs a hyperplane that separates positive classes (+1) from negative classes (-1), while maximizing the distance between classes from the hyperplane. The hyperplane is constructed by calculating the boundaries of the training data. There will be many potential candidates of hyperplanes, but the one that will be chosen is one which exhibits the maximum margin between two classes. Points that situated along the boundaries are called support vectors, meanwhile, the line located at the middle of the margin is the separating hyperplane.

3 Proposed Method

This study proposed a combination of classical CAMshift algorithm and Support Vector Machine (SVM) as an addition, with the intention to improve the tracking accuracy. Two binary classifiers trained by SVM were embedded into classical CAMshift which are back-projected classifier and target and non target classifier. The back-projected classifier is intended to verify the representation of back-projected images while the target and non target classifier is used to discriminate between target object and non-target object respectively.

This study implemented an orange coloured ball as the target object. For the back-projected classifier, the verification involved authenticating four types of orange ball's back-projected representations as presented in Table 1. Based on the table, representation 1 and 2 were classified as positive class as CAMshift traces a single coloured target object efficiently. In cases where another object located apart, accurate tracking was achieved as the peak (center) of probability distribution is computed only within the search window, thus, omitting the other objects that occur beyond it. Figure 2(a) shows the back-projected representation of an image of a single ball. While Figure 2(b) shows another example representing a ball with the presence of another object with similar colour located apart.

However, CAMshift is discovered to be incapable in distinguishing between ball and another object of same colour in condition when they are located adjacently. Figure 3(b) depicts this issue. Therefore, the target and non-target classifier is assigned to distinguish them in a state where the ball and non-ball object will be classified as a separate object. In addition, this classifier is also responsible to discriminate single non-ball object, particularly at times when the target object is fully occluded. The best example is shown in Figure 3(a). These two types of representations were classified as negative class.

Table 1. Back-projected representations of target object's colour

#	Back-projected images representations
1	Single orange coloured ball
2	Single orange coloured ball with presence of other non-ball objects apart
3	Non-ball objects
4	Single orange coloured ball adjacent with other non-ball objects

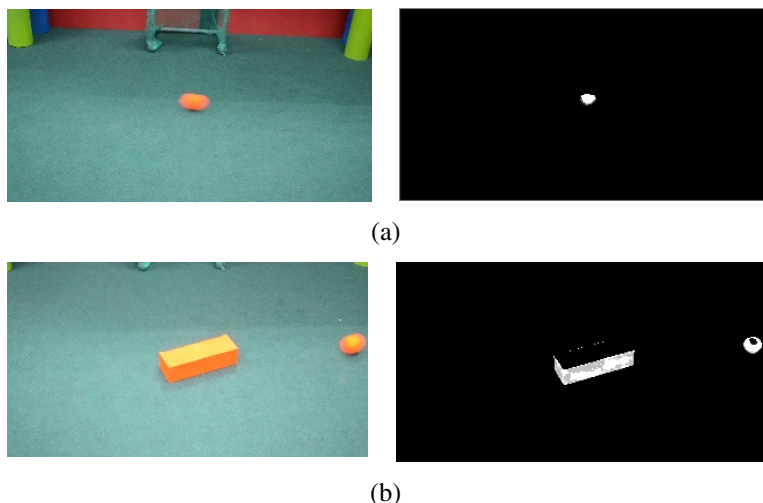


Fig. 2. (a) single ball (b) single ball with the presence of another non-ball object

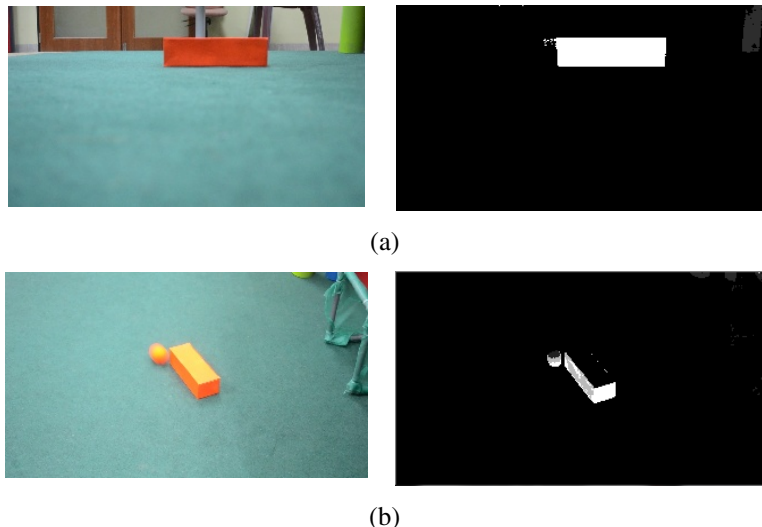


Fig. 3. (a) non ball object (b) ball and another non-ball object nearby

Figure 4 shows processes of the proposed method. At the beginning, images are captured using a video camera and arranged in a sequence of jpg files. Each file is formatted in RGB colour space with the size of 320×180 pixels (window size). During initialization of the first image, a search window or alternatively referred to as Region of Interest (ROI) is manually constructed that spans the region of the target object (orange ball). Then, the center location of search window (x, y) is computed. In the meantime, the RGB colour space is converted into HSV colour space. However, only Hue is selected, leaving Saturation (greyness) and Value (brightness) behind. In contrast with RGB, Hue facilitates colour representation by denoting single number for each colour. This is to alleviate the process of summing every colour for each pixel during colour histogram computation. Then, colour histogram within the search window is computed to determine the maximum colour distribution based on Hue values. Consequently, a colour histogram model is constructed. This model acts as a lookup table for reference of Hue values within search window on the subsequent images.

On the following images, by referencing to the distribution of Hue values, histogram back-projection technique is employed to rescale the maximum colour distribution (target object's colour) into a new value of 255, while other colours that do not correspond to the target object's colour will be regarded as 0. The next process is to verify the back-projected representation of target object by back-projected classifier trained by four types of representations as described in Table 1. The one that predicted as match to positive samples will be resumed to the tracking process by using spatial moments [6], while the one that indicates negative samples will be evaluated by target and non-target classifier. By this mean, exhaustive scan is performed through every sub-images of 40×30 pixels in 320×180 pixels image. The

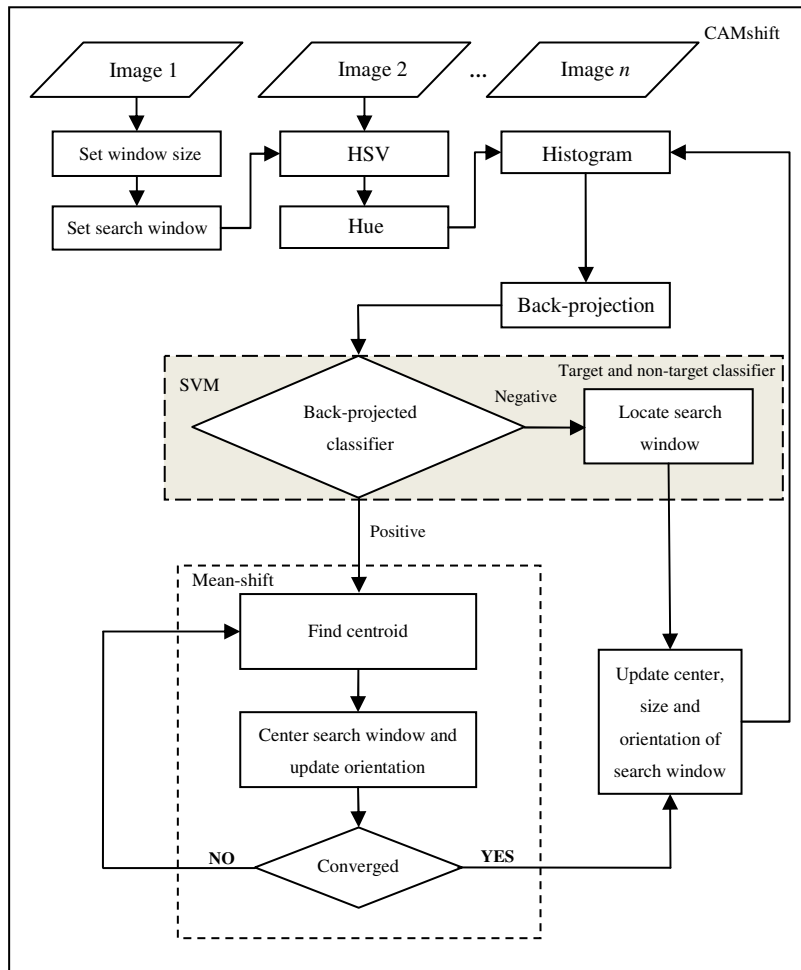


Fig. 4. The process of proposed method

scanning process is done by initializing a search window of 40×30 pixels. This search window is shifted incrementally both horizontally (x axis) and vertically (y axis). At first, the search window moves horizontally from position $x = 0$, until it reaches a threshold value. After completion, it will run the same process but with one increment added to y value. This process will be repeated until the value of y reaches a threshold value. The maximum threshold of (x,y) is set to $(280,150)$ respectively. These figures were opted to correspond the size of scanning search window during the movement along x and y axis in order to avoid over scanning. Each of the sub-image is predicted by the target and non-target classifier in order to verify if it is instance of a ball. The prediction resultant is the weight value ranging from 0 to 1 where 1 represents the highest possibility of a ball region. The x and y value of sub-image that represents the highest value of weight is stored in memory. Later, this value will be

chosen as reference point during the search window construction. By default, the search window is constructed 40×30 pixels in size, however, its size will be adjusted according to a search window that has been manually constructed by user during the initialization of ROI. If the size of search window during initialization is smaller than 40×30 pixels, the current search window is constructed 10% smaller while construction of 10% bigger takes place when the initialized search window is bigger than 40×30 pixels. The new center location and size of the current search window is updated for search window initialization on the next image. The pseudocode of this process is presented in Figure 5.

```

Input: Search window, s
Output: New search window, n
1. initialize search window, s
2. initialize probability value, p=0
3. initialize xp,yp
4. initialize percentage factor, f = 0.1
5. set s width, ws = 40, height hs = 30
6. start s at point (x,y) = s(0,0)
7. for y≤150 do
8.         for x≤280 do
9.                 svm predict p(s(x,y))
10.                if p(s(x,y)) > p then
11.                    p = p(s(x,y))
12.                    set xp,yp = x,y
13.                end if
14.                x=x+1
15.            end for
16.        y=y+1
17.    end for
18. if manually initialized search window size is lesser than
40 × 30 then
19.         set n width,wn = 40-(40×f), hn = 30-(30×f)
20.         draw rectangle of width xp+ wn,yp+ hn
21. end if
22. if manually initialized search window size is larger than
40 × 30 then
23.         set n width,wn = 40+(40×f), hn = 30+(30×f)
24.         draw rectangle of width xp+ wn,yp+ hn
25. end if

```

Fig. 5. Search window construction pseudocode

4 Experimental Setup

Experiments were conducted to test the performance of both classifiers. Training datasets contain of 1799 back-projected images with the size of 320×180 pixels each were used to train the back-projected classifier. All of these images were taken at different views and angles to give adaption for a dynamic environment. While target and non-target classifier was trained with 200 back-projected images of single orange coloured ball and another 200 of non-ball objects. To ensure the optimum classifier is constructed, the need of scaled datasets is crucial. Therefore, the training datasets were scaled between 0 and 1 prior training.

C-SVM was chosen as the SVM type and Radial Basis Function (RBF) was employed as kernel function to map the training data into feature space. As C-SVM requires parameter C and gamma, a cross validation process was done using existing scaled training datasets. As a result, the back-projected classifier managed to obtain C and gamma of 512 and 0.0001220703125 respectively. While for the target and non-target classifier, the C and gamma obtained was 128 and 0.00048828125 respectively. These parameters were then used during training the classifiers. In addition, both classifiers managed to get 92.62% and 93.3846% of accuracy tested on the training datasets.

The experiments were carried out by using testing data that constitutes 40% of the whole datasets under three cases namely easy, adjacent and cluttered. Each case contains 15 experiments. Every experiment holds images of the ball moving from one point to another point captured at different angles. These images were arranged in a sequence with 320×180 pixels in size each. As for the first case which is easy environment, the movement of the ball was visible and not interrupted or occluded by any object(s). Figure 6 depicts the scenario for the first case. The second case (adjacent) represents the ball was next to another object with same colour. In this case, there were also situations that the ball was fully occluded by any other object. Figure 7 illustrates the scenario for second case. Meanwhile, third case (cluttered) shares the same condition with second case but with the presence of more than one object, either sharing same colour attribute or maintain differently. This kind of state is best described in Figure 8.



Fig. 6. Example of easy case scenario



Fig. 7. Example of adjacent case scenario

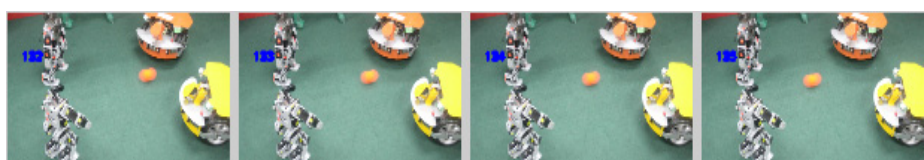


Fig. 8. Example of cluttered case scenario

5 Results

As for easy case, both methods managed to infer result by 100% of accuracy. In this case, it was proven that both methods performed very well on tracking a single ball with single colour. Figure 9(a) and 9(b) shows the image sequences showing the search window accurately covering the ball in every image.

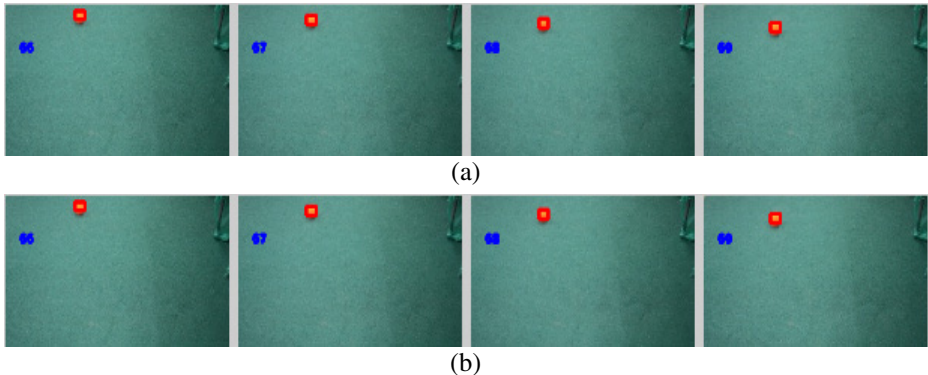


Fig. 9. Tracking using (a) classical CAMshift (b) proposed method for easy case

Experiment for adjacent case showing that the classical CAMshift managed to indicate accuracy by 51.96% out of 460 images while the proposed method managed to yield accuracy by 28.04% higher than classical CAMshift. Figure 10(a) shows the construction of search window in image sequence by adopting classical CAMshift. By observing on the images sequence, the search window became larger when the ball was nearer to the box, covering ball and box at the same time. This is explained as the box shared the same colour with the ball causing the probability distribution area was made up from two objects. As the ball moved, the search window lagged and eventually shifted to the box. Contrarily, by implementing the proposed method, with true prediction, the search window was constructed with only covering the ball area as shown in Figure 10(b).

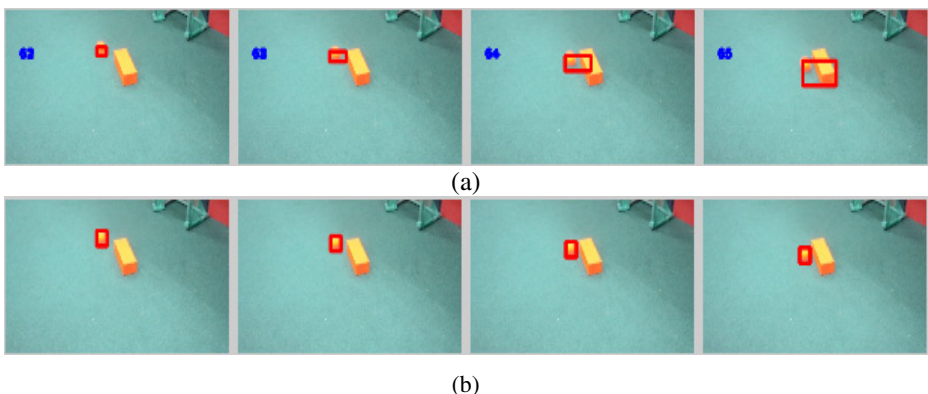


Fig. 10. Tracking using (a) classical CAMshift (b) proposed method for adjacent case

For cluttered case, the proposed method yielded 85.47% of accuracy while classical CAMshift resulted at 60.33% accuracy out of 358 images. As seen in Figure 11(a), the ball was fully occluded as it came to sequence number 2, causing the search window lagged in the next image sequence. As opposed to classical CAMshift, the proposed method was able to locate and construct a search window that covering the ball area after fully occluded by another object as shown in Figure 11(b).

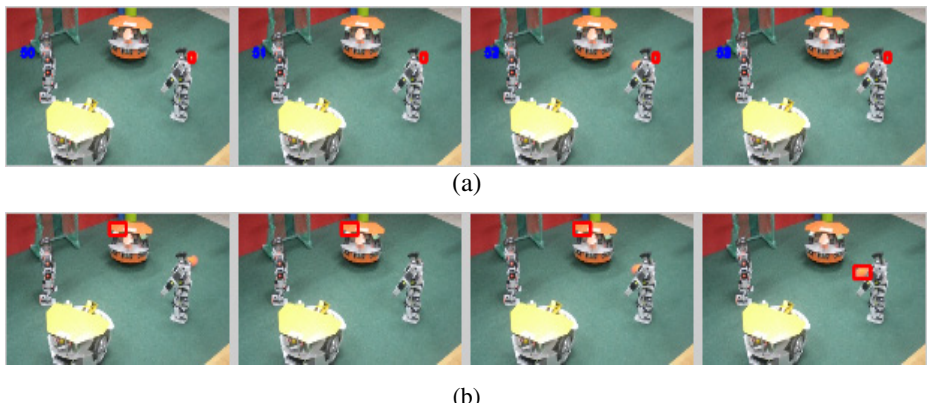


Fig. 11. Tracking using (a) classical CAMshift (b) proposed method for cluttered case

6 Conclusions and Future Works

This study proposed the embedment of two SVM classifiers into classical CAMshift. The back-projected classifier is served to learn a set of back-projected images that contains the orange coloured ball under 4 types of representations. The target and non-target classifier is developed to discriminate between a single orange coloured ball object with other non-ball objects. During tracking, if the back-projected image is predicted as a positive case, the search window is constructed traditionally by calculating zeroth, first and second order moments. However, if the back-projected image is predicted as a negative case, the search window is constructed by selecting the highest probability of sub-image that contains a single orange coloured ball classified by the target and non-target classifier. The performance of both classifiers was tested under three cases namely easy, adjacent and cluttered. From the experiments performed, the proposed method has significantly improved the tracking accuracy by 100% for easy case, 80% for adjacent case, 85.47% for cluttered case. The next possible future work would be reducing the complexity during exhaustive scanning by assigning a dynamic search region.

Acknowledgements. This project research was fully funded by FRGS/1/2012/SG05/UKM/02/8 project entitled “Generic Object Localization Algorithm For Image Segmentation”, PTS-2011-047 entitled “Empowering Robot Soccer Teaching and Learning in FTSM” and Centre for Research and Instrumentation (CRIM) PIP number UKM-UP-PIP-2012. It is part of robot soccer research development in National University of Malaysia.

References

1. Fukunaga, K., Hostetler, L.D.: The Estimation of the Gradient of a Density Function, with Applications in Pattern Recognition. *IEEE Transactions on Information Theory* 21(1), 32–40 (1975)
2. Bradski, G.R.: Computer Vision Face Tracking for Use in Perceptual User Interface. *Intel Technology Journal* 2(2), 12–21 (1998)
3. Huang, S., Hong, J.: Moving Object Tracking System Based on CAMshift and Kalman Filter. In: International Conference on Consumer Electronics, Communications and Networks, pp. 1423–1426 (2011)
4. Exner, D., Bruns, E., Kurz, D., Grundhoefer, A., Bimber, O.: Fast and Robust CAMshift Tracking. In: IEEE International Workshop on Computer Vision for Computer Games, pp. 9–16 (2010)
5. Nicole, M.A.: A Comparison of Mean-shift Tracking Methods. In: 12th Central European Seminar on Computer Graphics, pp. 197–204 (2008)
6. Horn, B.K.P.: Robot vision. MIT Press, Cambridge (1986)
7. Vapnik, V.: The Nature of Statistical Learning Theory. Springer, Berlin (1995)
8. Anthony, G., Gregg, H., Tshilidzi, M.: Image Classification using SVMs: One-Against-One vs One-Against-All. In: Proceedings of the 28th Asian Conference on Remote Sensing (2007)
9. Joachims, T.: Text Categorization with Support Vector Machines - Learning with Many Relevant Features. In: Nédellec, C., Rouveiro, C. (eds.) ECML 1998. LNCS, vol. 1398, pp. 137–142. Springer, Heidelberg (1998)
10. Huang, C., Davis, L.S., Townshed, J.R.G.: An Assessment of Support Vector Machines for Land Rover Classification. *International Journal of Remote Sensing* 23, 725–749 (2002)

Development of a Fall Detection System with Microsoft Kinect

Christopher Kawatsu, Jiaxing Li, and C.J. Chung

Department of Mathematics and Computer Science, Lawrence Technological University,
21000 West Ten Mile Road, Southfield, MI, 48075-1058, USA
{ckawatsu,jli,cchung}@ltu.edu

Abstract. Falls are the leading cause of injury and death among older adults in the US. Computer vision systems offer a promising way of detecting falls. The present paper examines a fall detection and reporting system using the Microsoft Kinect sensor. Two algorithms for detecting falls are introduced. The first uses only a single frame to determine if a fall has occurred. The second uses time series data and can distinguish between falls and slowly lying down on the floor. In addition to detecting falls, the system offers several options for reporting. Reports can be sent as emails or text messages and can include pictures during and after the fall. A voice recognition system can be used to cancel false reports.

1 Introduction

According to the Centers for Disease Control and Prevention [2], falls are the leading cause of injury and death for older adults, with one out of three adults 65 years and older falling each year. As a result, systems that detect falls have become a research topic of interest in recent years.

A variety of different approaches have been used to detect falls. Wearable sensors that detect acceleration can be used to detect falls. This approach is examined by Noury et al. [4]. These systems have the drawback that the user must remember to wear the sensors. Floor mounted sensors can also be used. Alwan et al. [1] use floor mounted vibration sensors to detect falls. This system eliminates the need for the user to wear a sensor; however, these systems are often expensive and are complex to install.

The present paper focuses on computer vision based systems. Fall detection systems using a variety of vision systems have been developed in recent years. Khan and Habib [3] developed a fall detection system which uses a single camera to detect falls. The system uses background subtraction to isolate the location of a person in the image. Motion gradient data is then used to determine if a fall has occurred. The drawback of this system is the motion gradient of a fall very near the camera will be much higher than that of a fall far from the camera. In order to solve this problem, the 3D rather than 2D location of the person must be known.

In the present paper an affordable but reliable way to develop fall detection systems using the Microsoft Kinect sensor is introduced. Rougier et al. [5] have developed a similar system which also uses the Microsoft Kinect sensor. This system also implements both a position based and velocity based algorithm for detecting falls. However,

the present paper uses the locations of 21 joints during the computation while Rougier et al. use only the centroid location. Additionally, the present paper provides methods for reporting falls and reducing false positive reports.

The paper is organized as follows. In Section 2 basic information about the Kinect sensor and the accompanying Standard Development Kit (SDK) is provided. Section 3 discusses the two algorithms used to detect falls. The voice recognition system used to validate falls is described in Section 4. Several methods of reporting falls are introduced in Section 5.

2 Kinect Overview

The Kinect contains three types of sensors: a standard camera, an IR camera, and a microphone array. The IR camera detects points projected by a laser and automatically converts them into a depth map. The cameras are calibrated so that the depth map pixels correspond to the pixels in the standard camera images.

The Kinect SDK is a free software package which provides a variety of useful tools. The software will automatically detect the 3D location of 21 joints for two people. No markers are required for the software to detect joint locations. Information about the algorithm used by this software is provided in [6]. In addition to joint locations, the Kinect SDK also detects the location of the floor plane.

3 Fall Detection Algorithms

We developed two algorithms to detect falls using the Kinect SDK. The first algorithm uses only joint position data. This algorithm calculates the distance from the floor to each joint. If the maximum distance is less than some threshold value, a fall is detected. The second algorithm calculates the velocity of each joint in the direction normal to the floor plane. The velocities are averaged over all joints and many frames. If this average velocity is lower (downward velocities are defined as negative) than some threshold value, a fall is detected.

3.1 Position Algorithm

The Kinect SDK provides data in frames at a rate of 30 frames per second. Each frame is processed by the fall detection algorithm to determine if the state is fall or not fall. For each joint on a skeleton 4 pieces of data are acquired from the Kinect SDK: the x, y, and z coordinates of the joint and the tracking information for the joint. Joints can be tracked, not tracked, or inferred. The x, y, and z coordinates are Cartesian coordinates in meters with the Kinect sensor located at the origin. In addition to joint information, the equation of the floor plane (in the same coordinate system as the joints) is acquired. The Kinect SDK provides the plane information in the form of the A , B , C , and D parameters from Equation (1).

$$Ax + By + Cz + D = 0 \quad (1)$$

In Cartesian space, the length of a vector normal to a plane ending at a point (x, y, z) can be calculated using [7]

$$d = \frac{Ax + By + Cz + D}{\sqrt{A^2 + B^2 + C^2}}. \quad (2)$$

Using this relation the normal distance from the floor to each joint is obtained.

The fall detection algorithm considers the distances only for joints which are tracked by the Kinect. If every tracked joint has a normal distance less than some threshold the algorithm sets the state to fall, otherwise not fall.

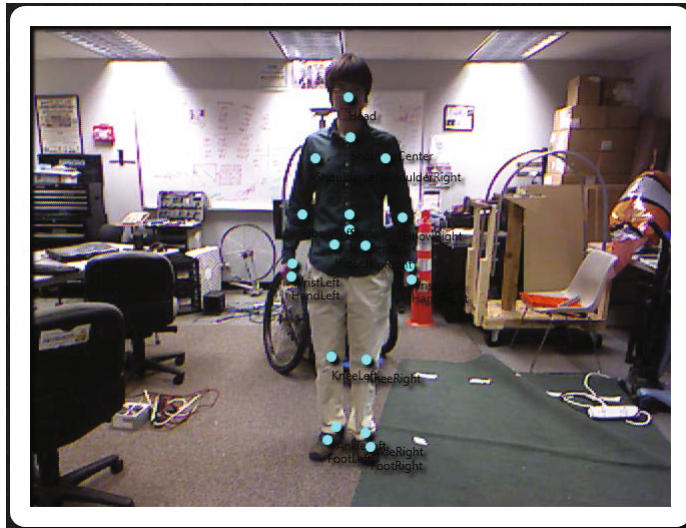


Fig. 1. Maximum joint distance from floor plane is above the threshold

3.2 Velocity Algorithm

The Kinect provides approximately 30 frames per second of data. From each frame we use the timestamp (in milliseconds) and the 3D Cartesian coordinate location of each joint. We also use the angle of the Kinect sensor which is assumed to not change throughout any calculations. Our algorithm also assumes that the Kinect is placed on a level surface.

Instead of using the floor plane equation provided by the Kinect (this is not always detected, particularly on stairs) we calculate our own floor plane. If we assume the Kinect is on a level surface then we can calculate the floor plane equation from the angle of the sensor as follows:

$$Ax + By + Cz + D = 0$$

where

$$\begin{aligned} A &= 0, \\ B &= \cos \theta, \\ C &= \sin \theta, \\ D &= 3. \end{aligned}$$



Fig. 2. Maximum joint distance from floor plane is below the threshold

A , B , and C are simply the vector normal to the floor and D shifts the floor plane 3 meters below the Kinect. The distance from the floor plane can then be calculated using:

$$d = \frac{Ax + By + Cz + D}{\sqrt{A^2 + B^2 + C^2}}.$$

For frame i and $i + 1$ the velocity for a particular joint normal to the floor is then:

$$v_i = 1000 \frac{d_{i+1} - d_i}{t_{i+1} - t_i}$$

Where t is the timestamp in milliseconds. The factor of 1000 allows us to work in more convenient units of meters per second instead of meters per millisecond. This velocity is averaged over N frames:

$$v_{avg} = \frac{1000}{N-1} \sum_{i=1}^{N-1} \frac{d_{i+1} - d_i}{t_{i+1} - t_i}.$$

If a joint is not tracked for frame i or $i + 1$, the velocity is not used and the value of N for the joint decreased. Finally we take v_{avg} from all 20 joints and average again:

$$v_{jointavg} = \frac{1}{20} \sum_{j=1}^{20} v_{avg,j}.$$

If $v_{jointavg}$ is less than -1 meters per second the algorithm detects a fall.

This algorithm has problems detecting falls in a few cases. First, if someone jumps in front of the camera it is detected as a fall. This occurs because the speed normal to

the floor is very high and the duration of the downward portion of the jump is about the same as a fall. Second, if a person walks out of the Kinect's vision range this is occasionally detected as a fall. The reason for this is because as the person walks off the camera, all of the tracked joints are shifted to the part of the person that is still visible to the Kinect's camera. For example, if only the lower half of a leg is visible to the Kinect, all 20 joints will be tracked within the area of the lower leg. This sometimes causes a very high downward velocity to be detected by the Kinect. Lastly, this algorithm does not perform very well on stairs. In order to detect falls on stairs the threshold velocity has to be lowered. Additionally, cases where someone falls forward when walking up stairs are very difficult to detect.

The first problem is not really possible to fix aside from using a different algorithm; however, it is unlikely people using this system will be jumping in front of the camera. For the second case we can eliminate most of the false reports by ignoring cases where all of the joints are very close to the left or right side of the camera's vision. Detecting falls on stairs will most likely require a different algorithm. For example, we could measure the angle of a person's posture while walking on stairs. If this angle deviates greatly from the "up" direction we detect a fall.

4 Validation

Voice recognition is used to reduce false positive reports. After a fall is detected, the event is validated using the Kinect microphone array and a voice recognition system. Once a fall is detected, a new thread is created to ask the user if the require assistance. The thread waits for a response of yes or no. In the case of a yes, a fall is reported. In the case of a no, the report is canceled. A timer is also set. If the timer ends without receiving a yes or no response, a fall is reported.

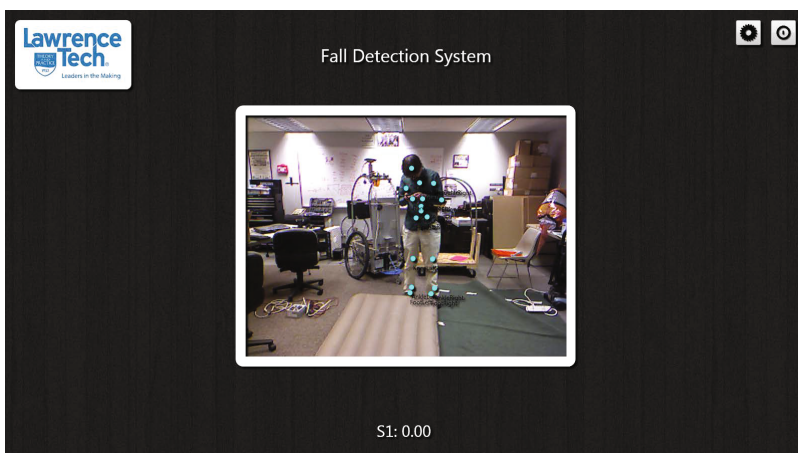


Fig. 3. The GUI when no fall has occurred (white border on image)

5 Fall Reporting

Falls are reported through email. After the algorithm detects a fall, pictures are taken 15 and 60 frames after the event. These pictures are sent to a user defined email address after passing the validation component. These pictures can also be sent to phones using Multimedia Messaging Service (MMS). Most mobile phone providers offer a service which forwards emails with attached pictures as MMS messages. This method is free but requires the user to know the form of the email address expected by the mobile phone provider. More robust services that only require a phone number are available; however these services are not free and charge for each message sent.



Fig. 4. The GUI after a fall has been detected and validated (red border on image)

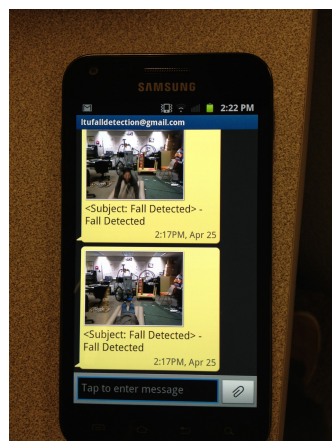


Fig. 5. MMS messages sent by the system

6 Experimental Results

The system has been tested quite extensively in our lab. All of the cases we observed where the system failed to detect or incorrectly reported a fall have been described in Section 3. One major concern is that a fall simulated in our lab may be significantly different from an actual fall. This could have a large impact on the velocity based algorithm. For example, if actual falls have a shorter duration or lower velocity than those recorded in our lab, the number of frames and threshold velocity would have to be adjusted.



Fig. 6. Picture taken during the fall



Fig. 7. Picture taken after the fall

7 Concluding Remarks

The fall detection system provides an affordable way to detect and report falls. The system has also been tested with people using canes, crutches, and walkers and works reliably. The software is available for download from <http://www.robofest.net/FDR>.

References

1. Alwan, M., Rajendran, P., Kell, S., Mack, D., Dalal, S., Wolfe, M., Felder, R.: A smart and passive floor-vibration based fall detector for elderly. In: 2nd Information and Communication Technologies, vol. 1, pp. 1003–1007 (2006)
2. Centers for Disease Control and Prevention. Falls Among Older Adults: An Overview, <http://www.cdc.gov/HomeandRecreationalSafety/Falls/adultfalls.html>
3. Khan, M.J., Habib, H.A.: Video Analytic for Fall Detection from Shape Features and Motion Gradients. In: Proceedings of the World Congress on Engineering and Computer Science, WCECS 2009, San Francisco, USA, October 20-22, vol. II (2009)
4. Noury, N., Fleury, A., Rumeau, P., Bourke, A., Laighin, G., Rialle, V., Lundy, J.: Fall detection - principles and methods. In: 29th Annual International Conference of the IEEE Engineering in Medicine and Biology Society, pp. 1663–1666 (2007)
5. Rougier, C., Auvinet, E., Rousseau, J., Mignotte, M., Meunier, J.: Fall detection from depth map video sequences. In: Abdulrazak, B., Giroux, S., Bouchard, B., Pigot, H., Mokhtari, M. (eds.) ICOST 2011. LNCS, vol. 6719, pp. 121–128. Springer, Heidelberg (2011)
6. Shotton, J., Fitzgibbon, A., Cook, M., Sharp, T., Finocchio, M., Moore, R., Kipman, A., Blake, A.: Real-time human pose recognition in parts from single depth images. In: Proceedings of the 2011 IEEE Conference on Computer Vision and Pattern Recognition, CVPR 2011, pp. 1297–1304. IEEE Computer Society, Washington, DC (2011)
7. Weisstein, E.W.: Point-Plane Distance. From MathWorld—A Wolfram Web Resource, <http://mathworld.wolfram.com/Point-PlaneDistance.html>

Strategic Decision-Making of MASTER Software Agent in Terms of the Behavior of Mobile Robot Agents

Mikulas Hajduk and Marek Sukop

Technical University of Kosice, Faculty of Mechanical Engineering,
Department of Production Systems and Robotics, B. Nemcovej 32, 042 00 Kosice, Slovakia
`{mikulas.hajduk,marek.sukop}@tuke.sk`

Abstract. This paper describes the strategic decision making of the master software agent in terms of behavior of robotic agents of mobile robot soccer team FME TUKE Robotics. The proposed approach is designed for category 5 vs. 5 MiroSot. The description is based on a hierarchy of multi-agent system with six agents. The proposed structure has one completely software master agent with inferior mobile robotic agents (players). In the first part of the paper there is a description of hardware and software modules and the overall strategy of system behavior. The body of paper describes process of decision making and strategy of master agent based on more information about the real situation on the field. Conclusion of the article gives an example of an attack strategy.

Keywords: mobile robot, agent, module.

1 Introduction

Control of a group of mobile robots is a complex issue that addresses many scientific institutions and universities around the world. There are many approaches to addressing this area and one of them is a multi agent approach with application to robot soccer. Robot soccer represents a very good opportunity for the development and application of artificial intelligence (AI) and for strategy development for cooperating mobile robots. The chosen strategy is based on the instantaneous real situation in the playfield and functions are assigned to the individual players accordingly [1, 5]. The autonomy of the robots consists in the fact that following the assigning of functions each player then makes his own decisions about his actions within the assigned function [1]. When deciding about the strategic arrangement, the system as well as each robot must see to it that none of the FIRA rules for the MiroSot league are violated [7].

2 Hardware and Software Modules and their Functions

Addressing the management of the mobile robots in robot soccer is based on the use of multiagent approach. Our proposed multi-agent system has a master agent and robot agents. Each robot is an agent, which integrates in itself:

- Elementary agent (the intelligence – software)
- Robot player (the body, hardware and software)

Comprehensive view of the software and hardware modules and their relationship to the agent system is proposed in fig. 1, where blocks with rounded edges represent hardware modules and blocks with sharp edges are software modules.

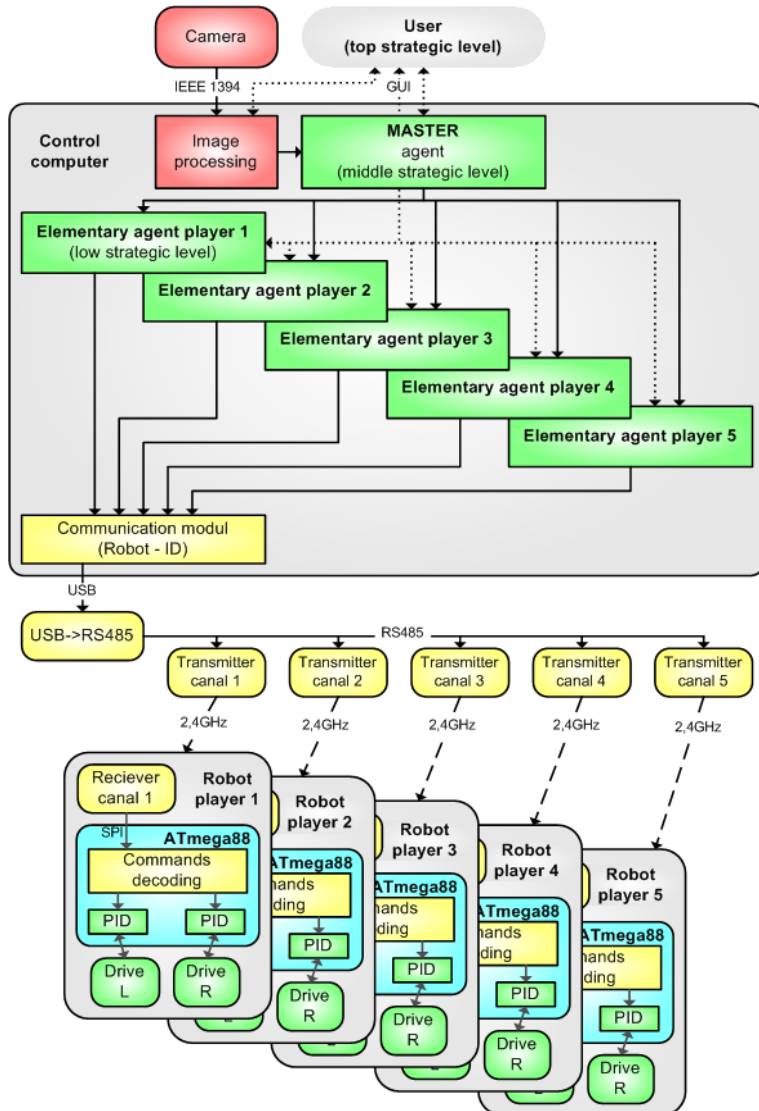


Fig. 1. Comprehensive view of the software and hardware modules

Control cycle begins with the camera modules. The image is transmitted using an IEEE 1394 (FireWire) to the image processing software module. The results of image processing are parameters of positions of the robots and the ball. All these parameters

are stored in memory (so-called sliding buffer) size of the last 67 frames. This memory is then available to the master agent and to elementary players' agents. Master agent uses this memory for estimating motion of the ball and opponent players and then selects one of pre-defined strategic actions. According to the chosen strategic actions MASTER agent selects five elementary players' agents who were in the development phase of an overall strategy assigned to the action. Subsequently, the agent assigns robots to elementary agents (ID). Master Agent decides to select strategic actions and elementary selection of players selected by the user basic strategy. Elementary players' agents have all the necessary information about the position of the ball and all robots on the field. Agents' players plan their moves from this information in order to get the ball into the opponent's gate, respectively to prevent an opponent scoring. After planning the moves, agents send the information to communication software module. After adjusting the data by pairing information with players, there is the data transfer via USB port to a hardware interface of the module for transforming the interface to RS485. Each robot has got its own transmitter set the channel used to transmit information wirelessly. The data is then sent parallel to each robot player cyclically, until new data is recorded. Robot player will change its parameters to the desired speed as quickly as possible after capturing the transmitted data packets. This will change the scene to the next recorded image.

3 Agents' Tasks and their Options

Before proposing a hierarchy of MAS there has been considered the fact that the basic strategy of behavior of robots is done by user who selects the control program. He can choose from predefined defensive or offensive strategies. The possibility of influencing the positional layout of the players is great but the choices of strategies are limited by the number of predefined strategies. The choice of the strategies is the choice of the highest level and can be carried out only during a stoppage in play or pause. The middle level possesses the strategic behavior of the system during the game as a dynamic response to the situation. The behavior of the system in the game is influenced by the chosen strategy at the highest level. The lowest level possesses the strategic behavior of each team member (robot-player). Individual strategy levels with its extent and influence towards strategic behavior of players is depicted in fig. 2.

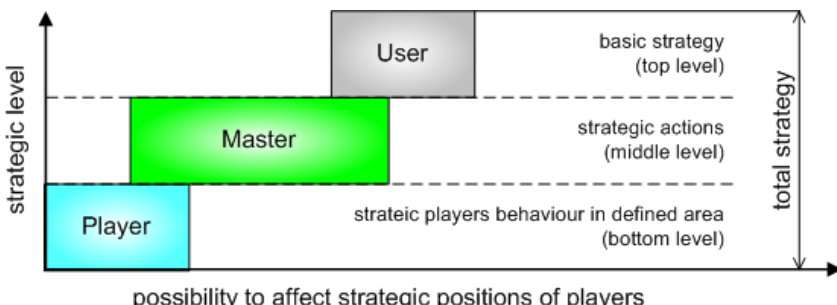


Fig. 2. Graphical representation of the possibility to affect strategic dispositions on the playing field

4 The Strategies Implemented in the Control Program

GUI of control program has a defined area in the main window fig. 3, in which the user sets the basic strategy at the highest level through a combination of the four selection menus. After the start of the game by the user, control program does the required redefinition of the parameters of an agent selected by the MASTER parameter. Ultimately, the behavior of the master agent during the game will depend on these settings.



Fig. 3. Strategy settings field in the main window of GUI of control program

All the basic strategies are derived from two or three cooperating attackers. The user has a choice of 24 combinations. The following strategic behavior of the middle level is dependent on the master agent's decision. The behavior at the lowest level is dependent on decisions of players. Graphical display of Figure 2 shows that the players have the opportunity to influence the overall strategy. This option is limited by movements of the player in its field of action.

5 Master Agent and Its Influence to Game Strategy

The possibility of user intervention and changes of strategies is limited to the referee interruption of the game. MASTER, unlike the user, decides on the strategic action after each processed image in the game. Decisions are influenced by adjusting the

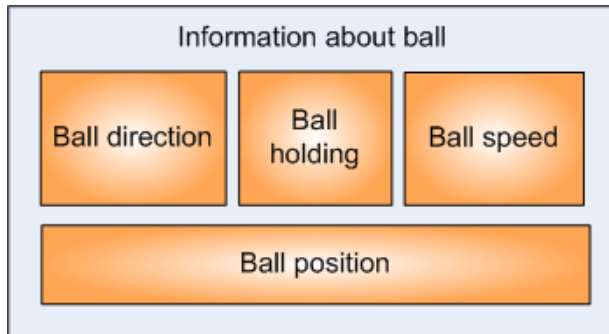


Fig. 4. Block scheme of the main parameters influencing master's deciding on strategy actions

basic strategy of the user and the immediate situation on the field. The immediate situation is based primarily on speed and positional parameters of the ball (Fig. 4). Positional parameters are the absolute position of the ball on the pitch and the relative position of the ball, related to the robot on the field.

Other parameters of a lesser extent affect the master's decisions depend on the master agent estimate of the situation in the very near future. The agent implements predicting near future which is maximum 1 second ahead. Eg.: Precondition of ball position if the ball is loose is performed by using a linear regression line, where in such a short period of time it does not count with the slowing down of movement. Agent uses the same rule of the reflection angle is the angle of impact to the sidewalls of the board.

Agent works with selected hysteresis widths due to stable condition monitoring which are defined in decision rules at the time of development of control software.

Master makes decisions according to information about:

- Ball location
- Players location and mutual positioning ($ID_n[x,y]$, φ_n) and speed parameters (v_n , ω_n), where $n=1,2,3,4,5$
- Opponent players position $Rs_n [x_{opst},y_{opst}]$, where $n=1,2,3,4,5$

Agent decides on immediate strategic action for the user selected basic strategy and carries out the selection of the five strategic actions shown in Figure 5. The strategic actions, during the games, overlap each other in a subsequent order and there should never be skipped any of the action unless there is defective vision and image processing, with consequent uncertainty introduced and causing significant error.

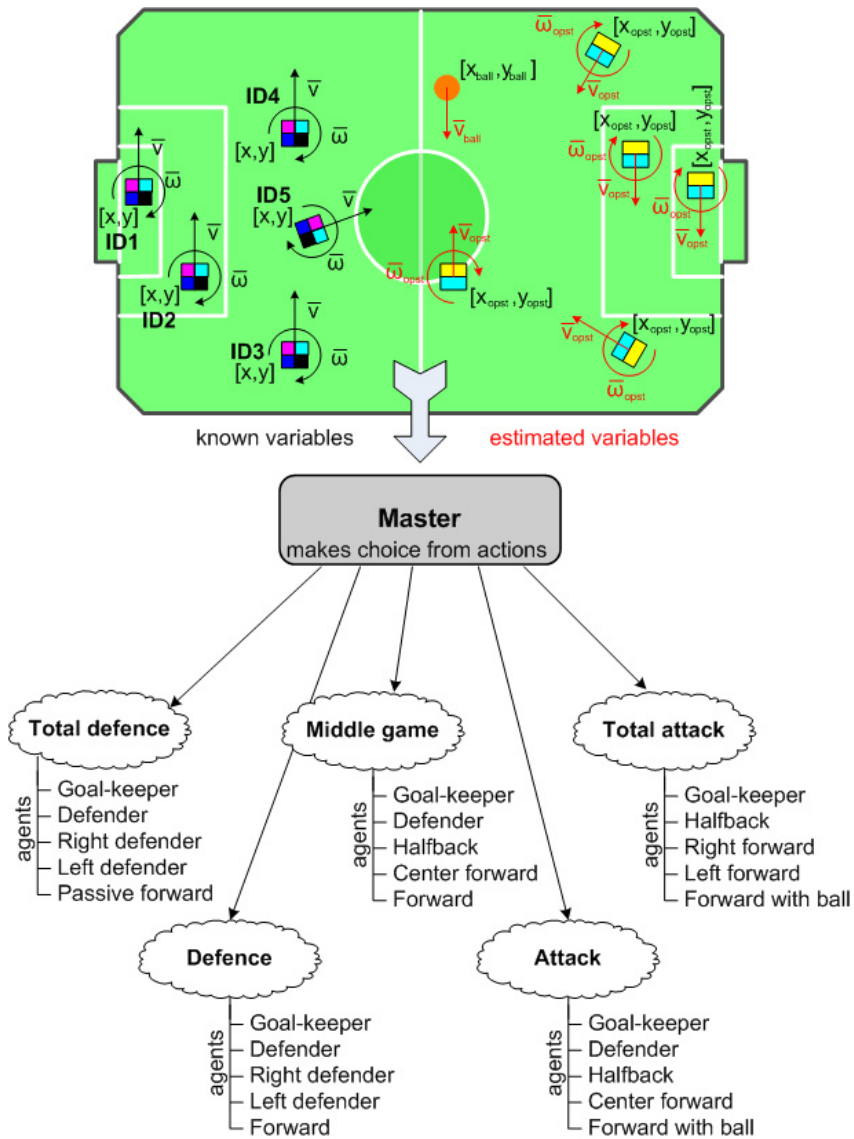


Fig. 5. variables in the system influencing decision making of the master agent on instant action out of all undefined actions

6 An Example of User's Strategy (Offensive Strategy)

User may select the strategy in the control program by combination of options in the field of strategy settings (fig.3)

- DEFENCE - Aggressiveness → active
- DEFENCE - STYLE → ahead
- Advances → active
- ATTACK → 2 gauge with extended defender

System strategy behavior is based on:

- 3 cooperating attackers/offenders
- Attackers without the ball run on the opponent sides of the gate
- Midfielder in the midfield is active in the movement to the sides
- 2 defenders before defense zone are in a position ahead
- Defenders in front of defense zone are active in taking over the opponent

This strategy is one of the two most offensively oriented basic strategies that were implemented in the program. When attacking, there are three attackers with one midfielder. All thresholds of strategic actions are shifted up towards our defensive zone. This strategy is intended to set the active defense of the backup and the chosen defenders in front of you (front and rear).

Master agent has this group of elementary agents available:

$$AH_1 = \left\{ \begin{array}{l} \text{goalkeeper, defender, back_defender, front_defender, midfielder,} \\ \text{forward, defensive_forward, right_forward, left_forward} \end{array} \right\}$$

Master agent uses 9 elementary agents for given strategy, fig. 6. Master agent decides on assigning them to the pitch (playground).

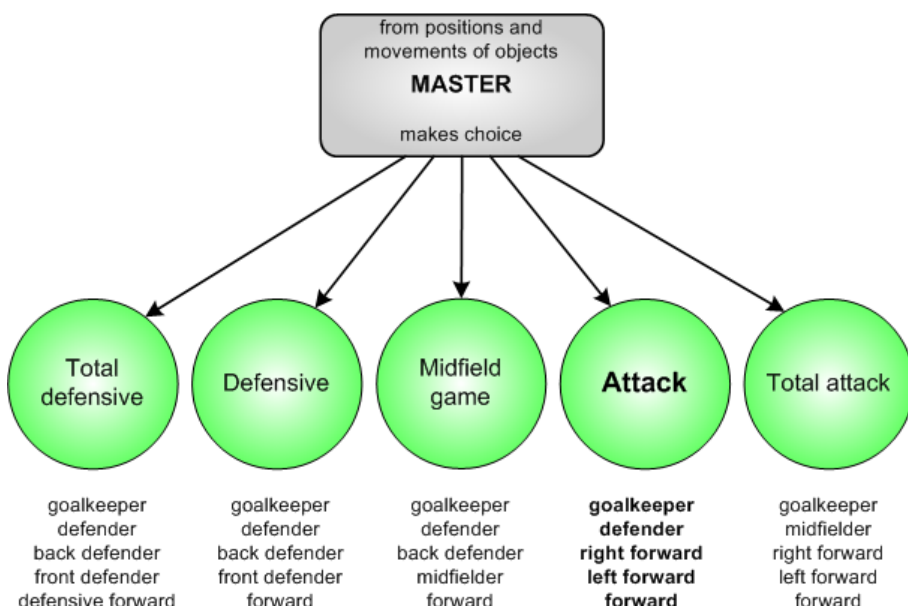


Fig. 6. Players' agents existence for strategic actions – strategy 2

7 Strategy Action Attack in Terms of Offensive Strategy

During the development of each strategy there was created an assignment key for assigning robots to elementary agent:

$$\begin{aligned} forward &\in \{ID5, ID4, ID3\} \\ right_forward &\in (\{ID5, ID4, ID3\} - u) \\ left_forward &\in (\{ID5, ID4, ID3\} - u - up) \\ goalkeeper &\in \{ID1, ID2\} \\ defender &\in (\{ID1, ID2\} - b) \end{aligned}$$

Rules were created according to this assignment key that were implemented in the master agent's decision making:

$$\begin{aligned} forward = IDn_1 &\Leftrightarrow SAP(IDn_1, forward); n_1 = 5,4,3 \\ right_forward = IDn_2 &\Leftrightarrow SAP(IDn_2, right_forward) \wedge right_forward \neq forward, n_2 = 5,4,3 \\ left_forward = IDn_3 &\Leftrightarrow SAP(IDn_3, left_forward) \wedge left_forward \neq (forward \vee right_forward), n_3 = 5,4,3 \\ goalkeeper = IDn_4 &\Leftrightarrow SAP(IDn_4, goalkeeper), n_4 = 1,2 \\ defender = IDn_5 &\Leftrightarrow SAP(IDn_5, defender) \wedge defender \neq goalkeeper, n_5 = 1,2 \end{aligned}$$

StatementAboutPosition(x, a)= Robot X has the best absolute and relative (with respect to the ball) position and velocity parameters for elementary agent a.

The rules for assigning robots to elementary agents are executed sequentially in that order. This maintains the priority and sequence assignment (Fig. 7).

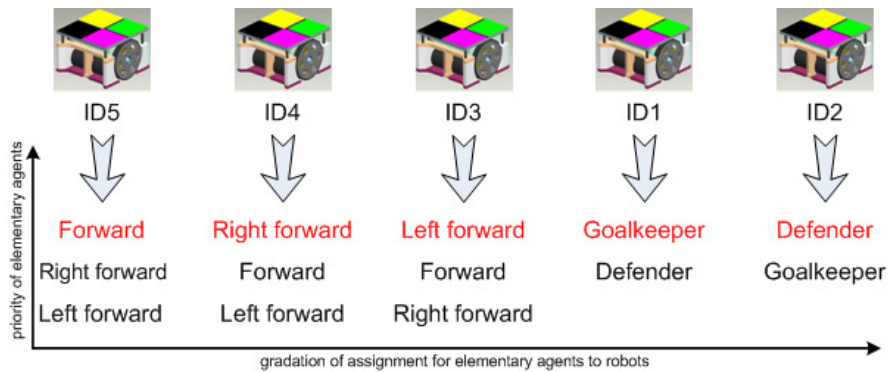


Fig. 7. Players' agents assignment options for offensive action

8 Conclusion

Robot soccer is an application where you can test and evaluate the appropriateness of an approach to solving collaboration of mobile robots on the field. The dynamic environment in which robots work, as well as influencing the situation on the field makes the application an excellent test of this application domain, where each team

has to count with these interventions. The suitability of MAS applications of FME TUKE Robotics used by the team showed was proved on several international competitions in which the team has excellent results (World Championship 2010 India - 1.place in MiroSot category).

References

1. Hajduk, M., Sukop, M.: Multiagents system with Dynamic Box Change for MiroSot. In: FIRA RobotWorld Congress 2009, Incheon, Korea. Springer, Berlin (2009) ISBN 3-642-03985-5; Clerk Maxwell, J.: A Treatise on Electricity and Magnetism, 3rd edn., vol. 2, pp. 68–73. Clarendon, Oxford (1892)
2. Han, K.-H. et al.: Robot Soccer System of SOTY 5 for Middle League MiroSot. In: FIRA Robot Congress 2002, Seoul, Korea (2002)
3. Kim, J.-H.: Soccer Robotics, s.326. Springer (2004) ISBN 3330000232678
4. DeLoach, S.A., Wood, M.: Developing Multiagent Systems with agentTool. In: Castelfranchi, C., Lespérance, Y. (eds.) ATAL 2000. LNCS (LNAI), vol. 1986, pp. 46–60. Springer, Heidelberg (2001)
5. Sukop, M.: Návrh štruktúry MAS v mobilnej robotike: dizertačná práca. Košice: SjF TU, s.117 (2008)
6. Yangmin, L., Wai, I.L., Xiaoshan, L.: Multi-Agent Control Structure for a Vision Based Robot Soccer System. In: 11th IEEE Internatiol Conference on Mechatronics and Machine Vision in Practice, Macau (2004)

Experimental Study of Grouser's Effect for Planetary Rovers Based on Terramechanics

Yuto Nakane¹, Kojiro Iizuka¹, and Takashi Kubota²

¹ Shinshu University

{12fm323f, iizuka}@shinshu-u.ac.jp

² Japan Aerospace Exploration Agency

kubota@isas.jaxa.jp

Abstract. In the future, the planetary exploration missions, planetary robots are required to traverse over very rough terrain. On the lunar surface and Mars surface, there are covered with loose soil, namely “Regolith”. The reason why the wheel is easy to occur the poor condition during traverse on loose soil is not yet clear in detail. We use Terramechanics model for analyzing the mechanism of slipping and sinking behavior. Terramechanics model which is widely used as locomotion model for some lunar rovers is applicable to only circular wheel. So, it is not easy to apply to wheel with grousers. Therefore, firstly, we simulated the conventional model to confirm the difference between the wheel without grousers and with grousers. Secondly, we carry out the running experiments using the rigid circular wheel (with and without grousers) to compare with simulation results. From these results, we consider the difference between the conventional model and the real wheel’s model.

1 Introduction

Rovers are one of the most important mission devices for planetary exploration. They are designed to move on planetary surfaces for the purpose of collecting precise information regarding the origin of the solar system etc. The NASA Mars mission in 1997 was accomplished using the micro rover Sojourner[1] that moved about and explored the surface of Mars. Sojourner transmitted important data and detailed images of the Martian surface to the Earth. The Sojourner mission demonstrated the importance of mobile exploration. Moreover, NASA/JPL sent MER to Mars in 2003(fig.1)[2]. MER transmitted importance data too.

In planetary exploration, rovers are required to traverse rough terrains such as those found in craters and cliffs which are scientifically important location for exploration. Further, when moving over such terrain rovers must avoid tipping over and getting stuck.

From this, we have to improve the capability of the rover which can traverse the ground like loose soil. Our target is to traverse lunar surface. The lunar surface is covered with regolith, the lunar ground is soft and it is easy to slide. Regolith is made of the fragment broken from the moon and other heaven bodies. Moreover, the regolith was suffered from the chemical change for granule



Fig. 1. Mars Exploration Rover [NASA/JPL][2]



Fig. 2. The rigid wheel of Mars Exploration Rover [NASA/JPL][2]

phenomenon. And the regolith is different from weathering soil of the Earth. On such a surface, a normally wheel are not gotten the traction efficiency for the movement.

Therefore the surface of the wheel of the rovers has grouser like fin's form. MER has the wheels with groupers like fig.2. However, it is not clear on what kind of form of groupers is appropriate. Therefore, this paper investigates about grouser's form. Especially, we carry out experiment that focus on the difference of wheel with groupers and that without groupers by measuring indices of the wheel's traversing efficiency.



Fig. 3. Digging condition of MER [NASA/JPL][2]

The paper is organized as follows. In the next section, we describe the condition while traversing loose soil. In Section 3, we describe the interaction model between the wheel with grousers and soil. Section 4 describes simulation and experiments, and the conclusion is reported by section 5.

2 Traverse on Loose Soil

Fig.3 shows the poor running condition of MER[2]. MER took lot of time to escape the loose soil like figure. Therefore, the circular rigid wheel is easy to sink when it traverses on loose soil. In this paper, the single wheel was traversed loose soil shown in fig.4[3]. This condition has many loose soil and slope. If there is slope to traverse, the wheel is not easy to traverse there like loose soil. As method which can traverse loose soil, we mounted grousers on surface of wheels. If the wheel has grousers, the wheel can traverse loose soil with slope. Therefore, we focus on interaction relation between form of grousers and running performance.

3 Interaction between Wheel and Soil

3.1 Model of Interaction between Wheel and Soil

Some researchers have studied robots with interaction between grousers and soil on a terrain[4]-[9]. Especially, Sutoh[10] proposes original slip model of wheel with grousers and experiment about slip of two wheel rover. Nakashima[11] proposes newel model about grousers called "Power Number" and simulated with discrete element method about single wheel. Irani[12] suggests a form for the



Fig. 4. Digging condition of Circular Wheel (Single)

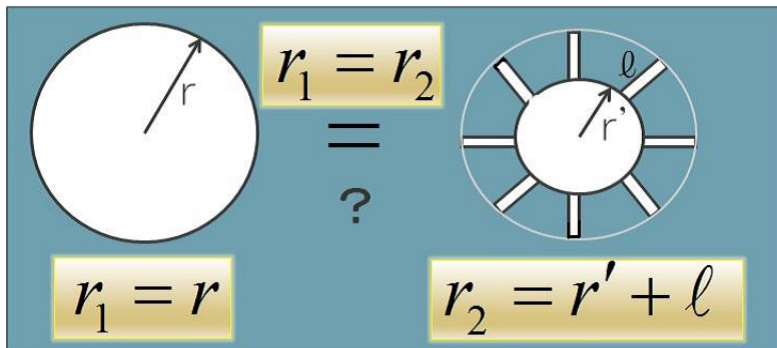


Fig. 5. Assumption for relation of wheel with grousers and normal wheel

pressure-sinkage relationship to capture the dynamic oscillations observed for a wheel with grousers. Obermayr[13] applied the DEM model to a simple case of a single cutting blade moving at constant speed under quasi-static conditions. Lyasko[14] presents an analysis and quantitative evaluation of the slip sinkage and its effect on the tractive performance of wheeled and tracked vehicles in different soils. Ding[15] carried out an experiment various kind of wheels and evaluate the effect of various parameter, such as velocity, the height of grousers, the number of grousers, and so on. However they do not develop the model of grousers with wheel. In 1969, Bekker started studying the interaction between wheel and soil, and proposed model of normal wheel and soil[16]. This study is called as Terramechanics. We'll show you about Terramechanics this section. When we apply the wheel with grousers to the model of the wheel without grousers, we regard the total amount of wheel radius and grouser height as new wheel radius (like Fig.5). We examined the accuracy of this theory, and the effect of grousers for wheel performance.

Therefore we examine the mechanism for drying using grousers. Fig.6. shows the interaction model between the wheel and soil.

The line which the wheel runs on slope is shown as "soil surface". h denotes the sinkage at a slope. θ is used to show the part of the wheel into soil. θ_f indicates the inserted angle into soil and θ_r indicates the escaped angle.

3.2 Drawbar Pull

The drawbar pull of wheel F_x is expressed by the total of force working the wheel. Therefore, the drawbar pull is expressed by intergrating a shearing stress $\tau(\theta)$ and a normal stress $\sigma(\theta)$ is intergrated using contacted area of wheel and soil. Then, the drawbar pull F_x is written as follows using the wheel radius r and the wheel width b .

$$F_x = rb \int_{\theta_r}^{\theta_f} \{ \tau_x(\theta) \cos(\theta) - \sigma(\theta) \sin(\theta) \} d\theta \quad (1)$$

If the angle which the value of normal becomes maximum is θ_m . θ_m is indicated follow.

$$\theta_m = (a_0 + a_1 s) \theta_f \quad (2)$$

Then, we describe the normal stress $\sigma(\theta)$ each area of theta

$$\theta_m \leq \theta < \theta_f$$

$$\sigma(\theta) = \sigma_m \left(\frac{\cos \theta - \cos \theta_f}{\cos \theta_m - \cos \theta_f} \right)^n \quad (3)$$

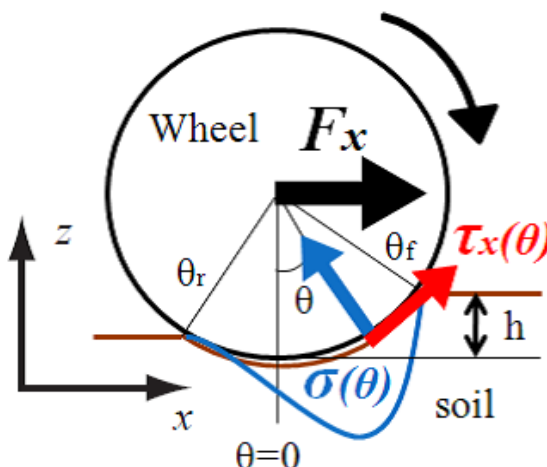
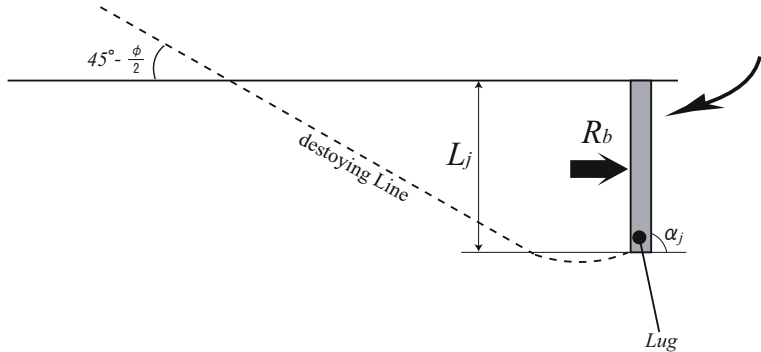


Fig. 6. Interaction Model between Wheel and Soil on Slope

**Fig. 7.** Model of Grouser

$$\theta_r < \theta \leq \theta_m$$

$$\sigma(\theta) = \sigma_m \left(\frac{\cos\{\theta_f - \frac{\theta-\theta_r}{\theta_f-\theta_m}(\theta_f - \theta_m)\} - \cos\theta_f}{\cos\theta_m - \cos\theta_f} \right)^n \quad (4)$$

a_0 and a_1 are constant values. Moreover, the maximum of σ_m is follow,

$$\sigma_m = (k_c/b + k_\phi) \{r(\cos\theta_m - \cos\theta_f)\}^n \quad (5)$$

The equations of the shearing stress is:

$$\tau(\theta) = (c + \sigma(\theta)) \tan\phi (1 - \exp^{-\frac{j(\theta)}{K}}) \quad (6)$$

where,

$$j_x(\theta) = r\{\theta_f - \theta - (1-s)(\sin\theta_f - \sin\theta)\} \quad (7)$$

c : adhesive power

j : shearing strain

ϕ : internal friction angle

The slip ratio λ is defined by the following formula here.

$$\lambda = \begin{cases} 1 - \frac{V_\omega}{r\omega} : drive(r\omega \geq V_\omega) \\ 1 - \frac{r\omega}{V_\omega} : brake(r\omega \leq V_\omega) \end{cases} \quad (8)$$

where,

- r : the radius of a wheel
 ω : angular velocity of a wheel
 V_ω : moving speed of a wheel

The interaction model between the wheel and the ground is shown like this. However, this model don't have the effect of grousers set on surface of the wheel. We should consider about the exist of grousers and the effect of these.

3.3 Drawbar Pull Produced by Grousers

$$R_b = \frac{\sin(\alpha_j + \phi)}{\sin \alpha_j} C \quad (9)$$

where

$$C = L_j c (N_c - \tan \phi) + \frac{1}{2} \gamma L_j^2 \left(\frac{2N_r}{\tan \phi} + 1 \right)$$

where,

- α_j : angle of approach
 γ : soil density
 L_j : grouser length
 c : cohesion stress
 ϕ : friction angle of soil
 N_c, N_r : coefficients of support force

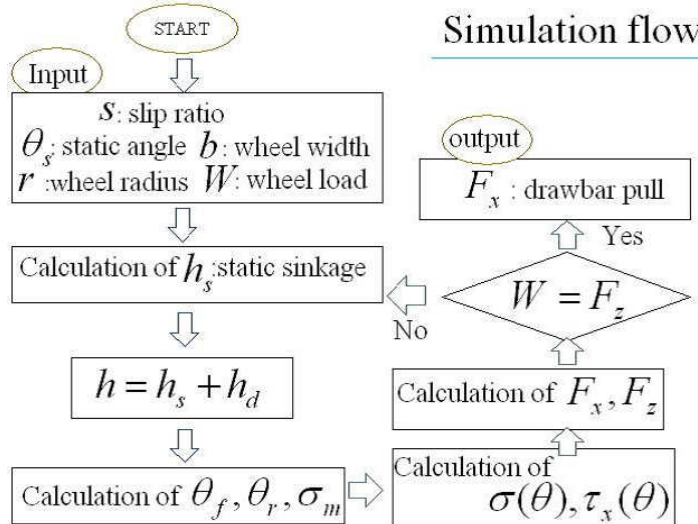
This is the effect of grousers, but the model of drawbar pull by grousers and wheel is not completely established. We carried out an experiment if the model of the normal wheel also can be applied for the wheel with grousers.

4 Simulation and Experiments

4.1 Simulation

We simulate to grasp a running state of the wheel with grousers when we apply them to the model of the wheel without grousers. The state of running wheel is hard to understand. So we made a simulation which can calculate the normal stress σ and the shear stress τ_x from the entry angle θ_f , and the exit angle θ_r , and a simulation which can calculate the drawbar pull from slip ratio. We show the simulation flow at Fig.8. We show the process at below.

1. Input of the parameters about the wheel and soil.
2. Input of slip ratio from 0.1 to 1.0 in units of 0.1.

**Fig. 8.** Simulation flow

3. Calculation of the amounts of sinkage of state wheel h_s and dynamic sinkage h_d , and want sum of sinkage h .
4. Calculation of maximum normal force angle θ_m , and maximum normal force σ_m .
5. Calculation of the wheel's entry angle θ_f , and exit angle θ_r .
6. Calculation of shearing strain j , normal stress σ , and shear stress τ_x .
7. Calculation of normal force F_z and drawbar pull F_x .
8. Repetition of the above 3'8 until normal force F_z exceeds wheel load W .
9. Calculation of normal force F_z and drawbar pull F_x when normal force F_z exceeds wheel load W .

4.2 Experimental System

Fig.9 is mechanism of this system and fig.10 is overview of this system. This system can control the slip ratio. The drawbar pull is obtained by inputting the slip ratio. This system is constituted by wheel, carriage, soil tank, measure system of sinkage, and load balancer. The depth of soil is 200 mm. The dimension of soil tank is 1700 mm(length), 900 mm(wide), and 500 mm(depth). The experimental system is configurated some mechanical parts and sensors. The velocity of motors for the wheel and the carriage are controloed by users to desired value. When the motor for the wheel rotates, the motor for the carriage rotates slower than that for wheel. From this control using two motors, we can control the slip ratio. The velocity of the wheel is determined by PID control using an encoder. The wheel has a force sensor which can measure forces and moments.

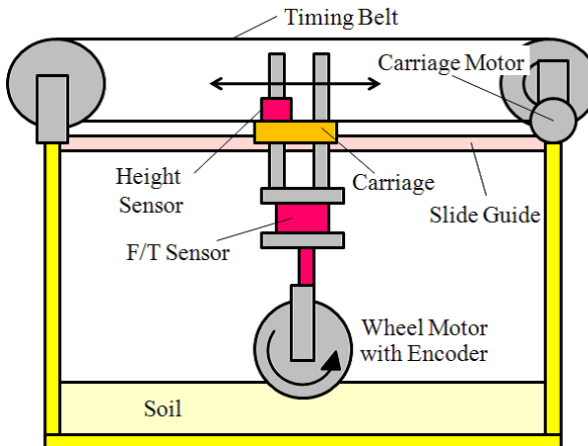


Fig. 9. Mechanism of experiment system

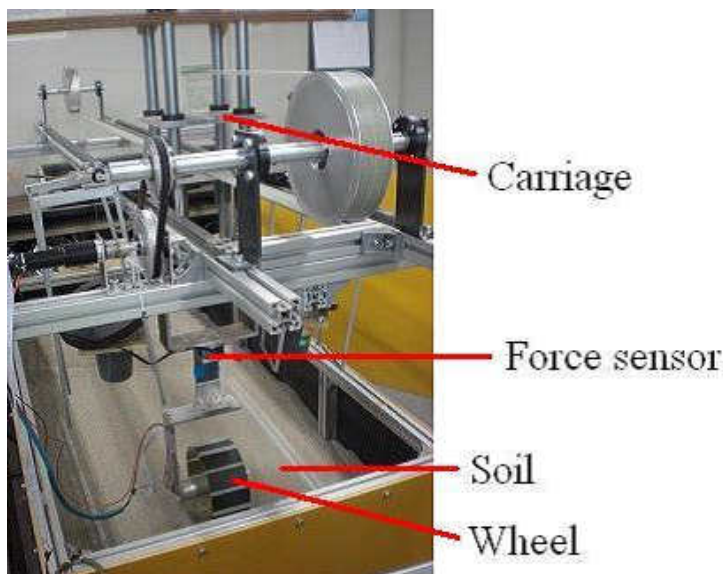
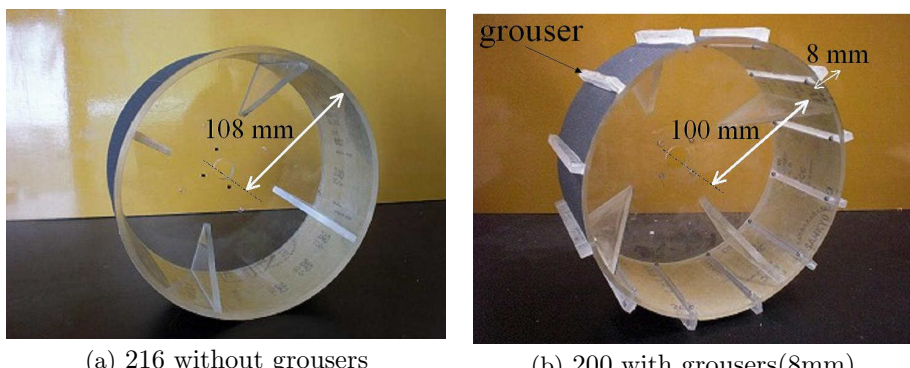
The experimental parameters are shown in table 1. The load of wheel is constant(2.0 kg).

Fig.11 shows the wheel for the experiments. The wheel's sinkage is measured by the hypersonic wave sencer. The force occurred by wheel's running is measured by force sencer set above the wheel (Force sensor is connected to wheel's stay).

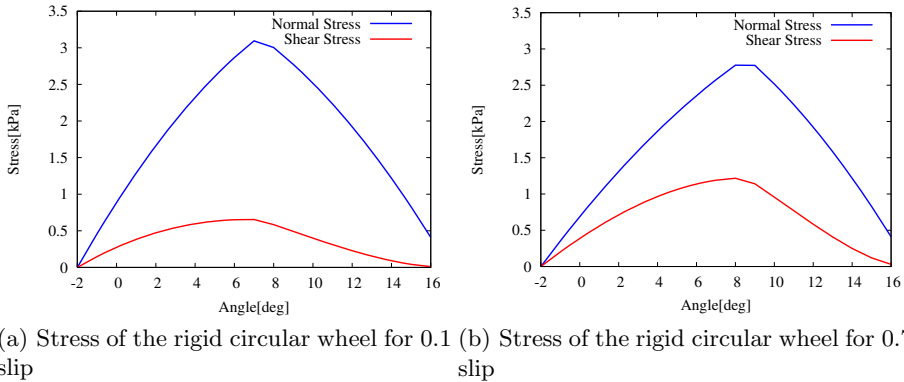
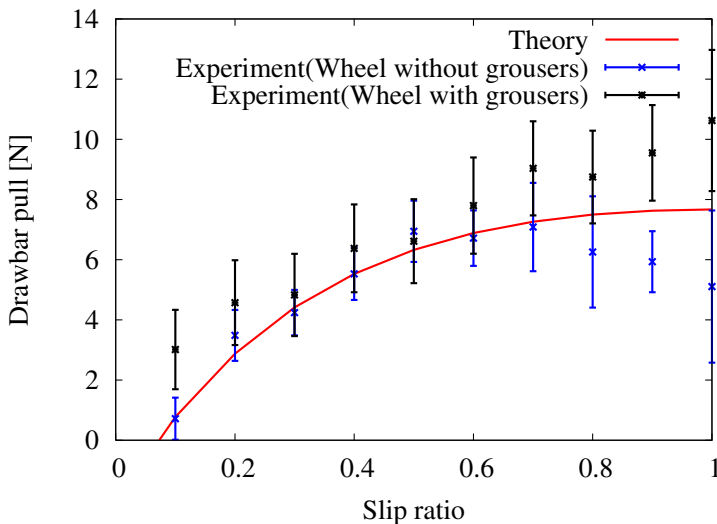
4.3 Results and Discussion

Fig.12 shows the normal stress and the shear stress calculated by simulation at slip 0.1 and 0.7. The red line shows the shearing stress, and the blue line shows the normal stress. When the slip ratio is set from 0.1 to 0.7, the shearing stress becomes bigger and the normal stress becomes smaller. When the slip ratio is set from 0.1 to 0.7, the maximum value and the distribution of the two stress are shifted to the front of the wheel toward the direction(maximum value of the two stress becomes from around 6 to around 9 deg).

Fig.13 shows the drawbar pull of wheel at the simulation, the experiment of the wheel without grousers, and the experiment of the wheel with grousers. When the slip ratio is less than 0.6, the value of the drawbar pull is almost match at the theory and the experiment of the wheel without grousers and the experiment of the wheel with grousers. When the slip ratio becomes more than 0.6, the drawbar pull of the wheel without grousers is smaller than that of simulation. When we set more than 0.6 slip ratio, the drawbar pull of the experiment of the wheel with grousers is bigger than that of simulation and the experiment of the wheel without grousers. It is good performance for wheel to be bigger drawbar pull at high slip. From fig.13, we can tell that the wheel with grousers does good performance at loose soil. The shear motion got by grousers is effect at loose soil.

**Fig. 10.** Overview of Experimental System**Fig. 11.** Wheels for experiments**Table 1.** Experimental Parameters

Load	2.0 kg
Speed	10 mm/s
Slip ratio	0, 0.1, 0.2, 0.3, 0.4, 0.5, 0.6, 0.7, 0.8, 0.9, 1.0
radius of wheel	108, 100 mm
length of grousers	0, 8 mm
used soil	Silica sand

**Fig. 12.** Stress of normal wheel**Fig. 13.** Drawbar pull at established slip ratio on simulation and wheel with and without grousers

5 Conclusion

We focused on grouser's effect for wheel of lunar rovers. From the experiments, the wheels with grousers have better performance than that without grousers. However, the simulation result doesn't match the experimental results of the wheel without grousers. Therefore the model including the effect of the grousers should be considered. In the future works, we will model including the effect of the grousers from various experimental results.

References

1. Mars Pathfinder, <http://mars.jpl.nasa.gov/MPF/>
2. MARS Rover, <http://marsrover.nasa.gov/home/index.html>
3. Iizuka, K., Kanamori, H., Kubota, T.: A Study of Terramechanics for Movement on Planetary Surface. *Robotics Symposia* 10, 33–38 (2005) (in Japanese)
4. European Space Agency, <http://www.esa.int/esaMI/ExoMars/index.html>
5. Michelin Group, <http://www.michelin.com/>
6. Yon, R.N., Fattah, E.A., Skidas, N., Kitano, M.: Run dynamics of off-road vehicles. The Japanese Society for Study Technology Education (1986)
7. Iagnemma, K., Kang, S., Shibly, H., Dubowsky, S.: Online Terrain Parameter Estimation for Wheeled Mobile Robots With Application to Planetary robots. *IEEE Transactions on Robotics* 20(5), 921–927 (2004)
8. Yoshida, K., Hamano, H.: Motion Dynamics Simulations and Experiments of an Exploration robot on Natural Terrain. In: The 11th Workshop on Astrodynamics and Flight Mechanics, pp. 306–313 (2001)
9. Iizuka, K., Kanamori, H., Kubota, T.: Wheeled Running Experiment with Mimic Physiognomy of Moon by Planetary Explore Robots. In: Conf. on Robotics and Mechatronics, No. 5 (2005) (in Japanese)
10. Sutoh, M., Nagatani, K., Yoshida, K.: Evaluation of influence of surface shape of wheel on traveling performance of planetary rovers over slope. In: Proc. of 17th Internal Conference of the International Society for Terrain-Vehicle Systems, pp. 18–22 (2011)
11. Nakashima, H., Fujii, H., Oida, A., Momozu, M., Kanamori, H., Aoki, S., Yokoyama, T., Shimizu, H., Miyasaka, J., Ohdoi, K.: Discrete element method analysis of single wheel performance for a small lunar rover on sloped terrain. *Journal of Terramechanics* 47(5), 307–321 (2010)
12. Irani, R.A., Bauer, R.J., Warkentin, A.: A dynamic terramechanic model for small lightweight vehicles with rigid wheels and grousers operating in sandy soil. *Journal of Terramechanics* 48(4), 307–318 (2011)
13. Obermayr, M., Dressler, K., Vrettos, C., Eberhard, P.: Prediction of draft forces in cohesionless soil with the Discrete Element Method. *Journal of Terramechanics* 48(5), 347–358 (2011)
14. Lyasko, M.: Slip sinkage effect in soil-vehicle mechanics. *Journal of Terramechanics* 47(1), 21–31 (2010)
15. Ding, L., Gao, H., Deng, Z., Nagatani, K., Yoshida, K.: Experimental study and analysis on driving wheels' performance for planetary rovers moving in deformable soil. *Journal of Terramechanics* 48(1), 27–45 (2011)
16. Bekker, M.: Theory of Land Locomotion. The University of Michigan Press (1955)

Evolving Story Narrative Using Surrogate Models of Human Judgement

Kun Wang¹, Vinh Bui¹, Eleni Petraki², and Hussein A. Abbass¹

¹ School of Engineering and IT, UNSW-Canberra, Australia

Kun.Wang@student.adfa.edu.au, vinhbq@gmail.com, H.Abbass@adfa.edu.au

² Faculty of Arts and Design, University of Canberra, Australia

Eleni.Petraki@canberra.edu.au

Abstract. Communication has been an active field of research in Robotics. However, less work has been done in the ability of robots to negotiate meanings of the world through storytelling. In this paper, we address this gap from the perspective of evolving stories. By approximating human evaluation of stories to guide the evolution, we can automate the story evolutionary process without interacting with humans. First, a multi-objective story evolution approach is applied where the approximated human story evaluation model automatically evaluates the subjective story metrics such as coherence, novelty and interestingness. We then use humans again to validate the stories narrated by the machine. Results show that for each of the human subjects, the stories collected after story evolution are regarded as better stories compared to the initial stories. Some interesting relationships are revealed and discussed in details.

Keywords: evolving story narrative, genotype-phenotype mapping, objective story metrics, human evaluation model.

1 Introduction

Storytelling has been regarded as an effective and interesting way of communication. In education industry, a storytelling agent, such as a storytelling humanoid robot [1], can serve as a learning tool for students. In entertainment industry such as computer Role Playing Games, storytelling technique has been a pillar in providing an immersive playing experience to human players [2]. Moreover, storytelling also plays an important role in planning and scenario generation [3].

Three major automatic storytelling approaches are observed in the literature: case-based reasoning [4,5], simulation-based [2] and the grammar-based approach [6,7]. In the grammar-based approach, story generation becomes a process of grammar derivation and evolution, in which a story grammar is designed by representing the underlying story structure in the form of formal grammar.

If a story can be represented as a genome, existing evolutionary algorithms can be applied to evolve the generated stories. However, to make the story evolution work, an appropriate fitness function must be defined to evaluate the story. This

raises one of the biggest challenges in automatic story generation—quantifying the story “qualitativeness” where a computational model of subjective story metrics such as coherence, novelty and interestingness are required.

At present, in the evolutionary computation (EC) field, a pragmatic approach for evaluating the “qualitativeness” is by using interactive EC (IEC) in which a human-in-the-loop evaluation is required. Example implementations of IEC to the story evolutionary generation field are [6,7]. However, a number of key challenges of IEC have been pointed out, such as human fatigue [8,9], granularity, user inconsistency [10] etc. As a result, it is difficult to evaluate a large number of stories using IEC.

A possible solution to automated story evolution is to predict the fitness values of individuals for fast IEC convergence, which can increase the searching capability by using a large population size equal to that of a normal EC [11]. In the literature of EC, the following techniques for predicting fitness functions have been observed: neural network [11], fuzzy logic [12] and heuristics using a defined measure of creativity [8]. In [9], a progressively interactive evolutionary multi-objective optimization (EMO) approach is proposed that utilizes the constructed value function in directing EMO algorithm’s search to more preferred solutions.

In this paper, we propose a multi-objective story evolution approach in which the approximated human story evaluation model calculated from a human-based experiment serves as the automatic story evaluator. This can contribute to the semi-automatic generation of good stories with reduced human involvement.

The rest of the paper is organized as follows: In Section 2, we give a rough explanation of our previous work—representing the generation of stories with flashback from the dependence network as a permutation problem which serves as the basis of this paper. Then in Section 3, subjective and objective story metrics are explained. Based on the data collected from a human-based experiment in our previous work, in Section 4, an approximation of human story evaluation model is obtained using simple multiple linear regression, which captures the mapping from objective story metrics space to the subjective story metrics space. Subsequently, in Section 5, a multi-objective story evolution approach is proposed to achieve evolutionary story generation with reduced human involvement where the approximation of human story evaluation model serves as the automatic story evaluator. In Section 6, another human-based experiment is carried out to test the performance of the story evolution approach. Finally, some concluding remarks are made and future work is discussed in Section 7.

2 Story Generation as Permutation Problem

In our previous work [13], we have represented the generation of stories with flashback as a permutation problem, that is, finding an appropriate permutation of the heterogeneous story information including event chains, parameters and flashback point in the story dependence network, so that diversified stories with different narration orders and parameter arrangements from the original story can be generated. A dependence network that reflects the dependence relations

between parameterized event chains in a story was firstly extracted. Then we encoded the new story generated from the story dependence network into a genome which is a valid permutation (*ie* a permutation under predefined constraints) of integers that represent heterogeneous story information. Finally, we generated different permutations in the genotype to change the phenotype—the corresponding text-form story.

3 Story Metrics

In this paper, which follows our previous work [13], the subjective story metrics selected for human story evaluation are coherence, novelty, interestingness and the overall quality of a story.

The objective story metrics defined are as follows: “*disOfFlashback*” means the distance of flashback feature of a story; “*consistChainOrders*” denotes the consistency of the chain order of a story with the chain order in the reference story, *ie* the original Little Red Riding Hood story (LRRH) or CaveLand story; “*consistPars*” denotes the consistency of the parameter arrangement with that of the reference story. Parameters are characters and objects; “*consistParRoles*” is the consistency of the arrangement of parameters roles with those in the reference story. They are calculated by the following equations:

$$disOfFlashback = \frac{\text{dependence network layer count} - \text{threshold layer}}{\text{dependence network layer count}} \quad (1)$$

$$consistChainOrder = \frac{\text{sorting cost to the reference story's chain order}}{n \times (n - 1)/2} \quad (2)$$

$$consistPars = 1 - \frac{\text{times of parameter change from reference story}}{\text{number of parameters in the story}} \quad (3)$$

$$consistParRoles = 1 - \frac{\text{times of role change from reference story}}{\text{number of parameters in the story}} \quad (4)$$

In (2), n denotes the number of chains in the dependence network and sorting cost is calculated according to the bubble sort.

4 Approximation of Human Story Evaluation Model

In this section, we discuss the procedure for developing an approximation of the human story evaluation model. This approximation is obtained by mapping the objective story metrics to the subjective story metrics whose data is collected from a human-based experiment in our previous work [13] where data of 240 stories are collected. Every human subject is required to evaluate 15 versions of a story in a continuous time slot of a day where a break less than 5 minutes is allowed; the reading order has been shuffled to reduce the impact of tiredness and context influence on the investigation result.

After the experiment, the objective story metrics are mapped with the collected subjective story metrics of the corresponding story using a multiple linear

regression using Ordinary Least Squares (OLS) [14] to obtain the approximated human story evaluation model.

The denotation used in the multiple linear regression model represented in equation (5) is explained as follows: Y is an $n \times 1$ vector of n cases of observed data about one subjective story metrics, each row corresponds to the average value of human evaluation scores among human objects for one of the n generated stories; β is a 5×1 vector of regression coefficients each of which denotes a corresponding objective story metrics' weight in determining the value of a subjective story metrics including the intercept; X is an $n \times 5$ matrix that gives all of the calculated values of the objective story metrics for each of the n stories and $x_{i1} = 1(i = 1, 2, \dots, n)$; e is the $n \times 1$ vector of statistical errors; the i th row of equation (5) is $y_i = y'_i + e_i$ where i denotes the i th case of observed data about the i th generated story.

$$Y = X\beta + e \quad (5)$$

The results of the approximation using linear regression are illustrated in Figure 1.

	LRRH story				CaveLand story			
	overall	coherence	novelty	interestingness	overall	coherence	novelty	interestingness
intercept	2.403512	1.40129912	3.87560692	3.059142906	2.56429757	2.29623523	2.20089605	1.157266475
disOffFlashback	-0.4496475	0.05310577	-1.5498338	-1.225707475	0.23619503	-0.0660218	0.77977309	1.478919836
consistChainOrder	2.17045649	2.99195121	0.63484671	1.289277834	5.84798377	6.12888124	5.16415601	6.807516244
consistChars	-0.2520972	-0.0112808	0.00759652	-0.748020471	0.58730031	0.57805004	0.27895474	0.450778111
consistCharRoles	1.60023519	1.66362622	0.87544643	1.821317403	-0.6527419	-0.495383	-0.4115191	-0.538917567

Fig. 1. Regression coefficients β of the approximated human story evaluation model

5 Multi-objective Story Evolution

In this section, a multi-objective story evolution approach is proposed where the approximation of human story evaluation model obtained in Section 4 serves as the automatic story evaluator. Compared to single-objective story evolution [6,7], multi-objective evolution has the advantage of enhancing diversity in the produced stories.

The genotype elaborated in our previous work [13] is used as the story chromosome. Among the subjective story metrics in Section 3, coherence, novelty and interestingness are selected as the multiple objectives for the story evolution.

In evaluating the quality of every generated story, the approximated human evaluation model mentioned in Section 4 is applied to automatically assign the values for each of the objectives (*ie* coherence, novelty and interestingness) of every generated story. This process involves the following steps: First of all, we extract the heterogeneous story information from the genotype (*ie* the threshold layer, chain list and parameter list) through a genotype-phenotype mapping elaborated in our previous work [13]. Then we calculate the objective story

metrics using the Equation (1) to (4) listed in Section 3 based on the story information just obtained from the last step. Finally, we calculate the subjective story metrics using the approximated human evaluation model mentioned in Section 4 based on the objective story metrics just obtained from the last step. The calculated subjective story metrics are the predicated human evaluations for the story during the evolution.

After assigning the values of each objectives, the elitism strategy in NSGA-II [15] is applied to maintaining elitist solutions in the population during the evolutionary process.

The genetic and search operators used in the multi-objective story evolution in this paper are listed below:

- **Crossover operators:** partially mapped (PMX), order (OX) and cycle (CX) crossovers explained in [16] which can maintain the validity of the permutation after crossover.
- **Mutation operators:** inversion, insertion, displacement and reciprocal exchange operators explained in [16].

After a mutation or crossover operator has been applied to produce offsprings, an extra work is to transform the genome of the offsprings into a genome that conforms to the predefined constraints mentioned in our previous work [13] to control the coherence in the generated stories to some degree.

6 Experimental Study

In this section, we present the experiment carried out to test the performance of the story evolution approach proposed in this paper—story evolution guided by the approximated human story evaluation model.

6.1 Experiment Design

Using the same initial story generation system with the previous experiment explained in [13], stories are randomly generated then evolved using the above multi-objective story evolution approach. After testing the performance of the story evolutionary process under different parameter settings, the following parameter setting is selected: population size—100; generation limit—1000; crossover rate—0.8 where PMX, OX and CX crossover operators have equal opportunities to work; mutation rate—0.2 where inversion, insertion, displacement and reciprocal exchange mutation operators share equal opportunities.

We run the above story generation and evolution process for several times—12 times for the LRRH story and 8 times for the CaveLand story and the following data is collected:

- (1) The non-dominated individuals in the final population of each run. The number of the overall non-dominated story individuals is 88 for the LRRH story and 487 for the CaveLand story.

- (2) Pareto fronts discovered in these runs of story evolutions, *ie* the non-dominated individuals in the data collected in (1).
- (3) Individuals with maximum value on at least one objective in the final population of each run. Within these individuals, 15 individuals with comparatively diversified objective values are selected for each of the LRRH story and CaveLand story.

Then present the text-form stories of the overall 30 individuals collected in (3) to the same six (out of eight since two are unavailable) participants to evaluate, then collect their scores on subjective story metrics of each of the stories. The scores of 180 new stories (*ie* 2 stories \times 15 versions \times 6 participants) are collected and analyzed.

6.2 Result and Analysis

To understand the effects of the story evolutionary process guided by the approximated human story evaluation model, Figure 2 presents a comparison between the objective metrics distribution of initial stories chosen in the previous experiment and the evolved stories chosen in the second experiment. Figure 2 provides the following insights:

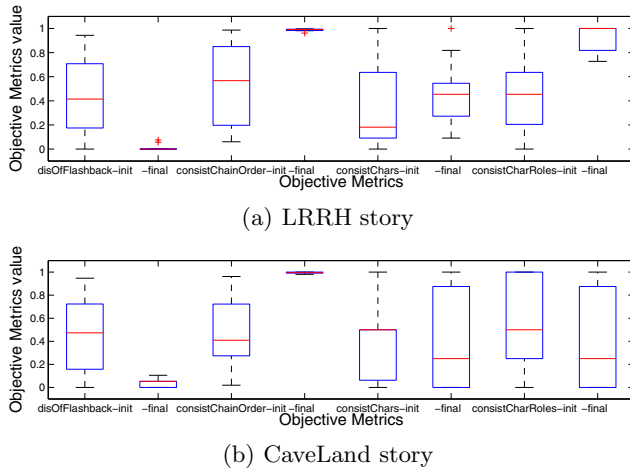


Fig. 2. Comparison between the objective metrics distribution of the collected initial stories (denoted by -init) and the evolved stories (denoted by -final)

Firstly, from the *disOfFlashback* and *consistChainOrder* objective story metrics of both the LRRH story and CaveLand story, the corresponding approximated human story evaluation model tends to guide the story evolutionary process to converge to stories whose chain orders are more consistent with the original stories. Secondly, the approximated human story evaluation model

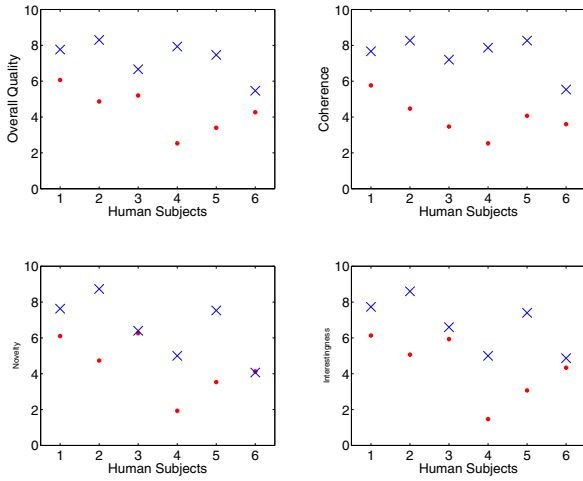


Fig. 3. Comparison between the subjective metrics of the initial stories (denoted by the solid points) and evolved stories (denoted by the crossed points) for LRRH

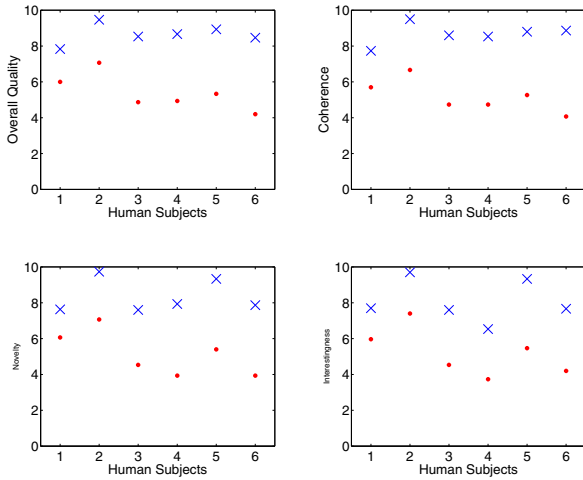


Fig. 4. Comparison between the subjective metrics of the initial stories (denoted by the solid points) and evolved stories (denoted by the crossed points) for CaveLand

of the unfamiliar CaveLand story tends to leave more diversity for the consistChars and consistCharRoles objective story metrics. This means the stories obtained through evolution can still enjoy diversified organization of characters compared to the original story, while for the familiar LRRH story, a comparatively high consistCharRoles objective story metrics is still preferred by the story evolutionary process.

To test the effectiveness of the story evolution guided by the approximated human story evaluation model in producing qualitatively better stories, Figure 3 and 4 each presents a comparison of the average subjective story metrics among different stories given by each of the human subjects between the initial stories obtained in the previous experiment and those for the evolved stories obtained in the second experiment.

It can be perceived from Figure 3 and 4 that the story evolution works. For each of the human subjects, the stories collected after story evolution are regarded as better stories compared to the initial stories, against the criteria set in this experiment.

7 Conclusion and Future Work

In this paper, we have demonstrated that we can evolve a story with minimal human input. The success of the methodology is judged based on the quality of the metrics derived from humans at the end of the evolution. It is possible that this process can take a mid point, where a human interacts with the evolution every now and then. This may produce a better quality stories at the end. This hypothesis is our current motivation for investigating the minimum human input required to generate quality stories. Future work includes improving the approximation model and the implementation of a semi-interactive multi-objective story evolution based on progressively approximated value functions.

References

1. Gelin, R., d'Alessandro, C., Le, Q., Deroo, O., Doukhan, D., Martin, J., Pelachaud, C., Rilliard, A., Rosset, S.: Towards a storytelling humanoid robot. In: AAAI Fall Symposium Series (2010)
2. Hsueh-Min, C., Von-Wun, S.: Planning-based narrative generation in simulated game universes. *IEEE Transactions on Computational Intelligence and AI in Games* 1(3), 200–213 (2009)
3. McKeever, W., Gilmour, D., Lehman, L., Stirzinger, A., Krause, L.: Scenario management and automated scenario generation. In: Kevin, S., Alex, F.S. (eds.) Modeling and Simulation for Military Applications, Florida, vol. 6228, pp. 62281A.1–62281A.12. SPIE (2006)
4. Díaz-Agudo, B., Gervás, P., Peinado, F.: A case based reasoning approach to story plot generation. In: Funk, P., González Calero, P.A. (eds.) ECCBR 2004. LNCS (LNAI), vol. 3155, pp. 142–156. Springer, Heidelberg (2004)
5. Pérez, R., Sharples, M.: Mexica: A computer model of a cognitive account of creative writing. *Journal of Experimental & Theoretical Artificial Intelligence* 13(2), 119–139 (2001)
6. Bui, V., Abbabass, H., Bender, A.: Evolving stories: Grammar evolution for automatic plot generation. In: 2010 IEEE Congress on Evolutionary Computation (CEC), pp. 1–8. IEEE (2010)

7. Wang, K., Bui, V.Q., Abbass, H.A.: Evolving stories: Tree adjoining grammar guided genetic programming for complex plot generation. In: Deb, K., Bhattacharya, A., Chakraborti, N., Chakraborty, P., Das, S., Dutta, J., Gupta, S.K., Jain, A., Aggarwal, V., Branke, J., Louis, S.J., Tan, K.C. (eds.) *SEAL 2010. LNCS*, vol. 6457, pp. 135–145. Springer, Heidelberg (2010)
8. Kowaliw, T., Dorin, A., McCormack, J.: Promoting creative design in interactive evolutionary computation. *IEEE Transactions on Evolutionary Computation* (2011)
9. Deb, K., Sinha, A., Korhonen, P., Wallenius, J.: An interactive evolutionary multiobjective optimization method based on progressively approximated value functions. *IEEE Transactions on Evolutionary Computation* 14(5), 723–739 (2010)
10. Brintrup, A., Ramsden, J., Tiwari, A.: An interactive genetic algorithm-based framework for handling qualitative criteria in design optimization. *Computers in Industry* 58(3), 279–291 (2007)
11. Takagi, H.: Interactive evolutionary computation: Fusion of the capabilities of ec optimization and human evaluation. *Proceedings of the IEEE* 89(9), 1275–1296 (2001)
12. Babbar-Sebens, M., Minsker, B.: Interactive genetic algorithm with mixed initiative interaction for multi-criteria ground water monitoring design. *Applied Soft Computing* (2011)
13. Wang, K., Bui, V., Petraki, E., Abbass, H.: From subjective to objective metrics for evolutionary story narration using event permutations (2012)
14. Weisberg, S.: *Applied linear regression*, vol. 528. Wiley (2005)
15. Deb, K., Pratap, A., Agarwal, S., Meyarivan, T.: A fast and elitist multiobjective genetic algorithm: Nsga-ii. *IEEE Transactions on Evolutionary Computation* 6(2), 182–197 (2002)
16. Michalewicz, Z., Fogel, D.: *How to solve it: modern heuristics*. Springer-Verlag New York Inc. (2004)

Distributed Multiobjective Quantum-Inspired Evolutionary Algorithm (DMQEA)

Si-Jung Ryu and Jong-Hwan Kim

Department of Electrical Engineering, KAIST, 291 Daehak-ro, Yuseong-gu, Daejeon,
305-701, Republic of Korea
{sjryu,johkim}@rit.kaist.ac.kr

Abstract. Most of the multiobjective evolutionary algorithm inherently has heavy computational burden, so it takes a long processing time. For this reason, many researches for reducing computational time have been carried out, in particular by using distributed computing such as multi-thread coding, GPU coding, etc. In this paper, multi-thread coding is used to reduce computational time and applied to multiobjective quantum-inspired evolutionary algorithm (MQEA). In MQEA, nondominated sorting and crowding distance assignment which take a long time are carried out in each subpopulation. By multi-thread coding, the processes in each subpopulation can be performed simultaneously. To demonstrate the effectiveness of the proposed distributed MQEA (DMQEA), comparisons with single-thread and multi-thread are carried out for seven DTLZ functions.

Keywords: Multiobjective evolutionary algorithm, Distributed computing, Quantum-inspired evolutionray algorithm, multiobjective quantum-inspired evolutionary algorithm.

1 Introduction

Quantum-inspired evolutionary algorithm (QEA) employs the probabilistic mechanism inspired by the concept and principles of quantum computing, such as a quantum bit and superposition of states [1,2,3]. In addition, multiobjective quantum-inspired evolutionary algorithm (MQEA) was developed with the purpose of solving multiobjective optimization problems [4]. MQEA provides high quality solutions close to Pareto-optimal solution set for multiobjective problems. Recently, preference-based sorting was applied to the nondominated solutions in an archive of MQEA to reflect the designer's preference in sorting them and selecting one preferred solution out of them [5,6]. However, MQEA also has a heavy computational burden like other multiobjective evolutionary algorithms. Especially, MQEA employs the nondominated sorting and crowding distance assigniment in the subpopulations, which leads to heavy computational burden.

There have been many researches for reducing the computational load for the multiobjective optimization problems [7,8,9]. This kind of research can be divided into two major issues; algorithmic development and computing power

development. Firstly, researches in terms of algorithmic development are progressed by modifying original algorithms efficiently and eliminating unnecessary parts of algorithms. Secondly, researches in terms of computing power development are progressed by distributing the computational burden of algorithms using multi-thread coding or GPU coding. The latter has much outstanding performance compared to the modification of algorithms.

In this paper, distributed computing is applied to develop distributed MQEA (DMQEA) to reduce the computational burden. It is also efficient to apply distributed computing to multiobjective evolutionary algorithms because there are many processes which can be performed simultaneously in the algorithms. Since subpopulation processes of MQEA are independent each other, the processes in each subpopulation can be performed simultaneously. To compare the performance of the proposed DMQEA, experiments are carried out for seven DTLZ functions.

The rest of this paper is organized as follows: MQEA is briefly introduced in Section 2. Section 3 proposes DMQEA. The experimental results are discussed in Section 4 and concluding remarks follow in Section 5.

2 Distributed Computing for MQEA

2.1 QEA

Building block of classical digital computer is represented by two binary states, ‘0’ or ‘1’, which is a finite set of discrete and stable state. In contrast, QEA utilizes a novel representation, called a Q-bit representation [1], for the probabilistic representation that is based on the concept of qubits in quantum computing [10]. Quantum system enables the superposition of such state as follows:

$$\alpha|0\rangle + \beta|1\rangle \quad (1)$$

where α and β are the complex numbers satisfying $|\alpha|^2 + |\beta|^2 = 1$.

Qubit is shown in Fig. 1, which can be illustrated as a unit vector on the two dimensional space as follows:

$$\begin{bmatrix} \alpha \\ \beta \end{bmatrix} \quad (2)$$

where $|\alpha|^2 + |\beta|^2 = 1$. Q-bit individual is defined as a string of Q-bits as follows:

$$\mathbf{q}_j^t = \begin{bmatrix} \alpha_{j1}^t & \left| \alpha_{j2}^t \right| & \cdots & \left| \alpha_{jm}^t \right| \\ \beta_{j1}^t & \left| \beta_{j2}^t \right| & \cdots & \left| \beta_{jm}^t \right| \end{bmatrix} \quad (3)$$

where m is the string length of Q-bit individual, and $j = 1, 2, \dots, n$ for the population size n . The population of Q-bit individuals at generation t is represented as $Q(t) = \{\mathbf{q}_1^t, \mathbf{q}_2^t, \dots, \mathbf{q}_n^t\}$.

Since Q-bit individual represents the linear superposition of all possible states probabilistically, diverse individuals are generated during the evolutionary process. The procedure of QEA and the overall structure for single-objective optimization problems are described in [1,2].

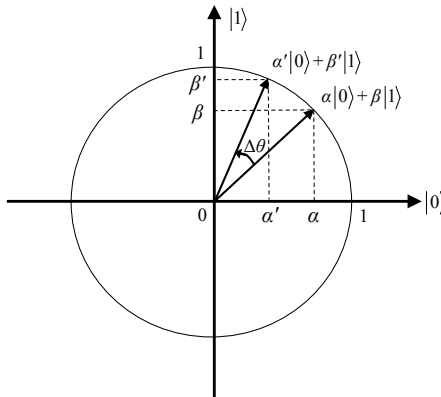


Fig. 1. Qubit described in two dimensional space

2.2 MQEA

Based on QEA, Multiobjective Quantum-inspired Evolutionary Algorithm (MQEA) was developed to solve multiobjective problems [4]. MQEA is designed by incorporating QEA with fast non-dominated sorting and crowding distance assignment. MQEA provides the solutions close to Pareto-optimal solution set for multiobjective problems. Overall procedure of MQEA is summarized in Algorithm 1. Each step is described in the following.

Algorithm 1. Procedure of MQEA

- 1: $t \leftarrow 0$
 - 2: Initialize $Q_k(t)$
 - 3: Observe the states of $Q_k(t)$ and form $P_k(t)$
 - 4: Evaluate $P_k(t)$ and store all solutions in $P_k(t)$ into $P(t)$
 - 5: Copy the nondominated solutions in $P(t)$ to $A(t)$
 - 6: **while** (not termination condition) **do**
 - 7: $t \leftarrow t + 1$
 - 8: Make $P_k(t)$ by observing the states of $Q_k(t - 1)$
 - 9: Evaluate $P_k(t)$
 - 10: Form $P_k(t)$ through the fast nondominated sorting and crowding distance sorting
 - 11: Store all solutions in every $P_k(t)$ into $P(t)$
 - 12: Form $A(t)$ by nondominated solutions in $A(t - 1) \cup P(t)$
 - 13: Migrate randomly selected solutions in $A(t)$ to every $R_k(t)$
 - 14: Update $Q_k(t)$ using Q-gates referring to the solutions in $R_k(t)$
 - 15: **end while**
-

1), 2) In this step, $Q_k(0)$ is initialized with $1/\sqrt{2}$, where $i = 1, 2, \dots, m$, $j = 1, 2, \dots, n$, and $k = 1, 2, \dots, s$. Note that m is the string length of Q-bit individual, n is the subpopulation size, and s is the number of subpopulations.

3) Binary solutions in $P_k(0)$ are formed by observing the states of $Q_k(0)$. One binary solution has a value either 0 or 1 according to the probability either $|\alpha_i^0|$ or $|\beta_i^0|$ as follows:

$$x_i^0 = \begin{cases} 0 & \text{if } \text{rand}[0,1] \leq |\alpha_i^0|^2 \\ 1 & \text{if } \text{rand}[0,1] > |\alpha_i^0|^2. \end{cases} \quad (4)$$

4) Each binary solution, \mathbf{x}_j^0 , in $P_k(0)$ is evaluated. All the solutions in $P_k(0)$ are stored in $P(0)$.

5) Archive $A(0)$ is filled with nondominated solutions in $P(0)$.

6), 7) The process terminates if the number of generation reaches the termination number.

8), 9) Binary solutions in $P_k(t)$ are generated through the multiple observing the states of $Q_k(t-1)$ and fitness values are calculated for each binary solution.

10) Individuals in the previous population and current population are sorted by the fast nondominated sorting and the crowding distance sorting and select n individuals [11]. $P_k(t)$ is formed with n selected individuals.

11) All solutions in every $P_k(t)$ are copied to $P(t)$.

12) An archive $A(t)$ is formed by nondominated solutions in the previous archive and global population ($A(t-1) \cup P(t)$)

13) Solutions in current archive are randomly selected and solutions in every reference population are randomly replaced by the selected solutions. Global random migration procedure occurs at each and every generation.

14) Fitness values in each subpopulation are compared, and then decided the update direction of Q-bit individuals. the rotation gate $U(\Delta\theta)$ is employed as an update operator for Q-bit individuals, which is defined as follows:

$$\mathbf{q}_j^t = \mathbf{U}(\Delta\theta) \cdot \mathbf{q}_j^{t-1} \quad (5)$$

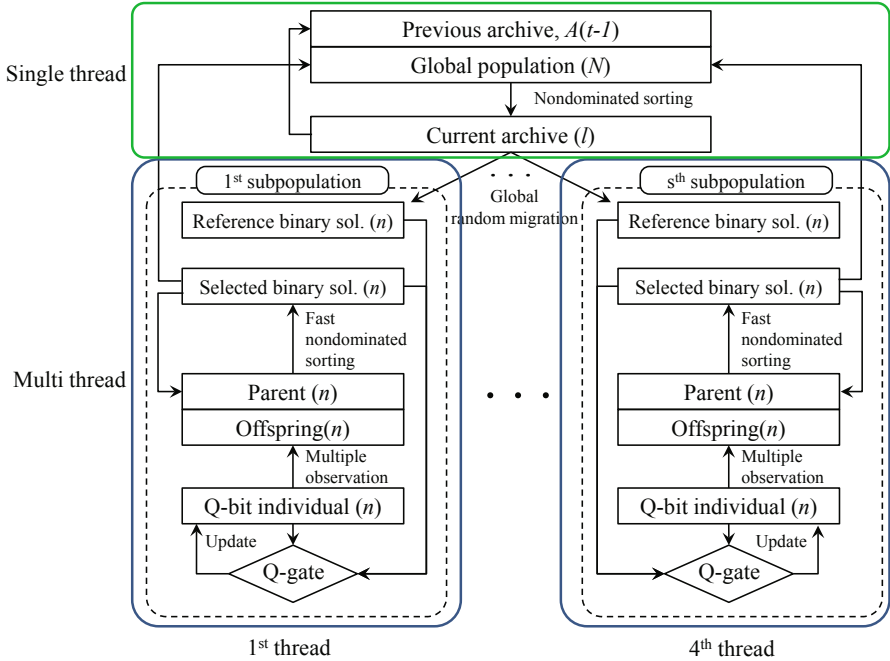
with

$$U(\Delta\theta) = \begin{bmatrix} \cos(\Delta\theta) & -\sin(\Delta\theta) \\ \sin(\Delta\theta) & \cos(\Delta\theta) \end{bmatrix}$$

where $\Delta\theta$ is the rotation angle of each Q-bit.

3 DMQEA

In recent years, computer-related technological advances such as multi-threading and GPU processing enable to reduce the computing time significantly. In this paper, DMQEA is proposed by applying multi-thread coding into MQEA. The main difference of DMQEA compared to MQEA is that each and every subpopulation, depicted in Fig. 2, goes through the evolutionary process simultaneously. The details of the subpopulation process of the DMQEA are as follows. Each subpopulation process is performed by the corresponding thread. In this paper, four subpopulations are executed at one time because experimental PC provides four threads. In this regard, thread synchronization is needed in each and every generation because computational times of threads are all different. Therefore, it

**Fig. 2.** Procedure of the DMQEA**Table 1.** Parameter setting of the DMQEA for DTLZ problems

Parameters	Values
The number of generations	3,000
The number of subpopulations (s)	4
The number of multiple observations	10
The rotation angle ($\Delta\theta$)	0.23π

is required to wait until all the thread processes are finished. And then, obtained solutions from the subpopulations are stored in the global population. The rest processes of DMQEA such as archive generation and migration are executed in single-thread because they are affected by the other processes.

4 Experimental Results

Experiments were carried out under Intel Core i5 650 CPU which provides four threads. Clock speed of PC is 3.20GHz and operating system is Windows 7 32bit. Parameter setting for experiments is given in Table 1. The experiments were carried out under three conditions of different sizes of the subpopulation and different numbers of objectives. The number of variables for each DTLZ

Table 2. Comparisons of computation times between single and multi-thread MQEAs for seven DTLZ functions (unit: second)

(a) subpopulation size: 25, objectives: 7

Problem	Single-thread	Multi-thread
DTLZ1	501.0	315.1
DTLZ2	532.0	370.6
DTLZ3	585.1	446.0
DTLZ4	515.6	308.6
DTLZ5	528.4	414.6
DTLZ6	539.9	442.8
DTLZ7	591.1	473.4
Average	541.9	395.9

(b) subpopulation size: 25, objectives: 3

Problem	Single-thread	Multi-thread
DTLZ1	427.1	298.1
DTLZ2	455.3	304.3
DTLZ3	492.8	361.1
DTLZ4	445.9	245.9
DTLZ5	479.5	324.3
DTLZ6	471.5	349.1
DTLZ7	498.5	354.3
Average	467.2	319.6

(c) subpopulation size: 50, objectives: 3

Problem	Single-thread	Multi-thread
DTLZ1	1438.8	1013.5
DTLZ2	1466.6	1017.7
DTLZ3	1513.3	1331.5
DTLZ4	1452.0	987.5
DTLZ5	1515.3	1259.4
DTLZ6	1498.9	969.7
DTLZ7	1596.4	1032.5
Average	1497.3	1087.4

function was set to 11 for DTLZ1, 16 for DTLZ2 to DTLZ6, and 26 for DTLZ7 function if the number of objectives is seven. Otherwise, the number of variables for each DTLZ function was set to 7 for DTLZ1, 12 for DTLZ2 to DTLZ6, and 22 for DTLZ7 function.

Table 2 shows the computation time of processing MQEAs by single-thread and multi-thread with three different conditions on subpopulation size and the number of objectives. As shown in the table, the processing time computed by multi-thread is about 70% lower than that by single-thread.

5 Conclusion

This paper proposed DMQEA to reduce the computational time of MQEA. The main difference of DMQEA compared to MQEA was that the processes in each subpopulation are executed in the multiple threads. The reason why distributed computing was applied to subpopulation processes is that they contains heavy computational processes such as nondominated sorting and crowding distance assignment. To demonstrate the effectiveness of the proposed DMQEA, comparisons of MQEAs with single-thread and multi-thread were carried out for seven DTLZ functions. Results showed that DMQEA reduces an execution time significantly. However, DMQEA still has a problem of computation time to be applied to real time applications. Therefore, it needs to be more improved as a future work.

Acknowledgments. This research was supported by the MKE (The Ministry of Knowledge Economy), Korea, under the Human Resources Development Program for Convergence Robot Specialists support program supervised by the NIPA (National IT Industry Promotion Agency) (NIPA-2012-H1502-12-1002).

References

1. Han, K.-H., Kim, J.-H.: Quantum-inspired evolutionary algorithm for a class of combinatorial optimization. *IEEE Trans. Evol. Computat.* 6(6), 580–593 (2002)
2. Han, K.-H., Kim, J.-H.: Quantum-inspired evolutionary algorithms with a new termination criterion, He gate, and two phase scheme. *IEEE Trans. Evol. Computat.* 8(2), 156–169 (2004)
3. Han, K.-H., Kim, J.-H.: On the analysis of the quantum-inspired evolutionary algorithm with a single individual. Paper presented at IEEE Congress Evolutionary Computation, pp. 9172–9179 (2006)
4. Kim, Y.-H., Kim, J.-H., Han, K.-H.: Quantum-inspired multiobjective evolutionary algorithm for multiobjective 0/1 knapsack problems. Paper presented at IEEE Congress Evolutionary Computation, pp. 2601–2606 (2006)
5. Kim, J.-H., Han, J.-H., Kim, Y.-H., Choi, S.-H., Kim, E.-S.: Preference-based Solution Selection Algorithm for Evolutionary Multiobjective Optimization. *IEEE Trans. Evol. Computat.* 16(1), 20–34 (2012)
6. Ryu, S.-J., Lee, K.-B., Kim, J.-H.: Improved version of a multiobjective quantum-inspired evolutionary algorithm with preference-based selection. Paper presented at IEEE Congress Evolutionary Computation, pp. 1–7 (2012)
7. Tan, K.C., Yang, Y.J., Goh, C.K.: A distributed Cooperative coevolutionary algorithm for multiobjective optimization. *IEEE Trans. Evol. Computat.* 10(5), 527–549 (2006)
8. Deb, K., Zope, P., Jain, A.: Distributed Computing of Pareto-Optimal Solutions with Evolutionary Algorithms. In: Fonseca, C.M., Fleming, P.J., Zitzler, E., Deb, K., Thiele, L. (eds.) *EMO 2003. LNCS*, vol. 2632, pp. 534–549. Springer, Heidelberg (2003)
9. Tan, K.C., Tay, A., Cai, J.: Design and implementation of a distributed evolutionary computing software. *IEEE Trans. Syst. Man Cybern. C, Appl.* 33(3), 325–338 (2003)

10. Hey, T.: Quantum computing: an introduction. *Computing and Control Eng. J.* 10(3), 105–112 (1999)
11. Deb, K., Pratap, A., Agarwal, S., Meyarivan, T.: A fast and elitist multiobjective genetic algorithm: NSGA-II. *IEEE Trans. Evol. Computat.* 6(2), 182–197 (2002)
12. Zitzler, E.: Evolutionary algorithms for multiobjective optimization: methods and applications. Berichte aus der Informatik. Shaker Verlag, Aachen-Maastricht (1999)

Neuro-Evolution of Escape Behaviour under High Level of Deception and Noise

Shir Li Wang, Kamran Shafi, Chris Lokan, and Hussein A. Abbass

School of Engineering and Information Technology,
University of New South Wales,
ADFA Campus,
Northcott Drive, Canberra ACT, 2600, Australia
shir.wang@student.adfa.edu.au,
{k.shafi,c.lokan,h.abbass}@adfa.edu.au

Abstract. Red teaming is an approach to studying a task by anticipating the actions of an adversary (“red”) who wishes to affect the achievement (by “blue”) of that task. Computational red teaming is a recent approach that extends in red teaming concept in cyber space and benefits from replacing the physical *red* and *blue* with simulated entities. In this study, we focus on the use of multiple strategies in computational red teaming and the factors that influence the selection of strategy. The reason for the use of multiple strategies is to simulate variability observed in human choice. The use of multiple strategies are demonstrated by the generation of diversified solutions by evolutionary robotics while the factors that influence the preferences of strategies are perception and deception. This paper presents an attempt at exploring and modeling the effect of *red* through the evolutionary method in a synthetic red teaming game environment.

Keywords: red teaming, computational red teaming, evolutionary robotics, perception, deception.

1 Introduction

Red teaming is an approach to study a task by anticipating adversarial behaviours. Two entities are involved, namely *red* and *blue*. A *blue* entity refers to the entity which would like to achieve the task while a *red* entity refers to the circumstances and/or entities which may have an adversarial impact on the task. In other words, the *blue* and *red* entities have conflicting interests. Red teaming is not a new concept and can be traced back to about 500 B. C. such as in The Art of War by Sun Tzu [5].

The red teaming concept has expanded from its original military and physical-realm-based applications to civilian and computational-based applications. The reason for its popularity is that the concept can be mapped into domains which share similar characteristics, such as adversarial learning, risk assessment, and behavioural decision making, as long the domains contain entities that have potential to influence the decision making process.

The focus of our paper is on the use of computational red teaming (“CRT”) to learn about the opponent behaviour, whereby we are interested to know the possible effects that *red* can cause on *blue* with an explicit representation of *red* and *blue* in a synthetic game environment. The purpose of our approach is to extract insights from the study and apply them to other related domains. There are two central elements that are considered in our setup of CRT, i.e., the use of multiple strategies in a task and the factors that influence the selection of strategies. The use of multiple strategies is motivated by the framing effects in humans. Although variability exists in human choice, it is undeniable that we will observe inconsistency of humans’ strategies in the same task, where the use of different strategies may lead to the similar or exactly the same outcome.

The characteristics of humans have played a very important role in determining the computational *red* in our setup of CRT. Highly complex systems, such as those found in humans, are robust and adaptive; this has led to the development of biologically-inspired approaches in solving a task. Therefore, we decide to use evolutionary robotics (“ER”), which is biologically inspired as well, for the computational *red*. ER refers to the use of evolutionary computation in the autonomous production of behavioral robot controllers. It is chosen as the approach to simulate the *red*’s behavior because it approximates the “bounded rationality” introduced by Simon [12], which lies on the ability to learn and evolve to produce functional behavior.

The rest of this paper is organised as follows. Section 2 presents related work on red teaming and its potential in other domains. In Section 3 we present the methodologies to synthesize the simulation environment. Section 4 describes the experimental setup followed by the results and discussion of the carried out experiments in Section 5. Finally, Section 6 presents the conclusion that we reach and also the future work.

2 Background Material

Although red teaming as a new concept can be traced back to thousand years ago, it still remains a developing and evolving concept which has great potential to offer. Only a few years ago, the importance of the red teaming concept was formally recognized in military community with the introduction of the Army Red Team Leader (ARTL) course at the University of Foreign Military and Cultural Studies (UFMCS), Fort Leaven in 2006. The Canadian military has also shown intention to establish the concept and its capability [7]. The concept was limited to the physical realm originally, but it has been extended to computer simulation owing to advancements in computer technology such as shown in [14,7]. CRT is no longer limited to military applications. Its implementation has been and can be further extended to security systems, commercial organizations, governments, and even countries to study the effectiveness of its strategies in anticipating adversarial behaviours.

Most of research studies on adversarial learning focus on either the possible adversarial attacks faced by machine learning algorithms, development of defence strategies against adversarial attacks, or both. Several research studies based on these areas can be found in [8,9,13,6,4].

The studies conducted in adversarial learning can mapped into a CRT problem, in which the adversarial attacks are referred as *red* while the underlying machine learning algorithms against the attacks are referred as *blue*. If the interest of the decision makers is to know the limitation/weakness of the underlying machine learning algorithms that are used to protect against adversarial attacks, CRT will be used to discover vulnerabilities. On the other hand, CRT can be used to learn about the opponents if the interest is to understanding an adversary's impact in a problem. Given that decision makers have sufficient information of the relevant aspects of the adversaries, if not absolutely complete, CRT can be used to study the possible action taken by the opponents in the environment. The exploration of action space allows decision makers to anticipate the actions from the opponents and organise their strategies in order to compete with opponents.

According to the definition from International Standards Organization (ISO) [3], risk is “the effect of uncertainties on objectives”. The definition consists of two important elements: uncertainty and objective. It means the effect of uncertainty needs to be measured relative to the objective, when risk assessment is performed. In risk assessment, the uncertainties in objective(s) are viewed as *red* while the actions taken to achieve the objective(s) are referred as *blue*. The use of CRT to explore a space of possibilities offers a great potential in risk assessment; the potential is demonstrated in [1,2], whereby a framework known as Multiobjective Evolutionary Based Risk Assessment (MEBRA) is developed to explore and evaluate the algorithms under risk.

Research on behavioural decision, especially the construction of preferences, plays an important role in decision making, because a better understanding on it could help us to manage our preferences more effectively. The construction of preferences depends highly upon task, context, and individual difference factors [11]. The study on the warfare in red teaming as shown in [14] shows a good example of research on behavioural decision, based on the implementation of CRT which involves evolutionary computation to simulate a warfare between the *blue* and *red* teams. From the study, the defence is able to know the possible appropriate combinations of personalities for the *blue* team that should be deployed for a given combination of personalities for the *red* team. In short, *CRT* has great potential to offer in above mentioned domains and any insight gained from *CRT* can be beneficial to these domains.

3 Methodology

In this section, we present the description of the simulation environment which includes the constraints of the environment, strategies for both agents, and parameter selection that influence the *blue*'s strategies.

3.1 Synthetic Simulation Environment

In this study, we represent CRT environment by a game. The game environment involves two agents, known as *blue* and *red*, where *blue* is represented by a cat and *red* is represented by a rat. The agents have opposite goals, *blue* tries to catch *red* while *red* tries to get away from *blue*. The whole scenario can be viewed exactly as a match between a cat and rat in nature. *Blue* and *red* are represented by coloured triangles. The perimeters of the circles surrounding *blue* and *red* (shown in dotted lines) represent the possible locations that the agents can move to in one time step, due to the constraints that have been imposed on them which will be explained in the following.

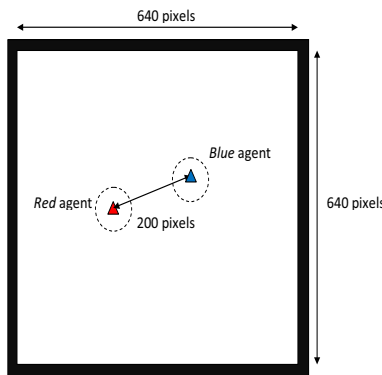


Fig. 1. Schematic representation of the initial setup of the *blue* and *red* agents in the game environment

Constraints. The environment is bounded by several constraints.

- Both agents are placed in a 2D grid environment of $16 \leq x \leq 640$ and $16 \leq y \leq 640$, where x and y refer to coordinates in pixels (the coordinates (x, y) start with the value 16 instead of 0 because the 2D grid environment is surrounded by rectangular walls).
- The speeds for the *blue* and *red* agents (represented by ξ_b and ξ_r respectively) are both fixed at 10 pixels per step ($\xi_b = \xi_r = 10$). The reason that the speeds for both agents are set to be equal is to emulate the scenario that both agents have equal capabilities, so that capturing can only occur through good strategy.
- The movements of the agent are determined by their travel angle; the travel angles for the *blue* and *red* agents are denoted as θ_b and θ_r respectively. The values of θ_b and θ_r are within the range of $[0, 2\pi]$. The generation of travel angles depends on the strategies used by the agents.

The game starts and ends as follows:

- The initial locations for both agents are randomly generated, with distance between them, $d_{opp} = 200 \text{ pixels}$.
- The game is terminated if one of the following constraints is met:
 - the distance between the *red* agent and *blue* agent, $d_{opp} < D_{min}$, with $D_{min} = 20 \text{ pixels}$. D_{min} refers to the distance at which *red* is considered to be caught by *blue*.
 - maximum number of time steps is reached, $S = 100$ steps.

Strategies. The movements for both agents are determined by their strategies to generate travel angles. In other words, the generation of travel angles depends on their decision models. *Blue*'s strategies are scripted. *Red*'s strategies are determined by ER.

The strategy of *blue* is based on the perception that it has of *red* and also with the acknowledgement of the existence of an intelligent *red* agent. *Blue*'s perception is affected by the noise in the observations. The noise is denoted $\hat{\alpha}^{(t)}$. Based on the perception, the *blue* arranges its action to deceive *red*. To model deception by *blue*, we introduced two parameters: namely deception cycle length, N_D ; and deception range, $\zeta^{(t)}$.

The pseudo code shown in Algorithm 1 describes the strategy used by *blue*. The parameters used in the strategy are as follows:

- $\hat{P}_b^{(t)}$ - Actual position of the *blue* agent at time t .
- $\hat{P}_r^{(t)}$ - Actual position of the *red* agent at time t .
- $\hat{P}_{ir}^{(t)}$ - Intel reporting on the position of the *red* agent perceived by the *blue* agent at time t .
- $\hat{\alpha}^{(t)}$ - the relative change in x and y coordinates due to the level of noise added to $\hat{P}_r^{(t)}$ and it is expressed as $\hat{\alpha}^{(t)} = (\Delta x, \Delta y)$.
- Counter - Game clock.

Blue uses the information it receives about *red* to generate deceptive movements, through the adjustment of N_D and $\zeta^{(t)}$.

For the *red* agent, ER is used to as the decision-making model to construct its decision behaviour. The main reason for the selection of ER is its abilities to learn and evolve, which are analogical to human's biological adaptation. These abilities are handled by the neural networks and genetic algorithm ("GA") respectively. Another reason that encourages the use of ER is its ability to produce a population of diversified solutions approximating the variability of human choice. Owing to the variability of human choice, we will observe inconsistency of humans' strategies in the same task.

Parameter Selection. $\hat{\alpha}^{(t)}$ represents the noise in the *blue*'s perception, while N_D and $\zeta(t)$ represent to the deception generated by the *blue* agent. The *blue* agent's strategies are influenced by the combinations these 3 parameters. Table 1 shows the 10 possible combinations of experimental setup based on $\hat{\alpha}^{(t)}$, N_D and $\zeta(t)$.

Algorithm 1. Update intel and position

```

while Counter is not stopped do
    Update intel:
     $\hat{P}_{ir}^{(t)} \leftarrow \hat{P}_r^{(t)} + \hat{\alpha}^{(t)}$ 
    Update position:
     $\theta_c = \hat{P}_{ir}^{(t)} - \hat{P}_b^{(t)}$ 
    if (Counter modulo  $N_D$ ) = 0 then
         $\theta_b^{(t)} = \theta_c^{(t)}$ 
    else {(Counter modulo  $N_D$ )  $\neq$  0}
         $\theta_b^{(t)} = \theta_c^{(t)} + \zeta^{(t)}$ 
    end if
end while

```

Table 1. The combinations of $\hat{\alpha}^{(t)}$, N_D and $\zeta^{(t)}$

Combination	$\hat{\alpha}^{(t)}$	N_D	$\zeta^{(t)}$
1		1	0
2		5	$U(-15^\circ, 15^\circ)$
3	0	5	$U(-30^\circ, 30^\circ)$
4		10	$U(-15^\circ, 15^\circ)$
5		10	$U(-30^\circ, 30^\circ)$
6		1	0
7		5	$U(-15^\circ, 15^\circ)$
8	$U(0, 20)$	5	$U(-30^\circ, 30^\circ)$
9		10	$U(-15^\circ, 15^\circ)$
10		10	$U(-30^\circ, 30^\circ)$

The first and sixth combinations in Table 1 represents the scenarios when the *blue* agent moves in the direction where it expects the *red* agent to be, $\hat{P}_{ir}(t)$. In simple words, these two scenarios mean that the *blue* is not deceptive.

The other combinations represent scenarios in which the *blue* agent is deceptive, and deviates from its expected trajectory (which leads to the capturing of the *red* agent) once after a number of steps. The deviation from the trajectory depends on the values of $\zeta^{(t)}$, which is based on an uniform distribution. The maximum and minimum deviations are selected as 15° and 30° respectively, so that the *blue* agent does not deviate too far away from the original trajectory which may end up with a failure to capture.

4 Experimental Design

The main objective of this experiment is to understand the behaviours exhibited by a *red* agent facing a deceptive *blue* agent in the proposed game environment.

To achieve the objective, we need to fix the behaviour of *blue* and evolve *red*'s strategies. Given that the behaviour of *blue* is influenced by noise and deception, different scenarios are created based on the configurations of $\alpha^{(t)}$, N_D and $\zeta^{(t)}$.

The neuroevolution suggested by [10] is used as the controller of *red*, with GA responsible for evolving a population of neural networks. *Red* evolves in the direction of accomplishing its goal, without any preferences to how should it achieve its goal. For each scenario, *red* feeds the relevant input variables into the neural network and uses the decision variables from the neural network to arrange its movements.

The input and decision variables are represented by a vector of real number as following:

- Input variables:
 1. the relative angle between the *blue* and *red*, $\beta^{(t)}$.
 2. the relative distance between the *blue* and *red* agents at time t , $d_{opp}^{(t)}$.
 3. the relative change of β at time t , $\Delta\beta^{(t)}$.
 4. the relative change of d_{opp} at time t , $\Delta d_{opp}^{(t)}$.
 5. the relative distance to the wall that the *red* agent faces at time t , $d_{wall}^{(t)}$.
- Decision variables:
 1. travel angle of the machine *red* agent from the machine, $\theta_{mr}^{(t)}$
 2. travel angle of the *blue* agent, $\theta_{pb}^{(t)}$

When the input information received by *red*'s sensor, the input variables are in their actual ranges; but they are mapped into the range of [0, 1] before they are fed into the neural networks to produce the output variables. The output variables are also in the range of [0, 1] and they are mapped accordingly to their actual ranges before they are used by *red*. The movements for both agents are updated simultaneously based on their strategies until the game is terminated. The learning task for the neural network is to predict the travel angle of the *blue* agent, $\theta_{pb}^{(t)}$ which is different from the evolutionary goal. The difference between the predicted ($\theta_{pb}^{(t)}$) and actual travel angle $\theta_b^{(t)}$ of the *blue* agent is used to adjust the connection weights of the network through back-propagation.

The goal of the *red* agent is to survive as long as possible. As long as the *red* agent is not caught by the *blue* agent, it is considered to succeed in achieving its goal. The longer the *red* agent can survive, the more likely it is that it will win in the game. The fitness function is defined as follows:

$$F = \frac{1}{N_G} \sum_{g=1}^{N_G} h_g \quad (1)$$

$$h_g = \begin{cases} 1 & \text{if } d_{opp} > D_{min} \\ 0 & \text{otherwise} \end{cases}$$

where h_g refers to the frequency of the *red* agent meeting the constraints ($d_{opp} > D_{min}$) in the g^{th} game, with $1 \leq g \leq N_G$, where N_G refers to the number of games that are repeated for each scenario (we use $N_G = 10$ in this experiment;

thus results are averaged over 10 games). The frequency of meeting the constraint is calculated as F , and is accumulated for each step. Based on the above equations, the fitness function measures the performance of the *red* agent to extend its life span.

The strategies in the population are used by *red* as a decision-making model to determine its movements in the grid environment. These strategies are evolved based on selection, crossover, mutation and elitism to form a new generation of strategies (*gen 1*) from the previous generation (*gen 0*). In GA, individuals from the population that have the highest fitness are selected to reproduce based on the *binary tournament* selection method. Once the new population has been created by selective reproduction, *one point* crossover and mutation are performed on the offspring. The individuals that have gone through selective reproduction, crossover and mutation form the new generation *gen 1*. Then, the top 10% parents (from *gen 0*) are copied to the offspring population (*gen 1*), replacing the worst 10% of the members of from *gen 1*. The whole process is repeated until the maximum number of generations is met, *gen* = 200.

The ultimate goal of our research is not to use evolutionary computation to win or lose in the game but rather to use the advances in computation models to mimic or reproduce the limited computational capabilities of humans interacting with the task environment to produce bounded rationality. Since the focus of the research is not on system optimization, we do not focus much on tuning the parameters involved in either GA or neural networks. A fixed neural network architecture is used, and GA is used to evolve the connection weights of the neural network. The neural network for the *red* agent's control system is a multi-layer perceptron of sigmoid units. That is, instead of letting the network size be adjusted as part of the evolutionary process, a fixed network size is adopted beforehand. The input layer, hidden layer and output layer consist of 5, 7 and 2 neurons respectively. Other relevant parameters such as learning rate and momentum rate are also fixed for all neural networks. The learning rate η for the network is set as 0.1, and the momentum rate γ is set as 0. Each connection weight of the neural network ranges in the interval $[-1, 1]$. Given that the architecture of the neural network is fixed, each chromosome in the evolutionary process represents a vector of weights for the input-hidden layers and the hidden-output layers.

5 Analysis and Result

For ease of discussion, Table 2 summarizes the combinations of perception and deception.

Figure 2 shows the best capture times (averaged over 30 runs) for *blue*, for different combinations of perception and deception

Referring to Figures 2(a) to 2(b), it is no surprise to observe that *blue* takes longer to capture *red* when the received information changes from being accurate to noisy, when it has the same frequency and degree of deception. A delay and/or some noise in the received information will affect *blue*'s perception of *red*'s actual position, thus requiring longer *best capture time* from *blue*.

Table 2. Description about perception and deception

Definition	Parameter	Value	Description
Perception	Noise	$\alpha = 0$ $\alpha = U(0, 20)$	Accurate Noisy
Deception	Deception frequency	$N_D = 10$ $N_D = 5$	Infrequent Frequent
	Deception degree	$\zeta^{(t)} = U(-15^\circ, 15^\circ)$ $\zeta^{(t)} = U(-30^\circ, 30^\circ)$	Low High
	Combination	$N_D = 1, \zeta^{(t)} = 0$	No deception

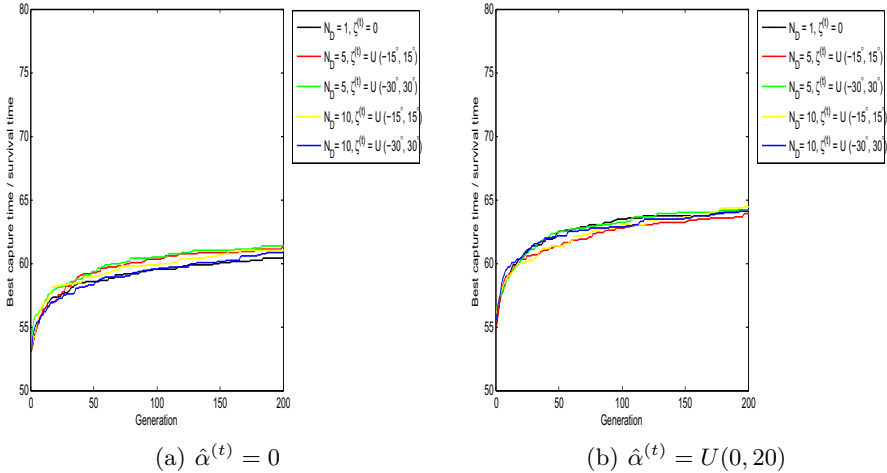
**Fig. 2.** The plots of *best capture time* by fixing $\hat{\alpha}^{(t)}$ and varying $N_D, \zeta^{(t)}$

Figure 3 zooms in on the last 50 generations of Figure 2. Figure 3(a) shows the *best capture times* of the *blue* associated with different deceptions upon receiving accurate information. Under such conditions, the non-deceptive *blue* requires a shorter *best capture time* than the deceptive *blue*. By comparing Figures 3(a) and 3(b), it is interesting to observe that best capture times of the deceptive *blue* becomes closer to or even better than the non-deceptive *blue* as the received information changes from being accurate to noisy.

From *red*'s perspective, the *best capture time* of *blue* is the converse of the *best survival time* of *red*. Continuous increments of the best survival time of *red* can be observed in Figures 2(a) and 2(b). This observation means learning does occur within the *red* agent.

These findings lead us to believe that that the use of deception helps to improve the performance of *blue* in capturing *red*, given that the perception of *blue* about *red* contains noise. In other words, deception could be used as a potential solution to counterbalance the effects of noise in the received information.

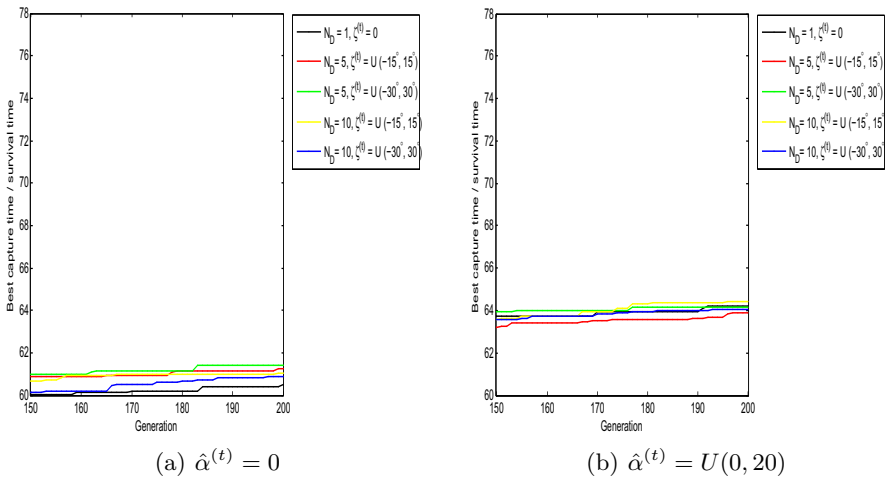


Fig. 3. Zoom in of Figure 2 for the last 50 generations

6 Conclusion

This study focuses on two central elements of decisions: the use of multiple strategies in CRT, and the factors that influence the use of strategies. In our study, the use of multiple strategies is demonstrated by the generation of diverse solutions by ER. On the other hand, the factors that influence the preferences of strategies are perception and deception.

The results shown in this study demonstrate the ability of deception to counterbalance the effects of noise and delay that exist in received information.

References

1. Abbass, H.A., Alam, S., Bender, A.: Application notes: Mebra: multiobjective evolutionary-based risk assessment. Computational Intelligence Magazine 4, 29–36 (2009), <http://dx.doi.org/10.1109/MCI.2009.933098>
2. Alam, S., Shafi, K., Abbass, H.A., Barlow, M.: An ensemble approach for conflict detection in free flight by data mining. Transportation Research Part C 17(3), 298–317 (2009)
3. Australia, S.: AS/NZ 4360: Risk Management. Standards Australia, Standard, AS/NZS 4360 (1999)
4. Barreno, M., Nelson, B., Joseph, A.D., Tygar, J.: The security of machine learning. Machine Learning (2010)
5. Griffith, S.B.: Sun Tzu - The Art of War. Oxford University Press (1963)
6. Jorgensen, Z., Zhou, Y., Inge, M.: A multiple instance learning strategy for combating good word attacks on spam filters. Journal of Machine Learning Research 9, 1115–1146 (2008)
7. Lauder, M.: Red dawn: The emergence of a red teaming capability in the canadian forces. Canadian Army Journal 12, 25–36 (2009)

8. Nelson, B., Joseph, A.D.: Bounding an attack's complexity for a simple learning model. In: Proceedings of the First Workshop on Tackling Computer System Problems with Machine Learning Techniques (SysML), pp. 1–5 (2006)
9. Newsome, J., Karp, B., Song, D.: Paragraph: Thwarting signature learning by training maliciously. In: Zamboni, D., Kruegel, C. (eds.) RAID 2006. LNCS, vol. 4219, pp. 81–105. Springer, Heidelberg (2006)
10. Nolfi, S., Parisi, D., Elman, J.L.: Learning and evolution in neural networks. *Adaptive Behavior* 3(1), 5–28 (1994),
<http://adb.sagepub.com/content/3/1/5.abstract>
11. Payne, J.W., Bettman, J.R.: Behavioral decision research: A constructive processing perspective. *Annual Review of Psychology* 43(1), 87–131 (1992)
12. Simon, H.A.: A behavioral model of rational choice. *The Quarterly Journal of Economics* 69(1), 99–118 (1955), <http://www.jstor.org/stable/1884852>
13. Veloso, A., Meira Jr., W.: Lazy associative classification for content-based spam detection. In: The Proceedings of the Latin American Web Congress (2006)
14. Yang, A., Abbass, H.A., Sarker, R.: Characterizing warfare in red teaming. *IEEE Transactions on Systems, Man, and Cybernetics, Part B: Cybernetics* 36(2), 268–285 (2006)

A Homogeneous Distributed Computing Framework for Multi-objective Evolutionary Algorithm

Ki-Baek Lee, Jong-Hwan Kim, and Fellow, IEEE

Department of Electrical Engineering, KAIST,
335 Gwahangno, Yuseong-gu, Daejeon 305-701, Republic of Korea
{kblee,johkim}@rit.kaist.ac.kr

Abstract. This paper proposes a homogeneous distributed computing (HDC) framework for multi-objective evolutionary algorithm (MOEA). In this framework, multiple processors divide a work into several pieces and carry them out in parallel. Every processor does its task in a homogeneous way so that the overall procedure becomes not only faster but also fault-tolerant and independent to the number of processors. To implement this framework into an evolutionary algorithm, the evolutionary process of multi-objective particle swarm optimization (MOPSO) is employed. The effectiveness of the proposed framework is demonstrated by empirical comparisons between the results with the different numbers of processors, one and four. Seven DTLZ functions are used as benchmark functions and hypervolume, diversity, and evaluation time are used as comparison metrics. The results indicate that the evaluation time is significantly reduced by the proposed framework without any loss of overall solution quality and diversity.

Keywords: Distributed computing, Multi-Objective Evolutionary Algorithm, Particle Swarm Optimiztion.

1 Introduction

Recently in most of real world problems, the importance of multi-objective evolutionary algorithm (MOEA) has been in the limelight. MOEA is inspired from evolution phenomena of nature and searches for solutions through an evolutionary process. By using MOEA, the parameters of the problems can be efficiently optimized considering multiple objectives simultaneously [1–4]. However, MOEA may require significant computation time as the number of objectives or the number of parameters increases. In this case, some techniques to handle time-consuming tasks can be helpful.

Distributed computing is one of the most promising techniques. Through distributed computing scheme, tasks can be distributed to available processors and processed in parallel. K. Deb *et al.* proposed an approach for finding multiple Pareto-optimal solutions with a distributed computing system [5]. In this approach, each process was in charge of a particular portion of Pareto optimal region for distributed computing. K. C. Tan *et al.* suggested a distributed cooperative coevolutionary algorithm (DCCEA) [6]. To design this algorithm suitable for distributed computing, each parameter was assigned to a subpopulation and these subpopulations were partitioned into groups depending on the number of available peer processors. These studies showed that not only

the computation time was reduced but also the diversity of the obtained solution set was improved by incorporating distributed computing within MOEA. However, in spite of the successful results of them, there is still room for improvement. First of all, the algorithms may fail by even one faulty processor because each processor has its unique role and cannot assist each other. In addition, it is inconvenient to adjust the number of processors. Some equations or structures of the algorithms should be modified according to the number of processors. To solve those problem, homogeneous distributed computing framework can be a solution. There are several advantages of homogeneity which means every processor does the same task. Firstly, it makes algorithms more fault-tolerant. Secondly, the number of processors can be readily controlled. Thirdly, there is no need for communication between processors.

Therefore, in this paper, a homogeneous distributed computing (HDC) framework for MOEA is proposed and to implement this framework into an evolutionary algorithm, the evolutionary process of multi-objective particle swarm optimization (MOPSO) is employed. MOPSO is one of the well-known evolutionary algorithms and in particular, it is easy to implement and fast [7]. To demonstrate the effectiveness of the proposed framework, empirical comparison is carried out between the results with the different numbers of processors, one and four. Seven DTLZ functions are used as benchmark functions and hypervolume, diversity, and evaluation time are used as comparison metrics [8–10].

This paper is organized as follows. Section II proposes HDC framework and introduces multi-objective particle swarm optimization with homogeneous distributed computing (MOPSO-HDC), an implementation of it. In Section III, the experimental result of MOPSO-HDC is discussed. Finally, concluding remarks follow in Section IV.

2 Homogeneous Distributed Computing Framework for Multi-objective Evolutionary Algorithm

In this section, HDC framework for MOEA is described. The distinguishing feature of HDC framework is that multiple processors divide a work into several pieces and carry them out in parallel. In addition, every processor does its task homogeneously and as a result, it is expected that the overall procedure becomes not only faster but also fault tolerant and independent to the number of processors. As an example implementation, multi-objective particle swarm optimization with homogeneous distributed computing (MOPSO-HDC) is introduced. MOPSO is one of the well-known evolutionary algorithms and in particular, it is easy to implement and fast. Thus MOPSO-HDC is a good example for verifying the effectiveness of HDC framework.

2.1 The Proposed HDC Framework

As categorized in [11], distributed computing can be implemented through three different approaches, i.e., master-slave model, island model, and diffusion model. In the master-slave model, a master processor executes overall MOEA and slave processors handle function evaluations only. In the island model, each processor has their own sub-population and executes MOEA independently. Some solutions are migrated between the processors with certain frequency as necessary. The diffusion model is a fine-grained

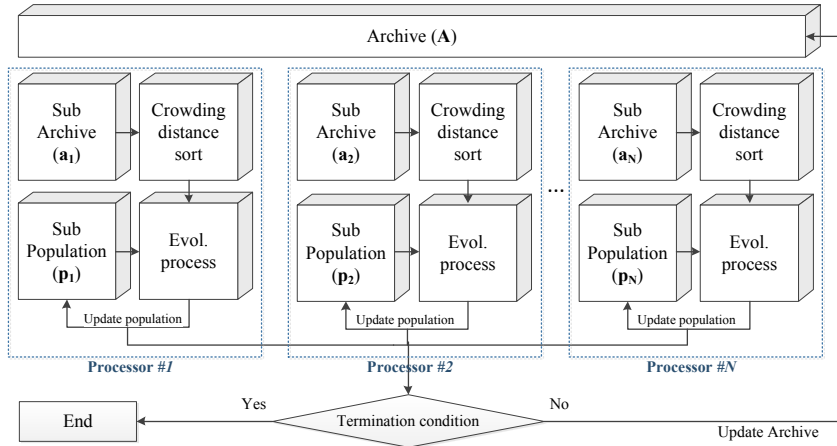


Fig. 1. Flow diagram of HDC framework

variation of the island model. The master-slave model and diffusion model cannot be implemented in homogeneous way. Therefore, in HDC framework, the island model is adopted and the task is homogeneously divided and processed.

Fig. 1 shows the flow diagram of HDC framework. In HDC framework, there are two important sets, population and archive. A population consists of individuals, which search for the solutions by updating themselves through evolutionary process. An archive consists of the non-dominated solution found by the individuals. The individuals in a global population and the non-dominated solutions in a global archive are equally distributed to the sub-population and the sub-archive of each available processor. Each processor evaluates the evolutionary process to update its sub-population with its sub-archive. After every processor finished its update, i.e. synchronization, the global archive is updated by domination test with the updated sub-populations. Finally, the global population is updated by uniting the sub-populations. By repeating these steps until a termination condition is met, desired solutions can be obtained.

2.2 The Overall Procedure of MOPSO-HDC

The overall Procedure of MOPSO-HDC can be summarized as Algorithm 1 and each step of the algorithm is described in the following.

1. Initialize a population and an archive.

The velocity and position of the individuals in a population are randomly initialized. The velocity \mathbf{v}_k and position \mathbf{x}_k of the k -th individual are the D -dimensional vectors as follows:

$$\mathbf{v}_k \in \mathbb{R}^D, \mathbf{x}_k \in \mathbb{R}^D.$$

The objective function values of each individual are calculated initially and the personal best position of each individual $p\mathbf{x}_k^t$ is also set as itself. The archive is initialized as a null set.

Algorithm 1. Multi-Objective Particle Swarm Optimization with Homogeneous Distributed Computing

1. Initialize a population and an archive.
 2. Divide the task for N available processors.
 - Split the population and the archive equally into N subgroups each.
 - Distribute them to the processors so that each processor has its own sub-population and sub-archive.
 3. Update each sub-population.

for each processor **do**

 - Calculate the crowding distances of the solutions in the sub-archive.
 - Sort the solutions based on their crowding distances.
 - for** each individuals in the sub-population **do**
 - Choose the global best position ${}^g \mathbf{x}_k^t$ from upper half of the sub-archive.
 - Update its velocity and position.
 - Evaluate the objective function values.
 - Update the personal best position ${}^p \mathbf{x}_k^t$. - end for**
 - end for**
 4. Update the global population.
 5. Update the global archive.
 6. Go back to step 2 and repeat until the termination condition is met.
-

2. Divide the task for N available processors.

The population and the archive are equally divided into N sub-populations and N sub-archives. Each processor has its own sub-population and sub-archive.

3. Update each sub-population.

To update an individual in PSO, its personal best position and a global best position are used. The personal best position has been determined from the previous step and the global best position is selected from the sub-archive. To maintain the diversity of the individuals, the crowding distances of the solutions in the sub-archive are calculated and the solutions are sorted by their crowding distances [12]. By selecting the global best position ${}^g \mathbf{x}_k^t$ randomly from the upper half of the sub-archive, the individuals can be guided with sufficient diversity. The velocity and position of each individual are updated as follows:

$$\begin{cases} \mathbf{v}_k^t = w \cdot \mathbf{v}_k^{t-1} + c \cdot \{\phi_k^{1,t}({}^p \mathbf{x}_k^{t-1} - \mathbf{x}_k^{t-1}) \\ \quad + \phi_k^{2,t}({}^g \mathbf{x}_k^t - \mathbf{x}_k^{t-1})\} \\ \mathbf{x}_k^t = \mathbf{x}_k^{t-1} + \mathbf{v}_k^t \end{cases} \quad (1)$$

where w and c are constants and $\phi_k^{1,t}$ and $\phi_k^{2,t}$ are random real values uniformly distributed in $[0, 1]$. \mathbf{v}_k^t and \mathbf{x}_k^t represent the velocity and position of the k -th individual at generation t , respectively. New random values are generated for each individual at each

Table 1. The parameter settings of the algorithm

Parameters	Values
Population size (N)	100
Number of generations	5000
Maximum archive size	500
Inertia weight (w)	$1/(2 \cdot \log 2)$
Cognitive/Social parameter (c)	$0.5 + \log 2$

and every generation. After that, objective function values of each particle are evaluated. Finally, the personal best position of each individual ${}^p\mathbf{x}_k^t$ is updated.

4. Update the global population.

The global population is updated by uniting the sub-populations.

5. Update the global archive.

The previous global archive and the updated global population is united and dominance test is performed on the union. By discarding dominated solutions, the global archive is updated.

6. Go back to step 2 and repeat until the termination condition is met.

By repeating these steps until the termination condition is met, the desired solutions can be obtained.

Note that computational complexity of the proposed algorithm is governed by the sort process, i.e. the crowding distance-based sort. Since the sort process is done by the quick sort, the algorithm has the average computational complexity of $O(n \log(n))$.

3 Experimental Result

3.1 Configurations

The parameters used in the experiment are given in Table 1. As benchmark functions, seven DTLZ functions were employed [8]. The number of objectives was set to three for every DTLZ function. The number of variables of each DTLZ function was set to 11 for DTLZ1, 16 for DTLZ2 - DTLZ6, and 26 for DTLZ7 function.

Two performance metrics, hypervolume, i.e. the size of dominated space, and diversity measure, were employed to evaluate the performance of the MOPSO-HD. Brief explanation of the metrics is provided in the following. The size of dominated space, \mathcal{S} is defined by the hypervolume of nondominated solutions [9]. The reference point to calculate \mathcal{S} was set to $(10, 10, 10)$. The quality of obtained solution set is high if this space is large. Diversity, \mathcal{D} is to evaluate the spread of nondominated solutions, which is defined as follows [10]:

$$\mathcal{D} = \frac{\sum_{k=1}^n (f_k^{(max)} - f_k^{(min)})}{\sqrt{\frac{1}{|N_0|} \sum_{i=1}^{|N_0|} (d_i - \bar{d})^2}} \quad (2)$$

where N_0 is the set of nondominated solutions, d_i is the minimal distance between the i th solution and the nearest neighbor, and \bar{d} is the mean value of all d_i . $f_k^{(max)}$ and $f_k^{(min)}$ represent the maximum and minimum objective function values of the k -th objective, respectively. A larger value means a better diversity of the nondominated solutions.

3.2 Comparison Result

Since multiple processors shared the overall optimization task, MOPSO-HDC could obtain the optimized solutions more quickly. Table 2 shows the average evaluation time

Table 2. Evaluation time ratio

Problem	$\frac{t_{\text{two processors}}}{t_{\text{one processor}}}$	$\frac{t_{\text{three processors}}}{t_{\text{one processor}}}$	$\frac{t_{\text{four processors}}}{t_{\text{one processor}}}$
DTLZ1	0.38	0.32	0.30
DTLZ2	0.51	0.40	0.31
DTLZ3	0.83	0.76	0.60
DTLZ4	0.47	0.38	0.30
DTLZ5	0.50	0.42	0.32
DTLZ6	0.44	0.39	0.30
DTLZ7	0.47	0.40	0.31

Table 3. Hypervolume and diversity measure [average(standard deviation)]

Problem	Hypervolume		Diversity	
	One processor	Four Processors	One processor	Four Processors
DTLZ1	884.37(51.51)	998.20(9.28)	29.18(17.28)	86.47(35.55)
DTLZ2	999.19(0.03)	998.74(0.39)	78.32(2.77)	78.24(3.10)
DTLZ3	100.04(221.28)	399.15(380.81)	16.48(10.08)	33.19(22.18)
DTLZ4	999.31(0.02)	998.35(1.63)	58.10(0.86)	57.92(0.96)
DTLZ5	988.64(0.23)	987.46(1.89)	54.54(0.18)	54.54(0.19)
DTLZ6	989.01(0.04)	985.96(2.59)	54.09(0.01)	54.17(0.71)
DTLZ7	708.07(1.53)	707.45(1.67)	59.07(0.26)	59.21(0.27)

Table 4. Hypothesis test ($H_0: X_{\text{four processors}} - X_{\text{one processor}} > 0$, Significance level: 0.05)

Problem	Hypervolume			Diversity		
	p-value	Reject H_0	Bayes Factor	p-value	Reject H_0	Bayes Factor
DTLZ1	0.6261	No	4.2747	0.9999	No	335.0568
DTLZ2	0.4991	No	5.0990	0.4979	No	5.0989
DTLZ3	0.9996	No	57.2779	0.9954	No	5.5556
DTLZ4	0.4981	No	5.0989	0.4938	No	5.0984
DTLZ5	0.4977	No	5.0989	0.5005	No	5.0990
DTLZ6	0.4939	No	5.0984	0.5031	No	5.0989
DTLZ7	0.4982	No	5.0990	0.5046	No	5.0987

ratio over 50 runs. As the table shows, the evaluation time decreases with increasing number of processors for every DTLZ function. Since every processor is synchronized at each iteration, time loss can occur. That is why the ratio is not exactly the same with the inverse of the number of processors.

The hypervolume and diversity of MOPSO-HDC are shown respectively in Table 3. The values were averaged over 50 runs. As the table shows, both hypervolume and diversity of MOPSO-HDC with four processor were similar to those of MOPSO with single processor. This means that there is no significant difference between the solution qualities of the two cases. To confirm this result clearly, hypothesis test was performed with those 50 pairs of sample data. Null hypothesis for every metric was defined as $X_{\text{four processors}} - X_{\text{one processor}} > 0$ and significance level was set to 0.05. As shown in Table 4, for every DTLZ function and metric, the null hypothesis could not be rejected. Bayes factor was also sufficiently large for every DTLZ function and metric which means that the odds are the null hypothesis will be turned out to be correct. As a result, the evaluation time was significantly reduced by the proposed framework without any loss of overall solution quality and diversity.

4 Conclusion

This paper proposed a homogeneous distributed computing (HDC) framework for multiobjective evolutionary algorithm (MOEA). As an implementation of this framework, multi-objective particle swarm optimization with homogeneous distributed computing (MOPSO-HDC) was also introduced. It could solve the multi-objective optimization problems (MOPs) distributing its work to several processors homogeneously. As a result, the algorithm became not only faster but also fault-tolerant and independent to the number of processors. The effectiveness of this algorithm was demonstrated by empirical comparison between the results with the different numbers of processors, one and four. The comparison result indicated that the evaluation time was significantly reduced by the proposed framework without any loss of overall solution quality and diversity.

Acknowledgement. This research was supported by Basic Science Research Program through the National Research Foundation of Korea (NRF) funded by the Ministry of Education, Science and Technology (2012-0000150).

References

1. Kim, Y.-H., Kim, J.-H., Han, K.-H.: Quantum-inspired multiobjective evolutionary algorithm for multiobjective 0/1 knapsack problems. Paper presented at IEEE Congress on Evolutionary Computation, pp. 2601–2606 (2006)
2. Lee, K.-B., Kim, J.-H.: Mass-spring-damper motion dynamics-based particle swarm optimization. Paper presented at IEEE Congress on Evolutionary Computation, pp. 2348–2353 (2008)
3. Lee, K.-B., Kim, J.-H.: Particle swarm optimization driven by evolving elite group. Paper presented at IEEE Congress on Evolutionary Computation, pp. 2114–2119 (2009)
4. Lee, K.-B., Kim, J.-H.: Multi-Objective Particle Swarm Optimization with Preference-based Sorting. Paper presented at IEEE Congress on Evolutionary Computation (2011)

5. Deb, K., Zope, P., Jain, S.: Distributed computing of pareto-optimal solutions with evolutionary algorithms. In: Fonseca, C.M., Fleming, P.J., Zitzler, E., Deb, K., Thiele, L. (eds.) EMO 2003. LNCS, vol. 2632, pp. 534–549. Springer, Heidelberg (2003)
6. Tan, K.-C., Yang, Y.-J., Goh, C.-K.: A distributed cooperative coevolutionary algorithm for multiobjective optimization. *IEEE Transactions on Evolutionary Computation* 10(5), 527–549 (2006)
7. Coello, C., Lechuga, M.: MOPSO: A proposal for multiple objective particle swarm optimization. Paper presented at IEEE Congress on Evolutionary Computation, pp. 1051–1056 (2002)
8. Deb, K., Thiele, L., Laumanns, M., Zitzler, E.: Scalable multi-objective optimization test problems. Paper presented at IEEE Congress on Evolutionary Computation, pp. 825–830 (2002)
9. Zitzler, E.: Evolutionary algorithms for multiobjective optimization: Methods and applications. Doctoral dissertation ETH 13398, Swiss Federal Institute of Technology (ETH), Zurich, Switzerland (1999)
10. Li, H., Zhang, Q., Tsang, E., Ford, J.A.: Hybrid estimation of distribution algorithm for multiobjective knapsack problem. In: Gottlieb, J., Raidl, G.R. (eds.) EvoCOP 2004. LNCS, vol. 3004, pp. 145–154. Springer, Heidelberg (2004)
11. Rivera, W.: Scalable parallel genetic algorithms. *Artififial Intelligence Review* 16(2), 153–168 (2001)
12. Raquel, C., Naval Jr., P.: An effective use of crowding distance in multiobjective particle swarm optimization. Paper presented at Conference on Genetic and Evolutionary Computation, pp. 257–264 (2005)

Personalized Emotional Expressions to Improve Natural Human-Humanoid Interaction

Maria Vircikova¹, Peter Sincak¹, and Dong Hwa Kim²

¹ Center for Intelligent Technologies

Dept. of Cybernetics and Artificial Intelligence, Technical University of Kosice
9 Letna, Kosice 040-01, Slovakia

{Maria.Vircikova, Peter.Sincak}@tuke.sk

² Dept. of Instrumentation and Control, Engineering, Hanbat National University
16-1 Duckmyong dong Yuseong gu Daejeon, South Korea 305-719
kimdh@hanbat.ac.kr

Abstract. We need to prepare robots for the shift from laboratories and industrial environments to join human residential areas. This is one of the reasons why current trends in the field of human-robot interaction are expanding into the social experience of users often involving artificial emotions. Emotional technology in its two forms – as an expression of artificial emotions of the systems and as systems capable of recognizing human emotions – contributes to the creation of personalized systems. We try to move from the knowledge about human emotional processes to implement a model of artificial emotions based on Plutchik's theories. The emotional model is a part of the autonomous mode for the humanoid robot. The proposed system is able to adapt to the user's expectations and thus, to evolve during the interaction process. The inputs to the system are user's expressions of emotions detected from his/her body movements and gestures. Fuzzy logic approach is used for blending of basic emotions to primary mixed emotions. We used humanoid robot Nao as an experimental setup and the user's expressions are mapped to the humanoid's body. The expressions are used to communicate robot's internal states much like non-verbal signals indicates feelings in human society. As the experiments show, the personalized expressions help users to understand the system and they improve the human-robot interaction.

Keywords: emotions, fuzzy logic, human-robot interaction, robot Nao.

1 Introduction

When dealing with people in our everyday life, in many situations we can notice that, metaphorically, we are dealing with, rather than creatures of logic, creatures of emotions [2]. To the human emotions, which act as a system with feedback provided by the body, we often attach greater weight than to the rational justifications while deciding or doing something.

How is it in case of cooperating with machines? Should machines remain creatures of pure logic? Would the enrolment of the emotions drift towards intuitive mutual cooperation man-machine?

Interacting with agents that have a model of emotions can form a better understanding of the user's moods, emotions and preferences and can thus adapt itself to the user's needs. Software agents may use emotions to facilitate the social interactions and communications between groups of agents and this way they can help in coordination of tasks, such as among cooperating robots.

As robots increasingly make their way into functional roles in human environments (e.g. homes, schools, and hospitals), they need to react appropriately to human expectations and behavior. Moreover, a person working with a robot should not be required to learn a new form of interaction. Thus, we need to develop computational models of social intelligence for these robots that will allow them to have interactions that are natural and intuitive for a human partner. When the robot expresses his internal states via his non-verbal and verbal expressions during communication, humans should better understand him. The question is, if robot can express emotions understandable by human society, he should learn to recognize people's intentions to help him as a team partner in collaboration tasks.

These motivations were proposed for giving machines certain emotional abilities by Picard [12]:

- to build robots and synthetic characters that can emulate living humans and animals – for example, to build a humanoid robot,
- to make machines that are intelligent, even though it is also impossible to find a widely accepted definition of machine intelligence,
- to try to understand human emotions by modeling them and
- to make machines less frustrating to interact with.

In recent years huge progress was made in the effort to express emotions with humanoids, mainly with facial expressions. Our results with the implementation based on the body movement expressions suggest that a humanoid robot, such as Nao, should be able to display emotions using body movement. The specific positioning that the body takes during a timeframe, are an effective medium to express emotion, also many emotions are differentiated by characteristic body movements, and that these are effective cues for judging the emotional state of other people even in the absence of facial and vocal cues.

Body movements include the movements themselves as well as the manner in which they are performed. Several studies observed how the whole body expresses emotion. To support this, discriminative features of emotions were found by [9] in the whole body posture and its movement quality analyzing correlations between emotion and gesture.

Although human beings share the same mental states, their expressions are different. For example, when humans become angry, some will remain calm, while others may clearly express anger. This means a wide variety of emotional expressions even though the mental state can be the same. For this purpose we present a framework in which the body movements of different expressions are stored in the database and the robot, depending on his human partner, expresses the emotions in the same manner as his partner.

The personalization of the expressions makes our system different from other proposed approaches. The emotional expressions of users are mapped from their bodies to the motors of the robot.

2 Background

2.1 Related Works

The design of computational model of emotions is not based only on computing technology, but is closely linked to the research findings of many areas and disciplines that study human emotional processes. Incorporation of an emotional model should improve the machine performance – its decision making, action selection, and management of behaviors, autonomy and the interaction with people.

During the history of artificial intelligence many attempts tried to make models describing the human mind and some of these involved emotional processes. Probably one of the first famous projects interested in emotions in artificial intelligence was the work of Simon, which around 1967 constructed a model based on the motivational states like hunger and thirst. The simulation consisted in the following process: if the level of hunger achieved some level, the process of thinking was interrupted. Several projects in which emotions were important for decision making processes or for the communication with robots appeared in 90-ties (e.g Sugano and Ogata [14]; Breazeal [1]).

Nasr [10] constructed the system FLAME, a computational model of emotions, in which the adaptive components represent a basis for evaluation of the interaction by users. It involves also learning in three different forms: the association of an emotion and an object which triggered the emotion in past, reinforcement learning to estimate the event depending on the agent's goals and the probabilistic approach for learning patterns of events and the heuristic approach for learning of actions which were pleasant or unpleasant for the agent as well as for the user.

Buy [15] designed ParlE, a quantitative, flexible, adaptive model of emotions for a conversational agent in a multi-agent environment which assesses events based on learning and a probabilistic planning algorithm. It also models personality, as well as motivational states and their role in determining the manner in which the agent experiences emotions.

Breazeal's [1] Kismet is considered a first robot (robotic head, in fact) expressing emotion. It simulates social interactions between people and based on this idea the robot had its own robotic teacher – an assistant helping him achieve better communication skills. Emotions are modelled from the functional perspective.

ALMA by Gebhard [7] is an architecture that integrates three major affective characteristics: emotions, moods and personality that cover short, medium, and long-term affect. The use of this model consists of two phases: In the preparation phase appraisal rules and personality profiles for characters must be specified. In the run-time phase, the specified appraisal rules are used to compute real-time emotions and moods as results of a subjective appraisal of relevant input. They use affective states to color simulated dialogs and through verbal and non-verbal expression of emotions.

MOEGPP by Kim and Le [8], a multi-objective evolutionary generation process for artificial creatures' specific personalities, is a model where the dimension of the personality model is defined as optimization objectives. An artificial creature is created as an autonomous one, which behaves depending on his internal state. This is composed of motivation, emotion and homeostasis, influences by perception, referring to the knowledge stored in memory and considering the context of the environment.

2.2 Plutchik's Psychoevolutionary Model of Emotions

Our emotional model is inspired by Plutchik's psychoevolutionary model of emotions [11], proposed with belief that a scientific and therapeutically useful understanding of emotions is possible. Assuming humans have eight native basic emotions that developed evolutionary; his model contains eight basic emotion dimensions. 1. Joy, 2. Trust, 3. Fear, 4. Surprise, 5. Sadness, 6. Disgust, 7. Anger and 8. Anticipation.

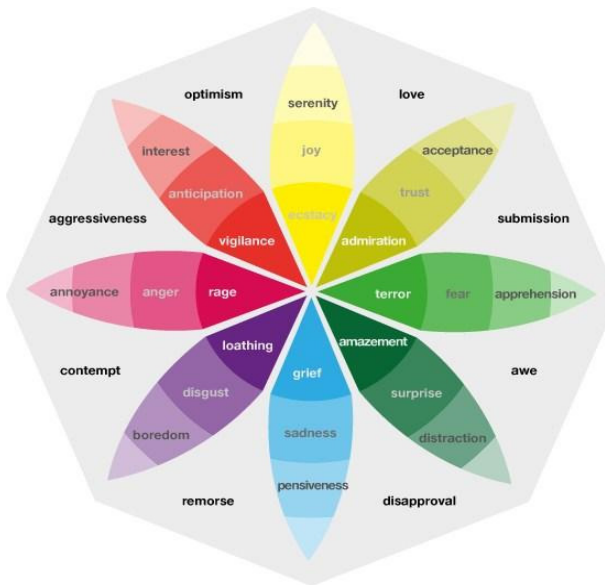


Fig. 1. Plutchik's wheel of emotion which defines a model of human emotions and their relations and combinations. The model resulted in a circumplex where emotions and variations are represented by different colors and hues.

All other emotions derive from these emotions. Following the pattern used in color theory and research, we can obtain judgments about combinations—the emotions that result when two or more fundamental emotions are combined, in the same way that red and blue make purple. Depression and grief, for instance, are varieties of sadness. Pleasure is a variety of happiness, and horror is a variety of fear. Secondary emotions form by combining varying degrees of basic emotions. Thus, surprise and sadness produce disappointment, while disgust and anger produce contempt. Multiple emotions can produce a single emotion, as well. For instance, anger, love, and fear produce jealousy.

Furthermore Plutchik defined that opposite emotions are joy and sadness, trust and disgust, fear and anger, surprise and anticipation. At the picture bellow is Wheel of Emotions, where can be found basic emotions with various intensities and also primary mixed emotions. Colors at the wheel have symbolic meaning, because like colors can have different shades, emotions can have different intensities and like colors can blend, emotions can too.

2.3 Fuzzy Logic for Artificial Emotions

Fuzzy logic is known for its ability to capture the uncertainty and the complex character of emotions. It has shown that it can achieve smooth transitions in behaviors with a relatively small set of rules, as mentioned by Nasr [10]. It is clear that emotions are vague, thus it is impossible to construct a credible emotional model in which some discrete values would be associated with different emotional states without any continuous transition between each other. One can be sad to some extent – in the word of fuzzy logic, one can be sad with an appropriate level of membership to the set of sadness. Fuzzy logic provides an expressive language to work with both quantitative and qualitative (linguistic) descriptions of the model and it allows the model to produce complex emotional states or the output behaviors. Our system basically uses fuzzy mapping to map the mixture of emotions on behaviors.

3 The Proposed System

3.1 Overview of the Overall System

We designed a system which represents an autonomous mode for the humanoid robot.

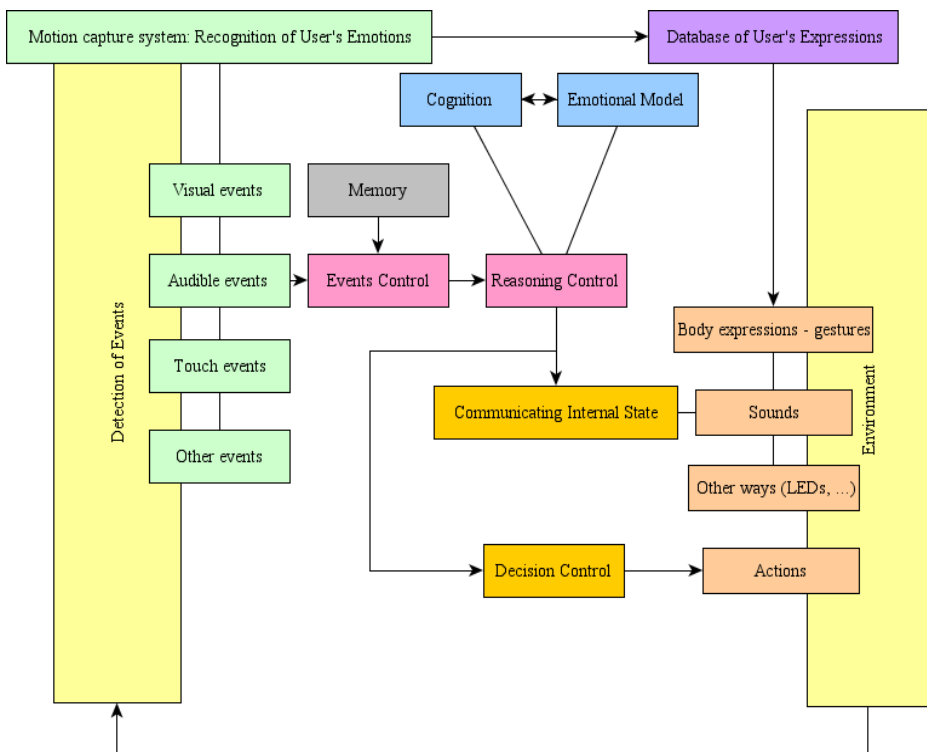


Fig. 2. The overall architecture of the system. It acts as a loop where the inputs are detected events and outputs are expressions of the robots to communicate its internal state and the actions of the robot.

It acts like a closed loop of stimulus → reaction. The stimulus can be detected by humanoid's sensors (camera, microphones, touch sensors or others, depending on the platform).

One special form of the input are recognized emotions of the human partner what is performed by the motion capture system. New expressions of emotions are stored in the database of user's expressions, different for each of the users. The outputs of the system serve to communicate the internal state of the agent (robotic expressions of emotions) and to perform actions. Body expressions of the robot are the same expressions of the concrete emotion as the expression of this particular emotion of its human partner.

This paper explains the part where the personalized gestures are generated from the data provided by the motion capture system, stored in the database and mapped from the human's to the humanoid's body. The robot labels each of the emotions with the expression observed from the user and thus evolves its expressions to communicate its internal state resulting from the emotional model as an output from the events control and the memory of the robot.

3.2 Personalized Emotional Expressions

1. Motion capture system was developed. It is based on Kinect sensor which features a depth scanner. This, for the needs of our model, separates human bodies from the environment and capture full-body 3D motion.
2. We asked 20 subjects to show their expressions of 8 basic emotions: joy, trust, fear, surprise, sadness, disgust, anger and anticipation.
3. We captured these expressions where one training pattern consists of 270 (15 records of angles x 18 frames) samples. Each input pattern is an M-dimensional vector (I_1, \dots, I_M), where each component I_i represents a position of one point of human body in time.



Fig. 3. User expresses his emotion of Joy – view from the sensor Kinect which separates the human body from the environment

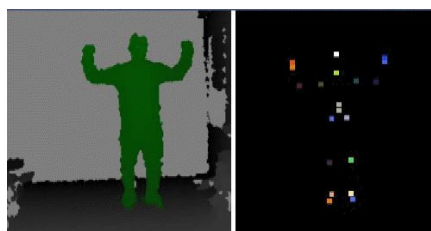


Fig. 4. Left image from depth sensor is displayed, on the right the base points of human body are detected



Fig. 5. Expressions from users mapped to the 25 motors of Nao. Joy.



Fig. 6. Expressions from users mapped to the 25 motors of Nao. Fear.



Fig. 7. Expressions from users mapped to the 25 motors of Nao. Anger.

3.3 The Fuzzy Inference System

The whole evolution of FIS can be summarized in these steps. We proposed membership functions (fuzzy sets) and their linguistic labels that compose the term emotion. Then we determined input and output linguistic variables and write a list of linguistic variables that form a data base of FIS. Afterwards we suggested fuzzy rules that forms rule base of the system and chose the method of the defuzzification.

Triangular membership functions were more suitable to simulate intensities of emotions than others for instance trapezoidal membership functions. All input and output linguistic variables are composed of three linguistic values:

1. low – trapezoidal function with parameters 0, 35, 50
2. medium – trapezoidal function with parameters 30, 50, 70
3. high – trapezoidal function with parameters 50, 75, 100

The rule base consists of two types of rules for each primary mixed emotion:

1. IF anger IS medium AND anticipation IS medium THEN aggressiveness IS low.
2. IF anger IS high AND anticipation IS high THEN aggressiveness IS medium.
3. IF anticipation IS medium AND joy IS medium THEN optimism IS low.
4. IF anticipation IS high AND joy IS high THEN optimism IS medium.
5. IF joy IS medium AND trust IS medium THEN love IS low.
6. IF joy IS high AND trust IS high THEN love IS medium.
7. IF trust IS medium AND fear IS medium THEN submission IS low.
8. IF trust IS high AND fear IS high THEN submission IS medium.
9. IF fear IS medium AND surprise IS medium THEN awe IS low.
10. IF fear IS high AND surprise IS high THEN awe IS medium.
11. IF surprise IS medium AND sadness IS medium THEN disappointment IS low.
12. IF surprise IS high AND sadness IS high THEN disappointment IS medium.
13. IF sadness IS medium AND disgust IS medium THEN remorse IS low.
14. IF sadness IS high AND disgust IS high THEN remorse IS medium.
15. IF disgust IS medium AND anger IS medium THEN contempt IS low.
16. IF disgust IS high AND anger IS high THEN contempt IS medium.

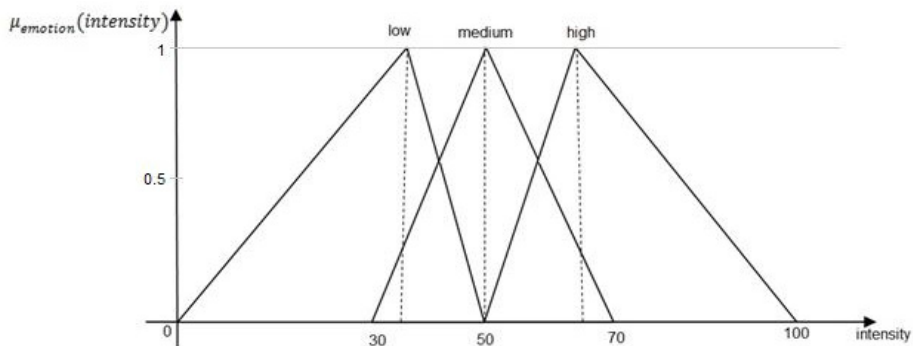


Fig. 8. The term emotions with linguistic values low, medium and high

Generally, when a human feels two basic emotions they both have to have enough intensities to blend and express like mixed one. For example, when person is little disgusted and little angry, he will never fell contempt (the intensities of the emotions are of linguistic terms of medium or high). With the concept of these two types of rules is blending of emotion human-like.

Our system contains personality types of sanguine, choleric, melancholic and phlegmatic.

Table 1. Types of personalities: sanguine, choleric, melancholic, phlegmatic with the intensities of positive and negative emotions

Personality	Intensity of positive emotion	Intensity of negative emotion
sanguine	95	25
choleric	80	60
melancholic	60	60
phlegmatic	40	40
none	50	50

During work of the fuzzy inference system is as implication method used operator minimum and for aggregation process is employed operator maximum. To the last fifth point, centroid method of aggregation is used to get numeric output of the intensity of primary mixed emotion.

The dynamic graph with the x-axis rolling from the beginning when program is run to the end when program is closed by user was designed with the aim to represent the emotional model. Bell shaped first derivative of the sigmoid function is used for figuring the emotional state. It can be seen on the graph that when two colors that represents two basic emotions are blended the shade is very similar to the color that represents the mixture.

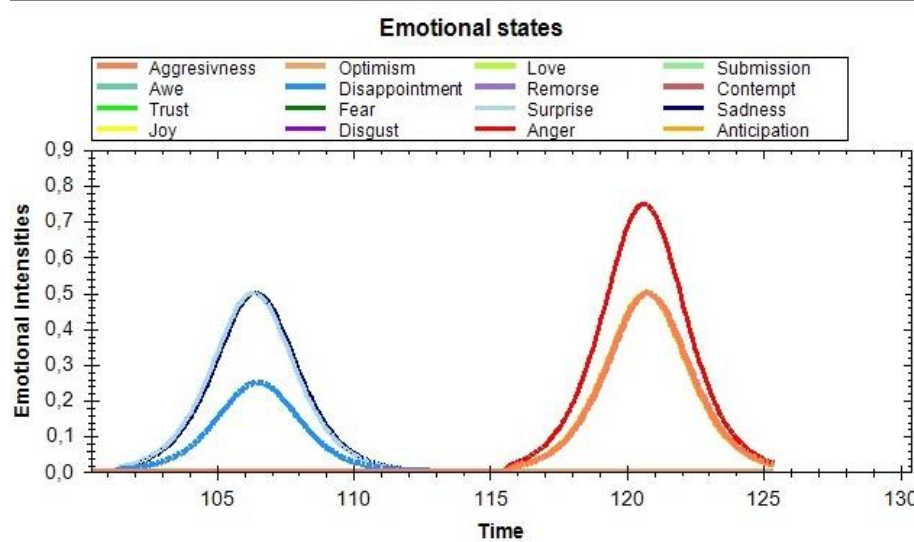


Fig. 9. The graph representing the output of the emotions

Type of emotions	Name of emotion	% Correct [expressions at the beginning of interaction]	% Correct (personalised) expressions after the interaction]
Basic emotions	anticipation	60	95
	joy	65	100
	trust	55	95
	fear	85	100
	surprise	90	100
	sadness	90	100
	disgust	85	100
	anger	85	100
Mixed emotions	optimism	45	95
	love	70	100
	submission	55	90
	awe	40	90
	disappointment	75	95
	remorse	45	95
	contempt	50	90
	aggressiveness	60	100

Fig. 10. Results of the evaluation of the system

4 Experiment

4.1 Experiment Method

To explore how the personalized expressions helped people to recognize Nao's expressions, we asked 20 users to tell which expression is Nao representing at the beginning of the interaction and after, when the expressions are adapted to the current user.

At the beginning of the interaction a set of preprogrammed expressions is shown to the users.

All of them were students, age 18-24, and saw the expressions of the robot for the first time. The second set of the experiment stands for the personalized expressions – the one that were mapped from the users to the humanoid.

4.2 Experimental Results

These interaction studies showcase one of the significant contributions of the personalisation of Nao's expression system. The subjects's responses argue that the adaptation of expressions to the specific user significantly contributes to the understanding of the expressions. The fuzzy inference system helps to produce complex emotional states.

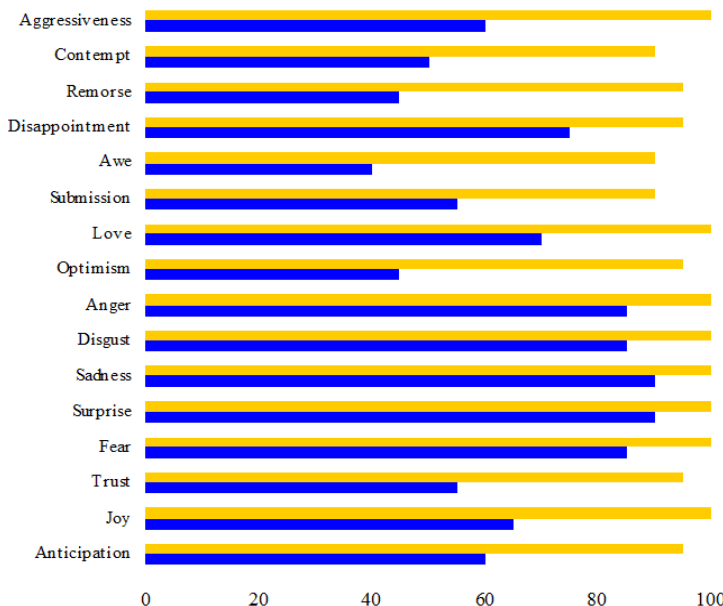


Fig. 11. The comparison of recognition of pre-programmed expressions (blue) and the adapted, personalized robotic expressions (yellow)

5 Conclusion

A wide spectrum of existing projects and applications try to better understand human emotional behavior and make a model according to their needs and expectations, implement this model to machines that interact with people. Such projects believe that during the process of machine migration to the human society they will be considered beneficial and intuitive partners. The future cooperation between machines and us how we believe it will be can be summed up with these words: machines fully adapting to man – that man no longer has to adapt his behavior to machines.

The idea is that communication and interaction should be easy and enjoyable, both for unfamiliar users and trained professionals. Researchers want to construct robots to behave more like people, so that people do not have to behave like robots when they interact with them. Our emotional model can be used for any humanoid-type robot. The experiments show that the personalizations of the robotic expressions help people understand the machine. We believe it could improve the quality of interaction between non-technical individuals and robots.

Acknowledgements. Research supported by the National Research and Development Project Grant 1/0667/12 “Incremental Learning Methods for Intelligent Systems” 2012-2015 and the project implementation “Center of Information and Communication Technologies for Knowledge Systems with the ITMS code 26220120030 supported by the R&D Operational Program funded by the ERDF.”

References

1. Breazeal, C.: Function Meets Style: Insights From Emotion, Theory Applied to HRI. *IEEE Trans. on Systems, Man and Cybernetics* 34(2) (2004)
2. Carnegie, D.: How to win friends and influence people. Pocket Books (1936)
3. Davis, D.N.: Modelling emotion in computational agents (2000),
<http://www2.dcs.hull.ac.uk/NEAT/dnd/papers/ecai2m.pdf>
(revised: April 15, 2012)
4. Fellous, J.M.: From Human Emotions to Robot Emotions. Architectures for Modeling Emotions: Cross-Disciplinary Foundations. In: AAAI Spring Symposium, pp. 37–47 (2004)
5. Fong, T., Nourbakhsh, I., Dautenhahn, K.: A survey of Socially Interactive Robots: Concepts, Design, and Applications. Technical report CMU-RI-TR-02-29 (2002)
6. de Freitas, J.S., Gudwin, R., Queiroz, J.: Emotion in Artificial Intelligence and Artificial Life Research: Facing Problems. In: Panayiotopoulos, T., Gratch, J., Aylett, R.S., Ballin, D., Olivier, P., Rist, T. (eds.) IVA 2005. LNCS (LNAI), vol. 3661, pp. 501–501. Springer, Heidelberg (2005)
7. Gebhard, P., Kipp, K.H.: Are Computer-generated Emotions and Mood Plausible to Humans? In: Gratch, J., Young, M., Aylett, R.S., Ballin, D., Olivier, P. (eds.) IVA 2006. LNCS (LNAI), vol. 4133, pp. 343–356. Springer, Heidelberg (2006)
8. Kim, J.K., Le, C.H.: Multi-objective Evolutionary Generation Process for Specific Personalities of Artificial Creature. *IEEE Computational Intelligence Magazine* (2008)
9. Kipp, M., Martin, J.C.: Gesture and Emotion: Can basic gestural form features discriminate emotions? In: 3rd International Conference on Affective Computing and Intelligent Interaction and Workshops, ACII 2009 (2009) ISBN 978-1-4244-4800-5
10. Nasr, E., et al.: FLAME: Fuzzy Logic Adaptive Model of Emotions. *Autonomous Agents and Multi-Agent Systems* 3(3), 219–257 (2000)
11. Plutchik, R.: A general psychoevolutionary theory of emotion. In: Plutchik, R., Kellerman, H. (eds.) *Emotion: Theory, Research, and Experience. Theories of Emotion*, vol. 1, pp. 3–33. Academic, New York (1980)
12. Picard, R., Klein, J.: Computers that recognize and respond to user emotion: theoretical and practical implications. *Interacting with Computers* 14, 141–169 (2002)
13. Ogata, T., Sugano, S.: Emotional communication between humans and the autonomous robot which has the emotion model. In: *IEEE International Conference on Robotics and Automation*, vol. 4, pp. 3177–3182 (1999)
14. Bui, T.D., Heylen, D., Poel, M., Nijholt, A.: ParleE: An Adaptive Plan Based Event Appraisal Model of Emotions. In: Jarke, M., Koehler, J., Lakemeyer, G. (eds.) KI 2002. LNCS (LNAI), vol. 2479, pp. 129–143. Springer, Heidelberg (2002)
15. Russel, J.A.: Core Affect and the Psychological Construction of Emotions. *Psychological Review* 110(1), 145–172 (2003)

Adaptive Fuzzy Cognitive Maps Using Interactive Evolution: A Robust Solution for Navigation of Robots

Daniel Lorencik, Jan Vascak, and Maria Vircikova

Center for Intelligent Technologies, Department of Cybernetics and Artificial Intelligence,
Technical University of Kosice
Bozeny Nemcovej 3, 04001 Kosice, Slovak Republic
`{daniel.lorencik,jan.vascak,maria.vircikova}@tuke.sk`

Abstract. Fuzzy cognitive maps belong to emerging approaches used for various tasks in artificial intelligence. They are especially useful for solving the problem of navigation of vehicles as fuzzy systems are very robust in general. Therefore, they are suitable for the real world applications. One of disadvantages of fuzzy systems is their inability to learn. In this paper, we propose the use of fuzzy cognitive maps for navigation of a humanoid robot Nao and also an adaptive mechanism based on interactive evolution. To get data about the surrounding world, we are using the robot's camera. Depending on the situation in the arena, the best direction is selected with the use of membership functions for target and obstacles. Parameters of these functions can be set manually from a program interface or the optimal parameters can be found using interactive evolution. The interactive evolution was selected to obtain the best results in the shortest time. Two approaches to the interactive evolution were tested. The first type was a simple interactive evolution, the second type used thresholds to find the most promising individuals to hold the ideal parameters and only these were presented to a human for evaluation. Experiments were made using manual setting of the parameters as well as using the adaptation mechanism of the first and the second type, where the second type was able to find the right set of parameters in a shorter time than the first one.

Keywords: Adaptation, Fuzzy Cognitive Maps, Nao, Robot, Navigation.

1 Introduction

Navigation system proposed in this paper is based on the solution from [1] for the use of fuzzy cognitive maps for solving the “Bago” problem in robot soccer. Bago is an exercise in the football game, where players stood in the circle with one in the middle. The task of players is to pass the ball between them without the player in the middle gaining it, and the task of the player in the middle is to intercept the pass and to catch the ball. The objects on the field were internally represented by the angle at which they were positioned with the regards of robot position. This system of representation can be easily adapted for navigation purposes where the obstacles and target are represented by: the angle at which they are detected by the robot, by their relative distance to the robot and by their width. The goal of this work is also to implement

the adaptation system as the fuzzy cognitive maps are unable to learn and adapt themselves. For this task, the interactive evolution was selected, where the parameters, which influence the creation (and shape) of membership functions, are evolved. As stated in [8], interactive evolution is used in cases where it is difficult to define adequate fitness function. Interactive evolution uses much smaller population size compared to the genetic algorithms because human evaluator can distinguish only small number of slightly different examples. Because of this, along the classic approach we used the pre-evaluation of individuals. From the experiments conducted we observed than when the individual has certain qualities, it has a higher chance to be successful than without them. Based on this observation and on approach used in [9], we defined the set of conditions, which were used to select only small number of individuals for human evaluation. So we were able to use bigger population to search for optimum, and yet use only small subset of it for interactive evaluation. This approach somewhat combines the benefits of the genetic algorithm with the benefits of interactive evolution. The experiments were conducted using manual input of parameters for membership functions creation and by using adaptive systems of the two proposed types.

This paper is organized as follows: in section 2, the fundamentals of fuzzy cognitive maps are presented as well as results from related works. In section 3, the problem of navigation of a Nao robot is described, and the solution is proposed and explained in detail. In section 4, results from experiments are presented, and finally, in section 5 the conclusion is made.

2 Fuzzy Cognitive Maps

Cognitive maps were created by psychologist E. C. Tolman [2] to describe how rats understand the world around them. Due to the interaction with the outside environment the image of the environment is created in the brain of the living agent, which is refined by every next interaction with the environment. Cognitive maps are a very robust system, which can model very complex behaviour [3].

Fuzzy cognitive maps (FCM) were created by Bart Kosko (in [4]) as fuzzy extension of cognitive maps. Fuzzy cognitive maps have a clearly defined knowledge base as every fuzzy system, which is clearly separated from the structure. This fact allows modifying this basis without change of structure and therefore modifying the functionality. But the fuzzy cognitive maps do not have the ability to learn, so this ability has to be implemented with the use of adaptive system.

As stated in [5] evolutionary strategies are exceptionally well suited for adapting FCM because their main advantages are numerical optimization, robustness, adaptability and flexibility; they also use specific knowledge about a problem in order to solve it. They differ from evolutionary algorithms by use of real parameters instead of the binary representation. Common terms used in evolutionary strategies are individuals, population, parents and offsprings.

An **individual** represents the solution to a given problem. Depending on the problem, the individual can have one value or multiple parameters. Individual also represents one point in the solution space.

Population is a group of individuals in one generation.

Parents are individuals used to create new offsprings by use of crossover. Most commonly, only the best individuals are used as parents.

Offspring is a new individual created either as a product of crossover between two or more parents, or as a product or mutation of one individual from population.

Conclusion from [5] states several interesting points:

- Big populations do not guarantee better results as small populations. Small populations tend to create more generations, which is more suitable for finding an optimal solution.
- The process, which uses the complete replacement of the population, is more successful than process using partial replacement.
- To learn FCM it is necessary to choose the right type of examples.
- The success of learning is dependent on the quality and number of examples, but the dependence on the structure and complexity of FCM is not significant.

The navigation of robot using adaptive FCM was presented in [6] although the system was tested on Lego robots and has used SOMA (self-organizing migration algorithm) for adaptation.

3 Problem Description and Implementation

As stated in the section 1, for solving the navigation problem of robot Nao, the solution proposed in [1] was used. Robot had been to navigate in arena seen in Fig. 1

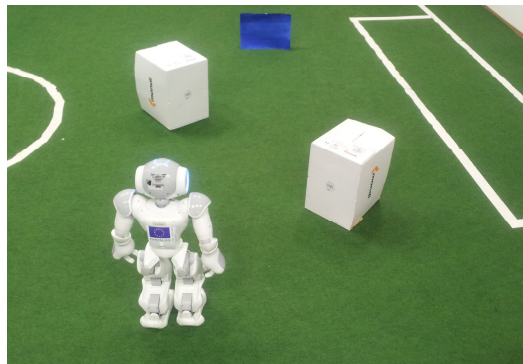


Fig. 1. Arena used to test adaptation of FCM

3.1 Processing the Image

For image processing, methods from AForge framework [7] are used. For initial filtering (to remove the arena floor from the image), Euclidean colour filter is used. Floor colour is picked as average colour from the middle of the image received from camera – so for getting the floor colour, robot must have a clear space before it.

After the floor is removed, objects remaining in the image are objects of real world which are marked and counted. The target is an object with specified colour.

3.2 Representation of Objects in the Arena

Since the arena is perceived by robot via a visual system only data about objects, which are available, are their position on the image and their size. For the use of FCM a conversion to the internal coordinate system is proposed, see Fig. 2.

After the conversion, the object has following properties:

- Angle – angle between the robot and a given object (regarding to the robot).
- Distance – a relative distance between object and robot, where 1 means that the object is in the immediate vicinity of the robot, and when the object is far, this number is lower.
- Mass – object width in degrees

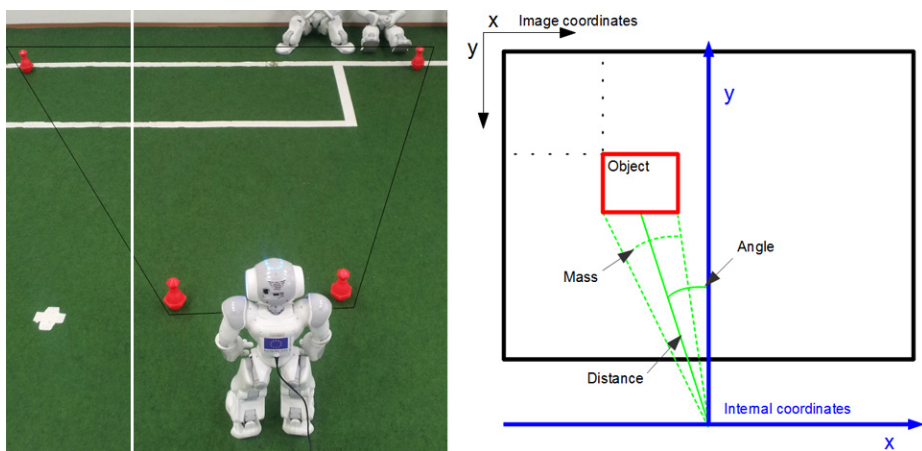


Fig. 2. Robot vision cone (left) and internal coordinate system (right)

Zero point of this new coordinate system has been chosen in such a way that the angle of object in the image would represent the angle of the object to the robot in the real word.

3.3 Finding the Most Suitable Direction for Movement

Finding the most suitable direction for movement uses membership functions of obstacles and target. These functions show the dependence of validity of motion on the angle of motion. The creation of function depends on the object parameters and also on the adaptation parameters.

The centre of the maximum of the function is located at the same angle value as the object is located; the width of maximum directly corresponds to the mass of the object, and height of maximum to the distance of the object.

For the target, this function is flipped – it is a result of subtraction of the target function from constant function with the function value of 1.

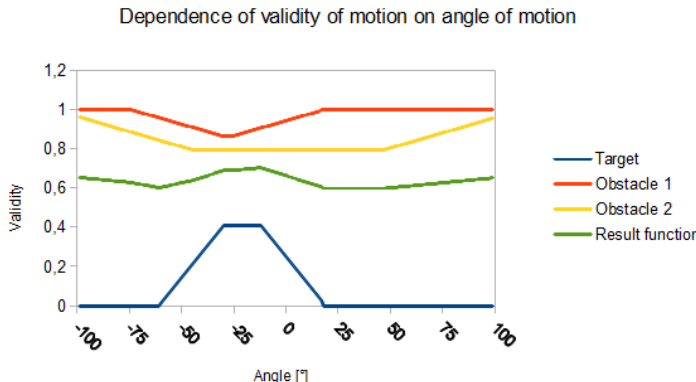


Fig. 3. Example of functions used in the process of finding the best direction for movement

After that, all functions are summed – values of functions at the same angles are summed up, and the result is divided by the number of functions, so it is normalized to the interval of [0; 1].

Then the maximum of the resulting function shows the optimal direction for a robot to reach the target. In case there are multiple maximums of the same value, the chosen maximum is the one closer to the zero angle. An example is in Fig. 3.

3.4 Design of Fuzzy Cognitive Map

The result of finding process is one of the input parameters – the most suitable direction. Output parameters are directly speeds for robot movement. The proposed FCM is in the Fig. 4.

The most suitable direction influences the turn speed of the robot, so the more is the target to the margin of robot view, the faster the robot turns.

Closest obstacle distance directly influences motion speed (forward or backward motion), as well as lateral motion of the robot. If the obstacle detected in the image from the camera is closer than a threshold, the speed is negative, so the robot moves backward, away from the obstacle. In other cases the speed depends on the distance – the closer the obstacle, the lower the speed. The distance to the obstacle is also measured by a sonar. If this distance is less than a given threshold, the collision avoidance mode will be performed – the robot will move backwards and move laterally to the side depending on the target position

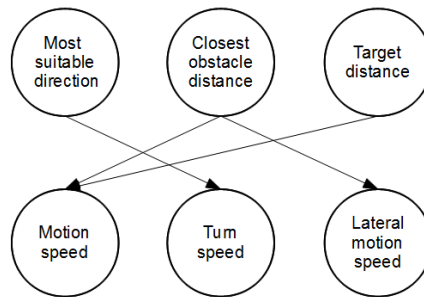


Fig. 4. FCM used in the solution

3.5 Adaptation System

To adapt these functions, parameters for height, width and slope are used.

The parameter for height is from interval $[0; 1]$ and it influences the height of the function. The height of the function is calculated as distance of the object multiplied by height parameter. This parameter is then equal to the weight that this object has on the decision.

The parameter for width is from interval $[0.1; 1]$ and the width of the function maximum is calculated as mass of the object divided by the width parameter. This will ensure that the object in the image appears wider for the decision process; thus it will be avoided by a greater distance.

The slope parameter is from interval $[0; 89]$ and determines the slope of the function.

These parameters can be set manually, or with the use of a genetic algorithm and they are set for obstacles and target.

Additionally, the turn speed and the walk speed are also parametrized and subject to the optimization with the use of genetic algorithm.

The proposed solution of adaptive system uses interactive evolution to optimize these parameters. Interactive evolution was selected because the fitness function here is not clearly defined, as the fitness of one set of parameters (which we will call an individual) cannot be defined based solely on numerical values of parameters.

Individuals consist of a set of parameters – height, width and slope parameters for target, height, width and slope parameters for obstacles. In one generation, there are 5 individuals; every one of them has to be evaluated by a human operator.

Two types of genetic algorithms were used, which differ in the creation of new generation.

In the first type, a new generation is created by using these rules:

- The best individual from the old generation is copied without any change to the new generation.
- The remainder of the generation is created by a cross-over and by applying a mutation operator.

In the second type, a new generation is created by using these rules:

- All possible offsprings are created by using crossover (each with each).
- For every parameter a condition is defined. If the parameter of the offspring meets the given condition, the value of the offspring is raised by 1; otherwise it is lowered by 1.
- Only the best valued offsprings are accepted to the new generation. The crossover used in both types creates a new individual, where the new parameters correspond to a mean of parameters of both parents.

We used five individuals in one population for both types of adaptation.

4 Experiments

4.1 Manual Entry of Parameters

Experiments were conducted in the arena shown in Fig. 1. Since the method used for image processing is colour-based, the target must be clearly differentiable from other objects in the arena. Firstly, the manual entry was used to set the parameters of membership functions, to test if the proposed solution is able to navigate robot.

With these settings the robot was able to get to the target and avoid any contact with obstacles. The time needed to traverse the distance was under 1 minute. Such a case is an example of a good navigation, so if the individual from the adaptation process is able to mimic this performance, it was considered as a good set of parameters and therefore it received a higher score (higher value of fitness).

4.2 Evaluation

The final score of an individual was determined by a human, who was assessing following aspects:

- if the robot was able to find the target,
- if the robot collided with an obstacle,
- if the robot followed the ideal route through the arena.

All experiments were assessed by the same human operator.

4.3 Adaptive System of the First Type

When using an adaptive system of the first type, the suitable set of parameters was found in the third generation and in the fifth generation all individuals have been on the same level of fitness – there were virtually no differences in navigation quality through the arena. They were able to navigate in the arena without any collisions and to find the target. Also, they were able to find the target in the arena with rearranged obstacles. Since the parameters are not converging, we can assume that there is no simple fitness function that can be calculated solely from these parameters. Therefore, this was the reason to use the interactive evolution in the first place.

4.4 Adaptive System of the Second Type

For the second type of adaptation system, we need to provide the conditions for evaluation of offsprings. The used conditions are in the Table 1.

An adaptive system of the second type was able to find two suitable sets of parameters in the second generation, and in the third generation 80% of individuals were rated as suitable solutions. Although the number of generations is lower than using the adaptive system of the first type, the number of generated individuals is much higher (which according to [5] is the reason of quick finding of the solution). The conditions used for pre-evaluating the individuals were based on estimation of parameters, which represented the human knowledge about which sets of parameters are more likely to be ideal than others. From the theoretical point of view, these conditions narrow the space searched for ideal individuals (set of parameters), and therefore the ideal solution should be found sooner than by the use of adaptive system of the first type.

Table 1. Evaluation conditions for the Adaptive system of the second type

Turn speed	$\geq 0.1 \& \& \leq 0.4$
Move speed	$\geq 0.3 \& \& \leq 0.7$
Obstacle height	≥ 0.5
Obstacle width	≥ 0.5
Obstacle slope	$\geq 45^\circ$
Target height	≥ 0.5
Target width	≥ 0.5
Target slope	$\geq 45^\circ$

Membership functions for the best individual found by the second type of adaptive system can be seen on Fig. 3.

5 Conclusions

In this paper, we used the adaptive fuzzy cognitive maps for the navigation of robots. The proposed approach how to find a suitable direction of movement also uses principles from adaptive fuzzy cognitive maps, and it was shown that this approach can simplify the task of navigation to the task of finding the function maximum. This system can be further improved by the use of more sophisticated membership functions.

As the FCM used for navigation in the first arena was successfully used also for navigation in changed arenas, and since fuzzy systems are inherently robust, we can assume that the proposed system can be used in more complex situations, although it may be necessary to adapt it again to receive better results.

We have proposed two adaptive systems for FCM, both using interactive evolution, where the second one used the pre-evaluation of individuals. This approach allows the use of bigger population to search for optimum, and then provides only small subset of individuals with the highest chance to be optimal for interactive evaluation.

Acknowledgements. This work is the result of the project implementation: Development of the Center of Information and Communication Technologies for Knowledge Systems (ITMS project code: 26220120030) supported by the Research & Development Operational Program funded by the ERDF and by the National Research and Development Project Grant 1/0667/12 “Incremental Learning Methods for Intelligent Systems” 2012-2015.

References

1. Lorenčík, D.: Fuzzy Cognitive Maps in Mobile Robotics. Bachelor thesis, Technical University in Košice (2010) (in Slovak),
<http://www.student.ui.sk/DanielLorencik>
2. Tolman, E.C.: Cognitive maps in Rats and Men. *The Psychological Review* 55(4), 189–208 (1948)
3. Axelrod, R.: Structure of Decision: The Cognitive Maps of Political Elites. Princeton University Press, New Jersey (1976)
4. Kosko, B.: Fuzzy Cognitive Maps. *International Journal of Man-Machine Studies* 24(1), 65–75 (1986)
5. Koulouriotis, D.E., Diakoulakis, I.E., Emiris, D.M.: Learning Fuzzy Cognitive Maps using Evolution Strategies: A Novel Schema for Modelling and Simulating high-level Behaviour. In: Proc. of the 2001 Congress on Evolutionary Computation, Seoul, vol. 1, pp. 364–371 (2001)
6. Vaščák, J., Paťa, M.: Adaptation of Fuzzy Cognitive Maps for Navigation Purposes by Migration Algorithms. *International Journal of Artificial Intelligence* 8(S12), 20–37 (2012)
7. AForge.NET framework, home page of the project, <http://www.aforgenet.com/>
8. Sims, K.: Interactive Evolution of Dynamical Systems. In: Proc. of the First European Conference on Artificial Life, Massachusetts Institute of Technology, pp. 171–178 (1994) (second printing)
9. Krizsán, Z., Kovács, S.: FRI model based pre-evaluation in IEC. In: Applied Computational Intelligence and Informatics, SACI 2009, May 28-29, pp. 35–40 (2009)

Tuning Fuzzy-Based Hybrid Navigation Systems Using Calibration Maps

Napoleon H. Reyes, A.L.C. Barczak, and T. Susnjak

Massey University, Albany, New Zealand
N.H.Reyes@massey.ac.nz

Abstract. We present a novel approach for the tuning and assessment of a cascade of fuzzy logic systems, working cohesively for robot soccer navigation. We generate calibration maps to comprehensively examine the performance of the cascades, allowing for both the visualisation and quantification of the overall system performance. The experiments demonstrate how the proposed method captures the aggregate effect on system's efficiency of even the slightest changes to the fuzzy rules. It also provides feedback on the mechanics of the fuzzy systems that could be held responsible for any shortcomings. Interestingly, without the aid of the proposed techniques, these minute changes are very difficult, if not impossible to identify through human visual inspection per se. Although the example provided in the paper reflects navigation in the Mirosoft league robot soccer scope, the proposed calibration method lends itself amenable to other problem domains where target pursuit and obstacle avoidance behaviours are a necessity. It is also worth-noting that the calibration method can be utilised as a fitness function to a Genetic Algorithm or other optimisation techniques, for a fully-automated calibration. Lastly, we discuss how the calibrated cascade of fuzzy systems neatly integrate with the A* algorithm to produce a hybrid system for near-optimal navigation.

1 Introduction

A novel fine-tuning method for fuzzy logic-based navigation systems is presented. The method has its merits in dealing with a fusion of a conglomeration of fuzzy systems, which are difficult to optimise in practise, due to the large number of possible outcomes that can be influenced even by a few fuzzy parameters tweaking. In scenarios like these, usually the change in a few parameters can improve the results in one particular system state, but may worsen the others. As an example, the method was used to analyse and tune a cascade of four fuzzy systems, working together to produce target pursuit and obstacle avoidance robot behaviours. We show how an initial configuration of four fuzzy systems can be further improved with the aid of calibration maps. It is worth-noting that the techniques and ideas proposed are not limited to fuzzy systems alone, but also generalises to fine-tuning other computational intelligence-based navigation algorithms proposed in the literature [1], [2], [3].

The paper is structured as follows: first, a brief literature review discusses the challenges of the calibration task within the scope of this work. Thereafter, the subsequent sections describe the details of the proposed calibration method and experiments used to verify the efficiency of the different sets of fuzzy parameters detailing the performance of the initial and tuned configurations of the navigation algorithm. A discussion of the results is then provided, followed by the conclusions and future work.

2 Related Work

This research draws its inspiration from [4], where an evolutionary and multi-objective optimisation technique is presented for approaching a ball (target pursuit) as quickly as possible, then kicking it accurately towards the goal. Their fitness function takes into account the elapsed time, heading angle error and posture angle errors. On the other hand, this research focuses on simultaneously calibrating a cascade of 4 fuzzy systems implementing two robot behaviours (objectives) that work synergistically in tandem: target pursuit and obstacle avoidance, in a dynamic environment. The calibration set-up utilises the accumulated elapsed time and number of collisions for an army of robots distributed evenly on the space of exploration. Another inspiration comes from the visualisation diagrams presented in [1], for the vector field based approach to navigation. It has sparked an idea that led to this research that a comprehensive mapping of the robot behaviour is vital for accurate system analysis and design. The treatment and generation of the visualisation of the robot trajectories presented in this paper, however are different, as we only use it for calibration purposes, and not for determining the actual path when running the navigation system live.

The calibration method proposed in this work falls within the context of MiroSot soccer robot navigation. For more than a decade, the MiroSot [5] platform has served as a research initiative that fosters the development of novel algorithms in the fields of computer vision, robotics, computational intelligence and other related fields. In the area of robot navigation, many algorithms were proposed to tackle the problem. Pure deterministic algorithms, such as Dijkstra's algorithm, A* and D* are good candidates for robot navigation. They operate on graphs with a guarantee of optimality, but their choice of movements are constrained along graph edges or discrete transitions between grid cells [6]. Therefore, the resulting path would not be smooth, not unless the grid is defined very finely, but that would drastically affect the computation time. Genetic Algorithms (GA), on the other hand, do not guarantee returning an optimal solution and are not generally amenable to be employed in solving real-time problems. However, there is a GA-based system that appears in the literature for real-time robot soccer navigation [7].

Reactionary/Reactive algorithms [8] [9] can respond well, with smooth navigation, without the need for a global map, but are susceptible to getting trapped at local minima. As an example of this class of algorithms, potential field methods have been observed to suffer from the following limitations: oscillatory behaviours in narrow corridors and getting trapped in closely spaced obstacles [9]

and U-shaped obstacles. Moreover, system calibration is a major issue for most reactive algorithms. Considering the number of parameters that can be altered, the problem is non-trivial and is still considered to be a challenge. Fuzzy systems are one among many of the reactive algorithms that are considered to be tedious to calibrate and requires careful analysis and fiddling with the rules and membership functions, at the very least. Furthermore, the defined fuzzy rules may be plagued with incoherence, non-completeness or inconsistencies in the control actions [10]. This poses a particular problem in the navigation algorithms based on fuzzy logic because the number of possible scenarios is very large, and therefore it is even difficult to verify if a calibration is effective, let alone automate the calibration.

Lastly, fuzzy-based hybrid navigation systems [11], [12] and [13] also require fine-tuning due to the presence of fuzzy system components in its architecture.

This paper proposes the use of calibration maps, dealing with both visual and parametric data, helping a user to modify the fuzzy rules and parameters, until a satisfactory performance is achieved. The proposed method can also be easily automated.

3 The Hybrid System and the Calibration Method

A MiroSot [5] simulation system was developed in our laboratory with the objective of allowing different navigation algorithms and scenarios (obstacles, targets, etc.) to be easily configured and investigated. The system is capable of dealing with a large number of robots that concurrently run the navigation algorithm, while storing data that can be analysed later.

Fig. 1 depicts a highly simplified version of the complete hybrid navigation system. The system is highly reconfigurable, with optional components for optimal path-planning, and follows a layered architecture. On top of the hierarchy is the environment processor, which works out the position of all relevant objects in the scene. It feeds an optional component for generating either the Voronoi diagram or grid-world representation of the exploratory space, based on the position of all the obstacles, robots and the target destination. This component is responsible for generating the set of traversable points that will be used in turn by an optimal path-planning algorithm, called the A* algorithm. A* combined with the traversable points from the Voronoi diagram allows for the calculation of the shortest-safest path. On the other hand, when A* operates on the grid-world, it returns the shortest path to the target. In turn, the A* component feeds the cascade of fuzzy systems with the next immediate waypoint towards the target. A* is a deterministic algorithm with a guarantee of returning the optimal path, if one exists. It serves as a global path-planner. This combination guarantees that the robot will never get trapped in U-shaped enclosures and local minima. The complete details of the architecture and its components can be found in [14]. The focus of this paper is on the cascade of 4 fuzzy systems (Algorithm 2) which require proper fine-tuning. Target pursuit is implemented using 2 fuzzy systems: one for calculating the steering angle adjustment and

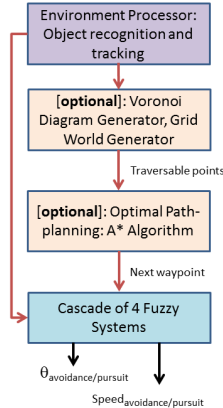


Fig. 1. General system architecture of the navigation system

another for calculating the absolute speed of the robot. Similarly, the obstacle avoidance behaviour requires 2 fuzzy systems for the same functionalities.

The tuning algorithm, as depicted in Algorithm 1, employs Algorithm 2 on each instance of the robot. It is worth-noting that tuning is applied on the pure target pursuit fuzzy systems first (Fuzzy systems 1 and 2 of Algorithm 2) by disengaging lines 10 to 19 (which corresponds to the obstacle avoidance behaviour). Once target pursuit is calibrated satisfactorily, the combined target pursuit and obstacle avoidance fuzzy systems are calibrated together. The calibration maps are configured to represent a discretised version of the exploratory space. A number of non-overlapping robots are initially arranged with a pre-defined orientation at time=1 (see Fig. 2). Note that during the calibration process, some of the robots may not eventually reach their target due to the prevailing incorrect parameter settings; therefore, a threshold-based stopping criteria is necessary. In order to quantify the performance of the navigation systems, we look at several factors. For instance, the accumulated time to reach the target will tell us which algorithm is the fastest. Secondly, the accumulated number of collisions will reflect the safest path-planning algorithm, in the presence of obstacles. Furthermore, the standard deviation of the heading angle of the robot relative to the target destination, as well as the number of fluctuations indicate whether we have an non-smooth, oscillatory motion. In this work, we measure the angle of the robot relative to the target, and set the sign (+/-) of the value depending on whether the target is on the left or right-hand side of the robot's heading angle. This also allows us to observe the number of fluctuations.

4 Experiment Results and Discussion

In this section we present an example of tuning the system using the visual cues and statistical measures derived from the calibration maps. Note that we actually utilise more graphs than what is shown in the figures.

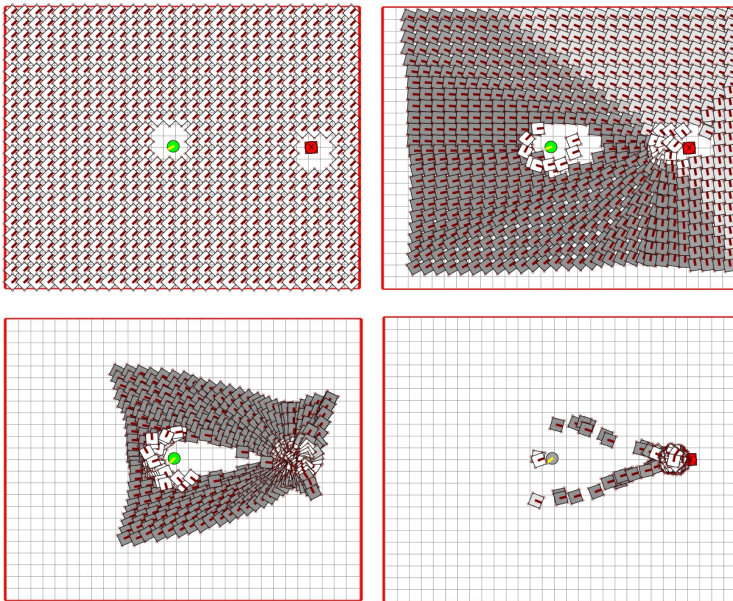


Fig. 2. Calibration maps for the combined target pursuit and obstacle avoidance behaviours. The target is the red square robot, and the obstacle is the green circle. Shown clock-wise, starting from the top-left, are the robot movements at time $t=1$, $t=4$, $t=14$ and $t=47$.

4.1 One Obstacle

The simulation set-up for the simplest case of a single obstacle is shown in Fig. 2. The target is the red square marked with an 'x', and the obstacle is represented by the green circle. At time $t=1$, all robots were initialised with the same heading angle of 45 degrees relative to the x-axis. At time $t=4$, it can be observed that some of the robots changed darker in colour, indicating that they have started accelerating towards the target. The increase in speed is due to either line 9 or line 17 of Algorithm 2, depending on whether there is no imminent danger along the heading direction of the robot and if it is pointing somewhat towards the target. The same pattern can be observed at $t=14$. However, at $t=47$, it can be seen that two of the robots eventually collided with the obstacle. Interestingly, the generated x-y-t graph in Fig. 3.a, and the x-y-collisions graph in Fig. 3.b, tells us more story than what can be observed from Fig. 2. The peak and the mountainous region in Fig. 3.a indicate that the robots that originated from that area took more time to travel towards the target, than any of the other robots. The peak indicate the positions that suffered the most delay. On the other hand, the peaks in Fig. 3.b tells us about the positions that incurred the collisions.

Based on the location of the problem areas, the recorded data, the membership functions and rules with the highest degree of firing during the collision

Given: Robots r_i , obstacles o_j , target Tg and $maxTime$

Output: 2-D array of structure containing the elapsed time t_r , standard deviation of the robot's heading angle relative to the target destination $stdDev_r$ and number of collisions cl_r incurred by all the robots.

- 1: Discretise the entire MiroSot soccer field, using the robot's size as the cell size for generating the grid-world.
- 2: Initialize the 2-D array of structure to match the grid. position the target, obstacles and robots, while avoiding overlaps. Use the grid as a guide for the placement of all objects. Fill-up the entire grid by adding more robots if necessary.
- 3: **for** $t = 0$ to $maxTime$ **do**
- 4: For each robot r_i , compute the steering angle and speed adjustments according to Algorithm 2.
- 5: Calculate the new position of all the robots. Check for any collision with obstacles (record if any is found).
- 6: Update the array of structure to reflect the new values for the accumulated elapsed time t_r , robot's heading angle relative to the target $angleFromTarget_r$, and number of collisions cl_r incurred by each of the robots.
- 7: If all robots have hit the target already, then break out of the loop.
- 8: **end for**
- 9: For each robot, calculate the standard deviation of the robot's heading angle relative to the target (store as $stdDev_r$).
- 10: Plot the contents of the array of structure to generate the 3-D graphs: X-Y-Time, X-Y-Standard Deviation and X-Y-Number of Collisions.
- 11: For each graph, identify the individual robot corresponding to the maximum peak. Run this robot alone, starting from its original position in the grid-world, and observe the degree of firing of all the fuzzy sets to get an idea of which membership functions and fuzzy rules need changing.
- 12: Edit the fuzzy system structures based on the observations made. (e.g. the range for the fuzzy set SMALL might need to be extended, for instance.)
- 13: Repeat from Step 2.

Algorithm 1: Tuning algorithm

instances, one can use these as clues to change the specific fuzzy parameters to tune the system. The improved results are shown in Fig. 4.a, where the peak has disappeared. Moreover, in support of this improvement, the number of collisions in Fig. 4.b has also decreased.

4.2 Three Obstacles

The scenario depicted in Fig. 5 raises the level of difficulty for the navigation system, where there are 3 obstacles present, in front of the target. Similarly, the initial angles of the robots for this experiment were fixed at 45 degrees, at time $t=1$ (not shown in the figure). Therefore, the results shown in Figs. 6 and 7 are slightly non-symmetrical, as it would be expected from the initial angles.

Given: coordinates of the target (x_t, y_t) , coordinates of the robots $(x_1, y_1), (x_2, y_2), \dots, (x_N, y_N)$, coordinates of the obstacles $(x_1, y_1), (x_2, y_2), \dots, (x_M, y_M)$, robots' angle to target $\alpha_1, \alpha_2, \dots, \alpha_N$, robots' angle to the nearest obstacle $\sigma_1, \sigma_2, \dots, \sigma_N$, target's position relative to the heading angle of each robot TP_1, TP_2, \dots, TP_N (*RIGHT* or *LEFT*), robots' distance to target DT_1, DT_2, \dots, DT_N , robots' distance to the nearest obstacle DO_1, DO_2, \dots, DO_N , distance coefficients K_1, K_2 , obstacle position OP_1, OP_2, \dots, OP_N (*RIGHT* or *LEFT*), angle of the robots $\beta_1, \beta_2, \dots, \beta_N$

4 structures with fuzzy information:
 pursuit steering PA , pursuit speed PS avoidance steering angle AA , avoidance speed AS

Output: robots' angle $\beta_1, \beta_2, \dots, \beta_N$

robots' speed s_1, s_2, \dots, s_N

```

1: for  $i = 1$  to  $R$  do
2:   if  $(DT_r > K1)$  then
3:     {Fuzzy system 1}
4:      $\theta = Fuzzy(\alpha_r, DT_r, PA)$ 
5:     if  $(TP_r = RIGHT)$  then
6:        $\theta = -\theta$ 
7:     end if
8:     {Fuzzy system 2}
9:      $FS = Fuzzy(\alpha_r, DT_r, PS)$  {calculate absolute robot speed }
10:    if  $(DO_r < K2 \&\& OP_r == TP_r)$  then
11:      {Fuzzy system 3}
12:       $\theta = Fuzzy(\sigma_r, DO_r, AA)$ 
13:      if  $(OP_r == LEFT)$  then
14:         $\theta = -\theta$ 
15:      end if
16:      {Fuzzy system 4}
17:       $FS = Fuzzy(\sigma_r, DOr, AS)$ 
18:       $RS = FS$  {conditionally overrides RS}
19:    end if
20:     $s_r = FS$ 
21:     $\beta_r = \beta_r + \theta$ 
22:     $r = move(s_r, \beta_r)$  {move robot}
23:  end if
24: end for

```

Algorithm 2: Integrated Target Pursuit and Obstacle Avoidance

Comparing the figures also prove that the calibration method was able to help in the fine-tuning of the system. The calibration map and the supporting 3-D plots of accumulated elapsed time and accumulated number of collisions show how much improvements (lesser number of peaks) were gained after tuning the fuzzy system structures.

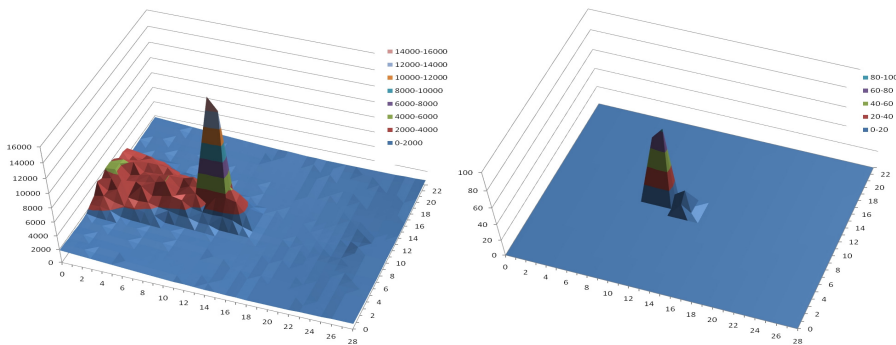


Fig. 3. Navigation performance results using the initial system configuration with the presence of a single obstacle. (Left-side) accumulated elapsed time, (Right-side) accumulated collisions.

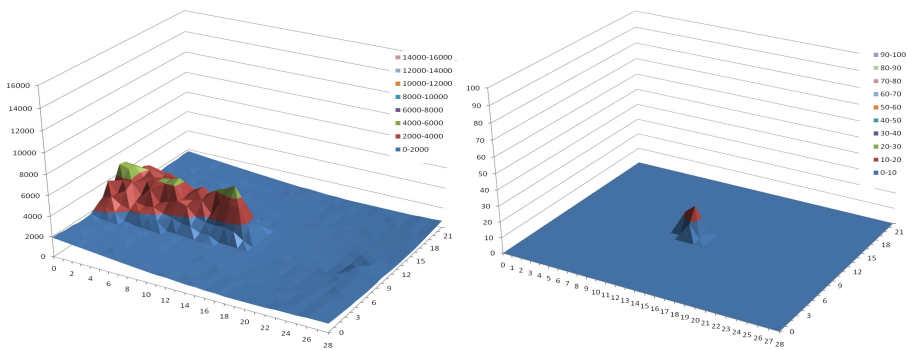


Fig. 4. Navigation performance results after system tuning, with the presence of a single obstacle. Note that the peaks disappeared. (Left-side) accumulated elapsed time, (Right-side) accumulated collisions.

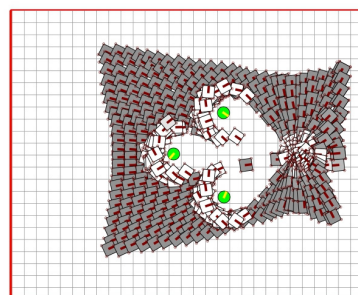


Fig. 5. Simulation with three obstacles (time = 10)

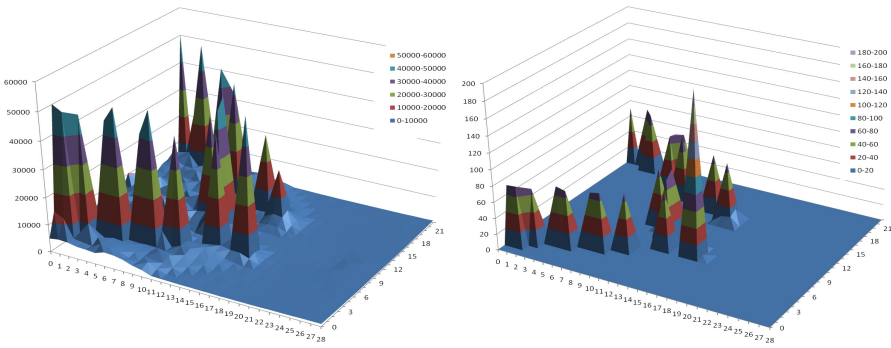


Fig. 6. Navigation performance results using the initial system configuration with the presence of 3 obstacles. (Left-side) accumulated elapsed time, (Right-side) accumulated collisions.

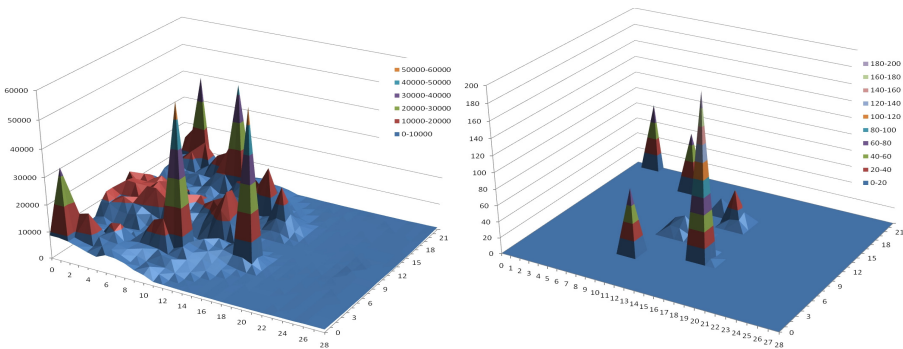


Fig. 7. Navigation performance results after system tuning, with the presence 3 obstacles. Note that the number of peaks were significantly reduced, as compared to the performance of the initial configuration. (Left-side) accumulated elapsed time, (Right-side) accumulated collisions.

5 Conclusion

We have proposed a new calibration method that is best suited for calibrating complex robot navigation systems, where it is neither trivial nor obvious to see if certain parameter tweaking makes any difference to the overall system performance. The new method allows for an easy to comprehend visualisation of the system's performance, quantification of the overall efficiency and provides some useful clues to the system designer to locate the faulty components/parameter settings. In this paper, we demonstrated the calibration method using a cascade of 4 fuzzy systems. In the future, the calibration method can be used to formulate a fitness function for an optimisation algorithm (e.g. genetic algorithm, particle swarm optimisation). Using this approach, most, if not all system parameters can be automatically determined.

References

1. Kim, J.H., Kim, K.C., Kim, D.H., Kim, Y.J., Vadakkepat, P.: Path planning and role selection mechanism for soccer robots. In: International Conference on Robotics and Automation (1998)
2. Patnaik, S.: Robot Cognition and Navigation: An Experiment with Mobile Robots. Springer (2007)
3. Park, J.-H., Stonier, D., Kim, J.-H., Ahn, B.-H., Jeon, M.-G.: Recombinant rule selection in evolutionary algorithm for fuzzy path planner of robot soccer. In: Freksa, C., Kohlhase, M., Schill, K. (eds.) KI 2006. LNCS (LNAI), vol. 4314, pp. 317–330. Springer, Heidelberg (2007)
4. Kim, J.H., Kim, Y.H., Choi, S.H., Park, I.W.: Evolutionary multi-objective optimization in robot soccer system for education. IEEE Computational Intelligence Magazine 2, 31–41 (2009)
5. Kim, J.H.: Federation of robot-soccer association, <http://www.fira.net/>
6. Garrido, S., Moreno, L., Blanco, D., Jurewicz, P.: Path planning for mobile robot navigation using voronoi diagram and fast marching. International Journal of Robotics and Automation 2, 154–176 (2011)
7. Linquan, Y., Zhongwen, L., Zhonghua, T., Weixian, L.: Path planning algorithm for mobile robot obstacle avoidance adopting belzier curve based on genetic algorithm. In: IEEE Chinese Control and Decision Conference, pp. 3286–3289 (2008)
8. Jayasiri, A., Mann, G., Gosine, R.: Behavior coordination of mobile robotics using supervisory control of fuzzy discrete event systems. IEEE Transactions on Systems, Man, and Cybernetics, Part B: Cybernetics 41, 1224–1238 (2011)
9. Calisi, D.: Mobile Robots and Vehicles Motion Systems: a unifying framework. PhD thesis, Sapienza Universita di Roma (2009)
10. Matia, F., Jimenez, A., Martinez, G.: Calibration of fuzzy control systems. In: Third IEEE Conference on Fuzzy Systems, Orlando, FL, pp. 7–12 (1994)
11. Gerdelen, A., Reyes, N.: A novel hybrid fuzzy a star robot navigation system for target pursuit and obstacle avoidance. In: 1st Korean-New Zealand Joint Workshop on Advance of Computational Intelligence Methods and Applications, pp. 75–79 (February 2006)
12. Gerdelen, A., Reyes, N.: Synthesizing adaptive navigational robot behaviours using a hybrid fuzzy a star approach. In: Reusch, B. (ed.) Computational Intelligence, Theory and Applications, pp. 699–710. Springer, Heidelberg (2006)
13. Gerdelen, A.P., Reyes, N.H.: Towards a generalised hybrid path-planning and motion control system with auto-calibration for animated characters in 3D environments. In: Köppen, M., Kasabov, N., Coghill, G. (eds.) ICONIP 2008, Part I. LNCS, vol. 5506, pp. 1079–1086. Springer, Heidelberg (2009)
14. Reyes, N., Barczak, A., Fatahillah, S.T.: A reconfigurable hybrid intelligent system for robot navigation. Research Letters in the Information and Mathematical Sciences 15, 21–34 (2011)

Distributed and Incremental Visual Object Categorization for Humanoid Platform NAO

Peter Sincak, P. Smolar, M. Vircik, and M. Pala

Center for Intelligent Technologies, Department of Cybernetics and Artificial Intelligence,
Faculty of Electrical Engineering and Informatics, Technical University of Kosice, Slovakia,
{peter.smolar, peter.sincak, maria.vircik, martin.pala}@tuke.sk

Abstract. Robotics is an essential component of current and future technological existence of mankind. Interaction between human and technology such as robots and their coexistence with humans will be extremely important. In fact, a fully embodied intelligence is one version of the future but another option is distributed intelligence when a part of intelligence is “somewhere in the Cloud”, and the second part is on the robot itself. Certainly there are several questions about connectivity and reduced activity in case of off-line robot life comparing to life in on-line robot existence. Meanwhile, a notion of Cloud Robotics came out, and it brings new challenges and endless possibilities for the future. The paper gives theoretical and experimental research about utilization of selected Neural technology specifically modified MF-ARTMAP neural network for object categorization. We used the categorization test-bed a Humanoid platform NAO connected to Global framework (MASS), which categorize in distributive and incremental approach objects. This approach creates a power of sharing knowledge among other robots and building collective intelligence. Papers gives the results of a pilot study and refers about preliminary results on different experimental data with building a database of objects on off-robot ecosystem. The system also works with fuzzy logic relations among objects and maintain a list of statements about the relationship between objects seen by the robot.

Keywords: distributed intelligence, image object recognition, ART neural networks, MF-ARTMAP neural network, fuzzy cluster, category, humanoid platform NAO, MASS.

1 Introduction

The power of living organisms to obtain information from the environment is essential for survival in the nature. If we focus only on visual perception, they are tasks such as detection, recognition of the enemy, finding a food, orientation in the surroundings. However, scientists try to understand these processes, replicate them and use in artificial intelligence systems. So far, however, nature handles with these tasks much better than scientists in laboratories [1]. Now, it gives attention to the solution of the object recognition or object categorization due to growing application areas of using, especially

in robotics, industrial, healthcare and other services. It is a particularly interesting comparison between humans and machines in recognition performance. Based on [2] humans are much better in categorization to general classes than machine, but in classification into more classes, machines can often be handled more efficiently or reliably using artificial vision systems. In [3] describes that humans can perform ultra-rapid categorization tasks in time less than 150 milliseconds. Also, it is fascinating information that humans can organize into about 30,000 different categories [4]. This paper deals with a neural system for image recognition related to the categorization process tested on the NAO humanoid robot. Results and pilot experiments presents with object categorization for NAO humanoid platform.

2 Background

Image processing in general has some theoretical and practical steps which are extremely important to understand. There are a number of approaches image processing, and we can generalize the basic structure of these principles consisted of individual processes. Much information can be found in [1,2,9]. These are as follows:

Definition of Feature Measurement – In this stage we propose methods for features measurement. Some features may give better categorization results than the others. It is exceptionally difficult to predict which features of the objects will have a positive effect for the entire result of the categorization process. Therefore, in this step we should perform detailed analysis of input data. **Measurement of Features** – Here, we extract features from the image using the method chosen in the Definition step.

Selection of Features – Here, we implement the method chosen in the Definition of Feature selection step. Computation complexity could decrease with fewer features and dimensionality of the feature space is smaller. **Definition of Classification Method** – The right choice of classification method is crucial, too. It is advantageous to use relevant a priori knowledge. **Classification** - After the definition of classification method, we use this method for a classification of input patterns to the categorization classes. **Definition of the Categorization** – In this block we propose methods for Categorization. Usually we choose one from clustering methods. The selected method depends on character of data. **Categorization** - in terminal block, selected method of categorization is running.

After application of every phase, we evaluate the current block, and we propose an improvement of the method in definition blocks. The expert can interfere with all blocks of Definition. In some cases, process of classification and categorization can be solved together in one technology as in **MF ARTMAP neural network** [10,11]. We can find other aspects of categorization system in [2]. Learning for Categorization is extremely important. A visual categorization system learns from the training set (images or sequences of images). Learning we can divide into supervised approaches and unsupervised approaches. In the case of supervised learning, training example contains visual input sample (training sets) and also label of the category. Categorization system learns from these training sets and labels. Obtained results from learning of categorization system are influencing boundaries between categories (discriminative hyper-planes) in features spaces. Unsupervised manner presents trained only with the visual inputs but without labels of categories.

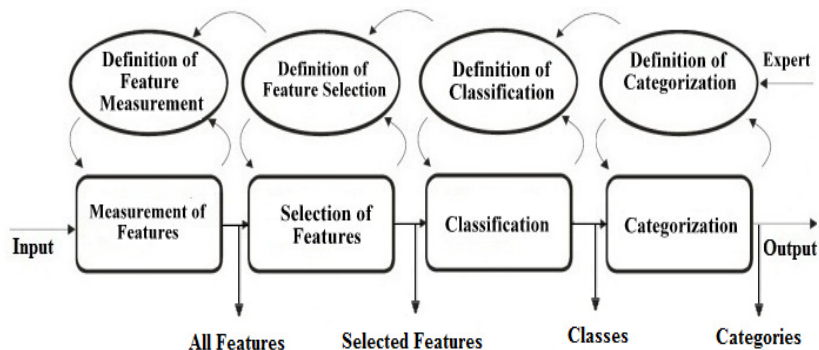


Fig. 1. Process of categorization based on original ideas on research of [14]

In research on object categorization, we can meet with the term “weak supervision” and “strong supervision”. Number of categorization approaches used in research and real-world environment including a nearest-neighbor method [5], support vector machines [6], Boosting [7], neural networks and genetic algorithms and some others.

The power of distributive intelligence partly on the Cloud and partly embedded on the Robots is the approach what this paper is advocating.

We have developed some pilot framework Multi Agent Sophisticated System (MASS) for experimenting with this idea [8].

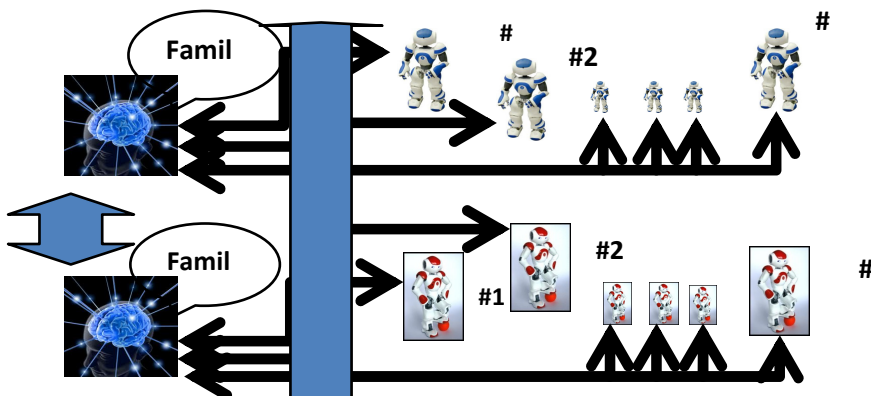


Fig. 2. Distributed Intelligence – partly on the Cloud and partly Embodied on the Robot

3 Membership Function ARTMAP Neural Network

We can find the motivation for this network in ambition to propose an algorithm with the ability better understand the data and to represent knowledge in a comprehensible form in various applications [1,11,12]. Considering supervised categorization is often particularly difficult to label the of input sample to the class if the samples can be classified into various classes. Neural network MF ARTMAP tries to solve this problem by a combination of the theory of Fuzzy Sets¹ and ART-like neural network. The neural network tries to compute so-called “membership” of the sample related to all classes. Thus, the final result of the classification is not “crisp” decision about classification of the unknown input to the one class, but it is a vector of values presenting membership function to classes. We do consider that number of “fuzzy clusters” are in the feature space, and this feature space is the universe of fuzzy sets. Considering each point x from this space, we can calculate the value of membership $\mu_A(x)$ to the each fuzzy set related to each fuzzy class A , where index A presents a fuzzy cluster².

Fig. 3 below shows an example of function of fuzzy relation in two-dimensional input feature space and a shape of this function can be changed with parameters E and F (see equation 1).

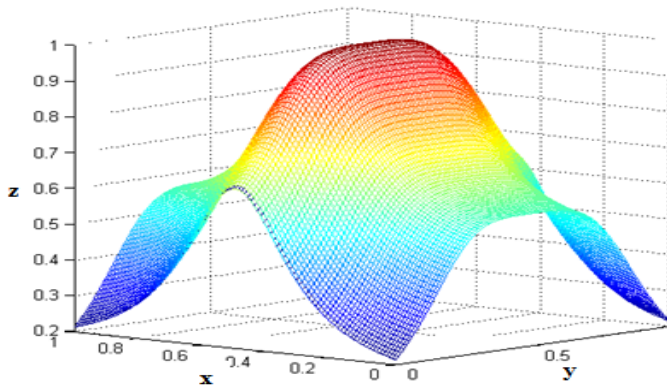


Fig. 3. Shape of the cluster in two-dimensional input features space Axes x and y represent dimensions of the feature space, axis z represents the value of the membership function of samples to the fuzzy cluster.

In respect to these requirements, the membership function for cluster k as a fuzzy set, the calculation in the MF-ARTMAP network (for m -dimensional feature space) we define as follows:

¹ For understanding of MF-ARTMAP network is important to have basic knowledge from Theory of Fuzzy Sets. This information is possible to find in [11,12].

² In this work we consider terms „fuzzy set“ and „fuzzy cluster“ as semantically equivalent.

$$\mu_k(\bar{x}_i) = \frac{1}{1 + \left| \left(\frac{\bar{x}_{sk} - \bar{x}_i}{E_k} \right)^{F_k} \right|} \quad (1)$$

Where:

- m is the number of dimensions of input feature space,
- $i=1, \dots, m$ is the index of the dimension of the input feature space,
- n is the number of all the samples in the training set,
- p is the number of created fuzzy clusters,
- $k = 1, 2, \dots, p$ is the index of the actual fuzzy cluster,
- $\mu_k(\bar{x}_i)$ is the membership of the sample \bar{x}_i to the fuzzy cluster k ,
- \bar{x}_i is the vector of an arbitrary point in the input feature space,
- \bar{x}_{sk} represents the center of fuzzy cluster k the feature space
- E_k and F_k are the parameters of fuzzy cluster k – shape related

We can define fuzzy class CL as union of fuzzy clusters that belong to this fuzzy class. If we consider A as a cluster in the feature space and the fuzzy set in the feature space can be expressed as

$$A_{CL} = \left\{ \bigcup_{k=1}^s A_k \right\} \quad (2)$$

Where parameter s defines number of fuzzy clusters that belong to the fuzzy class CL and operation of union defines as unification of fuzzy clusters.

Next, we can express the relation between membership function $A(x)$ of an arbitrary point x to the class CL and membership functions of all clusters of this class as follows:

$$\mu_{A_{CL}}(x) = \max(\mu_{A_1}(x), \dots, \mu_{A_s}(x)) \quad (3)$$

Where A_{CL} is a fuzzy cluster, which belongs to fuzzy class CL and “ s ” defines the number of fuzzy clusters of fuzzy class CL . The MF ARTMAP neural network computes membership value for arbitrary input samples from the feature space related

to fuzzy class from the training set. The topology is similar to the topology of ARTMAP neural networks [11]. The neural network topology stores knowledge of the training procedure in parameters of neural network.

4 Experiments on NAO Humanoid Platform Using MASS

4.1 Experiment with Single Object

We have tested an image of Juice box to categorize by Nao Robot. The input image was the Juice placed in front of the NAO robot. We have used some SIFT feature for learning phase. The algorithm is sensitive to light conditions but robust to the angle change considering turning of classified objects.



Fig. 4. Robot Nao learns the object "Juice".

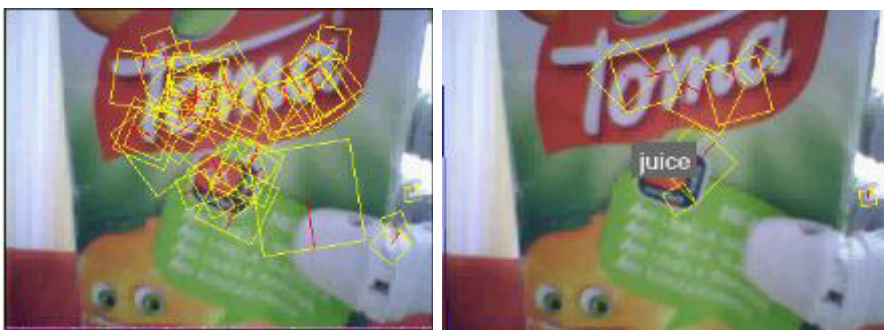


Fig. 5 SIFT descriptors detection

Fig. 6 Result of categorization is "Juice"

This approach was implemented in MASS system and presented by Reiff and Sincak in [15] and is partly similar with the intention of project RobotEarth by [16]. We do intend to converge MASS project into progressive RoboEarth concept

The overall systems provide categorization service that if one NAO learns a Juice Object all the NAOs will be able to recognize it. The importance is in Incrementality of the system which means IF 10 Robots are learning one object and are in the “family” of Robots according to fig. 2. each of the robots can recognize 10 objects in a very moment.

4.2 Experiment with More Complex Image

The power of MF ARTMAP was tested also on the different image where relations between objects were under the main focus of experiments. The input image of the robot was a scenario of the house and a distributed intelligent system was able to comment a relation among the objects on the image. Captured objects are as follows: “house”, “door”, “window”, “roof”, “balcony”, “face of the house”. There were objects trained separately including the overall picture. The clusters were optimized, and also MF ARTMAP investigate the inter and intra relations between and within categories.

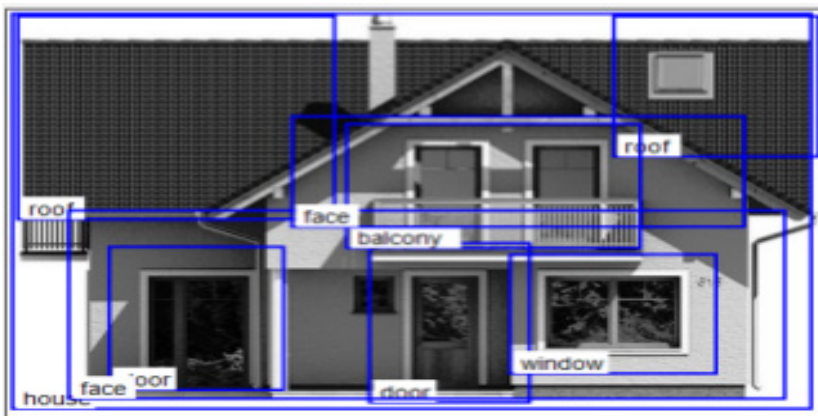


Fig. 5. Image with objects : house, door, window, roof, balcony, face of the house.

The MF-ARTMAP system was able to generate a list of statements which can give information about the interrelations of objects and increase intelligence of robots. The MASS environment computes this knowledge which in off robot mode. Examples of Intra-class and Interclass statements are as follows:

- Class house is **strongly homogenous** with membership (0.02).
- Class house is **homogenous** with membership (0.1).
- Class house is **heterogeneous** with membership (0.9).

- Class roof is **partly similar** to class house with membership (0.05).
- Class roof is **similar** to class house with membership (0.94).
- Class roof is **very similar** to class house with membership (0.04).

Using fuzzy sets the user fully define the notions “strong homogenous”, “homogenous”, “heterogeneous”, “partly similar”, “similar” and “very similar”.

5 Conclusion

The results are presenting research on a pilot study towards distributed intelligence for Robots. We do believe that Incrementally and Distributive manner of intelligence for Robots is very important part of the future of Robotics. Full Embodiment of Intelligence is not a way to get intelligent man made machine done. The research reports about experiments done on NAO Humanoid platform as fixed hardware and presenting experimental results towards building distributed intelligence for robots. MF-ARTMAP neural network have incremental learning ability and also we have developed a modification to extract any mutual relation among objects. This advantage is extremely significant for distributed intelligence implementation. The relations describe the human-like statements using fuzzy logic and. We will focus to establish an open framework for Cloud based Robotics in the future where we do see an important direction in Intelligent Robotics.

Acknowledgements. Research partly supported by a number of projects including the project implementation of “Development of the Center of Information and Communication Technologies for Knowledge Systems” (ITMS project code: 26220120030) supported by the Research & Development Operational Program funded by the ERDF. These results are also thanks to the project "Center of Competence of knowledge technologies for product system innovation in the industry and service", with ITMS project number: 26220220155 for the years 20012-2015 and also the research is partly supported by the National Research and Development Project Grant 1/0667/12 “Incremental Learning Methods for Intelligent Systems” 2012-2015.

References

1. Duda, R., Hart, R.P.E., Stork, D.G.: Pattern Classification, 2nd edn. John Wiley & Sons (2000)
2. Pinz, A.: Object Categorization, Foundations and Trends. Computer Graphics and Vision 1(4) (December 2005)
3. Van Rullen, R., Thorpe, S.: Is it a bird? Is it a plane? Ultra-rapid visual categorization of natural and artificial objects. Perception 30, 655–668 (2001)

4. Biederman, I.: Visual object recognition. In: Kosslyn, S.F., Osherson, D.N. (eds.) *An Invitation to Cognitive Science. Visual Cognition*, vol. 2, ch. 4, pp. 121–165. MIT Press (1995)
5. Lowe, D.G.: Object recognition from local scale-invariant features. In: Proc. International Conference on Computer Vision, pp. 1150–1157 (1999)
6. Vapnik, V.: *The nature of statistical learning theory*. Springer (1999)
7. Opelt, A., Fussenegger, M., Pinz, A., Auer, P.: Weak hypotheses and boosting for generic object detection and recognition. In: Pajdla, T., Matas, J(G.) (eds.) *ECCV 2004, Part II. LNCS*, vol. 3022, pp. 71–84. Springer, Heidelberg (2004)
8. Reiff, T., Sincak, P.: Multi-agent sophisticated system for intelligent technologies. In: International Conference on Computational Cybernetics, ICCC 2008, pp. 37–40 (2008) ISBN 9781424428755
9. Veregin, H., Sinčák, P., Kopčo, N.: Enhancement of Classification Accuracy Using Conflation Procedures. *Geocarto International, A Multi-disciplinary Journal of Remote Sensing* 15(1) (2000)
10. Sonka, M., Hlavac, V., Boyle, R.: *Image Processing, Analysis, and Machine Vision*, 3rd edn. Thomson-Engineering (2007) ISBN:049508252X
11. Sincak, P., Hric, M., Vascak, J.: Pattern recognition with MF-ARTMAP neural networks. In: Tech 2001, pp. 282–291. Assumption University, Bangkok (2001) ISBN 9746150685
12. Sincak, P., et al.: Financial fraud identification using MF-ARTMAP neural network. In: *Advances in Soft Computing*, pp. 95–106. Physica-Verlag, Heidelberg (2002) ISBN 3-7908-0005-8
13. Bodnarova, A., Olevicova, K.: MF-ARTMAP Neural Network Prediction Of the Market Position of the Company. In: IADIS European Conference on Data Mining (2007) ISBN 978-972-8924-40-9
14. Personal communication with prof. Jim Bezdek, University of West Florida, USA
15. Reiff, T., Sinčák, P.: Towards intelligent systems with incremental learning ability. In: Rudas, I.J., Fodor, J., Kacprzyk, J. (eds.) *Towards Intelligent Engineering and Information Technology. SCI*, vol. 243, pp. 627–638. Springer, Heidelberg (2009)
16. Roboearth project, EU FP7 FP7/2007-2013, web page seen (November 2012),
<http://www.roboearth.org/>

Computational Intelligence for Creating Autonomous Robots

Pitoyo Hartono

Dept. of Mechanics and Information Technology
Chukyo University, Toyota, Japan
hartono@ieee.org

Abstract. In this paper, some computational intelligence methods that can be applied for generating autonomous robots, proposed by the author, are outlined. Through these on-going studies, the author argues that these methods are promising candidate in at least complementing conventional design process for assembling robots.

Keywords: learning algorithm, self-configuration, module robotics, autonomous robots.

1 Introduction

Recently the roles of robot in our daily life have become increasingly important. This is symbolized by the increasing choices for commercially available floor-sweeping robots. Following this trend, in the near future it is not difficult to foresee that many robots will play more important roles in the fields of medicine, welfare, entertainment, education and so on. Hence, soon we will need to produce robots with variety of multitask-solving abilities and morphologies. However, the designing and the production processes of robots remain very complicated and expensive. It is obvious that to be able to effectively deal with the ever increasing variety of demands for those robots in various contexts, new methods for constructing robots need to be considered. Soon the conventional manufacturing process will be overwhelmed by these increasingly demands, not only in number but in complexity as well. On the other hand, it is known that nature and society are able to produce complicated artifacts using methods that are substantially different from our industrial manufacturing process. Evolution has been successful in producing rich collection of living organisms with very complex structures that nicely adapt to their various environments. In shorter temporal range, the learning abilities of the living organisms allow them to modify their behavior and sometimes their environments as well in order to increase their fitness. Self-organization is a strong method in producing natural and social structures, such as geological landscapes and snow crystal and social interaction. It also produces complex behaviors, such as the foraging in insects [1,2], the collective intelligence of the slime mold [3] to the formation of large scale synchronized system [4,5], market systems, language and even human civilizations [6,7].

In the past decades, with the help of the increasing availability of computational resources, we have seen the emerging of new problem-solving methods that are inspired by nature and social systems (not necessarily that of human), for creating artifacts, including robots. Rich collections of evolutionary calculations methods, such as Genetic Algorithm [8], Genetic Programming [9] and Evolutionary Programming [10] have been successfully applied to solve complicated optimization problems, designing complicated structures such as trains and some parts of airplanes, generating electrical circuits, and so on. Many types of learning algorithm [11], such as supervised learning, unsupervised learning, the combinations of both, and reinforcement learning [12] have been proposed for capturing the underlying rules of the problems that are difficult to extract using conventional calculations methods. The applications of neural networks cover the fields of not only engineering but also natural science, social science, medical science, industry, linguistic and so on.

It is only natural, that these computational intelligence methods should be included at least to complement the manufacturing process of robots, not only to partially relax the manufacturing complexity, but also to improve the flexibility, resiliency and adaptability of the robots in facing various users, running environments and task in physical environments.

The objective of this paper is to give a brief outline on some examples of the utilization of computational intelligent methods in generating autonomous robots that have been done by the author in the recent years.

2 Creating Robots: From Designing to Nurturing

The conventional manufacturing of a robot usually contains a string of processes shown in Fig. 1.

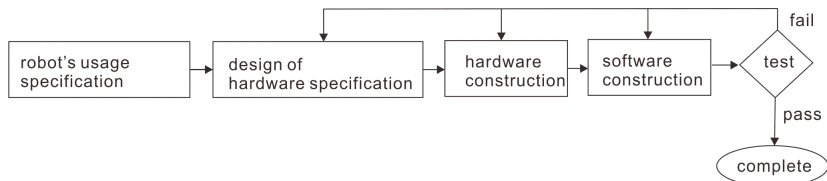


Fig. 1. Conventional Manufacturing Process of Robots

The first step is to decide the usage of the robot, for example the intended task, users and running environments of the robot. The second process is to design the physical structure that can satisfy the specifications decided in the first step, while the third and the fourth steps are the processes of physically assembling the hardware, and building the software for hardware-control. Any diffraction from the specification requires costly reiteration of one or more of those processes. This designing process of robots is expensive mainly because it still involves human resources. Furthermore with this conventional process, the robot can rarely be used outside its initial usage specification. Many of the problems of the design-based robots can be solved by introducing computational intelligence methods in the production process of the robots. A few examples of the currently introduced methods are explained as follows.

2.1 Training of Physical Robots

Many methods for training robots have been proposed [13-15]. In this paper, a fast training algorithm [16] that can be implemented in robots with limited power and computational resources.

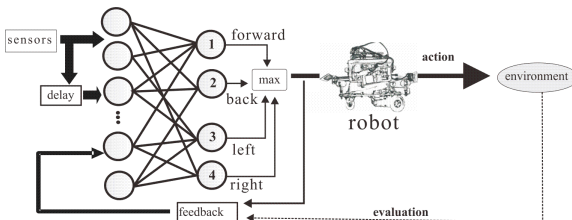


Fig. 2. Neural Network as Controller

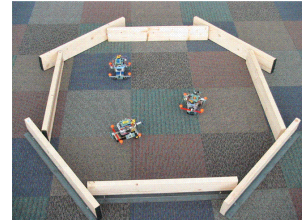
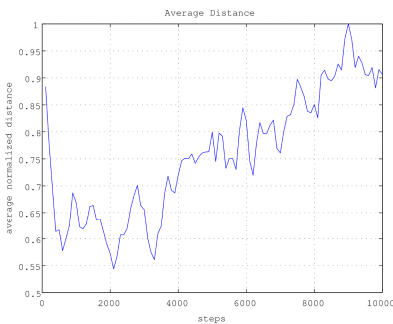
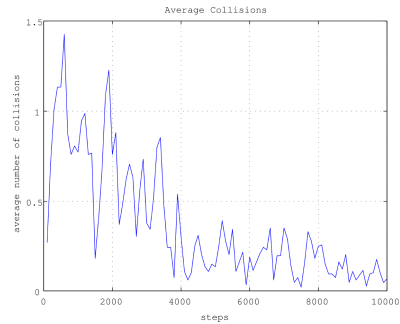


Fig. 3. Learning Environment

In this study, a fast neural network, illustrated in Fig. 2 was proposed. The inputs to the neural network are the sensory information obtained through the sensors attached to the robot, while the output is the actions of the robot. In this learning mechanism, when the selected action brings good evaluation, the learning process rewards that action by reinforcing the value of the output neuron associated with that action, and at the same time suppressing the output neurons associated with other actions. Inversely, when the selected actions generated poor evaluation, the learning process punishes that action and enhances the values of the output neurons associated with other actions. The learning algorithm here is a kind of Reinforcement Learning, but implemented in a layered structure that requires significantly less computational resources. The mathematical details of this learning process is explained in [16]. Using this learning algorithm, three small robots were trained in the same arena, thus generating a dynamic environment, as shown in Fig. 3. The robots were trained to acquire obstacle-avoidance behavior. Figure 4 shows the average distance between the robots and the obstacles during the learning process. This graph shows that the robots gradually acquire a strategy that allows them to move away from the obstacle by always executing actions that maximize their distance from the obstacles. Figure 5 indicates the successful learning of the robots in decreasing the frequency of collisions with each other or environmental obstacles. The efficiency of this learning algorithm is also tested with regards to robots with different mechanical structure. This learning mechanism allows real time learning of physical robots without requiring any computer simulations. The generality of the training algorithm was also tested against different morphologies.

A similar learning algorithm was also implemented on “survival” robots shown in Fig. 6. These robots are equipped with solar panels, thus can obtain their own energy. They were trained to “survive” in outdoors environment by acquiring good moving and energy management strategies. These robots were successfully tested in outdoors environments for several days without human intervention. The detail of this experiment is explained in [17].

**Fig. 4.** Average Distance**Fig. 5.** Average Collisions**Fig. 6.** Survival robots and the training environment

The experiments explained above show the promising possibilities of the learning mechanism in allowing the robots to autonomously acquire strategy in physical environments. It should be noted that both of the experiments were run on dynamic environments which are not easy to model, as required by hand-designed robots. This alone is a promising indication that learning mechanism is a strong candidate in replacing or at least complementing hand-coded strategies for robots running in real world environment.

Some techniques to include human, as evaluators, in the process of training physical robots were also proposed. Including human in the learning cycle may significantly improve the learning process of the robots, especially in the case when the learning objectives are hard to be mathematically expressed. A successful case was presented in [18], where a human coached a humanoid robot to learn to walk in real time.

2.2 Self-configuration of Physical Robots

As explained above, learning mechanisms enable the robots to autonomously acquire and adapt strategies in executing their task, thus relaxing the requirement for designing the controller software in the manufacturing process. However, learning mechanism does not usually allow the robots to configure and reconfigure their hardware morphologies. Recently many studies of modular robotics [19-23] are

dedicated to the development of hardware modules that can easily be configured to form various physical morphologies. The mechanisms for self-configuration and reconfigurations of those modules are also rigorously studied.

In this paper, an on-going study of the development of self-configuring hardware modules was introduced. The promising initial results of this study have been presented in [23]. In this study, many robotics modules (Fig. 7), each one containing limited computational and power resources, actuators, sensors and connectors, were built.

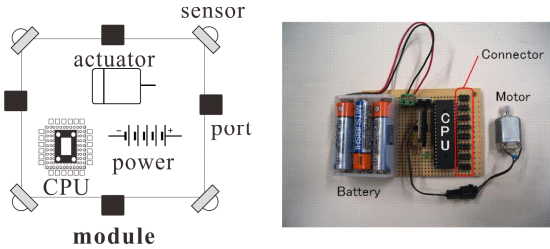


Fig. 7. Hardware Module

Each module is able to independently generate a simple behavior. The objective is to develop a mechanism that allows the randomly connected modules to self-configure the connection topology so that they collectively generate a coordinated movement as a single robot. In this case, the task of human is to generate an initial connection topology by arbitrarily connecting many modules and to provide an objective function that reflects the goal behavior of the robot. As illustrated in Fig. 8, the topology adaptation is gradually executed in where for a predefined time interval the behavior of the connected modules is evaluated, and mutated according to optimization mechanism, such as simulated annealing (SA). In [23], it is shown that the self-configuration mechanism can run in real time.

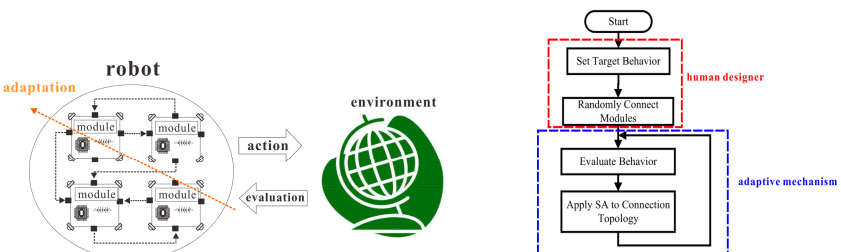


Fig. 8. Self-configuration of hardware modules

Here, module i , operates as an oscillator, producing periodical behavior which phase at time t is $\theta_i(t)$, shown in Eq. (1). In this equation, $\omega_i(t)$ denotes the angular velocity of the i -th module at time t , ε_{ij} denotes the asymmetrical connection between the i -th module and the j -th module, in which $\varepsilon_{ij} = 1$ indicates that the i -th

module is able to send signals to the j -th module, while $\varepsilon_{ij} = 0$ indicates the severance of this connection. ψ_{ij} denotes the ideal phase difference between the two modules, while $\eta(t)$ is a small random noise, and T_j is the time when the phase of the j -th module reaches 2π , and N is the number of modules.

$$\frac{d\theta_i(t)}{dt} = \omega_i(t) - \sum_{j=1}^N \varepsilon_{ij} \sin(\theta_i(t) - \psi_{ij} + \eta(t)) \delta(T_j - t)$$

$$\forall i, j \quad \varepsilon_{ij} \in \{1, 0\} \quad \varepsilon_{ii} = 0 \quad (1)$$

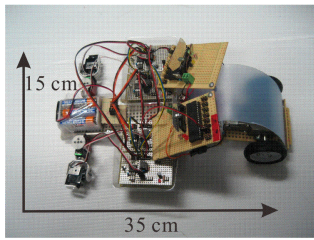
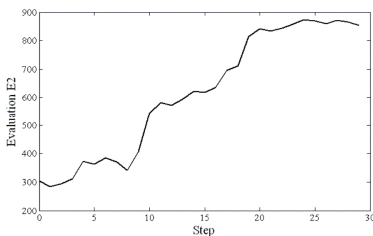
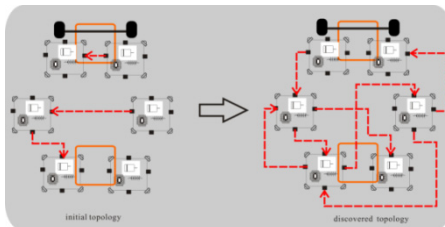
$$\delta(x) = \begin{cases} 1 & x = 0 \\ 0 & x \neq 0 \end{cases}$$

From Eq. (1), it is obvious that the collections of these modules generate a Central Pattern Generator (CPG), while the network topology of this CPG is decided by the collection of inter module connections indicated by matrix $E = [\varepsilon_{ij}]$. Hence, the target of topology self-configuration mechanism is the matrix $E = [\varepsilon_{ij}]$.

In the initial experiments reported in [23], this self-configuration mechanism is utilized for the formation of connection topologies of a group of modules that constitute many morphologies of robots. One of them is shown in Fig. 9. This robot is assembled from six modules, four of them have servo motors as their actuators and two of them have DC motors as their actuators. The objective is to create a robot that can generate a large movement from the collection of these randomly connected six modules. Four acceleration sensors are attached to the robot to periodically evaluate the movement of the robot periodically. A large movement generates a large value for the evaluation function, hence the objective is to maximize the evaluation function. The development of the evaluation function is shown in Fig. 10. It is obvious that the self-configuration mechanism allows the group of six modules to gradually discover a connection topology that enables them to move as one robot.

Figure 11 shows the initial topology and the final topology discovered through the self-configuration mechanism. It is clear that the mechanism is able to self-configure a complex topology that is not easy to design. The self-configuration process of the connection topology of various robots with different morphologies can be observed in <http://www.st.chukyo-u.ac.jp/z110118/module.html>.

The self-configuration mechanism proposed in this study also significantly improves the resiliency of the robots. In the conventional hand-designed robots, a partial malfunction in the robots' components most often will halt the robots. This is a significant drawback for autonomous robots operating in real world environment. With this mechanism, because of the continuous topology adaptation, a malfunction in one of the module causes the decline in the evaluation function and thus, triggering the mechanism to search for an alternative topology that allows to robot to continue its operation, albeit with a reduced performance. The proposed self-configuration mechanism also allows us to add new modules to the already operational robots in real time, an important feature in building robots that is difficult to achieve through the conventional designing process.

**Fig. 9.** Module Robot**Fig. 10.** Self-configuration Process**Fig. 11.** Topology Self-Configuration

3 Conclusions

In this paper, some studies of the utilization of computational intelligence methods for producing autonomous robots, proposed by the author, are outlined. The author argues that in the face of the increasing applications of robots into various fields in human society, the conventional design-based manufacturing process will encounter many difficulties. The results of the on-going studies indicate that the computational intelligence methods are promising in at least complementing the conventional manufacturing process. In adopting the computational intelligence methods, based on learning, relearning, adaptation and self-configuration, we can change the manufacturing process to include a concept of “nurturing” artifacts. For example it will be interesting to observe robots, produced from a same factory, are allowed to develop different abilities and maybe even personalities, because they are nurtured by different users in different environments. This will significantly improve the ability of the robots to customize themselves according to their users, tasks and running environments. The self-configuration mechanism expands this customization ability to the physical morphologies, and thus physical functionalities of the robots. In this paper, the author only limited the argument to robots, but the concept of nurturing physical robots can be expanded to include other artifacts, such as large scale software, electronics appliances, buildings, vehicle, network systems and so on. Will this concept bring us closer to the seminal idea of von Neumann [24] ?

Acknowledgements. P.H. thanks Artificial Intelligence Research Promotion Foundation and The Hibi Science Foundation for supporting this study.

References

1. Dorigo, M., Stutzle, T.: *Ant Colony Optimization*. The MIT Press, Cambridge (2004)
2. Gordon, D.: *Ants at Work*. The Free Press, New York (1999)
3. Nakagaki, T., et al.: Maze-solving by an amoeboid organism. *Nature* 407, 470 (2000)
4. Richmond, C.: Fireflies flashing in unison. *Science* 71, 537–538 (1930)
5. Strogatz, S.: *SYNC: The Emerging Science of Spontaneous Order*. Hyperion, New York (2003)
6. Mitchell, M.: *Complexity*. Oxford University Press, Oxford (2009)
7. Buchanan, M.: *Social Atom*. Marshall Cavendish Limited, London (2007)
8. Holland, J.: *Adaptation in Natural and Artificial Systems*. Univ. of Michigan Press, Ann Harbor (1975)
9. Koza, J.: *Genetic Programming*. The MIT Press, Cambridge (1992)
10. Fogel, L., et al.: *Artificial Intelligence through Simulated Evolution*. John Wiley (1966)
11. Widrow, B., et al.: Layered Neural Nets for Pattern Recognition. *IEEE Trans. on Acoustics, Speech, and Signal Processing* 36(7), 1109–1118 (1988)
12. Watson, R., et al.: *Reinforcement Learning*. MIT Press, Cambridge (1998)
13. Qiao, J., et al.: Application of Reinforcement Learning Based on Neural Network to Dynamic Obstacle Avoidance. In: Proc. IEEE Int. Conf. on Inf. and Aut., pp. 784–788 (2008)
14. Smart, W., Kaelbling, L.: Effective Reinforcement Learning for Mobile Robots. In: Proc. IEEE Int. Conf. on Robotics and Automation 2002, vol. 4, pp. 3404–3410 (2002)
15. Yamaguchi, T., et al.: Realtime Reinforcement Learning for a Real Robot in the Real Environment. In: Proc. IEEE Int. Conf. on Intelligent Robots and Systems, pp. 1321–1328 (2006)
16. Hartono, P., Kakita, S.: Fast Reinforcement Learning for Simple Physical Robots. *Memetic Computing* 1(4), 305–313 (2009)
17. Hartono, P., et al.: Strategy Acquirement by Survival Robots in Outdoor Environment. In: Proc. IEEE Int. Conf. on Robotics and Automation, vol. 3, pp. 3571–3535 (2003)
18. Nakatani, M., et al.: Subjective-Evaluation Oriented Teaching Scheme for a Biped Humanoid Robot. In: Proc. 2003 IEEE-RAS Int. Conf. on Humanoid Robots (2003)
19. Kamimura, A., et al.: Automatic Locomotion Design and Experiments for a Modular Robotic System. *IEEE/ASME Trans. on Mechatronics* 10(3), 314–325 (2005)
20. Yim, M., et al.: Modular Self-reconfigurable Robot System. *IEEE Robotics and Automation Magazine* 14(1), 43–52 (2007)
21. Gilpin, K., et al.: Modular Robot Systems. *IEEE Robotics and Automation Magazine* 17(3), 38–55 (2010)
22. Meng, Y., et al.: Autonomous Self-Reconfiguration of Modular Robots by Evolving a Hierarchical Mechanochemical Model. *IEEE Computational Intelligence Magazine* 6(1), 43–54 (2011)
23. Hartono, P., Nakane, A.: Robotics Modules with Real-time Adaptive Topology. *International Journal of Computer Information Systems and Industrial Management* 3, 185–192 (2011)
24. von Neumann, J.: *Theory of Self-Reproduction Automata*. Univ. Illinois Press, Urbana (1966)

Chapter III: Intelligent Robot Technologies and Applications

Peter Xu

Curiosity Rover on Mars, Da Vinci Robot in operation theatres, Robcoaster in theme parks, Asimo in dancing, Google Cars on roads, Predator Drone in aerial watching, Jiaolong in deep ocean are a few of ***today's intelligent robots***, adding to a list of hundreds of thousands of robots working tirelessly in production lines, milking stations, ovine slaughtering houses .

Ever-aging western society is demanding robots as companions to co-work and co-live with humans, such that our aged and less-abled people are cared, our wellbeing and quality of life are improved. More and more applications of intelligent robots have been trialed and ***tomorrow's intelligent robotic technologies*** are emerging today.

This chapter consists of seven groups of thirty-one scientific papers, showcasing a variety of intelligent robotic technologies, systems and applications. They are Intelligent Robots in Education, Intelligent Robots Applications, Interfaces for Robotic, Human and Cyber-physical Systems, Knowledge Representation for Robotics Applications, Design and Control of Intelligent Industrial Robots, Intelligent Systems Applications, and Interactive Session Papers.

Five papers below are included in **Intelligent Robots in Education**, where humanoid robot projects are found to be used as educational aids or tools for hands-on learning of engineering undergraduates. More interestingly, a humanoid robot as teacher was even used in an elementary school's science class.

- 1) Fostering Students' Spatial Skills through Practice in Operating and Programming Robotic Cells
- 2) Innovative Experimental System Supporting Mechatronics Education
- 3) Humanoids at the Assistive Robot Competition RoboWaiter 2012
- 4) Human-like Robot as Teacher's Representative in a Science Lesson: An Elementary School Experiment
- 5) Measuring the Information Quality of E-learning Systems in KSA: Attitudes and Perceptions of Learners

Intelligent Robots Applications has five papers in its group. A variety of applications of intelligent robots are showed, where a dynamic role assignment strategy was proposed for a team of Soccer robots to play based on a combinational performance index; an underwater flight vehicle was under intelligent blowing control; and behavior based intelligence was used for navigation of a humanoid robot.

- 1) Research on Distance-first Based Role Assignment Strategy of Soccer Robot
- 2) An Approach to the Specification of Security Concerns in UML
- 3) Intelligent Blowing Controller for Autonomous Underwater Flight Vehicle
- 4) Fuzzy Visual Navigation Using Behavior Primitives for Small Humanoid Robot
- 5) Development of Steer-by-Wire for Manned and Unmanned Electric Vehicle

The group of four papers of **Interfaces for Robotic, Human and Cyber-physical Systems** deals with the localization, collision avoidance and cooperation of a fleet of ground or aerial vehicles. Novel algorithms and techniques are found, where a passive RFID positioning system was proposed for localization of mobile robots; Evolutionary algorithm was developed for swarms of flapping-wing micro-air vehicles; a collision avoiding strategy was presented for a fleet of robots that are unable or unwilling to negotiate/communicate with one another; and a system was promoted for task competition communications among heterogeneous robots.

- 1) Passive RFID Positioning System Using RF Power Control
- 2) An Islands of Fitness Compact Genetic Algorithm Approach to Improving Learning Time in Swarms of Flapping-Wing Micro Air Vehicles
- 3) A Collision Control Strategy for Multiple Moving Robots
- 4) Communication for Task Completion with Heterogeneous Robots

Knowledge Representation for Robotics Applications is represented by three papers below, where the most interesting contribution lies in the use of ontology to describe the way a robot communicates with humans, other intelligent machines and agents. Ontological semantic technology has potential in enhancing robotic intelligence and establishing the communication in natural manner.

- 1) Robotic Reasoning with Ontological Semantic Technology
- 2) The Not So Simple Ontology of a "Primitive" Robot
- 3) Understanding and Processing Information of Various Grain Sizes

Four papers are contained in this group, **Design and Control of Intelligent Industrial Robots**. The first two papers present hardware, firmware and software design of a dual-arm robot for industrial applications, where the robot works in the way human operator does at the production cell. The third paper describes a novel gravitation compensated control method for a high-speed and high-precision parallel robot. The last paper is not exactly in the field of intelligent robotics, and presents the design and control of a novel magnetic bearing used in refrigeration compressor.

- 1) Software Platform for Industrial Dual-arm Robot
- 2) Design of Dual-arm Robot for Cell Production
- 3) Dynamic Control of Parallel Manipulator
- 4) Design of rotor and magnetic bearings for 200RT class turbo refrigerant compressor

Four papers below are a few representative applications of **Intelligent Systems Technologies**. An artificial neural networks method was presented to predict the locations of inductive heating that is needed in concave surface forming at shipyard. A wheelchair movement was controlled using the recognition of user's hand gesture,

when negotiating a curvature. An unnamed aerial vehicle (a quadrotor) was proposed to be controlled in Cartesian trajectory together with its altitude. A recursive projection profile cutting algorithm for image's character segmentation was developed, which is supposed to be used in the conversion of image-based documents to text-based documents.

- 1) Forming Complicated Surface in Shipyard using Neural Network System
- 2) A Method for Controlling Wheelchair Using Hand Gesture Recognition
- 3) Position Control of a Quad-rotor System
- 4) Mathematical formula Recognition based on Modified Recursive Projection Profile Cutting and Labeling with Double Linked List

This chapter ends with six more papers that were presented at Interactive Sessions. These papers show quite diversified applications of enabling technologies, models and algorithms for intelligent robots and systems.

- 1) Control for Smart Transportation Vehicle Based on Dynamic Model
- 2) Intelligent Camera for Object Identification and Tracking
- 3) Speaker Dependent Visual Speech Recognition by Symbol and Real Value Assignment
- 4) Automatic Image Segmentation Using Saliency Detection and Superpixel Graph Cuts
- 5) A Survey: Stereo Based Navigation for Mobile Binocular Robots
- 6) Wheel of Online Retailing Development in Saudi Arabia

Fostering Students' Spatial Skills through Practice in Operating and Programming Robotic Cells

Igor M. Verner¹, Sergei Gamer², and Avraham Shtub²

¹ Dept. of Education in Technology and Science

² Dept. of Industrial Engineering and Management,

Technion – Israel Institute of Technology, Haifa, Israel

ttrigor@technion.ac.il, gamer@tx.technion.ac.il,
shtub@ie.technion.ac.il

Abstract. This paper presents results of our educational experiments aimed to raise awareness of freshmen engineering and senior high school students on the importance of spatial skills and develop strategies for spatial learning through practice of remote operation and programming robot systems in automated manufacturing labs. In the first experiment senior high school students performed two assignments: (a) design of a multi-robot system for automatic labeling of blocks, and (b) picture puzzle assembly by teleoperating a robot manipulator. Pre-course and post-course paper-and-pencil spatial tests indicated considerable improvement in performing cube rotation tasks. An additional indicator of spatial learning was the substantial reduction of the assembly completion time with training. In the second experiment undergraduate freshmen students majoring in industrial engineering performed an exercise: to program the robot to assemble a structure consisting of blocks of different types in a virtual robotic environment RoboCell. Responses to the questionnaire conducted after the exercise indicated that almost all the students aware on importance of spatial skills for their future profession. Majority of them noted that the exercise effectively presented spatial problems in planning and programming robot systems.

Keywords: robot operation, robot programming, spatial skills, engineering education.

1 Introduction

Engineering practice commonly depends on visual information and relies on the abilities of spatial perception, reasoning, and visualization in physical and virtual environments. Researchers have found that the aptitude of creating spatial representations of objects is critical for success in engineering careers. Cognitive scientists believe that spatial ability can be developed through experience and exercises [1] and that computer technology can facilitate effective training spatial skills in different contexts [2]. Spatial instruction was included in undergraduate engineering graphics and CAD courses [3]. As found, this change affected significant improvement in students' achievements in the course and their spatial reasoning and

visualization skills. Similar effects were observed by Hsi, Lynn and Bell [4] who included spatial instruction in an introductory engineering course. The authors recommend fostering spatial skills throughout the engineering curriculum.

Spatial instruction is a strong necessity in robot teleoperation which requires from the operator high level of perceptual and cognitive skills. The experiments of Lathan and Tracey [5] showed that the level of performance in teleoperating the robot through a maze using a single camera significantly correlated with that in performing standard spatial reasoning tests. The experiment of Menchaca-Brandan et al. in the area of space teleoperation [6] indicated that spatial skills, particularly perspective taking and mental rotation, are essential in operating robotic manipulation systems. Research shows that spatial ability is also essential for success in programming. Jones and Burnett [7] found a positive correlation between programming skills of debugging and code navigation and the ability of mental rotation. Their study indicated that students with higher spatial ability performed better in the information technology course.

There is a great body of literature which characterizes spatial ability as particularly relevant for learning mathematics, science and technology in schools, and as a prerequisite for related professional education and careers. Wai et al. [8] summarize the findings of their longitudinal study and other research in the following general conclusions: (1) Spatial ability is a salient predictor of advanced educational and occupational achievements in science, engineering, and mathematics; (2) The role of spatial ability is critical both among learners in general and among intellectually talented individuals; (3) Spatial ability is a significant measure of intellectual giftedness together with mathematical and verbal abilities. As follows from the above discussion, there is a growing understanding of the need for purposeful spatial instruction in engineering and pre-engineering programs.

Despite the wide interest in different approaches to training spatial skills, only few studies consider spatial learning in robotic environments. Among them is our previous study [9], in which we considered the use of a programmable robot manipulator as a means for training spatial skills of school students (grades 7-10). A more recent study by Gomer and Pagano [10] dealt with spatial learning through operating mobile robots. This paper presents results of our educational experiments aimed to raise awareness of freshmen engineering and senior high school students on the importance of spatial skills and develop strategies for spatial learning through practice of remote operation and programming robot systems in automated manufacturing labs.

2 Spatial Reasoning for Robot Manipulations

Programming robot movements is based on point-to-point control, where the basic commands are to move the mechanical arm from a present position to the next one and to open or close the gripper. In order to arrange a robot manipulation, the operator has to design the overall trajectory of the robot motion, assign a sequence of intermediate positions (points) and program a set of point-to-point translations.

Activities in designing and programming robot manipulations involve various types of spatial reasoning. Robot manipulation design includes a number of subtasks, such as rotating an object, which require the operator to design the manipulation as a

sequence of primitive mechanical arm movements. A mechanical arm is primitive in comparison with the human arm and hand, and the performance of rotation is quite dissimilar. Robot grippers are usually intended only for simplified grasping operations and not for substituting the human hand in performing sophisticated movements required in skilled craftwork. Therefore, the way of manipulating objects in space by the mechanical arm differs from the human hand operation.

While human locomotion is controlled at the unconscious level, the designer of a robot operation has to use his/her spatial skills to plan robot movements. Every operation has to be designed in a way that is executable by the mechanical arm, without, of course, disturbing the stability of the entire set-up. Designing robot manipulations involves spatial perception, spatial reasoning and visualization skills. Different spatial representations of the robot and the environment are required to perform analysis of robot movements, their visual verification and physical manipulation of objects in the robot workspace. The designer "thinks with a robot," i.e. uses it as a frame of reference for the performance of spatial operations.

Observing the spatial tasks required for manipulating robot movements led us to the conclusion that programming and operating robot systems can become a meaningful learning activity for fostering development of spatial skills. This motivated our experiments discussed in the paper. The goal of the study is to identify spatial skills required for operating and programming multi-robot systems and develop strategies for training the skills.

3 Experimental Environment

We setup an experimental environment for spatial learning using the facilities of the Computer Integrated Manufacturing and Robotics Lab of the Technion Faculty of Industrial Engineering and Management:

- A semi-industrial CIM/FMS facility (Figure 1A)
- Workstations running CAD tools for graphic design and simulation
- A miniature FMS cell
- A robot farm which contains five semi-industrial robots that can be operated either individually or as a group (Figure 1B)
- AGV area for experiments with mobile robots
- A teaching class.

Similar laboratories exist in other universities [11]. The laboratory provides hands-on experimentation in various aspects of design, control and operation of automated manufacturing cells, while supporting several courses and activities. It also serves as a test bed for research experimentation of faculty and graduate students. From our teaching experience, students have difficulties in programming and operating robot systems to manipulate objects in 3D workspace. A frequent reason of mistakes in programming robot movements both in on-line and off-line modes is deficiency of spatial imagination.



Fig. 1. The CIM and Robotics Laboratory: A. CIM/FMS facility; B. Robot farm

3.1 Outreach Project Experiment

Assignments. The experiment included two learning assignments. The first assignment was to create a multi-robot system for manufacturing spatial test cubes (STCs) by attaching stickers to sides of cubic parts. The manufacturing system was composed from the appropriate set of the robot farm devices: three robots of different types, a pneumatic feeder, a conveyor belt, and a rotating table (Fig. 2). The programming language used for operating and programming the robots was Advanced Control Language.

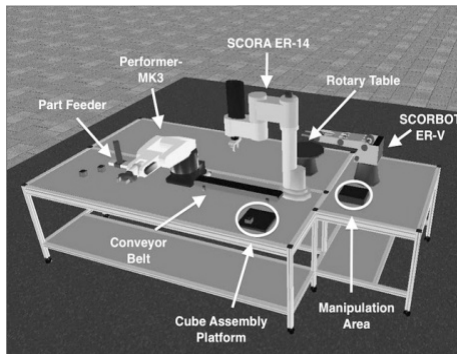


Fig. 2. Multi-Robot Assembly Cell

The second assignment was to assemble a 6-pieces puzzle through remote operation of a 5 DOF robot-manipulator, while getting on-screen visual feedback from cameras positioned around the workspace (Fig. 3). The puzzle pieces were scrambled and placed in a disorderly manner on the table. The operator had to pick up each cube, rotate it to the correct position, and place in the assembly.

Spatial Learning Follow-Up. The outreach experiment was conducted with participation of two senior high school students in the framework of the 2011

Technion International Youth Summer Research Program SciTech. The students performed the abovementioned assignments, while the follow-up included pre-course and post-course spatial tests, as well as analysis of remote operation performance and students' reflections. The tests were similar and included tasks of two types (to be performed in a given time): 3D rotation of cubes and 2D orientation of flat figures [12]. Results of the tests indicated that both students significantly improved their performance in cube rotation tasks (62% and 38% respectively), while in figure orientation tasks the improvements were small (5% and 3%).

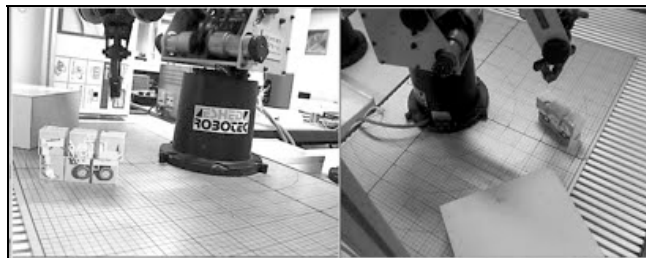


Fig. 3. Operator's on-screen feedback from the workspace

The tests were similar and included tasks of two types (to be performed in a given time): 3D rotation of cubes and 2D orientation of flat figures [12]. Results of the tests indicated that both students significantly improved their performance in cube rotation tasks (62% and 38% respectively), while in figure orientation tasks the improvements were small (5% and 3%).

In the remote operation assignment each of the students performed five trials of assembling the same puzzle, each time with different initial positions of the cubes. The task completion times were measured. As found, the first student significantly improved her performance, reducing the completion time from 41 min to 22 min while results of the second student kept at about the same level of 26-31 min. In the reflection the student mentioned difficulties in remote planning the mechanical arm movements for rotating and maneuvering the puzzle cubes. Possible reasons for the different progress are:

- When programming and operating robot manipulations the students extensively practice mental rotations of cubes, while did not have practice with flat figures.
- In the first assignment the group work was divided, so that the first student focused on programming spatial manipulations, while the second student dealt mainly with integration of the multi-robot system.

Despite the abovementioned differences, the students in the final project report noted that they significantly improved their spatial skills.

3.2 Freshmen Engineering Course Exercise

Viewing the need to raise awareness of freshmen students on the importance of spatial skills in industrial engineering and to extend their opportunities for spatial learning, we developed a laboratory exercise "Robot Assembly Planning" and implemented it

in the Technion course "Introduction to Industrial Engineering and Systems Integration". The course was delivered in the fall semester 2011.

The students were assigned to program a 5 DOF robot to assemble a structure consisting of blocks of three types: $50 \times 50 \times 50 \text{ mm}^3$, $100 \times 50 \times 50 \text{ mm}^3$, $150 \times 50 \times 50 \text{ mm}^3$. They worked with the virtual robotic environment (Fig. 4A) that was created using the RoboCell software [13]. Criteria for evaluation of the exercise performance included the following:

- The minimum of robot movements and used parts;
- Correct and precise calculation of positions of blocks in the robot workspace;
- Accuracy of the robotic assembly;
- Report quality.

Each pair of the students got a plan (top view) of the structure to be assembled. Performing the exercise included selection of suitable parts and defining their dispositions in the assembly, as well as defining positions and programming robot pick-and-place operations to assemble the structure (Fig. 4B).

After performing the exercise, the students were asked to answer the attitude questionnaire that included five questions (four semi-open and one open). The first and second questions requested students' opinion about the extent to which an industrial engineer is involved in solving spatial problems of manufacturing layout and robotic material handling. The third question asked students' views about the importance of spatial skills in planning manufacturing processes. The fourth and fifth question asked to what extent the laboratory exercise helped to understand the spatial problems of programming and operating robotic systems and difficulties faced by the engineer.

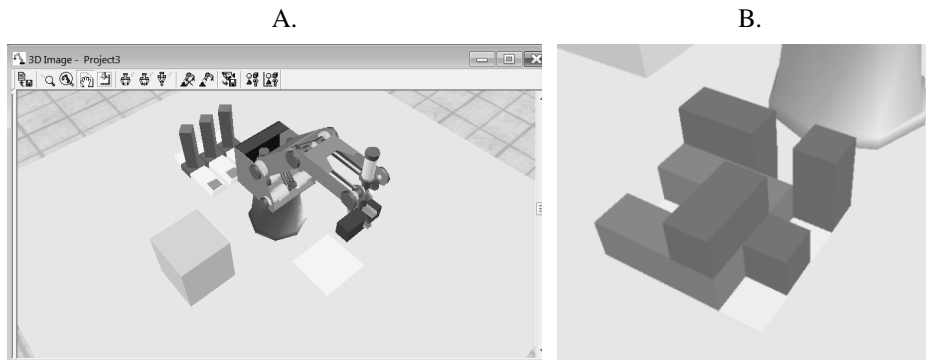


Fig. 4. A. Robotic environment; B. Assembled structure

Responses were accepted from 111 students. Absolute majority of the freshmen (93.7%) believe that industrial engineers actively participate in solving spatial problems of manufacturing. With regard to robotic material handling students' opinions are divided: 51.4% think that the industrial engineer is closely involved in planning robotic production processes, while others are of opposite opinion but believe that understanding these processes is required. 93.5% of the students consider

spatial ability as important or very important for planning and management of manufacturing processes. 71.4% noted that the laboratory exercise helped them to understand problems in planning and programming robot systems, among them 38.1% evaluated this impact as strong.

92.7% of the students mentioned difficulties in solving spatial problems of the laboratory exercise. In the analysis we divided the difficulties into three categories: spatial perception, mental operation and visualization. Perception related difficulties, mentioned by the students, were in positioning and perspective taking in the robot workspace. The challenges of mental operation were in imagination of spatial movements (especially in the presence of obstacles), describing positions of the mechanical arm by coordinates, and understanding spatial locations of objects from their on-screen representations. The difficulties of visualization were related mainly to on-screen design and verification of spatial operations. Following this finding, in further experiments we plan to combine spatial learning activities in both virtual and real robotic environments.

4 Conclusion

Engineering departments at many universities have CIM and robotics laboratories similar to our lab. The labs are equipped with expensive systems that need continuous professional maintenance. They are used mostly by manufacturing majors in advanced undergraduate courses and projects that focus on robot control and systems integration. The approach proposed in our paper significantly expands the use of such laboratories, particularly in introductory engineering courses for freshmen and in engineering outreach for school students.

We focus laboratory practice of these learners on training spatial reasoning skills, which are of great importance for engineering studies. In the past experiments we found that school students of grades 7-10 after practice in programming and operating robot manipulations demonstrated significant progress in performing spatial tasks.

The new experiments in the CIM and Robotics Lab indicate that even basic assignments of programming and operating robotic cells in physical and virtual environments, being focused on spatial tasks, can facilitate meaningful spatial learning of university freshmen and senior high school students.

The novelty of these experiments was that robotic manipulations were executed with spatial test cubes instead of regular cubes. Using STCs significantly raised the complexity of the spatial reasoning tasks. In the first experiment we carefully observed performing the robot programming and teleoperation assignments by two high school students. The evidence of their better results in the spatial tests, and their reflections convinced us in the potential of using these assignments for spatial instruction. Of course further investigation and careful measurement of outcomes of such spatial learning is required. In the second experiment the spatial task proposed to a quite large group of freshmen engineering students was to assemble a given block structure from blocks of different lengths placed in different orientations. The attitude questionnaire after the exercise indicated that absolute majority of the students did not have prior experience of such exercises. Many students mentioned that the exercise

helped them to understand spatial problems of computer aided manufacturing which an industrial engineer solves. The students suggested that the spatial task could be more complex, but also reported difficulties in performing it in the virtual environment. We plan to continue the study and explore spatial skills, required for operating and programming multi-robot systems in manufacturing processes, and develop strategies for training these skills in CIM and robotics laboratories.

Acknowledgement. This work is supported by the Technion Gordon Center for Systems Engineering research grant.

References

1. Lohman, D.F.: Spatial abilities as traits, processes, and knowledge. In: Sternberg, R.J. (ed.) *Advances in the Psychology of Human Intelligence*, vol. 4, pp. 181–248 (1988)
2. Péruch, P., Belingard, L., Thinus-Blanc, C.: Transfer of spatial knowledge from virtual to real environments. In: Habel, C., Brauer, W., Freksa, C., Wender, K.F. (eds.) *Spatial Cognition 2000. LNCS (LNAI)*, vol. 1849, pp. 253–264. Springer, Heidelberg (2000)
3. Sorby, S.A.: Developing 3D spatial skills for engineering students. *Australasian Journal of Engineering Education* 13(1), 1–11 (2007)
4. Hsi, S., Linn, M., Bell, J.: The role of spatial reasoning and the design of spatial instruction. *Journal of Engineering Education* 86(2), 151–158 (1997)
5. Lathan, C.E., Tracey, M.: The effects of operator spatial perception and sensory feedback on human-robot teleoperation performance. *Presence* 11(4), 368–377 (2002)
6. Menchaca-Brandan, M.A., Liu, A.M., Oman, C.M., Natapoff, A.: Influence of perspective-taking and mental rotation abilities in space teleoperation. In: Proc. of the 2nd ACM/IEEE International Conference on Human-Robot Interaction HRI 2007 (2007)
7. Jones, S., Burnett, G.: Spatial ability and learning to program. *Human Technology: An Interdisciplinary Journal on Humans in ICT Environments* 4(1), 47–61 (2008)
8. Wai, J., Lubinski, D., Benbow, C.P.: Spatial ability for STEM domains: Aligning over fifty years of cumulative psychological knowledge solidifies its importance. *Journal of Educational Psychology* 101, 817–835 (2009)
9. Verner, I.: Robot manipulations: A synergy of visualization, computation and action for spatial instruction. *International Journal of Computers for Mathematical Learning* 9(2), 213–234 (2004)
10. Gomer, J., Pagano, C.: NASA task load index for human-robot interaction workload measurement. *ITTEA Journal* 32, 210–214 (2011)
11. Goldstain, O., Ben-Gal, I., Bukchin, Y.: Remote learning for the manipulation and control of robotic cells. *European Journal of Engineering Education* 32(4), 481–494 (2007)
12. Eliot, J., Smith, I.: An international directory of spatial tests. NFER-Nelson (1983)
13. RoboCell for Controller USB, http://www.intelitek.com/ProductDetails.asp?Product_ID=57&CategoryID=7&Industrial=&Education=yes

Innovative Experimental System Supporting Mechatronics Education

Fusaomi Nagata¹, Akimasa Otsuka¹, Sakakibara Kaoru², Keigo Watanabe³,
and Maki K. Habib⁴

¹ Tokyo University of Science, Yamaguchi

1-1 Daigaku-dori, Sanyo-onoda 756-0884, Japan

nagata@rs.tus.ac.jp, otsuka_a@rs.tus.ac.jp

C-TASK Co. Ltd.

² 48-7 Oyama Kanai-machi, Itabashiku, Tokyo 173-0024, Japan

sakaki@c-task.co.jp, <http://www.c-task.co.jp/>

³ Graduate School of Natural Science and Technology, Okayama University,

3-1-1 Tsushima-naka, Kita-ku, Okayama 700-8530, Japan

watanabe@sys.okayama-u.ac.jp

⁴ American University in Cairo

113, Kasr El Eini St., P.O. Box 2511, Cairo 11511, Egypt

maki@aucegypt.edu

Abstract. Recently, many studies on educational system are conducted. In this paper, a unique educational experiment system is proposed for undergraduate students to be able to efficiently learn basic mechatronics techniques. The system is composed of three subsystems. The first subsystem is used to learn input/output port operations, periodically LED lights ON/OFF and a stepping motor control. The second subsystem is effective to learn AD transformation for several sensor information, DA transformation for DC motor control and a PID control method. Further, the third subsystem is designed by using a robot arm with four-DOFs to learn PWM (Pulse Width Modulation) control of a DC motor and force control of an end-effector. The effectiveness of the proposed system was confirmed through experimental instructions in Tokyo University of Science, Yamaguchi.

Keywords: Mechatronics educational system, Stepping motor, Photo interrupter, Photo reflector, Mobile robot with two wheels, Robot arm ABOT, PWM control, Force control.

1 Introduction

Recently, many studies on mechatronics education system are being conducted. For example, Stockmans-Daou presented a development system that provided a basic model, framework and automated tools for building mechatronics platforms. A case of use, where the development system had been used for educational robotics, was described by combining a LEGO Mindstorms system [1]. Also, Yilmaz and Tuncalp

investigated the effect of a Web-based mixed learning approach model on mechatronics education, in which the model combined different perception methods such as reading, listening, and speaking and practice methods developed in accordance with the vocational background of students [2].

In this paper, a unique educational system is proposed for undergraduate students to be able to efficiently learn basic techniques of mechatronics. Here, Microsoft Visual Studio C# is recommended as a software development environment, because which is one of the professional technical skills required from industrial fields. The system is composed of three subsystems. The first subsystem is used for second year students to learn input/output port operations with hexadecimal number, periodically LED lights ON/OFF by using Windows Timer, e.g., with a sampling period of 10 ms, and stepping motor controls built in a position control module and in a mobile robot with two wheels. The second subsystem is also used for third year students to learn AD transformation for several sensor information, DA transformation for the excitation of a DC motor and PID control method for velocity regulation. Further, the third subsystem is designed by using a robot arm ABOT with 4-DOFs for the graduation study of fourth year students to learn PWM (Pulse Width Modulation) control of a DC motor and force control for grasping motion. The effectiveness of the proposed experiment subsystems are evaluated through experimental instructions in Tokyo University of Science, Yamaguchi.

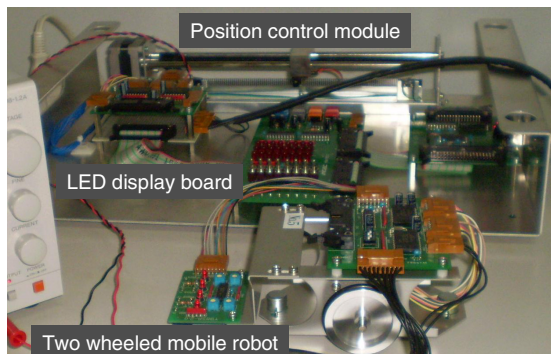


Fig. 1. Mechatronics system consisting of an LED display board, a position control device and a mobile robot with two wheels

2 Mechatronics System I

Figure 1 shows the first mechatronics system consisting of an LED display board, a position control device and a mobile robot with two wheels. The system is used in the experimental lecture of “Mechanical Engineering Experiments I” for the second year students [3]. Figure 2 shows the block diagram of the LED display experiment. Sixteen LEDs are arrayed with two rows as shown in figure 3 and each row is related to output port B and C, respectively. In figure 3, hexadecimal number 0x55 and 0xAA are set to port B and port C, respectively. Lighting pattern can be designed by giving the hexadecimal number, also lighting period can be changed by using Windows timer interrupt of 10 ms.

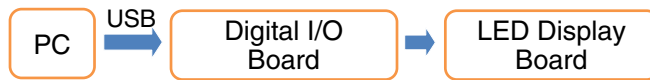


Fig. 2. Block diagram of LED display experiment

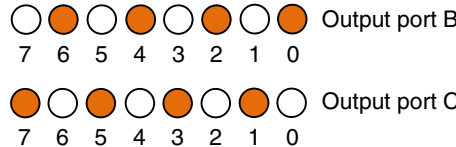


Fig. 3. Relation between two-arrayed LEDs and output port B, C

Figure 4 shows the position control device driven by a stepping motor. A photo interrupter is attached to the head to detect the position of the slit, i.e., black or transparent. The stepping motor is driven by pulse signals. One pulse signal rotates the stepping motor with 1.8 degrees, and this moves the head 6.25 μm through a ball screw. The pulse signal is generated by the lower four bits of output port B. Relation between binary number given to the port B and the corresponding motion is tabulated in Table 1.

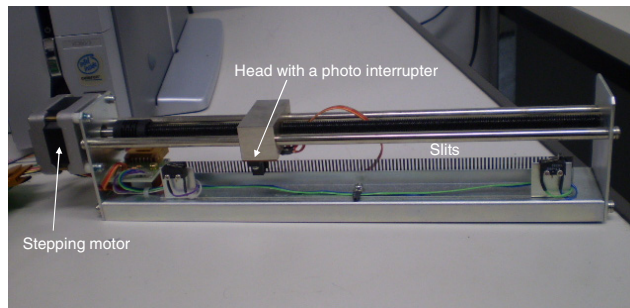


Fig. 4. Position control device driven by a stepping motor

Table 1. Binary number given to the lower four bits of port B and corresponding motion of stepping motor

0110	Low level signal for clockwise motion
0111	High level signal for clockwise motion
0010	Low level signal for counterclockwise motion
0011	High level signal for counterclockwise motion
1000	Excitation of motor is OFF

Figure 5 illustrates the mobile robot with two wheels and four photo reflectors. Wheels 1 and 2 are driven by stepping motors 1 and 2, respectively. The stepping motors 1 and 2 are excited by the lower four bits of output port B and C, respectively. In figure 5, v and ω are the forward translational velocity and the rotational velocity

of the robot in robot coordinate system; $2L$ is the distance between the two wheels and R is the radius of each wheel. The robot can perform forward/backward motions or rotational motion. When forward or backward motion is applied, the velocity of each wheel, v_1 , v_2 , is given by

$$v = v_1 = \omega_1 R = v_2 = -\omega_2 R \quad (1)$$

Also, when the rotational motion is conducted, the rotational velocity ω is given by

$$\omega = \frac{\omega_1 R}{L} = \frac{\omega_2 R}{L} \quad (\omega_1 = \omega_2) \quad (2)$$

where ω_1 and ω_2 are the rotational velocities of two wheels, respectively.

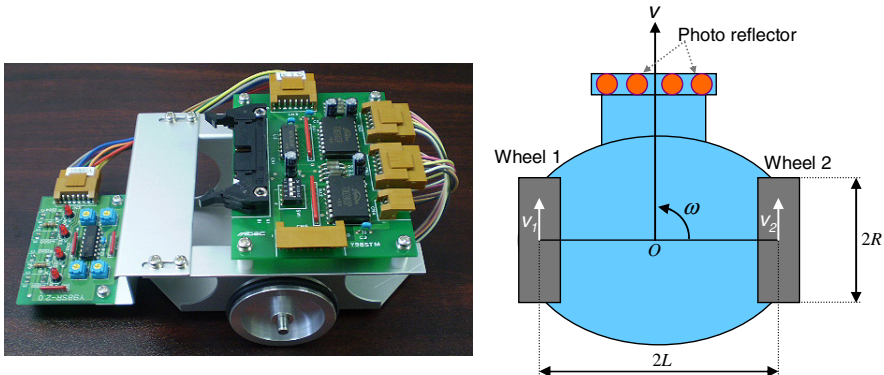


Fig. 5. Top view of two-wheeled mobile robot with four photo reflectors

3 Mechatronics System II

Figure 6 shows the second mechatronics system consisting of three sensors for measuring temperature, distance and brightness, AD/DA transformation interfaces, an LCD display panel, a stepping motor and a DC motor with a sensor of photo interrupter. The basic hardware is provided by C-TASK Co., Ltd. The system is used in the experimental lecture of “Mechanical Engineering Experiments II” for the third year students [3].

Here, the basic software developed for velocity control of the DC motor is explained. A ladder type DA converter is connected to the output port 1, so that the voltage within the range from 0 to 3.3 V can be outputted to the DC motor with the resolution of 256 steps. The velocity control of the DC motor can be performed by changing the voltage. The velocity of the motor is controlled by a proportional and integral action given by

$$\tau(k+1) = \tau(k) + \Delta\tau(k) \quad (3)$$

$$\Delta\tau(k) = K_p \{ v_d - v_s(k) \} + K_i \sum_{n=1}^k \{ v_d - v_s(n) \} \quad (4)$$

where $\tau(k)$ is the output torque to the DC motor at the discrete time k ; K_p and K_i are the proportional gain and integral gain, respectively; v_d is the reference value of rotational velocity and $v_s(k)$ is the rotational velocity measured by using a photo interrupter shown in figure 7. A rotational wheel with a small hole is fixed to the DC motor. The pass of the hole can be counted by detecting the change of signal form the photo interrupter, i.e., from HIGH level to LOW level. The rotational velocity is defined as counted number of the hole per a constant time period.

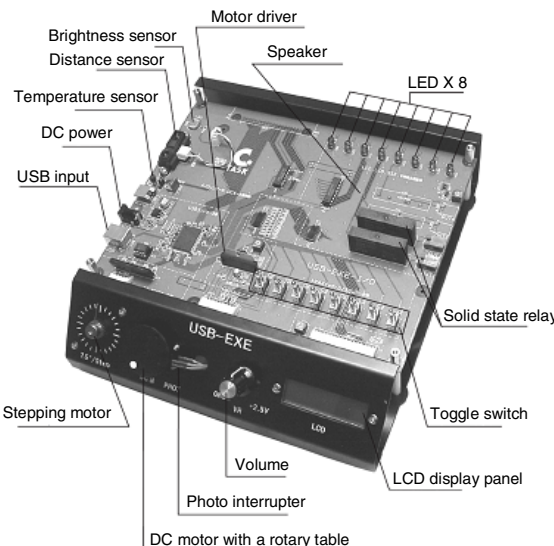


Fig. 6. Mechatronics system consisting of three sensors for measuring temperature, distance and brightness, AD/DA transformation interfaces, an LCD display panel, a stepping motor and a DC motor with a photo interrupter.

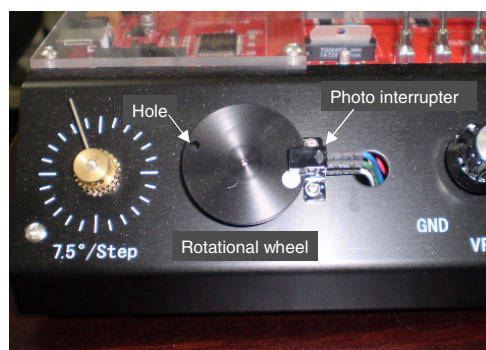


Fig. 7. Rotational wheel fixed to a DC motor with a sensor of photo interrupter

4 Basic Dialogues for Students' Experiment

In this section, basic dialogues developed for mechatronics experiment systems I and II are introduced. Students can effectively design a control program by using the dialogues and learn basic peripheral techniques concerning basic mechatronics.

4.1 Dialogue for Mechatronics Experiment System I

Mechatronics experiment I is considered for second year students in department of mechanical engineering, that is composed of three subjects, i.e., an LED lights ON/OFF experiment, a positioning experiment of a position control module and a line trace experiment of a two-wheeled mobile robot. As an example, figure 8 shows the windows dialogue designed for the line trace experiment using the mobile robot in mechatronics experiment I. At first, the students learn how to program important basic functions such as moving forward/backward, turning to left/right and sensing four photo-reflectors through the dialogue developed by using Microsoft Visual C#. Then, students can make a program for a line trace by making use of the basic functions. Fifteen hours (five hours, three days) are allotted to the mechatronics experiment I.

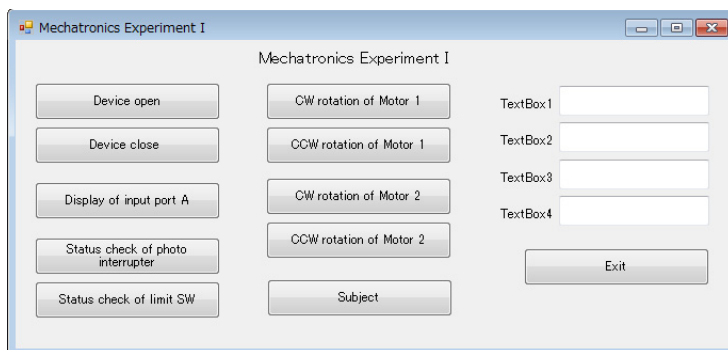


Fig. 8. Windows dialogue designed for an experiment using a two-wheeled mobile robot in mechatronics experiment I

4.2 Dialogue for Mechatronics Experiment System II

Mechatronics experiment II is considered for third year students, that is mainly composed of three subjects, i.e., AD transformation of several sensor signals such as distance, temperature and brightness, and DA transformation for velocity control of a DC motor. Students try to design a discrete-time PID controller for the velocity control of the DC motor. Figure 9 shows the windows dialogue designed for the mechatronics experiment system II. Ten hours (five hours, two days) are allotted to the mechatronics experiment II.

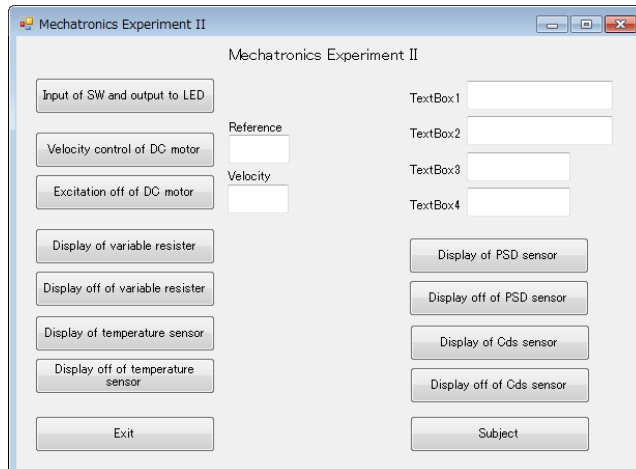


Fig. 9. Windows dialogue designed for an experiment using a DC motor in mechatronics experiment II

5 Robot Arm ABOT for Graduation Study

Students, who have gone through the experimental lectures by using the mechatronics experiment systems I and II, can smoothly cope with the graduation study at fourth year. We already developed a multiple mobile robots system for students to basically learn the subsumption architecture for schooling behavior [4]. The subsumption architecture is deeply concerned with the behavior-based robotic controller, which was introduced in 1986 by Brooks [5] and has influenced autonomous robotics and artificial intelligence.

In this section, another system for the students' graduation study is introduced, in which 4-DOFs robot arm called ABOT as shown in figure 10(*left*) is constituted for learning of joint velocity control with a well-known PWM (Pulse Width Modulation) control method and grasping control with a force control method. A thin film-type force sensor is attached to each finger as shown in figure 10(*right*). When the force given to the sensor becomes large, the resistance value tends to decrease. Therefore, the controller can monitor the change of force by measuring the voltage of the sensor. In this system, the voltage was digitally measured by using a small A/D converter module AGB65-ADC provided by AsakusaGiken Co., LTD.

Four DC motors are built in four joints of ABOT, respectively. Joint velocity can be regulated by varying the duty ratio of excitation pulse called as PWM control. Figure 11(*left*) shows a grasping control scene, in which a force controller is easily realized by regulating the open/close velocity based on the force sensor information. Also, figure 11(*right*) shows the desirable force control result, in which the largest value obtained from among the three force sensors is plotted at each discrete time.

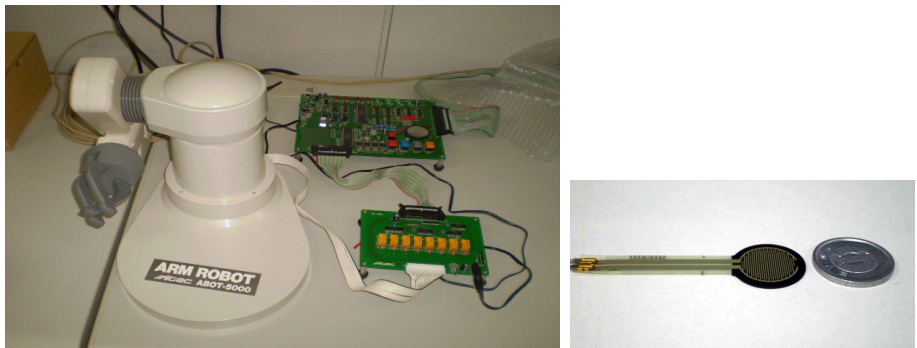


Fig. 10. 4-DOFs robot arm called ABOT(*left*), in which a film-type force sensor is put on the inside of each finger(*right*).

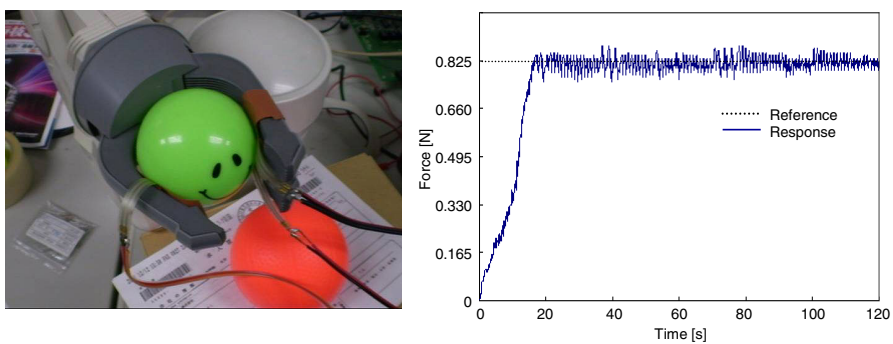


Fig. 11. Experiment scene of grasping a soft ball(*left*) and a force control result(*right*)

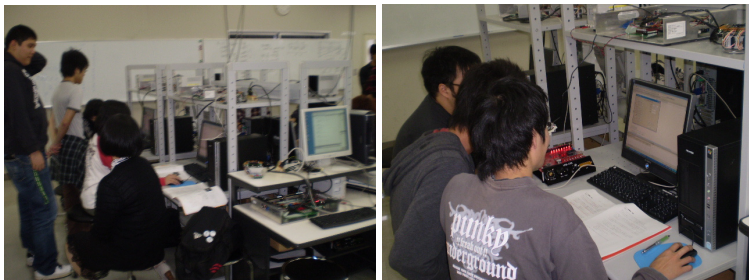


Fig. 12. Experimental lecture scene of “Mechatronics Experiment I” included in “Mechanical Engineering Experiments I” for the second year students in the department of mechanical engineering.

6 Conclusion

In this paper, a unique education system has been proposed for undergraduate students to practically learn basic mechatronics techniques. The system was constituted by three subsystems. The first subsystem was used for second year

students to mainly learn input/output port operations, periodically LED lights ON/OFF and stepping motor control. The second subsystem was effective for third year students to efficiently learn AD transformation for several sensor information, DA transformation for a DC motor control and the design of a PID controller. Further, the third subsystem was designed based on a 4-DOFs robot arm for one of graduation studies so that the fourth year students could learn PWM control for regulating the joint velocity and force control for simple grasping motion. The effectiveness of the proposed mechatronics education system was evaluated through experimental instructions in Tokyo University of Science, Yamaguchi as shown in figure 12.

References

1. Stockmans-Daou, C., Cruz-Martin, A., Fernandez-Madrigal, J.A.: A heterogeneity-enabled development system for educational mechatronics. In: Procs. of IEEE International Conference on Mechatronics (ICM 2009), pp. 1–6 (2009)
2. Yilmaz, O., Tuncalp, K.: A mixed learning approach in mechatronics education. IEEE Transactions on Education 54(2), 294–301 (2011)
3. Kitahara, N., Nagata, F., Otsuka, A., Sakakibara, K., Watanabe, K., Habib, M.K.: A proposal of experimental education system of mechatronics. In: Procs. of 17th International Symposium on Artificial Life and Robotics (17th AROB 2012), pp. 166–169 (2012)
4. Nagata, F., Yamashiro, T., Watanabe, K.: Cooperative swarm control for multiple mobile robots using only information from PSD sensors. Artificial Life and Robotics 16(1), 116–120 (2011)
5. Brooks, R.A.: A robust layered control system for a mobile robot. IEEE Journal of Robotics and Automation 2(1), 14–23 (1986)

Humanoids at the Assistive Robot Competition

RoboWaiter 2012

Igor M. Verner¹, Dan Cuperman¹, and Amit Cuperman¹, David Ahlgren²,
Steve Petkovsek², Vlad Burca², Binay Poudel², and Junius Santoso²

¹ Department of Education in Technology and Science, Technion-Israel Institute of Technology

² Department of Engineering, Trinity College, Hartford, CT 06106 USA

ttrigor@technion.ac.il, david.ahlgren@trincoll.edu

Abstract. This paper presents the rationale for focusing educational robotics projects on the development of humanoid assistive robots. We discuss our first experience of such projects and their presentation at the international assistive robotics competition RoboWaiter 2012. The RoboWaiter challenge is to create a robot that autonomously, accurately, and efficiently performs an assistive food fetch task in a model kitchen. Since its inception in 2009, only wheeled robots have participated in the competition, while our effort is to introduce a humanoid category. In the paper we describe the design considerations of our humanoid robots, named "Technion Ed" and "Trinity College Maximus", and their performance at the competition. The educational implementation of the Technion project was in the framework of a school outreach robotics course, the Trinity project was carried out by an independent study team.

Keywords: Educational robotics, humanoid robot, robot competition, Bioloid construction kit, RoboWaiter.

1 Introduction

There is a growing body of research focused on the creation of robots to assist people with reduced mobility. One important task is the daily need to move things around the house. A number of fetch-and-carry robots, addressing this need, have been recently developed and tested as laboratory prototypes for further research. Tapus, Mataric and Scassellati [1] suggest that establishing robot competitions, directed to challenging problems of assistive robotics, can have a stimulating effect on research and accelerate its practical implementation in the field. This suggestion is supported by evidence that robot search and rescue competitions significantly promote robotics research, particularly with regard to technical and human-centered aspects of HRI [2].

Sharing this view, the assistive robotics competition RoboWaiter has been established in order to inspire students and young researchers in the subject and involve them in socially responsible education. The inspiration for an assistive robotics competition came from the Connecticut Council on Developmental Disabilities. Persons with disabilities have been engaged in choosing the theme and developing the rules, and they attended the RoboWaiter events. Since 2009, the

assistive robotics project has been integrated in ENGR 120 (Introduction to Engineering Design—Mobile Robots), a first-year course at Trinity College and by the Trinity Robot Study Team.

The initiative of a humanoid RoboWaiter project came from the Technion, being motivated by the educational potential of humanoid robotics. We were also interested in exploring new opportunities opened by the innovative robot construction kit, Bioloid [3]. The initiative received sponsorship of the ROBOTIS Co. The Trinity College Robot Study Team and the Technion Educational Robotics Group took the challenge of creating a humanoid RoboWaiter and participation in the competition. This paper presents the RoboWaiter 2012 competition, the rationale and design considerations that underlie our humanoid robot projects, and the performance demonstrated by our robots "Technion Ed" and "Trinity College Maximus".

2 The RoboWaiter Challenge

Challenging characteristics of robot operation in human environments include the following: presence of autonomous actors (people, pets, and robots), variability, combining manipulation and mobility, and use of specialized tools. These characteristics appear in varying degrees in the RoboWaiter contest task. The task simulates a situation where Grandpa, a person with a disability, wishes, by means of an assistive robot, to move a plate of food from a refrigerator to the table where he is sitting in a wheelchair. Grandma is standing in the kitchen during the robot operation.

The action takes place in the arena that simulates a household kitchen (Fig. 1). The "kitchen" is furnished with scaled miniature items including a table, a sink, a refrigerator, and a chair. When performing the task, the robot, directed by a signal from the judge, should move from a fixed home position to the refrigerator, pick up the plate, move to the table where Grandpa sits, place the plate on the tabletop, and return to the home position. This action must be fully autonomous. Robots must avoid collisions with the kitchen items and with the doll that represents Grandma. The judge examines the robot operation and measures the time from the start signal until the plate is placed on the tabletop. The full description of the RoboWaiter rules may be found on the contest website [4].



Fig. 1. The RoboWaiter Advanced Division Arena

The primary measure of success in RoboWaiter is reliability, as measured by the number of successful runs among the three allowed trials. Robots finishing in this most reliable group are ranked according to overall task completion time. The secondary measure of success is the total number of tasks completed, based on the following task definitions: found shelf, picked up plate, transported plate at least 20 cm, and found table.

Twenty-six robots competed in RoboWaiter 2012, representing teams from the U.S., Canada, Indonesia, Israel, Portugal, and China. The participants ranged from children as young as 8th grade to university undergraduates and graduate students. These 2012 results were the best recorded in RoboWaiter's four-year history.

3 Why Humanoid Assistive Robots?

In recent years assistive robots are taking a growing role in supporting people with disabilities in their everyday home activities. Researchers note that when serving people in domestic environments, especially people with disabilities, assistive robots have to be sociable; i.e., they must act so as to create feelings of protection, comfort, and sympathy [5]. There is lively discussion on the need to endow such robots with human-like appearance and social identity.

When comparing a machine-like to a humanoid robot, the latter is usually more complex, more expensive and less technically efficient for carrying out similar tasks. Biped walking is a complex and inefficient motion strategy for a robot, when used in a home environment suitable for simple wheeled motion [6]. With this, there are practical and psychological considerations in favor of using humanoid robots in a home environment. As humanoid robots are designed to resemble humans, they are often fit to manage in a home environment and use the space, equipment and tools designed for human use [7]. This characteristic makes it possible to quickly adapt the robot to new tasks in this designated home environment.

From a psychological perspective, to engage in meaningful social interaction with people, a robot should have humanlike characteristics, whether in form, behavior or both [6]. The study conducted by Nass and Moon [8] indicated that people might attribute social rules and even gender stereotypes to technological devices. This no doubt applies also to humanoid robots that may be viewed as machines employing humanlike qualities; users might interact with these machines as if the machines were human. In fact, studies on human robot interaction showed that people tend to favor humanoid type domestic robots [9] and even find them more trust worthy and fit to share responsibility than machine-like robots [10].

In addition, there is growing interest in designing, building and operating humanoid robots for educational purposes [11]. As a humanoid robot is an analogical model of a human, the use of such a robot can facilitate a profound inquiry into engineering, science and humanities. Developing a robot locomotion scheme, for example, requires close look into the way in which motions are accomplished by the human body. Those complex but fascinating issues are less relevant when dealing with machine-like robots.

4 The Bioloid Platform

The platform chosen to be used for building the humanoid robots for the RoboWaiter challenge was the Bioloid Premium kit [3]. This kit can be used to assemble different robot models including three types of humanoid robots. The design chosen for the RoboWaiter competition was the most advanced one, consisting of 18 actuators controlled by a CM-510 or a CM-530 controller. Both controllers provide 6 analog inputs for sensors, 5 Dynamixel I/O ports for Dynamixel actuators and other devices, a RS 232 Communication port and a Serial port. The Bioloid premium kit also contains four sensors: a 2-axis gyro, a DMS-80 infrared distance measuring sensor, and two IR sensors. The kit includes dedicated software: RoboPlus Motion, for designing the robot's motions, and RoboPlus Task, for writing programming code for the robot, enabling it to use the motions created with RoboPlus Motion.

5 Humanoid RoboWaiter Projects

5.1 Technion Ed

Finding and Picking Up the Plate

Our first objective was to detect the LEDs marking the location of the plate, for this purpose we have selected the HaViMo 2.0 vision module [13] that is compatible with the Robotis CM-510 controller and RoboPlus programming tool. Mounting the HaViMo inside the robot's head would have exceeded the contest's height limit, so it was mounted on the robot's abdomen, under a clear plastic covering that protects the sensitive HaViMo (Fig.4a).

The Vision Module includes a camera and a dedicated image processor that is pre-calibrated by the user to identifying up to 16 different colors. For each color, the HaViMo returns coordinates, which are used to create a bounding box describing the location and size of the color area present in the image. It is possible to use this data not only to locate the LEDs, but also, to a limited extent, for determining the distance to the LEDs by inferring from the image size. This method was proved insufficient for shorter distances, which we measured using an IR distance-measuring sensor.

When getting near the shelf, the robot must determine when it is close enough to pick up the plate (Fig. 2a). The DMS-80 supplied with the kit proved to be insufficient for accurately measuring the distance of about 45 cm between the robot and the wall behind the shelf. The sensor was replaced by a Sharp GP2Y0A02YK0F infrared distance-measuring sensor that has a good voltage to distance resolution up to a range of 70 cm.

In the 2012 RoboWaiter competition, the shelf's height was given as being between 20 and 24 cm. Thus a motion should be created that allows the robot to pick up the plate regardless of the shelf height. This was achieved by first moving the robot's arms forward by 45 degrees (Fig.2b), lowering the arms while horizontal by bending at the knee, resting the grippers on the shelf and then positioning the grippers under the rim of the plate (Fig.2c).

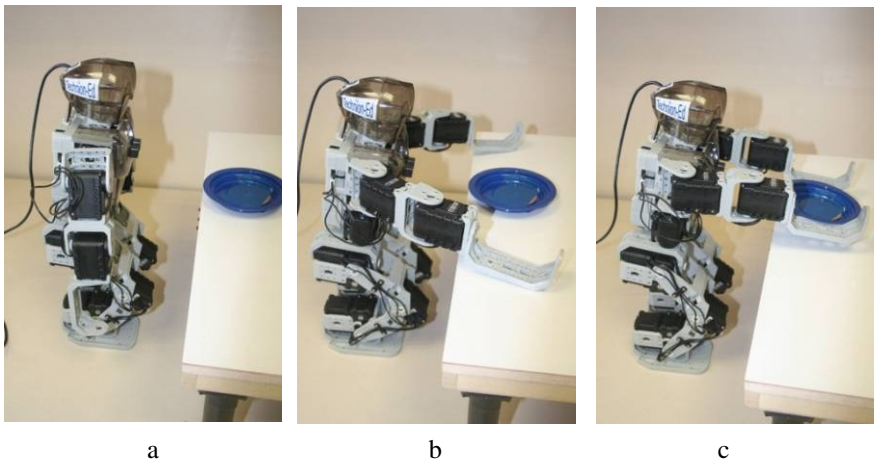


Fig. 2. The motion sequence for picking up the plate

Walking with the Plate

The challenge of walking to the table with the plate in the robot's hands, while still using the same walking steps, proved quite difficult. Though the plate does not weigh much, to carry it the robot needs to keep its arms stretched forward. The weight of the arms themselves cannot be neglected, as each arm contains two Dynamixel actuators.

Before the robot picks up the plate, its center of gravity is almost directly above the center of its feet (Fig.3a). If the robot holds the plate in a normal posture, its center of gravity moves upwards and forward to a location above the front of the robot's feet (Fig.3b). This move severely upsets the robot balance, causing it to topple forwards.

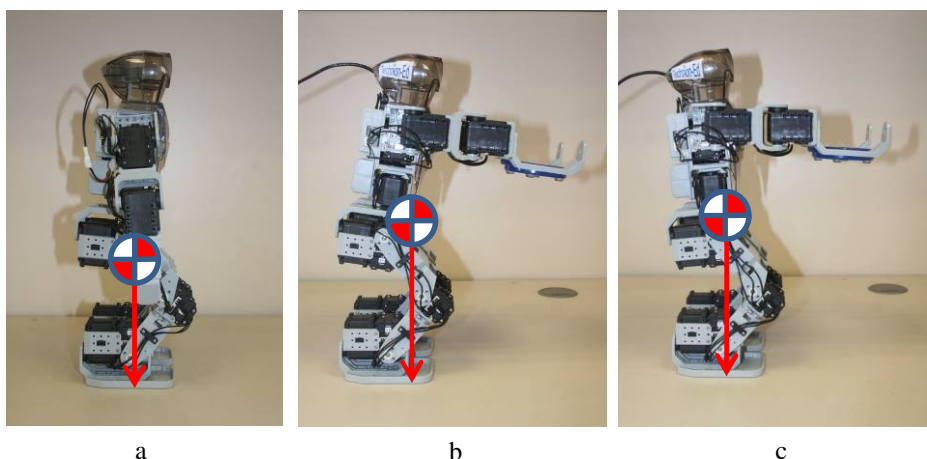


Fig. 3. Calculated center of gravity

To restore balance, the robot was leaned back at the upper leg actuators, causing the whole upper body to move backward, while the shoulder actuators were adjusted to keep the arms horizontal (Fig. 3c). This returned the center of gravity to a location above the center of the robot's feet and allowed using normal walking steps.

Orientation and Navigation

Because of The limited resolution of 160×120 pixels, the HaViMo can only detect a LED at a distance just over one meter. The first approach we considered for bringing the robot to viewing distance of the LEDs was wall following. To maintain a constant distance to the wall, a second infrared distance-measuring sensor was installed on a mounting behind the robot's right arm (Fig. 4b). To make sure the robot measures the distance being perpendicular to the wall, the robot aligned itself by performing several measurements and turning steps. As the wall following method was found very time consuming, we decided to add a compass to the robot.

Because the CM-510 does not support a standard I²C communication protocol, most compasses available on the market could not be used. We selected the CMPS-10 compass, which used Pulse Width Modulation to read the data. The compass generates pulses with a duration representing the measured angle. The pulses are detected via the CM-510 analog input. To measure the length of the pulse in order to calculate the angle, the controller must use a timer. However, the CM-510 does not have the necessary timer resolution and had to be replaced by the CM-530 which has a high-resolution timer that can measure in increments of 1ms. This resolution allowed us to calculate a directional reading in increments of 10 degrees. This directional resolution is quite sufficient as our robot has relatively rough directional control compared to wheeled platforms. The compass was placed on one of the robot's feet (Fig. 4c) where the actuator's magnetic field was the weakest.

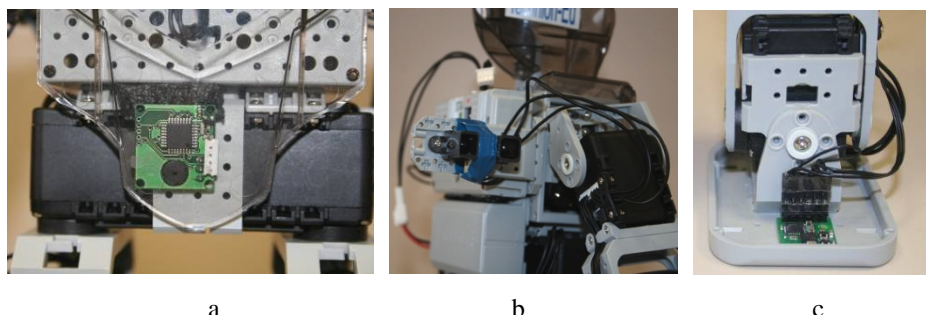


Fig. 4. CM-530 sensor mounted on the Bioloid

Using the compass for navigation in the arena significantly reduced the time needed to complete the RoboWaiter mission and increased the overall success rate.

Improvements and Fine Tuning

To improve the success rate for plate pick-up, a forward facing distance measurement was done to identify the plate. Since the plate is held below the measuring area of the sensor, a motion was created to raise the grippers so that the plate, if present, will be detected by the sensor. If the sensor does not detect the presence of the plate, the robot will move backward and retry to pick up the plate.

Adhesive strips were applied to the bottoms of the robot's feet, to improve the robot's traction on slippery surfaces, where the robot had trouble turning.

Participation in the Contest

The practice session held the day before the RoboWaiter 2012 was our first opportunity to test the robot in the competition arena. First runs were unsuccessful with the robot failing to reach the plate. The robot even could not walk more than a few steps without toppling. This walking problem was caused by the extremely high friction coefficient of the arena floor. We partially solved the problem by replacing the adhesive strips used to raise the feet's friction coefficient with ones that lowered it. In addition, the number of steps for each walking sequence was lowered and waiting periods between walking sequences were raised, allowing the robot to regain its balance.

One more problem was that the compass sensor intended for robot navigation could not be used in the competition venue. There were several areas in the arena in which the compass was off by as much as 90 degrees. An attempt was made to map these areas so that they could be bypassed, but they proved to be too large, and some were located in critical areas. Since the deviation from north was not constant, it was impossible to compensate for it through programming. As a result, it was necessary to use the wall following navigation method.

In the competition, each robot was given three attempts to complete the mission. In the first run, the robot successfully reached the shelf, picked up the plate and approached the table, but dropped the plate a few paces away from destination table. In view of this problem, we modified the gripper to prevent the plate from sliding off. In the second run, the robot picked up the plate, reached the destination table, but for some unforeseen navigation problem turned right 90 degrees and placed the plate beside the table. The third run was disqualified because the robot hit the chair on its way to the shelf.

Assessing Ed's Strengths and Weaknesses

Ed proved to be a promising robot. It is versatile and easy to program. Being a humanoid robot, Ed elicited emotional responses from spectators during the practice sessions and during the contest itself. People were excited to watch a humanoid robot perform the RoboWaiter mission, were happy when it succeeded, and disappointed when it failed.

Ed's primary weakness is its navigation capabilities. This weakness is exacerbated when its key navigational sensor, the compass, cannot be used. Solutions must be found to allow the robot to navigate without using the wall following method, which proved to be time consuming and inaccurate. To answer this need, we recommend adding an I²C port to the CM-530. Such an interface can broaden the variety of

sensors and accessories compatible with the robot. Another problem we encountered is the robot's stability. When holding the plate, the robot has a very high center of gravity, causing it to be unstable. To answer this problem, design modifications are needed.

5.2 Trinity MAXIMUS

Maximus was also based on the Bioloid Premium kit, which offered a mechanical base and a software development system. The design team addressed such issues as balance, localization, motion control, intelligence, and fault recovery. Limitations regarding the number of sensors and CPU processing speed were encountered and will be described below. Where possible, sensors not included in the Bioloid kit were avoided in order to reduce the overall cost of the project.

Design Approach

Five sensors were used to enable navigation and localization (Fig. 5& 6). For navigation, an accelerometer and two GP2Y0A21Sharp IR ranging sensors (10 – 80 cm range) were used. The accelerometer allowed the robot to determine its orientation relative to the floor. Differential signal of two photoresistors was used to find the shelf and table LEDs and to localize the robot position. One photoresistor used a hardware comparator to determine sensitivity for rapid calibration during the competition. The second photoresistor was wired in parallel with a touch sensor, effecting multiplexing of an analog port, which were in short supply (there are only four A/D ports on the CM-510 controller, and the team needed to use five sensors). The touch sensor was closed when the gripper of *Maximus* were touching the shelf, whose height could vary from trial to trial in the contest. De-multiplexing of the shared port was performed in a straightforward manner in the software.

Robot motions were made by referencing tables of positions for each of Maximus's 18 servos. These motions included "step forward", "get up", "turn left", "turn right", "shuffle left", "shuffle right", "open arms", "close arms", "crouch to pick up the plate", and "return to standing position". The grabbing mechanism (Fig. 6) was an enclosure made from Styrofoam plates fixed to the hands of Maximus. The enclosed nature of this grabber design prevented food from spilling out of the payload (the plate) during walking. The enclosure was held out in front of Maximus by its arms to allow clearance for its leg motions and its sensors. The arms and payload were heavy enough to topple the robot if the standard walking routine was used. To maintain balance while walking, Maximus leaned back and held the plate at an upward angle at a height above the tables and furniture in the arena.

The team used an algorithm that had four main modules (Fig. 7): Wall Following, Table Approach, Plate Pick-Up, and Plate Drop. The modules ran in a pre-configured series. Each new module was triggered by a particular sensor data signature (e.g. red LEDs on the table).

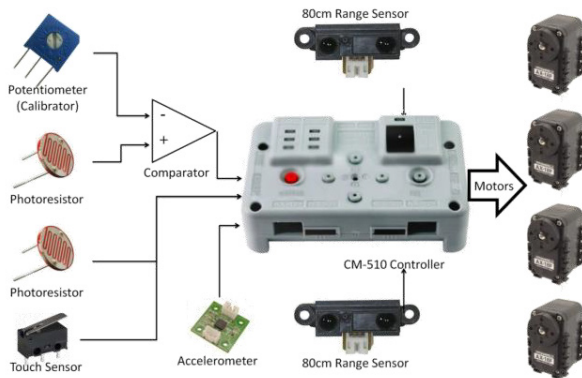


Fig. 5.Sensing and Computing Elements used by Maximus

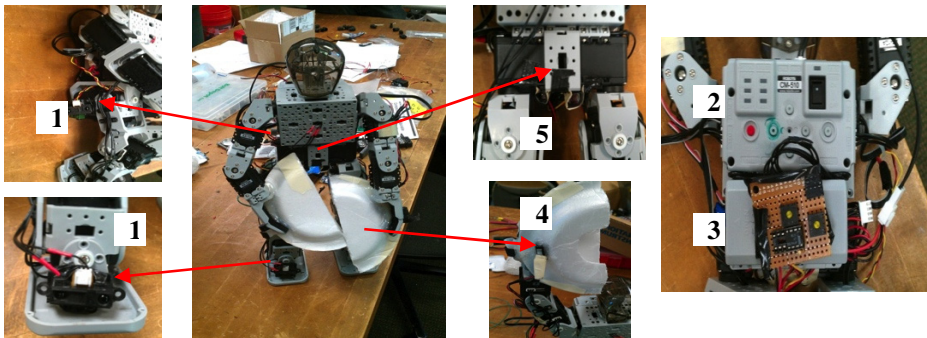


Fig. 6. Design and hardware placement on *Maximus*

1: distance sensors. 2: theCM510 controller. 3: Comparator circuit.

4: Grabbing mechanism and touch sensor. 5: Photoresistors (differential).



Fig. 7. Operational Sequence used by Maximus

Wall following (Fig. 8 a) was accomplished by following the right wall with a single range sensor. Control instability resulted in large fluctuations in distance readings. The value was read several times during each step, and when a step was completed the average distance reading for those cycles was used to determine the next motion.

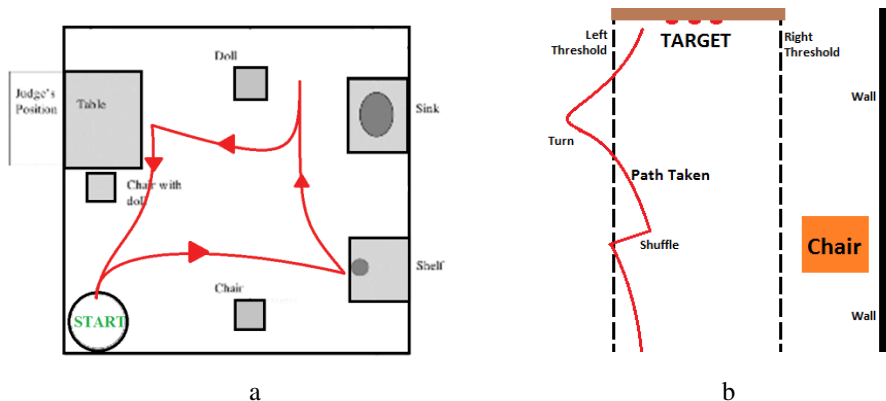


Fig. 8. Wall Following through the Arena

Maximus tended to veer left when using the step motion, so a combination of steps, shuffles, and turns was used. A distance tolerance was programmed where the robot would move forward (Fig. 8b). If it moved too far from the wall or too close to it, the robot would shuffle (slide sideways) back into the tolerable range and step forward. If the same tolerance was violated for several cycles, it was determined that the robot was heading in the wrong direction, and *Maximus* would turn its entire body back toward the center of the tolerance range and step forward. When the LEDs were seen, wall-following terminated and the differential signal of the two photoresistors was used to determine whether the robot should shuffle left or right when standing in front of the table. A range sensor, placed facing forward, detected the distance of *Maximus* to the rear wall, and when the appropriate distance was achieved and the robot was centered, the Pick-Up Plate routine was run. *Maximus* had to run separate motions for different table heights. The limited control allowed by the software prevented a continuous motion until the touch sensor was tripped. Rather, *Maximus*, after opening its arms, squatted in increments until the touch sensor was activated, then closed its arms and scooped up a large area in front of it, corralling the plate into the enclosed grabber. *Maximus* turned left, and repeated the same wall-following process until the drop-off target was located. The same “Approach Table” routine was run. To drop the plate, the arms were simply opened.

Technical Issues

C code can be used for programming the Bioloid but requires firmware reconfiguration. RoboPlus was used due to the short development time available to the design team and the library of functions available (such as reading from the motion module). Only one motion sequence may run at a time. If a sensor (i.e. range finder) sends a reading to the CM-510, the robot must finish its motion before acting on that reading. This increases reaction time and reduces control, making wall-following algorithms difficult (see *Algorithms: Wall Following*). Balance issues and foot slippage compounded this control issue. To counter slippage, several different

textures were applied to the feet of *Maximus*, including tape and sandpaper. The result was that friction was too great, and *Maximus* would tip itself over when pushing off the floor to shuffle or take a step.

Future Improvements

There are workarounds to the limitations of the Robotis Bioloid package that hindered *Maximus* performance. Installation of the Havimo vision module [13] could provide color recognition of the plate and LEDs, increasing detection redundancy and allowing fault detection and recovery if the robot does not pick up the plate. An external I/O development/extension board such as ArbotiXRobo controller from Vanadium Lab [14] or General I/O board from Huvrobotics [15] could be added to increase the number of sensor ports and consequently the number and effectiveness of the sensors. Furthermore, it is possible to improve the software development tools; for example ArbotiXsystem provides alternatives for the RoboPlus Motion software. Finally, pressure sensors [16] could be added on the robot's feet which could allow precise stability control. The sensors could be used to control the ankle servos, giving *Maximus* the ability to shift its weight if it begins to fall.

Observations

Maximus was successful in walking, navigating, and finding the plate during the Robowaiter competition. “*Maximus*” reached the shelf and deployed its gripper on one of the three runs but was hampered by the loss of its main sensor, a small camera programmed to recognize the plate and the bright LED beacon on the shelf edge. This failure gave clear proof of the need for adequate sensors to provide information for navigation and object recognition algorithms.

6 Conclusion

The three-year experience of the RoboWaiter competition directed to challenging problems of assistive robotics has demonstrated its value for promoting engineering education at undergraduate and school levels. This value has engineering, pedagogical, and social components. The engineering component is driven by practice of solving the robot design problems emerged in the RoboWaiter project. The pedagogical component focuses on the human aspects of engineering design and on promoting creative thinking and teamwork practices. The social component engages students in public presentation of their projects and in communication with other participants of the event, including people with disabilities. Interactions promoted by the assistive competition helped the participants to recognize the social challenge of assistive robotics and to learn that engineering work can have importance beyond pure technical achievement.

The first experience of humanoid RoboWaiter projects has indicated their promising advantages in achieving the mentioned educational values. These projects pose new challenging engineering problems of robot locomotion, navigation, manipulation, and human-robot interaction. Innovative robot construction kits, such

as Bioloid, enable educators to introduce humanoid robot projects even in introductory robotics courses. The projects inspire a deeper look into the needs and behaviors of people with disabilities and their caregivers, opening room for creative robotic modeling of these behaviors. In addition, humanoid robots are likely to be more interesting and attractive to the public, and they may lead to greater emotional involvement by their users.

Acknowledgements. This research has been supported in part by ROBOTIS, Co.

References

1. Tapus, A., Matarić, M.J., Scassellati, B.: The grand challenges in socially assistive robotics. *IEEE Robot. and Autom. Mag.* 14, 35–42 (2007), doi:10.1109/MRA.2007.339605
2. Yanco, H., Drury, J.: Rescuing interfaces: A multiyear study of human-robot interaction at the AAAI Robot Rescue Competition. *Autonomous Robots* 22(4), 333–352 (2007)
3. http://www.robotis.com/xe/bioloid_en (accessed July 17, 2012)
4. Trinity College Fire-Fighting Home Robot Contest, <http://www.trincoll.edu/events/robot> (accessed July 17, 2012)
5. Breazeal, C.: Towards sociable robots. *RAS* 42(3-4), 167–175 (2003)
6. Duffy, B.R.: Anthropomorphism and the social robot. *Robotics and Autonomous Systems* 42, 177–190 (2003)
7. Knoll, A., Dillmann, R.: Editorial: Humanoid Robots - Hype or Hope? *International Journal of Humanoid Robotics* 1(3) (2004)
8. Nass, C., Moon, Y.: Machines and mindlessness: Social response to computers. *Journal of Social Issues* 56(1), 81–103 (2000)
9. Scopelliti, M., Giuliani, M.V., Fornara, F.: Robots in a domestic setting: A psychological approach. *Universal Access in the Information Society* 4, 146–155 (2005)
10. Hinds, P., Roberts, T., Jones, H.: Whose job is it anyway? A study of human-robot interaction on a collaborative task. *Human Computer Interaction* 19, 151–181 (2004)
11. Chang, C.-W., Lee, J.-H., Chao, P.-Y., Wang, C.-Y., Chen, G.-D.: Exploring the Possibility of Using Humanoid Robots as Instructional Tools for Teaching a Second Language in Primary School. *Educational Technology & Society* 13(2), 13–24 (2010)
12. http://www.robotis.com/xe/bioloid_en (accessed July 17, 2012)
13. http://robosavvy.com/store/product_info.php/products_id/639 (accessed July 17, 2012)
14. <http://www.vanadiumlabs.com/arbotix> (accessed July 17, 2012)
15. <http://www.huvrobotics.com/shop/index.php?a=viewProd&productID=6> (accessed July 17, 2012)
16. <http://www.bioloid.info/tiki/tiki-index.php?page=Foot+Pressure+Sensors> (accessed July 17, 2012)

Human-Like Robot as Teacher's Representative in a Science Lesson: An Elementary School Experiment

Takuya Hashimoto¹, Igor M. Verner², and Hiroshi Kobayashi¹

¹ Dept. of Mechanical Engineering, Tokyo University of Science
1-14-6, Kudankita, Chiyoda-ku, Tokyo 102-0073, Japan
[{tak, hiroshi}@kobalab.com](mailto:{tak,hiroshi}@kobalab.com)

² Dept. of Education in Technology and Science, Technion-Israel Institute of Technology
Haifa, 32000, Israel
ttrigor@tx.technion.ac.il

Abstract. This paper reports results of our experiment aimed to investigate the educational process in an elementary school science class, in which teaching functions are carried out by an android robot remotely operated by a human instructor. The robot SAYA, used in the experiments, has human-like appearance and behaviors such as facial expressions, head and eye movements, and speech. In the experiment the instructor remotely controlled SAYA's behaviors, thus managing the interaction of the robot with the students. The experiment recreated a typical lesson on levers that was given to two ordinary groups of sixth graders (23 and 22 students) in their science classroom. The lesson included theoretical learning, experiments with lever balances, and assessment activities. The study utilized qualitative research methods so as to elicit characteristic features of the educational process related to in-class communication, instructional strategies, learning activities, and knowledge acquisition. The paper presents our findings and discusses directions of further research.

Keywords: android robot, robot teacher, human-robot interaction in education.

1 Introduction

Implementation of digital technologies in education and their impact on teaching and learning attract strong professional and social interest. Intensive research is directed toward finding ways to use these technologies for reducing the load of routine drudgery and liberating the teacher for guiding constructivist and individualized learning activities. Studies of learning in online, distance and other computer mediated environments indicated that the effectiveness of learning largely depends on the teacher immediacy – accessible psychological distance between the teacher and the learners [1]. Great effort in the research and development of such learning environments is made to provide opportunities of the teacher's virtual presence, i.e. accessibility for cognitive and social interactions [2].

One promising direction is the use of robots as mediators of the educational process [3]. Human-like robots have here a significant advantage, facilitating the

face-to-face communication by means of gestures [4]-[6] and facial expressions [7][8]. A number of applications of human-like robots as educational mediators have been recently developed. For example, Kanda et al. [9] utilized a humanoid robot, named “Robovie” which speaks only English, at elementary school to investigate long-term interaction between children and the robot, and to investigate whether such instruction motivated children to learn English. That experiment was conducted for two weeks, and the result showed that children were interested in the robot and interacted actively at the earlier phase even though children’s interest to the robot was decreased at the start of the second week along with time.

Polishuk et al. [10] reported on a spectrum of robotic programs developed at the Israel National Museum of Science, Technology and Space (MadaTech) in collaboration with the Technion. In particular, the robot theatre program included different pieces performed by the humanoid robot “Nao”. In the workshop “Human and humanoid robot motion” middle school students studied mechanics of human locomotion through operating Nao to simulate body motions. The follow-up study indicated the educational effectiveness of the humanoid robots as protagonists of the robotics programs. Hashimoto et al. [11][12] have recently initiated an experimental research aiming to utilize an android robot, created in the Tokyo University of Science and named “SAYA”, as a role of an elementary school science teacher. In the proposed setting SAYA serves as a mediator of the educational process, so that its behaviors and interactions with students in class are remotely controlled by a human instructor. Experiments have yielded promising results and indicated the need for a deeper investigation into the mediated learning interactions and their educational outcomes.

This paper presents first results of our collaborative study aimed to answer this need. We carefully designed and conducted an experiment in which a science lesson mediated by SAYA was given in one of elementary schools in Tokyo for two sixth grade classes. Qualitative methods were applied to analyze the lesson and determine characteristic features of students’ interactions with SAYA and of the educational process mediated by the robot. In the following sections of the paper we present the robot, the learning environment, the lesson, as well as research tools and findings.

2 Education Setting

2.1 Robot Teacher SAYA

We use a human-like robot, so-called “android robot”, which is named SAYA and has human like appearance as a teacher (Figure 1). It possesses the Face Robot [13] in the head part, which is capable of human-like facial expression (nineteen DOFs, including mouth movements), head-movements (four DOFs) and eye-movements (two DOFs) for communicating effectively with human beings. Facial movements and head movements are controlled by McKibben artificial muscle which is one of pneumatic actuator, and eye movements are driven by DC servo motors. These actuators are located in the head part.

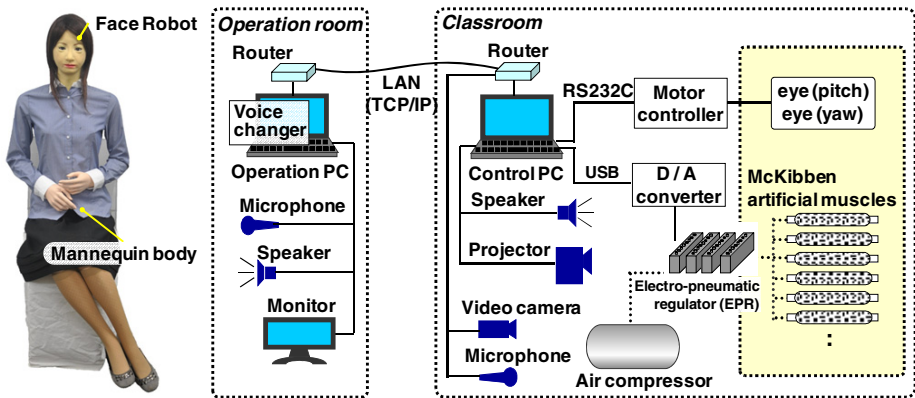


Fig. 1. The android robot used as “robot teacher” (*left*) and the hardware configuration of the proposed educational system (*right*)

2.2 Interaction between Students and Robot in Education

SAYA has some communicative behavior to interact with students, and a human instructor is able to manage SAYA’s behavior by remote control. For example, in giving explanation, when the instructor talk to microphone to give explanation to students, SAYA’ mouth moves in synchronization with instructor’s voice volume and its head and eyes move semi-autonomously to look around a room. The operator is also able to make SAYA to look at a student and to call his/her name individually in asking question. Of course, the instructor can converse with students and reply to them through SAYA without any inhibition. These SAYA’s behaviors are fundamental in educational communication, even though there are various kinds of interaction between human teacher and student. The distinctive behavior of SAYA is to emotionally interact with human through facial expressions. For example, when the instructor warns students, he says “Be quiet!” and he makes SAYA’s facial expression “anger” at the same time.

2.3 Educational Environment

Figure 1 shows the configuration of our proposed educational system, where the android robot SAYA is used as a teacher. In the classroom, SAYA is located in front of the room, as in the actual layout shown in Figure 3 (Section 3.2). A video camera and a microphone are also placed behind students to obtain sight and sound of the classroom. These visual and sound information are transmitted to an operation room. Operation commands of the operator are also sent to the control PC of SAYA in the classroom through LAN, and SAYA’s behaviors are controlled based on the commands.

In the operation room, there are an operation PC, an observation monitor, a microphone, and a speaker in front of a human instructor. The instructor is able to observe students’ behaviors because video and sound of the classroom are reproduced

via the observation monitor and the speaker respectively. When the instructor talks into the microphone, his voice is changed to SAYA's voice by a voice changer and replayed via the speaker of the classroom in real time. SAYA's mouth is moved in synchronization with amplitude of sound pressure of instructor's voice. GUI-based operation interface is displayed on the operation PC, thus the instructor can control SAYA's head and eye directions and facial expressions by clicking buttons allocated for SAYA's behavior on the display. In this way, the instructor is able to react to students' behavior through SAYA in real time. In addition, the instructor is also able to switch slides easily by clicking the button of the operation interface.

2.4 Lesson Plan

We adopted "Function and Law of Lever" as a lesson topic. This lesson topic is contained in a regular textbook along the educational guideline of science class for 6th grade of elementary school in Japan. The topic includes both theoretical and practical aspects. We organized a science lesson for our experiment referring to regular textbooks, and Table 1 shows detailed content of the science lesson concerning the topic "Function and Law of Lever". The lesson takes about 30 minutes and is started with greetings. Then, SAYA introduces itself and converses with children briefly. After that, SAYA introduces important points of a lever: the fulcrum, the point of effort, the point of load. The robot continues showing typical applications of a lever in our daily life such as scissors, bottle-opener, tweezers, and so on through conversation with children. Then, children conduct experiments with an experimental lever kit following SAYA's instruction, and they fill in the experiment worksheet. Through experiments, children explore different ways to balance the lever. After experiments, SAYA analyzes its results and formulates the lever law.

Table 1. The time schedule of the science lesson

Scene	Time (min.)	Content
1	1	Self introduction of SAYA
2	8	Lecture on basic theories and mechanical advantages of leverage
3	2	Lecture on familiar examples of leverage in daily life
4	15	Experiments with experimental lever kit
5	4	Conclusion

2.5 Instructional Material

We made original presentation slides using Microsoft Office PowerPoint® according to the textbook which is widely used in elementary schools in Japan. In order to offer attractive presentation, the slides contain animations that demonstrate familiar examples of a lever, to explain how a lever is balanced, to instruct how students should do experiment, to explain the principle of leverage, and so forth.

We prepared an experimental kit which has a lever with a scale to clarify the position of weights and some weights with hooks. We organized a worksheet, a fragment of which is shown in Figure 2(left), to help students to progress experiments in accordance with a lesson scenario. In the worksheet, students can write down experimental conditions: the number of weights, the position of weights, and experimental result which shows whether the lever is balanced at an experimental condition.

We also organized an assessment test, a fragment of which is shown in Figure 2(right), including nine questions concerning the lesson topic “Function and law of lever”. It has not only basic questions but also practical questions. First three questions check the capability to identify important points of the lever. Questions 4 and 5 checked the understanding of a dependency between an effort and a lever arm distance. Question 6 and 7 asked how to counterbalance a given weight put on one side of the lever. These questions checked the knowledge of a condition for balancing a lever. Questions 8 and 9 requested to analyze the use of leverage in two every-day life situations: wallet holding and seesaw swinging. Students answer the test after the lesson to assess their learning level.

<p>Work Sheet — The lever — How can you balance the lever in each condition?</p> <p>Condition 1: A weight is hung on the position 3 on the left side</p> <table border="1" style="margin-top: 10px;"> <thead> <tr> <th>The number of weights</th> <th>The position of weights</th> </tr> </thead> <tbody> <tr><td>1</td><td>1</td></tr> <tr><td>2</td><td>2</td></tr> <tr><td>3</td><td>3</td></tr> <tr><td>4</td><td>4</td></tr> <tr><td>5</td><td>5</td></tr> <tr><td>6</td><td>6</td></tr> </tbody> </table>	The number of weights	The position of weights	1	1	2	2	3	3	4	4	5	5	6	6	<p>5. In fig.3, Which of the boys to apply by his hands greater effort to hold the wallet? Answer: The boy of No. _____ apply greater effort to hold the wallet.</p> <p>No. 1 No. 2</p> <p>Figure 3 Boys holding the wallet</p>
The number of weights	The position of weights														
1	1														
2	2														
3	3														
4	4														
5	5														
6	6														

Fig. 2. The work sheet of the experiment (left) and the assessment test (right)

2.6 Evaluation Method

We developed a questionnaire as shown in Table 2 to collect students’ impressions of the human-like robot SAYA as a “robot-teacher” and their reflections on the lesson. We attempted to outline topics that are central for HLR mediated learning and formulate questions that can help to categorize them. The questionnaire was designed as a step in the study of this learning based on the principles of the grounded theory [14]. The main sources for outlining the topics were: results of the pilot questionnaire [11, 12], the Godspeed Human-Robot Interaction Questionnaire [15], and videos of pilot lessons conducted through mediation of SAYA. The three topics addressed in the questionnaire were: robot appearance, robot behaviors, and impression of the robot and the lesson. To characterize the robot appearance, we used the features “natural” and “human-like” from the Anthropomorphism section of the Godspeed Questionnaire, as they were relevant to our case and easy to understand for primary school students. From the Animacy section of the Godspeed we used the features “Responsive” and “Friendly” as characteristics of the robot behavior. Some more features from these sections were added after revision aimed to make them more relevant for our case. In particular we used “Like real teacher” instead of “Lifelike”

and “Energetic” instead of “Alive”. We did not include in our questionnaire features from the Godspeed’s section “Perceived Intelligence”. These features “Competent”, “Knowledgeable”, “Responsible”, “Intelligent”, and “Sensible” in our case were demonstrated by the instructor, not by the robot. In fact, robot SAYA does not have cognitive intelligence, but it has certain features of social and emotional intelligence, particularly related to speech generation and facial expressions [13]. We added a question related to these features, asking students “Did SAYA express emotions during the lesson?” To address students’ impressions of the robot, we included the feature “Like” from the Godspeed’s section Likeability. We revised the feature “Pleasant” of this section and asked the question “Was SAYA’s lesson pleasant?”. We made this revision because interaction with SAYA was inseparable part of the lesson. Our questionnaire also related to students’ impression of the lesson effectiveness. In HRI (Human-Robot Interaction) research, effectiveness is considered as an important metric. As the Godspeed questionnaire does not address the issue of HRI effectiveness, we added a relevant question for our case: “Was SAYA’s lesson interesting?”

Table 2. The questionnaire including 10 questions and their evaluation indices

Question	Evaluation			
Q. 1:Was SAYA’s appearance natural or unnatural?	Unnatural	Somewhat unnatural	Quite natural	Natural
Q. 2:Is SAYA machine-like or human-like?	Machine-like	Somewhat machine-like	Quite human-like	Human-like
Q. 3:Was SAYA responsive to the class?	Not care the class	Little responsive	Often responsive	Responsive
Q. 4:Was SAYA friendly during the lesson?	Not friendly	Not so friendly	Quite friendly	Friendly
Q. 5:Did SAYA behave like a real teacher?	Unusual behavior	Not typical behavior	Quite typical behavior	Teacher-like behavior
Q. 6:Was SAYA energetic during the lesson?	Inert	Quite inert	Quit energetic	Energetic
Q. 7:Do you like SAYA?	Dislike	Not so like	Like	Much like
Q. 8:Was SAYA’s lesson pleasant?	Unpleasant	Not so pleasant	Pleasant	Very pleasant
Q. 9:Was SAYA’s lesson interesting?	Not interesting	Little interest	Quite interesting	Interesting
Q. 10:Did SAYA express emotions during the lesson?	No emotions	Little emotion	Emotional	Very emotional

3 Experiment Implementation

3.1 Collaboration with an Elementary School

The experiment was conducted in cooperation with one of elementary schools in Tokyo, Japan. The school teachers discussed and accepted “Function and Law of

Lever” as a topic for the experimental lesson and gave recommendations related to the lesson content and teaching strategy. On their recommendation, the robot’s lesson followed the conventional lesson conducted by a teacher at which the topic “Function and law of lever” was introduced. In addition, we decided to conduct the science lesson twice for two classes in a day within a regular lesson.

3.2 Experimental Environment

We used a lunch room of the school for the lesson and an adjoining room for an operation. Figure 3 shows the experimental environment in the lunch room, and Figure 3 also shows a sight of the experiment. SAYA was located in front of the room as the role of a teacher, and a plasma display to show videos and slides was put next to SAYA. In the back of the room, a camera and a microphone were put for the operation. In addition, two additional cameras which were put at the front corners of the room were used to record the experiment. Four or five children sat on each table, and an experimental lever kit was put on each table.

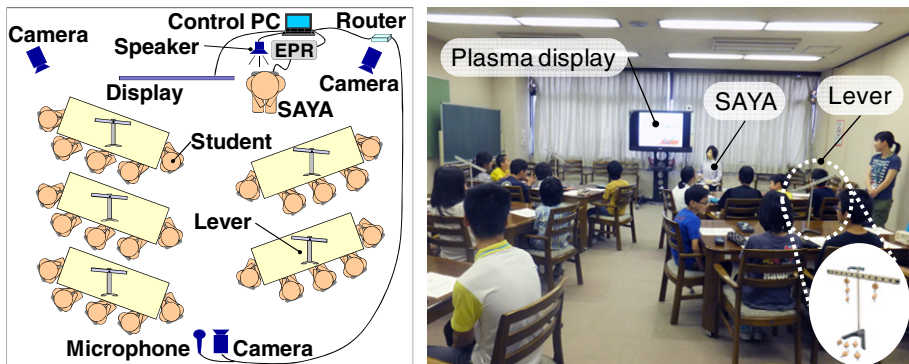


Fig. 3. The experimental setup in the class (*left*) and the sight of the lesson (*right*)

3.3 Participants

We conducted the science lesson twice for 45 students who aged 11-12 years and belonged to 6th grade. They had been divided to two classes, a class has 23 students (male: 14, female: 9) and the other class has 22 students (male: 13, female: 9). They had already studied the lesson topic “Function and law of lever” in regular class. Therefore, they were not unfamiliar with the topic.

Homeroom teachers of two classes and some teachers who were interested in our experiment also attended the lesson.

3.4 Procedure

First of all, an experimenter made children sit at assigned positions so that an instructor was able to distinguish children, and it allowed the instructor to make

SAYA look at a child or call a child's name individually. After that, the experimenter gave brief explanations about the experiment to children, and the experimenter exited the room. Then, the instructor controlled SAYA to ask children answer the assessment test (i.e. "pre-course test") to assess children's initial learning level because they had already learned the science lesson topic "Function and law of lever" and to compare their learning level before and after the lesson. After three minutes, SAYA gave children a greeting and begun the science lesson. After the lesson, SAYA also asked children to answer the same assessment test (i.e. "post-course test") and answer the questionnaire. Figure 4 shows the photos of the experiments.



Fig. 4. The photos of the experiments in the elementary school

4 Findings and Discussion

4.1 Analysis of Worksheets

All students in the first group actively participated in the experiments, filled the worksheet and presented results of the experiments correctly. In the second group the students also actively participated in the experiments, but only small part of them filled the worksheet. A possible reason is that the first class was more motivated to study the science topic than the second class. Other possible reason is that the request to fill the worksheet came as SAYA's own request, not teacher's request. The students from the second class did not accept this request.

4.2 Analysis of Assessment Test

In question 1, 2, and 3 of pre-course test, all students in both groups perfectly identified the important points of a lever: the fulcrum, the point of effort, and the point of load. The majority of the students (more than 80%) in both groups correctly answered Questions 4, 5, and 6. Questions 7, 8, and 9 were more difficult to the students: the percentage of incorrect answers for them was correspondingly 31%, 29%, and 38%. In the post-course test the percentage of incorrect answers reduced to 6.7%, 13.3%, and 26.7%. More than 85% of the students correctly answered all questions of the post-course test, except question 9. To summarize this comparison between pre-course test and post-course test, significant improvement of students' learning performance is indicated as shown in Table 3.

Table 3. The comparison of students' learning performances before and after the lesson

	Avg. score of pre-course test	Avg. score of post-course test	Improved results
First group	81.6	90.3	60.9%
Second group	90.4	97.0	36.4%

4.3 Analysis of Questionnaire

1) Robot appearance

Students' evaluations of SAYA as "Natural" (in Q. 1) and "Human like" (in Q. 2) can be summarized as follows. As indicated, one third of the students perceived SAYA's appearance as unnatural, about half as somewhat unnatural, i.e. having unnatural and natural attributes, and for 20% of the students SAYA looked natural or quite natural. The perceptions of SAYA as "human like" were more positive than that of "natural". One-third of the students perceived the robot as human-like, other one-third noted that SAYA combines machine-like and human-like attributes, and only one-third saw it as machine-like. To summarize the aforesaid, majority of the students perceived SAYA as a human-like robot.

2) Robot behaviors

The results of students' impressions of the robot's responsiveness ("Responsive") (Q. 3) and friendliness ("Friendly") (Q. 4) can be summarized as follows. 58% of them noted that SAYA was responsive or often responsive at the lesson, 27% considered its responsiveness as little and only 15% pointed that the robot did not care the class. From our observations, possible explanation for this fair evaluation is that SAYA missed part of students' comments and its responses sometimes were delayed. Students' evaluations of friendliness were slightly less positive than of responsiveness. 46% of the students perceived SAYA as friendly, 36% responded that it was not so friendly, and 18% considered the robot not friendly. A possible reason is that SAYA (the instructor) used formal official language to communicate with the students in the lesson.

In Q. 5, 55% of the students responded that for their opinion SAYA behaved "like a real teacher", 38% perceived its behaviors as not typical, and 7% as unusual for a teacher. A possible reason for the mixed results is that SAYA's implementations of teachers' behaviors had some unusual nuances such as making a mistake with calling student's name, missing eye-contact, and being unable to fit student's personality, even though SAYA did teacher-like behaviors: looking at a student, calling a name, giving explanations and instructions in experiments.

The question about SAYA's vitality (in Q. 6) brought us unexpected results. Two third of the students noted that in the lesson the robot was energetic or quite energetic, while 29% perceived it as quite inert and only 4% as inert. A possible reason for this response is that SAYA was unable to use many gestures and walk around the class, and was sometimes slow to respond, even though SAYA was able to interact with students fluently through words and facial expressions.

3) Student's impression of SAYA and of the lesson

In Q. 7, mixed results were accepted with regard to impressions about SAYA: 60% of the students noted that they like or much like the robot, 31% not so liked, and 9% disliked it. In addition, we could find out students' high positive impressions of the lesson in Q. 8: 89% of the students evaluated the lesson as pleasant or very pleasant, 7% as not so pleasant and only 4% as unpleasant. We observed numerous indications of students' joy: enthusiasm in learning activities and in communication with the robot, applauses to show agreement with answers given by classmates. In Q. 9, we found that the lesson raised interest of the class: 76% of the students found it interesting or quite interesting, 15% mentioned little interest and 9% no interest. This high evaluation was achieved in spite of the fact that the students had already studied the lesson subject "Function and law of lever" in regular science lessons.

4) Social and emotional intelligence of SAYA

When answering the question "Did SAYA express emotions during the lesson?" in Q. 10, 75% of the students perceived SAYA as emotional or very emotional, while only some students noted little emotion (18%) or no emotion (7%). We also asked the students on the kinds of SAYA's emotions that they observed during the lesson and suggested to select them from the list of typical facial expressions that can be expressed by SAYA. As indicated, absolute majority of the students observed expressions of positive emotions, namely smile (98%) and surprise (76%), while only small number of students paid attention to negative emotions such as angry (9%), fear (7%), disgust (2%), and sadness(7%), even though the instructor didn't express "fear" and "disgust" at all.

5) Communication with SAYA

About half of students answered positively to the question: Did limitations of SAYA's movement disturb your communication with the robot teacher in the lesson?" They noted difficulties in communication with SAYA due to the lack of movements and the slow response.

We also asked the question "Did you actively participate in the lesson? Please describe your activities". 80% of students answered that they actively participated in the lesson by raising their hands many times and doing experiment actively. Meanwhile, 13% of students indicated that they were not involved actively. Their typical explanations: "I have already known the lever. So I didn't participate actively", "I could not concentrate on the lesson because I was obsessed with SAYA".

We finally asked the question "What was most interesting to you in the lesson? Please explain". Most of students were interested in SAYA's behaviors and facial expressions, and functions (calling student's name and voice synthesizing) as well as the experiments using the experimental lever kit, the mechanism and the advantage of a lever.

5 Conclusion

In this paper we report an experimental study of the educational process in an elementary school science class, in which teaching functions were carried out by an

android robot, named SAYA, remotely controlled by a human instructor. The specific innovative features of our experiment were:

- Aspiration to recreate a typical science lesson (regular groups of students, a habitual classroom, typical learning activities, a topic from the curriculum, SAYA's simulation of teacher's behavior).
- Careful design of the developed lesson, including assessment of learning outcomes. Close collaboration with the school in implementing the lesson.
- Careful design of the educational experiment through collaboration of robot developers and an educator. Collecting data of observations, students' performances and reflections.

The experiment was a step in our study of educational processes in which a teleoperated robot plays the role of a teacher. It provided evidence for the following conclusions:

1. The experiment showed that the science lesson, conducted through robot mediation in the proposed setting, can successfully achieve its learning objectives.
2. The absolute majority of the students were closely involved in the lesson and actively participated in learning activities throughout it.
3. The observed learning behaviors were mostly typical for a science class. When the students had questions or wanted to answer questions posed by SAYA, they raised hands. When SAYA called students by name, they stood up and answered the posed questions. The students sought to personally communicate with SAYA. Those who did not have face-to-face contact with the robot were less engaged in the lesson.
4. The students were strongly impressed by SAYA. Seeing that SAYA is a robot, during the lesson they did not know how SAYA succeeded to act like a real teacher. The students were intrigued and interacted with the robot teacher with great interest. At the end of the lesson the students asked about how the robot is constructed and controlled and got explanation with great attention.
5. Students' answers about their perceptions of SAYA's appearance and behavior contain important data for the analysis of learning interactions with the robot and their optimization.

In conclusion, we acknowledge the potential of using human-like robots as mediators of science education and continue the study of the proposed approach towards deeper understanding and wider implementation of learning interactions with robots.

References

1. Swan, K.: Learning effectiveness: what the research tells us. In: Bourne, J., Moore, J.C. (eds.) *Elements of Quality Online Education*, pp. 13–45 (2003)
2. Baker, C.: The impact of instructor immediacy and presence for online student affective learning, cognition, and motivation. *The Journal of Educators Online* 7(1), 1–30 (2010)
3. Verner, I., Polishuk, A., Klein, Y., Cuperman, D., Mir, R., Wertheim, I.: A Learning Excellence Program in a Science Museum as a Pathway into Robotics. *International Journal of Engineering Education* 28(3), 523–533 (2012)

4. Ogawa, H., Watanabe, T.: InterRobot: a speech driven embodied interaction robot. In: Proceedings of 9th IEEE International Workshop on Robot and Human Interactive Communication (RO-MAN 2000), pp. 322–327 (2000)
5. Kamasima, M., Kanda, T., Imai, M., Ono, T., Sakamoto, D., Ishiguro, H., Anzai, Y.: Embodied Cooperative Behaviors by an Autonomous Humanoid Robot. In: Proceedings of IEEE/RSJ International Conference on Intelligent Robots and Systems (IROS 2004), pp. 2506–2513 (2004)
6. Kozima, H., Vatikiotis-Bateson, E.: Communicative criteria for processing time/space-varying information. In: Proceedings of 10th IEEE International Workshop on Robot and Human Interactive Communication, pp. 377–382 (2001)
7. Breazeal, C., Scassellati, B.: How to build robots that make friends and influence people. In: Proceedings of the 1999 IEEE/RSJ International Conference on Intelligent Robots and Systems (IROS 1999), vol. 2, pp. 858–863 (1999)
8. Kato, S., Ohshiro, S., Itoh, H., Kimura, K.: Development of a communication robot Ifbot. In: Proceedings of the 2004 IEEE International Conference on Robotics and Automation (ICRA 2004), pp. 697–702 (2004)
9. Kanda, T., Hirano, T., Eaton, D., Ishiguro, H.: Interactive Robots as Social Partners and Peer Tutors for Children: A Field Trial. *Human Computer Interaction* 19(1-2), 61–84 (2004)
10. Polishuk, A., Verner, I.: Interaction with animated robots in science museum programs: how children learn? In: Proceeding of the 7th Annual ACM/IEEE International Conference on Human-Robot Interaction (HRI 2012), pp. 265–266 (2012)
11. Hashimoto, T., Kato, N., Kobayashi, H.: Field Trial of Android-type Remote Class Support System in Elementary School and Effect Evaluation. In: Proceedings of IEEE International Conference on Robotics and Biomimetics (ROBIO 2009), pp. 1135–1140 (2009)
12. Hashimoto, T., Kato, N., Kobayashi, H.: Educational System with the Android Robot SAYA and Field Trial. In: Proceedings of 2011 IEEE International Conference on Fuzzy Systems (FUZZ-IEEE 2011), pp. 766–771 (2011)
13. Hashimoto, T., Hiramatsu, S., Tsuji, T., Kobayashi, H.: Development of the Face Robot SAYA for Rich Facial Expressions. In: Proceedings of SICE-ICASE International Joint Conference 2006, pp. 5423–5428 (2006)
14. Charmaz, K.: Grounded theory: Objectivist and constructivist methods. In: Denzin, N., Lincoln, Y.S. (eds.) *Handbook of Qualitative Research*, 2nd edn., pp. 509–536 (2000)
15. Bartneck, C., Croft, E., Kulic, D.: Measuring the anthropomorphism, animacy, likeability, perceived intelligence and perceived safety of robots. In: Proceedings of the Metrics for Human-Robot Interaction Workshop in Affiliation with the 3rd ACM/IEEE International Conference on Human-Robot Interaction (HRI 2008), Technical Report 471, pp. 37–44 (2008)

Measuring the Information Quality of e-Learning Systems in KSA: Attitudes and Perceptions of Learners

Salem Alkhafaf, Anne T.A. Nguyen, Steve Drew, and Vicki Jones

School of ICT, Griffith University Gold Coast, QLD, Australia

{salem.alkhalaf, a.nguyen, s.drew, v.jones}@griffith.edu.au

Abstract. The introduction of e-learning, with the easy availability of course materials and related resources, has had a major impact on students and lecturers in higher education. However, few studies have been conducted to measure the information quality of e-learning on educational institutions in Saudi Arabia. This paper looks at the issues of using e-learning systems and the effect on higher education institutions in the Kingdom of Saudi Arabia (KSA). The findings of this study show positive attitudes towards e-learning systems in higher education, as well as learning improvement and the positive effect of employing a collaborative style of e-learning.

Keywords: e-Learning; IS success; IS impact; Kingdom of Saudi Arabia, Information Quality

1 Introduction

One of the emerging technologies in education is collaborative e-learning, which plays a significant role in the growing number of students enrolled at universities, especially in Saudi Arabia. With the increased number of students, many higher-education institutions have introduced e-learning systems to improve the delivery of course content and enhance access to courses and subjects by both students and teachers [1-3].

Collaborative e-learning environments are also advantageous. Tomsic & Suthers [4] believe that the information sharing associated with social networks, can help establish new collaborative ties for students, and can have a more significant impact on learning than interaction and frequency of exposure to data, which is found in traditional systems. Collaborative e-learning environments are based on collaborative environments and are built on the research conducted on how students learn [5]. In collaborative e-learning environments, information technology facilitates increased interaction between the learners, promoting the exchange of knowledge. Collaborative e-learning environments can offer learners extensive opportunities for open learning, controlled by the learners themselves.

2 IS-Impact Measurement Model

There have been many studies conducted on web-based learning to measure the effectiveness of this sort of learning compared with traditional classroom learning for different courses at different educational levels [6]. However, according to [7], there is little in the literature on the effectiveness of e-learning systems.

This study adopted the IS-impact measurement model, which is also used to measure IS evaluation, as it considers the success of educational systems by measuring four aspects of the system [8]. Delone and McLean's [9] IS success/impact model was chosen, as it suits any educational environment due to the fact that it incorporates the whole e-learning environment. Previous research supports the notion that the model is suitable for any educational environment. Therefore, dimensional theory was used to measure the effectiveness of the IS success/impact model. Another reason this model is thought to be the most useful for measuring e-learning systems, is because it comprises 41 measures including six dimensions [8,10]:

- System Quality
- Information Quality
- Use
- User Satisfaction
- Individual Impact
- Organisational Impact

According to Wang, Wang, & Shee [7], system quality and information quality both affect use and user satisfaction, leading to user satisfaction being measured indirectly through Information Quality, System Quality and related variables in other studies [10]. However, this paper focuses on measuring the Information Quality of e-learning systems on learners.

3 Information Quality

A survey questionnaire was distributed to e-learning students in both Qassim University and King Abdualaziz University in order to evaluate the current e-learning system, already in use in these universities. The questionnaire was designed based on the IS measurement model [10]. It includes questions which measure the four dimensions: System Quality, Information Quality, Individual Impact, and Educational Impact. As mentioned above, only those survey questions that measure the organisational impact of e-learning systems were included. The questionnaire was presented to 800 students and 560 were returned but 32 were excluded as they deemed incomplete. Therefore, 528 questionnaires were included in the analysis. More specifically, the sample of males is 328 students while 200 participants were from female students. Table 1 shows the relative numerical distribution of responses regarding Information Quality.

Table 1. Relative numerical distribution of responses regarding "Information Quality"

N	Questions/Items	Strong agree	Agree	Neutral	Disagree	Strong disagree	Mean	SD	χ^2	Relative weight	Order
		Frequency									
1	The eLearning system provides information that is exactly what you need (Content Accuracy)	103	189	157	33	16	3.66	0.982	228.15	.73	7
2	The eLearning system provides information you need at the right time (Availability)	138	172	10	52	23	3.71	1.121	151.07	.74	6
3	The eLearning system provides information that is relevant to your course (Usability, relevance)	136	242	82	28	8	4.05	2.46	357.15	.81	1
4	The eLearning system provides sufficient information for your purposes (Quantity of information)	105	220	125	37	11	3.74	0.946	270.47	.74	4
5	The eLearning system provides information that is easy to understand (Understandability)	101	211	134	34	12	3.72	0.948	259.81	.74	5
6	The eLearning system provides up-to-date information (Current)	135	216	91	30	19	3.85	1.016	266.87	.77	3
7	The eLearning system provides information that appears readable, clear and well formed (User interface)	135	221	95	35	8	3.89	0.941	289.19	.77	2
8	The eLearning system provides required information on time. (Timeless)	112	178	126	52	26	3.6	1.105	148.55	.72	9
9	The eLearning system provides information that is suitable concise	98	187	145	42	20	3.61	1.026	196.64	.72	8

A statistical analysis of the questionnaires was carried out using the Statistical Package from the Social Sciences (SPSS) software package. As mentioned above, only those survey questions that measure the organisational impact of e-learning systems were included. The frequency and percentage of the responses for each of the ten variables was analysed, and their Chi-square values and their levels of significance.

The Chi-square Goodness of Fit Test value for all phrases that relate to each individual response to sample the first dimension of the questionnaire Information Quality and on the "Information Quality" greater than the value of Chi-square spreadsheet, which amounted to 7.78 at the 0.05 level of significance and 4 degrees of

freedom, indicate that the difference between duplicates renders the expected viewing of the dimension "Information Quality" statistically significant.

It is clear that the most important responses of the sample for Information Quality are as follows: "The e-learning system provides information that is relevant to your course (Usability, relevance)" and "The e-learning system provides information that appears readable, clear and well formatted (User interface)". The average variable number is between 3.60 and 4.05 and the relative weight of importance is between 72% and 88%; all variables nearly 72%, with standard deviation ranging from 0.941 to 2.460.

The results indicate the following: For statement 1, 189 respondents (38%) said that dealing with an educational system based on e-learning provides the information needed by the learner and the administration at one time, and is accurate in content and content due to dealing with electronic systems by computer programs designed for this purpose, which is providing the information well and accurately. For statement 2, 172 respondents (34.7%) reported that an e-learning system provides the information needed at the right time (availability), which helps them to do their jobs. For statement 3, 242 respondents (48.8%) confirmed that an e-learning system provides information relevant to their studies and is easy to use and compatible with their abilities and needs. For statement 4, 220 respondents (44.2%) confirmed that an e-learning system provides sufficient information for all purposes and for all students, and is commensurate with the needs of each individual student (the amount of information). For statement 6, 216 respondents (44%) confirmed that an e-learning system provides the latest information (resolution). For statement 7, 221 of respondents (44.7%) confirmed that an e-learning system provides information to readers in an easy, simple, clear and well-coordinated way (user interface), which helps them use the system correctly. In statement 8, 178 respondents (36%) confirmed that an e-learning system provides the required information on time (timing), which helps solve the problem of time in traditional systems, which may have access to information in these systems an obstacle to moving the business. For statement 9, 178 respondents (38%) confirmed that an e-learning system provides a summary of information compared to other systems that provide a lot of information.

4 Conclusion

With regard to item number 1, the results demonstrate that the majority of students feel that they have learnt a great deal through the use of the e-learning system, but with different levels of agreement. While 40% of the students agree that they have learnt a lot, 26% state that they strongly agree. Thus, it appears that the use of e-learning systems has had a positive impact on their education. Their conviction suggests that e-learning plays an effective role in the development of educational processes. These findings are in line with several previous studies. For instance, Williams and Jacobs [11] stated that student learning through blogs or similar collaboration tools is more effective than from teachers or textbooks. This reinforces the fact that the students need to have sufficient knowledge and proficient computer skills to achieve the higher level of success by using collaborative e-learning technology.

The results further indicate that most of the students (72%) either agree or strongly agree that e-learning systems enhance their awareness of the requirements of educational processes. Also according to one interviewee, students benefited from the e-learning system as it enhanced their understanding of information in this system. They have become more aware of sources of information. Multimedia information can be overwhelming as there are many forms. However, after using e-learning systems, they began to use more forms of multimedia, allowing them to receive information faster, due to the connectivity both within the university or from outside.

This paper helps confirm that the use of e-learning systems helps students get all the information they need in an accurate and timely way.

References

1. AlSaif, A.: The motivating and inhibiting factors affecting the use of Web-Based Instruction at the University of Qassim in Saudi Arabia. ETD Collection for Wayne State University (2005)
2. AlGhamdi, R., Drew, S., Alshehri, M.: Strategic Government Initiatives to Promote Diffusion of Online Retailing in Saudi Arabia. In: Pichappan, P. (ed.) Sixth International Conference on Digital Information Management, Melbourne, Australia, pp. 217–222 (2011)
3. Alkhalfaf, S., Drew, S., Alghamdi, R., Alfarraj, O.: E-Learning System on Higher Education Institutions in KSA: Attitudes and Perceptions of Faculty Members. Procedia-Social and Behavioral Sciences 47, 1199–1205 (2012)
4. Tomsic, A., Suthers, D.: Discussion tool effects on collaborative learning and social network structure. Educational Technology & Society 9(4), 63–77 (2006)
5. Liaw, S.-S., Huang, H.-M.: Developing a Collaborative e-Learning System Based on Users' Perceptions. In: Shen, W., Luo, J., Lin, Z., Barthès, J.-P.A., Hao, Q. (eds.) CSCWD. LNCS, vol. 4402, pp. 751–759. Springer, Heidelberg (2007)
6. Zhang, D., Nunamaker, J.: Powering e-learning in the new millennium: an overview of e-learning and enabling technology. Information Systems Frontiers 5(2), 207–218 (2003)
7. Wang, Y., Wang, H., Shee, D.: Measuring e-learning systems success in an organizational context: Scale development and validation. Computers in Human Behavior 23(4), 1792–1808 (2007)
8. Cao, L., Elias, N.: Validating the IS-Impact model: two exploratory case studies in China and Malaysia. In: Bapna, R., Sambamurthy, V. (eds.) Proceedings of the Pacific Asia Conference on Information Systems 2009, Association for Information Systems (AIS), Hotel Novotel, Hyderabad, India, pp. 1–14 (2009)
9. DeLone, W., McLean, E.: Information systems success: the quest for the dependent variable. Information Systems Research 3(1), 60–95 (1992)
10. Gable, G., Sedera, D., Chan, T.: Re-conceptualizing information system success: the IS-Impact Measurement Model. Journal of the Association for Information Systems 9(7), 377–408 (2008)
11. Williams, J.B., Jacobs, J.S.: Exploring the use of blogs as learning spaces in the higher education sector. Australasian Journal of Educational Technology 20(2), 232–247 (2004)

Research on Distance-First Based Role Assignment Strategy of Soccer Robot

Da-Lei Song¹, Bing-Wei Wu¹, Xiu-Fang Li², Li-Ping Chen¹, and Chuan-Jun Liu¹

¹ College of Engineering, Ocean University of China

² College of Information Science and Engineering, Ocean University of China

No.238, Songling Road, Laoshan District, Qingdao, Shandong, China

songdalei@ouc.edu.cn, wubingweide@gmail.com,

{1xf123279, liuchuanjun1990}@163.com, chen0037@foxmail.com

Abstract. This paper studies a dynamic role assignment strategy in robot soccer game and illustrates the disadvantages of the shortest distance assigning algorithm. Based on that algorithm, the distant role-first assigning algorithm is proposed. The algorithm takes the factors into account, such as the obstacle-avoiding when the players position their places, balance of power consumption of the players and short moving distance. Finally, the simulation experiment is conducted to verify the advantages of the distant role-first assigning algorithm based on typical defense formation and half-encircled formation. The results show that the algorithm we proposed performs well in practical applications.

Keywords: Role assignment, Formation, Distance-first, Robot soccer, Power consumption.

1 Introduction

The robot soccer game is the typical application platform of MAS (Multi-Agent System) [1; 2], and is a high technology intensive project with challenges in the artificial intelligence robot field. For the study of MAS, it emphasizes the interaction and influence between the multi-agents. Role assignment of multi-agent is the basic unit of the activity in the robot soccer, and any fiery match is inseparable from the role assignment of multi-agent. At present, there are many algorithms about role assignment of multi-agent, such as the shortest distance algorithm [3], Genetic algorithm [4], artificial neural network [5] and fuzzy control [6]. Genetic method, the artificial neural network and fuzzy control belong to artificial intelligence algorithms. At present, hohai university "e dragon" team is one of the best semi-autonomous robot football teams adopted the shortest distance algorithm to robot soccer and has achieved excellent results in the robot soccer game. In this paper, the distant role-first assigning algorithm is proposed based on the shortest distance algorithm.

The shortest distance algorithm has many advantages, such as strong real-time performance, speed fast and switching slowly of role resolution, but it has many disadvantages such as collision with each other, imbalance of power consumption of

the players and short moving distance, and so on. So this paper introduces the dynamic role assignment strategy for soccer robot that is the distant role-first assigning algorithm. The algorithm has been verified that it has advantages of obstacle-avoiding when the players positioning their places [7], balance of power consumption of the players and short moving distance, so it has important significance in the assisted research of soccer robot.

2 Decision-Making Subsystem

Soccer robot based on vision system is mainly composed of the vision subsystem, decision-making subsystem, communication subsystem and robot car subsystem. It is also the basic structure of Mirosoft [8] series robot system in China. Firstly visual subsystem gathers and processes images in time to get position coordinates of all robots and balls, and the direction angle of robots. After that, it sends these messages in the form of a matrix to decision-making system. Secondly the decision-making subsystem analyses the situation of robots, determines what kind of action the robot should take, calculates the speed of both left and right wheel for each robot, and drives the robot in accordance with the designated trajectory [9].

Decision-making system needs a series of processing according to the incoming information of robots and balls, and then return robot control instructions. The detailed process is shown as in fig1. Because the game in the twinkling of an eye, the original role may not be for now situation, if we want to keep a favorable situation, we must dynamically assign role of robots in play. For example Mirosoft 5:5, when the formation unit determined the formation one time and determined five robot main tasks, the role assignment unit will assign these tasks to corresponding robots, and each robot will play a certain role. Assume that the stadium situation is shown as in fig2: No.0 player is a goalkeeper, its role is fixed and its position is in goal area. The position of No.1~No.4 is shown as in this figure, and A, B, C, D are goals, so the role of No.1~No.4 are needed to assign rationally.

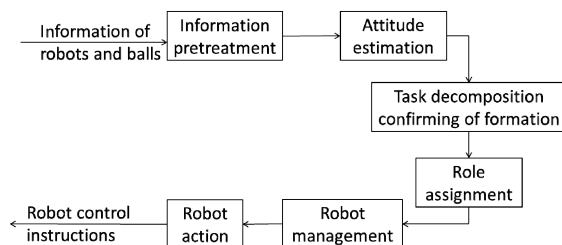


Fig. 1. The process of decision-making subsystem

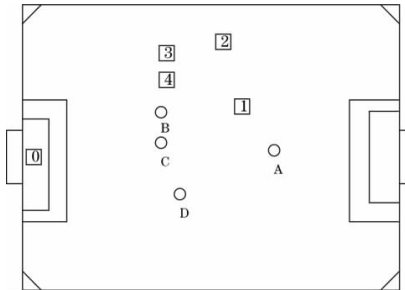


Fig. 2. The position assignment of players

3 The Distant Role-First Assigning Algorithm

The traditional shortest distance assigning algorithm needs to calculate the distance between the every robot and the role position, and elects a robot to act the role according to the minimum value of distance. As fig 2 shows, we can assign role of A,B,C,D to corresponding robot according to this shortest distance algorithm: 1 → A (No.1 to the position A), 4 → B, 3 → C, 2 → D .But this assignment algorithm has some shortcomings: (1) The path from No.3 to C go through B, however the No.4 arrives at B first, and the No.4 becomes the obstacle of No.3, so the No.3 needs to bypass the No.4. So this kind of role assignment leads to players' trajectory complex. (2) The distance between No.4 and its role is the shortest, and its power consumption is the least, however the power consumption of No.2 and No.4 are larger.

For the shortcomings of the shortest distance algorithm, we reanalyze the role assignment of Fig 2. If the order of role position is D,A,C and B, we reassign the role of robot according to the shortest distance algorithm, the result is $1 \rightarrow D, 4 \rightarrow A, 3 \rightarrow C, 2 \rightarrow B$. This kind of role assignment strategy is rational, which avoids the disadvantages of the former. This paper presents a new role assigning algorithm that is distant role-first assigning algorithm. The algorithm is a dynamic role assigning lgorithm, which combines the distance role and traditional shortest distance algorithm. The implementation ideas are described as follows:

- (1) Determine the role positions P_1, P_2, \dots, P_n of n roles, and the position R_1, R_2, \dots, R_n of n robots.
- (2) Calculate $\sum_{i=1}^n d(P_i, R_j)$ the sum of distance, which is between the position P_i and the positions of all robots. $\sum_{i=1}^n d(P_i, R_j)$ is the maximum of $\sum_{i=1}^n d(P_i, R_j)$, in other words the most distance role position is P_{i1} , and sort P_{i1} .
- (3) Judging whether all the role position are sorted, or turn to step (2).
- (4) Determine the reordered role positions G_1, G_2, \dots, G_n of n roles, and the positions R_1, R_2, \dots, R_n of n robots.
- (5) Calculate $d(G_i, R_j)$ the distance between the position G_i and the positions of all robots. Assign the role to the robot (the distance between the position G_i and this robot is the minimum of $d(G_i, R_j)$).

- (6) Judging whether all the role position are assigned to robot, or turn to step (5).
- (7) Robot management realizes the executive.

4 Simulation Platform

Newneu soccer robot 3D simulation platform [10] based on Microsoft Robotics Studio is a new type of soccer robot 3D simulation platform. Newneu soccer robot 3D simulation platform is composed of simulation engine service, Newneu simulation services and human-computer interactive service. The simulation platform has realized the major functions, such as the 3 D / 2 D real-time display, 4s real-time playback, the referee logic, human-computer interaction and so on. The simulation platform can well simulate the soccer robot game process except for wireless communications and visual processing. And because the platform can simulate 3D collision effects, it provides a good experimental platform for soccer robot system research. The small car system uses wheel structure, which installs driving wheels to the left and right side of the car, and support wheels to the front and end of the car to keep the balance of the car. Simulation platform is shown in fig 3.



Fig. 3. Control panel

The superiority of distant role-first assigning algorithm is verified by simulation experiment using this platform. Specific algorithm pseudo code as follows:

- (1)Information Preprocessing preProcess(), which do some simple processing of the information from the visual processing. For example, the transformation of coordinates, the records of object position, the prediction of robots and the balls.
- (2)Posture analysis GetAreaNo(), the field is parted according to the position of the balls, and take corresponding formation in view of the different partition.
- (3)Task decomposition and formation determine taskDecompose().
- (4) Distant role-first assigning charAllot().
- (5)Robot management RobotManager(), assign the corresponding role to each robot according to the results of the assignment.
- (6)Action Process actProcess(), achieve the form of each robot's left and right wheel according to the result of the role assignment.

5 Simulation Experiment

The formation problem in multi-robots systems is defined as the coordination of a group of robots to maintain a formation with a desired shape and reach a particular destination without collisions. Formation control is a typical and universal multi-robot coordination problem and at the same time it is also the foundation of the robot coordination problems [11]. The MiroSot 5:5 has the distributed physical structure, so it is necessary to study the formation control. According the real situation, we divide the formation into sever formations: triangle formation, waiting formation, level formation, half encircled formation, encircled formation, T formation, and so on.

This paper takes the half encircled formation as the object to study, which is shown in fig 4, No.0 player is a goalkeeper, its role is fixed and its position in goal area. The goal positions of No.1~No.4 are A, B, C, D respectively. The information pretreatment can gather the positions of players and robots. We fix the positions of No.0, No.1, No.2, No.4 and change the Y-coordinate of No.3 to verify the advantages of distant role-first assigning algorithm.

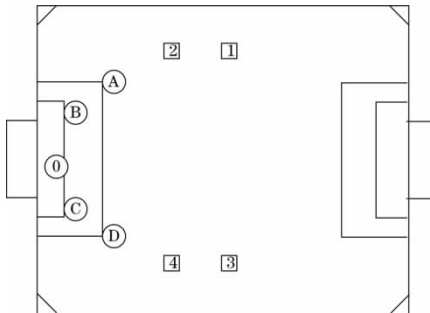


Fig. 4. Half encircled formation

When $y_3 \in (0, 180)$, the relationship of size between $\{sumA, sumB, sumC, sumD\}$ is shown in fig 5, and after analyzing fig 5 we can get the order of role assignment which is shown in Table 1.

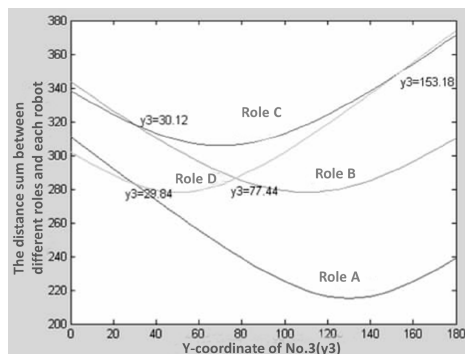


Fig. 5. Relationship between different roles and the sum of distance from roles to every robot

Table 1. The order of role assignment

The value of y3	The order of role assignment
(0,29.84)	BCAD
(29.84,30.12)	BCDA
(30.12,77.44)	CBDA
(77.44,153.18)	CDBA
(153.18,180)	DCBA

5.1 Collision Phenomenon Analysis

As the role order is $\{BCAD\}$, we can get two different movement tracks of robots by using these two algorithms, which can be shown in fig 6 and 7. As the role order is $\{CDBA\}$, we can get two other different movement tracks which can be shown in fig 8 and 9. Analyzing fig 6 to fig 9, it clearly shows that the algorithm 1 has collision phenomenon obviously in fig 6, however, it is not obvious in other figures. After experimenting and studying of other range respectively, we can achieve the collision phenomenon of these two algorithms, which is shown in Table 2. It is obvious that the all experiments using the shortest distance assigning algorithm have collisions phenomena, however using distant role-first assigning algorithm have not collision phenomena. Therefore the shortest distance assigning algorithm could not resolve the problem of robot collision well, because collision probability is very high. The distant role-first assigning algorithm can well resolve this problem, and collision probability is very low. The value $y_3=70$ represents that role assignment sequence switching using the shortest distance assigning algorithm.

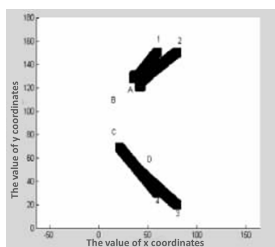


Fig. 6. Algorithm 1: movement track of very robot

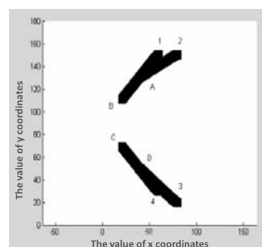


Fig. 7. Algorithm 2: movement track of very robot

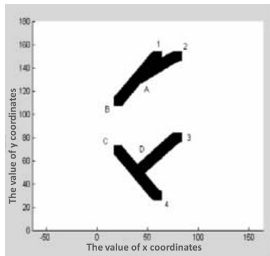


Fig. 8. Algorithm 1: movement track of very robot.

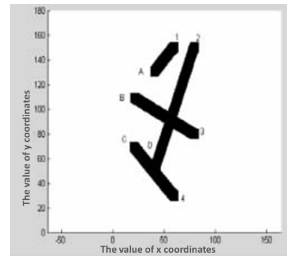


Fig. 9. Algorithm 2: movement track of very robot.

Table 2. The comparison of the two algorithms' collision results

	movement tracks of robots	movement tracks of robots
The value of y3	Shortest distance assigning algorithm	Distant role-first assigning algorithm
(0,29.84)	Has collision phenomenon	Has not collision phenomenon
(29.84,30.12)	Has collision phenomenon	Has not collision phenomenon
(30.12,77.44)	Has not collision phenomenon	Has not collision phenomenon
(77.44,153.18)	Has not collision phenomenon	Has not collision phenomenon
(153018,180)	Has collision phenomenon	Has not collision phenomenon

5.2 Movement Distance Analysis

As $y3 \in (70, 77.4)$ and $y3 \in (77.4, 146.25)$, there are not collision phenomenon using the two algorithms, so we study the sum of movement distance using the two algorithms respectively. And the simulation results are shown as in fig 10 and fig 11. They obviously show that when there is not collision phenomenon using the two algorithms, the distance sum of distance role-first assigning algorithm is shortest, and this algorithm itself is the embodiment of the energy balance. There is consumption of physical model, robot and battery, so the factors of balance of power consumption of the players and short moving distance are crucial. And these factors are taken into account in this algorithm.

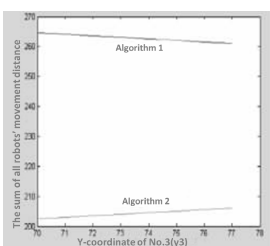


Fig. 10. Movement distance comparison of these two algorithms

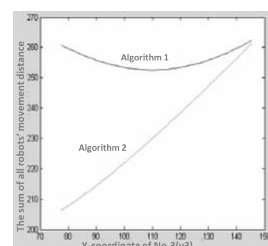


Fig. 11. Movement distance comparison of these two algorithms

6 Conclusion

Role assignment is a very important strategy in the robot soccer decision-making system. Good role assignment strategies can greatly improve the performance of this system and increase the chance of scoring in the match. This paper introduces distant role-first assigning algorithm, which is verified to be reasonable and effective by simulation experiment. This role assignment strategies has successfully applied to the 2008 Chinese robot competition—RoboCup, won the second runner-up in the Microsoft MS wheeled Micro Machines 11:11, and won the second prize in the ninth robot contest in 2009 FIRA World Cup of "Changchun engineering college cup". This role assignment strategy can be suitable for role assignment in the game in any of the complex conditions. It is not only suitable for all kinds of robot soccer game, but also can also be applied to other high real-time, high-confrontational multi-agent system of the task assignment.

References

1. Stone, P., Veloso, M.: Multiagent systems: A survey from a machine learning perspective. *Autonomous Robots* 8, 345–383 (2000)
2. Kim, J.H., Vadakkepat, P.: Multi-agent systems: A survey from the robot-soccer perspective. *Intelligent Automation and Soft Computing* 6, 3–18 (2000)
3. Ribeiro, V., Riedi, R., Baraniuk, R., Navratil, J., Cottrell, L.: pathchirp: Efficient available bandwidth estimation for network paths. In: *Passive and Active Measurement Workshop* (2003)
4. Lijuan, W., Xinhe, X.: Design of an obstacle-avoidance strategy based on genetic algorithms in robot soccer competition. *Robot* 23, 142–146 (2001)
5. Yan-duo, Z., Feng, M.: Application of reinforcement learning based on artificial neural network to robot soccer. *Journal of Harbin Institute of Technology* (2004)
6. Li, T.H.S., Lai, C.A., Guo, Y.J.: Design of fuzzy field control for a one-on-one robot soccer system. In: *IEEE 2002 28th Annual Conference of the Industrial Electronics Society, IECON 2002*, pp. 2605–2610. IEEE (2002)
7. Yang, W.J.L.S., Xiangfu, M.: Dynamic Assignment of Roles in Robot Soccer Competition. *Computer Applications and Software* (2009)
8. Han, K.H., Lee, K.H., Moon, C.K., Lee, H.B., Kim, J.H.: Robot soccer system of SOTY 5 for middle league MiroSot. In: *Proceeding of FIRA Robots World Congress*, pp. 2002–251 (2002)
9. Chen, X., Wu, M., Che, X.: Design and Analysis of the Decision-Making Subsystem of a Soccer-Robot System. *Computing Technology and Automation* (2001)
10. Duan, Y., Liu, Q., Xu, X.H.: Application of reinforcement learning in robot soccer. *Engineering Applications of Artificial Intelligence* 20, 936–950 (2007)
11. Ren, D.H., Lu, G.Z.: Thinking in formation control. *Control and Decision* 20, 601 (2005)

An Approach to the Specification of Security Concerns in UML

Vinh Xuan Tran¹, Ninh-Thuan Truong¹, and Anne T.A. Nguyen²

¹ VNU University of Engineering and Technology, Xuan Thuy, Cau Giay, Hanoi, Vietnam
evinh.trantx@gmail.com
thuantn@vnu.edu.vn

² School of Information and Communication Technology, Griffith University, Nathan,
QLD 4111, Australia
a.nguyen@griffith.edu.au

Abstract. The Object Oriented methodology has been applied in software engineering for a wide range of large and critical systems. One of the modeling languages frequently used for this purpose is UML. As yet, however, the means provided by UML to specify and deal with security concerns are rather sparse. In this paper we propose a practical approach that could readily be incorporated into existing software development processes. We begin by reviewing the main types of security concerns in the various phases of the software development cycle, and set up stereotypes to specify those concerns. The stereotypes are then attached to use case diagrams and later to activity diagrams (and other derived diagrams). At the implementation stage, security concerns can be transformed into more detailed aspects via AOP (aspect oriented programming) techniques. By maintaining the consistency of security stereotypes from phase to phase, the concerns about system security are implemented in a traceable fashion. Such use of security stereotypes does not require a high level of skills or deep knowledge of UML, and can therefore be integrated, with relatively little effort, with many current system development methodologies.

Keywords: security concerns, UML, AOP, security stereotypes.

1 Introduction

UML is a modeling language in which a system is modeled through its actors' behaviors. Despite the fact that UML is widely adopted, it does not provide security specification notions. UMLSec is one of UML profiles specified by OMG to represent security concerns in analysis and design of modern information systems. However, UMLSec is a complex profile which requires highly-skilled engineers in order to apply it and it is therefore not comfortably suitable to medium projects conducted in short term (less than 6 months, for example). This paper will introduce a feasibly practical approach to specify those concerns via a set of stereotypes.

To begin with, let's study 2 typical diagrams in UML: use case diagram and activity diagram. The use case diagram (Fig 1 as sample) represents relationships between actors and use cases into which actors are incorporated. This diagram does not show the time order in which an actor employs use cases to interact with a system.

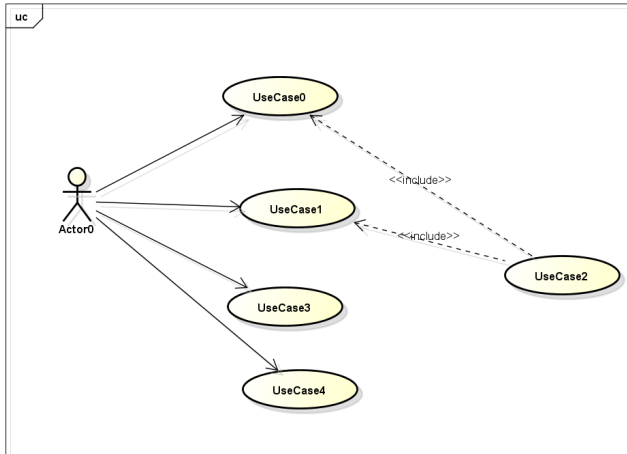


Fig. 1. Use case diagram sample

Activity diagram is one of most frequently used types of diagram in UML. This diagram represents a series of actions of actor(s) in a scenario. In Fig 2, actor A starts the scenario with action0, then depends on some conditions, it may continue action1 or action2 and in both cases, the next action is action3. Following that, 2 actions Action5 and Action4 are concurrently carried out then actor continues with action6 and finishes the scenario.

Activity diagram can be used for many purposes. In this paper, it is employed to describe a use case (a series of activities in a use case).

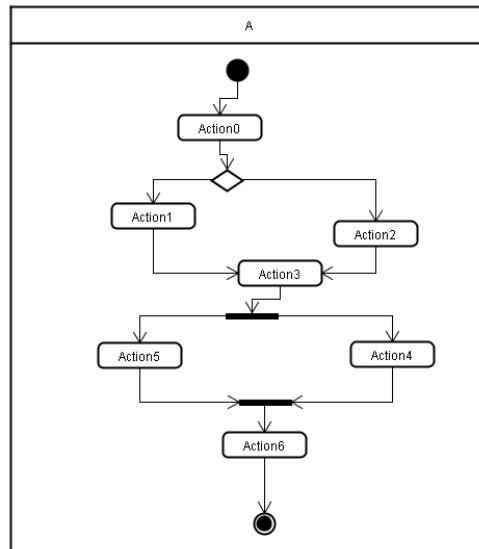


Fig. 2. Activity diagram sample

2 Background

2.1 Characteristics of Information System on Internet

There are a number of security related characteristics of an Internet information system. First of all, unlimited number of users accessing the system is one of important features. Secondly, users can be from various levels of computer skill, from novice to expert level. Thirdly, transport environment cannot be secured because information traverses multiple routers before reaching its destination. Fourthly, not able to physically manage users because the system operator can only know its users through identification, not the physical body. Fifthly, the Internet information system is the target of various attacks for different purposes such as: attack from competitors, attack for self-challenging.

2.2 Security Concerns in Designing an Internet Information System

From the analysis of security-related characteristics of an Internet information system, it can be listed some security concerns in designing an Internet information system as below:

- Denial of service attack: this is very basic type of attack with an increasing number of users accessing the system at one moment. This is because the system operator cannot assume and set a limit for the number of users.
- SQL injection: this type of attack exploits coding bug implemented by novice programmer, by sending special values to server, to inject into SQL query and retrieve critical values.
- Packet capturing: this type attack captures information on the transportation because the transport environment cannot be secure.
- User spoofing: an identification is used to access restricted area by cloning other's identification after logging into system.
- Cross access: an user logged into system and accessing other's information via some privacy holes in the system.

2.3 Related Works

Weaving security concerns in UML received the interest from many researchers.

Karine P. Peralta, Alex M. Orozco, Avelino F. Zorzo, Flavio M. Oliveira [3] proposed a set of stereotypes allowing specifying all security aspects as in 2.1. This is an overall proposal. And as such, it requires the applicator to own some knowledge level of UML and OCL. The scope of proposed solution is large, however focuses on modeling theoretical method and generating test cases with little implementation-related solution.

Mouheb, Djedjiga and Talhi, Chamseddine and Lima, Vitor and Debbabi, Mourad and Wang, Lingyu and Pourzandi, Makan [4] focus on generalized solution to weave security concerns into UML analysis diagrams, and then into

design. This work defines clearly join point, point-cut to weave security concerns into system designs. As result, the work is a mathematical model proofing oriented with little practical concern.

Several other works analyze general security threats [1], provide mathematical proofing for weaving security concerns into UML diagrams [2]. Those studies mainly concentrate on theory matters and not provide the distinct solution for cross access problem.

3 An Approach to Specifying Security Concerns in UML

This paper will focus on proposing a practical approach for specifying security concerns in UML and implementing them using Java aspect oriented programming techniques.

To illustrate the above ideas, the paper is scoped with “propose a method to specify security concerns for cross access“. This scope is selected because it relates to privacy policy which is often one of the top concerns of users when accessing a system. On the other hand, solution to other concerns mentioned in above section can be implemented on other layers: Denial of service is feasibly implemented on firewall or reverse-proxy, packet capturing can be solved by adding encryption. In contrast, the solution for privacy protection shall be covered by the application itself.

The solution will comprise 3 stages. At first, we build a security concern list and assign stereotype to each concern. Next, these stereotypes are attached to each type of UML diagram. And lastly, we use aspect-oriented programming technology to realize these concerns in system.

3.1 Build a Security Concern List

Assuming that we are building a system of cargo tracking which is often used by logistic service companies to provide their customers with updated information of where their cargos are, what the cargos’ status are. The tracking process starts when the buyer (importer) places an order with the seller (exporter). The tracking system shall provide information for multiple companies who have account to access the system. The list of cross access security concerns could be:

- Accessing other users’ information: this action is often carried out by system administrator and therefore there is a need for a clear policy to limit unexpected access.
- Accessing related company’s information: there must be a policy governing the case in which one user from company A wants to access company B’s information with which it has an invoice or an order.
- Accessing third party company’s information: this action is often carried out by third party’s (logistic service company) users. The seller (exporter) company will hand over cargos to a logistic party. This logistic party has no business relationship with the buyer (importer) but it needs to know information about the buyer because it has to forward the cargo to the buyer.

3.2 Assign Stereotypes to Security Concerns

Our purpose is clear: specify security concerns on existing UML diagrams in a way that supports maintaining the traceability between phases of software development lifecycle. This goal will help reducing efforts in integrating our solution to existing software development methodologies.

To achieve our target, we shall employ a facility of UML named «stereotype» by which each security concern will be represented by a stereotype. To unify our notions, we'll use prefix “sec:” for all proposed stereotypes. For example, we can have a list as in Table 1.

Table 1. Sample of stereotype

Stereotype	Description
«sec:other's info»	Accessing other's information
«sec:related company»	Accessing related company's information
«sec:third party»	Accessing third party company's information

3.3 Attach Stereotype to Use Case Diagram

For use case diagram, our approach is to write appropriate stereotype on the connector between an actor and a use case. This can be done through analyzing use case's business nature. The stereotype signifies that when this actor uses specific use cases, the concern specified by that stereotype should be raised.

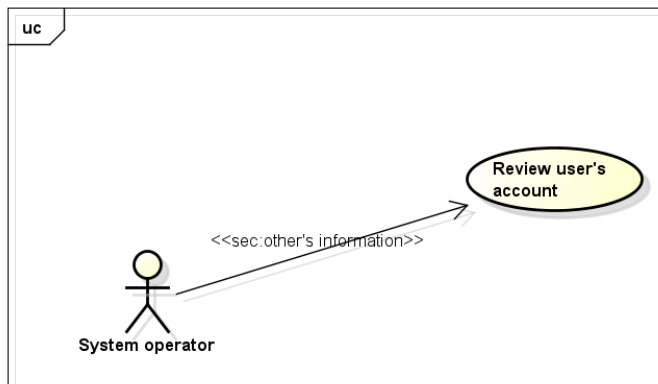


Fig. 3. Use case diagram with security stereotype

3.4 Attach Stereotype to Activity Diagram

An activity diagram is used to describe the details of a use case. In Fig 4, we detail a series of actions which realizes the use case in Fig 3. And because we attached the

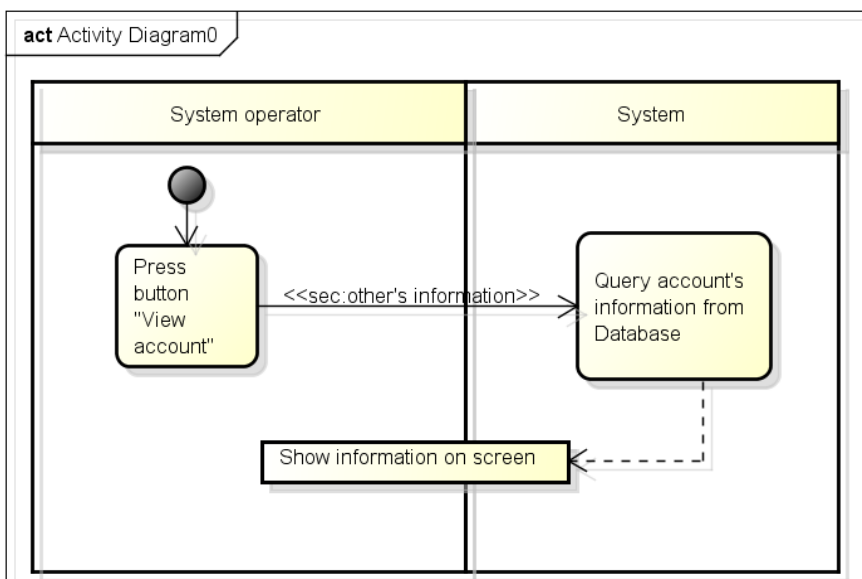


Fig. 4. Activity diagram with security stereotype

stereotype to use case diagram, we shall attach same stereotype to each connector between the actor and the system. This signifies next derived system development activities to raise the concern at appropriate step.

3.5 Implement Security Stereotypes Using AOP

From activity diagram, in implementation phase, in simplest approach, we shall raise appropriate “aspect” to be called before any request from user toward the system. An example of such aspect is provided in Fig 5, using Java AOP and Spring framework (this is suitable for Web system). The framework shall launch aspect code (method “check”) prior to any method execution whose class name ending with “BLogic”.

```

@Aspect
abstract class SecurityAspect{
    @Before ("bean(*BLogic)")
    public void check(JoinPoint jp) {
        ...
    }
}

```

Fig. 5. Applying AOP to realize security check

If for example, we want to detail activity diagram to other diagram or design (sequence diagram, process request design), we can follow a similar strategy i.e: attaching security concern to any interaction between user and system. This ensures that our security concerns are consistently maintained between different phases of software development lifecycle.

4 Conclusion

By inserting security stereotype into existing UML diagram, it can be assured that security requirements are fully covered from early phase of software development and it can also be traceable between various analysis, design and implementation activities. This approach does not introduce new type of diagram or require complex mathematical knowledge and can therefore be integrated into existing development models.

References

1. Chizmadia, D.: Security Risks in Systems of Distributed Objects, Components, and Services. In: OMG 7th Workshop on Distributed Objects and Component Security, Baltimore, MD, USA (2003)
2. Pavlich-Mariscal, J., Michel, L., Demurjian, S.: Enhancing UML to Model Custom Security Aspects. In: Proceedings of the 11th International Workshop on Aspect-Oriented Modeling, AOM@ AOSD 2007 (2007)
3. Peralta, K.P., Orozco, A.M., Zorzo, A.F., Oliveira, F.M.: Specifying Security Aspects in UML Models. In: Proceedings of the Workshop on Modeling Security, International Conference on Model Driven Engineering Languages and Systems. Toulouse, France (2008)
4. Mouheb, D., Talhi, C., Lima, V., Debbabi, M., Wang, L., Pourzandi, M.: Weaving security aspects into UML 2.0 design models. In: AOM 2009, Proceedings of the 13th Workshop on Aspect-Oriented Modeling, New York, NY, USA (2009)

Intelligent Blowing Controller for Autonomous Underwater Flight Vehicle

Hyun-Sik Kim

Dept. of Robot System Engineering, Tongmyong University
428 Sinseon-ro, Nam-gu, Busan 608-711, Korea
hyunskim@tu.ac.kr

Abstract. In case of flooding, the underwater flight vehicle (UFV) usually executes the emergency blowing by blowing ballast tanks off using high pressure air (HPA) while it also uses control planes and a propulsion unit to reduce the overshoot depth caused by a flooding and blowing sequence. However, the conventional whole HPA blow-off method lets the body on the surface after blowing despite a slight flooding. This results in the unnecessary mission failure or body exposure. Therefore, it is necessary to keep the body at the near surface by the blowing control while reducing the overshoot depth. To solve this problem, an intelligent blowing controller (IBC) using expert knowledge and the fuzzy basis function expansion (FBFE) is proposed here. To verify the performance of the proposed controller, the blowing control of UFV is performed. Simulation results show that the proposed algorithm effectively solves the problems in the UFV blowing control system online.

Keywords: intelligent blowing control, expert knowledge, fuzzy basis function expansion, ballast tank, underwater flight vehicle.

1 Introduction

Recently, the research and development of the underwater robot [1] that has the ability of satisfying the contemporary requirements of a marine research, underwater defense and surveillance is gradually increasing. Among the mobile platform of the underwater robot, the underwater flight vehicle (UFV) [2] has low energy consumption and acoustic noise in terms of the dynamic control because it has the body shape of the lowest hydrodynamic drag and has a propulsion unit and control planes rather than a multitude of thrusters. In addition, the UFV has the good controllability in terms of the static control because it has control tanks that have the ability of weight and buoyancy control. From these reasons, the UFV has the merits in both civil and military application area.

For satisfying the requirements by the successful mission execution without the loss of life and property in a severe ocean environment, the UFV requires the autonomous control technique (ACT) that has hierarchical levels of a mission planning, mission control, navigation and execution. Among the execution level, the buoyancy autopilot as a basis of the ACT is rarely studied except a simple depth

regulation [3,4] or the emergency blow-off, while the depth autopilot as another basis of the ACT is widely studied in a PID control [5], a sliding mode control [6], a gain-scheduled control [7] and a fuzzy control [8]. However, the new necessity of the study is rising by the following requirement:

In case of flooding, the UFV usually executes the emergency blowing by blowing ballast tanks off using high pressure air (HPA), while it also uses control planes and a propulsion unit to reduce the overshoot depth caused by a flooding and blowing sequence. However, the conventional whole HPA blow-off method lets the body on the surface after blowing despite a slight flooding. This results in the unnecessary mission failure or body exposure. Therefore, it is necessary to keep the body at the near surface by the blowing control while reducing the overshoot depth. As a brief, the UFV blowing control system operates with the following problems: it is a multi-input multi-output (MIMO) system because the UFV contains weight, pitch and depth variables as well as control tanks and planes, it requires a simple blowing procedure because it has the complex procedure that depends on the flooding condition, it requires small and continuous control input because the system that has reduced power consumption and acoustic noise is more practical, and further, it requires robustness because it may encounter uncertainties such as parameter variations or disturbances.

To solve this problem, an intelligent blowing controller (IBC) based on the decomposition method expanding expert knowledge in the UFV depth control and the sub-control and composition method using fuzzy basis function expansions (FBFEs) in the form of a fuzzy sliding mode controller (FSMC) is proposed.

The proposed controller has the main contribution of the establishment of a new method by combining a static and dynamic depth control for blowing control as a basis of the ACT for autonomous UFV. Related to this, it has four major advantages with respect to the uncertain target maneuvering: 1) it enables to let the UFV have an expanded vertical operation range in terms of safety 2) it has a simple blowing procedure for the decomposition of a MIMO system and the independency with respect to initial flooding conditions 3) it has optimal performances satisfying the constraints such as robustness, small and continuous control input, and 4) it has simple fuzzy rule definition methods in comparison with the trial-and-error method.

The mathematical model of the UFV is introduced in section 2. The design of an IBC is described in section 3, and the simulation results of the IBC in the UFV blowing control are presented in section 4. Finally, the conclusions are summarized in section 5.

2 Mathematical Model of UFV

The UFV that usually employs the right-handed coordinate system is divided into two types in terms of hull shape: the submarine-type UFV having the vertically non-symmetric shape and the torpedo-type UFV having the vertically symmetric shape. The location of ballast tanks and control planes in the former considered in this paper is shown in figure 1.

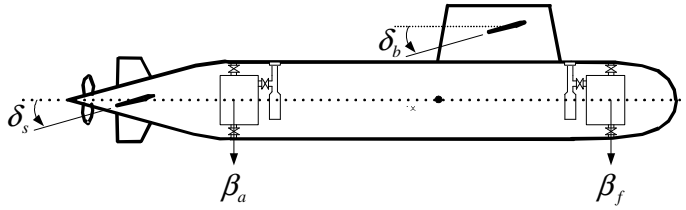


Fig. 1. Shape and notation of UFV

It has two horizontal control planes of a stern plane δ_s and a bow plane δ_b , and has two control tanks of a forward ballast tank β_f and an after ballast tank β_a . In the UFV dynamic equation mentioned by Kim and Shin [8], it can be described by the following components: translations x, y, z and rotations ϕ, θ, φ ; velocities u, v, w (surge, sway, heave) and angular velocities p, q, r (roll, pitch, yaw); accelerations $\dot{u}, \dot{v}, \dot{w}$ and angular accelerations $\dot{p}, \dot{q}, \dot{r}$; and $\mathbf{F} = [X \ Y \ Z]^T$ the resultant force vector and $\mathbf{G} = [K \ M \ N]^T$ the resultant moment vector [9]. From these descriptions, the motion equation based on Gertler's equation [10] is defined as

$$[\mathbf{m} + \mathbf{m}_a] \mathbf{Q} = -\begin{bmatrix} \mathbf{F}_I \\ \mathbf{G}_I \end{bmatrix} + \begin{bmatrix} \mathbf{F}_R \\ \mathbf{G}_R \end{bmatrix} + \begin{bmatrix} \mathbf{F}_H \\ \mathbf{G}_H \end{bmatrix} + \begin{bmatrix} \mathbf{F}_P \\ \mathbf{G}_P \end{bmatrix} \quad (1)$$

where \mathbf{m} is the mass, \mathbf{m}_a is the added mass that means the equivalent mass of the surrounding fluid accelerated with the vehicle, $\mathbf{Q} = [\dot{u} \ \dot{v} \ \dot{w} \ \dot{p} \ \dot{q} \ \dot{r}]^T$ the acceleration vector, $\mathbf{F}_I = [X_I \ Y_I \ Z_I]^T$ the inertia force vector, $\mathbf{G}_I = [K_I \ M_I \ N_I]^T$ the inertia moment vector, $\mathbf{F}_R = [X_R \ Y_R \ Z_R]^T$ and $\mathbf{G}_R = [K_R \ M_R \ N_R]^T$ are restoring force and moment vectors related to the weight and buoyancy, \mathbf{F}_H and \mathbf{G}_H are hull force and moment vectors related to the body shape, \mathbf{F}_P and \mathbf{G}_P are propulsion force and moment vectors generated by a propulsion unit and control planes.

Based on this formula, the modeling of flooding and blowing is executed as follows.

The force Z_R , which is an element of \mathbf{F}_R , is the dominant force in the blowing control because it includes the hydrodynamic forces B and W that generate the restoring force due to the non-neutral buoyancy. It is defined as

$$Z_R = (B - W + \Delta W(m_f, m_b)) \cos \phi \cos \theta \quad (2)$$

where B is the buoyancy, and W and ΔW are the weight and its change respectively. Both the flooding due to the damaged hole of the body and the blowing due to the blowing control can be modeled by ΔW . The water mass m_f related to

the water inrush due to the flooding is defined by applying the Bernoulli's equation that the water velocity is equals to $\sqrt{2gz}$:

$$m_f = C_n A \sqrt{2gz} \rho t \quad (3)$$

where $C_n \leq 1$ is the flooding constant depend on the shape of the hole and the state of ventilation, A is the hole area, g is the gravity constant, ρ is the density of water and t is the time period.

When the blowing subsystem composed of air bottles, pipes, valves, and ballast tanks is considered, the water mass m_b related to the water emission due to the blowing is defined by applying the perfect gas law $P = \rho RT = mRT/V$ [11,12]:

$$m_b = \frac{\dot{m}tR(T_m + T_k)}{P_m} \rho \quad (4)$$

where R is the gas constant, T_m and P_m are the temperature and pressure in the ballast tank respectively, T_k is the absolute temperature constant, and the change of the air mass \dot{m} is defined by

$$\dot{m} = \frac{A_p P_b}{\sqrt{R(T_b + T_k)}} \sqrt{\frac{2k}{k-1} \left\{ \left(\frac{P_m}{P_b} \right)^{2/k} - \left(\frac{P_m}{P_b} \right)^{(k+1)/k} \right\}} \quad (5)$$

where A_p is the pipe area, T_b and P_b are the temperature and pressure in the air bottle respectively, k is the specific heat ratio. The change of the air mass generates the water emission in the ballast tank.

3 Design of IBC

3.1 Expert Knowledge-Based Decomposition Method

The expansion and analysis of expert knowledge in the UFV depth control for decomposition are executed as follows.

As the UFV blowing control system is a MIMO system, it is convenient to decouple the system into subsystems in terms of controller design. Fortunately, the control tanks of β_f and β_a and the control planes of δ_s and δ_b perform the same function in terms of kinematics although they have different positions and polarities. Therefore, they can be interpreted as a single control tank β and a single control plane δ . In the proposed UFV blowing control expanding the expert knowledge [8] in depth control, if a flooding occurs at the flooding depth z_f , the blowing procedure of phases A to G is executed as figure 2.

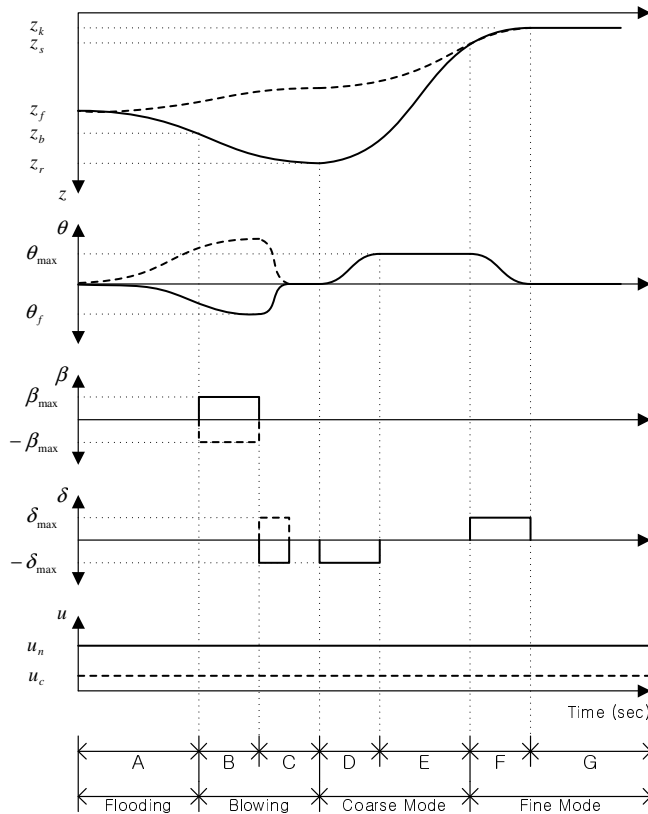


Fig. 2. UFV blowing control procedure by expert

The solid line expresses the blowing procedure in case of the forward-side flooding and the dotted line expresses the procedure in case of the after-side flooding. Here, the procedure is based on the fact that the recovering of the ship's static stability through the compensation of W is most important in terms of both controllability and practical use.

In phase A, the water inrush due to the flooding is blocked by the countermeasure. For a problem definition, the general 20/20 rule that has the assumption of both 20-mm hole diameter and 20-seconds countermeasure time is considered in this paper. In phase B, the water emission and free-flooding due to the blowing is executed by β until ΔW reaches zero. This phase is considered as a single-input single-output (SISO) system because it has a single β as well as a single W . In phase C, the pitch control is executed by δ until θ reaches zero. This phase is also considered as SISO system because it has a single δ as well as a single θ . In phases D to G, these phases are the same as the procedure in the UFV depth control [8]. This means that the blowing control system is decoupled into three subsystems of a weight, pitch and

depth control system by expanding the expert knowledge in the UFV depth control. The speed command in all phases has a constant normal speed u_n in case of the forward-side flooding and also has the constant critical speed u_c , which is the minimum speed for the UFV dynamic control using control planes, in case of the after-side flooding. Related to the procedure, the blowing property is expressed by

$$\text{Blowing Property} = f(P_b, N_a, C, u) \quad (6)$$

where N_a is the number of the air bottle and u is the speed. For reducing the overshoot depth $|z_r - z_f|$, it is important to transit the phase from B to C after recovering the weight as fast as possible employing the larger P_b and N_a . For reducing the keeping overshoot, especially, in case of after-side flooding, it is important to use the phase C in order to guarantee the stable control because the excessive positive-pitch generates the unexpected drag force and to reduce the speed in order to guarantee the normal blowing because small $|z_k - z_f|$ disables the proposed procedure. Therefore, this method is valid under the condition that $|z_k - z_f|$ is big in general. This implies the limit of the method.

Comparing with the complex procedure that should be differently executed according to the flooding conditions such as the flooding position with respect to the CG, A and z , these phase have only two procedures that are independent of the A and z except the CG. Note that the decomposition method addresses simple blowing procedure as well as decomposition of MIMO system for UFV blowing control.

3.2 FBFE-Based Sub-control and Composition Method

The design and analysis of FBFEs for sub-control and composition are executed as follows.

A general FBFE as a fuzzy technique used in the nonlinear function approximation equivalent to the fuzzy system with a singleton fuzzifier, a product inference, and Gaussian membership functions [13], is re-expressed as a weighted sum or weighted average of a family of FBF with different scaling and translations:

$$\hat{f}(\mathbf{x}) = \frac{\sum_{j=1}^N w^j g^j \left(\frac{\|\mathbf{x} - \xi^j\|}{\sigma^j} \right)}{\sum_{j=1}^N g^j \left(\frac{\|\mathbf{x} - \xi^j\|}{\sigma^j} \right)} \quad (7)$$

where g^j denotes a FBF, and $\xi^j = [\xi_1^j \ \xi_2^j \ \dots \ \xi_n^j]$ is the center.

The inference method for the proposed FBFE employs the simplified method [14]. The related rule, which has the form of a fuzzy sliding rule, is expressed by

$$R^j : \text{if } S \text{ is } A_1^j \text{ and } \dot{S} \text{ is } A_2^j \text{ then } \hat{f} = w^j \quad (8)$$

where S and \dot{S} are respectively the normalized values of an integral augmented sliding signal s and its derivative \dot{s} , and A_1^j and A_2^j are the membership functions, and the integral augmented sliding signal is defined as

$$s = \dot{e} + c_1 e + c_0 d \int e - \dot{e}(0) - c_1 e(0) \quad (9)$$

where e and \dot{e} are respectively a control error and its derivative, c_0 and c_1 are the constants. The integral augmented sliding mode controller (ISMC) using s in formula (9) has robustness as well as small and continuous control input because it has a reduced reaching phase [8]. Table 1 shows the proposed fuzzy sliding rule. The linguistic terms expressed by negative big (NB), negative medium (NM), zero (ZO), positive medium (PM), and positive big (PB).

Table 1. Proposed fuzzy sliding rule for FBFE

$S \backslash \dot{S}$	NB	NM	ZO	PM	PB
NB	-1.0	-0.7	-0.5	-0.3	0.0
NM	-0.7	-0.5	-0.3	0.0	0.3
ZO	-0.5	-0.3	0.0	0.3	0.5
PM	-0.3	0.0	0.3	0.5	0.7
PB	0.0	0.3	0.5	0.7	1.0

The table includes the following rules: if $S(k) > 0$, the output of FBFE is assigned in order to satisfy $\dot{S}(k+1) < 0$; otherwise, the output of FBFE is assigned in order to satisfy $\dot{S}(k+1) > 0$. It guarantees the stability of the FBFE because it satisfies the sliding mode existence condition $S(k)\dot{S}(k+1) < 0$ that drives the sliding mode phenomenon.

All sub-controllers for the decoupled subsystems commonly have the main FBFE, equivalent to the FMSMC, which uses both an integral augmented sliding signal and its derivative as fuzzy inputs and uses the simplified method as a fuzzy inference method. Only two sub-controllers of the pitch and the depth controller have additional FBFE equals to those of the expanded adaptive FMSMC (EAFMSMC) [8]; i.e., the weight controller has no additional FBFE because the effect of the weight control error can be ignored by using the robust pitch and depth controller of the EAFMSMC that has been verified with respect to 0.5% parameter variation of standard displacement (SD). Therefore, β is defined as

$$\beta = \begin{cases} C_w \hat{f}_w(\mathbf{x}_w) + K_w s_w, & |\Delta W| > W_s \\ 0, & \text{otherwise} \end{cases} \quad (10)$$

where W_s ($<< 0.5\%$ of SD) is the switching weight, C_w is the constant, \hat{f}_w is the FBFE for weight controller using formula (8), s_w is the sliding signal for weight controller using formula (9), $\mathbf{x}_w = [S_w \quad \dot{S}_w]$ is the normalized input vector of s_w and \dot{s}_w , and K_w is the gain.

β_f and β_a are easily obtained by applying formula (10) to the each side of UFV and they generally have the limitation that depends on the HPA capacity. δ_s and δ_b are the same as those of the EAFCMC. Note that the sub-control and composition method addresses robustness as well as small and continuous control input for UFV blowing control.

The block diagram of the proposed UFV blowing control system is presented in figure 3.

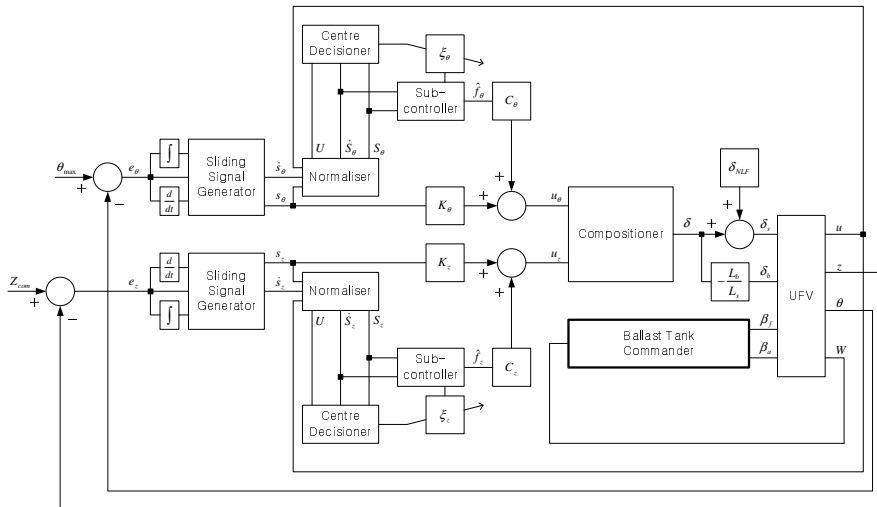


Fig. 3. Block diagram of proposed control system

From the above mentioned procedure, an IBC using expert knowledge and the FBFEs was designed.

4 Simulation Results

The performance of the proposed IBC is tested with the UFV blowing control problem that deals with the full 6-DOF equation considering no sea-wave effect in the vertical plane and no course change in the horizontal plane. The simulation scenario for the UFV blowing is given in table 2.

Table 2. Scenario for UFV blowing

Time [s]	Z_{com} [m]	Z_k [m]	u_{com} [knots]	Flooding (%) of SD
1–100	—	—	4	None
100–300	40	—	4	None
300–320	—	30	4	Forward-side, 2.5
320–600	—	30	4	None
600–620	—	20	2	After-side, 2.5
620–900	—	20	2	None
900–920	—	5	4	Both-side, 5.0
920–1200	—	5	4	None

In case of both-side flooding, the amount is increased for the meaningful verification of the proposed controller because the system is more stable in terms of the pitch control related to the phase C. The parameters for the flooding and blowing model are given in table 3.

Table 3. Parameters for flooding and blowing model

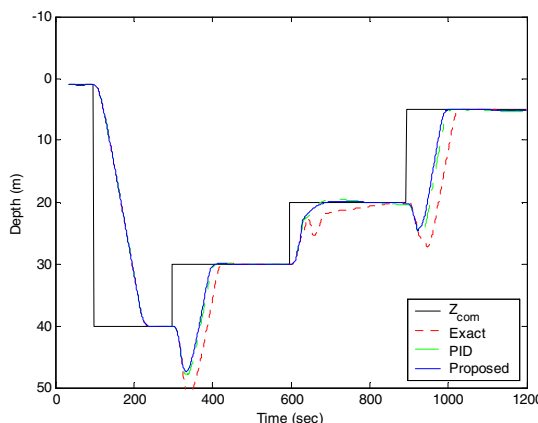
	Symbol	Value	Unit
Flooding constant	C_n	0.7	—
Water density	ρ	1000 (clean water)	kg/m^3
Tank temperature	T_m	20	$^\circ C$
Pipe area	A_p	0.00001256	m^2
Air bottle temperature	T_b	10	$^\circ C$
Air bottle pressure	P_b	1,000,000	N/m^2
Specific heat ratio	k	1.4 (air)	—

Here, the values satisfies the normal blowing condition $P_b > P_m$ because the operating depth is within 50 m ($=500,000 N/m^2$). The switching weight is $W_s = 13.5$ (0.01% of SD). In order to compare the IBC with conventional controllers, an exact blower that employs the feed-forward weight control having the same time and same weight change rate as those of the flooding under the condition of $N_b = 1$, a PID that employs the PID weight control under the condition of $N_b = 1$, and the IBC that employs the proposed weight control under the condition of $N_b = 2$ are considered. They all have the proposed procedure and the EAFSMC for the pitch and depth control. The parameters of pitch and depth control are the same as the EAFSMC and those of weight control are given in table 4. These parameters are chosen by a trial-and-error method.

Table 4. Parameters for weight control

	Exact	PID	Proposed
Forward-side control	—	$\begin{bmatrix} K_P = 1.0 \\ K_I = 0.1 \\ K_D = 0.01 \end{bmatrix}$	$\begin{bmatrix} c_1 = 8.0 \\ c_0 = 5.9 \\ K_w = 0.3 \end{bmatrix}, C_w = 0.7$
After-side control	—	$\begin{bmatrix} K_P = 1.0 \\ K_I = 0.1 \\ K_D = 0.01 \end{bmatrix}$	$\begin{bmatrix} c_1 = 10.0 \\ c_0 = 5.7 \\ K_w = 0.3 \end{bmatrix}, C_w = 0.7$

Figures 4–6 show the performances of depth, pitch and weight control in various flooding condition. The IBC is superior to the others in terms of the overshoot depth near time 300 in figure 4, the keeping overshoot near time 700 in figure 4, the maximum pitch near time 600 in figure 5, and the weight recovering in the severe case of $|z_f - z_k| \leq 10$ in figure 4. Although the exact blower solves the problems of the weight recovering and the overshoot depth using both the proposed procedure and the feed-forward weight control and also solves the problem of the keeping overshoot using both the proposed procedure and the EAFSMC, it exceeds the positive-pitch limit of 40° . The PID has better performance in terms of all problems including the maximum pitch because it has the feedback weight controller. The IBC has the best performance in terms of all problems because it has increased HPA number. In addition, considering the further study on the nonlinear characteristics of valves in ballast tank, this FBFE-based weight control comparing the PID-based control [15] may be more effective in terms of the robustness. These mean that the proposed procedure and the FBFEs act well and the weight control performance is very important in the blowing control based on the proposed procedure.

**Fig. 4.** Performance of depth control

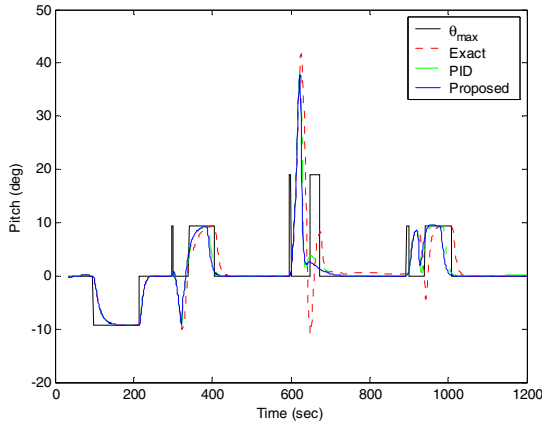


Fig. 5. Performance of pitch control

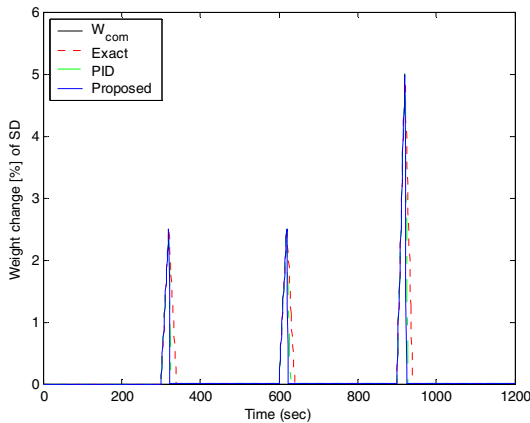


Fig. 6. Performance of weight control

Figures 7 and 8 show the commands of stern and forward and after ballast tanks respectively. The proposed controller is superior to the others in terms of the small and continuous control input in figure 7. Here, the outputs of the bow plane are omitted because it is similar to the outputs of the stern plane. Although the maximum value of the proposed controller is the larger than the others, the duty area is smaller than that of exact blower and similar to that of PID in figure 8. This means that the FBFEs act well and the larger N_a is more effective in terms of both controllability and redundancy.

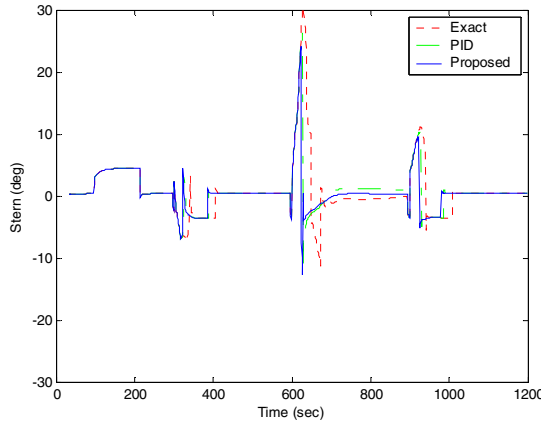


Fig. 7. Stern command

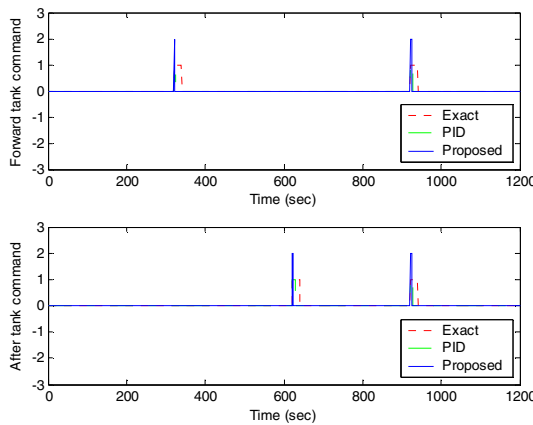


Fig. 8. Ballast tank command

Table 5 shows the numerical comparison of the proposed IBC and the others. $|e_z|_{avg}$ and $|e_\theta|_{avg}$ are respectively the average absolute values of the depth and pitch control errors in fine mode, $|e_w|_{avg}$ is the average absolute value of the weight control error in phase B. $|\delta_s|_{avg}$ and $|\dot{\delta}_s|_{avg}$ are respectively the average absolute values of the stern and its derivative in coarse and fine mode. $|\beta_f|_{avg}$ and $|\dot{\beta}_f|_{avg}$ are respectively the average absolute values of the forward ballast tank and its derivative in phase B. These values quantitatively verify the fact that the IBC is most effective in terms of both performances and control efforts with respect to the overall UFV blowing.

Table 5. Comparison of performances

	Exact	PID	Proposed
$ e_z _{avg}$	0.450	0.320	0.242
$ e_\theta _{avg}$	0.716	0.591	0.542
$ e_w _{avg}$	0.168	0.120	0.101
$ \delta_s _{avg} (\dot{\delta}_s _{avg})$	2.445 (0.163)	1.959 (0.148)	1.683 (0.155)
$ \beta_f _{avg} (\dot{\beta}_f _{avg})$	0.033 (0.003)	0.010 (0.003)	0.010 (0.006)

Although the comparisons are not executed under the same conditions with respect to the controllers because there does not yet exist a controller capable of solving all the problems in the UFV blowing control system online, the IBC is proven to have meaningful procedure and control terms for UFV blowing control in various flooding conditions such as the flooding position with respect to the CG and z .

5 Conclusion

In this paper, an IBC using expert knowledge and FBFEs has been proposed to address all problems regarding decomposition of MIMO system, a simple blowing procedure, small and continuous control input, and robustness in UFV blowing control. The issues of a simple blowing procedure as well as decomposition of MIMO system was solved by using expert knowledge, and the issue of robustness as well as continuous control input was solved by using the FBFEs. The proposed controller has four major advantages: 1) it enables to let the UFV have an expanded vertical operation range in terms of safety 2) it has a simple blowing procedure for the decomposition of a MIMO system and the independency with respect to initial flooding conditions 3) it has optimal performances satisfying the constraints such as robustness, small and continuous control input, and 4) it has simple fuzzy rule definition methods in comparison with the trial-and-error method. To verify the performance of the proposed IBC, the UFV blowing control in various flooding condition was performed. The simulation results showed that the proposed IBC effectively solves the problems in the UFV blowing control system online. Through this, an IBC as a basis of the ACT for autonomous UFV has been established.

Acknowledgements. This work (Grants No. C0026621) was supported by Business for Cooperative R&D between Industry, Academy, and Research Institute funded Korea Small and Medium Business Administration in 2012.

References

1. Antonelli, G.: Underwater robots. Springer (2006)
2. Lea, R.K., Allen, R., Merry, S.L.: A comparative study for control techniques for an underwater flight vehicle. *International Journal of System Science* 30, 947–964 (1999)
3. DeBitetto, P.A.: Fuzzy logic for depth control of unmanned undersea vehicles. *IEEE Journal of Oceanic Engineering* 20(3), 242–248 (1995)
4. Xu, M., Smith, S.M.: Fuzzy rule based depth controller for variable ballast system of autonomous underwater vehicles. In: *Proceedings of the 2005 Systems and Information Engineering Design Symposium*, vol. 30, pp. 947–964 (1999)
5. Jalving, B.: The NDRE-AUV flight control system. *IEEE Journal of Oceanic Engineering* 19(4), 497–501 (1994)
6. Cristi, R., Papoulias, F.A., Healey, A.J.: Adaptive sliding mode control of autonomous underwater vehicles in the dive plane. *IEEE Journal of Oceanic Engineering* 15(3), 152–160 (1990)
7. Liceaga-Castro, E., van der Molen, G.M.: A Submarine depth control system design. *International Journal of Control* 61(3), 279–308 (1995)
8. Kim, H.S., Shin, Y.K.: Expanded adaptive fuzzy sliding mode controller using expert knowledge and fuzzy basis function expansion for UFV depth control. *Ocean Engineering* 34, 1080–1088 (2007)
9. Yuh, J.: Modeling and control of underwater robotic vehicles. *IEEE Transactions on Man and Cybernetics* 20(6), 1475–1483 (1990)
10. Gertler, M., Hagen, G.R.: Standard equation of motion for submarine simulation. *Naval Ship Research and Development Center Report* 2510 (1967)
11. Lino, P., Maione, B., Amorese, C.: Modelling and predictive control of a new injection system for compressed natural gas engines. *Control Engineering Practice* 16, 1216–1230 (2008)
12. Zucrow, M., Hoffman, J.: Gas dynamics. Wiley, New York (1976)
13. Leondes, C.T.: Fuzzy theory systems. Academic Press (1999)
14. Takagi, T., Sugeno, M.: Fuzzy identification of system and its applications to modeling and control. *IEEE Transactions on Man and Cybernetics SMC-15*, 116–132 (1985)
15. Kim, H.S.: Adaptive blowing control algorithm for autonomous control of underwater flight vehicle. *Journal of Fuzzy and Intelligent Systems* 18(4), 482–487 (2008)

Fuzzy Visual Navigation Using Behavior Primitives for Small Humanoid Robot

Yong-Tae Kim¹ and Su-Hee Noh²

¹ Dept. of Electrical, Electronic and Control Engineering, Hankyong National University
327 Joongang-ro, Anseong, Gyeonggi-do, 456-749, Korea

² Kohyoung Technology, 345-90 Gasan-dong, Seoul, 153-802, Korea
ytkim@hknu.ac.kr

Abstract. In this paper, we present a fuzzy visual navigation method that uses behavior primitives for humanoid robots. We define behavior primitives that consist of locomotion and motion primitives. The fuzzy navigation system consists of four control algorithms: autonomous walking, target tracking, obstacle avoidance, and behavior control based on marker recognition. We verify the proposed method through navigation experiments by using a developed small humanoid robot. The experimental results demonstrate that the humanoid robot can navigate efficiently and stably to the target and show improved performance of behavior planning for humanoid navigation.

Keywords: fuzzy navigation, visual navigation, humanoid, behavior primitive.

1 Introduction

Humanoid robots can walk, turn, step on small objects, climb up or down stairs, climb ladders, climb ramps, step over obstacles, and crawl through narrow passages[1~5]. However, due to high degree of actuation, it is difficult to generate the robot's pose and stable motions on the complex cluttered environment that has various types of obstacles. Also, motion planning of humanoid robots is computationally expensive and require significant amount of memory and computation time. Therefore, path planning and navigation through a cluttered 3D environment, and collision avoidance with obstacles have been studied [6~8].

The generation of stable and efficient gaits for humanoid robots has been studied considering dynamic stability constraints [9~13]. The behavior generation problem of humanoid robots can be solved by using preplanned patterns of motions, which begin and end with a static and stable pose. These patterns can be generated and reused in sequence to make a walking and behavior motion. The preplanned motion is referred to as motion primitives [14~15]. If these motion primitives are optimized, behaviors of humanoid robot are more efficient, optimal, and robust. The behaviors planning of the humanoid robot is to design many motion primitives in order to deal with various situations and to select an optimal sequence of suitable motion primitives [16~17]. If these behavior primitives are used for a humanoid's behavior planning, navigation on

easy and flat ground is considered as the searching problem for a sequence of feasible behavior primitives. Humanoid robots need to move to a specific location to perform various tasks in the workspace. Navigation of humanoid robot is one of essential research areas. The robot plans a shortest path from its current coordinates to the goal coordinates in a dynamic environment and selects a behavior primitives to move to the target, while avoiding obstacles and following the command signs in the environment.

In this paper, we propose a fuzzy visual navigation method by using behavior primitives for a small humanoid robot. The proposed navigation system consists of autonomous walking, target tracking, obstacle avoidance, and behavior selection based on marker recognition. The rest of this paper is organized as follows: we describe the humanoid robot system and the behavior primitives in Section 2. In section 3, we propose a visual navigation system based on a target tracking and obstacle avoidance algorithm. In section 4, we present experimental results. Finally, we conclude with a discussion in Section 5.

2 Biped Robot and Behavior Primitive

We design a small humanoid robot as depicted in Fig. 1. The hardware platform consists of a main controller, a motion controller, a sensor module, and a battery. The main controller is an Intel PXA 272 embedded board with a Linux operating system. The embedded controller performs on-board image processing, behavior planning, and motion control. The motion controller is a micro-controller board that interfaces with a sensor module, and controls 24 motors in real time. We use six types of sensors and a 18.5 V battery. The humanoid robot has a height of 600 mm, a weight of 6 Kg including its batteries, 24 DOFs, and an aluminum body structure. The robot's joints consist of 24 servo motors. We assign a number to each motor, based on the position of each actuator, as shown in Fig. 1. The humanoid robot's right leg employs motors M1 through M6, while the left leg employs motors M11 through M16. The design of the robot incorporates roll, pitch, and yaw joints at the hip. The roll joint accommodates tilting at the pelvis, and the pitch joint allows for lateral displacement, as well as the minimum foot clearance required by the desired gait pattern. Knee and ankle joint interaction is achieved via the combination of pitch joints in the hip, knee, and ankle. A roll joint is also envisioned in the ankle, in order to avoid the foot from being placed upon its edge. This provides us with six degrees of freedom in each leg.

The purpose of the embedded vision system is to analyze input images captured by a camera in order to recognize the target, an obstacle, a wall, or a marker. The humanoid robot then plans its target path in real time, and identifies the best available locomotion primitives, based on the results produced by the vision system. We employ an NT-385 color CCD camera module. A field programmable gate array on the embedded board supports a variety of functions: image pre-processing, image sub-sampling, image conversion, and interfacing with the main processor. Input images are converted into 160×120 RGB images to decrease the on-board image processing time. The RGB image is used for image recognition, to identify targets and obstacles. The humanoid robot recognizes objects by detecting their edges, while excluding the noise.

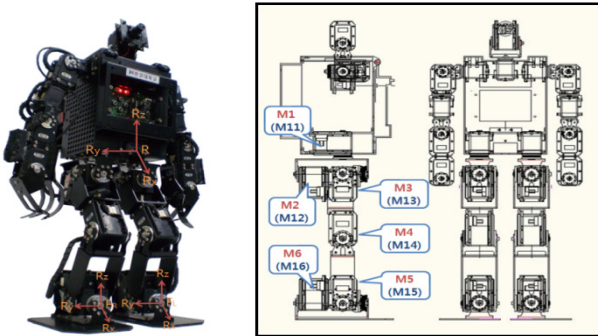


Fig. 1. Mechanical design and photo of the developed humanoid robot

A humanoid robot has high degree of freedom and its configuration space typically consists of more than twelve dimensions. Therefore, it is difficult to generate stable pose and set of motions available to the robot in time. In order to solve this difficulty, we use a set of behavior primitives for the humanoid robot [1][17]. Let a humanoid robot's behavior primitive be defined as a pattern of motion that begins and ends with a static stable posture. Behavior primitives can be classified as motion primitives and locomotion primitives as shown in Fig. 2.

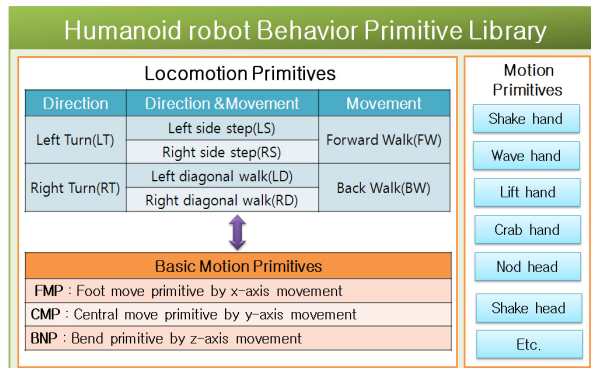


Fig. 2. Overall structure of behavior primitive library [17]

We use basic motion primitives (i.e., FMP, CMP, BNP) to develop a set of locomotion primitives. Locomotion primitives are the combined sequence of basic motion primitives. We design four types of locomotion primitives: walk(W), turn(T), diagonal walk(D), and side step(S). Each locomotion primitive is divided on the basis of its direction of travel(e.g., front(F), back(B), left(L), right(R)). Also, locomotion primitives are classified on the basis of the distance or angle of motion into big scale primitives and small scale primitives. If the robot rotates, it selects LT (Left Turn) or RT (Right Turn) according to the desired direction. If the robot selects RT, it will also choose either RBT (Right Big Turn) or RST (Right Small Turn) depending on the desired angle.

3 The Fuzzy Visual Navigation Method

3.1 Fuzzy Region Division and Input Variables

The ideal scenario is one in which the humanoid robot is capable of tracking a target while simultaneously avoiding obstacles. We propose a visual navigation system that depends on the target, obstacle, and marker.

The input image is divided into a set of sub-regions for the purpose of path planning as shown in Fig. 3. There are two types of regions: the target region and the obstacle region. The target region and obstacle region are then further divided on the basis of the distance and angle. There are nine fuzzy areas—NBB, NB, NM, NS, ZO, PS, PM, PB, and PBB—defined by their variance in angle from the robot's center of view, and there are five fuzzy areas—ZO, PS, PM, PB, and PBB—defined by their distance from the robot. A humanoid robot requires a wide area of analysis in order to find the target. Therefore, we use all nine areas based on angle, and five areas based on distance. However, we need to limit the region for obstacle avoidance; thus, we employ seven regions, based on angle, from NB to PB, and three regions based on distance, from ZERO to PM. The humanoid robot navigates in response to the location of objects, such as the target, obstacles, and markers. Fig. 3 shows the input variables to navigation system of the humanoid robot.

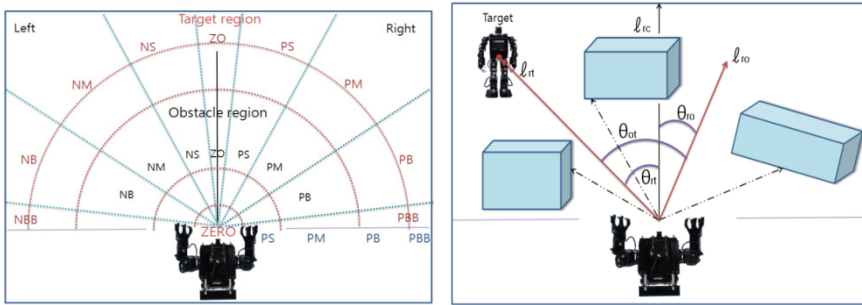


Fig. 3. Fuzzy region partition and input variables

3.2 Fuzzy Visual Navigation Method

The output of the proposed visual fuzzy navigation system can be divided on the basis of three types of objects, as shown in Table 1. The motion planning of the robot addresses eight cases depending on the presence of target, obstacle, or marker. The robot receives the input image through the camera and recognizes objects. If no object is recognized, the robot assumes that no objects are present. In this case, the robot selects Case 1, which is used to enact autonomous walking of the humanoid robot. If objects are recognized, the robot distinguishes between object types for motion planning. If only a target exists, the robot selects Case 2, to track the target. Case 3 is selected if the robot recognizes only obstacles. The robot selects Case 4 when it recognizes only markers.

Table 1. Distinction of navigation environment

Case No.	Target	Obstacle	Marker
1	X	X	X
2	O	X	X
3	X	O	X
4	X	X	O
5	O	O	X
6	O	X	O
7	X	O	O
8	O	O	O

Fig. 4 shows the case selection algorithm of the visual navigation system. The proposed navigation system has a set of basic cases (i.e., Case 1, 2, 3, 4) and a set of complex cases (i.e., Case 5, 6, 7, 8). Basic cases consist of scenarios in which no object or one type of object is present, while complex cases are scenarios involving the presence of two or three types of objects. If more than two types of objects are present, the robot must determine the priority of the object, in order to identify an optimal path of navigation. The object of greatest priority is the target, because the humanoid robot plans its path while continually tracking the target. If the robot recognizes a marker while it is tracking the target or avoiding obstacles, it performs the behavior command associated with the marker. The marker assists the robot in identifying navigation paths; thus, it receives second priority in most cases, except when there is an obstacle present in front of the marker, in which case the robot first seeks to avoid the obstacle.

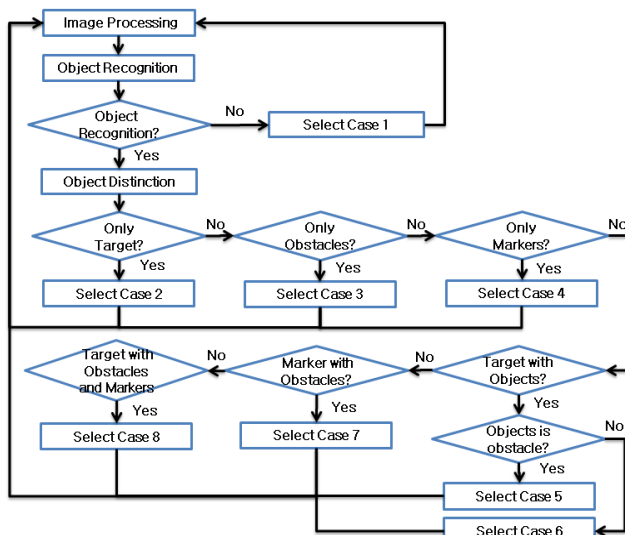
**Fig. 4.** Visual navigation selection algorithm

Fig. 5 depicts the autonomous walking algorithm as defined in Case 1. If no object is recognized, the robot selects the minimum angle path with maximum distance. ℓ_{pr} represents the robot's distance in following a given path. We are able to determine the number of considered paths, as this is related to the robot's motion planning time. θ_{pr} represents the angle between ℓ_{rc} and robot's path ℓ_p . Considering the angle and distance between the robot and its target, Fig. 6 presents a fuzzy membership function of θ_{pr} and ℓ_{pr} . We design fuzzy rules for autonomous walking as shown in Table 2.

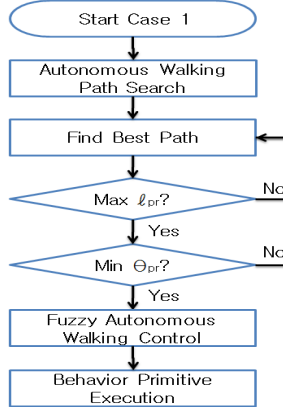


Fig. 5. Autonomous walking algorithm

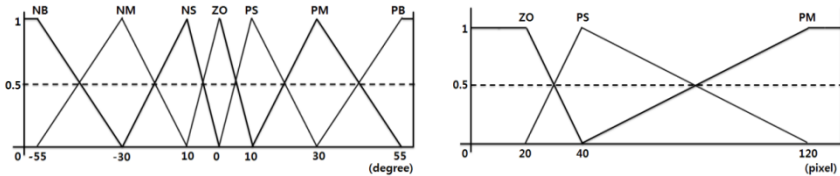


Fig. 6. Membership function of θ_{pr} (left) and of ℓ_{pr} (right)

Table 2. Fuzzy control rules for autonomous walking

ℓ_{pr}	θ_{pr}	NB	NM	NS	ZO	PS	PM	PB
ZO	BBW	BBW	BBW	BBW	BBW	BBW	BBW	
PS	LBT	LBD	LSD	FSW	RSD	RBD	RBT	
PM	LBT	LBT	LST	FBW	RST	RBT	RBT	

If the humanoid robot recognizes the marker while navigating, it selects an appropriate behavior primitive depending on the nature of the recognized marker. Fig. 7 depicts the behavior control algorithm based on marker recognition results. Obstacles may be divided into two types: walls and other obstacles. The humanoid robot will attempt to avoid those obstacles that it cannot pass, as identified by a marker. We display this marker on walls of the experiment environment.

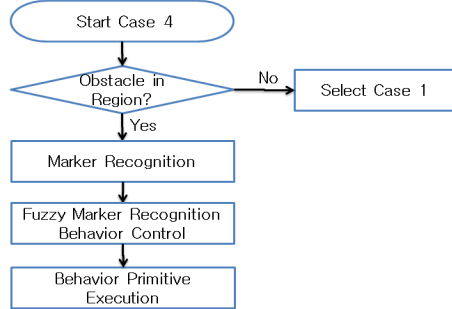


Fig. 7. Behavior control based on marker recognition results

We account for the distance and angle of direction between the robot and any obstacles in the obstacle avoidance algorithm as shown in Fig. 8. First, assuming that obstacles are located in the robot's obstacle avoidance region, if it does not have a target, the robot selects the longest path in order to avoid the obstacles. If there are multiple long equivalent paths, the robot will compare the angle between the various paths and the robot centerline. The robot will then select the best path based on minimization of the angle. Obstacles that do not reside within the obstacle avoidance region are ignored. We define an allowable obstacle pass range; NS to PS. If more than two obstacles exist within this field, the robot will not attempt to pass the obstacles. In this scenario, the robot will employ a right turn primitive to avoid the obstacles.

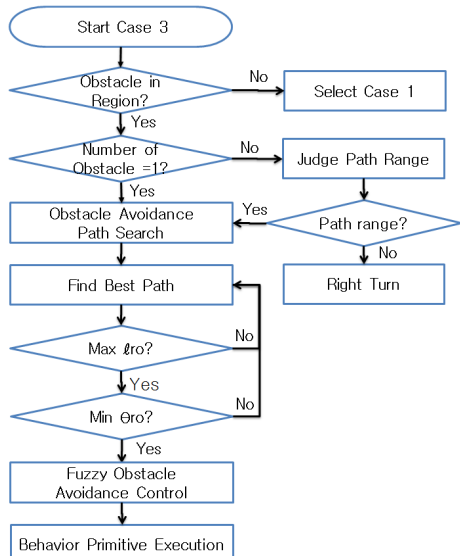


Fig. 8. Obstacle avoidance algorithm

The fuzzy membership function for distances and direction angles is shown in Fig. 9. We derive fuzzy control rules for the avoidance of obstacles as shown in Table 3. The humanoid robot will navigate in the direction opposite of the obstacles' positions.

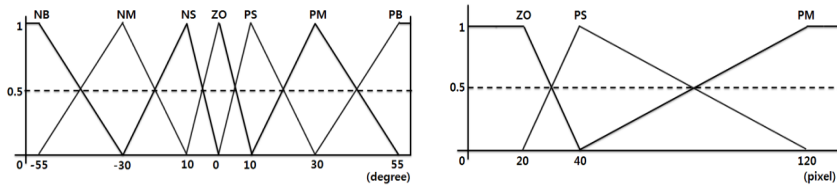


Fig. 9. Membership function of θ_{ro} (left) and of ℓ_{ro} (right)

Table 3. Fuzzy control rules for obstacle avoidance

ℓ_{ro}	NB	NM	NS	ZO	PS	PM	PB
ZO	BBW						
PS	LBT	LBD	BSW	BSW	BSW	RBD	RBT
PM	LBT	LST	LSD	FW	RSD	RST	RBT

In tracking the target, we first consider an obstacle free environment. The input image data is processed in an attempt to identify the target via the vision system. If the robot is successful in recognizing the target, the robot then identifies the target's center. The robot then proceeds to search for available paths to the target. We consider the angle and distance between the robot and the center of the target. ℓ_{rt} and θ_{rt} are input variables to the fuzzy navigation system used in target tracking. The robot selects the maximum distance ℓ_{rt} and minimum angle θ_{rt} . Fig. 10 presents the fuzzy membership function of the angle θ_{rt} and the distance ℓ_{rt} . We implement fuzzy control rules as defined in Table 4. If the target is not located upon analysis of the input image, the robot performs a random search. The robot attempts to maintain the presence of the target within the input image at all times. If the target is located in front of the robot, the robot determines that it can move straight to the target. As such, the robot executes a forward walk primitive. The robot selects the FSW(forward small walk primitive) or the FBW(forward big walk primitive) depending on ℓ_{rt} . If ℓ_{rt} is small but θ_{rt} is big, the robot executes a side step primitive. However, the side step primitive selected is not always the same.

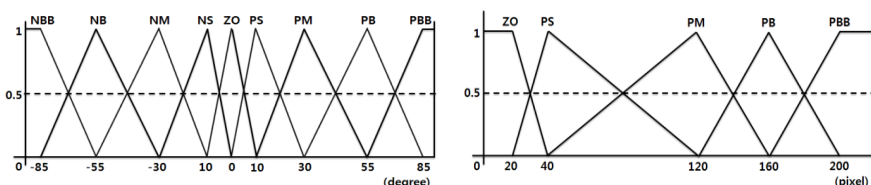
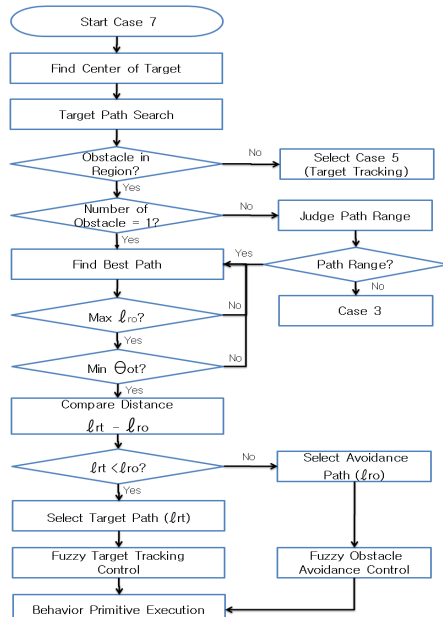


Fig. 10. Membership function of θ_{rt} (left) and of ℓ_{rt} (right)

Table 4. Fuzzy control rules for target tracking

θ_{rt}	NBB	NB	NM	NS	ZO	PS	PM	PB	PBB
ZO	BW								
PS	ST	LSS	LSD	ST	ST	ST	RSD	RSS	ST
PM	LSS	LBS	LBD	LSD	FSW	RSD	RBD	RBS	RSS
PB	LBT	LBT	LST	LST	FBW	RST	RST	RBT	RBT
PBB	LBT	LBT	LST	LST	FBW	RST	RST	RBT	RBT

We propose the visual navigation algorithm as depicted in Fig. 11. This visual fuzzy navigation algorithm incorporates two types of objects; targets and obstacles. The robot will always seek to avoid obstacles while tracking the target. The robot attempts to recognize the target. If the robot fails to recognize the target, it uses a geomagnetic sensor to determine the direction of the target. If the robot succeeds in recognizing the target, it subsequently locates the center of the target in order to identify the associated tracking path. The robot then proceeds to identify obstacles. Obstacles are considered to be any objects within the robot's obstacle avoidance region. We select a path on the basis of the number of recognized obstacles. If the humanoid robot does not recognize any obstacles, it will choose a path tracking the target. If there is one obstacle in the obstacle avoidance region, the robot will search for an obstacle avoidance path. If the robot recognizes two or more obstacles, it will default to a right turn primitive in order to avoid the obstacles.

**Fig. 11.** Visual navigation algorithm

4 Experimental Results

We verify the proposed method by using a developed biped robot. Fig. 12 shows the results of an experiment testing a humanoid robot's autonomous walking. This is an experiment of case 1, target tracking navigation. If a humanoid robot recognizes the target, the robot then finds the path in order to track the target. The robot plans motion planning to move to the target and selects an appropriate behavior primitive to perform. We confirmed that the humanoid robot moved to the target quickly and stably in the experiment results. However, there are the errors between pre-planned primitives and actual performed primitives. We importantly consider the current state of the robot configuration, the bottom state, and the disturbance to decrease the errors next time. If the target is far away or target path has many rotations, the results showed lower success rate of tracking the target by the cumulative errors.

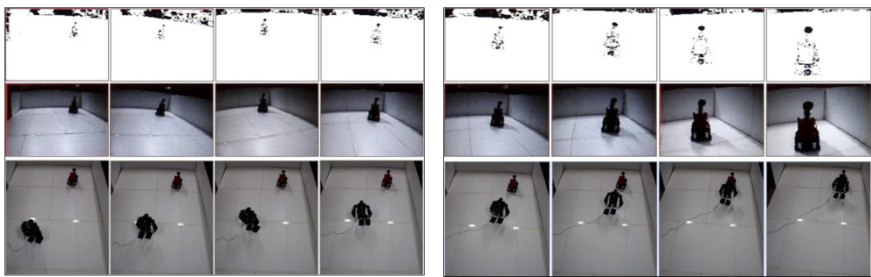


Fig. 12. Experimental results of target tracking algorithm

A humanoid robot is required sensors, which collect the current environmental information, to plan the path. The input images are processed such as color model conversion, noise exclusion, and edge detection by the vision system. We extract and recognize the patterns depending on features. Fig. 13 presents the results of an experiment testing a humanoid robot's behavior based on markers recognition. We confirmed that the humanoid robot effectively moved depending on recognition of markers in the experiment results.

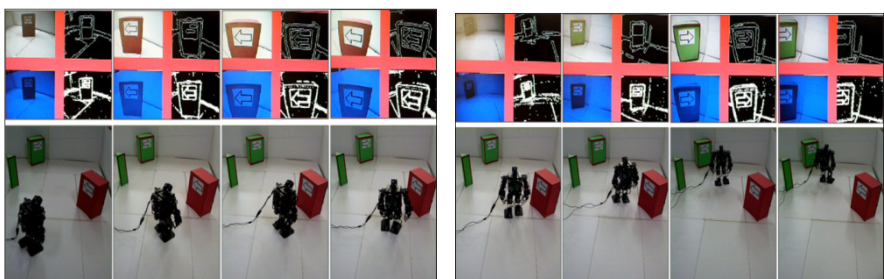


Fig. 13. Experimental results of marker recognition

Fig. 14 shows the results of an experiment testing a humanoid robot's autonomous walking. This is an experiment of case 3, obstacle avoidance navigation. Our obstacle avoidance method is regardless of color and shape of the obstacles in 3D experimental environment. If the obstacles location is moved, the humanoid robot can recognize and avoid the obstacles in real time. Sometimes the robot is in conflict with obstacles while walking. To solve this problem, we equipped the IR sensors to the humanoid robot in order to prevent collisions with obstacles.

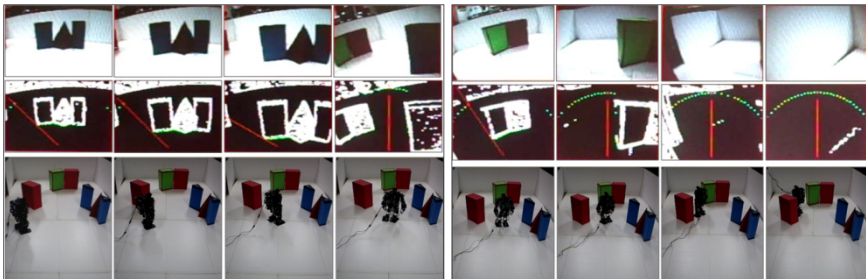


Fig. 14. Experimental results of obstacle avoidance algorithm

5 Conclusion

In this paper, we have presented a fuzzy visual navigation method that uses behavior primitives for humanoid robots. A fuzzy navigation algorithm using autonomous walking, target tracking, obstacle avoidance, and marker recognition was proposed to finds feasible sequence of behavior primitives to reach the target. We verified the proposed approach through navigation experiments using a developed small humanoid robot. The experimental results demonstrate that the robot is capable of autonomous walking and displays improved performance of behavior planning for navigation in the complex environment.

Acknowledgements. This research has been supported by the Basic Research Program for General Researchers through the National Research Foundation of Korea(NRF) funded by the Ministry of Education, Science and Technology(No.2010-0023291).

References

1. Kim, Y.-T., Noh, S.-H.: Behavior Planning for Humanoid Robot Using Behavior Primitive. *Journal of Fuzzy Logic and Intelligent Systems* 19(1), 108–114 (2009)
2. Hauser, K., Bretl, T., Latombe, J.-C.: Using Motion Primitives in Probabilistic Sample-Based Planning for Humanoid Robots. In: *Proceedings of the Workshop on the Algorithmic Foundations of Robotics*, WAFR (2006)
3. Kuffner, J., Nishiwaki, K., Kagami, S., Inaba, M., Inoue, H.: Motion planning for humanoid robots. In: *Int. Symp. Rob. Res.*, Siena, Italy (2003)

4. Hirai, K., Hirose, M., Haikawa, Y., Takenaka, T.: The Development of Honda humanoid robot. In: Int. Conf. on Robotics and Automation, pp. 1321–1326 (May 1998)
5. Okada, K., Kagami, S., Inaba, M., Inoue, H.: Plane segment finder: Algorithm, implementation, and applications. In: Int. Conf. on Robotics and Automation, Korea (2001)
6. Lau, M., Kuffner, J.J.: Behavior Planning for Character Animation. In: Eurographics/ACM SIGGRAPH Symposium on Computer Animation (2005)
7. Kanehiro, F., Yoshimi, T., Kajita, S., Morisawa, M., Fujiwara, K., Harada, K., Kaneko, K., Hirukawa, H., Tomita, F.: Whole body locomotion planning of humanoid robots based on a 3D grid map. In: Int. Conf. on Robotics and Automation, Spain (2005)
8. Gutmann, J.-S., Fukuchi, M., Fujita, M.: Real-time path planning for humanoid robot navigation. In: Int. Joint Conference on Artificial Intelligence (IJCAI), Edinburgh, Scotland (2005)
9. Choset, H., Lynch, K.M., Hutchinson, S., Kantor, G., Burgard, W., Kavraki, L.E., Thrun, S.: Principles of Robot Motion: Theory, Algorithms, and Implementations. MIT Press, Boston (2005)
10. Chestnutt, J., Kuffner, J.J.: A tiered planning strategy for biped navigation. In: Int. Conf. on Humanoid Robotics, Humanoids (2004)
11. Gutmann, J.-S., Fukuchi, M., Fujita, M.: Stair climbing for humanoid robots using stereo vision. In: Int. Conf. on Intelligent Robots and Systems (IROS), Sendai, Japan (2004)
12. Chestnutt, J., Kuffner, J.J., Nishiwaki, K., Kagami, S.: Planning biped navigation strategies in complex environments. In: Int. Conf. on Humanoid Robotics, Humanoids (2003)
13. Hirai, K., Hirose, M., Haikawa, Y., Takenaka, T.: The development of Honda humanoid robot. In: Int. Conf. on Robotics and Automation (ICRA), pp. 1321–1326 (May 1998)
14. Kim, Y.T., Noh, S.H., Lee, H.J.: Walking and Stabilization Algorithm of Biped Robot on the Uneven Ground. Journal of Fuzzy Logic and Intelligent Systems 15(1), 907–913 (2005)
15. Kroki, Y., Fujita, M., Ishida, T., Nagasaka, K., Yamaguchi, J.: A small biped entertainment robot exploring attractive applications. In: Int. Conf. on Robotics and Automation, ICRA (2003)
16. Lau, M., Kuffner, J.J.: Behavior Planning for Character Animation. In: Eurographics/ACM SIGGRAPH Symposium on Computer Animation (2005)
17. Noh, S., Kim, Y.T.: Stable Behavior Trajectory Generation for Humanoid Robot using Locomotion and Motion Primitives. International Journal of Assistive Robotics and Systems 11(2), 31–40 (2010)

Development of Steer-by-Wire for Manned and Unmanned Electric Vehicle

Yong-Jun Lee and Young-Jae Ryoo

Dept. of Engineering and Robotics, Mokpo National University
1666 Youngsan-ro, Chyungye-Myun, Muan-Gun, Chonnam, Korea
{yongjun,yjryoo}@mokpo.ac.kr

Abstract. In this paper, a steer-by-wire system for a manned and an unmanned electric vehicle using an electric clutch is proposed. When electric vehicles have unmanned driving function, an automatic steering system for the vehicle to follow along the path would be required. A steering mechanism was developed of electric vehicles for unmanned driving. The Steering motor using BLDC motor and an electric clutch are used to transmit motor power to steering axis steering mechanism. Also, the electric vehicle was tested to examine usefulness of the developed steering mechanism. The developed steer-by-wire system may be enable or enhance vehicle control technologies related to collision avoidance, lane keeping, and enhanced stability control.

Keywords: Steer-by-Wire, Unmanned Vehicle, Electric Vehicle.

1 Introduction

Steer-by-wire systems offer the potential to enhance steering functionality by enabling features such as automatic lane keeping, park assist, variable steer ratio, and advanced vehicle dynamics control. Steer-by-wire systems replace the conventional mechanical linkages with electronic sensors, controllers and actuators.

Depending upon the design, a steer-by-wire system can offer several benefits compared to conventional mechanical steering systems. Elimination of the mechanical linkage between the steering wheel and the steering gear can provide an enhancement to design flexibility.

There are several significant challenges associated with the commercial application of steer-by-wire technology to automobiles. Safety and security objectives must be met. A steer-by-wire system contains electrical components that have lower reliability than the mechanical components found in conventional steering systems. Redundancy of electrical components may be an effective method to assist steer-by-wire systems in meeting safety objectives.

However, component redundancy may also have a negative impact on cost and reliability. Despite the continuous cost reduction of electronic sensors, controllers, and actuators, the steer-by-wire system cost remains a significant obstacle to application in passenger cars.

In unmanned driving system, precise steering angle control is an important task for stable driving. Electric Power Steering (EPS) has a representative in the steer-by-wire system. But, the EPS has a problem that steering bar could be locked to protect itself from overheating of motors.

In this paper, how to overcome the problem of EPS as steering system using electric clutch is proposed. When Vehicle is unmanned driving, the automated steering system is connected to steering axis by electric clutch turn on. When vehicle isn't unmanned driving, the automated steering system is disconnected from steering axis by electric clutch turn off. Thus, steering bar locking problem can be overcome.

To implement the proposed method, a steering system has been developed. Usefulness and practicality of the proposed method was tested by the developed electric vehicles. For an unmanned driving electric vehicle uses magnetic guidance system. The unmanned vehicle is a battery powered demonstration vehicle. For experiments on the road to the magnetic path to install a magnetic marker, the electric vehicle was tested. When electric vehicle was driving, developed steering system was tested control vehicle's steering.

2 System Configuration

2.1 Structure of Steering System

The Steering actuator is using geared BLDC motor. BLDC motors are efficient because it has high torque and speed. For the common of the unmanned driving, 12v electric clutch was installed and BLDC motors have composed the unmanned steering system by using 12V 100W class as shown in a Fig.1.

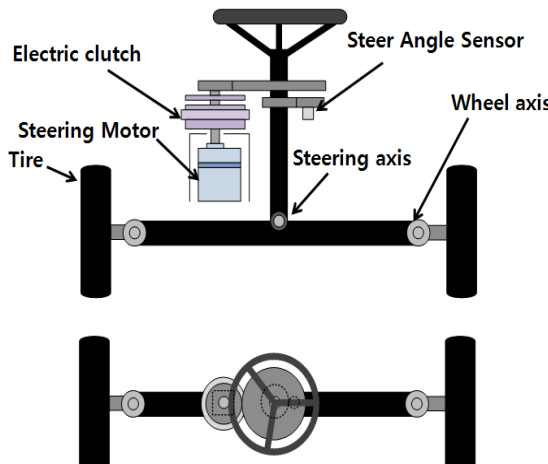


Fig. 1. Structure of steering system

Table 1. Specification of BLDC motor

Rated Output (W)	Rating			Rated Torque (kgf.cm)	Rated speed (rpm)	Operation range (rpm)
	Voltage (V)	Frequency (Hz)	Current (A)			
100	14	-	13.5	3.2	3000	300 ~ 3000

Table 2. Specification of BLDC motor driver

Maximum Current (RMS)	10A
Rated Input Voltage	DC 12 ~ 24 V ±15%
Controllable Signal	1. Run/Stop 2. Speed 3. Brake 4. Direction
Control Method	3 Phase PWM
Operating Temperature	0°C ~ 50°C
Protection	Shut down at aver current

2.2 Mechanism of Steering Actuator

The structure of the steer-by-wire system is that BLDC motors, steering axis and angle sensor was connected to gears. The BLDC motor axis is connected with the clutch. The steering axis and the wheel axis are connected with the universal joint. The gear of clutch axis and the steering axis are consisted of a 24:80. The steering axis and angle sensor axis was consisted of 24:120.

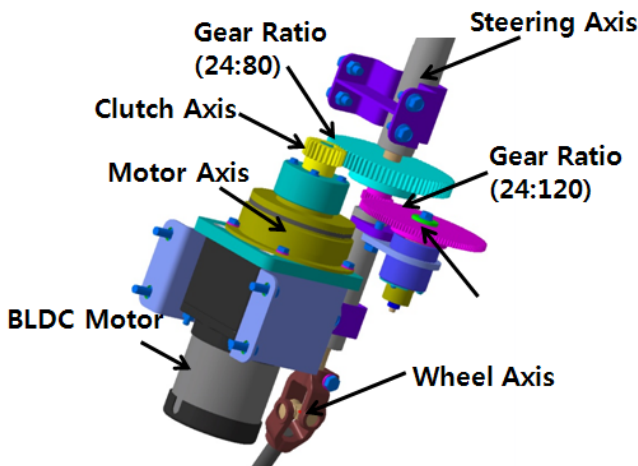
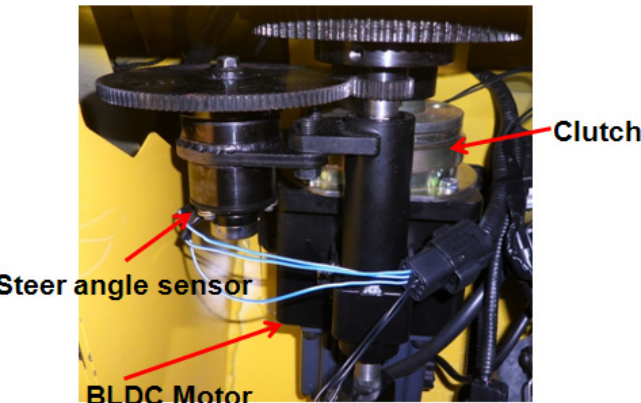
**Fig. 2.** Mechanism of Steering Actuator

Table 3. Result of calculate gear ratio

Motor Axis	Motor Axis	Angle Sensor Axis
0.5 turn/sec	0.15 turn/sec	0.03 turn/sec
180°/sec	54°/sec	10.8°/sec

**Fig. 3.** Developed mechanism of steering actuator

The angle sensor has an operation range of $\pm 145.44^\circ$ and the wheels of the vehicles have an operation range of medial 37° and external 27° .

3 Design of Control System

In order to control the steering of unmanned electric vehicle, a control system was designed and developed. The steering controller using a microprocessor was designed to control steering. BLDC motor driver for BLDC motor control was used. The steering controller enters a PWM signal that determines the steering speed based on steering angle values received from main controller and a control signal that determines ON/OFF of the BLDC motor and CW/CCW to the BLDC motor driver.

In order to protect the circuit from the back EMF that can be generated from the BLDC motor, the steering controller using a photo coupler insulates the output. Also, it was developed to protect the malfunction of the steering controller caused by the noise through a combination of the circuit using a TTL device. The angle value generated in the potentiometer was converted by the AD Converter in the main controller and it can measure the steering angle.

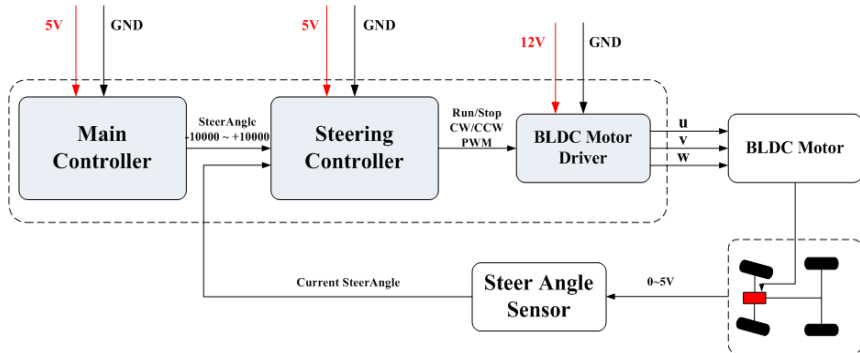


Fig. 4. Block diagram of steering control system

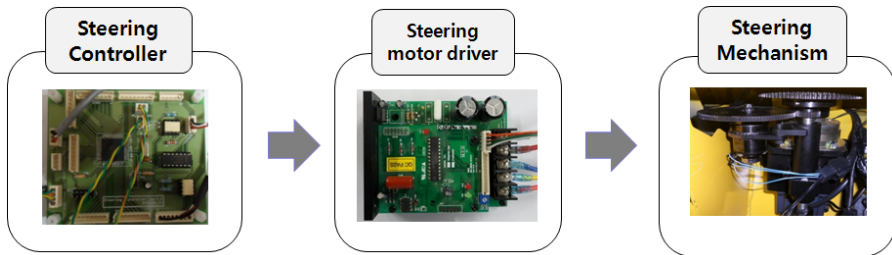


Fig. 5. Configuration of steering control system

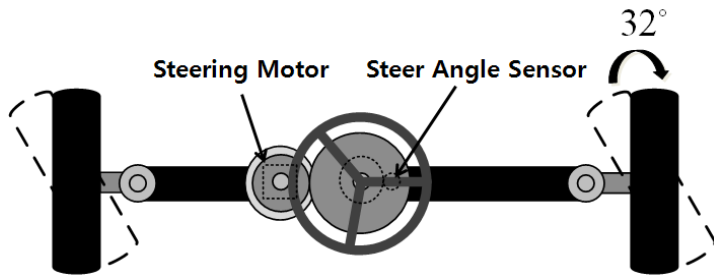
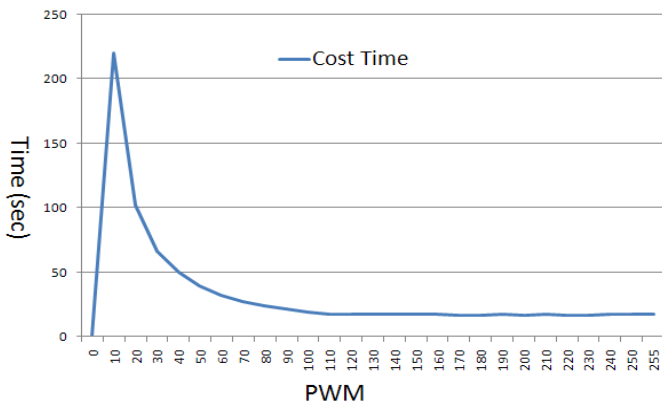
4 Experiment

In this chapter, the usefulness of the unmanned driving electric vehicle using the developed steer-by-wire system would be verified through the experiment. The characteristic experiment of the BLDC motor for the steering of unmanned driving electric vehicles was implemented and this result was analyzed.

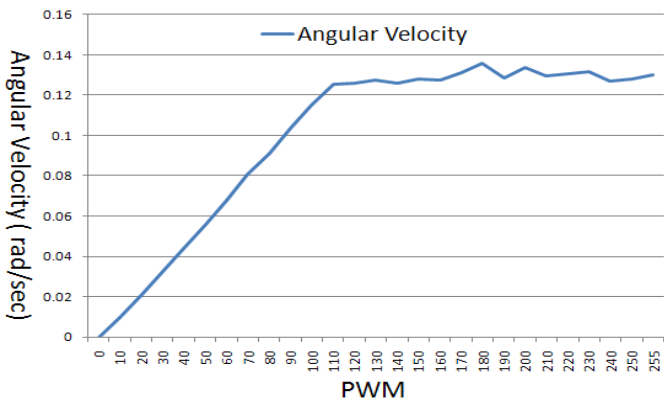
4.1 Characteristics of Steering System

For the steering of developed unmanned driving electric vehicles, the motion experiment of the BLDC motor was implemented. According to the PWM value, the motion experiment of the BLDC motor was implemented and data was compared and analyzed.

The minimum PWM value to operate the BLDC motor, dead-zone and proportional constant value k_p for the steering control was determined. In order to obtain the characteristic curve of the behavior of the BLDC motor,

**Fig. 6.** Configuration of steering test

(a) Cost Time.



(b) Angular Velocity.

Fig. 7. Characteristic of Steering Actuator

The steering actuator's characteristics of electric vehicle is shown as Fig. 7. For the operation of the unmanned steering device, input 0~5V is put to the steering motor driver. Main controller outputs the PWM value 0~255 and 0~5V control signal.

To confirm the minimum PWM value for the operation of the unmanned steering device, PWM values increase with starting at 0 by 10 units and the experiment was implemented.

Fig. 7 (a) shows that depending on the value of the PWM is a measure of the time when it takes to move the steering angle from -32° to 0° . Fig. 7 (b) is measure of the steering angular speed of the unmanned steering device depending on the increase of PWM.

When it is setting the PWM value within 110, we can get a result that close to linear other while PWM value is over the 110, we get a result of nonlinear.

Through characteristic experiment of the unmanned steering device, the optimal PWM control range for the steering of unmanned driving electric vehicles is selected from 0 to 110 was confirmed.

4.2 Closed-Loop Control

After the operating characteristic of the unmanned steering device was checked according to the PWM value, the experiment was conducted in order to check the steering motion of the actual vehicle and the motion of the steering motors according to the proportion constant value.

The steering angle of the unmanned driving electric vehicle is from -32° to $+32^\circ$. The value of the steering angle from -255 to 255 the steering angle is converted to the integer from -10000 to +10000. Therefore, the $C_{\text{integer Steer-dwm}}$ for converting the integer 10000 to PWM value is 0.0255. We entered 0.02, 0.04, 0.07 into the proportional constant K_p and analyzed the motion results

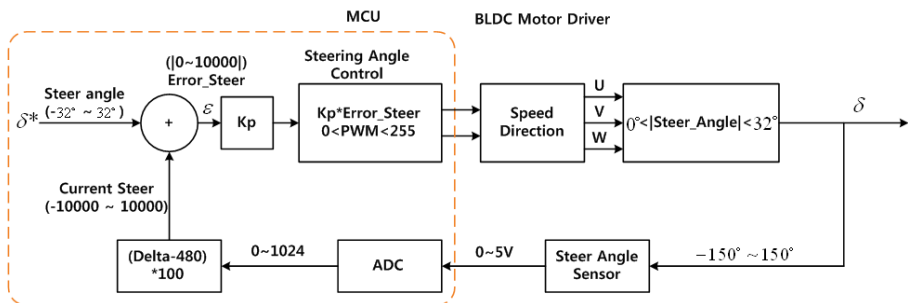


Fig. 8. Closed-Loop steering control block chart

The steering error was obtained through comparing the steering command value with the current steering angle value and calculate the steering speed by multiplying the proportional constant by the steering error.

The dead zone was set up to be able to stop the motion when the steering error values was from -400 to 400 and the marginal zone was set up to be able to stop the steering if the value is greater than 10000 or less than -10000.

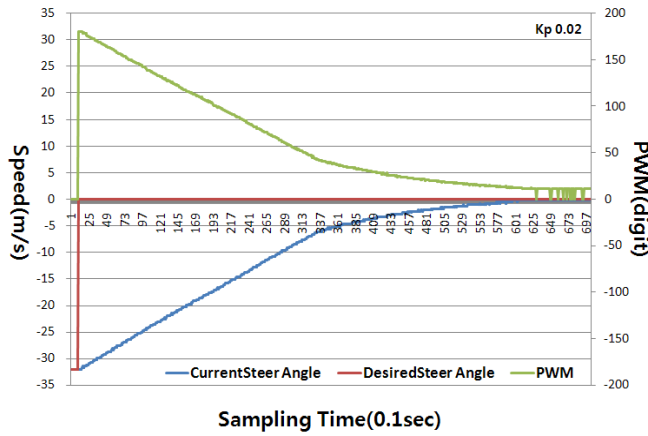
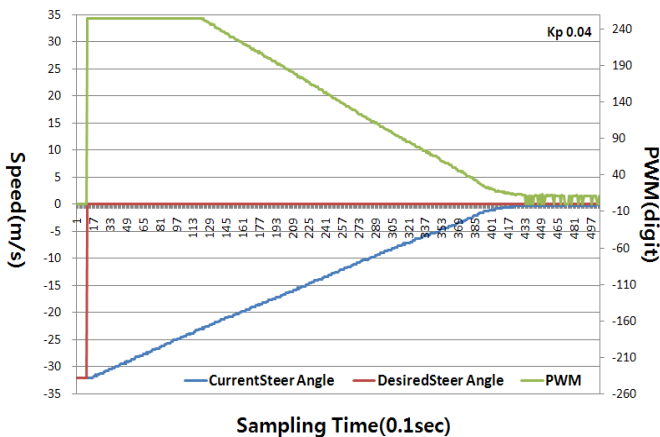
**Fig. 9.** Result of Steering Control (Kp:0.02)

Fig. 9 was the result of the steering experiment in case of setting the constant value K_p to 0.02. The current steering angle value is -10000 and we enter the command to go to 0 at that time the steering angle value and the change of the PWM value was analyzed. The time required of the steering angle value to reach the target spot was from 55sec up to 57sec.

**Fig. 10.** Result of Steering Control (Kp:0.04)

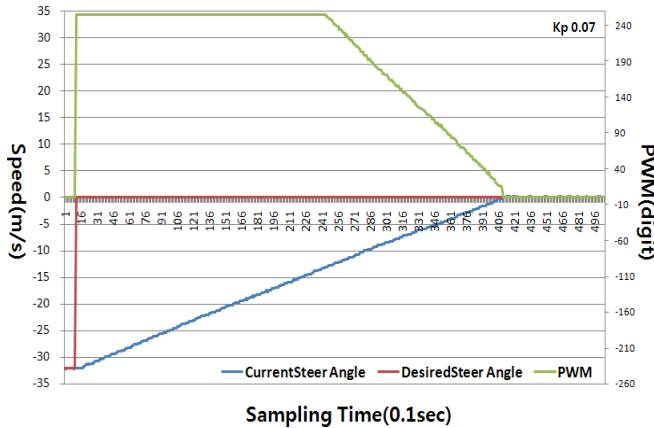


Fig. 11. Result of Steering Control (Kp:0.07)

Fig. 10, 11 was the result of the steering experiment in case of setting proportional constant value to 0.04 and 0.07. The current steering angle value is -10000 and we enter the command to go to 0 at that time the steering angle value and the change of the PWM value was analyzed. The time required of the steering value to reach the target spot was 41s when the k_p was 0.04 and we confirmed that the error occurs when the steering angle reach 0 degrees. The time required is about 40 seconds when the K_p is 0.07 and that there is no error was confirmed in case of reaching 0 degree.

Based on the results of the experiment, the steering proportion constant value of the unmanned driving electric vehicles was set up to 0.07.

5 Conclusion

In this paper, a steer-by-wire system was developed for manned and unmanned electric vehicle. How to overcome the problem of EPS as steering system using electric clutch was proposed. When the vehicle works with unmanned driving mode, the automated steering system is connected to the steering axis by electric clutch's turning on. When the vehicle works with manned driving mode, the automated steering system is disconnected from steering axis by electric clutch's turning off. Thus, the steering bar locking problem could be overcome.

To implement the proposed method, a steering system has been developed. Usefulness and practicality of the proposed method was tested by the developed electric vehicles. For the est of unmanned driving, the magnetic guidance system used. While electric vehicle was driving, the developed steer-by-wire system was suitable to control the vehicle.

The proposed steer-by-wire system could enhance vehicle technology related to collision avoidance, lane keeping, and stability control.

Acknowledgements. This research was financially supported by the Ministry of Education, Science Technology (MEST) and National Research Foundation of Korea(NRF) through the Human Resource Training Project for Regional Innovation

References

1. Heitzer, D., Seewald, A.: Development of a fault-tolerant steer-by-wire steering system. In: SAE Conference Proceedings, vol. 387, pp. 355–362 (2004)
2. Zara, N.: Rear-to-front steer algorithm for four-wheel-steer, full-size trucks-analytical assessment. In: SAE Special Publications 2005-01-0405, vol. 1916, pp. 37–46 (2005)
3. Nagai, M., Yamanaka, S., Hirano, Y.: Integrated control law of active rear wheel steering and direct yaw moment control. In: Proceedings of the International Symposium on Advanced Vehicle Control (AVEC), vol. 1, pp. 451–470 (1996)
4. Segawa, M., Nishizaki, K., Nakano, S.: A study of vehicle stability control by steer by wire system. In: Proceedings of the International Symposium on Advanced Vehicle Control (AVEC), pp. 233–240 (2002)

Passive RFID Positioning System Using RF Power Control

Sang Yup Lee¹, Byung-Cheol Min², Dong Hoe Kim¹, Jae Seok Yoon¹,
and Dong Han Kim¹

¹ Department of Electronics and Radio Engineering, Kyung Hee University, Yongin-si,
Gyeonggi-do, Korea

{leedanny, genesis130, blackyjs, donghani}@khu.ac.kr

² Department of Computer and Information Technology, Purdue University,
West Lafayette, IN, USA
minb@purdue.edu

Abstract. This research proposes a method which can be applied into location recognition of mobile robots using patterns and the numbers of recognized tags. As passive RFID tags can only measure existence of tags that are located in a recognizable range of a RFID reader, the physical position of each tag cannot be measured; thus, in order to receive information about positions of tags, a proper method to measure the positions should be selected. Also, in a real environment, results differ from ideal results based on characteristics of antennas and surrounding environments, characteristics of tags. Thus, this paper discusses a method to estimate locations according to values of power control with passive RFID tags in a real environment. In an experiment, a UHF-900MHz RFID reader was utilized with placement of passive RFID tags on a floor; the power of the reader was controlled with 30 different levels. In this paper, the differences according to the levels will be discussed with details. This research can be applied to location recognition with RFID power control in a real environment.

Keywords: position recognition, location recognition, RFID power control, mobile robot.

1 Introduction

Location recognition of mobile robots utilizes GPS, ultrasonic sensors, infrared sensors, LRF or multiple cameras in a number of researches [1-4]. Recently, there are several researches to provide self-local recognition services and localization services for robots in USN (ubiquitous sensor network) environments [5].

There have been many ongoing researches on RFID Technologies like this research, and, especially, researches to improve location estimation of mobile robots are representative [6-9]. In the researches, locations were estimated using RFID tags which were distributed in a space; by receiving location information which was saved in tags, a mobile robot could understand its location and then estimate its independent

position from other robots and obstacles. Also, as methods to place tags in a space, a square grid and an equilateral triangle grid were proposed, and it was concluded that location estimation would decrease with an equilateral triangle grid. However, the simulations and the experiments in the researches assumed that recognition ranges of the utilized RFID readers were ideal; in a real environment, it is meaningless in that RFID system depends on surrounding environments, performance of an antenna, and performance of tags in a real environment. Also, recognition rates of RFID readers used in the experiments were low and recognizable ranges were short; the use of RFID technologies was very limited in the experiments and advantages of RFID technologies were not fully utilized. There have been other researches about applications of navigation for cleaning robots using RFID technologies [10-11], an application of mobile robots understanding its current position and reaching a destination with a placed RFID tag [12], an application to measure a speed of a car with placement of RFID tags on a road and a car [13].

This paper will illustrate how location recognition can be applied in a real environment with improvements by using RFID power control. We utilized UHF RFID systems, operating at 900MHz, to compare patterns of recognized tags in a real environment and the different numbers of recognized tags when dynamic outputs are given, and to understand a difference between an estimated location and a real location by using min-max and mean operations with location information of recognized tags as variables.

2 RFID Power Control

This research proposes a method to receive positional information of coordinated tags using values of RF power control and then to estimate a location of a mobile robot with the positional information. The physical positions of tags are unknown as only existence of tags can be checked with passive RFID tags so that a method to estimate locations by receiving positional information should be selected.

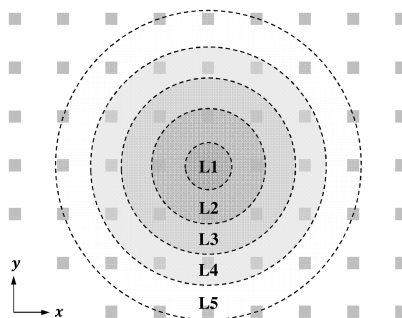


Fig. 1. The ideal RFID power control

Ideal RFID power control should look like Figure 1. In the figure, small rectangles represent RFID tags and the circle labeled as L1 (Level 1) is the minimum range of a RFID reader recognizing tags, and the circle labeled as L5 (Level 5) is the maximum range. As the level of power is greater, the reader is able to recognize more tags. However, recognized patterns and the number of recognized tags can vary, depending on characteristics of antennas and tags, and surrounding circumstances.

Mostly, tags are placed in a rectangle grid or a triangle grid [5]. Each tag has each x-y coordinate that is inputted in advanced, and the RFID reader receives coordinates from tags that are placed in a recognizable range according to values of RF power.

A position of a mobile robot can be estimated by using the coordinates of recognized tags. There are, roughly, two operations to estimate positions: min-max operation and mean operation. In this paper, a rectangle grid was selected, and it was assumed that positions of tags are all the same for the both operations.

Min-max operation calculates the minimum value and the maximum value of x and y from coordinates of recognized tags. And then, a position of a mobile robot is calculated by the mean of the two values as following:

$$(x_{min-max}, y_{min-max}) = \left(\frac{x_r^{min} + x_r^{max}}{2}, \frac{y_r^{min} + y_r^{max}}{2} \right) \quad (1)$$

Also, we can estimate its location by calculating the mean of coordinates of recognized tags with mean operation, as following. n refers to the number of recognized tags.

$$(x_{mean}, y_{mean}) = \left(\frac{1}{n} \sum_{i=1}^n x_r^n, \frac{1}{n} \sum_{i=1}^n y_r^n \right) \quad (2)$$

With the above operations, we can ultimately get a margin of error in estimating locations; if the result is closer to 0, the performance of estimating locations gets better.

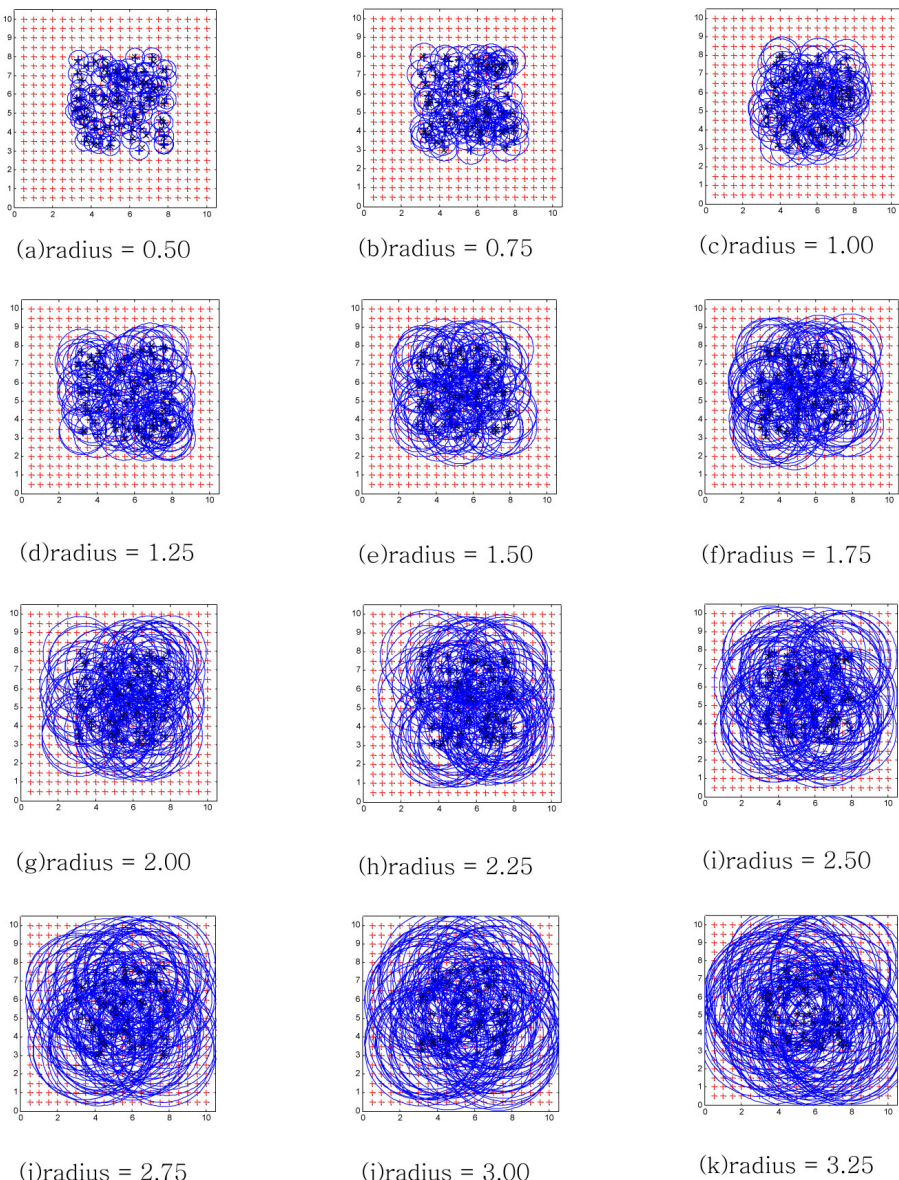
$$d_{error} = \sqrt{(x_{real} - x_{estimate})^2 + (y_{real} - y_{estimate})^2} \quad (3)$$

Both of the two operations are methods to estimate locations using coordinates of recognized tags, and if the recognizable range is not ideal, the margin of error will be greater; in this case, tags can be placed with a small interval from other tags though time and efforts to adapt in a real environment will be highly required.

3 Experiments

3.1 Simulation

The simulation has performed with MATLAB. The method was to arrange 400 tags as 20 x 20 and give a 0.5m space each other. RFID output was replaced by diameter of circle which can be seen in Figure 2. The experiment was held 100 times. The aim was to see the tolerance of the actual antenna's location and the estimated location between 0.5m to 3.25m radiuses.

**Fig. 2.** The result of the RF power control simulation

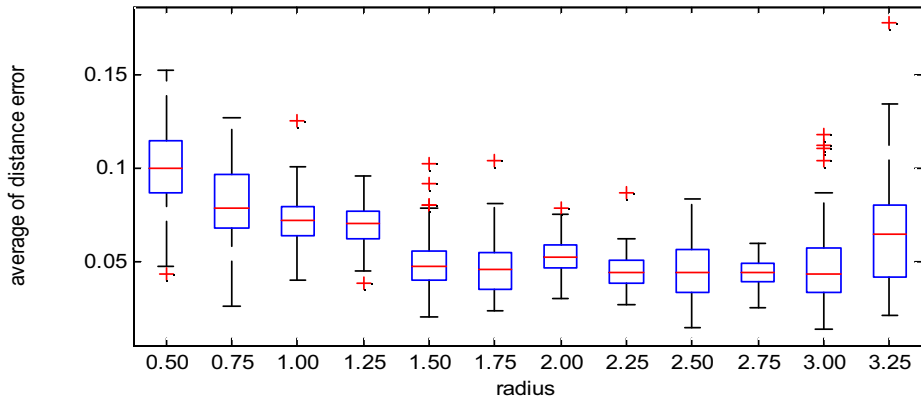


Fig. 3. The tendency of the distance error from each radius

The result of the radius per distance tolerance is shown in Figure 3. As the radius gets wider, the tolerance reduced. However, if output goes above the certain point, tolerance increased. This shows that when there is dramatic increase in output, power goes out of the tag area, which would result in increase of tolerance. As per result, it is able to assume that the distance tolerance can be decreased if the maximum output does not get off the RF tag area. The tolerance was increased at radius 2.00 and it is because the output was increased when the tag number was the same. Thus, if the detective tag number is the same, it is better to set the location at the less output area.

3.2 RFID System

Figure 4 shows placement of tags and an antenna, which are utilized in the experiment. MKUR-300 from Minerva was chosen as a RFID reader since this model is the most ideal and operates at a frequency of 900MHz.

And metal passive tags were selected as RFID tags in the experiment since metal tags are noise-resistant and accurate in recognition [14]. 25 of the metal tags were spaced 5×5 with an equal 30cm distance from one another; in the center, the (2, 2) point, the antenna was placed 50cm above from the floor. This placement is not idealized, and patterns and rates of recognition can differ, depending on the antenna, the placement of tags, and other effects from a dynamic environment.

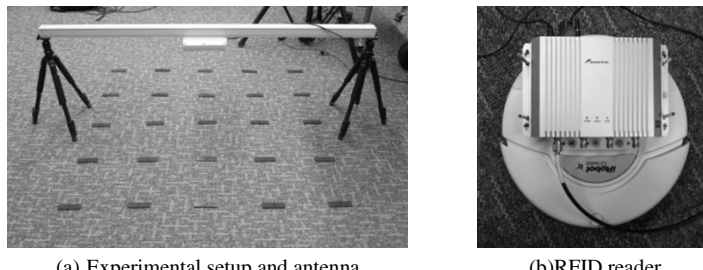


Fig. 4. RFID system

3.3 Experiment Results

In the experiment, we estimated patterns of recognized tags and the number of the tags for different values of power, by decreasing the value of power from 30dBm , the maximum power of the RFID reader, to 0dBm . And then, we estimated locations with calculation of min-max operation and mean operation, and calculated a distance error between a real position and an estimated position.

3.3.1 The Number of Recognized Tags

The number of recognized tags at each value of RF output is shown in Figure 5. The highest number of recognized tags was 24 at 27dBm or greater, and at the values of RF output less than 10dBm , tags were not recognized. As a result, in the environment of the experiment, the minimum value of RF output to be able to recognize tags was 10dBm . And at 10, 15, 20, 25, and 30dBm , the location was estimated with x-y coordinate information since there were variances in the numbers of recognized tags.

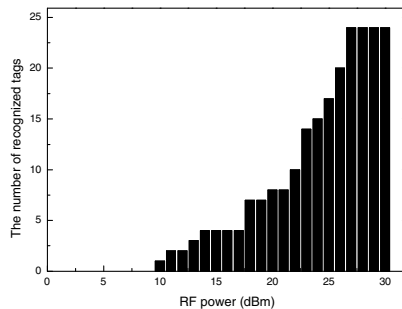


Fig. 5. The number of recognized tags by RF power control

3.3.2 Tag Patterns by RF Power

Figure 6 shows patterns by RF power. In an ideal environment, a constant pattern is shown; however, in the real experiment, there was no constant pattern found. It is due to characteristics of antenna and tags and influences from surrounding circumstances or environments. Especially, because performance of each tag is not the same, differences in results were found even when the same power was provided.

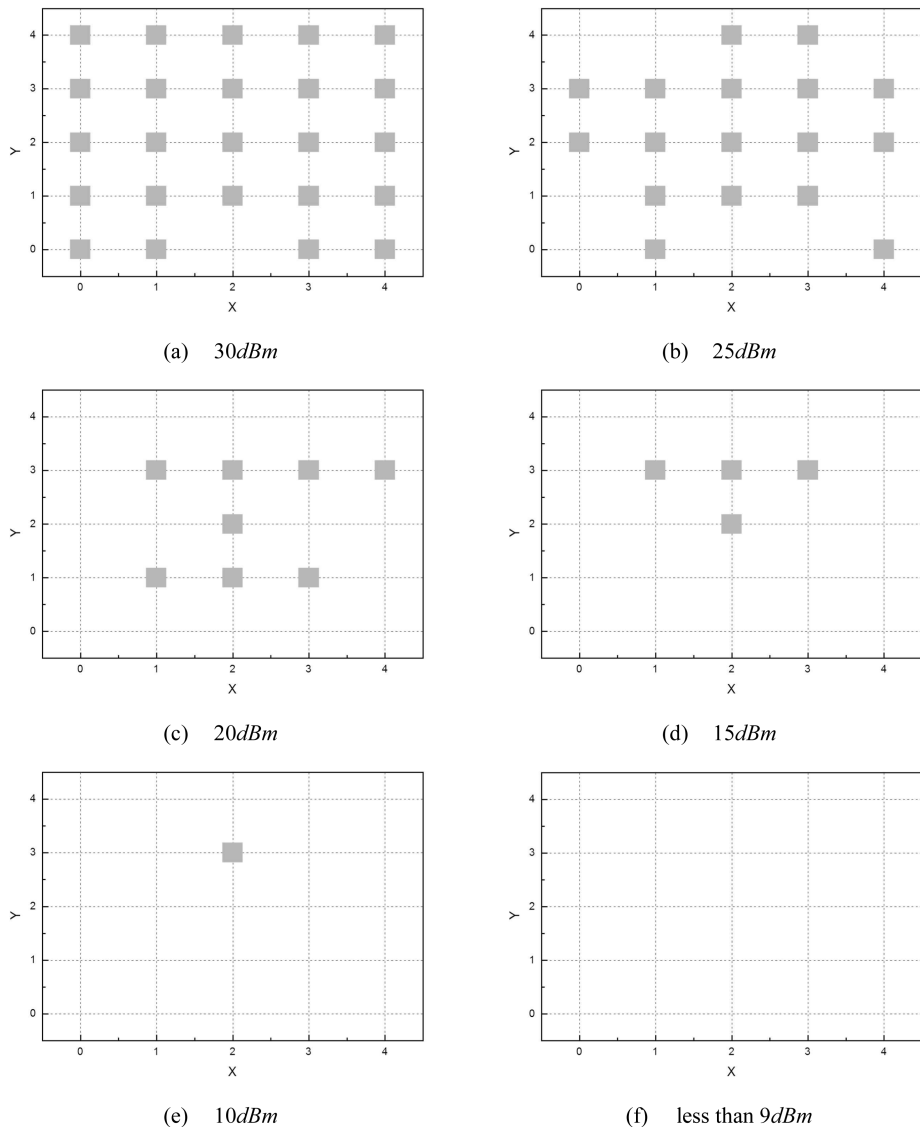


Fig. 6. Patterns of recognized tags in accordance with RF power

3.3.3 Location Estimate

Location estimation was made by using positional information from recognized tags, and we calculated the distance errors from real locations and estimated locations of the antenna. The results are shown in Table 1; as the value of power output increases, the value of distance error decreases and vice versa.

Table 1. The distance error of real and estimation position

RF power (dBm)	min-max		mean	
	Coordinate	Real	Coordinate	Real
	space	space(cm)	space	space(cm)
30	0.000	0.000	0.083	2.490
25	0.000	0.000	0.166	4.980
20	0.500	15.000	0.279	8.370
15	0.500	15.000	0.750	22.500
10	1.000	30.000	1.000	30.000

Table 2. Reductions (%) of the error of a distance by RF power

	10dBm	15dBm	20dBm	25dBm	30dBm
min-max	0.000	50.000	50.000	100.000	100.000
mean	0.000	25.000	72.050	74.503	100.000

Table 2 shows reduction rates of distance errors by the values of RF power. In 10dBm , the distance error was set as a standard of comparison among the reduction rates. As a result of the comparison, the distance error in 30dBm which was calculated from min-max operation and mean operation decreased at a rate of 100%. As a final result, when tags are recognized at most with the maximum output, the real position is closer to the estimated position; that is, the distance error decreases at the maximum output and the distance error at the maximum is the lowest value comparing to other distance errors at different values of RF outputs.

4 Conclusion and Future Work

In this paper, we estimated location recognition of tags with RF power control. When the maximum output was provided, the most tags were recognized, and the margin of error was the lowest in the environment. However, no ideal pattern of recognized tags was found in the experiment as it was affected by surrounding environmental elements and characteristics of an antenna or tags. The experiment was conducted with an antenna placed in the center of tags, which was at (2, 2) point; however, in each edge, there was a large margin of error because of constraints of tags in spite of the maximum power to recognize the most tags. In the case, the more accurate recognition can be realized with the lower value of power, and further improvements and researches will be necessary in the future.

Acknowledgements. This research was supported by a grant from the Construction Technology Innovation Program (CTIP) (No. 10CCTI-A050948-04) funded by the Ministry of Land, Transportation and Maritime Affairs (MLTM) of the Korean government, Basic Science Research Program Through the National Research Foundation of Korea (NRF) funded by the Ministry of Education, Science and

Technology (No. 2012R1A1A2043822), and the Technology Innovation Program of the Knowledge economy (No. 10041834) funded by the Ministry of Knowledge Economy(MKE, Korea)

References

1. Borenstein, J.: Mobile Robot Positioning Sensors and Techniques. *Journal of Robotic Systems*. Special Issue on Mobile Robots 14(4), 231–249 (1997)
2. LeBlanc, K., Saffiotti, A.: Cooperative Anchoring in Heterogeneous Multi-Robot Systems. In: *IEEE International Conference on Robotics and Automation*, Pasadena, CA, USA (May 2008)
3. Jia, S., Yang, H., Xiuzhi, L., Fu, W.: LRF-Based Data Processing Algorithm for Map Building of mobile robot. In: *International Congerence on Information and Automation*, Harbin, China (2010)
4. Oh, H., Won, D., Huh, S., Park, B., Shim, D.H., Tahk, M.: Indoor UAV Pose Estimation from Multicamera System Using EKF. In: *2nd International Symposium on Unmanned Aerial Vehicles*, Reno, Nevada (2009)
5. Kang, S.H., Kim, Y.H., Lee, E.J., Lee, S.G., Min, B.C., An, J., Kim, D.H.: Implementation of Smart Floor for Multi-Robot System. In: *Conference on Automation, Robotics and Applications*, New Zealand, December 6-8 (2011)
6. Choi, B.S., Lee, J.W., Lee, J.J.: Localization and map- building of mobile robot based on RFID sensor fusion system. In: *Conference on Industrial Informatics*, Daejeon, Korea, July 13-16 (2008)
7. Choi, B.S., Lee, J.M.: An Efficient Localization of Mobile Robot in RFID Sensor Space. *Journal of Control, Automation, and systems Engineering* 12(1) (January 2006)
8. Lim, H.S., Choi, S.Y., Lee, J.M.: An Efficient Localization Algorithm for Mobile Robotsin RFID Sensor Space. *Journal of Control, Automation, and Systems Engineering* 13(10) (October 2007)
9. Choi, B.S., Lee, J.W., Lee, J.J.: An Improved Localization System with RFID Technology for a Mobile Robot. *Industrial Electronics* (2008)
10. Johansson, R., Saffiotti, A.: Navigating by Stigmergy: A Realization on an RFID Floor for Minimalistic Robots. In: *2009 IEEE International Conference on Robotics and Automation*, Japan, May 12-17 (2009)
11. Kim, H.: User-centered approach to path planning of cleaning robots: analyzing user's cleaning behavior. In: *Conference on Human-Robot Interaction*, New York, USA (2007)
12. Kim, M., Chong, N.Y.: Direction Sensing RFID Reader for Mobile Robot Navigation. *IEEE Transactions on Automation Science and Engineering* 6(1) (January 2009)
13. Lee, E.K., Yoo, Y.M., Park, C.G.: Installation and Evaluation of RFID Readers on Moving Vehicles. In: *Proceedings of the Sixth ACM International Workshop on Vehicul Ar. Inter. Networking*, NY, USA (2009)
14. Nam, S.Y., Kim, D.H.: Evaluation of RFID System for Location Based Services in the Building. *Journal of IEEK* 48(1) (2011)

An Islands-of-Fitness Compact Genetic Algorithm Approach to Improving Learning Time in Swarms of Flapping-Wing Micro Air Vehicles

John C. Gallagher

Dept. of Computer Science and Engineering
Wright State University
Dayton, OH 45435, USA
john.gallagher@wright.edu

Abstract. Insect-Scale Flapping-Wing Micro-Air Vehicles (FW-MAVs) may be particularly sensitive to degradation of pose and position control caused by ongoing or pre-existing damage to the airframes. Previous work demonstrated that in-flight recovery of sufficient pose and position control precision via use of an adaptive oscillator component inside traditional SISO controllers. This work will replace previously used oscillator learning algorithms with a hyperplane sampling Evolutionary Algorithm (EA) that employs cross-vehicle islands-of-fitness. It will be demonstrated that this strategy allows swarms of vehicles to cooperatively, and more quickly, find and correct for simulate manufacturing errors that appear in all vehicles – even in the presence of randomized vehicle specific errors that are not common to all vehicles in the swarm. The paper will present specific simulation results demonstrating efficacy of this scheme and discussion of future applications of islands-of-fitness methods in this problem domain.

Keywords: Flapping-Wing Micro Air Vehicle, Evolvable and Adaptive Hardware, Evolutionary Algorithms.

1 Introduction

The first uncontrolled flight of an insect-scale flapping-wing vehicle [1] has triggered significant interest in developing flight control methods for this specific class of winged insect-scale airframes [2] [3] [4]. The controllers function by constructing a model that relates wing motion shape parameters to torques and forces applied to the body. Inverting that model, one obtains a desired force/torque to wing beat shape parameter mapping that, when combined with a conventional error correcting flight controller, can command wing motions to continuously correct vehicle position and pose errors. Vehicles at insect-size scales, however, seem particularly susceptible to pose and position control errors even for relatively small damage to wings and airframes. For example, altitude errors of up to ten times the height of the vehicle are possible for even fairly light damage [5]. In response to this, there has been some initial work in modifying those controllers with adaptive hardware to enable recovery

of control precision in the face of airframe damage suffered in service or due to fabrication faults [5] –[8]. Although these initial explorations were effective, in-service adaptation of flight controllers entail several challenges. Samples of controller efficacy, for example, collected during normal service are potentially deceptive due to a number of factors, including unexpected physical perturbations and ordering effects due to necessary serialization of measurements. In the past, we have dealt with these issues through judicious oversampling of candidates (I.E. relying on more than one measurement). In this work, we will consider implicit parallelization of controller evaluations across swarms of vehicles. Although the work reported here does represent an application of oversampling, here we will use it to address a different problem, that of speeding the acquisition of quality controllers by exploiting vehicle damage types common across the swarm. Such damage could happen due to common fabrication faults across a production run or due to extended exposure to some environmental condition that degrades each airframe similarly. This paper will outline the specifics of the problem to be addressed, discuss the techniques employed, and provide experimental evidence that the techniques are effective for these vehicles. The paper will conclude with discussion of additional future work that can exploit the lessons learned for attacking other practical difficulties that remain.

2 Background

2.1 Vehicle and Basic Controller Description

This work employs a variant of the Harvard RoboFly [1] with one piezoelectric actuator per wing instead replacing the single effector that drives both wings. The basic wing motion can be best described relative to the top view component of Figure 1. The 15mm lines extending from each side of the body in the top view represent wing span spars that can be independently moved to angles ϕ_L and ϕ_R for the left and right wings respectively. The triangular wing planforms (see the front view in lower left hand part of Figure 1) hang down from the support spars to which they are passively hinged. As the wing spars stroke forward and backward, dynamic air pressure lifts the triangular plan forms to an angle α under the plane of the spars (see the side view in the lower right hand part of Figure 1). The moving wings produce lift and drag forces that one can resolve into net body forces and torques using the kinematics and dynamics models derived in related work [2]. We presume that the wings can be excited independently and that position control of the wingtips is possible.

Vehicles of this type under the given assumptions can be controlled in a *cycle-averaged* manner. That is, one creates a family of whole wing beat cycle wing shape motions parameterized by a small number of shape parameters and creates a model that relates those motions to average force and torque produced over the course of the whole wing beat. One can employ standard error feedback controllers to determine desired whole body forces and torques, then select wing motions that produce those forces and torques over the course of a whole wing beat. In split-cycle control, each wing is provided a wing beat frequency and a waveform shape parameter at the beginning of its wing stroke. In the current generation of controllers, the wing motion

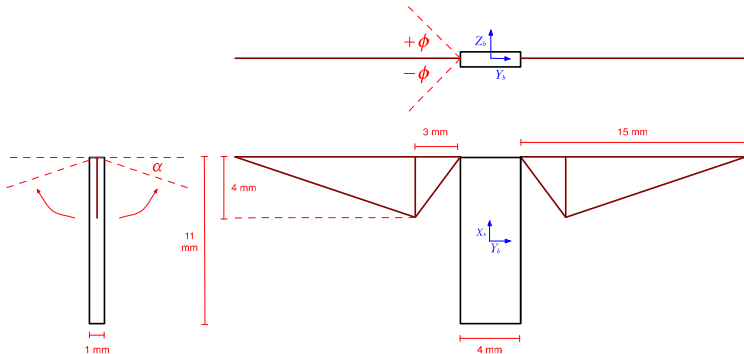


Fig. 1. Orthographic View of Insect-Scale Flapping-Wing Vehicle

envelopes are defined by a split-cycle cosine wave in which the upstroke phase (motion from +1 to -1 radians) is a cosine whose frequency is impeded or advanced by an amount δ rad/sec, and whose down stroke phase (motion from -1 radians back to 1 radian) is governed by a cosine that is impeded or advanced so that it reaches 1 radian at the same time it would have if it had been driven by a nominal cosine with the base frequency. Using blade element analysis, it is possible to relate wing beat cycle-averaged body forces and torques to wing frequency and shape parameter. Corrections to any aspect of body pose or position can be made by a SISO control law that computes desired body force or torque followed by a mapping of the desired force or torque to wing shape parameters, which are given to the appropriate wing for the next wing beat.

In this work, we will consider only the control of altitude. Under this restriction, the split-cycle parameter δ is always set to zero, meaning that we control wing frequency only. Also, under this restriction, both wings beat at the same frequency. On a cycle-averaged basis, all vehicle forces and torques, save for a single component of force upward around the spine of the vehicle, cancel. The effect is not dissimilar to a human treading water. A controller that combines basic altitude error feedback control and the cycle-averaged control concept is given in Figure 2.

2.2 Adaptive Oscillator Controller Concept

In this and previous work, the oscillator component of the ACTC (Fig.2) was replaced with an Evolvable and Adaptive Hardware (EAH) [9] oscillator that learns new wing motion schedules that restore the appropriate relationships between commands issued by the ACTC and cycle-averaged forces and torques applied by the wings to the body. The adaptive oscillator maintains an internal library of pre-computed wing motion basis functions, eight of which are averaged for each wing to produce the specific wing motions taken by each of the wings. Machine learning, in previous work a stochastic hill climber [5] – [8] and in this work a modified Genetic Algorithm, is used to combine basis functions to enable near-optimal control for specific vehicles

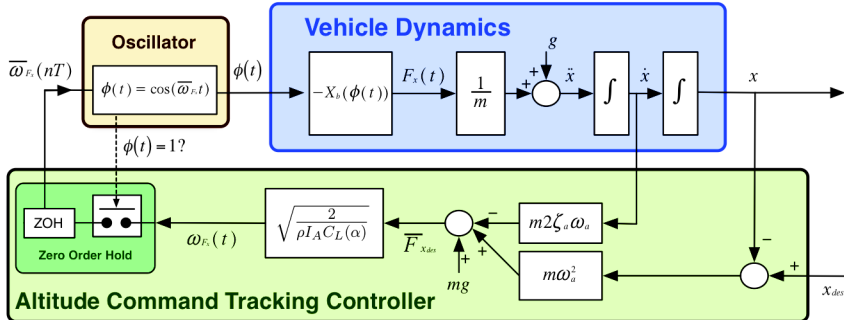


Fig. 2. Altitude Command Tracking Controller

damaged in service or suffering from manufacturing flaws in the wings. In all cases, both the basis functions mixed and the learning algorithm were designed to minimize the amount of digital components required for implementation and to limit the number of computational cycles required to achieve learning. A reference implementation of the required hardware can be found in previous work [6] and a simplified schematic of the adaptive oscillator is provided in Fig. 3. The shown adaptive oscillator is a drop-in replacement for the oscillator component shown in the top left part of Fig. 2.

Previous work used the MAV_MINIPOP algorithm [6] as the learning engine. MAV_MINIPOP, once every one hundred wing flaps, received a measure of desired and actual vehicle altitude and used this as an objective function to decide how to mix basis functions to produce unique left and right wing motion functions. Internally, each of the two wing motion functions was stored as an eight-element integer coded vector where each integer was index into a table of pre-computed wing positions. The combined 16-element index vector was learned and modified by the MAV_MINIPOP algorithm. During operation, the oscillator uses the 16-element index vector by a digital timer advances though one of 256 time steps and adjusts each wing's position to the average of the eight basis function values associated with that wing.

Previous work exercised MAV_MINIPOP by conducting learning trials on simulated vehicles in constrained hover and with random damage applied to the two wings. Wings were damaged so that they randomly produced anywhere from 75% to 100% of expected lift during a wing flap. This range is actually a superset of situations one would expect to observe in practice and was chosen on the assumption that an ability to recover proper flight behavior in the extended case would demonstrate that recovery was possible in what are presumably less difficult conditions in reality. MAV_MINIPOP has been observed to be able to recover altitude precision of less than 0.001 M in less than ten minutes flight time on average.

3 Islands-of-Fitness and FW-MAV Swarms

3.1 Motivation

In-flight controller adaptation is, naturally, fraught with difficulties. Among them is the relative dearth of controller assessments available to any learning algorithm. Since learning is being done in normal service, one does not have the luxury of landing the vehicle and conducting evaluations in laboratory conditions. Therefore, it is critical that one extract the maximum amount of useful information from each evaluation.

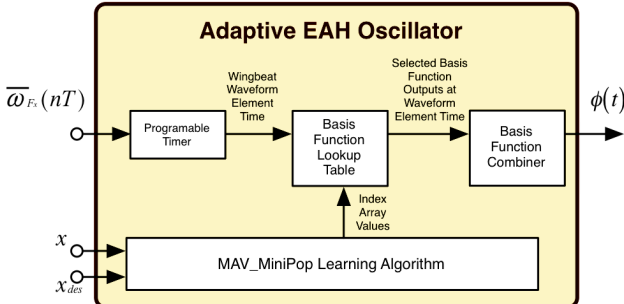


Fig. 3. Adaptive Oscillator Schematic

Consider a situation in which vehicles contain two types of physical faults. The first type are those common to all vehicles in a fabrication run and would be introduced due to some systematic flaw in a manufacturing process. The second type are those unique to each vehicle and would be introduced due to some variation in service conditions. Controller evaluations made on any vehicle containing the same type one fault would possess information potentially useful to other vehicles with that same type one fault. Methods to exploit that information, especially when confounded by type two faults, are not immediately clear.

3.2 Compact Genetic Algorithm and Islands of Fitness Modifications

In this work, the MAV-MINIPOP learning algorithm will be replaced with MAV_ICGA, which is a modification of the existing Compact Genetic Algorithm (CGA) [10]. CGA was chosen as a base because it is efficient to implement in digital hardware [11][12] and represents a fundamentally different kind of search than MAV_MINIPOP (hyperplane sampler as opposed to a stochastic hill climber). Islands-of-Fitness models maintain sub-populations of solutions that occasionally supply immigrants into other sub-populations [13]. In this work, each FW-MAV vehicle will maintain a single MAV_ICGA population and form a single island of fitness. On a random basis, each vehicle will occasionally broadcast its current champion genome (oscillator index vector). This will serve as an immigrant into all other vehicles in the swarm. Additionally, elitism is implemented by retaining the champion of the previous CGA tournament as a participant in the next tournament.

The other participant in each tournament is generated from a CGA simulated population in the conventional manner. As done in previous work, the current champion oscillator is allowed to control the vehicle without being evaluated for a user selectable period of time before true candidates are evaluated. This is done to minimize the effects of deceptive evaluations due to serialized evaluations of novel, and possibly bad, candidates. Also, in MAV_ICGA, each vehicle has a small chance of broadcasting its current champion. Upon broadcast, all other vehicles in the swarm import the 16-element vector and enter it as the challenger in the next available tournament inside itself. In this respect, each FW-MAV serves as an island-of-fitness with an independent population of search candidates. MAV_CGA is described in more detail in [14]. MAV_ICGA represents two trivial modifications to MAV_CGA, so readers are directed to that other work to expand upon operational and hardware details of the both algorithms.

3.3 Experimental Setup and Results

In this work, we are controlling simulated vehicles in constrained hover using the ACTC of Fig. 2. Every vehicle shares a common type one error in which the right wing can only travel to 75% of its full backward extension (this simulates a fabrication fault where the wing's travel distance is incorrect). In addition, each individual vehicle has a unique type two error of a random degradation of force and drag produced in each wing of up to 10%. This fault roughly simulated random damage to wing membranes and is unique to each vehicle. All results reported are based on 250 separate simulations of four-vehicle swarms each attempting to optimize performance using MAV_ICGA. In each vehicle, the CGA population size was 16384. CGA and its variants simulate a simple genetic algorithm with uniform crossover and no mutation. MAV_ICGA inherits these properties, therefore no crossover or mutation rates are reported.

Table 1. Flight Time Required to Achieve Hover Error < 0.001 meters. Columns represent different rates of immigrant broadcasts among members of the four-vehicle swarms.

	0.00%	6.25%	12.5%
01% Maximum Type II Damage	3.20	1.82	1.97
05% Maximum Type II Damage	3.75	3.11	3.67
10% Maximum Type II Damage	5.36	4.48	5.27

Six sets of 250 runs were performed under the conditions of immigrant rates of 0%, 6.25%, and 12.5% and type 2 wing errors randomly selected in the ranges of [0%..1%], [0%..95%], and [0%..90%]. All vehicle experiments were allowed to run to CGA convergence or 250,000 wing flaps, whichever came first.

Table 1 shows the average flight time required to achieve hover performance with an error of less than 1mm. The 0.00% column represents the performance of CGA with elitism and no immigrants among vehicles. Note that in both cases where immigrants were allowed (at levels of 6.25% and 12.5%) average time to achieve sub-

millimeter precision were better. The 6.25% level is considered superior due to fewer inappropriate immigrants being broadcast. The collected data seems to suggest that the islands-of-fitness modification does produce faster acquisition of quality controllers in broken vehicles.

Of additional interest is the average performance of the vehicle until the emergence of acceptable control. Table 2 provides the online errors corresponding to each of the experiment groups in Table 1. Online error is defined as the average vehicle position error from time zero up until the time that an acceptable controller (defined as a controller with less than 0.001 meters of position error) emerged. Note that this error measurement is calculated for all moments of flight, even those not explicitly measured by the MAV-ICGA algorithm. Note also that it includes the effects of candidate controllers that, being randomly selected from an early un-converged population, might not be of particularly high quality. We can see that, on average, the vehicle is no more than 2.5 cm from its intended target at any time during its learning flights. It should also be noted that none of the 9000 vehicle controllers evolved in any of the six reported experiments suffered a catastrophic control failure.

Table 2. Average Online Error Until Error < 0.001 meters. Columns represent different rates of immigrant broadcasts among members of the four-vehicle swarms.

	0.00%	6.25%	12.5%
01% Maximum Type II Damage	0.022	0.022	0.021
05% Maximum Type II Damage	0.023	0.023	0.021
10% Maximum Type II Damage	0.024	0.023	0.022

4 Conclusion

In this paper, we demonstrated the basic efficacy of both a hyperplane sampling EA and an Islands-of-Fitness modification for improving the learning time of adaptive oscillators for swarms of flapping-wing micro-air vehicles. Two lessons are particularly salient. First, even without the islands-of-fitness based swarm learning, it appears that the modified CGA acquired solutions more quickly than previously used stochastic hill climbers. Although this observation is exciting, more study of the relative merits of the two approaches is still required before declaring one approach or the other superior. Second, and perhaps more surprisingly, this relatively simple immigrant method seems able to disambiguate the contributions of type one and type two errors and significantly shorten the time required to acquire good control solutions. This is true even in the relatively difficult conditions of 10% maximum type two damage. It also seems true that the addition of immigrants does not severely impact online error and we have not triggered vehicle crashes. Although more comprehensive parameter sweeps and the inclusion of parameter adaption modifications to MAV-ICGA are ahead, this work seems to strongly suggest that islands-of-fitness in the context of a CGA adaptation engine positively impacts performance in this, and possibly related, problems.

Acknowledgements. This material is based upon work supported by the National Science Foundation under Grant No. CNS-1239196.

References

1. Wood, R.: The first takeoff of a biologically-inspired at-scale robotic insect. *IEEE Trans. on Robotics* 24(11), 341–347 (2008)
2. Doman, D., Oppenheimer, M., Sigthorsson, D.: Dynamics and control of a minimally actuated biomimetic vehicle: part I – aerodynamic model. In: Proceedings of the AIAA Guidance, Navigation, and Control Conference (2009)
3. Oppenheimer, M., Doman, D., Sigthorsson, D.: Dynamics and control of a minimally actuated biomimetic vehicle: part II – control. In: Proceedings of the AIAA Guidance, Navigation, and Control Conference (2009)
4. Doman, D., Oppenheimer, M., Bolender, M., Sigthorsson, D.: Altitude control of a single degree of freedom flapping wing micro air vehicle. In: Proceedings of the AIAA Guidance, Navigation, and Control Conference (2009)
5. Gallagher, J., Doman, D., Oppenheimer, M.: Practical in-flight altitude control learning in a flapping-wing micro air vehicle (submitted)
6. Gallagher, J., Oppenheimer, M.: An improved evolvable oscillator for all flight mode control of an insect-scale flapping-wing micro air vehicle. In: Proceedings of the 2011 IEEE Congress on Evolutionary Computation (2011)
7. Gallagher, J., Oppenheimer, M.: Cross-layer learning in an evolvable oscillator for in-flight control adaptation of a flapping-wing micro air vehicle. In: The 45th Asilomar Conference on Signals, Systems, and Computers (2011)
8. Gallagher, J., Doman, D., Oppenheimer, M.: The technology of the gaps: an evolvable hardware synthesized oscillator for the control of a flapping-wing micro air vehicle. *IEEE Trans. on Evolutionary Computation* (in press)
9. Greenwood, G., Tyrrell, A.: *Introduction to Evolvable Hardware: A Practical Guide for Designing Self-Adaptive Systems*. IEEE Press (2005)
10. Harik, G., Lobo, F., Goldberg, D.: The compact genetic algorithm. *IEEE Transactions on Evolutionary Computation* 2(2), 287–297 (1999)
11. Aporntewan, C., Chongistivatana, P.: A hardware implementation of the compact genetic algorithm. In: Proc. of the 2001 Congress on Evolutionary Computation, pp. 624–629 (2001)
12. Gallagher, J., Vigraham, S., Kramer, G.: A family of compact genetic algorithms for intrinsic evolvable hardware. *IEEE Transactions on Evolutionary Computation* 8(2), 111–126 (2004)
13. Cohoon, J., Hedge, S., Martin, W., Richards, D.: Punctuated equilibria: a parallel genetic algorithm. In: Proc. of the 2nd International Conference on Genetic Algorithms and Their Applications (1987)
14. Timmerman, K., Gallagher, J.: A hardware compact genetic algorithm adaptive oscillator for hover improvement in an insect-scale flapping-wing micro air vehicle. In: Proc. of the National Aerospace and Electronics Conference (2012)

A Collision Control Strategy for Multiple Moving Robots

Pejman Kamkarian and Henry Hexmoor

Electrical and Computer Engineering Department, Southern Illinois University,
Carbondale, IL 62901, USA

Computer Science Department, Southern Illinois University, Carbondale, IL 62901, USA
pejman@siu.edu, hexmoor@cs.siu.edu

Abstract. We present a solution to prevent collisions among robots that are moving toward their respective goals. A robot may start moving at any time from its station to its goal. For a moving robot, the probability of conflict increases proportionately to the complexity of other robots' respective routes. In terms of lowering possibilities of collision, a proper strategy for controlling robot behaviors before encounters is essential. Prior research presented a negotiation-based solution through a broadcasting method. In our solution, we assume robots are unable or unwilling to negotiate or broadcast data among one another. They should possess a strategy to detect and predict conflict zones, and hence determine strategies to avoid collisions independently.

Keywords: Moving Robots, Robot Collision Control.

1 Introduction

Imagine a factory floor with hundreds of unmanned guided vehicles rushing to complete tasks at disparate but route-crossing destinations. Similarly, on a busy street in a major metropolitan city like NYC, people mitigate collisions by the rapid uptake of others' trajectories (i.e., intention inferencing) as well as instantaneous velocity adjustments. People either mutually accommodate one another by modifying their own trajectory or select strategies from a predetermined set of conventions that minimize collisions. Negotiated trajectory adjustments for multirobots is one possible solution as found in [7]. The majority of negotiations in a multi-robot environment operate in multiphases where each robot shares a trajectory with all other robots operating in the common workspace. Motion planning methods provide mechanisms to detect potential collisions. In order to detect collisions, robots preplan the paths each robot will follow together with the associated trajectories along these paths. Straight line paths have been reported with advantages for multi-robot systems [1]. Another approach to multirobotic collision avoidance is found in [10]. Founded on A* algorithm, M* can be proven to find an optimal path in finite time. In this paper we offer an alternative solution. Section 2 provides our basic assumptions and section 3 defines a collision zone. Section 4 outlines a multiphase reasoning whereas section 5 describes validation on specific cases. Conclusions are drawn in section 6.

2 Concepts and Premises

In order to develop our strategy, we made following five main assumptions.

(1) As a typical mobile robot system, we assumed a set of four co-located robots, which are located at the different four corners of a room. Each robot A_i has a separate destination assigned to it, which is located on the opposing perimeter of the room. Each robot independently operates on its task. There is no goal sharing among robots. Each destination cannot be assigned to more than one robot at a time. At each moment, the status for a robot is given by $A_i = \{P_i, V_i, \partial_i\}$, where P_i is the priority rate, V_i is the velocity at moment t , and ∂_i is the current direction of robot i . The priority rates vary for each destination and will be determined based on the local status of the tasks, goals, and robot circumstances. Initially, it can be a randomly assigned number to each robot. It can be as a rate based on the robot ability or task urgency for each robot. ∂_i is the destination i and direction to it.

(2) All robots are circular in shape and all robots to have same size [2], [5], [9]. For simplicity, robots can only move forward in a straight line. They are unable to move backwards or turn.

(3) Each robot will have a different trajectory to move towards its goal location. For example, robots will have a constant speed without stops before reaching their goals.

(4) Robots may or may not be able to directly communicate with one another. Broadcasting information is used by many multi robot systems such as [2] and [5]. Since our solution is a non-communication approach we are not focusing on the broadcasting data. Our robots are unable to share information.

(5) Each robot is equipped with a vision sensor, which enables them to detect other robots within a fixed distance. The sensor is located in front (i.e., the moving direction). Vision is used in many applications such as optical motion planning mapping [6], [8], or the motion sensors themselves [4], [3], [11].

3 Collision Zone

Since each agent is equipped with a vision sensor, it is able to detect objects in a certain range. Each agent is represented by a set of specifications as it denoted by $A_i = (S_i, R_i, D_i)_t$, where S_i represents speed of the i^{th} agent, R_i captures the maximum detection range, and D_i indicates direction of the relevant agent, at timet. In figure 1, we assumed two moving agents that encounter a collision zone.

By definition, a collision zone is formed when more than a single agent, which is moving toward its goal, detects and recognizes another moving agent. A collision incident will be considered by moving agents that detect collision zones and hence need to perform evaluation and decision for preventing collisions. Our strategy specifies a complete halt (i.e., full stop) for moving agents until the risk of collision expires. For simplicity, all moving agents have the same speed and hence take the

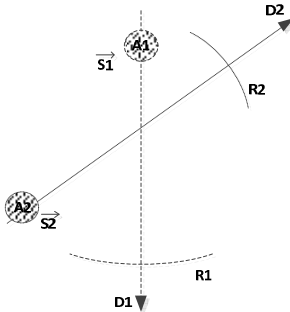


Fig. 1. Two moving agents in a collision zone

same time to perform a full stop. However, in the real world, we will have different types of moving agents with different speeds. A faster speed means a greater distance to travel before a complete stop. Based on that, we considered a direct relationship between decision making when confronting a collision zone and velocity, reaction time, and stopping mechanism, as follows. $DM_i \propto (\alpha, \beta, \gamma)_i$. α represents robot speed, β is the reaction time, and γ denotes the stopping mechanism for the i^{th} moving agent. In order to adjust the reaction time we need to consider the processor in the agent, which leads us to focus on the mechanical properties. The velocity may vary based on the objective of the agent and the environmental specifications.

4 A Two Phase Solution of Collision Prevention

The main consideration of this paper is to develop a strategy that is able to control moving agents toward their goals with potential risks of collision. Each agent is in either one of three conditions at any time.

- (i) Waiting status, which indicates the agent either will not begin to move from the start, or is already dwelling in a collision zone and is waiting for the agents with higher priority to vacate the zone,
- (ii) Moving status represents that the agent is either free of collision zones or located in a collision zone but is permitted to continue moving toward its goal due to its priority that is higher than others in the zone,
- (iii) Has reached its goal and hence removes itself from consideration.

The collision zone specifications, as well as conditions for entering to decision phase, are already discussed. In the remainder of this section, we propose a two phase solution to avert collision among moving agents while they are in a collision zone. Decision making process consists of two separate processes of *detection* and *decision*. Each process is governed by its own rules and conditions and we will discuss them in more details next.

4.1 Detection

The aim of this phase is to determine collision zones for moving agents. As discussed earlier, each agent is equipped with a visual sensor. The agent detects moving agents when they are within detection range. The sensitivity of each sensor can vary based on the agent speed. The detection range must be long enough for a moving agent to stop in a reasonable amount of time before collision. Assume two agents $A_1, A_2 \in A_i$, detect one another while moving toward their goals with V_1 and V_2 indicating speeds respectively. If $V_1 > V_2$, which represents a higher speed for A_1 , the detection range R_1 , must increase enough to avoid collision.

4.2 Decision

A set of n robots enter a decision phase when they enter a collision zone. They have to decide which one is allowed to continue movement toward its goal while all others must stop and wait in the collision zone. Assume the set of n agents A_i , are present with a collision zone. Consider a flag with an identification value to represent the priority of that agent such that it is visible and hence can be detected using the vision sensor. The number is unique and reflects the robot urgencies for performing its task. At the beginning of the movement process priority is assigned and is determined by the following steps.

- (i) Priorities have to be comparable.
- (ii) They have to start based on their priorities.
- (iii) All values must be assigned to agents at the beginning of the general movements.
- (iv) Each priority remains the same until the task is completed.
- (v) The total number of agents are numbered from 1 to $|A| - 1$.

Each agent has a unique value and hence there is a set of n priorities at the beginning of movement process as follows: $P_i = \{P_1, P_2, \dots, P_n\}$, where P_n , is the priority of agent n^{th} agent. With a set of g agents in a collision zone, the priority set becomes $P_i = \{P_1, P_2, \dots, P_g\}$, where $(P_1, P_2, \dots, P_g) \in P_i$.

At each moment, an agent compares the set of priorities to recognize the agent with the highest priority. Once found, if the highest priority belongs to self, the robot will continue toward its goal unabated; otherwise, it stops until the condition of collision changes by either a new agent entering to the current zone or the highest priority agent leaves the zone. The process then continues and allows the next highest priority agent to move toward its goal.

5 Solution Algorithm and Experimental Results

In this section we illustrate our solution strategy in detail. Figure 2 presents a general flowchart of collision control strategy.

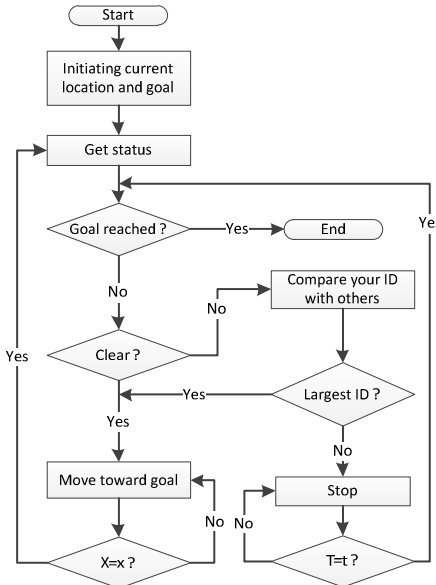


Fig. 2. General outline of collision control strategy in flowchart format

Once each robot is assigned a goal it becomes active and starts to move toward it. The process of movement continues until it reaches the goal. The mechanism of checking the status can be implemented by either distance or time measurements. In order to check status by distance, each active robot measures the status when passing a certain distance x . Active robots check the status when a certain time t has passed, if the checking status is based on the time. For simplicity, all robots may follow a single strategy for measuring status. However, in the real world they can follow different rules to measure status. Reasons are many folds. They can be made to perform different activities and goals. They can be made with different structures and speeds and hence need different times to reduce their velocities and to eventually stop. Each robot has a reference list of priorities for all other robots, at the beginning of movement process.

To implement our strategy we are assuming a two dimensional (2D) space where there are four different robots parked. We also assume that each goal is located at the center of each edge. The goals will randomly be assigned to each robot and hence they start moving toward them consequently. Figure 3 shows the indicated situation for robots and their goals.

We considered robot movements only inside the 2D space and hence each robot can accept only the goals that are not located on the same edge with them such that they can accept between either one of two goals. For simplicity, we also assume that the robots only can move toward a straight line and are not able to change their route while moving toward their goals. Goal assignment can be without restrictions, in terms of sharing. On the other hand, it is possible to assign the same goal to more than

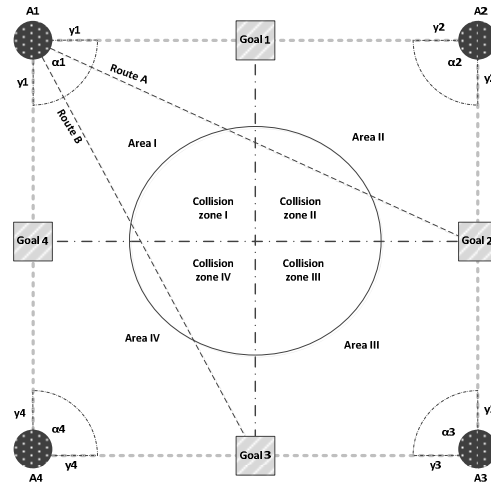


Fig. 3. 2D scope with 4 robots and 4 goals

one robot. Although in the real case, the proportion of numbers of robots and goals may vary in our space we assume the number of robots is the same as the number of goals. The space that each robot needs to pass before reaching goals is the same. However, the required time before reaching the goals vary and will be determined by the number of collision zones that leads them to be stopped and wait until detection status indicated a clear status.

We considered the following algorithm as our solution. However, they can vary in different situations and robot constructions. The algorithm is given next.

Algorithm 1. Collision avoidance algorithm

1. Initialize current location.
 2. Initialize goal location.
 3. Set your movement direction toward goal.
 4. Determine status from vision cameras.
 5. If status is clear then go to step 7; otherwise, go to step 9.
 6. If distance to the goal is negligibly small, stop.
 7. Move toward goal.
 8. If the traveled distance is x , then go to step 4; otherwise, go to step 7.
 9. Initialize other robots inside the common collision zone.
 10. Compare others' identifications with self.
 11. If self has the highest identification, then go to step 6; otherwise, go to step 12.
 12. Stop and count up wait time.
 13. If wait time reached t , then go to step 4.
-

The amount of needed time to perform a movement until reaching the desired goal will be larger when a larger number of robots with shared goals start to move toward their goals at the same time. To form our experimental analyses, we considered starting moving status, sharing goals conditions, as well as sharing areas probabilities. Figure 4 consists of three different series of experiments. The first series show the time diagram; when all robots start moving toward their goals at the same time, they do not share their goals with one another, and also none of them pass through other robot areas, during movement toward reaching its goal. In the second series, however, robots might pass through areas belonging to one other with a 50% chance. In other words, at least one robot from any other area will pass through any other robot area. Series three assumes each area will be occupied by at least two other robots during experiment. On the other hand, the probability of passing other robots through each area is 100%.

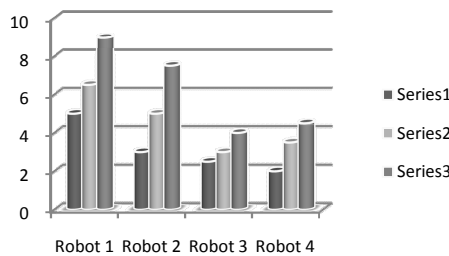


Fig. 4. Time diagram for robots when all robots start to move at the same time without sharing their goals and different situations for passing through one another's area

For the second round of experiments, we assumed goals to be shared by more than a single robot. Figure 5 consists of three different series of experiments. The first series show the time diagram. As all robots start moving toward their goals at a same time, they share their goals to one other; however, none of them pass through other robot areas, during movement toward reaching its goal. In the second series, however, robots might pass through areas belongs to one other with the 50% chance. In other words, at least one robot from any other area will pass through any other robot's area. Series three assumes each area will be occupied by at least two other robots during experiment. On the other hand, the probability of passing other robots through each area is 100%.

For the third round of our experiments, we assumed randomized scheduling time for the time that each robot starts moving toward its goal. Figure 6 consists of three different series of experiments. The first series show the time diagram when all robots start moving toward their goals in a random time. They do not share their goals with one other and also none of them pass through other robot areas, during movement toward reaching its goal. In the second series, however, robots might pass through areas belongs to one other with the 50% chance. In other words, at least one robot from any other area will pass through any other robot area. Series three assumes each area will be occupied by at least two other robots during experiment. On the other hand, the probability of passing other robots through each area is 100%.

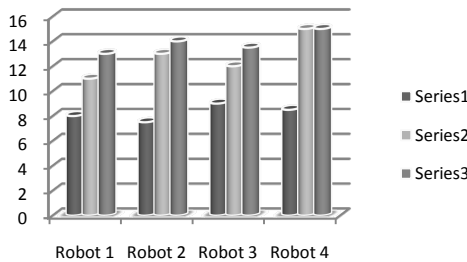


Fig. 5. Time diagram for robots, when all start to move at the same time, they occupy each goal with more than a single robot, and with different situations for passing through one another's area

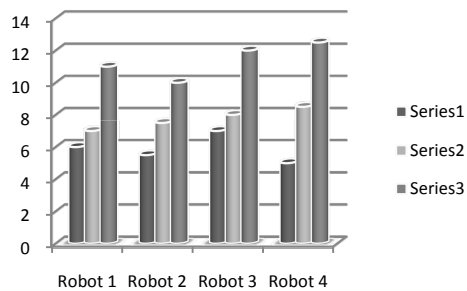


Fig. 6. Time diagram for robots when they start to move at random times without sharing their goals and with different situations for passing through one another's area

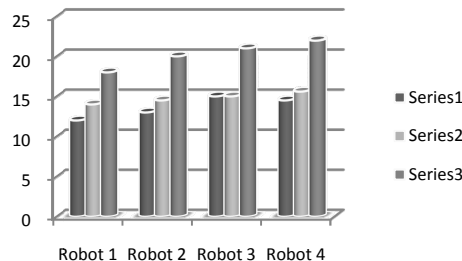


Fig. 7. Time diagram for robots, when they start moving at a random time, with sharing goals, and having different situations for passing through one other area

For the final round of experiments, we considered the robots to start moving at a random time and occupy each goal by more than a single robot. Figure 7 consists of three different series of experiments. The first series show the time diagram when all robots start moving toward their goals at a random time. The goals are shared between more than single robots. Also none of them pass through other robot areas, during movement toward reaching its goal. In the second series, however, robots might pass through areas

belonging to one another with the 50% chance. In other words, at least one robot from any other area will pass through another robot's area. We assumed for the third series that each area is occupied by at least two other robots during the experiment. On the other hand, the probability of passing other robots through each area is 100%.

6 Conclusion

This paper proposed a non-market based method to prevent multiple moving robots from collisions. Based on this strategy, the robots are able to decide how to avoid collision, without broadcasting data among them. This method is useful, when having different types of multiple moving robots that are not able to communicate with one another because of having some differences, such as different programmed or different type of usage. When a robot states that is in a conflict zone with many other robots, it compares its priority with all other robots in a same zone, and hence will decide how to perform a decision based on avoiding collision.

References

1. Calliess, J.D., Lyons, D., Hanebeck, U.D.: Lazy Auctions for Multi-robot Collision Avoidance and Motion Control under Uncertainty. In: AAMAS Workshops 2011, pp. 295–312. ACM Press (2011)
2. Clark, C.M., Rock, S.M., Latombe, J.C.: Motion planning for mobile robots using dynamic networks. In: Proc. IEEE Int. Conf. on Robotics and Automation (2003)
3. Expert, F., Viollet, S., Ruffier, F.: Outdoor field performances of insect-based visualmotion sensors. *Journal of Field Robotics* 28(4), 529–541 (2011)
4. Gaspar, J., Winters, N., Santos-Victor, J.: Vision-based Navigation and Environmental Representations with an Omni-directional Camera. *IEEE Transactions on Robotics and Automation* 16(6), 890–898 (2000)
5. Guo, Y., Parker, L.: A distributed and optimal motion planning approach for multiple mobile robots. In: Proc. IEEE Int. Conf. on Robotics and Automation, pp. 2612–2619 (2002)
6. Karaman, S., Frazzoli, E.: Sampling-based algorithms for optimal motion planning. *International Journal of Robotics Research* 30(7), 846–894 (2011)
7. Krishna, M., Chellappa, S., Hexmoor, H.: Reactive Navigation of Multiple Moving Agents by Collaborative Resolution of Conflicts. *Journal of Robotic Systems* 22(5), 249–269 (2005)
8. Mazzini, F., Kettler, D., Guerrero, J., Dubowsky, S.: Tactile Robotic Mapping of Unknown Surfaces. *IEEE Transactions on Instrumentation and Measurement With Application to Oil Wells* 60, 420–429 (2011)
9. Srivastava, P., Satish, S., Mitra, P.: A distributed fuzzy logic based n-body collision avoidance system. In: Proc. of the 4th Int. Symposium on Intelligent Robotic Systems, Bangalore, pp. 166–172 (1998)
10. Wagner, G., Choset, H.: M*: A Complete Multi robot Path Planning Algorithm with Performance Bounds. In: IEEE/RSJ International Conference on Intelligent Robots and Systems, pp. 3260–3267. IEEE Press (2011)
11. Zhang, L., Zhang, T., Wu, H., Borst, A., Uhnlenz, K.K.: Visual Flight Control of a Quadrotor Using Bioinspired Motion Detector. *International Journal of Navigation and Observation*, 9 (2012)

Communication for Task Completion with Heterogeneous Robots

Danielle Erickson¹, Max DeWees², John Lewis³, and Eric T. Matson⁴

¹ Dickinson College, Carlisle, Pennsylvania

² Embry-Riddle Aeronautical University, Daytona Beach, Florida

³ M2M Lab, Purdue University, West Lafayette, Indiana

⁴ RICE Research Center, Purdue University, West Lafayette, Indiana

`ericksond@ dickinson.edu, deweesm1@my.erau.edu,`

`ematson@ purdue.edu`

Abstract. The field of robotics and particularly the area of multiagent systems has been growing steadily. There is hope to one day have robots that not only interact with humans, but also interact among themselves. Before this goal can be reached, work must be done to create a system that promotes heterogeneous robotic agents and allows for change in the number and type of robots it commands. This paper presents a system that accomplishes this by taking vocal commands as input and relaying the commands to three robots of different builds by two different means of communication. The network is tested for accuracy of speech recognition and time response to the execution of commands.

Keywords: heterogenous robotics, multiagent robots, speech recognition, centralized robotic networks.

1 Introduction

Robots have traditionally been designed and used to function in a singular, isolated way for a specific task. However, in recent years the need for several robotic agents working together to achieve a common goal has become more necessary. A heterogeneous robotic network is made up of several different robots that potentially vary in design and functionality with differences in programming environments. Some robots may have differences or share similarities with others in physical appearance, hardware components, range of abilities, communication, and development. The applications of environment-agnostic robots can be beneficial when a task cannot feasibly or effectively be completed by one or more robots of the same type. Since each robot has inherent strengths and weaknesses, their abilities can be analyzed to determine the best way for a network of robots to carry out a job.

The purpose of this project is to create a network of heterogeneous robots capable of performing vocally administered tasks, meaning that an individual would be able to speak a command into a centralized control mechanism that will relay the command to the correct robot. The goal of this project is to be able to control various robots with spoken commands, regardless of design or communication protocol of the robot

and have the commands be executed by the correct robot each time. The system should have the capability to easily adapt to the addition or deletion of robots of same or differing types. This will require:

- A centralized control system
- One or more robots of similar or different types
- Speech-to-text software
- Well-defined tasks or commands
- Software to analyze the command once spoken
- A program to determine where to send the command and how to send it
- Communication protocol(s) to send the command to the correct robot

A system to communicate between robots should take full advantage of new robotic technologies [10]. These technologies may be model-based [6, 7] where the standard exchange of natural language communication comes from a common standard. The models may also be based on ontological structures [13] or structured as service oriented architectures [12]. The technology must also display some level of indistinguishability, where commands and queries are issued with no respect to the target, except for capability to complete the command or answer the query [8]. This can lead to a consciousness-based approach [11], which fits well if humans are in the organization or society [9].

2 Scenario

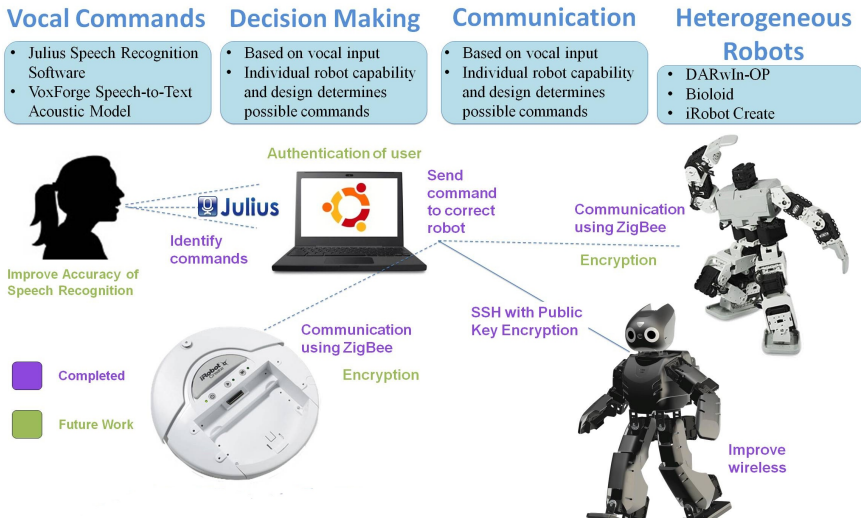


Fig. 1. Scenario of robot speech interaction

2.1 Components

This project utilizes three different robots for task execution: DARWIN-OP [1], Bioloid [2], and iRobot Create [3], as shown in Fig. 1. A computer acts as the

command center to accept, interpolate, and process the voice commands as well as send the commands to the correct agent. A summary of the components utilized by each robot follows:

DARwIn-OP [1]

- Biped Humanoid Robot
- Full Operating System: Currently running Ubuntu 10.04
- CM 730 microcontroller with 20 Dynamixel MX-28 servo motors for motion in elbows, hips, knees and ankles
- SSH capabilities for communication
- Camera for recognition of objects based on color hue
- Speakers
- Microphones (which can also be used as sensors)
- Currently developing actions as C++ programs which are precompiled and run on-demand

Bioloid [2]

- Biped Humanoid Robot
- No Operating System
- Robotis CM-510 microcontroller with Dynamixel AX-12A servo motors
- ZigBee ZIG-110A for communication
- Actions sent via ZigBee as low-level instructions on-demand

iRobot Create [3]

- Vehicular robot
- 10 built-in demo programs
- ZigBee ZIG-100 for communication
- Actions sent via ZigBee as low-level instructions on-demand

Computer (control center)

- Macbook Pro
- Ubuntu 10.04 running as a virtual machine
- Julius 4.2.1 [4] for Speech Recognition
- VoxForge HTK Acoustic Model [5], Build 726
- Bash script for decision-making process on how to send the commands and to which agent
- ZigBee ZIG-100 and SSH for communication to appropriate agent

2.2 Details

The commands are administered as a series of four words: the initiator, agent, preparatory command, and execution command. The initiator is simply a greeting used to initiate the command and serves to stand out from other speech in the environment. For example, the word "hello" was employed as the initiator during this experiment. The agent is an arbitrary name assigned to each robot to distinguish them from each other (DARwIn is "Harry," Bioloid is "Steve," and iRobot Create is "George"). The preparatory command is the first part of the action the robot should

perform, with the execution command being the second part (the parameter) of the command. For instance, the command could be “turn” with an execution of “left” or “right.” Examples of correctly formatted commands include:

“Hello Harry, stand up.”

“Hello George, move forward.”

“Hello Steve, turn left.”

It is important to note that this grammar system is user-defined and may vary for different implementations. For example, although no terminator term is used and is implicit, another implementation might find it necessary to include a defined word or phrase for termination. Furthermore, commands could be developed that use a variable number of words or call upon multiple agents.

Once the command is spoken, Julius Open-Source Speech Recognition [4] is used to interpret spoken words and convert them to text. To accomplish this, Julius is supplied with an acoustic model by VoxForge [5]. The vocabulary for the commands was manually written to fit these needs and is expandable depending on what functionality is desired. Because of the way the structure of the four-word phrase has been defined, each word is defined as being of a particular type (initiator, agent, preparatory command, or execution command) and by the phonemes used in the pronunciation of the word. Examples of the phonemes for several words in the grammar include:

“[HARRY] hh ae r iy”

“[STEP] s t eh p”

“[EXECUTE] eh k s ih k y uw t”

After the words were chosen and their appropriate phonemes were defined, the grammar must be built to allow the computer to interpret what is being said. A script is executed on the computer (control center) to see if a spoken command is correct and can be relayed to the correct robot. If any part of the command is incorrect or missing, the command is rejected. If the command is understood and can be sent to the robot, the script must then decide how to send the command to the appropriate robot.

Communication to DARwIn is achieved with secure shell (SSH) since DARwIn supports it with a complete Ubuntu environment. This can be set up either wired or wirelessly and utilizes Public Key Encryption to avoid the necessity of a password once the connection has been initiated.

For communication to the Bioloid and the iRobot Create, the ZigBee wireless protocol was used. ZigBee communication can be used in a “broadcast mode,” which means that the module attached to the computer issues the commands to all available modules. Although the commands are different for Bioloid and iRobot Create, if there are multiple robots of each type present in the network, all robots of a particular type will execute the command. In other words, if a command is sent to the Bioloid but multiple Bioloids exist in the network, they will all execute the command regardless

of the names given to each individual unit. This can be solved by masking the communication or using a form of Public Key Encryption implemented through hardware but this is outside the scope of this project. For the purposes of this project, there was no visible interference in sending each robot the commands every time. For example, if a command formatted for Bioloid was sent in broadcast mode to both robots, the iRobot Create simply ignored the command. This was true for the Bioloid as well in the case of commands being sent via broadcast mode to the iRobot Create.

3 Experiment

For all of the experiments, the constants include using a 15" MacBook Pro with a built-in microphone. The MacBook Pro was running Linux Ubuntu 10.04 through Virtualbox virtual machine. The dependent variables to be tested were the accuracy of the speech recognition software with the particular setup and the time it took for a command to be recognized, sent, and received by the robot.

3.1 Testing Procedure

To determine the accuracy of the voice recognition program, an experiment was devised to take into account the independent variables of the individual's sex, accent or vocal idiosyncrasies, and background noise level. In this experiment, the subjects spoke to the computer from roughly a foot away or from a natural distance. They were told to speak as naturally as possible as they read a list of 30 valid commands in random order. The commands were only converted from speech to text and not sent to the robots for testing purposes of this experiment.

To test the different ranges of the male and female voice, one male and one female each were instructed to complete five trials of reading the 30 commands. Both the male and the female subjects were Caucasian and were in their late teens to early twenties. Additionally, both subjects were from the United States and spoke with minimal accents.

To test the difference in background noise, the male and female participants began by completing five trials in a space within the academic laboratory that held a substantial amount of background noise. The second location chosen for trials was a room free of any background noise. The male and the female performed three trials each in the second location.

To determine if there were time differences when communicating with the three different robots, a stopwatch was used to record the time it took for a robot to react to or receive a command. To accomplish this, the stopwatch was started as soon as the command was finished and stopped once there was an indication that the robot had received the command. To accommodate for the possible human error involved in using a stopwatch, ten trials were completed with a list of 17 commands: 5 commands each to DARwIn-OP and Bioloid, and 7 to the iRobot Create. These commands when spoken by a Caucasian male were accurate 84% of the time. The commands were processed by the computer, which then determined if the command had the correct initiator and if the action requested existed for the agent of the desired name.

3.2 Results

In terms of accuracy, the male voice was more accurate than the female voice in a large majority of the trials, as shown in Fig. 2. More specifically, the male voice had a much greater accuracy in the area with background noise and a slightly greater accuracy in the quiet area. It was also noted that both the male and the female voices had lower accuracy rates in the quiet area than in the loud area.

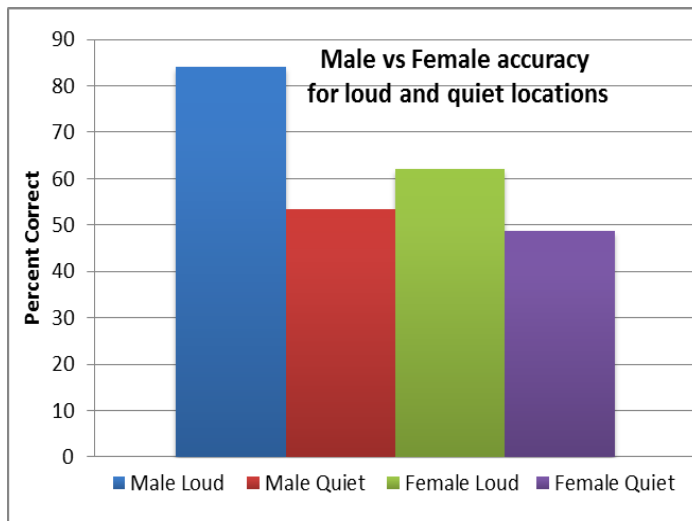


Fig. 2. Accuracy rating for both male and female voices in both a quiet environment and one where background noise was present

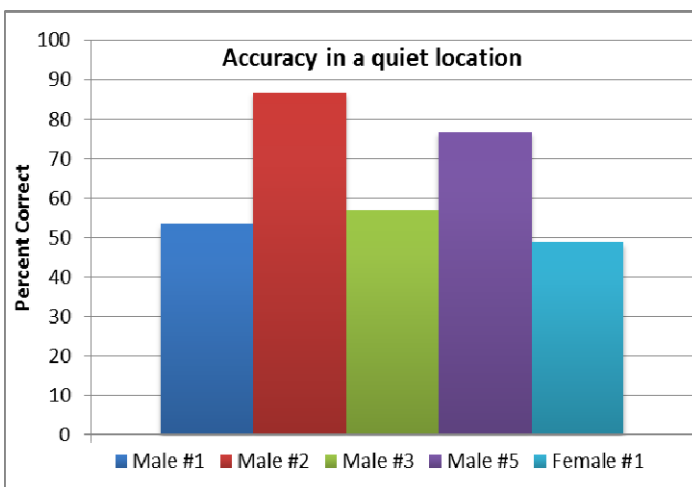


Fig. 3. Differences in accuracy ratings in a quiet environment among several people, both male and female

All of the trials with the male voice were more accurate than that of the female voice, even though there was a lot of variation amongst the male voices, as shown in Fig. 3. This is indicative that despite the possibility that there are some males with lower accuracy than some females, a male voice is more accurate overall with the voice recognition software and acoustic model utilized in this testing. To further support this hypothesis, more trials must be done with more male and female participants.

Certain combinations of words were mistaken for others quite often. For instance, fourteen out of fifteen times when an individual attempted to say “get mean,” the system identified his words as “kick mean.” This could be due to the formation of the phonemes in the grammar model or when using the acoustic model for recognition. If more emphasis was placed on the word “get,” the system would respond more accurately but caused the individual to not speak in a natural manner. Nevertheless, the selection of words for a command is important to achieve correct speech recognition.

For the time experiment, there was no clear correlation between type of command and time, but there was a correlation between robot and time. The average time it took for the Bioloid to process a command was significantly less than the average time for the other two robots. Additionally, the DARwIn-OP took more time on average to receive a command than the iRobot Create, as shown in Fig. 4.

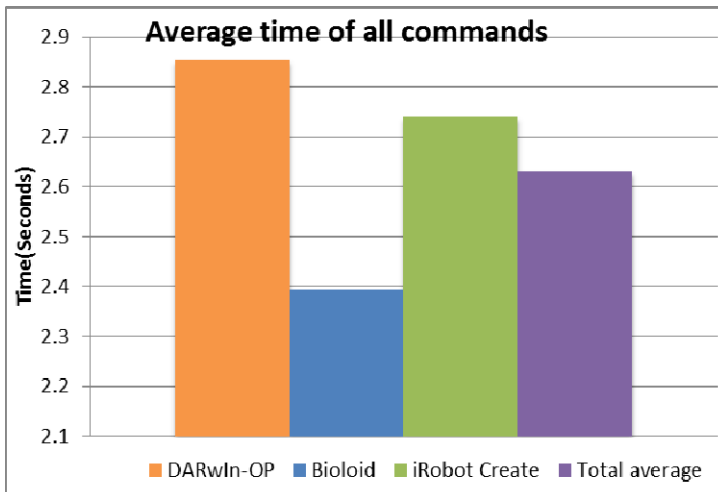


Fig. 4. Average time response for each robot from the time the command was spoken until the execution started

3.3 Analysis

The first trend that was noticed upon analyzing the results was that up to five seconds after the microphone was first turned on, the recorded sample did not sound like natural speech. To investigate this, audio recording software was used on the virtual

machine and it was found that the first few seconds of a recorded voice sounded distorted when played back. This phenomenon can most likely be attributed to the fact that the program was being run within a virtual machine hosted on the computer. The microphone itself was eliminated from suspect after it was tested using the recording software on the host machine. In this environment, the recording sounded completely natural from the beginning.

The difference in accuracy between the male and female voices can be attributed to the VoxForge acoustic model used for speech recognition. In the future, it would most likely benefit the accuracy to make and employ a custom acoustic model. As for the difference between the area with a large amount of background noise and the area with very limited background noise, the speakers having less accuracy in the quiet area was a surprising result. More trials are necessary to conclusively verify that this is the truth and not the result of error.

Regarding the command accuracy test, it must be mentioned that as they did more trials, the male and female speaker who completed 5 trials in each location began to recognize what inflections of their voice would help the system recognize their command. Because they became conscious of their speech in this sense, it is hard to have confidence in these trials. However, three of the male participants only did one trial each and still were not consistent throughout the list of 30 commands.

For the timed trials, it was interesting that Bioloid had faster average communication time than the other two robots. It was expected that, because the Bioloid and the iRobot Create shared a communication to via ZigBee, each command for these robots would take about the same time to be received. There is no current explanation besides human error as to why it took longer to communicate with the iRobot Create. However, it was expected that it would take longer to communicate with DARwIn-OP as the script used an SSH tunnel to navigate to an executable program on DARWIN-OP's internal computer each time a command was sent. This process is more time consuming than communication via ZigBee.

This experiment did have a large factor of human error. Because the ten trials were completed using a stopwatch, it is possible that the averages represented are not entirely accurate.

4 Future Work

After completing the experiments and building a system, a few issues were noticed. First, when sending a command via ZigBee, the communication is transmitted in a broadcast mode with all receiving parties accepting transmission. The process for initiate commands for Bioloid and iRobot Create are slightly different. However, if more than one Bioloid or iRobot Create were added to the network, both would execute commands sent out regardless of the names given in the spoken commands.

One way this issue could be resolved is through an implementation of a separate wireless transmission protocol. Otherwise, certain security measures could be employed, such as Public Key Encryption of the ZigBee communication. This would ensure that using multiple iRobot Create robots or multiple Bioloid robots, only the intended robot would receive the command and not all of the robots of that type.

Another avenue for improvement is full duplex communication for the agents and control. This would consist not only of communication from the computer to the robots, but also communication from the robots to the computer as well as inter-robot communication in a decentralized manner. This additional communication would allow the robots to cooperatively perform a common task. Ultimately, the robots in a given network could work together to combine their strengths (i.e. the iRobot Create could explore and build a map of a particular room and DARwIn-OP could then use the map to accomplish a task).

Further improvements are related to the limitations faced. These include using wireless on DARwIn-OP and using a central control system without the virtual machine. As mentioned previously in Section 3.3, there is work to be done in improving the accuracy of the voice recognition program. Much of this can be accomplished simply by making a unique acoustic model. It might also be helpful to use a better microphone in addition to making efforts to speed up the software used to transfer commands to the correct robot.

5 Conclusion

Robotics is a steadily growing field ripe with innovation, particularly in the area of multiagent systems. The achievements within the discipline to date are both numerous and notable, but the promise of robotics has yet to come to full fruition. In order to realize the goal of robots interacting with both humans and other robots, work must be done to create a system that promotes heterogeneous robotic networks and allows for change in the number and type of robots it commands.

This paper has demonstrated the use of three robots together in a heterogeneous centralized network that can perform tasks via voice commands. Testing was done for voice recognition accuracy and time response, and it was shown that there are areas of improvement for both of these aspects. In the future, there is work to be done in attempting to have various different robotic systems work together, realizing each agent's strengths and weaknesses, to perform a common task.

References

1. DARWIn robot, ROBOTIS (2012), <http://www.robotis.com>
2. Bioloid Premium, ROBOTIS (2012), <http://www.robotis.com>
3. iRobot Create, iRobot, Inc. (2012), <http://www.irobot.com>
4. Julius Speech Recognition (2012), <http://julius.sourceforge.jp>
5. VoxForge (2012), <http://code.google.com/p/voxforg>
6. Matson, E.T., Min, B.C.: M2M infrastructure to integrate humans, agents and robots into collectives. In: 2011 IEEE International Instrumentation and Measurement Technology Conference (I2MTC 2011), Hangzhou Binjiang, Hangzhou, China, May 10-12 (2011)
7. Matson, E.T., Taylor, J., Raskin, V., Min, B.C., Wilson, E.C.: A natural language exchange model for enabling human, agent, robot and machine interaction. In: Proceedings of ICARA 2011: The 5th IEEE International Conference on Automation, Robotics and Applications, Wellington, New Zealand, December 6-8 (2011)

8. Lewis, J., Matson, E.T., Wei, S.: Using Indistinguishability in Ubiquitous Robot Organizations. In: Ubirobots Workshop, ACM Conference on Ubiquitous Computing, Pittsburgh, PA (September 8, 2012)
9. Rani, P., Liu, C., Sarkar, N.: Interaction between Human and Robot - an Affect-inspired Approach. *Interaction Studies* 9(2), 230–257 (2008)
10. Kim, J.H., Kim, Y.D., Lee, K.H.: The third generation of robotics: Ubiquitous robot. In: Proc. of the 2nd Int. Conf. on Autonomous Robots and Agents, Palmerston North, New Zealand (2004)
11. Raskin, V., Taylor, J., Matson, E.T.: Towards an Ontological Modeling of Something Very Much Like Consciousness: The HARMS Way. In: SDPS 2012 Conference, Berlin, Germany, June 10-14 (2012)
12. Yachir, A., Tari, K., Amirat, Y., Chibani, A., Badache, N.: QoS based framework for ubiquitous robotic services composition. In: IEEE/RSJ International Conference on Intelligent Robots and Systems, IROS 2009, pp. 2019–2026 (2009)
13. Hidayat, S.S., Kim, B.K., Ohba, K.: Learning affordance for semantic robots using ontology approach. In: 2008 IEEE RSJ International Conference on Intelligent Robots and Systems, pp. 2630–2636 (2008)

Robotic Reasoning with Ontological Semantic Technology

Max Petrenko¹ and Christian F. Hempelmann²

¹ Princess Ekaterina R. Dashkova Moscow Humanities Institute
Ontological Semantics Technology Lab-Northeast Texas,
Texas A&M University-Commerce

maxpetrenko@alumni.purdue.edu

² Dept. of Literature and Languages
Ontological Semantic Technology Lab–Northeast Texas
Texas A&M University-Commerce
c.hempelmann@tamuc.edu

Abstract. The paper discusses the ways in which Ontological Semantic Technology (OST) can contribute to current robotic systems. Based on the example of a robotic car oil changer, the paper demonstrates how OST can represent background knowledge and drive object-based inference and anomaly detection rules as well as complex script-based behavior in field and service robots.

Keywords: robotics, artificial intelligence, ontology, knowledge representation, reasoning.

1 Introduction

The main aim of the paper is to demonstrate how the functionality of current robotic systems can be supplemented with ontological semantic technology (OST). While considerable progress has been achieved in the performance of current field and service robotic systems, a number of intrinsically intelligent capabilities remain unattainable: tenacity, resilience, robustness, and synergy [2]. Recasting these limitations in terms of the more conventional “control-perception” framework, current robotic systems are relatively solid control-wise and brittle perception-wise. The brittleness of perception, in our opinion, directly comes from the systems’ intrinsic limitations in how input is processed, which, in turn, is necessitated by engineering considerations.

The paper will illustrate how the integration of OST with current field and service robotic systems will enhance the current performance control- and perception-wise. We believe that OST-driven improvements in perception functionality can ensure better control by feeding back acquired and processed data for more refined navigation.

Most of the research, development, as well as commercialization efforts in robotic perception are currently concentrated around object detection/recognition. A set of

machine learning algorithms is typically deployed to first decompose, classify, and then label an item of input data represented as low-level features (scale invariants, RIFT and GLOH in computer vision, MFCC in speech recognition, etc.) or high-level features (e.g., edge and edge cluster representation in computer vision [3] or basis functions generated by sparse coding [11]).

Even a cursory look at the current research efforts in object recognition reveals that the notion of “recognition” is viewed as reliable detection of consistent patterns of data, which are then paired with pre-determined labels. Upon successful labeling, a recognition procedure is generally considered complete. The significance attributed to the recognition ability in the sense defined above can be demonstrated by various benchmarking initiatives (e.g., the Hollywood 2 benchmark for activity recognition) where improvement in the order of tenths of percent is considered a valuable achievement.

This limitation of object recognition to pattern labeling leaves out a number of important functionalities that commonly constitute a conventional definition of artificial intelligence [5]: the ability to reason (i.e., derive inferences) over the recognized object, predict its properties, their parameters and behavior, and plan the system’s behavior based on known and acquired data.

Since none of these capabilities are directly derivable from a feature-based machine learning algorithm, they have largely been left out of the current ambit of robotics. This oversight leads to a somewhat bizarre situation where a machine-learning-powered robotic system does not understand what it is supposed to have recognized: the only knowledge about a successfully detected object it acquires is that the pattern representing the object is consistently different from patterns representing other objects. The machine neither knows what this object is nor what to make of it. This limitation places severe constraints on reasoning, predictive and planning capabilities of robotic systems.

This paper is an effort to bridge this gap. It will introduce an efficient computational technology that will complement the output of feature-based machine learning applications with rich world, language, and common sense knowledge resources and reasoning capabilities. Within the framework of OST, the notion of perception can also be extended to include the capabilities summarized in the table below. Each capability utilizes a specific method, takes advantage of a particular set of features, and outputs a reasoning, planning or prediction procedure for object detection, reasoning, prediction, and planning.

Section 2 will provide a brief overview of ontological semantic technology focusing on aspects relevant for the capabilities outlined above. Sections 3 and 4 will explain how each capability is supported by OST. Section 5 will illustrate all four capabilities by emulating the recognition, reasoning, and behavior of an OST-powered car oil changing robot, and Section 6 will argue that OST-based applications differ from earlier toy expert systems in a number of critical ways.

Table 1. OST-supported capabilities

Capability	Method	Feature type	Input	Output
Object detection	Machine-learning algorithms	Pixels, edges, edge clusters, etc.	“Raw” sensory data	Consistently labeled patterns
Object knowledge	Ontology representation	Ontological domain, concepts	Consistently labeled patterns	Hierarchy of concepts, property fillers, and attribute values
Concept-based reasoning	Ontological semantic representation and inference rules	“concept-property-filler” triplets	Concept hierarchy, property fillers and attribute values	Rules of inference for property and behavior prediction and planning
Script-based reasoning	Ontology-, lexicon-, and onomasticon-based complex events	Ontological events, their property fillers and attribute values	Concept hierarchy, property fillers and attribute values + inference rules	Scenarios for reasoning, prediction, and planning for guiding perception and improved navigation

2 Ontological Semantic Technology Overview

OST is a much refined, proof-of-concept-tested and commercially implemented system of knowledge-based language computation. The architecture and functionality of OST has been extensively described and reviewed in the literature [1, 6, 7, 9, 10, 11, 12]. A notable effort of applying OST to facilitate human-human, human-robot, and robot-robot interaction by building a communication and knowledge sharing platform as part of a comprehensive multilevel infrastructure has been made in [4].

OST is predicated on the explicit premise that intelligent language processing is only possible through a robust and universal knowledge base which furnishes the system with a computational world and language model.

OST knowledge base includes a language-independent ontology (circa 10,000 concepts) language-specific lexica (circa 100,000 senses), and supplementary resources (e.g. onomasticons.) The ontology models the world knowledge as a hierarchical lattice of concepts interconnected via multiple properties, whose fillers can be prioritized via default and non-standard facets. The ontology adopts a standard OBJECT-EVENT-PROPERTY branching and then bifurcates from other ontological resources by utilizing a broad range of properties well beyond the usual IS-A or HAS-PART inventory. Language-independent concepts, hundreds of properties interacting with prioritized fillers gives the ontology unprecedented representational capability. General purpose domains could be extended into specific areas and subareas, based on the objectives of an application.

The lexicon’s role is to provide complete coverage of the semantics, morphology, and syntax of a particular language. Closed classes (prepositions, conjunctions), non-compositional (i.e., idiomatic) units, synonyms are also covered. Supplementary resources include a constantly updated proper noun vocabulary.

The static knowledge resources are accessed by a multi-modular processor component whose core functionality includes processing multi-clausal sentences, heeding syntactic agreement, which handles multiword expressions, accommodating unattested lexical items, and centrally disambiguation and ellipsis. The output text meaning representation results from semantic, syntactic, and morphological mapping of an input segment with ontological concepts and their property fillers onto lexicon senses. Enhanced capabilities (e.g., inference, reasoning, non-literal language use detection, and humor recognition) have been developed based on the application's need. The picture below is a generic illustration of the OST architecture and its basic functionality.

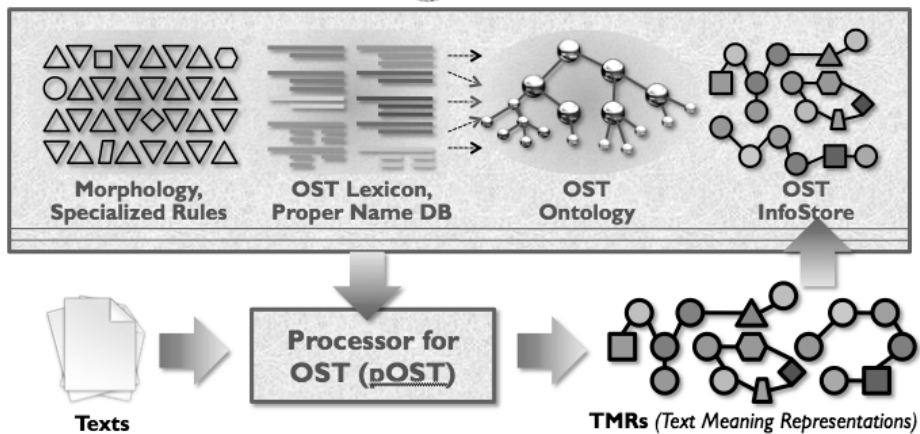


Fig. 1. OST architecture and functionality

Unlike many of today's language processing technologies, OST rejects the (often implicit) unsubstantiated premise that constructing knowledge resources is hard, expensive, and prone to brittleness. Several decades of team projects developing OTS resources and implementing OST-powered applications demonstrated that (a) knowledge resources can be acquired consistently, (b) when acquired and utilized, knowledge resources effectively obviate many statistical processing algorithms by giving direct and immediate access to world knowledge and language meaning.

Given OST's extensive and robust static knowledge resource base, it is easy to see how any field and service robotic system would benefit by being able to reason about, predict and plan its behavior based on the in-depth knowledge about real-life objects it interacts with, which the further sections will illustrate.

3 OST Support for Object-Based Knowledge

After the feature-based algorithm has detected and labeled an object, higher-level knowledge resource will pair it with an instance of an underlying concept carrying the identical label, at which point the machine gains access to a broad body of hyper-hyponimic, mereological, and other types of property-based knowledge about the concept. The grain size of the acquired domain can be calibrated to the needs of a

particular application. To illustrate, in order to reason, predict, and plan its behavior over an oil changing procedure, the robot would have to know about oil and its typical parameters (viscosity, color, etc.). It would also have to know about a typical location of oil in car engines, which necessitates knowledge about engines, and, of course, cars. This type of open-ended knowledge is represented in OST via the ontology.

```
(car
  (definition
    (value("a motor vehicle used for carrying
           passengers")))
  (is-a
    (hier(land-vehicle motor-vehicle)))
  (has-physical-object-as-part
    (sem(car-part)))
)
(car-engine
  (is-a
    (hier car-part))
  (has-object-as-part
    (default(car-engine-part)
      (sem(artifact)))
)
)
(dipstick
  (definition
    (value("a rod for measuring the depth of a liquid;
           especially, a thin metal rod used to measure
           the oil level in the crankcase of an automotive
           engine."))
)
  (is-a
    (hier(engine-part)))
)
  (has-object-as-part
    (sem(handle shaft tip)))
)
  (made-of
    (sem(steel plastic)))
)
)
(lubricating-oil
  (definition
    (value("lubricating oils")))
  (is-a
    (hier(oil petroleum-product)))
)
)
(oil
  (definition
```

```

(value("hydrophobic compound that is liquid
      at room temperature"))
(is-a
  (hier(hydrophobic-compound liquid-material)))
(subclasses
  (hier(cooking-oil crude-oil fuel-oil
        lubricating-oil)))
)
(viscosity
  (value(0.8-1.0))
)
)
)
(viscosity
  (definition
    (value("measure of the resistance of a fluid
           which is being deformed by either shear stress
           or tensile stress."))
  (domain
    (sem(liquid)))
  (range
    (value(0-1))
  )
)
)
)

```

4 OST Support for Inference Rules

Inference rules constitute an intermediary layer between object-based knowledge and script-based behavior. Using ontological concepts and their property fillers, inference rules provide the machine with actionable knowledge over objects and underlie the structure of sub-scripts, scripts, and reasoning operations. The number of inference rules is potentially large, so the section will only provide representations for causal inference rules which have the IF-THEN structure and are widely used in script development. A rule regulating oil change decision, for example, would check multiple parameters of oil and call multiple procedures depending on the obtained values in the IF part.

Rule 1: oil change decision

IF engine-oil

or quantity less-than x
 or viscosity less-than y
 or color value z

THEN call procedure:
 drain-oil
 and select-oil-type
 and add-oil

ELSE terminate

One of advantages of OST over currently and previously existing knowledge bases is its universality. Top concept branching, language independence and rich properties allow for formulating broad, overarching inference rules covering remote domains. To illustrate, combining specific values from the WEATHER and CARS domains, an inference rule could be constructed, which would recommend switching to appropriate oil type depending on the current and upcoming season and thus expected temperature changes.

```

IF current-month ∈ MONTH
THEN
  current-season = current-month(part-of-season(season))
  upcoming-season = current-season(before(season))
  suggested-oil-type1 = season(optimal-oil-type(oil-type))
  suggested-oil-type2 = upcoming-season(optimal-oil-type(oil-type))
ELSE
  terminate

```

5 OST Support for Scripts

A typical task that can be carried out automatically is an oil change on a vehicle with an internal combustion engine. It is an extremely frequent task with largely enumerable variations, while all deviations are assumed to be handled with general world knowledge, as can be captured by an OST system. The task is frequent because of the ubiquity of vehicles and the degradation of oil. Oil aging (thermal and mechanical degradation) is tracked over time (correlating to heating cycles) and mileage (correlating to length of exposure to high temperature and shear). From this comes the controversial rule of thumb recommending oil changes every 3 months or 3,000 miles, whatever comes first.

Oil change as a typical task where the robot has to have near-universal in mechanical versatility, so that trained humans are still the more economic method. An advantage of this sample task is that it has a finite domain in that generally car makes and models are enumerable. But there are variations in that aftermarket, replacement, or incorrect parts may have been installed. The system needs to be able to handle the majority of these and only fall back to human help in exceptional cases. In addition to, as well as in the process of, changing the oil on the vehicle, the engine should be checked for obvious problems, like leaks. This task can be extended to a more complete checkup beyond the engine's oil system, for example to lubrication and inspection of suspension parts.

The formalism that OST uses for handling complex events with temporal and causal chaining of sub-events is scripts, a type of event concept allowing for several additional relations between sub-events and tracking of objects and properties from one subscript to another. It was first developed in more detail for the financial event of bankruptcy [13].

In this section we will outline the general outline of the script of an oil change, with detailed focus on one of its subscripts. The full script with all subscripts, as well as the concepts for all objects and properties would take up more space than the whole paper in its current form.

For most of the subscripts there is a list of model-specific events and objects that are part of it, as well as a generic fall-back script that locates the relevant object types and manipulates them.

Outline of the OIL-CHANGE script

1. Is the vehicle make, model, and year known (identified by customer)?
 - no: go to 2.
 - yes: go to 4.
2. open-hood
3. identify-vehicle (subscript)
4. remove-oil-plug.
 - If plug is not in position or of type expected, go back to 2.
5. check-oil-level (subscript)
 - note if low, to check for leak or cause of loss (burning oil)
6. check-vehicle-position above oil drain receptacle
7. Loosen and remove drain plug
8. Check for obvious leaks (subscript)
9. Loosen and remove oil filter
 - note if type correct
10. Monitor draining oil
11. Install new filter
12. Refill oil of correct type and amount
13. Start-car (subscript) for 5 seconds
 - a. check if in neutral
 - b. check parking brake is set (unless told it's broken by customer)
 - c. turn/press ignition (key)
14. Check oil level (subscript)
15. Top off oil level if necessary
16. Put oil cap back on
17. Put drain plug back in
 - use correct torque for vehicle type/standard torque
 - note if threads are stripped (torque can't be reached)
18. Inspect-used-oil
 - visually/chemically for contamination with other liquids, metal shavings
19. Create final report
 - noting all problems and procedures carried out

check-oil-level

```

is-a      vehicle-maintenance-event
has-event-as-part
          check-oil-level-sensor-reading
          or
          check-oil-dipstick
  
```

check-oil-dipstick

```

is-a      vehicle-maintenance-event
has-even-as-part
  
```

open-hood (subscripts)
 grab-dipstick (subscripts)
 pull-dipstick (subscripts)
 create-image-dipstick-tip (subscripts)
 process-image-dipstick-tip (subscript)

- different outside temperatures require different viscosity grades
- in moderate climates one can use the same viscosity all year, but in places like here you should use a different oil in summer than in winter
- there's rare cases where it's contaminated, e.g., with engine coolant
- if the head gasket fails or the head is cracked
- the latter is something for which the oil should be monitored after being drained
- then a repair suggestion should be made
- it should also be monitored for metal shavings that indicate unusual wear
- finally, there can be gasoline in the old oil, which indicates a problem with the piston rings most likely

6 Summary

The paper is a preliminary effort to introduce OST in robotics. We discussed a standard task of oil changing in cars to illustrate how reasoning, predicting and planning capabilities of a field or service robotic system could be improved by pairing the output of feature-based machine learning applications with the universal, robust and computer tractable knowledge resources of OST. The integration of OST knowledge resources revisits the question of using knowledge-based systems in robotics and revises major issues that emerged from earlier efforts. Unlike earlier applications, OST offers general purpose, domain independent and non-toy intelligence by featuring a universal, robust, parsimonious and language-independent world model called the ontology. OST ontology allows for broader reasoning capabilities by deploying knowledge domains not directly pertinent to the given task. OST ontology also leads to higher robustness by making the system less vulnerable to unexpected or anomalous input. In the paper, we first discussed how object knowledge and inference rules can be represented in OST. We also provided a brief overview of OST focusing on relevant components and functionality. The ontological domain of CARS was partially demonstrated with concepts, properties and fillers explained. The representation of inference rules in OST was then illustrated by a rule regulating oil change decision and a rule recommending an appropriate oil type based on the current and upcoming season.

References

- [1] Hempelmann, C.F., Taylor, J.M., Raskin, V.: Application-guided ontology engineering. In: Proc. ICAI 2010, Las Vegas (July 2010)
- [2] Kuniyoshi, Y.: Autonomous Adaptive Emergent Systems. Advanced Robotics 23, 1481–1485 (2009)

- [3] Lee, H., Raina, R., Teichman, A., Andrew, Y.N.: Exponential Family Sparse Coding with Application to Self-taught Learning. In: Proceedings of the Twenty-First International Joint Conference on Artificial Intelligence, IJCAI 2009 (2009)
- [4] Matson, E.T., Taylor, J., Raskin, V., Min, B.-C., Wilson, E.C.: A natural language exchange model for enabling human, agent, robot and machine interaction. In: Proc. of the 5th Int. Conf. on Automation, Robotics and Applications (ICARA), pp. 340–345 (2011)
- [5] Murphy, R.: Introduction to AI robotics. MIT Press (2000)
- [6] Nirenburg, S., Raskin, V.: Ontological Semantics. MIT Press, Cambridge (2004)
- [7] Petrenko, M.: Lexicon Management in Ontological Semantics. Papers from the Annual international Conference Dialogue 2010, Moscow, Russia (2010)
- [8] Petrenko, M.: The Architecture and Functionality of Ontological Semantics. In: Proceedings of the 29th International Conference on Lexis and Grammar, Belgrade, Serbia, pp. 262–271 (2010)
- [9] Raskin, V., Taylor, J.M., Hempelmann, C.F.: Guessing and knowing: Two approaches to semantics in natural language processing. Papers from the Annual Int. Conf. “Dialogue”, Moscow, vol. 9(16), pp. 642–650 (2010)
- [10] Smith, E., Lewicki, M.S.: Efficient auditory coding. Nature 439(23), 978–982 (2006)
- [11] Taylor, J.M., Hempelmann, C.F., Raskin, V.: On an automatic acquisition toolbox for ontologies and lexicons. In: Proc. ICAI 2010, Las Vegas, USA (July 2010)
- [12] Raskin, V., Nirenburg, S., Hempelmann, C.F., Nirenburg, I., Triezenberg, K.E.: The Genesis of a Script for Bankruptcy in Ontological Semantics. In: Proc. HLT-NAACL 2003, pp. 30–37. ACL, New York (2003)

The Not So Simple Ontology of a “Primitive” Robot

Victor Raskin

Linguistics and CERIAS Purdue University
656 Oval Drive, West Lafayette, Indiana 47907-2086, USA
vraskin@purdue.edu

Abstract. The paper addresses the important issue of (enhancing) robotic intelligence and enhancing the robots’ communication with humans, intelligent agents, sensors and machines. First, it proposes a way to achieve communication in natural language for the agents in hybrid groups with the help of the Ontological Semantic Technology (OST), currently the only approach to accessing deep and comprehensive meaning of language and other data, thus turning it into information, but in principle, one of potentially numerous competing proposals that may ultimately eclipse this early bird. The main thrust of the paper and, I believe, the main reason my colleagues are not ready (yet) to jump into my boat, as it were, is in the second, much more tentative and controversial part of the paper which is philosophical, at least in part. It is attempting to build up a theoretical foundation for a close look at the world of a “primitive” robot and argues that its ontology is not so primitive at all, and it is the theoretical foundation which brings it all to the surface in a pretty straightforward fashion. Contrary to what it may sound, that does not make the OST or any other rich-ontology-based approach to robotic intelligence and communication any more complicated—on the contrary, it reduces it to the well-traveled and -tested situation of domain expansion, a standard feasible procedure, increasingly automated but still including a limited and highly constrained/templates participation by a native speaker.

Keywords: ontological semantic technology, robotic intelligence and communication, natural language, robot world ontology, hybrid agent collaboration.

1 Introduction

The paper addresses the important issue of (enhancing) robotic intelligence and enhancing the robots’ communication with humans, intelligent agents, sensors and machines. First, it proposes a way to achieve communication in natural language for the agents in hybrid groups with the help of the Ontological Semantic Technology (OST), currently the only approach to accessing deep and comprehensive meaning of language and other data, thus turning it into information, but in principle, one of potentially numerous competing proposals that may ultimately eclipse this early bird.

The first part of the paper deals with the OST view of the hybrid human-agent-robot-sensor-machine (HARMS) communication in natural language, covering the

area of current research at the M2M Laboratory in the Department of Computer and Information Technology at Purdue University. The project is co-led by Eric Matson and Julia Taylor, with this author's participation, and includes a powerful cohort of their (and our) graduate students, several of them Korean—and it is the active collaboration with Korean universities and companies, often supported by the Government of the Republic of Korea (along with Purdue University and Purdue Research Foundation), that makes Korean the second natural language, after English, for which the system may be built: practically, it means only the addition of the OST lexicon for the language. Many ideas in the first part were developed in close cooperation with these fine people, especially Dr. Taylor, and it is magnanimous of her/them to allow me the sole authorship of this paper, with this strong acknowledgment, even though I am (re)using primarily the unpublished paragraphs from our internal working papers and reports that were drafted by myself.

The main thrust of the paper and, I believe, the main reason my colleagues are not ready (yet) to jump into my boat, as it were, is in the second, much more tentative and controversial part of the paper which is... er, philosophical, at least in part. It is attempting to build up a theoretical foundation for a close look at the world of a “primitive” robot and argues that its ontology is not so primitive at all, and it is the theoretical foundation which brings it all to the surface in a pretty straightforward fashion. Contrary to what it may sound, that does not make the OST or any other rich-ontology-based approach to robotic intelligence and communication any more complicated—on the contrary, it reduces it to the well-traveled and -tested situation of domain expansion, a standard feasible procedure, increasingly automated but still including what is now monikered as “human computation” [1], a limited and highly constrained/templates participation by a native speaker.

The recognition of the role of philosophy underlying any domain of research and captured in its theory is not widespread, to put it mildly, and the fact that my high-powered colleagues can only muster politeness (Eric) and tolerance (Eric and Julia) towards my preoccupation with theory and a strong, well-tested belief that only theory can provide direction and justification of research and practice, indicates that philosophy and theory have a long way to go to establish their role in cognition, science and engineering.

2 Part One: The OST Road to HARMS

While there has apparently been no prior work on porting the Natural Language Processing (NLP) technology, let alone Computational Semantic or any meaning processing technology into supporting the robot/agent communication without limiting it to specific commands or menus, there have been pertinent efforts in NLP involving intelligent agents, for instance, [2] or [3]. Their focus has been on emulating dialog participation by the computer with a single human, and valuable insights have been achieved but not concerning real-life robotic agents nor dealing directly with their native systems of communication. Part of the reason for that paucity of robot-human communication research would be that active collaboration

between agent and NLP research groups has yet to take off, and, hopefully, this effort may lead to more such interdisciplinary efforts. Another reason may be that the problem of the communication system among humans, robots, agents and machines lacks the main premises and constituents for the successful applications of currently dominant non-representative, non-rule-based, non-semantic methods. The syntax-, statistics-, and machine-learning-based approaches have dominated NLP for several decades and have made very significant inroads into classifying and clustering texts without understanding them and without spending efforts on acquiring such resources as machine-tractable repositories of meanings.

Throughout this time, computational semantics, or meaning- and rule-based NLP, has been addressing applications, where the very nature of the task calls for comprehensive and direct meaning access, and we proceed on the premise that the hybrid communication does not have—nor will or should it generate multi-million-word corpora that lend themselves to the statistical methods. Essentially, it is not a text-clustering or data-mining application, where a considerable level of inaccuracy is tolerated, but rather one, in which immediate and precise understanding of every command, report, or directive is of essence. Rule-based approaches have their own limitations: they function well where we have knowledge. After they yield meaning-based results, machine learning may still need to kick in for matters of reasoning, and especially abduction.

To facilitate robot-human communication, a radically different approach has been attempted, the one similar to the natural development of Pidgin English in the 19th century to mitigate English-Chinese communication in the ports of sea trade, or the invention of Esperanto, a naive attempt to develop the “easiest” natural language that combines the features of the “most efficient languages” so that it could be adopted as the international language. ROILA 2011, a spoken language for talking to robots makes both of these claims: it is billed as simple, easy, and exception-free—and it is foreign to both sides, human and robotic, and has to be learned from scratch. Nor does it afford any access to meaning.

Probably the closest NLP has ever come to handling problems that are similar to the ones we deal with in this proposal is in the never-dying dream to program in natural language, a dream that recurs with almost every new approach to NLP—for the latest efforts in this direction, see, for instance, Mihalcea et al. (2006), Veres (2008). This is not to be confused with the Computing with Words initiative by Zadeh 2002, which limits its purview to computational interpretations, or “precisions,” of just a handful of words, mostly scalarized quantifiers.

Contrary to hybrid human-robot-agent-machine collaboration, inter-human collaboration has been studied intensely from several disciplinary and interdisciplinary perspectives: those of sociology, management, industrial engineering/ergonomics, human factors, rhetoric/usability. More pertinent to this research, some of aspects of inter-human collaboration were subsequently extended to intelligent agents, and dominant among those are the belief-desire-intention (BDI) studies of intelligent agents (Rao and Georgeff 1991, 1995); rooted in Bratman’s (1999/1987) influential scholarship on plans and intentions—see also Wooldridge (2000). BDI studies focused on hybrid teams’ joint intentions (Cohen and Levesque

1991a,b; Levesque, Cohen and Nunes 1990); shared plans (Grosz and Sidner 1990, Grosz 1996, Grosz and Kraus 1996), and some other aspects of intelligent agents architecture and implementation (Vikhorev et al. 2009, Sonenberg et al. 1994, Dunin-Keplicz and Verbrugge 1996).

Even more to the point, work has been done on the construction of practical, domain-independent teamwork models and architectures (Tambe 1997, Pynadath et al. 1999, Yen et al. 2001, Pynadath and Tambe 2002). Somewhat less pertinently perhaps but not without inherent fascination, there have been some reverberations (e.g., Churchland and Churchland 1990) of the 1980 philosophical discourse about ways to separate human intelligence from machine intelligence, in which the Turing (1950) test was loosely metaphorized, if not actually parodied (Searle 1980, 1984-cf. also Dennett 1980 or Dreyfus and Dreyfus 1980).

Somewhat amazingly, in spite of all of this research activity, not much attention has been paid to the actual communication medium: what language or languages are to be used for agent or robot communication, and we speculated on the possible reasons for this above. An important goal of this research is to fill the gap—or at least to start the process.

The ability to communicate in natural language for the model is provided by the Ontological Semantic Technology (see, for instance, Raskin et al. 2010, Taylor et al. 2010). For the prototype implementation, a limited world of an individual limited-capability robot is interesting to be considered in the context of hybrid interaction. This world has a limited number of objects, such as the robots themselves, their sensors, various obstacles, robot parts, etc. The movements of robots, their assignments, capabilities communication acts are described by events. The events and objects are considered to be concepts and are interconnected with properties. All of these entities must be accommodated by an ontology, a language independent conceptual representation of the considered world.

The full-fledged ontological semantic technology (OST) strives to address the real world as it is known to humans, including common sense knowledge, some of which it reflects in the ontology and some in the first approximations of common sense rules (Taylor et al. 2011). At the core of OST, are repositories of world and linguistic knowledge, acquired semi-automatically within the approach and used to disambiguate the different meanings of words and sentences and to represent them. These repositories, also known as the static knowledge resources, consist of the ontology, containing language independent concepts and relationships between them; one lexicon per supported language (English, Russian, etc), containing word senses anchored in the language-independent ontology which is used to represent their meaning; the Onomasticon, which contains names of people, countries, organizations, etc., similar to gazetteers (Mikheev et al. 1999) and their description anchoring them in ontological concepts and interlinking them with other Onomasticon entries (very unsimilar to gazetteers); and a common sense rules resource. A conforming lexicon and ontology, as well as - when needed - onomasticons and common sense rules, are used by a semantic analyzer, a text interpretation mechanism of Ontological Semantic Technology that produces Text Meaning Representations (TMRs) from the text that it reads. The format of TMRs conforms to the format and interpretation of the ontology.

The processed TMRs are entered into Information Storage, a dynamic knowledge resource of OST, from which information is used for further processing and reasoning.

Every ontological concept is represented in the form: (concept(property(facet (filler+))+)+). A filler can be a concept itself or a literal value, depending on a property. The ontology is property rich but compact: in the largest ontology acquired within the approach so far, there are some 6,000+ concepts. Unlike other ontologies developed within different approaches and for different purposes in the government and industry, the ontology is not designed to cover all the words in a text but rather serve as the basis for the conceptual definition of all possible word senses of natural language. This is why ontology is the same for all languages but the lexicons are language-specific, i.e., one for each natural language, such as English, Chinese, etc.

In the HARMS model, an actor is executing its instructions until it comes to a message that it needs to send: for instance, it finds that its voltage is below some threshold and it needs to send a request for battery charge or replacement. At this point, OST translation mechanism kicks in producing the TMR for the called method from the Robotese lexicon information. A similar situation occurs when a human types a message on their system in any supported natural language. Since natural language is ambiguous and vague, such ambiguity and vagueness are mitigated by OST in its TMR production. It is the TMRs, then, that are sent to the addressee(s), be it/they human(s) or robot(s), via unicast, multicast or broadcast. Since all TMRs conform to the same formalism, the messages themselves are thus not marked as to whether the sender is human or otherwise. Next, in two similar processes, the same TMR is translated into Robotese for a robot or into a supported natural language of choice for a human.

The capability of the Ontological Semantics Technology to represent the meanings of English sentences with the help of the English lexicon and language independent ontology is thus mirrored with regard to the communication system used in the software, robotic and machine environments. In other words, any robot to robot, or more generically, agent-to-agent communication is represented by OST in the same format. This allows for a seamless meaning-preserving translation of Robotese (more generically, Agentese) into English and vice-versa. Moreover, it also means that a different system

3 Part Two: Towards a Philosophy and Practice of Robotic Intelligence and Communication

Philosophy, science, and engineering should form one happy team, closely cooperating together in the cognition of the world, understanding it, and enhancing it for human survival, well-being, and convenience. Nothing could be further from reality, however. The philosophy of science is not: it has mostly physics, now in deep crisis, in its sight, followed by biology, and elements of psychology, rarely economics (see, for instance, Hempel 1965; cf. Rosenberg 2011)—no other field or discipline has received much attention from the discipline. Its own concerns may be legitimate, and

of those, the very complex notion of simplicity (Good 1969) and the thorny issue of justification (Haack 1993, 1997; Bonjour) warrant attention, but if in the latter, for instance, the focus remains on empirical verification, that naturally leaves out any non-empirical discipline, including philosophy itself, which is this denied justification.

What should have come out of a true philosophy of science is a clear notion of theory. As a result, many sciences and academic disciplines operate without a proper theory, often using the term casually, as in *I have a theory why Nicole left Jason*. Let's have a look at what a true theory should look like and then apply it to the area of robotic intelligence and communication only to discover that it has had none to speak of so far.

A real theory is a complex entity (see Nirenburg and Raskin, 2004: Ch. 2). It consists of the following components:

- body of the theory: set of explanatory and predictive statement about its purview
- purview: the phenomena that the theory takes on itself to deal with—or what it is the theory of
- premises: the implicit axiomatic statements that the theory takes for granted—these are not stated clearly by many theories and cause most misunderstanding
- goals: the final results of the successful formulation of a theory;
- methods of falsification: the clearly stated hypothetical situation which would prove the theory wrong, a counterexample—we follow here Popper's (1972) view that a hypothesis that is unfalsifiable in principle is not only not a theory but is actually a faith: this includes Marxism and phenomenology
- method of justification/evaluation: a set of statements on how to check the veracity of the body statements and, wherever possible, on how to compare the theory to its competition, if any.

Let us see now how it practically applies to HARMS. One essential premise of this approach is that all communication, by any agent, human or otherwise, has content that describes, states, reports a certain element of or situation in the real world, which is typically an event or a state involving one or more objects. Thus, a simple distance-measuring sensor describes a situation in which two objects, itself and a target are located at a certain distance from each other. The related premise is that each such situation can be captured in a formalized and computable engineering ontology. The introductory information about OST in Part 1 belongs in the body of the HARMS theory. The goals of the HARMS theory are stated clearly enough: to ensure a seamless and precise system of communication among the diverse agents. The theory is falsified if and/or when, following all of its rules, the HARMS system fails. These hypothetical failures, if any, are assessed in the process of evaluation and justification of the theory, especially if there is competition. The falsification and justification/evaluation process are greatly simplified in comparison to these abstract issues in the philosophy of science because HARMS is going to be used in specific applications, and success and failure of the system will be pretty obvious or at least easier to determine.

We will not discuss here the advantages of choosing natural language as the common basis of the hybrid system communication (see Matson et al. 2011)—they are mostly built into the body of the theory underlying OST but it is appropriate to note here the same consideration that underlay the preference for the interlingua approach to machine translation some 50 years ago versus the direct transfer approach. In that context, for n different languages, one needed $n(n-1)/2$ direct transfer systems but only n interlingua-based systems using common resources and software with the sole exception of the lexicons (if they include the morphological and syntactic information for each language). Similarly, for 5 types of agents in HARMS, one would need 10 different translation modules versus just 4 for the proposed system because, of course, humans will not need a translation to or from natural language. If the assumption that all agents of the same type is waved, this numerical advantage of the OST-based system over any non-interlingua-based approaches only increases.

The initial attraction of becoming aware of the world of any non-human agent, with its objects, events, and properties, was its apparent paucity and simplicity. If we have a distance-measuring sensor, and this is all it does, it may appear that only distance characterizes its world. A closer look reveals more: first, its world divided into two major classes of objects, itself and everything else; second, the latter category distinguishes the objects that it sees from those it does not. This is based on those properties of objects that make it visible to the sensor or otherwise, and the action or state of sensing is related to these properties. What started out as one phenomenon has already grown into two numerous and potentially infinite subclasses of objects as well as a set of properties contributing to their (in)visibility plus some states or actions.

If such a sensor is self-propelled it can, besides measuring the distance, calculate how fast it can get to the target object. If it itself does not have the intelligence to figure it out but its distance report is broadcast, another device or the system as a whole (the collective intelligence module of the HARMS system) may calculate that as well as which agent can get there faster. This will also presuppose the separation of those objects that need to be approached, e.g., a device that needs recharging, from those which do not, e.g., obstacles that cannot be removed.

All of this brings up the real value of the ontological representation for even the most impoverished world of a dumb device. Any one phenomenon, such as a distance value, is connected through a network of properties to various other objects and actions, thus providing each device with potential or actual understanding capability of the part of the world that its functionality prepares it for. And it folds each device, with its actual and potential functionalities, into the entire system of collective intelligence. By the same token, the system may automatically calculate, with the help of the ontology, which functionalities are missing and should be acquired or developed. Most importantly, the OST allows a smooth transition from the ontology to any natural language for which there is an OST lexicon, thus making the entire HARMS system of communication expandable and scalable.

References

1. Law, E., von Ahn, L.: Human Computation. In: Synthesis Lectures on Artificial Intelligence and Machine Learning. Morgan & Claypool (August 2011)
2. Wilks, Y. (ed.): Artificial Companions in Society: Scientific, Economic, Psychological and Philosophical Perspective. John Benjamins, Amsterdam (2009)
3. Ruttkay, Z., Kipp, M., Nijholt, A., Vilhjálmsson, H.H. (eds.): IVA 2009. LNCS, vol. 5773. Springer, Heidelberg (2009)
4. Ravi, N., Dandekar, N., Mysore, P., Littman, M.: Activity recognition from accelerometer. In: Proc. Seventeenth Innovative Applications of Artificial Intelligence Conf., pp. 11–18 (2005)
5. Parkka, J., Ermes, M., Korppi, P., Mantyjarvi, J., Peltola, J., Korhonen, I.: Activity classification using realistic data from wearable sensors. IEEE Trans. Information Technology in Biomedicine 10(1), 119–128 (2006)
6. Subramanya, A., Raj, A., Bilmes, J., Fox, D.: Recognizing activities and spatial context using wearable sensors. In: Proc. of Conf. on Uncertainty in Artificial Intelligence (2006)
7. Cox, E.: Fuzzy fundamentals. IEEE Spectrum 29(10), 58–61 (1992)
8. Bodymedia, Sensewear behavior prescribed,
http://www.sensewear.com/images/bms_brochure.pdf
9. Jang, J., Sun, C., Mizutani, E.: Neuro-fuzzy and soft computing. Prentice Hall (1997)
10. Korb, K., Nicholson, A.: Bayesian artificial intelligence. Chapman and Hall/Crc Computer Science and Data Analysis (2004)
11. Domingos, P., Pazzani, M.: On the optimality of the simple Bayesian classifier under zero-one loss. Machine Learning 29(2-3), 103–130 (1997)

Understanding and Processing Information of Various Grain Sizes

Julia M. Taylor

Computer and Information Technology, Purdue University
401 N. Grant St., West Lafayette, IN 47906, USA
jtaylor1@purdue.edu

Abstract. This paper explores the ideas of humor communication with robots by issuing commands in natural language. Special attention is being paid to vague commands and similar commands and whether it is possible for a robot to process them. The paper discusses various aspects of similarity of information in general as well as in relation to a particular physical capability that a robot may or may not have. All aspects are addressed on the Ontological Semantic Technology foundation.

Keywords: language recognition, grain size, similarity, robotics applications.

1 Introduction

This paper will address the issues of semantic equivalence, information duplication, information redundancy and semantic overlap in the context of robotic communication in natural language. It is assumed here that one or more persons can communicate with one or several robots in natural language. Ontological Semantics is used here to interpret the commands given in natural language and translate it to the Text-Meaning-Interpretation (TMR) that removes ambiguity from the commands and presents information at a specified grain level. We assume here that a robot can communicate in TMRs, and a direct translation from TMR to natural language can be done. The question becomes, which TMRs would be misunderstood by a person and potentially compromise further communication.

The following metrics will be discussed:

- Semantic equivalence, which detects sentences with identical, explicitly stated information. This metric is useful when a communicating entity wants to find out repetitive information that another entity should be aware of, and remove any supposedly known knowledge from consideration. This can be also useful when there is a potential for assumptions by one entity, leading to a certain text interpretation, to be different from the assumptions by another entity.
- Duplication of information between texts or utterances based on previously accessed text, which determines if information repeats what is already contained in the previously processed information. This is necessary for relating information implicit in text at hand, especially if the information was already

explicitly stated before. This output could be used in determining how information will be interpreted depending on what prior knowledge a reader accesses.

- Redundancy of information, detecting cases of no equivalence nor duplication when the difference between two sentences is limited to the grain sizes of one or more elements of information. The sentence with the coarser grain size is, then, redundant. It is in principle possible, of course, that a sentence may be redundant to another on one piece of information but the situation is reversed on another piece of information, and in this case, the algorithm will store the information on the finer grain size on both pieces. Here again, the output may be used in conjunction with prior knowledge to predict how coarser grain size information could be interpreted.
- Semantic overlap between two sentences based on the outputs of the previous 3 algorithms as well on some elements of pre-semantic similarity metrics developed by the NLP community. The calculation of the overlap will, of course, detect the non-overlaps that serve as input for the last algorithm as well as the detection of (potential) contradictions and deception, which is not part of the this paper.
- Novelty relative to any set of sentences based on calculating the non-overlaps with the time/sequence of sentences factored in, unlike the previous 4 algorithms. This algorithm can serve as a bridge to determine the interestingness/significance of the information, which will also vary from user to user depending on their prior knowledge. For the purposes of this paper a maximally informed user is considered for novelty detection.

2 Definitions of Semantic Metrics

The assumption is that robots and humans communicate, both describing events that they sense and giving and performing commands. What is of interest is using the notions described above to record and report events of interest and command at the appropriate grain size. In other words, we use semantic equivalence, duplication, and semantic overlap in building causal and temporal chains and then report them at the grain size necessary to show these chains. We take into account the frequency with which some information is duplicated in highlighting the chains, but we do not ignore infrequent information, as that may be the most salient¹ piece. Because of the natural of the approach that we use – an ontological approach – it is always possible to drill down the hierarchy of the events of interest for more information about the subsumed events.

The working definition of **semantic equivalence** is two or more sentences such that either of them can be paraphrased to result in the other sentence without any loss of information in either. For example, *Rumba reported that a couch was moved from*

¹ Saliency computation *per se* is, however, outside the scope of this paper. See Giora 2003 and references there.

its typical position and according to Rumba, somebody moved the couch from its normal position are semantically equivalent.

The working definition of both **duplicated** and **redundant information** is two or more sentences where information in one sentence supersedes information in the other sentence(s). Duplication and redundancy are, however, different phenomena. If a sentence does not contain any information that another does not already contain, the information is duplicated. For example, given two sentences *One of the devices reported that a couch was moved from its place* and *A couch was moved from its normal position*, the second sentence contains duplicated information, even though the sentences are not semantically equivalent. In *One of the devices reported that a couch was moved 3 feet forward* and *Some large furniture was rearranged*, the second sentence contains redundant but not necessarily duplicated information since the second sentence doesn't make clear the what type of furniture, even though it can be easily inferred. We differentiate between duplicated and redundant information in that, in the latter case, it is due to the hierarchical nature of the concepts used in the sentence (*couch ⊂ furniture*).

The **semantic overlap** of two sentences is the shared information between them, it is a semantically equivalent part of the two sentences. Thus, in *One of the devices reported that a couch was moved 3 feet forward* and *A couch was rearranged*, the overlap is in that *a position of the couch has changed*; yet some facts fall outside of the information overlap, namely that it moved *3 feet forward*, that it was either an accident or done on purpose, and who reported the change of position.

Finally, in the definitions of semantic equivalence, duplication, redundancy and overlap, no temporal order to reports is assumed. In other words, an intelligent system may read a report from one device or another about a particular event, and if one of them reports more information than the other one, the temporal order of reading should not matter for the final summarized report. The **novelty**, on the other hand, is dependent on the temporal order, and the first story detection (FSD—see Allan et al. 1998b, 2000, 2001; Kumaran and Allan 2004; Luo et al. 2007) was a really hot subfield of topic detection and tracking (TDT—see, for instance, Allan et al. 1998a, DARPA 1999, NIST 1999) in the last decade and a half or so. Thus, we define novel information with respect to all of the definitions above while watching and recording the order of appearance of the sentences. For example, if the two sentences are semantically equivalent, then the one received later is not novel. If the second sentence is redundant to the first one, then it has no novel information either. On the other hand, if the first sentence is redundant to the second one, then both may contain novel information as information in the second sentence supersedes information in the first. Similarly, for the semantic overlap, only the non-overlapping parts of the second sentence are novel.

It should be stated right away that we differentiate between novelty and informativeness (see Taylor and Raskin 2011c) as there might be plenty of new information that is irrelevant to the task at hand, and similarly, there might be a very limited amount of novel information that may tie two pieces of the puzzle together, and thus it becomes very informative. This paper will not address the informativeness algorithm.

3 Overview of the Method

As stated above the paper relies on the Ontological Semantic Technology (Nirenburg and Raskin 2004, Raskin et al. 2010a, Taylor et al. 2010a, Hempelmann et al. 2010, Taylor et al. 2011a,b; Taylor and Raskin 2011a) for information processing. In order to make our results useful for systems that do not yet speak the OST language, as it were, we can only use OST for computational purposes and then results of the algorithms can be reported in a way that could be compatible with other systems, after the results have been “de-OSTified” or at least simplified (see Figure 1).

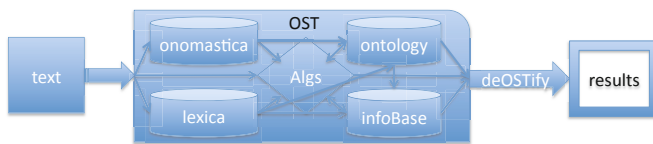


Fig. 1. Text process flow

Typical algorithms of OST are focused on the so-called Text Meaning Representation (TMR), an automatic translation of natural language text into a directed graph-like structure where vertices correspond to ontological concepts as defined in the ontology and edges correspond to properties, both dictated by natural language (see Figure 2). How TMRs are calculated is described, for instance, in Taylor and Raskin (2010).



Fig. 2. Graphical representation of TMR of “*A couch was moved from its typical position in the room*” where green corresponds to ontological events, blue to ontological objects, and red to unknown entities.

It should be noted that in order for an entity to detect that something was moved, it needs to either observe the event, or determine that an item was moved based on its prior and present positions. In the latter case, the entity reporting this information must have access to prior knowledge and must understand it at the grain size that it needs to report it. It is possible that in its knowledge base it has information to the millimeter of where the couch was and it can measure it with the same accuracy where it is now. However, if it is reporting it to a human, such accuracy is likely not be needed and this information should be reported not the most known level, but to the most useful level. The usefulness, again, is user-dependent.

3.1 Semantic Equivalence Detection

We assume that several robots may observe the same event and will report on it. The task then is to summarize their report to the most usable level. The first part of it is to remove semantically equivalent information. The lexicon gives definition in the normalized form. For example, the normalized subject a physical event is an animate or a force. In order to use these definitions often enough, semantic equivalence interpretations must be considered. To get an interpretation of *A couch was moved from its typical position in the room* to the TMR in Figure 2 several operations should be performed. One is to create a semantically equivalent sentence with *couch* being a syntactic object (*unknown moved the couch*), and another one is to create a transformation where both previous and current position of the chair belong to the space that is in the room.

The first transformation is a straightforward rule that converts a passive sentence without prepositional phrases to an active one. Such rules are well studied and can typically be found in many textbooks. The interest for semantic equivalence comes from the observation that passive and active sentences do not have to be semantically equivalent, as the agent of the action may be unknown in the passive sentence. Active sentences also don't have to be semantically similar. In other words, syntactic equivalence by itself does not guarantee semantic equivalence: wind (force) moved leaves; I (agent) moved leaves; shovel (instrument) moved leaves.

The transformations are the key to the semantic equivalence measure. The transformations are computed based on the support of a syntax (sub-)tree whose terminal nodes are concepts instead of words. The instrument is a semantic ontological term; the subject comes from surface syntax. It is this combination of OST-lite, as it were, with natural language syntax, a much more attainable task that promises, in our experience (Taylor et al. 2012), significant gains that are increasingly emerging as knowledge- and hence meaning-thirsty. The frequency of the verb-event concept and the concepts corresponding to the heads in the noun phrases are calculated. Their grain size is manipulated according to the ontological hierarchy until they satisfy the desired threshold. Transformation candidates are created from the resulting trees.

The use of sentential and subsentential paraphrases in various NLP applications has been based substantially on Harris (1985) distributional structure hypothesis, according to which items that occur in the same context are similar in meaning. The influential DIRT article (Lin and Pantel 2001a—see also Lin and Pantel 2001b) redefined those contexts as dependency paths in a syntactic parser, extending and somewhat relaxing the hypothesis in the process. This allowed the establishment of similarities between such expressions “as “X is author of Y ≈ X wrote Y”, “X solved Y ≈ X found a solution to Y”, and “X caused Y ≈ Y is triggered by X” (Lin and Pantel 2001a: 323). Various statistical methods based on distributional structure have been tried with a reasonable degree of success on both monolingual and bilingual corpora—see a useful survey in Bouamor (2010) and references there as well as, additionally, Barzilay and McKeown 2001, Dolan et al. 2004, and Rus et al. 2008. The same distributional similarity basis has been recently explored in a study of textual

entailments, advocating a further extension of the hypothesis from the symmetrical relationship to directional, thus replacing mere similarity with inference and textual entailment—see Kotlerman et al. (2010) and references there.

3.2 Redundancy Detection

Our approach to redundancy detection is based on the assumption that when a lot of information is available it should be prioritized by the level of interestingness (see Taylor and Raskin 2011c and references there). What is interesting for a particular robot is information that it can use. Thus, informing it that a couch moved when it has no sensors to detect distance or location of something is not of particular use. On the other hand, if a robot can sense an object in front of it and be able to tell its length, sending it a message that there is an obstacle without providing any specific details is also not very useful, and since the robot already has a more specific information, redundant.

Redundancy has not been sufficiently explored in the aspect that is needed here, even though the term is used in different areas of language studies. In linguistic pragmatics, following Grice (1975), various versions of rules have been suggested to identify and interpret the extra information (see Carston 2005; Horn 2004; Levinson 2000—to name just the latest few). Davies (2011) provides a convenient compendium of this effort. Much closer to the proposed approach have been attempts to deal with redundancy and its reduction in the NLP strand of research on novelty (Taylor and Raskin 2011c): closely related to sentential and substantial paraphrase alignments (see also about relevant paraphrase research that in the previous section), various statistical approaches have been developed to remove the repeating ‘snippets’ of information (see, for instance, Thadani & McKeown 2008 and extensive references there). This use of ‘redundancy,’ however, is closer to our definition of duplicated information, while our use of the term involves the finer-grain-size NER. No matter what term is used to describe the efforts, the statistical approaches do not have access to sufficient semantic information (usually, limited to no more than a list of synonyms), and that adversely affects their precision (Schiffman and McKeown 2005).

In our redundancy detection, each sentence will be processed through the OST-lite system (Taylor et al. 2012). The results, in the forms of TMRs, will be compared to ontological knowledge as a basis for determining the subsumption relation. Within any set of concepts, the most specific concepts are considered non-redundant. If there is no unique most specific concept, the least general concept that also appears in the text is considered redundant. For example, let us compare two sentences *A large piece of furniture changed its position* and *Rumba reported that a couch was moved 3 feet forward* are compared. The first sentence contains a lot of redundant information: *furniture* is more general than *couch*; *changing position* is more general than *moving 3 feet forward*. Thus, if one compares the description of events involved one sentence is much more general (and therefore redundant) than the other.

Finally, a sentence is redundant if every single constitute of it is either redundant or equivalent to something.

3.3 Duplication Detection

The detection of duplicated information is very similar to that of the redundant one. The difference is that our definition of duplication does not allow for the grain size change. In other words, while information about *furniture* in the example above is redundant, it is not a duplicate. On the other hand, in the sentences *A couch changed its position* and *Rumba reported that a couch was moved* the latter one is a duplicate of the former one because no conceptual hierarchy traversal is necessary to detect “similarity” between the two.

Similarly to the redundant sentence definition, a sentence is a duplicate if every single constituent of it is a duplicate.

3.4 Overlap Detection

Typically, an entire sentence will not be redundant or duplicated. Overlap detection serves to point out those sub-sentential segments that carry information that has been stated already. In other words, for each sentence that is not fully redundant or duplicated, its detected components will be marked. It is possible that a sentence has one part that overlaps with sentence A and another part that overlaps with sentence B.

As with any semantic processing, the detection of relationships between concepts plays a very important role. For example, there is a huge difference between an agent of the action and the recipient or the experiencer of that action (*Troops killed a civilian in an attack* vs. *Troops were killed by a civilian in an attack*). This difference is the reason why semantic processing should be done. However, such processing is not always easy to implement for a generic architecture.

The knowledge of what type of a robot reports the first-hand information or can help determining the exact relationships as they are dependent on the robot’s capabilities. It should also be stated that various capabilities should be considered for interpretations of commands in semantic processing. Thus, a command *walk 3 feet forward* given to a humanoid is perfectly reasonable. The same command given to a robot on wheels is not only overlapping with the previous one, but is also somewhat puzzling, assuming that walking requires the presence of “legs.”

There are several ways to address such commands. One of them is to assume that if the same command (command overlap?) can be given to multiple entities, it was the coarser grain event that was meant (moving vs. walking) and thus command could be executed. Another approach, of course, is to report that the entity has no ability to walk and wait for further instructions. The answer to which scenario to follow should be application specific. Moreover, careful considerations should be given to the grain size at which all commands should be exact.

3.5 Novelty Detection

We defined novelty as the lack of duplication with an added temporal factor: the subsequent non-duplicating sentence contains novel information relative to the previous sentence. The amount of semantic overlap between these sentences

determines the amount of novelty. What is more significant for the system is the novelty relative to the InfoBase, i.e., all the previously processed TMRs (see also Taylor and Raskin 2011c). The novelty may introduce a new lexical entry which will require the robust unattested input treatment we discussed above; less frequently, a new concept; a new relation between two concepts, which is an instantiation of an existing relationship; and most consequential for the resources, a new property that will then need to be assigned to each concept that has it, leading also to modifications, albeit simple and mostly monotonous, in all related lexical entries.

A more sophisticated metric of novelty, however, is interestingness. We touched on interestingness before. This depends on how significant the novelty is for the current user in a current situation, and this may vary significantly from user to user as well as situation to situation. Interestingness can be dynamically predefined as anything related to a particular position on the field, a political role, or a celebrity, an event, etc. But in general, interestingness ultimately depends on saliency, an important category of now-ness.

4 Summary

In this paper, a brief sketch of various facets of semantic similarity useful for human robot communications were discussed. While no experimental results are provided, this work is an important step forward understanding not only explicit commands and information between robots and humans but also catering it to a specific environments and capabilities. It is assumed here that information gathered from robotic intelligence (used here in a different sense than intelligent robotics), as collected by various entities can be summarized at a level useful to a human being automatically.

Acknowledgements. Part of this research was done in collaboration with Victor Raskin of Purdue University.

References

1. Allan, J., Carbonell, J., Doddington, G., Yamron, J., Yung, Y.: Topic detection and tracking pilot study: Final report. In: Proc. DARPA Broadcast News Transcription and Understanding Workshop, pp. 194–218 (1998a)
2. Allan, J., Gupta, R., Khandelwal, V.: Temporal summaries of news topics. In: Proc. SIGIR 2001, pp. 10–18 (2001)
3. Allan, J., Lavrenko, V., Jin, H.: First story detection in TDT is hard. In: Proc. CIKM 2000, pp. 374–381 (2000)
4. Allan, J., Papka, R., Lavrenko, V.: On-line new event detection and tracking. In: Proc. SIGIR 1998, pp. 37–45 (1998b)
5. Barzilay, R., McKeown, K.: Extracting paraphrases from a parallel corpus. In: Proc. 39th Annual Meeting of the Association for Computational Linguistics, pp. 50–57 (2001)
6. Bouamor, H., Max, A., Vilnat, A.: Comparison of paraphrase acquisition techniques on sentential paraphrases. In: Loftsson, H., Rögnvaldsson, E., Helgadóttir, S. (eds.) IceTAL 2010. LNCS, vol. 6233, pp. 67–78. Springer, Heidelberg (2010)

7. Carston, R.: A note on pragmatic principles of least effort. UCL Working Papers in Linguistics (17), 271–278 (2005)
8. DARPA, Proc. DARPA Broadcast News Workshop, Herndon, VA (1999)
9. Davies, C.: Over-Informativeness in Referential Communication. Ph.D. Dissertation, Cambridge University, Cambridge, UK (2011)
10. Dolan, W.B., Quirk, C., Brockett, C.: Unsupervised construction of large paraphrase corpora: Exploiting massively parallel news sources. In: Proc. COLING 2004 (2004)
11. Giora, R.: On Our Mind: Salience, Context, and Figurative Language. Oxford University Press, New York (2003)
12. Grice, H.P.: Logic and conversation. In: Cole, P., Morgan, J. (eds.) Syntax and Semantics, 3: Speech Acts, pp. 41–58. Academic Press, New York (1975); Reprinted in Grice, H. P.: Studies in the Way of Words, pp. 22–40. Harvard University Press, Cambridge (1989)
13. Harris, Z.: Distributional structure. In: Katz, J.J. (ed.) The Philosophy of Linguistics, pp. 26–47. Oxford University Press, New York (1985)
14. Hempelmann, C.F., Taylor, J.M., Raskin, V.: Application-guided ontological engineering. In: Proc. ICAI-2010: International Conference on Artificial Intelligence, Las Vegas, NE (2010)
15. Horn, L.: Implicature. In: Horn, L., Ward, G. (eds.) The Handbook of Pragmatics, pp. 3–28. Blackwell, Oxford (2004)
16. Kotlerman, L., Dagan, I., Szpektor, I., Zhitomirsky-Geffet, M.: Directional distributional similarity for lexical inference. Natural Language Engineering 16(4), 359–389 (2010)
17. Kumaran, G., Allan, J.: Text classification and named entities for new event detection. In: SIGIR 2004, pp. 297–304 (2004)
18. Levinson, S.: Presumptive Meanings. MIT Press, Cambridge (2000)
19. Lin, D., Pantel, P.: DIRT – discovery of inference rules from text. In: Proc. ACM SIGKDD Conference on Knowledge Discovery and Data Mining, San Francisco, CA, pp. 323–328 (2001a)
20. Lin, D., Pantel, P.: Discovery of inference rules for question answering. Natural Language Engineering 7(4), 343–360 (2001b)
21. Luo, G., Tang, C., Yu, P.S.: Resource-adaptive real-time new event detection. In: Proc. SIGMOD 2007, Beijing, China, June 11–14 (2007)
22. Nirenburg, S., Raskin, V.: Ontological Semantics. MIT Press, Cambridge (2004)
23. NIST, topic detection and tracking evaluation project, TDT3 (1999)
24. Raskin, V., Hempelmann, C.F., Taylor, J.M.: Guessing vs. knowing: The two approaches to semantics in natural language processing. In: Kibrik, A.E. (ed.) Proceedings of Annual International Conference Dialogue. AABBY/Yandex, Moscow, Russia (2010a)
25. Rus, V., McCarthy, P.M., Lintean, M.C., McNamara, D.S., Graesser, A.C.: Paraphrase identification with lexico-syntactic graph submission. In: Proc. AAAI 2008 (2008)
26. Schiffman, B., McKeown, K.R.: Context and learning in novelty detection. In: Proc. TREC 2005 (2005)
27. Taylor, J.M., Raskin, V.: Fuzzy ontology for natural language, Proc. NAFIPS 2010 (2010)
28. Taylor, J.M., Raskin, V.: Graph decomposition and its use for ontology verification and semantic representation. In: Intelligent Linguistic Technologies Workshop at International Conference on Artificial Intelligence, Las Vegas, NE (July 2011a)
29. Taylor, J.M., Raskin, V.: Understanding the unknown: Unattested input processing in natural language. In: FUZZ-IEEE Conference, Taipei, Taiwan (June 2011b)

30. Taylor, J.M., Raskin, V.: Working Paper on Informativeness and Novelty. Technical Report 2011-84, CERIAS, Purdue University (2011c)
31. Taylor, J.M., Raskin, V., Hempelmann, C.F.: On an automatic acquisition toolbox for ontologies and lexicons in Ontological Semantics. In: Proc. ICAI-2010: International Conference on Artificial Intelligence, Las Vegas, NE (2010a)
32. Taylor, J.M., Raskin, V., Stuart, L.M.: Matching human understanding: Syntax and semantics revisited. In: Proc. IEEE SMC 2012, Seoul, Korea (2012)
33. Thadani, K., McKeown, K.: A framework for decreasing textual redundancy. In: Proc. 22nd International Conference on Computational Linguistics (COLING), Manchester, England (2008)

Software Platform for the Industrial Dual-Arm Robot

Taeyong Choi, Hyunmin Do, Chanhun Park, Dongil Park, Seunghwi Lee,
and Jinho Kyung

The Department of Robotics and Mechatronics, Korea Institute of Machinery & Materials,
Daejeon, 305-343, Korea
`{taeyongc, hmdo, chpark, parkstar, leesh, jhkyung}@kimm.re.kr`

Abstract. Human rights at poor working condition is the severe problem in modern manufacturing system. The industrial dual-arm robot is being developed to meet these social issues fundamentally. The software platform for the industrial dual-arm robot is also being developed, which have many differences compared to the conventional robot software platforms. The software platform for the industrial dual-arm robot which are being developed should have the realtime control capability, the precise motion command interface and the convenience of usage. A special architecture for the mentioned functions is introduced. The proposed architecture consists of the multiple user command input tools, the translator for the unique robot language and the robot control framework with the realtime control property controlled by the unique robot language.

1 Introduction

Industrial robot systems, has been widely used for the purpose of manufacturing such as laser welding, object transfer and repetitive processes. They can work all day without stop and error. The most advanced conventional industrial robot is a single manipulator robot such as the PUMA. In case of serial robot, it usually consists of 6 degrees of freedom (DOF) serially linked joint, that is used to position the end-effector of robot to exact position with orientation. However, they have limitation to replace human worker due to their low DOF in one arm. Human has many degree of freedom in his arms. For example, a shoulder can be represented by 6 DOF. Recently, dual-arm robots such as [1–3] are becoming upcoming technology for manufacturing in the cell production line. They have more DOF than conventional industrial robots to be similar to human. They can have 6 DOF or 7 DOF in one arm depending on the shoulder motion. Cell production lines to assemble small product is good example for them to be used. Currently, they have limit to handle heavy payload because of its complex structure to be implemented.

Commonly, industrial robot need to be taught to memory their repetitive actions. To teach industrial robot is tedious and hard process. Teaching pendant and command console is used to program their task. Their operation trajectory must be programmed in detail using special robot language [4–6]. To overcome conventional tedious teaching process, some intuitive method like direct teaching [7, 8] were introduced. These kinds of teaching method for conventional single manipulator are not suitable for dual-arm robot because of their complex task. Dual-arm robot assembles small and complicated parts. Sometimes, his two arms cooperates to handle a heavy objects like human.

For more easy program in robot such as humanoid, mobile robot and toy robot, novel robot program method based on flow chart scheme and graphical user interface (GUI) were introduced such as [9–14]. They have common structure. They have similar GUI. User can define the robot motions by state diagram or flow chart using the mouse. Each parts of state or flow is described by action such as ‘go’, ‘stop’, ‘do something’ and so on. Robot moves by the programmed actions. Of course, each action can be easily reconfigured to make new motion like object oriented program (OOP) method. In these methods, it is difficult to define detailed motion trajectory and to assure the precision of end effector. The precision of motion is the most important index for industrial robot.

Here, the sheme of novel program framework for industrial dual-arm robot is introduced. User can program dual-arm robot using both way; One is by console based program method to teach detailed motion. Other one is by GUI with state diagram. Implementation of the physical industrial dual-arm robot is in progress.

2 Surroundings

2.1 Industrial Dual-Arm Robot

Cell line for IT product manufacturing is designed like Fig. 1. Currently, IT products such as mobile phone and TV are made by human, who works all day at the designated area with standing. Their work is repetitive. Robot, specifically, Dual-arm robot which have functions like human can be a proper substitution for this kinds of tedious and repetitive works. In our senario, two or three robots cooperate to assemble mobile phone. Also, they can pack the mobile phone. Because dual-arm robot have two arms like human, then can manage objects as human do without additional tools for automation.

The dual-arm robot to apply the factory as in Fig.1 is designed like as Fig.2. Its physical properties are described in Tabel.1. It has 7 DOF in each arms and 2 DOF

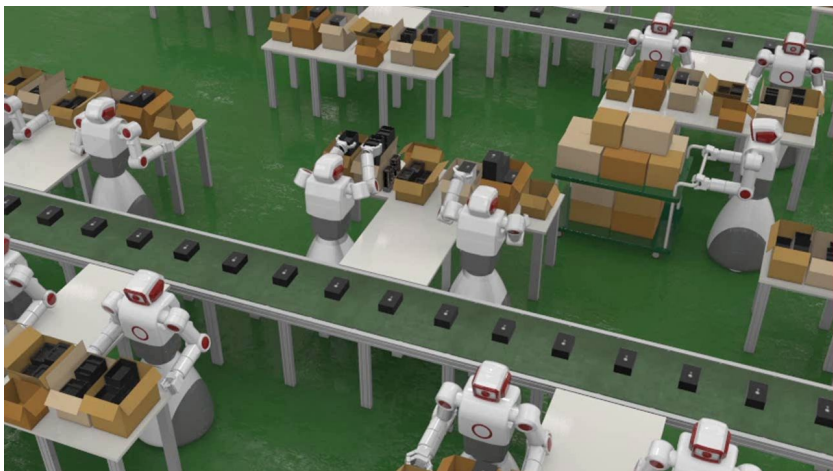


Fig. 1. Designed cell line for production of IT products

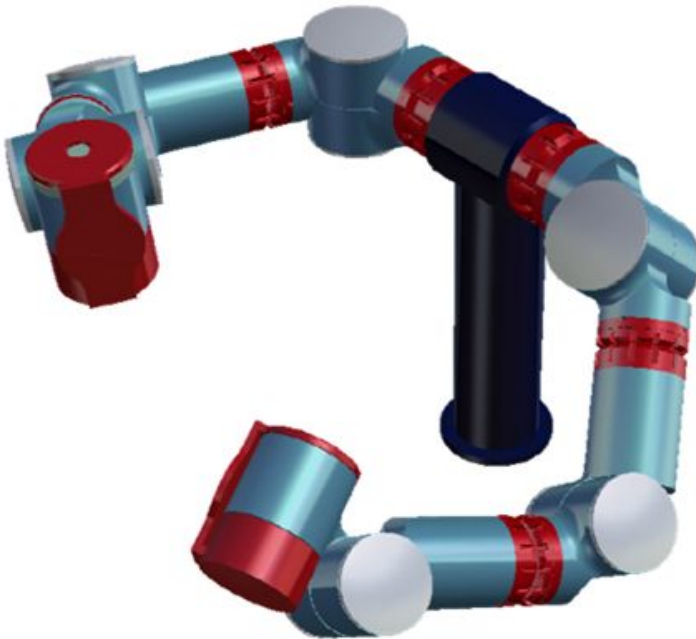


Fig. 2. Designed dual-arm robot

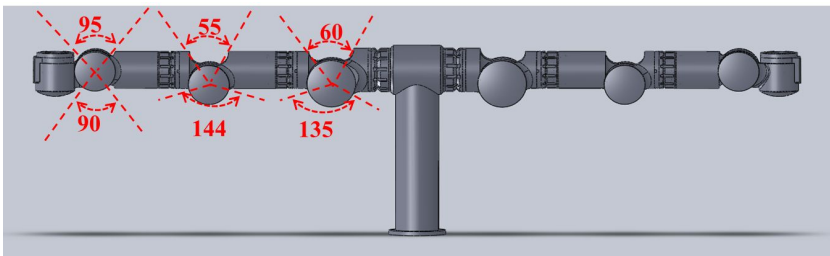


Fig. 3. Joint's work range of the designed dual-arm robot

Table 1. Dual-arm robot dimension

	DOF	Weight(Kg)	Length(mm)
Left arm	7	14.5	700
Right arm	7	14.5	700

in the waist. The aim of payload is 1/2 of the arm weights at least. All actuators and force-torque sensors are communicated by the ethercat protocol [15]. The ethercat is the communication standard introduced by BECKHOFF inc.. It use the conventional local area network (LAN) physical layer and hardware, so user don't need to add any special equipments without ethernet protocol support hardwares. It also use the daisy chain topology for connection. In our robot, the hollow axis actuators and sensors are

used and all signal lines go through the hole. In this reason serial connection method of ethercat is very useful. Actually, there are many serial connection methods. However, only the ethercat guarantee the realtime communication in PC surrounding.

2.2 Realtime Control

Dual-arm robot needs real-time control. Required performance for speed and precision is more higher than the other normal robot such as serving, walking and mobile robots. The control output with strictly regular intervals more than 1Khz is usually necessary to guarantee the required performance in industrial application. Developers prefer microsoft windows environment with visual studio developer tools due to its comfort. However, unfortunately user friendly operating system (OS), the windows, is hard to schedule with regular interval because of its heavy background processing. Commercial software RTX kernel [16] is used to meet the realtime control requirement. Actually, ethercat communication method works on the realtime kernel.

3 Software Framework for the Industrial Dual-Arm Robot

3.1 Scheme

We aim to develop the user command program with easy usage and strictly fixed-time control property. There are many user friendly robot operating platforms such as [9–13]. However, they are not suitable for industrial application but Roboticslab owing to realtime control architecture. Conventional robot software platform is designed for service robot that lack precision and strictly fixed-time control. Robotics software platform which is desired for our dual-arm robot have to both the easy usage like component based motion command using GUI and the realtime control. Usual competent based motion teaching lack precision command for teach robot to follow detailed trajectory. Novel scheme to secure the precision command and the easy usage command is devised like Fig.4. Dual-arm task script language (DTSL) is developed, with which user can control robot motion with high precision in detail. DTSL is similar to the conventional industrial robot language. Most of industrial robot is taught by robot language. The sequence of DTSL is defined as robot work to produce somethings. User describe the sequence of DTSL, that means the robot teaching. This process is hard and tedious.

Actually, Not all industrial robot works need precision command. Precision command is necessary for those actions like welding, precision positioning and so on. Simple transfer, grip and etc. don't need high precision command. For the easy usage of the robot software platform, component based command with GUI can be used for the part of robot works that is not the precision command. Finally, dual-arm robot platform consist like Fig.4. DTSL is configured from the many methods. Each method have its own advantages.

3.2 Framework

Desired dual-arm robot software platform is more concretized. Multiple user program method is configured like follows; One is the original DTSL to secure motion

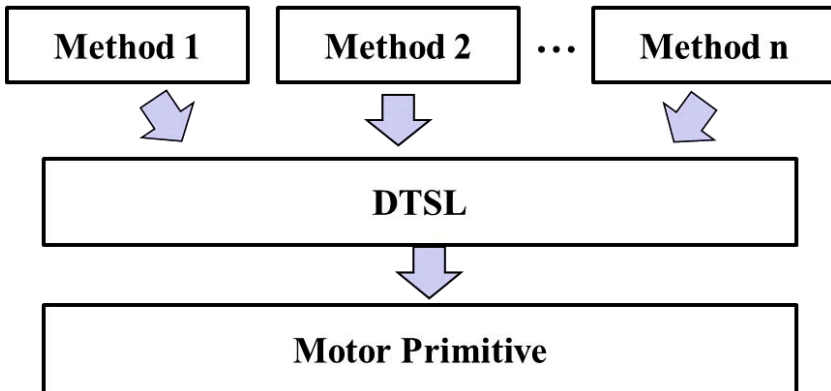


Fig.4. Simple overview of dual-arm robot software platform. Dual-arm robot is controlled through the DTSL. DTSL is made by many method pass.

precision. Another is the direct teaching tool (DTT) to be easy user command. One another can be the indirect teaching tool (ITT) to teach brief motion trajectory. DTT is one of the intuitive teaching methods shown in Fig.5. An operator pushes or pulls the end-effector of a manipulator and it is controlled to comply with the operator's teaching force/moment; as a result, it moves as an operator intends. The manipulator records the teaching trajectory and playback by operator's request. This method is very easy and effective compared to conventional method like teaching by teaching-pendant. Conatrary to DTT, ITT is motion-capture based teaching method. User show the motion to teach. Then robot estimate the motion and its trajectory and mimic the user's motion.

Layer stacks of the desired dual-arm software platform is shown in Fig.6. Framework consists of;

- Job planner: Job planner is the GUI tools to describe robot works. Here user put the command components which can be DTSL, ITT or DTT in our options. Dual-arm robot works is determined by the sequence of the positioned components.
- Task monitor: Task monitor display the current work process over the whole process.
- Simulator: User can simulator the robot motion on the simulator of the dual-arm robot without the control program.
- Indirect teaching tool: ITT is a kinds of robot teaching tool. User show the actual motion. Robot learn the brief motion using vision system.
- Direct teaching tool: DTT is a kinds of robot teaching tool User teach the robot directly by tracking the robot end-effector.
- Common Command Interface: Common command interface (CCI) translate the results from various teaching tools to a DTSL format.
- Dual-arm Task Script Language: DTSL is robot operation language with running engine.

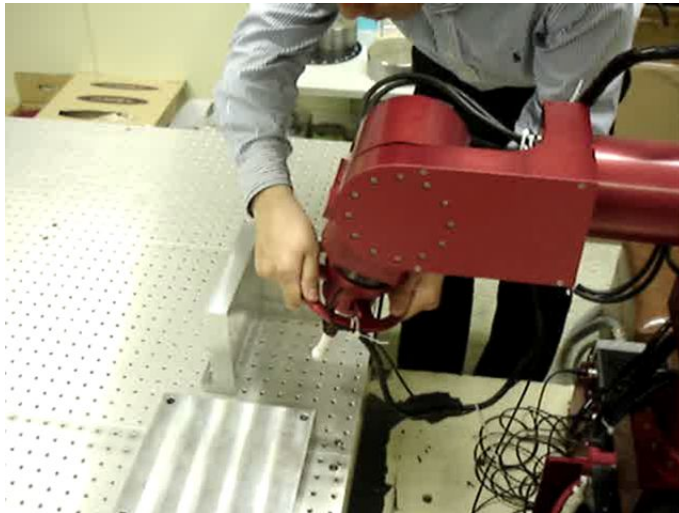


Fig. 5. DTT to teach deburring trajectory

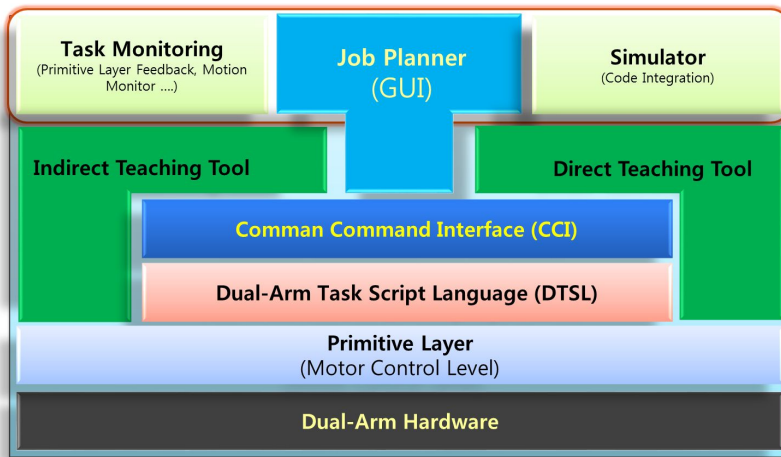


Fig. 6. Software platform layer for dual-arm robot. User can teach the robot through the job planner interface.

3.3 Realization

We do not build up all layers. Among conventional robot software platforms the Roboticslab [13] is used as the motor control level framework because it adopted RTX kernel. Ethercat driver for the Roboticslab is also available. Other layers are being implemented. DTSL is linked to the Roboticslab framework via message port. Message port transfer the command message from the DTSL engine to the Roboticslab engine using process communication or TCP/IP protocol. Commanded robot motion is

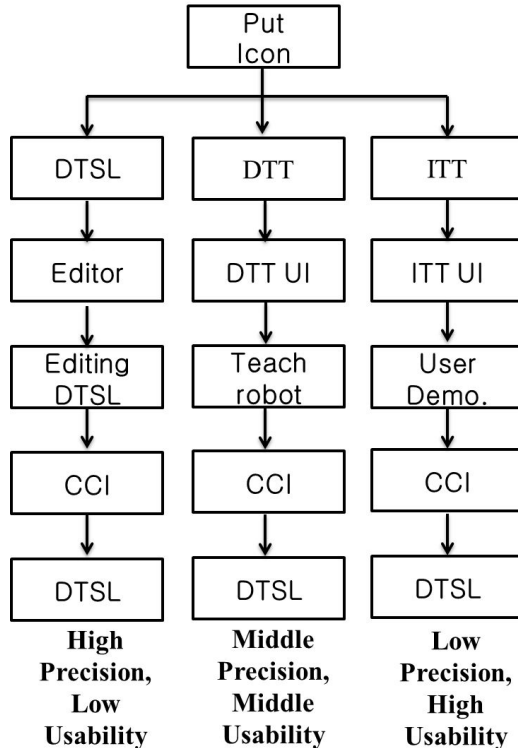


Fig. 7. User can select teaching method among provided methods. Each method have its own advantages and disadvantages.

controlled by control algorithms on the roboticslab framework, and control output from the roboticslab control layer is passed through the RTX kernel to ethercat output.

The job planner is the final user interface. The command depth of icon blocks on the job planner is more higher than that of other software platform. In other software platform the variable declaration, the motor axis, the individual algorithm and etc. are declared in GUI. However, in our job planner, unit robot action is declared, that is filled by each teaching method of Fig.7. The usage is like follows; User put the components or icon in the job planner. Each icon have its link to ITT, DTT or DTSL. In case of DTT, DTT program is executed by double click DTT icon. That icon represent the robot trajectory taught by DTT, and it is described in DTSL in real. User can modify DII's teaching trajectory directly using DTSL.

Actually, The output of ITT and DTT is also DTSL format by passing the CCI layer. In the view of the dual-arm robot DTSL is the unique commanding method. For example, the teaching trajectory from the DTT consists of many path points. It is kinds of DB contains path points, and is changed to DTSL command such as *trajectory(*DB)* or *move(*points)*.

DTSL works for both the physical dual-arm robot and simulator model. Currently, simulator model of the designed robot is implemented on the Roboticslab simulator

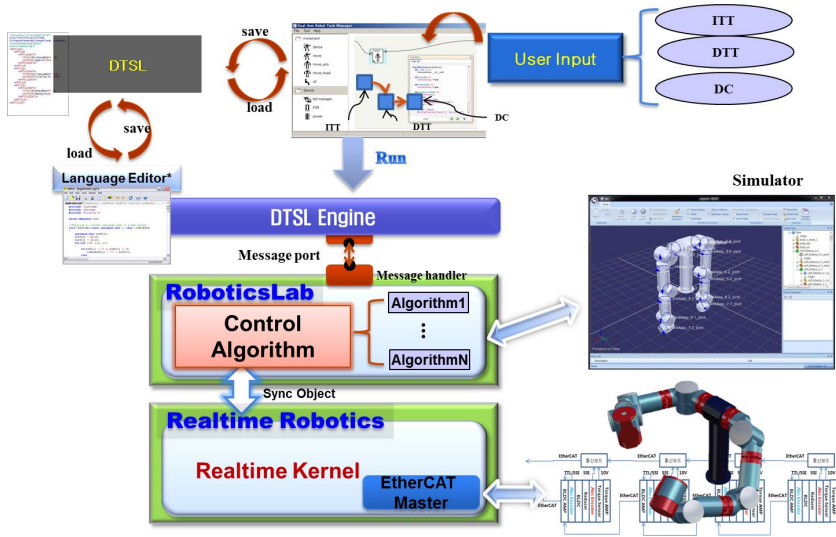


Fig. 8. The data relations and flows in the desired software platform

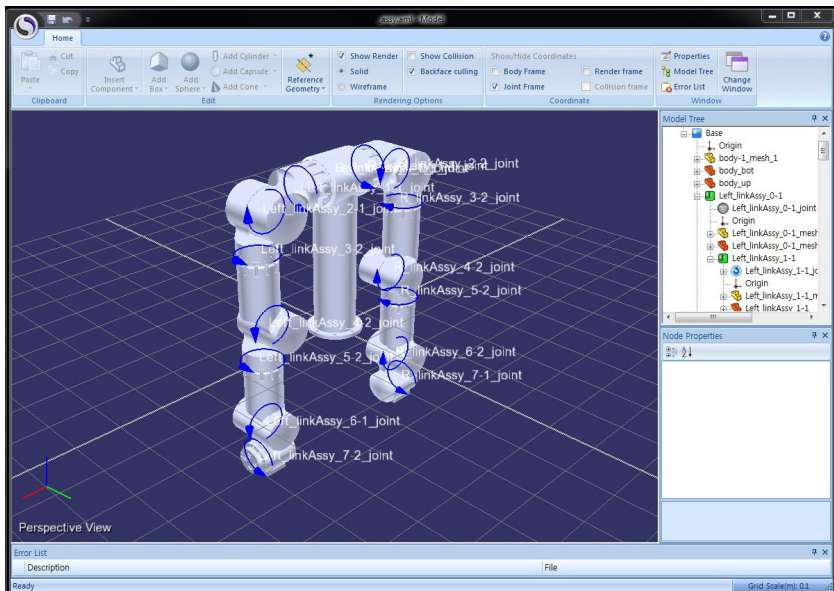


Fig. 9. Simulator model of the dual-arm robot

environment shown in Fig.9. Simulator is not simplified as the simple rigid models. Simulator model contains the detail information of the robot hardware model including motor inertia, sensor mass, each part positions and so on.

4 Conclusion and Furthur Works

4.1 Conclusions

Dual-arm robot is a novel industrial robot. It has both property of conventional industrial robot and service robot. Dual-arm robot requires the high precision motion and human-like action. New robot software platform to manage multiple user input is proposed to achieve both property in uniform software platform. Some parts of robot work is taught by DTT, and some parts of robot work is taught by DTSL. Using this software platform, user can easily teach dual-arm robot with GUI by securing precise motion.

4.2 Future Works

Now, we are building the software platform for the dual-arm robot. Implementations of DTSL, ITT, DTT, Job planner, Task monitor and motor level control algorithms are in progress.

Next time, we hope to show the results of the implemented software platform.

References

1. Yaskawa inc.: Motoman Robotics, <http://www.motoman.com/products/robots/assembly-robots.php>.
2. Kawada inc.: Nextage Humanoids, <http://www.kawada-nextage-humanoids.com>
3. ABB inc.: FRIDA concept robot, <http://www.abb.com>
4. Simmons, R., Apfelbaum, D.: A Task Description Language for Robot Control. In: IEEE International Conference on Intelligent Robots and Systems, Victoria, Candada, pp. 1931–1937 (1998)
5. Pires, J.N.: Industrial Robot Programming, Building Applications for the Factories of the Future. Springer, New York (2006)
6. Pires, J.N., Godinho, T., Nilsson, K., Haage, M., Meyer, C.: Programming industrial robots using advanced input-output devices: test-case example using a CAD package and a digital pen based on the Anoto technology. In: REV 2007, pp. 1–7 (2007)
7. Park, C.H., Kyung, J.H., Park, D.I., Park, K.T., Kim, D.H., Gweon, D.G.: Direct Teaching Algorithm for a Manipulator in a Constraint Condition using the Teaching Force Shaping Method. Advanced Robotics (24), 1365–1384 (2010)
8. Choi, T.Y., Park, C.H., Kyung, J.H.: Feature Point Recognition for the Direct Teaching Data in Industrial Robot. In: Incheon, C.D. (ed.) International Conference on Ubiquitous Robots and Ambient Intelligence, CD, Incheon, Korea, November 23-26 (2011)
9. Robot Operating System, <http://www.ros.org/wiki>
10. Open Platform for Robotic Service, <http://www.opros.or.kr>
11. Microsoft inc.: Microsoft Robotics Developer Studio, <http://www.microsoft.com/robotics>
12. Bruyninckx, H., Soetens, P., Koninckx, B.: The real-time motion control core of the Orocoss project. In: IEEE International Conference on Robotics and Automation, pp. 2766–2771 (2003)

13. Simlab inc.: Roboticslab, <http://rlab.co.kr>
14. Simões, A.S., Colombini, E.L., Matsuura, J.P., Franchin, M.N.: TOPR: The Open Robot Project. *Journal of Intelligent Robots and Systems* 66, 3–22 (2012)
15. Ethercat Technology Group,
<http://www.ethercat.org/en/technology.html>
16. RTX Real-Time Platform,
<http://www.intervalzero.com/products/rtx-at-a-glance>

Design of Dual-Arm Robot for Cell Production

Hyunmin Do, Chanhun Park, Kyoungtaik Park, and Jin Ho Kyung

Dept. of Robotics and Mechatronics, Korea Institute of Machinery and Materials
156 Gajeongbukno, Yuseoung-gu, Daejeon 305-343, Korea
hmdo@kimm.re.kr

Abstract. Needs for an automation in a cell production line is recently increasing with an increasing number of aged people and a decreasing number of population. Since skilled workers are required more due to the nature of a cell production line, much attention is given to a dual arm robot as a solution for an automated cell production system. Dual arm robot can work in a very similar way with a human worker and thus it is very proper for a cell. This paper presents a design of a dual-arm robot for an application to the cell production line in packaging and assembling of IT products like cell phone, television and so on. A requirement for a design parameter is suggested and the design concept and some implementation results are proposed.

Keywords: dual-arm robot, cell production, IT products.

1 Introduction

Conventional industrial robot works in the structured environment and always does the already scheduled job. Thus the environment should be setup for robots and should be separated from human worker. That causes the application of a robot in a manufacturing spot to be restrictive and difficult. Such a concept is good for the mass production system and the most representative production site is an automobile factory.

Nowadays, the production system is changing into a small quantity batch production line because a variety of product is required from the market in many areas (e.g. cell phone, tablet PC, et. al.) and thus the cell production system is widely introduced especially around IT products. In the cell production line, the flexibility is the most important factor and the conventional industrial robot is not appropriate in this point. A human worker is the best in the view point of the flexibility and a robot should have an ability of handling a variety of product flexibly. The flexibility of a human worker comes from the ability of handling several shapes of products and monitoring the state of a current job and correcting errors. An arm and a hand of a human can be used to achieve various missions. Thus an arm like a human's one is needed for a robot. That is the starting point of a research on a dual-arm robot. Many studies have been done during several decades and focused on the design and control of a dual-arm robot [1,2,3]. The most important point of a dual-arm robot is an ability of doing a jig-less job like a human worker. Thus it can improve the flexibility in the production line compared to the conventional robot.

To conduct given jobs in the manufacturing site effectively, a commercial product of dual-arm robot is firstly proposed by YASKAWA as MOTOMAN series (SDA 5D / SDA10D / SDA 20D) [4]. Recently, several kinds of dual-arm robot towards industrial application have been developed such as FRIDA by ABB Inc. [5], BAXTER by Rethink robotics [6] and so on. Dual-arm robot by YASKAWA aims at doing a job separated from human worker and so the function of safety is not emphasized. This is the installation condition of the conventional industrial robot. On the other hand, FRIDA by ABB sets a goal of working with a human. Many functions for safety are implemented in FRIDA considering the collision with a human worker who works together with her.

This paper gives attention to a dual-arm robot, which has similar structure of human and can work in a similar way with a human, as a key component of an automated cell production system. Especially, some IT products like cell phone, LCD television and so on are considered as target products of an automated production system. This paper is organized as follows: Section 2 describes the design of dual-arm robot. Section 3 describes an application of dual arm robot to cell phone production line. Discussion and concluding remarks are made in Section 4.

2 Design of Dual-Arm Robot

In this section, a design concept of a dual arm robot is described. A fundamental concept in the design of a dual arm robot, which will be applied to a cell production line, is like a human. A structure, a length of an arm, a height of a robot and a workspace are all designed to meet those of a human. Therefore, it is possible to apply a designed robot to a current production system without dramatic change of a structure of production cell line.

2.1 Elicitation of Design Parameters

The most important point in designing a robot is a light-weight arm with a function of a safety. Even though a robot has a safety function, risk of safety accident is increasing as weight of an arm increases. Thus to secure an intrinsic safety, we try to reduce the weight of an arm as far as possible and to add a function of safety. Since the robot should handle the needed payload, also, the target is to design a single arm, of which the weight is less than 10kg and the payload is more than 5kg. To derive the required specification, firstly, an average size of a human body was investigated. It is important to minimize the change of current production line in order to apply a robot to many industrial sites easily and thus it would be better to design a robot similar to a human body with respect to overall size; height, length of arm, etc. An average size of men and the designed robot is shown in Figure 1. Important point is a length from a shoulder to wrist and position of a shoulder.

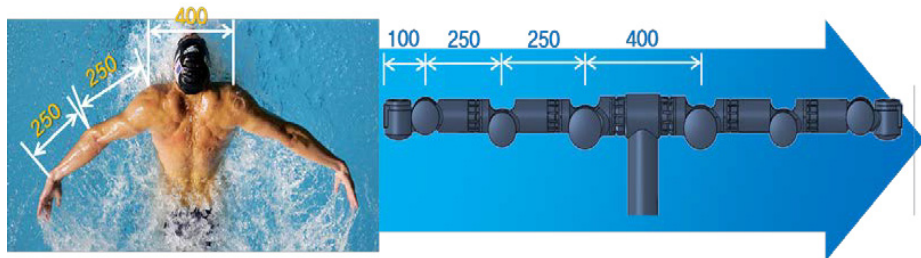


Fig. 1. Comparison of a length of an arm between a men and a designed robot

Also dynamic property to decide the specification of an actuating module was investigated. A packaging job of cell phone was conducted by a human worker and the motion was captured and analyzed. Figure 2 shows the position of sensor attached on a worker and Figure 3 shows the configuration of experiments and results of motion capture. Through this procedure, the maximum speed and time of acceleration of each joint were decided. The angular velocity of each joint should be more than $150^{\circ}/\text{sec}$ and the needed torque for each joint is calculated with the time of acceleration 0.2sec. Then, the parts of an actuator module were selected to meet such a specification. First of all, an actuator module is comprised of commercial products only. To meet the required specification, a motor and a reducer were selected to be light weight and plat among those which can provide a required torque. As a result, a robot arm was designed to meet the required payload and the weight of a single arm was about 15kg because of the limitation of selectable products. Therefore, the necessity of developing a customized actuator parts was clarified to satisfy the desired specification. Also, an actuator module was designed as hollow type for the compactness of the structure and the convenience of the maintenance like other dual arm robots which are already developed.

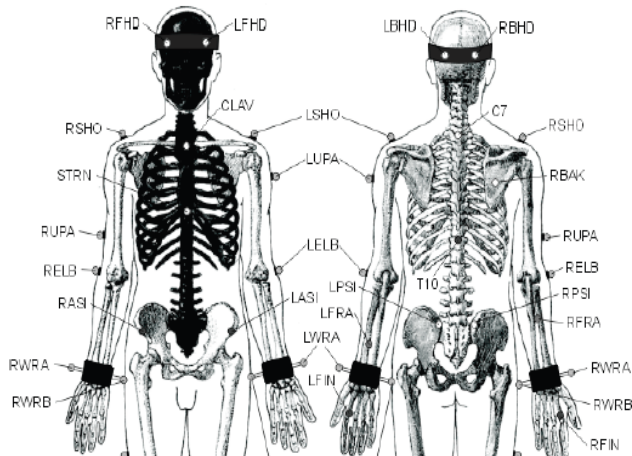


Fig. 2. Attached position of markers

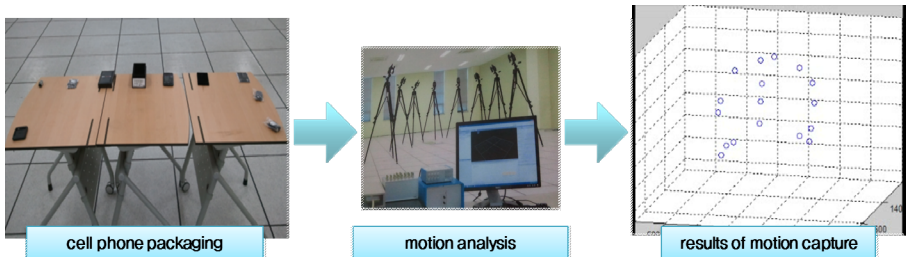


Fig. 3. The configuration for experiments and results of motion capture

2.2 Workspace Analysis

In dual-arm robot, the dual-arm workspace should be identified as well as the workspace of each arm respectively. Dual-arm workspace means the intersection of the workspace of each single arm and that is meaningful point because the merit of a dual-arm robot is a dual-arm operation. In the proposed robot, each joint has an asymmetrical structure in the view of an angle of rotation and thus the dual-arm workspace can be expanded. Figure 4 shows the shape and the angle of rotation of the designed robot. Also the workspace was investigated and it can be checked that the required dual-arm workspace was secured. Figure 5 shows results.

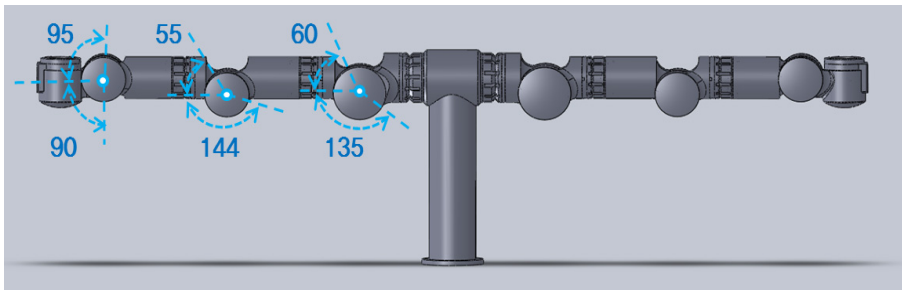


Fig. 4. Shape and angle of rotation of the designed robot (asymmetrical structure)

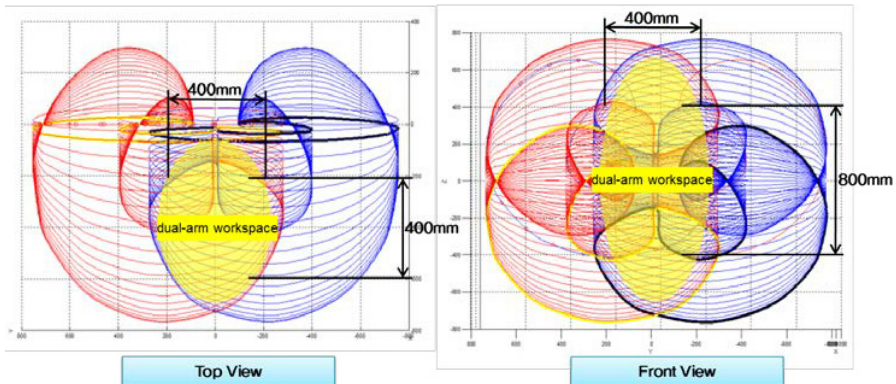


Fig. 5. Results of workspace analysis

2.3 Design and Specification

To meet the required specification, a motor and a reducer were selected to be light weight and flat among those which can provide a required torque. As a result, a robot arm was designed to meet the required payload and the weight of a single arm was about 15kg because of the limitation of selectable products. To reduce the weight of an arm, several customized parts of an actuator module are being developed. Maximum reach of each arm is 680mm. Each arm has 7 degrees of freedom and each joint have a joint torque sensor to measure an external force applied to an arm. Then a safety function can work if there is an impact between a robot and a human or an object and an active safety can be implemented. An actuator was designed as a modular structure and thus it has a merit in the aspect of maintenance. Figure 6 shows possible posture for a jig-less job, which is one of merits of dual arm robot and Figure 7 shows final design of the proposed dual-arm robot.

Table 1. Specification of each joint

Joint #	Max. speed (degree/sec)	Motion Range (degree)
1	150	+180 ~ -180
2	150	+135 ~ -60
3	150	+180 ~ -180
4	150	+144 ~ -55
5	240	+180 ~ -180
6	240	+90 ~ -90
7	240	+90 ~ -90

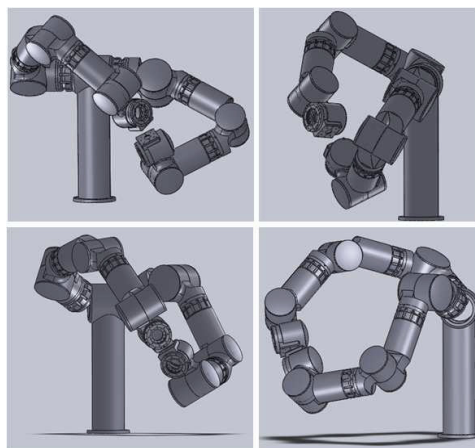


Fig. 6. Possible posture for a jig-less job



Fig. 7. Final design of the proposed robot

2 Implementation

In this section, a design concept and implementation results of actuator modules are proposed. An actuator module is composed of a motor, a reducer, an encoder, a torque sensor. Also, to measure the modification by a reducer and a torque sensor, double encoder is used. An actuator module is designed as a hollow shaft type for compactness and ease of maintenance of a robot. Figure 8 shows the concept of an actuator module.

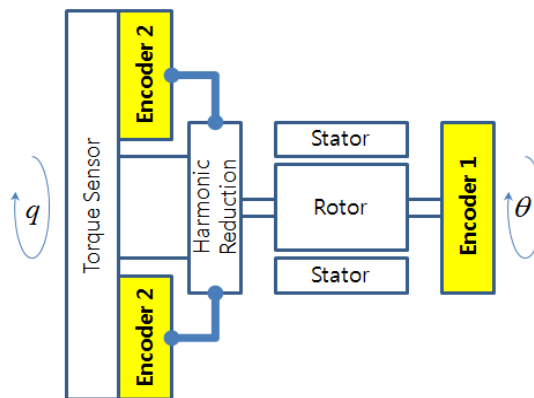


Fig. 8. Concept design of an actuator module

All four types of actuator modules are made, i.e., for joint 1, 2, for joint 3, 4, for joint 5, 6, and for joint 7. Each module was tested and improved to minimize the vibration and noise. Figure 9 shows implemented actuator modules and Figure 10 shows a prototype of a designed dual arm robot which is an assembly of seven modules and links.



Fig. 9. Each actuator module



Fig. 10. Prototype of a designed dual-arm robot

3 Cell Production System for Packaging IT Products

Nowadays, the requirement of robotic manufacturing system is increasing in many industrial sites [6] and this is closely related to the movement from the mass production system to the batch process cell production system. Even though the dramatic change in production line does not happen after the application of a robot, the manufacturing process appropriate for robots should be developed. Since a robot cannot do all tasks which a human worker does, a process should be categorized and automation equipment can be introduced to reduce a tact time. Overall concept of robotic cell production system is shown in Figure 11. In this system, robots and human works share the space and fulfill the mission which is given to each.



Fig. 11. Concept image of robotic cell production system

4 Conclusion

In this paper, we proposed a dual-arm robot for packaging of IT products like a cell phone. The procedure for the derivation of the needed specification was shown. Based on the derived specification, a robot design and workspace analysis was conducted. Also, some implementation results of actuator modules and the prototype of dual-arm robot was suggested. Finally, cell production system for robotic manufacturing process was described.

Acknowledgements. This research was supported by the Ministry of Knowledge Economy and the Korea Evaluation Institute of Industrial Technology (KEIT) with the program number of “10038660”.

References

1. Do, H.M., Park, C., Kyung, J.H.: Dual arm robot for packaging and assembling of IT products. In: IEEE Int. Conf. Automation Science and Engineering, pp. 1063–1066 (2012)

2. Park, C., Park, K., Park, D.I., Kyung, J.H.: Dual arm robot manipulator and its easy teaching system. In: IEEE Int. Symp. Assembly and Manufacturing, pp. 242–247 (2009)
3. Park, C., Park, K.: Design and kinematics analysis of the dual arm robot manipulator for precision assembly. In: IEEE Int. Conf. Industrial Informatics, pp. 430–435 (2008)
4. <http://www.motoman.com/products/robots/assembly-robots.php>
5. <http://www.abb.com/cawp/abbzh254/8657f5e05ede6ac5c1257861002c8ed2.aspx>
6. <http://www.rethinkrobotics.com/index.php/products/baxter/>
7. <http://spectrum.ieee.org/automaton/robotics/industrial-robots/abbfactory-robot-frida>

Dynamic Control of Parallel Manipulator

Kap-Ho Seo, Yongsik Park, Sungjo Yun, Sungho Park, Jungsoo Jun,
and Jeongtack Min

Applied Technology Division, Korea Institute of Robot and Convergence,
San 31, Hyoja-dong, Nam-gu, Pohang, Gyeongbuk, 790-784, Korea
neoworld@kiro.re.kr

Abstract. Parallel manipulator with longer legs and heavy load is applied in most of the current high fidelity simulators, which is used to simulate various motions in different environments by exporting varying displacement and orientation.

A novel model-based controller for 6-DOF parallel manipulator with gravity compensation is developed, in order to improve the control precision of 6-DOF parallel manipulator with high speed and heavy load. The effectiveness of the proposed algorithm will be discussed based on experiments.

Keywords: Parallel manipulator, dynamic control.

1 Introduction

The parallel manipulators have attracted many researchers since the early 1990's due to their advantages of high stiffness, high payload, high accuracy, and so on. The typical parallel manipulator is Gough Stewart Platform which is constructed by D. Stewart [1]. It consisted of six legs which are actuated by hydraulic actuators. There are several advantages in the application which includes large output force and torque, higher rigidity and accuracy due to the parallel path and averaged link to end effector error, compared with serial manipulator.

Another approach is the 6-DOF parallel manipulator with revolute actuators. These manipulators are faster since they use electrical motors. This type of parallel manipulator was introduced by Hunt in 1983 for the first time.

Parallel manipulator has been extensively studied due to its high force-to-weight ratio and widespread application [2]. Earl and Rooney analyzed the kinematic structures for robotic applicaitons and their interconnections including both serial and parallel mechanisms [3]. Hunt researched the kinematics of parallel manipulators based on screw theory and enumerated promising kinematics structures.

The control approaches of six degrees of freedom (6-DOF) parallel manipulator, which is a nonlinear system for its complex architecture, various variables, multi-degree of freedom, have been extensively studied recently. Some previous approaches intended to realize force control by assuming that the six ledges of 6-DOF parallel manipulator are absolutely independent. But, the control performances are not so ideal because they have ignored the mechanical coupling



Fig. 1. Developed stewart platform

between the six extensible legs. In this paper, the neural network controller is applied to compensate the friction and gravity of manipulator. The neural network controller is no more difficult to implement on actual systems than modern adaptive control algorithms. Neural network control also embodies some notions from robust control. However, in addition to these advantages, neural network control offers several advantages over adaptive control that virtually guarantee its acceptance within the industrial controls community during the next few years.

In this research, we developed a 6-DOF parallel manipulator, which can handle the 300kg payload for motion simulation. In order to implement the original motion of handling contents, the gravity of platform should be compensated. Section 2 describes the configuration of the developed platform, and section 3 and 4 shows the proposed algorithm and experimental results, respectively. The efficiency of the developed system is evaluated by the experiments. Concluding remarks are discussed in section 5.

2 System Description of 6-DOF Parallel Manipulator

2.1 Geometric Analysis of 6-DOF Parallel Manipulator

Generally, parallel manipulators consist of two platforms and six legs, where one platform is generally fixed to the ground, called the base platform, and the other is movable, called the moving platform. The developed platform is described in figure 1.

Each of the six legs has one end located in the base and the other end in the platform. Though the location of the six mounting points in either base or platform is not restricted, not all configurations result in controllable mechanisms. In each of the bodies, a coordinate frme is located; B denotes the base and P the platform in figure 2.

In practice, Stewart platform are not completely arbitrary arrangements, but rather are implemented as geometrically symmetrical mechanisms due to

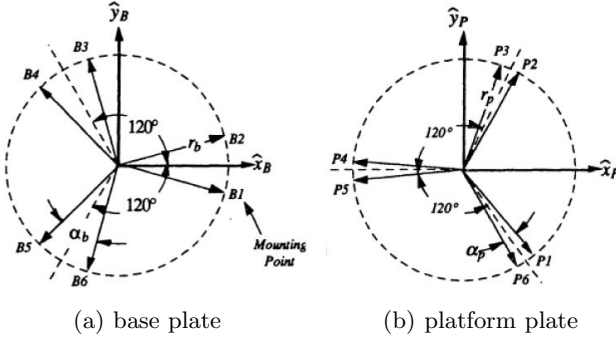


Fig. 2. Symmetrical stewart platform geometry

mechanical design constraints. The most common configuration uses six legs mounted in semi-regular hexagons on two plates. Since the vertices of the semi-regular hexagons may be inscribed in a circle, the geometry of both the base and platform plates can be described using only 4 parameters as shown in figure 2. It should be understood that for this paper only this configurations considered to be of interest and that all subsequent discussion implicitly refers to this particular type of Stewart platform. In figure 2, r_b means the base plate radius, r_p the radius of platform plate, α_b the base mounting angle, and α_p the amounting angle of platform plate.

2.2 Dynamic Model of 6-DOF Parallel Manipulator

The parallel manipulator allows full position and orientation control of the upper platform's center. The six legs are telescoping joints; as they extend and contract, they move and rotate the upper platform. The parallel manipulator has position accuracy and force exertion capabilities far exceeding that of standard serial-link robot arms.

Unfortunately, the parallel manipulator has a problem in fine position and force control. The dynamics for parallel-link robots are indeed of the form of equation 1.

It's not easy to control the 6-DOF parallel manipulator system well due to the high nonlinearity in system dynamics, system uncertainties, and complex kinematics. In this paper, we consider the dynamics of the 6-DOF parallel manipulator with Lagrange method. Lagrange equation describes the conervation of energy, which is suitable for analyzing the multi-link movements with restraints:

$$M(q)\ddot{q} + C(q, \dot{q})\dot{q} + F(q, \dot{q}) + \tau_d = \tau \quad (1)$$

where $q \in \mathbb{R}^p$ denotes the p generalized coordinates, $M(q) \in \mathbb{R}^{p \times p}$ is the symmetric and positive definite inertia matrix, $C(q, \dot{q}) \in \mathbb{R}^{p \times p}$ represents the centripetal and Coriolis matrix, $F(q, \dot{q}) \in \mathbb{R}^p$ represents the friction and gravitational vector, $\tau_d \in \mathbb{R}^p$ denotes bounded unknown disturbances including unstructured dynamics, and $\tau \in \mathbb{R}^{p-r}$ is the torque input vector.

This is because when determining the kinematics solution for parallel-link arms, it is necessary to solve a set of coupled nonlinear equations. Thus, the dynamics computation takes the form of a computer algorithm, wherein the kinematics problem is first solved numerically, then two Jacobians are computed, and finally the arm dynamics equations are computed.

The upshot of this situation is that, due to the impossibility of finding a closed-form expression for regression matrices, it is fruitless to apply standard adaptive control techniques to parallel-link arms. Neural network controllers should finally open the way for parallel-link arms in industrial and machining applications involving position and force control.

3 System Control

Since it is very difficult to model dynamics of this system due to its complex structure, and also due to disturbances or varying loads on it when the user exerts his ambulation on it we incorporated neural network based control methodology. The dynamics of a mobile manipulator subject to kinematic constraints can be obtained using Lagrangian approach as shown in equation 1.

The generalized coordinates q consist of system parameter, $q = (x, y, z, \phi, \theta, \psi)^T$, where (x, y, z) are the platform center of mass cartesian coordinates, (ϕ, θ, ψ) are the Euler angle on the platform center.

In this stage, to design a controller, we consider a Lyapunov function candidate for manipulator as:

$$V = V_1(e_x) + V_2(r) \quad (2)$$

where e_x is not a position error in the world coordinate space but a position error in the robot coordinate space, $r = \dot{e} + ke$ is a filtered tracking error in manipulator joints. The first term in (2) was considered to maintain the user's position within the clearance area in robot. The second term for joint position and velocity error enable us to control robot manipulator which should adjust the predetermined height and support the specified portion of the user's weight.

Now, take a Lyapunov function candidate of the following form [6] [7] [8]:

$$V = V_1(q_{vd} - q_v) + \frac{1}{2}r^T Mr. \quad (3)$$

Assuming that there exist a Lyapunov function $V_1(q_{vd} - q_v, t)$, a positive continuous function, $Q_1(t) > 0$, a reference smooth feedback velocity α , such that

$$\frac{\partial V_1}{\partial t} + \frac{\partial V_1}{\partial (q_{vd} - q_v)} \frac{d(q_{vd} - q_v)}{dt} \Big|_{\dot{q}_v = S(q_v)\alpha} \leq -Q_1(t). \quad (4)$$

Taking the time derivative of (3), we obtain

$$\dot{V} = \dot{V}_1 + \dot{V}_2. \quad (5)$$

Performing detailed mathematical derivation with (4) yields

$$\begin{aligned}\dot{V} \leq & -Q_1(t) + r^T \{-\tau + Mkr - (Mk - C)ke \\ & + f + \tau_d\}\end{aligned}\quad (6)$$

Once simplified

$$\begin{aligned}\dot{V} \leq & -Q_1(t) + r^T \{-\tau + Mkr - (Mk - C)ke + f\} \\ & + r^T \tau_d \\ = & -Q_1(t) + r^T \{-\tau + \Psi\} + r^T \tau_d\end{aligned}\quad (7)$$

with the unknown nonlinear terms which should be estimated through the learning algorithm with neural networks.

$$\begin{aligned}\Psi &= Mkr - (Mk - C)ke + f \\ &= Mkr - (Mk - C)ke + M\ddot{q}_{rd} + C\dot{q}_{rd} + F\end{aligned}\quad (8)$$

Neural networks such as an RBF network has been shown to have a universal approximation ability to approximate any smooth function on a compact set. Two RBF networks with a sufficiently many number of hidden units such that

$$\Psi = W^T h(x) + \epsilon(x) \quad (9)$$

where x is the input pattern to the neural networks. The ideal and unknown weights $W \in \Re^{n_1 \times (m-r)}$ in that respect are assumed to be constant and bounded by

$$\|W\|_F \leq W_B \quad (10)$$

where W_B is known positive constants. The numbers of hidden-layer neurons of the two RBF neural networks are n . The approximation errors $\epsilon \in \Re^{m-r}$ is bounded by $\|\epsilon\| \leq \epsilon_N$, with ϵ_N being positive constant; The properly chosen RBFs for the hidden-layer neurons are $h(x) : \Re^{5m+5n-3r} \rightarrow \Re^{n_1}$.

The basis functions of neural networks were defined to be Gaussian:

$$h_{ij} = \exp\left(\frac{-\|x - c_{ij}\|^2}{\sigma_{ij}^2}\right), i = 1, 2, j = 1, 2, \dots, N \quad (11)$$

The centers c_{ij} and widths σ_{ij} are all chosen *a priori* and kept fixed for simplicity. Therefore, only the weights W is adjustable during the learning process.

The estimates of Ψ is given by

$$\hat{\Psi} = \hat{W}^T h(x). \quad (12)$$

Theorem 1. *By choosing the control law as*

$$\tau = kr + \hat{\Psi} \quad (13)$$

where r is filtered tracking error for the manipulator, and the weight update law for the neural networks is

$$\dot{\hat{W}} = +\beta hr^T - \mu\beta\|P\|\hat{W} \quad (14)$$

where

- $P = (r)$, control gains;
- $k > 0$
- $\beta > 0$ positive constants representing the learning rates of the two neural networks;
- $\mu > 0$ small positive design parameter.

By choosing them properly, the tracking errors of error dynamics and the neural network estimation weights are all guaranteed to be uniformly ultimately bounded.

Proof. Substitute the control law (13) into the derivative of Lyapunov function (7), so that

$$\begin{aligned} \dot{V} &\leq -Q_1(t) + r^T\{-kr - \hat{\Psi} + \Psi\} + r^T\tau_d \\ &\leq -Q_1(t) - kr^Tr + r^T(\tilde{W}^Th) + r^T\epsilon + r^T\tau_d \end{aligned} \quad (15)$$

where $\tilde{W} = W - \hat{W}$.

Let a new Lyapunov function candidate with neural network learning dynamics be defined as

$$V = V + \frac{1}{2\beta}\text{tr}\{\tilde{W}^T\tilde{W}\} \quad (16)$$

Differentiating (16) yields

$$\begin{aligned} \dot{V} &\leq -kP^TP + r^T(\tilde{W}^Th) \\ &\quad + P^T(\epsilon + \tau_d) - \frac{1}{\beta}\text{tr}\{\tilde{W}^T\dot{\hat{W}}\} \\ &\leq -k\|P\|^2\|P\|(\epsilon_N + \tau_N) \\ &\quad - \frac{1}{\beta}\text{tr}\{\tilde{W}^T(\dot{\hat{W}} + \beta hz^T)\} \end{aligned} \quad (17)$$

where $\|\epsilon\| \leq \epsilon_N$, $\|\tau_d\| \leq \tau_N$, and $\|W\|_F \leq W_B$. Applying weight update law,

$$\dot{V} \leq -k\|P\|^2\|P\|(\epsilon_N + \tau_N) + \mu\|P\|\text{tr}\{\tilde{W}^T\hat{W}\} \quad (18)$$

From the matrix theory, the following property holds [9]:

$$\text{tr}\{\tilde{W}^T\hat{W}\} \leq \|\tilde{W}\|_F\|W\|_F - \|\tilde{W}\|_F^2. \quad (19)$$

From (18) and (19),

$$\begin{aligned} \dot{V} &\leq -\|P\|\left[\bar{k}\|P\| + \mu\left(\|\tilde{W}\|_F - \frac{W_B}{2}\right)^2\right. \\ &\quad \left.- \left(\frac{\mu W_B^2}{4} + \epsilon_N + \tau_N\right)\right] \end{aligned} \quad (20)$$

which is guaranteed to be negative provided

$$\|P\| > \frac{\frac{1}{4}\mu W_B^2 + \epsilon_N + \tau_N}{\bar{k}} \quad (21)$$

or

$$\|\tilde{W}\|_F > \frac{W_B}{2} + \sqrt{\frac{\mu W_B^2}{4} + \frac{\epsilon_N + \tau_N}{\bar{k}}}. \quad (22)$$

By Lemma 4.1.1 in [9], for all x in the compact set $S_x \equiv \{x \mid \|x\| < b_x\}$, since \tilde{q}_v is asymptotically stable, there exist computable positive constants q_B , c_0 and c_1 , such that

$$\|x(t)\| \leq q_B + c_0\|P(0)\| + c_1\|P(t)\| \quad (23)$$

where $P(0) = r(0)$, and b_x , q_B are constants representing the boundness, $b_x > q_B$.

To ensure that the approximation property of the two neural network on-line estimators holds throughout, the tracking error-vector P should be always kept in the compact set $S_p \equiv \{P \mid \|P\| < (b_x - q_B)/(c_0 + c_1)\}$. This may be achieved by selecting the minimum control gain \bar{k} to satisfy

$$\bar{k} > \frac{(\frac{1}{4}\mu W_B^2 + \epsilon_N + \tau_N)(c_0 + c_1)}{b_x - q_B}. \quad (24)$$

Thus, if the parameters are appropriately chosen, the uniform ultimate boundedness of the tracking errors z and r , and the neural network weights can be guaranteed. ■

4 Experimental Results

In this paper, simple simulation was conducted for evaluating the effectiveness of the proposed control algorithm. The parallel manipulator was controlled to

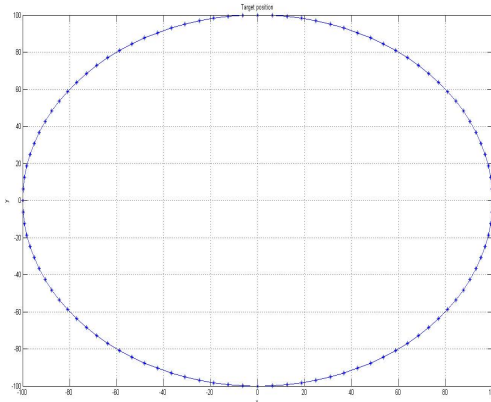
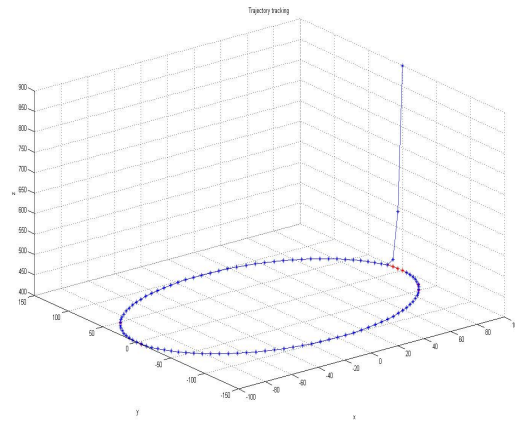
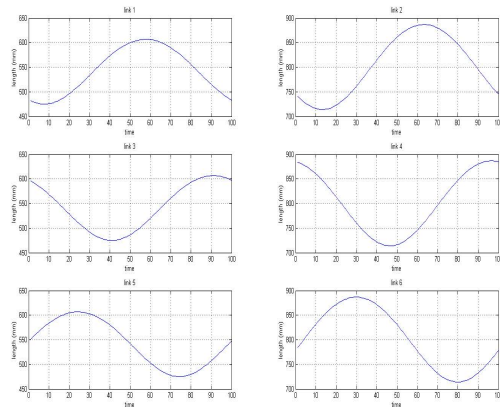
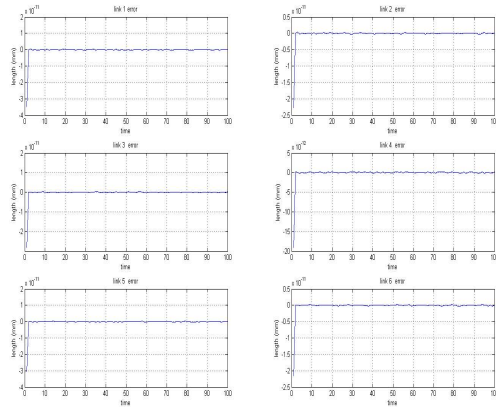
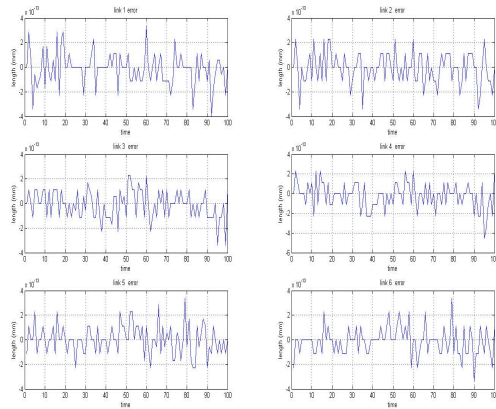


Fig. 3. Target position

**Fig. 4.** Trajectory tracking**Fig. 5.** Link Length

follow a predefined trajectory. The desired trajectory is a circle with a diameter of 100mm and a height from a base plate of 400mm as shown in figure 3. The initial position of manipulated is assumed at $q = [x, y, z, \phi, \theta, \psi]^T = [100, 0, 900, 0, 0, 0]^T$.

The tracking is conducted as shown in figure 4. After a few step, the parallel manipulator followed the desired trajectory. Each link adjusted its length, using a torque control with the proposed algorithm. The change of each link is depicted in figure 5. Its tracking error is plotted in figure 6. In the initial state, the error is very high as compared with the stable state. But, when it comes to the stable state, the error has a small value as shown in figure 7.

**Fig. 6.** Error**Fig. 7.** Detail Error

5 Conclusion

A novel model-based controller for 6-DOF parallel manipulator with gravity compensation is developed, in order to improve the control precision of 6-DOF parallel manipulator with high speed and heavy load. The effectiveness of the proposed algorithm was discussed based on experiments.

Acknowledgment. This research was partially supported by Ministry of Knowledge Economy (MKE), Korea Institute for Advancement of Technology (KIAT) and Daekyung Leading Industry Office through the Leading Industry Development for Economic Region, Ministry of Culture, Sports and Tourism(MCST) and Korea Creative Content Agency(KOCCA) in the Culture Technology(CT)

Research & Development Program (Immersive Game Contents CT Co-Research Center), Ministry of Knowledge Economy (MKE), Korea Institute for Advancement of Technology (KIAT) and Biomedical IT Convergence Center.

References

- [1] Stewart, D.: A Platform with six degrees of freedom. In: Proceedings of the Institution of Mechanical Engineers, vol. 180, pp. 371–386 (1965)
- [2] Merlet, J.P.: Parallel robots. Kluwer Academic Publisher, Netherlands (2000)
- [3] Earl, C.F., Rooney, J.: Some Kinematic Structures for Robot Manipulators. ASME, J. Mech. Trans. Auto. in Design, 15–22 (1983)
- [4] Hunt, K.H.: Structural Kinematics of in-parallel-actuated Robot-arms. ASME, J. Mech. Trans. Auto. in Design, 705–712 (1983)
- [5] Lewis, F.L.: Neural Network Control of Robot Manipulators. IEEE Expert 11, 64–75 (1996)
- [6] Lee, C., Seo, K., Oh, C., Lee, J.: A System for Gait Rehabilitation System with Body Weight Support: Mobile Manipulator Approach. Journal of HWRS-ERC 2(3), 16–21 (2001)
- [7] Lee, C., Seo, K., Kim, C., Oh, S., Lee, J.: A System for Gait Rehabilitation: Mobile Manipulator Approach. In: Proc. IEEE Conf. Robot. Automat. 2002, vol. 3, pp. 3254–3259 (2002)
- [8] Lin, S., Goldenberg, A.A.: Neural-Network Control of Mobile Manipulators. IEEE Trans. Neural Networks 12(5), 1121–1133 (2001)
- [9] Lewis, F.L., Jagannathan, S., Yesildirek, A.: Neural Network Control of Robot Manipulators and Nonlinear Systems. Taylor and Francis, London (1999)

Design of Rotor and Magnetic Bearings for 200RT Class Turbo Refrigerant Compressor

Cheol Hoon Park and Sang Kyu Choi

Dept. of Robotics & Mechatronics Research, KIMM
104 Sinseongno, Yuseong-gu, Daejeon, 305-343, Korea
{parkch,skchoi}@kimm.re.kr

Abstract. For turbo refrigerant compressor, oil-free bearing has merits that the continuous operation is possible because the lubrication system is not required and the refrigerant is not contaminated by the oil. Magnetic bearing is one of oil-free bearing and recently it started to be applied to a few turbo refrigerant compressors because of easy maintenance thanks to no friction and no wear in bearing. 200RT class turbo refrigerant compressor using oil-free bearing is under development after finishing the development of 145RT compressor. This paper presents the design modification from 145RT compressor and design procedure of hybrid thrust magnetic bearing using both of permanent magnet and electromagnet. Thrust magnetic bearing are designed to support 2,000N thrust force by compressor at 18,000rpm operating speed. The controller for magnetic bearing was designed and the rotordynamic analysis such as critical speed, and unbalance response in case that the rotor is supported by magnetic bearings are simulated by using finite-element method.

Keywords: Turbo refrigerant compressor, magnetic bearings, rotordynamics.

1 Introduction

The rotor of turbo refrigerant compressors cannot be supported by the ball bearings because the refrigerant melts the lubricant which is used in the ball bearings. Therefore, turbo refrigerant compressors should adopt the oil-free bearings. Air foil bearings are a kind of oil-free bearings, but they have disadvantages that the maintenance cost is high because there is friction and wear between air foil bearing and rotor at the moment of start-up and the stability is not so high because the damping is low. The other oil-free bearings are magnetic bearings. In contrast to air foil bearing, magnetic bearings have advantages that the maintenance cost is very low because there is no friction and wear in all operation speed range including initial start and the energy efficiency is very high because friction loss is less than 1/500 of friction loss in the typical oil bearings [1, 2]. In this study, we present the design procedure of magnetic bearings to support 200RT class turbo refrigerant compressor. Magnetic bearings here consist of hybrid homopolar type radial bearings and hybrid thrust bearing using both of permanent magnet and electromagnet. Magnetic bearings are designed to support 2,000N thrust force by compressor at 18,000rpm operating

speed. The controller for magnetic bearings was designed and the critical speed, and unbalance response are simulated through rotordynamic analysis using finite element method.

2 Previous Works

Several turbomachinery companies have already released compressor using magnetic bearings. TURBOCOR Co. in USA developed centrifugal compressor using permanent/electromagnet magnetic bearings as shown in figure 1, which has been equipped in the chiller of UNILAIR Co. SKF Co. in Sweden developed turbo refrigerant compressor using electromagnet magnetic bearings as shown in figure 2 of which radial and thrust magnetic bearing could generate 1,320 N and 2,200 N respectively. The other company in Sweden, abs also developed turbo compressor using electromagnet magnetic bearings as shown in figure 3.

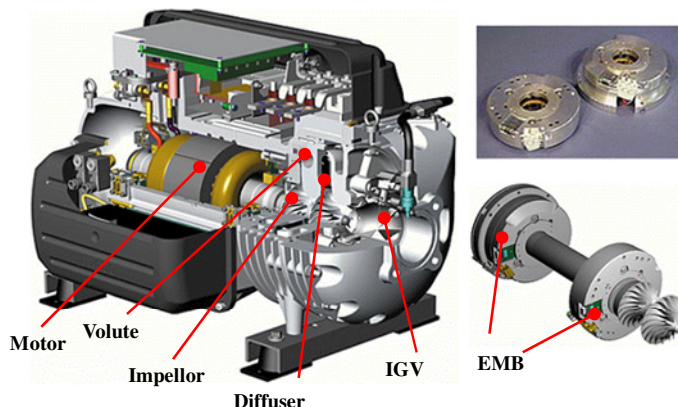


Fig. 1. Centrifugal compressor of Danfoss TURBOCOR, USA

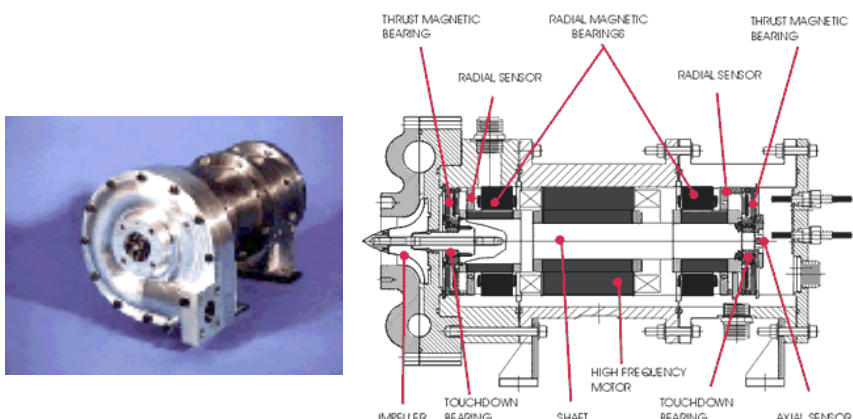


Fig. 2. Turbo refrigerant compressor of SKT, Sweden

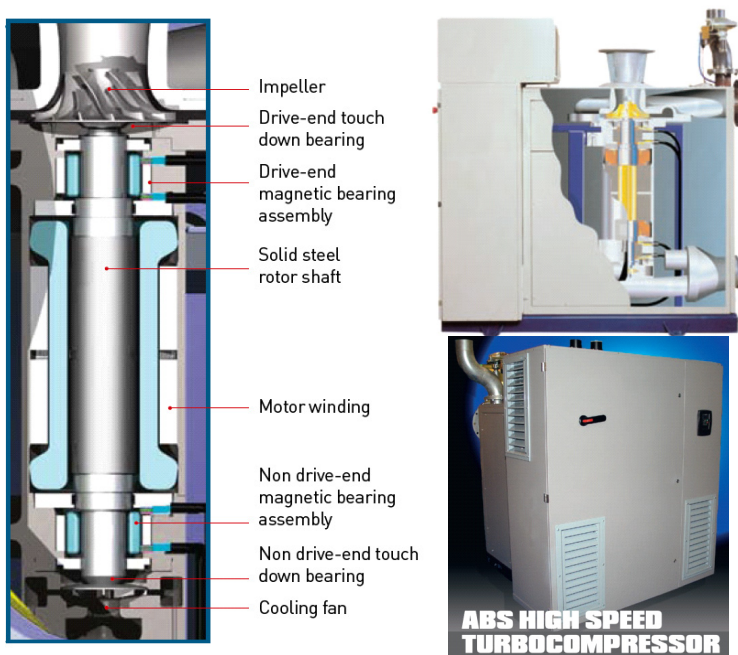


Fig. 3. Turbo compressor of abs, Sweden

Previously, we have developed 145RT class turbo refrigerant compressor which has a configuration as shown in Fig. 4. It was composed of shaft, high efficient impellers, magnetic bearings and high speed BLDC. The rotor was located to stand vertically so that the radial magnetic bearings could be free from the necessity to support the weight of rotor and the force requirement for the radial magnetic bearings could be minimized. In addition to this, this layout is helpful to reduce the force requirement for the thrust magnetic bearing because the gravity force by rotor would act in the opposite direction to the thrust force by compressor. The magnetic bearings to support the rotor were composed of radial magnetic bearings and thrust magnetic bearings. Magnetic bearings are classified based on the way how to generate magnetic flux such as active magnetic bearings (AMB) using electromagnet only, permanent magnetic bearings (PMB) using permanent magnet only and hybrid magnetic bearings (HMB) using the combination of electromagnet and permanent magnet [3]. While PMB have a merit that they don't need energy, there is a demerit that it is difficult to be used for vibration control because of low stiffness and damping [4]. AMB show the fast dynamic response but they need continuous bias current to generate bias flux and the efficiency becomes low. In contrast, HBM don't need bias current because the permanent magnets located adjacent to the electromagnet core generate bias flux, and they have merits that they can generate more magnetic force than AMB with the same amount of current and they can be more efficient. On the basis of these reasons, HMB were selected for the radial magnetic bearings so that the size of magnetic bearings could be minimized and the efficiency could be maximized. For the thrust bearing, the

use of both HMB and PMB was selected. While double-acting type thrust HMB generates the dynamic force to take care of the pulsation of thrust force by compressor, thrust PMB located at the end of the rotor generates bias force in the opposite direction to the thrust force by compressor.

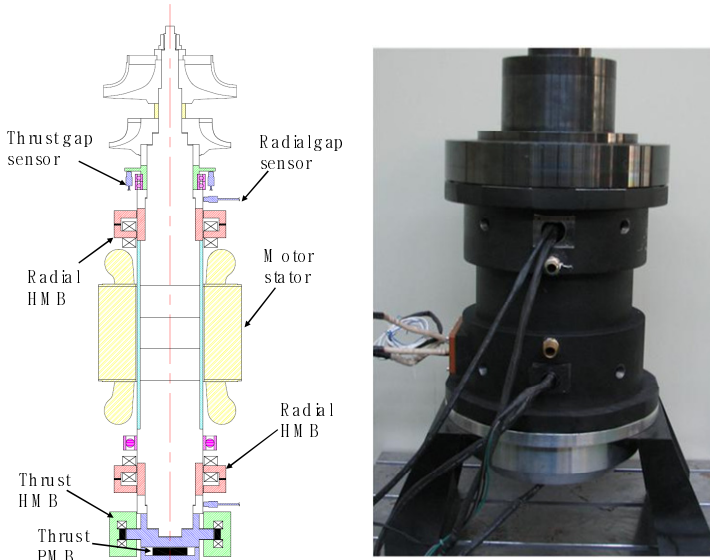


Fig. 4. 145RT class turbo refrigerant compressor (Previous work of this study)

However, there were several problems in the configuration of 145RT class turbo refrigerant compressor. Firstly, there was no space to install the axial gap sensor at the end of shaft because thrust PMB was installed at that location. Therefore, thrust target plate should be installed right below the second impeller in the rotor. Moreover, correct axial displacement could be measured by averaging the outputs of 2 axial sensors. The additional axial sensor resulted in the increase of the cost. Secondly, thrust HMB was equipped with a radially magnetized ring magnet. Because it is almost impossible to magnetize the entire ring magnet in the radial direction, in practice, a ring magnet is segmented into 6 or 8 pieces, and each segment is separately magnetized in the radial direction. One of the problems with a segmented ring magnet is that it is not easy to assemble all the pieces of the magnet into one ring magnet again and control the gap between the magnet and the thrust collar. Another problem is that the radial magnetic flux becomes non-uniform on the boundaries of the segmented magnets, which results in performance degradation.

3 Configuration of 200RT Class Turbo Refrigerant Compressor

Figure 5 shows the configuration of 200RT class turbo refrigerant compressor. In order to solve the problems in the previous work, some configuration has been modified in developing 200RT compressor. Inductive type gap sensor to measure

both axial and radial displacement with one PCBA was developed and installed at the upper side of upper radial HMB and lower side of lower radial HMB. The structure of thrust HMB has been modified to install the axially magnetized ring magnet. Because it is easy to magnetize the ring magnet in the axial direction, the segmentation of the ring magnet for magnetization is not required and the assembly process can be simplified. The rotor length of 200RT compressor is 707 mm, which is increased by 25 mm compared to the rotor length of 145RT compressor. Therefore, it is predicted that the first bending mode critical speed would be reduced, but it would not make any problem because the operating speed is also reduced from 21,000 rpm of 145RT compressor to 18,000 rpm.

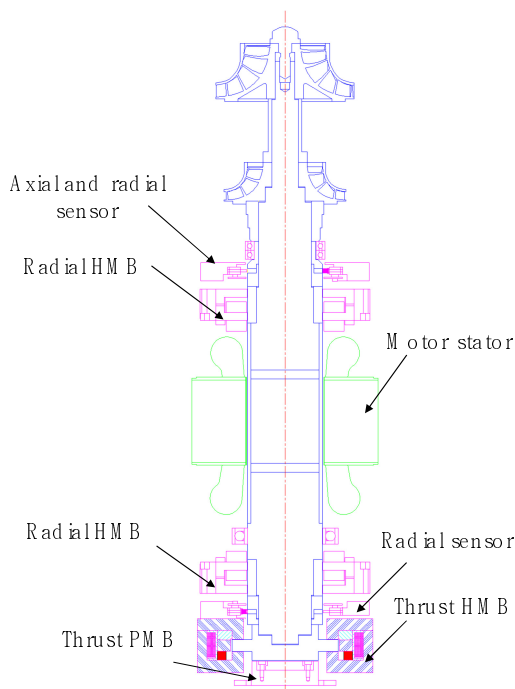


Fig. 5. Configuration of rotor and magnetic bearings of 200RT class turbo refrigerant compressor

4 Design of Magnetic Bearings

In order to design thrust magnetic bearing, the thrust force to be supported must be identified first. Because turbo refrigerant compressor is the vertical-rotor type, the sum of the thrust force by compressor and the weight of rotor can be considered as the total thrust force to be supported. It is predicted that the mass of rotor will be about 22kg and the thrust force by compressor at the operating speed will be maximum 2,000N. Hence, thrust force covering all speed range is from -200N at a standstill to

1,800N at the operating speed. Thrust magnetic bearing consists of HMB which can dynamically control the magnetic force by changing the amount of current and PMB which generates bias force in the opposite direction to the thrust force by compressor. Ring-shaped coil is located inside of HMB stator made of pure iron. Ring-shaped permanent magnet which is axially magnetized and generates bias flux for HMB is positioned inner side of coil, and pure iron ring which provides a flux path from PM to thrust collar is located on the ring-shaped magnet. PMB using coin-shaped permanent magnet is located inside of pure iron stator at a distance of air gap, g_0 apart from the end of the rotor [5]. The integral pure iron structure of thrust collar and U-shape core which is attached at the end of the rotor serves the flux path from HMB and PMB to the rotor. Based on the requirements in Table 1, thrust HMB and PMB were designed by referring [6]-[9]. The dynamic force requirement of thrust HMB is determined to have enough range so that the net magnetic force by HMB and PMB could have a safety factor of more than 1.5.

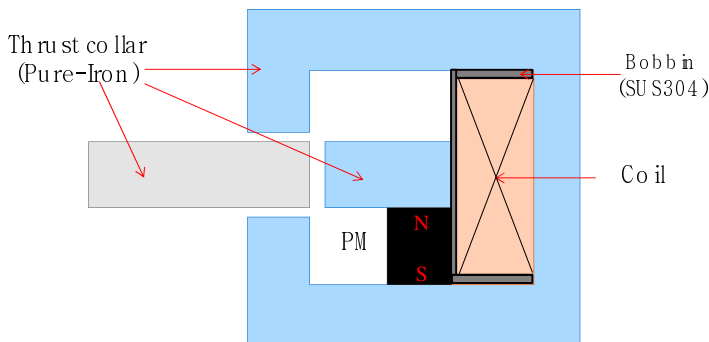


Fig. 6. Configuration of thrust HMB of 200RT class turbo refrigerant compressor

Table 1. Design requirements for thrust HMB and PMB

Item	Value
Thrust force to be supported	-200~1,800
Force requirement for HMB and PMB[N]	-1,800~200
Bias force by PMB[N]	-1,000
Dynamic force by HMB[N]	-2,000~2,000
Net magnetic force by HMB and PMB[N]	-3,000~1,000

In order to check the design validity, magnetic flux density analysis shown as Figure 7 was performed under 3 cases of conditions by using electromagnetic analysis software, Maxwell. The analysis results in Table 3 show that this design would result in generating almost same forces as the design requirements.

Radial HMB was designed to meet the same specifications as 145RT compressor.[1]

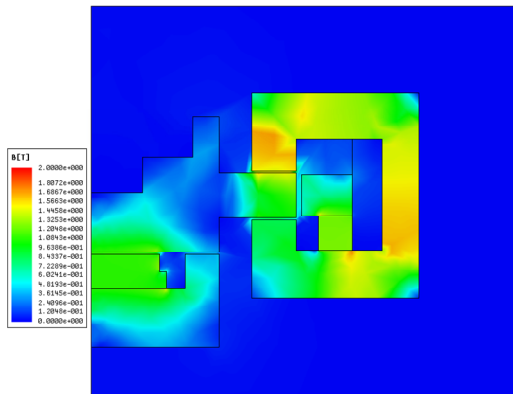


Fig. 7. Magnetic flux density analysis of thrust HMB and PMB with 10A current

Table 2. Analysis results for magnetic forces of thrust HMB depending on conditions

Condition	Magnetic force[N]
Force by PMB only	-729
Force by HMB only with 10A current	2,081
Force by PMB and HMB with 10A current	1,607

5 Rotordynamic Analysis

The rotor in Figure 5 is divided into 38 elements as shown in Figure 8 to perform the rotordynamic analysis of the flexible rotor by using finite element method. All other components on the rotor except the shaft are considered as the added mass. The analytical model for the rotor suspended by the radial HMB can be obtained by combining the finite element model of the flexible rotor and the linearized model of the radial HMB [10]. PID controller was designed to compensate the radial disturbances such as unbalance force. The analysis to get the eigenvalues and unbalance response was performed for the speed range from 0 to 24,000rpm, and Damped natural frequency map is shown in Figure 9. It is predicted that free-free first and second bending mode frequency would be 471 Hz and 952 Hz, respectively, and the translational and conical rigid body mode would be met at 1,500rpm and 1,800rpm each and the frequency of backward 1st bending mode at 2,1000rpm would exist at 441Hz which is far enough from the operating speed, 18,000rpm (300Hz). Unbalance response was calculated assuming unbalance is evenly located at 17th and 32nd node with the phase difference of 180deg, and it is predicted that there would be zero-to peak displacement of the rotor at nodes of the location of radial HMB less than 2 μ m in all speed range.

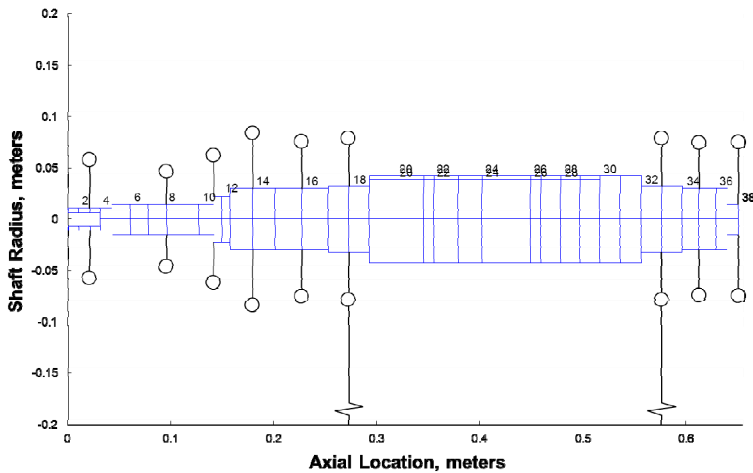


Fig. 8. Rotordynamic model for FEM analysis

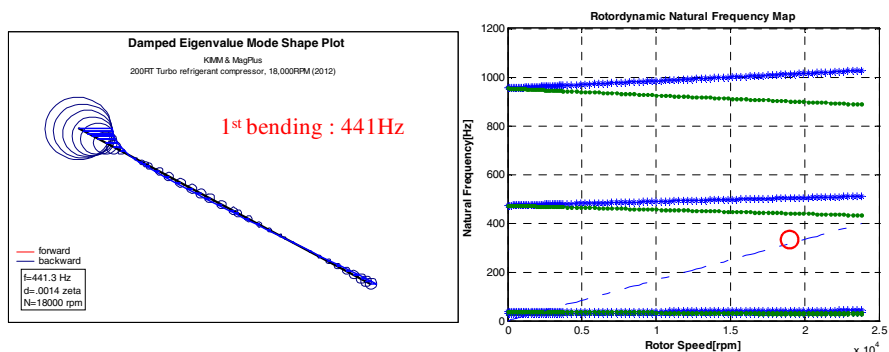


Fig. 9. Mode shape of 1st bending mode and Campbell diagram

6 Conclusion

The magnetic bearings to support 200RT class turbo refrigerant compressor were designed. Basically, they are based on those of 145RT compressor, but new sensors and thrust HMB was adopted to overcome several issues of 145RT compressor. Through the rotordynamic analysis, it was predicted that first bending mode would be located at the high frequency with enough margin from the operating speed. Also, it is predicted that even with PID controller, zero-to-peak displacement caused by unbalance response would be less than 2 μm , and it would be possible to run the stable operation in all the speed range. In the future, we have a plan to build the test rig to verify the performance of the radial and thrust magnetic bearings.

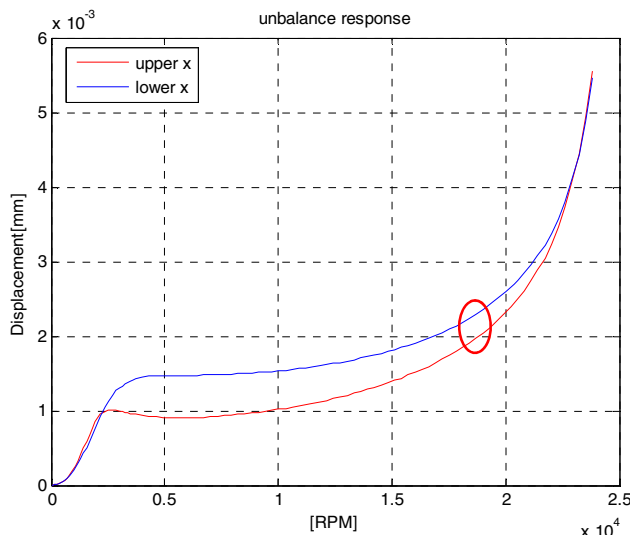


Fig. 10. Unbalance response in 200RT class turbo refrigerant compressor

References

1. Park, C.H., Choi, S.K., Park, J.Y., Yun, D.W.: Design of hybrid magnetic bearings for turbo refrigerant compressor. In: Proc. 17th International Congress on Sound & Vibration, pp. 1–8 (2010)
2. Allaire, P.E., Maslen, E.H., Humphris, R.R., Sortore, C.K., Studer, P.A.: Low power magnetic bearing design for high speed rotating machinery. In: Proceedings of the NASA International Symposium on Magnetic Suspension, pp. 317–329 (1992)
3. Rao, J.S., Tiwari, R.: Design optimization of double-acting hybrid magnetic thrust bearings with control integration using multi-objective evolutionary algorithms. Mechatronics 19, 945–964 (2009)
4. Morales, W., Fusaro, R.: “Permanent magnetic bearing for spacecraft applications”, NASA/TM-2003-211996/REV1
5. TURBOCOR INC., “Device to relieve thrust load in a rotor-bearing system using permanent magnets”, PCT patent, 2004007984
6. Lee, A.C., Hsiao, F.Z., Ko, D.: Analysis and testing of magnetic bearing with permanent magnets for bias. JSME International Journal Series C 37, 774–782 (1994)
7. Lee, A.C., Hsiao, F.Z., Ko, D.: Performance limits of permanent-magnet-biased magnetic bearings. JSME International Journal Series C 37, 783–794 (1994)
8. Maslen, E.H., Allaire, P.E., Noh, M.D., Sortore, C.K.: Magnetic bearing design for reduced power consumption. Journal of Tribology 118, 839–846 (1996)
9. Fan, Y.H., Lee, A.C.: Design of a permanent/electromagnetic magnetic bearing-controlled rotor system. Journal of the Franklin Institute 334B, 337–356 (1997)
10. Yoo, S.Y., Park, C.H., Choi, S.K., Noh, M.K.: Flexible rotor modelling for a large capacity flywheel energy storage system. In: Proceedings of 11th International Symposium on Magnetic Bearing 2008, Nara, Japan, pp. 238–242 (2008)

Forming Complicated Surface in Shipyard Using Neural Network System

Nguyen Truong-Thinh, Tuong Phuoc Tho, and Trinh Duc Cuong

Dept. of Mechatronics, Ho Chi Minh City University of Technical Education

1 Vo Van Ngan, Thu Duc, Ho Chi Minh, Vietnam

thinhnt@hcmute.edu.vn, {tuongphuoctho,cuongtd91}@gmail.com

Abstract. Determining the positions of triangle heating in and parameters of heating process are important for deforming the concave surfaces in shipyard, as well as airplane. The objective of this study was to develop an artificial neural network (ANN) model to predict positions of induction heating and parameters of heating process based on analytical solutions. This model of ANN can help manufacturers determine the positions of induction heating lines and their heating parameters to form a desired shape of plate. The back-propagation neural network systems for determining line-heating positions from object shape of plate are presented in this paper. An artificial neural network model is developed with the relationship between the desired shape of plate and the paths of induction heating. The input data are vertical displacements of plate and the output data are selected heating lines composed by the areas. The outputs of the models were positions of induction heating on plate as well as their parameters. Simulated values obtained with neural network correspond closely to the experimental results.

Keywords: Neural Network, Induction heating, Back propagation, deformation, forming.

1 Introduction

Line heating is an important production process that is widely used to produce various curved thick plate for ship industry [1]. The line heating technique is base on human skill and is plate forming for producing desired curve plates. In ship building, it has been an important problem in manufacturing process. Thermal strains and stresses are generated by non-uniform temperature gradients, which are produced in the plate by the heating and cooling cycles that occur in the line heating process. When thermal stresses exceed the elastic limit, residual distortions appear. Using these deformations, objective curved surface is manufactured. Since the line heating process is very complex transient thermo-elastic-plastic procedure, the predictions of residual deformation are relatively difficult. Many researches have focus on the prediction of the shape of the metal plate, when the line heating condition and material properties are known. In order to calculate the shape of plate, finite element method or plate theory is applied. Research on design of the proper heating and cooling processes is based on the experience of forming simple shape surfaces from rectangular plates.

In order to determine heating line, strain or curvature analysis is needed. It is thought that process automation can be possible, using differential geometry and numerical analysis. In shipbuilding industry, plates are so thick that temperature gradient is main mechanism which induces the bending of thick plates in line heating process. Thermal strains and stress are generated by non-uniform temperature gradient, which are produced in the plate by the heating and cooling cycles that occur in the line heating process. Line heating process is very complex transient thermo-elastic-plastic procedure, and the predictions of residual deformation are relatively difficult. Also computation time is very long in case of three-dimensional finite element analysis. Therefore, three-dimensional model is not suitable for real time analysis. In order to reduce computation time, simplified models have been developed, but there are more work needs to be done to apply it in the line heating process.

In the present study an attempt has been made towards the applications of ANN system in modeling the processing route with predictability of the systems parameters in induction line heating [2,3]. They are being used in the areas of prediction and classification, areas where nonlinear models and other related statistical techniques have traditionally been used. A comparative study between the above mentioned modeling tool and FEM modeling has also been made to assess the effect of the different input parameters on the shrinkage and displacement after induction triangle heating by inductor. To deform a more complex surface, the number of induction heating triangles increases and the positions of them exist at random, and estimation of the deformed shape of plate is more difficult. Long time and high cost are disadvantage of experimental and numerical method to estimate the heating positions including heating parameters for a desired shape of the plate. In this study, an ANN model to predict the heating positions for a desired curved surface is developed with the relationship between the heating-triangle positions including the heating parameters and the deformations of steel plates obtained by the analytical solution. The training and testing data for the ANN are obtained by use of the analytical solution. The network uses the back-propagation algorithm to learn the training patterns and its architecture is optimized with the trial-and-error method. The results of the prediction with the ANN model are used in an experiment of induction heating to validate usefulness and effectiveness of the model to determine the heating positions including heating parameters for the desired shape of a plate in induction heating process. In this paper model of Neural Network for predicting positions of induction triangle heating is discussed and compared to FEM models as well as results from experiments.

2 Analysis of Induction Heating

An alternating voltage applied to induction coil results in an alternating current in the coil circuit. Alternating coil current will produce in its surrounding a time-variable magnetic field that has the same frequency as the coil current. This magnetic field induces eddy current in the steel plate located near the coil. These induced currents have same frequency as the coil current, whereas, their direction is opposite to coil current. The induced current generates electric-resistance heat by the Joule effect in the plate and this can be used to bend the plate. It is assumed that plastic strains,

driving force to make angular distortion and transverse shrinkage, are produced in a critical heating region.

Heat generation which is calculated from the electro-magnetic analysis is used as heat source in three dimensional temperature analysis. Magnetic vector potential can be evaluated. From the theory of Maxwell's electromagnetism, and the eddy current can be calculated using the magnetic vector potential and is given by

$$J_e = \sigma E = -j\omega\sigma A \quad (1)$$

Where E is the electric field intensity and J_e is the Eddy current density. Heat source is expressed as

$$q = \frac{[\operatorname{Re}(J_e)]}{\sigma} \quad (2)$$

Where q is the heat source. For the special case where the source current density is assumed to be time harmonic, the heat input for the average time can be calculated as

$$\bar{q} = \frac{1}{\tau} \int_0^\tau q dt \quad (3)$$

The heat input for the average time can be written as

$$\bar{q} = \frac{1}{2} \omega^2 \sigma A^* A \quad (4)$$

Where \bar{q} is the heat input for the average time and $*$ is complex conjugate. Meanwhile, the magnetic properties change with the temperature. Therefore, the mathematical model for induction heating normally involves three main physical phenomena related to electromagnetism, heat transfer and solid mechanics. That is to say, the electromagnetic phenomenon is coupled with the thermal problem of the plate. In this study, the model of the coupled problem is first developed to obtain the heat flux distribution over a steel plate during the induction heating. The temperature gradient field changes since the sources moves in the induction heating process. For the simplification of the transient heat flow problem, with the assumption that moving speed of the inductor is much faster than that of heat conduction, the quasi-stationary state is adopted for the process. In the analyses, iterations are carried out at each step with updated material properties until the convergence limit by comparing the temperature distributions of subsequent iteration steps. The comparisons finally produce a heat flux at each node from the inductor. The heat flux obtained is then utilized as the heat input onto the plate in the following transient heat flow analysis. The deformations of plate are dominated by the distributions of plastic strains in induction heating. It is assumed that plastic strains, driving force to make angular distortion and transverse shrinkage, are produced in a critical heating region. The area reaching the critical temperature during the induction heating process is defined as the plastic region which has the eigenstrains. The widths and depths of the plastic regions for heating parameters are obtained depending on the types of inductor, pattern, electrical current... The width and depth of a plastic region for a set of heating

parameters are used as those of an inclusion in the plate for the deformation analysis with the plate theory. The area reaching the critical temperature during the induction heating process is defined as part of the plastic region. The plastic strain zone is defined as the region where peak temperature is equal to or greater than the critical temperature at which material strength becomes minimal. The dimensions of the plastic strain zone vary with the heating conditions such as moving velocity of heat source and intensity of heat flux. This shape of plastic strain region is determined by the depth of heat penetration and the heat flow analysis. Plastic strains and its region correspond to eigenstrains and size of inclusion. Each section of the shape of the eigenstrain region can be modeled to have a half-elliptical shape shown in figure 1.

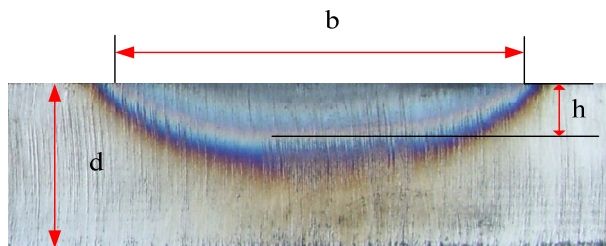


Fig. 1. The shape of plastic zone in induction heating

In this paper, a simplified analysis model for deformation of plate in induction heating can be given as mechanical strain regions of plastic and elastic regions. The deformations of steel plate in induction heating can be calculated based on [4] with the magnitude and size of the plastic strains. The vertical deformations in terms of material properties, plate thickness, and heat input as follows at different shapes of inclusions of trapezoid and ellipse for the steel plate in induction heating, respectively is given like as:

$$u_3 = -\frac{3\pi(1+\nu)h_t}{8\pi(h^0)^3} \left[\alpha T_c - \sigma_{yl} \left(\frac{1}{Kb_t} + \frac{1-\nu}{E} \right) \right] \left(h^0 - \frac{\pi h_t}{4} \right) [H(x_1, x_2) - H(0,0)] \quad (5)$$

3 Using Neural Network in Prediction

Artificial Neural Networks are revolutionary computing paradigms that try to mimic the biological brain. A part of the training data can then be used by the ANN to predict unknown output values for a set of input values. Artificial neural network are a functional abstraction of the biological neural structure of the central nervous system. In the induction heating process, the deformed shape of plate can be changed with the number and position of induction heating area. The deformation analysis in the forming process requires much time and cost with the calculation procedure of the coupled problem associated with magnetic, thermal, mechanical phenomena. In the proposed model, ANN is used to solve the problem selecting the positions of induction heating areas as well as heating time at one's area.

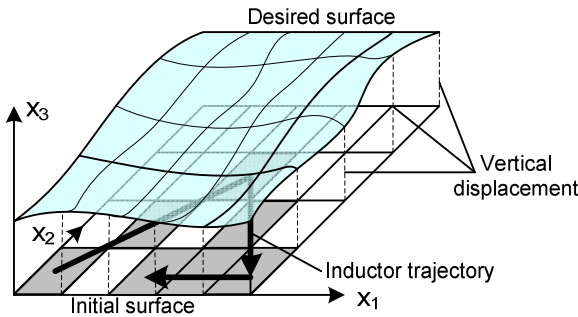


Fig. 2. Displacement and deformation of plate meshing in heating

The network is trained for positions of induction heating area and deformation of plate after heating. Initial shape is a square plate, and it is divided into $n \cdot m$ points to get displacements with equal distance from a point to another on the planar area. The point's vertical displacement of gridded plate along z-axis is measured as input of network. Therefore, each input vector had $n \cdot m$ units representing a deformed shape of plate expressed as a pattern of displacements at grid points. The displacements of a plate in induction heating process can be calculated with Eq.(5). As values of output units, induction heating paths are needed to generate the deformed plate. The output layer is recognized by parameters as number of induction zones, direction of heating path, and heating time. A heating path includes heated areas (heat or no heat) with heating time, and direction of path. The areas are indexed shown in figure 2 with $M \cdot N = 4(n-1)(m-1)$ where they are able to be horizontal lines, vertical lines, or diagonal lines along which the inductor moves. Values of output layer are binary. Each induction heating line is predicted with 2 parameters.

- Parameter 1: Active Area, (1 = Heating, 0 = no heating);
- Parameters 2 and 3: Active heating area (00 = 5 seconds, 01 = 10 seconds, 10 = 15 seconds, 11 = 20 seconds);

When first parameter of group i (i^{th} induction heating path) is 0, the area of i^{th} does not heat and therefore heating time is not available. Meanwhile, the relationship between numbers n and m is set to be as follows.

$$\begin{aligned} M &= 2(m-1) \\ N &= 2(n-1) \end{aligned} \quad (6)$$

In figure 3, the performance of inputs and outputs for ANN is shown. To decrease the input neurons, each 4-areas is enclosed by 4 nodes at corners. The number of outputs is larger than input, it make to determine the positions of areas easily. A general ANN using in this paper is a form of a multiplayer feed-forward network is. Output value of a neuron in ANN is determined as

$$y_j = f\left(\sum_{i=1}^n x_i w_{ij}\right) \quad (7)$$

Where x is input vector, w_{ij} are weights on output unit j , y is output vector, and $f(\cdot)$ is a defined function as transfer function.

In this study, the back-propagation algorithm is selected as the training method because it has been proven to be highly successful in training of multi-layered neural network. The back-propagation neural network (BPN) technique employs a gradient descent learning algorithm that is commonly used by the neural network community.

One of most important tasks in ANN studies is to determine the optimal network architecture which related to the number of hidden layers and neurons in it. The number of neurons in hidden layer was determined through a trial and error method, in order to accommodate the converge error. In this study, the best architecture of the neural network was obtained by trying different number of hidden layers and neurons. The structures of ANN including 1-2 hidden layers with different number of neurons in the hidden layer were investigated.

4 Results and Discussions

The proposed ANN is applied for the initial dimension of plate of 500x500x20 (mm³). Distance between 2 points of grid for calculating displacements was 50 (mm). Architecture of ANN was formulated with 121 input units, which represent vertical displacement of the plate established as input variables, and the estimated paths of induction heating line among 400 groups (800 units) established as output variables. The trial started one hidden layer with 200 neurons, and the accuracy of the predicted values checked before optimal structure of ANN selected. The goal is to maximize accuracy to obtain a network with the best generalization.

In training for NN, it can be observed that increment of the number of neurons used in the hidden layers did not improve the performance of network. It was found that increase of the number of neurons in the hidden layer does not ensure the decrease of the average training process's error or increase accuracy. Based on this analysis, the optimal architecture of the ANN was constructed as 121 – 600 – 800 presenting the number of inputs, neurons in hidden layers, and output, respectively. After training, the ANN model is tested by using only the feed-forward phase of the training algorithm. As the specific case, a desired surface was the saddle surface with equation like as:

$$z = \frac{(x - c_x)^2}{a^2} - \frac{(y - c_y)^2}{b^2} \quad (8)$$

The values of the displacements were saved at input vector for testing the ANN. The outputs of the test result gave the heating-area numbers to be heated, which are schematically presented on the plate as figure 3(a). The continuous areas make the path of the induction heating. At first, the heating parameters of 400 groups were examined, when the predicted heating area parameters were 1, paths of group number heated by induction heating, then other parameters of these group were checked. The initial shape of plate is planar, after the plate was heated, the deformed shape of plate

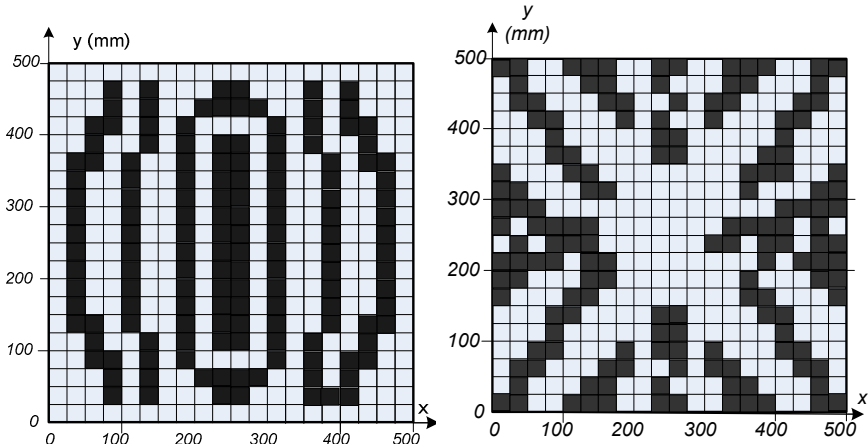


Fig. 3. Line heating predicted by NN with (a) saddle and (b) pillow shape

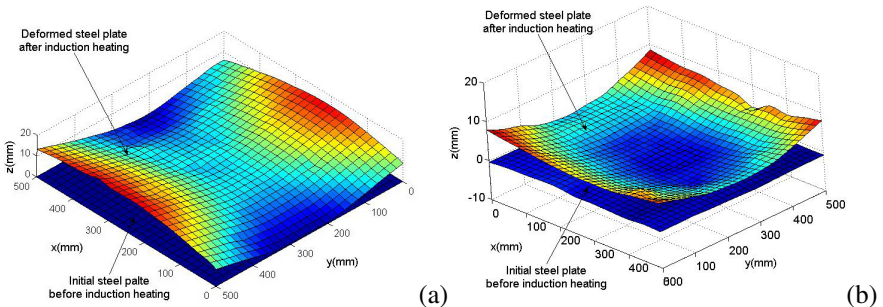


Fig. 4. Deformed shape (a)saddle and (b) pillow shape of plate after heating compared to initial shape

is shown as figure 4(a), where the vertical displacement values of plate at points were measured by Coordinate Measuring Machine (CMM). Besides, experiment was carried out with pillow shape like in figure 3(b) and 4(b).

Especially, the desired and experimental results of saddle shape for vertical displacements when induction heating process was performed on the flat plate of 20 mm thickness are compared as shown in Fig. 5 at the positions of $y = -500$ (mm), -300 (mm), -100 (mm), 100 (mm), 300 (mm) and 500 (mm). The vertical displacements reveal that the experimental results are almost near the desired ones. Compared desired displacements, we can see that the small differences between the desired and experimental values may be attributed to the following reasons: first, numbers of training data are not enough with random distributions for predicting parameters. To improve the problem, the ANN model should be trained with larger number of data and patterns chosen randomly with equilateral distributions as well as more combination of pieces of the heating lines.

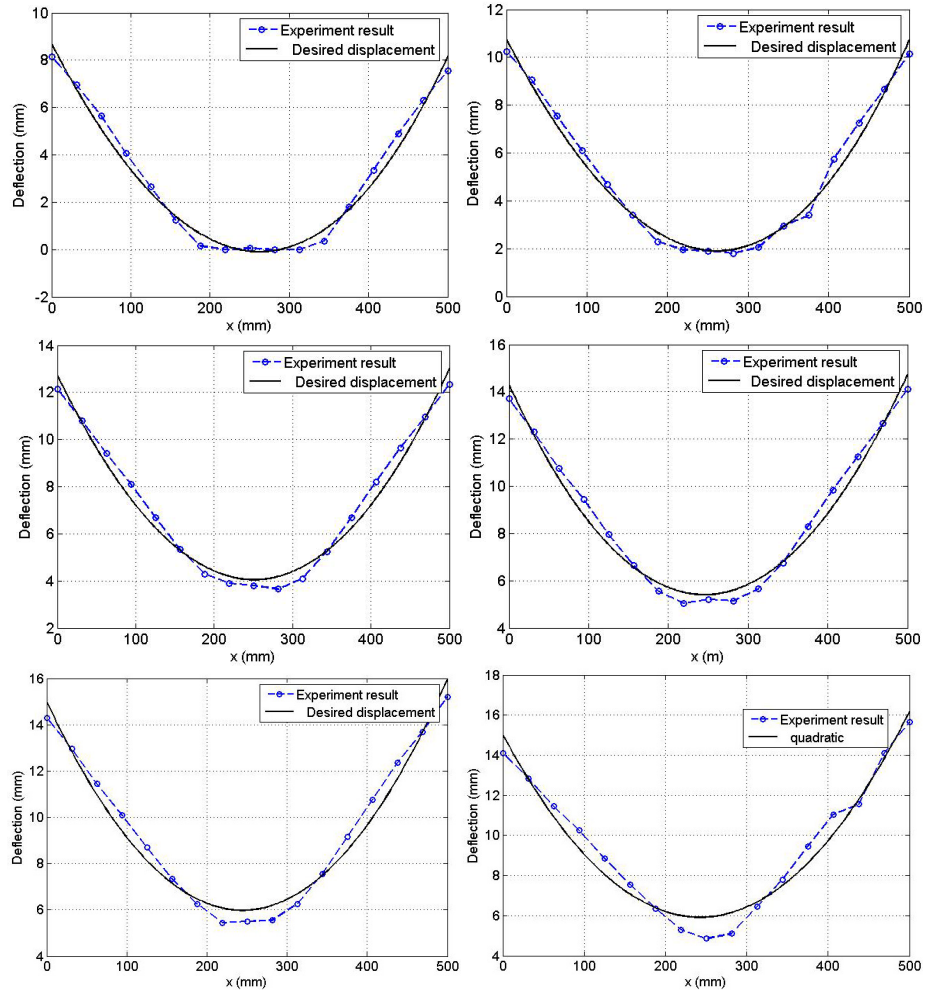


Fig. 5. Vertical displacements of induction heated plate for saddle shape

Secondly, several chosen velocities have large different levels, therefore, they may affect on errors of deformed plate. To reduce the errors, number of bits to encode velocity used should be more than a bit or differences between 2 velocities should be smaller. The improvements will bring better results for predictions of induction heating paths. Nevertheless, the test case reveals that predicted results of vertical displacements with the parameters obtained by the ANN model are good matched with the desired results. The result of the tests shows that the developed ANN model can help predict the induction heating paths from the desired surface of a plate.

5 Conclusions

In this paper, an Artificial Neural Network model capable of predicting the heating parameters including heating positions from the given desired shape of a plate are developed. The model can be implemented and learned with the back-propagation algorithm. The inputs and outputs for the learning and testing the model are obtained by the induction heating parameters and the derived analytic solution for the plate deformation with the parameters. The tests proved the ANN model as a predictive tool for determining heating paths in induction heating process. The ANN model can effectively reduce not only the time required to solve the problem of matching deformation of plate with induction heating line positions but also the time required to solve the problem of predicting induction heating paths.

References

1. Kawaguchi, H., Enokizono, M., Todaka, T.: Thermal and magnetic field analysis of induction heating problem. *J. of Materials Processing Technology* (161), 193–198 (2005)
2. Bae, K.-Y., Yang, Y.-S., Hyun, C.-M., Cho, S.-H.: Derivation of simplified formulas to predict deformations of plate in steel forming process with induction. *International Journal of Machine Tools and Manufacture* 48, 1646–1652 (2008)
3. Nguyen, T.-T., Yang, Y.-S., Bae, K.-Y., Choi, S.-N.: Prediction of Deformations of Steel Plate by Artificial Neural Network in Forming Process with Induction Heating. *Journal of Mechanical Science and Technology* 23, 1211–1221 (2009)
4. Nguyen, T.-T., Yang, Y.-S., Bae, K.-Y.: The development of an artificial neural network model to predict heating-line positions for plate forming in induction heating process. *Mechanics Based Design of Structures and Machines An International Journal* 37(2), 201–227 (2009)

A Method for Controlling Wheelchair Using Hand Gesture Recognition

Nguyen Kim-Tien, Nguyen Truong-Thinh, and Trinh Duc Cuong

Dept. of Mechatronics, Ho Chi Minh City University of Technical Education

1 Vo Van Ngan street, Thu Duc district, Ho Chi Minh City, Viet Nam

{nguyenkmtien90, cuongtd91}@gmail.com, thinkhnt@cmute.edu.vn

Abstract. This paper presents an approach for controlling wheelchair movement using hand gesture recognition. This method was developed based on the curvature of a hand shapes contour. It is simple and has some features to recognize and offers robustness recognizing gestures of one hand. The curvature based hand gesture recognition algorithms recognizes hand gestures using a combination of hand shape contour geometry and calculating the distance from the center of hand to the convex hull on the fingertips. In this paper, this method is able to recognize 5 different hand gestures in same backgrounds for five status movement of wheelchair like as: forward, reverse, left, right and stop. Experiments are presented to show that the wheelchair is able to move and avoid obstacles autonomously while controlled by its user via the hand gesture.

Keywords: Hand gesture recognition, Wheelchair, mobile robot.

1 Introduction

The wheelchair is an important way of transfer for handicapped and aged. As the development of science and technology, the assistive systems are more and more popular in human lives. Intelligent wheelchairs, as a kind of rehabilitation robots, play an important role in helping the handicapped and the elderly people to live more independently at home and have a low cost on their healthcare. The manual wheelchairs have been around for hundreds of years, and have become a pseudo-standard in hospitals, shopping malls, homes and many other facilities to assist immobile patients. Many researches have been developing intelligent wheelchairs due to increasing requirement of safer and more comfortable wheelchairs. A wheelchair has been designed and developed. By using some input methods such as joystick, electronic controllers and motors instead of hand propulsion or a guardian, people with disabilities have been able to loco-mote with less effort than before, not just in mobility but also in reduction of effort and discomfort. However, some physically disabled people are not able to use such devices as they may have difficulty in handing the controls. The recognition of human activity is a concerning problem to provide interactive service with the user in various environments. Research about activity recognition is emerging recently, using various sensory resources. Some users

have difficulty in using powered wheelchairs because they lack the necessary motor skills, strength, or visual acuity. These are the people who would benefit the most from using an automated wheelchair system. Hence, the powered wheelchairs require additional functions, such as autonomous navigation, obstacle avoidance, hands gesture and bio-signal control, to make the lives of the extremely disabled and the elderly easier. Hand gesture one of the most popular human communication ways just lower than oral language. Hand gesture is the meaningful or intentional movements of human hands and arms. It's used as methods of non-verbal communication in our daily lives to represent meaning or emphasis on the idea while communicating, such as communicating of speech-impaired instead people, controlling the traffic, etc. Nowadays, assistive robotic wheelchair can improve the quality of life for disable people. They allow user to travel more efficiently and with greater ease based on hand gesture signals.

The aim of this study is to develop a fully operational semi-autonomous wheelchair. The user is able to control the speed and the steering of the wheelchair using hand gestures. The user can select functions for controlling wheelchair by changing the hand gestures. In order to develop such algorithm of recognizing hand gestures, the algorithm is implemented with two parts: the hand gesture recognition and the control input application.

2 Hand Gesture Recognition Based on the Curvature of a Hand Shapes Contour

Many people, including paraplegics, quadriplegics and elders, depend permanently or temporarily on wheelchair for locomotion. The controlling of an electric wheelchair when joysticks are not an option. Computer vision is being explored in the development of wheelchair control mechanisms based on gesture, facial expression, head movements and eye gaze [2].

Once the hand contour, which is a set of coordinates of boundary pixels of a hand shape, is selected and filtered with the filter. The curvature calculated from this contour is severely noisy. After the process of Hand shape contour filtering the curvatures along the contours are calculated. The hand gesture recognition algorithm is presented based on a few transformation and calculating contour of images. The coordinates of all the closed contours are stored in two-dimensional arrays. Among the detected contours, the hand shape contour is decided. Firstly, the images received from camera will be converted to gray-level. The captured image is converted to a grey level image, and thresholded and filtered to detect the boundary lines of objects in the image. Then the Gauss filter is used for pre-processing images, it can help to reduce noise and unwanted losing details of the hand. Every pixel in image was compared with a variable threshold value to detect the edge of image.

All data will be processed at edge detection and finding contour. This is the core of the whole algorithm of hand gesture recognition. A contour is a list of points that represent a curve in an image. In this hand gesture recognition method, Freeman Chain code method was used as extremely useful method to find contour and represent a boundary by a connected sequence of straight-line segment of specified

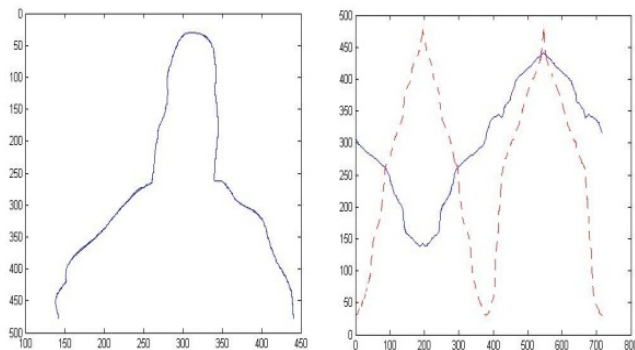


Fig. 1. Contour of hand gesture is processed and created by the list of points

length and direction. With a Freeman chain code, a polygon is represented as a sequence of steps in one of eight directions; each step is designated by an integer from 0 to 7 and the centre represents the current pixel being investigated [3]. The process starts from the bottom left corner of the image and find the first pixel which has the value equal to 1. As soon as the first pixel was found in the neighbouring pixels, the current pixel location is saved in a contour array and moved to the position where the pixel location was found. After the process was end, we have a list of points. All of them created a contour of a hand (figure 1). Since the determined number of contour in finding process is more than 1, the auto-tuning percent threshold value algorithm is continuously tuning the percent threshold value until the number of contour equal to 1. This algorithm tunes the percent threshold value (L) by increasing it by 0.01 per every step.

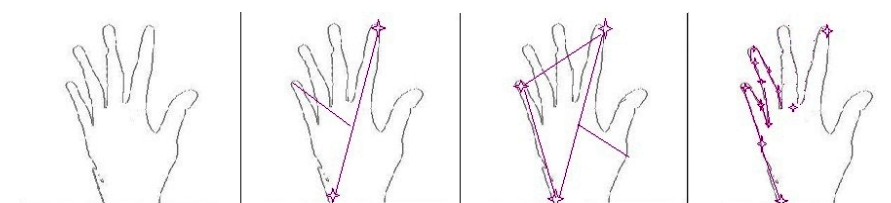


Fig. 2. Polygon approximations method

And then Douglas – Peuker algorithm was used to combine these points by a polygon approximations method. The polygon begin with a line was created by two points which have maximum distance and the third point have maximum distance from that line. The process will continue until the distance from a line to a point (x) less than value β (const), the contour of hand was created (figure 2)

After that, the calculating principal distance process will be found based on convex points which were detected by Sklansky's algorithm on the contour of hand. The system extracts skin-color regions by color segmentation. It also extracts moving regions by subtraction between consecutive frames. Regions around those extracted in

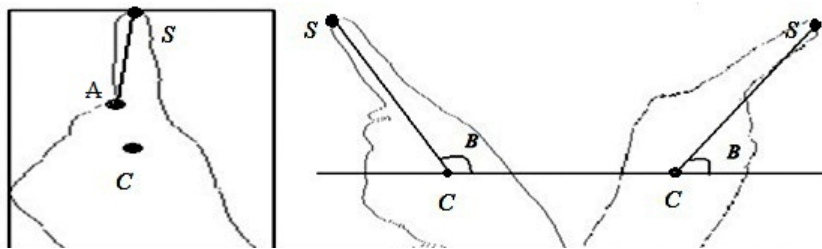


Fig. 3. Calculate distance and find feature of hand shape for motion state forward, left and right

both processes are considered as hand gesture. The system zooms in on each hand candidate one by one, checking whether or not it is really a hand by examining the existence of hand gesture features. Then, the selected hand region data is fed into the hand gesture recognition process based on the hand gesture recognition method proposed. Images of the user from various angles are compressed in an eigenspace in advance.

In order to evaluate the accuracy of this method, some hand gestures are tested for several times. Table 1 is results after 5 times had changed state from forward to left or right. The angle desired is 68° for left state and 106° for right, but in fact it is about errors $1^\circ \div 3^\circ$. Because the image was captured continuously by camera, the state of hand wasn't fixed, so the convex hull points on finger (S) wasn't fixed, either.

Table 1. Testing hand gesture

Output: 67.42 Expected: 68	Output: 65.8 Expected: 68	Output: 67.56 Expected: 68	Output: 67.4 Expected: 68
Output: 114.3 Expected: 106	Output: 106.8 Expected: 106	Output: 107.04 Expected: 106	Output: 106.2 Expected: 106

3 Wheelchair Control Using Hand Gesture Recognition

In this paper, a multifunction wheelchair is used as an application of hand gesture Recognition algorithm. The multifunction wheelchair system consists of a chair equipped with a mechanical system that can help people in personal activities such as moving, going to the toilet, getting high objects, rehabilitation.



Fig. 4. Modeling of multi-function wheelchair

Table 2. Multifunction wheelchair's specification

Unit	Wheelchair specifications
Size of Mobility configuration	1200 x 600 x 1620 (mm)
Size of full lifted configuration	1200 x 600 x 2270 (mm)
Weight(unload)	122 (kg)
Limit load	80 (kg)
Max speed moving	0.88 (m/s)
Max speed changing high level	1 (m/min)
Rotation speed of frame 3	2 (r/min)
Rotation angle of frame 3	180 degree (left and right)
Active wheel diameter	260 mm
Passive wheel diameter	4x10 mm
Power supply	Battery 12V/40A
Driving	1 motor and bevel gear
Steering	1 motor and transmission pulley

Table 2 shows the specifications of the multifunction wheelchair. In figure 4, the robotic system consists of an electrical wheelchair which design and developed based on the core of the hand lift truck in order to getting high object and in rehabilitation. The structure of wheelchair includes three main frames. The first frame is a hand lift truck which is driven and steered by its rear axles. The second frame is connected with the first one by the prismatic joints, one ball screw and two slide bar to lift the occupant up or down following user's intention. And the last one is chair that

connected to the second frame by the revolute joint. The chair with the special seat rest, arm rest and feet rest that can be autonomous adjusted when user go to the toilet or in rehabilitation mode. The motion of wheelchair like mobile robot but the driving and pushing structure was combined together, more flexible in small space.

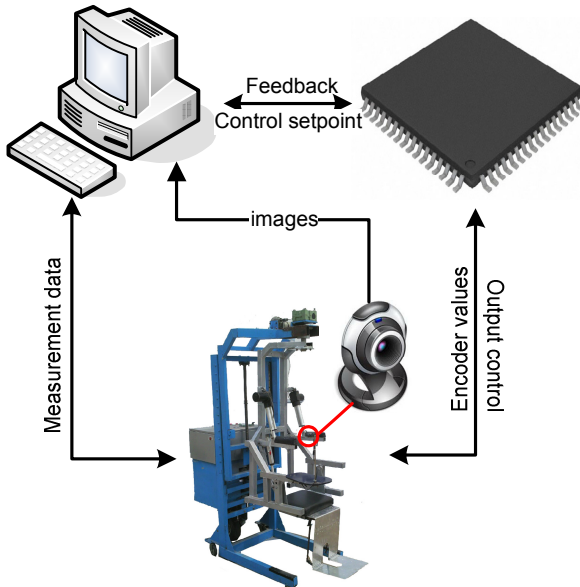


Fig. 5. Controlling wheelchair diagram

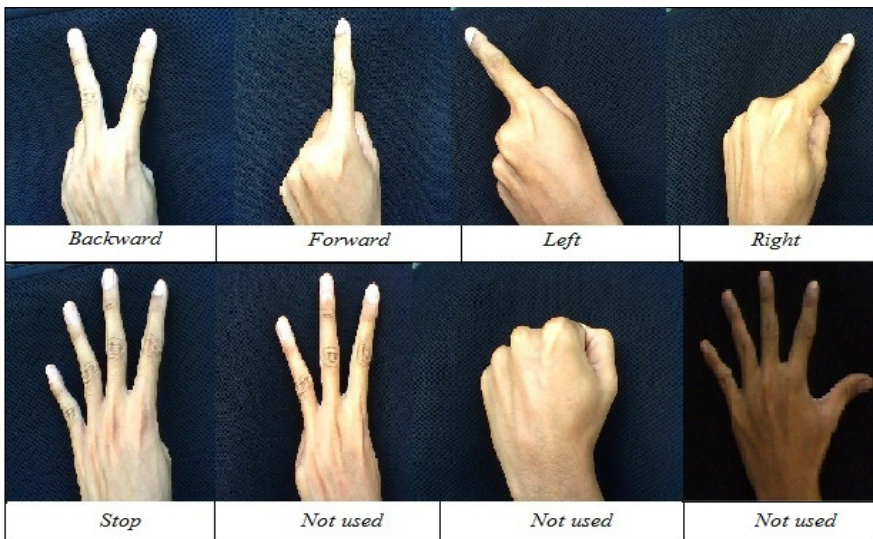
In order to develop the human-machine interfaces for the wheelchair system, the computational cost of the interface method must be considered because the wheelchairs must be operated in real-time. The wheelchair system which equipped with a standard PC (Pentium 466 MHz, 128MB RAM). The hand gesture recognition system using geometric properties of static hand gestures developed in this study is on the basis of the regular moment calculation method. In this paper we use a vision system consists of a 300x200 pixel color camera which was placed upper the armrest platform 50 cm (figure 5). The armrest platform is made of plastic and covered by a black material to avoid the light reflect to the camera. The camera was connected with PC by a USB cable. In this case, the images of user's hand captured through cameras attached to the wheelchair are interpreted and used to produce the driving commands. The system controls its motion based on computing the hand gesture direction from images of the user-observing camera. However, the problem is that users move their fingers for various other reasons than controlling the wheelchair's direction. The system needs to discern wheelchair-control behaviors from others. This is the intention-understanding problem in the current system. Our basic assumption is that users move their fingers slowly and steadily when they are told that the wheelchair moves in their hand gesture's direction. Thus, the system ignores quick finger's movements and only responds to slow, steady movements.

For more safety, four ultrasonic sensors were used to see the environment and detect obstacles around the wheelchair. If any obstacles are detected, the wheelchair is controlled to avoid them. This obstacle-avoidance behavior overrides other behaviors except those done manually with the joystick to ensure safety.

The process for controlling wheelchair was shown in figure 5. First, the hand image which was captured from controller will be handled, where the computer determines the state of motion and rotation angle calculation for state turn left or right. Then, these parameters are sent to microcontroller via RS-232 interface. Rotation of the wheel will be continuously feedback from encoder to microcontroller and the PID position control algorithm will ensure the wheelchair's response will approach the desire of user. Then microcontroller will feed back to computer.

The hand gesture recognition algorithm based on the curvature of a hand shapes contour was applied for control wheelchair in different light conditions. The control actions are simple and change easily. We have defined five control states for the wheelchair, namely "Stop", "Forward", "Backward", "Left", and "Right" in Table 3. Users use hand gesture to switch between different control states. The stop state of wheelchair is always priority when it appears. So, it is different with other states. Forward, left and right state shared a gesture but the angle of them isn't same. The left motion state was defined from 45° to 68° (experiment) when the hand gesture rotates an angle compare with horizontal plane. Similarly, the right motion state was defined from 106° to 140° and the forward motion state was defined from 69° to 105° . All of angles were chosen from the experiences for user's comfort.

Table 3. Hand gesture for controlling wheelchair



4 Experiments and Discussion

The goal of Human-Machine Interface (HMI) research is to provide humans with a new communication channel that allows translating Human's will states via a computer into application specific actions. In experiments of hand tracking, the skin color using the HSV (Hue, Saturation and Value) color model was applied. The skin color model is adapted during tracking. In the first frame, the skin color region is found by hand, and used to initialize the color model. In the tracking process, we use the track result to update the skin color model. Figure 6 shows the status of the wheelchair which moving in an orbit identification using hand gesture recognition. The developed system has been tested in the OpenLab – Mechatronics at the Ho Chi Minh City University of Technical Education, experimental area is a rectangular shaped room with a length of approximately 20m. The task is to switch the system from non-control state to control state, drive the wheelchair from position A to B, and then switch the system back to non-control state. To complete the task, the user has to make at least 4 turns and travel about 12~15 meters.

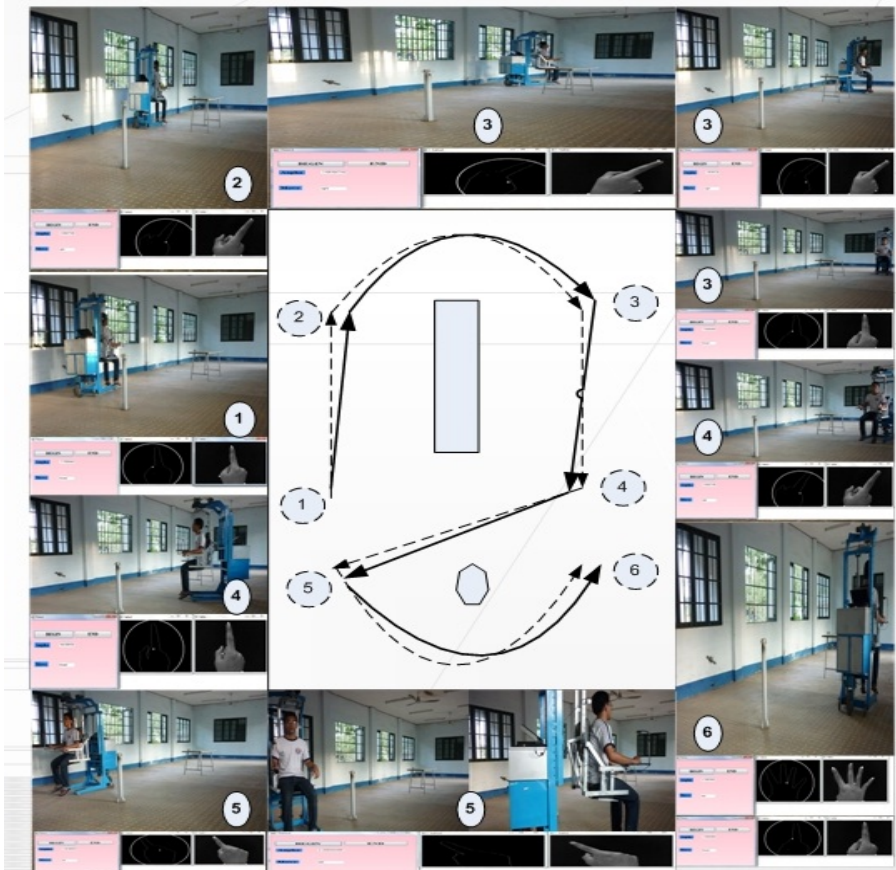


Fig. 6. Experiment on an indindentified trajectory

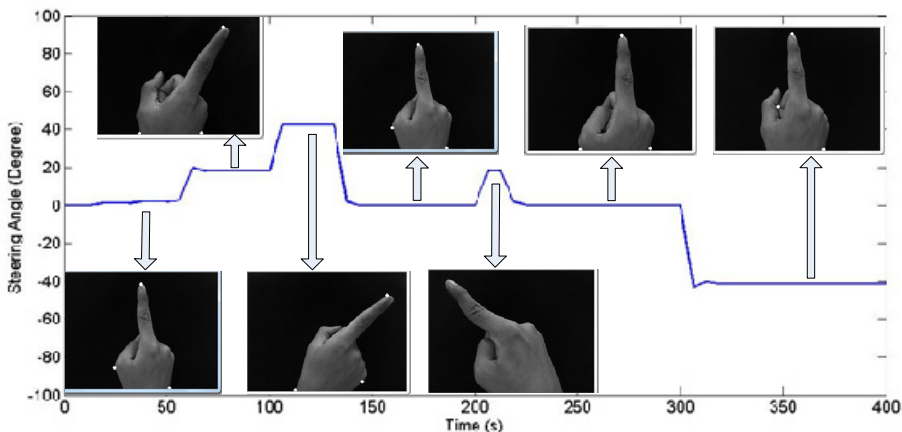


Fig. 7. Response of encoder during the test

The test was repeated several times, and the average completion time is 400 seconds. From position start moving straight to position 2 and turn right to bypass obstacles, in this process the steering wheel rotation is changed and update on the computer through the encoder, the computer continuous treatment and compared with the value of hand rotation to control wheelchair moving in the right orbit to position 3. This process continuous until the stop position 6. Although the trajectory of movement had errors but it is not significant. This difference may be due to a number of reasons. First, the steering wheel is erroneous a little angle compared to the straight position. Second, movement speed should be slower to easily change the hand states. Third, the limiting effect of light requires classification threshold process must take place continuously, in a few time to reach max or min threshold value. Although, this process was happen very fast but there are also affecting the identification process, particularly is angle of rotation.

This paper presented an overview of some recent work related to the use of computer vision techniques to improve human-machine interaction for people with special needs. The two problems presented in this paper, namely the hand gesture recognition and wheelchair control have been investigated based on sensors and devices.

5 Conclusions

In this paper, we propose an electric wheelchair system that is operated by using stereo camera to recognize hand gestures. This paper presented the developed algorithms of virtual human-machine interface (HMI) of multifunction wheelchair. The developed HMI employs hand gesture recognition to replace the conventional control inputs, such as button, joystick, tactile screen, etc. the user can operate the wheelchair by posing hand gesture on the hand putting flat. Each hand gesture has its own purposes based on its position and the direction of hand gesture, the appropriate

command, such as turn left, right, move forward, reverse, break and also the speed and steering of the wheelchair will be determined. This method is more comfortable and lower cost than the others for smart wheelchair. It does not require any special outfits and does not interfere with the user behavior. This algorithm can determine seven hand gestures and does not matter the user's hand size. But only five hand gestures are used in this paper in order to control the movement of wheelchair.

References

1. Pavlovic, V., Sharma, R., Huang, T.: Visual interpretation of hand gestures for human-computer interaction: a review. *IEEE Trans. Pattern Anal. Mach. Intell.* 19(7), 677–695 (1997)
2. Tien, N.K., Thinh, N.T.: Using Electrooculogram and Electromyogram for powered wheelchair. In: *IEEE ROBIO 2011 - International Conference on Robotics and Biomimetics*, pp. 1585–1590 (2011)
3. Kang, S.-P., Katupitiya, J.: A hand gesture controlled semi-autonomous wheelchair. In: *Intelligent Robots and Systems (IRON 2004)*, vol. 4, pp. 3565–3570 (2004)
4. Kathuria, P.: Hand Gesture Recognition. Japan Advanced Institute of Science and Technology (2011)

Position Control of a Quad-Rotor System

Seungho Jeong and Seul Jung

Dept. of Mechatronics Engineering, Chungnam National University
220 Gung-dong, Yuseong-gu, Daejeon 305-764, Korea
cimdream@naver.com, jungs@cnu.ac.kr

Abstract. Research on unmanned aerial vehicles (UAV) has been quite active in robotics and control communities. Most of UAVs have been utilized for military missions in war zones. Recently, quad-rotor systems as one of UAVs are getting more attention in civilian applications since they have an omni directional movement capability and their control is relatively simple. In this paper, the Cartesian trajectory control of a quad-rotor system is presented along with attitude control. In order for a quad-rotor to perform the Cartesian position control task, global positioning sensors are required to locate the position. Here we are using a camera as a global sensor. Simulation and experimental studies are performed to test the feasibility of the proposed control method.

Keywords: quad-rotor system, attitude control, position control.

1 Introduction

Recently, autonomous robotic vehicles are paid attention by the industries as well as militaries. Specially, research on unmanned aerial vehicles (UAV) has been increased in robotics and control communities. Successful performances of military operations in war zones have accelerated research on UAV. Most of military UAVs are categorized into a conventional take-off and landing (CTOL) structure that can perform a long range mission.

Recently, research on UAVs with a vertical take-off and landing (VTOL) structure is actively conducted as civilian applications of UAVs are intensively demanded. As a VTOL structure, quad-rotor systems as one of UAVs are getting more attention in civilian applications. Quad-rotor systems have four rotors to generate six motions, which is a kind of under-actuated systems. Quad-rotor systems have a unique advantage of an omni-directional movement capability over single rotor systems. Dynamics of quad-rotor systems is relatively simple so that control can be done with ease.

In the literature, there have been many research results on quad-rotor systems from theoretical studies to experimental implementation. Research is focused on the attitude control of quad-rotor system which is relatively simple to control. Since a global sensor is not necessary for the attitude control, experimental verification can be easily done [1]. Besides the attitude control performance, one major task of quad-rotor systems is navigation which requires localization and trajectory control by

global sensors [2]. Neural network control applications to trajectory control are presented [3,4].

Research on quad-rotors systems is getting more challenging that experimental results of indoor position control have been successfully demonstrated as a group of quad-rotors in University of Pennsylvania and ETH Zurich. Optical sensors are used to help trajectory following control and landing control of quad-rotors [5,6]. Based on position control, interaction control and gripping control of quad-rotor systems are introduced.

In the previous research, experimental studies of attitude control of a quad-rotor system were performed. Flymobile has been developed for both driving and flying capabilities [9]. Flymobile has been controlled remotely by an operator, which is not autonomous.

All of applications of quad-rotor systems are dependent upon not only attitude control performance but also accurate position control performance. Therefore, in this paper, position control of a quad-rotor system is presented. The quad-rotor is required to follow the Cartesian trajectory along with attitude control. Simulation studies are performed to verify the Cartesian space control performances.

To confirm the feasibility of the simulation results, experimental studies are also conducted. The quad-rotor system is required to maintain desired position under the camera that is used as a global sensor to locate the position of the quad-rotor system. Experimental results are evaluated.

2 Quad-rotor System

2.1 Modeling of a Quad-Rotor System

A quad-rotor system is an under-actuated system that has four rotors to control six-axis motions. Three translational movements, x, y, z , and three rotational angles, ϕ, θ, ψ , which are a roll, pitch, and yaw angle, respectively are induced by four rotors. A pair of two rotors rotates in the clockwise direction and another pair in the counter clockwise direction.

Regulating thrust forces controls the motion of the quad-rotor system. Fig. 1 describes the coordinate of the quad-rotor system. F_F, F_L, F_B, F_R are the thrust forces of the front, left, back, and right rotor, respectively.

The dynamic equations of a quad-rotor system are described as

$$\begin{bmatrix} f \\ T \end{bmatrix} = \begin{bmatrix} m(\dot{V}_V + \omega_V \times V_V) + G \\ I\dot{\omega}_V + \omega_V \times (I\omega_V) \end{bmatrix}, \quad (1)$$

where $f \in R^{3 \times 1}$ is the translational force, $T \in R^{3 \times 1}$ is the rotational torque, $m \in R$ is the mass, $G \in R^{3 \times 1}$ is the gravitational force and $I \in R^{3 \times 3}$ is the moment of inertia of the system.

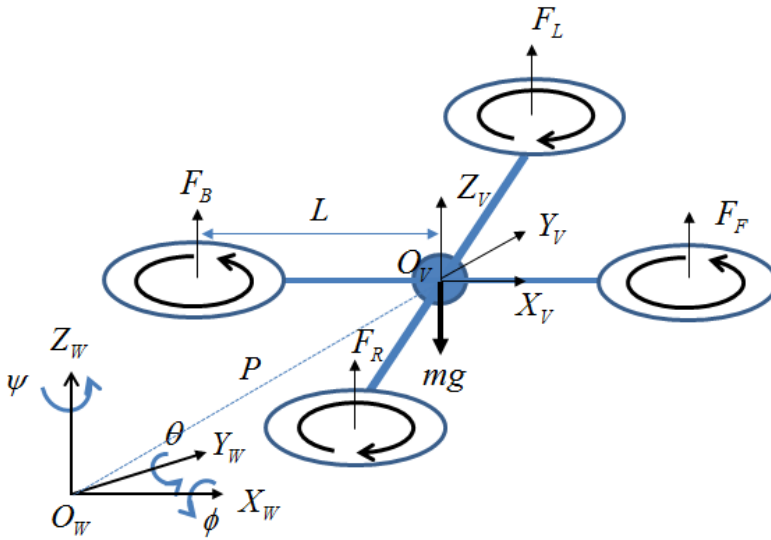


Fig. 1. Model of a quad-rotor system

The linear velocity, V_v , in the vehicle frame has the relationship with the linear velocity, V , in the global coordinate by the rotational transformation.

$$V_v = R_T^{-1}V, \quad (2)$$

where

$$R_T^{-1} = \begin{bmatrix} c\theta c\psi & c\theta s\psi & -s\theta \\ s\phi s\theta c\psi - c\phi s\psi & s\phi s\theta s\psi + c\phi c\psi & s\phi c\theta \\ c\phi s\theta c\psi + s\phi s\psi & c\phi s\theta s\psi - s\phi c\psi & c\phi c\theta \end{bmatrix}, \quad (3)$$

where $c\phi = \cos\phi$, $s\phi = \sin\phi$, $c\theta = \cos\theta$, $s\theta = \sin\theta$, and $c\psi = \cos\psi$, $s\psi = \sin\psi$.

The angular velocity, ω_v , in the vehicle coordinate has the relationship with ω in the global coordinate as

$$\omega_v = R_A^{-1}\omega, \quad (4)$$

where R_A is the Euler kinematic equation defined as

$$R_A^{-1} = \begin{bmatrix} 1 & 0 & -\sin(\theta) \\ 0 & \cos(\phi) & \sin(\phi)\cos(\theta) \\ 0 & -\sin(\phi) & \cos(\phi)\cos(\theta) \end{bmatrix} \quad (5)$$

Substituting (2)-(5) into (1) yields the following simplified dynamics equations under the assumption of neglecting Coriolis terms.

$$\begin{aligned} m\ddot{x} &= f_{th}(\cos \phi \sin \theta \cos \psi + \sin \phi \sin \psi) \\ m\ddot{y} &= f_{th}(\cos \phi \sin \theta \sin \psi - \sin \phi \cos \psi) \\ m\ddot{z} &= f_{th} \cos \theta \cos \phi - mg \\ I_{xx}\dot{\phi} &= \tau_\phi \\ I_{yy}\dot{\theta} &= \tau_\theta \\ I_{zz}\dot{\psi} &= \tau_\psi \end{aligned} \quad (6)$$

where f_{th} is the total thrust force, g is the gravitational acceleration and I_{xx}, I_{yy}, I_{zz} are moments of inertia about x, y, z axis, respectively.

3 Control Schemes

Each torque has the following relation with the induced force from each rotor.

$$\begin{aligned} f_{th} &= F_F + F_B + F_R + F_L \\ \tau_\phi &= L(F_L - F_R) \\ \tau_\theta &= L(F_B - F_F) \\ \tau_\psi &= C(F_R + F_L - F_F - F_B) \end{aligned} \quad (7)$$

where $\tau_\phi, \tau_\theta, \tau_\psi$ are the torques of roll, pitch, and yaw angle, respectively, L is the distance from the center of the mass to the center of each rotor and C is a constant factor.

From (7), we can derive the equation for thrust forces. Thus the control can be done by designing the thrust force of each rotor with linear controllers such as

$$\begin{aligned} F_F &= au_{th} - bu_\theta - cu_\psi \\ F_B &= au_{th} + bu_\theta - cu_\psi , \\ F_R &= au_{th} - bu_\phi + cu_\psi \\ F_L &= au_{th} + bu_\phi + cu_\psi \end{aligned} \quad (8)$$

where $a = \frac{1}{4}, b = \frac{1}{2L}, c = \frac{1}{4C}$ and $u_{th}, u_\phi, u_\theta, u_\psi$ are control inputs for thrust, and roll, pitch, yaw angles, respectively.

3.1 Attitude Control

For attitude control, roll angle, ϕ , pitch angle, θ , yaw angle, ψ , and elevation, z , are regulated. The control input vector, U has the form of linear controllers.

$$U_A = K_A E \quad (9)$$

where $U_A = [u_{\text{th}}, u_{\phi}, u_{\theta}, u_{\psi}]^T$, $E = [e_{\text{th}}, e_{\phi}, e_{\theta}, e_{\psi}]^T$ and K_A is a control gain matrix. Parameters of K_A can be founded from linear controllers.

$$\begin{aligned} u_{\phi} &= k_{p\phi}(\phi_d - \phi) + k_{i\phi} \int (\phi_d - \phi) dt + k_{d\phi}(\dot{\phi}_d - \dot{\phi}) \\ u_{\theta} &= k_{p\theta}(\theta_d - \theta) + k_{i\theta} \int (\theta_d - \theta) dt + k_{d\theta}(\dot{\theta}_d - \dot{\theta}) \\ u_{\psi} &= k_{p\psi}(\psi_d - \psi) + k_{i\psi} \int (\psi_d - \psi) dt + k_{d\psi}(\dot{\psi}_d - \dot{\psi}) \end{aligned} \quad (10)$$

For the elevation control, we have

$$u_{\text{th}} = (u_z + mg) \frac{1}{\cos \theta \cos \phi} \quad (11)$$

where

$$u_z = k_{pz}(z_d - z) + k_{iz} \int (z_d - z) dt + k_{dz}(\dot{z}_d - \dot{z}) \quad (12)$$

where k_{pz}, k_{iz}, k_{dz} are PID controller gains and z is the height from the ground.

The thrust force can be generated by the following relationship.

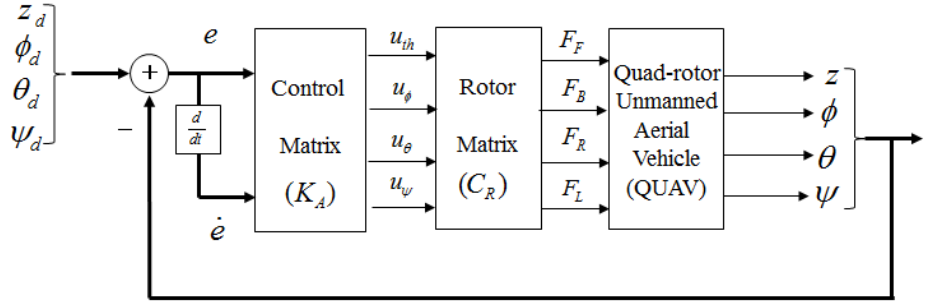
$$F = C_R U_A \quad (13)$$

where $C_R = \begin{bmatrix} a & 0 & -b & -c \\ a & 0 & b & -c \\ a & -b & 0 & c \\ a & b & 0 & c \end{bmatrix}$.

The attitude control block diagram is shown in Fig. 2

3.2 Cartesian Trajectory Control

For a quad-rotor to navigate, position control based on a global sensor is required. Localization from sensor fusion should be done *a priori* like other unmanned systems. The Cartesian control loop is added to the attitude control block diagram of Fig. 2.

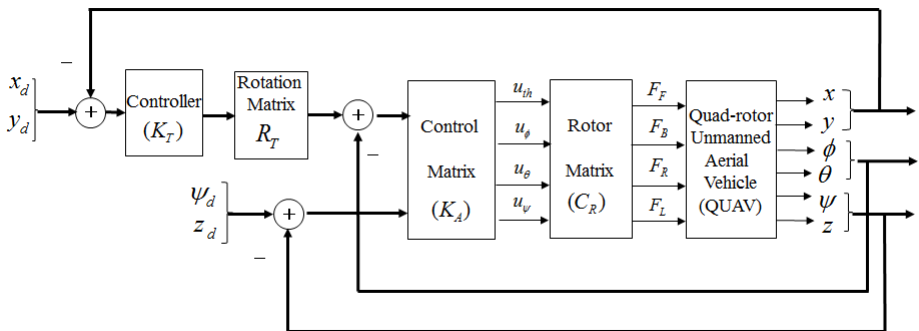
**Fig. 2.** The attitude control block diagram

Since the elevation control requires gravity compensation as in (11) and (12), it is separately controlled so that the corresponding part of the rotation matrix, R_T , are used to generate desired roll and pitch angles.

The Cartesian position errors are defined and used in controllers.

$$\begin{aligned} u_x &= k_{px}(x_d - x) + k_{ix} \int (x_d - x) dt + k_{dx}(x_d - x) \\ u_y &= k_{py}(y_d - y) + k_{iy} \int (y_d - y) dt + k_{dy}(y_d - y) \end{aligned} \quad (14)$$

A linear control method is used for the Cartesian trajectory control and its output is transformed through the rotation matrix, R_T . The Cartesian tracking errors of x and y axis are transformed into desired roll and pitch angles to be controlled in the inner loop. Fig. 3 shows the Cartesian trajectory control block diagram.

**Fig. 3.** The Cartesian trajectory control block diagram

4 Simulation

4.1 Attitude Control Performance

Firstly, the attitude of a quad-rotor system is controlled. Fig. 4 shows the attitude control results based on Fig. 2. Roll, pitch, and yaw angles are well controlled. Initial angles are

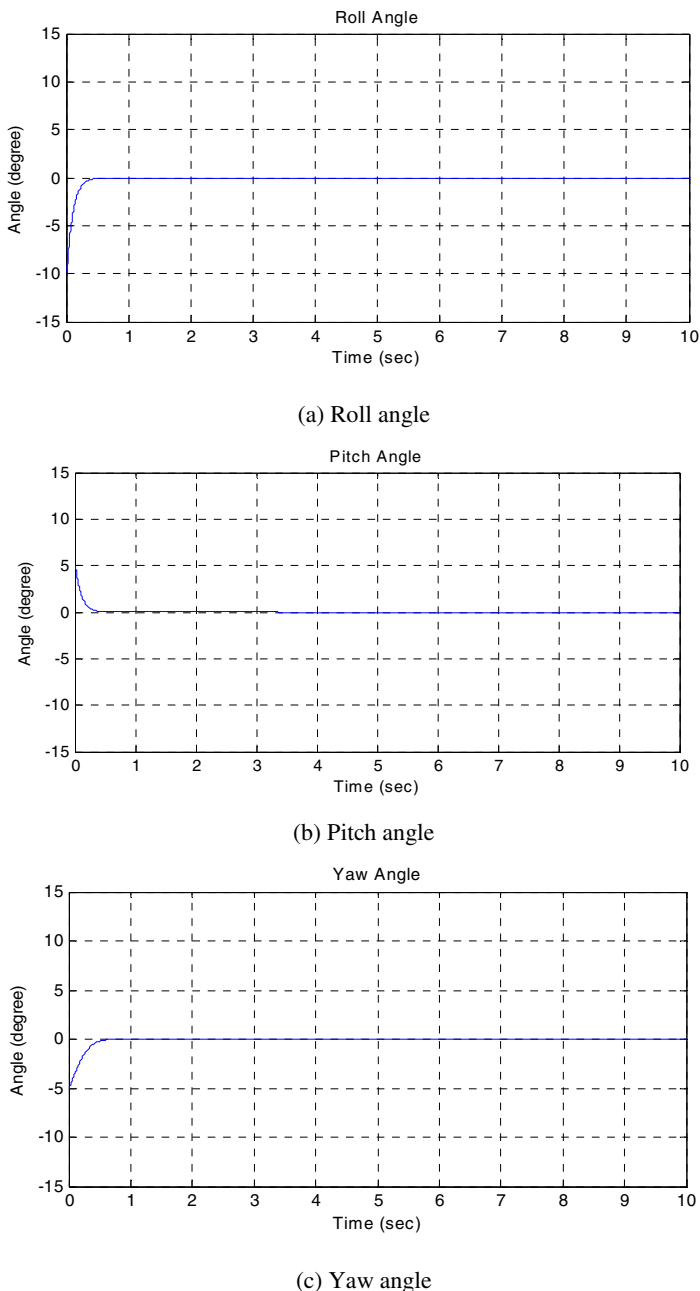


Fig. 4. Attitude control performance

set to -10, 5, -5 degrees for roll, pitch, yaw angles, respectively. The attitude control is desired to have zero angles in roll, pitch and yaw angles.

4.2 Circular Trajectory Tracking Control Performance

The quad-rotor system is required to follow the Cartesian circular trajectory as shown in Fig. 5. Each axis in the Cartesian space is well regulated as shown in Fig. 5 (a), (b), and (c). The corresponding roll, pitch, and yaw angle errors are plotted in Fig. 5 (d). The overall Cartesian trajectory tracking result is shown in Fig. 5. (e). We see the tracking errors in the Cartesian trajectory tracking performances by the transformation error from the Cartesian space to the joint space due to the coupled effects and unknown dynamics.

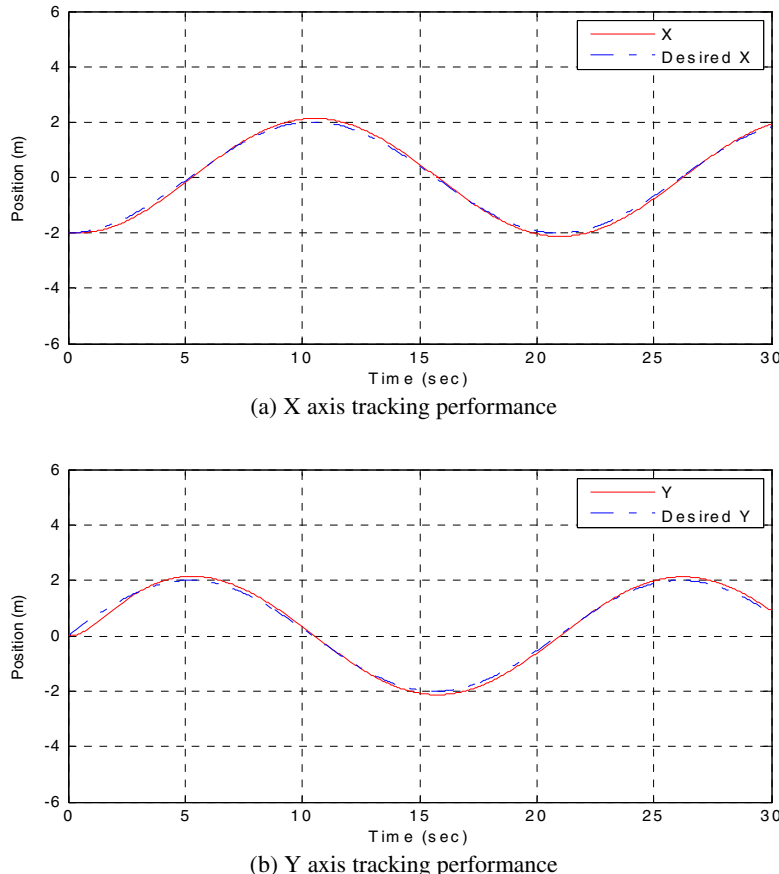


Fig. 5. Position tracking control performance

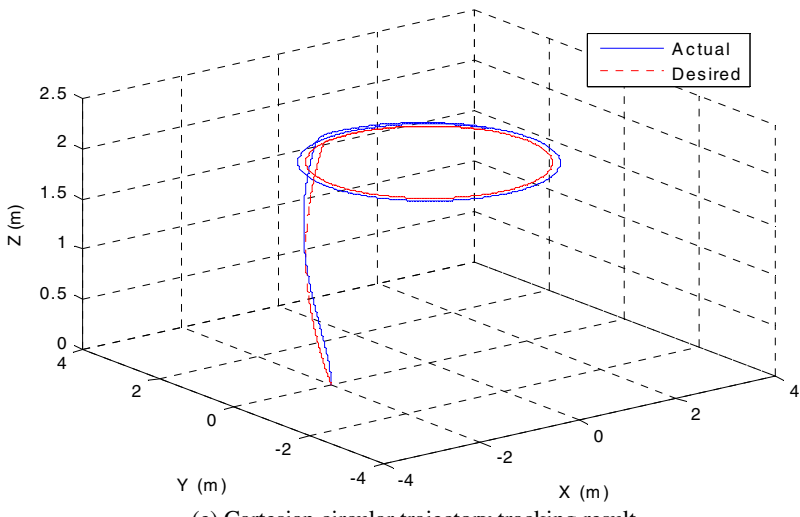
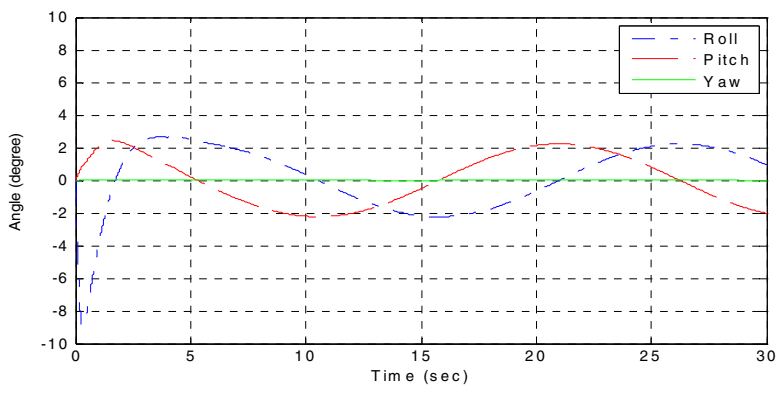
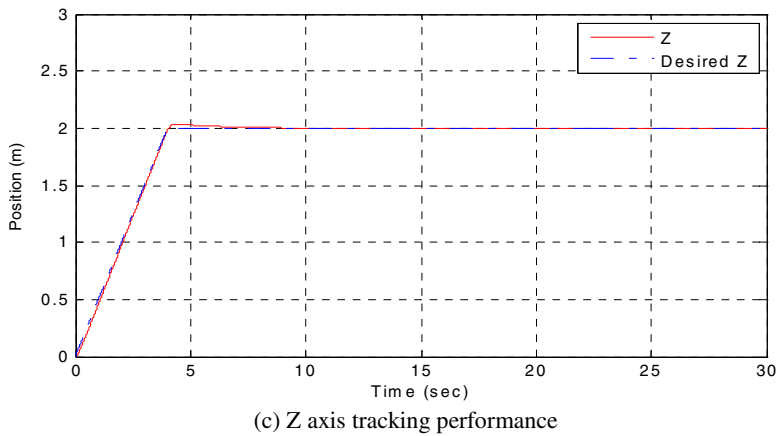


Fig. 5. (continued)

5 Experimental Studies

To confirm the feasibility of the control schemes, experimental studies are presented. A camera is used as a global sensor to detect the position and orientation of the quad-rotor system. Red and yellow markers are used to detect the heading angle of the system. The quad-rotor system is required to maintain desired position. Fig. 6 shows the image-cut of the real movement of the quad-rotor system.



Fig. 6. Position control performance

6 Conclusion

In this paper, the Cartesian position control of a quad-rotor system was presented. Kinematics and dynamics of a quad-rotor system were derived. Simulation studies were conducted to demonstrate control performances of the Cartesian trajectory control. A circular trajectory tracking control task has been conducted along with the attitude control. Both control performances were well realized. To confirm the feasibility of the control schemes, experimental studies of maintaining desired position under the camera are conducted. Although an experimental result of maintaining position of a quad-rotor system is conducted, the trajectory following control is not presented. Another problematic issue is to improve the control performance.

Acknowledgements. This research has been supported by Korea Research Foundation (KRF) through the general research program (2012R1A1A2A004668981) in Korea and the center for autonomous intelligent manipulation (AIM) for service robots of MKE (The Ministry of Knowledge Economy), Korea, under the Human Resources Development Program for Convergence Robot Specialists support program supervised by the NIPA (National IT Industry Promotion Agency) (NIPA-2012-H1502-12-1002).

References

1. Zhang, R., Quan, Q., Cai, K.Y.: Attitude control of a quad-rotor aircraft subject to a class of time-varying disturbances. *IET Control Theory and Applications* 4(9), 1140–1146 (2010)
2. Zuo, Z.: Trajectory tracking control design with command-filtered compensation for a quad-rotor. *IET Control Theory and Applications* 4(11), 2343–2355 (2010)
3. Dierks, T., Jagannathan, S.: Output feedback control of a quad-rotor UAV using neural networks. *IEEE Trans. on Neural Networks* 21(1), 50–66 (2010)
4. Efe, M.: Neural network assisted computationally simple PID control of a quad-rotor UAV. *IEEE Trans. on Industrial Informatics* 7(2), 354–361 (2011)
5. Schwager, M., Jullian, B., Angermann, M., Rus, D.: Eyes in the sky: Decentralized control for the deployment of robotic camera networks. *Proceeding of IEEE* 99(9), 1514–1516 (2011)
6. Herrise, B., Hamel, T., Mahony, R., Russotto, F.: Landing a VTOL unmanned aerial vehicle on a moving platform using optical flow. *IEEE Trans. on Robotics* (2011)
7. Ng, W.S., Sharlin, E.: Collocated interaction with flying robots. In: *IEEE Conf. on Robot and Human Interactive Communication (ROMAN)*, pp. 143–149 (2011)
8. Ghadiok, V., Goldin, J., Ren, W.: Autonomous indoor aerial gripping using a quad-rotor. In: *IEEE Conf. Intelligent Robots and Systems (IROS)*, pp. 4645–4651 (2011)
9. Jeong, S.H., Lee, M.K., Jung, S.: Calibration and control of rotor actuation of flymobile by force measurements. In: *URAI*, pp. 395–398 (2010)

Mathematical Formula Recognition Based on Modified Recursive Projection Profile Cutting and Labeling with Double Linked List

Yong-Ho Yoo and Jong-Hwan Kim

Department of Electrical Engineering, KAIST
335 Gwahangno, Yuseong-gu, Daejeon, Republic of Korea
`{yhyoo,johkim}@rit.kaist.ac.kr`

Abstract. Recognizing mathematical expression is important to reduce time in converting image-based documents like PDF to text-based documents that are easy to use and edit. In case of general character recognition, the sequence of character segmentation is from left to right, and from top to bottom. However, mathematical expression is a kind of two-dimension visual language. Thus, segmentation is more complex than one-dimension language. This paper proposes a modified recursive projection profile cutting method of character segmentation in images of mathematical formula, using depth first search for arranging and double linked list for re-arranging. The proposed method is demonstrated through various kinds of experiments, and shows this method can yield results of high accuracy for the recognition of mathematical formula.

Keywords: Mathematical Expression, Baseline Structure Analysis, Character recognition, Neural Network.

1 Introduction

Mathematical formula is very important in science and engineering reference because it is easily understood and expressed. Nowadays, many science references are composed of images like PDF. When we need to quote mathematical formula in PDF or modify a little, we have to convert two-dimension images into one-dimension texts via L^AT_EX. This job is very cumbersome as complexity of formula structures are very complex. Thus, many researchers have tried to convert two-dimension images into one-dimension texts automatically.

Over the past, there have been a number of approaches in formula recognition. There are three main issues in formula recognition. One is how to detect formula region in PDF. Xiaoyan Lin *et al.* proposed mathematical formula identification in PDF Documents [1]. They proposed to identify regions of both the isolated and embedded mathematical expressions in PDF documents. They used rule-based and learning-based method to adapt to wide range formula types. Rule-based rule proposed by them means that a line is filtered out only when it does not satisfy any of following two rules: 1) A named function appears in the line: 2)

At least one math symbol appears in the line. And proposed learning-based rule means LIBSVM, an optimized implementation of Support Vector Machine (SVM) for classifying.

Second issue is how to segment each letter in formula region that is already detected in PDF. Okamoto et al. outline a method of obtaining a structural representation of scanned images of mathematics notation using recursive projection profile cutting [2]. A projection corresponds to projecting pixels onto the x and $y - axes$ of images. The cutting process is to separate adjacent sub-expressions horizontally using a vertical projection, followed by horizontal projection to separate baselines. This process is applied recursively. However, it would happen two or more character could be recognized as one character by using this method solely.

The other is how to analysis already segmented characters and convert to one-dimension texts. Zanibbi and Blostein used seven baseline to analyze the formula structure, constructed one BST (Baseline Structure), achieved structure description, it's an adaptive method for most of the formula type [3]. However, it is restricted to detect structure correctly for formula that has multi-baseline.

In this paper, we propose modified recursive projection profile cutting method to improve character segmentation and the method how multi-baseline could be detected. The proposed scheme could solve problems, mentioned above, and the recognition result could be improved better.

The rest of paper is organized as follows: Section 2 reviews relevant work. Section 3 describes character segmentation method using double linked list, modified recursive projection cutting method and classifying method based on neural network. Structure analysis by detecting multi-baseline is described in Section 4. Experiments and results are presented in Section 5, and this paper is concluded with a future research plan in Section 6.

2 Related Work

Nowadays, there are many researches on mathematical formula recognition. Among them, the recognition method is divided by BST and projection profile cutting method. BST, an abbreviation of baseline structure analysis is to recognize the character in baseline. Subsequently, each character is classified by position based on baseline. On the other hand, projection profile cutting is to segment two-dimension images to each character by projecting toward $x - axis$ and $y - axis$ alternatively.

2.1 Baseline Structure Tree

The meaning of mathematical formula could be changed by position as well as shape. Thus, each character has to be classified by position. For correct classifying, character region could be designed like Fig. 1. The field of text node is the region of baseline, which has following seven kinds of type: Above, Below, Super, Subsc, Tleft, Bleft and Hor [3].

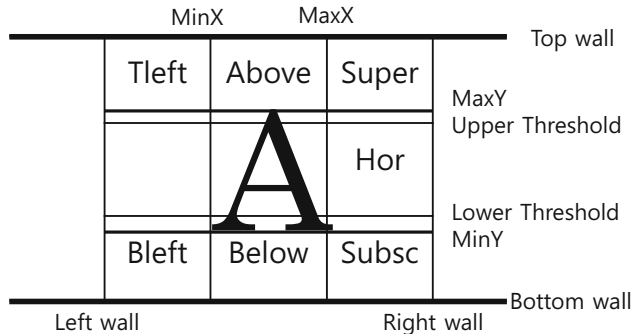


Fig. 1. Character region design

Using character region design, formula is represented by base structure trees. Components of base structure tree could be divided by character node and field node. Character node means the character which is located at baseline. And field node means the character which is located side of character region centered by character node. Equation (1) could be represented as BST like Fig. 2.

$$\bar{x} = \frac{1}{n} \sum_{i=1}^n x_i \quad (1)$$

In the structure tree, ‘x’, ‘=’, ‘-’, ‘ Σ ’, ‘x’ is designated as character located at baseline and they are called as parent nodes. And child nodes are defined nodes that have parent nodes. There are a number of advantages to structural representation via this baseline structure tree. The recognizing sequence could be easily found from left to right through baseline detection. Also, using baseline structure tree, the characters that have same depth and same parents could be grouped by binding ‘(’ and ‘)’. By doing this, transforming to one-dimension texts works more easily. However, the character relation of off-line formula is

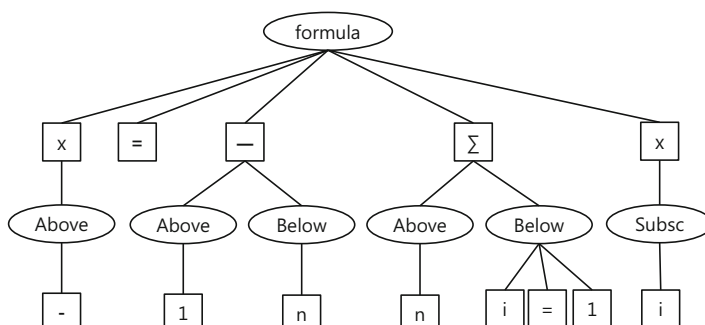


Fig. 2. Structure analysis process

so uncertain that some characters may not be classified any field. To solve this problem, the field region is overlap with other field. Using this method can avoid recognition failure caused by uncertain position relation [4]. However, although there are multi-baselines in formula, this method assumes that there is only one baseline. To solve this problem, other additional processing is needed.

2.2 Recursive Projection Profile Cutting Method

In formula, the character's sequence for reading is not linear so that recognizing properly is very complicated. By projection profile cutting method, proper sequence of formula could be detected. Histogram could be drawn by projection horizontally or vertically. Next, this method cut the image along with positions whose number of pixels has under threshold value. This method is repeated until there are no positions whose number of pixels have no under threshold value any more.

Fig. 3 represents structural expression by using recursive projection profile cutting method. By this method, segmentation sequence is ‘∞’, ‘ \sum ’, ‘n’, ‘=’, ‘0’, ‘x’, ‘n’, ‘=’, ‘1’, ‘-’, ‘1’, ‘-’ and ‘x’. As the form of this formula in L^AT_EX is $\backslash sum_{n=0}^{\infty} x^n = \frac{1}{1-x}$, this segmentation sequence is almost correct. However, this approach is not appropriate to detect superscripts, subscripts, matrices, limit expression (e.g. summations) or expressions within square roots, each of which requires additional processing [5].

Furthermore, they have the chance that two or more character would be recognized as one character based on histogram. Therefore, there are many limitation of recognizing formula by using only recursive projection profile cutting method.

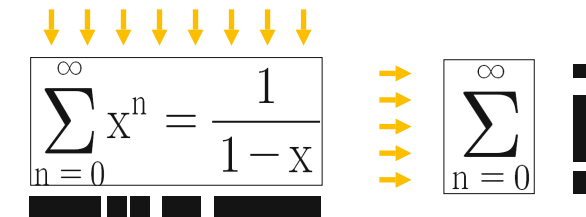


Fig. 3. Character region design Cutting Method horizontally(*left*) and cutting method vertically(*right*)

3 Character Segmentation

3.1 Applied Double Linked List

General character segmentation is implemented according to priority of position, from top to bottom, and left to right. However, when this method is used at

formula recognition, they are chances of making error in the arrangement of words. To overcome this problem, we use double linked list to correct sequence between characters easily.

Fig. 4 and Fig. 5 show how double linked list is applied. Fig. 4 represent the structure that memorizes feature of each character. In this structure, position, size and normalized image's pixel value could be saved. And to access adjacent character or to change character sequence easily, address variables like 'prev' and 'next' are defined. Fig. 5 represent the whole structure of formula. It is composed of structure of one character. All variables and functions related to recognition are also declared in this class. (e.g. linked lists' insertion, deletion, addition, binarization, interpolation for normalizing image of each character etc.)

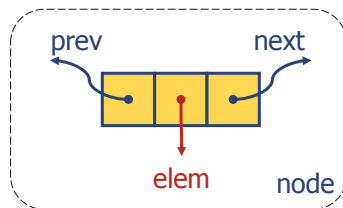


Fig. 4. Structure of one character

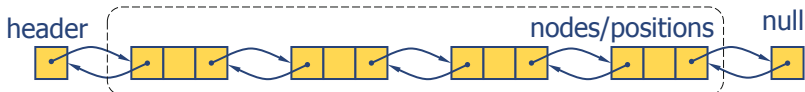


Fig. 5. Whole structure of formula

3.2 Modified Projection Profile Cutting Method

When previous projection profile cutting method is applied, it could be at risk for recognize two or more characters as one character. This problem is described in Fig. 6. When projection profile cutting method is used, trough between two characters' histogram could be over the threshold value designated so that these characters are recognized as one character.

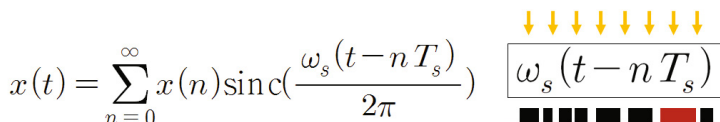


Fig. 6. A projection cutting problem based on histogram

Although one character is segmented by projection profile cutting, this cannot be always convinced so that additional processing is needed. The solution is labeling after projection. This problem is almost happened during projection not vertically but horizontally. Therefore, labeling sequence has priority from left to right than from top to down. So, it could be overcome by using labeling after projection.

3.3 Classifying Individual Characters or Words

One character could be recognized after using projection profile cutting method followed by labeling. This character could be translated text for representing in L^AT_EX. The general formula character is shown in table 1[4].

Table 1. The general formula character samples

Number	Description	Character example
1	Digital number	0123456789
2	English character	ABCDEFGHIJKLMNPQRSTUVWXYZ abcdefghijklmnoprstuvwxyz
3	Greece character	ΑΒΓΔΕΖΗΘΙΚΑΜΝΞΟΠΡΣΤΥΦΧΨΩ αβγδεζηθικαμνξοπρστυφχψω
4	Mathematical character	+ ×÷/±^() [] = <> % * &# $\in \sum \prod \int \phi \forall \neg \vee \therefore \leq \geq \neq$
5	Special character	,?";,:;"ΔΛΔ

To classify characters, characters that have same histogram distribution must be thought as separate groups. A horizontal axis is divided into three equal parts. Among each part, assign 1 when the number of pixels has more pixels than average number of pixels. Otherwise, assign 0. Therefore, each character could be grouped as 8 groups from “000” to “111”. Also, same process is applied to a vertical axis. The total number of group could be 64. In this process, each character is allowed being overlapped multiple groups. Some examples of this process are described in Fig. 7. ‘4’ is classified “001” vertically and “010” horizontally. ‘+’ is classified “010” vertically and “010” horizontally.

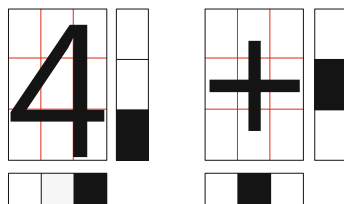


Fig. 7. Example of classifying one character ‘4’ and ‘+’

Artificial neural network is applied to classify and give a name to express text among characters in same groups. As each character is normalized 16×12 sizes, 16×12 input neurons are used. The number of neuron in hidden layer is 150. And, the number of characters in each groups could be the number of output neuron. This structure is described in fig. 8.

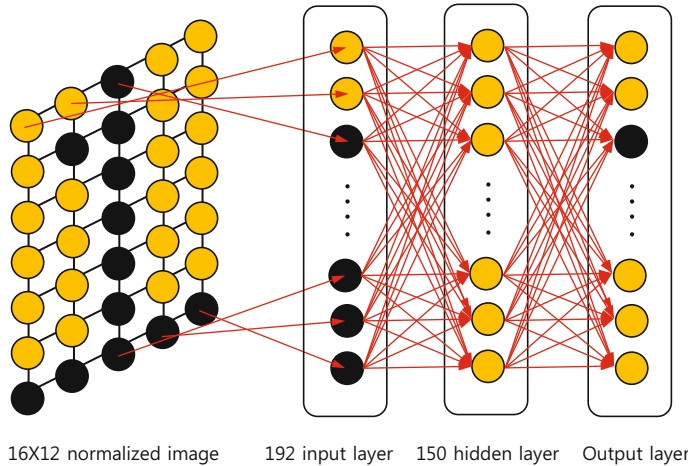


Fig. 8. Neural network structure of character recognition

4 Structure Analysis

General character recognition is completed by classifying. Though, in case of formula recognition, the position of each character is important as the meaning of position determine whether scripts or not. Therefore, classifying has to be followed by structure analysis.

4.1 Baseline Detection

Baseline Detection method proposed by Zanibbi and Blostein could be used in single baseline [3]. By using this method, superscripts, subscripts and matrices could be classified in a simple formula. However, there are formulae that have many baseline like (2).

$$\frac{(x - m)^2}{a^2} + \frac{(y - n)^2}{b^2} = 1 \quad (2)$$

To detect multi-baseline, a depth of recursive projection profile cutting function is saved. Depth means that how many function is called until no more projection is excuted. The segmentation order above formula is ‘(’, ‘-’, ‘m’, ‘)’, ‘2’, ‘_’, ‘a’

Depth	Character															
0																
1																
2																
3																

Fig. 9. A formula that has multi-baseline

and ‘2’ by projection profile cutting method. The depth of each character is described in Fig. 9.

Each baseline could be detected from depth information. Baseline is started from depth-increasing point and ended depth-decreasing point. This example is represented in Fig. 9. Each detected baseline could be recognized using BST method. This method could be a solution of single BST method.

4.2 Correcting Relation

The sequence of recognized order using projection cutting method, labeling and BST method couldn’t be always reasonable. Some structurers which contain Σ , \prod , etc. in formula have to be modified. Generally, the sequence of equation is symbol, superscript and subscript. However, the sequence of recognized order for equations included Σ or \prod is superscript to symbol followed by downscript. These special characters have to be executed by exception processing. The relationship between characters is represented by double linked list. Therefore, change of order is easily executed by changing address which indicates about previous or next character.

5 Experiment Result

We carried out experimental recognition for a wide variety of off-line mathematical expressions. Fig. 10 shows the original images used and the recognition results reproduced by LATEX.

Most formula could be recognized correctly. However, some formula failed to recognize partially. Last formula in Fig. 10 failed to recognize ωt and kz . These fail came from narrow spaces between two letter. It means that two separate letter was recognized one letter during projection.

6 Conclusions

This paper proposed a modified recursive projection cutting method with labeling and demonstrated its effectiveness through the experiment with neural network. To classify normal letter, superscript and subscript, depth of recursive projection was used. Altough most of formula could be recognized correctly,

Original Image	Transformed Text Format	Representation in LATEX
$\epsilon m f = \oint EdL = -\frac{d}{dt} \int BdS$	$\text{emf}=\oint \text{EdL}=-\frac{d}{dt}\int \text{BdS}$	$\text{emf} = \oint EdL = -\frac{d}{dt} \int BdS$
$x(t) = \sum_{n=0}^{\infty} x(n) \sin c\left(\frac{w_s(t-nT_s)}{2\pi}\right)$	$x(t)=\sum_{n=0}^{\infty} \{n=0\}^{\{\infty\}} x(n)\text{sinc}(\frac{\omega_s(t-nT_s)}{2\pi})$	$x(t) = \sum_{n=0}^{\infty} x(n) \text{sinc}\left(\frac{\omega_s(t-nT_s)}{2\pi}\right)$
$\nabla \times H = J + \frac{\partial D}{\partial t}$	$\nabla \times H = J + \frac{\partial D}{\partial t}$	$\nabla \times H = J + \frac{\partial D}{\partial t}$
$\frac{(x-m)^2}{a^2} + \frac{(y-n)^2}{b^2} = 1$	$\frac{(x-m)^2}{a^2} + \frac{(y-n)^2}{b^2} = 1$	$\frac{(x-m)^2}{a^2} + \frac{(y-n)^2}{b^2} = 1$
$c_n = \int_{T_0} x(t) e^{-jn\omega_0 t} dt$	$c_n=\int_{T_0} x(t) e^{-jn\omega_0 t} dt$	$c_n = \int_{T_0} x(t) e^{-jn\omega_0 t} dt$
$x[n] = x(t) \sum \delta(t - nT_s)$	$x[n]=x(t)\sum \delta(t-nT_s)$	$x[n] = x(t) \sum \delta(t - nT_s)$
$1 + x + x^2 + x^3 + \dots = \sum \frac{1}{1-x}$	$1+x+x^2+x^3+\cdots=\sum \frac{1}{1-x}$	$1 + x + x^2 + x^3 + \cdots = \sum \frac{1}{1-x}$
$\epsilon_x(z; t) = \text{Re}[E_x^- e^{j(\alpha z + \phi_z)}] = E_x \cos(\alpha z + k z + \phi_z)$	$\epsilon_x(2; t) = \text{Re}[E_x^- e^{j(a+b)}] = E_x \cos(a + k z + \phi_x)$	$\epsilon_x(2; t) = \text{Re}[E_x^- e^{j(a+b)}] = E_x \cos(a + k z + \phi_x)$

Fig. 10. Experiment results

there are some problems to solve. As the space between two characters is narrower, it would be harder to recognize correctly so that projection method is very sensitive to noise. Therefore, it is also important to reduce noise in pre-processing to yield results of high accuracy for recognition. Another important problem is that there are many similar characters in formula expression, for example, ‘a’ and ‘α’. These kind of letters couldn’t be always recognized without knowing context of formula. Therefore, it is needed to comprehend contextual information by analyzing adjacent letters.

In future research, these two problems will be the main issues in formula recognition. As well as off-line recognition, this research could also be extended to on-line formula recognition.

Acknowledgements. This research was supported by the MKE (The Ministry of Knowledge Economy), Korea, under the Human Resources Development Program for Convergence Robot Specialists support program supervised by the NIPA (National IT Industry Promotion Agency) (NIPA-2012-H1502-12-1002)

References

1. Lin, X.Y., Gao, L.C., Tang, Z., Lin, X.F., Hu, X.: Mathematical formula identification in PDF documents. Paper presented at Int. Conf. Document Anal and Recognition, Beijing, China, pp. 1419–1423 (September 2011), doi: 10.1109/ICDAR.2011.285
2. Okamoto, N., Miao, B.: Recognition of mathematical expressions by using the layout structures of symbols. Paper presented at Int. Conf. Document Anal and Recognition (1), Saint-Malo, France, pp. 242–250 (September 1991)
3. Zanibbi, R., Blostein, D., Cordy, J.: Baseline structure analysis of handwritten mathematics notation. Paper presented at Int. Conf. Document Anal and Recognition, Seattle, WA, USA, pp. 768–773 (February 2001), doi:10.1109/ICDAR.2001.953892
4. Li, Y., Wang, K., ShangGuan, W., Tang, L.: The research of mathematical formula recognition method base on baseline structure analysis. Paper presented at Int. Conf. Internet Computing in Sci. and Eng., Harbin, China, pp. 53–59 (January 2008), doi:10.1109/ICICSE.2008.102
5. Zanibbi, R.: Recognition of mathematics notation via computer using baseline structure. Technical Report ISBN-0836-0227-2000-439, Dept. Computing and Information Science, Queen's University, Kingston, Ontario (August 2000)

Control for Smart Transportation Vehicle Based on Dynamic Model

Phan Le Hung, Trinh Duc Cuong, and Nguyen Truong Thinh

Dept. of Mechatronics, Ho Chi Minh City University of Technical Education
1 Vo Van Ngan, Thu Duc, Ho Chi Minh, Vietnam

lephan_hung@yahoo.com, cuongtd91@gmail.com,
thinhnt@hcmute.edu.vn

Abstract. In this paper, we mention the design, modelling and development of a mobile robot based on the structure of smart transportation vehicle carrying passengers. Smart transportation vehicle is being driven by electric motor automatically and is modeled dynamical systems with non-holonomic movement is rolling and non-sliding. This vehicle is being used increasingly often for a range of tasks. The contents of this article will address the control tracking for desired trajectories, kinematic, dynamics. Then the results of the method of problem-driven dynamics and kinematics followed a given trajectory is evaluated based on experimental data.

Keywords: Smart transportation vehicle, Kinematics, Dynamics.

1 Introduction

A significant proportion of robotics research involves developing vehicle-like robots [1]. In addition, mobile robots have been used in many application such as moving material between work stations. They can also be found in many areas such as industrial, medical, environmental and even domestic machines. However, some research has also addressed some topics related to dynamic characteristics of the movement which are essential to tracking trajectory. It has shown the problem of computing suitable trajectories in the face of varying terrain topography and under road holding constraints. This paper presents the work that has been done to explore the issue of kinematic and dynamic model. This leads to the development of a dynamic model for smart vehicle. The moving dynamic for the smart transportation vehicle can be achieved by applying a number of forces acting at any point and in any direction. It can be used to obtain general free body motion dynamics. This can be divided into kinematics trajectory planning and translation into the dynamic motor rotation trajectories. In order to execute accurate trajectories, the motor moving trajectories must consider both constraints due to the motors and load dynamics and those due to characteristic [2]. The reminder of this paper is organized as follow. After discussing model for smart transportaion vehicle, we describe the trajectory planning and moving control in section 3. Our experiments and results are present in section 4. Finally, section 5 summarizes the conclusions drawn from this vehicle.

2 Model for Smart Transportation Vehicle

2.1 Kinematic Model

The modelling will be derived taking the non-holonomic constraints into account. Non-holonomic constraints for smart transportation vehicle are non-integrable and are related to its velocity.

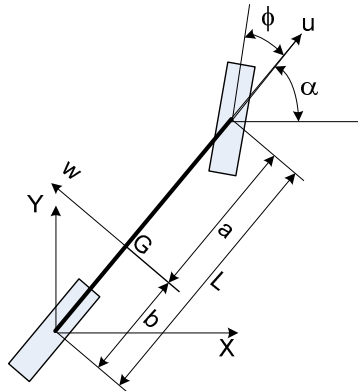


Fig. 1. Bicycle model for four-wheeled vehicle

Four wheels of smart transportation vehicle can be modeled as a bicycle for rotation angles of steering. The kinematic bicycle model collapses the left and right wheels into a pair of single wheels at the center of the front and rear axles as shown in figure 1. The wheels are assumed to have no lateral slip and only the front wheel is steerable. Let (x, y) denote the center of gravity (G) of the robot. The distance from G to the rear and front wheels be a and b respectively. Let θ denote the heading angle of the smart transportation vehicle with respect to the x-axis and ϕ denotes the steering angle between the front wheel and the body axis [3].

From above kinematic model, the non-holonomic constraints is given by:

$$\begin{aligned}\dot{x} \sin(\theta) - \dot{y} \cos(\theta) + b\dot{\theta} &= 0 \\ x \sin(\theta + \phi) - \dot{y} \cos(\theta + \phi) - a\dot{\theta} \cos(\theta) &= 0\end{aligned}\tag{1}$$

Let v_u and v_w be the longitudinal and lateral velocities of the smart transportation vehicle, we can define as follow.

$$\begin{aligned}\dot{x} &= v_u \cos(\theta) - v_w \sin(\theta) \\ \dot{y} &= v_u \sin(\theta) + v_w \cos(\theta)\end{aligned}\tag{2}$$

Substituting (2) in (1) and derived we get

$$v_w = b\dot{\theta}\tag{3}$$

$$v_w = \frac{b \tan \phi}{L} v_u \quad (4)$$

From equations (2) through (4) the kinematic model of the smart transportation vehicle is given by

$$\dot{x} = v_u \cos(\theta) - v_u \frac{b \tan \phi}{L} \sin(\theta) \quad (5)$$

$$\dot{y} = v_u \sin(\theta) + v_u \frac{b \tan \phi}{L} \cos(\theta) \quad (6)$$

$$\dot{\theta} = \frac{\tan \phi}{L} v_u \quad (7)$$

2.2 Dynamic Model

The dynamic model is derived with the following assumptions: there is no slip at the wheel, the rear wheels cannot be steered and are always in the same direction as the orientation of the vehicle, and the drive force and drive torque are assumed to act at the center of the rear wheels. In order to obtain the dynamic model of the smart transportation vehicle, forces must be applied, analyzed and moments must be taken about some point on the smart transportation vehicle, in this case the centre of gravity.

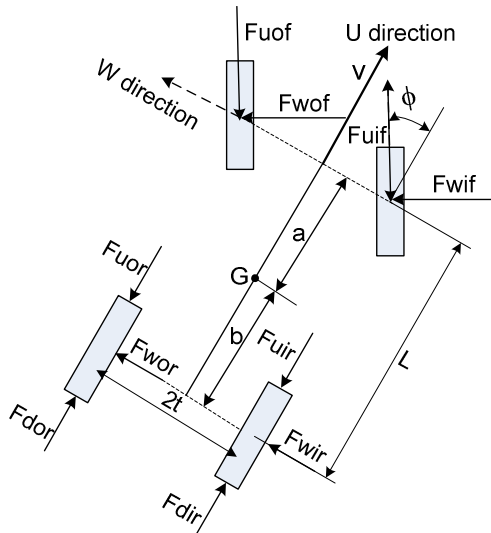


Fig. 2. Free Body Diagram

The forces acting on the smart transportation vehicle are as shown in figure 2. F_u , F_w , F_d denote the frictional force, the force acting perpendicular to each wheel as a

result of the slippage assumption made and the drive force respectively. Balancing the forces (Figure 3) acting along the u and w direction we have.

$$m(\dot{v}_u - v_w \dot{\theta}) = -F_{ur} + F_{dr} - F_{uf} \cos \phi - F_{wf} \sin \phi \quad (8)$$

$$m(\dot{v}_w + v_u \dot{\theta}) = F_{wr} - F_{uf} \sin \phi + F_{wf} \cos \phi \quad (9)$$

Where

$$F_{wir} + F_{wor} = F_{wr} \quad (10)$$

$$F_{uir} + F_{uor} = F_{ur} \quad (11)$$

$$F_{wif} + F_{wof} = F_{wf} \quad (12)$$

$$F_{uif} + F_{uof} = F_{uf} \quad (13)$$

$$F_{dir} + F_{dor} = F_{dr} \quad (14)$$

Also steering system dynamics of the smart transportation vehicle can be modeled by a first order linear system represented by the differential equation

$$\dot{\phi} = \frac{1}{\tau_s} (u - \phi) \quad (15)$$

Where τ_s , u denote the time constant and steering control respectively.

3 Trajectory Planning and Moving Control

Trajectory planning is the subject that deals with the moving of the smart transportation vehicle in a previous known environment. It plays a major role in building an effective sophisticated. Trajectory planning as well as trajectory generation are required prior to the movement. The movement is desired to move from a starting position to a goal point in the workspace. In this paper an effective method for trajectory planning and trajectory generation is adopted. This method consists of straight lines joined by circular arc segments with a specified radius and turning angle. Given a goal configuration, the trajectory planner computes a nominal trajectory for the smart transportation vehicle, i.e. a time-ordered sequence of (configuration, velocity) couples between the current configuration of the smart transportation vehicle and its goal. The termination of this trajectory relies upon a priori information on the environment and velocity as well as sensor data.

In this paper, a first approach would consist in applying open-loop steering control laws like those. However, it is known that this type of control is not robust to modelling errors (the sources of which are numerous) and that it cannot guarantee that the vehicle will follow the desired trajectory as planned. For this vehicle, such structure is useful because it constrains the available actions and reduces the

complexity of the navigation task [4]. The task of the controller is to achieve various goals and desired features for vehicle moving. It is also designed to execute the planned sequences of moving correctly in the presence of any error. The control strategies in this work are based on controlling the traction forces causing the motion as well as maintaining the tracking of the desired trajectory without any slippage or deviation.

In public environments where there is trajectory information to guide, the smart transportation vehicle must use a more general approach for navigation. In order to arrive at its intended destination address, it could use the local planning component of its system and orientation objective in figure 3.

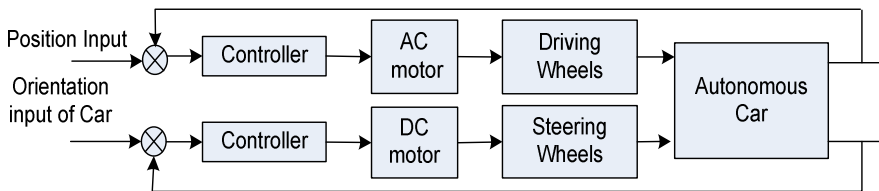


Fig. 3. The block diagram steering and driving system for smart transportation vehicle

The controller tasks consist of two parts to control the steering wheel of the vehicle. The first part is the 'High level' controls trajectories which collects signals from sensors and compares it to reference trajectory then command rotate the steering wheel as request. In this vehicle, four ultrasonic sensors SRF05 were equipped to detect obvious obstacles at long ranges in front and back of the car. Two were amounted in the front bumper and the others were amounted in the back bumper. Moreover, one GPS U-BLOX 6 Kit was used to provide current location and time information for this vehicle. The GPS Kit was put in the vehicle and the antenna was mounted on the ceiling. In addition, accurate direction estimation is one of the foremost concerns in smart transportation vehicle. In order to solve this problem, a module digital compass CMPS03 is used to identify accurately direction. This vehicle used two encoders, one is used to identify the steering wheel position and the other has function measures speed as well as moving distance of driving wheels.

The second one to control is the 'Low level' which uses PID controller and it received rotating signals from 'High level' to control request position of steering wheel. The combined "Low level" moving control is shown in figure 4.

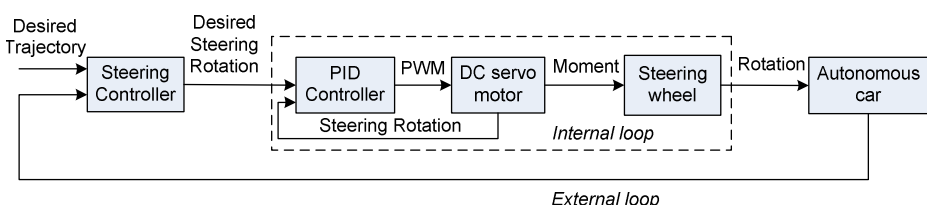


Fig. 4. Block diagram of Low level controller

In order to respond accurately requests from combined controller, this vehicle control system have 4 inputs including: GPS data, orientation, speed, and steering-wheel angle. These inputs provide surrounding environment data to combined controller which commands the steering-wheel actuator and receives the actual steering-wheel position from steering-encoder. Moreover, in this strategy, a moving control algorithm based on self-turning control is considered. The controller has been designed with a PID structure to estimate the changes in the system dynamic parameters. The self-tuning control structure offers a good framework to estimate the model parameters. This can be achieved through the estimation mechanism. Then controller implements and is able to cope with the dynamic changes and take the proper action to control the moving. However, it cannot estimate or cope with the changes in the surface conditions. The basic block diagram for the self-turning moving controller is shown in figure 5.

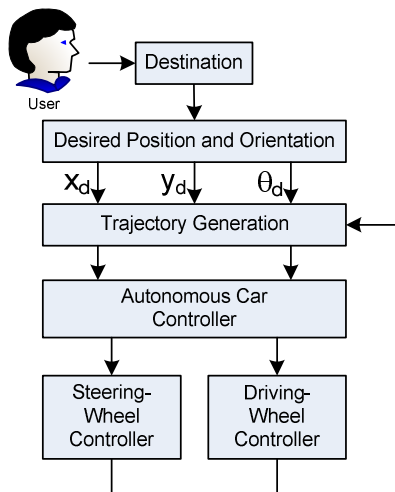


Fig. 5. Block diagram of automatic moving

4 Experiments and Results

In order to evaluate the responding of the vehicle, some experiments are implemented in a real environment (Figure 6). A general dynamic model to represent the smart transportation vehicle as a three dimensional rigid body has been built using Matlab software. The model will calculate the mass, centre of gravity and the inertia of the entire body. These values are used in the dynamic model which the controller operates on. Moreover, the results indicate that the combined controller is able to compensate and cope with the changes on the trajectory condition and provide better trajectory-tracking. Also the displacement error in the overall trajectory-tracking are presented to show the advantages of the combined controller.



Fig. 6. Smart transportation was used in the experiment

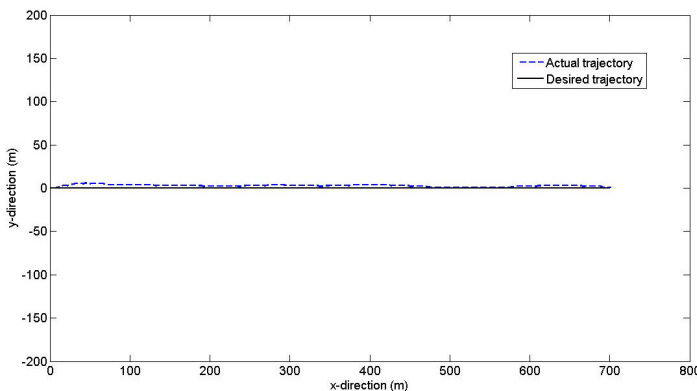


Fig. 7. Respond to straight trajectory

The response of movement following checked trajectory is shown in figure 7. In this figure, the actual trajectory followed a desired straight trajectory very well, however in real moving trajectory of smart transportation vehicle there sometimes were the errors as shifts in reference request because of controlling error of the steering wheel angle as well as compass's evaluated value. The errors caused by mechanical transmissions and vehicle's inertia.

Figure 8 illustrates the basic behavior of the smart transportation vehicle trajectory behavior. Based on moving control, the actual trajectory is the same as the desired trajectory. Although the actual trajectory has different performance with the desired trajectory, there is not much different in straight trajectory part (figure 8). Then the actual trajectory turned the smart transportation vehicle right with a large angle ($\approx 90^\circ$), but there was not much different with the desired trajectory. The processing of rotation 90° is as well as required. However, after turning, the smart transportation vehicle move straight and this process began to emerge error can be seen. The error after turning is due to the transmission errors accumulated make the steering system generate errors and oscillate around point 0 of the steering vector. Thus errors in the process is not by the control algorithm that generated by errors in mechanical transmission.

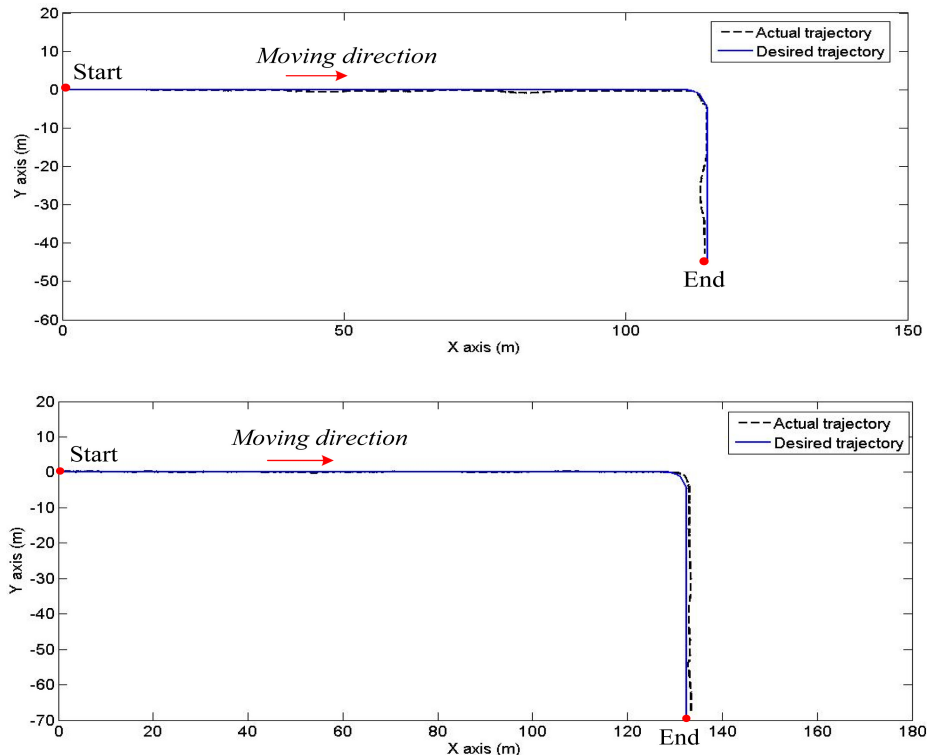


Fig. 8. Respond to desired trajectories

5 Conclusion

In this paper two control strategies are developed, and tested on the smart transportation vehicle. The 'low' level controller performance deteriorated with the changes in the surface condition such as the traction condition (friction coefficient). Meanwhile the combined controller detects the changes and copes with them in an adequate manner, maintaining a largely consistent performance. Some of the issues concerning the environmental structure and the high level control have been presented. Determining the location of the smart transportation vehicle plays a vital role in maintaining fast, smooth trajectory-tracking. Measuring the position of the smart transportation vehicle in the workspace gives the high level controller an indication of whether the smart transportation vehicle is experiencing any slippage or not. All these issues are important for the motion control. The combined control system has been investigated and tested on the differential drive smart transportation vehicle. Simulation results show that the performance of the smart transportation vehicle under the combined system has improved and the accuracy of trajectory-tracking also improved significantly.

References

1. Urmson, C., et al.: Autonomous Driving in Urban Environments: Boss and the Urban Challenge. In: Springer Tracts in Advanced Robotics, vol. 56, pp. 1–59 (2009)
2. Albagul, A.: Dynamic modeling and adaptive traction control for mobile robots. In: Industrial Electronics Society IECON 2004 - 30th Annual Conference of IEEE, vol. 1, pp. 614–620 (2004)
3. Panimadai Ramaswamy, S.A., Balakrishman, S.N.: Formation Control of Car-like Mobile Robots: A Lyapunov Function Based Approach. In: American Control Conference, pp. 657–662 (2008)
4. Ferguson, D., Bellino, M., Siegwart, R.: Autonomous Driving in Structured and Unstructured Environments. In: Intelligent Vehicles Symposium, pp. 558–563. IEEE (2006)

Intelligent Camera for Object Identification and Tracking

Donald G Bailey, Gourab Sen Gupta, and Miguel Contreras

School of Engineering and Advanced Technology
Massey University, Palmerston North, New Zealand
{D.G.Bailey,G.SenGupta}@massey.ac.nz

Abstract. Intelligent cameras extend the concept of smart camera by directly processing the pixels as they stream from the sensor. Working in a synchronous streamed pipeline processing mode, an FPGA incorporated into the camera is able to operate at the camera pixel clock rate. With careful design, this scheme minimizes memory accesses and reduces the latency over DSP based smart cameras. The transformation of the software image processing algorithm to an efficient intelligent camera implementation is demonstrated for global vision within robot soccer. The resulting intelligent camera requires no memory outside of the FPGA, and is able to provide the position and orientation of the objects while the image is being streamed from the sensor.

Keywords: FPGA, robot vision, robot soccer, real-time vision.

1 Introduction

Processing speed is critical in many vision applications. This is especially so when vision is used as a sensor in a control system, as is frequently encountered in robotics, machine vision and surveillance. The processing latency limits the usefulness of the data derived by image processing, because increased delays within a feedback loop can severely impact the controllability of a system. The consequences are poorer performance, or in extreme cases, instability.

Mobile robotics imposes additional constraints on vision processing. System size and weight are often limited, and since mobile robots are usually battery powered, power consumption is important. The complexity of many vision algorithms often requires high performance computing to manage the high data rates from cameras. This usually entails processors running with high clock speeds just to maintain the high pixel throughput. High clock speeds result in higher power requirements.

This state of affairs is exacerbated by the increasing resolution of low cost digital cameras. While the increased resolution generally improves the performance of many vision algorithms, this comes at the cost of an increased computational burden. The increased processing cost reduces the time available for other processing tasks, such as strategy and control functions.

To overcome some of these problems, processing is increasingly being moved to within the camera. Consequently, the last decade or so has seen the advent of

so-called “smart cameras”, where the camera is no longer solely responsible for capturing the images, but performing some of the processing, and communication of the processed images or results (Bramberger et al. 2006).

A general purpose processor struggles to keep up with the processing demands of image processing applications. For this reason, digital signal processors (DSPs) are commonly used for implementing smart cameras (Wills 1999; Bramberger et al. 2004; Novak and Mahlknecht 2005; Bramberger et al. 2006). The architecture of DSPs has been optimized for signal processing in a number of ways. The use of a Harvard architecture doubles the memory bandwidth by separating instruction and data memories. The CPU also has single cycle multiply and accumulate functions which speeds up filtering and other related operations.

Low-level vision processing operates independently on individual pixels, enabling the associated parallelism to be readily exploited (Downton and Crookes 1998). This has led to parallel processors which work simultaneously on multiple parts of an image. One example of this is described in (Kleihorst et al. 2001). They developed a dedicated chip that operates a bank of 320 processors in parallel on the pixels within one or more rows using a SIMD (single instruction multiple data) architecture. The input had a serial to parallel conversion to convert the incoming pixel stream to make the image rows available to the processor in parallel. A similar unit transformed the parallel processed data back to a serial stream for output.

In recent years, field programmable gate array (FPGA) technology has matured to the stage where it is practical for image processing tasks. FPGAs have been used in a wide range of ways within smart cameras. One has been through the use of a SIMD architecture to exploit spatial parallelism (Fatemi 2007). For these, a set of identical processing elements (PEs) is used in parallel. Another common architecture for image processing is the window processor (Dias et al. 2007). Here a series of dedicated PEs is used to perform identical processing to the pixels within a window, which are then reduced by another PE to give a single window output. Such an architecture enables a wide range of filters to be implemented, including linear filters, grayscale morphology, and sum of absolute difference. The window architecture exploits functional parallelism (Bailey 2011a), where the same function is applied to all of the pixels within a window. At the other end of the FPGA spectrum, dedicated logic is developed for the particular application, and implemented on the FPGA. One example of this is described in (Leeser et al. 2004). Such approaches generally have the smallest resource requirements, but are less general purpose. However, blocks of logic, such as memory management, camera interfacing, and some basic operations can be reused from one design to the next.

In software, most images are operated on at the image level. That is, an operation is applied to an image by reading the image from memory, performing the operation, and writing the results back to memory. The time required for such processing is dominated by memory accesses, rather than the actual processing performed. With general purpose processors, this also strongly relies on the processor cache to prevent the algorithm speed from being dominated by slow memory. Within a smart camera, though, processing can be moved from an image based computation to a pixel based computation (Bramberger et al. 2004). Here, rather than processing operations on

complete images, a sequence of image processing operations are performed on each pixel, with the intermediate results stored in local registers. The resulting reduction in memory bandwidth required can give significant savings. Where necessary, memory bandwidth can be increased further by operating multiple banks as ping-pong buffers.

Most smart cameras save the incoming image into a frame buffer before beginning processing, even if they begin processing before the complete frame has been captured. On an FPGA, it is possible to process the image as it is directly streamed from the camera. If all of the processing can be implemented in this manner, then the memory requirements (and associated bandwidth required) can be significantly reduced (Bailey 2011a). The strict timing constraint requires not just porting the algorithm from software into the camera, but transforming the algorithm so that it can use stream processing. We term this type of smart camera as an “intelligent camera”.

In this paper we will demonstrate this transformation process through the description of an intelligent camera for the global vision processor for robot soccer. The rest of the paper is structured as follows. Section 2 briefly overviews the typical architecture of robot soccer, in particular the robot soccer systems which use global vision. It outlines the changes to the system that result from using an intelligent camera. Section 3 outlines the vision processing algorithms performed by the intelligent camera in this application. The transformation of these algorithms for stream processing is described in some detail. Section 4 describes our implementation of an intelligent camera. Section 5 concludes the paper by discussing the costs and benefits of using an intelligent camera.

This is the first description (that we are aware of) of using an FPGA based intelligent camera for global vision for robot soccer. A further novel aspect of this paper is the description of the algorithm transformations from conventional software to an intelligent camera for this application.

2 Robot Soccer Architecture

Since robot soccer was introduced to the world in the mid nineties, most teams have relied on using global vision to track the robots and the ball. In a global vision system, a camera is mounted over the centre of the soccer platform at a prescribed height so that the playing field (robots’ workspace) is in its field of view. The video signal from the camera is fed to the PC based game controller. For analog cameras, the video signal is digitized using a frame grabber card before further processing. FireWire (IEEE 1394) is by far the most popular digital camera interface used. Where the field size is too big to be seen by one camera, some teams have resorted to using multiple cameras and combining the processed data output from them (Ball et al. 2004).

The typical architecture of a robot soccer global vision system is shown in Fig. 1. The image from the camera is first stored in a frame buffer. The vision processing software then analyses the image to identify objects of interest and this information is passed on to the strategy processor which decides the behaviour of individual robots (Sen Gupta et al. 2005). Based on the roles assigned to the robots, the global control processor generates the commands for the movement of the robots. The commands are sent to the robots by the communication layer.

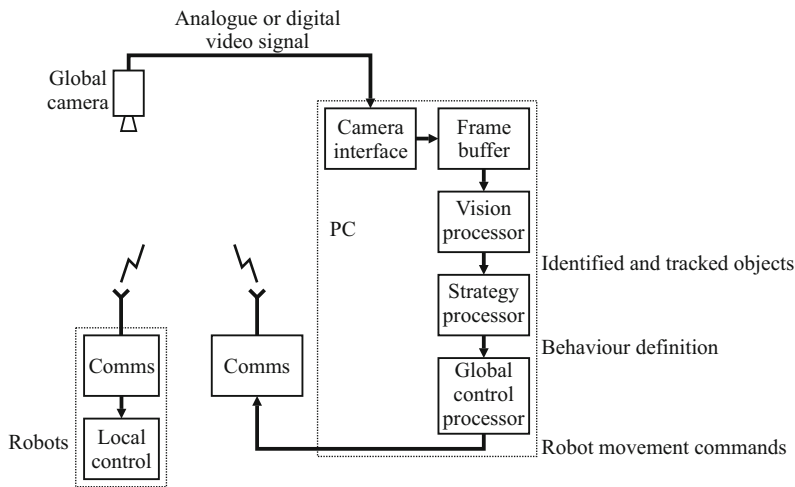


Fig. 1. Typical architecture of a robot soccer global vision system

The robot soccer game has graduated from 3-a-side in the early years of its inception to 11-a-side. Consequently the field size has also increased several fold. Recently, the trend has been to move to local vision based systems, partly dictated by the revised and challenging rules of the game. In a local vision based system, robots carry the vision system on board the mobile platform to perceive the world around them. This places many constraints on the system hardware and software such as size and processing throughput. A local vision system has been described in (Weiss and Jesse 2004). (Novak and Mahlknecht 2005) have implemented a high-speed onboard vision system comprising a small digital CMOS camera and a very fast and low power signal processing unit.

While there are several examples of use of smart cameras for local vision, research in the area of smart cameras for global vision is still in its infancy. (Wills 1999) designed and partially built a smart camera for robot soccer global vision using a DSP. His smart camera eliminates the frame grabber and PC hardware from the system. (Weiss and Hildebrand 2004) have presented the architecture of a flexible global vision system for robot soccer; the design is such that it can be adapted for multiple cameras and also for local vision systems.

The reduced system from using an intelligent camera is shown in Fig. 2. The intelligent camera incorporates the image sensor and the processing hardware to process the image. The intelligent camera generates the data, notably the coordinates and orientation of the identified objects, which is passed to the strategy layer of the software running on a PC. This effectively removes a lot of the processing overheads from the PC and offloads them onto the intelligent camera. The time available to the PC program for strategy and global control processing is increased resulting in quicker and better control of the robots.

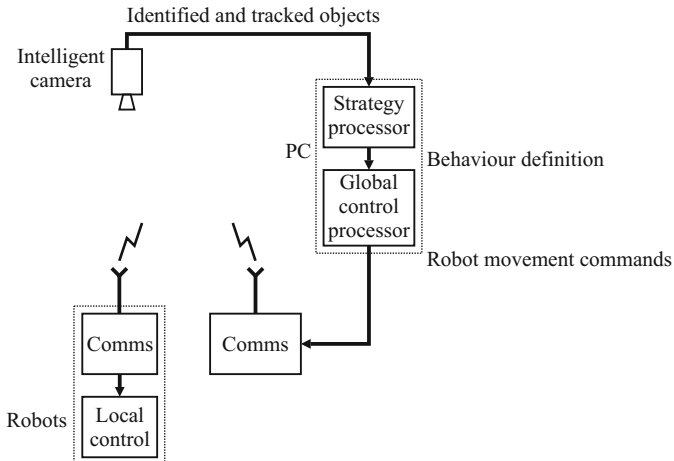


Fig. 2. Reduced system from using an intelligent camera

With FPGAs making tremendous progress in terms of speed and number of processing blocks, it is feasible now to implement the vision processing in FPGAs and derive the benefits of parallel processing in hardware. In this paper we present the design of a FPGA based intelligent camera for global vision applications and enumerate how software algorithms may be transformed to run on FPGAs utilizing hardware parallelism.

3 Algorithm Transformation for Intelligent Camera

The software algorithm used by the vision processor is outlined in Fig. 3. An RGB colour image from the camera is captured into a frame buffer by a frame grabber card. This image is converted from RGB to a simplified YUV colour space using only integer additions and shifts (Sen Gupta et al. 2004). The RGB colour space is not good for segmentation since changes in lighting significantly affect all 3 components. By converting to YUV, most of the lighting change is reflected in Y with only smaller changes to U and V. This allows significantly better colour selectivity when thresholding to detect the colours. The individual coloured pixels are detected by thresholding the Y, U and V channels independently, effectively using rectangular boxes within YUV space. The detected pixels are then grouped together and assigned unique labels using connected components labeling.

Processing within the next section is on each connected component, or blob, rather than on pixels. First, the coordinates of the centre of gravity of each blob are calculated, with the resulting coordinates corrected for parallax, lens and perspective distortion (Bailey and Sen Gupta 2004). The blobs are then grouped together and associated with robots based on proximity. From the set of blobs, the robot position and orientation can be estimated.

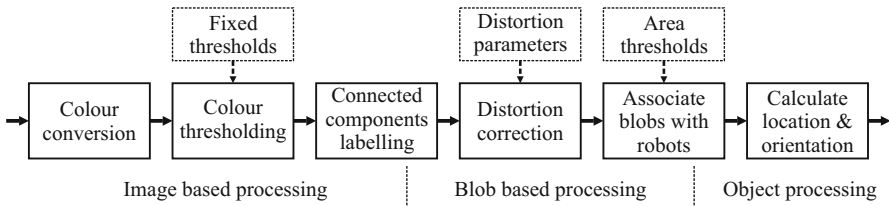


Fig. 3. Software algorithm implemented within the vision processor

From an image processing perspective, the basic algorithm can be implemented on the FPGA. Since the raw pixel stream directly from the camera is being processed, it is necessary to extend the colour conversion module to include Bayer pattern demosaicing.

However, rather than directly port the software algorithm, the algorithm needs to be transformed to exploit parallelism. Bailey has identified 9 transformation principles to consider when transforming an image processing algorithm from hardware to software implementation (Bailey 2011b). These are

1. Exploit Appropriate forms of Parallelism

Image processing algorithms consist of a sequence of operations. Building a separate processor for each operation and pipelining the results from one operation accelerated the processing by enabling each processor to operate in parallel. Other forms of parallelism spatial parallelism (unrolling the outer loop which steps through pixels, and build a separate processor for each instance), and functional parallelism (unrolling the inner loop to implement the low level operations in parallel).

The software algorithm in Fig. 3 can be directly be pipelined by building hardware on the FPGA for each operation. Functional parallelism is used to enable each operation to process one pixel per clock cycle.

2. Use Stream Processing where Possible

Stream processing converts the processing from an image basis to a pixel basis. This means operating the pipelines at a pixel level of granularity rather than at the image level. This significantly reduces latency, because it is unnecessary to wait for the whole image to be available before beginning the processing. Stream processing introduces a hard timing constraint, which can be overcome through low-level pipelining. This spreads the time required for each operation over several clock cycles, while maintaining a throughput of one pixel per clock cycle.

Stream processing is the basis of intelligent cameras, because the processing starts as soon as the pixels start arriving from the camera. By operating on the pixels as they arrive from the camera, external memory accesses are minimized.

3. Reduce Memory Access through Local Caches

For many image processing operations, the output pixel depends on several input pixels. Filters are a good example; caches save the pixels which are going to be reused later into memory blocks on the FPGA to minimize external memory bandwidth. Custom cache design is made easier by the regular access patterns of most low level image processing operations (simple row buffers are sufficient in many cases).

The algorithm above requires caches for the filtering associated with demosaicing, and for label propagation as part of connected components labeling. Edge enhancement and noise reduction filters are also introduced into the algorithm to improve the segmentation accuracy. These also require row buffers to cache previous rows.

4. Strip Mining and Multiplexing

Strip mining is another form of loop unrolling, where separate hardware is built for operating on separate sections of data. When processing pixels, usually each pixel only belongs to one class, enabling a single processor to be multiplexed between the associated data.

This is the case when calculating the area and centre of gravity of each of the blobs. Each pixel only belongs to one blob, so the pixel label can be used to select the corresponding data to be updated.

5. Rearrange Algorithm and Substitute Operations to Simplify Processing

Many algorithms can be simplified by rearranging the order of the operations, or replacing complex operations with simpler approximations.

In the robot soccer algorithm, this is exploited in several ways. First, rather than calculate the true YUV, which requires multiplications, the simplified YUV can be implemented purely with additions (Johnston et al. 2005). Connected components labeling typically requires two passes through the image. By extracting the data associated with each blob as the image is being labeled, the second pass is no longer necessary (Bailey and Johnston 2007; Ma et al. 2008). In fact the connected components processing can be simplified further since each of the blobs is convex.

6. Reduce Data Volume through Coding

In some applications, processing can be accelerated by compressing the data. In particular, run-length coding has been found useful in a number of applications, including connected components labeling (Appiah et al. 2008).

Run-length coding can simplify the connected components labeling of convex blobs. If a run overlaps matching pixels in the previous line then the whole run can be added to the blob, completely eliminating the need for merger processing.

7. Transform the Complete Algorithm, not Just Individual Operations

This principle suggests investigating interactions between operations, rather than implementing each operation in isolation (even if using pipelined stream processing).

8. Select Data and Memory Structures Based on H/W not S/W Requirements

In software almost all data structures are based within a single monolithic memory. On an FPGA, there are a large number of independent small dual-port memories which can be used to implement many of the data structures. The independence of the memory blocks gives a potentially wide bandwidth, although with stream processing it is still necessary to keep in mind the pixel rate – only one memory access may be made per port per clock cycle.

Caching is one example of the use of this principle. Another is using a block of memory to maintain the data structures associated with each connected component.

When implemented correctly, this enables data associated with a region to be output even before the image has been completely scanned (Ma et al. 2008).

9. Use Software for Software Tasks and Hardware for Hardware Tasks

Not all algorithms map well to hardware. Low level pixel processing is ideally suited to FPGA implementation. The higher level object based processing often consists of complex primarily sequential code, which if mapped to hardware would result in the hardware sitting idle for much of the time. These tasks are best implemented in software.

The robot level processing is one example of this. In this case, the processing to correct for distortion and determine the robot position and orientation is relatively simple. It could either be implemented in hardware, or in software on a soft core processor implemented within the FPGA.

The resulting transformed algorithm is shown in Fig. 4. It is shown in a little more detail than its software counterpart in Fig. 3. Note that the complete algorithm is implemented using pipelined stream processing, and no external frame buffer or other memory is required.

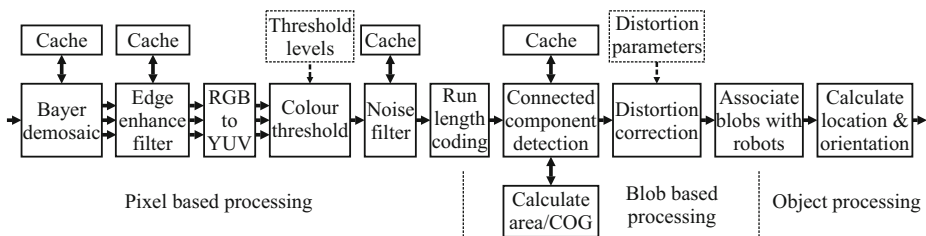


Fig. 4. Hardware implementation of the global vision algorithm on an FPGA

4 System Implementation

We are currently implementing the algorithm in Handel-C, compiled for the Cyclone IV FPGA on an Altera DE0-Nano board. Connected directly to the DE0-Nano, is a 5 megapixel D5M camera module. This provides a very compact, yet flexible development platform for prototyping our design.

Configuring the camera in skipping mode, we can output a VGA resolution image (640×480) at 127 frames per second. The pixels are streamed from the camera module at 96 MHz, and the FPGA is able to maintain a throughput of 1 pixel per clock cycle at this rate. The Bayer demosaicing filter has a latency of just over 1 row (using edge directed bilinear interpolation requires a 3×3 window). Edge enhancement and noise filtering similarly use 3×3 windows, with a latency of just over 1 row for each of those operations. Colour conversion and thresholding have a latency of one clock cycle each, and run length coding provides the run of coloured pixels one clock cycle after the end of the run. Connected components detection operates on runs of coloured pixels at a time. It accumulates the area and centre of gravity of the blob as the runs arrive. However, it must wait until the row after the end of the blob to determine that

the region is completed. This adds between 1 and 2 rows latency. Distortion correction takes only a few clock cycles, as does associating the blob to a robot. Once the last coloured patch has been detected for a robot, the position and orientation can be determined, and can be output to the strategy processor. The total latency is just over 5 image rows, with the results for an object output approximately 85 µs after the last pixel for the object is sent from the camera. Note that the last object is output before the end of the frame has been reached.

5 Discussion and Conclusions

In moving the vision system from a conventional camera and video processor to an intelligent camera, we have achieved a number of benefits. Processing pixels directly at the rate provided by the sensor can maximize the resolution-frame rate product. This allows an increase in either the resolution, or frame rate, or both, over a conventional camera. Being able to directly control the sensor features also gives increased flexibility, because in a conventional camera, many of the low level features are not user accessible. Processing the data with a synchronous streamed pipeline processor also minimizes the latency. On an FPGA, each stage of the processing pipeline is built with separate hardware, so all can operate in parallel. This allows the clock rate of the system to be reduced to the native rate of the pixels being streamed from the camera. Careful transformation of the algorithm allows the objects to be identified and tracked, even before the frame has completed loading into the FPGA. On a conventional system, the video processor will not have started processing the frame yet. The higher frame rate, combined with reduced latency, can significantly improve the system controllability.

The disadvantage of an intelligent camera is the difficulty in transforming the serial, memory based, software algorithm into one suitable for synchronous streamed pipeline processing. Simply porting the algorithm generally gives disappointing results, because it is usually necessary to modify the algorithm to fully exploit the parallelism available on an FPGA.

Further enhancements which we plan to introduce within the camera are:

- Use wireless communication to transmit object data to the strategy processor. This will simplify setup and reduce the need for wires.
- Integrate calibration within the camera as outlined in (Bailey and Sen Gupta 2010). The full sensor resolution could be used to give greater accuracy for the calibration. This would significantly reduce setup time.
- Modify the colour thresholding to use adaptive thresholding rather than fixed thresholds. This would overcome the perennial problem of sensitivity to light and light distribution. Again it would reduce setup time by avoiding the need to determine suitable thresholds each time the system is set up.

Overall, we have demonstrated the significant benefits that can be obtained through using FPGAs to create an intelligent camera for object identification and tracking within the robot soccer environment. We have moved the processing burden from

computer for performing the strategy and control processing. This has enabled a significant decrease in latency (to approximately 85 µs) and increase in frame rate (to 127 fps) for VGA resolution images. We anticipate that this would lead to better control.

Acknowledgements. This research has been supported in part by a grant from the Massey University Research Fund (11/0191).

References

- Appiah, K., Hunter, A., Dickenson, P., Owens, J.: A run-length based connected component algorithm for FPGA implementation. In: International Conference on Field Programmable Technology, Taipei, Taiwan, pp. 177–184 (2008)
- Bailey, D., Sen Gupta, G.: Error assessment of robot soccer imaging system. In: Image and Vision Computing New Zealand (IVCNZ 2004), Akaroa, New Zealand, pp. 119–124 (2004)
- Bailey, D.G., Johnston, C.T.: Single pass connected components analysis. In: Image and Vision Computing New Zealand (IVCNZ), Hamilton, New Zealand, pp. 282–287 (2007)
- Bailey, D.G., Sen Gupta, G.: Automated camera calibration for robot soccer. In: Papic, V. (ed.) Robot Soccer, pp. 311–336. In-Tech, Vukovar (2010)
- Bailey, D.G.: Design for embedded image processing on FPGAs. John Wiley & Sons (Asia) Pte. Ltd., Singapore (2011a)
- Bailey, D.G.: Invited paper: Adapting algorithms for hardware implementation. In: 7th IEEE Workshop on Embedded Computer Vision, Colorado Springs, Colorado, pp. 177–184 (2011b)
- Ball, D.M., Wyeth, G.F., Nuske, S.: A global vision system for a robot soccer team. In: 2004 Australasian Conference on Robotics and Automation, Canberra, pp. 1–7 (2004)
- Bramberger, M., Brunner, J., Rinner, B., Schwabach, H.: Real-time video analysis on an embedded smart camera for traffic surveillance. In: 10th IEEE Real-Time and Embedded Technology and Applications Symposium (RTAS 2004), Toronto, Canada, pp. 174–181 (2004)
- Bramberger, M., Doblander, A., Maier, A., Rinner, B., Schwabach, H.: Distributed embedded smart cameras for surveillance applications. IEEE Computer 39(2), 68–75 (2006)
- Dias, F., Berry, F., Serot, J., Marmoiton, F.: Hardware, design and implementation issues on a FPGA-based smart camera. In: First ACM/IEEE International Conference on Distributed Smart Cameras (ICDSC 2007), Vienna, Austria, pp. 20–26 (2007)
- Downton, A., Crookes, D.: Parallel architectures for image processing. IEE Electronics & Communication Engineering Journal 10(3), 139–151 (1998)
- Fatemi, H.: Processor architecture design for smart cameras. PhD Thesis, Technische Universiteit Eindhoven (2007)
- Johnston, C.T., Bailey, D.G., Gribbon, K.T.: Optimisation of a colour segmentation and tracking algorithm for real-time FPGA implementation. In: Image and Vision Computing New Zealand (IVCNZ 2005), Dunedin, New Zealand, pp. 422–427 (2005)
- Kleihorst, R.P., Abbo, A.A., van der Avoird, A., Op de Beeck, M.J.R., Sevat, L., Wielage, P., van Veen, R., van Herten, H.: Xetal: a low-power high-performance smart camera processor. In: IEEE International Symposium on Circuits and Systems (ISCAS 2001), Sydney, Australia, vol. 5, pp. 215–218 (2001)

- Leeser, M., Miller, S., Yu, H.: Smart camera based on reconfigurable hardware enables diverse real-time applications. In: 12th Annual IEEE Symposium on Field-Programmable Custom Computing Machines (FCCM 2004), Napa, California, USA, pp. 147–155 (2004)
- Ma, N., Bailey, D., Johnston, C.: Optimised single pass connected components analysis. In: International Conference on Field Programmable Technology, Taipei, Taiwan, pp. 185–192 (2008)
- Novak, G., Mahlknecht, S.: TINYPHOON: a tiny autonomous mobile robot. In: ISIE 2005, Dubrovnik, Croatia, vol. 4, pp. 1533–1538 (2005)
- Sen Gupta, G., Bailey, D., Messom, C.: A new colour-space for efficient and robust segmentation. In: Image and Vision Computing New Zealand (IVCNZ 2004), Akaroa, New Zealand, pp. 315–320 (2004)
- Sen Gupta, G., Messom, C.H., Demidenko, S.: Real-time identification and predictive control of fast mobile robots using global vision sensing. *IEEE Transactions on Instrumentation and Measurement* 54(1), 200–214 (2005)
- Weiss, N., Hildebrand, L.: An exemplary robot soccer vision system. In: CLAWAR/EURON Workshop on Robots in Entertainment, Leisure and Hobby, Vienna, Austria (2004)
- Weiss, N., Jesse, N.: Towards local vision in centralized robot soccer leagues: A robust and flexible vision system also allowing varying degrees of robot autonomy. In: FIRA World Congress 2004, Busan, Korea (2004)
- Wills, P.: The hardware design of a smart camera for the robot soccer environment. BE (Hons) Thesis, Department of Computer Science and Electrical Engineering, University of Queensland (1999)

Speaker Dependent Visual Speech Recognition by Symbol and Real Value Assignment

Jeongwoo Ju¹, Heechul Jung², and Junmo Kim²

¹ Division of Future Vehicle, Korea Advanced Institute of Science and Technology

² Dept. of Electrical Engineering, Korea Advanced Institute of Science and Technology

291 Daehak-ro, Yuseong-gu, Daejeon 305-701, Korea

{veryju, heechul}@kaist.ac.kr, junmo@ee.kaist.ac.kr

Abstract. In this paper, we propose a visual speech recognition method using symbol or real value assignment. Our method is inspired by Bag of Word (BoW) [1] model which is usually applied to an object matching problem. In the BoW model, a codebook is produced by using K-means clustering, and a feature vector extracted from an image is converted to corresponding symbol. Similarly, we generate codebook by running K-means algorithm on a pool of pHog (Pyramid Histogram of Oriented Gradients) feature vectors extracted from a subset of lip database. Then, the remaining lip images are assigned a particular value after comparing the chi-square distance to each cluster. Based on the type of this value, two methods are suggested so as to assign the value to a lip image frame. The first method is to find the cluster whose element image has the minimum chi square distance to the processing frame, and assign the cluster label to the frame. Second one is to calculate the distances between the frame and all cluster's centroids, obtain multi-dimensional vector for the frame which directly becomes an assigned value for the frame. Following these methods, each time sequence is converted into symbolized or multi-dimensional real valued sequence. To measure the similarity between two time sequences, we use Dynamic Time Warping for real valued time sequence and Edit distance for symbolized sequences.

Keywords: Visual Speech Recognition, Edit distance, Dynamic Time Warping, pHog, Codebook.

1 Introduction

Audio-based speech recognition (ASR) system has shown a satisfying performance, but its recognition rate rapidly decreases when the audio signal is degraded by acoustic noise [2] which is one of the limitations of ASR. A few examples for this case are as follows; running ASR system inside a car having a lot of noise source (engine, aerodynamic noise and tire) and making sense of a particular person's speech among crowded people.

To tackle this problem, supplementary information should be added to the speech recognition system. In general, a speech is generated by articulators such as tongue,

vocal tract and lip which is a highly observable organ. Hence, speaker utterance is partly interpretable from lip movement. By this intuition, a lot of previous works have focused on integrating audio and visual information to enhance speech recognition performance [3], [4].

In this paper, we focus on speech recognition problem only using visual information. Since a speech is produced by lip movement as time goes on, making use of not only spatial but also temporal information is essential for recognition. However this attempt can lead to different dimension or length for each speech data, as the speed or rate of speech changes every time, which yields difficulty in handling the data afterwards, e.g. comparing sequences of different lengths. To eliminate this problem, for instance, in G. Zhao et.al [5] they divide each image sequence into the same number (typically 3 in time axis) of blocks and construct a LBP feature from each block to equalize the dimension between speech sequences. In contrast to the above approach, which loses lots of temporal information, we try to use as many frames as possible not to lose temporal information even though we encounter the problem of unequal dimensions in data. To achieve this goal, we propose a new method utilizing pHog-based time sequences.

We divide all images in database into three groups; subset data for codebook, training and test, and then pHog features extracted from the individual image are used to represent a frame. K-means algorithm runs on all frames included in subset data for codebook based on chi-square distance between two pHog histograms. Once clustering finished, each frame of the remaining images belonging to training is summarized by a value, which is either a symbol or a real value as explained below. We propose two ways of assigning value to the image frame. The first one is to assign each frame a symbol using one nearest neighbor chi-square distance with the subset data. This implies that Bag of Word (BoW) concept is applied in modified way compared with original version, which has conversion from image to visual word followed by histogram generation denoting visual word occurrence. However, in this paper histogram step is omitted to prevent it from losing temporal information. The other method is that the frame obtains multi-dimensional vector after comparison its pHog histogram to that of centroids from clusters. In either way, time sequence data with different form corresponding to a specific utterance are obtained. In classification procedure, one nearest neighbor (1NN) using edit distance to compare between two symbol sequences is utilized, and 1NN multi-dimensional dynamic time warping for two real value vectors. The evaluation of proposed methods is conducted on 10 classes of isolated words and sentences using OuluVS database [5].

This paper is organized as follows. Section 2 presents the method on how to cluster lip image data based on pHog feature. Section 3 explains symbolizing procedure as well as introducing metric suitable for analyzing similarity between symbol sequences. Section 4 addresses the method of converting an image to multi-dimensional real value vectors to be successively applicable for dynamic time warping for dissimilarity measure. Section 5 describes our experimental setup and results. Section 6 summarizes our method and results with a conclusion. Section 7 suggests future work for further research.

2 Codebook Generation Based on pHog

A Histogram of Oriented Gradients (Hog) feature describes gradient occurrences and formulates it as histogram. Pyramid Histogram of Oriented Gradients (pHog) divides an image into sub-region, and Hog features are extracted inside sub-regions. For more information, reader may refer to [6], [7].

Originally, J. Sivic et al. [1] map high dimensional feature descriptor that occurs in an image to visual word using K-means. In a similar manner, we conduct mapping training data to a corresponding visual word. Since pHog feature takes histogram form, dissimilarity measure suitable for histogram is required to compare images. Among several measure options, chi-square distance is chosen as equation (1) in this work, where G, H denote slice histogram, n is the number of bin.

$$\chi^2(G, H) = \sum_{i=1}^n \frac{(G_i - H_i)^2}{(G_i + H_i)} \quad (1)$$

We separate a subset data from original database to use them for codebook construction, and then K-means algorithm runs on this group with the number of clusters, which we denote by N , being set to be 20. Subsequently, lip images of cluster group begin to gather according to the chi-square dissimilarity. The final clusters are utilized as codebook as in [1]. The schematic of flow chart is shown in Fig.1.

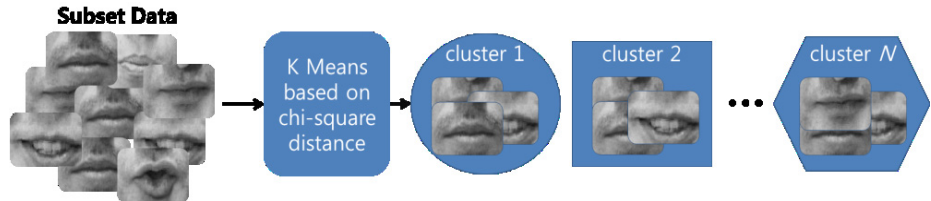


Fig. 1. Subset data clustering for codebook generation

3 Symbol Assignment and Classification

In this section, we propose a method of converting a lip image sequence to a sequence of discrete symbols, which we call visual word time sequence, as illustrated in Fig. 2. For instance, in Fig.2, one training data from the ‘Excuse me’ class has k frames. For each image frame, we select a cluster that is closest to the frame and we assign the cluster label as a symbol for the image frame, where the closest cluster is simply the cluster that contains the element closest to the image frame in terms of the chi-square distance between pHog feature vectors. For example, if a frame from training data is closest to the image which is part of cluster 13, Symbol 13 is assigned to the frame.

It is obvious that visual word is not a real value rather a symbol. Usually, Dynamic Time Warping (DTW) is chosen to measure dissimilarity between two time series. However, in this case DTW is unable to compare symbol sequences (e.g. Euclidean distance calculation between character ‘C’ and ‘D’ is impossible). Instead, the Edit

distance, a well-known metric for string matching, can measure dissimilarity between two symbol sequences. Given string or symbol sequence X and Y , edit distance between X and Y describes how many times the fundamental operations (deletion, insertion and exchange) are carried out to transform X into Y . The larger the number of conducted fundamental operations, the more dissimilar X and Y are. Furthermore, edit distance is non-negative and symmetric operation ($d(X, Y) = d(Y, X)$), if costs for all operations are equal. For more detailed study regarding this measurement, the literature [8] is a helpful material.

For the classification, we store a full training set of symbol sequences. During classification, a test data is compared with each cluster to become a symbol sequence. The symbol sequence of the test data is used for computing edit distance with all stored training data. Finally, the test data is recognized as one of possible utterances by 1NN.

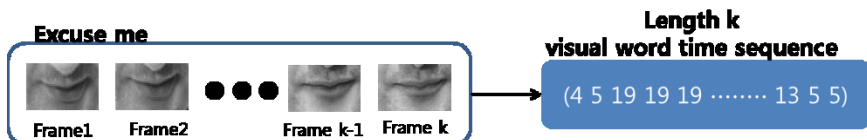


Fig. 2. Conversion of frames to visual words

4 Real Value Assignment and Classification

In this section, we propose an alternative approach to represent a lip image sequence by time series, which consists of real valued vectors. The way a real valued vector is assigned to each image frame is illustrated in Fig. 3. The idea is to represent an image frame by N dimensional vector (N is the number of clusters) whose l -th element is a chi-square distance between the pHog feature of the image frame and centroid of pHog feature vectors in the l -th cluster.

DTW is widely known metric to measure the dissimilarity between two time series having real values. To begin with, it requires building cost matrix. Once cost matrix construction finished, dynamic programing finds the optimal path having overall minimal cost. Given two time sequences U and V having length u and v , respectively, DTW aims to compute the similarity distance between two sequences as formulated below (2).

$$\text{DTW}(U, V) = D(u, v), \quad D = u \times v \text{ accumulated cost matrix}$$

$$D(i, j) = \min\{D(i - 1, j - 1), D(i - 1, j), D(i, j - 1)\} + C(U_i, V_j) \quad (2)$$

Where C denotes cost matrix and, U_i, V_j represents the i -th, j -th element of U, V sequences, respectively.

Since a particular utterance contains a number of frames, say M frames, after converting each frame to N dimensional vector, we would obtain M by N matrix with each row corresponding to the N dimensional vector. Thus, classical DTW designed for one dimensional time series is not applicable for this case. Instead, multi-dimensional

dynamic time warping (MDDTW) is utilized. The difference between DTW and MDDTW is the way of constructing cost matrix. Given matrix A and B from two utterances, we build cost matrix as follows.

$$\text{Cost Matrix}(i, j) = \sum_{k=1}^N (A(i, k) - B(j, k))^2 \quad (3)$$

Where i, j represents i -th and j -th frame from A and B utterance, respectively. Another option for constructing cost matrix is Manhattan distance as in [9]. More details for dynamic time warping are summarized in the literature [10].

In the classification, a test data is converted to a real value vector and the test data is classified as one of possible utterances by 1NN classifier based on MDDTW distance.

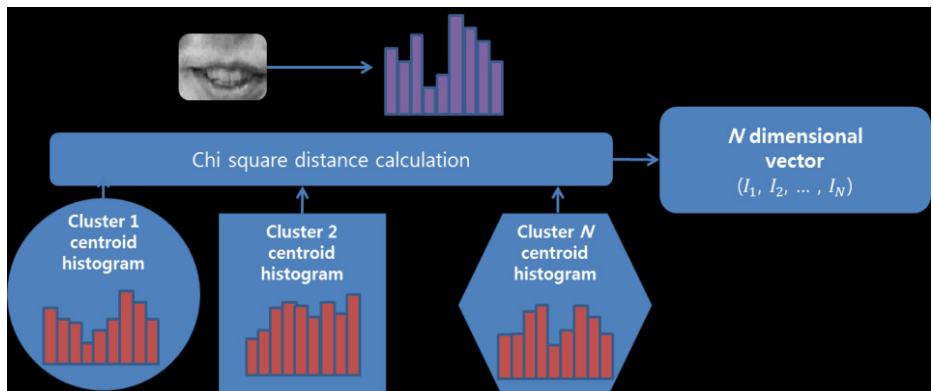


Fig. 3. Conversion from a frame to real value

5 Experiment

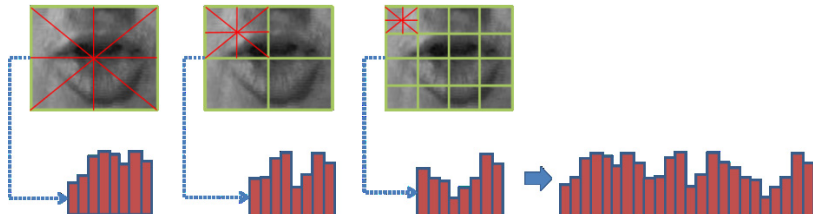
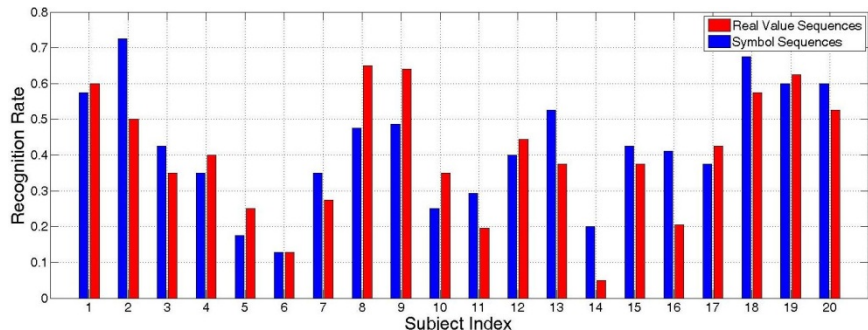
In contrast to the abundance of audio only corpora, there exist only a few databases available for visual speech. G. Zhao et.al established OuluVS database [5], which contains 10 classes of simple isolated sentences and words. The individual speaker repeats each phrase about 5 times. The database includes 817 sequences from 20 speakers in total. The phrases spoken in the database are listed in table 1.

For speaker-dependent experiments, the leave-one utterance-out was utilized for cross validation on the OuluVS database because there are not abundant samples of each phrase of each speaker. A pool of images being necessary for codebook generation is chosen from first repeat of each phrase. The remaining images from the rest repeats were used as test and training. While running the K-means algorithm, K is set to be 20 for producing both symbolized sequences and real valued sequences. The necessary parameters for pHog feature extraction algorithm is set as follows; the number of bin is 36, dividing 360 degree of angle so that one bin represents 10 degree, and pyramid levels are set to be 2 as shown in Fig.4.

Table 1. The list of phrases

“Excuse me”	“See you”
“Thank you”	“Good bye”
“Hello”	“I am sorry”
“How are you”	“Nice to meet you”
“Have a good time”	“You are welcome”

Experimental results are shown in Fig.5. As depicted in Fig.5, depending on the subject, it shows different performances. Note that neither symbol sequence nor real value vector always outperforms the other for all subjects.

**Fig. 4.** pHog feature extraction from a lip image**Fig. 5.** The recognition rates using symbol sequences or real value vectors for every subject on OuluVS database

6 Conclusion

This paper proposed two approaches for representing time series by real value or symbol assignment to solve the visual speech recognition problem. The difference between two approaches is in the method of assigning value to a frame and corresponding dissimilarity measurement. In the case of real value assignment, a frame from training data has its own real valued vector after computing the distance from the centroid of each cluster. In the symbol case, a frame has the cluster label

after comparison to pre-defined codebook. Finally, lip image sequences are converted into real value vectors or symbol sequences. Dynamic time warping and Edit distance play a role of measuring dissimilarity between two real value vectors and two symbol sequences, respectively. To classify test data as one of 10 possible utterance classes, we use 1 NN classifier. Experimental results show that both types of sequences have exhibited similar performances.

7 Future Work

In this work, classification method virtually depends on simple 1NN. Thus, it is worthwhile utilizing widespread classification machine, Support Vector Machine (SVM), in order to determine performance according to classification.

Neuhaus et al. [11] introduced kernel function based on edit distance. They defined pattern space of strings χ and a training set pattern space $\chi^t \subseteq \chi$. Successively, a basic kernel function $k_{x_0}: \chi \times \chi \rightarrow \mathbb{R}$ is established as in equation (4). $d(\cdot, \cdot)$ denotes edit distance, x_0 represents fixed pattern or zero string $x_0 \subseteq \chi^t$. Also they proposed two kernel function; sum kernel and product kernel to express more complex kernel function. In the future, we may use product kernel as in equation (5), since equation (5) is reported to mostly outperform sum kernel. $I \subseteq \chi^t \subseteq \chi$ denotes a set of zero string included in the training set. For detail explanation regarding edit distance based kernel function, refer to [11].

$$k(x, x') = k_{x_0}(x, x') = \frac{1}{2}(d(x, x_0)^2 + d(x_0, x')^2 - d(x, x')^2) \quad (4)$$

$$k_I^*(x, x') = \prod_{x_0 \in I} k_{x_0}(x, x') \quad (5)$$

C. Bahlmann et.al [12] defined Gaussian DTW (GDTW) for time sequence as equation (6), where d_{DTW} denotes one dimensional dynamic time warping distance, x and x' are real value vectors. Unfortunately, it is unable to prove that equation (6) is positive definite which is the necessary condition to guarantee that SVM algorithm yields global maximum. However, the paper [12] reported that GDTW kernel has shown reasonable good result despite its possibly non-positive definite. In the future work, we can use equation (7) with changing from d_{DTW} to d_{MDDTW} for SVM to run on classification.

$$K(x, x') = e^{(-\gamma d_{DTW}(x, x'))} \quad (6)$$

$$K(x, x') = e^{(-\gamma d_{MDDTW}(x, x'))} \quad (7)$$

Acknowledgements. This research was **supported** by the MKE (The Ministry of Knowledge Economy), Korea, under the Human Resources Development Program for Convergence Robot Specialists support program supervised by the NIPA (National IT Industry Promotion Agency) (NIPA-2012-H1502-12-1002).

References

1. Sivic, J., Zisserman, A.: Video Google: A Text Retrieval Approach to Object Matching in Videos. In: Proc. Ninth Int'l Conf. Computer Vision, pp. 1470–1478 (2003)
2. Dupont, S., Luettin, J.: Audio-visual speech modeling for continuous speech recognition. *IEEE Trans. Multimedia* 2, 141–151 (2000)
3. Potamianos, G., Neti, C., Luettin, J., Matthews, I.: Audio-Visual Automatic Speech Recognition: An Overview. In: Bailly, G., Vatikiotis-Bateson, E., Perrier, P. (eds.) *Issues in Visual and Audio-Visual Speech Processing*. MIT Press (2004)
4. Neti, C., Potamianos, G., Luettin, J., Matthews, I., Glotin, H., Vergyri, D., Sison, J., Mashari, A., Zhou, J.: Audio-visual speech recognition. In: Final Workshop 2000 Report, vol. 764 (2000)
5. Zhao, G., Barnard, M., Pietikainen, M.: Lipreading with local spatiotemporal descriptors. *IEEE Transactions on Multimedia* 11(7), 1254–1265 (2009)
6. Dalal, N., Triggs, B.: Histograms of oriented gradients for human detection. In: IEEE Computer Society Conference on Computer Vision and Pattern Recognition, CVPR 2005, vol. 1, pp. 886–893. IEEE (2005)
7. Bai, Y., Guo, L., Jin, L., Huang, Q.: A novel feature extraction method using pyramid histogram of orientation gradients for smile recognition. In: 2009 16th IEEE International Conference on Image Processing (ICIP), vol. 2, pp. 3305–3308. IEEE (2009)
8. Duda, R.O., Hart, P.E., Stork, D.G.: *Pattern classification*. John Wiley, New York (2001)
9. Ten Holt, G.A., Reinders, M.J.T., Hendriks, E.A.: Multi-dimensional dynamic time warping for gesture recognition. In: Proc. of the Conference of the Advanced School for Computing and Imaging, ASCI 2007 (2007)
10. Senin, P.: Dynamic time warping algorithm review, Information and Computer Science Department University of Hawaii at Manoa Honolulu, USA (2008)
11. Neuhaus, M., Bunke, H.: Edit distance based kernel functions for structural pattern classification. *Pattern Recognition* 39(10), 1852–1863 (2006)
12. Bahlmann, C., Haasdonk, B., Burkhardt, H.: On-line handwriting recognition with support vector machines—a kernel approach. In: Proc. 8th Int. Workshop Front. Handwriting Recognition (IWFHR), pp. 49–54 (2002)

Automatic Image Segmentation Using Saliency Detection and Superpixel Graph Cuts

Sandeul Kang, Hansang Lee, Jiwhan Kim, and Junmo Kim^{*}

Dept. of Electrical Engineering, Korea Advanced Institute of Science and Technology,
291 Daehak-ro, Yuseong-gu, Daejeon 305-701, South Korea
junmo@ee.kaist.ac.kr

Abstract. Image segmentation, which divides an image into foreground and background, is an important task for several applications in vision area such as object detection and classification. In this paper, we introduce a novel algorithm for automatic image segmentation technique which does not require further learning processes to perform segmentation. To achieve this automatic image segmentation, we incorporate saliency map for an image as an initial cue for image segmentation. An enhanced saliency detection method for generating saliency map is proposed. With over-segmented superpixels for an image and the generated saliency map, we perform image segmentation using graph cuts. To adapt graph cut segmentation to superpixel graph and saliency map, we suggest edge costs for superpixel graph based on Gaussian mixture models (GMM). As a result, superpixel graph enhances computational efficiency for our image segmentation technique and saliency map provides helpful cue for foreground region. We evaluate the performance of our algorithm on MSRA database demonstrate experimental results.

Keywords: automatic image segmentation, saliency detection, graph cuts, superpixels.

1 Introduction

Object recognition and classification are still challenging problems in computer vision. One of the major issues in these problems is how we extract meaningful information from an image, an array of pixels. Foreground/background segmentation, which extracts meaningful regions, called foreground, from its surroundings, called background, is thus a crucial task for not only object recognition and classification problems, but also several applications in computer vision including image retrieval and annotation. Foreground/background segmentation has been widely investigated with various types of data clustering techniques. Most of them are semi-automated, which relies on users' guidance such as bounding box [15, 18], scribble [4], and set of points [12]. These interactive techniques, however, have limitations such as sensitivity to quantity and quality of manual cues, also called seeds. On the other hand, one common approach for automatic foreground/background segmentation is to identify foreground region which has highest correlation with trained foreground

^{*} Corresponding author.



Fig. 1. Experimental results of our algorithm: Original test images (top row) and their segmented foreground images (bottom row)

detector or mask. [5, 17] Underlying concept of this approach is that a set of general images, which contain objects of single category, shares similar appearances of foreground regions. Since this approach usually requires a large training database and its learning step, it is not sufficient for some cases such as detecting unexpected object from an image or detecting object without training database.

In this work, we propose a fully automatic foreground segmentation algorithm which requires only a given single image. To achieve automatic segmentation, we incorporate saliency map as an initial cue for foreground segmentation. Saliency detection, which extracts visually salient regions from an image and creates saliency map, is widely researched as a useful tool for detecting visual information from general images. Several works has proposed various methods for saliency detection, including center-surround differences [8, 9], spatiotemporal cues [20], graph-based visual saliency [7], pixel-wise differences [1, 2], visual context [6], and psychological attention model [13]. In this research, we propose a novel saliency detection method which enhances a saliency map by combining global and local saliency features. With the proposed saliency map, we use graph cuts [4, 18], one of the most popular and powerful segmentation and optimization techniques, for foreground segmentation. To apply our saliency map into graph cut segmentation properly, we suggest modified terminal and neighboring edge costs based on statistical measures using Gaussian mixture models (GMM), which is in a similar way to them of grab cut approach [18]. Additionally, to reduce the computational complexity while still obtaining reliable boundaries, we utilize over-segmentation [14], which partitions an image into set of boundary-preserving segments called superpixels, prior to segmentation step, and construct the graph with these superpixels for graph cuts, not with whole image pixels. As a result, Fig. 1 shows some test images and their corresponding results segmented by the proposed algorithm. Our main contributions in this paper are summarized as follows:

- We propose a fully automatic foreground segmentation method, which does not require any user interactions.
- Neither training database nor learning process is required for the proposed segmentation algorithm.
- We propose a novel saliency detection method at full-resolution
- We propose superpixel graph cuts with modified edge costs based on GMM.

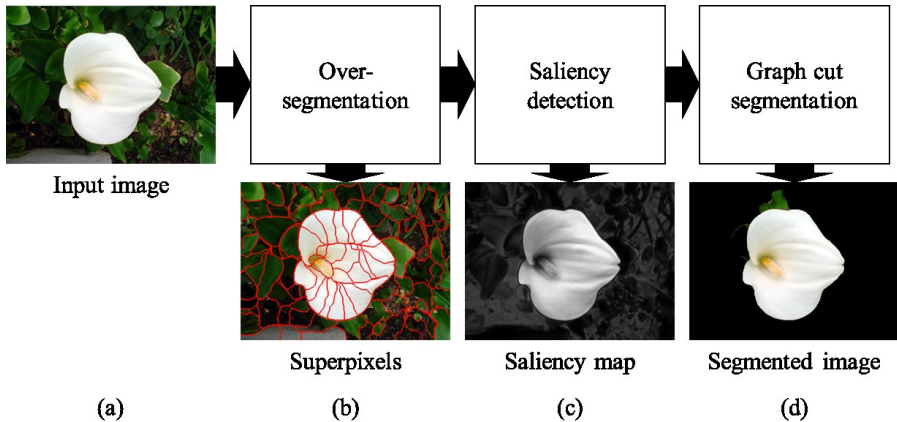


Fig. 2. Schematic overview of our segmentation algorithm: (a) An input image, (b) an over-segmentation step and its output superpixels, (c) a saliency detection step and its output saliency map, (d) a graph cut segmentation step and its output segmented foreground image

The outline of the paper is as follows: In section 2, we introduce the structure of our segmentation algorithm and its implementation. In section 3, we show experimental results of our segmentation algorithm on test images and evaluations of their performances. In section 4, we discuss our work and conclude the paper.

2 Algorithm

Fig. 2 shows the main structure of our segmentation method. First, we apply over-segmentation [14] on the given image to obtain superpixels. With the given image and obtained superpixels, we perform saliency detection to create the saliency map. In the saliency detection step, we find salient regions which are visually outstanding in two levels: local and global. With the saliency map created in this saliency detection, we create a tri-map for initial foreground and background GMMs using thresholding. In graph cut segmentation step, superpixel graph with modified edge costs is constructed and graph cuts [4] are performed on this graph to segment foreground and background from the given image. In the following subsections, we describe details of each step.

2.1 Over-segmentation

Over-segmentation is an algorithm which clusters pixels of an image into groups of pixels called superpixels which have similar properties such as color, brightness, and texture. Fig. 2 (b) shows an example of over-segmented image. As shown in the figure, over-segmented superpixels preserve boundaries inside an image and each superpixel is visually consistent. Furthermore, this over-segmentation step simplifies the computational complexity of later steps including graph cuts, by decreasing the number of graph nodes from the total number of pixels in an image to the number of superpixels, which can be determined by the user in the over-segmentation step. As

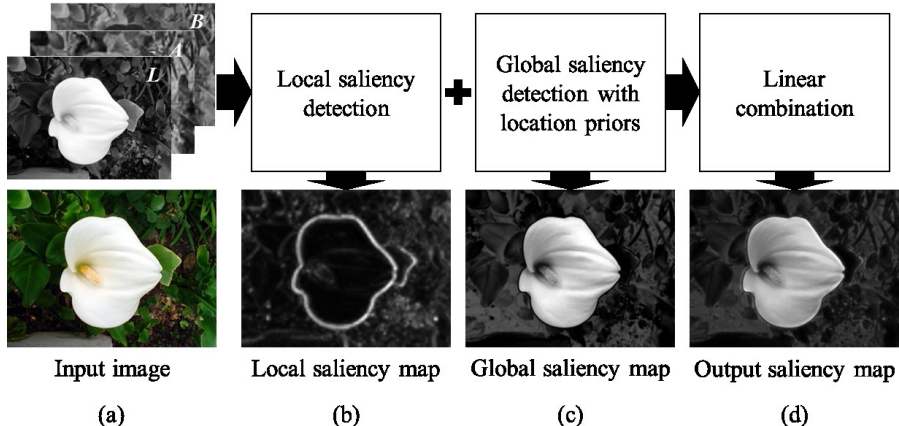


Fig. 3. Outline of saliency detection method: (a) An input image and its CIE Lab color components, (b) local saliency detection step and its output saliency map, (c) global saliency detection step with location prior maps and its output saliency map (d) output saliency map

shown in Fig. 2, both our saliency detection step and graph cut segmentation step use over-segmented superpixels for the given image. We use an over-segmentation method proposed by Mori et al. [14] which is based on the normalized cuts [16]. In our experiments, we choose the number of superpixels as $N_{sp} = 100$.

2.2 Saliency Detection

Saliency detection is to extract salient regions from images, which are visually outstanding and perceptually attractive. In photographic environment, foreground is represented as salient region since people usually focus cameras on the foreground. Under this assumption, we use saliency of the given image as an initial cue for foreground/background segmentation. For saliency detection, we construct three principles which are modified from principles suggested in Goferman et al. [6] based on psychological and biological evidence [11]:

P1. (Local saliency) Salient region has different feature properties, such as color, intensity, and texture, from its surroundings.

P2. (Global saliency) Salient region appears uniquely among the image, i.e. it does not occur concurrently.

P3. (Location prior) Salient region is usually located at the center of the image, or it includes the center of the image.

Based on these three principles, we propose a novel saliency detection method which is outlined in Fig. 3. As shown in the figure, our saliency detection method consists of three major steps: First, we extract locally salient region from an image according to the principle P1. Next, we find globally salient region from an image with the principle P2. In global saliency detection step, we apply the location prior map, which is determined in the principle P3, into global saliency map generation. We then create

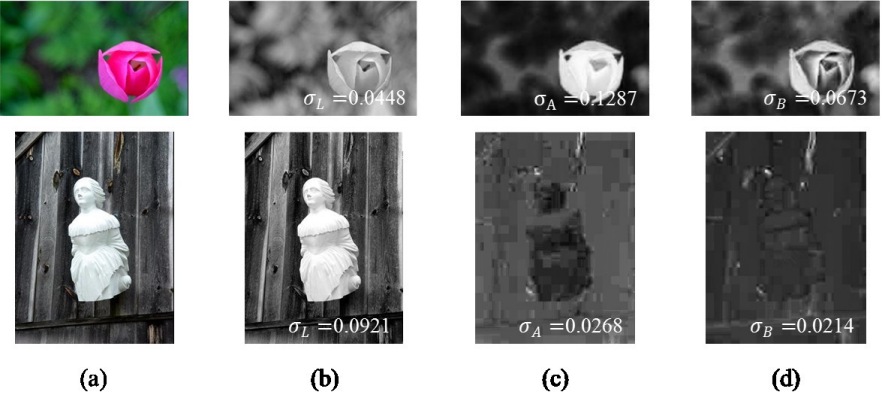


Fig. 4. Color channel selection for global saliency map: For each row, (a) input images, (b), (c), (d) visualized color channel components for L, a, b channels, respectively. Standard deviation values for each channel are written at the bottom of each image.

the saliency map by computing linear combination of local and global saliency maps we obtained. In our saliency detection method, we use CIELAB color space for the given image, which is known to represent color components proper for human visual perception.

According to the principle P1, people tend to give more attention to region which is locally distinctive from its neighbors. This local level approach has been accepted to several early saliency detection methods [7, 8, 9]. In this research, we find the locally salient region from the given image using center-surround differences which is originally proposed by Itti et al. [8, 9]. First, we make several scales for the input image in L , a , and b color channels. Then, we compute differences between a “center” fine scale $c \in \{1, 2, 3, 4\}$ and a “surround” coarser scale $s = c + \delta$, $\delta \in \{3, 4\}$ for each color channel as follows:

$$I(c, s) = |I(c) - I(s)| \quad (1)$$

where $I \in \{L, a, b\}$ is color channel for each scale and the across-scale difference between two images is obtained by expanding both images to the size of original scale image with neighbor-padding interpolation. We compute the local saliency map by combining center-surround differences for each scale pair and for each color channel:

$$S_L = \sum_{I \in \{L, a, b\}} \sum_{c=1}^4 \sum_{s=c+3}^4 \overline{N}(I(c, s)) \quad (2)$$

where $\overline{N}(I(c, s))$ is a normalized center-surround difference for each scale pair (c, s) . Fig. 3 (b) shows an example of local saliency map extracted by our local saliency detection method.

From the principle P2, since the salient region usually occurs uniquely among entire image, we extract global saliency by measuring outlying degrees for superpixels of an image. First, we pick the superpixel sp_j and calculate the

differences between the image for each color channel $I \in \{L, a, b\}$ and $m(sp_j)$, the mean value of sp_j . We then compute the average of differences among all the superpixels, and add the difference between the image I and the mean value of entire pixels $m(I)$:

$$I_G = \frac{1}{N_{SP}} \left(\sum_{j=1}^{N_{SP}} (I - m(sp_j))^2 \right) + (I - m(I))^2 \quad (3)$$

Before combining computed global saliency maps for each color channel to produce the final global saliency map, we select color channels to be combined among three color channels, L , a , and b . Fig. 4 shows some motivating examples for this channel selection process. If the given image has enough color information including both intensity and contrast, as shown at the top row in Fig. 4, only a and b channels provide a sufficient result without L channel, since L channel represents luminance, which usually interrupts color-based salient region. On the contrary, if the given image doesn't have enough color information as shown at the bottom row in Fig. 4, only L channel provide a sufficient result without a and b channels. Thus, we select channels for each image adaptively, based on comparing standard deviation values for each color channel which scale is normalized. For standard deviation values σ_L , σ_a , and σ_b for L , a , and b channels, respectively, the set of selected color channels $D \subseteq \{L, a, b\}$ is determined by following conditions:

$$D = \begin{cases} \{L\} & \text{where } \sigma_L \gg \sigma_a, \sigma_b \\ \{a, b\} & \text{where } \sigma_a, \sigma_b \gg \sigma_L \\ \{L, a, b\} & \text{otherwise} \end{cases} \quad (4)$$

where \gg means “twice greater than.” With the selected color channels, we then compute global saliency map by combining global saliency maps for selected channels:

$$S_G = \sum_{I \in D} I_G \quad (5)$$

According to the principle P3, people tend to give more attention at near the center of the image [11]. We thus create a location prior map and refine our global saliency map by applying this map to each color channel image. The location prior map is defined by a Gaussian distribution based on the distance between the pixel and the center of the image C :

$$P = \exp(-dist(p, C)/2\sigma_N^2) \quad (6)$$

where $dist(p, C)$ is the Euclidean distance between the pixel p and the center of the image C , and σ_N^2 is a constant. In our experiment, we choose σ_N as 2. We multiply this prior map with the global saliency computed for each color channel before combining them. Fig. 3 (c) shows an example of global saliency map extracted by our



Fig. 5. Tri-map generation: (a) An input image, (b) our saliency map, (c) tri-map generated by thresholding, (d) Superpixel graph with yellow edges

global saliency detection method. With local saliency map and refined global saliency map, we finally obtain our saliency map by computing linear combination of them:

$$S = \alpha S_L + \beta S_G \quad (7)$$

where α, β are constants. In our experiments, we set α, β as 0.25 and 0.75, respectively. Fig. 3 (d) shows our final saliency map obtained from our saliency detection method.

2.3 Graph Cut Segmentation

We then perform foreground/background segmentation using graph cuts with the saliency map for the given image obtained in the previous subsection as initial cues. First, to apply the saliency map as prior information for graph cuts, we transform the saliency map into tri-map, which consists of tri-nary regions: foreground, background, and unknown regions. We define two threshold values Th_f and Th_b for foreground and background regions, respectively, and determine the tri-map by thresholding with these two thresholds as follow:

$$M = \begin{cases} \text{foreground} & \text{if } S > Th_f \\ \text{background} & \text{if } S < Th_b \\ \text{unknown} & \text{otherwise} \end{cases} \quad (8)$$

Fig. 5 shows the saliency map and its corresponding tri-map. In Fig. 5 (c), initial foreground, background, and unknown regions are colored white, gray, and black, respectively. In our experiments, we set Th_f and Th_b as 5% and 60%, respectively.

With the obtained tri-map, we extract initial cue information for foreground and background regions using Gaussian mixture models in a similar way to grab cut approach [18]. From these extracted Gaussian components, we define sets of mean values for each Gaussian as follow:

$$G_F = \{\mu_{F1}, \mu_{F2}, \dots, \mu_{FK}\} \quad (9)$$

$$G_B = \{\mu_{B1}, \mu_{B2}, \dots, \mu_{BK}\} \quad (10)$$

where G_F, G_B are sets of mean values for foreground and background regions, respectively, K is the number of Gaussian components. In our experiment, we

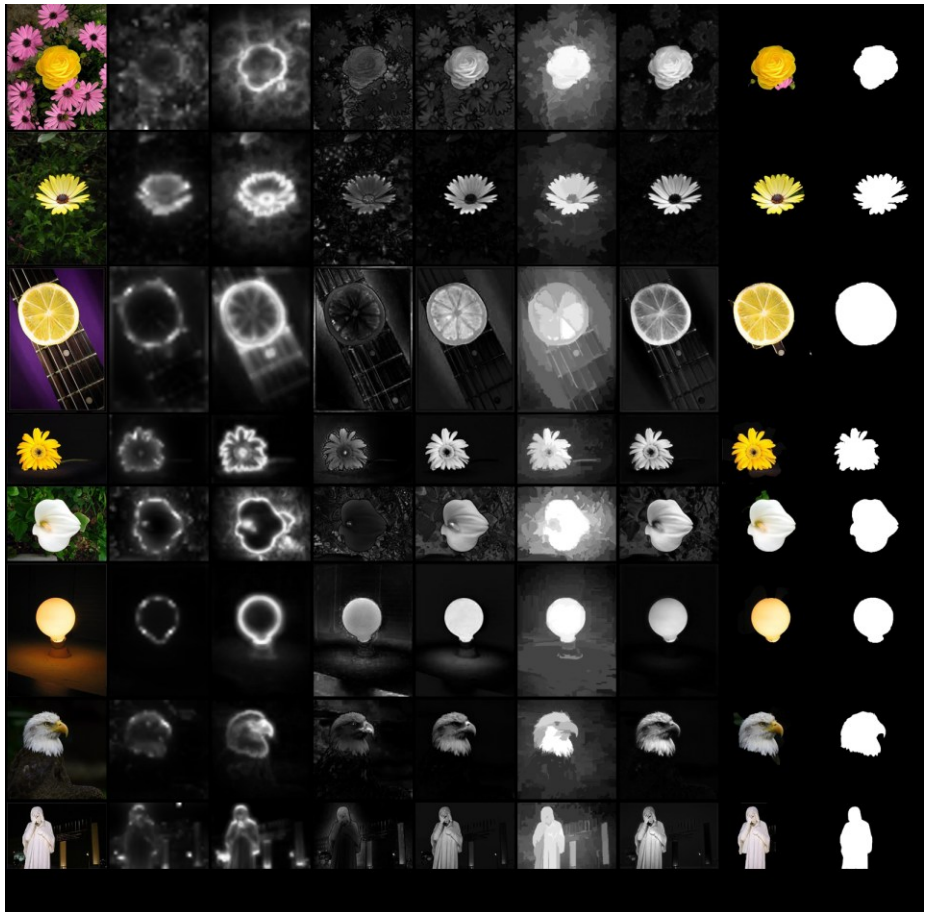


Fig. 6. Experimental results and their comparisons: (a) Input images, (b)~(g) saliency maps generated by (b) HR [7] , (c) CA [6], (d) AC [21], (e) IG [1], (f) RC [22], and (g) ours, (h) our segmentation results, (i) ground truth masks

choose the number of Gaussians as 5. Once initial GMMs are created, then we construct graph with over-segmented superpixels for graph cut segmentation. We use Delaunay triangulation to connect each superpixel to adjacent superpixels and for each superpixel sp_j , we compute mean color μ_j and use it as pixel color in pixel-wise graph cuts [4]. Fig. 5 (d) shows superpixel graph with edges connecting adjacent superpixels. For N-links which connect between adjacent superpixels, we compute modified edge costs defined as follows:

$$E_N(sp_j, sp_k) = \exp\left(-(\mu_j - \mu_k)^2 / 2\sigma_T^2\right) \quad (11)$$

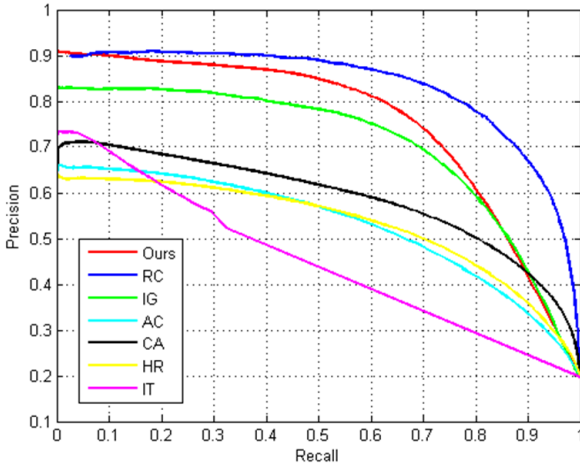


Fig. 7. Precision-recall curves for our saliency detection method with 6 state-of-the-art methods (RC [22], IG [1], AC [21], CA [6], HR [7], IT [9])

where σ_T is a constant. In our experiment, we choose σ_T as 1. For T-links which connect between superpixels and terminals representing foreground and background, we also compute modified edge costs defined as follows:

$$E_T(sp_j, F) = \min_{\mu_B \in G_B} (\mu_j - \mu_B)^2 \quad (12)$$

$$E_T(sp_j, B) = \min_{\mu_F \in G_F} (\mu_j - \mu_F)^2 \quad (13)$$

where F, B are terminals for foreground and background regions, respectively. With the constructed superpixel graph, we perform graph cut segmentation using min-cut max-flow algorithm [4] to obtain the final segmented foreground region. Fig. 2 (d) shows an example of segmentation results.

3 Experimental Results

We experiment our algorithm on the MSRA salient object database, which includes 1000 images selected by Achanta et al. [1] as test images with ground truth binary masks. On this dataset, we compare our saliency detection results with 6 state-of-the-art saliency detection methods including Cheng et al. (RC) [22], Achanta et al. (IG) [1], Achanta et al. (AC) [21], Goferman et al. (CA) [6], Harel et al. (HR) [7], and Itti et al. (IT) [9]. We also measure the performance of our segmentation results by comparing with the ground truth masks of test images. Our parameter settings on the experiment are presented in the previous sections.

We test our algorithm on an Intel® Core™ i5 with 2.67 GHz CPU with 8GB memory. The algorithm is implemented on the MATLAB platform. Except the over-segmentation step, our saliency map generation takes average 0.67 seconds per image. To compare saliency detection results, we test our method on every 1000 images provided in the given MSRA dataset. Fig. 6 shows selected test images and their corresponding saliency maps resulted from several saliency detection methods mentioned above and ours. With these results, we obtain the precision-recall rate curve by changing threshold values from 0 to 255 where the entire saliency maps are represented as grayscale images. We compare these thresholded binary masks of salient with ground truth masks and compute average precision and recall values over 1000 images. Fig. 7 shows precision-recall curves for our method with others. As shown in the figure, our saliency maps present high precision and recall as their own. We also measure precision and recall rates to evaluate the performance of our segmentation algorithm. With 1000 segmented masks on MSRA database, we compute overlapping ratios between our segmented masks and ground truth masks to calculate mean precision and recall rates. As a result, we obtain average values of precision and recall as 73.81% and 73.57%, respectively.

4 Conclusion

In this paper, we proposed a fully automatic foreground segmentation algorithm based on saliency detection and superpixel graph cuts. We introduced a novel saliency detection method which combines local and global saliency features to produce an accurate saliency map. Compared to state-of-the-art saliency detection algorithms, our saliency maps show fine performances as saliency detection itself. We further used our saliency map as an initial cue for the graph cut segmentation. In graph cuts, we utilized over-segmentation to construct the superpixel graph and computed modified edge costs on this superpixel graph. To evaluate our segmentation method quantitatively, we tested on 1000 images of MSRA database and compared with the ground truth and segmented regions resulted from state-of-the-art saliency detection algorithms. As a result, our saliency model shows proper performances for graph cut segmentation compared to other saliency detection algorithms. Moreover, our segmentation method achieves accurate segmentation performances without user inputs and learning processes, which makes our segmentation method a useful pre-processing tool for object detection and classification.

Acknowledgements. This research was supported by the MKE (The Ministry of Knowledge Economy), Korea, under the Human Resources Development Program for Convergence Robot Specialists support program supervised by the NIPA. (National IT Industry Promotion Agency) (NIPA-2012-H1502-12-1002).

References

1. Achanta, R., Hemami, S., Estrada, F., Süstrunk, S.: Frequency-tuned salient region detection. In: Proceedings of the 2009 IEEE Conference on Computer Vision and Pattern Recognition, pp. 1597–1604 (2009)
2. Achanta, R., Süstrunk, S.: Saliency detection using maximum symmetric surround. In: Proceedings of the 2010 17th IEEE International Conference on Image Processing, pp. 2653–2656 (2010)
3. Arbelaez, P., Maire, M., Fowlkes, C., Malik, J.: From contours to regions: An empirical evaluation. In: Proceedings of the 2009 IEEE Conference on Computer Vision and Pattern Recognition, pp. 2294–2301 (2009)
4. Boykov, Y.Y., Jolly, M.-P.: Interactive graph cuts for optimal boundary & region segmentation of objects in N-D images. In: Proceedings of the 2001 8th IEEE International Conference on Computer Vision, vol. 1, pp. 105–112 (2001)
5. Brox, T., Bourdev, L., Maji, S., Malik, J.: Object segmentation by alignment of poselet activations to image contours. In: Proceedings of the 2011 IEEE Conference on Computer Vision and Pattern Recognition, pp. 2225–2232 (2011)
6. Goferman, S., Zelnik-Manor, L., Tal, A.: Context-aware saliency detection. In: Proceedings of the 2010 IEEE Conference on Computer Vision and Pattern Recognition, pp. 2376–2383 (2010)
7. Harel, J., Koch, C., Perona, P.: Graph-based visual saliency. In: Proceedings of the Conference on Advances in Neural Information Processing Systems, vol. 19, pp. 545–552 (2006)
8. Itti, L., Braun, J., Lee, D.K., Koch, C.: Attentional modulation of human pattern discrimination psychophysics reproduced by a quantitative model. In: Proceedings of the 1998 Conference on Advances in Neural Information Processing Systems, vol. 2, pp. 789–795 (1998)
9. Itti, L., Koch, C., Niebur, E.: A model of saliency-based visual attention for rapid scene analysis. *IEEE Transactions on Pattern Analysis and Machine Intelligence* 20(11), 1254–1259 (1998)
10. Jung, C., Kim, C.: A unified spectral-domain approach for saliency detection and its application to automatic object segmentation. *IEEE Transactions on Image Processing* 21(3), 1272–1283 (2012)
11. Judd, T., Ehinger, K., Durand, F., Torralba, A.: Learning to predict where humans look. In: Proceedings of the 2009 IEEE 12th International Conference on Computer Vision, pp. 2106–2113 (2009)
12. Kim, T.H., Lee, K.M., Lee, S.U.: Nonparametric higher-order learning for interactive segmentation. In: Proceedings of the 2010 IEEE Conference on Computer Vision and Pattern Recognition, pp. 3201–3208 (2010)
13. Klein, D.A., Frintrop, S.: Center-surround divergence of feature statistics for salient object detection. In: Proceedings of the 2011 IEEE International Conference on Computer Vision, pp. 2214–2219 (2011)
14. Mori, G.: Guiding model search using segmentation. In: Proceedings of the 2005 10th IEEE International Conference on Computer Vision, vol. 2, pp. 1417–1423 (2005)
15. Pham, V.-Q., Takahashi, K., Naemura, T.: Foreground-background segmentation using iterated distribution matching. In: Proceedings of the 2011 IEEE Conference on Computer Vision and Pattern Recognition, pp. 2113–2120 (2011)
16. Ren, X., Malik, J.: Learning a classification model for segmentation. In: Proceedings of the 2003 9th IEEE International Conference on Computer Vision, pp. 10–17 (2003)

17. Rosenfeld, A., Weinshall, D.: Extracting foreground masks towards object recognition. In: Proceedings of the 2011 IEEE International Conference on Computer Vision, pp. 1371–1378 (2011)
18. Rother, C., Kolmogorov, V., Blake, A.: GrabCut: interactive foreground extraction using iterated graph cuts. ACM Transactions on Graphics 23(3), 309–314 (2004)
19. Sinop, A.K., Grady, L.: A seeded image segmentation framework unifying graph cuts and random walker which yields a new algorithm. In: Proceedings of the 2007 IEEE 11th International Conference on Computer Vision, pp. 1–8 (2007)
20. Zhai, Y., Shah, M.: Visual attention detection in video sequences using spatiotemporal cues. In: Proceedings of the 14th Annual ACM International Conference on Multimedia, pp. 815–824 (2006)
21. Achanta, R., Estrada, F., Wils, P., Süstrunk, S.: Salient region detection and segmentation. In: Proceedings of the 6th International Conference on Computer Vision Systems, pp. 66–75 (2008)
22. Cheng, M.-M., Zhang, G.-X., Mitra, N.J., Huang, X., Hu, S.-M.: Global contrast based salient region detection. In: Proceedings of the 2011 IEEE Conference on Computer Vision and Pattern Recognition, pp. 409–416 (2011)

A Survey: Stereo Based Navigation for Mobile Binocular Robots

Da-Lei Song, Qian-li Jiang, Wei-cheng Sun, and Le-le Yao

College of Engineering, Ocean University of China
No.238, Songling Road, Laoshan District, Qingdao City, Shandong Province, China
songdalei@ouc.edu.cn

Abstract. Stereo based navigation is essential and crucial in the domains of both vision and control. It is becoming more and more common and important in autonomous navigation and it has been applied in traditional Autonomous Ground Vehicles (AGV), Unmanned Aerial Vehicles (UAV) and Autonomous Underwater Vehicles (AUV). So this survey presents those related works, which constitute a wide progress in stereo-based navigation techniques such as land navigation techniques, aerial navigation techniques and autonomous underwater vehicles navigation techniques. The paper deals with two key major approaches: camera calibration and stereo matching. The camera calibration is the basis of accurate navigation. In this paper, we discuss and analyze three camera calibration methods and their latest progress and applications. Also, we propose the latest stereo matching algorithms that suited for the robot navigation and the progress of various real-time stereo methods. The challenges the stereo matching methods confront are analyzed, and the recent algorithms proposed aim to tackle the real-time demands and the robustness problem.

Keywords: robot navigation, camera calibration, real-time stereo matching.

1 Introduction

Navigation can be roughly described as the process of determining a suitable and safe path between a starting and a goal point for a robot travelling between them [1, 2]. Different sensors have been used to this purpose, which has led to a varied spectrum of solutions. In particular, in the last three decades, stereo-based navigation for mobile robots has become a source of countless research contributions since navigation strategies based on vision can increase the scope of application of autonomous mobile vehicles. Among the different proposals, this paper surveys the most recent ones. In many cases, the performance of a good navigation algorithm is deeply joined to accurate robot localization in the environment. Therefore, some vision-based localization solutions applied and developed for autonomous vehicles have also been included in this survey.

Stereo-based navigation solutions are applied not only in traditional Autonomous Ground Vehicles (AGV), but also in Unmanned Aerial Vehicles (UAV). UAVs offer great perspectives in many applications, such as surveillance, patrolling, search and

rescue, outdoor and indoor building inspection, real-time monitoring, high risk aerial missions, mapping, fire detection or cinema recording. Since UAVs move in 3D space they do not have the limitations of ground robots, which usually cannot overcome rocks, climb stairs or get access to ceilings. Nevertheless, UAVs need to exhibit a notable degree of awareness and exactness to accomplish their navigation and obstacle avoidance tasks successfully. Besides, the typically reduced size of UAVs limits their payload capabilities so that they cannot carry sensors available for ground vehicles, such as lasers or certain brands of sonars. In contrast, cameras used in robot vision-based navigation strategies are light and provide a perception of the environment in a single shot. However, the image resolution can be restricted due to the fact that UAVs fly at high altitude. For underwater environments, there is still a preference for more traditional navigation solutions (i.e. acoustic-based) because of the special characteristics of light propagation undersea. However, sonar based navigation system are limited in resolution and size, which are imposed by the acoustic frequency used and the need of accommodation space. Stereo-based navigation systems reduce space and cost and increase the resolution, although their range dramatically decreases in muddy or turbid waters. At present, a number of solutions for Autonomous Underwater Vehicles (AUV) can already be found for many undersea critical applications: undersea infrastructures or installations inspection and maintenance, for any of power, gas or telecommunications transport cases, sea life monitoring, military missions, sea bed reconstruction in deep waters, inspection of sunken ancient ships, etc. Vision has become essential for all these applications, either as a main navigation sensor or as a complement of sonar. Consequently, there exists a good motivation to improve AUVs navigation techniques by expanding their autonomy, capabilities and their usefulness [3].

Whatever applications types are the stereo-based navigations used, the systems are required to be robust and accurate. The accuracy is mainly determined by the calibration of the cameras. Camera calibration is the key and precondition of the intelligent vehicle's correct and safe navigation. There are three kinds of calibration methods most popular in camera calibration field, which are traditional calibration techniques, self-calibration techniques and active vision based camera calibration techniques.

In order to realize real-time navigation, feature-based matching is used to reduce compute cost [4, 5, 6]. However, feature-based matching algorithm could not get dense disparity map, which is more and more important for robot navigation. With the rapid development of the embedded MCU, the computing frequency improves rapidly while the cost reduces greatly. Real-time matching algorithms based on local area, are studied and proposed by many authors. Martin et al. [7] presented the fast local stereo matching algorithm based the classic Census transform, and the algorithm can reach a frame rate of up to 75 fps for 640×480 images and 50 disparities. To meet the real-time demand, many stereo algorithms are based on DSP implementation, which can improve the speed of the embedded stereo system efficiently [8, 9, 10].

The rest of the paper is organized as follows: firstly, section 2 gives the most prominent approaches of the camera calibration; secondly, section 3 reviews new approaches of stereo matching algorithms for real-time navigation; finally, section 4 concludes the paper.

2 Camera Calibration

Binocular stereo vision-based robot navigation algorithms typically assume that the camera intrinsic parameters (i.e. internal camera geometric and optical characteristics) and extrinsic parameters (i.e. the 3-D position and orientation of the camera frame relative to a certain world coordinate system) have been determined in advance and do not change over time unless specifically controlled by the robot.

Knowledge of these parameters enables the projection of points on the image plane into rays in the robot body frame, allowing the robot to use its two cameras to reason geometrically about the world [11]. But it is difficult to balance the precision and the real-time of calibration.

Due to its importance to robot navigation, much work has been done in this field and all kinds of approaches have been proposed. Methods for camera calibration fall into three types: 1. Traditional calibration techniques. 2. Self-calibration techniques. 3. Active vision based camera calibration techniques.

2.1 Traditional Calibration Techniques

The traditional calibration technique is source from the traditional method of photogrammetry. It involves placing a calibration target carefully in the field of view. Based on the correspondences between known 3D features on the target and their 2D locations in the image, the calibration can be obtained.

Fraig [12] used the coplanar constraint conditions of pinhole camera model to establish the equations, and achieved parameters of cameras by solving the equations. But it has a high computation cost and a poor result. So, Abdel-Aziz and Karara proposed a DLT (Direct linear transformation) method, and this method can get parameters of cameras by solving the linear equations directly. But these two methods carry even greater errors because they do not consider perspective distortion.

As people aware of this problem, the nonlinear camera calibration method was born. In 1986, Tsai [13] proposed a two-step method (the initial parameter values are computed linearly and the final values are obtained with nonlinear minimization). But it has shortcomings such as it only considers the radial distortion, and it is not suitable for simple calibration because it needs high accuracy requirements. And then Weng [14] made an important improvement and development of the two-step method by taking the two kinds of distortion into the novel method. In 2000, Zhang [15] proposed a flexible new technique for Camera based on planar template. This method is simple, and can solve the lens distortion factors.

In addition, there are also many practical new methods proposed by Hu Zhaozheng [16], H Zhang [17], X Ying [18], and these new methods provide more new directions for the study of the camera calibration.

However, requirement of calibration targets limits the practicability robot navigation to any situation. The reasons are that the calibration targets and equipment are not available in one situation, the methods require human intervention, and calibration target are not available in wide-field scenes (their projections are of very small size on image plane to supply poor accuracy for calibration) [19].

2.2 Self-calibration Techniques

Self-calibration methods seem to be a more suitable way to robot navigation. Self-calibration, introduced by Maybank [20, 21], assumed that the internal camera parameters are constant over the image sequence. Recently, many researchers have been working on this subject and mostly self-calibration algorithms are concerned with unknown but constant intrinsic camera parameters.

The first self-calibration method was proposed by Maybank [20, 21] based on the Kruppa equations. Luong and Faugeras [22] improved this approach by using the Kruppa equations to derive systems of polynomial equations. The main advantage of this technique is that it only relates pairwise epipolar calibration, not all the images in a single projective frame. The drawback of this technique is that it involves high computational costs and it is difficult to take the uncertainty into consideration, such as the estimate of the epipolar geometry and any a priori knowledge regarding the intrinsic parameters. In 1996, Heyden and Astrom [23] proposed a method which is the Variants of the basic approach.

The complexity of the self-calibration problem might be reduced when using a stratified approach. Hartley proposed this kind of approach, which consists of two steps, first in retrieving the plane at infinity, and then linearly solving Kruppa's equations.

Pollefeys in [24, 25] introduced the modulus constraint to this stratified approach, which represents a major advancement in the category of stratified approaches. The new stratified approach starts from projective calibration, augments it with the homography of the plane at infinity to yield affine calibration and finally upgrades to Euclidean calibration. And this method was developed further in [26] to obtain the metric calibration of a camera setup from only three images.

In 1997, Triggs [27] is the recovery of the absolute quadric. In this method the absolute quadric and conic are recovered simultaneously using an efficient constrained nonlinear optimization technique or a quasi-linear method. Also in 1997, Steinhage [28] proposed a self-calibration based on invariant view recognition, which is a dynamic approach to navigation.

Lourakis and Deriche [29] propose a simplification of the Kruppa equations and show how it can be employed for self-calibration. The simplification is derived in a purely algebraic manner and is based solely on the fundamental matrix. Estimates of the epipoles, which are known to be difficult to compute accurately, are not needed.

The work of Schaffalitzky [30] shows that out of the 64 planes that satisfy the modulus constraint for a triplet of images, at most 21 are of interest. However, Pollefeys' approach requires a fairly long sequence of images in order to isolate a unique solution. Although Schaffalitzky's equations are univariate, they are highly nonlinear (of degree 21) and are known to be illconditioned in general.

In 1999, Roy et al. [31] proposed an online self-calibration for mobile robots. The advantage to this approach is that the calibration parameters adapt to change in the environment rapidly and without human intervention.

Lei et al. [32] propose a method to solving the Kruppa equations for camera self-calibration. First, the method determines the scale factors by a Levenburg-Marquardt (LM) optimization or Genetic optimization technique. Then the camera's intrinsic parameters are derived from the resulting linear constraints.

In a comparative study [26], Pollefey has pointed out that the quality of self-calibration results depends more on a good localization of the plane at infinity rather than on the DIAC.

In a more recent work, many novel self-calibration techniques have been proposed by many people, such as A Martinelli [33, 34], H Chen, K Matsumoto [35], J Kelly [36] and so on.

The area of camera self-calibration has drawn the attention of tens of robot navigation scientists and researchers in these years following the break through paper [21]. In order to calibrate the camera on-line, researches have used the camera intrinsic constraints separately and in conjunction with the camera motion constraints or the scene constraints. Most of the self-calibration algorithms are concerned with unknown but constant intrinsic camera parameters. A group of researchers have also analyzed the developed self-calibration algorithms, estimated the errors, and identified critical motion.

2.3 Active Vision Based Camera Calibration Techniques

Active vision based camera calibration techniques is the important branch of self-calibration techniques. Firstly it obtains images by controlling the movement of the camera, and then achieves the internal and external parameters through building the relationships between these images and the camera motion trajectory. At present, there are typical methods based on active vision such as the method proposed by Ma S D.[37], and the method proposed by CJ Yang et al. [38].

The advantages of the active vision based camera calibration techniques are that they are simple and we can get linear solution. The disadvantage is that the instrument which must control camera movement precisely is expensive. So this technique is not suitable to the robot navigation.

Three camera calibration methods are analyzed with their latest progress and applications. The traditional calibration methods require human intervention and calibration target are not available in wide-field scenes; Most of the self-calibration algorithms are concerned with unknown but constant intrinsic camera parameters; According to pros and cons of the active vision based camera calibration, the technique is not suitable to the robot navigation. Above all the self-calibration algorithms are relatively suitable for the robot navigation, but most of them are concerned with unknown and constant intrinsic camera parameters. So it is urgent to develop more real-time and more accurate self-calibration algorithms which can adapt to varying intrinsic camera parameters.

3 Stereo Matching

Perception is a crux part of the design of mobile robots operated in unknown and unstructured environments. So, the robot navigation system must make the robot perceive its environment sufficiently to be operated safely. Especially, 3D information about the area around the robot is vital important for reliable operations in human environments. In the initial stage of study, most researchers use sonar transducers or laser range sensors to obtain 3D information and do robot navigation

[39, 40, 41]. That is either rough or has low resolution with respect to time and space. Stereo vision is a technology that is well suited for delivering a precise description in robot navigation field [42, 43, 44].

The navigation problem can be viewed as a 3D reconstruction problem [45, 46]. However, stereo matching methods [47, 48], which try to find a set of points in one image that can be identified as the same points in another image, are widely used to do 3D reconstruction. An accurate disparity map can help robots to navigate in real environment.

3.1 Stereo Matching Algorithms

In general, the stereo matching algorithms can be divided into two categories: global methods and local methods.

Global algorithms make explicit smoothness assumptions and then solve it through various optimization techniques. Most of the global algorithms are based on energy minimization. Global algorithms give very good results but these methods are computationally very expensive which makes them impractical for real-time systems. Global methods use the scanline or the whole image to assign a disparity value to each pixel. In general, global methods are dynamic programming [49; 50], graph cuts [51], or belief propagation [52]. Recently, the most accurate methods on the Middlebury Stereo Evaluation website [53], which is the standard benchmark platform for the stereo community, are the global algorithms. Anyway, the computational burden they require is far from meeting real-time or near real-time requirements. However, a few real-time global algorithms have been presented in recent years. Morris, J. et al. use symmetric dynamic programming stereo (SDPS) to achieve 1% depth accuracy and a disparity range of 128 in a system processing high resolution (1 Mpixel) images at 30 fps, which has a small, compact hardware realization [54]. Most real-time global stereo matching algorithms accelerate based on the FPGA and GPU hardware implementation.

Local algorithms are statistical methods and can be sub-divided into two broad categories: area-based algorithms [55] and feature based algorithms. Area-based algorithms use a small image window centered at a given pixel to find the suitable match within a finite corresponding neighboring window in another image by using the intensity values of the pixels, which generate dense disparity maps. The performance of area-based algorithms is highly dependent on the size of the matching window. Feature based algorithms rely on feature extraction and match local cues (e.g. edges, corners). These algorithms work very fast but generate sparse disparity map. Accordingly, featured based stereo matching algorithms are rarely studied in recent years. In the robot navigation field, most people adopt local stereo matching algorithms to do 3D reconstruction.

3.2 Local Stereo Matching

The difficult problems for robot navigation are the matching robustness and the real-time demand. And the illumination is always variant in the environment of robots and

it can lead to bad matching for many classical stereo matching algorithms. So the trade-off between execution time and robustness of matching must be handled with care and is a difficult task.

The taxonomy and categorization scheme for dense correspondence algorithms is proposed by Scharstein and Szeliski firstly [47]. It is based on the observation that stereo algorithms generally perform the following four steps: a) matching cost computation; b) cost (support) aggregation; c) disparity computation / optimization; d) disparity refinement. Generally, the emphasis is on the matching cost computation and cost aggregation steps for the local stereo matching algorithms.

(1) Similarity measures

For any dense stereo matching algorithm, a similarity measure, which compares pixel values in order to determine how likely they are to be in correspondence, is the first step. In this section, we briefly review the similarity measures used commonly.

The most common window-based matching costs include sums of squared intensity differences (SSD, formula (1)) and absolute intensity differences (SAD, formula (2)).

$$SSD = \sum_{i=n} \sum_{j=m} (I_1(u+i, v+j) - I_2(u+d+i, v+j))^2 \quad (1)$$

$$SAD = \sum_{i=n} \sum_{j=m} |I_1(u+i, v+j) - I_2(u+d+i, v+j)| \quad (2)$$

Another traditional matching cost is normalized cross-correlation (NCC, formula (3)).

$$NCC = \frac{\sum_{i=n} \sum_{j=m} I_1(u+i, v+j) I_2(u+d+i, v+j)}{\sqrt{\sum_{i=n} \sum_{j=m} I_1(u+i, v+j)^2 \sum_{i=n} \sum_{j=m} I_2(u+d+i, v+j)^2}} \quad (3)$$

In contrast to SAD and SSD, NCC accounts for gain difference (a multiplicative change) in the matching windows due to normalization [56; 57]. A constant offset (bias) of pixel values is often compensated by the zero-mean versions ZSAD (formula (4)), ZSSD, and ZNCC (formula (5)).

$$ZSAD = \sum_{i=n} \sum_{j=m} |(I_1(u+i, v+j) - \bar{I}_1) - (I_2(u+d+i, v+j) - \bar{I}_2)| \quad (4)$$

$$ZNCC = \frac{\sum_{i=n} \sum_{j=m} (I_1(u+i, v+j) - \bar{I}_1)(I_2(u+d+i, v+j) - \bar{I}_2)}{\sqrt{\sum_{i=n} \sum_{j=m} (I_1(u+i, v+j) - \bar{I}_1)^2 \sum_{i=n} \sum_{j=m} (I_2(u+d+i, v+j) - \bar{I}_2)^2}} \quad (5)$$

$$\text{In formula (4) and (5), } \bar{I} = \frac{1}{nm} \sum_{i=n} \sum_{j=m} (I(u+i, v+j))$$

Non-parametric local measures introduced by Zabih and Woodfill [58] are different matching strategies to the images, such as Rank and Census transforms. The Rank and Census methods can be implemented as a filter followed by a comparison using the absolute difference or hamming distance. The Rank transform compares the intensity of center pixel with the neighbor pixels in a local region as shown in formula (6), where the function T is defined to return 1 if its argument is true and 0 otherwise.

$$I_{Rank} = \sum_{i=n} \sum_{j=m} T(I(u+i, v+j) < I(u, v)) \quad (6)$$

where $I(u, v)$ represents the center pixel, and $I(u+i, v+j)$ is the neighbor pixel.

Then the intensity of the center pixel is replaced by I_{Rank} value and use the SAD to aggregate the costs. The Census transform converts each pixel inside a moving window into a bit string representing which neighbors are above or below the central pixel as shown in formula (7). Different from Rank transform, Census takes the Hamming distance between Census-transformed pixels to aggregate the costs. The non-parametric local transform is invariant to multiplicative intensity differences caused by lighting conditions.

$$I_{census} = \bigotimes_{i=n} \bigotimes_{j=m} (\xi(I(u, v), I(u+i, v+j))) \quad (7)$$

where $\xi(p_1, p_2) = \begin{cases} 0 & p_1 \leq p_2 \\ 1 & p_1 > p_2 \end{cases}$, and the operator \otimes denotes a bit-wise catenation.

(2) Real-time stereo matching methods

Local and widow-based methods aggregate the matching cost by summing or averaging over a support region in the DSI, which is a three-dimensional data structure with size disparity \times width \times height. Recently, more and more real-time area-based stereo matching methods are presented that are evaluated on the Middlebury Stereo Evaluation website.

Martin et al. [7] proposed a fast stereo matching algorithm on embedded system for robotic applications. The most important change of the algorithm in comparison with the classic Census transform is the usage of a sparse census that halves the processing time but not unchanged the matching quality. The algorithm is implemented on various hardware platforms, e.g. a PC, a DSP and a GPU, reaching a frame rate of up to 75 fps for 640×480 images and 50 disparities. It is robust to illumination change in the robot environment and improves the performance of the vision system to meet the real-time demands.

A real-time Adaptive Binary Window is presented by Raj et al. [59], which gives very good results and reduces the algorithm's running time to milliseconds. The algorithm divides the stereo matching process into two steps: initial disparity estimation and disparity map refinement. Firstly, the initial disparity estimation is obtained with an adaptive binary window based approach which uses the windows of dynamic shapes and sizes for matching. After that, disparity map refinement process presents a simple but very effective single pass approach which uses the reference image's color information to improve the accuracy without much affecting the computation cost.

Adaptive support-weight approach developed by Yoon and Kweon consistently has the best tradeoff between performance and speed [60; 61]. The local weighting technique, in particular, is interesting because, instead of using square windows with uniform weighting, each pixel within an aggregation window influences the final matching cost based on its color similarity and spatial distance. This method, however, is computationally a little more expensive than other area-based methods and can work

well for real images with little image noise. It can obtain high accuracy disparity map. In recent years, most real-time algorithms are based on the DSP implementation.

Computing the final disparities is trivial: simply choose at each pixel the disparity associated with the minimum cost value. Thus, these methods perform a local “winner-take-all” (WTA) optimization at each pixel. A limitation of this approach (and many other correspondence algorithms) is that uniqueness of matches is only enforced for one image (the reference image), while points in the other image might match multiple points, unless cross-checking. However, for applications such as robot navigation, these may be perfectly adequate.

However, there are many challenges for local stereo matching algorithms, such as discontinuity regions, homogeneous regions, object boundaries, low textured areas and so on. Around robot environment, the illumination is variant so as to the intensity changes for a specified object. Therefore, the recent local stereo matching algorithms focus on the robust and real-time research to apply the robot navigation and embedded systems.

4 Conclusions

In this paper, we have reviewed the technologies for binocular robot navigation, which includes camera calibration and stereo matching. Three camera calibration methods are analyzed with their latest progress and applications. The self-calibration algorithms are relatively suitable for the robot navigation, but most of them are concerned with unknown and constant intrinsic camera parameters. So it is urgent to develop more real-time and more accurate self-calibration algorithms which can adapt to varying intrinsic camera parameters. With respect to stereo matching, the real-time and robust algorithms suited for the robot navigation are introduced. The challenges and the difficult problems that the recent stereo matching methods confront are analyzed. Recently, the stereo matching algorithms focus on the robust and real-time research.

References

1. Jean-Claude, L.: Robot motion planning. Springer, Kluwer Academic Publishers (1991)
2. Choset, H., Lynch, K., Hutchinson, S., Kantor, G., Burgard, W., Kavraki, L., Thrun, S.: Principles of Robot Motion (2005)
3. Bonin-Font, F., Ortiz, A., Oliver, G.: Visual navigation for mobile robots: a survey. *Journal of Intelligent & Robotic Systems* 53, 263–296 (2008)
4. Grimson, W.E.L.: Computational experiments with a feature based stereo algorithm. *IEEE Transactions on Pattern Analysis and Machine Intelligence*, 17–34 (1985)
5. Hsieh, Y.C., McKeown Jr., D.M., Perlant, F.P.: Performance Evaluation of Scene Registration and Stereo Matching for Artographic Feature Extraction. *IEEE Transactions on Pattern Analysis and Machine Intelligence* 14, 214–238 (1992)
6. Lane, R.A., Thacker, N.A., Seed, N.L.: Stretch-correlation as a real-time alternative to feature-based stereo matching algorithms. *Image and Vision Computing* 12, 203–212 (1994)
7. Humenberger, M., Zinner, C., Weber, M., Kubinger, W., Vincze, M.: A fast stereo matching algorithm suitable for embedded real-time systems. *Computer Vision and Image Understanding* 114, 1180–1202 (2010)

8. Khaleghi, B., Ahuja, S., Wu, Q.: An improved real-time miniaturized embedded stereo vision system (MESVS-II). In: IEEE Computer Society Conference on Computer Vision and Pattern Recognition Workshops, CVPRW 2008, pp. 1–8 (2008)
9. Zinner, C., Humenberger, M., Ambrosch, K., Kubinger, W.: An optimized software-based implementation of a census-based stereo matching algorithm. In: Bebis, G., Boyle, R., Parvin, B., Koracin, D., Remagnino, P., Porikli, F., Peters, J., Klosowski, J., Arns, L., Chun, Y.K., Rhyne, T.-M., Monroe, L. (eds.) ISVC 2008, Part I. LNCS, vol. 5358, pp. 216–227. Springer, Heidelberg (2008)
10. Deng, C., Honghuan, B.: Census Stereo Matching based on DSP. Bulletin of Science and Technology (2008)
11. Koch, O., Walter, M.R., Huang, A.S., Teller, S.: Ground robot navigation using uncalibrated cameras. In: 2010 IEEE International Conference on Robotics and Automation (ICRA), pp. 2423–2430. IEEE (2010)
12. Faig, W.: Calibration of close-range photogrammetric systems: mathematical formulation. Photogrammetric Engineering and Remote Sensing (1975)
13. Tsai, R.Y.: An efficient and accurate camera calibration technique for 3D machine vision. In: Proc. IEEE Conf. on Computer Vision and Pattern Recognition (1986)
14. Weng, J., Cohen, P., Herniou, M.: Camera calibration with distortion models and accuracy evaluation. IEEE Transactions on Pattern Analysis and Machine Intelligence 14, 965–980 (1992)
15. Zhang, Z.: A flexible new technique for camera calibration. IEEE Transactions on Pattern Analysis and Machine Intelligence 22, 1330–1334 (2000)
16. Zhaozheng, H., Zheng, T.: Camera Calibration with Conics Fitting and Circular Points. Journal-Xian Jiaotong University 40, 1065 (2006)
17. Zhang, H., Wong, K.Y.K., Zhang, G.: Camera calibration from images of spheres. IEEE Transactions on Pattern Analysis and Machine Intelligence 29, 499–502 (2007)
18. Ying, X., Zha, H.: Geometric interpretations of the relation between the image of the absolute conic and sphere images. IEEE Transactions on Pattern Analysis and Machine Intelligence 28, 2031–2036 (2006)
19. Zhang, Z., Li, M., Huang, K., Tan, T.: Practical camera auto-calibration based on object appearance and motion for traffic scene visual surveillance. In: IEEE Conference on Computer Vision and Pattern Recognition, CVPR 2008, pp. 1–8. IEEE (2008)
20. Faugeras, O., Luong, Q.T., Maybank, S.: Camera self-calibration: Theory and experiments. In: Sandini, G. (ed.) ECCV 1992. LNCS, vol. 588, pp. 321–334. Springer, Heidelberg (1992)
21. Maybank, S.J., Faugeras, O.D.: A theory of self-calibration of a moving camera. International Journal of Computer Vision 8, 123–151 (1992)
22. Luong, Q.T., Faugeras, O.D.: Self-calibration of a moving camera from point correspondences and fundamental matrices. International Journal of Computer Vision 22, 261–289 (1997)
23. Heyden, A., Astrom, K.: Euclidean reconstruction from constant intrinsic parameters. In: Proceedings of the 13th International Conference on Pattern Recognition, pp. 339–343. IEEE (1996)
24. Pollefeys, M., Van Gool, L.: Self-calibration from the absolute conic on the plane at infinity. In: Sommer, G., Daniilidis, K., Pauli, J. (eds.) CAIP 1997. LNCS, vol. 1296, pp. 175–182. Springer, Heidelberg (1997)
25. Pollefeys, M., Van Gool, L., Oosterlinck, A.: The modulus constraint: a new constraint self-calibration. In: Proceedings of the 13th International Conference on Pattern Recognition, pp. 349–353. IEEE (1996)

26. Pollefeys, M., Van Gool, L.: Stratified self-calibration with the modulus constraint. *IEEE Transactions on Pattern Analysis and Machine Intelligence*, 707–724 (1999)
27. Triggs, B.: Autocalibration and the absolute quadric. In: *Proceedings of the IEEE Computer Society Conference on Computer Vision and Pattern Recognition*, pp. 609–614. IEEE (1997)
28. Steinhage, A., Schöner, G.: Self-calibration based on invariant view recognition: Dynamic approach to navigation. *Robotics and Autonomous Systems* 20, 133–156 (1997)
29. Lourakis, M.I.A., Deriche, R.: Camera self-calibration using the singular value decomposition of the fundamental matrix: From point correspondences to 3D measurements (1999)
30. Schaffalitzky, F.: Direct solution of modulus constraints. In: *Proc. Indian Conf. on Computer Vision, Graphics and Image Processing*, pp. 314–321 (2000)
31. Roy, N., Thrun, S.: Online self-calibration for mobile robots. In: *Proceedings of the IEEE International Conference on Robotics and Automation*, pp. 2292–2297. IEEE (1999)
32. Lei, C., Wu, F., Hu, Z., Tsui, H.T.: A new approach to solving kruppa equations for camera self-calibration. In: *Proceedings of the 16th International Conference on Pattern Recognition*, pp. 308–311. IEEE (2002)
33. Martinelli, A., Tomatis, N., Siegwart, R.: Simultaneous localization and odometry self calibration for mobile robot. *Autonomous Robots* 22, 75–85 (2007)
34. Martinelli, A., Scaramuzza, D., Siegwart, R.: Automatic self-calibration of a vision system during robot motion. In: *Proceedings 2006 IEEE International Conference on Robotics and Automation, ICRA 2006*, pp. 43–48. IEEE (2006)
35. Chen, H., Matsumoto, K., Ota, J., Arai, T.: Self-calibration of environmental camera for mobile robot navigation. *Robotics and Autonomous Systems* 55, 177–190 (2007)
36. Kelly, J., Sukhatme, G.S.: Visual-inertial sensor fusion: Localization, mapping and sensor-to-sensor self-calibration. *The International Journal of Robotics Research* 30, 56–79 (2011)
37. De Ma, S.: A self-calibration technique for active vision systems. *IEEE Transactions on Robotics and Automation*, 12, 114–120 (1996)
38. Yang, C.J., Wang, W., Hu, Z.Y., Ma, S.D.: An active vision based camera intrinsic parameters self-calibration technique. *Chinese Journal of Computers-Chinese Edition*-21, 428–435 (1998)
39. Brooks, R.: A robust layered control system for a mobile robot. *IEEE Journal of Robotics and Automation* 2, 14–23 (1986)
40. Nickerson, S.B., Jenkin, M., Milios, E., Down, B., Jasiobedzki, P.: Autonomous Navigation of a Mobile Robot in a Known Environment. In: *IAS-3: an International Conference on Intelligent Autonomous Systems*, Pittsburgh, Pennsylvania, February 15–18, p. 288. Ios Pr Inc. (1993)
41. Tomatis, N., Nourbakhsh, I., Siegwart, R.: Simultaneous localization and map building: A global topological model with local metric maps. In: *Proceedings of the 2001 IEEE/RSJ International Conference on Intelligent Robots and Systems*, pp. 421–426. IEEE (2001)
42. DeSouza, G.N., Kak, A.C.: Vision for mobile robot navigation: A survey. *IEEE Transactions on Pattern Analysis and Machine Intelligence* 24, 237–267 (2002)
43. Murray, D., Little, J.J.: Using real-time stereo vision for mobile robot navigation. *Autonomous Robots* 8, 161–171 (2000)
44. Kriegman, D.J., Triendl, E., Binford, T.O.: Stereo vision and navigation in buildings for mobile robots. *IEEE Transactions on Robotics and Automation* 5, 792–803 (1989)
45. Pollefeys, M., Nistér, D., Frahm, J.M., Akbarzadeh, A., Mordohai, P., Clipp, B., Engels, C., Gallup, D., Kim, S.J., Merrell, P.: Detailed real-time urban 3d reconstruction from video. *International Journal of Computer Vision* 78, 143–167 (2008)

46. Seitz, S.M., Curless, B., Diebel, J., Scharstein, D., Szeliski, R.: A comparison and evaluation of multi-view stereo reconstruction algorithms. In: 2006 IEEE Computer Society Conference on Computer Vision and Pattern Recognition, pp. 519–528. IEEE (2006)
47. Scharstein, D., Szeliski, R.: A taxonomy and evaluation of dense two-frame stereo correspondence algorithms. *International Journal of Computer Vision* 47, 7–42 (2002)
48. Brown, M.Z., Burschka, D., Hager, G.D.: Advances in computational stereo. *IEEE Transactions on Pattern Analysis and Machine Intelligence* 25, 993–1008 (2003)
49. Birchfield, S., Tomasi, C.: Depth discontinuities by pixel-to-pixel stereo. *International Journal of Computer Vision* 35, 269–293 (1999)
50. Salmen, J., Schlipring, M., Edelbrunner, J., Hegemann, S., Lüke, S.: Real-time stereo vision: making more out of dynamic programming. In: Jiang, X., Petkov, N. (eds.) CAIP 2009. LNCS, vol. 5702, pp. 1096–1103. Springer, Heidelberg (2009)
51. Hong, L., Chen, G.: Segment-based stereo matching using graph cuts. In: Proceedings of the 2004 IEEE Computer Society Conference on Computer Vision and Pattern Recognition, CVPR 2004, pp. I-74–I-81. IEEE (2004)
52. Felzenszwalb, P.F., Huttenlocher, D.R.: Efficient belief propagation for early vision. In: Proceedings of the 2004 IEEE Computer Society Conference on Computer Vision and Pattern Recognition, CVPR 2004, pp. I-261–I-268. IEEE (2004)
53. Tappen, M.F., Freeman, W.T.: Comparison of graph cuts with belief propagation for stereo, using identical MRF parameters. In: Proceedings of the Ninth IEEE International Conference on Computer Vision, pp. 900–906. IEEE (2003)
54. Morris, J., Jawed, K., Gimel'Farb, G., Khan, T.: Breaking the ‘Ton’: achieving 1% depth accuracy from stereo in real time. In: 24th International Conference on Image and Vision Computing New Zealand, IVCNZ 2009, pp. 142–147. IEEE (2009)
55. Stefano, L.D., Marchionni, M., Mattoccia, S.: A fast area-based stereo matching algorithm. *Image and Vision Computing* 22, 983–1005 (2007)
56. Hirschmuller, H., Scharstein, D.: Evaluation of cost functions for stereo matching. In: IEEE Conference on Computer Vision and Pattern Recognition, CVPR 2007, pp. 1–8. IEEE (2007)
57. Hirschmuller, H., Scharstein, D.: Evaluation of stereo matching costs on images with radiometric differences. *IEEE Transactions on Pattern Analysis and Machine Intelligence* 31, 1582–1599 (2009)
58. Zabih, R., Woodfill, J.: Non-parametric local transforms for computing visual correspondence. In: Eklundh, J.-O. (ed.) ECCV 1994. LNCS, vol. 800, pp. 151–158. Springer, Heidelberg (1994)
59. Gupta, R.K., Cho, S.Y.: Real-time stereo matching using adaptive binary window. In: Proceedings of the 3DPVT (2010)
60. Yoon, K.J., Kweon, I.S.: Adaptive support-weight approach for correspondence search. *IEEE Transactions on Pattern Analysis and Machine Intelligence* 28, 650–656 (2006)
61. Yoon, K.J., Kweon, I.S.: Locally adaptive support-weight approach for visual correspondence search. In: IEEE Computer Society Conference on Computer Vision and Pattern Recognition, CVPR 2005, pp. 924–931. IEEE (2005)

Wheel of B2C E-commerce Development in Saudi Arabia

Rayed AlGhamdi¹, Anne T.A. Nguyen², and Vicki Jones²

¹ Faculty of Computing & IT, King Abdulaziz University

Jeddah, Kingdom of Saudi Arabia

raalghamdi8@kau.edu.sa

² School of ICT, Griffith University

170 Kessels Rd, Nathan, QLD 4111, Australia

{a.nguyen, v.jones}@griffith.edu.au

Abstract. Online retailing (a model of B2C e-commerce) is growing worldwide, with companies in many countries showing increased sales and productivity as a result. It has great potential within the global economy. This paper looks at the current status of online retailing in Saudi Arabia, with particular focus on what inhibits or enables both the customers and retailers. It also analyses the status of Government involvement and proposes a layered model, known as the “Wheel of Online Retailing” which illustrates how Government intervention can benefit the e-commerce in Saudi Arabia.

Keywords: online retail, e-commerce, development, Saudi Arabia.

1 Introduction

Although, the commercial industry is generally considered to be responsible for developing e-commerce within a country, the government should play a significant role in accommodating the e-commerce network particularly in: creating a favourable policy environment for e-commerce; and becoming a leading-edge user of e-commerce and its applications in its operations, and a provider to citizens of e-government services, to encourage its mass use [1].

Government support can take many forms from country to country. However, Government regulation can be critical in supporting e-commerce [2]. Comparing developing countries to developed countries, it is apparent that government incentive is most important in the developing world [2]. The aggressive driver for governments in some countries to take active role supporting e-commerce development is achieving economic success (e.g. Singapore, Taiwan, and Germany). In a rich developing nation like Saudi Arabia this is not such an aggressive motivator so government support is already taking its own unique form (and pace) but can still be guided effectively by the study of these successful cases.

Although Saudi Arabia has a large ICT marketplace, the growth of e-commerce activities is relatively slow [3,4]. The Saudi Government introduced e-commerce in 2001 in response to the fast expansion of e-commerce throughout the world. A permanent technical committee for e-commerce was established by the Saudi

Ministry of Commerce. However, this Committee no longer exists, and from 2006, e-commerce supervision and development has been managed by the Ministry of Communications and Information Technology (MCIT). Unfortunately, there has been little progress since then.

2 E-government in Saudi Arabia

An e-government plan was set up with the following vision “By the end of 2010, everyone in the Kingdom will be able to enjoy from anywhere and at any time – world class government services offered in a seamless user friendly and secure way by utilizing a variety of electronic means” [5]. However, this vision has not been achieved as set up in a timely manner, which means the plan was not realistic [6]. The main problem, which was not taken into consideration, was the ICT infrastructure and assessing the e-readiness of the different government departments [7-11]. As a result, an e-government second action plan with the vision: “Enable use of efficient, integrated customer friendly and secure multiple e-Government services” (covering the period 2012-2016) has been launched; considering human resource training and development, promote cooperation and innovation culture, and maximizing efficiency of e-services provided by government agencies, [12].

E-government and e-commerce share some similarity in terms of transaction requirements. Therefore, development in e-government can serve as an engine to power e-commerce development [13]. The similarity between e-government and e-commerce is that both of them depend on ICT infrastructure, online payment systems and mailing/post systems to reach their users/customers and deliver their services/products [14].

3 Government Role in E-commerce Promotion

Government support takes various forms from country to country; however, government regulation can be critical to supporting e-commerce [2]. Online shopping shows rapid growth in the developed world. Significantly, the South Korean government has played a key role promoting e-commerce. The Malaysian government is encouraging small and medium enterprises (SMEs) to adopt e-commerce solutions, and in Australia, the Government is providing support in various forms [15].

4 Inhibitors and Enablers for the Customers and Retailers

The factors (inhibitors and enablers), which were detailed and discussed in [16-19], can be categorized into seven groups for the purpose of formulating possible explanation. The factors are categorized into the following groups: Cultural Issues (CI), Legislative Infrastructure (LI), Financial Infrastructure (FI), Logistics/Post Infrastructure (PI), ICT Infrastructure (II), Government Support (GS), and Internal Factors (IFs). From discussing the results, it is apparent that there is a distinct lack of government support of online retailing in Saudi Arabia

4.1 Cultural Issues (CI)

Online retailing and e-commerce in general is fairly new in the Saudi environment, and retailers are not selecting to sell online because their customers are not buying online [16,17]. Retailers in Saudi Arabia do not want to invest money opening online stores unless customers demand it. In contrast, a significant number of the customers surveyed say that, the fact that they are not familiar with the online retailers in Saudi Arabia is an inhibitor [18,19]. It looks like we are in vicious circle; customers say that there are not enough retailers online and retailers say there are not enough customers encouraging us to invest in online stores. For this reason, an intermediate third party is needed to facilitate change.

4.2 Legislative Infrastructure (LI)

The empirical evidence of this research continues to raise this problem as a major issue challenging online commerce in Saudi Arabia. Most of the transactions done by online businesses are paperless and signatures are digital. Consumers Protection - Currently, there is a consumer protection body that regulates traditional commerce. However, Saudis are frustrated that this body is not acting as expected and does not cover online commerce [20].

In Saudi Arabia, there is not yet any specific legislation related to e-commerce [21]. Both retailers and customers emphasized that the lack of clear regulations and legislation and the need for government supervision and support as being a significant inhibitor to their adoption of e-commerce.

4.3 Financial Infrastructure (FI)

In Saudi Arabia, many consumers are reluctant to use credit cards, both because of a lack of trust and because some consumers are culturally averse to carrying out transactions linked with conventional interest rates [22]. Therefore, it is apparent that provision of an alternative, trustworthy, and easy-to-use payment system has the potential to significantly influence the successful adoption of e-retailing in the KSA [21]. Some local banks in KSA, have started making normal ATM cards that are to be used as debit cards. Other possible solutions include the use of trusted third party payment systems, such as Paypal, which act as link between the credit card holders and the sellers.

Another option is the electronic bill presentment and payment system called SADAD that Saudi Arabia developed for billers and payers who are residents of the country. In essence, SADAD facilitates data exchange between registered billers and the nation's commercial banks. It relies on existing banking channels (such as Internet banking, telephone banking, ATM transactions and even counter transactions) to allow bill payers to view and pay their bills via their banks (for more details, see [22]). Currently, SADAD is limited to 100 billers only. This means that only the biggest billers in Saudi Arabia have access to this system.

4.4 Logistics/Post Infrastructure (PI)

Effective logistics infrastructure is a key for e-commerce. In Saudi Arabia the lack of housing mailboxes is an inhibitor to online retailing in Saudi Arabia. A program to accelerate allocation of house addresses and citizen adoption of mail boxes will have a positive effect on the adoption of e-commerce by providing the necessary infrastructure to support secure goods delivery to homes.

Unlike most developed nations, until 2005 nobody in Saudi Arabia had a house address to which deliveries could be made. Individuals had to subscribe to have a mailbox in the town's central post offices. In 2005, the new project for addressing and delivering mails to homes and buildings was announced and approved by the Saudi Post [3,23].

4.5 ICT Infrastructure (II)

The widespread availability of the Internet, especially broadband services, is an important indicator for strong ICT infrastructure [24]. Internet users in Saudi Arabia increased from one million (5% of the population) in 2001 to an estimated 13 million (46%) at the end of the third quarter of 2011 [25], while mobile broadband subscriptions reached 11.5 million, representing a penetration of 40.5% of the population, and the fixed broadband penetration rate stood at 30.6% of households for the same period [25]. However, most of the services provided by these companies were predominately from the main cities. Most small towns and villages are still not well served by Internet connections or have no Internet connections at all [20]. Internet connection fees in Saudi Arabia are considered high compared to the leading developing countries and developed countries [3]. Prices need to be reviewed to make it attractive for most of the households to connect to the Internet [20].

4.6 Government Intervention (GI)

The empirical evidence of this research suggests that the government interventions and support for e-commerce is very important factor in terms of flourishing e-commerce in Saudi Arabia [26]. The Saudi government does not give enough attention to e-commerce environment development [27].

While it is generally agreed that the commercial industry has to take the main responsibilities in developing e-commerce within a country, the government plays a significant role in promoting e-commerce particularly in (1) creating a favorable policy environment for e-commerce; and (2) becoming a leading-edge user of e-commerce and its applications in its operations, and a provider to citizens of e-government services, to encourage its mass use [1,28].

The empirical evidence of this research suggests that the government interventions and support for e-commerce is very important factor in terms of flourishing e-commerce in Saudi Arabia. It is ranked the second highest enabler for both customers and retailers.

The Saudi government does not give enough attention to e-commerce environment development. E-commerce requires an appropriate environment of

legislative, financial, communicational, technological, and delivery infrastructures and building awareness among other issues [20].

The Saudi government has put its efforts towards e-government development [29]. E-government working plans and projects have been implemented to reach the vision “Enable use of efficient, integrated customer friendly and secure multiple e-Government services” by 2016 [20,21]. Surely, e-government and e-commerce share some similarity and well development in e-government can service as an engine to power e-commerce development as well [13]. However, e-commerce has different features which need to be considered

4.7 Internal Factors (IFs)

All the previously discussed issues: cultural issues, legislative infrastructure, financial infrastructure, logistics infrastructure, ICT infrastructure, and government support, seem external to the primary stakeholders, which require third parties: e.g. change agents, as Rogers [30] suggests, to take action. The factors discussed in this section are internal or related to individuals and organizations that make decisions to adopt change internally. The internal factors include: the lack of experiences for customers to purchase online and retailers to deal with e-commerce, customers looking for competitive prices, retailers’ products are not suitable to be sold online, retailers’ resistance to change, retailers distrust of e-commerce, e-commerce setup costs, perceived lack of profitability, and the difficulty for retailers to compete online.

5 A Way Forward: Towards Online Retailing Diffusion in KSA

The way toward online retailing diffusion in Saudi Arabia requires developing a strategic plan. The strategic planning for online retailing diffusion in Saudi Arabia is based on the results of this research.

- Very few retailers adopt e-commerce in Saudi Arabia
- Habit of Saudis in terms of buying online is the most influencing factor inhibiting retailers in Saudi Arabia to adopt e-commerce
- Lack of e-commerce experiences play significant role for both retailers and consumers to sell and purchase online
- There is not yet any specific legislation and regulations related to e-commerce in Saudi Arabia
- There is no government agency/body is clearly responsible for e-commerce in Saudi Arabia
- There is a need to develop trustworthy and secure online payment systems

A model called “*wheel of online retailing development in KSA*” is suggested in order to address the issues raised in this research and contribute to the development of online retailing, and e-commerce diffusion in Saudi Arabia.

The enhancement and development of these four areas (e-commerce legal framework, ICT infrastructure, logistic/post infrastructure, and financial

infrastructure) would enable the online environment and making it attractive for online businesses.

As Figure 1 illustrates, Government Support (GS) is placed in the external layer; legal framework, financial infrastructure, post infrastructure and ICT infrastructure are placed in the middle layer; cultural issues are placed in the second middle layer; and internal factors are placed in the central layer. The IFs are placed in the central layer because they are involved with the participants (i.e. customers and retailers) which means an individual (person/ organization) has to take the decision to change internally. However, the progress of the IFs is limited to the progress/ development/ maturity/ change in the surrounding layers (Cultural Issues (CI), Legislative Infrastructure (LI), Financial Infrastructure (FI), Logistics/Post Infrastructure (PI), and ICT Infrastructure (II)). Similarly, the progress/ development/ maturity/ change in CI, LI, FI, PI, and II are limited to the progress of government (the external layer).



Fig. 1. Wheel of online retailing development in KSA

In the light of the above findings, what actions could the government take to facilitate further development of online retailing in Saudi Arabia? There is little doubt that the clarification and enhancement of legislation and regulation in this area would be an appropriate priority for the government, as such matters are clearly part of its responsibilities. Similarly, further development of the IT infrastructure and domestic IT capabilities would benefit not only the e-retail industry but also the whole economy and the wider society. The government may also wish to facilitate or assist the development and growth of online payment systems (like SADAD) that would benefit consumers, businesses and the economy generally. A program to accelerate allocation of house addresses and citizen adoption of mail boxes and providing the necessary infrastructure to support secure goods delivery to homes is an urgent requirement not only for e-commerce but also to support all other e-services. The enhancement and development of these four areas (e-commerce legal framework,

ICT infrastructure, logistic/ post infrastructure, and financial infrastructure) would enable the online environment and making it attractive for online businesses. There is no point to look at what inhibit consumers and businesses from purchasing or selling online while the environment is not ready to support this type of business. For this reason, a government body should be allocated for e-commerce development in Saudi Arabia. This government body then should work with the chambers of commerce and private sectors to sponsor solutions of e-commerce.

The second stage is to work on the cultural issues by meeting the concerns and contributes to resolve them. For example, lack of trust due to security and privacy would be change with the presence of customer protection law, old buying habit which dies hard and inhibit the growth of online shopping habit can be in somehow overcome by increasing the awareness and providing e-commerce educational programs. Even with the lack of products' physical inspection which is the most inhibiting factors for online shopping by consumers, leading retailers, good reputation vendors, brand name products would not encounter problems in this regard when they sell online. The empirical evidence shows that more than half of the consumers would buy online from leading/ good reputations/ brand names retailers. This indicates the opportunity of success for leading retailers, good reputation and strong brand name/familiar products firms entering online sales environment. Therefore, focusing on those retailers and encouraging them to adopt e-commerce would create an active online environment in Saudi Arabia for consumers making them more likely to be accepted to purchase online from them and motivate other retailer to enter online environment as this will create competitive pressure in the online environment.

References

1. Scupola, A.: Government Intervention in SMEs' E-Commerce Adoption. In: Khosrow-Pour, M. (ed.) *Encyclopaedia of Information Science and Technology*, 2nd edn., pp. 1689–1695. IGI Global (2009)
2. Kraemer, K., Dedrick, J., Melville, N., Zhu, K.: *Global e-commerce: impacts of national environment and policy*. Cambridge Univ. Press, New York (2006)
3. Alfuraih, S.: E-commerce and E-commerce Fraud in Saudi Arabia: A Case Study. In: 2nd International Conference on Information Security and Assurance Busan, Korea, pp. 176–180 (2008)
4. CITC, IT Report 2010 On the Internet Ecosystem in Saudi Arabia, Communications and Information Technology Commission, Riyadh (2010)
5. AL-Shehry, A.M.: Transformation towards E-government in The Kingdom of Saudi Arabia: Technological and Organisational Perspectives. In: The School of Computing, CCSR, De Montfort University (2008)
6. Alfarraj, O., Nielsen, S., Vlacic, L.: eGovernment initiatives and key factors causing the delay of their implementation in Saudi Arabia. In: 5th Conference on Qualitative Research in IT, Brisbane, Australia, pp. 130–141 (2010)
7. Alfarraj, O., Drew, S., AlGhamdi, R.: EGovernment Stage Model: Evaluating the Rate of Web Development Progress of Government Websites in Saudi Arabia. *International Journal of Advances Computer Science and Applications* 2(9), 82–90 (2011)

8. Abu Nadi, I.: Success Factors for eGovernment Adoption: Citizen Centric Approach. LAP LAMBERT Academic Publishing Gold Coast, Australia (2010)
9. Abu Nadi, I., Sanzogni, L., Sandhu, K.S., Woods, P.R.: Success Factors Contributing to eGovernment Adoption in Saudi Arabia: G2C approach. In: Saudi International Innovation Conference SiiC 2008 Proceeding, Leeds, UK, pp. 1–8 (2008)
10. Alshehri, M., Drew, S., Alfarraj, O.: A Comprehensive Analysis of E-government services adoption in Saudi Arabia: Obstacles and Challenges. International Journal of Advanced Computer Science and Applications (IJACSA) 3(2), 1–6 (2012)
11. Alshehri, M., Drew, S., Alhussain, T., Alghamdi, R.: The Effects of Website Quality on Adoption of E-Government Service: AnEmpirical Study Applying UTAUT Model Using SEM. In: Lamp, J. (ed.) 23rd Australasian Conference On Information Systems (ACIS 2012), Melbourne, Australia, pp. 1–13 (2012)
12. Yasser eGov Program. The e-Government Second Action Plan (2012-2016) (2012), http://www.yesser.gov.sa/en/MechanismsandRegulations/strategy/Pages/-second_Implementation_plan.aspx (cited March 7, 2012)
13. Blakeley, C., Matsuura, J.: E-government: An engine to power e-commerce development. In: Proceedings of the European Conference on e- Government, Dublin, Ireland, pp. 39–48 (2001)
14. AL-Shehry, A., Rogerson, S., Fairweather, N., Prior, M.: The Motivations for Change Towards E-Government Adoption: Case Studies from Saudi Arabia. In: eGovernment Workshop, London, UK, vol. 6, pp. 5–11 (2006)
15. DBCDE (Australian Department of Broadband Communication and the Digital Economy), Background to the online retail forum, Department of Broadband, Communication and the Digital Economy (2011), http://www.dbcde.gov.au/digital_economy/online_retail_forum/background_to_the_online_retail_forum (viewed May 14, 2011)
16. AlGhamdi, R., Drew, S., Al-Ghaith, W.: Factors Influencing Retailers in Saudi Arabia to Adoption of Online Sales Systems: a qualitative analysis. Electronic Journal of Information System in Developing Countries (EJISDC) 47(7), 1–23 (2011)
17. AlGhamdi, R., Nguyen, J., Nguyen, A., Drew, S.: Factors Influencing E-Commerce Adoption by Retailers in Saudi Arabia: A Quantitative Analysis. International Journal of Electronic Commerce Studies (IJECS) 3(1), 85–100 (2012)
18. AlGhamdi, R., Drew, S., Alfarraj, O.: Issues Influencing Saudi Customers' Decisions to Purchase from Online Retailers in the KSA: A Qualitative Analysis. European Journal of Scientific Research 55(4), 580–593 (2011)
19. AlGhamdi, R., Nguyen, A., Nguyen, J., Drew, S.: Factors Influencing Saudi Customers' Decisions to Purchase from Online Retailers in Saudi Arabia: A Quantitative Analysis. In: IADIS International Conference e-Commerce 2011, Roma, Italy, pp. 153–161 (2011)
20. Aleid, F., Rogerson, S., Fairweather, B.: A consumers' perspective on E-commerce: practical solutions to encourage consumers' adoption of e- commerce in developing countries - A Saudi Arabian empirical study. In: International Conference on Advanced Management Science, Chengdu, China, vol. 2, pp. 373–377 (2010)
21. Alwahaishi, S., Nehari-Talet, A., Snasel, V.: Electronic commerce growth in developing countries: Barriers and challenges. In: First International Conference on Networked Digital Technologies, Ostrava, Czech Republic, pp. 225–232 (2009)
22. SADAD, About SADAD Payment System (2004), <http://www.sadad.com/English/SADAD+SERVICES/AboutSADAD> (viewed October 10, 2010)

23. Saudi Post, Saudi Post: Establishment and Development, Saudi Post (2008), <http://www.sp.com.sa/Arabic/SaudiPost/aboutus/Pages/establishmentanddevelopment.aspx> (viewed November 21, 2009)
24. Sleem, A.: E-Commerce Infrastructure in Developing Countries. In: Kamel, S. (ed.) Electronic Business in Developing Countries: Opportunities and Challenges, pp. 349–385. Idea Group Inc., USA (2006)
25. MCIT (Saudi Ministry of Communication and Information Technology). ICT indicators in K.S.A, H1-2011 (2011), <http://www.mcit.gov.sa/english/Development/SectorIndices/> (cited December 11, 2011)
26. AlGhamdi, R., Drew, S., Alshehri, M.: Strategic Government Initiatives to Promote Diffusion of Online Retailing in Saudi Arabia. In: Pichappan, P. (ed.) Sixth International Conference on Digital Information Management, Melbourne, Australia, pp. 217–222 (2011)
27. AlGhamdi, R., Drew, S., Abugabah, A.: Designing Government Strategies to Facilitate Diffusion of Online Commerce: A focus on KSA. Journal of Information & System Management 1(3), 97–106 (2011)
28. Padmannavar, S.: A Review on E-Commerce Empowering Women's. International Journal of Computer Science and Telecommunications 2(8), 74–78 (2011)
29. Alkhalaif, S., Drew, S., Alghamdi, R., Alfarraj, O.: E-Learning System on Higher Education Institutions in KSA: Attitudes and Perceptions of Faculty Members. Procedia-Social and Behavioral Sciences 47, 1199–1205 (2012)
30. Rogers, E.M.: Diffusion of Innovations, 5th edn. Simon & Schuster, New York (2003)

Author Index

- Abbass, Hussein A. 179, 653, 671
Abdullah, Azizi 33, 611
Abdullah, Siti Norul Huda Sheikh 33, 611
Ahlgren, David 763
AlGhamdi, Rayed 1047
Alkhalfaf, Salem 787
Al-Wahedi, Khaled 415
Amandine, Charmasson 301
An, Sung-Tae 599
Ax, Markus 525
Bailey, Donald G 1003
Barczak, A.L.C. 713
Bautista-Hernández, Antonio 505
Boguslavsky, A.A. 463
Bui, Vinh 653
Burca, Vlad 763
Chen, Li-Ping 793
Choi, Han-Lim 599
Choi, Sang Kyu 941
Choi, Seung-Hwan 65
Choi, Taeyong 911
Chung, C.J. 623
Chung, Jae H. 571
Chung, Timothy H. 561
Confreras, Miguel 1003
Cuong, Trinh Duc 951, 961, 993
Cuperman, Amit 763
Cuperman, Dan 763
Darwish, Aya 415
DeWees, Max 873
Do, Hyunmin 911, 921
Drew, Steve 787
Enoki, Shuji 55
Eqlouss, Enas A.A. 33
Erickson, Danielle 873
Figueiredo, Karla T. 187
Gallagher, John C. 855
Gamer, Sergei 745
Golden, Lisa J. 283
Golden, Zachary T. 283
González, María Laura 327
Gupta, Gourab Sen 1003
Habib, Maki K. 753
Hajduk, Mikulas 631
Hamada, Nozomu 453
Han, Jianda 537
Han, Ji-Hyeong 127, 549
Han, Seung-Beom 23, 263
Hartono, Pitoyo 733
Hashimoto, Hideki 91, 493
Hashimoto, Takuya 775
Hempelmann, Christian F. 883
Hexmoor, Henry 863
Hong, Young-Dae 209
Hoshino, Koshi 105
Ierache, Jorge Salvador 327, 337
Iizuka, Kojiro 169, 641
Irribaren, Juan 337
Ishigami, Genya 405
Jayasekara, Peshala G. 493
Jeong, In-Bae 273

- Jeong, Seungho 971
 Jiang, Qian-li 1035
 Jo, Jun 85
 Jo, Sungho 241, 441
 Jones, Vicki 787, 1047
 Jong-Hwan, Kim 301
 Joo, Sihyun 241
 Ju, Jeongwoo 1015
 Jun, Jungsoo 931
 Jung, Chang-Young 383
 Jung, Heechul 1015
 Jung, Il-Kyun 375
 Jung, Jongdae 5
 Jung, Philhwan 431
 Jung, Seul 971
- Kalashankar, B.A. 45
 Kamkarian, Pejman 863
 Kang, Sandeul 1023
 Kaoru, Sakakibara 753
 Kapolka, Marek 561
 Kawatsu, Christopher 623
 Kim, Christopher 571
 Kim, Deok-Hwa 423
 Kim, Dong Han 845
 Kim, Dong Hoe 845
 Kim, Donghoon 395
 Kim, Dong Hwa 691
 Kim, Gon-Woo 255
 Kim, Hanguen 147
 Kim, Hyongjin 395, 485
 Kim, Hyun-Sik 809
 Kim, Jiwhan 1023
 Kim, Jong-Hwan 23, 65, 75, 127, 137, 209,
 223, 263, 273, 315, 383, 423, 477, 549,
 589, 663, 683, 983
 Kim, Jung-Hoon 375
 Kim, Junmo 1015, 1023
 Kim, Jun-Yeup 231
 Kim, Minho 241
 Kim, Sung-Hoon 599
 Kim, Yong-Tae 823
 Kim-Tien, Nguyen 961
 Ko, Kwang-Eun 115, 231
 Ko, Woo-Ri 65, 75
 Kobayashi, Hiroshi 775
 Kodiah, Basma 415
 Komatsu, Hirofumi 169
 Kubota, Takashi 91, 169, 199, 405, 493,
 641
- Kuhnert, Klaus-Dieter 525
 Kuhnert, Lars 525
 Kunii, Yasuharu 105
 Kyung, Jin Ho 911, 921
- Langerwisch, Marco 525
 Lee, Bum-Joo 359
 Lee, Donghwa 395, 485
 Lee, Dong-Hyun 549
 Lee, Hansang 1023
 Lee, Honggu 441
 Lee, Hyoung-Ki 5
 Lee, Jung-Woo 293
 Lee, Keonhong 441
 Lee, Ki-Baek 683
 Lee, Sang Yup 845
 Lee, Seon-Woo 431
 Lee, Seunghwi 911
 Lee, Seung-Jae 477
 Lee, Seung-Mok 395, 517
 Lee, Sung G. 315
 Lee, Yong-Jun 835
 Le Hung, Phan 993
 Lewis, John 873
 Li, Jiaxing 623
 Li, Ming 537
 Li, Xiu-Fang 793
 Lim, Jong-Tae 293
 Lim, Sun 375
 Liu, Chuan-Jun 793
 Lokan, Chris 671
 Lorencik, Daniel 703
- Matson, Eric T. 283, 873
 McAtee, James Michael 283
 Meng, Lijun 537
 Miao, Yu 537
 Min, Byung-Cheol 845
 Min, Jeongtack 931
 Myung, Hyun 5, 147, 395, 485, 517
- Nagata, Fusaomi 753
 Nakane, Yuto 641
 Nakazawa, Kazuo 453
 Nguyen, Anne T.A. 787, 801, 1047
 Niitsuma, Mihoko 91
 Noh, Su-Hee 823
- Ok, Jung Seul 315
 Otsu, Kyohei 405

- Otsuka, Akimasa 753
 Otsuki, Masatsugu 405
- Pala, M. 723
 Park, Byeolteo 147
 Park, Chang-Soo 223
 Park, Chanhun 911, 921
 Park, Cheol Hoon 941
 Park, Chung-Woon 293
 Park, Dongil 911
 Park, Kyoungtaik 921
 Park, Seung-Min 115, 231
 Park, Sungho 931
 Park, Yongsik 931
 Pereira, Gustavo 337
 Petkovsek, Steve 763
 Petraki, Eleni 653
 Petrenko, Max 883
 Poudel, Binay 763
 Prasad, N.N.S.S.R.K. 45
- Qi, Juntong 537
- Ramos-Quintana, Fernando 505
 Raskin, Victor 893
 Remmersmann, Thomas 525
 Reyes, Napoleon H. 713
 Ryoo, Young-Jae 835
 Ryu, Si-Jung 663
- Samusudin, Mohamad Faizal bin 13
 Santoso, Junius 763
 Sattolo, Iris 337
 Sawatsubashi, Yoshito 13
 Sekikawa, Masashi 453
 Seo, Kap-Ho 931
 Shafi, Kamran 179, 671
 Shibata, Katsunari 13, 55
 Shimizu, Taku 199
 Shin, Chang-Seop 255
 Shin, Jae-uk 395
 Shtub, Avraham 745
 Sim*, Kwee-Bo 115
 Sim, Kwee-Bo 231
 Sincak, Peter 347, 691, 723
 Smolar, P. 723
 Sokolov, S.M. 463
 Son, Hyoung Il 91
 Song, Da-Lei 537, 793, 1035
- Song, Seong-Ho 431
 Song, Young Eun 91
 Stevens, Ann 85
 Su, Daobilige 453
 Suiffet, Nicolás 337
 Sukop, Marek 631
 Sun, Wei-cheng 1035
 Susnjak, T. 713
 Suzuki, Satoshi 155
- Tan, Clarence 85
 Taylor, Julia M. 901
 Tehrani, Kambiz Arab 301
 Thamke, Stefan 525
 Thinh, Nguyen Truong 993
 Tho, Tuong Phuoc 951
 Tran, Vinh Xuan 801
 Trifonov, O.V. 463
 Truong, Ninh-Thuan 801
 Truong-Thinh, Nguyen 951, 961
- Valencia, Cesar H. 187
 Vanny, Makara 115
 Vascaik, Jan 703
 Vasilyev, A.I. 463
 Vellasco, Marley M.B.R. 187
 Verner, Igor M. 745, 763, 775
 Vircik, M. 723
 Vircikova, Maria 347, 691, 703
- Wang, Kun 653
 Wang, Shir Li 671
 Wang, Ziming 537
 Watanabe, Keigo 753
 Woo, Seung Je 315
 Wu, Bing-Wei 793
- Yang, Ji Hyun 561
 Yao, Le-le 1035
 Yoo, Bum-Soo 137
 Yoo, Jeong-Ki 23, 263
 Yoo, Yong-Ho 983
 Yoon, Jae Seok 845
 Yun, Sungjo 931
- Zaheer, Sheir Afgen 589
 Zhang, Bin 179
 Zhao, Shuaike 537
 Zin, Nur Ariffin Mohd 611